NATURE INDEX
Science cities

nature

THE INTERNATIONAL WEEKLY JOURNAL OF SCIENCE

DIVERSITY UNMASKED

Cellular atlas offers insights into neuronal structure and function in the cortex

PAGES 38, 72 & 79

QUANTUM PHYSICS

MECHANICAL POWER

Measurement-based quantum control of motion

PAGES 39 & 53

ARTIFICIAL INTELLIGENCE

ACCIDENTS WILL HAPPEN

The moral dilemma presented by self-driving cars

PAGE 59

MEDICAL RESEARCH

WALKING AGAIN

Spinal-cord stimulation reverses effects of paralysis

PAGE 65

NATURE.COM
1 November 2018
Vol. 563, No. 7729

THIS WEEK

EDITORIALS

PARALYSIS Spinal-cord treatment can restore leg function **p.6**

WORLD VIEW The practical problems of the need for visas **p.7**

VIKINGS Early tar production protected ships and sails **p.9**

Anatomy does not define gender

Proposals in the United States to classify people on the basis of anatomy or genetics have no scientific basis and should be scrapped.

According to a draft memo leaked to *The New York Times*, the US Department of Health and Human Services (HHS) proposes to establish a legal definition of whether someone is male or female based solely and immutably on the genitals they are born with. Genetic testing, it says, could be used to resolve any ambiguity about external appearance. The move would make it easier for institutions receiving federal funds, such as universities and health programmes, to discriminate against people on the basis of their gender identity.

The memo claims that processes for deciding the sex on a birth certificate will be "clear, grounded in science, objective and administrable".

The proposal — on which HHS officials have refused to comment — is a terrible idea that should be killed off. It has no foundation in science and would undo decades of progress on understanding sex — a classification based on internal and external bodily characteristics — and gender, a social construct related to biological differences but also rooted in culture, societal norms and individual behaviour. Worse, it would undermine efforts to reduce discrimination against transgender people and those who do not fall into the binary categories of male or female.

Furthermore, biology is not as straightforward as the proposal suggests. By some estimates, as many as one in 100 people have differences or disorders of sex development, such as hormonal conditions, genetic changes or anatomical ambiguities, some of which mean that their genitalia cannot clearly be classified as male or female. For most of the twentieth century, doctors would often surgically alter an infant's ambiguous genitals to match whichever sex was easier, and expect the child to adapt. Frequently, they were wrong. A 2004 study tracked 14 genetically male children given female genitalia; 8 ended up identifying as male, and the surgical intervention caused them great distress (W. G. Reiner and J. P. Gearhart *N. Engl. J. Med.* **350**, 333–341; 2004).

Even more scientifically complex is a mismatch between gender and the sex on a person's birth certificate. Some evidence suggests that transgender identity has genetic or hormonal roots, but its exact biological correlates are unclear. Whatever the cause, organizations such as the American Academy of Pediatrics advise physicians to treat people according to their preferred gender, regardless of appearance or genetics.

The research and medical community now sees sex as more complex than male and female, and gender as a spectrum that includes transgender people and those who identify as neither male nor female. The US administration's proposal would ignore that expert consensus.

The idea that science can make definitive conclusions about a person's sex or gender is fundamentally flawed. Just ask sports organizations such as the International Olympic Committee (IOC), which have struggled with this for decades. In the 1960s, concerned that men would compete in women's events, officials tried classifying athletes through genital exams — an intrusive and humiliating process. DNA tests that check for the presence of a Y chromosome did not prove reliable, either: people with XY chromosomes can have female characteristics owing to conditions including an inability to respond to testosterone.

Nowadays, the IOC classifies athletes by measuring their testosterone levels, but this, too, is flawed. Certain medical conditions can raise women's testosterone levels to the typical male range, and the tests leave them unable to compete among women.

If the Trump administration does attempt to impose genetic testing, it will have many surprises. For instance, genetic recombination can transfer Y chromosome genes to X chromosomes, resulting in people with XX chromosomes who have male characteristics.

"Attempts to pigeonhole people have nothing to do with science and everything to do with stripping away rights."

Political attempts to pigeonhole people have nothing to do with science and everything to do with stripping away rights and recognition from those whose identity does not correspond with outdated ideas of sex and gender. It is an easy way for the Trump administration to rally its supporters, many of whom oppose equality for people from sexual and gender minorities. It is unsurprising that it appeared just weeks before the midterm elections.

This is not the first time that the administration has attacked legal protections for transgender and non-binary people. Last year, Trump declared that transgender people would no longer be allowed to serve in the US military, and rescinded guidelines suggesting that schools should let pupils use the lavatory of their choice. An October 2017 memo from the US Department of Justice stated that laws prohibiting employment discrimination should not apply to gender identity.

Instituting a policy with a narrow definition of sex or gender and no basis in science would be a major step backwards for the United States in gender-identity issues. Sadly, the move is only the latest in a series of proposals that misuse and ignore science and harm marginalized groups as part of a quest to score cheap political points. ■

False promises

Brazil's new president is a threat to global science.

A decade ago, under the leadership of Luiz Inácio 'Lula' da Silva, Brazil seemed like a tropical juggernaut that could play a leading part in the fight against climate change. The economy was booming, helping Lula's government to lift millions out of poverty. Beer and soya-bean production was steadily increasing, even as deforestation — one of Brazil's largest sources of carbon emissions — in the Amazon plummeted. Today, Lula is in jail on corruption charges, the economy is a shambles, violence is on the increase and deforestation is back on the rise. And now Brazil has elected as president Jair Bolsonaro, a right-wing demagogue with an anti-environmental agenda.

© 2018 Springer Nature Limited. All rights reserved.

Scientists, academics and environmentalists in Brazil have been raising the alarm about Bolsonaro's environmental policies — as well as his anti-democratic leanings — for months. But his vitriol and fiery rhetoric carried the day. Bolsonaro captured 55% of the vote in the second round of the election on 28 October against Fernando Haddad, former mayor of São Paulo and political scientist who became the Workers' Party candidate only after the jailed — but still popular — Lula was barred from running. There are many reasons to worry — for people both inside and outside the country.

A former army captain and long-time legislator from Rio de Janeiro, Bolsonaro has earned his 'Tropical Trump' moniker by denigrating women and minority groups, threatening to take land away from Indigenous communities and declaring he would prefer his son to be dead rather than gay. His solution to the epidemic of violence is to put guns in the hands of citizens — and make it easier for police to use lethal force. He speaks fondly about the military dictatorship that ran Brazil from 1964 to 1985, and his vice-president, Hamilton Mourão, a former army general, has openly discussed the possibility of military intervention to quell the political chaos that has reigned during the past few years. His election is another blow for those who value free thinking and free expression.

Bolsonaro's position on science and the environment is just as worrying. He promotes development at all costs and has at times threatened to follow US President Donald Trump and pull Brazil out of the 2015 Paris climate accord (although two days before the election, Bolsonaro said Brazil would stay in). He has promised to merge the environment ministry — the function of which includes the protection of the Amazon rainforest — with the agriculture ministry. Regardless of whether he can get such changes through the Brazilian Congress, his election sends the wrong signals to landowners and businesses who hold considerable sway over the future of the largest tropical rainforest on the planet — and the carbon that it contains. Globally, deforestation produces around 10% of greenhouse-gas emissions.

The tale of Bolsonaro's rise to power is by now sadly familiar. He unleashed incendiary anti-establishment rhetoric that spread like wildfire on social media and found fertile ground with a legitimately angry populace. Brazil is still recovering from a crippling two-year recession that began in 2014, and the country is reeling from ongoing investigations into political corruption. The Brazilian public's desire for change is entirely justified, but Bolsonaro is no saviour. He represents the biggest test yet for Brazil's young democracy, and academics will soon find themselves on the front line fighting for evidence-based policies. They have allies. His environmental agenda will face intense domestic and international opposition — including from many powerful beef and soya-bean exporters that do not want to deal with the stigma of deforestation. Scientists everywhere should add their voices to the protests.

"The tale of Bolsonaro's rise to power is by now sadly familiar."

On the same day that Bolsonaro announced his reversal on the Paris accord, Brazilian media reported that police and election authorities had conducted raids on at least 17 universities, questioning students and academics about illegal election activities — the law prohibits electoral publicity in public spaces. The authorities apparently seized protest materials, including pro-democracy and anti-fascist banners and flyers.

Brazil's budgetary woes have meant that researchers have struggled for years to fulfil the nation's potential to be a scientific giant; the federal science ministry's budget is now roughly one-third of its 2010 level, and further cuts are expected next year. Luiz Davidovich, a theoretical physicist and president of the Brazilian Academy of Sciences, has said that conducting research in Brazil is "an act of resistance". That resistance will be even more crucial when Bolsonaro takes the helm. ■

First steps

People paralysed by spinal injuries are being helped to walk again.

Not so long ago, the hope that someone paralysed for years by a severe spinal-cord injury would ever be able to walk again was just that — hope. But recent advances are bringing those hopes closer to reality.

In this week's *Nature* (page 65), researchers describe a treatment — a combination of electrical stimulation of the spinal cord and physical therapy — that has enabled three men with spinal-cord injury to walk (F. B. Wagner *et al. Nature* **563**, 65–71; 2018). And this is not just in controlled laboratory conditions: they have been able to take walks outside again.

It's an extraordinary development that could have implications for hundreds of thousands of people around the world. And it's also the result of decades of cross-disciplinary research that has steadily built an evidence base in animal experiments — with the scientists involved sometimes facing criticism for doing them — and taken that work carefully into the clinic.

Researchers have long pursued diverse strategies to repair and reactivate the spinal cord after injury. Many approaches are remarkably effective in regenerating and achieving functional recovery in mice and other animals, but fail to translate to human therapies. The advance in the current study was that, rather than delivering a constant electric current — as had been tried before — the researchers applied patterns of stimulation calculated to activate the correct groups of leg muscles at the correct time during stepping. In this way, specific locations in the spinal cord could be targeted, to activate the muscles in a coordinated fashion. This patterned stimulation protocol not only allowed the unprecedented restoration of walking ability, but also enabled the individuals to regain control over previously paralysed muscles when electrical stimulation was turned off. This indicates that the brain and spinal cord had re-established functional connections, revealing an unexpected degree of plasticity.

In light of such progress, the prognosis for what was long considered an irreversible condition seems a lot brighter. But there is much more work to do. Spinal injuries vary enormously in their location, severity and outcome, and it will take many more studies to understand who will benefit from this technology. The current research is a proof of concept in a small number of participants who had a range of residual leg function at the start of the study. A major challenge is to understand what determines successful recovery. For example, one source of variability might be how much sensory information the damaged spinal cord can still transmit to the brain.

In a related study published this week in *Nature Neuroscience*, the same team shows that continuous stimulation (which is enough to restore locomotion in rodents) is less effective in humans because it interferes with the transmission to the brain of sensory feedback about an individual's own movements and body position (E. Formento *et al. Nature Neurosci.* https://doi.org/10.1038/s41593-018-0262-6; 2018). This is another reason why temporally patterned stimulation could be more effective, and might have been one key to success for the three participants in the *Nature* study. However, different stimulation methods might turn out to be more or less useful for different individuals.

It's also important to temper this exciting success story with caution about access. According to the World Health Organization, between 250,000 and 500,000 people around the globe are affected by a spinal-cord injury each year — most caused by road accidents, falls or violence. Spinal stimulation is a complex and expensive medical procedure, and recovery also seems to require intensive rehabilitation. It will not be available to all — at least, any time soon. But it is a first step. ■

© 2018 Springer Nature Limited. All rights reserved.

JOSUA PIORR

Tear down visa barriers that block scholarship

If we want a diverse, equitable and inclusive research community, academics from the global south must be able to meet freely, says **Connie Nshemereirwe**.

These days, I feel as though I live my life from one visa application to another. Last week, I was supposed to travel from Uganda to Panama. This was for my role as co-chair of the Global Young Academy (GYA), an organization focused on science education and policy that advocates for early-career researchers around the world. Instead, I'm stuck at home working on a long-overdue proposal for a research project on science leadership in Africa while filling in forms for the next trip, hoping for better luck.

On 25 July, I contacted the closest Panama embassy (in South Africa), and learnt that I had to submit my visa application in person; that every page of my passport had to be photocopied and notarized; that anything scratched out on a form would invalidate my entire application; and that all my documents had to be translated into Spanish — including bank statements, the air ticket, the hotel booking and all invitation letters — by a certified translator (now, how was I going to find such a person in Uganda? Or pay them?).

My hosts in Panama were able to work with immigration authorities so that I could send paperwork by a document-delivery service instead of taking a US$500, 4-hour flight to Pretoria, but hiccups such as delayed hotel reservations and having the wrong format for dates in translated documents meant that paperwork had to be resubmitted several times, and there was not enough time to process the visa. These requirements feel so arbitrary; had it not been so last minute, my co-chair, a British national, could have attended without needing a visa. (Nor did Panama require visas for attendees from countries including Malaysia, Poland or the United States, although my Polish colleague had to pay more than $160 and go through an interview to transit through a US airport.)

Visa problems present an obstacle for many researchers in the global south to participate in the broader scientific community. Earlier this year, a poll by the RAND Corporation found that African and Asian researchers are, respectively, three to four times as likely as European or North American ones to report visa-related obstacles for work travel (see go.nature.com/2z9dabn). With the US ban on travel for citizens of some countries, and Brexit in the United Kingdom, things will only get worse.

My Panama experience is extreme, but not atypical. When I worked at a rural university, 100 kilometres from the nearest city, applying for a visa often wiped out at least 2 workdays: 1 day to gather all the documents required and to submit the package, and another day to go pick up the visa. That doesn't count time needed to work out what each country requires, pick up certified bank statements, take the precise photographs required and coordinate proof of employment and invitation letters.

Even when other expenses are covered, researchers (or their institutions) are expected to meet visa costs. These costs are punishing in light of the average Ugandan academic's salary. My top take-home pay as a senior lecturer with a PhD from Twente University in the Netherlands, after 15 years in academia, was about 60,000 Ugandan shillings (US$16) a day. For me, a South African visa costs $36, plus $90 as a 'processing' fee; the UK visa costs $120 and takes 3 weeks. I paid about $100, plus bank-transfer charges, for the attempted trip to Panama. The Schengen (European Commission) visa is among the most forgiving: just under $70, with a 1-week wait.

I was elected as co-chair in May, and have had to travel to seven countries — four to represent the GYA — between September and November. If all goes to plan, I will be in Japan when this column appears, a trip that required me to find a Japanese national, who could send me an official invitation; guarantee my adherence to the country's laws; and have documents sent by post, because the embassy does not accept fax or e-mail. I have been to the Japanese embassy in Kampala multiple times, because I missed or misunderstood some details of the application (not all of which were explained online).

APPLYING FOR VISAS SHOULD NOT BE A FULL-TIME JOB.

On the same day that I read that disheartening e-mail from the Panama embassy, I received an invitation to speak at an annual conference of the InterAcademy Partnership — a global network of academies worldwide that work together on public policy — in South Korea in April 2019. Instead of elation, all I felt was the dread of having to decipher yet another sea of visa procedures, just because I am a citizen of Uganda.

I appreciate that countries need to control entry, but common sense should rule. Applying for visas should not be a full-time job: there must be better ways for the academic and research communities to vouch for each other, and for governments to ease international scholarship.

I've heard some promising ideas for reform. South Africa is considering creating a category for academic visas that would be valid for ten years. Colleagues in the GYA are working on a concept called the Global Passport for Scholars. We are also collecting stories of scholars' visa tribulations to press the case (please e-mail yours to me). Yes, scholars face many more — and more-significant — barriers than visas: we lack job opportunities, access to funding and equipment, and have poor mentorship. Still, visa problems should be among the easiest to fix.

In April 2019, the GYA will have its 10-year anniversary in Germany, and all 200 of our members, plus our 216 alumni — together representing 83 countries — are invited. Although we will make every effort to assist them with their travel, a good number will undoubtedly not make it, simply because they were born in the wrong country. ■

Connie Nshemereirwe *is an independent science and policy facilitator, serves on the steering committee of the Africa Science Leadership Programme and co-chairs the Global Young Academy in Kampala.*
e-mail: cnshemereirwe@gmail.com

© 2018 Springer Nature Limited. All rights reserved.

SEVEN DAYS *The news in brief*

FUNDING

UK budget released

The UK government's budget, released on 29 October, contained few surprises for science. Chancellor of the Exchequer Phillip Hammond announced £1.6 billion (US$2 billion) of "new investments" in science and innovation. But the advocacy group Campaign for Science and Engineering says this mostly represents allocation of funds that the government had already committed. The money includes £235 million to develop quantum technologies and £150 million for international research fellowships. The government has previously promised to increase spending on research and development to 2.4% of gross domestic product by 2027. But in a statement, Venki Ramakrishnan, president of the Royal Society, said that the 2018 budget "does not provide any more clarity on how it is going to get there".

EVENTS

Conference furore

More than 1,400 people have signed a petition calling for a machine-learning conference to change its controversial name. Anima Anandkumar at the California Institute of Technology in Pasadena set up the petition after the board of the annual Neural Information Processing System conference, widely known as NIPS, said on 22 October that it would keep its name on the basis of a poll that the petition says was flawed. Some researchers say that the connotations of the conference acronym have been used by some attendees to make unwelcome sexual jokes, so the board issued a poll asking people who had attended the event over the past five years whether they supported a name change. Around one-third of the 2,270 respondents supported the change, including 44% of the 300 or so women.

ANDRE COELHO/BLOOMBERG/GETTY

Brazil's new president worries scientists

Right-wing politician Jair Bolsonaro won Brazil's presidential election on 28 October, leaving many researchers stunned, and worried about the future of their country. He captured around 55% of the vote in a run-off election against Fernando Haddad, former mayor of São Paulo. None of the 13 presidential candidates garnered a majority during the first round of voting on 7 October, prompting the run-off between the top two candidates. Bolsonaro has promised to crack down on violent crime and government corruption, roll back environmental regulations and promote economic development. Although he has backed down from an earlier promise to pull Brazil out of the 2015 Paris climate accord, Bolsonaro has said that he will merge the environment and agriculture ministries as part of a broader effort to loosen regulations on the agricultural industry. See go.nature.com/2q1wrgc for more.

Hubble-law change

Members of a major international organization of astronomers have voted to change the name of the Hubble law. The law states that the velocity at which a galaxy seems to be receding is proportional to its distance from Earth, and it provided evidence for the expansion of the Universe. The International Astronomical Union recommends that the law should now be known as the Hubble–Lemaître law, to pay tribute to the Belgian priest and astronomer Georges Lemaître, who derived the speed–distance relationship two years earlier than did US astronomer Edwin Hubble. Of the 4,060 votes (out of some 11,070 eligible members) 78% were in favour of the change.

Research chief

Structural biologist Shekhar Mande is the new director-general of India's Council of Scientific and Industrial Research (CSIR), one of the country's largest and oldest research and development organizations. Mande says he will use his appointment to help address some of the country's most intractable problems, such as malnutrition, disease epidemics and access to clean drinking water. But Mande arrives at a time when the CSIR faces major challenges of its own. The organization's 38 institutes are still reeling from a government order, three years ago, to increase their own funding. Subsequent hikes to employers' pension-scheme contributions then put a dent in the council's already stretched budget. "My highest priority is to take stock of CSIR's funding situation," Mande says. Scientists also hope he will

© 2018 Springer Nature Limited. All rights reserved.

tackle the agency's entrenched bureaucracy. See go.nature.com/2ay7smt for more.

Climate lawsuit

New York state attorney general Barbara Underwood filed a lawsuit against oil and gas giant ExxonMobil on 24 October, alleging that the company misled its investors about the financial risks that global warming posed to its business. The suit alleges that the company told investors that it was taking into consideration the impact that potential climate-change regulations could have on future demand for fossil fuels. But ExxonMobil either used low estimates of those costs or failed to consider them at all in business activities such as evaluating its oil and gas reserves and assessing demand for its products in the transportation sector. The lawsuit also alleges that the company's senior management was aware of these activities. ExxonMobil did not respond to *Nature*'s requests for comment. See go.nature.com/2qw4ky1 for more.

POLICY

Hungary departure

An international university in Budapest that has been at the centre of a struggle between Hungarian liberals and the country's right-wing government has decided to transfer its next batch of master's and doctoral students to Vienna (**pictured**). The decision to move new students to Austria ends an 18-month struggle to keep the Central European University (CEU) fully in Hungary after the government passed a law in April 2017 requiring international universities to operate as higher-education institutes in their country of origin, as well as in Hungary. Founded by philanthropist billionaire George Soros, the CEU has been based in Budapest since 1993, even though it is legally registered in New York state. Michael Ignatieff, rector of the CEU, announced the move in a 25 October statement, in which he referred to various laws introduced by the Hungarian government earlier this year that also impinged on CEU activities — and which Ignatieff described as a crackdown on academic freedom.

GERHARD TRUMLER/IMAGNO/GETTY

Research rejected

Australian universities and researchers have condemned the actions of a government minister who vetoed projects that had been selected for funding by peer-review panels. On 25 October, it emerged that in June 2018 and November 2017, Simon Birmingham, the then-minister for education, used his ministerial powers to stop funding for 11 humanities research projects, worth a combined AUS$4.2 million (US$3 million). Birmingham's intervention went against the recommendations of independent peer-review panels that had assessed the projects as high-quality and worthy of funding from the Australian Research Council, a major funder of science and humanities research. Although the education minister has the power to reject recommended projects, the right is rarely exercised. Researchers are worried that the minister's actions undermine the country's competitive research-funding system.

CLIMATE CHANGE

Canada carbon tax

Canadian Prime Minister Justin Trudeau unveiled the details of a federal carbon tax programme on 23 October. It will apply to provinces that don't already have carbon tax plans that meet federal requirements, such as Ontario, Manitoba and New Brunswick. The programme, announced in 2016, is aimed at helping Canada to reduce its greenhouse-gas emissions by 30% below 2005 levels by 2030. The federal tax for consumers is due to start at Can$20 (US$15) per tonne of carbon dioxide in 2019, rising to $50 per tonne in 2022. It will be applied as a fuel surcharge, although 90% of the proceeds will be returned to consumers as a rebate. Major industrial facilities will be taxed through a separate programme, the final details of which the government plans to announce early next year.

TREND WATCH

Studies that fail to find a positive result are often left unpublished, which leads to a publication bias that compromises the credibility of scientific literature.

An analysis now suggests that registering and peer-reviewing study protocols before research is conducted could help to correct the bias towards positive findings.

Researchers from Cardiff University, UK, report what they say is the first analysis of whether such a practice is effective. Chris Allen and David Mehler analysed the outcomes of 113 registered reports in the biomedical and psychological sciences. They identified 296 discrete hypotheses across those studies, and found that, overall, 61% of them were not supported by the final results in the published papers. By contrast, just 5–20% of hypotheses in the general scientific literature lead to null results, they estimate (C. Allen and D. M. A. Mehler Preprint at PsyArXiv https://psyarxiv.com/3czyt; 2018).

For replication studies, the percentage of null results was slightly higher, at 66%, whereas this figure was 55% for original research. So far, only 130 registered reports have ever published final results, and some 140 journals use the format.

REGISTERED REPORTS CUT PUBLICATION BIAS

Pre-registering research protocols in a 'registered reports' format could reduce publication bias skewed towards positive results. Studies that pre-register their protocols publish more negative findings that don't support their hypothesis than those that don't.

HYPOTHESES NOT SUPPORTED BY RESEARCH PAPERS (%)

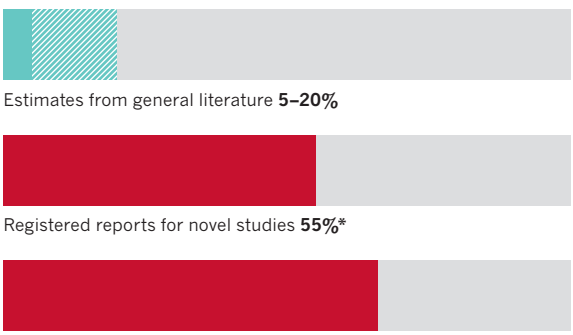

*Sample size: 296 hypotheses across 113 studies in biomedicine and psychology

SOURCE: C. ALLEN & D. M. A. MEHLER PREPRINT AT PSYARXIV HTTPS://PSYARXIV.COM/3CZYT (2018)

© 2018 Springer Nature Limited. All rights reserved.

NEWS IN FOCUS

GENETICS Court ruling on gene-edited crops hits research projects **p.15**

DRUG DISCOVERY Speedy atomic structures thrill organic chemists **p.16**

NEPAL Hope for future of mothballed Himalayan climate observatory **p.17**

PSYCHOLOGY Emotion-tracking technology is speeding to market **p.20**

CHRISTOPHE COURTEAU/GAMMA-RAPHO/GETTY

Ethnic groups in Africa, including San communities in Botswana, are working with scientists to unravel early human history on the continent.

GENETICS

Rare DNA sequences bring early human history to light

Genome studies unlock clues to our ancient family tree and migration patterns in Africa.

BY AMY MAXMEN

Humanity's early history in Africa is coming into sharper focus with a recentstudy of 180 genomes from a dozen ethnic groups on the continent — some of which have never before been analysed.

These preliminary results suggest that more than 40,000 years ago, two of the groups — the San and the Baka Pygmy — were roughly twice the size of other ethnic groups present at the time, and that the San and Baka overlapped in central-eastern or southern Africa. Researchers presented these as-yet unpublished results at an American Society of Human Genetics (ASHG) meeting in San Diego, California, in mid-October.

This is the most comprehensive whole-genome-sequencing study of groups that represent the ancestral diversity of humans, says Sarah Tishkoff, a human geneticist at the University of Pennsylvania in Philadelphia, who co-led the project. Together with genetic analyses of ancient human remains from Africa published last year[1,2], the latest data are starting to fill in the nearly blank canvas of early human history.

Although *Homo sapiens* originated in Africa roughly 250,000 to 315,000 years ago, geneticists have devoted their attention almost exclusively to the small subset of Africans that migrated ▶

© 2018 Springer Nature Limited. All rights reserved.

north to Europe tens of thousands of years later. A handful of African genomics projects are now beginning to address this imbalance.

In 2009, Tishkoff and her colleagues published a study[3] assessing small sections of the genome from people belonging to about 100 of the more than 2,000 ethnic groups in Africa today. The results suggested that the San and the Baka might have descended from a single lineage of hunter-gatherers.

But Tishkoff needed whole genomes from them and other ethnic groups to test this idea. Her team spent years getting approvals for the project from government and institutional ethical review boards in countries in eastern, southern and western Africa. Tishkoff and her colleagues partnered with local researchers and spoke about genetics with the communities that they hoped to enrol in the project, explaining what the scientists and the groups could learn about their early ancestry. Many of the communities live in remote regions — such as the Sabue people of southwestern Ethiopia — and geneticists know little about them.

"There is nothing in Africa that is not possible since we have no idea what humans were doing on the continent 5,000 years ago."

Genomics research in Africa can be contentious, and many scientists engage in such outreach to involve the communities they work with in their research. The Human Heredity and Health in Africa (H3Africa) Initiative — an African-led consortium that supports genomics research — has called for a greater role for Africa-based scientists in such projects. And last year, an Indigenous group in South Africa introduced research-ethics guidelines for scientists looking to work with them.

Tishkoff and her colleagues make sure to follow up with the communities that participate in their studies. For example, some of the Fulani, a traditionally nomadic group, are interested in what their genetics can reveal about their migration history, says Alfred Njamnshi, a neurologist at the University of Yaoundé in Cameroon.

ANCESTRAL LINKS

Nearly one-fifth of the genetic variation that the team uncovered has never before been reported. Statistical models of the data indicate that the Hadza and the Sandawe people of Tanzania shared an ancestor in the past 30,000 years. The findings also suggest that there was intermingling during that period between the Hadza, the San in southern Africa and the Baka in central Africa, all of whom were traditionally hunter-gatherers. "I think we are seeing an ancient common ancestry between the major hunter-gatherer groups in Africa," Tishkoff says.

Some of the findings align with signals of mixed Hadza and San ancestry in DNA extracted from human remains[1] dated to between 2,500 and 8,100 years old, says Pontus Skoglund, a palaeogeneticist at the Francis Crick Institute in London.

Other researchers want to see further statistical analyses of the data before they accept the idea that the Hadza, San and Baka overlapped geographically. Earlier studies have given little indication that people from these groups mixed with each other, says Deepti Gurdasani, a genetic epidemiologist at the Wellcome Sanger Institute in Hinxton, UK. But it's plausible, she adds. "There is literally nothing in Africa that is not possible since we have no idea what humans were doing on the continent 5,000 years ago."

This knowledge gap might dissipate in the coming years as more teams working on African genome projects publish their results. Gurdasani presented findings from an analysis of whole genomes from 2,000 Ugandans at the ASHG meeting. And H3Africa has sequenced more than 400 genomes from African individuals, says Charles Rotimi, a Nigerian genetic epidemiologist at the National Human Genome Research Institute in Bethesda, Maryland, who founded the initiative.

After conducting further analyses, Tishkoff plans to publish the results and share the anonymized genomes publicly, so that scientists can pool their data.

This last bit is essential, says Shaohua Fan, a molecular biologist at Fudan University in Shanghai, China. As of 2016, about 80% of people in genetic studies were of European descent. "We know humans originate in Africa," says Fan, "but we don't know what we did before we left — we don't know our own history." ■

1. Skoglund, P. *et al. Cell* **171**, 59–71 (2017).
2. Schlebusch, C. M. *et al. Science* **358**, 652–655 (2017).
3. Tishkoff, S. A. *et al. Science* **324**, 1035–1044 (2009).

PHYSICS

Quantum projects get cash

European Commission has announced the first-round winners of its new flagship.

BY DAVIDE CASTELVECCHI

Plans to build two working quantum computers are among the first winners to be announced in a €1-billion (US$1.1 billion) funding initiative of the European Commission. On 29 October, the commission announced the first batch of fund recipients of its Quantum Flagship. The 20 international consortia, including public research institutions and industry, will receive a total of €132 million over 3 years for technology-demonstration projects (see 'Quantum windfall').

The efforts add to a global rush to turn early-stage laboratory experiments into applications such as practical quantum computers, which promise to improve certain tasks — for example, predicting chemical reactions exponentially faster than classical computers do. Most recently, in August, Germany's federal government quietly announced a quantum initiative worth €650 million. The US Congress is considering a proposal to set aside more than $1.2 billion for quantum computing, and China, which has already made major investments in

QUANTUM WINDFALL

Europe's Quantum Flagship programme will spend €132 million (US$150 million) overall on 20 projects spanning 6 themes for its first 3 years.

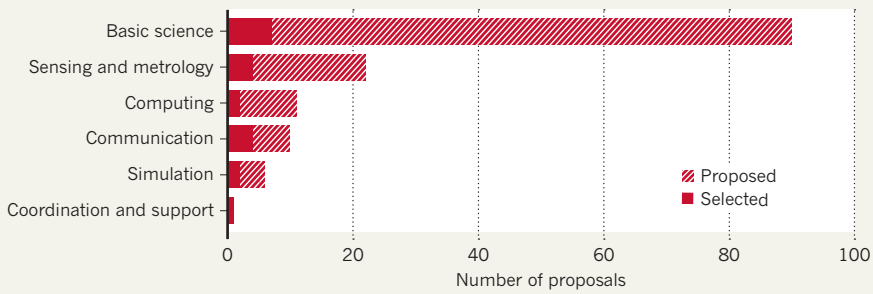

SOURCE: QUANTUM FLAGSHIP

© 2018 Springer Nature Limited. All rights reserved.

the field, is rumoured to be planning a quantum-research centre in Hefei worth billions of US dollars.

The European Union initiative is the commission's third flagship scheme, after the Human Brain and Graphene flagships started in 2013. It was announced in 2016 in response to a 'Quantum Manifesto' written by a group of experts. The two previous flagships have been criticized, in part about how they awarded the grants. The organizers of the Quantum Flagship have been mindful of those controversies, says Tommaso Calarco, who was an author of the original Quantum Manifesto and is a theoretical physicist at the Helmholtz Centre in Jülich, Germany. "Grants are decided with open calls, evaluated by external collaborators," he says.

Other grants announced this week included those for a range of projects. Some of the proposed technologies are relatively close to having market applications, including ultra-precise, portable, atomic clocks, and chip-sized devices that produce random numbers for use in secure networks. For most labs involved, the flagship funds will not make a substantial difference to buying machinery or hiring researchers: the money is distributed over ten years and dozens of laboratories. (The EU provides half of the €1 billion; member countries must provide the remaining half.)

Lieven Vandersypen, a physicist at the Delft University of Technology in the Netherlands, says that the flagship is a missed opportunity to provide a 'Moonshot' on a single focused goal, such as building a large quantum computer. Instead, "only €20 million goes to computing" in this round of funding, says Vandersypen, who is leading an effort to build a quantum computer on a silicon chip, in collaboration with US semiconductor giant Intel. "I don't see the Moon."

But others say that the main advantage of the flagship is that it has forced groups to pool their efforts and knowledge — in particular, those in academia and industry. "It is a strong incentive to make sure that we collaborate on a European scale," says Thomas Monz, a physicist at the University of Innsbruck in Austria.

Major public funding will be necessary merely to keep a pipeline of experts, says Rodney Van Meter, an engineer at Keio University in Tokyo. "You need to build quantum programmes inside universities simply to train the people that Google and Intel are going to need." Public funders worldwide, from Canada to Japan, and major corporations are betting that quantum technologies will grow into multi-billion-dollar markets. The "decisive stimulus" for the European Commission to select quantum physics as its third flagship project, says Calarco, was a dramatic increase in investment in the field from US technology giants such as Google and IBM. ■

AVALON

A project to protect bananas from disease is among those affected by a European court decision.

RESEARCH

EU gene-editing rule squeezes science

Researchers protest about impacts of stricter legislation.

BY ANDREW J. WIGHT

Three months after the European Union's top court gave gene-edited crops the same stringent legal status as genetically modified (GM) organisms, researchers across the world are starting to feel the pinch. And some are becoming increasingly vocal in their opposition to the ruling.

The ruling by the European Court of Justice (ECJ) imposes extensive risk evaluations before gene-edited organisms can be planted or sold as crops.

Much basic research on gene editing in plants isn't affected because these evaluations apply only to organisms released into the environment, and so pose hurdles at the field-trial or commercialization stage. But some applied-research projects are feeling the strain.

"A maize field trial we've been conducting in Belgium for over a year and a half was suddenly considered a GM field," says Dirk Inzé, science director at the VIB–UGent Center for Plant Systems Biology in Ghent, Belgium.

As a result of the ruling, he says, local authorities have insisted on extra precautionary measures, such as placing a fence around the researchers' plot and completing extensive documentation.

Meanwhile, a Belgian start-up that planned to use CRISPR technology to help Africa's banana industry says it lost its financing. And a company in Brazil says it has put millions of dollars' worth of gene-editing projects focused on soya beans on hold because its major market is in Europe.

A 2001 EU Directive required GM organisms to be identified, tracked and monitored for their effects on the environment and consumers. The new ruling imposes those restrictions on gene-edited crops, even though gene editing mostly involves small, precise changes to DNA — and not inserting foreign genes, as in the case of GM organisms.

"We see a chilling effect on plans for performing research with CRISPR-edited plants in the field," says René Custers, manager of regulatory and responsible research at the VIB life-sciences research institute in ▶

© 2018 Springer Nature Limited. All rights reserved.

Belgium. "The climate for precision breeding in general and CRISPR in particular has worsened after the ECJ ruling."

SCIENTISTS GET VOCAL

Scientists are also making public demands for exemptions from the ruling, which they say is not in line with scientific evidence. On 24 October, 170 European scientists from 75 research centres in more than a dozen countries released a position paper urging that the law should change so that crops with small DNA adaptations made through gene editing would follow the regulations for varieties produced through conventional methods such as selective breeding, not for GM organisms.

In August, the organizers of the International Plant Molecular Biology congress in Montpellier, France, started an online petition calling for a review of the ruling. The petition has now attracted more than 5,200 signatures, including Inzé's. It declares that there is "no scientific rationale" for the ruling and that the EU should regulate crop genetic techniques on the basis of science.

And on 13 September, researchers from 33 UK science, farming and agricultural–technology organizations sent an open letter to the UK government to encourage recognition of gene editing as a non-GM method.

Outside Europe, Alexandre Garcia, who heads soya-bean research and development at the Brazilian plant-breeding company Tropical Melhoramento & Genética, says that the company had been expanding partnerships and investing in several research initiatives in soya-bean gene editing, but now needs to factor in the extra compliance work needed to meet the EU rules.

"For at least the past six years, the European Union has been the second biggest market for Brazilian soya beans, and Brazil is the main provider to the EU — so if any farmer plans to plant soya beans on Brazilian land, they need to worry about EU rules," he says.

Garcia says that the decision was a "cold water bath" on the company's research activities, and that research partnerships and investments that it valued at millions of dollars are now on hold while their viability is evaluated. The company might permanently cull research projects involving gene-editing unless they are expected to recoup the higher regulatory costs, he says.

The Belgian start-up faces similar challenges. It had wanted to use CRISPR technology to develop an edible banana that is resistant to Panama disease and black Sigatoka, two fungal pests that put 80,000 African growers at risk of losing their entire crops.

Biotech entrepreneur Roel Sterken, who leads the business side of the project, says that the company had secured venture capital financing of more than €1 million (US$1.14 million), and a distribution partner. Then, within days of the July ruling, Sterken says, the finance "blew up" and the partner backed out. He attributes this to fears that consumers would conflate the new product with the bad press that GM organisms receive.

Legal experts say that there is no mechanism for appealing the European court's ruling. "We have reached the end of the road as regards the ruling," says Julian Hitchcock, a partner at the London-based law firm Marriott Harrison. The only way to reverse the decision would be for the European Commission to revise the legislation and get it passed in parliament, he says. But he adds that the commission has been sluggish in responding to rapidly changing gene-editing technologies. ■

ORGANIC CHEMISTRY

Atomic structures solved in minutes

Cross-disciplinarity led to method's use on small molecules.

BY MATTHEW WARREN

Organic chemists, make sure you're sitting comfortably. The structure of small organic molecules, such as those used in drugs, can be deduced in minutes rather than weeks, thanks to a technique that uses beams of electrons.

Three-dimensional electron diffraction has been used by some inorganic chemists and materials scientists since the mid-2000s. But organic chemists, for whom the implications could be transformative, have not adopted it widely. In mid-October, two papers[1,2] appeared online describing a way to use the technique for drugs, making it much faster and easier to work out the structures of these small organic molecules than has been possible with previous techniques.

"I think there are a lot of people smacking their heads, saying, 'Why didn't we think to do this earlier?'" says John Rubinstein, a structural biologist at the University of Toronto in Canada who uses related techniques to study large molecules. Existing methods for determining the structure of small molecules require scientists to grow crystals for analysis, a laborious process that can take weeks or months. "Something that was a real barrier to their research is now basically removed," says Rubinstein.

Knowing how atoms are arranged in a molecule is necessary for understanding that substance's function. Chemists working to develop new drugs, for example, depend on this structure to understand how a compound acts in the body — and how it could be tweaked to bind more strongly to its therapeutic target or to reduce side effects.

"I think there are a lot of people smacking their heads, saying, 'Why didn't we think to do this earlier?'"

X-ray crystallography has been used for decades to deduce this arrangement. But it can take weeks of work — and is not always successful. First, scientists need to coax the molecules to crystallize. Then they blast the crystal with an X-ray beam. The crystal's lattice structure causes the X-rays to diffract, and a detector records the resulting pattern. Scientists then use software to analyse the pattern and work out the structure of the molecule.

The challenges arise because X-ray diffraction works only with large crystals, and these can take months to form. And some molecules are so hard to crystallize that it might not even be possible to analyse them in this way.

One alternative is to replace X-rays with electron beams, which can produce diffraction patterns for much smaller crystals. In 2007 and 2008, respectively, crystallographers at the Johannes Gutenberg University in Mainz, Germany, and at Stockholm University developed the first methods for detecting the 3D structures of molecules automatically using electron diffraction[3,4]. Previously, scientists had to laboriously merge multiple 2D diffraction patterns to get this 3D structure.

Initially, the technique was used mainly with inorganic structures, which are less affected by radiation than are organic molecules. Then, in 2013, Tamir Gonen, a structural biologist at the University of California, Los Angeles, developed a version of electron diffraction called MicroED, which could be used on large biomolecules such as proteins[5].

Now, Gonen's team and another group, based in Switzerland, have shown that electron diffraction can also be used to work out the structure of smaller organic molecules. It's an important demonstration of just how fast and easy this kind of analysis can be, says Xiaodong Zou, a structural chemist at Stockholm University.

A team led by crystallographer Tim Grüne at the Paul Scherrer Institute in Switzerland

© 2018 Springer Nature Limited. All rights reserved.

reports the creation of a prototype device for finding the structure of small molecules, using the beam from an electron microscope and a compatible detector[1].

TRIVIAL BUT TRANSFORMATIONAL

The diffraction patterns are analysed by software that is already used in X-ray crystallography. "Everything is composed of parts which have existed before," says Grüne. "It's just really the smooth integration of the system." His team used its set-up to find the structure of the painkiller paracetamol from minuscule crystals formed of the powder used inside capsules. These crystals were just a few micrometres long — much smaller than can be analysed using X-ray diffraction.

And Gonen's group adapted the MicroED technique to solve the structure of small molecules instead of proteins[2]. Gonen says that making this shift was "trivial". The main tweaks concerned the preparation of the samples, he says: whereas fragile proteins need to be treated with care, in this case, all he had to do was grind down pharmaceutical powders. The team used this adapted version of MicroED to find the structure of powders of pharmaceuticals including ibuprofen and the anti-epileptic drug carbamazepine.

These crystals were some 100 nanometres wide — a billion times smaller than those required for X-ray crystallography — and their structure could be resolved in under 30 minutes.

Rubinstein says it's surprising that a technique already used in other fields hasn't yet been widely adopted by organic chemists. "It's this great solution that's been sitting almost in plain sight," he says.

Gonen puts the oversight down to a lack of communication between disciplines. It was only when he began speaking to chemists, he says, that he became aware that they struggled to grow large crystals in order to analyse small molecules, leading him to realize he had a solution for them. "As a protein crystallographer, I never really thought very carefully about small molecules," he says. "For us, small molecules are the things we try to get rid of." ■

1. Gruene, T. *et al. Angew. Chem. Int. Edn* http://doi.org/cvw3 (2018).
2. Jones, C. G. *et al.* Preprint at ChemRxiv http://doi.org/cvvh (2018).
3. Kolb, U., Gorelik, T., Kübel, C., Otten, M. T. & Hubert, D. *Ultramicroscopy* **107**, 507–513 (2007).
4. Hovmöller, S. Electron Rotation Camera. Patent WO/2008/060237 A1 (2008).
5. Shi, D., Nannenga, B. L., Iadanza, M. G. & Gonen, T. *eLife* **2**, e01345 (2013).

FACILITIES

Himalayan observatory close to resurrection

Negotiations with Italian funding agency foster hope for climate station's future.

BY LOU DEL BELLO

EVK2CNR

The Nepal Climate Observatory-Pyramid is located near the base of Mount Everest.

Scientists hope that a Himalayan climate observatory that had its funding cut four years ago could be back in action by early next year. Managers of the Nepal Climate Observatory-Pyramid station say they are close to reaching an agreement with the Italian National Research Council (CNR). The council helped set up the station near the base of Mount Everest in 2006 but stopped funding it in 2014 because of how its budgets were managed.

"For the first time in four years, I am extremely optimistic about the fate of the station," says philanthropist and climber Agostino Da Polenza, who heads the Ev-K2-CNR Association, a non-profit group that promotes research in mountain areas and helped to set up the Nepal Climate Observatory-Pyramid, one of the highest climate observatories in the world.

If the deal goes through, the observatory will resume collecting data on atmospheric processes at high altitudes. Climate researchers say these measurements are crucial for understanding how pollution influences climate patterns.

HOPE IN THE HIMALAYAS

Da Polenza says that a meeting in October between the Ev-K2-CNR Association and the CNR to discuss the observatory's future was overwhelmingly positive, and he hopes that, come March, technicians will be on their way to the station to switch on its instruments. But he declined to reveal any further details, saying he did not want to jeopardize a potential deal before it has been finalized.

Antonello Provenzale, acting director of CNR's Institute of Geosciences and Earth Resources in Pisa, which manages funding for infrastructure, says that it is too early to disclose details of the observatory's fate, but there is a strong motivation to reinstate funding. "We all feel strongly that the Pyramid must resume activities."

The Nepal Climate Observatory-Pyramid is part of the Global Atmosphere Watch (GAW) network, run by the United Nations World Meteorological Organization in Geneva, Switzerland. The programme ▶

© 2018 Springer Nature Limited. All rights reserved.

combines data from hundreds of stations around the world to build a picture of global climate.

The Nepal observatory is perfectly positioned to study how the climate in the Himalayas is being influenced by pollution — such as anthropogenic emissions from biomass burning and agriculture — transported from South Asia, says Paolo Bonasoni, the observatory's research leader and a scientist with the Institute of Atmospheric Sciences and Climate at the CNR in Bologna.

Atmospheric scientist Oksana Tarasova, who heads the GAW network, says that various kinds of pollution travel up the sides of the Himalayan mountain chain and then mix together. When pollutants such as ammonia and oxides of nitrogen interact with other airborne chemicals and sunlight, they create compounds known as secondary aerosols, which alter the climate and affect the weather, she says.

The Nepal observatory is one of the few that can simultaneously measure aerosols, reactive gases and other compounds, she says. Its instruments have shown that the air surrounding the Himalayas changes quickly from clean to polluted when pulses of dirty air travel up from urban centres; when this happens before the monsoon period, it triggers bursts of cloud condensation.

SELF-FUNDED

Since 2014, members of the Ev-K2-CNR Association have donated their time or money to maintain the observatory at a vastly reduced capacity. Most of the instruments are not being used, and have been turned off to prevent them from deteriorating in the extreme winter conditions. Less than two months ago, the group feared it would have to close the station altogether, as its members struggled to secure a new source of money to update and run the instruments.

The observatory's reduced capacity has hampered scientists' ability to study complex environmental problems, says Bhupesh Adhikary, who models chemical transport at the International Centre for Integrated Mountain Development in Kathmandu.

Some researchers have suggested that satellite monitoring could fill the data gap. But Adhikary says this will not be sufficient. Satellite-based air-pollution detection is still rudimentary, and most sensors have problems over mountainous areas, he says. "Whatever tool you use to study the problem, whether it's satellite or computer, you need ground validation."

Tarasova is excited that the observatory could soon resume full data collection again. "This is an important station, a rare one and a real treasure in our programme," she says. ■

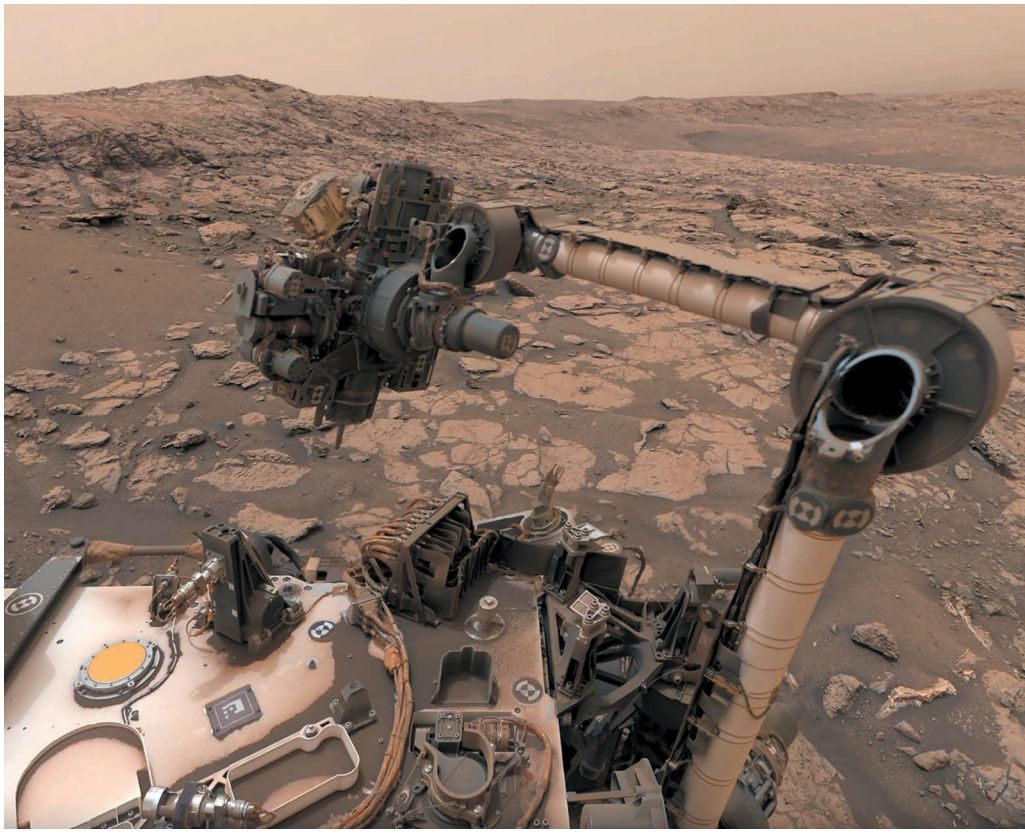

The Curiosity rover has tracked methane in Mars's atmosphere since it landed on the planet in 2012.

NASA/JPL

PLANETARY SCIENCE

Clues emerge to Martian mystery

Warming power of the Sun could help to explain why the level of methane in the atmosphere changes with the seasons.

BY ALEXANDRA WITZE IN KNOXVILLE, TENNESSEE

Planetary scientists are getting closer to solving the puzzle of methane on Mars. New calculations could help to explain why NASA's Curiosity rover detects peaks of methane gas in the Martian atmosphere during the planet's northern summer. As winter gives way to spring, the idea goes, the Sun's heat begins to warm the soil — allowing methane to percolate up from the ground and into the atmosphere, said John Moores, a planetary scientist at York University in Toronto, Canada. He presented the work on 24 October at the American Astronomical Society's Division for Planetary Sciences meeting in Knoxville, Tennessee.

Curiosity's methane measurements have been tantalizing researchers for years. The rover, which landed near Mars's equator in Gale crater in 2012, at first found mysterious spikes in atmospheric methane during the northern spring[1]. Earlier this year, mission scientists reported that methane levels waxed and waned with the seasons, peaking in northern summer[2].

FROM THE DEPTHS

Finding methane in Mars's atmosphere is intriguing because chemical reactions should destroy the gas after about 300 years. Its presence today suggests that something on the planet is still sending the gas into the atmosphere. The source could be geological, such as reactions between water and certain types of rock — or, more intriguingly, buried microbes or other forms of life. Most methane in Earth's atmosphere comes from living things.

Researchers have chased every whiff of methane they can find on Mars. Telescopes on

© 2018 Springer Nature Limited. All rights reserved.

Earth and spacecraft orbiting Mars have spotted the gas around the red planet from time to time — including an intense plume reported in 2009 (ref. 3). Curiosity was supposed to help solve the puzzle by measuring methane levels directly, but instead it has complicated it.

Now, it seems the answer might lie under Mars's surface. Moores and his colleagues analysed how methane might seep upwards through cracks and fissures in the Martian soil until it enters the atmosphere. Warming the soil could allow the gas to leak into the air, their calculations show. Seasons on Mars are complex, especially at Curiosity's location so close to the planet's equator. But the highest methane levels do appear just after the warmest time of the year, suggesting that heat spreading downward allows more of the gas to be released.

The amount of gas that the scientists estimate is entering the atmosphere is a good match for the measurements Curiosity has made at Gale crater, Moores said. The methane's ultimate source is still a mystery. But the work could help to explain the gas's seasonal ebb and flow, he added.

GAS LEAK

The idea builds on earlier suggestions that methane could be seeping out of Sun-warmed cliff faces on Mars, said Michael Mumma, a planetary scientist at NASA's Goddard Space Flight Center in Greenbelt, Maryland. When he and his colleagues reported[3] on the intense methane plume in 2009, they suggested that pores in the Martian soil might open up on cliffs or crater walls during certain seasons, allowing methane to make its way from the subsurface to the atmosphere.

More discoveries could come shortly. A European–Russian probe, the ExoMars Trace Gas Orbiter (TGO), has been hunting for methane and other gases in Mars's atmosphere since April.

At the meeting, project scientist Håkan Svedhem of the European Space Agency in Noordwijk, the Netherlands, hinted to the audience that the spacecraft's first results would be published soon. TGO measures methane all around the planet and at a range of altitudes, going far beyond what Curiosity can measure on the ground. The orbiter could help to settle some of the methane-on-Mars questions once and for all.

"There will be surprising results," said Mumma, who is part of the TGO team. He declined to elaborate. ■

1. Webster, C. R. *et al. Science* **347**, 415–417 (2015).
2. Webster, C. R. *et al. Science* **360**, 1093–1096 (2018).
3. Mumma, M. J. *et al. Science* **323**, 1041–1045 (2009).

CORRECTION

The News story 'Scientists criticize handling of animal-welfare charges' (*Nature* **558**, 13–14; 2018) stated that Nikos Logothetis was indicted on 20 February for allegedly violating animal-protection laws, and that a court had not yet considered those charges. In fact, on 20 February, the public prosecutor in Tübingen announced that earlier in the year, the district court had issued Logothetis with a penalty order — an accusation of a minor offence combined with a fine, which automatically becomes a conviction if the accused does not appeal — for alleged mistreatment of animals. Logothetis immediately appealed. The appeal will be heard in court, but no date has been set. The story also said that Stuttgart prosecutors had overturned an earlier settlement granted by the Tübingen court and pursued the case against Logothetis, leading to the indictment. In fact, the Stuttgart attorney general asked Tübingen prosecutors to reconsider their settlement decision, and it was these prosecutors who pursued the case, leading to the penalty order.

© 2018 Springer Nature Limited. All rights reserved.

HAPPY WITH A 20% CHANCE OF SADNESS

Researchers are developing wristbands and mobile phones to predict moods and even warn of suicide risk. But they also worry that emotion-tracking technology could lead to problems.

BY MATT KAPLAN

In the winter of 1994, a young man in his early twenties named Tim was a patient in a London psychiatric hospital. Despite a happy and energetic demeanour, Tim had bipolar disorder and had recently attempted suicide. During his stay, he became close with a visiting US undergraduate psychology student called Matt. The two quickly bonded over their love of early-nineties hip-hop and, just before being discharged, Tim surprised his friend with a portrait that he had painted of him. Matt was deeply touched. But after returning to the United States with portrait in hand, he learned that Tim had ended his life by jumping off a bridge.

Matthew Nock now studies the psychology of self-harm at Harvard University in Cambridge, Massachusetts. Even though more than two decades have passed since his time with Tim, the portrait still hangs in his office as a constant reminder of the need to develop a way to predict when people are likely to try and kill themselves. There are plenty of known risk factors for suicide — heavy alcohol use, depression and being male among them — but none serve as tell-tale signs of imminent suicidal thoughts. Nock thinks that he is getting close to solving that.

Since January 2016, he has been using wristbands and a phone application to study the behaviour of consenting patients who are at risk of suicide, at Massachusetts General Hospital in Boston. And he has been running a similar trial at the nearby Franciscan Children's Hospital this year. So far, he says, although his results have not yet been published, the technology seems able to predict a day in advance, and with reasonable accuracy, when participants will report thinking of killing themselves.

Nock's trial is one effort to make use of the burgeoning science of mood forecasting: the idea that by continuously recording data from wearable sensors and mobile phones, it will be possible not only to track and perhaps identify signs of mental illness in a person, but even to predict when their well-being is about to dip. Nock collaborates with Rosalind Picard, an

© 2018 Springer Nature Limited. All rights reserved.

ILLUSTRATION BY LEANDRO CASTELAO

electrical engineer and computer scientist at the Massachusetts Institute of Technology (MIT) in Cambridge. Picard leads a team that has tracked hundreds of undergraduates in universities in New England with phones and wristbands, and reports being able to predict episodes of sadness in these students a day before symptoms arrive.

Hints that it might be possible to track impending emotional vulnerability have sparked strong commercial interest. Mindstrong Health, a company in Palo Alto, California, which has raised US$29 million in venture capital, tracks how people tap, type and scroll on their phones, to spot shifts in neurocognitive function. Paul Dagum, a physician and computer scientist who founded the firm, says that data from a person's touchscreen interactions can identify oncoming episodes of depression, although that work has not yet been published. Other companies are also researching the use of such 'digital phenotyping' to recognize symptoms of mental illness. Among them is Verily, a life-sciences firm owned by Google's parent company, Alphabet.

At this stage, the reliability of mood-prediction technology is unclear. Few results have been published, and groups that have released results say they have achieved only moderate rather than outstanding accuracy when it comes to forecasting moods. Picard, however, is confident that the concept will hold up. "I suffered from depression early in my career and I do not want to go back there," she says. "I am certain that by tracking my behaviours with my phone I can make it far less likely I will return to that terrible place."

But researchers including Picard have qualms about possible downsides of their creations. They worry that scientists and clinicians haven't thought enough about how to inform users of an imminent emotional downturn. There are also questions about whether such warnings could cause harm. And some wonder whether corporations or insurance companies might use the technology to track the future mental health of their employees or customers. "The [potential for] misuse of this technology is what keeps me up at night," Dagum says.

PREDICTING DEPRESSION

Picard got into mood-prediction research indirectly. A decade ago, she showed that it was possible to use wristbands to detect seizures, sometimes minutes before spasms shook the body, by tracking the electrical conductance on a person's skin. In 2013, she co-founded Empatica, a company in Cambridge that sells sensors, including a smartwatch approved by the US Food and Drug Administration to monitor signs of seizures and issue alerts to caregivers.

Working with her PhD student at the time Akane Sano, now at Rice University in Houston, Texas, Picard saw potential for wider applications. They hypothesized that it might be possible to combine data from wrist sensors and mobile phones to monitor stress, sleep, activity and social interactions to predict general mental health and well-being.

Sano and Picard collaborated with a team at Harvard Medical School to design a study that would track university students on a daily basis. Since 2013, the team has studied 300 students — 50 each semester, for 30 days at a time — by giving them watch-like devices to wear. The instruments measure the students' movements, note the amount of light they are exposed to, monitor their body temperature and record the electrical conductance of their skin. Sano and Picard also developed software, installed on participants' phones, which records data about their calls, text messages, location, Internet use, 'screen on' timing and social interactions. The team also recorded much of their e-mail activity. Students filled out surveys twice a day about their academic, extracurricular and exercise activities. They described their sleep quality, their mood, health, stress levels, social interactions and how many caffeinated and alcoholic drinks they were consuming. The students also reported their exam scores and filled out extensive surveys at the beginning and end of the 30-day studies.

"WE CAN PREDICT EPISODES OF DEPRESSION UP TO A WEEK IN THE FUTURE."

By 2017, the team had reported[1,2] training an algorithm to learn from these surveys and to weight the importance of hundreds of measurements. The system can accurately forecast, a day in advance, the students' happiness, calmness and health, Picard's team says. In the experiment, individuals had to be monitored for 7 days to reach forecast-accuracy levels of around 80%. Picard's analysis suggests that wristbands and mobile phones are not able to predict slight changes in mood. But when changes in well-being are large, predictions are more reliable. Some of the signals make intuitive sense — moving around before bed might suggest agitation, for instance — but the details are not always understood. As an example, social interactions might modify stress levels, which can be reflected in skin electrical conductance, but it's unclear whether many peaks of skin conductance in a day is good or bad, because it increases both when people are problem solving and when they are stressed.

Simply interpreting someone's mood using such signals is a great achievement, says computer scientist Louis-Philippe Morency at Carnegie Mellon University in Pittsburgh, Pennsylvania, who thinks artificial-intelligence technology could help with mental-health assessments. But he is cautious about its ability to forecast moods. "Since tomorrow's mood is often similar to today's mood, we need more research to be able to clearly decouple these two phenomena. It is possible that current forecasting technologies are mostly predicting spillover emotion from one day to the next," he says.

Picard thinks improvements will come: "We are the pioneers saying that this is truly possible and are showing data to back this claim up. Reliability will grow and grow with more data." She has made her algorithms open-source, so that others with access to the technology can try to reproduce her work.

"Picard is on to something, and her track record of transparency with her algorithms, models and data sets makes me even more confident of that. People don't make it so easy to recreate their work when they are unsure about their results," says Jonathan Gratch, a psychologist at the Institute for Creative Technologies at the University of Southern California in Playa Vista.

Nock's trial on suicidal thoughts grew out of a collaboration with Picard. So far, he has monitored 192 people, mainly using wristbands and by asking them how they are feeling, through a phone app or interview. For now, he has trained devices not on an individual's data, but on those of the entire group of participants, and he says that he has identified a few measurable signs that can predict later suicidal thoughts with an accuracy of 75%. Some of the most important factors, he says, are considerable movement in the evening, perhaps denoting restlessness or agitation at night, mixed with spikes in skin electrical conductance and an elevated heart rate. But he declined to give more details because his paper is under review at a journal.

MOVING TO MARKET

Commercial firms are less willing than are academics to discuss their results. But in March, Mindstrong, which is only 16 months old, reported finding digital biomarkers — patterns of swipes and taps on a phone — that correlate with scores on neuropsychological performance tests[3]. On its website, the firm says it has completed five clinical trials, the results of which have not been disclosed, and in February, it announced a partnership with Tokyo-based Takeda Pharmaceuticals to explore the development of digital biomarkers for conditions such as schizophrenia and treatment-resistant depression. It has competition: Verily says its digital phenotyping projects include one designed to detect post-traumatic stress disorder using smartphones and watches.

Mindstrong says it's moving beyond measuring brain function with smartphones, to predicting it. "When we take in the trajectory of numerous biomarkers over the course of six or seven days, we can predict episodes

© 2018 Springer Nature Limited. All rights reserved.

CHARLIE MAHONEY/NYT/REDUX/EYEVINE

Rosalind Picard, wearing a wristwatch that monitors electrical skin conductance.

of depression up to a week in the future," says Dagum — although he declined to say which signals his firm is using, because the company was submitting papers on its work to journals. The plan for Mindstrong's phone-based app (the company is not using wristbands) is to embed its touchscreen-interaction measures into a digital mental-health-care system. It has been sharing results with the state of California, which sees enough clinical potential to have granted the firm $10 million over 3 years from a state-managed, $60-million mental-health innovation fund. "Will all of this data that we are collecting ultimately have clinical utility? We don't know yet," says psychiatrist Tom Insel, who co-founded Mindstrong and had previously started the mental-health unit at Verily after a 13-year stint as head of the US National Institute of Mental Health.

Picard questions Insel's approach at Mindstrong. "I believe he has made a company with an idea that is not proven to work as well as other ideas," she says. Neither she nor Nock yet have commercial plans for their mood-prediction technology. (Besides Empatica, however, Picard has co-founded Affectiva, a firm in Boston that sells technology to analyse facial and vocal expressions.)

Insel says the technology needs testing in real-world settings, with patients and health providers. "We are not running before walking. California is paying us to learn how to walk," he says. He adds that he doesn't view Picard as a rival. "This is a hard problem that no one has solved. My best guess is that it will take all of us using many approaches to prove the clinical value of this technology — and, frankly, I'd love to have at least ten other groups of Roz's lab's calibre working on digital phenotyping," he says.

CHANGING BEHAVIOUR

Picard is confident that mood forecasting — even if it requires individualized training from a consenting user — will become a perfected art. The real question, she says, is whether it can be used to help change a forecasted dark mood.

Nock and psychologist Evan Kleiman, also at Harvard University, are working with 150 patients to encourage them to reappraise things that they are viewing negatively by using cognitive reframing exercises. These exercises are activated on the patients' phones when their wrist monitors detect signals that predict upcoming suicidal thoughts. Beyond this, Nock is unclear what to do with the data. "If we have someone who is predicted to be at high risk for suicidal thoughts, or who notes that they are 100% likely to kill themselves, what do we do? Do we send an ambulance? Contact their doctor? Do nothing?" he wonders. "The ethics of this are extremely challenging." Nock says he knows that those in his trial want the technology. "Patients say all the time how useful they would find an alert or guidance system," he says.

THE ACT OF PREDICTING A MOOD COULD AFFECT HOW PEOPLE FEEL.

Morency thinks that it is too soon for computers to be giving mental-health advice on their own. His research involves teaching computers to study facial expressions and language so that they can work out what is on a person's mind, and he is now collaborating with psychiatrists to install this technology in hospital mental-health wards. The goal is for machines to study people during their interactions with doctors, to discern whether psychiatric disorders are present. The physicians still do the diagnosis; the computer analysis provides a separate assessment that doctors can compare with their own. "The risks presented by a computer giving mental-health advice are significant. We need more research to understand the long-term impact of such technology," Morency says.

Another issue, says Picard, is that actions to improve mood are different for different people. In one of her experiments, Picard found that one cluster of students who had conversations with friends before going to sleep enjoyed brighter moods the following day, whereas another cluster experienced the inverse effect.

Barbara Fredrickson, a psychologist at the University of North Carolina at Chapel Hill, is concerned that the act of predicting a mood could affect how people feel. "It seems likely that people will give negative mood forecasts a great deal of attention, and for some, this could start an emotional negativity tailspin that could be truly damaging," she says.

Justin Baker, a researcher in mental illnesses who is the scientific director of the McLean Institute for Technology in Psychiatry in Belmont, Massachusetts, says: "I think it will be just as difficult for us to determine what advice a person needs as it will be to determine how to present that advice to them in a manner that does not get ignored or make them worse."

Picard has grand visions for digital mood forecasting. She thinks it could improve the health of the general public, and in particular that it might benefit corporations. "Why do so many amazing companies that give their employees every perk under the sun still lose so many staff to depression? Can we catch the coming transition before it takes place?" she says. But she also worries that the technology might be misused. Picard thinks that new regulations might be needed to prevent, say, corporations from targeting advertising at those whose bad or good moods can be seen coming, or to keep insurance companies from setting prices based on signs of their customers' mental health.

"A few bad actors who misuse this technology could spoil the benefits for patients with serious mental-health issues," says Insel. Mindstrong, he says, is working with a bioethics group at Stanford University, California and plans to publish a paper on these matters shortly.

Picard argues the research efforts are worthwhile. "Clinical depression is often emotional death by a thousand cuts," she says. "If we can help to identify the many little things that weigh us down over time and drive us into a perpetual sorrowful state, we can make a big difference." ■

Matt Kaplan *is a science journalist and author based in Hertfordshire, UK.*

1. Taylor, S. *et al. IEEE Trans. Affect. Comput.* https://doi.org/10.1109/TAFFC.2017.2784832 (2017).
2. Sano, A. *et al.* in *2015 IEEE 12th Int. Conf. Wearable and Implantable Body Sensor Networks.* https://doi.org/10.1109/BSN.2015.7299420 (2015).
3. Dagum, P. *Digit. Med.* **1**, 10 (2018).

© 2018 Springer Nature Limited. All rights reserved.

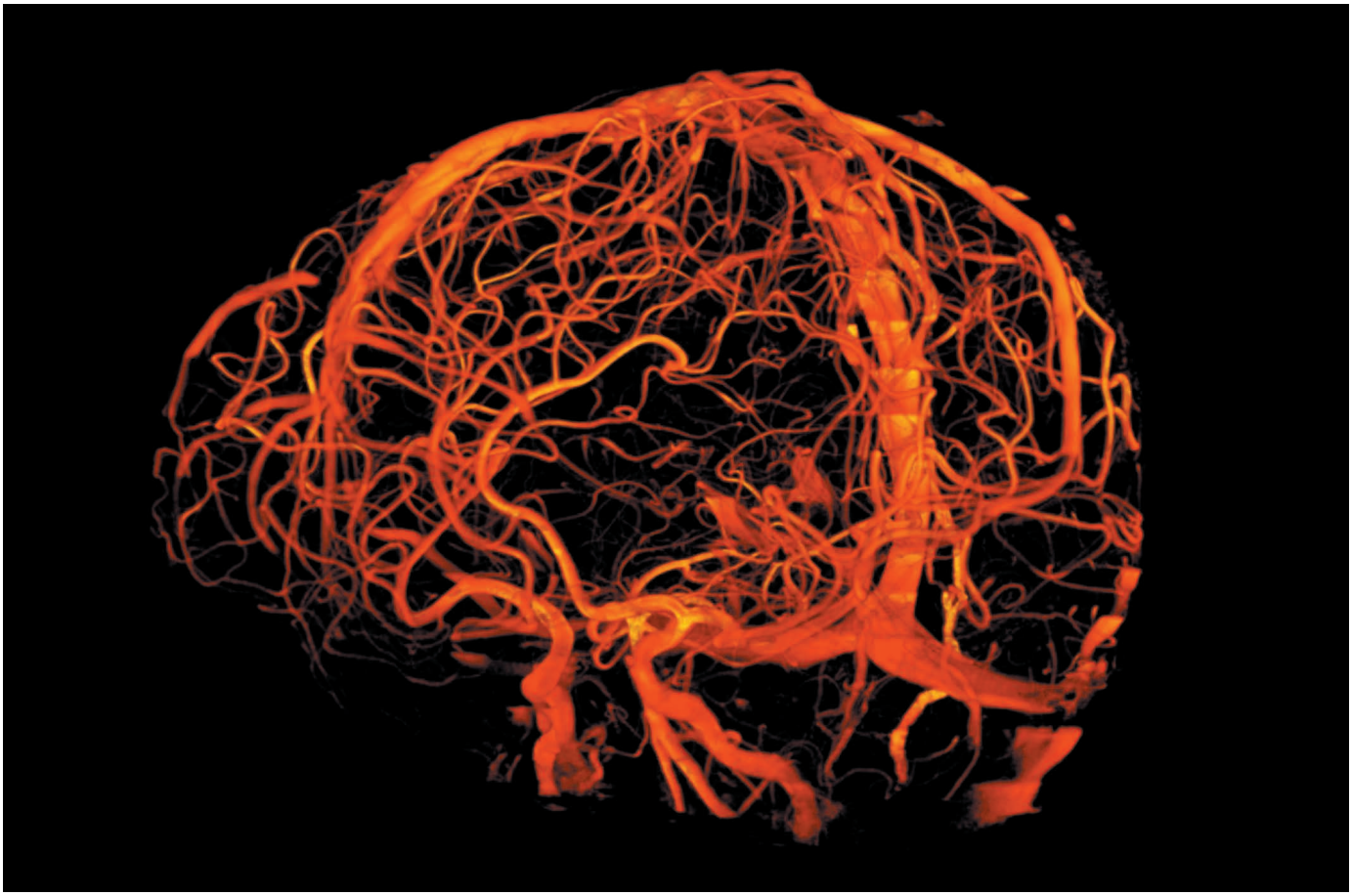

CENTRE FOR ADVANCED IMAGING, UNIV. QUEENSLAND

Cerebral blood vessels glow orange in this picture, generated by a 7-tesla magnetic resonance imaging scanner at the University of Queensland in Australia.

THE STRONGEST SCANNERS

Researchers are pushing non-invasive brain imaging to new limits.

BY ANNA NOWOGRODZKI

On a cold morning in Minneapolis last December, a man walked into a research centre to venture where only pigs had gone before: into the strongest magnetic resonance imaging (MRI) machine built to scan the human body.

First, he changed into a hospital gown, and researchers made sure he had no metal on his body: no piercings, rings, metal implants or pacemakers. Any metal could be ripped out by the immensely powerful, 10.5-tesla magnet — weighing almost 3 times more than a Boeing 737 aeroplane and a full 50% more powerful than the strongest magnets approved for clinical use. Days earlier, he had passed a check-up that included a baseline test of his sense of balance to make sure that any dizziness from exposure to the magnets could be assessed properly. In the MRI room at the University of Minnesota's Center for Magnetic Resonance Research, he lay down inside a 4-metre-long tube, surrounded by 110 tonnes of magnet and 600 tonnes of iron shielding, for an hour's worth of imaging of his hips, whose thin cartilage would test the limits of the machine's resolution.

The centre's director, Kamil Ugurbil, had been waiting for years for this day. The magnet faced long delays because the liquid helium needed to fill it was in short supply. After the machine was finally delivered, on a below-freezing day in 2013, it took four years of animal testing and ramping up the field strength before Ugurbil and his colleagues were comfortable sending in the first human. Even then, they didn't quite know what they'd see. But it was worth the wait: when the scan materialized on screen, the fine resolution revealed intricate details of the wafer-thin cartilage that protects the hip socket. "It was extremely exciting and very rewarding," Ugurbil says.

The US$14-million scanner is one of a handful around the world that are pushing

© 2018 Springer Nature Limited. All rights reserved.

MRI to new limits of magnetic strength. Today, hospitals routinely use machines with field strengths of 1.5 T or 3 T. But ultra-high-field scanners are on the rise. There are already dozens of 7-T machines in research labs around the world, and last year, the first 7-T model was cleared for clinical use in both the United States and Europe. At the extreme end are three scanners designed for humans that reach beyond 10 T. In addition to the University of Minnesota's machine, researchers are readying two 11.7-T devices for their first tests on people: a gargantuan one for whole-body scanning at the NeuroSpin Centre at CEA Saclay outside Paris, and a smaller one for head scans at the US National Institutes of Health (NIH) in Bethesda, Maryland. Germany, China and South Korea are considering building 14-T human scanners.

The appeal of ultra-high-field scanners is clear. The stronger the magnetic field, the greater the signal-to-noise ratio, which means the body can be imaged either at greater resolution, or at the same resolution, but faster. At 3 T, MRI machines can resolve details of the brain as small as 1 millimetre. That resolution can be as fine as 0.5 millimetres in a 7-T machine — enough to discern the functional units inside the human cortex and perhaps see for the first time how information flows between collections of neurons in a live human brain. Scanners with even higher field strengths are expected to have resolving power that is at least double that of the 7-T devices.

The push to achieve higher field strengths presents a range of challenges. The scanners are bigger, more expensive and more technically demanding. They also require more attention to safety. But work at 7 T has already resulted in gains, researchers say, for both neuroscience and clinical applications: clinicians can guide electrodes for deep-brain-stimulation treatments more accurately, and might also be able to detect osteoarthritis at an earlier stage than was possible before.

The scanners offer detail that was once seen only in thinly sliced postmortem samples imaged by powerful microscopes. "This is a window we've just never had in the intact human brain," says Ravi Menon, a neuroimaging scientist at Robarts Research Institute at Western University in London, Canada.

IF YOU BUILD IT

The nuts and bolts of MRI technology have not changed much since the first human scanner was developed in the mid-1970s. The heart of the MRI is still a tube-like superconducting magnet, which generates a static electromagnetic field that realigns a small fraction of the hydrogen protons inside water molecules. Once those protons are lined up, coils in the scanner emit a short burst of radio-frequency waves that cause the protons' magnetic fields to wobble. When the radio burst ends, the protons release energy, sending out a faint echo of the radio waves that is detected by receiver coils and gives a picture of the anatomy of the brain and other tissue.

The stronger the magnetic field, the greater the fraction of protons that become aligned, and the bigger the energy difference between them and those that remain unaligned. This produces a signal that can be better detected over background noise. But every jump in field strength comes with some uncertainty. "At the beginning of the MRI era, many scientists were thinking that 0.5 T would be the maximum magnet strength for MRI" because they thought the ion conductivity of live tissue would stop radio waves from penetrating far enough inside the body, says Victor Schepkin of the US National High Magnetic Field Laboratory in Tallahassee, Florida. Then, the 1980s saw the emergence of 1.5-T scanners for clinical use. And in 2002, 3-T scanners won approval. Even before then, researchers were pushing for higher field strength; the first 7-T research scanners began to emerge in 1999.

"EVEN THE STARTING IMAGES LOOK PRETTY SPECTACULAR."

The move from 3T to 7 T presented some challenges. Biological side effects, although temporary, are more pronounced: people can experience dizziness and vertigo when they move in and out of the scanner, researchers say. When people move inside the machine, they can sometimes taste metal, see white flashes or experience involuntary eye movements called nystagmus.

Tissue can also overheat. Because hydrogen nuclei resonate at higher frequencies as the field strength increases, ultra-high-field MRIs must use shorter-wavelength, and thus higher-energy, radio pulses to make the protons wobble. Human tissue absorbs more energy from these waves. So to avoid creating hotspots — and to make usable images — this energy must be smoothed out as much as possible inside the tube. Researchers have devised various ways of accomplishing this. One tactic, says Gregory Chang, a musculoskeletal radiologist at the New York University School of Medicine, is to generate the pulses using a ring of individually tunable transmitters arrayed around the patient.

The fine resolution is also a mixed blessing, because it makes scanners highly sensitive to the slightest motion. Some repetitive movements in the body, caused by breathing or heartbeats, can be modelled and removed. But Menon says that the biggest challenge at 7 T and above — one that is not present in lower-resolution scanners — is involuntary movements of the brain inside the skull. "If I stretch my toes while I'm in the scanner, my brain will move because my toes are connected through the spinal cord to the brain," Menon says. And thanks to the heartbeats, he adds, the brain pulsates "on the scale of half a millimetre to a millimetre". Tackling these artefacts is an ongoing area of research, he says.

Even so, scientists say, 7 T has already opened a new window onto the living brain, by revealing structures smaller than 1 millimetre. This regime, dubbed the mesoscopic scale by neuroscientists, is something that previously was accessible only by surgeons, says Klaus Scheffler, head of the magnetic-resonance centre at the Max Planck Institute for Biological Cybernetics in Tübingen, Germany. With 7 T, Scheffler says, "you see all the details without opening the brain".

Among the structures that have been revealed are the six layers of the cerebral cortex, the 3-millimetre-thick outer region of the brain that is responsible for humans' high level of cognition. Each layer has a specialization: one handles inputs from other brain areas, some process information and still others convey the outputs of that processing to other parts of the brain. The jump to 7-T machines has enabled researchers to measure the relative activity in different layers, which can reveal how that information is travelling. "That's the huge advance over imaging at 3 T or 1.5 T," says Menon. "Normally, we just say A is connected to B, and we can't tell much about which way the information is flowing."

Some teams have used this capability to measure activity as people undergo verbal and behavioural tests, and the results are illuminating how activity in different layers alters how various areas of the cortex process experiences (S. J. D. Lawrence *et al. NeuroImage* http://doi.org/cwbr; 2017). "It's not just that area A is in charge of vision, but that it is modulated by attention, mood, memory," says Menon. "And those kinds of questions are extremely difficult to answer in animal models. They obviously don't think or verbalize the way we can." Now, with 7-T scans of humans, "a picture of human memory is emerging that was really unavailable before", he says.

Researchers also hope to learn more about the columnar organization of the brain. Cortical columns are thought to carry out computations and respond preferentially to particular stimuli, such as the orientation of objects, although there's fierce debate over their exact role in this context. Measuring roughly 500-micrometres across, the columns run perpendicular to the cortical layers and communicate with each other through connections in one of the middle layers. If MRI could measure brain activity at a columnar level, scientists might be able to use that to draw conclusions about computations in individual neurons. This would be exciting because one of the limitations of MRI is that it can't measure neuronal activity directly.

© 2018 Springer Nature Limited. All rights reserved.

A 10.5-T magnet is delivered to the University of Minnesota in 2013.

CENTER FOR MAGNETIC RESONANCE RESEARCH, UNIV. MINNESOTA

MRI scans at 7 T also provide a better measure of brain connectivity, says Ugurbil, who is involved in the Human Connectome Project. The research effort, which aims to completely map links between neurons in the brain, has performed scans of 184 people at both 3 T and 7 T. At 7 T, they detected many more neural networks and connections between neurons than at 3 T. "In terms of what does that translate into, predicting or studying human diseases, this is still to come," says Ugurbil.

But Ugurbil says that the machines already show promise for clinical diagnosis and treatment. Deep-brain stimulation, which has been used to treat many people with Parkinson's disease, is often administered by inserting an electrode into the subthalamic nucleus, part of the basal ganglia deep inside the brain. MRI is used to help surgeons position the electrode, and once it seems to be in place, the electrode is activated to see whether it hit the correct target. But using 1.5- or 3-T machines, "it's a bit of a fishing expedition", says Ugurbil. "If you're not in the right place, you have to pull out your electrode and insert it again slightly differently." Each time, he says, there is a chance of hitting a blood vessel and causing bleeding. Images taken with 7-T scanners eliminate all this poking around. "You see your target, then you just go: one penetration and you have the result," he says.

Scans done with 7-T machines have also revealed more about the symptoms and progression of multiple sclerosis. New medications for the disease have helped to slow the advance of motor deficits, and the ensuing gain in patients' life expectancy and quality of life has meant that cognitive problems have been noticed for the first time. "A lot of these people have what they might describe as [attention deficit hyperactivity disorder]-like symptoms," says Menon. "We've never understood how that could be until now." Using a 7-T scanner, Menon's group has been able to spot lesions in areas where they previously had not been observed, including the dorsolateral prefrontal cortex, an area responsible for executive function and attention. "Historically, those were quite hard to see," he says. These lesions might explain why the patients develop cognitive symptoms. Menon is involved in a major project "looking at the relationship between cognitive function and the location of lesions", he says.

If greater resolution is not needed, clinicians can also use the higher signal-to-noise ratio in an ultra-high-field MRI to simply scan more quickly, creating images in seconds that would otherwise take minutes, and images in minutes that would otherwise take hours. For patients, this can make a big difference in comfort.

Researchers can also look beyond water. At field strengths of 7 T and higher, MRI can detect not only hydrogen nuclei, but also the nuclei of heavier elements, such as sodium, potassium, phosphorus and fluorine, which have a much lower intrinsic sensitivity to magnetic resonance than hydrogen nuclei do.

Chang has used New York University's 7-T scanner to look at sodium for biochemical changes that might presage osteoarthritis. The evidence suggests that in people with early stages of the disease, he says, "the sodium concentration in their cartilage goes down without any change in the structure of the cartilage". Several other groups have replicated the results in small studies. Chang hopes that if they hold up, the approach could be used to detect osteoarthritis early enough to prevent further damage by making lifestyle modifications and to allow researchers to perform clinical trials more quickly, because they get an early indicator of the disease.

BEYOND 7

The world's most powerful MRI scanner sits in the US National High Magnetic Field Laboratory. With an interior space just 10.5 centimetres in diameter, the 21.1-T machine is too small to be used on people. Schepkin and his colleagues there scan small animals instead. They have used the scanner to study, for instance, the sodium concentration in rat brain tumours, and their results suggest that the amount of sodium present in a tumour can indicate how resistant it would be to chemotherapy (V. D. Schepkin *et al. Magn. Reson. Med.* **67**, 1159–1166; 2012).

At first, Schepkin says, there was some hesitation around using the imager. "We had a rule that nobody can work near the magnet alone," he explains. That rule is no longer in place, but the group does still observe a strict 'no metal' policy.

It took years to prepare the scanner, which was not a fully commercial machine, for animal testing. The process has been similarly slow for many of the new human-research scanners beyond 10 T. The NIH, for example, is currently awaiting the return of its 11.7-T magnet. After it was delivered in 2011, the team turned some of the scanner components on and off too quickly, causing the magnet to overheat and damage some wiring, an imaging researcher at the agency says. The magnet needed a factory rebuild; it is expected back in 2019. The 5-metre-diameter magnet for the 11.7-T MRI at the NeuroSpin Centre in France was delivered last May. The scanner is slated to produce its first scans of live human brains in 2022.

Ugurbil received US Food and Drug Administration clearance in August 2017 to scan 20 people with his 10.5-T MRI (the man in December was the first). He expects to scan the first human brain in a few months. Scans at this field strength are at the point where researchers are not looking to answer any biomedical questions, but simply testing whether the process has any side effects. Still, he says, "even the starting images look pretty spectacular". He is part of a group discussing efforts to reach 20 T in humans.

The amount of heating generated by such machines could be even more problematic. Some researchers have speculated that scanners operating above 14 T could also cause nerve conductance to slow down, stimulate peripheral nerves or damage DNA, although Schepkin says he has seen none of these effects so far in animals, even at 21.1 T. Still, Scheffler thinks that at some point there will be a limit to field strength beyond which we can't go without damaging the body: "I don't think we can go higher and higher forever." ■

Anna Nowogrodzki *is a freelance journalist in Boston, Massachusetts.*

© 2018 Springer Nature Limited. All rights reserved.

COMMENT

ECOLOGY Domestic safari finds rich biodiversity down the back of the sofa **p.31**

HISTORY How the CIA co-opted science in the cold war **p.32**

CORRESPONDENCE Staff at the FAO can advise on data analysis and interpretation **p.35**

OBITUARY Thomas Steitz, ribosome Nobel laureate, remembered **p.36**

TAYLOR WEIDMAN/ZREPORTAGE.COM/ZUMA

A Xikrin woman walks back to her village from the Cateté River in Brazil.

Protect the last of the wild

Global conservation policy must stop the disappearance of Earth's few intact ecosystems, warn **James E. M. Watson, James R. Allan** and colleagues.

A century ago, only 15% of Earth's surface was used to grow crops and raise livestock[1]. Today, more than 77% of land (excluding Antarctica) and 87% of the ocean has been modified by the direct effects of human activities[2,3]. This is illustrated in our global map of intact ecosystems (see 'What's left?').

Between 1993 and 2009, an area of terrestrial wilderness larger than India — a staggering 3.3 million square kilometres — was lost to human settlement, farming, mining and other pressures[4]. In the ocean, areas that are free of industrial fishing, pollution and shipping are almost completely confined to the polar regions[5].

Numerous studies are revealing that Earth's remaining wilderness areas are increasingly important buffers against the effects of climate change and other human impacts. But, so far, the contribution of intact ecosystems has not been an explicit target in any international policy framework, such as the United Nations' Strategic Plan for Biodiversity or the Paris climate agreement.

This must change if we are to prevent Earth's intact ecosystems from disappearing completely.

LAST CHANCE

In 2016, we led an international team of scientists to map the world's remaining terrestrial wilderness[3,4]. This year, we produced a similar map for intact ocean ecosystems[2] (see 'Wild Earth'). The results of these efforts show that time is running out to safeguard the health of the planet — and human well-being.

Some conservationists contend that ▶

© 2018 Springer Nature Limited. All rights reserved.

particular areas in fragmented and otherwise-degraded ecosystems are more important than undisturbed ecosystems[6,7]. Fragmented areas might provide key services, such as tourism revenue and benefits to human health, or be rich in threatened biodiversity. Yet numerous studies are starting to reveal that Earth's most intact ecosystems have all sorts of functions that are becoming increasingly crucial[2,8,9].

Wilderness areas are now the only places that contain mixes of species at near-natural levels of abundance. They are also the only areas supporting the ecological processes that sustain biodiversity over evolutionary timescales[10]. As such, they are important reservoirs of genetic information, and act as reference areas for efforts to re-wild degraded land and seascapes.

Various analyses reveal that wilderness areas provide increasingly important refuges for species that are declining in landscapes dominated by people[11]. In the seas, they are the last regions that still contain viable populations of top predators, such as tuna, marlins and sharks[9].

Safeguarding intact ecosystems is also key to mitigating the effects of climate change, which are making the refuge function of wilderness areas especially important. A 2009 study, for instance, showed that Caribbean coral reefs that have low levels of pollution or fishing pressure recovered from coral bleaching up to four times faster than did reefs with high levels of both[12]. And a 2012 global meta-analysis revealed that the impacts of climate change on ecological communities are more severe in fragmented landscapes[13].

Many wilderness areas are critical sinks for atmospheric carbon dioxide. For example, the boreal forest is the most intact ecosystem on the planet and holds one-third of the world's terrestrial carbon. And intact forested ecosystems are able to store and sequester much more carbon than are degraded ones[8]. In the tropics, logging and burning now accounts for up to 40% of total above-ground carbon emissions[14]. In the ocean, seagrass meadows that are degraded (such as by sediment pollution) switch from being carbon sinks to major carbon sources[15].

Moreover, models based on geography, rainfall, degree of deforestation and so on are starting to reveal the degree to which wilderness areas regulate the climate and water cycles — locally, regionally and globally. Such areas also provide a buffer against extreme weather and geological events. Simulations of tsunamis, for instance, indicate that healthy coral reefs provide coastlines with at least twice as much protection as highly degraded ones[16].

Wilderness regions are home to some of the most politically and economically marginalized indigenous communities on Earth. These people (who number in the hundreds of millions) are reliant on intact marine and terrestrial ecosystems for resources such as food, water and fibre[17]. Many have established biological and cultural connections with their environment over millennia. Securing the wilderness is central to reducing their poverty and marginalization — and to achieving numerous UN Sustainable Development Goals, from reducing inequality to improving human well-being.

GLOBAL TARGETS

We believe that Earth's remaining wilderness can be protected only if its importance is recognized within international policy frameworks.

Currently, some wilderness areas are protected under national legislation such as the 1964 US Wilderness Act, which protects 37,000 km^2 of federal land. But in most nations, these areas are not formally defined, mapped or protected, and there is nothing to hold nations, private industry, civil society or local communities to account for their long-term conservation. What is needed is the establishment of global targets within existing international frameworks — specifically, those aimed at conserving biodiversity, avoiding dangerous climate change and achieving sustainable development.

There are several ways to do this immediately. The carbon sequestration and storage capacities of wilderness areas could be formally documented, and the importance of conserving them written into the policy recommendations of the UN Framework Convention on Climate Change (UNFCCC). Such a move would enable nations to make the protection of wilderness areas an integral part of their strategy for reducing emissions.

As an example, under the UNFCCC process for reducing emissions from deforestation and forest degradation (REDD+), landowners can be compensated if they refrain from clearing an area of tropical forest that they'd planned to develop. However, there are no incentives for nations, private industry or communities to protect crucial carbon sinks, even when no imminent development is identified. This means that there is nothing to stop the slow erosion of these places from small-scale and often unplanned industrial activity. Similar policies are needed to protect other carbon-rich ecosystems, such as seagrass meadows, and temperate and boreal forests, especially in developed countries that do not currently receive financial support under the UNFCCC.

Later this month, Egypt will host the 14th gathering of the Conference of the Parties to the Convention on Biological Diversity (CBD). Signatory nations, intergovernmental organizations such as the International Union for Conservation of Nature (IUCN), non-governmental organizations and the scientific community will meet to work towards a strategic plan for the protection of biodiversity after 2020. We urge participants at the meeting to

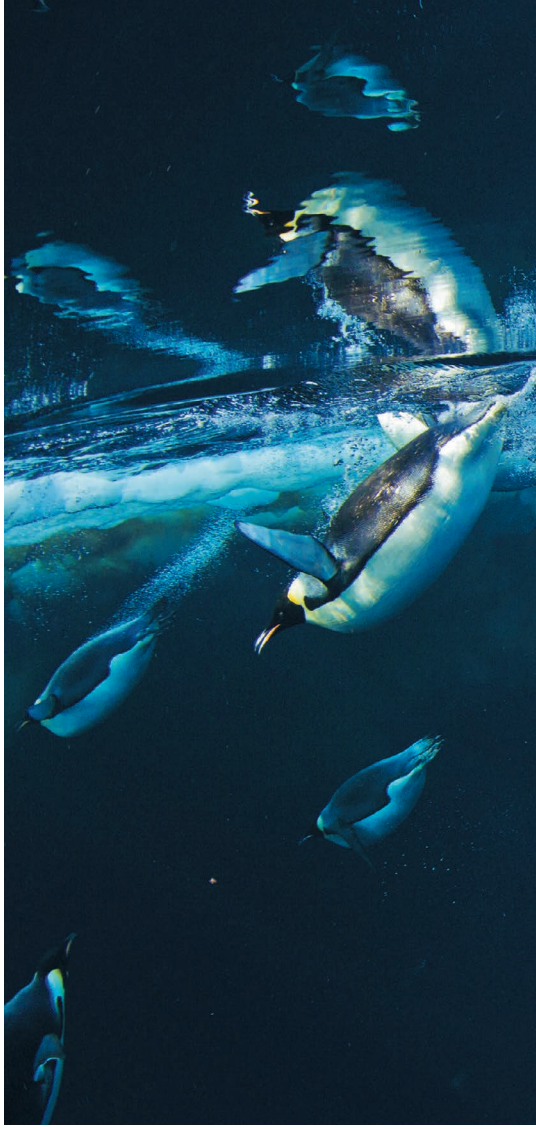

WILD EARTH

Mapping methods

To map Earth's remaining terrestrial wilderness, we used the best available data on eight indicators of human pressures at a resolution of 1 square kilometre. These were: built environments, crop lands, pasture lands, population density, night-time lights, railways, major roadways and navigable waterways[3,4]. (Data were collected in 2009.) For our map of intact ocean ecosystems, we used 2013 data on fishing, industrial shipping and fertilizer run-off, among 16 other indicators[2].

We identified wilderness land or ocean areas as those that were free of human pressures, with a contiguous area of more than 10,000 km^2 on land.

J.E.M.W. *et al.*

© 2018 Springer Nature Limited. All rights reserved.

Emperor penguins in the Ross Sea.

PAUL NICKLEN/NGC

include a mandated target for wilderness conservation. In our view, a bold yet achievable target is to define and conserve 100% of all remaining intact ecosystems.

A mandated global target will make it easier for governments, non-governmental organizations and entities such as the Global Environment Facility (a multinational funding programme that tackles environmental and sustainability problems) to leverage funding and mobilize action on the ground.

It will also help to enable action under the various conventions that are attempting to protect biodiversity. For example, officially recognizing the contribution that the wilderness makes to the 'outstanding universal value' of certain areas could lead to the designation of new Natural World Heritage Sites.

Under the UN World Heritage Convention, Natural World Heritage Sites are currently selected for their outstanding natural beauty, or because they contain unique biodiversity or ecological and geological features. The wilderness is associated with all of these criteria, but its importance has yet to be specifically acknowledged.

Almost two-thirds of marine wilderness lies in international waters, beyond the immediate control of nations. The United Nations Convention on the Law of the Sea is currently negotiating a legally binding agreement to govern high-seas conservation. Keeping Earth's remaining marine wilderness off-limits to exploitation should be a key component of the new treaty. Strict limits on government subsidies of harmful fishing will also be crucial here; without these, more than half of high-seas industrial fishing would be unprofitable[18].

Our maps exclude Antarctica because it is off-limits to direct resource exploitation such as mining, and the indirect effects of human activities there are harder to measure. But it is a crucial wilderness area that is urgently in need of protection. Antarctica's isolation and extreme conditions have prevented the levels of degradation experienced elsewhere. But invasive species, pollution, increased human activity and, above all, climate change are threatening its unique biodiversity and its ability to regulate the global climate.

"Mechanisms that enable the private sector to protect, rather than harm, wilderness areas will be crucial."

The Antarctic Treaty System's Committee for Environmental Protection has prioritized research and action targeted at minimizing human impacts in its latest five-year plan. Signatory nations must now commit to implementing measures targeted at reducing human impacts, such as strict biosecurity procedures that minimize the risk of visitors to Antarctica introducing invasive species.

LOCAL ACTION

How can changes in policy at the global level translate into effective national action?

By our measure, 20 countries contain 94% of the world's remaining wilderness (excluding the high seas and Antarctica). More than 70% is in just five countries — Russia, Canada, Australia, the United States and Brazil (see 'What's left?'). Thus, the steps these nations take (or fail to take) to limit the expansion of roads and shipping lanes, and to rein in large-scale developments in mining, forestry, agriculture, aquaculture and industrial fishing, will be critical.

One obvious intervention that these nations can prioritize is establishing protected areas in ways that would slow the impacts of industrial activity on the larger landscape or seascape[19]. Given the scale of wilderness areas, however, the expansion of strictly enforced protected areas won't suffice.

Several studies show that stopping industrial development to protect the livelihoods of indigenous people can conserve biodiversity and ecosystem services just as

© 2018 Springer Nature Limited. All rights reserved.

well as strictly protected areas can. As such, the recognition of local community rights to land ownership and management could be a key way to limit the impacts of industrial activity[8].

Mechanisms that enable the private sector to protect, rather than harm, wilderness areas will be crucial. Specifically, the preservation of intact ecosystems needs to feature among lenders' investment and performance standards, particularly for organizations such as the World Bank, the International Finance Corporation and the regional development banks. Initiatives that enable companies to declare their supply chains 'deforestation-free' (such as for products containing palm oil) should be expanded to help to secure more intact ecosystems.

In the oceans, regional fisheries management organizations (RFMOs), formed by countries to manage shared fishing interests, have effectively closed large areas of the high seas. For example, the North East Atlantic Fisheries Commission (an RFMO founded in 1980) has shut more than 350,000 square kilometres of the Atlantic to bottom trawling. The power of RFMOs could be increased to enable the creation of broader, scaled-up conservation agreements for the high seas.

Wild places are facing the same extinction crisis as species. Similarly to species extinction, the erosion of the wilderness is essentially irreversible. Research has shown that the first impacts of industry on wilderness areas are the most damaging[11]. And once it has been eroded, an intact ecosystem and its many values can never be fully restored.

As US President Lyndon B. Johnson observed when he signed the US Wilderness Act in 1964, "If future generations are to remember us with gratitude rather than contempt … we must leave them a glimpse of the world as it was in the beginning."

Already we have lost so much. We must grasp this opportunity to secure the wilderness before it disappears forever. ■

WHAT'S LEFT?

Earth's remaining wilderness areas are becoming increasingly important buffers against changing conditions in the Anthropocene. Yet they aren't an explicit target in international policy frameworks.

THE HUMAN FOOTPRINT

77% of land (excluding Antarctica) and 87% of the ocean has been modified by the direct effects of human activities.

REMAINING WILDERNESS: ■ Terrestrial ■ Marine

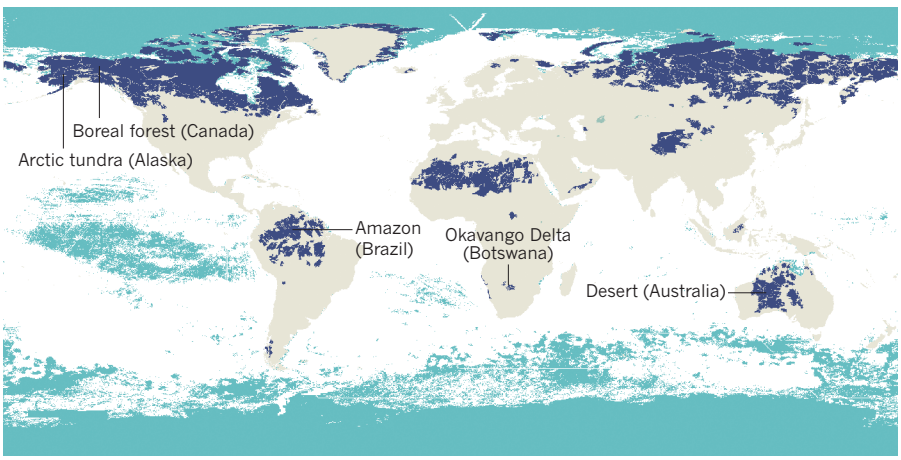

THE WILDEST COUNTRIES

Twenty countries contain 94% of the world's wilderness, excluding Antarctica and the high seas.

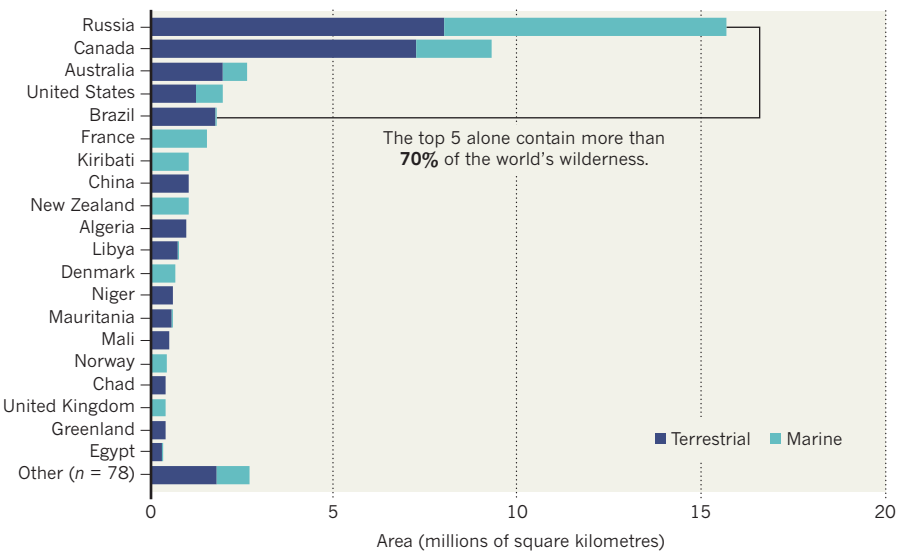

SOURCE: REFS 2 & 3

James E. M. Watson *is a professor of conservation science at the University of Queensland, and director of the Science and Research Initiative at the Wildlife Conservation Society, Bronx, New York, USA.* **Oscar Venter** *is an associate professor at the Natural Resource and Environmental Studies Institute, University of Northern British Columbia, Prince George, Canada.* **Jasmine Lee** *is a PhD candidate in the School of Biological Sciences, University of Queensland, St Lucia, Australia.* **Kendall R. Jones** *is a conservation planning specialist and* **John G. Robinson** *is executive vice-president of conservation and science at the Wildlife Conservation Society, Bronx, New York, USA.* **Hugh P. Possingham** *is chief scientist at The Nature Conservancy, Arlington, Virginia, USA.* **James R. Allan** *is a postdoctoral research fellow in the School of Biological Sciences, University of Queensland, St Lucia, Australia.*
e-mails: jwatson@wcs.org; james.allan@uqconnect.edu.au

1. Klein Goldewijk, K., Beusen, A., van Drecht, G. & de Vos, M. *Glob. Ecol. Biogeogr.* **20**, 73–86 (2011).
2. Jones, K. R. *et al. Curr. Biol.* **28**, 2506–2512 (2018).
3. Allan, J. R., Venter, O. & Watson, J. E. M. *Sci. Data* **4**, 170187 (2017).
4. Watson, J. E. M. *et al. Curr. Biol.* **26**, 2929–2934 (2016).
5. Halpern, B. S. *et al. Nature Commun.* **6**, 7615 (2015).
6. Kareiva, P. & Marvier, M. *BioScience* **62**, 962–969 (2012).
7. Ricketts, T. H. *et al. Proc. Natl Acad. Sci. USA* **102**, 18497–18501 (2005).
8. Watson, J. E. M. *et al. Nature Ecol. Evol.* **2**, 599–610 (2018).
9. D'agata, S. *et al. Nature Commun.* **7**, 12000 (2016).
10. Soulé, M. E. *et al. Pacific Conserv. Biol.* **10**, 266–279 (2004).
11. Betts, M. G. *et al. Nature* **547**, 441–444 (2017).
12. Carilli, J. E., Norris, R. D., Black, B. A., Walsh, S. M. & McField, M. *PLoS ONE* **4**, e6324 (2009).
13. Mantyka-pringle, C. S., Martin, T. G. & Rhodes, J. R. *Glob. Change Biol.* **18**, 1239–1252 (2012).
14. Houghton, R. A., Byers, B. & Nassikas, A. A. *Nature Clim. Change* **5**, 1022–1023 (2015).
15. Howard, J. *et al. Front. Ecol. Environ.* **15**, 42–50 (2017).
16. Kunkel, C. M., Hallberg, R. W. & Oppenheimer, M. *Geophys. Res. Lett.* **33**, L23612 (2006).
17. Millennium Ecosystem Assessment. *Ecosystems and Human Well-Being: Current State and Trends* (Island Press, 2005).
18. Sala, E. *et al. Sci. Adv.* **4**, eaat2504 (2018).
19. Watson, J. E. M., Dudley, N., Segan, D. B. & Hockings, M. *Nature* **515**, 67–73 (2014).

© 2018 Springer Nature Limited. All rights reserved.

EYE OF SCIENCE/SPL

A bedbug pictured in an image from a scanning electron microscope.

ECOLOGY

There's a jungle in your bed

William Foster enjoys Rob Dunn's hymn to the life in our homes and on our bodies.

Rob Dunn invites us on a safari in pursuit of the wildlife teeming on our bodies and in every corner of our homes. For him, the creatures that sprawl in the human navel and under the bathroom shower head elicit the kind of wonder most of us would feel only on seeing the denizens of Tanzania's Ngorongoro Crater or the Great Barrier Reef off Australia. Dunn is more than an informed and entertaining commentator, a David Attenborough of domestic biodiversity. He is a scientist whose research group at North Carolina State University in Raleigh made many of the discoveries described in his fascinating and illuminating book, *Never Home Alone*.

Dunn and his colleagues have used the concepts and techniques of community ecology to tease apart the functioning of a mostly ignored ecosystem: the human home. Their research enriches our understanding of ecosystem function, and — more grippingly — gives us insight into how our interactions with living things in the domestic habitat affect our health and well-being. The book is structured around sub-habitats in our homes — our bodies, rooms, water supply, pets and food. It considers an awesome range of organisms, from the rich fungal flora on bakers' hands to the diversity of fly larvae in our drains.

We discover that warm, moist shower heads are ideal for the growth of biofilms containing trillions of bacteria, including *Mycobacterium* species that are harmful to human health. Dunn and his colleagues invited thousands of volunteers globally to send in samples from their bathrooms. The researchers are finding, for instance, that the more a water supply is treated with chemicals designed to kill microbes, the greater the abundance of pathogenic strains of mycobacteria. We also learn that the numbers of plant and butterfly species in our gardens are correlated with the robustness of the community of microbes on our skin; that some German cockroaches have evolved to perceive glucose as bitter, thus avoiding poisoned bait; and that dogs can give us both heartworm and a top-up of beneficial bacteria from their microbiomes.

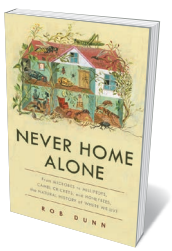

Never Home Alone: From Microbes to Millipedes, Camel Crickets, and Honeybees, the Natural History of Where We Live
ROB DUNN
Basic (2018)

The message of *Never Home Alone* is clear. The health of an ecosystem depends on its biodiversity: this is as true of our homes as of a mangrove swamp. Two factors, notes Dunn, are important. Simply by chance, a home containing more species is more likely to include organisms (especially microbes) that are vital in sparking our immune systems into life. And an ecosystem with niches fully occupied by diverse species is likely to be resilient and resistant to invasion by pests and pathogens.

We rightly fear the handful of domestic species that can harm us, such as lice and *Legionella* bacteria. But all-out chemical warfare is not a viable defence. It scythes down thousands of other species, and the target rapidly evolves resistance and flourishes on the blank slate we have thoughtlessly provided. This story is familiar from the overuse of antibiotics and pesticides, but Dunn's book is the first to apply it across the range of domestic wildlife, from bacteria to bedbugs.

Dunn is a man on a mission. He is determined to recruit others to his research programme, to hunt for camel crickets in basements and to send samples of armpit flora, face mites or sourdough starters. He champions citizen science — as long as ▶

© 2018 Springer Nature Limited. All rights reserved.

the citizens have curiosity and focus. The book opens and closes with a supreme exemplar of a lay scientist: seventeenth-century Dutch businessman Antonie van Leeuwenhoek, who pioneered microscopy and discovered bacteria and protozoa, opening up the universe of microbiology. His discoveries — based on everyday substances in his Delft home, such as saliva — and the wonder they excited in him epitomize the ideas in *Never Home Alone*.

Just one of Dunn's arguments fails to convince. He asserts that some organisms, such as fruit flies and house mice, are important because they have become iconic model lab species, or because, like the *Penicillium* fungus, they could be sources of drugs. He suggests that by understanding the biology of, for example, domestic camel crickets — which thrive on very poor diets — we might learn new ways of breaking down intractable materials such as plastic. Quite so; but none of it depends on the fact that these organisms can be found in homes. Biologists find useful animals anywhere, from the axolotl to the hagfish and the *Xenopus* frog.

The results of the projects described are important. The indoor biome is huge. Humans are an urbanizing species, and in most cities, the combined floor space of homes and apartments exceeds that of the ground space outside. If we are to chart a harmonious settlement with the species living with us, we need to understand as much as possible about them.

I think this research has even broader significance. Since the Darwinian revolution, we have accepted that, biologically, we are one species among millions, subject to the same laws of evolution by natural selection. It is less clear that we have accepted that we are also subject to the same ecological laws. We know we can control, disrupt and destroy the ecosystems of the world, but we tend to imagine that we do so from inside a hermetically sealed personal bubble. By reframing our homes and selves as ecosystems, we are forced to contemplate how we fit in with the complex community of organisms with whom we share our lives.

The book has one final message. We have "farsighted" ecologists (Dunn's term), whose eyes are fixed on the distant, charismatic ecosystems of rainforest and coral reef. We also need near-sighted ones who will study the half-hidden communities closely quartered with us in our homes. This book is their battle cry. ■

William Foster *is emeritus curator of insects at the University Museum of Zoology, Cambridge, UK; director of alumni relations in the Department of Zoology; and a fellow of Clare College.*
e-mail: waf1@cam.ac.uk

SPUTNIK/SPL

UK crystallographer Dorothy Hodgkin and Soviet physicist Moisey Markov at a 1983 Pugwash conference.

HISTORY

The covert politics of cold-war science

Ann Finkbeiner reflects on an era when research and education were co-opted to promote a government line.

In the late 1950s, students in a Hong Kong school were dissecting local earthworms and labelling the parts to match diagrams in a British textbook — even though the worms in Britain and Hong Kong were anatomically different. Watching the children, US herpetologist and educator Arnold Grobman noted that they were being directed to follow the textbook over their own observations.

The students' reliance on authority was not what worried Grobman. The real danger, he said, is that this choice "left the students vulnerable to the influence of Communism".

So begins science historian Audra Wolfe's *Freedom's Laboratory*, a study of how the United States won the cold war partly by embracing and promoting ideals embraced by science itself. Today, equating unquestioning trust in authority with vulnerability to Communism sounds overwrought. But at the time, the tense stand-off between the Soviet Union and the United States (which ran roughly from 1947 to 1989) was ramping up. Almost simultaneously with the start of the cold war, the Soviet Communist Party endorsed a pseudoscientific stance: Lysenkoism, the political campaign to reject Mendelian genetics, headed by agronomist Trofim Lysenko. Stocks of *Drosophila* fruit flies for research were destroyed, and Soviet geneticists were fired, imprisoned, exiled or executed.

Freedom's Laboratory: The Cold War Struggle for the Soul of Science
AUDRA J. WOLFE
John Hopkins University Press (2018)

One US countermeasure against Communism, as Wolfe shows, was to present democracy as a bastion of scientific freedom for nations aligned against a totalitarian state. This message fitted the ideals of scientists and scientific institutions, so they went along with it. Scientists are ideally driven by curiosity and logic, not politics. But politics, writes Wolfe, were crucial to how the US government "constructed and maintained" the equation of science with freedom.

This politicization took advantage of scientists' habits of international collaboration. In the early 1950s, the US government, in particular the Department of State and the CIA, tried using independent scientists as attachés — actually, spies. This mirrored Soviet practice. (I recall old US physicists' stories of visiting Soviet scientists announcing that they needed to take photos of, say, local military depots.) As Wolfe shows, however, the US scientist-spies proved ineffective.

Meanwhile, the State Department, CIA and National Academy of Sciences sponsored international conferences and travel to promote scientific freedom. The US government also used the international Pugwash

© 2018 Springer Nature Limited. All rights reserved.

organization, a group of nuclear scientists who promoted disarmament, to demonstrate the virtues of independent Western science.

Another avenue for politicizing science was education. In the early 1960s, the CIA, through a wide-ranging Asian–American partnership called the Asia Foundation, supported the high-school Biological Sciences Curriculum Study (BSCS). This taught pupils to ask their own questions, make their own observations and come to their own conclusions. Translations of the BSCS were promoted internationally and ultimately used in 35 countries. "Lysenko's name is never stated explicitly in these texts," writes Wolfe, but the "emphasis on rejecting received knowledge" is implicit throughout.

In 1967, the CIA's involvement in "youth groups, organized labor, cultural organizations, and private foundations" such as the Asia Foundation became public. Amid uproar, the administration of US president Lyndon B. Johnson announced the end of covert CIA support of private institutions. Some scientists were chagrined by what they saw as a cynical use of science in propaganda. The programmes, dubbed "CIA orphans", could not be overtly re-funded by the government or foundations. So the government looked for 100 "private voluntary organizations that 'did the kind of work'" the orphans had done. The Asia Foundation ended up being funded by the State Department.

With covert shenanigans suspended and the US government out of the "hearts and minds" business, the focus of the conflict between free and state-approved science moved to Soviet dissident scientists, including nuclear physicist Andrei Sakharov, who campaigned for human rights and was later arrested. Now scientists on both sides were acting not as agents of states, but as individuals — writing letters, raising funds, boycotting, signing petitions, lobbying, protesting. "By 1980," Wolfe writes, "there was only one 'science' and it looked remarkably like the vision advanced by the West." Sakharov was freed in 1986, the Soviet Union collapsed in 1991, and the cold war was over for good.

How, in hindsight, to assess this history? Were the scientists who worked knowingly or unknowingly with the government either collaborators or dupes? Cold-war history, Wolfe writes, is not a heroes-and-villains narrative: it must be told in "shades of gray". The government used scientists' ideals for its own political reasons. And the scientists, who saw themselves as apolitical, used the government's political messages and support to question, observe, conclude, write and speak — freely and in accord with their ideals. ■

Ann Finkbeiner *is a freelance science writer in Baltimore, Maryland, and author of* The Jasons. *She blogs at www.lastwordonnothing.com.*
e-mail: anniekf@gmail.com

Books in brief

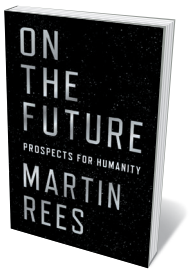

On the Future
Martin Rees PRINCETON UNIVERSITY PRESS *(2018)*
UK astronomer royal Martin Rees faces the future as scientist, citizen and "worried member of the human species". His bold, beautifully synthesized primer paces from human-driven challenges such as climate change to dizzying astronomical discoveries within and beyond the Solar System. Rees celebrates technological advance, but warns of the potential for abuse, reminding us that the benefits of progress can dim in the face of inequity and natural catastrophes. And he argues that a yen for Martian colonies must not leave Earth in the dust. A clarion call for global, rational, long-term thinking.

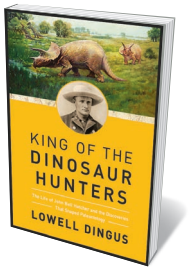

King of the Dinosaur Hunters
Lowell Dingus PEGASUS *(2018)*
By his death in 1904, US palaeontologist John Bell Hatcher had unearthed a vast trove of fossils, including scientifically important *Triceratops* remains and 66-million-year-old mammal teeth. His finds went on to seed prestigious US collections such as that in the Carnegie Museum of Natural History in Pittsburgh, Pennsylvania. Palaeontologist Lowell Dingus exhaustively tracks Hatcher's short but storied life, from early work for luminaries such as Othniel Charles Marsh to the astounding digs in fossil hotspots from Kansas to Patagonia that studded Hatcher's starry scientific trajectory.

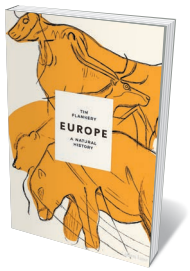

Europe: A Natural History
Tim Flannery ALLEN LANE *(2018)*
Some 100 million years ago, Europe was a tropical archipelago and, as a bridge between Africa, Asia and North America, a migratory hotspot. It became a protean, fecund region for hybridization. Palaeontologist Tim Flannery's natural history takes us from the dinosaurs' demise 66 million years ago to today. We meet the four-tusked elephant-like gomphothere, the nimravid (a sabre-toothed cat), and the hominin *Graecopithecus* (by way of footprints left on what is now Crete, 5.7 million years ago). The litany of extinctions ends in de-extinction projects such as the 'mammophant'. A rich, illuminating journey.

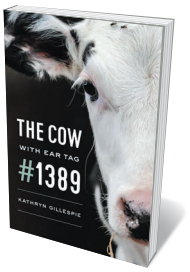

The Cow with Ear Tag #1389
Kathryn Gillespie UNIVERSITY OF CHICAGO PRESS *(2018)*
What price a glass of milk? In this trenchant examination of the dairy industry, animal-studies researcher Kathryn Gillespie investigates its workings, wastefulness (farmers in the US Midwest and Northeast dumped 300 million litres of milk in early 2017) and impacts on the environment, such as leaks from manure lagoons. Gillespie's central focus, however, is the effect on the cows, bulls and calves involved, before their inevitable slaughter. Her careful field research in auction yards and slaughterhouses shows how commodification of animals too often leads to severe, and disturbing, health and welfare issues.

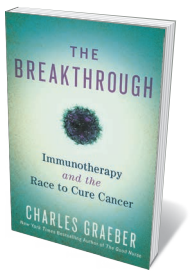

The Breakthrough: Immunotherapy and the Race to Cure Cancer
Charles Graeber TWELVE *(2018)*
In this deft, detailed study of cancer immunotherapy, journalist Charles Graeber traces the breakthroughs leading to cutting-edge treatments today. Interwoven with the advances and portraits of researchers and patients is a fascinating backstory of medics who, from the late nineteenth century onwards, saw a link between infection and spontaneous regression of cancers. From the once-discredited pioneer William Coley to immunologist and Nobel laureate James P. Allison, they form a brilliant, driven, admirably stubborn group that Graeber brings vividly to life. **Barbara Kiser**

© 2018 Springer Nature Limited. All rights reserved.

Correspondence

Get more out of FAO statistics

Papers on the sustainability of food systems (M. Springmann *et al. Nature* http://doi.org/gfb7ht; 2018) and the impacts of land use on global carbon budgets (G. Grassi *et al. Nature Clim. Change* **8**, 914–920; 2018) are among the latest examples of high-profile publications that rely on statistics compiled by the Food and Agriculture Organization of the United Nations (FAO). Authors of such high-profile publications might not always realize that they can find out more about the strengths and limitations of their data by engaging directly with the FAO.

The FAO disseminates statistics collected over more than 50 years for crop, livestock, forestry and fisheries production, and for trade, food security and balance sheets, land and water use, emissions and fertilizers (http://www.fao.org/faostat/en). It supports capacity development in more than 180 countries and territories to improve the collection and processing of national statistical information. And it disseminates all such data as common public goods — free of charge to users worldwide.

FAO specialist staff are on hand to advise researchers on any uncertainties or limitations relating to these national statistics. This service can help them to improve their analyses and to identify emerging data needs.

Francesco N. Tubiello *Food and Agriculture Organization of the United Nations, Rome, Italy.*
francesco.tubiello@fao.org

Risks of WHO listing traditional medicine

The World Health Organization's decision to include traditional oriental medicines in its International Statistical Classification of Diseases and Related Health Problems effectively approves them for primary medical care (see *Nature* **561**, 448–450; 2018). In my opinion, incorporating such contentious treatments into these guidelines is risky.

The antimalarial artemisinin is so far a lone active compound to emerge from the multi-billion-dollar industry of traditional oriental medicines. Active ingredients in such medicines need to be identified by rational investigation based on the scientific method. A long tradition doesn't obviate the need for evidence: the galenic concoctions popular in ancient Greece were discarded with good reason.

Irrespective of their cultural origins, medicines should improve people's lives. Legitimizing traditional oriental medicines at this point could cause sick people to forgo proven treatments and subject them to unknown and unnecessary side-effects. And because some of the treatments come from endangered species, it also risks driving animals such as the rhino to extinction.

Andreas Bietz *University of Heidelberg, Germany.*
bietz@stud.uni-heidelberg.de

Good leaders boost ethical science

Mariam Aly's laboratory manual and wiki collate multiple layers of information and guidance for her team members (see *Nature* **561**, 7; 2018). Translating research processes from scholarly concepts into good laboratory practice in this way aligns with established principles in effective leadership. In my view, investigators prepared to go that extra mile to help their teams are more likely to run ethical labs and produce better science.

Aly's advice on promoting the reproducibility of results and participation in open science — both topics frequently overlooked in education — safeguards against ethical lapses. By setting baseline expectations, openly sharing information and stimulating collaboration, she creates a more productive research environment.

Lab leaders need strong interpersonal skills to foster a culture of integrity — for example, by effectively handling difficult conversations, negotiating around shared interests and encouraging members to declare mistakes before they escalate.

Elizabeth A. Luckman *University of Illinois at Urbana-Champaign, Illinois, USA.*
eluckman@illinois.edu

Brighten outlook for long-term studies

Many governments have a legal obligation to monitor the status of their wildlife populations — for example, to document the effects of climate change or habitat loss on population numbers, structures, breeding success and survival. These are long-term studies, so funding can be challenging — particularly when government priorities shift.

My experience from a 46-year study of guillemots (*Uria aalge*) on Skomer Island in Wales has taught me the value of well-designed and well-managed population-monitoring programmes, which amount to a health check on the oceans.

After the Welsh government (through Natural Resources Wales) cut my modest, but adequate, funding four years ago, I was forced to turn to crowdfunding from a sympathetic public to support the continued monitoring of this vulnerable species (T. Birkhead *Nature* **514**, 405; 2014). I considered it essential not to lose track of the ongoing change in its populations.

Researchers are increasingly having to turn to alternative funding sources to keep their long-term studies going. Although crowdfunding has the advantage that it cannot be top-sliced or taxed, there is a risk that the more ecologists resort to it, the less inclined governments will be to provide financial support. However, it could end up as the only way to sustain long-term investigations.

Tim R. Birkhead *University of Sheffield, UK.*
t.r.birkhead@sheffield.ac.uk

Cure lure of India's predatory journals

The number of papers published in Indian predatory journals is still alarmingly high (see *Nature* **560**, 537–538; 2018) — despite the dramatic decline in such journals (from 518 to 254) over the past 5 years, and India's consequent fall from 4th to 15th in the Directory of Open Access Journals' ranking.

Simply excising predatory open-access journals from the government's current list of approved research journals is not enough. Its University Grants Commission also needs to prevent others from creeping in — for example, by appointing a committee to annually review the journals on the list. The commission could also organize workshops that raise researchers' awareness of predatory journals and dissuade them from using these to boost their publication record.

Jagadeesh Bayry *Institut National de la Santé et de la Recherche Médicale, Paris, France.*
jagadeesh.bayry@crc.jussieu.fr

CONTRIBUTIONS

Correspondence may be submitted to **correspondence@nature.com** after consulting the author guidelines and section policies at **http://go.nature.com/cmchno**.

© 2018 Springer Nature Limited. All rights reserved.

Thomas A. Steitz

(1940–2018)

Crystallographer who shared the ribosome Nobel.

One Nobel prize sometimes leads to another. As a student in 1963, Thomas Steitz heard Max Perutz talk about the structure of myoglobin, the first protein to be solved at the resolution of individual atoms. Perutz had shared the Nobel Prize in Chemistry the year before with his colleague John Kendrew, of the MRC Laboratory of Molecular Biology in Cambridge, UK. Steitz later recalled that he was stunned, thanks to the diminutive Perutz's stereoscopic slides, to see the structure "pop out in three dimensions over Max's head".

Grasping that this technique could answer questions about the molecular basis of life, Steitz joined a protein crystallography lab for his doctoral research. His scientific insight and deft hand with the notoriously tricky experiments led him eventually to the Sterling Professorship of Molecular Biophysics and Biochemistry at Yale University in New Haven, Connecticut.

In 2009, he received his own Nobel Prize in Chemistry (shared with Venkatraman Ramakrishnan and Ada E. Yonath) for his contribution to solving the immensely complex structure of the ribosome, the structure that translates genetic information into proteins in cells.

Steitz had an unerring eye for important problems. He set himself the task of unravelling the molecular basis of what Francis Crick had dubbed the central dogma of biology: that genes, made of DNA, direct the production of proteins through the mediation of RNA. His early work confirmed predictions that enzymes would change their 3D shape on binding to their substrates, and this led to work on interactions between proteins and nucleic acids. His group was the first to solve the structure of a protein that binds to DNA (a transcription factor), and the first to solve the structure of one of the enzymes that synthesizes DNA molecules, a DNA polymerase.

Born and raised in Milwaukee, Wisconsin, Steitz spent his school holidays picking radishes and weeding onions on his grandfather's nearby farm. At his local high school, he played the saxophone in the school band, and briefly considered becoming a professional musician. Instead, he won a scholarship to Lawrence College, a small liberal-arts school in Appleton, Wisconsin, where

LUCAS JACKSON/REUTERS

he majored in chemistry but also took courses in a range of humanities subjects. This brought opportunities to question the narrow beliefs of his upbringing, and to experience laboratory research.

At a summer school in Cambridge, Massachusetts, taught by faculty members from Harvard University and the Massachusetts Institute of Technology, he came across the field of biophysics and decided to go to Harvard for his doctoral work in that field. It was in his first year at Harvard that he had the lecture-room epiphany that determined the course of his career. He joined the lab of 'The Colonel' William Lipscomb, and became a protein crystallographer, helping to solve the structure of the versatile enzyme carboxypeptidase A.

On receiving his PhD, Steitz married fellow Harvard graduate student, Joan Argetsinger. She had been working on bacteriophage RNA in the laboratory of James Watson. Argetsinger was also a Midwesterner with a bachelor's degree from a small liberal-arts college; their careers continued to progress independently, yet in parallel. Both went to the United Kingdom for postdoctoral work at the MRC Laboratory of Molecular Biology. Tom worked with David Blow on interactions of the enzyme chymotrypsin with its substrates, and Joan with Francis Crick, Sydney Brenner and Mark Bretscher on messenger RNA.

Tom started an assistant professorship at the University of California, Berkeley, but soon resigned, on the grounds that the institution would not accept Joan into a faculty position because she was a woman. Yale was only too pleased to recruit them both, and from 1970, they each developed their own research groups. Tom's was part of the Yale Center for Structural Biology, with colleagues including Donald Engelman and Peter Moore. He continued to work on enzymes and their substrates, increasingly focusing on enzymes involved in DNA synthesis and RNA transcription.

In 1995, he began to collaborate with Moore on the structure of the ribosome, the 'final frontier' in sorting out the molecular basis of the central dogma. By 2000, their team had solved the structure of the '50S subunit' of the bacterial ribosome, the part that assembles amino acids into proteins.

This immediately clarified the action of antibiotics that work by binding to this subunit in the bacterial cell and inhibiting the synthesis of proteins. Steitz and his team founded a company, Rib-X Pharmaceuticals (now Melinta Therapeutics, in New Haven), to develop new antibiotics targeting the same binding site.

Steitz was genial, generous and gregarious, and a scientific mentor to many. His beard gave him the look of an Amish farmer or a New England whaler. As well as music, he loved sport and the outdoors, playing baseball with his son Jon (who later became a professional player); impersonating his wife as 'Dr Steitz' to gain access to the tennis courts of the University of Cambridge college that had admitted her as its first woman member; and skiing with scientific friends and their families.

He was not deflected from his fascination with new problems, either by the demands of his status as a Nobel laureate or by the diagnosis of pancreatic cancer that led to his death on 9 October. His long-standing colleague Peter Moore called him "the most accomplished structural biologist of his generation". ■

Georgina Ferry *is a science writer specializing in the history of the life sciences in Oxford, UK. Her many books include biographies of the crystallographers Dorothy Hodgkin and Max Perutz.*
e-mail: mgf@georginaferry.com

© 2018 Springer Nature Limited. All rights reserved.

NEUROSCIENCE

A picture of diversity

A single-cell sequencing study reveals how different types of neuron are distributed in the brain. An analysis then demonstrates how these data can improve our understanding of neuronal functions. SEE ARTICLES P.72 & P.79

APARNA BHADURI & TOMASZ J. NOWAKOWSKI

Imagine an art curator preparing for an exhibition. Paintings in the gallery can be arranged into various ensembles — for example by artist, medium, style or theme. Similarly, neurons can be categorized according to a variety of features, such as their size, shape or location in the brain. Writing in *Nature*, Tasic *et al.*[1] (page 72) and Economo *et al.*[2] (page 79) delve deep into the gallery of neuronal types in the cortex of the mouse brain, and use cutting-edge technologies to uncover previously unknown facets of these cells.

Around the turn of the twentieth century, Spanish neuroscientist Santiago Ramón y Cajal created a 'portrait gallery' of neurons by carefully examining slices of brain tissue to produce detailed drawings of the cells that captured their diverse shapes. Since then, neurons have been further characterized using measurements of shape, physiology or function. Now, technologies to analyse the gene-expression profile of single cells enable unbiased exploration of cell types.

The brain's cerebral cortex is responsible for cognition and memory, and contains regions involved in sensory and motor functions. Tasic and colleagues used single-cell sequencing to profile the gene-expression landscapes of more than 20,000 cells, mostly neurons, from two anatomically distinct cortical areas in adult mice — the visual cortex, which processes visual sensory information from the eye, and the anterior lateral motor cortex, which is involved in movement. By doing so, they could compare cells of the same type located in regions with different functions (Fig. 1).

Broadly speaking, neurons of the cortex can be classified as excitatory or inhibitory, depending on the type of neurotransmitter molecule they produce and whether their activation leads to increased or decreased activity of neural circuits. The authors identified more than 100 different cell types, including 61 types of inhibitory neuron and 56 types of excitatory neuron. They found that most cell types were present in both cortical areas — with the exception of excitatory neurons.

These cells are the primary activity-generating units of cortical circuits, and have long been hypothesized to be identical across all cortical areas[3]. But Tasic *et al.* found that nearly every subtype of excitatory neuron was specific to either the visual or the anterior lateral motor cortex. The authors injected the cells with fluorescent tracers to track their neuronal projections into distant brain areas. Surprisingly, neurons with different gene-expression profiles also showed different patterns of long-range projection, suggesting that molecular definitions of cell types based on gene expression can provide information about multiple properties of an excitatory neuron.

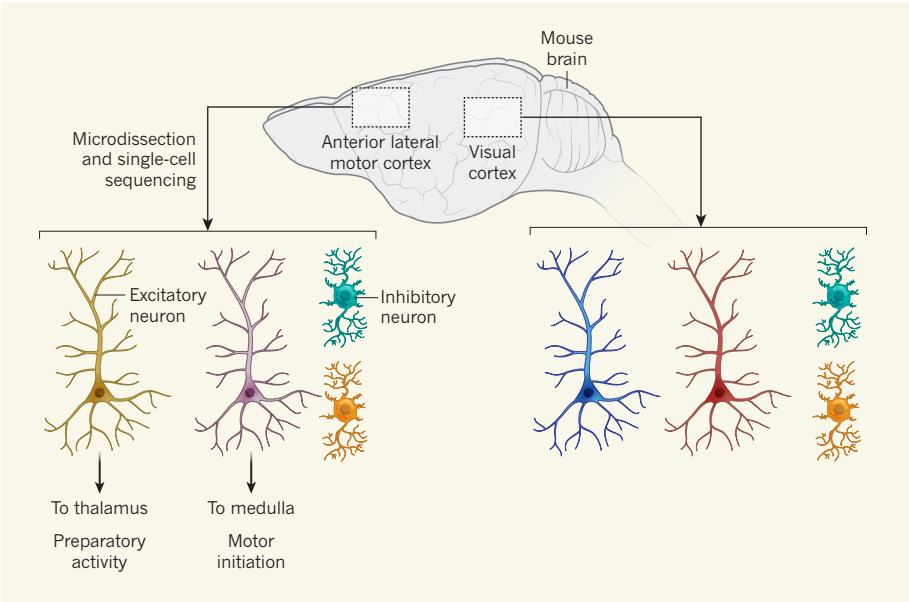

Figure 1 | Cell-type diversity in the mouse cortex. Tasic *et al.*[1] microdissected the anterior lateral motor cortex and the visual cortex of the mouse brain, and subjected neuronal cells from these regions to single-cell sequencing. The authors identified 133 cell types on the basis of gene-expression profiles. The analysis revealed that types of inhibitory neuron are shared between regions (colours indicate cell types), but that types of excitatory neuron are area-specific. Economo *et al.*[2] performed in-depth characterization of two subpopulations of excitatory neurons in the motor cortex. They found that the two connect to distinct brain regions (the thalamus and medulla) and perform different functions in respectively preparing and initiating motion.

A study published last year[4] also found area-specific excitatory neurons in the developing human cortex, even before the cortical circuits begin to process sensory information. This, together with Tasic and colleagues' observations, suggests the need to revise our framework for understanding how cortical areas process diverse types of information. In particular, these findings suggest that the functional specialization of cortical areas might rely not only on differences in microcircuits and connectivity patterns, but also on the use of different cell types to process information. Future work is needed to sample cells from more cortical areas to establish how many area-specific excitatory-neuron types exist and how their distribution affects cortical function.

Whereas Tasic and colleagues present an entire gallery of cortical neurons, Economo *et al.*[2] zoom in to look at nuanced differences between neurons in one layer of the cortex — much like studying paintings of the same style on one gallery floor. Excitatory pyramidal tract neurons, which reside in a region called layer 5 in the anterior lateral motor cortex, communicate with other neurons located many thousands of cell diameters away by establishing physical contacts. Pyramidal tract neurons were presumed to all have similar functions[5]. However, Tasic and colleagues' analysis revealed that these cells fall into different subtypes on the basis of their gene-expression profiles. Economo and colleagues sought to

© 2018 Springer Nature Limited. All rights reserved.

dissect the differences between subgroups.

Pyramidal tract neurons located primarily in the upper part of layer 5 send signals to a brain region called the thalamus that sends projections back to the cortex, forming a loop involved in preparing for motor activity. Tasic *et al.* demonstrated that these neurons are molecularly distinct from those located in a lower portion of layer 5 that project to the medulla, which is associated with the execution of movement. Economo *et al.* engineered each subpopulation of neurons to express the protein channelrhodopsin — a light-sensitive ion channel. This enables neuronal activity to be precisely controlled using light (a method known as optogenetics), and so allowed the authors to dissect the roles of the upper and the lower layer-5 neurons in different types of motor function.

Economo and colleagues used light to independently activate the pyramidal tract populations in mice, and simultaneously monitored both the activity patterns of the cells and the behaviour of the animals as they engaged in a motor-learning exercise. These experiments confirmed that the two populations of pyramidal tract neurons have separate roles: one in preparing for motor activity and the other in initiating movement. The authors' results also provide a compelling demonstration of how understanding the molecular taxonomy of the brain can lead us to an understanding of how neurons connect and function.

Together, the two studies highlight the transformative potential of atlas-scale data sets in modern neuroscience[6,7]. They make a strong case for conducting similar studies of more cell types and of the brains of animals of different species, including humans, at various ages. In support of the need for data from different species, a recent single-cell sequencing study[8] has reported a greater diversity of neurons in a cognition-associated region of the human cortex than has been described for mice — this might explain our ability for higher-order cognition. Further characterization of both neuronal and non-neuronal cell classes could also yield fresh insights into their selective vulnerabilities to disease states, and instruct the development of protocols to generate these cell types from stem cells *in vitro*, for use as disease models and for drug testing.

In the future, researchers will undoubtedly make use of the genetic markers of specific neuronal populations identified by Tasic and colleagues' cell atlas. For example, these markers could be used to design more optogenetic experiments that target specific neuronal populations; to investigate whether 'area-specific' cell types can be found in other cortical regions; and to isolate populations of cells for further functional characterization.

However, translating the cellular composition of the brain into biologically meaningful insights will require new strategies for interrogating neuronal function. Technologies to manipulate cell types currently being developed through the support of the US National Institutes of Health BRAIN Initiative[9] might enable these analyses. In doing so, they could allow us to fully appreciate the portrait gallery of cells that control brain function. ■

Aparna Bhaduri *and* **Tomasz J. Nowakowski** *are at the Eli and Edythe Broad Center for Regeneration Medicine and Stem Cell Research, University of California, San Francisco, San Francisco, California 94143, USA.*
e-mail: tomasz.nowakowski@ucsf.edu

1. Tasic, B. *et al. Nature* **563**, 72–78 (2018).
2. Economo, M. N. *et al. Nature* **563**, 79–84 (2018).
3. Creutzfeldt, O. D. *Naturwissenschaften* **64**, 507–517 (1977).
4. Nowakowski, T. J. *et al. Science* **358**, 1318–1323 (2017).
5. Harris, K. D. & Shepherd, G. M. G. *Nature Neurosci.* **18**, 170–181 (2015).
6. Zeisel, A. *et al. Cell* **174**, 999–1014 (2018).
7. Saunders, A. *et al. Cell* **174**, 1015–1030 (2018).
8. Hodge, R. D. *et al.* Preprint at bioRxiv https://doi.org/10.1101/384826 (2018).
9. Ecker, J. R. *et al. Neuron* **96**, 542–557 (2017).

QUANTUM PHYSICS

Mechanical quantum systems controlled

The control of quantum systems offers great potential for advanced information-processing and sensing applications. An approach has been demonstrated that enables such control over the motion of mechanical oscillators. **See Article p.53**

MICHAEL R. VANNER

People tend to behave differently when they are being watched. It turns out that objects in the quantum world do, too, and that the very act of measurement can modify their behaviour. This effect is a consequence of Heisenberg's uncertainty principle, which states that, if we measure the position of a moving object precisely, we cannot simultaneously know the object's momentum. On page 53, Rossi *et al.*[1] report an experiment that beautifully demonstrates this tenet of quantum physics. The authors use their measurements to apply a feedback force to a mechanical oscillator — an object akin to a vibrating drumhead — to greatly suppress the oscillator's motion. The work opens up an avenue for controlling mechanical quantum systems by continuously monitoring and manipulating their dynamics.

The use of measurements and feedback to stabilize a system is a well-developed technique in engineering and is applied in many everyday technologies. For example, the technique is used to stabilize the motion of lifts, and is also used to reduce the effects of turbulence during flights in many types of aircraft. Researchers have now extended these concepts so that measurement and feedback can be used to control the properties of individual quantum systems[2].

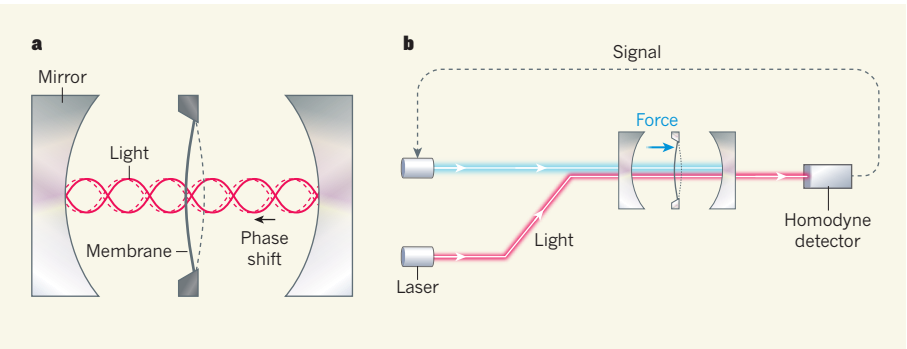

Figure 1 | Quantum measurement and feedback. a, Rossi *et al.*[1] report an experiment in which a millimetre-sized mechanical membrane interacts with light that bounces back and forth between a pair of mirrors known as an optical cavity. The drumhead-like motion of the membrane causes the light to acquire a phase shift that depends on the position of the membrane. The black and red dashed lines indicate a mechanical displacement and such a phase shift, respectively. **b**, The authors continuously supplied the cavity with light (red) from a laser. They monitored the phase shift of light that was transmitted through the cavity using a device called a homodyne detector, thus enabling a continuous measurement of the membrane's position. The signal from the detector was then used to control the intensity of a second laser. The light (blue) from this laser applied a feedback force to the membrane that brought the membrane's motion close to its ground state — a convenient starting point for future quantum experiments.

© 2018 Springer Nature Limited. All rights reserved.

Prominent experimental examples of quantum control include preparing and stabilizing quantum states of a microwave signal that bounces between a pair of mirrors known as an optical cavity[3], and controlling the state of a superconducting quantum bit of information[4]. Progress in quantum control has been rapid during the past few decades, and researchers have been extending these techniques to other physical systems to exploit the advantages that different systems provide.

One such area under development is cavity quantum optomechanics, in which laser light inside an optical cavity is used to control the motion of a mechanical oscillator. Central to this field of research is the radiation–pressure interaction, whereby the reflection of light from an object modifies the object's momentum and, concurrently, causes the light to acquire a phase shift — a shift in the crests and troughs of the light's electric field — that depends on the object's position. Using this interaction, physicists can both precisely measure and control mechanical motion.

A key goal in optomechanics research has been to bring mechanical motion close to its ground state — the state that describes the tiny amount of jiggling that is imposed by quantum mechanics, even at absolute zero temperature. Realizing this state is a convenient starting point for future quantum experiments that would otherwise be unfeasible because of random heat-induced fluctuations of the mechanical motion.

A common route to achieving this goal is sideband cooling — a technique that uses light to reduce mechanical fluctuations and that was previously applied to trapped ions. The method requires the light in the optical cavity to have a lifetime that is much longer than the period of the mechanical motion. This configuration of experimental parameters is known as the resolved-sideband regime, and precludes fast measurements of the mechanical motion because the cavity accumulates a signal of such motion over a relatively long timescale.

Rossi and colleagues developed an optomechanical experiment that operates well outside the resolved-sideband regime. The authors placed a millimetre-sized mechanical membrane inside an optical cavity that was continuously supplied with light from a laser (Fig. 1). They monitored the resulting phase shifts in the light using a device known as a homodyne detector, which enabled the membrane's position to be measured continuously.

The authors then passed the signal from the detector through a filter, which essentially converted the information about the membrane's position into information about its momentum, and used this new signal to control the intensity of a second laser. The light from the second laser applied a feedback force to the membrane that greatly suppressed the membrane's motion. Using this approach, the team achieved a mean thermal occupation of approximately 0.3, which means that the oscillator was in the ground state for more than 75% of the time.

Rossi and co-workers' achievement can be viewed as the culmination of decades of research in engineering and quantum physics, and it builds on the work of several other groups around the globe that are too numerous to list here. The use of laser light to both monitor mechanical motion and apply a feedback force was first studied theoretically[5] in the late 1990s, and a proof-of-concept experiment was carried out shortly thereafter[6]. Since then, improvements in optomechanical experiments have enabled researchers[7] to achieve a thermal occupation of about 5.3, which is equivalent to a ground-state probability of 16%. The technique has also been used to stabilize the mirrors in gravitational-wave detectors[8].

Key to the present work's success was the fact that the speed with which the experiment precisely measured the position of the membrane was much faster than the rate at which the membrane returns to thermal equilibrium. Such a regime is said to have high 'quantum cooperativity', and allowed the physics of the Heisenberg uncertainty principle to be clearly visible in Rossi and colleagues' experimental results.

The authors' work not only demonstrates the utility of quantum measurement and feedback, but also highlights the richness of optomechanical experiments that operate well outside the resolved-sideband regime. Among many applications, working in this regime allows optomechanical interactions to be carried out that, when combined with the authors' control method, offer a route towards producing 'quantum-superposition' states of mechanical motion[9]. Such states would be useful to both develop quantum technologies and probe the foundations of physics. ■

Michael R. Vanner *is at the Quantum Measurement Laboratory, Department of Physics, Imperial College London, London SW7 2BW, UK.*
e-mail: m.vanner@imperial.ac.uk

1. Rossi, M., Mason, D., Chen, J., Tsaturyan, Y. & Schliesser, A. *Nature* **563**, 53–58 (2018).
2. Wiseman, H. M. & Milburn, G. J. *Quantum Measurement and Control* (Cambridge Univ. Press, 2009).
3. Sayrin, C. *et al. Nature* **477**, 73–77 (2011).
4. Vijay, R. *et al. Nature* **490**, 77–80 (2012).
5. Mancini, S., Vitali, D. & Tombesi, P. *Phys. Rev. Lett.* **80**, 688–691 (1998).
6. Cohadon, P. F., Heidmann, A. & Pinard, M. *Phys. Rev. Lett.* **83**, 3174–3177 (1999).
7. Wilson, D. J. *et al. Nature* **524**, 325–329 (2015).
8. Abbott, B. *et al. New J. Phys.* **11**, 073032 (2009).
9. Ringbauer, M., Weinhold, T. J., Howard, L. A., White, A. G. & Vanner, M. R. *New J. Phys.* **20**, 053042 (2018).

MICROBIOLOGY

Chromatin clues to a parasite's coat switch

The parasite *Trypanosoma brucei* causes sleeping sickness. It evades human defences by changing the version of a protein that coats its surface. Analysis of its genome and nuclear structure clarifies this variation process. SEE LETTER P.121

STEVE KELLY & MARK CARRINGTON

Most infections don't usually cause prolonged illness in humans because the body's immune system recognizes the presence of a molecular fragment made by the pathogen, termed an antigen, as alien, and triggers a defence response that eliminates the pathogen. However, pathogens use a range of strategies to evade such destruction. One approach is called antigenic variation, whereby a pathogen population keeps changing the antigens that are expressed. If antigenic variation occurs more rapidly than the host can respond to a newly expressed antigen, infection can persist. Müller *et al.*[1] report on page 121 that in the parasite *Trypanosoma brucei*, the structure of the DNA–protein complex known as chromatin has a role in how antigenic variation occurs in this organism.

The process of antigenic variation has evolved independently in many organisms[2–5]. It has certain common features, such as the presence of a reservoir of many versions of a particular gene, and hence the possibility that many different antigens can be expressed that correspond to that gene or gene family. Another aspect central to infection persistence is the presence of mechanisms to ensure that only one version of such a gene is expressed at a time, with all the other versions existing in a silenced state that might later be reversed[6].

Antigenic variation has been studied intensively in *T. brucei*, which causes African trypanosomiasis, historically known as sleeping sickness, in humans, and a range of diseases in livestock. The disease can be fatal if trypanosomes enter the brain, causing a range of neurological symptoms that including the disturbance of sleep patterns[7]. Although the incidence of the human disease is in decline[8], the animal illness remains a major cause of poverty among farmers in sub-Saharan Africa[9].

The surface of a *T. brucei* trypanosome is

© 2018 Springer Nature Limited. All rights reserved.

covered with closely packed molecules of a glycoprotein termed VSG (Fig. 1). During an infection, switching events occur that result in a different version of the VSG being expressed from a reservoir of thousands of VSG genes, most of which are substantially different from each other[10,11]. This switching process enables the parasite to evade immune-mediated destruction, and the infection can thus persist for decades[12].

Most of the parasite's VSG-encoding gene repertoire occurs in tandem arrays close to DNA sequences called telomeres, which are found at the ends of chromosomes[13]; these arrays are known as subtelomeric arrays. In addition, at any given time, approximately 15 other VSG-encoding genes — including the one being expressed[6] — are present in expression sites. These are regions of chromosomes next to telomeres that are specialized for the expression of VSG-encoding genes. Only one expression site is active, and it is located in a nuclear structure termed the expression-site body[14]. The other expression sites are inactive, and all the genes are said to be silent. Antigenic variation can occur either by a change in the sequence of the VSG gene in the active expression site through a DNA-mediated process called recombination[5], or by the replacement of one expression site with another in the expression-site body[5].

The processes involved in gene silencing must operate on all copies of the VSG-encoding gene apart from the one being expressed. Müller and colleagues' study addressed three questions about this process. How are the subtelomeric arrays of VSG-encoding genes kept silent? Is the same mechanism used for all the silenced expression sites? And how is this silencing reversed?

Müller and co-workers report a newly generated assembly of the *T. brucei* genome that adds substantially to the one previously reported[15]. The authors reconstructed 33 subtelomeric arrays of VSG-encoding genes, and determined on which of the chromosomes 27 of these were located. This advance in our understanding of the trypanosome genome reveals that approximately half of the parasite's DNA is devoted to VSG-encoding genes.

Their genome assembly allowed the authors to investigate the silencing of VSG-encoding genes. They first confirmed by RNA sequencing that the subtelomeric arrays of VSG-encoding genes are not expressed. Second, using a DNA-crosslinking technique called Hi-C to monitor the physical proximity of DNA sequences to each other in the nucleus, the authors report that there is a greater compaction of subtelomeric arrays than of other regions of the chromosomes. Such compaction is characteristic of silenced chromatin in which genes are not expressed. The telomeres of *T. brucei* are located near the outermost region of the nucleus[16], termed the nuclear periphery, and it is probable that the silent VSG-encoding arrays are located there, too.

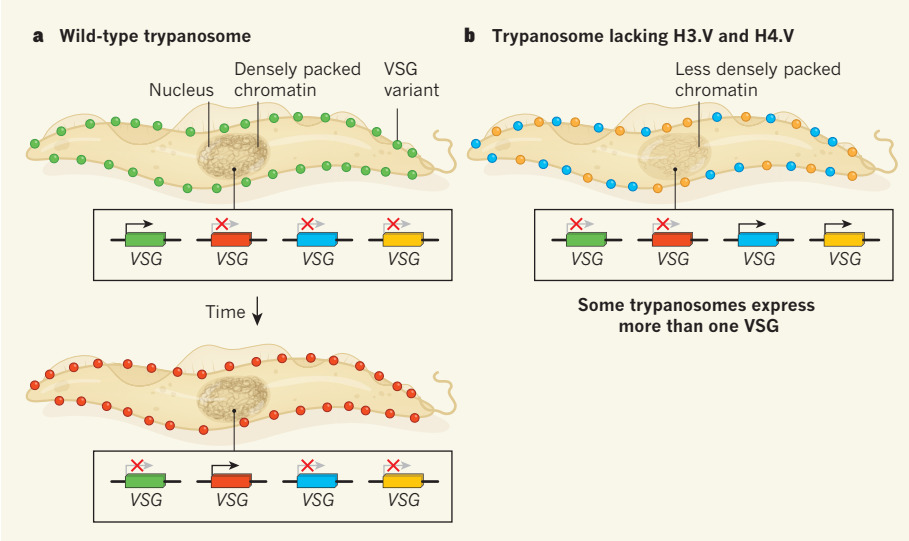

Figure 1 | Coat switching in the parasite *Trypanosoma brucei*. **a**, The trypanosome parasite, which causes sleeping sickness, evades destruction by the immune system by varying over time the version of a glycoprotein called VSG that coats its surface. The parasite usually expresses only one copy of its many versions of VSG-encoding genes at a time, enabling its surface coat to change more rapidly than its host can target a defence response against it. VSG-encoding genes can be found in the periphery of the nucleus in a densely packed region of chromatin (the complex of DNA and protein). **b**, Müller *et al.*[1] shed light on how the coat-switching process occurs, and report that if trypanosomes lack H3.V and H4.V, which are DNA-binding proteins called histones, the chromatin surrounding VSG-encoding genes exists in a conformation that is less densely packed than the conformation in wild-type trypanosomes. Such less densely packed chromatin favours gene expression, and some of the trypanosomes that lack both H3.V and H4.V can express more than one VSG at a time.

How might gene silencing and localization of silent arrays of VSG genes to the nuclear periphery be maintained? The answer is probably complex. Several factors influence the silencing of VSG-encoding genes[17,18]. Müller and co-workers report that two variant versions of histone proteins, called H3.V and H4.V, also have a role in this silencing process. These histones are a component of chromatin, and mark sites in the genome of *T. brucei* at which the synthesis of RNA transcripts by the enzyme RNA polymerase II is terminated[19].

The authors engineered *T. brucei* to lack either H3.V or H4.V, or both, and investigated how this affected the structure of the nucleus and chromatin and the silencing of VSG-encoding genes. Experiments using Hi-C and assessing the localization of telomeres in the nucleus indicated that the absence of H3.V, but not of H4.V, altered nuclear organization and resulted in increased clustering of telomeres at the nuclear periphery.

The authors next analysed chromatin structure using a technique called ATAC-seq, which assesses the ability of an enzyme to access specific sequences of DNA. If the enzyme can access a particular sequence, the DNA is probably in an uncompacted chromatin structure that might facilitate access for the components needed to drive gene expression. Müller *et al.* found that, if both H3.V and H4.V were absent, chromatin accessibility of VSG-encoding sequences in expression sites was increased compared with accessibility in the wild-type situation. To address how these changes affected the expression of VSG-encoding genes, the authors used single-cell RNA sequencing to determine the number of expression sites being expressed in individual cells. They found that, although most cells still expressed just a single VSG in the absence of H3.V and H4.V, some cells in the population expressed up to four different VSGs. It is not known why all the expression sites were not activated when the chromatin accessibility for these genes increased more than usual. But there are probably many levels of control to limit VSG expression to just one at a time, given that this capacity is a key element of pathogen survival.

Many questions remain to be answered. What happens to the expression-site body in the cells that lack H3.V and H4.V? Does its location change, and might the number of these structures increase? Perhaps the cell's ability to construct multiple expression-site bodies is restricted, which might therefore limit the number of active expression sites in parasites that lack H3.V and H4.V. Another interesting issue is whether changes in chromatin accessibility alter the ease with which expression-site sequences can move into an expression-site body. Answers to these questions might help to illuminate the intimate relationship between genome architecture and the mechanism of antigenic variation in one of the world's most puzzling, problematic and pugnacious pathogens. ■

Steve Kelly *is in the Department of Plant Sciences, University of Oxford, Oxford OX1 3RB, UK.* **Mark Carrington** *is in the*

© 2018 Springer Nature Limited. All rights reserved.

Department of Biochemistry, University of Cambridge, Cambridge CB2 1QW, UK.
e-mails: steven.kelly@plants.ox.ac.uk; mc115@cam.ac.uk

1. Müller, L. S. M. *et al. Nature* **563**, 121–125 (2018).
2. Deitsch, K. W. & Dzikowski, R. *Annu. Rev. Microbiol.* **71**, 625–641 (2017).
3. Foley, J. *Comput. Struct. Biotechnol. J.* **13**, 407–416 (2015).
4. Gargantini, P. R., Serradell, M. C., Ríos, D. N., Tenaglia, A. H. & Luján, H. D. *Curr. Opin. Microbiol.* **32**, 52–58 (2016).
5. Mugnier, M. R., Stebbins, C. E. & Papavasiliou, F. N. *PLoS Pathog.* **12**, e1005784 (2016).
6. Duraisingh, M. T. & Horn, D. *Cell Host Microbe* **19**, 629–640 (2016).
7. Kennedy, P. G. *Lancet Neurol.* **12**, 186–194 (2013).
8. Simarro, P. P. *et al. PLoS Negl. Trop. Dis.* **9**, e0003785 (2015).
9. Shaw, A. P. M. in *The Trypanosomiases* (eds Maudlin, I., Holmes, P. H. & Miles, M. A.) 369–402 (CABI, 2004).
10. Schwede, A., Macleod, O. J. S., MacGregor, P. & Carrington, M. *PLoS Pathog.* **11**, e1005259 (2015).
11. Bartossek, T. *et al. Nature Microbiol.* **2**, 1523–1532 (2017).
12. Sudarshi, D. *et al. PLoS Negl. Trop. Dis.* **8**, e3349 (2014).
13. Callejas, S., Leech, V., Reitter, C. & Melville, S. *Genome Res.* **16**, 1109–1118 (2006).
14. Navarro, M. & Gull, K. *Nature* **414**, 759–763 (2001).
15. Berriman, M. *et al. Science* **309**, 416–422 (2005).
16. Chung, H. M. *et al. EMBO J.* **9**, 2611–2619 (1990).
17. Stanne, T. *et al. J. Biol. Chem.* **290**, 26954–26967 (2015).
18. Glover, L., Hutchinson, S., Alsford, S. & Horn, D. *Proc. Natl Acad. Sci. USA* **113**, 7225–7230 (2016).
19. Siegel, T. N. *et al. Genes Dev.* **23**, 1063–1076 (2009).

This article was published online on 17 October 2018.

NEURODEVELOPMENT

Pruned to perfection

During development, some synaptic connections between neurons are removed by immune cells called microglia, and others are retained. The discovery of a 'don't eat me' signal that prevents excess pruning sheds light on this process.

SERGE RIVEST

The signals transmitted between neurons through synaptic connections are responsible for most, if not all, brain functions, from learning to decision-making. During brain development, synapses that are stimulated less often than others are eliminated through a process called pruning, whereas those that are highly stimulated are retained. This refines the brain's ability to respond to stimuli and environmental cues. Microglia, the brain's innate immune cells, have a key role in pruning — they engulf and digest synapses through a process called phagocytosis. But the mechanism that determines which synapses they avoid has been unclear. Writing in *Neuron*, Lehrman *et al.*[1] describe a 'don't eat me' signal, involving a protein called cluster of differentiation 47 (CD47), that prevents inappropriate synaptic pruning by microglia.

About a decade ago, it was shown that synapses requiring elimination send an 'eat me' signal to microglia[2] (Fig. 1a). This signal involves the proteins C1q and CR3, which are part of the complement cascade — a complex series of interactions that is best known for activating cells of the innate immune system to eliminate disease-causing organisms and damaged cells. 'Don't eat me' signals act to limit the effects of 'eat me' signals in the immune system, but it was not known whether the same process occurs during synaptic pruning in the developing brain.

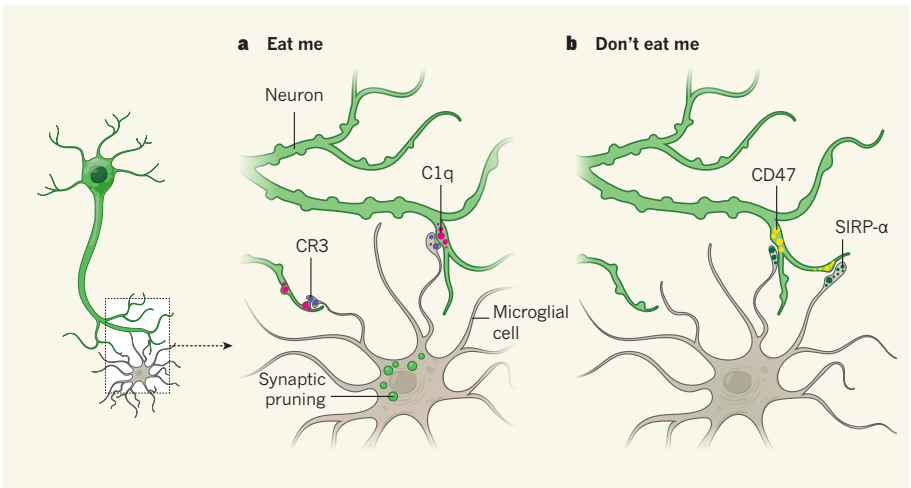

Figure 1 | Opposing signals in synaptic pruning. **a**, Unnecessary synaptic connections between neurons can be removed during brain development in a process called pruning, in which the termini of neurons leading into synapses are engulfed and digested by microglia — the brain's innate immune cells. Synapses destined for elimination release an 'eat me' signal, in which an immune protein called C1q signals to the protein CR3 on microglia to promote pruning. **b**, Lehrman *et al.*[1] report an opposing 'don't eat me' signal. The protein CD47 is expressed on active synaptic termini, and signals to its receptor SIRP-α on microglia, discouraging the immune cells from digesting the synaptic terminal.

CD47 is a cell-surface protein that has many immune functions, including acting as a 'don't eat me' signal for macrophages[3], microglia's sister cells, which exist outside the brain. Lehrman *et al.* analysed whether CD47 is expressed in the dorsal lateral geniculate nucleus (dLGN), a region of the brain involved in vision. This region receives inputs from neurons called retinal ganglion cells (RGCs) that originate in the retina. The authors demonstrated in mice that, at five days after birth, synapses from RGCs to other neurons in the dLGN are being pruned at high levels.

Lehrman and colleagues found that CD47 was expressed at higher levels in the dLGN than in other brain regions at this time. Moreover, the protein SIRP-α, which acts as a cell-surface receptor for CD47, was highly expressed by microglia at the same developmental stage. Using a super-resolution imaging technique, the researchers showed that CD47 was located in 25% of synapses in the mouse dLGN 5 days after birth.

Next, the group investigated whether CD47 functions as a 'don't eat me' signal in this context. First, they measured phagocytosis of synaptic material in mice genetically engineered to lack CD47. They found that microglia engulfed more RGC inputs in CD47-deficient mice than in their wild-type siblings. The mutant mice also displayed higher levels of pruning than did controls, and had fewer synapses in the dLGN by ten days after birth — a change that persisted into adulthood. The authors observed a similar phenomenon in mice lacking the gene that encodes SIRP-α, indicating a possible CD47–SIRP-α interaction on microglia.

The researchers used various *in vitro* approaches to test whether CD47–SIRP-α signalling could prevent the phagocytosis of isolated synaptic termini, called synaptosomes. These analyses revealed that microglia lacking SIRP-α engulfed synaptosomes more efficiently than did wild-type microglia, and that microglia preferentially engulfed synaptosomes lacking CD47 over wild-type ones. Together, these data indicate that CD47–SIRP-α signalling acts as a 'don't eat me' signal to protect against excessive microglia-mediated pruning and synapse loss (Fig. 1b).

Blocking or disrupting neuronal stimuli and environmental cues to neurons can alter synaptic pruning and refinement in

© 2018 Springer Nature Limited. All rights reserved.

many brain regions[4]. To investigate whether activity-dependent changes in synaptic CD47 might determine which synapses are removed, Lehrman *et al.* set up an artificial competition assay, in which they used the neurotoxin tetrodotoxin (TTX) to suppress neuronal activity in one eye in mice. They found that CD47 levels were higher in synaptic inputs from RGCs that originated in the more-active control eye than in the inputs from the TTX-treated eye, suggesting that CD47 is either degraded or moves away from synapses in RGCs of the less-active eye.

Finally, Lehrman and colleagues showed that, in wild-type mice, CD47 levels were higher in more-active than in less-active synapses, and that, in CD47-deficient animals, microglia showed no preference for less-active inputs. Together, the authors' data indicate that protective 'don't eat me' signals prevent aberrant microglial engulfment in the dLGN.

As Lehrman *et al.* point out, a major challenge for the immune system is to remove dying cells, disease-causing organisms and toxic molecules without removing or damaging healthy cells. This study is particularly interesting in that regard, because the 'eat me' and 'don't eat me' signals from synapses both act on microglia. Whether the complement system and CD47–SIRP-α act separately or interact to ensure that the correct synapses are removed or protected remains an open question. This aspect is also not clear for macrophages in the immune system.

The mechanisms by which synapses that are either unwanted or to be retained send these signals to microglia remain to be demonstrated — in particular, the interaction between CD47 and SIRP-α in microglia as a leading factor in constraining synaptic pruning has not been shown directly and has been validated using *in vitro* models. The physiological relevance of this signalling pathway also needs to be examined, because CD47-deficient mice do not seem to have major defects in brain development[5].

Another question is whether these events modulate other innate immune responses in the brain, such as those involved in disease. For instance, in multiple sclerosis, a sheath of a fatty substance called myelin that insulates neurons becomes damaged. Microglia have a key role in removing damaged sheaths to enable remyelination[6]; perhaps 'eat me' and 'don't eat me' signals help the microglia to determine whether myelin should be removed.

Synaptic protection is essential for normal brain development. The identification of a 'don't eat me' signal in microglia reveals a new aspect of this crucial developmental phenomenon. ■

Serge Rivest *is at the CHU de Québec Research Center and in the Department of Molecular Medicine, Faculty of Medicine, Laval University, Quebec City G1V 4G2, Canada.*
e-mail: serge.rivest@crchudequebec.ulaval.ca

1. Lehrman, E. K. *et al. Neuron* **100**, 120–134 (2018).
2. Stevens, B. *et al. Cell* **131**, 1164–1178 (2007).
3. Oldenborg, P.-A. *et al. Science* **288**, 2051–2054 (2000).
4. Stellwagen, D. & Shatz, C. J. *Neuron* **33**, 357–367 (2002).
5. Koshimizu, H., Takao, K., Matozaki, T., Ohnishi, H. & Miyakawa, T. *PLoS ONE* **2**, e89584 (2014).
6. Lampron, A. *et al. J. Exp. Med.* **212**, 481–495 (2015).

ASTRONOMY

Evidence of ancient Milky Way merger

An analysis of data from the Gaia space observatory suggests that stars in the inner halo of the Milky Way originated in another galaxy. This galaxy is thought to have collided with the Milky Way about ten billion years ago. SEE LETTER P.85

KIM VENN

From studying the exquisite images collected by ground- and space-based telescopes over the past century, astronomers have learnt that galaxies can collide. On page 85, Helmi *et al.*[1] use data from the Gaia space observatory to determine that the Milky Way was hit by a satellite galaxy roughly ten billion years ago. Stars from this galaxy are still around us today to tell the story.

Gaia was launched in 2013 by the European Space Agency as the successor to Hipparcos — a satellite that in 1997 produced the first high-precision catalogue of nearby stars[2]. Gaia was designed to conduct ongoing observations of the visual characteristics and positions of more than one billion objects in the sky[3] (Fig. 1). Such map-making might seem like tedious work, but repeated measurements made by Gaia can also be used to determine precise distances and velocities across the sky for about 1% of all the stars in our Galaxy[3].

The information from Gaia can be combined with spectroscopic measurements of velocities along the observer's line of sight to make videos that show the precise motions of the stars (see, for example, go.nature.com/2atris8). Playing these videos backwards allows astronomers to study how our Galaxy was assembled and how it has evolved.

Helmi and colleagues used the Gaia mission's second data release, which was published earlier this year[4], to analyse the motion of stars near the Sun (within a distance of about 10 kiloparsecs). The authors compared these observations with predictions from simulations in which the Milky Way and a satellite galaxy with 20% of the mass of our Galaxy merged in the past[5]. The similarities are striking, particularly the detailed motions of some high-velocity stars that orbit the Galactic Centre in the opposite direction to the Sun.

Using astronomical-data catalogues that provide the ages and chemical compositions of stars[6], Helmi *et al.* determined that the Milky Way's inner halo — a region that surrounds the thick stellar disk — is made up mainly of stars from the satellite galaxy. These stars provide a record of the galactic collision, which the authors estimate took place approximately ten billion years ago.

Several other research groups working with the Gaia data have reached a similar conclusion to that of Helmi and colleagues, using other analytical methods or data catalogues[7–9]. However, there are small differences between the results of Helmi *et al.* and those of the other groups, such as the mass of the satellite galaxy, when the collision occurred and whether the event involved a single satellite galaxy or a few smaller galaxies.

One conclusion on which all of the groups agree is that the event might have contributed to the formation of the Milky Way's thick stellar disk. If a thin disk of stars encircled the Galactic Centre at the time of the merger, the orbits of the stars would have been disrupted. Originally, the stars would have had a specific chemical composition that reflected the young age of the Milky Way. But today, they would be old and relatively poor in metals (elements heavier than helium), and on orbits in a thickened disk. All the research groups reported the possible identification of these old stars in the Gaia data.

Astronomers have speculated for several decades that an ancient satellite galaxy merged with the Milky Way in the past, because such an event could explain differences in the motions and chemical compositions of stars in the neighbourhood of the Sun. For example, one of the most unusual objects in our Galaxy is Omega Centauri — a cluster of stars so distinctive that it is thought to be the core of a satellite galaxy that was disrupted and absorbed by the Milky Way. Researchers have suggested that some of the stars found in the Gaia data might be debris from this event[10,11].

Obtaining proof that some stars are associated with a merger required the high precision and large survey area of Gaia, in combination

© 2018 Springer Nature Limited. All rights reserved.

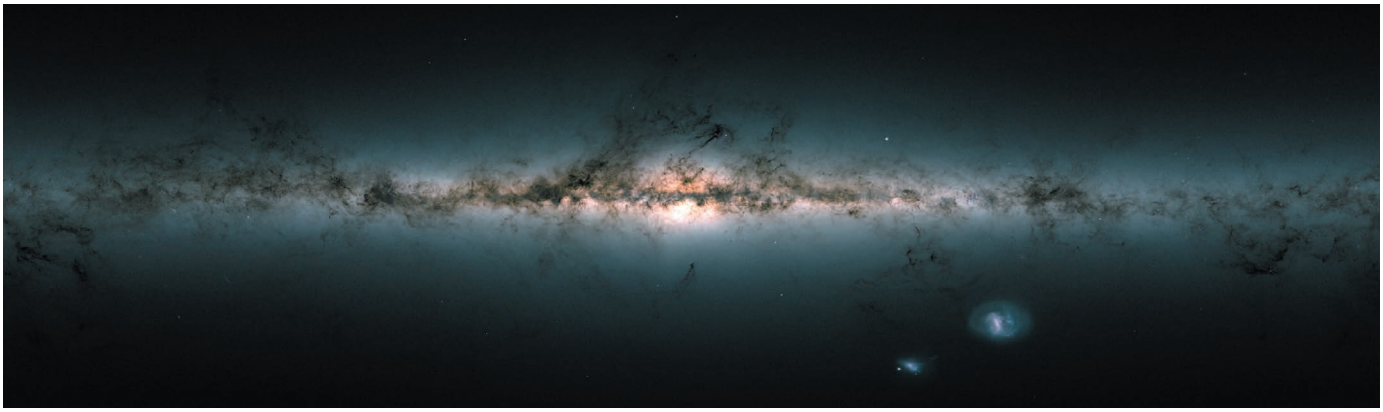

ESA/GAIA/DPAC

Figure 1 | View of the Milky Way based on data from the Gaia space observatory.

with large databases of the spectral and chemical properties of stars. Over the next decade, several international observatories will carry out massive surveys of the spectra of stars throughout the Milky Way. These surveys will provide new data to identify the characteristics of more stars from the satellite galaxy.

The Gaia mission will continue for another few years, sharpening our vision of the Milky Way. With Gaia's detection of even more stars that originated in the satellite galaxy, astronomers will be better able to determine the mass of this galaxy, and when the merger occurred. It might even be possible to learn about the star-formation history of the satellite galaxy before it collided with the Milky Way.

Helmi and colleagues named the satellite galaxy Gaia–Enceladus, in honour of the space observatory that provided the crucial data and after one of the Giants of Greek mythology. Enceladus was the offspring of Gaia (Earth) and Uranus (the sky). He was said to be buried under Mount Etna in Italy and responsible for earthquakes in the region. The authors suggest that this is an appropriate name because Gaia–Enceladus was a giant compared with other past and present satellite galaxies of the Milky Way. Furthermore, it shook our Galaxy, leading to the formation of the thick stellar disk. Regardless of the name, it is clear that the history of the merging event is written in the stars. ■

Kim Venn *is in the Department of Physics and Astronomy, University of Victoria, Victoria, British Columbia V8P 1A1, Canada.*
e-mail: kvenn@uvic.ca

1. Helmi, A. *et al. Nature* **563**, 85–88 (2018).
2. Perryman, M. A. C. *et al. Astron. Astrophys.* **323**, L49–L52 (1997).
3. Gaia Collaboration. *Astron. Astrophys.* **595,** A1 (2016).
4. Gaia Collaboration. *Astron. Astrophys.* **616**, A1 (2018).
5. Villalobos, Á. & Helmi, A. *Mon. Not. R. Astron. Soc.* **391**, 1806–1827 (2008).
6. Abolfathi, B. *et al. Astrophys. J. Suppl. Ser.* **235**, 42 (2018).
7. Belokurov, V., Erkal, D., Evans, N. W., Koposov, S. E. & Deason, A. J. *Mon. Not. R. Astron. Soc.* **478**, 611–619 (2018).
8. Koppelman, H. H., Helmi, A. & Veljanoski, J. *Astrophys. J. Lett.* **860**, L11 (2018).
9. Haywood, M. *et al. Astrophys. J.* **863**, 113 (2018).
10. Myeong, G. C., Evans, N. W., Belokurov, V., Sanders, J. L. & Koposov, S. E. *Mon. Not. R. Astron. Soc.* **478**, 5449–5459 (2018).
11. Myeong, G. C., Evans, N. W., Belokurov, V., Sanders, J. L. & Koposov, S. E. *Astrophys. J. Lett.* **856**, L26 (2018).

BIOLOGICAL TECHNIQUES

Complementing the forebrain

A new technique, in which forebrain-precursor cells are ablated from early-stage mouse embryos and replaced with embryonic stem cells, promises to facilitate our ability to study the central nervous system. **See Letter p.126**

JIMENA ANDERSEN & SERGIU P. PAŞCA

For the past few decades, it has been possible to directly manipulate an organism's genes early in development, to generate, for example, mice that harbour genetic modifications. Such transgenic mice have been powerful model systems in which to study human disease[1], but conventional approaches for generating these animals can be costly and time-consuming. On page 126, Chang *et al.*[2] describe an alternative approach to building complex mouse models with which to interrogate the function and diseases of the forebrain. The authors' approach could also be used to produce models focused on other regions of the central nervous system (CNS).

In conventional transgenic approaches, genes are modified in mouse embryonic stem (ES) cells, which are pluripotent — they can give rise to all cell types of the animal's body. The genetically engineered cells are then injected into a mouse embryo at an early stage of development called the blastocyst stage. The result is a chimaeric mouse, in which some cells are genetically modified and some are not. If the animal's eggs or sperm contain the genetic modification, it can be bred to produce offspring in which all the cells are modified (Fig. 1a). This approach, although recently accelerated by gene-editing technologies such as CRISPR–Cas9, remains expensive and labour-intensive. Moreover, unless the genetic modification is engineered to be expressed in only certain cell types, this approach is limited to genes that are not essential for early embryonic development.

More than two decades ago, the laboratory that performed the current study devised a technique called blastocyst complementation, to circumvent these limitations in the immune system[3]. The approach is based on the fact that, if the development of a particular organ in the host is disabled, a vacant niche is created that can be filled by tissue derived from newly introduced ES cells. In that paper, the authors used RAG2-deficient mice, which do not have mature immune cells called T and B cells. They showed that embryos of this strain could give rise to mice that generated T and B cells normally if blastocysts were injected with wild-type mouse ES cells. Moreover, these immune cells were exclusively of donor origin.

Blastocyst complementation has since been used to generate the lens of the eye[4], the kidney[5] and the heart[6]. The technique has also been used to generate pancreases made mainly of cells from another species, by injecting mouse cells into pancreas-disabled rat blastocysts and vice versa[7]. This type of animal, called an interspecies chimaera, offers great potential both for understanding fundamental principles

© 2018 Springer Nature Limited. All rights reserved.

in biology and for regenerative medicine, in which the ultimate goal is to grow organs that carry the genome of a specific individual.

Chang *et al.* developed an approach that they call neural blastocyst complementation (NBC), which involved disrupting the developing mouse forebrain — the region that will generate the brain's hippocampus, cerebral cortex and olfactory bulbs, among other structures (Fig. 1b). They crossed existing transgenic mouse strains to produce embryos in which diphtheria toxin subunit A was expressed specifically in forebrain progenitor cells. This led to the death of these cells, and therefore to mice that lacked forebrain structures. But wild-type ES cells injected into blastocysts of this strain could repopulate the forebrain niche. The authors found that the forebrain structures in the resulting animals were reconstituted. These mice were indistinguishable from controls in a set of behavioural assays.

The researchers next showed that this approach could be coupled with CRISPR–Cas9 editing of donor ES cells as a way of interrogating the function of genes of interest in the forebrain. As a proof of principle, they focused on the gene *doublecortin* (*Dcx*), which encodes a protein involved in neuronal migration and causes malformations of the cerebral cortex when mutated in patients. Chimaeras produced using *Dcx*-deficient donor ES cells exhibited hippocampal defects that mimicked those observed[8] in transgenic mice lacking *Dcx*.

Chang and colleagues' NBC approach could facilitate the study of brain development and disease in several ways. First, generating transgenic animals in which both copies of a gene are mutated requires multiple breeding steps: even if both copies of the gene are mutated in the injected ES cells, the chimaeric mice must be crossed to wild-type partners to produce offspring with one normal copy, and an extra step is needed to produce animals in which both gene copies are mutated. The need for these breeding steps is eliminated with NBC. Similarly, numerous modifications can be introduced into donor ES cells at the same time using CRISPR–Cas9, rather than being brought together through complex breeding strategies. This could accelerate studies into disorders involving more than one gene, such as autism spectrum disorders, and improve our understanding of gene–gene interactions during development.

Second, although Chang *et al.* chose to ablate forebrain progenitors, the same principle can be applied to other regions or cell types in the CNS. Moreover, alternative approaches for targeted genetic ablation could also be used, such as the removal of genes essential for development of a specific brain region, or the forced expression of proteins that induce programmed cell death. However, because most of the proteins that regulate development have roles in various cell types and at a range of

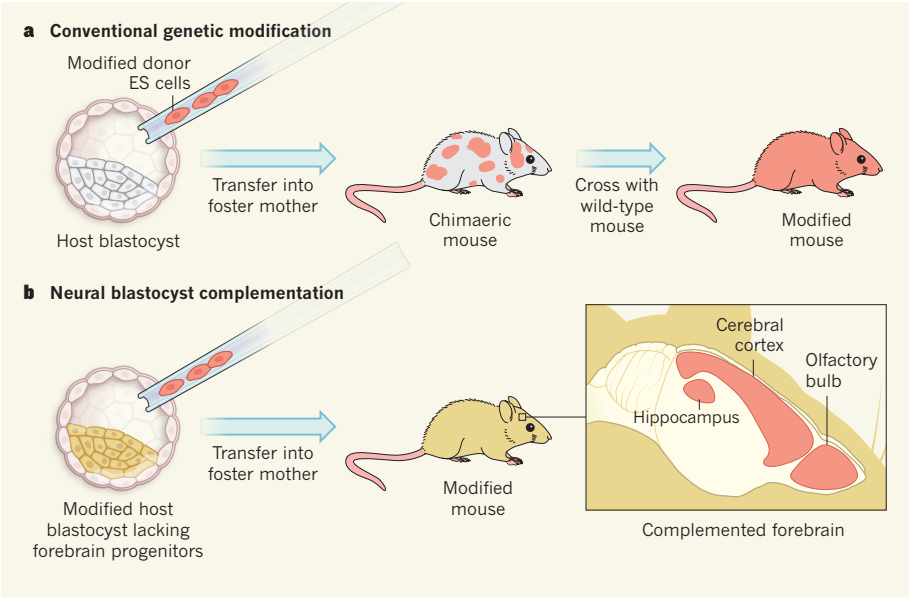

Figure 1 | Two ways to generate genetically modified mice. **a**, Genetically modified mice are usually generated by engineering mouse embryonic stem (ES) cells to harbour a desired mutation, and injecting the modified cells into a host embryo at the blastocyst stage. The embryo is then implanted into a foster mother. The donor and host ES cells mingle, giving rise to chimaeric mice consisting of both cell lineages (indicated by colouring). By breeding with wild-type mice, chimaeric animals can pass the mutation down through their eggs or sperm, producing offspring in which all cells are genetically modified. **b**, Chang *et al.*[2] describe an alternative approach called neural blastocyst complementation to produce mice whose forebrain cells all carry a desired genetic modification. The authors generated host embryos in which diphtheria toxin subunit A was expressed only in forebrain progenitor cells — these cells therefore died, leaving a vacant niche. The group injected the host blastocysts with donor ES cells that harboured a genetic modification of interest, and implanted them into foster mothers. The donor cells filled the vacant niche, repopulating the forebrain (but not other brain regions) of the resulting mice.

embryonic stages, caution is warranted when designing targeted ablation strategies, to avoid undesired side effects.

Third, this study raises the possibility of generating interspecies chimaeras of the CNS. In particular, the generation of human–animal chimaeras, in which human cells are integrated into an animal's neural circuits, would allow some human-specific brain features to be studied in a more physiological environment than can be provided by current *in vitro* systems[9]. However, the ethical implications of this work need to be closely considered[10]. Indeed, organizations such as the International Society for Stem Cell Research recommend restrictions on experiments that incorporate human cells into animals early in development, together with specialized oversight and review of the research[11].

There are technical difficulties, too. Although human cells such as neural-precursor cells have successfully been transplanted into mouse embryos to generate chimaeric tissues[12], it has proved harder to efficiently generate whole-organism chimaeras from blastocyst injections. This barrier could be overcome by strategies that confer a selective advantage on or enhance the survival of donor human cells, or by the development of techniques to better monitor the state of human pluripotent stem cells. For instance, human pluripotent stem cells that are in a ground state known as naive can be engrafted into pig and cattle blastocysts, but show little chimaera-forming abilities; by contrast, pluripotent stem cells in a different cell state known as intermediate can be engrafted and generate differentiated progeny[13].

Nonetheless, the model developed by Chang *et al.* provides a powerful tool for neuroscientists to study mammalian brain development and evolution. It will no doubt expand our ability to investigate the mechanisms of neuropsychiatric disorders. ■

Jimena Andersen *and* **Sergiu P. Pașca** *are in the Department of Psychiatry and Behavioral Sciences, Stanford University, Stanford, California 94305, USA.*
e-mail: spasca@stanford.edu

1. Capecchi, M. R. *Nature Med.* **7**, 1086–1090 (2001).
2. Chang, A. N. *et al. Nature* **563**, 126–130 (2018).
3. Chen, J., Lansford, R., Stewart, V., Young, F. & Alt, F. W. *Proc. Natl Acad. Sci. USA* **90**, 4528–4532 (1993).
4. Liégeois, N. J., Horner, J. W. & DePinho, R. A. *Proc. Natl Acad. Sci. USA* **93**, 1303–1307 (1996).
5. Usui, J. *et al. Am. J. Pathol.* **180**, 2417–2426 (2012).
6. Fraidenraich, D. *et al. Science* **306**, 247–252 (2004).
7. Kobayashi, T. *et al. Cell* **142**, 787–799 (2010).
8. Corbo, J. C. *et al. J. Neurosci.* **22**, 7548–7557 (2002).
9. Pașca, S. P. *Nature* **553**, 437–445 (2018).
10. Farahany, N. A. *et al. Nature* **556**, 429–432 (2018).
11. Hyun, I. *et al. Cell Stem Cell* **1**, 159–163 (2007).
12. Cohen, M. A. *et al. Proc. Natl Acad. Sci. USA* **113**, 1570–1575 (2016).
13. Wu, J. *et al. Cell.* **168**, 473–486 (2017).

This article was published online on 10 October 2018.

© 2018 Springer Nature Limited. All rights reserved.

Assumptions for emergent constraints

ARISING FROM P. M. Cox, C. Huntingford & M. S. Williamson *Nature* **553**, 319–322 (2018); https://doi.org/10.1038/nature25450

Uncertainty in equilibrium climate sensitivity (ECS) can potentially be narrowed by using an emergent constraint that relates a currently observable variable to climate-model-simulated ECS. A recent study[1] reports an emergent constraint that reduces ECS uncertainty by about 60% and shifts the central estimate of ECS to a lower value than that reported by the Intergovernmental Panel on Climate Change (IPCC). However, we show here that the assumptions that underpin the theoretical basis of the emergent constraint from Cox et al.[1] are not necessarily fulfilled. Alternative methods that more fully satisfy the theoretical assumptions indicate that the emergent constraint from Cox et al.[1] reduces ECS uncertainty by at most about 11% relative to the raw model spread that informs the analysis, and it is ambiguous whether the emergent constraint from Cox et al.[1] robustly lowers the central estimate of ECS. There is a Reply to this Comment by Cox, P. M. et al. *Nature* **563**, https://doi.org/10.1038/s41586-018-0641-x (2018).

The emergent constraint presented by Cox et al.[1] is based on the fluctuation–dissipation theorem, which "relates the mean response to impulsive external forcing of a dynamical system to its natural unforced variability"[2]. In the context of Cox et al.[1], ECS represents the mean response to external forcing, and the measure of natural unforced variability is represented by Ψ, a metric of global mean temperature variability. In addition, the relationship derived by Cox et al.[1] between Ψ and ECS (equation (2) in Cox et al.[1]) assumes that the residual global-mean forcing time series is stationary, consists of mutually independent random quantities and for any given year is independent of the global-mean temperature of the previous year[3,4]. Consequently, it is important to remove any non-random forced variability from the modelled and observed time series before calculating Ψ.

Cox et al.[1] calculate Ψ using time series of annual global-mean temperature that have been linearly de-trended in time within moving 55-year windows. We test whether this procedure can remove non-random forced temperature variability, which if not removed would undermine the theory relating Ψ to ECS. We do so by calculating the correlation between the de-trended time series of global-mean temperature (in models and observations) and the corresponding CMIP5 historical model-mean time series (representing forced temperature variability) within each of the moving 55-year windows considered in Cox et al.[1]. We find correlations that indicate that the linearly de-trended temperature residuals retain substantial forced variability (Fig. 1a, black lines). By not adequately removing forced temperature variability (from volcanic and greenhouse gas forcing; Extended Data Fig. 1), Ψ is inflated over the later portion of the historical record (figure 2a in Cox et al.[1]). This causes the modelled forcing ($Q = N + \lambda\Delta T$, where N is the top-of-atmosphere radiative imbalance, λ is the net feedback parameter and T is the global-mean temperature) to display non-trivial one-year-lag autocorrelation (Fig. 1b, black line). When the forcing exemplifies temporal persistence, a relationship between the forcing for a given year and the temperature of the previous year will be induced, which undermines the premise in Cox et al.[1] that temperature variability can be modelled as a first-order autoregressive process[3–5] (progression from equation (3) to equation (7) in Cox et al.[1]).

The issue of forced temperature variability leaking into the residual of the linearly de-trended temperature time series and of the forcing displaying non-random characteristics motivated us to test three alternative de-trending approaches.

In the first approach, we estimate unforced temperature variability as the residual of the linear regression between the temperature time series of each model (and of each observational dataset) and the corresponding historical multi-model-mean within each 55-year window (red lines in Fig. 1; Fig. 2d). This approach has been shown to be more effective at removing long-term forced variability than is temporal linear de-trending[6–10].

In the second approach, we select a 55-year segment of the temperature time series from the (linearly de-trended) pre-industrial control run of each model over each moving window (blue lines in Fig. 1; see also Supplementary Information). Pre-industrial control runs contain only unforced temperature variability by construction, so their use eliminates the need to remove forced temperature variability statistically. The trade-off, however, is that there are no observations that correspond to pre-industrial periods. Therefore, in the implementation of the emergent constraint for this approach (Fig. 2e), we use Ψ calculated from observations that were de-trended in the same way as the first alternative approach (discussed above; that is, the residual of linear regression against the model-mean temperature). These temperature residuals contain much less forced variability than those obtained in Cox et al.[1] via linear de-trending in time[6–10]. However, any forced variability that remains after de-trending tends to bias the central estimate of ECS in the positive direction.

Using these two approaches, we find that the one-year-lag autocorrelation of the forcing is closer to zero than it is using the method of Cox

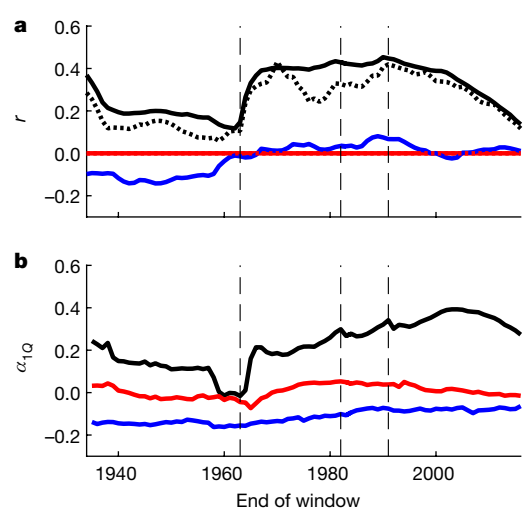

Fig. 1 | Analysis of simulated and observed time series using three methods to isolate unforced variability. a, b, Analogous to figure 2a in Cox et al.[1]; r is the correlation coefficient and α_{1Q} is the one-year-lag autocorrelation of the forcing. Solid lines are model-mean values for 55-year time periods that end in the given year. Dotted lines in **a** are the mean across four observational datasets (GISTEMP, HadCRUT4, NOAA and Berkeley Earth). Black lines correspond to time-series residuals after the temporal linear trend has been removed (using the method from Cox et al.[1]). Red lines correspond to residuals after the linear relationship with the historical multi-model-mean time series (representing forced variability) has been removed[6–10]. Blue lines correspond to time-series segments selected from the pre-industrial control runs of the models. Vertical dashed lines mark the major volcanic eruptions of Mount Agung, El Chichón and Mount Pinatubo.

© 2018 Springer Nature Limited. All rights reserved.

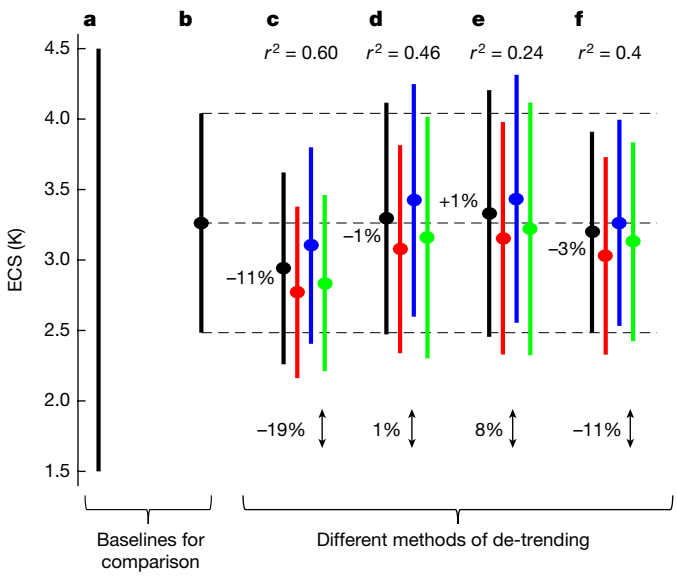

Fig. 2 | Comparison of the central estimate and likely range of ECS for various methods and for four observational datasets. a, IPCC likely range. **b**, Raw models used in Cox et al.[1]. **c**, Method of Cox et al.[1], with linear de-trending applied within each 55-year moving window. **d**, Residual of a linear regression against model-mean temperature within each 55-year moving window (first alternative method). **e**, Same as **d** for the observations, but using pre-industrial control runs of the models (our second alternative method). **f**, Same as **d**, but using the entire historical record rather than a moving window. In all cases, filled points show the central estimates and error bars the likely (more than 66%) ranges. Average changes in the central estimates of ECS across the four observational datasets are reported within the range defined by the dashed lines (which correspond to the estimate in **b**). Average changes in uncertainty ranges are reported at the bottom of the figure (doubled-headed arrows). r^2 values (the coefficient of determination) of the Ψ–ECS relationship are reported at the top of the figure. Results corresponding to observations from GISTEMP, HadCRUT4, NOAA and Berkeley Earth are shown in black, red, blue and green, respectively. Changes in uncertainty are reported relative to the raw model range ($\pm$0.95 standard deviations across the ECS values of CMIP5 models) used to inform the analysis (**b**) rather than relative to the broader IPCC range used as the baseline in Cox et al.[1] (**a**). See 'ECS uncertainty baseline for comparison' in Supplementary Information for further discussion.

et al.[1] (Fig. 1b). These alternative approaches are therefore better suited to inform the proposed[1] relationship between Ψ and ECS.

In the third approach, instead of using a moving-window method, we calculate Ψ over the entire historical record after forced temperature variability has been removed via regression against model-mean temperature variability[6–10] (Fig. 2f). The motivation for this approach is that the use of moving windows becomes less necessary when better methods than linear de-trending in time are used to remove non-random forced variability.

In Fig. 2d–f we summarize our calculations of the emergent constraint using these three alternative methods. We find that the more complete removal of forced temperature variability from Ψ produces central estimates of ECS that lack a consistent sign shift across the observational datasets. In addition, the statistical relationship ranges from providing no reduction in ECS uncertainty relative to the raw model baseline (Fig. 2d, e) to providing a reduction of at most about 11% (compared to the roughly 19% reduction in uncertainty relative to the raw model baseline obtained using the method of Cox et al.[1]; compare Fig. 2c, f). See 'ECS uncertainty baseline for comparison' in Supplementary Information for further discussion. We take this as evidence that the results of Cox et al.[1] depend, at least in part, on Ψ containing a specific mixture of information from both short-term unforced and longer-term forced temperature variability (probably from volcanic, greenhouse gas and other forcings; Extended Data Fig. 1), rather than containing information on only the ability of the climate system to dissipate internally generated temperature fluctuations. This is counter to the fluctuation–dissipation framework[2] and raises questions about the validity of the Ψ–ECS relationship derived in Cox et al.[1]. Nevertheless, the results of Cox et al.[1] raise interesting questions relating to why the specific blend of forced and unforced temperature variability captured by their Ψ metric can potentially provide a constraint on ECS.

Data availability

The CMIP5 data used for this study can be accessed at http://pcmdi9.llnl.gov. We used the same set of CMIP5 models as Cox et al.[1]. The GISTEMP observations can be accessed at https://data.giss.nasa.gov/gistemp. The HadCRUT4 observations can be accessed at https://crudata.uea.ac.uk/cru/data/temperature. The NOAA observations can be accessed at https://www.ncdc.noaa.gov/data-access/marineocean-data/mlost. The Berkeley Earth observations can be accessed at http://berkeleyearth.org/data. Other data are available from the corresponding author on request.

Code availability

The primary code used to make the plots is available on request.

Patrick T. Brown[1]*, Martin B. Stolpe[2] & Ken Caldeira[1]
[1]Department of Global Ecology, Carnegie Institution for Science, Stanford, CA, USA. [2]Institute for Atmospheric and Climate Science, ETH Zurich, Zurich, Switzerland. *e-mail: pbrown@carnegiescience.edu

Received: 7 February 2018; Accepted: 11 July 2018

1. Cox, P. M., Huntingford, C. & Williamson, M. S. Emergent constraint on equilibrium climate sensitivity from global temperature variability. *Nature* **553**, 319–322 (2018).
2. Leith, C. E. Climate response and fluctuation dissipation. *J. Atmos. Sci.* **32**, 2022–2026 (1975).
3. Brockwell, P. J. R. A. D. *Introduction to Time Series and Forecasting* (Springer, Berlin, 1996).
4. Wilks, D. S. *Statistical Methods in the Atmospheric Sciences* Vol. 100 (Elsevier, Amsterdam, 2011).
5. Foster, G., Annan, J. D., Schmidt, G. A. & Mann, M. E. Comment on "Heat capacity, time constant, and sensitivity of Earth's climate system" by S. E. Schwartz. *J. Geophys. Res.* **113**, D15102 (2008).
6. Ting, M., Kushnir, Y., Seager, R. & Li, C. Forced and internal twentieth-century SST trends in the North Atlantic. *J. Clim.* **22**, 1469–1481 (2009).
7. Mann, M. E., Steinman, B. A. & Miller, S. K. On forced temperature changes, internal variability and the AMO. *Geophys. Res. Lett.* **41**, 3211–3219 (2014).
8. Cheung, A. H. et al. Comparison of low-frequency internal climate variability in CMIP5 models and observations. *J. Clim.* **30**, 4763–4776 (2017).
9. Steinman, B. A., Mann, M. E. & Miller, S. K. Atlantic and Pacific multidecadal oscillations and Northern Hemisphere temperatures. *Science* **347**, 988–991 (2015).
10. Frankcombe, L. M., England, M. H., Mann, M. E. & Steinman, B. A. Separating internal variability from the externally forced climate response. *J. Clim.* **28**, 8184–8202 (2015).

Author contributions P.T.B. and M.B.S. performed the analysis. P.T.B. wrote an initial draft of the manuscript. All authors contributed to interpreting the results and refining the manuscript.

Competing interests Declared none.

Additional information
Extended data accompanies this Comment.
Supplementary information accompanies this Comment.
Reprints and permissions information is available at http://www.nature.com/reprints.
Correspondence and requests for materials should be addressed to P.T.B.

https://doi.org/10.1038/s41586-018-0638-5

© 2018 Springer Nature Limited. All rights reserved.

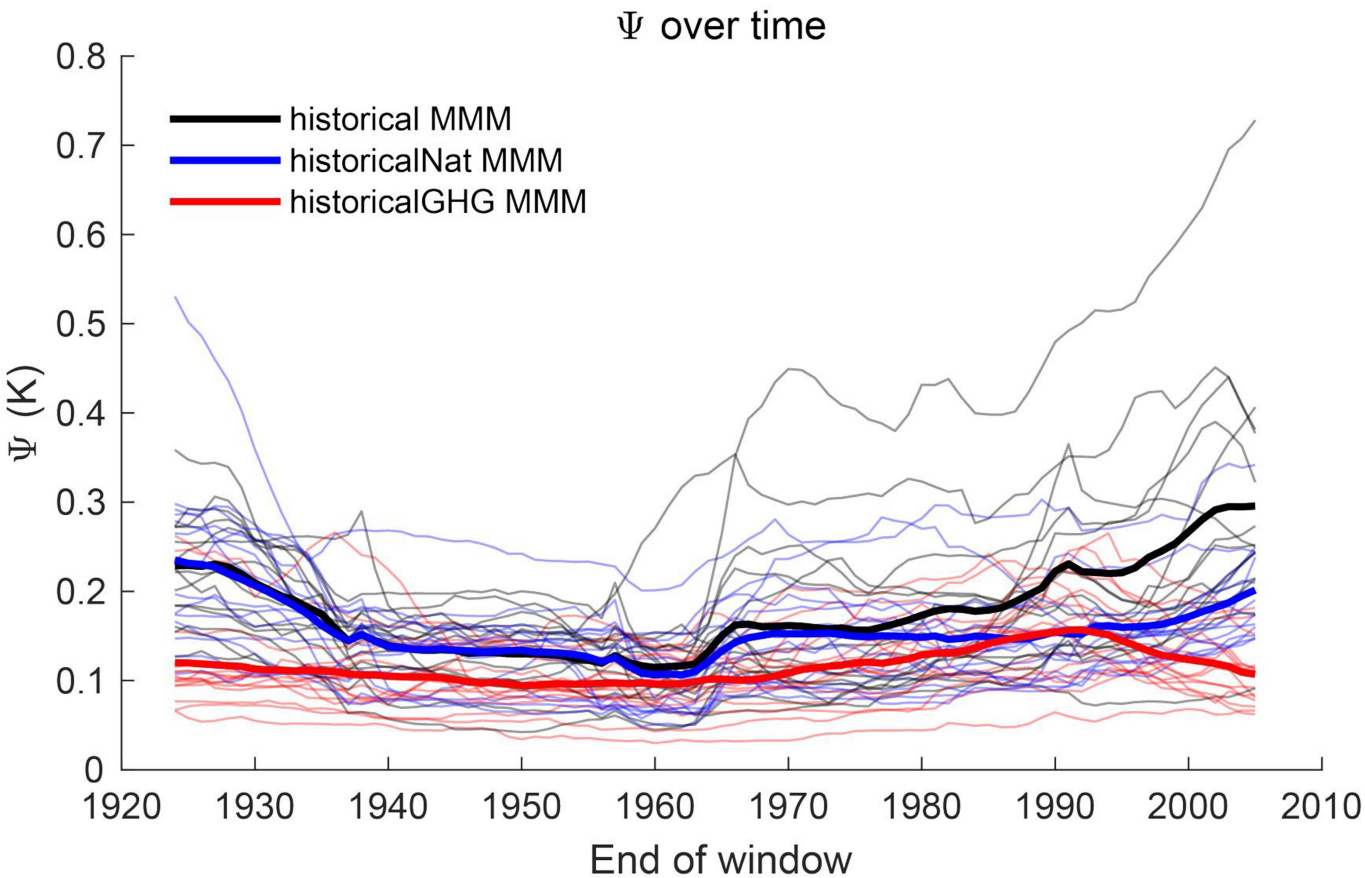

Extended Data Fig. 1 | *Ψ* metric of temperature variability versus time. This figure is analogous to figure 2a in Cox et al.[1], but without data from ACCESS1-0, inmcm4, IPSL-CM5B-LR, MPI-ESM-LR, GFDL-ESM2G, MIROC5 and bcc-csm1-1-m because not all required simulations were available for these models. Black lines correspond to *Ψ* calculated from the historical experiment, which includes all forcings. Blue lines correspond to *Ψ* calculated from the historical–natural experiment ('historicalNat'), which includes only forcings from changes in incoming solar radiation and volcanic aerosols. Red lines correspond to *Ψ* calculated from the historical greenhouse gas experiment ('historicalGHG'), which includes only forcing from well-mixed greenhouse gases (and ozone in some models). Thin lines are individual model-ensemble members (r1i1p1) and thick lines are multi-model means (MMMs). The data show that *Ψ* (as calculated by Cox et al.[1]) is non-stationary and inflated towards the end of the record, even in the case where models are forced by only greenhouse gases.

© 2018 Springer Nature Limited. All rights reserved.

Emergent constraints on climate sensitivity

ARISING FROM P. M. Cox, C. Huntingford & M. S. Williamson *Nature* **553**, 319–322 (2018); https://doi.org/10.1038/nature25450

The Intergovernmental Panel on Climate Change[1] (IPCC) has estimated the likely range of equilibrium climate sensitivity (ECS) to be 1.5–4.5 K. Recently, Cox et al.[2] claimed to have reduced this uncertainty to a likely range of 2.2–3.4 K. However, we believe that their results are derived from incorrect physics and are sensitive to arbitrary methodological choices. The study therefore does not represent a credible constraint on either the IPCC likely range or the range observed in the selected set of climate models. There is a Reply to this Comment by Cox, P. M. et al. *Nature* **563**, https://doi.org/10.1038/s41586-018-0641-x (2018).

The rationale of the approach of Cox et al.[2] is an emergent relationship between ECS in climate models and a metric Ψ, which characterizes the correlation structure of the solution to the stochastic, one-layer energy balance model:

$$C\frac{\mathrm{d}\Delta T}{\mathrm{d}t} = -\lambda\Delta T + Q \qquad (1)$$

where C is the effective heat capacity, T is the global temperature anomaly, t is time, λ is the feedback parameter and Q is a random noise term that represents the stochastic forcing from atmospheric weather. Equation (1) does not take into account energy uptake in the deep ocean and implies that the temperature response ΔT to radiative forcing is characterized by a single timescale $\tau = 1/[-\log(\alpha_{1T})] = C/\lambda$, where α_{1T} is the one-year-lag autocorrelation of ΔT. More relevant models for characterizing ECS are the two-layer energy balance model[3] or the three-layer model[4], which include two or three exponential responses, respectively, with time constants ranging from a few years to several hundred years. These models have been shown to accurately describe the response of global-mean temperature to forcing in Earth system models (ESMs).

The ECS in the one-layer energy balance model (equation (1)) is $Q_{2\times CO2}/\lambda$, where $Q_{2\times CO2}$ is the radiative forcing that corresponds to a doubling of CO_2 concentration. The forcing Q is a white-noise process with scale parameter σ_Q, and the solution is an Ornstein–Uhlenbeck process in which ΔT has variance $\sigma_T^2 = \sigma_Q^2/(2\lambda C)$ and autocorrelation function $\mathrm{e}^{-t/\tau}$. Thus, we have the emergent relationship

$$\mathrm{ECS} = \frac{Q_{2\times CO2}}{\lambda} = \sqrt{2}\,\frac{Q_{2\times CO2}}{\sigma_Q}\Psi \qquad (2)$$

where $\Psi = \sigma_T/\sqrt{-\log(\alpha_{1T})}$ is a metric that depends on the variance and autocorrelation time of the stochastic process. For the more realistic, multi-layer models, the solution is a multivariate Ornstein–Uhlenbeck process with a more complex autocorrelation structure than that described by Ψ, and equation (2) is not satisfied. When Ψ is defined as above, it is determined by the shortest of several timescales in the system, which provides no information about the long-term responses.

Cox et al.[2] contend that Ψ can be estimated from the instrumental temperature record and that there is an emergent relationship between ECS and estimates of Ψ (denoted $\hat{\Psi}$) in ESMs, which allows $\hat{\Psi}$ observed in the instrumental record to constrain the model-based estimate of ECS. They used sample estimators of σ_T and α_{1T} after linear de-trending in running time windows. However, the result of their analysis depends on the window length and on which part of the instrumental record is used for the analysis.

The estimated ECS versus window size is shown in Fig. 1a, which is a reproduction of figure 4a in Cox et al.[2] but with an extended range of window sizes. We observe that the expected value of the ECS increases from 2.5 K for 25-year windows to 3.0 K for 70-year windows. The constraint on the ECS found by Cox et al.[2] depends critically on their choice of window size (around 55 years). This choice was made by selecting the window size that made the slope of the regression line $\mathrm{ECS} = a\hat{\Psi} + b$ match the constant of proportionality $\sqrt{2}\,Q_{2\times CO2}/\sigma_Q$ derived from equation (2), when this constant is estimated as its mean over the ensemble of ESMs.

We also dispute the addition in Cox et al.[2] of a positive constant b to the emergent relationship without any theoretical justification. This adds a positive bias to the ECS that conceals the negative bias that is introduced by using the one-layer model. If, hypothetically, a non-zero b could be justified on the basis of a more complex model than equation (1), the slope a would have a different physical interpretation and there would no longer be any reason to assume that it would take the value $\sqrt{2}\,Q_{2\times CO2}/\sigma_Q$. But if this were the case, the rationale for using a 55-year window width would not be valid.

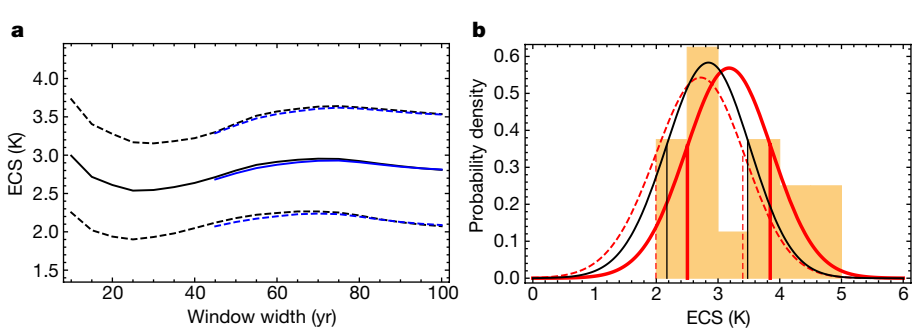

Fig. 1 | Analysis of the robustness of the emergent constraint on ECS. **a**, Mean (solid black line) and 66% confidence intervals (dashed black lines) for a broader range of window widths than included in figure 4a in Cox et al.[2]. The estimation method is described in Methods and gives similar results to the method by Cox et al.[2] (blue lines). **b**, The distribution shown as the black line and the yellow histogram are reproduced from figure 3a in Cox et al.[2]. In addition, we show the corresponding distributions if we use only data from 1880–1975 (thick red curve) or 1920–2016 (dashed red curve). The vertical lines represent 66% confidence intervals for the distributions.

© 2018 Springer Nature Limited. All rights reserved.

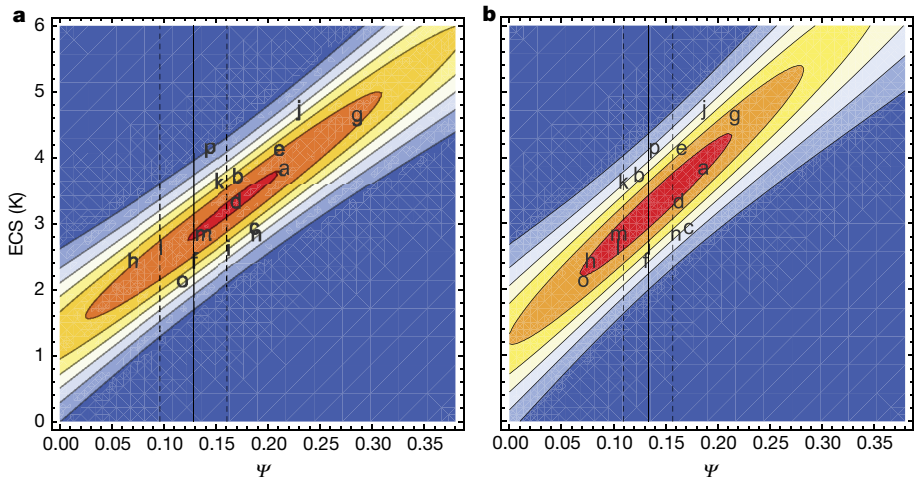

Fig. 2 | Dependence of the emergent constraint on the time period. **a**, Scatter plot (letters correspond to different ESMs; see extended data table 1 of Cox et al.[2]) similar to figure 2b in Cox et al.[2], but using the entire record (1880–2016) for the instrumental period. We also show a contour plot (colour scale) of the conditional probability density $P(\mathrm{ECS} \mid \Psi)$. The solid vertical line shows $\hat{\Psi}$ for the instrumental temperature record and the dashed vertical lines indicate the uncertainties (± 1 standard deviation). **b**, Same as **a**, but using only data for the period 1880–1975.

We believe that the approach in Cox et al.[2] is valid only if $\hat{\Psi}$ actually measures the theoretically informed metric Ψ, which depends on only the properties of the Ornstein–Uhlenbeck process. However, this is not the case because $\hat{\Psi}$ in Cox et al.[2] is strongly influenced by the anthropogenic trend in the temperature record, and more so towards the last forty years with stronger historical forcing. This is apparent from the estimates shown in figure 2a in Cox et al.[2]. In Fig. 1b we demonstrate the effect that this influence has on the probability density function for the ECS by repeating their analysis but omitting the last forty years of the temperature record. By doing so, $\hat{\Psi}$ is closer to the theoretically informed metric that characterizes the unforced variability. The resulting probability density function for the ECS has an expected value of 3.2 K and a standard deviation of 0.7 K. For comparison, the ECS values of the ESM ensemble have a mean of 3.3 K and a standard deviation of 0.7 K. The success of the emergent constraint should be measured against the range of this ESM ensemble and not against the IPCC likely range, which is an expert assessment of all available evidence on ECS.

We demonstrate why $\hat{\Psi}$ in Cox et al.[2] does not constrain the probability density function obtained directly from the ESM ensemble in Fig. 2; Fig. 2a shows the relationship between ECS and $\hat{\Psi}$ for all of the models when $\hat{\Psi}$ is obtained from the entire record, and corresponds to figure 2b of Cox et al.[2]. Because most models have $\hat{\Psi}$ much greater than the value of 0.13 K estimated from the instrumental temperature record, they have very low weight in the estimate of the posterior probability density function of the ECS. On the other hand, in Fig. 2b we show the same relationship but when the truncated temperature record is used. In this case, the $\hat{\Psi}$ values of the models do not differ as much from each other and are closer to the value estimated from the observational record. Consequently, the models are more equally weighted and the model results are not constrained effectively by the observational data.

The only way to obtain the probability density function of Cox et al.[2] is to use the last part of the record. To justify doing so, the existence of an emergent relationship between the ECS and the estimate $\hat{\Psi}$ obtained from the strongly forced part of the record must be assumed—a relationship that is not theoretically informed by the energy balance equation. However, even with this assumption, Fig. 1a demonstrates a range of probability density functions, with centre values ranging from 2.5 K to 3.0 K depending on an arbitrary choice of window width.

Methods

Our methods are identical to Cox et al.[2], with a few minor exceptions. We estimate the standard deviation of $\hat{\Psi}$ from ensembles of ESM runs rather than from the instrumental record. In Fig. 1a (and only there), we average estimates of σ_T and α_{1T} over all windows before computing $\hat{\Psi}$. We thus avoid problems with negative one-year-lag correlations for small window sizes. For the ESMs we used run r1 for each model and RCP8.5 data for the period 2006–2016. This yields similar results to Cox et al.[2].

Data availability

Relevant data are available from the corresponding author on reasonable request.

Martin Rypdal[1]*, Hege-Beate Fredriksen[1], Kristoffer Rypdal[1] & Rebekka J. Steene[1]
[1]Department of Mathematics and Statistics, UiT—The Arctic University of Norway, Tromsø, Norway. *e-mail: martin.rypdal@uit.no

Received: 23 February 2018; Accepted: 11 July 2018

1. Collins, M. et al. in *Climate Change 2013: The Physical Science Basis. Contribution of Working Group I to the Fifth Assessment Report of the Intergovernmental Panel on Climate Change* (eds Stocker, T. F. et al.) Ch. 12 (Cambridge Univ. Press, Cambridge, 2013).
2. Cox, P. M., Huntingford, C. & Williamson, M. S. Emergent constraint on equilibrium climate sensitivity from global temperature variability. *Nature* **553**, 319–322 (2018).
3. Geoffroy, O. et al. Transient climate response in a two-layer energy-balance model. Part I: analytical solution and parameter calibration using CMIP5 AOGCM experiments. *J. Clim.* **26**, 1841–1857 (2013).
4. Fredriksen, H.-B. & Rypdal, M. Long-range persistence in global surface temperatures explained by linear multibox energy balance models. *J. Clim.* **30**, 7157–7168 (2017).

Author contributions M.R., H.-B.F., K.R. and R.J.S. designed the study. H.-B.F. and R.J.S. collected data from the CMIP5 ensemble. M.R. and H.-B.F. performed the analyses. M.R., H.-B.F. and K.R. wrote the paper, with input from all authors.

Competing interests Declared none.

Additional information
Reprints and permissions information is available at http://www.nature.com/reprints.
Correspondence and requests for materials should be addressed to M.R.

https://doi.org/10.1038/s41586-018-0639-4

© 2018 Springer Nature Limited. All rights reserved.

Climate constraint reflects forced signal

ARISING FROM P. M. Cox, C. Huntingford & M. S. Williamson *Nature* **553**, 319–322 (2018); https://doi.org/10.1038/nature25450

A recent paper by Cox et al.[1] introduces Ψ, "a theoretically informed metric of global temperature variability", which scales with equilibrium climate sensitivity (ECS) across 16 general circulation models (GCMs). Cox et al.[1] report that Ψ provides a strong constraint on ECS, ruling out both high and low values. Our analysis shows that this constraint is sensitive to the GCMs considered, primarily reflects the forced climate response rather than climate variability and does not narrow the uncertainty in ECS. It is therefore premature to rule out the possibility of large ECS values. There is a Reply to this Comment by Cox, P. M. et al. *Nature* **563**, https://doi.org/10.1038/s41586-018-0641-x (2018).

Cox et al.[1] build on fundamental physical principles, making use of the fluctuation–dissipation theorem, which relates the statistical properties of a system in thermal equilibrium to the sensitivity of the system to forcing. The authors apply the fluctuation–dissipation theorem to the 'Hasselmann model' of global climate under white-noise forcing. Using this highly idealized model, they define Ψ as the ratio of temperature variability to a measure of the one-year-lag autocorrelation of annual-mean temperature and show Ψ to be proportional to ECS. Their work extends previous research on the fluctuation–dissipation theorem and climate[2–5] by demonstrating that Ψ scales with ECS in historical simulations performed with GCMs. Using the instrumental surface-temperature record as an observational constraint on Ψ, Cox et al.[1] propose bounds on ECS that are narrower than in previous assessments. They provide what appear to be the essential ingredients[6] for an emergent constraint on climate sensitivity: their metric Ψ is observable, scales with ECS values in GCMs and has a sound theoretical basis.

An implicit assumption by Cox et al.[1] is that Ψ primarily reflects internal climate variability. In simulations and observations of historical climate change, Ψ is also influenced by natural (volcanic and solar) and anthropogenic forcings. To determine whether Ψ scales with ECS in simulations without changes in external forcing, we use pre-industrial control experiments, in which global temperature variations are due to internal climate variability alone. Following Cox et al.[1], we calculate Ψ using de-trended, overlapping 55-year windows of global-mean surface temperature. The average of the individual windows in an entire control simulation of a model is denoted by $\bar{\Psi}$. Consistent with the findings of Cox et al.[1] for historical simulations, a strong relationship exists between $\bar{\Psi}$ and ECS in GCM control experiments (Fig. 1a).

However, there is substantial spread in the regression between $\bar{\Psi}$ and ECS in individual segments of the control simulations. For consistency with the length of the historical record (1880–2016), we randomly sample 137-year periods from each pre-industrial control simulation, compute $\bar{\Psi}$ and then calculate the correlation between $\bar{\Psi}$ and ECS. Repeating this calculation, we find that only about 7% of our samples yield a relationship that rivals or exceeds the correlation coefficient found by Cox et al.[1] ($r = 0.77$). This result suggests that the observational record is too short to act as a strong ECS constraint[7] and that forced temperature changes probably enhance the strength of the $\bar{\Psi}$–ECS relationship in historical simulations.

Compared to the historical simulations used by Cox et al.[1] (Fig. 1b), the pre-industrial control simulations exhibit a different $\bar{\Psi}$–ECS scaling (Fig. 1a), with a narrower range of $\bar{\Psi}$ values across GCMs. This difference in scaling has important implications. Applying the observational $\bar{\Psi}$ estimate to the pre-industrial control simulations yields a 95% confidence interval for the ECS of 2.6–5.4 °C (Fig. 1a). This is substantially higher than that found by Cox et al.[1] using historical simulations (1.6–4.0 °C; Fig. 1b). We therefore infer that the strong constraint on the high end of ECS reported by Cox et al.[1] arises primarily from the response to historical forcing, not from internal variability.

The physical derivation of the relationship between Ψ and ECS by Cox et al.[1] is valid only for stationary white-noise forcing. It is therefore important to remove forced temperature signals. Cox et al.[1] assume that forced temperature variability can be removed by linearly de-trending the temperature time series. An alternative method (which does not require this assumption) is to remove the ensemble-mean response of a model to external forcing. We contrast these two methods for signal removal using ten realizations of historical climate change from the CSIRO-Mk3-6-0 model (Fig. 2a). The approach of Cox et al.[1] yields Ψ values that are inflated after about 1950 relative to those based on

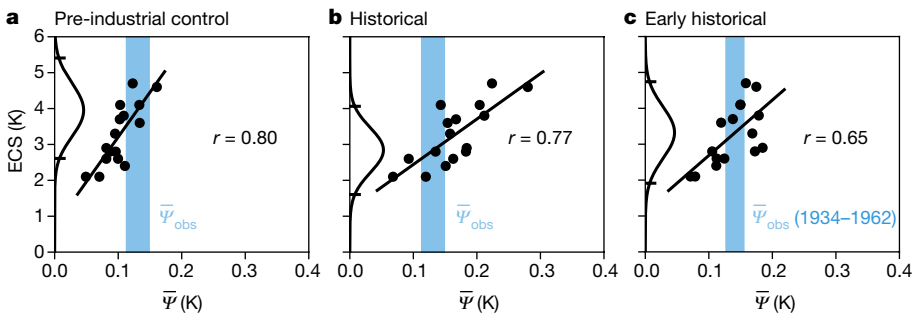

Fig. 1 | The ECS constraint depends on the underlying forcing. **a**, Relationship between $\bar{\Psi}$ and ECS derived from the entire length of the pre-industrial control simulation available for each model. **b**, As in **a**, but for simulations of historical climate change over the period 1880–2016. **c**, As in **b**, but considering only global temperature data before 1963. In each panel, the black circles represent the original 16-model subset highlighted by Cox et al.[1]. The black line is a linear fit and the vertical blue shading is the observational $\bar{\Psi}$ value (±1 standard deviation). In **a** and **b**, the observational range is derived from the entire temperature record (1880–2016), whereas the instrumental record before 1963 is used in **c** (Ψ values ending between 1934 and 1962). The implied probability distribution of ECS is displayed on the vertical axis. The median ECS value and 95% confidence interval for **a**–**c** are 4.0 ± 1.4 °C, 2.8 ± 1.2 °C and 3.3 ± 1.4 °C, respectively. The corresponding 95% confidence interval is denoted by horizontal lines along the *y* axis.

© 2018 Springer Nature Limited. All rights reserved.

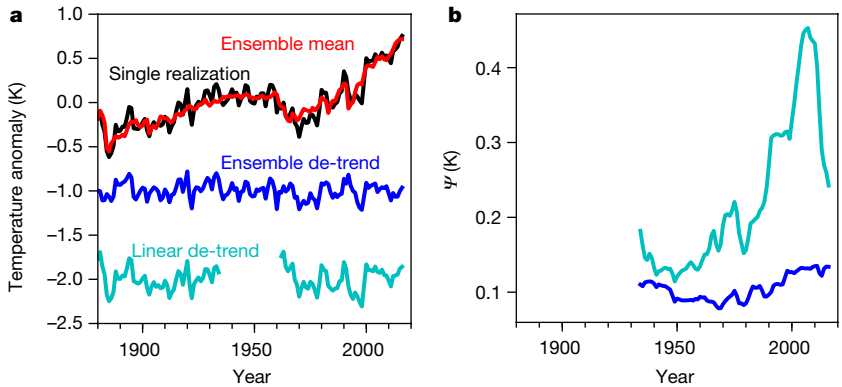

Fig. 2 | Forced temperature changes contaminate Ψ. a, Annual temperature anomaly of the CSIRO-Mk3-6-0 model for a single realization (black) and the ensemble average of ten realizations (red). The blue line shows the single realization de-trended using the ensemble average and the cyan line shows the first and last 55-year period of the single realization de-trended using a linear fit. The blue and cyan lines are offset by −1 K and −2 K for clarity. **b**, Ψ values for the end of each 55-year period using a moving linear fit to remove forced temperature changes (cyan), and Ψ values calculated after first removing forced temperature variability (as represented by the ensemble average, blue).

the removal of the ensemble-mean forced signal (figure 2a in Cox et al.[1]; Fig. 2b). The increase in Ψ occurs when there is a pronounced change in anthropogenic radiative forcing. Our results suggest that late twentieth-century forcing contaminates this variability-based constraint on ECS, undermining the physical interpretation of Ψ.

To understand the sensitivity of the ECS constraint to the time period selected, we consider the implications of using Ψ values from the early part of the historical record, before the rapid increase in anthropogenic forcing. We calculate $\bar{\Psi}$ from observational temperature data for the period 1880–1962, thus excluding forcing from the eruption of Mt Agung in 1963 (Fig. 1c). The resulting $\bar{\Psi}$ values are relatively small during the early historical period. The median ECS estimate is larger (3.3 °C; 95% confidence interval of 1.9–4.7 °C) than the result of Cox et al.[1] for the full historical record (2.8 °C). This indicates that the central ECS estimate and its bounds are sensitive to the time period considered.

The strength of the $\bar{\Psi}$–ECS correlation is also sensitive to the subset of GCMs considered. If we include six additional models that were listed in extended data table 1 of Cox et al.[1] but were not included in the primary analysis, then the $\bar{\Psi}$–ECS correlation decreases both in historical simulations ($r^2 = 0.59$ to $r^2 = 0.42$) and in pre-industrial control simulations ($r^2 = 0.63$ to $r^2 = 0.43$; Extended Data Fig. 1). Including additional GCMs that were not considered in the original research further degrades the $\bar{\Psi}$–ECS relationship (Extended Data Fig. 1), indicating that the ECS variance explained by $\bar{\Psi}$ depends on the models considered. The justification for the smaller, 18-model subset was "to avoid biasing the emergent constraint towards the centres with the most model runs". However, different models developed at the same centre can have widely varying $\bar{\Psi}$ and ECS values (Extended Data Fig. 1), so the inclusion of multiple models from the same institution does not necessarily weight $\bar{\Psi}$ and ECS values towards a particular centre. Our finding that the use of larger model subsets degrades the correlation between $\bar{\Psi}$ and ECS undermines the robustness of the constraint[6].

Emergent constraints are most convincing when they are based on a solid theoretical understanding of the underlying physical mechanisms. The constraint presented by Cox et al.[1] was developed assuming that forced changes are negligible. As we have shown, their constraint is influenced by climate forcings in the latter half of the twentieth century. This introduces ambiguity in the interpretation of $\bar{\Psi}$. Despite this ambiguity, the fact remains that GCMs exhibit a relationship between $\bar{\Psi}$ and ECS. This suggests that $\bar{\Psi}$ may reflect an indirect constraint on ECS through a dependence on aerosol forcing[8], volcanic response[9] and transient warming[10]. Although the original[1] Ψ constraint implies an ECS value near the centre of the likely range found by the Intergovernmental Panel on Climate Change (IPCC; 1.5–4.5 °C)[11], credible emergent-constraint studies[12] suggest ECS values that are greater than the likely estimate of Cox et al.[1]. In the absence of additional efforts to understand the dependence of the constraint of Cox et al.[1] on climate forcing and model selection, $\bar{\Psi}$ alone does not provide a sufficient basis for narrowing the range of ECS reported by the IPCC, which is based on multiple lines of evidence[11].

Data availability

The datasets generated during this study are available from the corresponding author on reasonable request.

Code availability

The Python code used to produce the figures in this paper is available from the corresponding author on reasonable request.

Stephen Po-Chedley[1]*, Cristian Proistosescu[2], Kyle C. Armour[3] & Benjamin D. Santer[1]

[1]Lawrence Livermore National Laboratory, Livermore, CA, USA. [2]Joint Institute for the Study of the Atmosphere and the Ocean, University of Washington, Seattle, WA, USA. [3]Department of Atmospheric Sciences and School of Oceanography, University of Washington, Seattle, WA, USA.
*e-mail: pochedley1@llnl.gov

Received: 21 March 2018; Accepted: 11 July 2018

1. Cox, P. M., Huntingford, C. & Williamson, M. S. Emergent constraint on equilibrium climate sensitivity from global temperature variability. *Nature* **553**, 319–322 (2018).
2. Leith, C. E. Climate response and fluctuation dissipation. *J. Atmos. Sci.* **32**, 2022–2026 (1975).
3. Wigley, T. M. L. & Raper, S. C. B. Natural variability of the climate system and detection of the greenhouse effect. *Nature* **344**, 324–327 (1990).
4. Langen, P. L. & Alexeev, V. A. Estimating 2 × CO_2 warming in an aquaplanet GCM using the fluctuation-dissipation theorem. *Geophys. Res. Lett.* **32**, L23708 (2005).
5. Schwartz, S. E. Heat capacity, time constant, and sensitivity of Earth's climate system. *J. Geophys. Res.* **112**, D24S05 (2007).
6. Klein, S. A. & Hall, A. Emergent constraints for cloud feedbacks. *Curr. Clim. Change Rep.* **1**, 276–287 (2015).
7. Kirk-Davidoff, D. B. On the diagnosis of climate sensitivity using observations of fluctuations. *Atmos. Chem. Phys.* **9**, 813–822 (2009).
8. Kiehl, J. T. Twentieth century climate model response and climate sensitivity. *Geophys. Res. Lett.* **34**, L22710 (2007).

© 2018 Springer Nature Limited. All rights reserved.

9. Bender, F. A.-M., Ekman, A. M. L. & Rodhe, H. Response to the eruption of Mount Pinatubo in relation to climate sensitivity in the CMIP3 models. *Clim. Dyn.* **35**, 875–886 (2010).
10. Flato, G. et al. in *Climate Change 2013: The Physical Science Basis. Contribution of Working Group I to the Fifth Assessment Report of the Intergovernmental Panel on Climate Change* (eds Stocker, T. F. et al.) 741–866 (Cambridge Univ. Press, Cambridge, 2013).
11. Collins, M. et al. in *Climate Change 2013: The Physical Science Basis. Contribution of Working Group I to the Fifth Assessment Report of the Intergovernmental Panel on Climate Change* (eds Stocker, T. F. et al.) 1029–1136 (Cambridge Univ. Press, Cambridge, 2013).
12. Caldwell, P. M., Zelinka, M. D. & Klein, S. A. Evaluating emergent constraints on equilibrium climate sensitivity. *J. Clim.* **31**, 3921–3942 (2018).

Author contributions All authors collaborated on the design of the study, the interpretation of the results and writing the manuscript. S.P. performed the analysis using CMIP5 data.

Competing interests Declared none.

Additional information
Extended data accompanies this Comment.
Supplementary information accompanies this Comment.
Reprints and permissions information is available at http://www.nature.com/reprints.
Correspondence and requests for materials should be addressed to S.P.

https://doi.org/10.1038/s41586-018-0640-y

© 2018 Springer Nature Limited. All rights reserved.

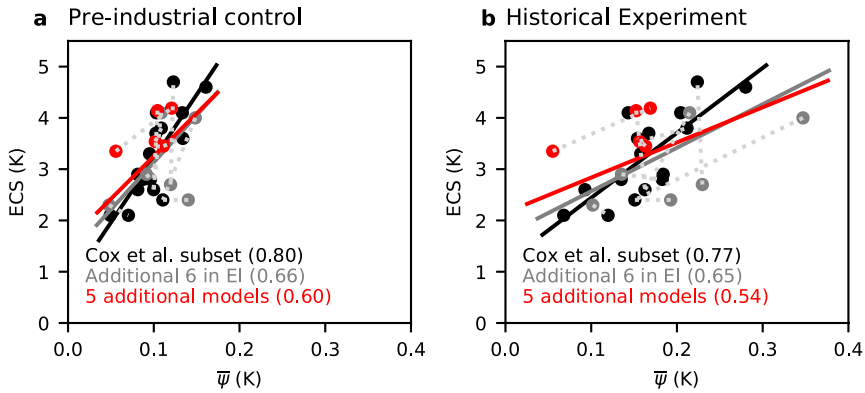

Extended Data Fig. 1 | The strength of the $\bar{\Psi}$–ECS relationship depends on the models considered. a, $\bar{\Psi}$ versus ECS for the pre-industrial control experiment (as in Fig. 1a), but including six additional models listed in extended data table 1 of Cox et al.[1] (grey) and five additional models not included in their original analysis (red; see Supplementary Information). The black line represents the regression obtained with the original 16-model subset of Cox et al.[1], the grey line represents the regression with the 22-model subset (grey and black dots) and the red line represents the regression using all 27 models. The dotted grey lines connect models from a common modelling centre. The correlation coefficient is listed in parentheses for each set of models considered. **b**, As in **a**, but for the historical experiment. Using all models and the early historical period (1880–1962) to compute $\bar{\Psi}$ (as in Fig. 1c), we arrive at a median ECS of 3.4 °C (95% confidence interval of 1.9–4.9 °C).

© 2018 Springer Nature Limited. All rights reserved.

Cox et al. reply

REPLYING TO P. T. Brown, M. B. Stolpe & K. Caldeira *Nature* **563**, https://doi.org/10.1038/s41586-018-0638-5 (2018); M. Rypdal, H.-B. Fredriksen, K. Rypdal & R. J. Steene *Nature* **563**, https://doi.org/10.1038/s41586-018-0639-4 (2018); S. Po-Chedley, C. Proistosescu, K. C. Armour & B. D. Santer *Nature* **563**, https://doi.org/10.1038/s41586-018-0640-y (2018)

The accompanying Comments[1–3] make several common points on our original study[4], which we address here. The main point in all three Comments relates to the role of external forcing, with each assuming that external forcing contaminates our emergent constraint. Each Comment goes on to suggest alternative methods for removing external forcing, including using pre-industrial control runs[1,3], using shorter periods of the historical record[2,3] or de-trending using the CMIP5 model mean[1]. All of these alternative methods are reported to weaken our emergent constraint on equilibrium climate sensitivity (ECS)[4]. Here we show that these alternative methods are neither necessary nor justified. Although residual external forcing after de-trending affects the gradient of the linear relationship between ECS and our metric of global temperature variability (Ψ), it does not undermine our original emergent constraint, which depends on only the linear proportionality between Ψ and ECS. Using outputs from the CMIP5 models, as well as one-box[5] and two-box[6] conceptual models, we show that the linear ECS–Ψ relationship is not only present but also strengthened by the presence of residual external forcing, which therefore serves to usefully reduce the uncertainty in the resulting emergent constraint on ECS.

In the context of our theory based on the one-box Hasselmann model[5], the response of global-mean temperature to a perturbation depends on climate sensitivity, regardless of whether the perturbation arises from internal variability or external forcing. This is consistent with all forcing being on the right-hand side of the Hasselmann equation, which therefore represents both internal and forced variability. We demonstrate this point by running Hasselmann models with and without external forcing (Fig. 1, experiments (i) and (iii), respectively; Extended Data Table 1; Methods). The correlation in the resulting ECS–Ψ relationship is stronger with external forcing. When random internal variability is removed, leaving only the common forcing, the linear relationship is almost perfect (Fig. 1, experiments (ii) and (iv)), with the reason for non-perfect correlation being differences between the models in the radiative forcing that corresponds to a doubling of CO_2 concentration ($Q_{2\times CO2}$).

The differences in the gradients of the ECS–Ψ relationship in Fig. 1 arise from differences in the magnitude of the residual forcing. As can be seen in equation (2) of Cox et al.[4], we expect ECS to scale with Ψ/σ_Q:

$$\mathrm{ECS} = \sqrt{2}\,Q_{2\times CO2}\left(\frac{\sigma_T}{\sigma_Q}\right)\frac{1}{\sqrt{-\log_e \alpha_{1T}}} = \sqrt{2}\,\frac{Q_{2\times CO2}}{\sigma_Q}\Psi$$

where σ_T and σ_Q are the standard deviation of the global-mean temperature and radiative forcing, respectively, and α_{1T} is the one-year-lag autocorrelation of the global-mean temperature. The simulations that include variations in forcing that arise from both residual external forcing (after de-trending) and internal variability have increased σ_Q and therefore led to shallower ECS–Ψ gradients. These forced runs produce higher correlations between ECS and Ψ because the time series of residual forcing is more common across the models. The dependence of the ECS–Ψ relationship on the magnitude of the forcing is the reason that Ψ varies in time in Cox et al.[4] (see figure 2a of Cox et al.[4]). It is also the reason why it is inappropriate to derive emergent constraints on ECS by combining ECS–Ψ relationships from control runs with estimates of observed Ψ from the historical period[1,3], as we show in Fig. 2.

In Fig. 2a we show the ECS–Ψ relationships for historical and control CMIP5 runs (using the 55-year window of Cox et al.[4]). The historical and control runs both fit around linear regression lines, suggesting a robust link between ECS and Ψ. However, the historical runs are on a line with a shallower gradient. This is because the historical runs experience larger σ_Q associated with residual external forcing, which is not present in the control runs. In addition, the correlation between ECS and Ψ in the historical runs ($r = 0.83$) is slightly larger than for the control runs ($r = 0.75$). The non-zero intercepts[2] are primarily due to regression dilution[7] that arises from the error in Ψ estimated from relatively short, 125-year time series and from the variation in $Q_{2\times CO2}$ across the model ensemble. This effect is evident even in pure Hasselmann models, as can be seen in Fig. 1. We suspect that a smaller, additional contribution to the intercept in the ECS–Ψ relationship across the CMIP5 models arises from slow feedbacks that are not captured in our Ψ statistic.

In Fig. 2b we plot ECS versus Ψ/σ_N, where σ_N is the standard deviation of the net top-of-atmosphere flux ($\Delta N = \Delta Q - \lambda\Delta T$, where ΔQ is the change in net radiative forcing, λ is the net feedback parameter and ΔT is the change in global-mean temperature). Net radiative forcing is not routinely available from the CMIP5 models, but σ_N is strongly correlated with σ_Q across the CMIP5 ensemble. Once Ψ is normalized by σ_N, the historical and control runs fit on a similar regression line in ECS–Ψ/σ_N phase space. This is because normalizing by σ_N essentially removes the dependence of the temperature response (given by Ψ) on the amplitude of the residual radiative forcing. The ECS–Ψ relationship that we reported[4] therefore depends on de-trending to remove aspects of the radiative forcing trend that differ most among the models. However, it does not require that all external forcing is removed. On the contrary, residual forcing sharpens the ECS–Ψ relationship when that residual forcing is similar across the models.

De-trending with a moving window is also important because it isolates the shorter timescale of the global temperature response. Previous studies have shown that the global temperature response in CMIP5 models is inconsistent with the single timescale represented in Hasselmann models[8]. However, a two-box model (with separate timescales representing the atmosphere or mixed-layer and deep ocean) gives a much better fit to the longer-timescale and transient responses of models[6]. Moving-window de-trending removes the longer-timescale response, revealing the shorter-timescale response, which is most likely to be well approximated by the one-box Hasselmann model. We chose our 55-year window to minimize the uncertainty in the emergent constraint (rather than to fit the theoretical gradient expected from the Hasselmann model, as suggested by Rypdal et al.[2]). However, this window length neatly separates the short (roughly 5-year) and long (roughly 200-year) timescales of climate models[6]. By contrast, alternative approaches that de-trend without high-pass filtering[1] contaminate the ECS–Ψ relationship with longer timescales (Extended Data Fig. 1).

In response to suggestions that the Hasselmann model is an inappropriate underlying model[2], we tested the generality of the ECS–Ψ emergent relationship by considering two-box models that have been shown to emulate the transient responses of CMIP5 models[6]. In Extended Data Fig. 2 and Extended Data Table 1 we show results

© 2018 Springer Nature Limited. All rights reserved.

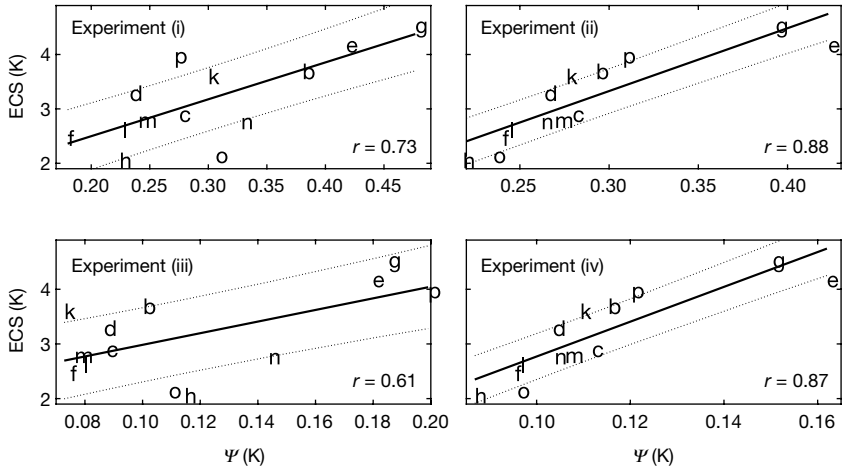

Fig. 1 | Typical results for experiments with the one-box Hasselmann model. Experiments are as follows (see also Methods): (i) historical runs with both external forcing factors and random variability in forcing; (ii) historical runs with external forcing factors only; (iii) control runs with random variability in forcing; and (iv) control runs with common random forcing. See extended data table 1 in Cox et al.[4] for the letter–model correspondence. Solid lines indicate the emergent relationship and dotted lines are the prediction error. The historical forcing (top panels) is taken from Meinshausen et al.[10] and the random component of the radiative forcing (right panels) is assumed to have a standard deviation of 0.25 W m^{-2}.

from four separate 125-year numerical experiments. In all cases, the global-mean temperatures were processed as in Cox et al.[4], using a 55-year moving window. As for the Hasselmann models (Fig. 1), there is always a linear relationship between ECS and Ψ, but it is stronger in the historical runs (Extended Data Fig. 2, (i)) than in the control runs (Extended Data Fig. 2, (iii)). A strong correlation ($r = 0.95$) is produced if the models experience a common forcing time series, whether this is external Intergovernmental Panel on Climate Change (IPCC) forcing (Extended Data Fig. 2, (ii)) or the same sequence of internal variability in Q (Extended Data Fig. 2, (iv)). The ECS–Ψ relationship is weakened when the residual forcing time series has no commonality between models. In this case, estimates of Ψ have an error that scales inversely to the square-root of the sample size, so longer time series are required to properly reveal the ECS–Ψ relationship.

The two-box model experiments therefore back-up our four main conclusions in response to the accompanying Comments[1–3]. First, although we agree that some residual external forcing remains after our de-trending, it actually helps to tighten the emergent constraint on ECS. It is therefore counterproductive to exclude periods during which there is substantial external forcing because doing so inevitably leads to a weaker relationship between ECS and Ψ[1–3] (Fig. 1). Second, the gradient of ECS versus Ψ depends inversely on the magnitude of the residual forcing (internal plus external). Therefore, it is inappropriate to derive emergent constraints on ECS by combining ECS–Ψ relationships from control runs with estimates of observed Ψ from the historical period[1,3]. Doing so will lead to an overestimate of ECS because residual σ_Q values are lower in the control runs, which leads to a steeper ECS–Ψ relationship (Fig. 2). Third, de-trending is important to eliminate the longer timescales of the climate response, which helps to reveal the ECS–Ψ relationship. In the absence of such high-pass filtering, the emergent relationship is contaminated by the longer timescale[1] (Extended Data Fig. 1). Last, although we originally explained the ECS–Ψ relationship in terms of the response of the one-box Hasselmann model[4], we also find similar relationships in de-trended data from more complex models[9], such as two-box models that are known to emulate CMIP5 models more effectively[2] (Extended Data Fig. 2).

The strength of our emergent constraint comes in part from the year 1960 onwards. This is due to this being a period when forcing is comparatively high, so the larger responses in Ψ from the more sensitive, higher-ECS models (figure 2a in Cox et al.[4], magenta lines) differentiate them from the lower-ECS ones (figure 2a in Cox et al.[4], green lines). We have shown here that this sharper differentiation would be expected in the Hasselmann model and in the two-box models in the

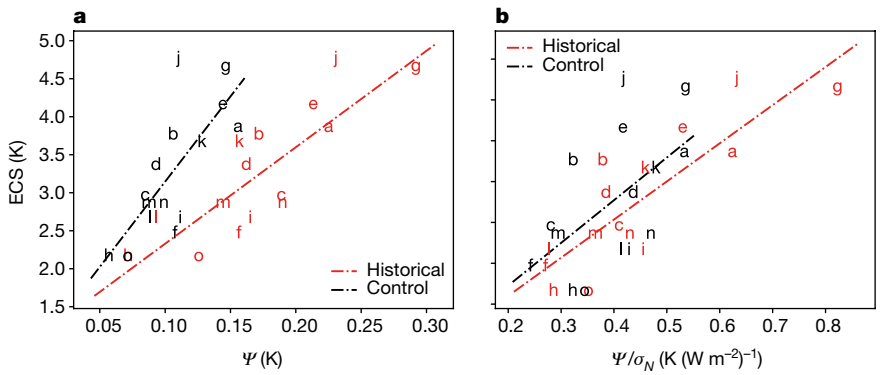

Fig. 2 | Comparison of different emergent relationships. a, **b**, ECS versus Ψ (**a**) and ECS versus Ψ/σ_N (**b**) for CMIP5 historical (red) and control (black) runs. In both cases, a 55-year window is used, as in Cox et al.[4]. The model data are taken from 1880–2016 for the historical runs (as in Cox et al.[4]) and from the first 239 years of each control run. Only models with the necessary data available for both of these runs are shown. As in Fig. 1, letters represent models given in extended data table 1 in Cox et al.[4].

© 2018 Springer Nature Limited. All rights reserved.

presence of common forcing. The observations do not share the large Ψ response of the more sensitive models, which leads to the lower-ECS emergent constraint (figure 2a in Cox et al.[4], black circles). The additional analyses presented here thus support the overall conclusions of our original work[4].

We acknowledge funding from the ERC ECCLES project (P.M.C., F.J.M.M.N.), the EU CRESCENDO project (P.M.C., M.S.W.) and the NERC CEH National Capability fund (C.H.) We also acknowledge the World Climate Research Programme's Working Group on Coupled Modelling, which is responsible for CMIP, and we thank the climate modelling groups (listed in extended data table 1 of Cox et al.[4]) for producing and making available their model output.

Methods

We use the parameters of the two-box models fitted to the CMIP5 models by Geoffroy et al.[6] (tables 3 and 4) for the two-box and Hasselmann model simulations. Because of the reduced number of parameters in the Hasselmann model, we use only the climate feedback parameter (λ), the radiative forcing due to a quadrupling of CO_2 ($F_{4\times CO2}$) and the effective heat capacity (C). ECS is calculated as $\mathrm{ECS} = F_{4\times CO2}/(2\lambda)$. We use the intersection of the sets of CMIP5 models in Cox et al.[4] and Geoffroy et al.[6]. The mean amplitude of the random forcing σ_Q is estimated from CMIP5 control runs and is fixed across the models to 0.25 W m^{-2} (relative standard deviation of about 10%) in the Hasselmann and two-box simulations. The time step is 0.01 years when integrating and we then take annual means to create an analogous time series to the CMIP5 data.

We perform five experiments: (i) full historical simulations from 1880 to 2005, with forcing being the sum of prescribed IPCC radiative forcing[10] from greenhouse gases, aerosols, volcanoes and so on, and a random component that represents internal variability; (ii) historical simulations with only IPCC radiative forcing, no random component; (iii) control simulations of 125 years, with only random forcing; (iv) same as experiment (iii), but with each model in the experiment forced with the same random time series; and (v) a control simulation of 300 years (same as experiment (iii) but longer).

For historical simulations we use the total radiative forcing time series from Meinshausen et al.[10]. We start the simulations at year 1765. The random forcing time series is generated from a zero-mean normal distribution with standard deviation σ_Q. A different random time series is generated for each model simulation, apart from experiment (iv), for which the same random sequence is used across the models. To obtain Ψ and the emergent relationships, we apply our original methodology[4], although we use the shorter historical period 1880–2005. When random forcing is used, the experiment is repeated 20 times to sample the range of possible values. The results are shown in Fig. 1 (Hasselmann model), Extended Data Fig. 2 (two-box model) and Extended Data Table 1.

Data availability

Relevant data are available from the corresponding author on reasonable request.

Peter M. Cox[1]*, Mark S. Williamson[1], Femke J. M. M. Nijsse[1] & Chris Huntingford[2]

[1]College of Engineering, Mathematics and Physical Science, University of Exeter, Exeter, UK. [2]Centre for Ecology and Hydrology, Wallingford, UK.
*e-mail: p.m.cox@exeter.ac.uk

1. Brown, P. T., Stolpe, M. B. & Caldeira, K. Assumptions for emergent constraints. *Nature* **563**, https://doi.org/10.1038/s41586-018-0638-5 (2018).
2. Rypdal, M., Fredriksen, H.-B., Rypdal, K. & Steene, R. J. Emergent constraints on climate sensitivity. *Nature* **563**, https://doi.org/10.1038/s41586-018-0639-4 (2018).
3. Po-Chedley, S., Proistosescu, C., Armour, K. C. & Santer, B. D. Climate constraint reflects forced signal. *Nature* **563**, https://doi.org/10.1038/s41586-018-0640-y (2018).
4. Cox, P. M., Huntingford, C. & Williamson, M. S. Emergent constraint on equilibrium climate sensitivity from global temperature variability. *Nature* **553**, 319–322 (2018).
5. Hasselmann, K. Stochastic climate models part I. Theory. *Tellus* **28**, 473–485 (1976).
6. Geoffroy, O. et al. Transient climate cesponse in a two-layer energy-balance model. Part I: analytical solution and parameter calibration using CMIP5 AOGCM experiments. *J. Climate* **26**, 1841–1857 (2013).
7. Frost, C. & Thompson, S. G. Correcting for regression dilution bias: comparison of methods for a single predictor variable. *J. R. Stat. Soc. Ser. A* **163**, 173–189 (2000).
8. MacMynowski, D. G. et al. The frequency response of temperature and precipitation in a climate model. *Geophys. Res. Lett.* **38**, L16711 (2011).
9. Williamson, M. S., Cox, P. M. & Nijsse, F. J. M. M. Theoretical foundation of emergent constraints: relationships between climate sensitivity and global temperature variability in conceptual models. *Dyn. Stat. Clim. Syst.* (in the press).
10. Meinshausen, M. et al. The RCP greenhouse gas concentrations and their extensions from 1765 to 2300. *Clim. Change* **109**, 213 (2011).

Author contributions The list of co-authors and their order are slightly different from the original study[4]. F.J.M.M.N. carried-out many statistical tests in response to the accompanying Comments, and has therefore been added to the author list for this Reply. Similarly, M.S.W. carried out substantial new work with simple models, and has therefore been moved to the second-author position. P.M.C. and M.S.W. drafted the response. C.H. provided the time-series data for the CMIP5 models. M.S.W. produced Fig. 1 and Extended Data Fig. 2 using the one- and two-box models. P.M.C. produced Fig. 2 and Extended Data Fig. 1 from the CMIP5 models. F.J.M.M.N. provided statistical expertise and analysed the impact of regression dilution. All authors contributed to the final version of the Reply.

Competing interests Declared none.

Additional information
Extended data accompanies this Reply.
Reprints and permissions information is available at http://www.nature.com/reprints.
Correspondence and requests for materials should be addressed to P.M.C.

https://doi.org/10.1038/s41586-018-0641-x

© 2018 Springer Nature Limited. All rights reserved.

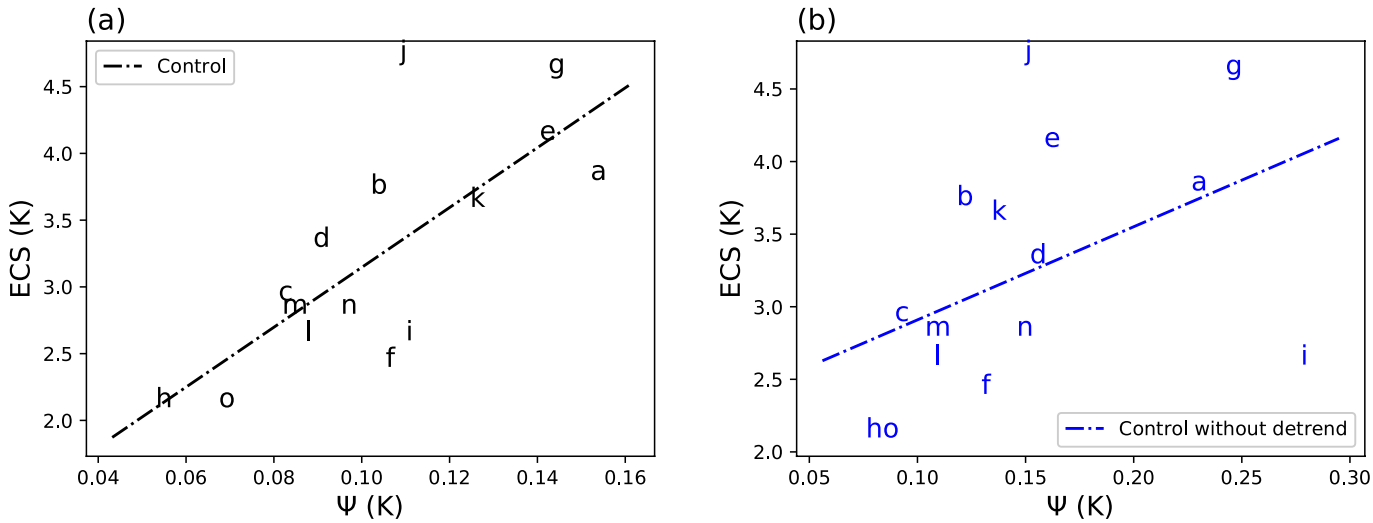

Extended Data Fig. 1 | Impact of de-trending on the ECS–Ψ relationship in CMIP5 models. a, Control runs linearly de-trended in a 55-year moving window ($r = 0.75$). **b**, Control runs without de-trending ($r = 0.45$).

© 2018 Springer Nature Limited. All rights reserved.

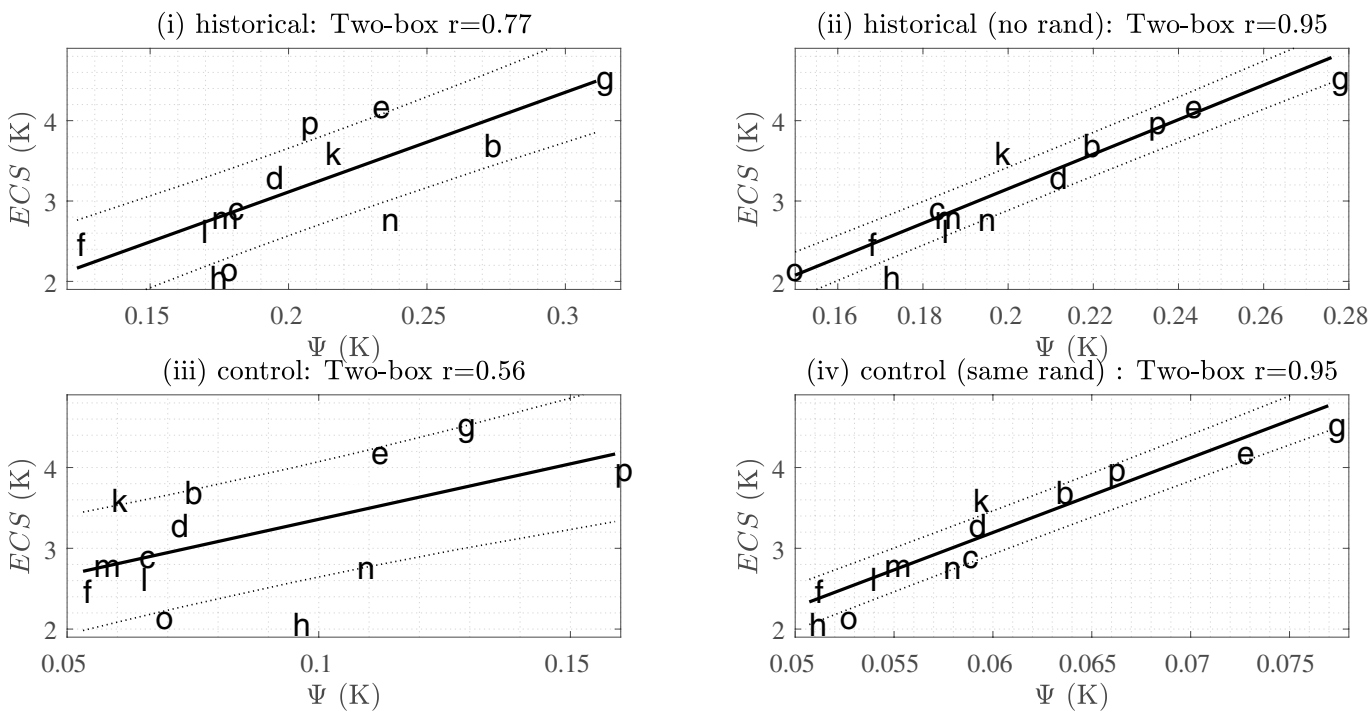

Extended Data Fig. 2 | Typical results for experiments (i)–(iv) with the two-box model. As in Figs. 1 and 2, letters represent models given in extended data table 1 in Cox et al.[4]. Solid lines indicate the emergent relationship and dotted lines are the prediction error.

© 2018 Springer Nature Limited. All rights reserved.

Extended Data Table 1 | Experiments with common models

		Model	r
(i)	Historical (IPCC and random forcing, 1880 - 2005)	H76	0.66 +/- 0.17
		Two-box	0.68 +/- 0.19
		CMIP5	0.73
(ii)	Historical (as above but no random forcing)	H76	0.88
		Two-box	0.95
		CMIP5	n/a
(iii)	Control, 125 years	H76	0.50 +/- 0.22
		Two-box	0.55 +/- 0.22
		CMIP5	0.69
(iv)	As (iii) but same random forcing in each model	H76	0.86 +/- 0.04
		Two-box	0.95 +/- 0.01
		CMIP5	n/a
(v)	As (iii) but 300 years	H76	0.63 +/- 0.17
		Two-box	0.69 +/- 0.16
		CMIP5	0.82

Models common to the sets of CMIP5 models in Cox et al.[4] and Geoffroy et al.[6] are used. We used our original method[4]. The Hasselmann (H76) and two-box models were run 20 times, with means taken if a random forcing component was present. Plus and minus values are standard deviations in the correlation of the ECS–Ψ relation.

© 2018 Springer Nature Limited. All rights reserved.

https://doi.org/10.1038/s41586-018-0631-z

Magnetism in two-dimensional van der Waals materials

Kenneth S. Burch[1], David Mandrus[2,3] & Je-Geun Park[4,5]*

The discovery of materials has often introduced new physical paradigms and enabled the development of novel devices. Two-dimensional magnetism, which is associated with strong intrinsic spin fluctuations, has long been the focus of fundamental questions in condensed matter physics regarding our understanding and control of new phases. Here we discuss magnetic van der Waals materials: two-dimensional atomic crystals that contain magnetic elements and thus exhibit intrinsic magnetic properties. These cleavable materials provide the ideal platform for exploring magnetism in the two-dimensional limit, where new physical phenomena are expected, and represent a substantial shift in our ability to control and investigate nanoscale phases. We present the theoretical background and motivation for investigating this class of crystals, describe the material landscape and the current experimental status of measurement techniques as well as devices, and discuss promising future directions for the study of magnetic van der Waals materials.

Magnetism in two dimensions has long been at the heart of numerous theoretical[1–6], experimental[7–10] and technological advances[7], such as the study of topology, the fluctuation-driven generation of new phases and the electrical manipulation and detection of spin. A particularly promising aspect of two-dimensional (2D) magnetism is the ability to rapidly fabricate various 2D heterostructures with engineered levels of strain, chemistry, optical and electrical properties[11–15]. Just as graphene and transition-metal dichalcogenides revolutionized condensed matter and materials engineering, the introduction of a new class of 2D atomic crystals, magnetic van der Waals (vdW) materials[11], is expected to open up a wide range of possibilities for applications and fundamental research[11,16]. These materials offer a new means to study 2D magnetism, where spin fluctuations are expected to be strongly enhanced[17–19]. Indeed, the wide flexibility of 2D atomic crystals with different elements and structures suggests straightforward tuning of the magnetic anisotropy, which is crucial for reducing or strengthening spin fluctuations and thus various forms of order[5–10,17,19,20].

The field of magnetic 2D atomic crystals is advancing rapidly[11,18], with numerous demonstrations of new systems in which 2D magnetism is realized by using only adhesive tape, chemical vapour deposition or molecular beam epitaxy, as was first achieved in graphene. In just the past two years, several notable examples of magnetic order have been observed in single atomic layers of $FePS_3$[21,22], CrI_3[23], $Cr_2Ge_2Te_6$[20], VSe_2[24] and $MnSe_2$[25]. This review aims to highlight some of the recent advances in this area and serve as a guide to some of the enormous opportunities provided by the arrival of magnetic vdW materials (see Fig. 1). These opportunities include the thorough examination of well-established theories, such as the Ising transition[3], the Berezinskii–Kosterlitz–Thouless (BKT) transition of the XY model[4,5] and the Mermin–Wagner theorem[6]. They also include the control and manipulation of magnetic states through coupling to external perturbations such as strain, light, gating, proximity and moiré patterns. In addition, further exotic quantum phases are expected to be revealed in these materials and their heterostructures, including the quantum Hall effect, quantum spin Hall effect, quantum spin liquids and the fractionalization of quasiparticles.

As an example, one can envision thorough experimental investigations of the widely used Mermin–Wagner theorem, which is a rare example of an exact result in many-body physics. The theorem is often misunderstood to imply that any order in two dimensions is theoretically excluded. Strictly speaking, however, such order is only ruled out for continuous rotational symmetries and short-range interactions. This is mainly due to the enhanced fluctuations in two dimensions, which make symmetry-breaking order unsustainable. However, by gapping the low-energy modes through the introduction of anisotropy, order could be established by providing stabilization of long-range correlations in two dimensions, which is similar to the presence of a magnetically ordered state in the 2D Ising model[20,23]. Given the ease with which anisotropy can be introduced into magnetic systems (for example, via spin–orbit coupling or lattice distortions), we expect to see many more 2D magnetic vdW materials hosting magnetically ordered phases. Moreover, the presence of the intrinsically enhanced and potentially novel fluctuations can produce other types of order that may be useful for producing new types of superconductor[1] and platforms for topological quantum computation[2].

Another interesting phenomenon observed in 2D magnetic vdW systems is the XY-type interaction. Berezinskii, Kosterlitz and Thouless[4,5] demonstrated in their seminal works that a new type of topological order can emerge that involves the creation of vortex–antivortex pairs. These topological objects are defined by their winding number and can create an ordered state by forming bound pairs of opposite winding numbers. A generalization of this idea is the skyrmion, which is found in certain magnetic systems without inversion symmetry[26]. Interestingly, order can also be suppressed by further enhancing the degeneracy of the ground state and the associated strong spin fluctuations. When these spin fluctuations become dominant, they can mediate the formation of otherwise hidden quantum phases. The arrival of 2D magnetic vdW materials opens up exciting opportunities for studying the emergence of such strong fluctuations and their role in creating novel phases, as well as for understanding new phenomena in the 2D limit. Moreover, because 2D materials do not require lattice matching, a wide range of material combinations become possible (for example, moiré folding of the Brillouin zone[14] or strain-induced effective fields[12]). Although the possibilities are endless, in this article we focus on those that we expect will lead to the biggest potential payoffs in the near future in relation to new physical phenomena and devices.

[1]Physics Department, Boston College, Boston, MA, USA. [2]Department of Materials Science and Engineering, University of Tennessee, Knoxville, TN, USA. [3]Materials Science and Technology Division, Oak Ridge National Laboratory, Oak Ridge, TN, USA. [4]Center for Correlated Electron Systems, Institute for Basic Science, Seoul, South Korea. [5]Department of Physics and Astronomy, Seoul National University, Seoul, South Korea. *e-mail: jgpark10@snu.ac.kr

© 2018 Springer Nature Limited. All rights reserved.

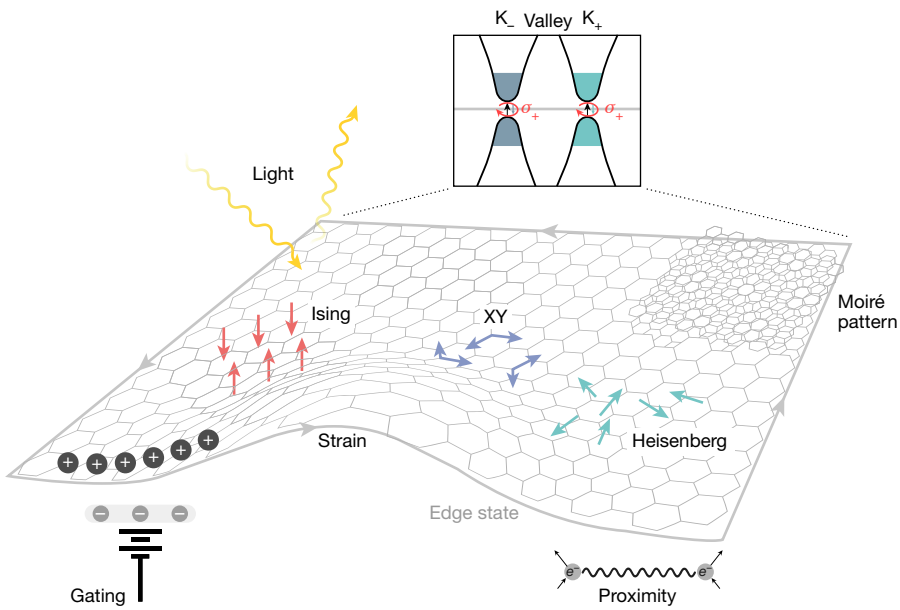

Fig. 1 | Physical phenomena that can be studied with magnetic vdW materials. 2D magnetic vdW materials are an ideal platform for investigating how the Hamiltonians of the fundamental magnetism models (the Ising, XY and Heisenberg models; magnetic moments indicated by the red, purple and cyan arrows, respectively) behave in the 2D limit. In addition, the magnetic ground states of these materials could be controlled by external perturbations, such as gating and strain, or via proximity effects and moiré patterns. Because of the intrinsic properties of their honeycomb lattice, there is also a possibility of light–matter interactions through valley coupling of K_- and K_+ points in the momentum space and the edge states (grey arrows).

Material landscape

Most of the magnetic vdW materials are layered, cleavable transition-metal chalcogenides and halides and typically have a layer of metal ions sandwiched between layers of chalcogens or halides. As with other vdW materials, the easy cleavage and lack of dangling bonds allow the creation of nearly perfect surfaces and interfaces, regardless of lattice matching (size or symmetry), providing a vast range of possibilities for such heterostructures[14,27]. These systems have diverse magnetic and electronic properties and include ferromagnetic semiconductors, such as $Cr_2(Si,Ge)_2Te_6$[28,29] and MSe_2 (M = V, Mn)[24,25], itinerant ferromagnets (FMs), such as Fe_3GeTe_2[30], and insulating antiferromagnets (AFMs), such as MPX_3 materials (M = transition metal, X = S or Se)[21,22,31]. There are also materials with strong bond-dependent interactions, such as α-$RuCl_3$[32,33]. The spin Hamiltonian and magneto-crystalline anisotropy vary widely from material to material, and they can be tuned through chemical doping, strain or proximity effects. In the near future, we envision efforts focused on developing various thin films via chemical vapour deposition and molecular beam epitaxy[24,25], as well as new materials with the super-exchange interactions, the spin–orbit interaction and the resulting anisotropy tuned by doping of the non-magnetic atom[34].

Optical probes of magnetism

A key challenge is detecting the long-range order, domains and associated magnetic fluctuations. Standard techniques (for example, superconducting quantum interference device (SQUID) magnetometry and neutron scattering) used for bulk crystals, large-area thin films and nanoparticles in solution are unlikely to be successful in magnetic vdW materials, which have small volumes[7]. To evaluate the utility of optical techniques, we consider the energy shifts in the band structure of magnetically ordered materials (Fig. 2a). Specifically, the energy splitting of the spin-up and spin-down states that are associated with the moment is proportional to the strength and sign of the magnetic exchange as well as the magnetization. Assuming that spin–orbit coupling is present, circularly polarized ($\hat{\sigma}^{\pm}$) light will cause a transition from a particular spin state. This is most easily detected by measuring the circular dichroism in the absorption or reflection, that is, the magneto-circular dichroism (MCD)[35]. Alternatively, one can use the fact that polarized light $(\hat{x},\hat{y})$ is a sum of circular polarizations with different phases, $\hat{x}/\hat{y} = \hat{\sigma}^{+} \pm i\hat{\sigma}^{-}$. Thus, upon transmission (Faraday effect) or reflection (Kerr effect), linearly polarized light will become elliptical, with the change in the polarization angle being proportional to the magnetization (assuming small angles and no magneto-elastic coupling-induced anisotropy). MCD is thus an important complement to Kerr rotation and magnetization studies, as it is only sensitive to time-reversal-symmetry breaking and generally immune to structural anisotropy. Nonetheless, we note that for both Kerr and MCD the direction and size of the magnetization probed depends sensitively on the wavelength, interference, film thickness and setup[8,36].

Studies of Kerr rotation versus the applied magnetic field produced the first evidence of order in thin layers of $Cr_2Ge_2Te_6$[23] and CrI_3[20] (see Fig. 2b). In CrI_3 the bilayer system showed zero out-of-plane magnetization up to a critical value of the magnetic field, whereas all other examined materials generally exhibited the hysteresis expected from a ferromagnet. This was interpreted as evidence for an antiferromagnetic configuration between the layers. Although one could expect this to indicate a change in the easy axis of the bilayer system, more recent MCD[37] and tunnelling[38–40] results have confirmed the initial interpretation. We anticipate that a number of more advanced optical approaches will soon be employed. For example, as achieved in magnetic semiconductors[35,41] spectroscopic MCD could measure the strength and sign of the exchange as well as the bands relevant to the magnetic order (Fig. 2a). Furthermore, by applying an a.c. magnetic field, one can measure the susceptibility[9]. This a.c.–Kerr technique, which was first applied to thin films, could be used to measure the Néel temperature and provide insights into low-energy fluctuations, moment size and magnetic frustration.

Alternatively, inelastic light scattering provides access to the energy, symmetry and statistics of lattice, electronic and magnetic excitations in nanomaterials. These techniques rely on the modulation of the optical constants by the fluctuations of some operator. The mixing of such modulations with the optical field produces a response in the sum (anti-Stokes) or difference (Stokes) frequency that results from the creation (annihilation) of an excitation. If the operator is the lattice displacement, the fluctuations are phonons. Via spin–orbit coupling we can also expect coupling to magnetic terms that allow the measurement of various magnetic excitations, including fluctuations of the magnetic energy

© 2018 Springer Nature Limited. All rights reserved.

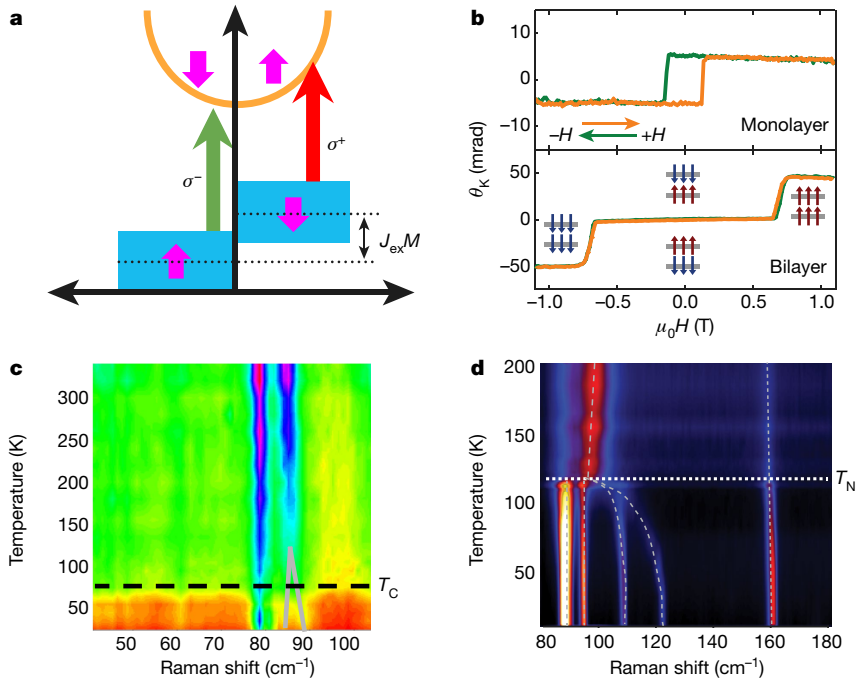

Fig. 2 | Optical probes of magnetism in two dimensions. a, Density of states for spin-up and spin-down electrons with possible optical transitions for left (green arrows; σ^-) and right (red arrows; σ^+) circularly polarized light, respectively. The band is split by the magnetic exchange (J_{ex}) and the net magnetization (M), allowing one to measure the magnetization from the resulting circular dichroism in the absorption or reflection and from the rotation of the light polarization upon reflection (Kerr effect) or transmission (Faraday effect). **b**, Polar Kerr rotation angle θ_K versus a magnetic field μ_0H applied along the c axis for single-layer (top) and bilayer (bottom) CrI_3[20] (H, magnetic field strength; μ_0, magnetic constant). The single-layer hysteresis loop is consistent with FM order, whereas the bilayer reveals a metamagnetic transition, consistent with AFM order between layers. The blue and brown arrows in the bottom graph show the direction of the moments in the layers (grey lines). Image reprinted with permission from ref. [20], Springer Nature Limited. **c**, **d**, Raman shift versus temperature for $Cr_2Ge_2Te_6$ (**c**; image reprinted from ref. [29]) and single-layer $FePS_3$ (**d**; image reprinted with permission from ref. [21]. Copyright 2016 American Chemical Society), with the ordering (Curie/Néel) temperature shown by the horizontal dashed lines. Both figures reveal changes in the phonons due to magnetic order; for example, degeneracy lifting in $Cr_2Ge_2Te_6$ (grey lines) and zone folding (indicated by the splitting of the low-energy peaks) for $FePS_3$. The broad background in **c** results from quasi-elastic scattering due to magnetic thermal fluctuations. The colour scales indicate the intensity (high intensity, red; low intensity, green (**c**) and high intensity, red; low intensity, black (**d**)).

density (that is, quasi-elastic scattering), acoustic and optical magnons, and spinons (fractional magnons expected in frustrated systems). One example is the Raman scattering from $Cr_2Ge_2Te_6$, shown in Fig. 2c. Here a broad background is seen for all temperatures above the Curie temperature (T_C), which results from thermal magnetic fluctuations[29]. Additionally, magneto-elastic coupling splits the optical modes for temperatures above T_C owing to the presence of short-range order.

Raman spectroscopy also provided the first evidence for long-range order in a single-layer magnetic vdW material[21,22]. Specifically, single-layer $FePS_3$ at high temperatures showed a broad feature at low energies (see Fig. 2d). Upon cooling below the Néel temperature (T_N), the broad feature splits into four modes. This results from zone-folding due to the presence of the zig-zag antiferromagnetic order and from the zone-boundary modes becoming Raman-active (that is, they are folded to the zone centre)[21,22]. Raman spectroscopy also first revealed the strength of the magnetic exchange in a magnetic vdW material via measurements of the two-magnon joint density of states[42]. For uncovering novel topology, Raman spectroscopy can also measure the non-trivial statistics associated with fractional spin excitations[43]. Lastly, Brillouin light scattering has been employed in thin films and devices to image the spin injection of electrons and the magnon chemical potential[44,45]. Considering that Brillouin light scattering has been used to measure acoustic modes in graphene[46], we anticipate that it will soon reveal the strength of the exchange, anisotropy and spin-injection efficiency in magnetic vdW materials and devices.

Initial devices and electrical probes

The surprising AFM state of the CrI_3 bilayer[20] was soon confirmed via tunnelling across heterostructures of graphene(ite)/CrI_3/graphene/hBN (hexagonal boron nitride) (Fig. 3a)[38–40]. Consistent with earlier studies of artificial multilayers[45,46], tunnelling was suppressed in the AFM configuration. Tuning the out-of-plane magnetic field produces a large and sudden increase in tunnelling, with switching from an AFM to an FM configuration (see Fig. 3a). This can be understood by considering CrI_3 as a perfect spin filter, such that in an FM configuration only 50% of the electrons at the Fermi surface of graphene can tunnel through it. Thus, in the AFM configuration one would expect zero tunnelling, because the two spin species are filtered by different layers. The actual degree of spin filtering will be less than 100%, leading to finite resistance even in the AFM state. In thicker CrI_3 layers, tunnelling has been shown to involve additional steps for out-of-plane fields but a smooth evolution for in-plane fields. Thus, tunnelling magnetoresistance (TMR) experiments have confirmed an AFM configuration between layers, with the moment along the c axis. Given the large TMR observed, these studies[38–40] have paved the way for the development of tunnelling-based memory, sensing and spin-filtering devices. Magnetic vdW materials are also expected to produce novel optoelectronic devices. Indeed, magnetic tuning of emission in heterostructures has already been observed[13] and predictions of electrical tuning of the Kerr effect have been reported[49].

As in a wide variety of materials[50–53], electric fields have been applied to manipulate the ordered phase in magnetic vdW materials. Many studies of CrI_3 have used structures with hBN spacers between the graphene layers and the CrI_3, with an additional graphene layer in direct contact with the magnetic layer[17,37]. This allowed probing the magnetism via MCD while either the doping level or the electric field across the layer was tuned. As shown in Fig. 2, the MCD is hysteretic and shows jumps with respect to an electric field applied across the layers. Interestingly, similar effects have been observed with doping and have been attributed to switching that results from reducing the critical

© 2018 Springer Nature Limited. All rights reserved.

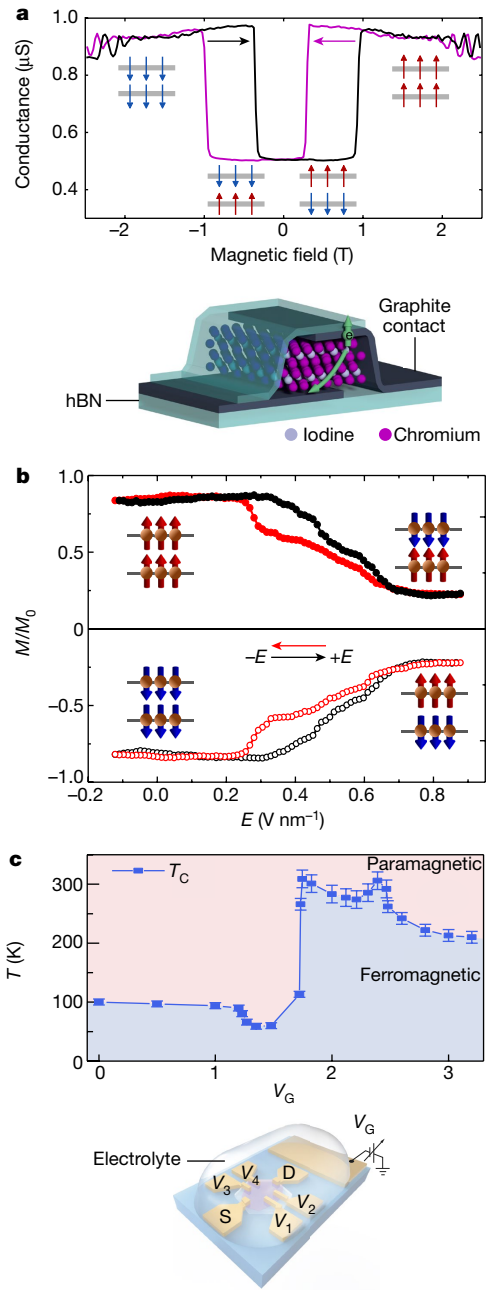

Fig. 3 | Electrical measurements and tuning of 2D magnetism. **a**, Tunnelling between graphene layers spaced by CrI_3 as a function of applied magnetic field and sweep direction (indicated by black and purple arrows). The device layout is shown in the inset and the magnetic configuration is shown by the red and blue arrows. The sudden increase in conductance is attributed to the enhanced net transmission that occurs when the two layers are aligned (bottom schematic; from ref. [39]. Reprinted with permission from AAAS.). **b**, MCD signal M of bilayer CrI_3, normalized by its saturation value M_0. The data were taken at 4 K with a magnetic field just above the critical value for the metamagnetic transition. Upon applying an electric field, the sample is tuned back to the AFM state[37]. Image reprinted with permission from ref. [37], Springer Nature Limited. **c**, The ferromagnetic (blue) and paramagnetic phases (pink) of Fe_3GeTe_2, with the transition temperature measured using the anomalous Hall effect. The critical temperature T_C (blue points) is tuned by applying a gate voltage V_G through an ionic liquid (see bottom schematic; S, source; D, drain; four probes (V1, V2, V3, V4))[30]. Image reprinted from ref. [30].

magnetic field for the metamagnetic transition. This suggests that the field across the layers results in doping across the device, such that the induced carriers mediate an enhanced ferromagnetic exchange[37], consistent with studies of non-vdW materials[54]. Electrostatic gating has also been applied to tune T_C in the vdW ferromagnetic semiconductors $Cr_2Ge_2Te_6$[55,56] and Fe_3GeTe_2[30]. In the latter, the use of an ionic liquid produced a T_C above room temperature. As shown in Fig. 3c, the dependence of the transition temperature on the gate voltage was highly non-monotonic, suggesting that the doping moved the Fermi level into a new band. However, because the Li ions were intercalated into Fe_3GeTe_2, disorder and strain effects may have also played a part. We anticipate that spectroscopic probes will be employed to uncover the origin of this enhancement, as well as comparison with the use of chemical doping of the initial bulk crystal to further enhance and tune T_c. This exciting development also holds promise for electrical control of magnetism in functional devices. From a fundamental perspective, we anticipate that electric fields and heterostructures applied to AFMs, topologically ordered materials and potential spin-liquid magnetic vdW materials will reveal novel superconducting states[1].

Table 1 | List of potential research topics in four categories for magnetic van der Waals materials

Research directions	Specific topics
New materials	Room-temperature ferromagnetic and antiferromagnetic materials Multiferroic materials Magnetic vdW materials with quantum spin ($S = 1/2$) Magnetic vdW materials with 4*d*/5*d* elements and strong spin–orbit coupling Unconventional superconductors
Fundamental issues	Evolution of magnetic fluctuations as a function of layer number: Ising, XY and Heisenberg models XY model: BKT transition, vortex–antivortex pair fluctuations Effects of interface, including substrate and capping layer Proximity with other quantum phases: *s*-, *p*- and *d*-wave superconductors, ferroelectrics, FMs, AFMs Spin–valley coupling Magnetic excitons
Devices and applications	Controllability via strain and gating Heterostructures Magnetic sensors Terahertz magneto-optical devices Multiferroics Spintronics Topological quantum computing
Quantum and topological phases	Quantum spin liquids Quantum critical phenomena induced by external variables Unconventional superconductivity in two dimensions Kitaev interaction, spin-liquid physics and fractionalization Quantum spin Hall effect Skyrmions Landscaping quantum phases

New quantum phases and outlook

Going forward, we believe that there are four main directions to be pursued in the study and use of magnetic vdW materials (see Table 1). The first is the discovery of new materials with specific functionality—for example, the recent development of magnetic 2D vdW materials with transition temperatures at or above room temperature[24,25]. Pushing T_C higher will be crucial for real applications and will simultaneously provide a wider range of possible probes and ground states, given the rather large exchange energies involved. One can envision further increasing T_C by optimizing two key parameters, the exchange interaction and the magnetic anisotropy, with the latter being crucial for suppressing fluctuations that destroy long-range order[57]. It will also be very interesting to speculate what will lie ahead once we synthesize systems with quantum spins or strong spin–orbit coupling—for example, materials with elements such as Cu^{2+} or 4*d*/5*d* transition metals. These should provide materials with strong fluctuations or fractional excitations that can be exploited to potentially mediate novel unconventional superconductors in 2D materials and heterostructures. Key to these efforts will be the simultaneous enhancement of the exchange interaction and tuning of the magnetic anisotropy[19,34].

© 2018 Springer Nature Limited. All rights reserved.

The second direction involves using these new materials to deepen our understanding of quantum materials. Specifically, numerous phases emerge when multiple physical effects compete, and it is often difficult to tune a single parameter in a material without inadvertently affecting the others (for example, doping level and disorder). It is entirely conceivable to achieve a detailed measurement of spin fluctuations for the four fundamental Hamiltonians—of the Ising, XY, Heisenberg and Kitaev models—as a function of layer number and temperature, with any combination of external variables of interest. Thus, one can study in detail the spatial and temporal map of vortex–antivortex pair creation and annihilation for the XY model below and above its BKT transition. It is also plausible to examine how these fluctuations vary in proximity with other materials, such as substrates, capping layers and materials with their own order (for example, superconductors or ferroelectrics). Other challenging, yet entirely possible, aims include spin–valley coupling and the magnetic exciton.

The third direction concerns the implementation of these materials in novel devices and applications. By building on the works summarized in 'Initial devices and electrical probes', there is room for novel concepts, such as the synaptic memory effects found in $CrPS_4$[58]. For successful implementation in real devices, it is of the utmost importance to understand and exploit the control of the ground state via strain and gating. The fact that magnetic vdW materials are intrinsically 2D makes them much more amenable to external stimuli. In addition, heterostructures unachievable by other techniques (for example, twists, periodic strain or lattice-mismatched materials) can be straightforwardly combined. Another important—and perhaps far-reaching, if realized—application is the use of 2D magnetic vdW materials in spintronics[13,18]. The intrinsic atomic limit of these materials renders them excellent platforms for future applications, such as spin injection through half-metallicity.

Last, but not least, it is very exciting to speculate on how one can realize quantum and topological phases using these materials. We note that most magnetic vdW materials form with the magnetic elements in a honeycomb lattice. With strong spin–orbit coupling and two neighbouring magnetic ions sharing an edge bond, we expect a Kitaev directional exchange interaction. Therefore, many magnetic vdW materials are subject to the competition among the Kitaev, Heisenberg and anisotropic exchange terms[59]. This competition can in principle lead to exotic quantum spin liquids, revealing fractionalized, magnetic Majorana fermions in real materials[2,32,43]. There is also the potential to realize other topological phases and particles in magnetic systems, such as the quantum spin Hall effect[60] or skyrmions[26]. Other interesting opportunities include taking advantage of the intrinsically strong spin fluctuations to produce unconventional superconductivity by doping, proximity or pressure.

In the 2D limit, fluctuations—either quantum or classical—are typically very strong, which suggests the possible presence of new quantum phases in some nearby corners of the material parameter space. Clever implementation of heterostructures and perturbations should provide access to these phases without falling into nearby, sometimes trivial, alternative states. In essence, magnetic vdW materials offer us an entirely new opportunity to landscape quantum phases.

Received: 14 May 2018; Accepted: 20 August 2018;
Published online 31 October 2018.

1. Lee, P. A. et al. Doping a Mott insulator: physics of high-temperature superconductivity. *Rev. Mod. Phys.* **78**, 17–85 (2006).
2. Kitaev, A. Anyons in an exactly solved model and beyond. *Ann. Phys.* **321**, 2–111 (2006).
3. Onsager, L. Crystal statistics. I. A two-dimensional model with an order–disorder transition. *Phys. Rev.* **65**, 117–149 (1944).
4. Berezinskii, V. Destruction of long-range order in one-dimensional and two-dimensional systems having a continuous symmetry group I. Classical systems. *Sov. Phys. JETP* **32**, 493–500 (1971).
5. Kosterlitz, J. M. & Thouless, D. J. Ordering, metastability and phase transitions in two-dimensional systems. *J. Phys. C* **6**, 1181–1203 (1973).
6. Mermin, N. D. & Wagner, H. Absence of ferromagnetism or antiferromagnetism in one- or two-dimensional isotropic Heisenberg models. *Phys. Rev. Lett.* **17**, 1133–1136 (1966).
7. Hellman, F. et al. Interface-induced phenomena in magnetism. *Rev. Mod. Phys.* **89**, 025006 (2017).
8. Zak, J., Moog, E. R., Liu, C. & Bader, S. D. Universal approach to magneto-optics. *J. Magn. Magn. Mater.* **89**, 107–123 (1990).
9. Arnold, C. S., Dunlavy, M. & Venus, D. Magnetic susceptibility measurements of ultrathin films using the surface magneto-optic Kerr effect: optimization of the signal-to-noise ratio. *Rev. Sci. Instrum.* **68**, 4212–4216 (1997).
10. Elmers, H.-J. et al. Critical behavior of the uniaxial ferromagnetic monolayer Fe(110) on W(110). *Phys. Rev. B* **54**, 15224–15233 (1996).
11. Park, J.-G. Opportunities and challenges of two-dimensional magnetic van der Waals materials: magnetic graphene? *J. Phys. Condens. Matter* **28**, 301001 (2016).
This paper highlighted the importance of magnetic vdW materials and the huge potential of this new class of materials.
12. Roldán, R., Castellanos-Gomez, A., Cappelluti, E. & Guinea, F. Strain engineering in semiconducting two-dimensional crystals. *J. Phys. Condens. Matter* **27**, 313201 (2015).
13. Zhong, D. et al. Van der Waals engineering of ferromagnetic semiconductor heterostructures for spin and valleytronics. *Sci. Adv.* **3**, e1603113 (2017).
14. Cao, Y. et al. Unconventional superconductivity in magic-angle graphene superlattices. *Nature* **556**, 43–50 (2018).
15. Buscema, M. et al. Photocurrent generation with two-dimensional van der Waals semiconductors. *Chem. Soc. Rev.* **44**, 3691–3718 (2015).
16. Sachs, B. et al. Ferromagnetic two-dimensional crystals: single layers of K_2CuF_4. *Phys. Rev. B* **88**, 201402 (2013).
17. Huang, B. et al. Electrical control of 2D magnetism in bilayer CrI_3. *Nat. Nanotechnol.* (2018).
This study demonstrated the controllability of 2D magnetism in the magnetic vdW material CrI_3.
18. Samarth, N. Magnetism in flatland. *Nature* **546**, 216–218 (2017).
19. Lado, J. L. & Fernández-Rossier, J. On the origin of magnetic anisotropy in two dimensional CrI_3. *2D Mater.* **4**, 35002 (2017).
20. Huang, B. et al. Layer-dependent ferromagnetism in a van der Waals crystal down to the monolayer limit. *Nature* **546**, 270–273 (2017).
This study demonstrated the layer dependence of the ferromagnetic transition in the magnetic vdW material CrI_3 as a function of layer number.
21. Lee, J.-U. et al. Ising-type magnetic ordering in atomically thin $FePS_3$. *Nano Lett.* **16**, 7433–7438 (2016).
This work showed that one can exfoliate an atomically thin monolayer of the antiferromagnetic vdW material $FePS_3$ and demonstrated the Onsanger solution for a real magnetic vdW material.
22. Wang, X. et al. Raman spectroscopy of atomically thin two-dimensional magnetic iron phosphorus trisulfide ($FePS_3$) crystals. *2D Mater.* **3**, 31009 (2016).
23. Gong, C. et al. Discovery of intrinsic ferromagnetism in two-dimensional van der Waals crystals. *Nature* **546**, 265–269 (2017).
This study demonstrated the layer dependence of the ferromagnetic transition in the magnetic vdW material $Cr_2Ge_2Te_6$ as a function of layer number.
24. Bonilla, M. et al. Strong room-temperature ferromagnetism in VSe_2 monolayers on van der Waals substrates. *Nat. Nanotechnol.* **13**, 289–293 (2018).
25. O'Hara, D. J. et al. Room temperature intrinsic ferromagnetism in epitaxial manganese selenide films in the monolayer limit. *Nano Lett.* **18**, 3125–3131 (2018).
26. Mühlbauer, S. et al. Skyrmion lattice in a chiral magnet. *Science* **323**, 915–919 (2009).
27. Geim, A. K. & Grigorieva, I. V. Van der Waals heterostructures. *Nature* **499**, 419–425 (2013).
28. Williams, T. J. et al. Magnetic correlations in the quasi-2D semiconducting ferromagnet $CrSiTe_3$. *Phys. Rev. B* **92**, 144404 (2015).
29. Tian, Y., Gray, M. J., Ji, H., Cava, R. J. & Burch, K. S. Magneto-elastic coupling in a potential ferromagnetic 2D atomic crystal. *2D Mater.* **3**, 025035 (2016).
30. Deng, Y. et al. Gate-tunable room-temperature ferromagnetism in two-dimensional Fe_3GeTe_2. Preprint at https://arxiv.org/abs/1803.02038 (2018).
31. Kuo, C. T. et al. Exfoliation and Raman spectroscopic fingerprint of few-layer $NiPS_3$ van der Waals crystals. *Sci. Rep.* **6**, 20904 (2016).
32. Banerjee, A. et al. Neutron scattering in the proximate quantum spin liquid α-$RuCl_3$. *Science* **356**, 1055–1059 (2017).
33. Plumb, K. W. et al. α-$RuCl_3$: a spin-orbit assisted Mott insulator on a honeycomb lattice. *Phys. Rev. B* **90**, 041112 (2014).
34. Abramchuk, M. et al. Controlling magnetic and optical properties of the van der Waals crystal $CrCl_{3-x}Br_x$ via mixed halide chemistry. *Adv. Mater.* https://doi.org/10.1002/adma.201801325 (2018).
35. Ando, K., Takahashi, K., Okuda, T. & Umehara, M. Magnetic circular dichroism of zinc-blende-phase MnTe. *Phys. Rev. B* **46**, 12289–12297 (1992).
36. Lange, M. et al. A high-resolution combined scanning laser and widefield polarizing microscope for imaging at temperatures from 4 K to 300 K. *Rev. Sci. Instrum.* **88**, 123705 (2017).
37. Jiang, S., Shan, J. & Mak, K. F. Electric-field switching of two-dimensional van der Waals magnets. *Nat. Mater.* **17**, 406–410 (2018).
38. Song, T. et al. Giant tunnelling magnetoresistance in spin-filter van der Waals heterostructures. *Science* **360**, 1214–1218 (2018).
39. Klein, D. R. et al. Probing magnetism in 2D van der Waals crystalline insulators via electron tunneling. *Science* **360**, 1218–1222 (2018).
40. Kim, H. H. et al. One million percent tunnel magnetoresistance in a magnetic van der Waals heterostructure. *Nano Lett.* **18**, 4885–4890 (2018).
41. Burch, K. S., Awschalom, D. D. & Basov, D. N. Optical properties of III-Mn-V ferromagnetic semiconductors. *J. Magn. Magn. Mater.* **320**, 3207–3228 (2008).

© 2018 Springer Nature Limited. All rights reserved.

42. Sandilands, L. J. et al. Stability of exfoliated $Bi_2Sr_2Dy_xCa_{1-x}Cu_2O_{8+\delta}$ studied by Raman microscopy. *Phys. Rev. B* **82**, 064503 (2010).
43. Nasu, J., Knolle, J., Kovrizhin, D. L., Motome, Y. & Moessner, R. Fermionic response from fractionalization in an insulating two-dimensional magnet. *Nat. Phys*. **12**, 912–915 (2016).
44. Bozhko, D. A. et al. Supercurrent in a room-temperature Bose–Einstein magnon condensate. *Nat. Phys*. **12**, 1057–1062 (2016).
45. An, K. et al. Magnons and phonons optically driven out of local equilibrium in a magnetic insulator. *Phys. Rev. Lett.* **117**, 107202 (2016).
46. Wang, Z. K., Lim, H. S., Ng, S. C., Özyilmaz, B. & Kuok, M. H. Brillouin scattering study of low-frequency bulk acoustic phonons in multilayer graphene. *Carbon* **46**, 2133–2136 (2008).
47. Worledge, D. C. & Geballe, T. H. Magnetoresistive double spin filter tunnel junction. *J. Appl. Phys*. **88**, 5277–5279 (2000).
48. Miao, G. X., Müller, M. & Moodera, J. S. Magnetoresistance in double spin filter tunnel junctions with nonmagnetic electrodes and its unconventional bias dependence. *Phys. Rev. Lett.* **102**, 076601 (2009).
49. Sivadas, N., Okamoto, S. & Xiao, D. Gate-controllable magneto-optic Kerr effect in layered collinear antiferromagnets. *Phys. Rev. Lett.* **117**, 267203 (2016).
50. Bollinger, A. T. et al. Superconductor–insulator transition in $La_{2-x}Sr_xCuO_4$ at the pair quantum resistance. *Nature* **472**, 458–460 (2011).
51. Leng, X., Garcia-Barriocanal, J., Bose, S., Lee, Y. & Goldman, A. M. Electrostatic control of the evolution from a superconducting phase to an insulating phase in ultrathin $YBa_2Cu_3O_{7-x}$ films. *Phys. Rev. Lett.* **107**, 027001 (2011).
52. Nojima, T. et al. Hole reduction and electron accumulation in $YBa_2Cu_3O_y$ thin films using an electrochemical technique: evidence for an n-type metallic state. *Phys. Rev. B* **84**, 020502 (2011).
53. Ahn, C. H., Triscone, J.-M. & Mannhart, J. Electric field effect in correlated oxide systems. *Nature* **424**, 1015–1018 (2003).
54. Ahn, C. H. et al. Electrostatic modification of novel materials. *Rev. Mod. Phys*. **78**, 1185–1212 (2006).
55. Xing, W. et al. Electric field effect in multilayer $Cr_2Ge_2Te_6$: a ferromagnetic 2D material. *2D Mater*. **4**, 24009 (2017).
56. Chen, Y. et al. Role of oxygen in ionic liquid gating on two-dimensional $Cr_2Ge_2Te_6$: a non-oxide material. *ACS Appl. Mater. Inter*. **10**, 1383–1388 (2018).
57. Irkhin, V. Y. & Katanin, A. A. Kosterlitz–Thouless and magnetic transition temperatures in layered magnets with a weak easy-plane anisotropy. *Phys. Rev. B* **60**, 2990–2993 (1999).
58. Lee, M. J. et al. Synaptic devices implemented with two-dimensional layered single crystal chromium thiophosphate ($CrPS_4$). *NPG Asia Mater*. **10**, 23–30 (2018).
59. Jackeli, G. & Khaliullin, G. Mott insulators in the strong spin–orbit coupling limit: from Heisenberg to a quantum compass and Kitaev models. *Phys. Rev. Lett.* **102**, 017205 (2009).
60. Lee, K. H., Chung, S. B., Park, K. & Park, J.-G. Magnonic quantum spin Hall state in the zigzag and stripe phases of the antiferromagnetic honeycomb lattice. *Phys. Rev. B* **97**, 180401 (2018).

Acknowledgements We acknowledge useful discussions with D. Xiao and X. Xu. K.S.B. was supported by the National Science Foundation through grant DMR-1709987 and D.M. acknowledges support from the National Science Foundation under grant DMR-1410428. J.-G.P. was supported by the Institute for Basic Science (IBS) of Korea (IBS-R009-G1).

Reviewer information *Nature* thanks M. Katsnelson and the other anonymous reviewer(s) for their contribution to the peer review of this work.

Author contributions J.-G.P. initiated the project and all authors wrote the manuscript.

Competing interests The authors declare no competing interests.

Additional information
Reprints and permissions information is available at http://www.nature.com/reprints.
Correspondence and requests for materials should be addressed to J.-G.P.
Publisher's note: Springer Nature remains neutral with regard to jurisdictional claims in published maps and institutional affiliations.

© 2018 Springer Nature Limited. All rights reserved.

https://doi.org/10.1038/s41586-018-0643-8

Measurement-based quantum control of mechanical motion

Massimiliano Rossi[1,2,3], David Mason[1,2,3], Junxin Chen[1,2,3], Yeghishe Tsaturyan[1] & Albert Schliesser[1,2]*

Controlling a quantum system by using observations of its dynamics is complicated by the backaction of the measurement process—that is, the unavoidable quantum disturbance caused by coupling the system to a measurement apparatus. An efficient measurement is one that maximizes the amount of information gained per disturbance incurred. Real-time feedback can then be used to cancel the backaction of the measurement and to control the evolution of the quantum state. Such measurement-based quantum control has been demonstrated in the clean settings of cavity and circuit quantum electrodynamics, but its application to motional degrees of freedom has remained elusive. Here we demonstrate measurement-based quantum control of the motion of a millimetre-sized membrane resonator. An optomechanical transducer resolves the zero-point motion of the resonator in a fraction of its millisecond-scale coherence time, with an overall measurement efficiency close to unity. An electronic feedback loop converts this position record to a force that cools the resonator mode to its quantum ground state (residual thermal occupation of about 0.29). This occupation is nine decibels below the quantum-backaction limit of sideband cooling and six orders of magnitude below the equilibrium occupation of the thermal environment. We thus realize a long-standing goal in the field, adding position and momentum to the degrees of freedom that are amenable to measurement-based quantum control, with potential applications in quantum information processing and gravitational-wave detectors.

Controlling the state of a quantum system is a delicate task because any observation of the system will inevitably perturb it[1,2]. Coherent quantum control avoids this issue by coupling the system to another quantum system, a 'controller', in such a way that the joint system converges to the target state without the need for measurement, at the expense of quantum resources in the controller. Measurement-based quantum control[3–5] is based on a different paradigm. It exerts control by measuring the quantum state and applying feedback that depends on the measurement outcome, much like classical control systems. However, in the quantum regime, the effect of the backaction of the measurement must be taken into account, and effectively cancelled. This requires an overall measurement efficiency η—in essence, the amount of information gained per decoherence induced—close to unity. So far, this challenging demand has been met only in the clean settings of cavity and circuit quantum electrodynamics[6,7] (for example, $\eta = 40\%$ in ref. [7]).

To prepare high-purity motional quantum states, researchers have traditionally relied on sideband cooling, a form of coherent quantum control. An engineered quantum optical bath acts as the controller, to which the motional degree of freedom couples through optical forces. The motion thermalizes to this bath, at a temperature that is determined by the quantum fluctuations of the forces. This temperature sets a fundamental limit to sideband cooling. In optomechanics, this limit requires that the cavity linewidth resolves the motional sidebands to enable ground-state cooling with coherent light[8]. Systems that operate in this regime have been prepared close to the ground state[9,10], and cooling 2 dB below the sideband-cooling limit was demonstrated recently by squeezing the electromagnetic vacuum fluctuations[11].

Within the paradigm of measurement-based quantum control, feedback cooling[12,13] can overcome this limit, given a sufficiently efficient measurement. This protocol has been explored in several fields, including atomic physics, optomechanics and gravitational-wave astronomy. However, despite two decades of research involving diverse mechanical systems, such as trapped atoms[14], ions[15], micro- and nanoparticles[16,17], cantilevers[18,19], nanomechanical resonators[20–23], mirror modes[13] and gravitational-wave detector masses[24,25], ground-state cooling, an elementary form of quantum control, has yet to be achieved. This is chiefly because previous measurements were too weak ($\Gamma_{\mathrm{meas}} \ll \gamma$, where Γ_{meas} is the measurement rate[2] and γ is the motional decoherence rate due to coupling to the environment) and/or the detection too inefficient ($\Gamma_{\mathrm{meas}} \ll \Gamma_{\mathrm{qba}}$, where Γ_{qba} is the motional decoherence rate due to the quantum backaction of the measurement) to realize an overall measurement efficiency of $\eta = \Gamma_{\mathrm{meas}}/(\Gamma_{\mathrm{qba}} + \gamma) \approx 1$. The closest previous approach to this ideal-efficiency limit is reported in ref. [20], in which $\eta = 0.9\%$ was reached in a feedback experiment on a nanomechanical resonator.

In contrast to previous attempts, we perform a motion measurement that is sufficiently strong and efficient to reach $\eta = 56\%$. This high efficiency is enabled by an extremely precise displacement measurement, which realizes the closest approach so far (within 35%) to the Heisenberg measurement–disturbance uncertainty limit and the standard quantum limit.

Experimental setting

We study the drumhead-like motion of a highly tensioned, millimetre-sized, 20-nm-thick Si_3N_4 membrane (Fig. 1). The resonance mode of interest is confined to a defect within a phononic crystal, created by patterning a periodic array of holes into the membrane. The frequency of the defect mode $\Omega_{\mathrm{m}}/(2\pi) = 1.14$ MHz lies in the bandgap of the surrounding phononic crystal, which minimizes radiative leakage of mechanical energy into the surrounding structure. In addition, the gentle confinement by the phononic crystal reduces mode curvature compared to membranes clamped to a rigid substrate. As demonstrated recently[26], such soft clamping greatly suppresses mechanical energy dissipation (Γ_{m}) and enables ultrahigh quality factors $Q = \Omega_{\mathrm{m}}/\Gamma_{\mathrm{m}}$;

[1]Niels Bohr Institute, University of Copenhagen, Copenhagen, Denmark. [2]Center for Hybrid Quantum Networks (Hy-Q), Niels Bohr Institute, University of Copenhagen, Copenhagen, Denmark. [3]These authors contributed equally: Massimiliano Rossi, David Mason, Junxin Chen. *e-mail: albert.schliesser@nbi.ku.dk

© 2018 Springer Nature Limited. All rights reserved.

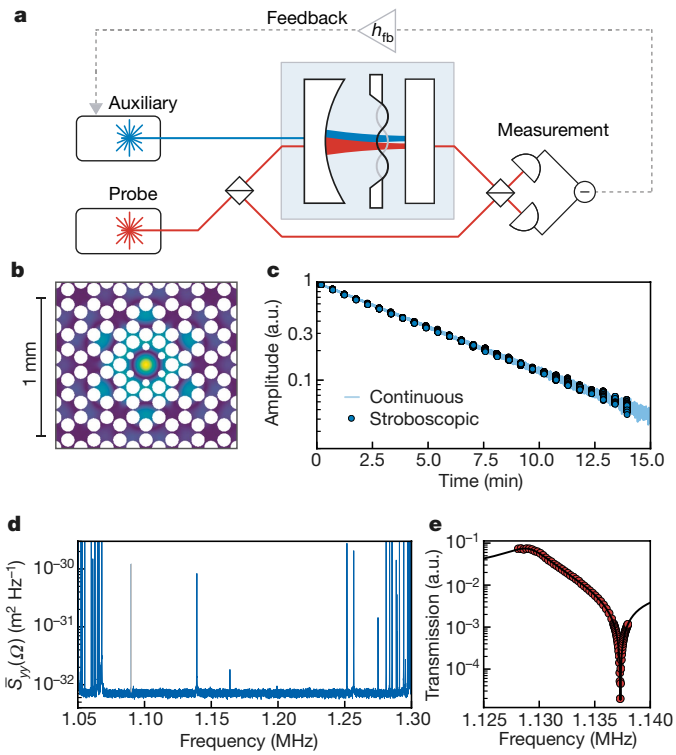

Fig. 1 | Optomechanical system. a, Sketch of experimental set-up. The mechanical resonator couples to a cryogenic optical cavity. Its motion is probed by a resonant laser (red), the phase of which is measured with a balanced homodyne detector. An additional auxiliary laser (blue) drives a different cavity mode. The probe signal can be used to control the auxiliary laser via an electronic feedback loop (h_{fb}). **b**, Simulated displacement pattern (colour scale; dark blue, small displacement; yellow, large displacement) of the mechanical mode of interest. The white circles correspond to holes in the membrane. **c**, Mechanical ringdown measurements. Light (dark) blue indicates continuously monitored (stroboscopic) ringdown. **d**, Displacement spectrum around the frequency region of the bandgap. Out-of-bandgap modes are visible at the edges of the spectrum, and five in-gap modes are visible. A phase calibration tone is shown in grey. **e**, An OMIT measurement (red symbols), used to characterize the optomechanical coupling strength (from the fit, black line). a.u., arbitrary units.

we find $Q = 1.03 \times 10^9$ in ringdown measurements, carefully ruling out artefacts (see Methods). This quality factor corresponds to a mechanical coherence time $\gamma^{-1} \approx (\bar{n}_{th}\Gamma_m)^{-1} = \hbar Q/(k_B T)$ (where $\hbar$ is the reduced Planck constant, k_B is the Boltzmann constant, T is the temperature of the environment and $\bar{n}_{th}$ is the occupation of the thermal bath) of the order of 1 ms, even at the moderate cryogenic temperatures ($T \approx 10$ K, $\bar{n}_{th} = \mathcal{O}(10^5)$) at which all reported experiments were conducted.

The membrane is introduced into a 1.6-mm-long, high-finesse Fabry–Pérot resonator, so that displacement by its zero-point amplitude $x_{zpf} = \sqrt{\hbar/(2m\Omega_m)}$ (where m is the mass of the resonator) dispersively shifts[27,28] (Methods) the optical-mode frequency by the vacuum optomechanical coupling rate g_0. Populating the cavity with a coherent field of average photon number $\bar{n}_{cav}$ then leads to the field-enhanced optomechanical coupling $g = g_0\sqrt{\bar{n}_{cav}}$ in a linearized, quantum-non-demolition-type interaction Hamiltonian $H' = -\hbar g(a^\dagger + a)(b^\dagger + b)$ between the shifted annihilation (creation) operators a ($a^\dagger$) and b ($b^\dagger$) of the cavity field and the mechanical motion, respectively[8,29]. A probe laser (Fig. 1a, red) is used to probe the frequency fluctuations of an optical cavity mode of linewidth $\kappa/(2\pi) = 15.9$ MHz. We measure the mechanical position by monitoring the phase of the transmitted light using balanced homodyne detection. In an unresolved sideband system ($\kappa \gg \Omega_m$), this measurement occurs at a rate[29] $\Gamma_{meas} = 4\eta_{det}g^2/\kappa$, for a detection efficiency η_{det}. Careful optimization of the entire detection chain (Methods) leaves us with $\eta_{det} = 77\%$.

In addition, we frequently use an auxiliary laser (Fig. 1a, blue), which populates a different longitudinal cavity mode (linewidth, $\kappa_{aux}/(2\pi) = 12.9$ MHz) and has a polarization that is orthogonal to the probe beam to avoid unwanted interference. This laser has several purposes, including laser cooling and, in combination with an amplitude modulator, exerting a force on the mechanical resonator via radiation pressure. Its exact role is specified in each section, in which the different experiments that we performed are described.

To gauge the possible strength of the measurement, we perform optomechanically induced transparency (OMIT) measurements[30] to extract g. We find (Fig. 1e) values up to $g/(2\pi) = 329$ kHz, which suggests that the effect of measurement-induced quantum backaction ($\Gamma_{qba} = 4g^2/\kappa$) exceeds that of thermal decoherence (γ) by a large margin. The ratio of these parameters defines the quantum cooperativity parameter[8,29] $C_q = \Gamma_{qba}/\gamma$; we achieve values of up to $C_q = 119$. We therefore expect a close-to-unity overall measurement efficiency $\eta = \eta_{det}/(1 + 1/C_q)$, as required for successful quantum control.

Quantum backaction in sideband cooling

For further characterization and direct comparison with a coherent control technique, we proceed with a sideband-cooling experiment. While monitoring the mechanical motion with a weak ($C_q \ll 1$), resonant probe beam, we lock the auxiliary laser (Fig. 1, with no feedback loop, $h_{fb} = 0$) at a finite detuning ($\Delta_{aux}/(2\pi) = -4.2$ MHz). Increasing the power of this auxiliary beam results in two competing processes: cooling of the motion by optical damping (at rate Γ_{opt}) and heating by quantum backaction (radiation-pressure quantum noise) on top of the constant thermal noise. At sufficiently high powers, these processes equilibrate[8,11,29,31] and the mechanical phonon occupancy $\bar{n} = (\Gamma_{opt}\bar{n}_{min} + \Gamma_m\bar{n}_{th})/(\Gamma_{opt} + \Gamma_m)$ asymptotes to the (sideband-cooling) quantum backaction limit $\bar{n}_{min} = [(\Omega_m + \Delta_{aux})^2 + (\kappa_{aux}/2)^2]/(-4\Delta_{aux}\Omega_m)$.

Comparison of this model with our data (Fig. 2) yields several conclusions. First, Fig. 2b confirms that the regime of dominating quantum backaction can indeed be accessed deeply ($\Gamma_{opt}\bar{n}_{min} \gg \Gamma_m\bar{n}_{th}$). Second, the quantum backaction limit ($\bar{n}_{min} = 2.64$) precludes sideband cooling to the ground state because of the 'bad' cavity ($\kappa_{aux} \approx \kappa \gg \Omega_m$) that we use. Third, the excellent agreement, even towards the highest Γ_{opt}, indicates the absence of substantial excess backaction, such as classical radiation-pressure noise. This finding is consistent with independent measurements of the noise of the lasers (Supplementary Information). Fourth, equilibration to an optical bath is beneficial for calibrating the vacuum optomechanical coupling rate g_0 of the probe using a standard frequency-modulation technique[32] (Methods), which requires reference data with known phonon occupation $\bar{n}$. The temperature of the phonon thermal bath $T \approx \bar{n}_{th}\hbar\Omega_m/k_B$ (which is usually difficult to ascertain) is negligible for the largest Γ_{opt}; it contributes only $(1 + \Gamma_{opt}\bar{n}_{min}/\Gamma_m\bar{n}_{th})^{-1} \approx 4\%$ to the occupation $\bar{n}$. Instead, $\bar{n} \approx \bar{n}_{min}$ is determined by only the parameters κ_{aux}, Δ_{aux} and Ω_m, which can be easily and robustly determined spectroscopically. In physical terms, this calibration means that we use vacuum fluctuations as a temperature reference[33] to extract g_0. A fit (Methods) to the whole dataset for all Γ_{opt}, based on standard theory of optomechanical sideband cooling[8], yields $g_0 = 2\pi \times (127 \pm 2)$ Hz and $T = 11 \pm 2$ K (where the uncertainties quoted indicate the confidence interval of the fit). This value of g_0 compares well to that of $g_0 = g/\sqrt{\bar{n}_{cav}} = 2\pi \times 129^{+2}_{-3}$ Hz (where the uncertainty indicates the full range of measured values) determined from an OMIT fit with a calibrated intracavity photon number $\bar{n}_{cav}$. Both methods are subject to different systematic uncertainties (Methods); their excellent agreement underscores a thorough understanding of our system and lends further support to the calibration of the measured spectra in terms of the number of quanta based on this value of g_0.

Quantum measurement

In the next experiment we characterize the quality of the measurement to gauge the possibility of overcoming the sideband-cooling limit via measurement-based quantum feedback with $\eta \approx 1$. We reduce the auxiliary laser power and arrange it to provide only mild pre-cooling

© 2018 Springer Nature Limited. All rights reserved.

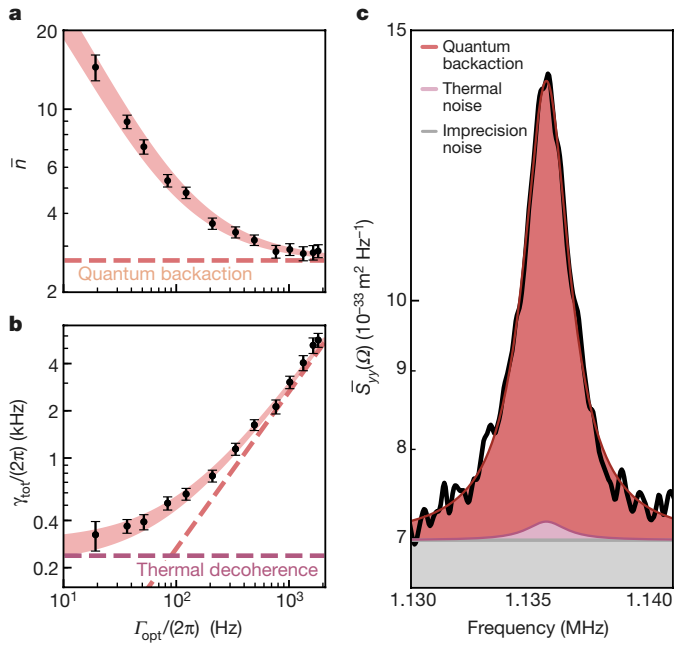

Fig. 2 | Quantum backaction in sideband cooling. a, **b**, Phonon number $\bar{n}$ (**a**) and total heating rate $\gamma_{tot} = \bar{n}(\Gamma_{opt} + \Gamma_m) = \Gamma_{opt}\bar{n}_{min} + \Gamma_m\bar{n}_{th}$ (**b**) obtained from fitting calibrated displacement spectra (Γ_m, mechanical energy decay rate; Γ_{opt}, optical damping rate; $\bar{n}_{min}$, occupancy in the sideband-cooling limit; $\bar{n}_{th}$ occupancy of the thermal bath). The shaded areas show fits of a theoretical model to these data (Supplemetary Information), with the width reflecting the confidence interval of the fit. Dashed lines indicate contributions from thermal decoherence (purple) and quantum backaction (red). Error bars indicate two standard deviations. **c**, Calibrated displacement spectrum (black line) corresponding to the highest cooling power, with a Lorentzian fit (red line). The grey line represents the imprecision noise. Thermal noise (pink) contributes about 4% of the total force noise, the remainder being due to quantum backaction (red).

on the mechanical mode of interest ($\Gamma_{opt}/(2\pi) = \mathcal{O}(10)$ Hz), and on all other modes of the membrane (Supplementary Information), to stabilize the system. At the same time, we increase the probe power in several steps into the regime $C_q > 1$.

In Fig. 3 we show the corresponding measured mechanical displacement spectra $\bar{S}_{yy}(\Omega)$, obtained from the calibrated time-dependent homodyne photocurrent $y(t) = x(t) + x_{imp}(t)$, which includes the actual mechanical position x and the measurement-imprecision noise x_{imp} (Supplementary Information). When increasing the probe strength, the imprecision noise floor decreases and the total force noise on the resonator increases due to quantum backaction. We fit the spectra to a Lorentzian peak, driven by a total force noise $\bar{S}_{FF}^{tot}$ and with an imprecision noise floor $\bar{S}_{xx}^{imp}$:

$$\bar{S}_{yy}(\Omega) = |\chi_{eff}(\Omega)|^2\, \bar{S}_{FF}^{tot} + \bar{S}_{xx}^{imp} \qquad (1)$$

where $\chi_{eff}(\Omega)$ is the effective mechanical susceptibility, with resonance frequency Ω_{eff} and damping Γ_{eff}, which is affected by the (largely irrelevant) dynamical backaction of the lasers[8,29].

For the sake of comparability, we reference these measurement noises to the resonant spectral density associated with mechanical zero-point fluctuations. Doing so yields the number of imprecision noise quanta $n_{imp} = \bar{S}_{xx}^{imp}/(8x_{zpf}^2/\Gamma_m)$ and force noise quanta $n_{tot} = \bar{S}_{FF}^{tot}/(8p_{zpf}^2\Gamma_m)$, where p_{zpf} is the zero-point amplitude of the momentum such that $x_{zpf}p_{zpf} = \hbar/2$. For the strongest measurement we find $n_{imp} = 5.8 \times 10^{-8}$. This constitutes an improvement of three orders of magnitude over the best previous measurement[20]. All measured values agree with the expectation $n_{imp} = \Gamma_m/(16\Gamma_{meas})$ to within a factor of 1.03 ± 0.06 (where the uncertainties correspond to ± 1 standard deviation). The force acting on the system can be broken down into three contributions, $\bar{S}_{FF}^{tot} = \bar{S}_{FF}^{th} + \bar{S}_{FF}^{aux} + \bar{S}_{FF}^{qba}$, due to thermal noise and quantum backaction of the auxiliary and probe beams. For each dataset, the fit results agree with the $\bar{S}_{FF}^{tot}$ predicted from the parameters of the system (Supplementary Information) to within a factor of 1.08 ± 0.02 (where the uncertainties correspond to ± 1 standard deviation), with $\bar{S}_{FF}^{aux}/\bar{S}_{FF}^{th} \approx 0.18$ and $\bar{S}_{FF}^{qba}/\bar{S}_{FF}^{th} = C_q$.

We use these findings to evaluate the measurement efficiency of the probe, $\eta = (16n_{imp}n_{tot})^{-1} = 56\%$, which is on par with circuit quantum electrodynamics systems[7] and sufficient to exert high-fidelity quantum control. Using $\eta = \hbar^2/(\bar{S}_{xx}^{imp}\bar{S}_{FF}^{tot})$ further allows comparison to the Heisenberg measurement–disturbance uncertainty relation[1,8,29] $\sqrt{\bar{S}_{xx}^{imp}\bar{S}_{FF}^{qba}} \geq \hbar$. The measured total noises $1.33\hbar = \sqrt{\bar{S}_{xx}^{imp}\bar{S}_{FF}^{tot}} \geq \sqrt{\bar{S}_{xx}^{imp}\bar{S}_{FF}^{qba}}$ constrain the deviation from an ideal measurement to at most 33%. To our knowledge, this is the best mechanical realization of the Heisenberg microscope gedanken-experiment so far. Consequently, the experimental displacement sensitivity of equation (1) is also closer to the standard quantum limit (SQL) than that of any previous measurement of this kind. We find that away from the mechanical resonance ($\delta\Omega = \Omega - \Omega_{eff} \approx 2\pi \times 3.3$ kHz), at which the uncorrelated imprecision and backaction noises are optimally balanced, our mechanical sensor reaches $\bar{S}_{yy}(\Omega_{eff} + \delta\Omega) = 1.35\bar{S}_{yy}^{SQL}(\Omega_{eff} + \delta\Omega)$, where $\bar{S}_{yy}^{SQL}(\Omega) = 2\hbar\,|\chi_{eff}(\Omega)|$. This result is better than what is currently achievable in Advanced LIGO[34], with ultracold atoms[35] or with ultracold mechanical resonators[10], even when probed with squeezed light[11] or with nominally sub-SQL variational techniques[36].

Ground-state cooling by feedback

We now use the signal $y(t)$ obtained from this near-ideal quantum measurement to control and stabilize the quantum state of the mechanical system. We electronically convolve the signal with a filter kernel $h_{fb}(t)$ and apply the output $F_{fb}(t) = h_{fb}(t) * y(t)$ as a force to the mechanical resonator (feedback interaction, $H_{fb} = F_{fb}(t)x(t)$). To exert this force we modulate the amplitude of the auxiliary laser beam, the power of which is kept small, as in the previous experiment. In the domain of linearized quantum optomechanics, assuming Gaussian noise only, the quantum dynamics of the system can be mapped to a classical control problem, with the caveat that process and measurement noises must be included that mimic the quantum-mechanically required backaction and imprecision, respectively. Linear–quadratic–Gaussian control theory then provides a straightforward way of obtaining the optimum controller for cooling, the objective of which is to reduce a quadratic cost function—in this case, the mechanical position and momentum variance of a single mechanical mode[3,4,29,37–39] (Supplementary Information).

Although inspired by these results, our feedback filter $h_{fb}(\Omega) = h_{main}(\Omega) + h_{aux}(\Omega)$, with

$$h_{main}(\Omega) = g_{fb}e^{i\Omega\tau - i\phi}\left(\frac{\Gamma_{fb}\Omega}{\Omega_{fb}^2 - \Omega^2 - i\Gamma_{fb}\Omega}\right)^2 \qquad (2)$$

accommodates a more complex experimental reality (Supplementary Information). In particular, it contains a predominantly electronic loop delay of $\tau \approx 300$ ns, a high-order bandpass filter (with bandwidth Γ_{fb}, gain g_{fb} and global phase ϕ) peaked at the centre frequency Ω_{fb}, close to the centre of the phononic bandgap, to suppress gain for out-of-gap modes, and an auxiliary filter h_{aux} that suppresses instabilities of other mechanical modes far away from Ω_m. The phase ϕ is electronically adjusted so that $\arg(h_{fb}(\Omega_m)) \approx -\pi/2$. The feedback force is then approximately proportional to the velocity of the resonator, providing a quantum-noise-limited friction force, which is sometimes referred to as 'cold damping'[12,13,40]. Together with standard optomechanical theory[8,29], equation (2) can be incorporated into a simple control-theoretical model that predicts the spectra of the measured displacement, $\bar{S}_{yy}(\Omega)$, and the underlying fluctuations in the position and momentum of the resonator, $\bar{S}_{xx}(\Omega)$ and $\bar{S}_{pp}(\Omega)$, respectively (Supplementary Information).

© 2018 Springer Nature Limited. All rights reserved.

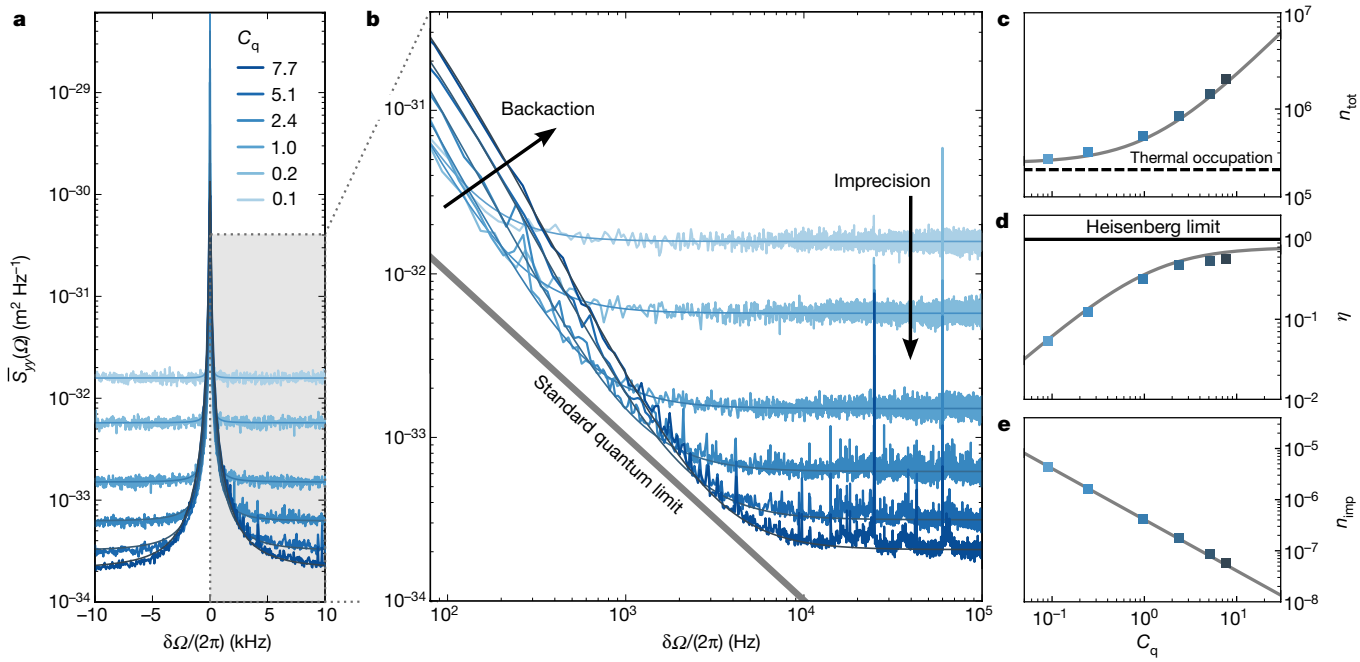

Fig. 3 | Quantum measurement. a, Displacement spectra around the effective mechanical frequency Ω_{eff}, for different quantum cooperativities C_q of the probe. **b**, Off-resonant tails of the spectra from **a** with Lorentzian fits (smooth, slightly darker lines). The standard quantum limit is indicated by the grey line. **c**, **e**, Imprecision noise n_{imp} (**e**) and the total force noise n_{tot} (**c**), from the fits in **b**. The former is visible as a decrease in the noise floor, whereas the latter appears as an increase in the wings of the Lorentzian (see arrows in **b**). The black dashed line in **c** indicates the thermal occupation. **d**, From these values, we calculate the measurement efficiency $\eta = 1/(16 n_{imp} n_{tot})$, which reaches 0.56. The Heisenberg limit corresponds to ideal efficiency, $\eta = 1$. The grey lines in **c**–**e** are fits of a theoretical model to the data (Supplementary Information).

To assess the cooling performance, we fit the predicted $\bar{S}_{yy}(\Omega)$ to measured spectra, adjusting n_{tot}, n_{imp}, g_{fb} and ϕ. The fit values for n_{tot} and n_{imp} agree with independent, first-principles calculations to within factors of 1.06 ± 0.07 and 1.01 ± 0.05, respectively (where the uncertainties correspond to ± 1 standard deviation). We then calculate the occupation of the mechanical resonator from its position variance:

$$\bar{n} = \langle b^{\dagger} b \rangle \approx \frac{1}{2}\left(\frac{1}{2\pi}\int_0^{\infty} \bar{S}_{xx}(\Omega) x_{zpf}^{-2} \mathrm{d}\Omega - 1\right)$$

In Fig. 4 we show the results as a function of controller gain (expressed as the effective resonator damping $\Gamma_{eff} = \Gamma_m + \mathrm{Im}[h_{fb}(\Omega_m)]/(m\Omega_m) + \Gamma_{opt}$), for five different probing strengths up to $C_q = 7.8$. For each C_q, a minimum occupancy is reached for a certain gain, beyond which the resonator is heated again. This mechanism is known as noise 'squashing'[13,18,20] (Fig. 4b) and involves substantial imprecision noise being fed back to the mechanics. The lowest residual occupation observed is $\bar{n} = 0.29 \pm 0.03$ (where the uncertainty indicates the confidence interval of the fit; Fig. 4a).

We benchmark this cooling performance against the occupation $\bar{n}_{est}$ of the conditional state (that is, conditioned on the measurement

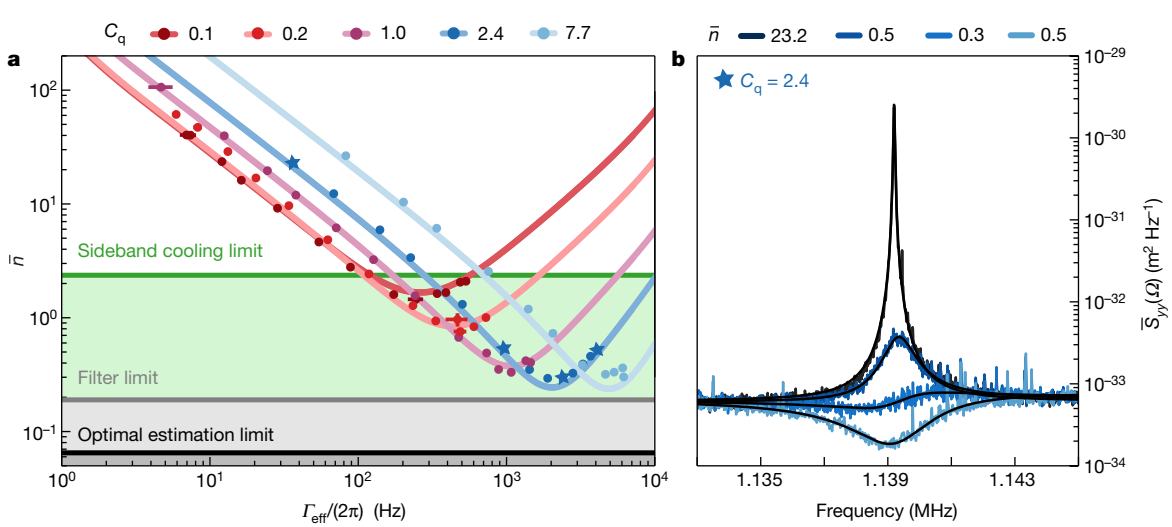

Fig. 4 | Feedback cooling to the quantum ground state. a, Mechanical occupancy for different quantum cooperativities C_q, as a function of loop gain, expressed here as an effective damping rate Γ_{eff}. Points are data; error bars indicate fit uncertainty; solid lines are theoretical calculations using independently estimated system parameters. The sideband-cooling limit for this system is shown as a green line. Grey and black lines indicate the limit of our implemented filter and of optimal state estimation, respectively (Supplementary Information). **b**, Exemplary spectra for $C_q = 2.4$, at the gain values marked by stars in **a**. Smooth black lines are Lorentzian fits.

© 2018 Springer Nature Limited. All rights reserved.

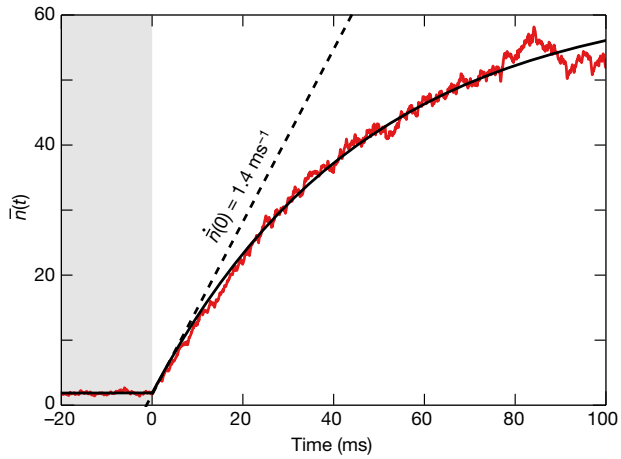

Fig. 5 | Heating from low phonon occupancy. Mechanical heating $\bar{n}(t)$ (red trace) measured by switching off the feedback at $t = 0$ ms. The black line is an exponential fit; its dashed tangent indicates $\dot{\bar{n}}(t=0) \approx \gamma_{\mathrm{tot}}$. The grey shading indicates the time interval during which the feedback is applied.

result)[29,41,42]. The lowest conditional occupation is reached by optimal state estimation from the available measurement record and coincides with the lowest occupation to which ideal feedback can bring the resonator. Under the idealized assumption of a single-mode, high-Q resonator coupled to a hot thermal bath[29,41], $\bar{n}_{\mathrm{est}} \approx (\sqrt{1/\eta} - 1)/2$. This expression yields $\bar{n}_{\mathrm{est}} \approx 0.07$ for our $\eta_{\mathrm{det}} = 0.77$ and for $C_{\mathrm{q}} \to \infty$, which corresponds to a state of high purity ($(1 + 2\bar{n}_{\mathrm{est}})^{-1} \approx 88\%$). The discrepancy with the achieved occupation indicates further room for improvement in engineering our feedback filter, the sub-optimal nature of which becomes apparent for high quantum cooperativity and gain (Supplementary Information). The performance compromise is a consequence of the need to avoid instabilities anywhere outside the bandgap—spectral regions that are crowded with other high-quality mechanical modes. Wider bandgaps, reduced loop delay and a filter that accounts for individual out-of-band modes are therefore routes to improved feedback.

By turning off the electronic feedback abruptly after cooling close to the ground state, we measure the heating rate of the resonator directly. In Fig. 5 we show the result of such a measurement, averaged over about 400 experimental iterations. The occupancy $\bar{n}(t)$ equilibrates exponentially to the level given by residual sideband cooling. At low probe power, we infer (Supplementary Information) a heating rate of 1.4 phonons per millisecond out of the ground state from the slope of this curve at $t = 0$ ms. This rate is consistent with the expected thermal decoherence rate $\gamma \approx \bar{n}_{\mathrm{th}} \Gamma_{\mathrm{m}}$ at the temperature of this experiment ($T \approx 9$ K) plus a contribution of 0.2 phonons per millisecond due to quantum backaction.

Discussion and outlook

Such millisecond coherence times compare favourably with other mechanical systems held at dilution refrigerator temperatures[11,31,43] and might be boosted to seconds if our system were made similarly cold. The very narrow linewidth of the mechanical mode (about 1 mHz) furthermore suggests the absence of substantial dephasing (Methods). Quantum memory applications are therefore conceivable.

With an overall measurement efficiency close to unity, mechanical systems such as the one presented here will allow tests and application of a wide range of quantum measurement and control techniques[3,4,29]. This includes time-continuous Bell measurements for state teleportation and entanglement swapping[44,45] and combination with mechanical parametric amplification[46] to create strongly squeezed mechanical states. An occupancy 9 dB below the sideband-cooling limit is promising for quantum control, in particular, of low-frequency mechanical systems such as those used for gravitational-wave detection; feedback-based protocols to enhance interferometric detectors have already been proposed[47]. Combination with nonlinear measurement schemes, such as photon counting[48], could allow non-Gaussian state preparation. Moreover, given that we achieved $C_{\mathrm{q}} > 100$ at 10 K, the prospect of quantum control of motion at room temperature appears more realistic than ever.

Online content

Any methods, additional references, Nature Research reporting summaries, source data, statements of data availability and associated accession codes are available at https://doi.org/10.1038/s41586-018-0643-8.

Received: 31 May 2018; Accepted: 13 September 2018;
Published online 31 October 2018.

1. Braginsky, V. B. & Khalili, F. Y. *Quantum Measurement* (Cambridge Univ. Press, Cambridge, 1992).
2. Clerk, A. A., Devoret, M. H., Girvin, S. M., Marquardt, F. & Schoelkopf, R. J. Introduction to quantum noise, measurement, and amplification. *Rev. Mod. Phys.* **82**, 1155–1208 (2010).
3. Jacobs, K. *Quantum Measurement Theory and its Application* (Cambridge Univ. Press, Cambridge, 2014).
4. Wiseman, H. M. & Milburn, G. J. *Quantum Measurement and Control* (Cambridge Univ. Press, Cambridge, 2009).
5. Zhang, J., Liu, Y.-X., Wu, R.-B., Jacobs, K. & Nori, F. Quantum feedback: theory, experiments, and applications. *Phys. Rep.* **679**, 1–60 (2017).
6. Sayrin, C. et al. Real-time quantum feedback prepares and stabilizes photon number states. *Nature* **477**, 73–77 (2011).
7. Vijay, R. et al. Stabilizing Rabi oscillations in a superconducting qubit using quantum feedback. *Nature* **490**, 77–80 (2012).
8. Aspelmeyer, M., Kippenberg, T. J. & Marquardt, F. Cavity optomechanics. *Rev. Mod. Phys.* **86**, 1391–1452 (2014).
9. Chan, J. et al. Laser cooling of a nanomechanical oscillator into its quantum ground state. *Nature* **478**, 89–92 (2011).
10. Teufel, J. D. et al. Sideband cooling of micromechanical motion to the quantum ground state. *Nature* **475**, 359–363 (2011).
11. Clark, J. B., Lecocq, F., Simmonds, R. W., Aumentado, J. & Teufel, J. D. Sideband cooling beyond the quantum backaction limit with squeezed light. *Nature* **541**, 191–195 (2017).
12. Mancini, S., Vitali, D. & Tombesi, P. Optomechanical cooling of a macroscopic oscillator by homodyne feedback. *Phys. Rev. Lett.* **80**, 688–691 (1998).
13. Cohadon, P. F., Heidmann, A. & Pinard, M. Cooling of a mirror by radiation pressure. *Phys. Rev. Lett.* **83**, 3174–3177 (1999).
14. Kubanek, A. et al. Photon-by-photon feedback control of a single-atom trajectory. *Nature* **462**, 898–901 (2009).
15. Bushev, P. et al. Feedback cooling of a single trapped ion. *Phys. Rev. Lett.* **96**, 043003 (2006).
16. Li, T., Kheifets, S. & Raizen, M. G. Millikelvin cooling of an optically trapped microsphere in vacuum. *Nat. Phys.* **7**, 527–530 (2011).
17. Jain, V. et al. Direct measurement of photon recoil from a levitated nanoparticle. *Phys. Rev. Lett.* **116**, 243601 (2016).
18. Poggio, M., Degen, C. L., Mamin, H. J. & Rugar, D. Feedback cooling of a cantilever's fundamental mode below 5 mK. *Phys. Rev. Lett.* **99**, 017201 (2007).
19. Kleckner, D. & Bouwmeester, D. Sub-kelvin optical cooling of a micromechanical resonator. *Nature* **444**, 75–78 (2006).
20. Wilson, D. J. et al. Measurement-based control of a mechanical oscillator at its thermal decoherence rate. *Nature* **524**, 325–329 (2015).
21. Lee, K. H., McRae, T. G., Harris, G. I., Knittel, J. & Bowen, W. P. Cooling and control of a cavity optoelectromechanical system. *Phys. Rev. Lett.* **104**, 123604 (2010).
22. LaHaye, M. D., Buu, O., Camarota, B. & Schwab, K. C. Approaching the quantum limit of a nanomechanical resonator. *Science* **304**, 74–77 (2004).
23. Gavartin, E., Verlot, P. & Kippenberg, T. J. A hybrid on-chip optomechanical transducer for ultrasensitive force measurements. *Nat. Nanotechnol.* **7**, 509–514 (2012).
24. Vinante, A. et al. Feedback cooling of the normal modes of a massive electromechanical system to submillikelvin temperature. *Phys. Rev. Lett.* **101**, 033601 (2008).
25. Abbott, B. et al. Observation of a kilogram-scale oscillator near its quantum ground state. *New J. Phys.* **11**, 073032 (2009).
26. Tsaturyan, Y., Barg, A., Polzik, E. S. & Schliesser, A. Ultracoherent nanomechanical resonators via soft clamping and dissipation dilution. *Nat. Nanotechnol.* **12**, 776–783 (2017).
27. Thompson, J. et al. Strong dispersive coupling of a high-finesse cavity to a micromechanical membrane. *Nature* **452**, 72–75 (2008).
28. Nielsen, W. H. P., Tsaturyan, Y., Møller, C. B., Polzik, E. S. & Schliesser, A. Multimode optomechanical system in the quantum regime. *Proc. Natl Acad. Sci. USA* **114**, 62–66 (2017).
29. Bowen, W. P. & Milburn, G. J. *Quantum Optomechanics* 103, 161, 163 (CRC Press, Boca Raton, 2016).
30. Weis, S. et al. Optomechanically induced transparency. *Science* **330**, 1520–1523 (2010).
31. Peterson, R. W. et al. Laser cooling of a micromechanical membrane to the quantum backaction limit. *Phys. Rev. Lett.* **116**, 063601 (2016).

© 2018 Springer Nature Limited. All rights reserved.

32. Gorodetksy, M., Schliesser, A., Anetsberger, G., Deleglise, S. & Kippenberg, T. Determination of the vacuum optomechanical coupling rate using frequency noise calibration. *Opt. Express* **18**, 23236–23246 (2010).
33. Purdy, T. P., Grutter, K. E., Srinivasan, K. & Taylor, J. M. Quantum correlations from a room-temperature optomechanical cavity. *Science* **356**, 1265–1268 (2017).
34. Martynov, D. V. et al. Sensitivity of the advanced LIGO detectors at the beginning of gravitational wave astronomy. *Phys. Rev. D* **93**, 112004 (2016).
35. Schreppler, S. et al. Optically measuring force near the standard quantum limit. *Science* **344**, 1486–1489 (2014).
36. Kampel, N. S. et al. Improving broadband displacement detection with quantum correlations. *Phys. Rev. X* **7**, 021008 (2017).
37. Doherty, A. C. & Jacobs, K. Feedback control of quantum systems using continuous state estimation. *Phys. Rev. A* **60**, 2700–2711 (1999).
38. Doherty, A. C., Habib, S., Jacobs, K., Mabuchi, H. & Tan, S. M. Quantum feedback control and classical control theory. *Phys. Rev. A* **62**, 012105 (2000).
39. Garbini, J. L., Bruland, K. J., Dougherty, W. M. & Sidles, J. A. Optimal control of force microscope cantilevers. I. Controller design. *J. Appl. Phys.* **80**, 1951–1958 (1996).
40. Genes, C., Vitali, D., Tombesi, P., Gigan, S. & Aspelmeyer, M. Ground-state cooling of a micromechanical oscillator: comparing cold damping and cavity-assisted cooling schemes. *Phys. Rev. A* **77**, 033804 (2008).
41. Doherty, A. C., Szorkovszky, A., Harris, G. I. & Bowen, W. P. The quantum trajectory approach to quantum feedback control of an oscillator revisited. *Phil. Trans. R. Soc. Lond. A* **370**, 5338–5353 (2012).
42. Wieczorek, W. et al. Optimal state estimation for cavity optomechanical systems. *Phys. Rev. Lett.* **114**, 223601 (2015).
43. Chu, Y. et al. Quantum acoustics with superconducting qubits. *Science* **358**, 199–202 (2017).
44. Hofer, S. G., Vasilyev, D. V., Aspelmeyer, M. & Hammerer, K. Time-continuous Bell measurements. *Phys. Rev. Lett.* **111**, 170404 (2013).
45. Hofer, S. G. & Hammerer, K. Entanglement-enhanced time-continuous quantum control in optomechanics. *Phys. Rev. A* **91**, 033822 (2015).
46. Szorkovszky, A., Doherty, A. C., Harris, G. I. & Bowen, W. P. Mechanical squeezing via parametric amplification and weak measurement. *Phys. Rev. Lett.* **107**, 213603 (2011).
47. Courty, J.-M., Heidmann, A. & Pinard, M. Quantum locking of mirrors in interferometers. *Phys. Rev. Lett.* **90**, 083601 (2003).
48. Ringbauer, M., Weinhold, T. J., Howard, L. A., White, A. G. & Vanner, M. R. Generation of mechanical interference fringes by multi-photon counting. *New J. Phys.* **20**, 053042 (2018).

Acknowledgements We acknowledge discussions with K. Hammerer, E. Zeuthen and D. Vitali, and early-stage sample fabrication by Y. Seis. This work was supported by funding from the European Union's Horizon 2020 research and innovation programme (European Research Council (ERC) project Q-CEOM, grant agreement no. 638765 and FET proactive project HOT, grant agreement no. 732894), a starting grant from the Danish Council for Independent Research and the Carlsberg Foundation.

Reviewer information *Nature* thanks D. Bouwmeester, M. Poggio and M. Vanner for their contribution to the peer review of this work.

Author contributions M.R., D.M. and J.C. built (with initial contributions from Y.T.) and performed the experiments, analysed the data and, together with A.S., discussed the results and wrote the paper. Y.T. designed and fabricated the membrane resonators. A.S. conceived and directed the project.

Competing interests The authors declare no competing interests.

Additional information

Extended data is available for this paper at https://doi.org/10.1038/s41586-018-0643-8.
Supplementary information is available for this paper at https://doi.org/10.1038/s41586-018-0643-8.
Reprints and permissions information is available at http://www.nature.com/reprints.

Correspondence and requests for materials should be addressed to A.S.

Publisher's note: Springer Nature remains neutral with regard to jurisdictional claims in published maps and institutional affiliations.

© 2018 Springer Nature Limited. All rights reserved.

METHODS

Soft-clamped mechanical resonator. The mechanical device used in the experiment is based on a 20 nm × 3.6 mm × 3.6 mm soft-clamped Si_3N_4 membrane[26]. As shown in Extended Data Fig. 1, a honeycomb hole pattern is fabricated into the membrane, producing phononic bandgaps for out-of-plane modes. In the centre of the membrane, a defect is created, supporting localized vibrational modes whose frequencies lie in one of these bandgaps. These mechanical modes are soft-clamped in the sense that their mode shapes decay into the phononic crystal structure gradually, as opposed to being clamped by a rigid frame. This reduced curvature, combined with stress redistribution due to the phononic pattern, results in ultrahigh mechanical quality factors. Here we focus on mode A, at $\Omega_m/(2\pi) = 1.139$ MHz. Compared to previous work[26], a modified defect design is used to shift mode A away from the left bandgap edge.

To measure the quality factor of this soft-clamped mode, we performed ringdown experiments. The laser is tuned to a wavelength where the finesse of the optical cavity is low ($F = \mathcal{O}(10)$), allowing interferometric displacement measurements without dynamical optomechanical effects. The transmitted light intensity is measured directly with a photodiode, and the photocurrent is demodulated at the mechanical frequency Ω_m to obtain a record of the motion. To excite a desired mechanical mode, the amplitude of an auxiliary laser is modulated at Ω_m. When the modulation is turned off, the oscillation amplitude decays according to $x(t) = x(0)\exp[-\Omega_m t/(2Q)]$, as shown in Extended Data Fig. 2a. From a fit we extract a quality factor of $Q = 1.03 \times 10^9$.

When measuring such extreme quality factors, it is important to ensure that the decay is not modified by any residual dynamical effects due to photothermal or radiation-pressure backaction. In Extended Data Fig. 2b, we confirm that the measured Q does not depend on laser power, as would be expected for these effects. We also conduct a 'stroboscopic' ringdown measurement, in which the motion was probed for only brief moments (duty cycle of about 4%, period of about 0.5 min). The continuous and stroboscopic ringdowns overlap well, yielding Q values of 1.03×10^9 and 1.02×10^9, respectively. The inset of Extended Data Fig. 2a shows the power spectral density of the continuous ringdown data. The width of this peak is Fourier-limited to 1.1 mHz for these data and thereby confirms the absence of substantial dephasing: the energy decay rate was found (by ringdown) to be 1.1 mHz.

Experimental set-up. Extended Data Fig. 3 shows more details about the set-up for the experiments described in the main text. A Ti:sapphire laser (red) at $\lambda \approx 795$ nm is used to probe the frequency fluctuations of an optical cavity mode whose linewidth is $\kappa/(2\pi) = 15.9$ MHz. To stabilize the laser frequency relative to the optomechanical cavity, we implement a Pound–Drever–Hall scheme[49], using a phase modulator on the probe beam. This phase modulator is also driven with a coherent tone at ν_{cal}, to calibrate the transduction of optical frequency fluctuations into detected voltage fluctuations[32]. At the wavelength of this probe beam, the reflectivities of the two cavity mirrors differ greatly, forming a strongly asymmetric optical resonator. To detect as much of the cavity light as possible, we drive the cavity through the higher-reflectivity port while detecting the light leaving the more transmissive port. We perform a phase-sensitive measurement on the transmitted light by means of a balanced homodyne receiver.

To stably measure the optical phase of the signal beam, on which the mechanical displacement information is imprinted, we stabilize the path difference of the signal and local oscillator arms. A feedback loop actuates a piezo-controlled mirror in the local oscillator path, minimizing the d.c. component of the photocurrent[50]. The information about the mechanics is contained in the a.c. part of the photocurrent, which is digitally acquired both from a data acquisition card to perform a Fourier analysis and from a digital lock-in amplifier to analyse the time evolution (Supplementary Information).

An auxiliary Ti:sapphire laser (blue) at $\lambda_{aux} \approx 796$ nm is frequently used in the experiment. To avoid unwanted interference, its polarization is orthogonal to the probe laser and it is locked to a different longitudinal cavity mode, whose linewidth is $\kappa_{aux}/(2\pi) = 12.9$ MHz. In the experiment described in Fig. 2, this laser provides the sideband cooling and acts as a source of strong quantum backaction. In the feedback cooling experiment (Fig. 4), the auxiliary laser is used (in combination with an amplitude modulator) to exert a force on the mechanical resonator via radiation pressure, that is, to actuate the feedback force. For this feedback, a field-programmable gate array (FPGA)-based digital controller (RedPitaya 125-14; https://redpitaya.com) is used to bandpass-filter the a.c. homodyne photocurrent close to the mechanical mode to be cooled. The filter is implemented in an open-source, Python-based software module[51] (https://github.com/lneuhaus/pyrpl), whereby the built-in I/Q modulation capability enables filters with continuously tunable phase. The processed signal is amplified and sent to a fibre-integrated optical amplitude modulator on the auxiliary beam. In the actual experiment we use several FPGA controllers. One of them is devoted to cooling the defect mode of interest, using the transfer function $h_{main}(\Omega)$ given in equation (2). An electronic switch is inserted just after this controller to toggle the feedback force on and off to measure transient dynamics (Supplementary Information). All other controllers can be grouped in a single transfer function $h_{aux}(\Omega)$, which is used to cool some of the low-frequency modes that correspond to motion of the entire Si_3N_4 membrane structure, as well as defect modes C and D. This is needed to avoid large frequency fluctuations and keep the whole system stable. This auxiliary controller is always on in the experiments reported in Figs. 3 and 4.

Optomechanical assembly. We largely use the same optomechanical assembly and optical characterization techniques as described previously[28], combining them here with a soft-clamped membrane[26]. In this membrane-in-the-middle geometry[27], the main optomechanical parameters—the optical-mode resonance frequency, the vacuum optomechanical coupling g_0, the cavity linewidth κ and the cavity outcoupling η_c—depend on the position z_m of the centre of mass of the membrane relative to the intracavity standing wave. Because the position of the membrane is constrained by the cavity assembly, we use a laser whose wavelength can be tuned (over about 200 nm) to control these parameters. Tuning the laser to the next longitudinal optical resonance introduces one more antinode in the intracavity standing wave, effectively changing the position of the membrane relative to the standing wave.

To predict how the other parameters behave as a function of λ, we use a transfer matrix model[52]. In this approach, the optomechanical system is modelled as a stack of component transfer matrices, whose total behaviour can be analysed to predict system parameters. We measure the shift of the optical resonance frequencies for several longitudinal modes and fit them with the transfer matrix model to estimate a cavity length $L = 1.6$ mm and a membrane position $z_m = 0.5$ mm relative to the flat, transmissive mirror. By using an independent measurement of the transmissivity of the mirrors, we also predict the cavity outcoupling $\eta_c = \kappa_{out}/\kappa$ to be modulated between 0.88 and 0.95, depending on membrane position. With the known laser wavelength and inferred z_m, the transfer matrix model predicts a unique value for η_c. We use this value to obtain an estimate of g_0 from an OMIT trace (η_c links the measured output power with the intracavity photon number) and find excellent agreement with the g_0 obtained from the quantum backaction calibration, which is independent of η_c (Supplementary Information). No other results reported here depend on η_c.

To measure the cavity linewidth κ, we sweep a phase-modulated laser across the cavity resonance and measure the transmitted intensity. The central feature is fitted with a Lorentzian and its linewidth is converted to frequency units using the phase-modulation sidebands as frequency markers. During the sweep the auxiliary laser is locked to the red side of a different cavity mode to laser-cool the mechanical modes of the entire membrane structure; large-amplitude excursions of these modes can otherwise lead to artificial broadening of the cavity line shape.

Detection efficiency budget. High detection efficiency is critical for our quantum measurements. To increase the quantum efficiency of the photodiodes, we removed the protective glass window. From the measured responsivity, we estimate a quantum efficiency of 93%, which is 2% below the specified values. We believe this difference comes from minor damage during the window removal process. In Extended Data Table 1 we report a breakdown of contributions to the total detection efficiency. Adding up all losses gives an expected efficiency of $\eta_{det} = 80\%$. However, we measure directly the losses between just after the cryostat window and just before the photodetection to be 92% instead of the expected 95%, which reduces the detection efficiency to $\eta_{det} = 77\%$. Electronic noise in all measurements is around 1% of the optical vacuum noise level.

Calibration of g_0 via quantum noise thermometry or OMIT. We implement two independent methods to measure the single-photon optomechanical coupling g_0 between a given cavity mode and the mechanical mode.

First, we lock the probe laser on the red side of the cavity and modulate its phase with a coherent tone. We observe OMIT[30] in the optical response function when the frequency of that tone is swept and the intensity of the transmitted beam is detected directly. If the laser detuning Δ and the cavity linewidth κ are measured independently then the measured trace can be fitted to extract the light-enhanced coupling g. From it, the single-photon coupling g_0 can be derived if the optical losses to the detector and the cavity outcoupling η_c are known.

In Extended Data Fig. 4 we show a series of OMIT traces with different detunings, with the corresponding fits. While the optical losses in the detection path are measured to be 5%, the cavity outcoupling cannot be measured directly. Therefore, we assume the outcoupling from the transfer matrix model for this particular cavity mode, $\eta_c = 95\%$. With this assumption, we estimate a single-photon coupling of $g_0/(2\pi) = 129^{+2}_{-3}$ Hz.

The second method to measure g_0 relies on precise knowledge of the temperature of the mechanical mode. When that is the case, we can compare the measured mechanical energy to a known frequency modulation to obtain g_0. This method is explained in more detail in Supplementary Information, but the result is $g_0/(2\pi) = 127 \pm 2$ Hz. The agreement between the two methods is particularly meaningful because they make very different assumptions. In brief, the first is essentially a calibration based on intracavity photon occupation, while the second is based on a certain mechanical phonon occupation.

© 2018 Springer Nature Limited. All rights reserved.

Data availability

Source Data for Figs. 1–5 are provided with the online version of the paper and are available in the UCPH ERDA repository (https://doi.org/10.17894/ucph.2612dd59-20ab-40d2-a33d-f53e4428c4cd).

49. Black, E. D. An introduction to Pound-Drever-Hall laser frequency stabilization. *Am. J. Phys.* **69**, 79–87 (2001).
50. Leonhardt, U. *Measuring the Quantum State of Light* Ch. 4.2 (Cambridge Univ. Press, Cambridge, 1997).
51. Neuhaus, L. et al. PyRPL (Python Red Pitaya Lockbox) — an open-source software package for FPGA-controlled quantum optics experiments. In *2017 Conference on Lasers and Electro-Optics Europe and European Quantum Electronics Conference* https://doi.org/10.1109/CLEOE-EQEC.2017.8087380 (Optical Society of America, 2017).
52. Jayich, A. M. et al. Dispersive optomechanics: a membrane inside a cavity. *New J. Phys.* **10**, 095008 (2008).

© 2018 Springer Nature Limited. All rights reserved.

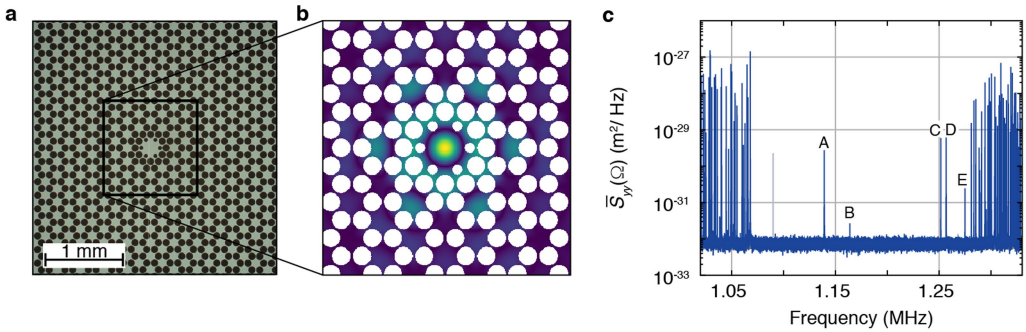

Extended Data Fig. 1 | Soft-clamped membrane. a, Photograph of the soft-clamped membrane. **b**, Simulated displacement pattern of defect-localized mode A. **c**, Mechanical spectrum of the lowest-frequency bandgap, with defect-localized modes labelled from A to E. The grey peak at 1.09 MHz is a phase-calibration tone.

© 2018 Springer Nature Limited. All rights reserved.

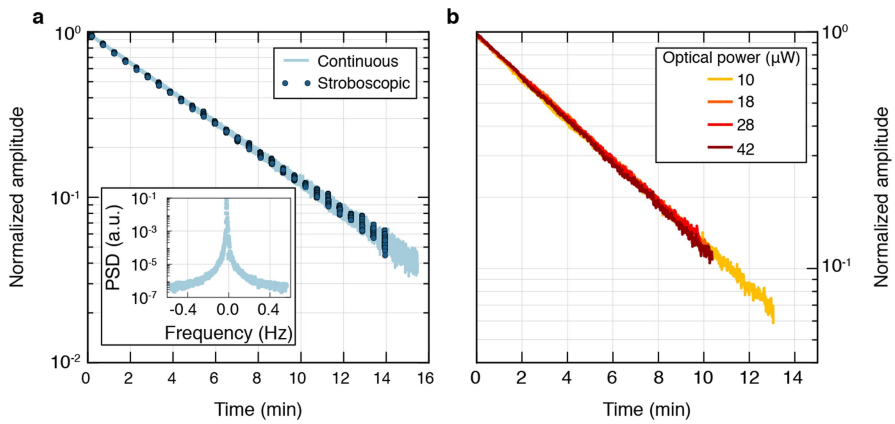

Extended Data Fig. 2 | Mode A ringdowns. a, Ringdowns with continuous and stroboscopic optical monitoring. The inset shows the power spectral density (PSD) of the continuous ringdown data. **b**, Ringdowns at different continuous optical powers. The Q values extracted are 1.02×10^9, 1.06×10^9, 1.07×10^9 and 1.04×10^9 from high to low optical power.

© 2018 Springer Nature Limited. All rights reserved.

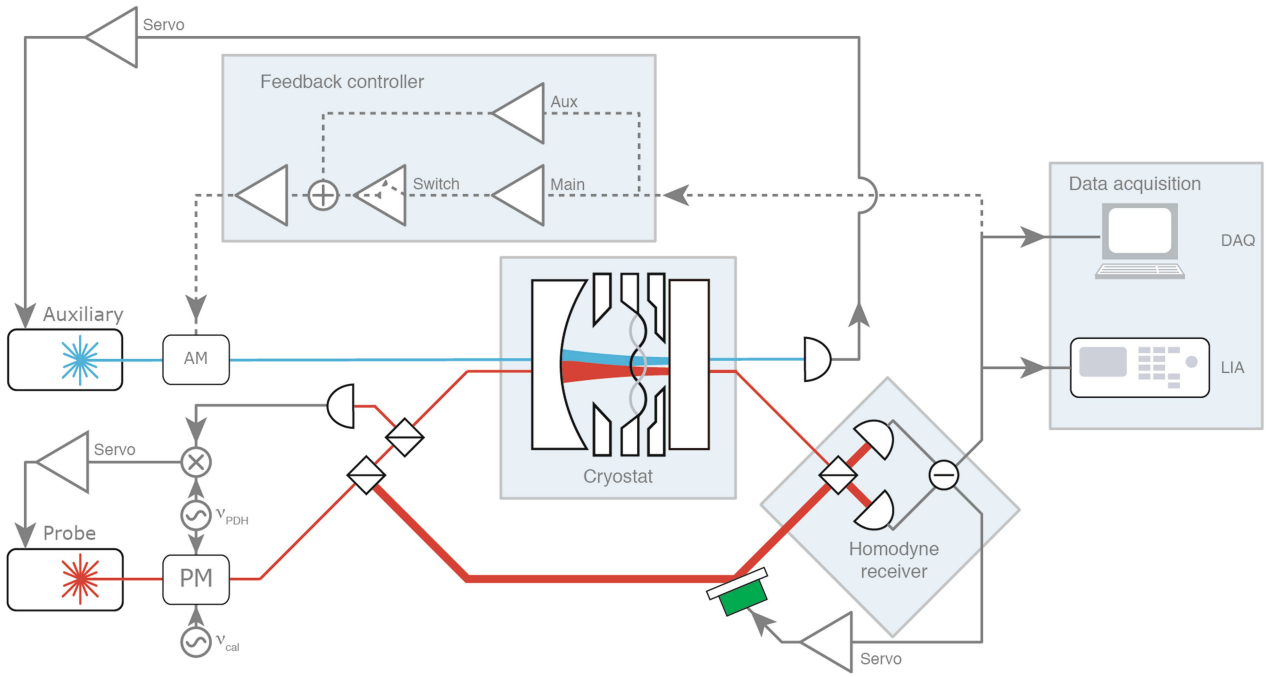

Extended Data Fig. 3 | Experimental set-up. An overview of the optical and electronic scheme used in the experiments is shown. AM, amplitude modulator; PM, phase modulator; DAQ, data acquisition card; LIA, lock-in amplifier; aux, auxiliary; ν_{PDH}, Pound–Drever–Hall modulation frequency; ν_{cal}, calibration tone frequency.

© 2018 Springer Nature Limited. All rights reserved.

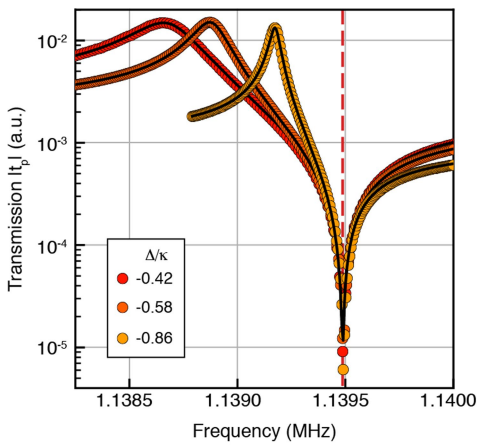

Extended Data Fig. 4 | OMIT. Measured traces of the transmission $|t_p|$ are shown for different laser detunings, close to the mechanical frequency Ω_m (dashed red line). Black lines are theoretical fits.

© 2018 Springer Nature Limited. All rights reserved.

Extended Data Table 1 | Contribution to detection efficiency

Optical element	Value	Origin
Cavity outcoupling	95%	TMM
Cavity window	99.6%	Specs
Lens	99.6%	Specs
PBS, transmission	99%	Measured
Lens	99.6%	Specs
Waveplate	99.2%	Specs
PBS, transmission	99%	Measured
PBS, reflection	99.5%	Specs
Diode quantum efficiency	93%	Measured
Interference visibility	98%	Measured

PBS, polarizing beam splitter; TMM, transfer matrix model.

© 2018 Springer Nature Limited. All rights reserved.

ARTICLE

https://doi.org/10.1038/s41586-018-0637-6

The Moral Machine experiment

Edmond Awad[1], Sohan Dsouza[1], Richard Kim[1], Jonathan Schulz[2], Joseph Henrich[2], Azim Shariff[3]*, Jean-François Bonnefon[4]* & Iyad Rahwan[1,5]*

With the rapid development of artificial intelligence have come concerns about how machines will make moral decisions, and the major challenge of quantifying societal expectations about the ethical principles that should guide machine behaviour. To address this challenge, we deployed the Moral Machine, an online experimental platform designed to explore the moral dilemmas faced by autonomous vehicles. This platform gathered 40 million decisions in ten languages from millions of people in 233 countries and territories. Here we describe the results of this experiment. First, we summarize global moral preferences. Second, we document individual variations in preferences, based on respondents' demographics. Third, we report cross-cultural ethical variation, and uncover three major clusters of countries. Fourth, we show that these differences correlate with modern institutions and deep cultural traits. We discuss how these preferences can contribute to developing global, socially acceptable principles for machine ethics. All data used in this article are publicly available.

We are entering an age in which machines are tasked not only to promote well-being and minimize harm, but also to distribute the well-being they create, and the harm they cannot eliminate. Distribution of well-being and harm inevitably creates tradeoffs, whose resolution falls in the moral domain[1–3]. Think of an autonomous vehicle that is about to crash, and cannot find a trajectory that would save everyone. Should it swerve onto one jaywalking teenager to spare its three elderly passengers? Even in the more common instances in which harm is not inevitable, but just possible, autonomous vehicles will need to decide how to divide up the risk of harm between the different stakeholders on the road. Car manufacturers and policymakers are currently struggling with these moral dilemmas, in large part because they cannot be solved by any simple normative ethical principles such as Asimov's laws of robotics[4].

Asimov's laws were not designed to solve the problem of universal machine ethics, and they were not even designed to let machines distribute harm between humans. They were a narrative device whose goal was to generate good stories, by showcasing how challenging it is to create moral machines with a dozen lines of code. And yet, we do not have the luxury of giving up on creating moral machines[5–8]. Autonomous vehicles will cruise our roads soon, necessitating agreement on the principles that should apply when, inevitably, life-threatening dilemmas emerge. The frequency at which these dilemmas will emerge is extremely hard to estimate, just as it is extremely hard to estimate the rate at which human drivers find themselves in comparable situations. Human drivers who die in crashes cannot report whether they were faced with a dilemma; and human drivers who survive a crash may not have realized that they were in a dilemma situation. Note, though, that ethical guidelines for autonomous vehicle choices in dilemma situations do not depend on the frequency of these situations. Regardless of how rare these cases are, we need to agree beforehand how they should be solved.

The key word here is 'we'. As emphasized by former US president Barack Obama[9], consensus in this matter is going to be important. Decisions about the ethical principles that will guide autonomous vehicles cannot be left solely to either the engineers or the ethicists. For consumers to switch from traditional human-driven cars to autonomous vehicles, and for the wider public to accept the proliferation of artificial intelligence-driven vehicles on their roads, both groups will need to understand the origins of the ethical principles that are programmed into these vehicles[10]. In other words, even if ethicists were to agree on how autonomous vehicles should solve moral dilemmas, their work would be useless if citizens were to disagree with their solution, and thus opt out of the future that autonomous vehicles promise in lieu of the status quo. Any attempt to devise artificial intelligence ethics must be at least cognizant of public morality.

Accordingly, we need to gauge social expectations about how autonomous vehicles should solve moral dilemmas. This enterprise, however, is not without challenges[11]. The first challenge comes from the high dimensionality of the problem. In a typical survey, one may test whether people prefer to spare many lives rather than few[9,12,13]; or whether people prefer to spare the young rather than the elderly[14,15]; or whether people prefer to spare pedestrians who cross legally, rather than pedestrians who jaywalk; or yet some other preference, or a simple combination of two or three of these preferences. But combining a dozen such preferences leads to millions of possible scenarios, requiring a sample size that defies any conventional method of data collection.

The second challenge makes sample size requirements even more daunting: if we are to make progress towards universal machine ethics (or at least to identify the obstacles thereto), we need a fine-grained understanding of how different individuals and countries may differ in their ethical preferences[16,17]. As a result, data must be collected worldwide, in order to assess demographic and cultural moderators of ethical preferences.

As a response to these challenges, we designed the Moral Machine, a multilingual online 'serious game' for collecting large-scale data on how citizens would want autonomous vehicles to solve moral dilemmas in the context of unavoidable accidents. The Moral Machine attracted worldwide attention, and allowed us to collect 39.61 million decisions from 233 countries, dependencies, or territories (Fig. 1a). In the main interface of the Moral Machine, users are shown unavoidable accident scenarios with two possible outcomes, depending on whether the autonomous vehicle swerves or stays on course (Fig. 1b). They then click on the outcome that they find preferable. Accident scenarios are generated by the Moral Machine following an exploration strategy that

[1]The Media Lab, Massachusetts Institute of Technology, Cambridge, MA, USA. [2]Department of Human Evolutionary Biology, Harvard University, Cambridge, MA, USA. [3]Department of Psychology, University of British Columbia, Vancouver, British Columbia, Canada. [4]Toulouse School of Economics (TSM-R), CNRS, Université Toulouse Capitole, Toulouse, France. [5]Institute for Data, Systems & Society, Massachusetts Institute of Technology, Cambridge, MA, USA. *e-mail: shariff@psych.ubc.ca; jean-francois.bonnefon@tse-fr.eu; irahwan@mit.edu

© 2018 Springer Nature Limited. All rights reserved.

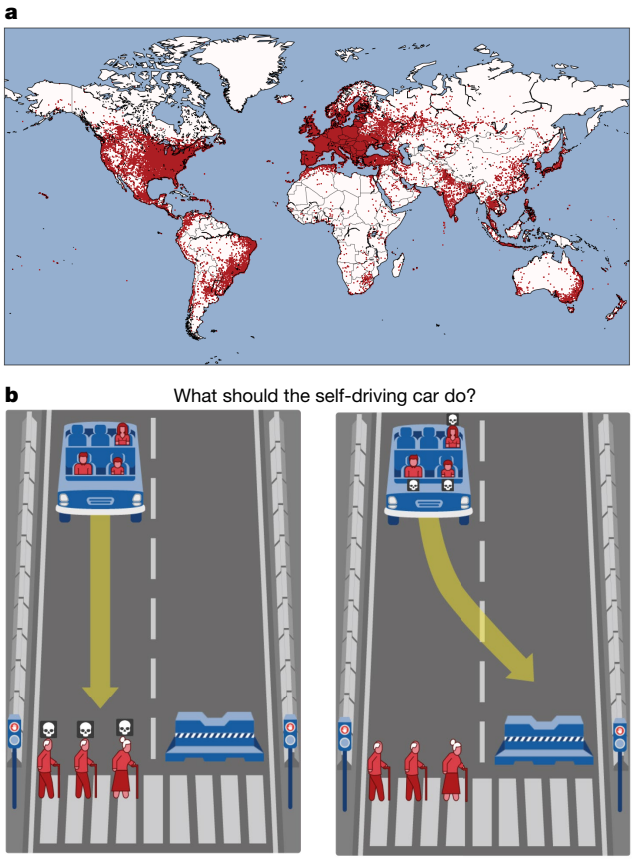

Fig. 1 | Coverage and interface. a, World map highlighting the locations of Moral Machine visitors. Each point represents a location from which at least one visitor made at least one decision ($n = 39.6$ million). The numbers of visitors or decisions from each location are not represented. **b**, Moral Machine interface. An autonomous vehicle experiences a sudden brake failure. Staying on course would result in the death of two elderly men and an elderly woman who are crossing on a 'do not cross' signal (left). Swerving would result in the death of three passengers: an adult man, an adult woman, and a boy (right).

focuses on nine factors: sparing humans (versus pets), staying on course (versus swerving), sparing passengers (versus pedestrians), sparing more lives (versus fewer lives), sparing men (versus women), sparing the young (versus the elderly), sparing pedestrians who cross legally (versus jaywalking), sparing the fit (versus the less fit), and sparing those with higher social status (versus lower social status). Additional characters were included in some scenarios (for example, criminals, pregnant women or doctors), who were not linked to any of these nine factors. These characters mostly served to make scenarios less repetitive for the users. After completing a 13-accident session, participants could complete a survey that collected, among other variables, demographic information such as gender, age, income, and education, as well as religious and political attitudes. Participants were geolocated so that their coordinates could be used in a clustering analysis that sought to identify groups of countries or territories with homogeneous vectors of moral preferences.

Here we report the findings of the Moral Machine experiment, focusing on four levels of analysis, and considering for each level of analysis how the Moral Machine results can trace our path to universal machine ethics. First, what are the relative importances of the nine preferences we explored on the platform, when data are aggregated worldwide? Second, does the intensity of each preference depend on the individual characteristics of respondents? Third, can we identify clusters of countries with homogeneous vectors of moral preferences? And fourth, do cultural and economic variations between countries predict variations in their vectors of moral preferences?

Global preferences

To test the relative importance of the nine preferences simultaneously explored by the Moral Machine, we used conjoint analysis to compute the average marginal component effect (AMCE) of each attribute (male character versus female character, passengers versus pedestrians, and so on)[18]. Figure 2a shows the unbiased estimates of nine AMCEs extracted from the Moral Machine data. In each row, the bar shows the difference between the probability of sparing characters with the attribute on the right side, and the probability of sparing the characters with the attribute on the left side, over the joint distribution of all other attributes (see Supplementary Information for computational details and assumptions, and see Extended Data Figs.1, 2 for robustness checks).

As shown in Fig. 2a, the strongest preferences are observed for sparing humans over animals, sparing more lives, and sparing young lives. Accordingly, these three preferences may be considered essential building blocks for machine ethics, or at least essential topics to be considered by policymakers. Indeed, these three preferences differ starkly in the level of controversy they are likely to raise among ethicists.

Consider, as a case in point, the ethical rules proposed in 2017 by the German Ethics Commission on Automated and Connected Driving[19]. This report represents the first and only attempt so far to provide official guidelines for the ethical choices of autonomous vehicles. As such, it provides an important context for interpreting our findings and their relevance to other countries that might attempt to follow the German example in the future. German Ethical Rule number 7 unambiguously states that in dilemma situations, the protection of human life should enjoy top priority over the protection of other animal life. This rule is in clear agreement with social expectations assessed through the Moral Machine. On the other hand, German Ethical Rule number 9 does not take a clear stance on whether and when autonomous vehicles should be programmed to sacrifice the few to spare the many, but leaves this possibility open: it is important, thus, to know that there would be strong public agreement with such programming, even if it is not mandated through regulation.

By contrast, German Ethical Rule number 9 also states that any distinction based on personal features, such as age, should be prohibited. This clearly clashes with the strong preference for sparing the young (such as children) that is assessed through the Moral Machine (see Fig. 2b for a stark illustration: the four most spared characters are the baby, the little girl, the little boy, and the pregnant woman). This does not mean that policymakers should necessarily go with public opinion and allow autonomous vehicles to preferentially spare children, or, for that matter, women over men, athletes over overweight persons, or executives over homeless persons—for all of which we see weaker but clear effects. But given the strong preference for sparing children, policymakers must be aware of a dual challenge if they decide not to give a special status to children: the challenge of explaining the rationale for such a decision, and the challenge of handling the strong backlash that will inevitably occur the day an autonomous vehicle sacrifices children in a dilemma situation.

Individual variations

We assessed individual variations by further analysing the responses of the subgroup of Moral Machine users ($n = 492{,}921$) who completed the optional demographic survey on age, education, gender, income, and political and religious views, to assess whether preferences were modulated by these six characteristics. First, when we include all six characteristic variables in regression-based estimators of each of the nine attributes, we find that individual variations have no sizable impact on any of the nine attributes (all below 0.1; see Extended Data Table 1). Of these, the most notable effects are driven by gender and religiosity of respondents. For example, male respondents are 0.06% less inclined to spare females, whereas one increase in standard deviation of religiosity of the respondent is associated with 0.09% more inclination to spare humans.

More importantly, none of the six characteristics splits its subpopulations into opposing directions of effect. On the basis of a

© 2018 Springer Nature Limited. All rights reserved.

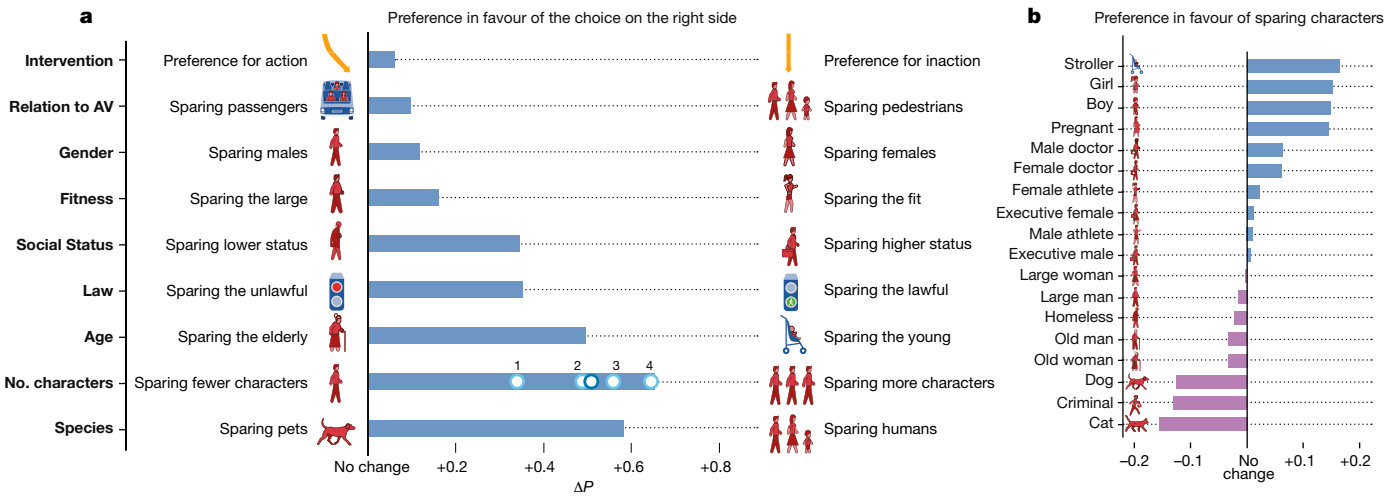

Fig. 2 | Global preferences. a, AMCE for each preference. In each row, ΔP is the difference between the probability of sparing characters possessing the attribute on the right, and the probability of sparing characters possessing the attribute on the left, aggregated over all other attributes. For example, for the attribute age, the probability of sparing young characters is 0.49 (s.e. = 0.0008) greater than the probability of sparing older characters. The 95% confidence intervals of the means are omitted owing to their insignificant width, given the sample size (n = 35.2 million). For the number of characters (No. characters), effect sizes are shown for each number of additional characters (1 to 4; n_1 = 1.52 million, n_2 = 1.52 million, n_3 = 1.52 million, n_4 = 1.53 million); the effect size for two additional characters overlaps with the mean effect of the attribute. AV, autonomous vehicle. **b**, Relative advantage or penalty for each character, compared to an adult man or woman. For each character, ΔP is the difference the between the probability of sparing this character (when presented alone) and the probability of sparing one adult man or woman (n = 1 million). For example, the probability of sparing a girl is 0.15 (s.e. = 0.003) higher than the probability of sparing an adult man or woman.

unilateral dichotomization of each of the six attributes, resulting in two subpopulations for each, the difference in probability (ΔP) has a positive value for all considered subpopulations. For example, both male and female respondents indicated preference for sparing females, but the latter group showed a stronger preference (Extended Data Fig. 3). In summary, the individual variations that we observe are theoretically important, but not essential information for policymakers.

Cultural clusters

Geolocation allowed us to identify the country of residence of Moral Machine respondents, and to seek clusters of countries with homogeneous vectors of moral preferences. We selected the 130 countries with at least 100 respondents (n range 101–448,125), standardized the nine target AMCEs of each country, and conducted a hierarchical clustering on these nine scores, using Euclidean distance and Ward's minimum variance method[20]. This analysis identified three distinct 'moral clusters' of countries. These are shown in Fig. 3a, and are broadly consistent with both geographical and cultural proximity according to the Inglehart–Welzel Cultural Map 2010–2014[21].

The first cluster (which we label the Western cluster) contains North America as well as many European countries of Protestant, Catholic, and Orthodox Christian cultural groups. The internal structure within this cluster also exhibits notable face validity, with a sub-cluster containing Scandinavian countries, and a sub-cluster containing Commonwealth countries.

The second cluster (which we call the Eastern cluster) contains many far eastern countries such as Japan and Taiwan that belong to the Confucianist cultural group, and Islamic countries such as Indonesia, Pakistan and Saudi Arabia.

The third cluster (a broadly Southern cluster) consists of the Latin American countries of Central and South America, in addition to some countries that are characterized in part by French influence (for example, metropolitan France, French overseas territories, and territories that were at some point under French leadership). Latin American countries are cleanly separated in their own sub-cluster within the Southern cluster.

To rule out the potential effect of language, we found that the same clusters also emerged when the clustering analysis was restricted to participants who relied only on the pictorial representations of the dilemmas, without accessing their written descriptions (Extended Data Fig. 4).

This clustering pattern (which is fairly robust; Extended Data Fig. 5) suggests that geographical and cultural proximity may allow groups of territories to converge on shared preferences for machine ethics. Between-cluster differences, though, may pose greater problems. As shown in Fig. 3b, clusters largely differ in the weight they give to some preferences. For example, the preference to spare younger characters rather than older characters is much less pronounced for countries in the Eastern cluster, and much higher for countries in the Southern cluster. The same is true for the preference for sparing higher status characters. Similarly, countries in the Southern cluster exhibit a much weaker preference for sparing humans over pets, compared to the other two clusters. Only the (weak) preference for sparing pedestrians over passengers and the (moderate) preference for sparing the lawful over the unlawful appear to be shared to the same extent in all clusters.

Finally, we observe some striking peculiarities, such as the strong preference for sparing women and the strong preference for sparing fit characters in the Southern cluster. All the patterns of similarities and differences unveiled in Fig. 3b, though, suggest that manufacturers and policymakers should be, if not responsive, at least cognizant of moral preferences in the countries in which they design artificial intelligence systems and policies. Whereas the ethical preferences of the public should not necessarily be the primary arbiter of ethical policy, the people's willingness to buy autonomous vehicles and tolerate them on the roads will depend on the palatability of the ethical rules that are adopted.

Country-level predictors

Preferences revealed by the Moral Machine are highly correlated to cultural and economic variations between countries. These correlations provide support for the external validity of the platform, despite the self-selected nature of our sample. Although we do not attempt to pin down the ultimate reason or mechanism behind these correlations, we document them here as they point to possible deeper explanations of the cross-country differences and the clusters identified above.

As an illustration, consider the distance between the United States and other countries in terms of the moral preferences extracted from the Moral Machine ('MM distance'). Figure 4c shows a substantial

© 2018 Springer Nature Limited. All rights reserved.

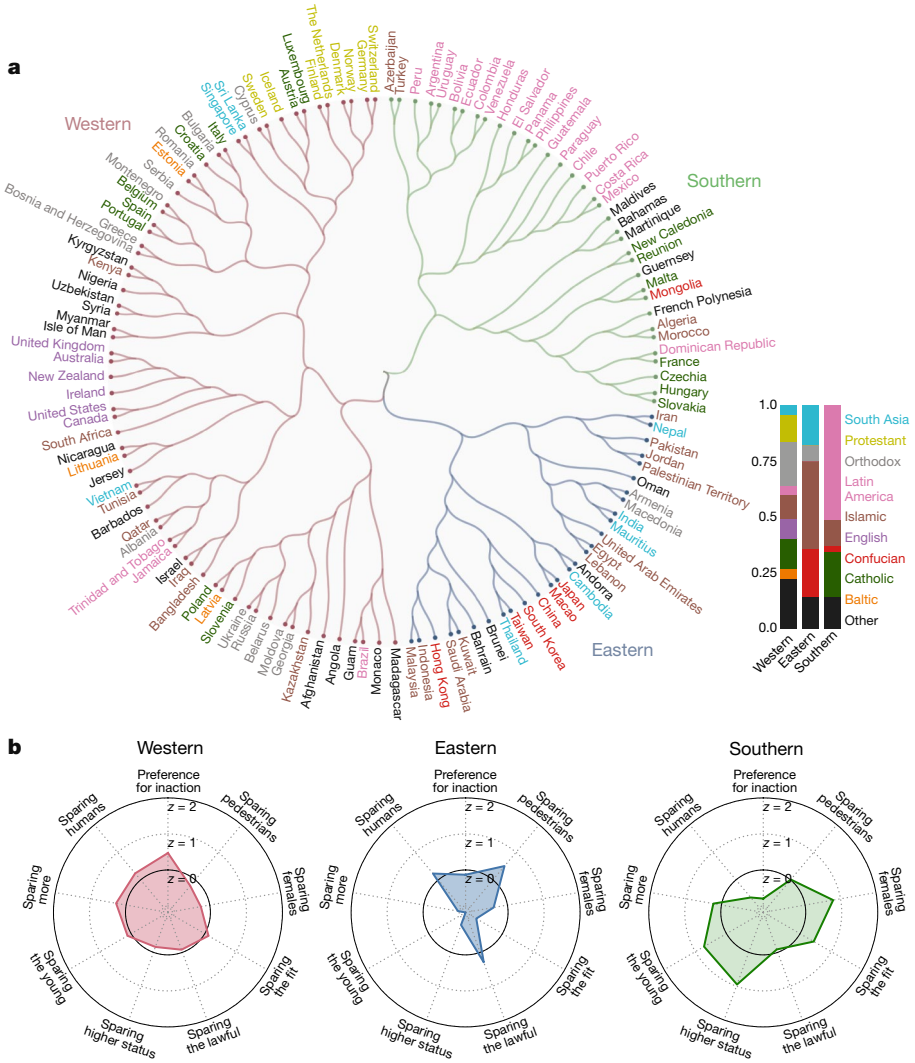

Fig. 3 | Country-level clusters. a, Hierarchical cluster of countries based on average marginal causal effect. One hundred and thirty countries with at least 100 respondents were selected (range, 101–448,125). The three colours of the dendrogram branches represent three large clusters—Western, Eastern, and Southern. Country names are coloured according to the Inglehart–Welzel Cultural Map 2010–2014[21]. Distributions across the three clusters reveal stark differences. For instance, cluster 2 (Eastern) consists mostly of countries of Islamic and Confucian cultures. By contrast, cluster 1 (Western) has large percentages of Protestant, Catholic, and Orthodox countries in Europe. **b**, Mean AMCE *z*-scores of the three major clusters. Radar plot of the mean AMCE *z*-scores of three clusters reveals a striking pattern of differences between the clusters along the nine attributes. For example, countries belonging to the Southern cluster show a strong preference for sparing females compared to countries in other clusters.

correlation ($\rho = 0.49$) between this MM distance and the cultural distance from the United States based on the World Values Survey[22]. In other words, the more culturally similar a country is to the United States, the more similarly its people play the Moral Machine.

Next, we highlight four important cultural and economic predictors of Moral Machine preferences. First, we observe systematic differences between individualistic cultures and collectivistic cultures[23]. Participants from individualistic cultures, which emphasize the distinctive value of each individual[23], show a stronger preference for sparing the greater number of characters (Fig. 4a). Furthermore, participants from collectivistic cultures, which emphasize the respect that is due to older members of the community[23], show a weaker preference for sparing younger characters (Fig. 4a, inset). Because the preference for sparing the many and the preference for sparing the young are arguably the most important for policymakers to consider, this split between individualistic and collectivistic cultures may prove an important obstacle for universal machine ethics (see Supplementary Information).

Another important (yet under-discussed) question for policymakers to consider is the importance of whether pedestrians are abiding by or violating the law. Should those who are crossing the street illegally benefit from the same protection as pedestrians who cross legally? Or should the primacy of their protection in comparison to other ethical priorities be reduced? We observe that prosperity (as indexed by GDP per capita[24]) and the quality of rules and institutions (as indexed by the Rule of Law[25]) correlate with a greater preference against pedestrians who cross illegally (Fig. 4b). In other words, participants from countries that are poorer and suffer from weaker institutions are more tolerant of pedestrians who cross illegally, presumably because of their experience of lower rule compliance and weaker punishment of rule deviation[26]. This observation limits the generalizability of the recent German ethics guideline, for example, which state that "parties involved in the generation of mobility risks must not sacrifice non-involved parties." (see Supplementary Information).

Finally, our data reveal a set of preferences in which certain characters are preferred for demographic reasons. First, we observe that higher country-level economic inequality (as indexed by the country's Gini coefficient) corresponds to how unequally characters of different social status are treated. Those from countries with less economic equality between the rich and poor also treat the rich and poor less equally in the Moral Machine. This relationship may be explained by regular encounters with inequality seeping into people's moral preferences, or perhaps because broader egalitarian norms affect both how

© 2018 Springer Nature Limited. All rights reserved.

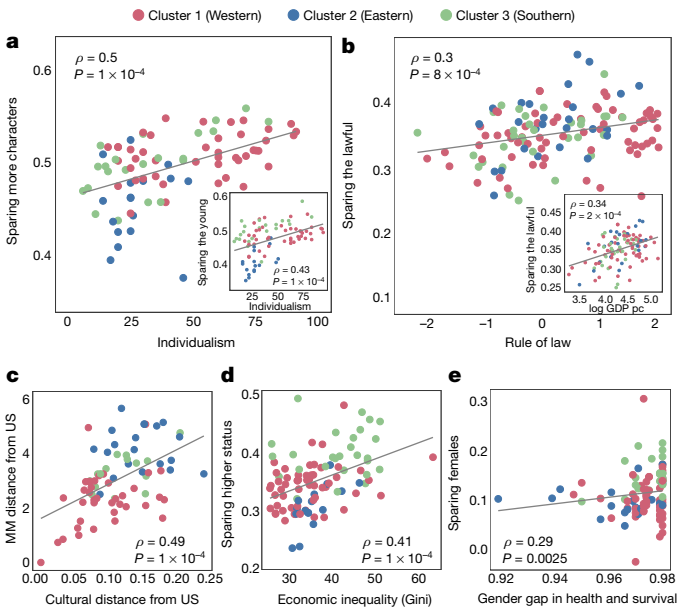

Fig. 4 | Association between Moral Machine preferences and other variables at the country level. Each panel shows Spearman's ρ and P value for the correlation test between the relevant pair of variables. **a**, Association between individualism and the preference for sparing more characters ($n = 87$), or the preference for sparing the young (inset; $n = 87$). **b**, Association between the preference for sparing the lawful and each of rule of law ($n = 122$) and log GDP per capita (pc) (inset; $n = 110$). **c**, Association between cultural distance from the United States and MM distance (distance in terms of the moral preferences extracted from the Moral Machine) from the United States ($n = 72$). **d**, Association between economic inequality (Gini coefficient) and the preference for sparing higher status ($n = 98$). **e**, Association between the gender gap in health and survival and the preference for sparing females ($n = 104$).

much inequality a country is willing to tolerate at the societal level, and how much inequality participants endorse in their Moral Machine judgments. Second, the differential treatment of male and female characters in the Moral Machine corresponded to the country-level gender gap in health and survival (a composite in which higher scores indicated higher ratios of female to male life expectancy and sex ratio at birth—a marker of female infanticide and anti-female sex-selective abortion). In nearly all countries, participants showed a preference for female characters; however, this preference was stronger in nations with better health and survival prospects for women. In other words, in places where there is less devaluation of women's lives in health and at birth, males are seen as more expendable in Moral Machine decision-making (Fig. 4e). While not aiming to pin down the causes of this variation in Extended Data Table 2, we nevertheless provide a regression analysis that demonstrates that the results hold when controlling for several potentially confounding factors.

Discussion

Never in the history of humanity have we allowed a machine to autonomously decide who should live and who should die, in a fraction of a second, without real-time supervision. We are going to cross that bridge any time now, and it will not happen in a distant theatre of military operations; it will happen in that most mundane aspect of our lives, everyday transportation. Before we allow our cars to make ethical decisions, we need to have a global conversation to express our preferences to the companies that will design moral algorithms, and to the policymakers that will regulate them.

The Moral Machine was deployed to initiate such a conversation, and millions of people weighed in from around the world. Respondents could be as parsimonious or thorough as they wished in the ethical framework they decided to follow. They could engage in a complicated weighting of all nine variables used in the Moral Machine, or adopt simple rules such as 'let the car always go onward'. Our data helped us to identify three strong preferences that can serve as building blocks for discussions of universal machine ethics, even if they are not ultimately endorsed by policymakers: the preference for sparing human lives, the preference for sparing more lives, and the preference for sparing young lives. Some preferences based on gender or social status vary considerably across countries, and appear to reflect underlying societal-level preferences for egalitarianism[27].

The Moral Machine project was atypical in many respects. It was atypical in its objectives and ambitions: no research has previously attempted to measure moral preferences using a nine-dimensional experimental design in more than 200 countries. To achieve this unusual objective, we deployed a viral online platform, hoping that we would reach out to vast numbers of participants. This allowed us to collect data from millions of people over the entire world, a feat that would be nearly impossibly hard and costly to achieve through standard academic survey methods. For example, recruiting nationally representative samples of participants in hundreds of countries would already be extremely difficult, but testing a nine-factorial design in each of these samples would verge on impossible. Our approach allowed us to bypass these difficulties, but its downside is that our sample is self-selected, and not guaranteed to exactly match the socio-demographics of each country (Extended Data Fig. 6). The fact that the cross-societal variation we observed aligns with previously established cultural clusters, as well as the fact that macro-economic variables are predictive of Moral Machine responses, are good signals about the reliability of our data, as is our post-stratification analysis (Extended Data Fig. 7 and Supplementary Information). But the fact that our samples are not guaranteed to be representative means that policymakers should not embrace our data as the final word on societal preferences—even if our sample is arguably close to the internet-connected, tech-savvy population that is interested in driverless car technology, and more likely to participate in early adoption.

Even with a sample size as large as ours, we could not do justice to all of the complexity of autonomous vehicle dilemmas. For example, we did not introduce uncertainty about the fates of the characters, and we did not introduce any uncertainty about the classification of these characters. In our scenarios, characters were recognized as adults, children, and so on with 100% certainty, and life-and-death outcomes were predicted with 100% certainty. These assumptions are technologically unrealistic, but they were necessary to keep the project tractable. Similarly, we did not manipulate the hypothetical relationship between respondents and characters (for example, relatives or spouses). Our previous work did not find a strong effect of this variable on moral preferences[12].

Indeed, we can embrace the challenges of machine ethics as a unique opportunity to decide, as a community, what we believe to be right or wrong; and to make sure that machines, unlike humans, unerringly follow these moral preferences. We might not reach universal agreement: even the strongest preferences expressed through the Moral Machine showed substantial cultural variations, and our project builds on a long tradition of investigating cultural variations in ethical judgments[28]. But the fact that broad regions of the world displayed relative agreement suggests that our journey to consensual machine ethics is not doomed from the start. Attempts at establishing broad ethical codes for intelligent machines, such as the Asilomar AI Principles[29], often recommend that machine ethics should be aligned with human values. These codes seldom recognize, though, that humans experience inner conflict, interpersonal disagreements, and cultural dissimilarities in the moral domain[30–32]. We have shown that these conflicts, disagreements, and dissimilarities, while substantial, may not be fatal.

Online content

Any methods, additional references, Nature Research reporting summaries, source data, statements of data availability and associated accession codes are available at https://doi.org/10.1038/s41586-018-0637-6.

© 2018 Springer Nature Limited. All rights reserved.

Received: 2 March 2018; Accepted: 25 September 2018;
Published online 24 October 2018.

1. Greene, J. *Moral Tribes: Emotion, Reason and the Gap Between Us and Them* (Atlantic Books, London, 2013).
2. Tomasello, M. *A Natural History of Human Thinking* (Harvard Univ. Press, Cambridge, 2014).
3. Cushman, F. & Young, L. The psychology of dilemmas and the philosophy of morality. *Ethical Theory Moral Pract.* **12**, 9–24 (2009).
4. Asimov, I. *I, Robot* (Doubleday, New York, 1950).
5. Bryson, J. & Winfield, A. Standardizing ethical design for artificial intelligence and autonomous systems. *Computer* **50**, 116–119 (2017).
6. Wiener, N. Some moral and technical consequences of automation. *Science* **131**, 1355–1358 (1960).
7. Wallach, W. & Allen, C. *Moral Machines: Teaching Robots Right from Wrong* (Oxford Univ. Press, Oxford, 2008).
8. Dignum, V. Responsible autonomy. In *Proc. 26th International Joint Conference on Artificial Intelligence* 4698–4704 (IJCAI, 2017).
9. Dadich, S. Barack Obama, neural nets, self-driving cars, and the future of the world. *Wired* https://www.wired.com/2016/10/president-obama-mit-joi-ito-interview/ (2016).
10. Shariff, A., Bonnefon, J.-F. & Rahwan, I. Psychological roadblocks to the adoption of self-driving vehicles. *Nat. Hum. Behav.* **1**, 694–696 (2017).
11. Conitzer, V., Brill, M. & Freeman, R. Crowdsourcing societal tradeoffs. In *Proc. 2015 International Conference on Autonomous Agents and Multiagent Systems* 1213–1217 (IFAAMAS, 2015).
12. Bonnefon, J.-F., Shariff, A. & Rahwan, I. The social dilemma of autonomous vehicles. *Science* **352**, 1573–1576 (2016).
13. Hauser, M., Cushman, F., Young, L., Jin, K.-X. R. & Mikhail, J. A dissociation between moral judgments and justifications. *Mind Lang.* **22**, 1–21 (2007).
14. Carlsson, F., Daruvala, D. & Jaldell, H. Preferences for lives, injuries, and age: a stated preference survey. *Accid. Anal. Prev.* **42**, 1814–1821 (2010).
15. Johansson-Stenman, O. & Martinsson, P. Are some lives more valuable? An ethical preferences approach. *J. Health Econ.* **27**, 739–752 (2008).
16. Johansson-Stenman, O., Mahmud, M. & Martinsson, P. Saving lives versus life-years in rural Bangladesh: an ethical preferences approach. *Health Econ.* **20**, 723–736 (2011).
17. Graham, J., Meindl, P., Beall, E., Johnson, K. M. & Zhang, L. Cultural differences in moral judgment and behavior, across and within societies. *Curr. Opin. Psychol.* **8**, 125–130 (2016).
18. Hainmueller, J., Hopkins, D. J. & Yamamoto, T. Causal inference in conjoint analysis: understanding multidimensional choices via stated preference experiments. *Polit. Anal.* **22**, 1–30 (2014).
19. Luetge, C. The German Ethics Code for automated and connected driving. *Philos. Technol.* **30**, 547–558 (2017).
20. Müllner, D. Modern hierarchical, agglomerative clustering algorithms. Preprint at https://arxiv.org/abs/1109.2378 (2011).
21. Inglehart, R. & Welzel, C. *Modernization, Cultural Change, and Democracy: The Human Development Sequence* (Cambridge Univ. Press, Cambridge, 2005).
22. Muthukrishna, M. Beyond WEIRD psychology: measuring and mapping scales of cultural and psychological distance. Preprint at https://ssrn.com/abstract=3259613 (2018).
23. Hofstede, G. *Culture's Consequences: Comparing Values, Behaviors, Institutions and Organizations Across Nations* (Sage, Thousand Oaks, 2003).
24. International Monetary Fund. *World Economic Outlook Database* https://www.imf.org/external/pubs/ft/weo/2017/01/weodata/index.aspx (2017).
25. Kaufmann, D., Kraay, A. & Mastruzzi, M. The worldwide governance indicators: methodology and analytical issues. *Hague J. Rule Law* **3**, 220–246 (2011).
26. Gächter, S. & Schulz, J. F. Intrinsic honesty and the prevalence of rule violations across societies. *Nature* **531**, 496–499 (2016).
27. O'Neil, C. *Weapons of Math Destruction: How Big Data Increases Inequality and Threatens Democracy* (Penguin, London, 2016).
28. Henrich, J. *et al*. In search of Homo Economicus: behavioral experiments in 15 small-scale societies. *Am. Econ. Rev.* **91**, 73–78 (2001).
29. Future of Life Institute. *Asilomar AI Principles* https://futureoflife.org/ai-principles/ (2017).
30. Haidt, J. *The Righteous Mind: Why Good People Are Divided by Politics and Religion* (Knopf Doubleday, New York, 2012).
31. Gastil, J., Braman, D., Kahan, D. & Slovic, P. The cultural orientation of mass political opinion. *PS Polit. Sci. Polit.* **44**, 711–714 (2011).
32. Nishi, A., Christakis, N. A. & Rand, D. G. Cooperation, decision time, and culture: online experiments with American and Indian participants. *PLoS ONE* **12**, e0171252 (2017).

Acknowledgements I.R., E.A., S.D., and R.K. acknowledge support from the Ethics and Governance of Artificial Intelligence Fund. J.-F.B. acknowledges support from the ANR-Labex Institute for Advanced Study in Toulouse.

Author contributions I.R., A.S. and J.-F.B. planned the research. I.R., A.S., J.-F.B., E.A. and S.D. designed the experiment. E.A. and S.D. built the platform and collected the data. E.A., S.D., R.K., J.S. and A.S. analysed the data. E.A., S.D., R.K., J.S., J.H., A.S., J.-F.B., and I.R interpreted the results and wrote the paper.

Competing interests The authors declare no competing interests.

Additional information
Extended data is available for this paper at https://doi.org/10.1038/s41586-018-0637-6.
Supplementary information is available for this paper at https://doi.org/10.1038/s41586-018-0637-6.
Reprints and permissions information is available at http://www.nature.com/reprints.
Correspondence and requests for materials should be addressed to A.S. or J.-F.B. and I.R.
Publisher's note: Springer Nature remains neutral with regard to jurisdictional claims in published maps and institutional affiliations.

© 2018 Springer Nature Limited. All rights reserved.

METHODS

This study was approved by the Institute Review Board (IRB) at Massachusetts Institute of Technology (MIT). The authors complied with all relevant ethical considerations. No statistical methods were used to predetermine sample size. The experiments were randomized and the investigators were blinded to allocation during experiments and outcome assessment.

The Moral Machine website was designed to collect data on the moral acceptability of decisions made by autonomous vehicles in situations of unavoidable accidents, in which they must decide who is spared and who is sacrificed. The Moral Machine was deployed in June 2016. In October 2016, a feature was added that offered users the option to fill a survey about their demographics, political views, and religious beliefs. Between November 2016 and March 2017, the website was progressively translated into nine languages in addition to English (Arabic, Chinese, French, German, Japanese, Korean, Portuguese, Russian, and Spanish).

While the Moral Machine offers four different modes (see Supplementary Information), the focus of this article is on the central data-gathering feature of the website, called the Judge mode. In this mode, users are presented with a series of dilemmas in which the autonomous vehicle must decide between two different outcomes. In each dilemma, one outcome amounts to sparing a group of 1 to 5 characters (chosen from a sample of 20 characters, Fig. 2b) and killing another group of 1 to 5 characters. The other outcome reverses the fates of the two groups. The only task of the user is to choose between the two outcomes, as a response to the question "What should the self-driving car do?" Users have the option to click on a button labelled 'see description' to display a complete text description of the characters in the two groups, together with their fate in each outcome.

While users can go through as many dilemmas as they wish, dilemmas are generated in sessions of 13. Within each session, one dilemma is entirely random. The other 12 dilemmas are sampled from a space of approximately 26 million possibilities (see below). Accordingly, it is extremely improbable for a given user to see the same dilemma twice, regardless of how many dilemmas they choose to go through, or how many times they visit the Moral Machine.

Leaving aside the one entirely random dilemma, there are two dilemmas within each session that focus on each of six dimensions of moral preferences: character gender, character age, character physical fitness, character social status, character species, and character number. Furthermore, each dilemma simultaneously randomizes three additional attributes: which group of characters will be spared if the car does nothing; whether the two groups are pedestrians, or whether one group is in the car; and whether the pedestrian characters are crossing legally or illegally. This exploration strategy is supported by a dilemma generation algorithm (see Supplementary Information, which also provides extensive descriptions of statistical analyses, robustness checks, and tests of internal and external validity).

After completing a session of 13 dilemmas, users are presented with a summary of their decisions: which character they spared the most; which character they sacrificed the most; and the relative importance of the nine target moral dimensions in their decisions, compared to their importance to the average of all other users so far. Users have the option to share this summary with their social network. Either before or after they see this summary (randomized order), users are asked whether they want to "help us better understand their decisions." Users who click 'yes' are directed to a survey of their demographic, political, and religious characteristics. They also have the option to edit the summary of their decisions, to tell us about the self-perceived importance of the nine dimensions in their decisions. These self-perceptions were not analysed in this article.

The country from which users access the website is geo-localized through the IP address of their computer or mobile device. This information is used to compute a vector of moral preferences for each country. In turn, these moral vectors are used both for cultural clustering, and for country-level correlations between moral preferences and socio-economic indicators. The source and period of reference for each socio-economic indicator are detailed in the Supplementary Information.

Data availability

Source data and code that can be used to reproduce Figs. 2–4, Extended Data Figs. 1–7, Extended Data Tables 1, 2, Supplementary Figs. 3–21, and Supplementary Table 2 are all available at the following link: https://goo.gl/JXRrBP. The provided data, both at the individual level (anonymized IDs) and the country level, can be used beyond replication to answer follow-up research questions.

© 2018 Springer Nature Limited. All rights reserved.

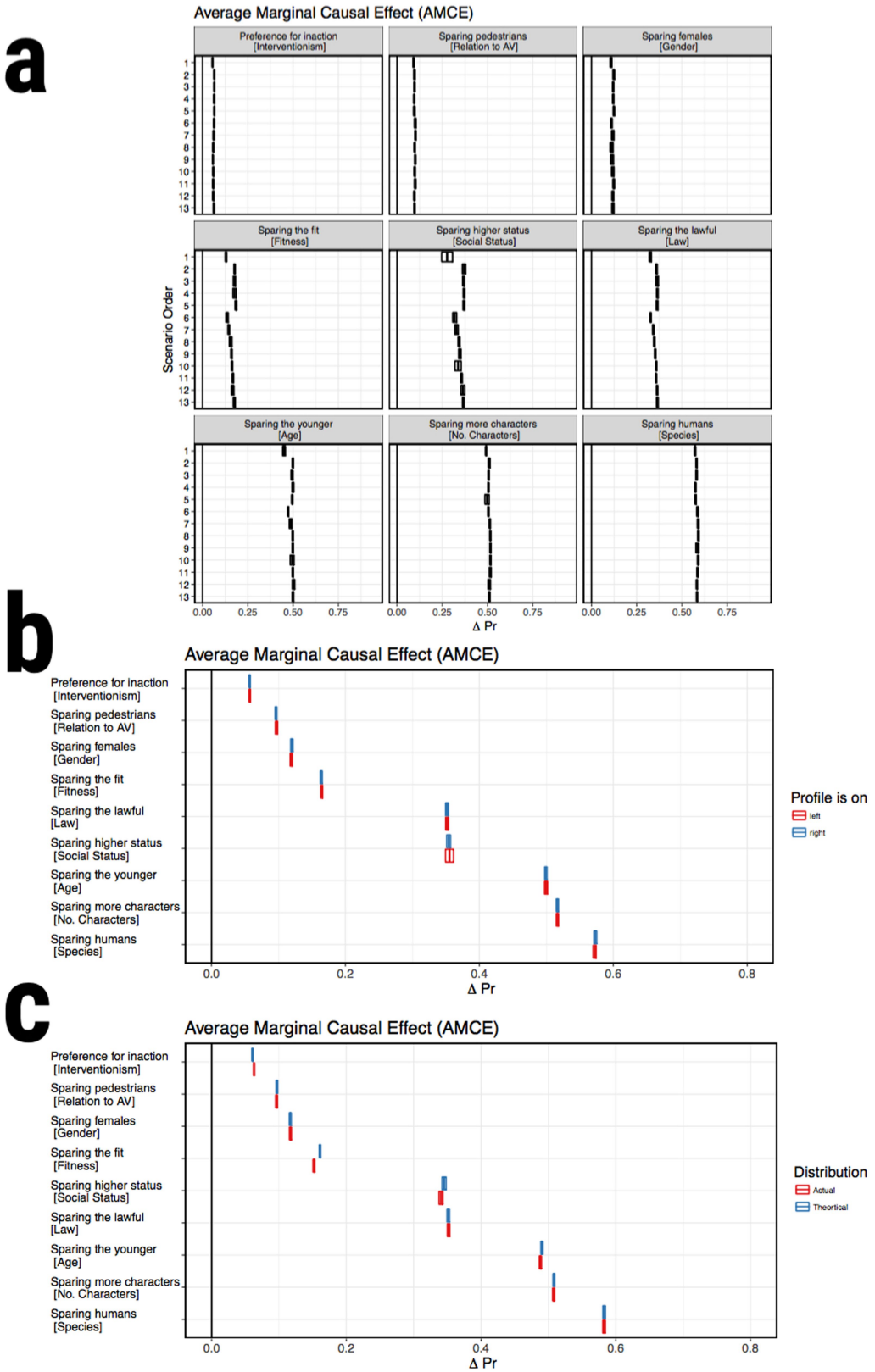

Extended Data Fig. 1 | Robustness checks: internal validation of three simplifying assumptions. Calculated values correspond to values in Fig. 2a (that is, AMCE calculated using conjoint analysis). For example, 'Sparing Pedestrians [Relation to AV]' refers to the difference between the probability of sparing pedestrians, and the probability of sparing passengers (attribute name: Relation to AV), aggregated over all other attributes. Error bars represent 95% confidence intervals of the means. AV, autonomous vehicle. **a**, Validation of assumption 1 (stability and no-carryover effect): potential outcomes remain stable regardless of scenario order. **b**, Validation of assumption 2 (no profile-order effects): potential outcomes remain stable regardless of left–right positioning of choice options on the screen. **c**, Validation of assumption 3 (randomization of the profiles): potential outcomes are statistically independent of the profiles. This assumption should be satisfied by design. However, a mismatch between the design and the collected data can happen during data collection. This panel shows that using theoretical proportions (by design) and actual proportions (in collected data) of subgroups results in similar effect estimates. See Supplementary Information for more details.

© 2018 Springer Nature Limited. All rights reserved.

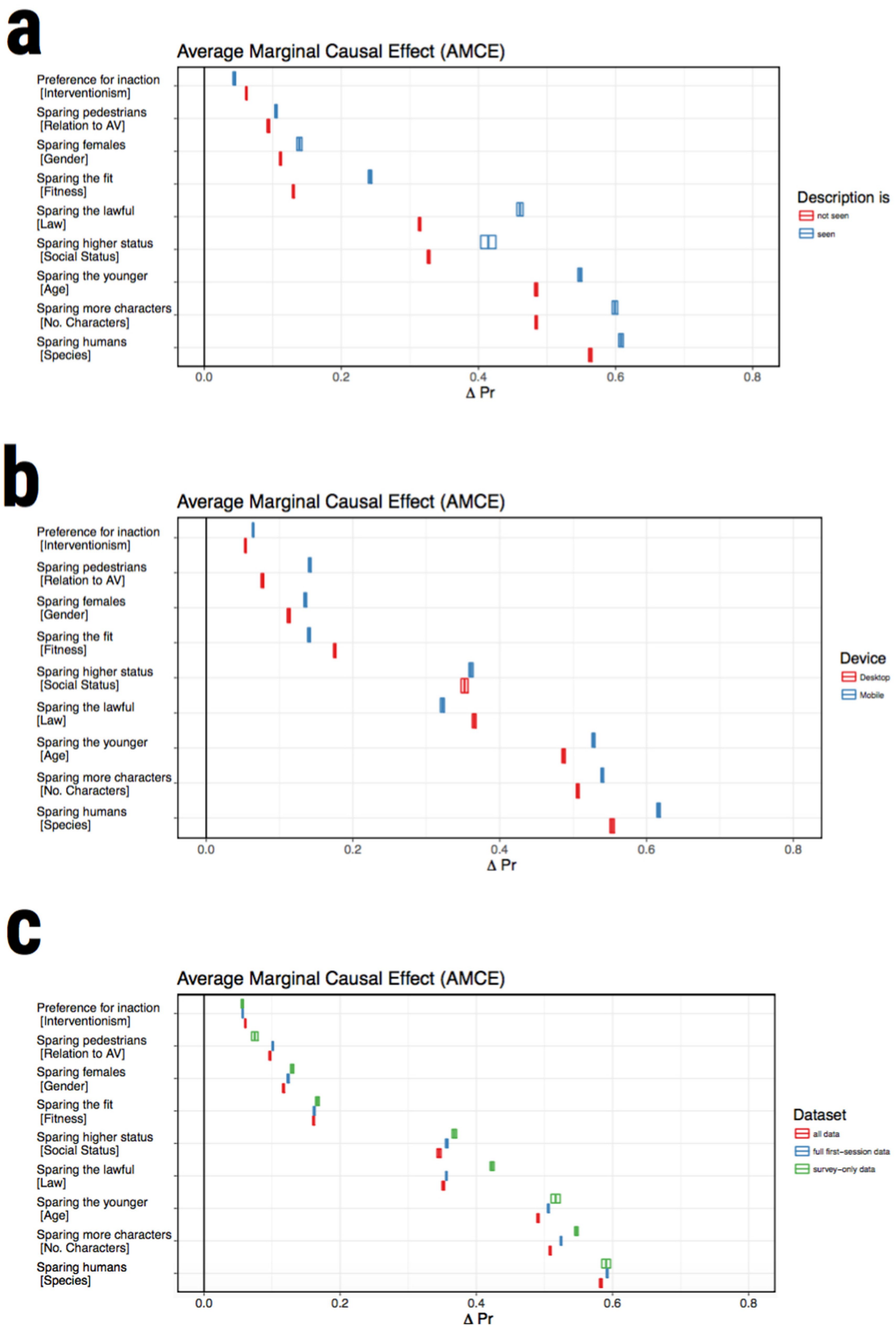

Extended Data Fig. 2 | See next page for caption.

© 2018 Springer Nature Limited. All rights reserved.

Extended Data Fig. 2 | Robustness checks: external validation of three factors. Calculated values correspond to values in Fig. 2a (AMCE calculated using conjoint analysis). For example, 'Sparing Pedestrians [Relation to AV]' refers to the difference between the probability of sparing pedestrians, and the probability of sparing passengers (attribute name: Relation to AV), aggregated over all other attributes. Error bars represent 95% confidence intervals of the means. **a**, Validation of textual description (seen versus not seen). By default, respondents see only the visual representation of a scenario. Interpretation of what type of characters they represent (for example, female doctor) may not be obvious. Optionally, respondents can read a textual description of the scenario by clicking on 'see description'. This panel shows that direction and (except in one case) order of effect estimates remain stable. The magnitude of the effects increases for respondents who read the textual descriptions, which means that the effects reported in Fig. 2a were not overestimated because of visual ambiguity. **b**, Validation of device used (desktop versus mobile). Direction and order of effect estimates remain stable regardless of whether respondents used desktop or mobile devices when completing the task. **c**, Validation of data set (all data versus full first-session data versus survey-only data). Direction and order of effect estimates remain stable regardless of whether the data used in analysis are all data, data restricted to only first completed (13-scenario) session by any user, or data restricted to completed sessions after which the demographic survey was taken. First completed session by any user is an interesting subset of the data because respondents had not seen their summary of results yet, and respondents ended up completing the session. Survey-only data are also interesting given that the conclusions about individual variations in the main paper and from Extended Data Fig. 3 and Extended Data Table 1 are drawn from this subset. See Supplementary Information for more details.

© 2018 Springer Nature Limited. All rights reserved.

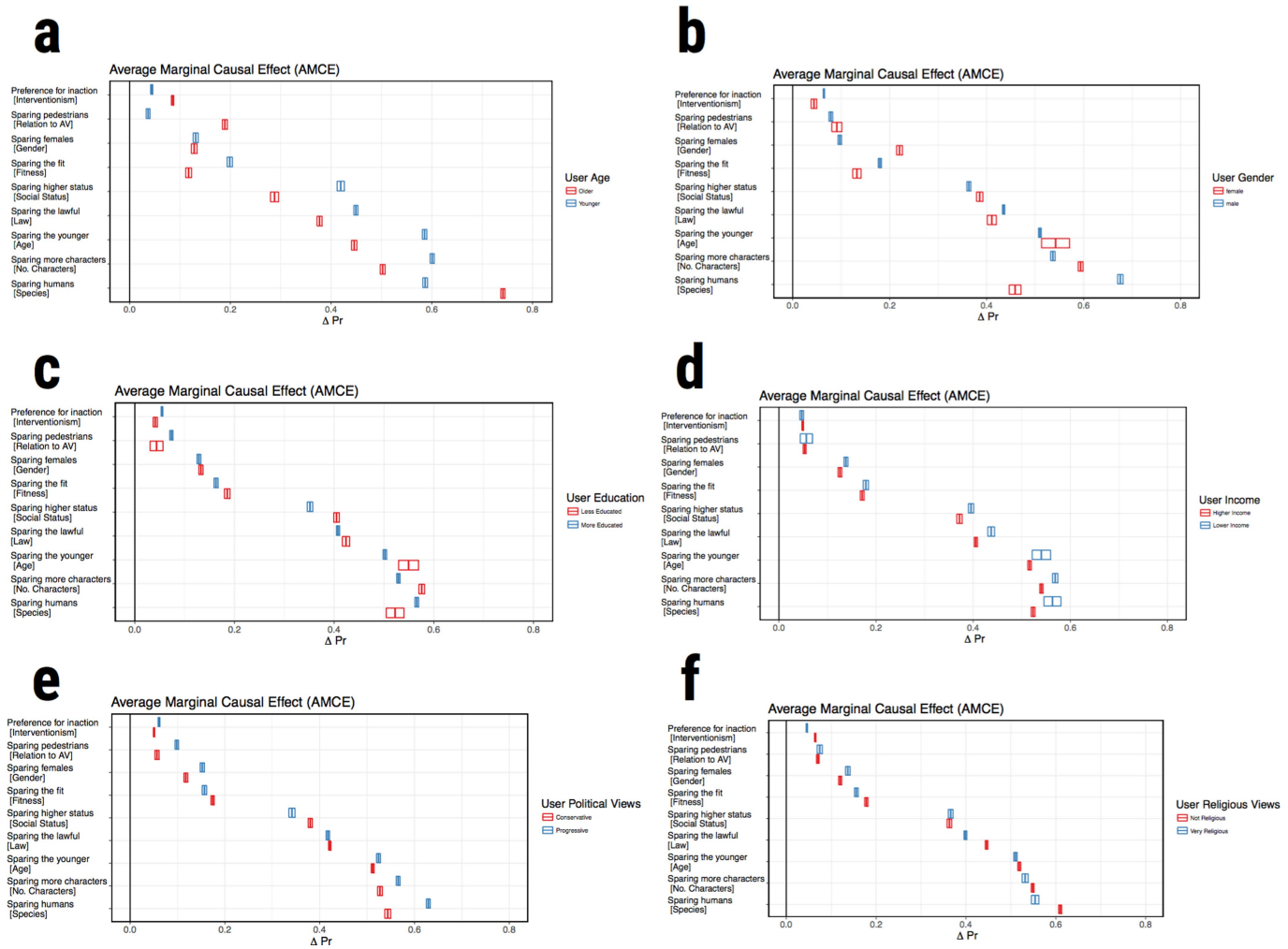

Extended Data Fig. 3 | Average marginal causal effect (AMCE) of attributes for different subpopulations. Subpopulations are characterized by respondents' age (**a**, older versus younger), gender (**b**, male versus female), education (**c**, less versus more educated), income (**d**, higher versus lower income), political views (**e**, conservative versus progressive), and religious views (**f**, not religious versus very religious). Error bars represent 95% confidence intervals of the means. Note that AMCE has a positive value for all considered subpopulations; for example, both male and female respondents indicated a preference for sparing females, but the latter group showed a stronger preference. See Supplementary Information for a detailed description of the cutoffs and the groupings of ordinal categories that were used to define each subpopulation.

© 2018 Springer Nature Limited. All rights reserved.

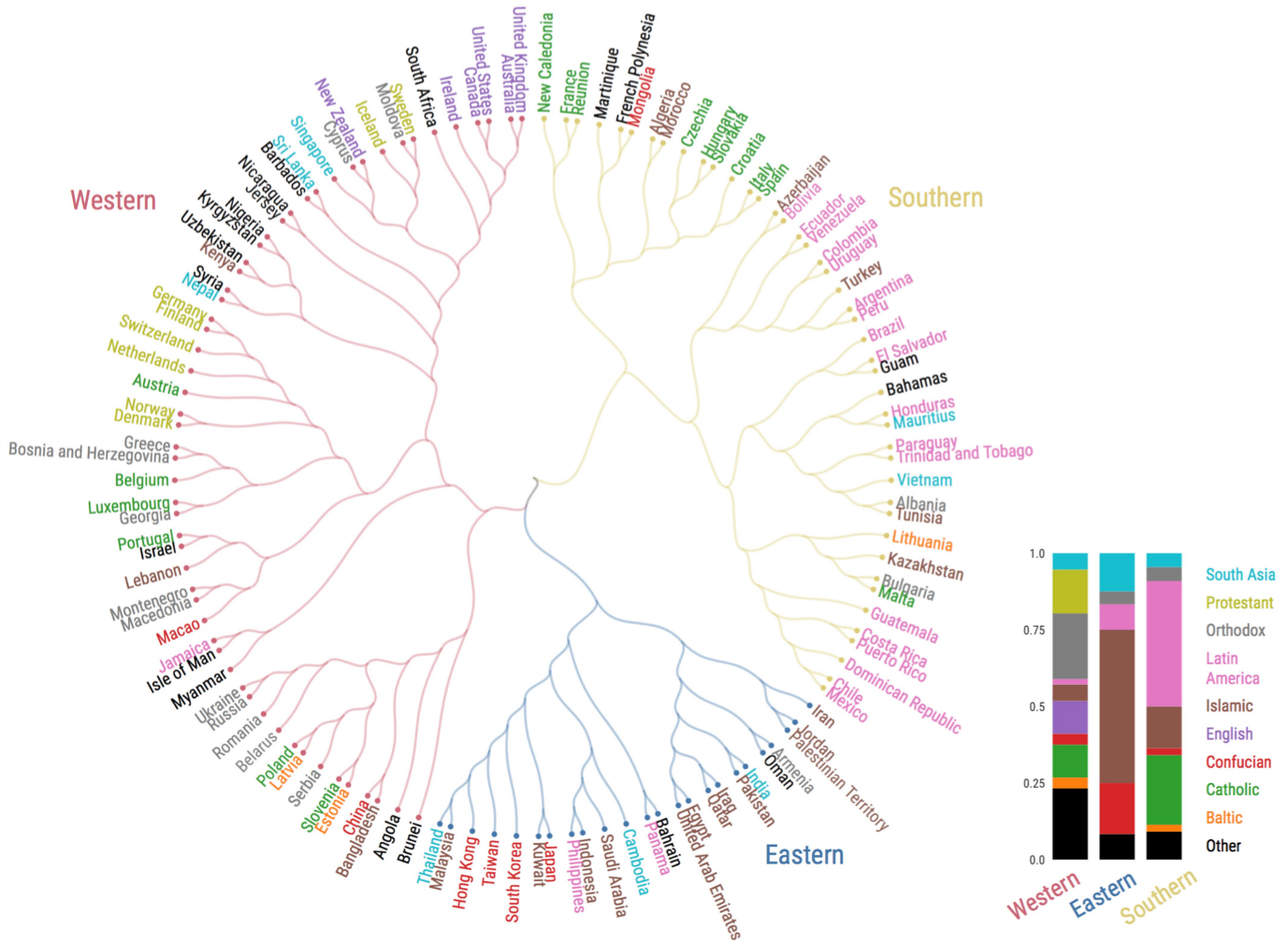

Extended Data Fig. 4 | Hierarchical cluster of countries based on country-level effect sizes calculated after filtering out responses for which the linguistic description was seen, thus neutralizing any potential effect of language. The three colours of the dendrogram branches represent three large clusters: Western, Eastern, and Southern. The names of the countries are coloured according to the Inglehart–Welzel Cultural Map 2010–2014[21]. See Supplementary Information for more details. The dendrogram is essentially similar to that shown in Fig. 3a.

© 2018 Springer Nature Limited. All rights reserved.

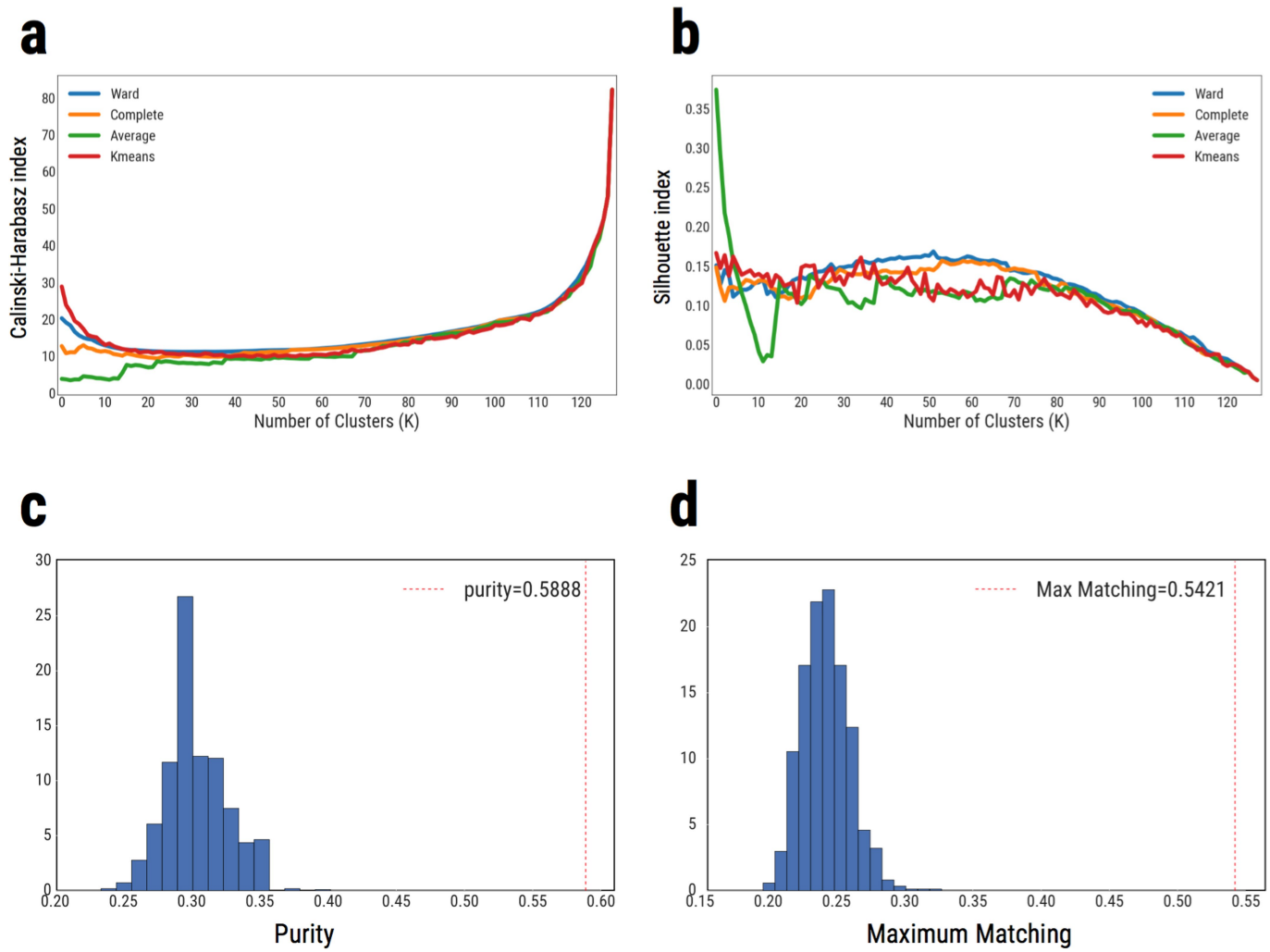

Extended Data Fig. 5 | Validation of hierarchical cluster of countries. **a**, **b**, We use two internal metrics of validation of three linkage criteria of calculating hierarchical clustering (Ward, Complete and Average) in addition to the *K*-means algorithm: **a**, Calinski–Harabasz index; **b**, silhouette index. The *x* axis indicates the number of clusters. For both internal metrics, a higher index value indicates a 'better' fit of partition to the data. **c**, **d**, We use two external metrics of validation of the used hierarchical clustering algorithm (Ward) versus those of random clustering assignment: **c**, purity; **d**, maximum matching. The histogram shows the distributions of purity and maximum matching values derived from randomly assigning countries to nine clusters. The red dotted lines indicate purity and maximum matching values computed from the clustering output of the hierarchical clustering algorithm using ACME values. See Supplementary Information for more details.

© 2018 Springer Nature Limited. All rights reserved.

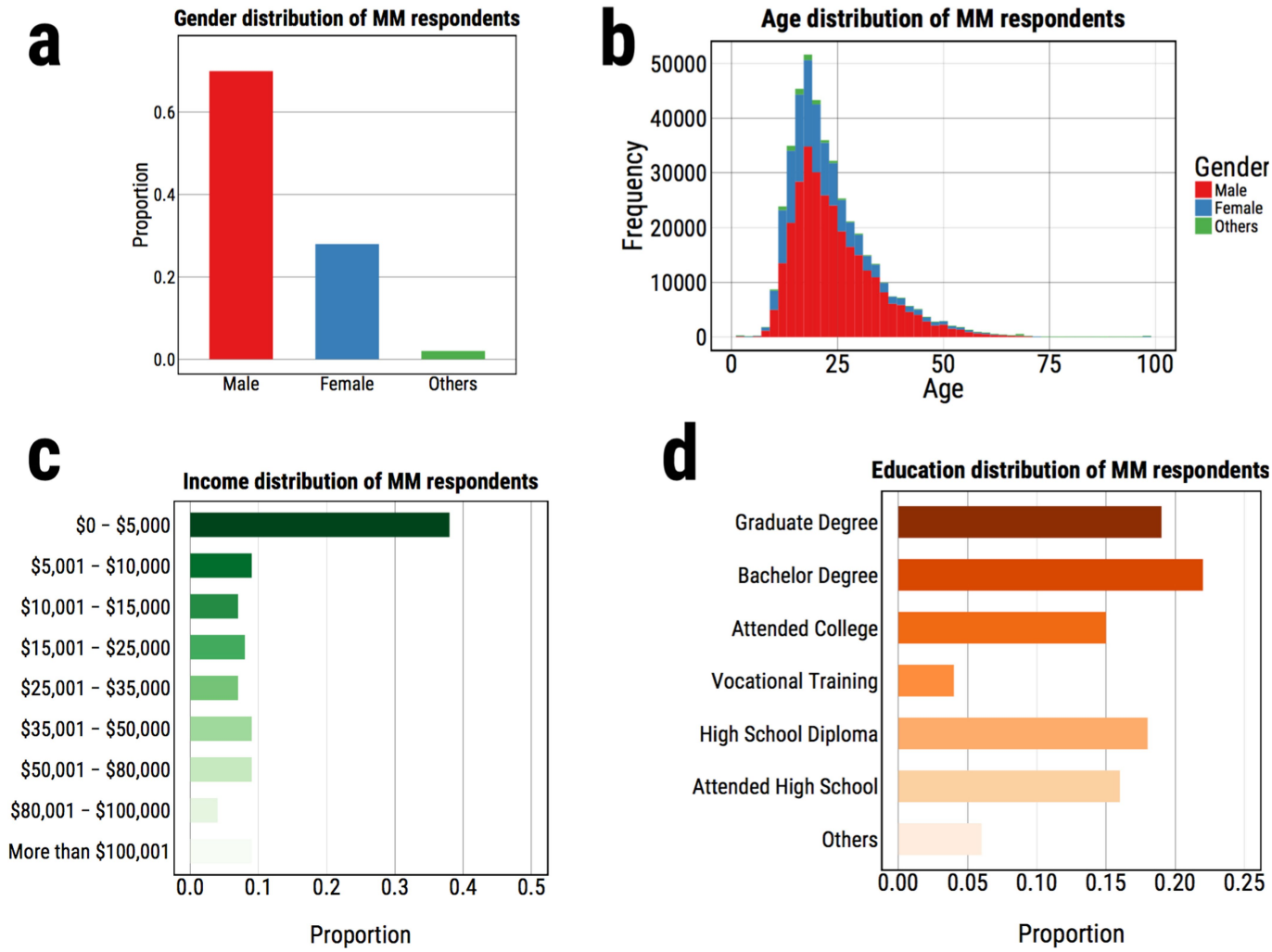

Extended Data Fig. 6 | Demographic distributions of sample of population that completed the survey on Moral Machine (MM) website. Distributions are based on gender (**a**), age (**b**), income (**c**), and education attributes (**d**). Most users on Moral Machine are male, went through college, and are in their 20s or 30s. While this indicates that the users of Moral Machine are not a representative sample of the whole population, it is important to note that this sample at least covers broad demographics. See Supplementary Information for more details.

© 2018 Springer Nature Limited. All rights reserved.

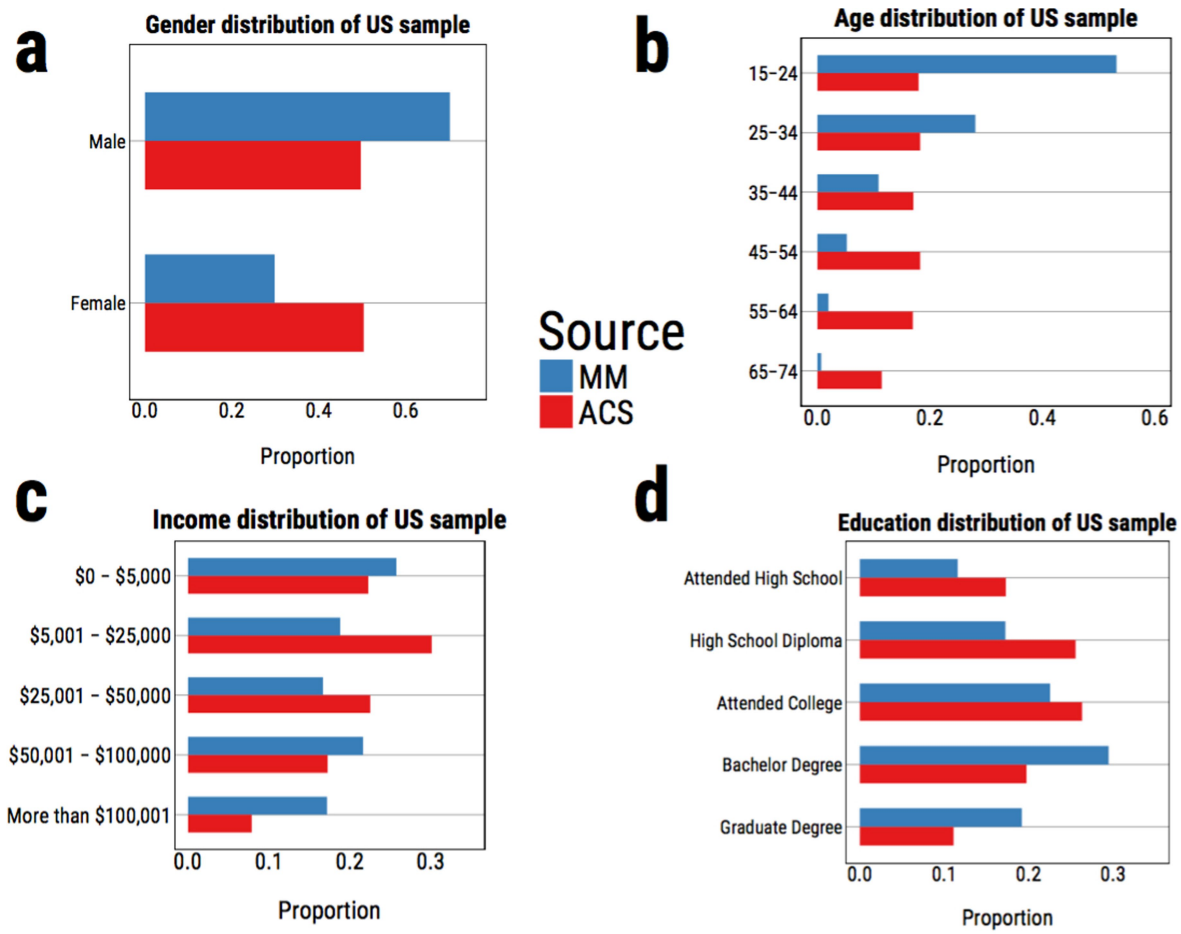

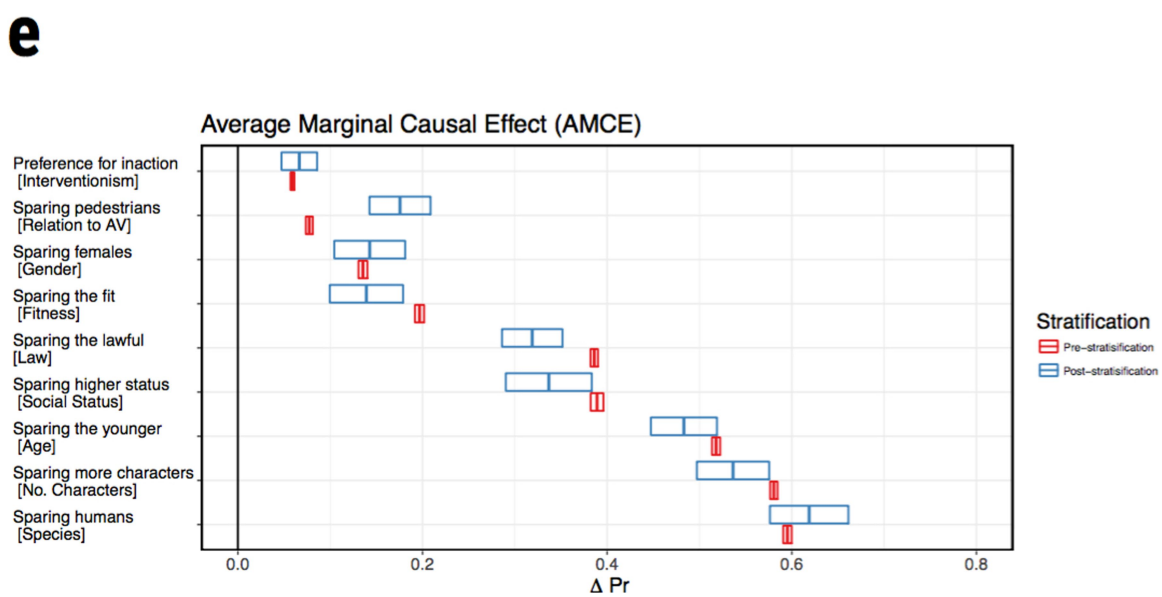

Extended Data Fig. 7 | Demographic distributions of US sample of population that completed the survey on Moral Machine website versus US sample of population in American Community Survey (ACS) data set. a–d, Only gender (**a**), age (**b**), income (**c**), and education (**d**) attributes are available for both data sets. The MM US sample has an over-representation of males and younger individuals compared to the ACS US sample. **e**, A comparison of effect sizes as calculated for US respondents who took the survey on MM with the use of post-stratification to match the corresponding proportions for the ACS sample. Except for 'Relation to AV' (the second smallest effect), the direction and order of all effects are unaffected. See Supplementary Information for more details.

© 2018 Springer Nature Limited. All rights reserved.

Extended Data Table 1 | Regression table showing the individual variations for each of the nine attributes

	Demographics								
	Preference for Inaction	Sparing Pedestrians	Sparing the Lawful	Sparing Females	Sparing the Fit	Sparing Higher Status	Sparing the Young	Sparing More Characters	Sparing Humans
	(1)	(2)	(3)	(4)	(5)	(6)	(7)	(8)	(9)
Male	-0.015***	-0.022***	0.020***	-0.061***	0.024***	-0.009***	-0.018***	-0.024***	0.085***
	(0.001)	(0.001)	(0.001)	(0.002)	(0.002)	(0.002)	(0.001)	(0.001)	(0.002)
Age	0.001*	0.037***	-0.014***	0.008***	-0.019***	-0.022***	-0.020***	-0.011***	0.019***
	(0.0004)	(0.001)	(0.001)	(0.001)	(0.001)	(0.001)	(0.001)	(0.001)	(0.001)
Income	-0.003***	-0.008***	-0.010***	-0.008***	0.004***	-0.002	-0.004***	-0.003***	-0.007***
	(0.0004)	(0.001)	(0.001)	(0.001)	(0.001)	(0.001)	(0.001)	(0.001)	(0.001)
Is college educated	-0.010***	0.001	0.016***	-0.001	-0.008***	-0.012***	-0.016***	-0.009***	0.037***
	(0.001)	(0.001)	(0.001)	(0.002)	(0.002)	(0.002)	(0.001)	(0.001)	(0.001)
Political views (conservative to progressive)	0.001	0.011***	-0.002*	0.014***	-0.007***	-0.012***	0.004***	0.009***	0.011***
	(0.0003)	(0.001)	(0.001)	(0.001)	(0.001)	(0.001)	(0.001)	(0.001)	(0.001)
Religiousity	0.038***	0.064***	-0.083***	0.054***	-0.059***	-0.003	-0.016*	0.010	0.091***
	(0.003)	(0.005)	(0.006)	(0.007)	(0.007)	(0.009)	(0.006)	(0.006)	(0.005)
Constant	0.503***	0.565***	0.696***	0.585***	0.545***	0.680***	0.751***	0.772***	0.743***
	(0.001)	(0.001)	(0.002)	(0.002)	(0.002)	(0.003)	(0.002)	(0.002)	(0.002)
Structural Covariates	Yes	Yes	Yes	Yes	Yes	Yes	Yes	Yes	Yes
Observations	6,477,161	2,542,020	1,547,713	1,100,816	993,252	356,165	1,064,506	1,168,238	1,105,292

Dependent variables are recorded as to whether the preferred option was chosen (for example, whether the respondent spared females). Continuous predictor variables are all standardized. All models include structural covariates (remaining attributes of a scenario). Coefficients are estimated using a regression-based estimator with cluster-robust standard errors. $^{*}P < 0.01$, $^{**}P < 0.001$, $^{***}P < 0.0001$. See Supplementary Information for more details.

© 2018 Springer Nature Limited. All rights reserved.

Extended Data Table 2 | Country-level OLS regressions showing the relationships between key ethical preferences and various social, political and economic measures

	Sparing...			
	More Characters	The Lawful	Higher Status	Females
Individualism	**0.88*****	-0.52***	0.02	-0.07
	(5.69)	(-2.96)	(0.11)	(-0.38)
Rule of Law	-0.37**	**0.53*****	-0.25	0.24
	(-2.60)	**(3.29)**	(-1.56)	(1.50)
Economic Inequality	0.23*	-0.30**	**0.32****	0.46***
	(1.86)	(-2.05)	**(2.28)**	(3.23)
Female Health/Survival	0.12	0.06	0.24*	**0.07**
	(1.15)		(1.96)	**(0.53)**
N	56	56	56	56
R^2	0.65	0.48	0.52	0.48

Pairwise exclusion was used for missing data. Predicted relationships are shown in bold. *$P < 0.10$, **$P < 0.05$, ***$P < 0.01$. See Supplementary Information for more details.

© 2018 Springer Nature Limited. All rights reserved.

https://doi.org/10.1038/s41586-018-0649-2

Targeted neurotechnology restores walking in humans with spinal cord injury

Fabien B. Wagner[1,2,15], Jean-Baptiste Mignardot[1,2,15], Camille G. Le Goff-Mignardot[1,2,15], Robin Demesmaeker[1,2], Salif Komi[1,2], Marco Capogrosso[3], Andreas Rowald[1,2], Ismael Seáñez[1,2], Miroslav Caban[4,5], Elvira Pirondini[1,2,6], Molywan Vat[7], Laura A. McCracken[1,2], Roman Heimgartner[1,2], Isabelle Fodor[2], Anne Watrin[4], Perrine Seguin[1,2], Edoardo Paoles[4], Katrien Van Den Keybus[2], Grégoire Eberle[2], Brigitte Schurch[2], Etienne Pralong[7], Fabio Becce[8], John Prior[9], Nicholas Buse[10], Rik Buschman[10], Esra Neufeld[11], Niels Kuster[11,12], Stefano Carda[2], Joachim von Zitzewitz[4], Vincent Delattre[4], Tim Denison[10,13], Hendrik Lambert[4], Karen Minassian[1,2,16], Jocelyne Bloch[2,7,14,16] & Grégoire Courtine[1,2,7,14,16]*

Spinal cord injury leads to severe locomotor deficits or even complete leg paralysis. Here we introduce targeted spinal cord stimulation neurotechnologies that enabled voluntary control of walking in individuals who had sustained a spinal cord injury more than four years ago and presented with permanent motor deficits or complete paralysis despite extensive rehabilitation. Using an implanted pulse generator with real-time triggering capabilities, we delivered trains of spatially selective stimulation to the lumbosacral spinal cord with timing that coincided with the intended movement. Within one week, this spatiotemporal stimulation had re-established adaptive control of paralysed muscles during overground walking. Locomotor performance improved during rehabilitation. After a few months, participants regained voluntary control over previously paralysed muscles without stimulation and could walk or cycle in ecological settings during spatiotemporal stimulation. These results establish a technological framework for improving neurological recovery and supporting the activities of daily living after spinal cord injury.

Spinal cord injury (SCI) disrupts communication within the nervous system, leading to the loss of essential neurological functions. At present, activity-based therapies are the only medical practices that can be used to enhance recovery[1–3]. The volitional production of active movements during training promotes reorganization of neuronal pathways and thereby augments recovery[4,5]. However, the most affected patients, who fail to produce active movements voluntarily, experience minimal benefits from these therapies[1].

This situation has prompted the development of multifaceted neurotechnologies[6], such as lower limb exoskeletons, bodyweight support systems, functional electrical stimulation of muscles, and spinal cord neuromodulation therapies, all of which share the same goal: to enable patients to sustain active movements during training to enhance the reorganization of neuronal pathways[4]. Three decades of clinical research using these neurotechnologies suggested that epidural electrical stimulation (EES) of the spinal cord may be pivotal to achieve this goal[7–10]. EES not only enables the brain to exploit spared but functionally silent descending pathways in order to produce movements of paralysed limbs[11,12], but also improves the ability of the spinal cord to translate task-specific sensory information into the muscle activity that underlies standing and walking[9,10,12–16].

To harness the therapeutic potential of EES, we studied its underlying mechanisms. We found that EES activates motor neurons by recruiting proprioceptive circuits within the posterior roots of the spinal cord[17–20]. This understanding translated into EES protocols that target individual posterior roots to access the motor neuron pools located in the spinal cord segment innervated by each root[21]. To engage motor neurons at the appropriate time, spatially selective EES trains are delivered with timing that coincides with the intended movement. Compared to empirical stimulation protocols, spatiotemporal EES enhances the potency of leg movements, which enabled weight-bearing locomotion in animal models of leg paralysis[21–23]. When combined with overground locomotor training enabled by a gravity-assist device[24], this stimulation promotes extensive reorganization of residual neural pathways that improves locomotion with and even without stimulation[21,25,26].

Here, we report the development of targeted neurotechnologies for delivering spatiotemporal EES during overground locomotor training with a gravity-assist device in humans[27]. We hypothesized that spatiotemporal EES would immediately enable voluntary locomotion despite chronic paralysis, and that the ability to sustain active movements during training would promote meaningful functional improvements with and even without stimulation.

Targeted neurotechnologies and surgery

We developed a wireless environment that allows real-time control over independently adjusted EES trains to the spinal cord during overground

[1]Center for Neuroprosthetics and Brain Mind Institute, School of Life Sciences, Swiss Federal Institute of Technology (EPFL), Lausanne, Switzerland. [2]Department of Clinical Neuroscience, Lausanne University Hospital (CHUV), Lausanne, Switzerland. [3]Platform of Translational Neuroscience, Department of Neuroscience and Movement Science, University of Fribourg, Fribourg, Switzerland. [4]GTXmedical, Lausanne, Switzerland. [5]Institute of Bioengineering, Swiss Federal Institute of Technology (EPFL), Lausanne, Switzerland. [6]Department of Radiology and Medical Informatics, University of Geneva, Geneva, Switzerland. [7]Department of Neurosurgery, Lausanne University Hospital (CHUV), Lausanne, Switzerland. [8]Department of Diagnostic and Interventional Radiology, Lausanne University Hospital (CHUV), Lausanne, Switzerland. [9]Department of Nuclear Medicine and Molecular Imaging, Lausanne University Hospital (CHUV), Lausanne, Switzerland. [10]Medtronic, Minneapolis, MN, USA. [11]Foundation for Research on Information Technologies in Society (IT'IS), Zurich, Switzerland. [12]Department for Information Technology and Electrical Engineering, Swiss Federal Institute of Technology (ETHZ), Zurich, Switzerland. [13]Department of Engineering Science, University of Oxford, Oxford, UK. [14]Faculty of Biology and Medicine, University of Lausanne (UNIL), Lausanne, Switzerland. [15]These authors contributed equally: Fabien B. Wagner, Jean-Baptiste Mignardot, Camille G. Le Goff-Mignardot. [16]These authors jointly supervised this work: Karen Minassian, Jocelyne Bloch, Grégoire Courtine. *e-mail: gregoire.courtine@epfl.ch

© 2018 Springer Nature Limited. All rights reserved.

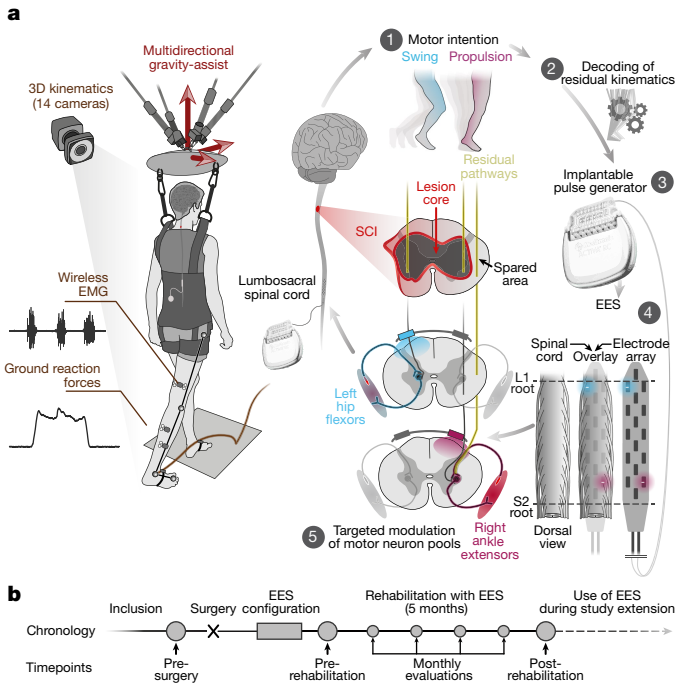

Fig. 1 | Technology and study design. a, Targeted neurotechnologies enable walking after SCI. Multidirectional assistance of trunk movements during overground locomotion while 3D kinematics, ground reaction forces and EMG activity are recorded wirelessly. An implantable pulse generator connected to a 16-electrode paddle array was used to target the posterior roots projecting to specific motor neuron pools, illustrated for hip flexors and ankle extensors. Real-time processing of residual kinematics ensures that targeted EES coincides with movement intent. **b**, Study timeline.

walking (Fig. 1a and Supplementary Video 1). A gravity-assist applied multidirectional forces to the trunk to provide personalized bodyweight support in a safe workspace[27]. A recording platform allowed real-time processing of whole-body kinematics, ground reaction forces and electromyographic (EMG) activity of leg muscles. To deliver stimulation, we upgraded an implantable pulse generator commonly used for deep brain stimulation with wireless communication modules[23] that enabled real-time control over EES parameters (Extended Data Fig. 1). EES sequences could be pre-programmed in an open loop or triggered in a closed loop on the basis of external signals[21,22]. The lumbosacral posterior roots were targeted using a 16-electrode paddle array designed for pain therapy.

We enrolled three males with a chronic cervical SCI who displayed severe lower limb deficits or complete paralysis that prevented them from walking overground (Extended Data Table 1).

To target the posterior roots that project to motor neuron pools that innervate leg muscles (Fig. 2a), we developed a surgical protocol consisting of pre-operative imaging combined with intraoperative electrophysiology and radiology that guided the precise placement of the paddle array (Extended Data Fig. 1b).

EES enables control of paralysed muscles

We aimed to identify electrode configurations that target the posterior roots that project to spinal cord regions, containing motor neurons involved in mobilizing the hip, knee and ankle joints.

We compiled an atlas of motor neuron activation maps underlying flexion or extension of each joint in healthy individuals. We projected the EMG activity from leg muscles onto the expected anatomical locations of the associated motor neuron pools[28,29]. We obtained consistent motor neuron activation maps. For example, hip flexion involved the activation of upper lumbar segments, whereas ankle extension activated motor neuron pools restricted to upper sacral segments (Fig. 2b).

To identify electrodes that could target the posterior roots that project to the spinal cord regions associated with these motor neuron activation maps, we performed simulations using hybrid computational models of EES[18]. Each model was personalized using magnetic resonance imaging (MRI) and computerized tomography (CT) scans. Simulations estimated the relative recruitment of each posterior root by each electrode of the array (Fig. 2c).

These simulations guided the identification of optimal electrode configurations. While participants laid supine, we delivered monopolar pulses of EES at increasing intensities through the electrodes that had the highest probabilities of activating the targeted posterior roots (Extended Data Fig. 2). Projection of muscle response amplitudes into circular plots described the spatial selectivity of each electrode, which we quantified with an algorithm (Fig. 2d). If the selectivity was insufficient, we steered the electrical field with multipolar electrode configurations (Extended Data Fig. 2).

For all participants, computer simulations and electrophysiological experiments confirmed high correlations between the identified electrode configurations and the recruitment of the posterior roots that project to each of the targeted spinal cord regions involved in mobilizing hip, knee and ankle joints (Extended Data Fig. 3).

We next tested whether spatially selective EES could facilitate force production from the targeted muscles. While seated, participants were asked to produce an isometric force restricted to a single joint. Participant 1 (P1) failed to produce hip flexion and ankle extension torques with his paralysed leg (Fig. 2e, f). EES immediately enabled voluntary activation of the targeted muscles to produce the desired torque. These observations were repeated for all targeted joints and participants (Extended Data Fig. 4).

Without any voluntary contribution, EES induced minimal muscle contraction (Extended Data Fig. 4). At the amplitudes used, EES augmented the excitability of the targeted motor neurons, which enabled residual but functionally silent descending inputs to activate muscles.

EES modulates cortical activity

These results opened the possibility that the recruitment of proprioceptive pathways with EES modulates cortical excitability, which may facilitate movement[30].

To study this hypothesis, we recorded electroencephalographic (EEG) activity when participants attempted to produce knee extension torques without and with EES (Extended Data Fig. 5a). EES triggered a robust response in the sensorimotor cortex (latency: 90–140 ms, Extended Data Fig. 5b), probably resulting from the recruitment of proprioceptive afferents.

Attempts to activate knee extensor muscles triggered event-related desynchronization (ERD) of the contralateral sensorimotor cortex in β-band frequencies, both without and with EES. This cortical activity has been linked to movement execution, and is followed by event-related resynchronization (ERS) after movement termination[31]. Previous studies showed that the amplitude of ERS decreases in proportion to severity of SCI[31]. Voluntary activation of paralysed muscles during EES led to an increase in ERS amplitude (Extended Data Fig. 5c, d). These results suggest that EES enhances cortical excitability, promoting more natural dynamics during movement execution[30].

Spatiotemporal EES enables walking

Walking involves reproducible sequences of muscle activation (Fig. 3a). The underlying motor neuron activation maps involve a succession of hotspots for which the migration reflects body mechanics[28], ensuring weight acceptance, propulsion and swing (Fig. 3b).

Targeted EES effectively activated the regions embedding these hotspots (Fig. 3c). To configure EES sequences (Fig. 3d, e), we fine-tuned the timing of each spatially selective stimulation train using a closed-loop controller that triggered EES on the basis of foot trajectory[21,22,32]. We adjusted the onset and duration of each train to approach the motor neuron activation maps of healthy individuals (Extended Data Fig. 6). Relatively small changes in the timing of each train altered performance (Extended Data Fig. 6b). Once optimized, EES could be delivered in an open loop: participants regulated the timing of their movements

© 2018 Springer Nature Limited. All rights reserved.

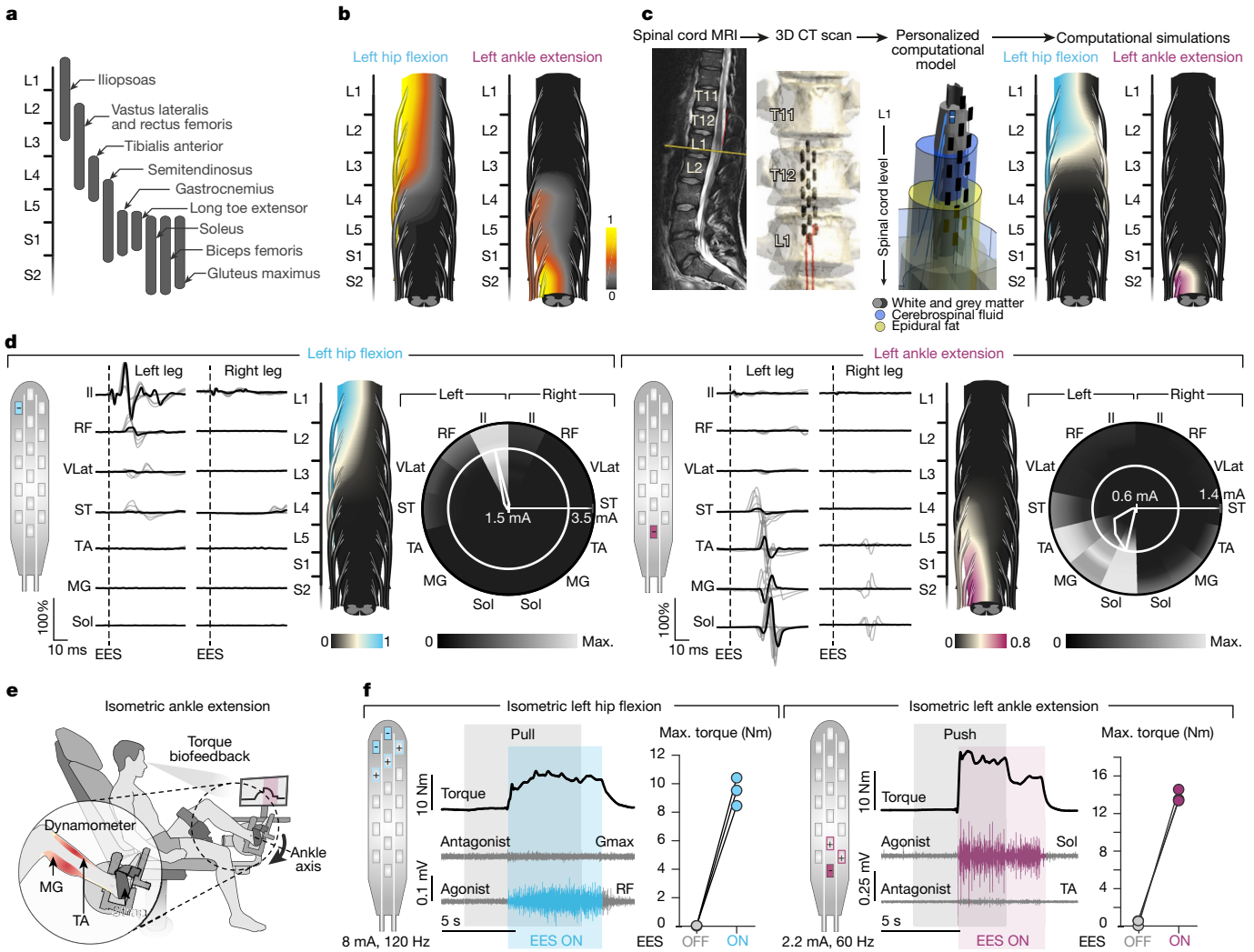

Fig. 2 | Configuration of targeted EES. a, Distribution of motor neuron pools within the spinal cord[46]. **b**, Map of motor neuron activation underlying isometric torque production in a healthy subject (consistent across three repetitions and subjects). **c**, Personalized computational model of EES. Simulated map of motor neuron activation following EES targeting the L1 and S2 posterior roots. **d**, Electrophysiological experiments were used to determine optimal electrodes and amplitudes for targeting specific spinal cord regions. EMG responses when delivering single-pulse EES at increasing amplitudes are shown (grey traces). Motor neuron activation maps correspond to optimal amplitudes (black traces). Circular plots report EMG amplitude (in grey scale) at increasing amplitudes (radial axis). White circles show optimal amplitudes; polygons quantify selectivity at this amplitude. **e**, Instrumented chair used to measure single-joint torques. **f**, Targeted EES enables voluntary force production by paralysed muscles. Isometric torque and EMG activity while delivering targeted EES, including quantification ($n = 3$ repetitions, P1). Gmax, gluteus maximus; Il, iliopsoas; MG, medial gastrocnemius; RF, rectus femoris; Sol, soleus; ST, semitendinosus; TA, tibialis anterior; VLat, vastus lateralis.

to pre-programmed EES sequences, which improved gait consistency (Extended Data Fig. 6c).

To tune muscle activity, we adjusted EES amplitudes and frequencies (Extended Data Fig. 6). As observed in animal models[21,22], we found a monotonic relationship between EES frequency and flexor muscle activity (Fig. 3f), such that increasing frequency proportionally enhanced flexion (Extended Data Fig. 6d). Unexpectedly, extensor motor neuron pools responded inversely. Proprioceptive afferents elicit strong monosynaptic responses in extensor motor neurons, whereas these afferents primarily engage flexor motor neurons through polysynaptic circuits[33]. In humans, monosynaptic projections are highly sensitive to low-frequency depression[34], which may explain the decrease in extensor motor neuron activation with increasing frequency.

Within five days, this procedure led to EES sequences (Fig. 3d, e) that enabled robust EMG activity in otherwise quiescent muscles during stepping on a treadmill (Extended Data Fig. 7).

Participants were then asked to walk overground using the gravity-assist and spatiotemporal EES. The stimulation enabled all participants to walk voluntarily until the stimulation was stopped. They could resume locomotion as soon as the stimulation was reintroduced (Fig. 4a, Extended Data Fig. 8a and Supplementary Video 2).

We next investigated participants' ability to adjust leg movements. First, we asked them to produce exaggerated step elevations without changing EES parameters. All participants were able to enhance their step elevation three-to-fivefold compared to regular steps (Fig. 4b and Extended Data Fig. 8b). Second, we asked them to adjust their stride to varying speeds. Not only were the participants able to adjust their stride length, but they also could stop locomotor movements despite the treadmill belt motion and ongoing stimulation (Extended Data Fig. 8b, e).

Finally, we asked participants to walk on a treadmill for one hour. All participants sustained more than 1,200 steps, covering distances as long as 1.0 km without showing muscle exhaustion or gait impairments (Fig. 4c and Extended Data Fig. 8c).

These results show that spatiotemporal EES not only enabled completely or partially paralysed individuals to walk overground, but also allowed them to adjust leg movements to stand and walk over a range of speeds for durations as long as one hour.

© 2018 Springer Nature Limited. All rights reserved.

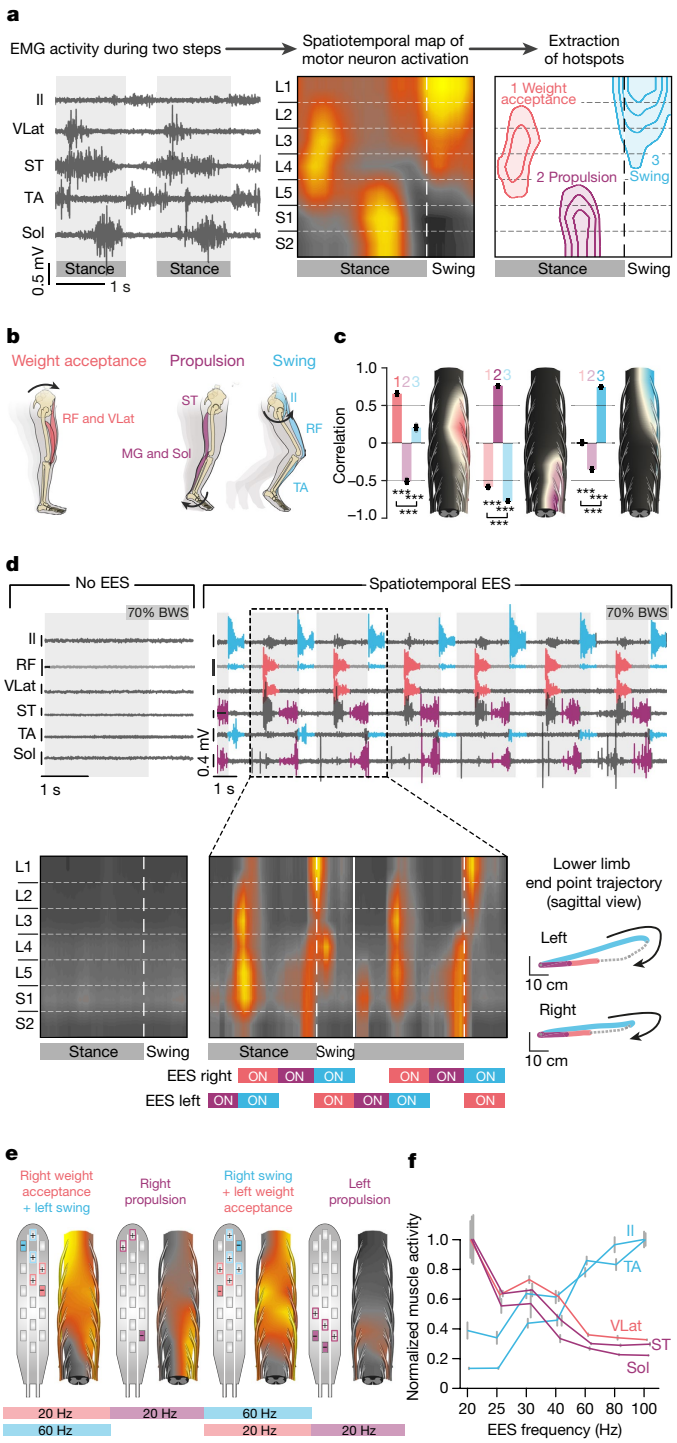

Fig. 3 | Configuration of spatiotemporal EES for walking. a, EMG activity during walking in healthy individuals. Spatiotemporal map of motor neuron activation highlights hotspots (mean, $n = 12$ gait cycles, representative subject). Equipotential lines represent 45–75% activation. **b**, Functional target of each hotspot. **c**, Map of motor neuron activation following 500-ms bursts of targeted EES during standing. Bar plots show Pearson's correlations for each hotspot (mean ± s.e.m., $n = 12$ bursts, $***P < 0.001$; one-way ANOVA, post hoc Tukey's honest significant difference (HSD) test). **d**, EMG activity and map of motor neuron activation during EES or without EES after a motor complete SCI while stepping on a treadmill with support and assistance (P3). EES timing is indicated along foot trajectories (bottom right; $n = 73$ steps) and below motor neuron activation maps. **e**, Spatiotemporal EES sequence for data shown in **d**. **f**, Mean (± s.e.m.) modulation of EMG amplitude in flexor and extensor muscles during walking with increasing EES frequencies ($n = 20, 15, 16, 17, 15, 16, 15$ gait cycles for 20, 25, 30, 40, 60, 80, 100 Hz, respectively; P3).

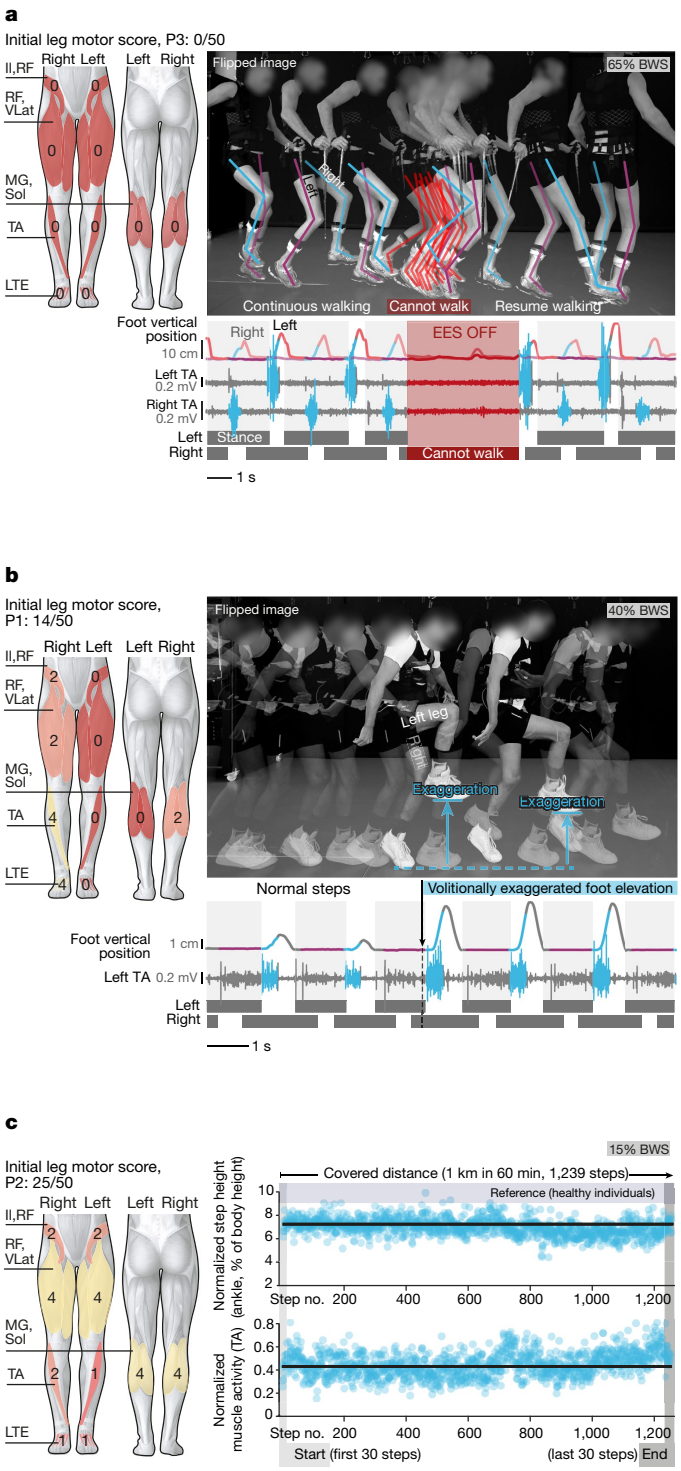

Fig. 4 | Voluntary control of adaptive and sustained locomotion. a, Spatiotemporal EES enables voluntary control of overground walking. Chronophotography, tibialis anterior (TA) EMG activity and foot vertical position during overground walking with gravity-assist and sticks while EES is switched on, then off, then on. Leg motor scores shown on muscles in diagrams: 0, total paralysis; 1, palpable or visible contraction; 2, active movement, gravity eliminated; 3, active movement against gravity; 4, active movement against some resistance; 5, active movement against full resistance. **b**, Spatiotemporal EES enables voluntary control of leg kinematics. Overground walking when participants were requested to perform steps with normal heights and then exaggerated step elevations. **c**, Spatiotemporal EES enables sustained walking. Consecutive values of step height and EMG activity over 60 min of walking with EES (P1: 1.2 km; P2, P3: 1 km). Experiments in **a**, **b** were repeated at least five times; the experiment in **c** was performed once, but participants routinely walked for 60 min during training. BWS, bodyweight support.

© 2018 Springer Nature Limited. All rights reserved.

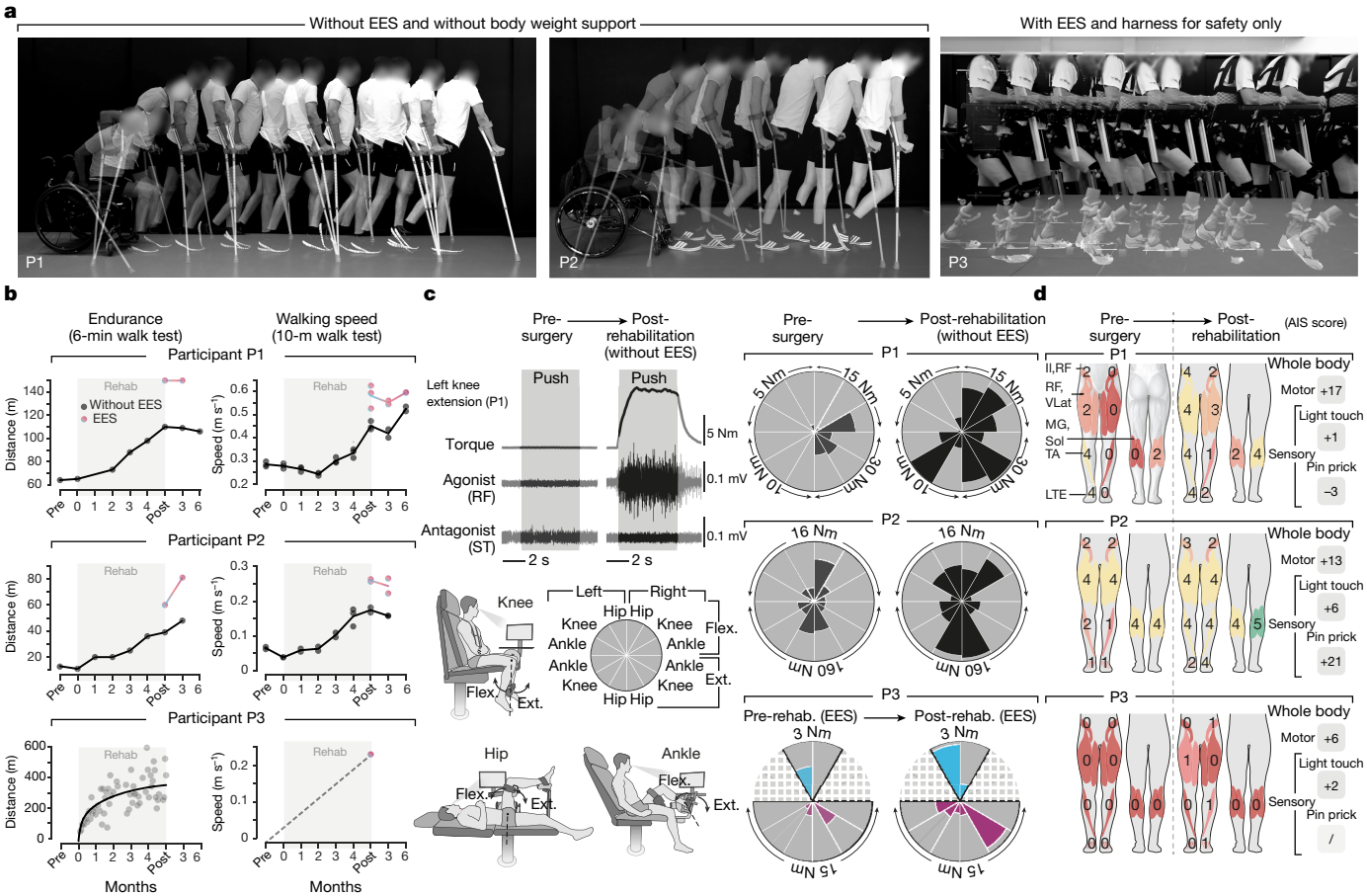

Fig. 5 | Rehabilitation mediates neurological recovery. a, Improved mobility after rehabilitation. Chronophotography shows P1 and P2 transiting from sitting to walking with crutches without EES; P3 progresses overground with a walker and EES; repeated at least three times on different days. **b**, Plots reporting changes in 6-min and 10-m walk tests for P1 and P2. Tests were performed without gravity-assist, following clinical guidance. For P3 plots report changes in walking distance during rehabilitation and walking speed with EES (with transparent body weight support). **c**, Evaluations of isometric torque production for each joint, quantified before surgery and after rehabilitation without EES for P1 and P2, and with EES for P3. **d**, Changes in lower limb motor and sensory scores after rehabilitation. Changes in motor and sensory scores on abbreviated injury scale (AIS) for all levels below injury are summarized (see Extended Data Table 1).

Continuous EES is poorly effective

Recent studies have shown that continuous EES enabled overground walking after nearly one year of intense training[9,10]. As spatiotemporal EES enabled locomotion within one week, we evaluated whether continuous EES could achieve similar efficacy.

We delivered widespread stimulation targeting the posterior roots associated with flexor motor neuron pools, as previously recommended[10]. However, we did not further optimize the stimulation. Continuous EES enhanced muscle activity, but was poorly effective in facilitating locomotion overground. All participants reported a loss of limb position awareness combined with co-activation across muscles (Extended Data Fig. 9 and Supplementary Video 3). These detrimental outcomes are due to the cancellation of proprioceptive information during continuous EES[35].

Rehabilitation improves walking with EES

Participants followed a rehabilitation program four to five times per week for five months (Fig. 1b), focused on walking on a treadmill and overground; this was complemented with muscle strengthening and standing, each of which was enabled by task-specific EES (Extended Data Fig. 10a).

With spatiotemporal EES, all participants improved their walking capacities following a reproducible chronology (Extended Data Fig. 10b): non-ambulatory participants initially required crutches and the gravity-assist to walk overground. After one to three months, they could walk hands-free when provided with hip support in the gravity-assist. Eventually, P1 and P2 regained independent walking while 35% of their bodyweight was supported against gravity. P3 needed a walker to progress overground with EES (Supplementary Video 4).

Neurological recovery without EES

Improvements were not limited to walking with EES. Rehabilitation promoted neurological recovery that translated into improvements without EES.

P1 and P2 could transit from sitting to standing and walking independently with crutches (Fig. 5a). P1 could even walk without an assistive device for several steps (Supplementary Video 5). Consequently, P1 and P2 increased their WISCI (walking index for spinal cord injury) scores from 13 to 16 and 6 to 13, respectively. They displayed substantial improvements in clinical evaluations such as ten-metre and six-minute walking tests without EES (Fig. 5b). Several months after completing the rehabilitation program, both participants, who continued practicing once or twice per week with EES, maintained or further improved their performance.

Participants also recovered voluntary leg movements without EES. For example, P1 and P3 could sustain a full extension of their previously paralysed legs against gravity (P3, lying only; Extended Data Fig. 11c and Supplementary Video 5). Quantified measurements revealed that P1 and P2 improved their ability to produce a torque at each joint of

© 2018 Springer Nature Limited. All rights reserved.

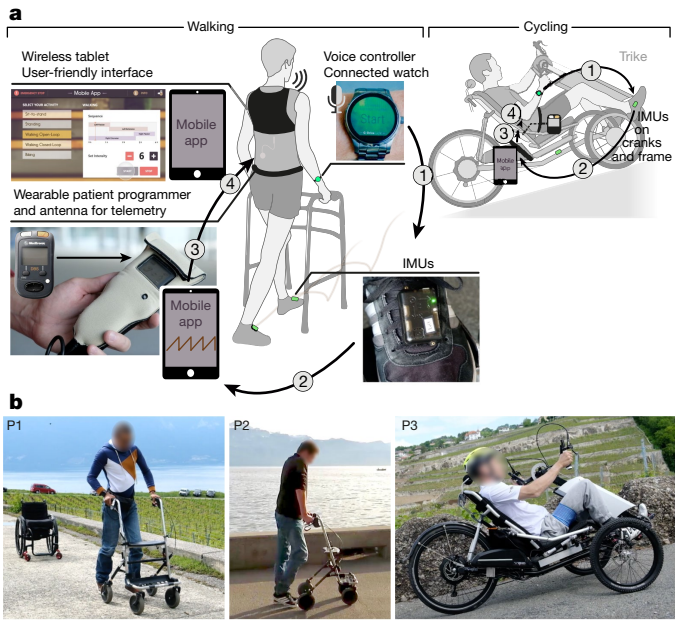

Fig. 6 | Spatiotemporal EES in ecological settings. a, System to support activities of daily living. Tablet featuring a mobile App allows participants to select EES sequences, delivered in open loop or closed loop based on inertial measurement units (IMUs) located on both feet or attached onto the cranks and frame of a trike. 1. A personalized voice-controlled watch allows the user to switch EES on or off. 2. IMUs detect foot or crank motion during walking or cycling. 3. Controller sends commands to the patient programmer. 4. Spatiotemporal EES is adjusted in a closed loop. **b**, Walking and cycling activities in ecological settings are enabled by spatiotemporal EES.

both legs (Fig. 5c). This recovery translated into an increase of 16 and 11 points in lower extremity motor scores, respectively (Fig. 5d). Both participants had previously followed extensive conventional rehabilitation without showing neurological recovery. The lower extremity motor score increased by 4 points in participant P3, but without EES this recovery was insufficient to produce measurable forces when seated. However, force production improved during EES (Fig. 5c). He showed a considerable increase in mass and quality of thigh and trunk muscles (Extended Data Fig. 11). P1, P2 and P3 also showed improvements in upper limb motor scores of 1, 2 and 2 points, respectively.

Support of activities in the community

Recovery of functional leg movements during spatiotemporal EES suggested that practical stimulation technologies could support activities of daily living. For this purpose, we engineered a solution based on a tablet to enable the selection of EES sequences that are switched on or off with a voice-controlled watch (Fig. 6a). To enable standing, walking or cycling, EES sequences must be synchronized to the intended movements. We conceived algorithms that trigger and adjust the timing of EES trains in a closed loop based on real-time acquisition of signals from wearable inertial measurement units.

Robust event-triggered detection allowed participants to transit from sitting to standing and walking freely in ecological settings (Fig. 6b and Extended Data Fig. 12). A stimulation program specific for cycling permitted participants to ride an adapted trike powered with the arms and legs (Supplementary Video 6).

Discussion

We developed targeted EES neurotechnologies that immediately restored voluntary control of walking in individuals with severe or complete paralysis. The electrode configurations targeted proprioceptive circuits through the recruitment of selected posterior roots[17–19,36]. This strategy was pivotal to enable the immediate control of walking despite chronic paralysis. This framework guided the rapid personalization of spatiotemporal EES sequences that continuously coincided with intended movements. Consequently, EES augmented the excitability of motor neuron pools that were concomitantly engaged by the natural flow of sensory information and residual supraspinal commands. This spatiotemporal convergence enabled more robust and natural control of leg movements compared to empirical stimulation paradigms such as continuous EES[9,10].

We hypothesize that this spatiotemporal convergence is responsible for the neurological recovery observed in all participants without EES. We showed that mice lacking proprioceptive circuits exhibit defective rearrangement of descending pathways after SCI, which abolishes recovery[37]. Conversely, we propose that the spatiotemporal contingence between residual supraspinal commands and proprioceptive circuit activations with EES may increase the strength and number of terminals from spared descending projections through bidirectional spike-timing-dependent plasticity[38,39]. Electrophysiological studies have documented such plasticity in humans with SCI[40,41]. This interpretation is consistent with the pronounced reorganization of cortico-reticulo-spinal circuits observed in rodents when EES enables gait training despite paralysis[25,26]. As we observed in humans, rodents regained cortical control of leg movements that persisted without EES[25] when rehabilitation commenced early after SCI. We therefore anticipate that this therapy will be even more efficacious early after SCI in humans, when the potential for plasticity is elevated and the neuromuscular system has not yet undergone the atrophy that follows chronic paralysis[42]. Furthermore, improvements in muscle mass and other physiological functions[43,44] suggest that EES may help to counteract these deteriorations.

Clinical trials starting early after SCI will require a stratification of participants who may benefit from the therapy, combined with statistical models that predict their potential for recovery[45]. Here, we validated our neurotechnologies in a few individuals. This proof-of-concept stresses the urgency of developing neurotechnologies that not only harness targeted EES to enable movement, but also provide the usability features to support rehabilitation in clinical settings and use in the community.

Data availability

Data that support the findings and software routines developed for the data analysis will be made available upon reasonable request to the corresponding author.

Online content

Any methods, additional references, Nature Research reporting summaries, source data, statements of data availability and associated accession codes are available at https://doi.org/10.1038/s41586-018-0649-2.

Received: 22 June 2018; Accepted: 1 October 2018;
Published online 31 October 2018.

1. Behrman, A. L., Ardolino, E. M. & Harkema, S. J. Activity-based therapy: from basic science to clinical application for recovery after spinal cord injury. *J. Neurol. Phys. Ther.* **41**, S39–S45 (2017).
2. Jones, M. L. et al. Activity-based therapy for recovery of walking in individuals with chronic spinal cord injury: results from a randomized clinical trial. *Arch. Phys. Med. Rehabil.* **95**, 2239–2246 (2014).
3. Field-Fote, E. C., Lindley, S. D. & Sherman, A. L. Locomotor training approaches for individuals with spinal cord injury: a preliminary report of walking-related outcomes. *J. Neurol. Phys. Ther.* **29**, 127–137 (2005).
4. Edgerton, V. R. et al. Training locomotor networks. *Brain Res. Rev.* **57**, 241–254 (2008).
5. Côté, M. P., Murray, M. & Lemay, M. A. Rehabilitation strategies after spinal cord injury: inquiry into the mechanisms of success and failure. *J. Neurotrauma* **34**, 1841–1857 (2017).
6. Borton, D., Micera, S., Millán, J. d. R. & Courtine, G. Personalized neuroprosthetics. *Sci. Transl. Med.* **5**, 210rv2 (2013).
7. Field-Fote, E. C. & Roach, K. E. Influence of a locomotor training approach on walking speed and distance in people with chronic spinal cord injury: a randomized clinical trial. *Phys. Ther.* **91**, 48–60 (2011).
8. Minassian, K., McKay, W. B., Binder, H. & Hofstoetter, U. S. Targeting lumbar spinal neural circuitry by epidural stimulation to restore motor function after spinal cord injury. *Neurotherapeutics* **13**, 284–294 (2016).
9. Angeli, C. A. et al. Recovery of over-ground walking after chronic motor complete spinal cord injury. *N. Engl. J. Med.* **379**, 1244–1250 (2018).

© 2018 Springer Nature Limited. All rights reserved.

10. Gill, M. L. et al. Neuromodulation of lumbosacral spinal networks enables independent stepping after complete paraplegia. *Nat. Med.* https://doi.org/10.1038/s41591-018-0175-7 (2018).
11. Barolat, G., Myklebust, J. B. & Wenninger, W. Enhancement of voluntary motor function following spinal cord stimulation-case study. *Appl. Neurophysiol.* **49**, 307–314 (1986).
12. Angeli, C. A., Edgerton, V. R., Gerasimenko, Y. P. & Harkema, S. J. Altering spinal cord excitability enables voluntary movements after chronic complete paralysis in humans. *Brain* **137**, 1394–1409 (2014).
13. Danner, S. M. et al. Human spinal locomotor control is based on flexibly organized burst generators. *Brain* **138**, 577–588 (2015).
14. Grahn, P. J. et al. Enabling task-specific volitional motor functions via spinal cord neuromodulation in a human with paraplegia. *Mayo Clin. Proc.* **92**, 544–554 (2017).
15. Carhart, M. R., He, J., Herman, R., D'Luzansky, S. & Willis, W. T. Epidural spinal-cord stimulation facilitates recovery of functional walking following incomplete spinal-cord injury. *IEEE Trans. Neural Syst. Rehabil. Eng.* **12**, 32–42 (2004).
16. Minassian, K. et al. Stepping-like movements in humans with complete spinal cord injury induced by epidural stimulation of the lumbar cord: electromyographic study of compound muscle action potentials. *Spinal Cord* **42**, 401–416 (2004).
17. Rattay, F., Minassian, K. & Dimitrijevic, M. R. Epidural electrical stimulation of posterior structures of the human lumbosacral cord: 2. Quantitative analysis by computer modeling. *Spinal Cord* **38**, 473–489 (2000).
18. Capogrosso, M. et al. A computational model for epidural electrical stimulation of spinal sensorimotor circuits. *J. Neurosci.* **33**, 19326–19340 (2013).
19. Moraud, E. M. et al. Closed-loop control of trunk posture improves locomotion through the regulation of leg proprioceptive feedback after spinal cord injury. *Sci. Rep.* **8**, 76 (2018).
20. Gerasimenko, Y., Roy, R. R. & Edgerton, V. R. Epidural stimulation: comparison of the spinal circuits that generate and control locomotion in rats, cats and humans. *Exp. Neurol.* **209**, 417–425 (2008).
21. Wenger, N. et al. Spatiotemporal neuromodulation therapies engaging muscle synergies improve motor control after spinal cord injury. *Nat. Med.* **22**, 138–145 (2016).
22. Wenger, N. et al. Closed-loop neuromodulation of spinal sensorimotor circuits controls refined locomotion after complete spinal cord injury. *Sci. Transl. Med.* **6**, 255ra133 (2014).
23. Capogrosso, M. et al. A brain-spine interface alleviating gait deficits after spinal cord injury in primates. *Nature* **539**, 284–288 (2016).
24. Dominici, N. et al. Versatile robotic interface to evaluate, enable and train locomotion and balance after neuromotor disorders. *Nat. Med.* **18**, 1142–1147 (2012).
25. Asboth, L. et al. Cortico-reticulo-spinal circuit reorganization enables functional recovery after severe spinal cord contusion. *Nat. Neurosci.* **21**, 576–588 (2018).
26. van den Brand, R. et al. Restoring voluntary control of locomotion after paralyzing spinal cord injury. *Science* **336**, 1182–1185 (2012).
27. Mignardot, J. B. et al. A multidirectional gravity-assist algorithm that enhances locomotor control in patients with stroke or spinal cord injury. *Sci. Transl. Med.* **9**, eaah3621 (2017).
28. Cappellini, G., Ivanenko, Y. P., Dominici, N., Poppele, R. E. & Lacquaniti, F. Migration of motor pool activity in the spinal cord reflects body mechanics in human locomotion. *J. Neurophysiol.* **104**, 3064–3073 (2010).
29. Yakovenko, S., Mushahwar, V., VanderHorst, V., Holstege, G. & Prochazka, A. Spatiotemporal activation of lumbosacral motoneurons in the locomotor step cycle. *J. Neurophysiol.* **87**, 1542–1553 (2002).
30. Asanuma, H. & Mackel, R. Direct and indirect sensory input pathways to the motor cortex; its structure and function in relation to learning of motor skills. *Jpn. J. Physiol.* **39**, 1–19 (1989).
31. Gourab, K. & Schmit, B. D. Changes in movement-related β-band EEG signals in human spinal cord injury. *Clin. Neurophysiol.* **121**, 2017–2023 (2010).
32. Capogrosso, M. et al. Configuration of electrical spinal cord stimulation through real-time processing of gait kinematics. *Nat. Protoc.* **13**, 2031–2061 (2018).
33. Schieppati, M. The Hoffmann reflex: a means of assessing spinal reflex excitability and its descending control in man. *Prog. Neurobiol.* **28**, 345–376 (1987).
34. Schindler-Ivens, S. & Shields, R. K. Low-frequency depression of H-reflexes in humans with acute and chronic spinal-cord injury. *Exp. Brain Res.* **133**, 233–241 (2000).
35. Formento, E. et al. Electrical spinal cord stimulation must preserve proprioception to enable locomotion in humans with spinal cord injury. *Nat. Neurosci.* https://doi.org/10.1038/s41593-018-0262-6 (2018).
36. Moraud, E. M. et al. Mechanisms underlying the neuromodulation of spinal circuits for correcting gait and balance deficits after spinal cord injury. *Neuron* **89**, 814–828 (2016).
37. Takeoka, A., Vollenweider, I., Courtine, G. & Arber, S. Muscle spindle feedback directs locomotor recovery and circuit reorganization after spinal cord injury. *Cell* **159**, 1626–1639 (2014).
38. Holtmaat, A. & Svoboda, K. Experience-dependent structural synaptic plasticity in the mammalian brain. *Nat. Rev. Neurosci.* **10**, 647–658 (2009).
39. Nishimura, Y., Perlmutter, S. I., Eaton, R. W. & Fetz, E. E. Spike-timing-dependent plasticity in primate corticospinal connections induced during free behavior. *Neuron* **80**, 1301–1309 (2013).
40. Perez, M. A., Field-Fote, E. C. & Floeter, M. K. Patterned sensory stimulation induces plasticity in reciprocal Ia inhibition in humans. *J. Neurosci.* **23**, 2014–2018 (2003).
41. Urbin, M. A., Ozdemir, R. A., Tazoe, T. & Perez, M. A. Spike-timing-dependent plasticity in lower-limb motoneurons after human spinal cord injury. *J. Neurophysiol.* **118**, 2171–2180 (2017).
42. Dietz, V. Behavior of spinal neurons deprived of supraspinal input. *Nat. Rev. Neurol.* **6**, 167–174 (2010).
43. West, C. R. et al. Association of epidural stimulation with cardiovascular function in an individual with spinal cord injury. *JAMA Neurol.* **75**, 630–632 (2018).
44. Herrity, A. N., Williams, C. S., Angeli, C. A., Harkema, S. J. & Hubscher, C. H. Lumbosacral spinal cord epidural stimulation improves voiding function after human spinal cord injury. *Sci. Rep.* **8**, 8688 (2018).
45. van Middendorp, J. J. et al. A clinical prediction rule for ambulation outcomes after traumatic spinal cord injury: a longitudinal cohort study. *Lancet* **377**, 1004–1010 (2011).
46. Sharrard, W. J. The segmental innervation of the lower limb muscles in man. *Ann. R. Coll. Surg. Engl.* **35**, 106–122 (1964).

Acknowledgements See Supplementary Notes. Support: International Foundation for Research in Paraplegia (IRP), Wings for Life, Wyss Center for Neuroengineering, European Union's Horizon 2020 No.785907 (Human Brain Project SGA2), Eurostars No. E10889, GTXmedical, National Center of Competence in Research (NCCR) Robotics of the Swiss National Foundation, the Commission of Technology and Innovation Innosuisse (CTI) No. 25761.1, Voirol Foundation, Firmenich Foundation, Pictet Group Charitable Foundation, Panacée Foundation, riders4riders, SOFMER (to P.S.), the Whitaker International Scholars Program (to I.S.) and the H2020-MSCA-COFUND-2015 EPFL Fellows program (No. 665667 to F.B.W.).

Reviewer information *Nature* thanks C. Moritz, J. Henderson and K. Moxon for their contribution to the peer review of this work.

Author contributions N.B. and T.D., Neural Research Programmer development. F.B.W., Mi.C., C.G.L.G.-M., R.H., V.D. and J.v.Z., technological framework. J.B., surgeries. F.B.W., J.-B.M., C.G.L.G.-M., Ma.C., E.Pi., K.M., R.D., S.K., I.S. and G.C. performed and analysed experiments. R.D., S.K. and Ma.C. contributed equally. F.B., muscle data. I.F., L.M., M.V., P.S., I.S., F.B.W., J.-B.M., C.G.L.G.-M., K.M., K.V.D.K. and G.E., neurorehabilitation. K.V.D.K., F.B., J.P., B.S., E.Pr., P.S. and S.C., clinical and neurological evaluations. A.R. and Ma.C., computational framework. A.R., E.Pa., E.N. and N.K., computational simulations. J.-B.M., C.G.L.G.-M., R.D., S.K. and F.B.W. generated figures. A.W., M.V., R.B., V.D. and H.L., regulatory affairs. K.M., J.B. and G.C., conception and supervision. G.C. wrote the paper with J.B., F.B.W. and K.M.

Competing interests G.C., J.B., Ma.C. and V.D. hold various patents in relation to the present work. T.D., R.B. and N.B. are Medtronic employees, and V.D., H.L., J.v.Z., A.W., Mi.C. and E.Pa. are GTXmedical employees. In review of the manuscript they contributed to technical accuracy but did not influence the results or the content of the manuscript. G.C., J.B., V.D., and H.L. are founders and shareholders of GTXmedical, a company with direct relationships to the presented intervention.

Additional information
Extended data is available for this paper at https://doi.org/10.1038/s41586-018-0649-2.
Supplementary information is available for this paper at https://doi.org/10.1038/s41586-018-0649-2.
Reprints and permissions information is available at http://www.nature.com/reprints.
Correspondence and requests for materials should be addressed to G.C.
Publisher's note: Springer Nature remains neutral with regard to jurisdictional claims in published maps and institutional affiliations.

© 2018 Springer Nature Limited. All rights reserved.

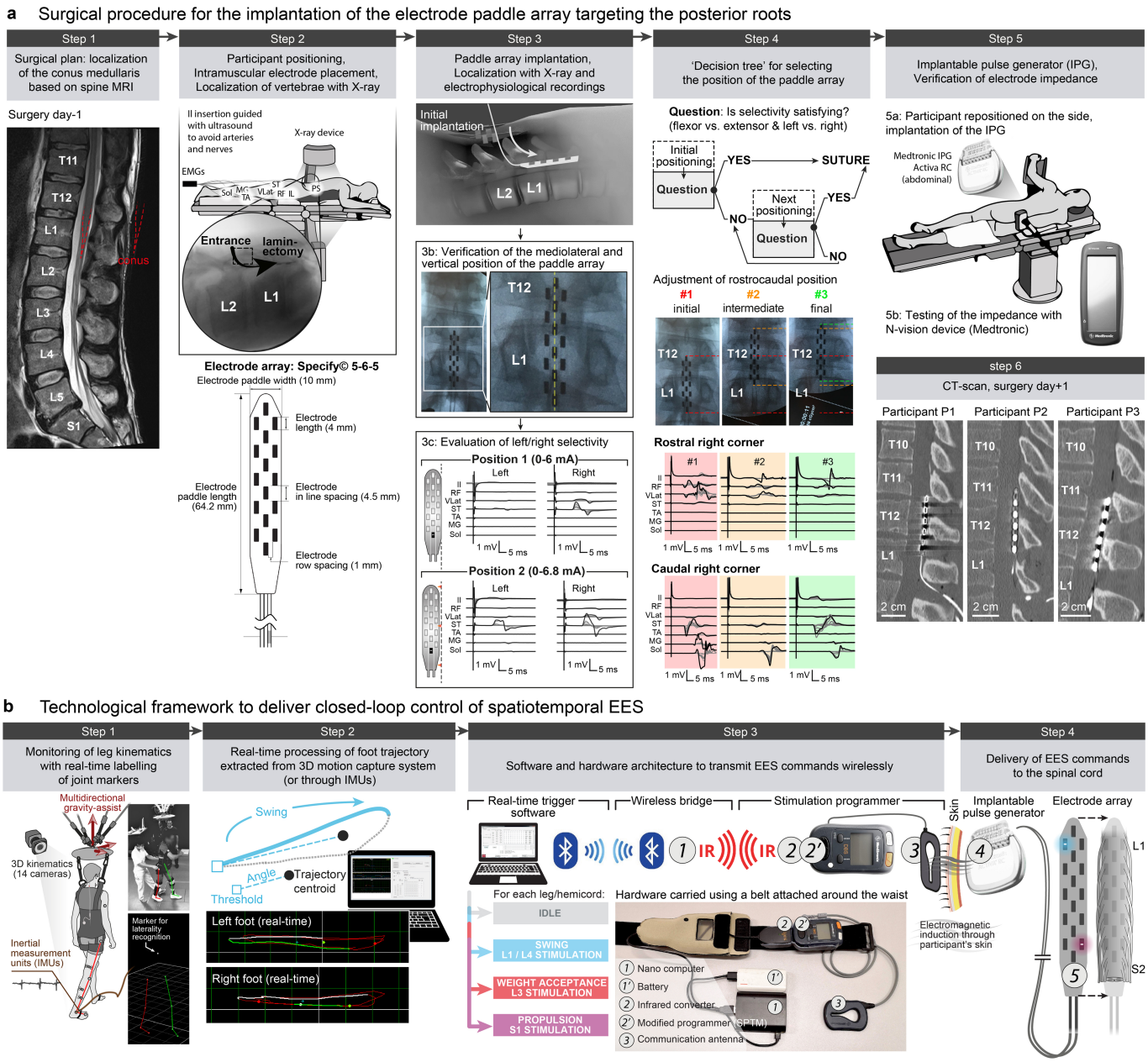

Extended Data Fig. 1 | Surgical procedure and technological framework. a, Surgery. Step 1: high-resolution MRI for pre-surgical planning. The entry point into the epidural space is based on the position of the conus. Step 2: placement of subdermal and intramuscular needle EMG electrodes for key leg muscles and paraspinal (PS) muscles. A subdermal needle is inserted over the sacrum and used as a return electrode for stimulation. Bottom, schematic of the 16-electrode paddle array. Step 3: surgical openings based on pre-surgical planning, typically between the L1 and L2 vertebrae, which are identified through intraoperative X-ray. The mediolateral positions of the paddle array are evaluated with X-ray and recordings of EMG responses following single pulses of EES delivered to the most rostral or most caudal midline electrodes. Step 4: the rostrocaudal position of the paddle array is optimized using EMG responses to single-pulse EES delivered to the electrodes located at each corner of the paddle array. The aim is to obtain strong ipsilateral responses in hip flexors with the most rostral electrodes and strong ipsilateral responses in ankle extensors with the most caudal electrodes. Step 5: implantable pulse generator (IPG) placed within the abdomen. Once connected to the paddle array, the impedance of the electrodes is evaluated to verify that all the components are properly connected. Step 6: post-surgical CT scan showing the location of the paddle array with respect to the vertebrae in each participant.
b, Technological framework and surgical procedure. Step 1: participants wear reflective markers that are monitored using infrared cameras. An algorithm assigns the markers to the joints in real-time. Step 2: the spatiotemporal trajectory of the foot around a calculated centre of rotation (centroid, updated every 3 s) is converted into angular coordinates that trigger and terminate EES protocols when a user-defined threshold is crossed. Step 3: EES commands are transmitted to the IPG via Bluetooth (1) to a module that converts them into infrared signals (2), which are then transferred to the stimulation programmer device (2′). Step 4: the stimulation programmer transmits EES commands into the IPG (4) via induction telemetry, using an antenna (3) taped to the skin and aligned to the IPG. EES is delivered through the paddle array (5).

© 2018 Springer Nature Limited. All rights reserved.

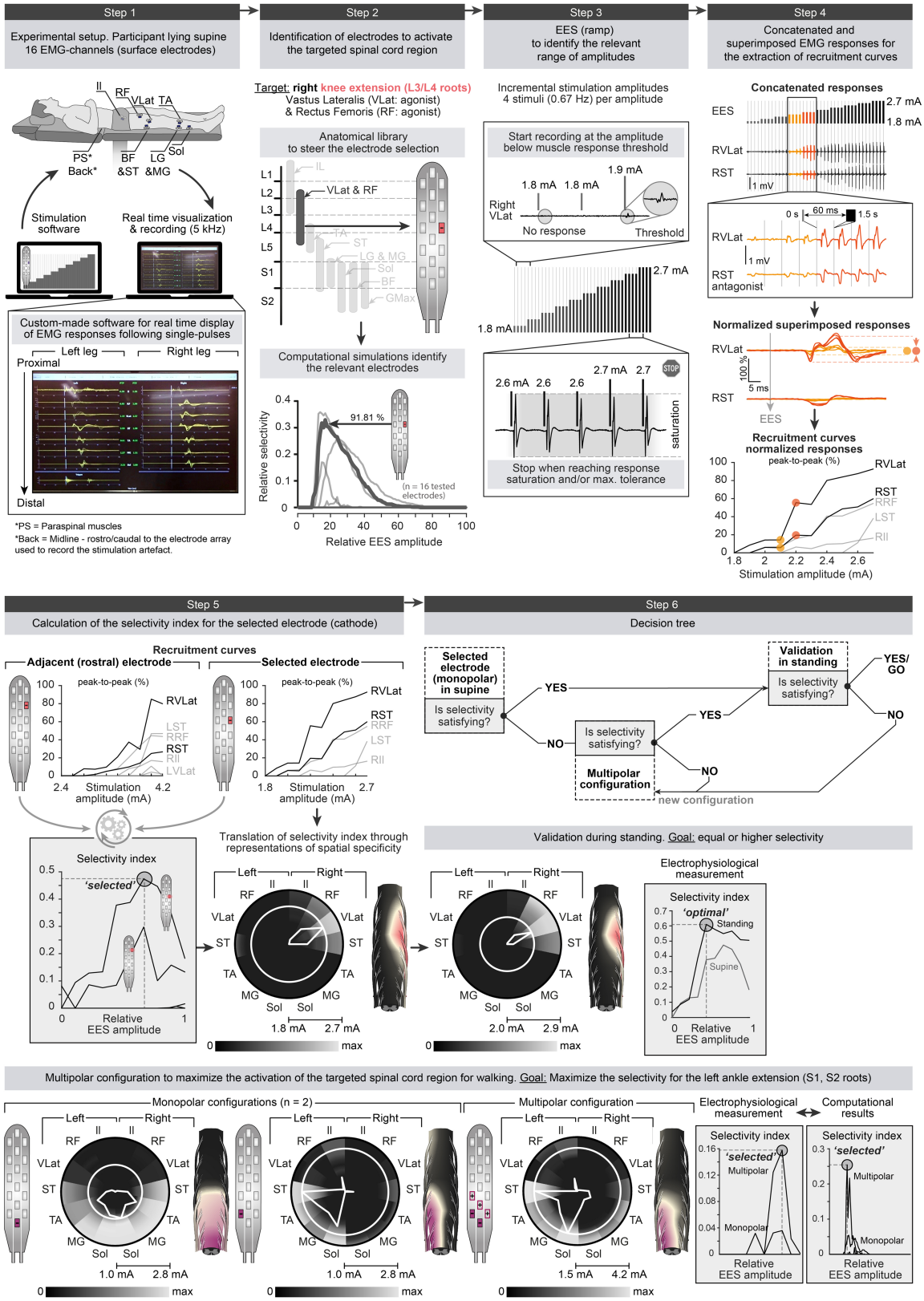

Extended Data Fig. 2 | See next page for caption.

© 2018 Springer Nature Limited. All rights reserved.

Extended Data Fig. 2 | Identification of electrode configurations to target selected posterior roots. Step 1: single-pulse EES and EMG recording setup. Step 2: motor neuron pools are located in specific segments, which provides information on the relative recruitment of each posterior root with EES. For example, electrodes targeting the L3 or L4 posterior roots will elicit the strongest EMG responses in the knee extensors. A personalized computational model of EES allows the performance of simulations that evaluate the relative activation of a given posterior root with a given electrode over the entire amplitude range. Each curve corresponds to an electrode. The highlighted curve corresponds to the electrode selected after steps 3–5. Step 3: single pulses of EES are delivered through the subset of electrodes identified by simulations. The EMG responses are recorded over a broad range of EES amplitudes. Step 4: the EMG responses are concatenated and averaged across $n = 4$ repetitions for each EMG amplitude, and the peak-to-peak amplitude of the average responses is calculated to elaborate a recruitment curve for each recorded leg muscle (black traces: targeted muscles). Step 5: the circular plots display the normalized EMG responses (greyscale) when delivering single-pulse EES at increasing amplitudes (radial axis), where the white circle highlights the optimal EES amplitude and the polygon quantifies the relative muscular selectivity at this amplitude (median response taken over $n = 4$ EES pulses). The motor neuron activation maps are shown for the optimal amplitudes. Step 6: decision tree to validate or optimize electrode configurations. The selected electrode is tested during standing as the position of the spinal cord with respect to the paddle array can change between supine and standing. In this example, the selectivity improves during standing. When the selectivity is deemed insufficient, the current is steered towards the targeted posterior roots using multipolar configurations. The example shows the increased selectivity of a multipolar configuration with two cathodes surrounded by three anodes, compared to the two corresponding monopolar configurations. These results were verified experimentally and with computer simulations.

© 2018 Springer Nature Limited. All rights reserved.

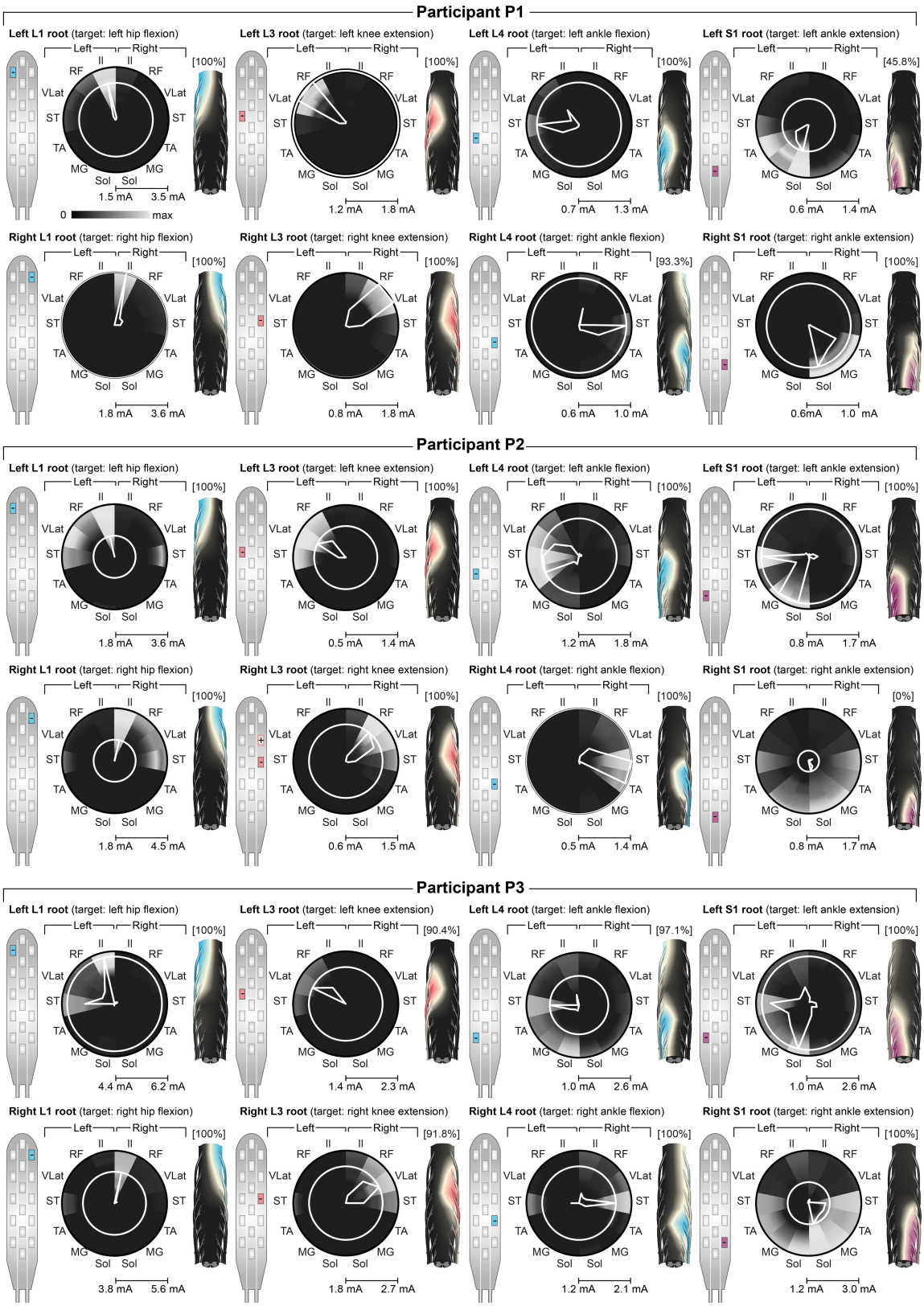

Extended Data Fig. 3 | Spatial selectivity of targeted electrode configurations. Monopolar configurations (shown on paddle array schematics) experimentally selected to target the left and right posterior roots associated with hip flexion (L1), knee extension (L3), ankle flexion (L4) and ankle extension (S1) for the three participants. The circular plots and motor neuron activation maps use the same conventions as in Fig. 2 and Extended Data Fig. 2 (median of $n = 4$ pulses). The normalized selectivity index is reported above each motor neuron activation map. This index represents the percentage of posterior root selectivity for the electrode configuration selected experimentally, with respect to the maximum posterior root selectivity that can be achieved among all monopolar configurations (all selectivity indices obtained from computational simulations). Note that in P2, the electrode selected experimentally to target the right S1 root was located on the midline and resulted in bilateral activation within computational simulations, which resulted in a normalized selectivity index of zero.

© 2018 Springer Nature Limited. All rights reserved.

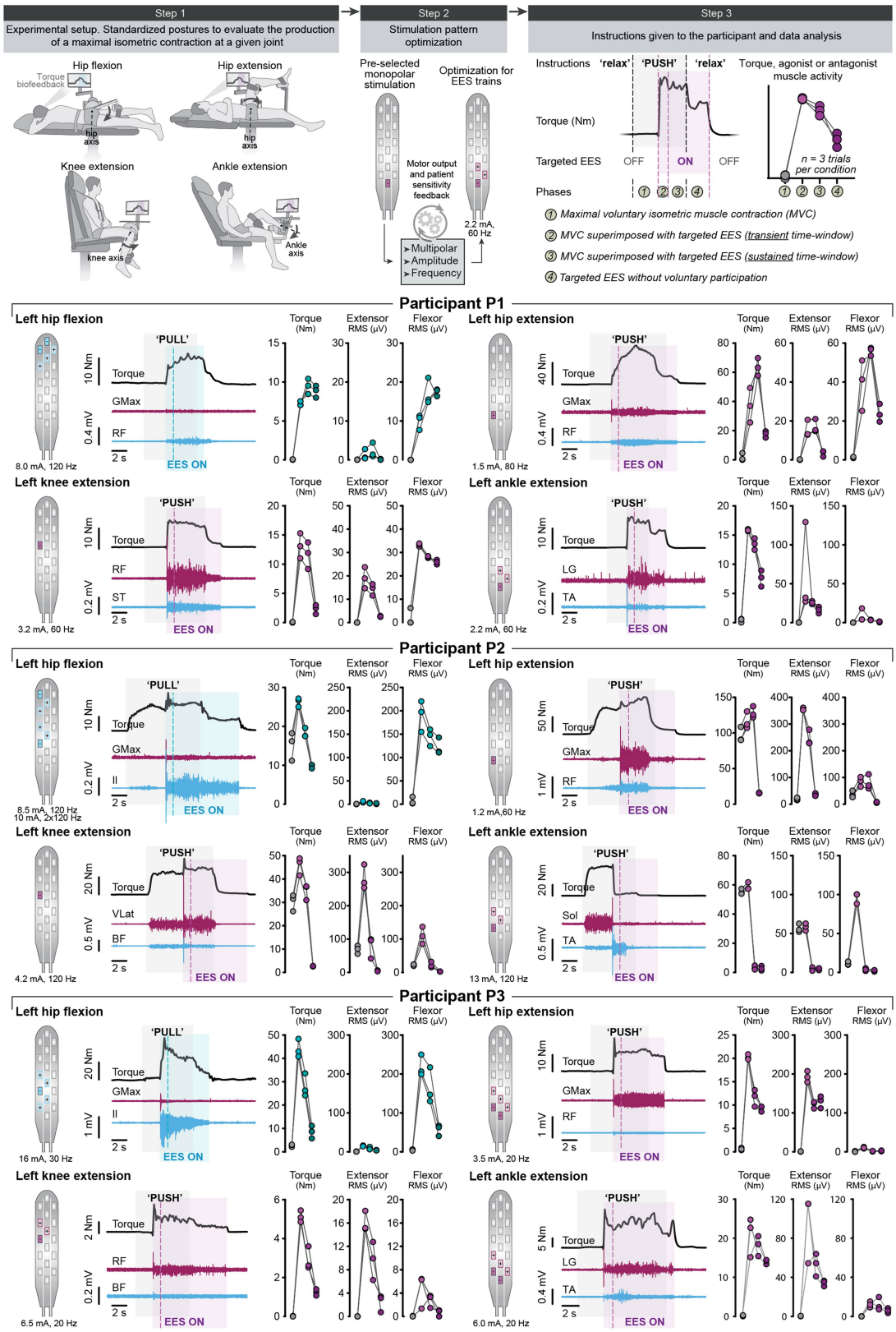

Extended Data Fig. 4 | See next page for caption.

© 2018 Springer Nature Limited. All rights reserved.

Extended Data Fig. 4 | Single-joint movements enabled by targeted EES. Step 1: participants are placed in standardized positions to allow assessment of voluntary torque production at a single joint (isometric contractions) without and with targeted EES. Step 2: EES protocols elaborated from single-pulse experiments (Extended Data Figs. 2, 3) are optimized for each task using multipolar configurations and adjustments of EES amplitude and frequency. Step 3: sequence of each trial. Participants were asked to produce a maximal voluntary contribution, but failed in most cases, as evidenced by the absence of EMG activity during this period. While they continued trying to activate the targeted muscle, EES was switched on. After a few seconds, participants were instructed to stop their voluntary contribution. After a short delay, EES was switched off. For each sequence, the produced torque and EMG activity of the key agonist and antagonist muscles acting at the targeted joint were calculated over the four indicated phases of the trial. Plots report the measured torques and EMG activity during the various phase of the trial for the left legs of all participants for the four tested joints (cyan, flexor; magenta, extensor), together with EES parameters and electrode configurations. All measurements were performed before rehabilitation, except for hip extension in P1 and P2 (not tested before), and ankle extension in P3 (no capacity before rehabilitation), which were carried out after rehabilitation. Targeted EES enabled or augmented the specific recruitment of the targeted muscle, which resulted in the production of the desired torque at the targeted joint, except for ankle extension of P2. Plots show quantification of the EMG activity and torque for $n = 3$ trials per condition. Note that hip flexion can be enabled or augmented with EES targeting L1 and/or L4 posterior roots (heteronymous facilitation of flexor motor neuron pools).

© 2018 Springer Nature Limited. All rights reserved.

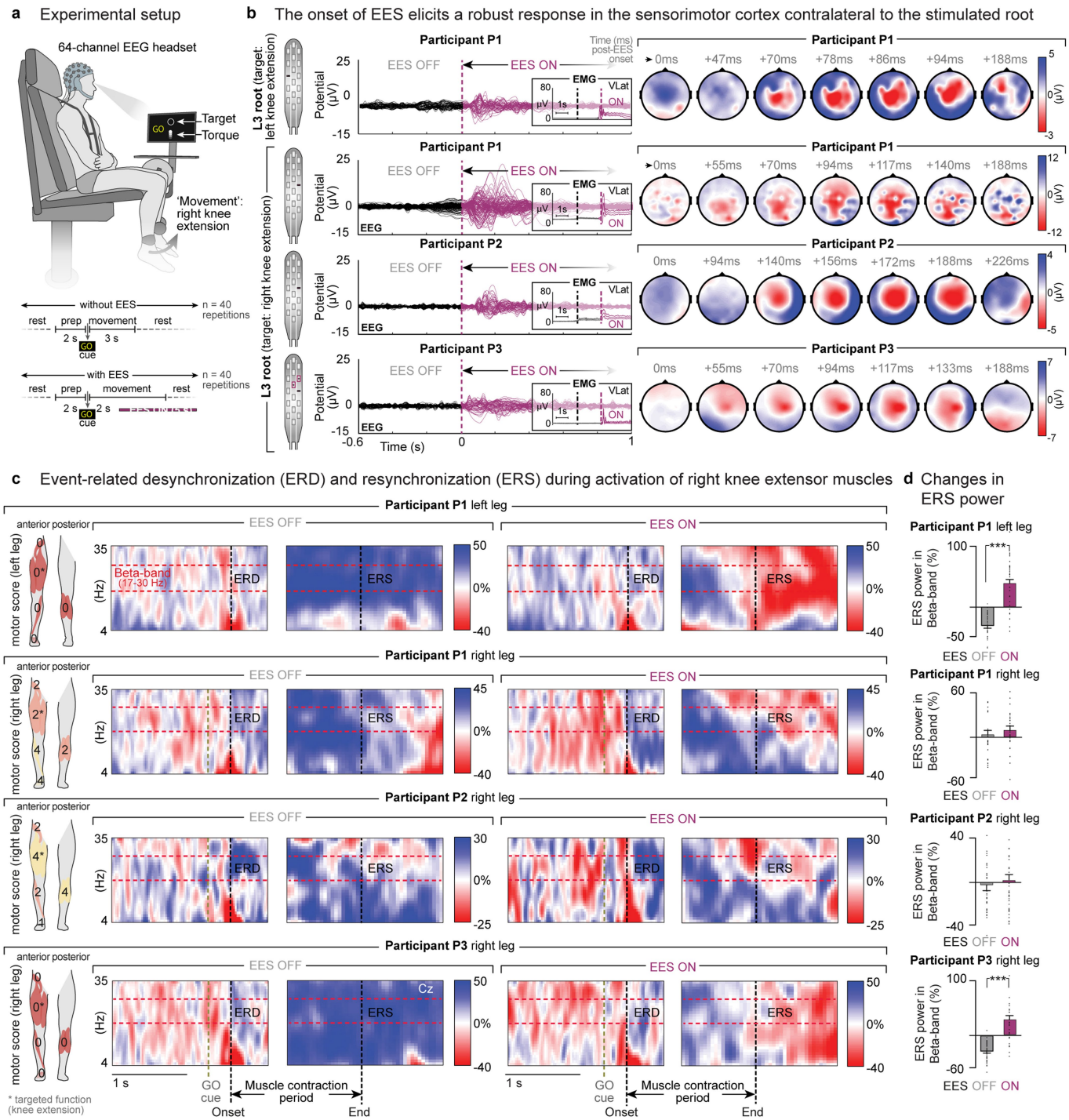

Extended Data Fig. 5 | Modulation of EEG activity during volitional contraction of leg muscles without and with EES. a, Recordings of EEG activity while participants were asked to produce an isometric torque at the knee joint without and with continuous EES targeting motor neuron pools innervating knee extensors, as shown in **b**. **b**, Superimposed EEG responses ($n = 40$ repetitions) and temporal changes in the topography of average activity over the cortical surface after the onset of EES, as indicated above each map. The onset was calculated from the onset of EMG responses in the targeted vastus lateralis muscle (insets). The stimulation elicited a robust event-related response over the left sensorimotor cortex with a latency of 90 ± 40 ms for P1 and P3, and of 170 ± 40 ms for P2 (full range of the peaks and middle of this range indicated). **c**, Average normalized time–frequency plots ($n = 40$ trials) showing ERD and ERS over the Cz electrode (central top electrode) for each individual during the voluntary activation of knee extensor muscles without and with EES. Schematic drawings (left) indicate the motor scores of the tested legs, including the targeted muscles (*), at the time of enrolment in the study. Both legs were tested in P1 owing to his asymmetric deficits. **d**, Normalized average power (mean ± s.e.m.) of the β-band over the Cz electrode during ERS from 0 to 500 ms after termination of contraction without and with continuous EES ($n = 40$ repetitions for each condition, individual data points shown except for outliers more than 3 median absolute deviations away from the median). ***$P < 0.001$ (permutation tests, see Methods).

© 2018 Springer Nature Limited. All rights reserved.

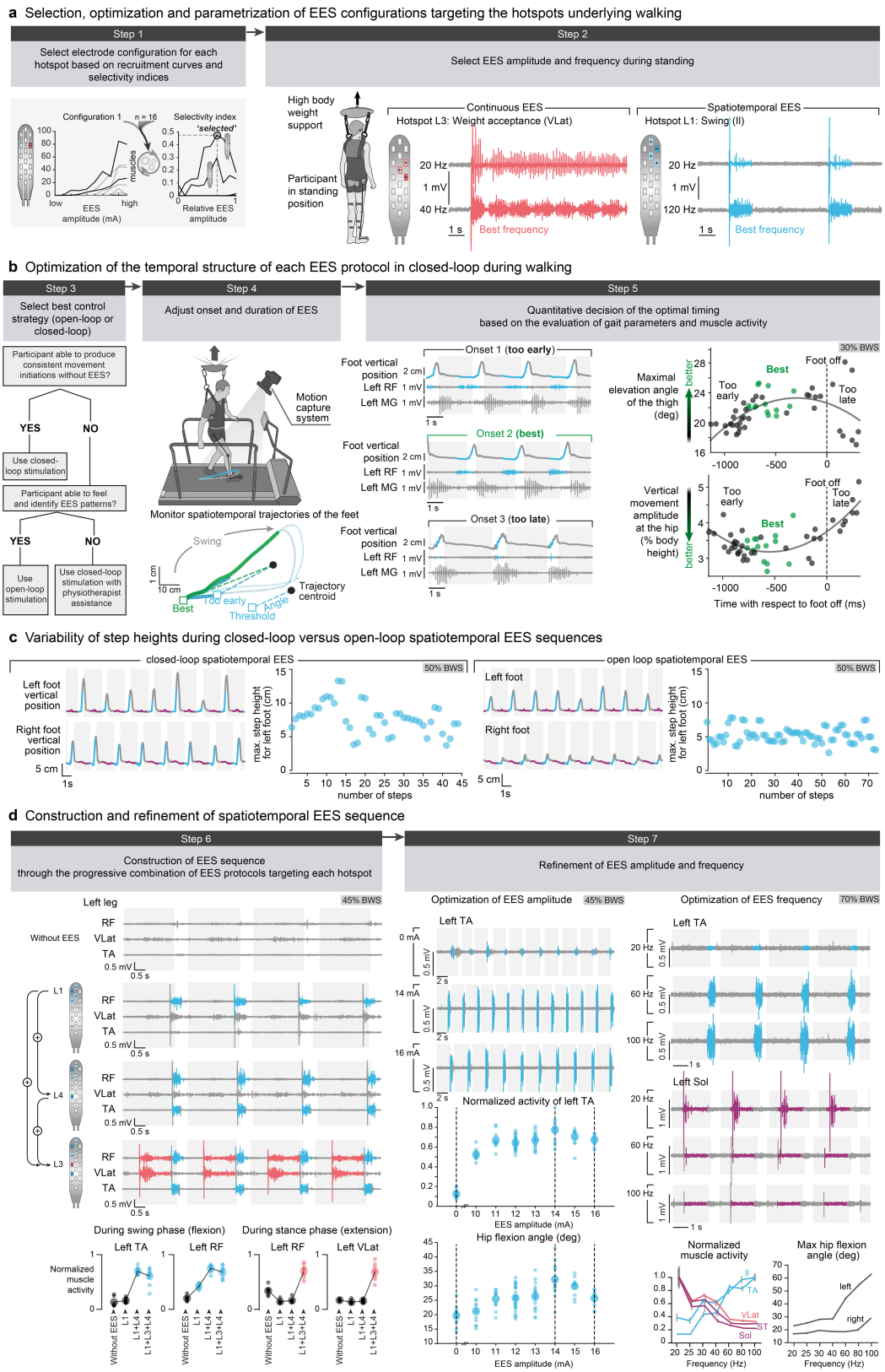

Extended Data Fig. 6 | See next page for caption.

© 2018 Springer Nature Limited. All rights reserved.

Extended Data Fig. 6 | Configuration of spatiotemporal EES to enable walking. a, Spatial configuration. Step 1: select electrode configurations from single-pulse experiments to target the three hotspots underlying the production of walking in healthy individuals (weight acceptance: L3; propulsion: S1; swing: L1/L4). Step 2: optimize EES amplitude and frequency while delivering EES during standing. Multipolar configurations can be used to refine selectivity of EES protocols. Example shows continuous EES targeting the right L3 posterior root to facilitate right knee extension during standing, and trains (500 ms) of EES targeting the right L1 posterior root stimulation to facilitate hip flexion. Two EES frequencies are shown (P3). **b**, Temporal configuration. Step 3: decision tree to select the best strategy to configure the temporal structure of EES protocols. If the participant is able to initiate leg movements consistently, use closed-loop EES based on real-time processing of foot trajectory. If the participant is not able to initiate consistent leg movements but can feel when EES is applied, use open-loop EES. If the participant is not able to generate movement and cannot feel EES, use closed-loop EES combined with physiotherapist assistance to move the legs. Step 4: real-time monitoring of the spatiotemporal trajectory of the feet. The trajectory is modelled as a foot rotating in space around the centroid of the movement (updated every 3 s). Angular thresholds determine the onset and end of EES protocols. Step 5: example showing the effect of three different angular thresholds on the onset of EES and resulting kinematics and EMG activity, including the quantification of kinematics for each step and condition that enables selecting the optimal onset of EES trains (P1). The same approach is used to optimize the duration of each train. **c**, Comparisons between closed-loop and open-loop EES. Plots show the vertical displacements of the left and right feet and successive step heights during walking with spatiotemporal EES delivered in closed loop versus open loop, showing the reduced variability of step height during pre-programmed EES sequences (P1). **d**, Resulting EMG patterns. Step 6: example of the progressive addition of EES protocols targeting specific hotspots. Plots show the quantification of EMG activity for the displayed muscles ($n = 7$ gait cycles for no EES and $n = 9$ gait cycles for each stimulation condition, P2). Step 7: EES amplitudes and frequencies are adjusted to avoid detrimental interactions between the different EES protocols and thus obtain the desired kinematic and EMG activity. Plots report the modulation of EMG activity and kinematics with increases in EES amplitude and frequency (mean ± s.e.m.; amplitude data: $n = 10, 12, 12, 30, 19, 12, 11, 10$ gait cycles for amplitudes in increasing order, P2; frequency data: $n = 20, 15, 16, 17, 15, 16, 15$ gait cycles for frequencies in increasing order, P3).

© 2018 Springer Nature Limited. All rights reserved.

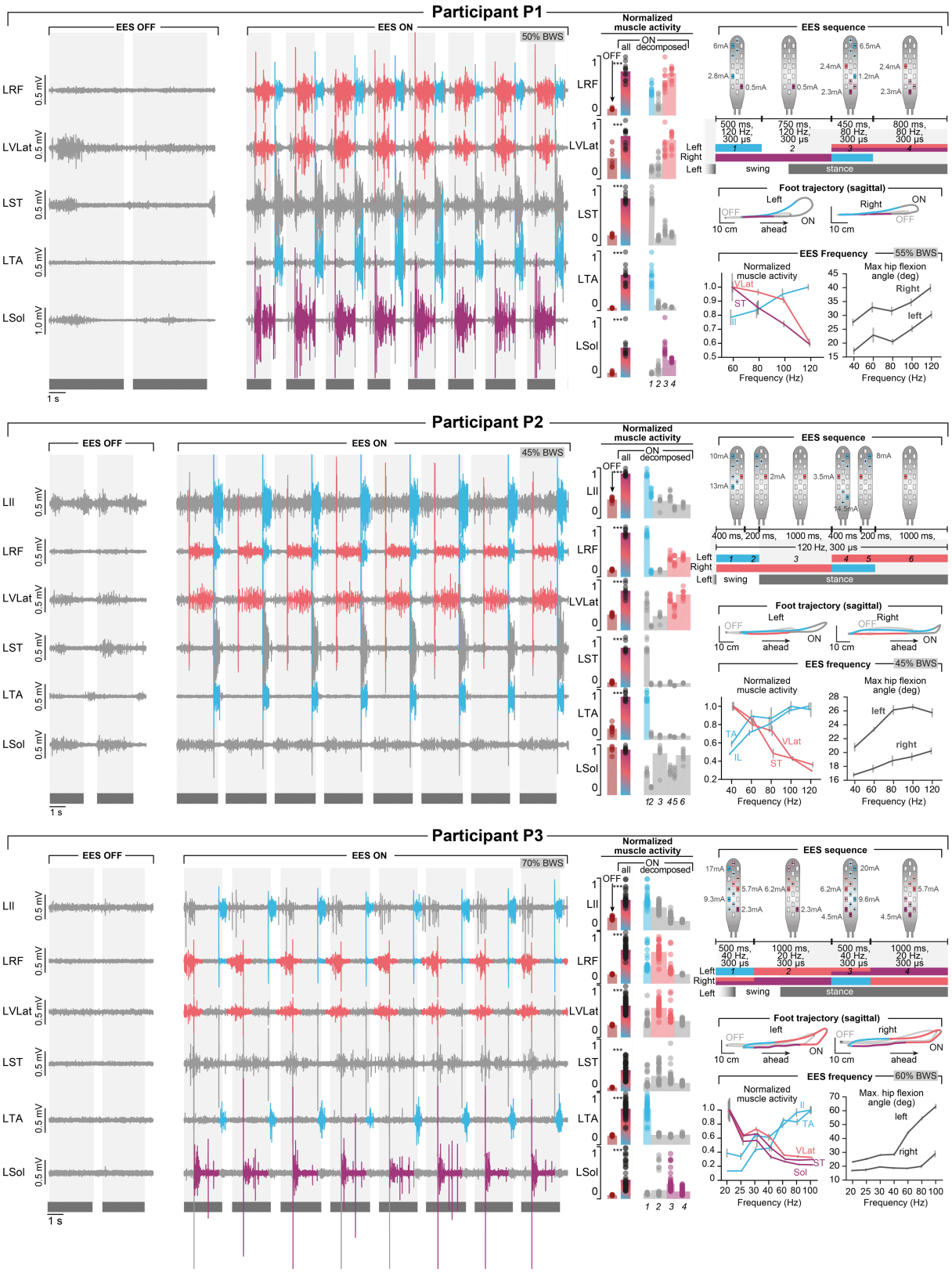

Extended Data Fig. 7 | See next page for caption.

© 2018 Springer Nature Limited. All rights reserved.

Extended Data Fig. 7 | Targeted modulation of muscle activity during walking. Each panel reports the same representative data and quantification for one participant. Left, EMG activity of leg muscles during walking on a treadmill without EES (EES OFF) and with spatiotemporal EES (EES ON) while applying 50%, 45% and 70% body weight support for participants P1, P2 and P3, respectively. Stance and swing phases are indicated by grey and white backgrounds, respectively. The personalized spatiotemporal EES sequence (open loop) is schematized at the top right. The colours of each EES protocol refer to the targeted hotspots: weight acceptance (salmon), propulsion (magenta) and swing (cyan). These colours are used in the EMG traces to indicate the temporal window over which each targeted EES protocol is active. The bar plots report the amplitude of muscle activity without EES and with spatiotemporal EES, for which the quantification was performed over the entire burst of EMG activity and during each temporal window with targeted EES. The temporal windows are labelled with a number that refers to the spatiotemporal EES sequence. These results show the pronounced increase in the EMG activity of the targeted muscles (P1, no EES: $n = 7$ gait cycles, EES: $n = 11$ gait cycles; P2, no EES: $n = 9$ gait cycles, EES: $n = 9$ gait cycles; P3, no EES: $n = 10$ gait cycles, EES: $n = 57$ gait cycles). The average spatiotemporal trajectories of both feet with respect to the hip in the sagittal plane are shown for walking without EES and with spatiotemporal EES. The presence of targeted EES is indicated with the same colour code. Plots at bottom right show the relationships between EES frequency and the modulation of the EMG activity of flexor (blue) and extensor (magenta or salmon) muscles and maximum amplitude of hip movements during walking (mean ± s.e.m.; P1: $n = 14, 17, 15, 19$ gait cycles for increasing frequencies; P2: $n = 13, 16, 10, 17, 12$ gait cycles for increasing frequencies; P3: $n = 20, 15, 16, 17, 15, 16, 15$ gait cycles for increasing frequencies). $^{***}P < 0.001$. Student's t-test.

© 2018 Springer Nature Limited. All rights reserved.

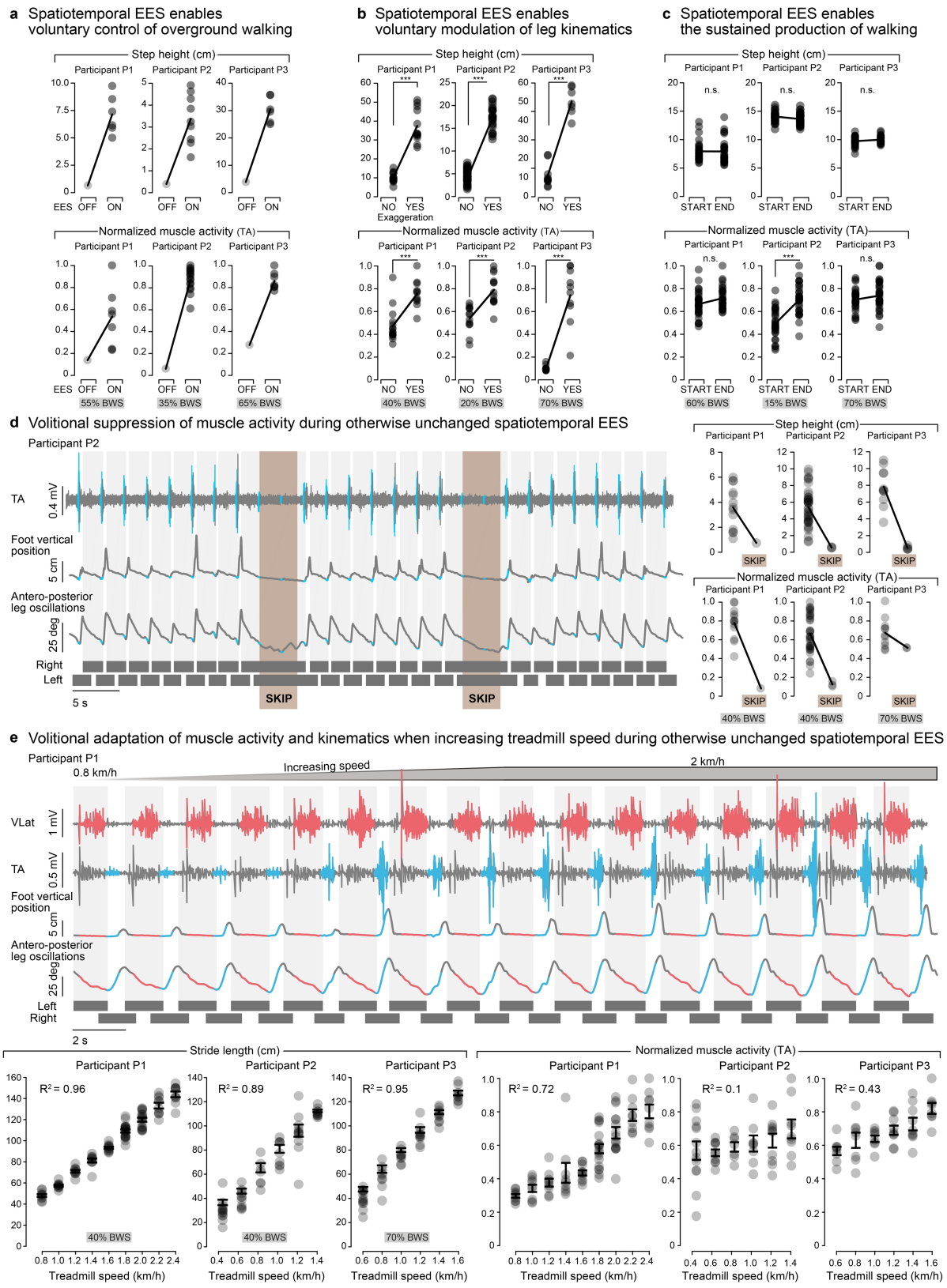

Extended Data Fig. 8 | See next page for caption.

© 2018 Springer Nature Limited. All rights reserved.

Extended Data Fig. 8 | Volitional adaptations of walking during otherwise unchanged spatiotemporal EES. a–c, Quantifications of experiments shown in Fig. 4a–c for each participant. **a**, Step height and TA EMG activity with and without EES during overground walking (P1, EES ON: $n = 7$ gait cycles; P2, EES ON: $n = 16$ gait cycles; P3, EES ON, $n = 7$ gait cycles). **b**, Step height and TA EMG activity during normal steps and when participants were requested to perform exaggerated step elevations during overground walking (P1, $n = 15$ normal gait cycles, $n = 11$ exaggerated gait cycles; P2, $n = 31$ normal gait cycles, $n = 23$ exaggerated gait cycles; P3, $n = 14$ normal gait cycles, $n = 10$ exaggerated gait cycles). **c**, Step height and TA EMG activity during the first and last 30 steps extracted from a sequence of 1 h of locomotion on a treadmill ($n = 30$ gait cycles for all conditions). ***$P < 0.001$; n.s., non-significant; Student's *t*-test. **d**, EMG activity of representative leg muscles, vertical displacements of the foot and anteroposterior oscillations of the leg (virtual limb joining the hip to the foot) while P2 was walking continuously on the treadmill with spatiotemporal EES (open loop). The participant was asked to suppress the effects of EES and stand during one cycle of open-loop spatiotemporal EES sequence, highlighted in brown (SKIP), whereas he actively contributed to the production of movement the rest of the time. Plots report the quantification of step height and TA EMG activity during walking and when skipping steps for each participant (P1, $n = 13$ normal gait cycles, $n = 1$ skipped cycles; P2, $n = 36$ normal gait cycles, $n = 3$ skipped gait cycles; P3, $n = 11$ normal gait cycles, $n = 2$ skipped cycles). **e**, EMG activity of two representative muscles, vertical displacements of the foot and anteroposterior oscillations of the leg while P1 was walking on the treadmill and the speed of the belt increased progressively from 0.8 to 2 km h^{-1}. Plots show relationships between treadmill speed and mean stride length and TA EMG activity in all participants (P1: $n = 9, 9, 9, 9, 10, 18, 15, 9, 9$ gait cycles for increasing speeds; P2: $n = 13, 10, 7, 8, 10, 9$ gait cycles for increasing speeds; P3: $n = 8, 8, 10, 9, 9, 8$ gait cycles for increasing speeds; s.e.m. shown). The range of tested speeds was adapted to the walking ability of each participant.

© 2018 Springer Nature Limited. All rights reserved.

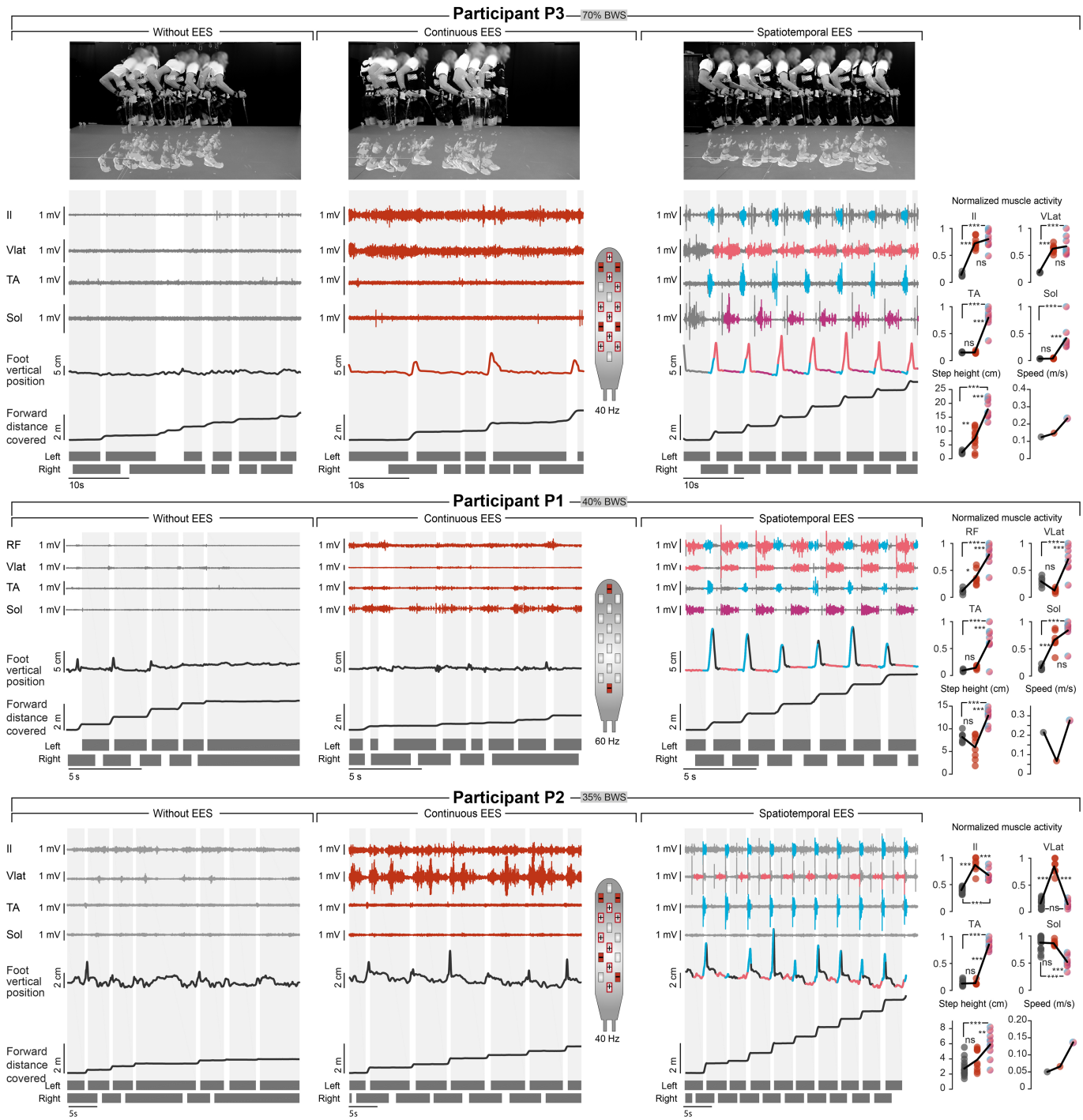

Extended Data Fig. 9 | Comparison between continuous and spatiotemporal EES during overground walking. Each panel represents one participant who is attempting to walk overground with gravity-assist without EES (left), with continuous EES (middle) and with spatiotemporal EES (right). EMG activity of representative leg muscles, vertical position of the foot and distance covered by the foot in the forward direction are displayed for each experimental condition. Continuous EES is applied throughout the trial (red). For P2 and P3, we optimized EES protocols that targeted the posterior roots on both sides, whereas EES was applied over the most rostral and most caudal midline electrodes for P1, as shown next to each plot. Spatiotemporal EES is represented using the same colour scheme as in Fig. 3 and Extended Data Fig. 7. The plots report quantification of EMG activity, step height and mean speed (based on distance covered) for the three experimental conditions (P1, $n = 6$, 7, 8 gait cycles for no EES, continuous EES and spatiotemporal EES; P2, $n = 17$, 7, 9 gait cycles for no EES, continuous EES and spatiotemporal EES; P3, $n = 6$, 10, 9 gait cycles for no EES, continuous EES and spatiotemporal EES). ***$P < 0.001$; **$P < 0.01$; n.s., non-significant. One-way ANOVA, post hoc Tukey's HSD. These recordings were repeated on at least three different days for each participant.

© 2018 Springer Nature Limited. All rights reserved.

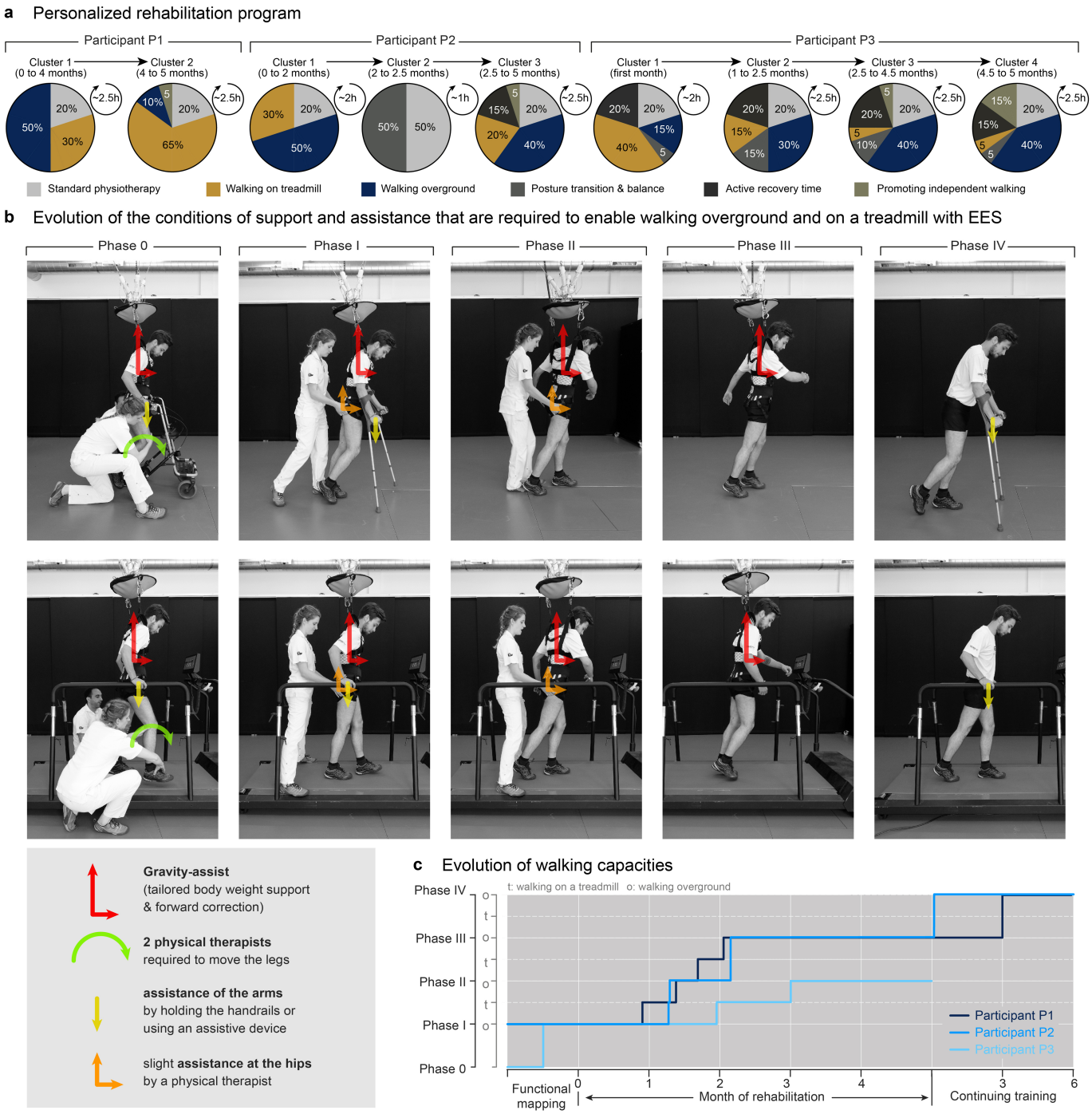

Extended Data Fig. 10 | Rehabilitation program and evolution of walking capacity. a, Rehabilitation programs were continuously personalized on the basis of the current motor performance of participants. Walking capacities evolved in phases (**b**). For this reason, the relative percentage of training in the various tasks has been divided into clusters, which correspond to the evolution of walking capacities. To facilitate the sustained production of reproducible locomotor movements (Extended Data Fig. 6c), EES was delivered in open-loop mode during gait rehabilitation. **b**, Walking capacities evolved through stereotypical phases that are illustrated in the snapshots. **c**, Plots showing the progression of the three participants along the phases of recovery during the rehabilitation program, and during the subsequent 6 months for P1 and P2. P3 had just completed the rehabilitation program at the time of submission of this study. See also Supplementary Video 4.

© 2018 Springer Nature Limited. All rights reserved.

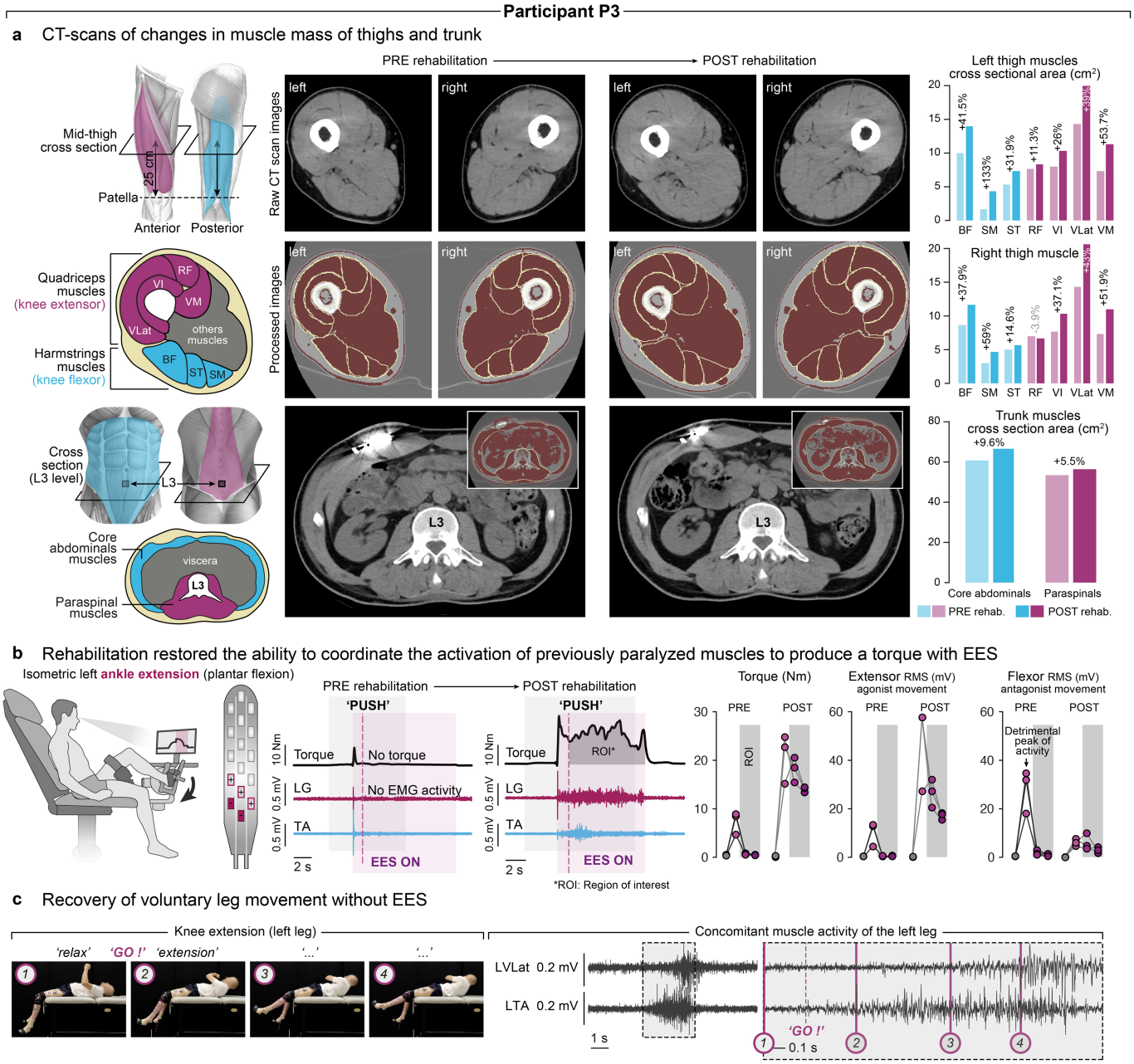

Extended Data Fig. 11 | Changes in muscle mass and quality and recovery of voluntary movements with and without EES in participant P3. a, Skeletal muscle mass and quality were assessed at the pre- and post-rehabilitation time points using X-ray attenuation from CT images obtained at the abdomen (L3 vertebra) and mid-thigh (25 cm above femorotibial joint space). Muscle mass was determined by measuring the cross-sectional areas (CSAs) of muscle tissues, while muscle quality was reflected by CT attenuation numbers (in Hounsfield units, HU) within the CSAs. Muscle segmentations were performed semi-automatically using ImageJ and muscle-specific HU thresholds (–29 to 150 HU). Plots report the substantial changes in muscle mass at mid-thigh, for both flexor and extensor muscles, and of trunk muscles. Muscle quality was also improved at both levels: total mid-thigh, left: 52.9 to 56.1 HU, right: 51.9 to 56.7 HU; total L3, 45.9 to 48.3 HU. This increase in CT attenuation numbers between the baseline CT scan and the follow-up imaging reflected the decrease in muscle fibre lipid content at the mid-thigh and abdomen. These evaluations were part of a protocol amendment obtained when enrolling P3. **b**, Assessment of voluntary torque production at the ankle (extension) with targeted EES before and after rehabilitation. Conventions are as in Extended Data Fig. 4. **c**, Snapshots showing voluntary extension of the left leg against the direction of gravity together with the concomitant sequence of EMG activity in the extensor and flexor muscles of this leg. The zoomed window shows the relationship between the movement and the EMG activity, indicated with the numbers. This participant presented flaccid paralysis, and had thus no control over leg muscles before the surgery. This movement was observed repeatedly at the end of the rehabilitation period (at least two days per week for several weeks).

© 2018 Springer Nature Limited. All rights reserved.

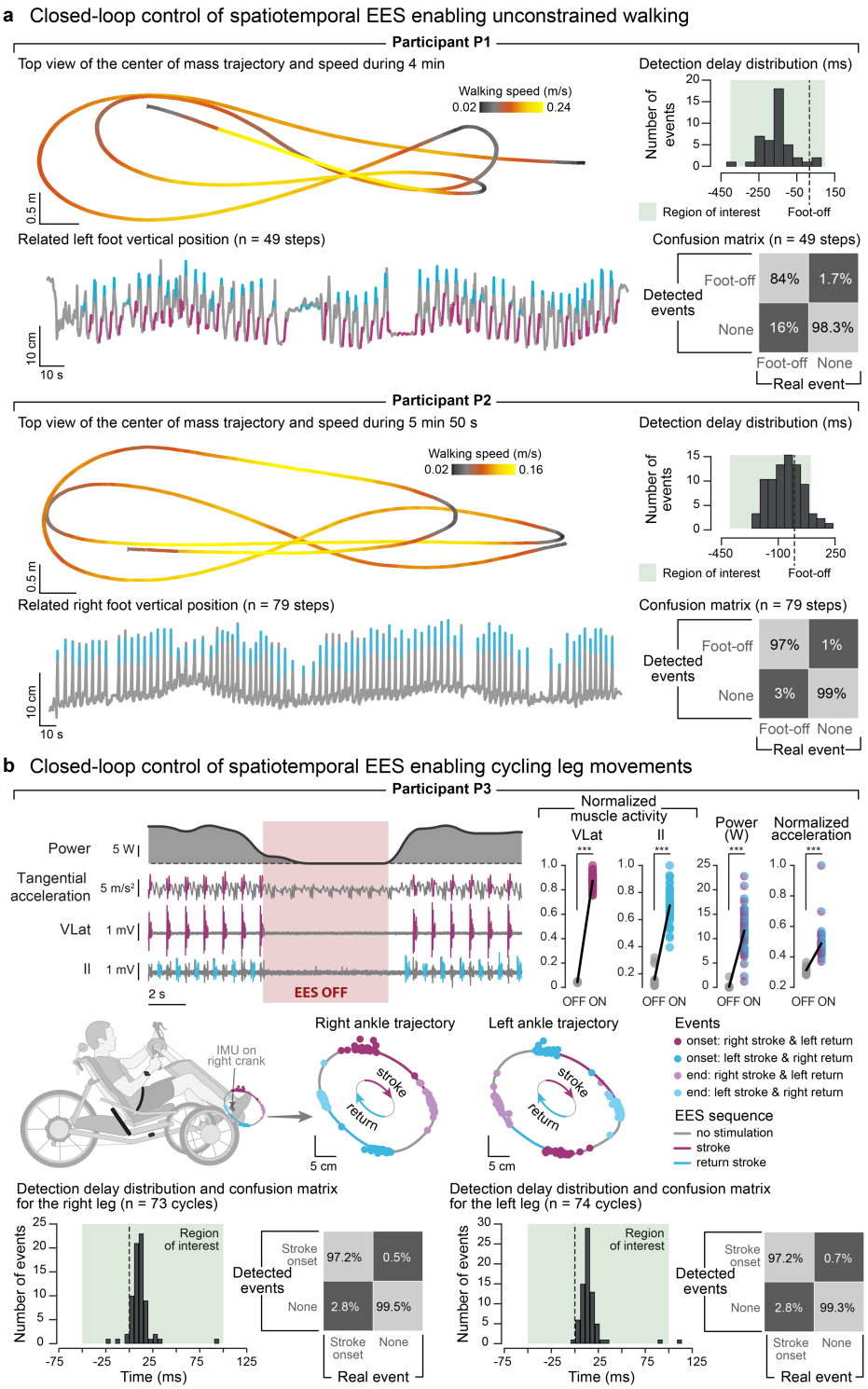

Extended Data Fig. 12 | Performance of closed-loop spatiotemporal EES to enable walking and cycling outside the laboratory. a, P1 and P2 were asked to walk freely overground with a walker (no body weight support) for 6 min. The concomitant vertical displacements of the foot show the consistency of EES triggering events despite variable foot kinematics and voluntary breaks. The trajectory of the centre of mass is shown from a top view to illustrate the ability to steer locomotion along any desired path. EES protocols took into account the deficits of each participant (cyan, EES targeting hip flexion; magenta, EES targeting knee and ankle extension). Histograms indicate the number of detected foot-off events for the represented leg as a function of the latency with respect to real foot-off events. The confusion matrix associated with these detections is represented below, as a percentage of the real events that were correctly or incorrectly classified. Detections were considered valid if they occurred between 400 ms before and 100 ms after real foot-off events, as highlighted in green on histograms (P1, $n = 49$ gait cycles; P2, $n = 79$ gait cycles). **b**, Closed-loop spatiotemporal EES was delivered in P3 using an electric trike powered by hand and foot pedals. Traces show EMG activities of the targeted hip flexor and knee extensor muscles on one leg together with the tangential acceleration of the pedal and power generated at the foot pedal. Plots report the quantification of flexor and extensor EMG activities, peak tangential accelerations and generated power without and with EES. Successive ankle trajectories during cycling are shown together with the timing of EES protocols targeting the hip flexor and knee extensor muscles. The histograms and confusion matrices report the performance of the controller following the same conventions as in **a**, except that the correct detection window was restricted to 50 ms before and 100 ms after the desired crank position (P3: $n = 73$ pedalling cycles). ***$P < 0.001$. Student's t-test.

© 2018 Springer Nature Limited. All rights reserved.

Extended Data Table 1 | Neurological statuses of participants

Participant		**P1**		**P2**		**P3**	
Gender		m		m		m	
Age (y)		28		35		47	
Years after SCI		6		6		4	
Assessments at study enrollment (Pre) and after rehabilitation period (Post)		Pre	Post	Pre	Post	Pre	Post
Walking index for spinal cord injury (WISCI II score; max. 20)		13	16	6	13	0	0
American Spinal Injury Association Impairment Scale (AIS)		C	D	D	D	C*	C
Neurological level of injury		C7	C8	C4	C4	C7	C7
Upper Extremity Motor Scores:							
C5, elbow flexors	(right | left)	5 | 5	5 | 5	5 | 5	5 | 5	5 | 5	5 | 5
C6, wrist extensors	(right | left)	5 | 5	5 | 5	5 | 4	4 | 4	5 | 5	5 | 5
C7, elbow extensors	(right | left)	5 | 5	5 | 5	4 | 4	4 | 4	5 | 4	5 | 5
C8, finger flexors	(right | left)	4 | 4	5 | 4	1 | 0	3 | 1	4 | 4	4 | 5
T1, finger abductors	(right | left)	4 | 4	4 | 4	3 | 0	3 | 0	4 | 4	4 | 4
(max. 5 per side)							
Total (max. 50)		46	47	31	33	45	47
Lower Extremity Motor Scores:							
L2, hip flexors	(right | left)	2 | 0	4 | 2	2 | 2	3 | 2	0 | 0	0 | 1
L3, knee extensors	(right | left)	2 | 0	4 | 3	4 | 4	4 | 4	0 | 0	1 | 0
L4, ankle dorsiflexors	(right | left)	4 | 0	4 | 1	2 | 1	4 | 4	0 | 0	0 | 1
L5, long toe extensors	(right | left)	4 | 0	4 | 2	1 | 1	2 | 4	0 | 0	0 | 1
S1, ankle plantar flexors	(right | left)	2 | 0	4 | 2	4 | 4	5 | 4	0 | 0	0 | 0
(max. 5 per side)							
Total (max. 50)		14	30	25	36	0	4
Light Touch Sensory Scores:							
L1-S2 dermatomes subscore	(right | left)	7 | 7	7 | 7	5 | 8	2 | 10	1 | 4	2 | 5
(max. 14 per side)							
Total (max. 112)		75	76	65	71	55	57
Pin Prick Sensory Scores:							
L1-S2 dermatomes subscore	(right | left)	0 | 0	0 | 0	4 | 8	1 | 13	0 | 0	0 | 0
(max. 14 per side)							
Total (max. 112)		33	30	65	86	28	28

Subjects' neurological status according to the International Standards for Neurological Classification of Spinal Cord Injury at study entry and after completion of the five-month training program.
*Reason for AIS C classification in spite of motor scores of 0 throughout all lower extremity key muscles is the presence of voluntary anal contraction.

© 2018 Springer Nature Limited. All rights reserved.

ARTICLE

https://doi.org/10.1038/s41586-018-0654-5

Shared and distinct transcriptomic cell types across neocortical areas

Bosiljka Tasic[1]*, Zizhen Yao[1,4], Lucas T. Graybuck[1,4], Kimberly A. Smith[1,4], Thuc Nghi Nguyen[1], Darren Bertagnolli[1], Jeff Goldy[1], Emma Garren[1], Michael N. Economo[2], Sarada Viswanathan[2], Osnat Penn[1], Trygve Bakken[1], Vilas Menon[1,2], Jeremy Miller[1], Olivia Fong[1], Karla E. Hirokawa[1], Kanan Lathia[1], Christine Rimorin[1], Michael Tieu[1], Rachael Larsen[1], Tamara Casper[1], Eliza Barkan[1], Matthew Kroll[1], Sheana Parry[1], Nadiya V. Shapovalova[1], Daniel Hirschstein[1], Julie Pendergraft[1], Heather A. Sullivan[3], Tae Kyung Kim[1], Aaron Szafer[1], Nick Dee[1], Peter Groblewski[1], Ian Wickersham[3], Ali Cetin[1], Julie A. Harris[1], Boaz P. Levi[1], Susan M. Sunkin[1], Linda Madisen[1], Tanya L. Daigle[1], Loren Looger[2], Amy Bernard[1], John Phillips[1], Ed Lein[1], Michael Hawrylycz[1], Karel Svoboda[2], Allan R. Jones[1], Christof Koch[1] & Hongkui Zeng[1]

The neocortex contains a multitude of cell types that are segregated into layers and functionally distinct areas. To investigate the diversity of cell types across the mouse neocortex, here we analysed 23,822 cells from two areas at distant poles of the mouse neocortex: the primary visual cortex and the anterior lateral motor cortex. We define 133 transcriptomic cell types by deep, single-cell RNA sequencing. Nearly all types of GABA (γ-aminobutyric acid)-containing neurons are shared across both areas, whereas most types of glutamatergic neurons were found in one of the two areas. By combining single-cell RNA sequencing and retrograde labelling, we match transcriptomic types of glutamatergic neurons to their long-range projection specificity. Our study establishes a combined transcriptomic and projectional taxonomy of cortical cell types from functionally distinct areas of the adult mouse cortex.

The neocortex coordinates most flexible and learned behaviours[1,2]. In mammalian evolution, the cortex underwent greater expansion in the number of cells, layers and functional areas compared to the rest of the brain, coinciding with the acquisition of increasingly sophisticated cognitive functions[3]. On the basis of cytoarchitectonic, neurochemical, connectional and functional studies, up to 180 distinct cortical areas have been identified in humans[4] and dozens in rodents[5,6]. Cortical areas have laminar structure (layers (L) 1–6), and are often categorized as sensory, motor or associational, on the basis of their connections with other brain areas. Different cortical areas show qualitatively different activity patterns. Primary visual (VISp) and other sensory cortical areas process sensory information with millisecond timescale dynamics[7–9]. Frontal areas, such as the anterior lateral motor cortex (ALM) in mice, show slower dynamics related to short-term memory, deliberation, decision-making and planning[10–12]. Categorizing cortical neurons into types, and studying the roles of different types in the function of the circuit, is an essential step towards understanding how different cortical circuits produce distinct computations[13,14].

Previous studies have characterized various neuronal properties to define numerous types of glutamatergic (excitatory) and GABAergic (inhibitory) neurons in the rodent cortex[15–20]. Reconciling the morphological, neurophysiological and molecular properties into a consensus view of cortical types remains a major challenge. We leveraged the scalability of single-cell RNA sequencing (scRNA-seq) to define cell types in two distant cortical areas. We analysed 14,249 cells from the VISp and 9,573 cells from the ALM to define 133 transcriptomic types and establish correspondence between glutamatergic neuron projection patterns and their transcriptomic identities. In the accompanying paper[21], we show that transcriptomic L5 types with different subcortical projections have distinct roles in movement planning and execution.

Overall cell type taxonomy

Building on our previous study[20], we established a standardized pipeline for scRNA-seq (Extended Data Figs. 1–4). Individual cells were isolated by fluorescence-activated cell sorting (FACS) or manual picking, cDNA was generated and amplified by the SMART-Seq v4 kit, and cDNA libraries were tagemented by Nextera XT and sequenced on the Illumina HiSeq2500 platform, resulting in the detection of approximately 9,500 genes per cell (median; Extended Data Fig. 4).

We report 23,822 single-cell transcriptomes with cluster-assigned identity, validated by quality control measures (Extended Data Fig. 2b). The cells were isolated from the VISp and ALM of adult mice (96.3% at postnatal day (P) 53–59, Supplementary Table 1) of both sexes, in the congenic C57BL/6J background (Extended Data Fig. 1a). We obtained 10,752 cells from layer-enriching dissections of ALM and VISp of pan-neuronal, pan-glutamatergic or pan-GABAergic recombinase driver lines crossed to recombinase reporters (referred to as the PAN collection; Extended Data Fig. 1, Supplementary Table 2). To sample non-neuronal cells, compensate for cell survival biases, and collect rare types, we supplemented the PAN collection with 10,414 cells isolated from a variety of recombinase driver lines and reporter-negative cells, with or without layer-enriching dissections (Extended Data Fig. 1b, h, i). To investigate the correspondence between transcriptomic types and neuronal projection properties, we analysed 2,656 retrogradely labelled cells (retro-seq dataset, Fig. 1a), resulting in 2,204 cells in the annotated retro-seq dataset (Extended Data Fig. 2c).

We defined 133 clusters by combining iterative, bootstrapped dimensionality reduction with clustering (Extended Data Fig. 2b). After clustering, we evaluated cluster membership to assign core versus intermediate identity to each cell: core cells (21,195 cells) are reliably classified into the original cluster (in more than 90 out of 100 trials); others are labelled intermediate[20] (2,627 cells; Extended Data Fig. 2b).

[1]Allen Institute for Brain Science, Seattle, WA, USA. [2]Janelia Research Campus, Howard Hughes Medical Institute, Ashburn, VA, USA. [3]Massachusetts Institute of Technology, Cambridge, MA, USA. [4]These authors contributed equally: Zizhen Yao, Lucas T. Graybuck, Kimberly A. Smith. *e-mail: bosiljkat@alleninstitute.org

© 2018 Springer Nature Limited. All rights reserved.

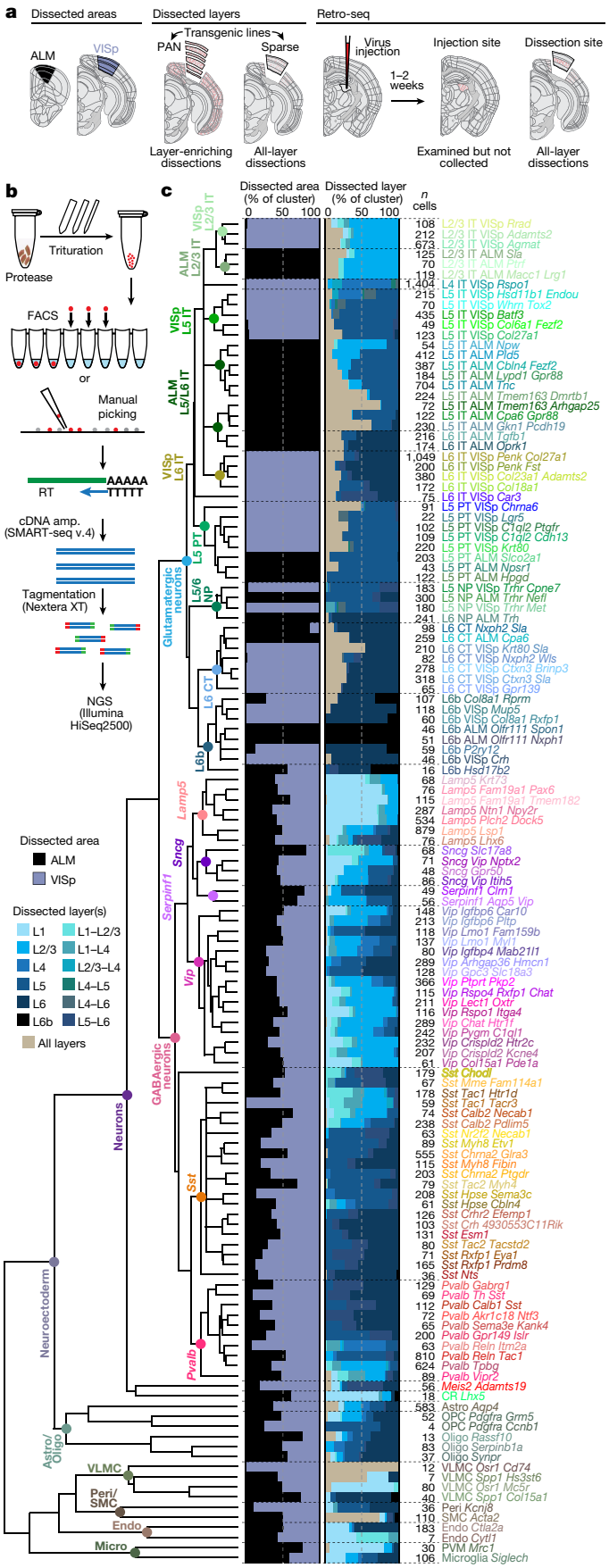

Fig. 1 | Cell type taxonomy in ALM and VISp cortical areas. **a**, Transgenically or retrogradely labelled cells and unlabelled cells were collected by layer-enriching or all-layer microdissections from the ALM or VISp. **b**, After dissociation, single cells were isolated by FACS or manual picking, mRNA was reverse transcribed (RT), amplified (cDNA amp.), tagmented and sequenced (next-generation sequencing, NGS). **c**, Clustering revealed 61 GABAergic, 56 glutamatergic, and 16 non-neuronal types organized in a taxonomy on the basis of median cluster expression for 4,020 differentially expressed genes, $n = 23{,}822$ cells and branch confidence scores > 0.4 (Extended Data Figs. 1–3). Cell classes and subclasses are labelled at branch points of the dendrogram. Bar plots represent fractions of cells dissected from the ALM and VISp, and from different layer-enriching dissections. Astro, astrocyte; CR, Cajal–Retzius cell; endo, endothelial cell; oligo, oligodendrocyte; OPC, oligodendrocyte precursor cell; peri, pericyte; PVM, perivascular macrophage; SMC, smooth muscle cell; VLMC, vascular lepotomeningeal cell; IT, intratelencephalic; PT, pyramidal tract; NP, near-projecting; CT, corticothalamic. Brain diagrams were derived from the Allen Mouse Brain Reference Atlas (version 2 (2011); downloaded from https://brain-map.org/api/index.html).

By assigning identity to each cluster based on previously reported and newly discovered differentially expressed genes (Extended Data Fig. 5), we identified 56 glutamatergic, 61 GABAergic and 16 non-neuronal types (Fig. 1). These types correspond well to the 49 types from our previous study[20], with better resolution provided in the current dataset (Extended Data Fig. 6). Sub-sampling analysis shows that for most clusters, we sampled many more cells than needed to define them (Extended Data Fig. 7). The use of many transgenic lines enabled focused access to select rare types, and allowed us to define cell types labelled by each line (Extended Data Fig. 8).

A clear hierarchy of transcriptomic cell types and their relationships emerged (Fig. 1). Consistent with previous reports[19,20], the biggest differences are observed between non-neuronal ($n = 1{,}383$) and neuronal ($n = 22{,}439$) cells. We refer to major branches as classes (for example, glutamatergic class), and related groups of types as subclasses (for example, L6b subclass) (Fig. 1c). We do not assign subclass or class to isolated branches (for example, CR–*Lhx5* cells). We detect all previously defined non-neuronal classes in the cortex (Extended Data Fig. 9).

Most neurons fall into two major branches corresponding to glutamatergic and GABAergic classes (Fig. 1). There are two exceptions: CR–*Lhx5* and *Meis2–Adamts19*, two distant branches preceding the major glutamatergic and GABAergic split. On the basis of marker expression and cell source, *Meis2–Adamts19* corresponds to the *Meis2*-expressing GABAergic neuronal type largely confined to white matter that originates from the embryonic pallial–subpallial boundary[22]. Among GABAergic types, this is the only type that reliably expresses the transcription factor *Meis2* mRNA, and transcribes the smallest number of genes (median = 4,965, Extended Data Fig. 4b). CR–*Lhx5* corresponds to Cajal–Retzius (CR) cells based on their location in L1 and expression of known Cajal–Retzius markers, such as *Trp73*, *Lhx5* and *Reln*[23,24] (Extended Data Fig. 5). Almost all GABAergic types contain cells from both ALM and VISp (Figs. 1c, 2a) with the exception of *Sst–Tac1–Tacr3* and *Pvalb–Reln–Itm2a* types, which are VISp-specific. By contrast, the glutamatergic types are mostly segregated by area (Figs. 1c, 2a), with the exception of five shared types: one L6 CT type, three L6b types and the CR–*Lhx5* type.

We performed differential gene expression tests between the best-matched ALM- and VISp-specific types (mostly glutamatergic; Extended Data Fig. 10c) and between ALM- and VISp-portions of shared types (mostly GABAergic and non-neuronal) (Fig. 2b). We find that the best-matched glutamatergic types have a median of 78 differentially expressed genes and average eightfold difference in expression (Fig. 2b, Supplementary Table 3). We find more ALM-enriched genes (Fig. 2c, d). We confirm the area-specific expression of several genes by RNA in situ hybridization (ISH) from the Allen Brain Atlas[25] (Extended Data Fig. 10d, e). By contrast, the GABAergic neurons from the two areas belonging to the same cluster have a median of 2 (and at most 19) differentially expressed genes, with an average 5.2-fold difference in expression (Fig. 2b, left).

Glutamatergic taxonomy by scRNA-seq and projections

Most cortical glutamatergic neurons project outside of their resident area, and genetic markers have been correlated with projection

© 2018 Springer Nature Limited. All rights reserved.

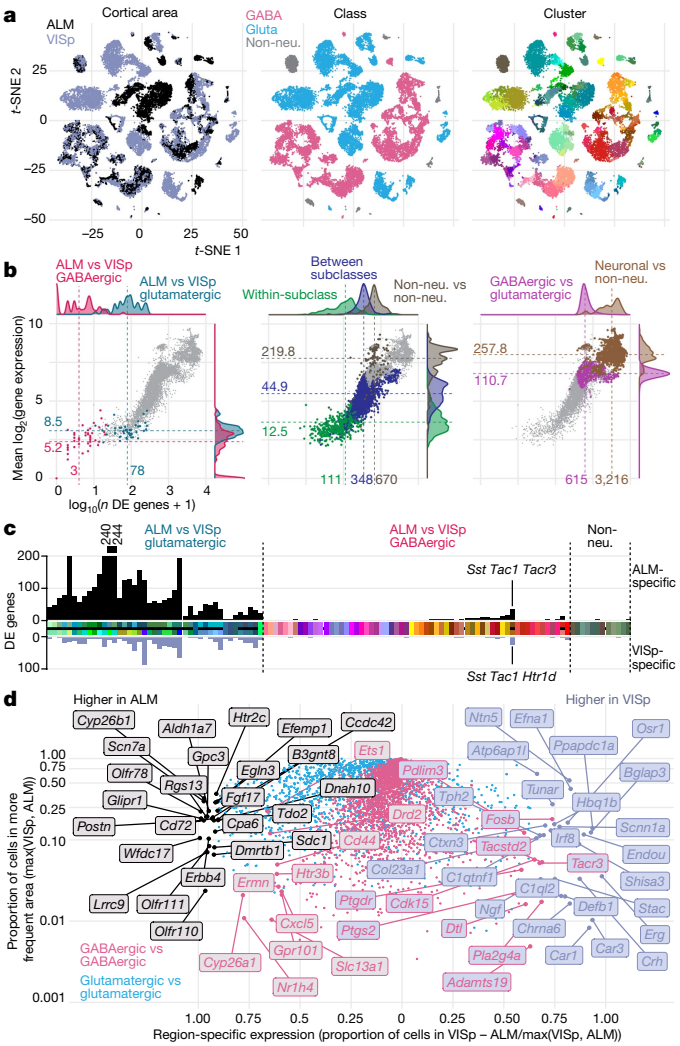

Fig. 2 | Comparison of gene expression differences among types across cortical areas. a, Two-dimensional *t*-distributed stochastic neighbour embedding (*t*-SNE) plots based on 4,020 differentially expressed genes for $n = 23{,}822$ cells, coloured by region, class and cluster. Most glutamatergic types are ALM- or VISp-specific. Most GABAergic types contain cells from both regions (salt-and-pepper clusters, left *t*-SNE). **b**, Number of differentially expressed (DE) genes (*x* axis) and mean difference in gene expression (*y* axis) for all 8,778 pairs of clusters. Left, comparisons between ALM and VISp portions of each GABAergic cluster (pink) and best-matched glutamatergic ALM and VISp clusters (blue). For comparison, centre and right panels show differences between: types within a subclass, types from different subclasses, non-neuronal types, types from different neuronal classes (GABA versus glutamate), and neuronal and non-neuronal types. Grey points represent all pairwise type comparisons; pink points are only in the left panel. **c**, Number of differentially expressed genes between best-matched ALM- and VISp-specific cell types (Extended Data Fig. 10c) or ALM and VISp portions for shared types. Cell types on the *x* axis are coloured as in Fig. 1; black horizontal line separates matched ALM and VISp types, but not the shared types. Black and grey bars denote the numbers of ALM- and VISp-enriched genes, respectively. **d**, ALM- or VISp-specific genes based on the proportion of cells in each region that express each gene, calculated separately for glutamatergic and GABAergic cells.

properties[15,26,27]. To inform our transcriptomic taxonomy with neuronal projection properties, we analysed the transcriptomes of 2,204 cells labelled by retrograde injections (retro-seq dataset; Fig. 3a, Extended Data Fig. 2c). Projection targets (Fig. 3b, Extended Data Fig. 10) were selected based on the Allen Mouse Brain Connectivity Atlas[28] and other anatomical data[29]. Retro-seq cells were processed through the same pipeline including clustering with all other cells.

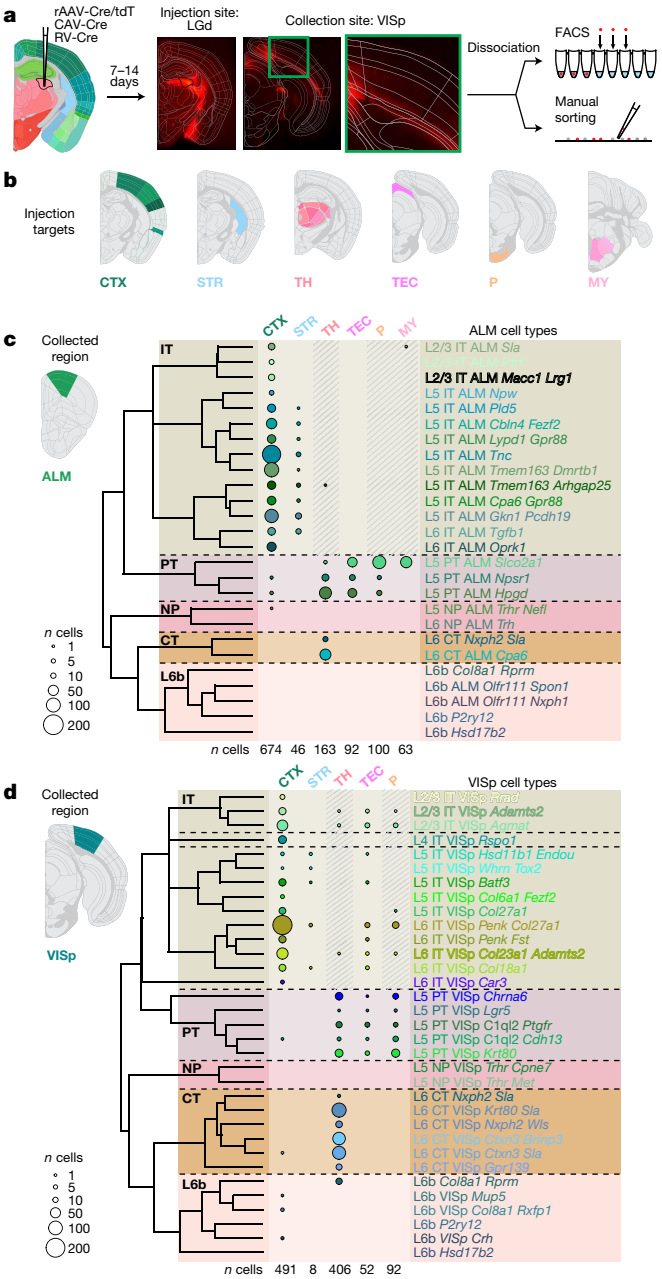

Fig. 3 | Glutamatergic cell types by scRNA-seq and projections. a, Retro-seq: after virus injections and brain sectioning, injection sites were imaged to determine injection specificity. Tissue was microdissected from the collection site (ALM or VISp) and processed as shown in Fig. 1b. **b**, Injection targets grouped into broad regions: cortex (CTX), striatum (STR), thalamus (TH), tectum (TEC), pons (P) or medulla (MY). **c**, Dendrogram of glutamatergic cell types in ALM followed by numbers of cells (represented by disc area) originating from retrograde labelling from regions on top. Shaded regions denote cells labelled unintentionally, directly or retrogradely through the needle (injection) tract. **d**, As in **c**, but for VISp. Only glutamatergic cells from the annotated retro-seq dataset were included: $n = 1{,}138$ out of 1,152 annotated cells in **c**, and 1,049 out of 1,052 annotated cells in **d**. See Extended Data Fig. 10a, b for further details. Brain diagrams were derived from the Allen Mouse Brain Reference Atlas (version 2 (2011); downloaded from https://brain-map.org/api/index.html).

We assigned identities to glutamatergic neuron types based on their projection patterns (Fig. 3c, d), dominant layer-of-dissection (Figs. 1c, 4b), and expression of marker genes (Fig. 4c, Extended Data Fig. 5). We represent the relationships between types by a constellation diagram and a dendrogram (Fig. 4a,b). VISp and ALM contain common subclasses

© 2018 Springer Nature Limited. All rights reserved.

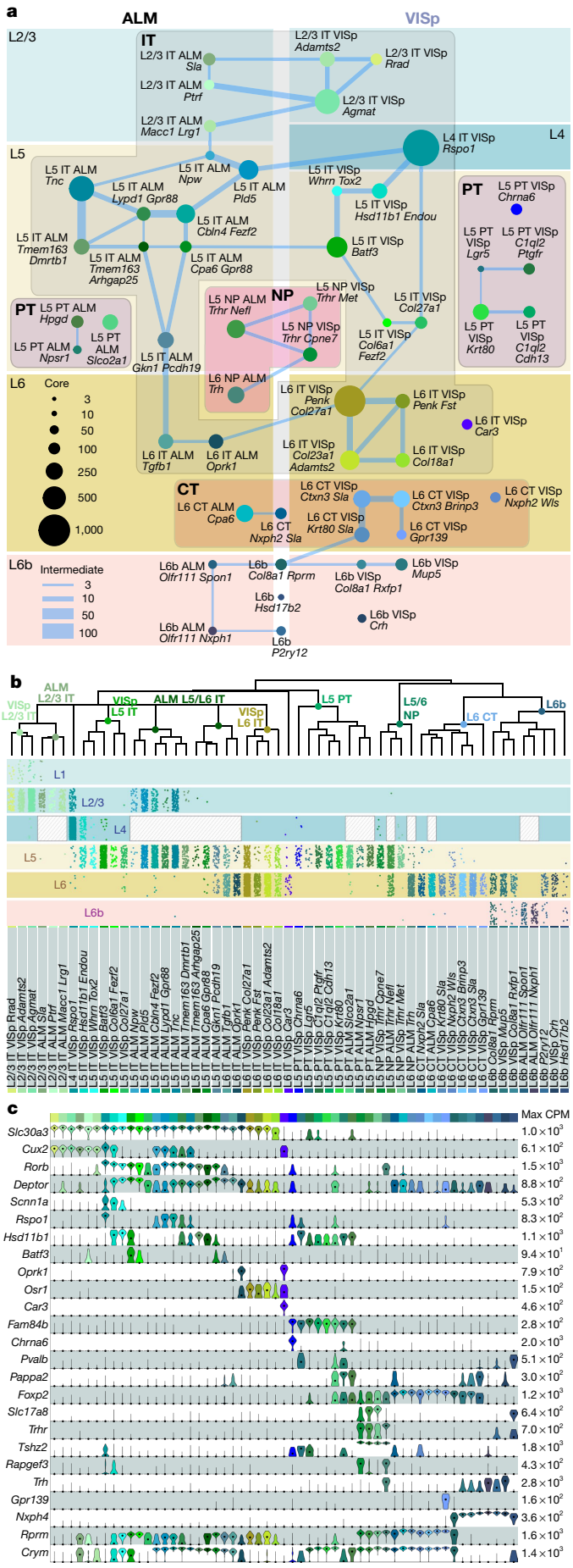

Fig. 4 | Glutamatergic cell types and markers. a, Constellation diagram of ALM and VISp types. Disc areas represent core cell numbers for each cluster ($n = 10{,}729$), edge weights represent intermediate cell numbers ($n = 1{,}136$). L6–CT–*Nxph2–Sla*, L6b–*Col8a1–Rprm*, L6b–*Hsd17b2* and L6b–*P2ry12* are found in both areas. Cajal–Retzius type was omitted. **b**, Dendrograms correspond to glutamatergic portion of Fig. 1c. Layer distribution for each type was inferred from layer-enriching dissections ($n = 8{,}477$ out of 11,871 cells in glutamatergic clusters): each dot represents a cell positioned at random within each layer. Distributions are approximate owing to sampling strategy (Methods). **c**, Marker gene expression distributions within each cluster are represented by violin plots. Rows are genes, black dots are medians. Values within each row are normalized between 0 and maximum detected, displayed on a $\log_{10}$ scale ($n = 11{,}827$ cells).

of projection neurons (Fig. 3c, d): intratelencephalic (IT), pyramidal tract (PT), near-projecting (NP) and corticothalamic (CT). We validated the preferential residence layer for neuronal cell bodies of select types by RNA fluorescent in situ hybridization (FISH) and neuronal projections by anterograde labelling (Extended Data Fig. 11).

Projection properties dominate the dendrogram structure. The IT types constitute the largest branch in both the VISp and ALM glutamatergic taxonomies (Figs. 1c, 3c, d), and span most layers. IT constellations include many intermediate cells, which connect types within a layer, between equivalent layers (for example, L2–L3 in ALM and VISp) or from neighbouring layers (Fig. 4a). We define many new markers (Fig. 4c), including a new pan-IT-type marker (*Slc30a3*) and a new L6-IT-type marker (*Osr1*). We also define a distinct IT type, L6–IT–VISp–*Car3*, which expresses a unique combination of markers including *Car3*, *Oprk1* and *Nr2f2* (Fig. 4). Some of these genes have been previously detected in the claustrum[30], and are detected in VISp L6 in the Allen Brain Atlas[25]. Anterograde labelling confirms these findings and refines our knowledge of cortico–cortical projections (Extended Data Fig. 11). For example, IT types preferentially target different laminae in same target areas—upper layers for L2–L3 and L5 IT types, and lower ones for L6 IT types (Extended Data Fig. 11f–h).

Pyramidal tract neurons, the descending output neurons in L5, share a separate branch in the taxonomy (Fig. 1c). They project to subcortical targets (Fig. 3c, d) and express the previously known marker *Bcl6*[26] and a new pan-pyramidal tract neuronal marker *Fam84b* (Fig. 4b, c). The three pyramidal tract transcriptomic types in the ALM correspond to two projection classes[21]: two project to the thalamus, whereas the third projects to the medulla (Extended Data Fig. 10a). The thalamus- and medulla-projecting ALM pyramidal tract neurons have distinct functions in planning and executing voluntary movements, respectively[21]. Similarly, it seems that pyramidal tract types from the VISp display differential subcortical projections (Extended Data Fig. 10b).

Corticothalamic (CT) L6 types (Fig. 3c, d) share the transcription factor marker *Foxp2* (Fig. 4b, c), and may have cell-type-specific preferences for different thalamic nuclei (Extended Data Fig. 10b).

L6b types share many markers, such as *Cplx3*, *Ctgf* and *Nxph4*[25,31,32], but display differential projections to the thalamus or anterior cingulate (Fig. 3d). The thalamus-projecting L6b–*Col8a1–Rprm* type is related to the L6–CT–VISp–*Krt80–Sla* type (Fig. 4a), and expresses shared markers (for example, *Rprm* and *Crym*; Fig. 4c). This relationship is captured in the constellation diagram (Fig. 4a), but not in the dendrogram (Fig. 4b). Three other L6b types in the VISp project to the anterior cingulate area (Extended Data Fig. 10b). For the remaining L6b types, we observed no long-distance projections. As recently reported[33], anterograde tracing in *Ctgf-2A-dgcre* knock-in mice (see Methods) confirms sparse long-range projections from the anterior VISp to the anterior cingulate area. In addition, it shows that L6b neurons in the VISp and ALM project to L1 within resident and neighbouring cortical areas (Extended Data Fig. 11j).

We define four related types in L5–L6 that express distinct markers including *Slc17a8*, *Trhr*, *Tshz2*, *Sla2* and *Rapgef3* (Fig. 4c). On the basis of the retro-seq dataset, they do not project to any of the

© 2018 Springer Nature Limited. All rights reserved.

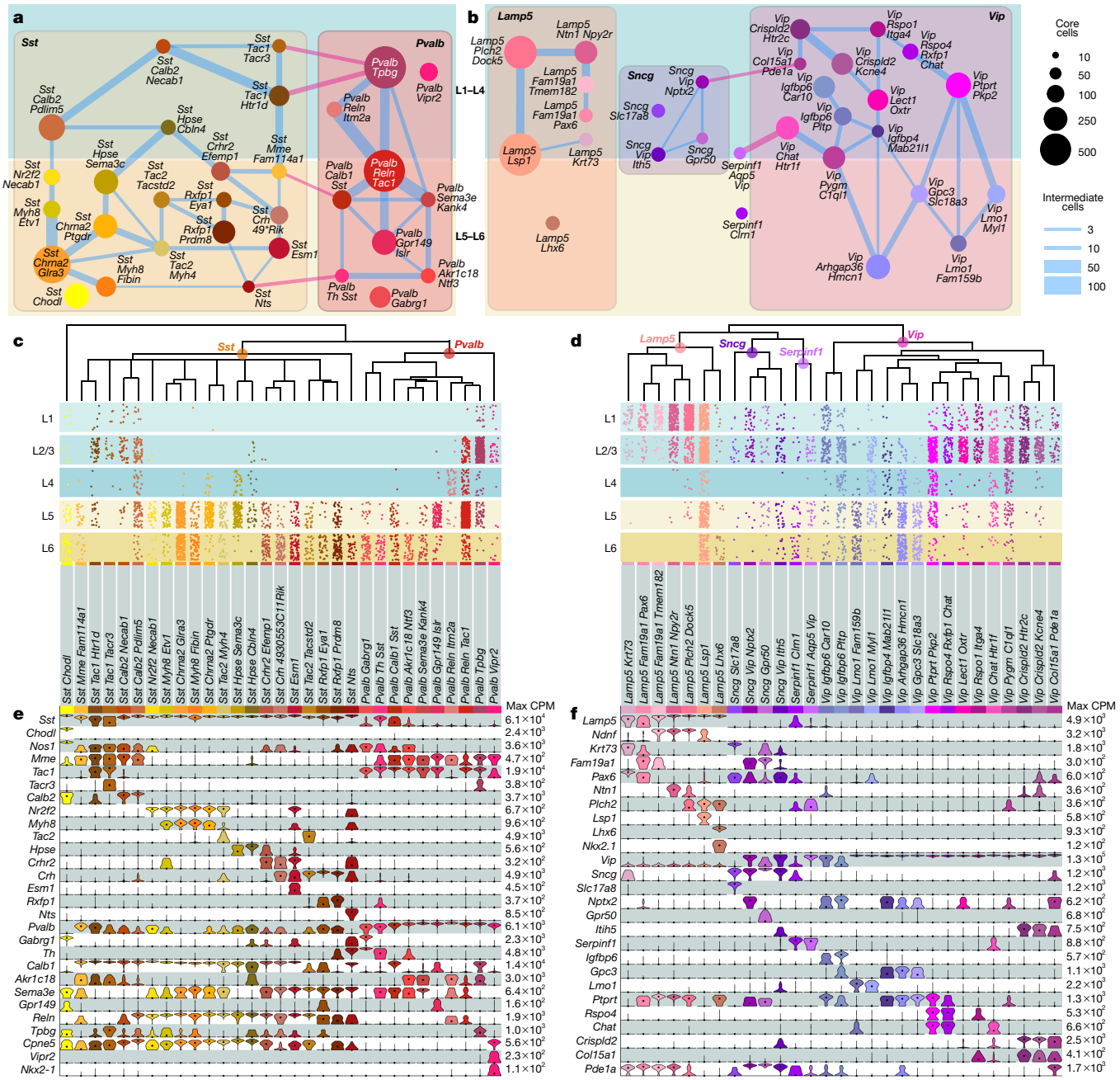

Fig. 5 | GABAergic cell types by scRNA-seq. a, **b**, Constellation diagrams for *Sst* and *Pvalb* (**a**) and *Lamp5*, *Serpinf1*, *Sncg* and *Vip* (**b**) types, as in Fig. 4a (n = 9,021 core cells; $n = 1,457$ intermediate cells). Edges connecting subclasses are pink. *Meis2* type was omitted. **c**, **d**, Dendrograms are portions of Fig. 1c focused on the main GABAergic branch. Below the dendrograms, layer distribution for each type was inferred as in Fig. 4b; only cells from single-layer dissections were used: $n = 4,675$ out of 5,365 cells in **c**, and 3,908 out of 5,113 cells in **d**. Distributions are approximate owing to the sampling strategy (Methods). **e**, **f**, Marker gene expression distributions within each cluster are represented by violin plots as in Fig. 4c. $n = 5,365$ cells in **e** and 5,113 cells in **f**.

assayed areas (Fig. 3c, d). Anterograde tracing of neurons labelled by a new Cre line *Slc17a8-IRES2-cre*, reveals only sparse projections to neighbouring areas (Extended Data Fig. 11k), earning this subclass the name 'near projecting'. Some of these cells probably correspond to previously reported *Slc17a8*$^+$ L5 cells[26], as well as cells labelled by *Efr3a-cre_NO108*[34].

GABAergic cell type taxonomy by scRNA-seq

We define six subclasses of GABAergic cells: *Sst*, *Pvalb*, *Vip*, *Lamp5*, *Sncg* and *Serpinf1*, and two distinct types: *Sst–Chodl* and *Meis2–Adamts19* (Fig. 1c). We represent the taxonomy by constellation diagrams, dendrograms, layer-of-isolation, and the expression of select marker genes (Fig. 5a–f). The major division among GABAergic types largely corresponds to their developmental origin in the medial ganglionic eminence (*Pvalb* and *Sst* subclasses) or caudal ganglionic eminence (*Lamp5*, *Sncg*, *Serpinf1* and *Vip* subclasses).

The *Sst* and *Pvalb* subclasses within the *Sst* and *Pvalb* constellation are connected by select upper and lower layer types (Fig. 5a, pink lines). The *Lamp5*, *Vip*, *Serpinf1* and *Sncg* subclasses are represented by four interconnected neighbourhoods in the constellation diagram (Fig. 5b). These complicated landscapes are the result of many genes expressed in a combinatorial and graded fashion (Extended Data Fig. 5), resulting in high co-clustering frequencies (Extended Data Fig. 3a) and many intermediate cells (Fig. 5a, b).

Our GABAergic transcriptomic taxonomy agrees with previously reported interneuron types based on marker gene expression,

© 2018 Springer Nature Limited. All rights reserved.

transgenic lines, published Patch-seq (patch-pipette-extracted single-cell RNA sequencing) and other scRNA-seq data (Supplementary Table 4, Extended Data Figs. 8, 12). *Sst–Chodl* corresponds to *Nos1*$^+$ long-range projecting interneurons based on marker expression, location, Cre-line labelling, and other RNA-seq data[20,35,36] (Supplementary Table 4, Extended Data Figs. 8, 12). *Sst–Calb2–Pdlim5* corresponds to *Sst*$^+$ and *Calb2*$^+$ L2/3 Martinotti cells[16,35,36] (Fig. 5e, Extended Data Fig. 12a), whereas some of the deep-layer *Sst* types (for example, *Sst–Chrna2–Glra3*) express *Chrna2*, a gene detected in L5 Martinotti cells[37].

For the Pvalb subclass, we confirm that the *Pvalb–Vipr2* type (*Pvalb–Cpne5* in our previous study[20]), corresponds to chandelier cells by mapping of the recently reported chandelier cell (CHC1) RNA-seq data[36] to our *Pvalb–Vipr2* type (Extended Data Fig. 12a). We used the new genetic marker *Vipr2* to develop *Vipr2-IRES2-cre* to access chandelier cells (Extended Data Figs. 8, 13a–f). Several other *Pvalb* types (*Pvalb–Gpr149–Islr*, *Pvalb–Tpbg* and *Pvalb–Reln–Tac1*) correspond to basket cells[36] (Extended Data Fig. 12a, b).

Within the *Lamp5*, *Vip*, *Sncg* and *Serpinf1* subclasses, we find evidence for neurogliaform, bipolar, single bouquet and cholecystokinin (CCK) basket cell types (Supplementary Table 1). The *Sncg* subclass corresponds to the *Vip*$^+$ and *Cck*$^+$ multipolar or basket cells and is distinct from cells of the *Vip* subclass that are also *Calb2*$^+$ and have bipolar morphologies[16,35,36] (Fig. 5f, Extended Data Fig. 12a). We previously assigned neurogliaform cell identity to *Ndnf* types[20], which correspond to several current *Lamp5* types (Extended Data Fig. 6). We confirm this finding by mapping of published Patch-seq data[38] to our data (Extended Data Fig. 12d–f) and find correspondence of neurogliaform cells to *Lamp5–Plch2–Dock5* and *Lamp5–Lsp1* types. In addition, we find that single bouquet cells map mostly to *Lamp5–Fam19a1–Tmem182*, and find a possible transitional single bouquet–neurogliaform cell type, *Lamp5–Ntn1–Npy2r* (Extended Data Fig. 12d).

The *Lamp5–Lhx6* type is unusual because it clusters with other *Lamp5* types, which are derived from the caudal ganglionic eminence, but expresses *Nkx2.1* (also known as *Nkx2-1*) and *Lhx6*, which encode transcription factors of the medial ganglionic eminence. This type is labelled by tamoxifen induction at embryonic day (E) 18 of *Nkx2.1-creERT2* mice (Extended Data Fig. 8) and was isolated previously[36] from the same Cre line (Extended Data Fig. 12a–c). We find that the RNA-seq data of chandelier type 2 cells (CHC2)[36] map primarily to our *Lamp5–Lhx6* type (Extended Data Fig. 12a, b), which is transcriptomically most related to *Lamp5* neurogliaform types.

Continuous variation and cell states

Cell classes are easily identified because they are driven by large differences in gene expression (Fig. 2b) and agree well with previous literature[19,20]. Gene expression differences between subclasses and types are smaller and sometimes graded (Fig. 2b), making interpretation more complicated. Constellation diagrams capture differences in gene expression among types as a combination of continuity and discreteness. However, they do not capture heterogeneity within types, which may be substantial. To illustrate this, we focus on the L4–IT–VISp–*Rspo1* type, which consists of 1,404 cells and displays heterogeneity along the first principal component (Extended Data Fig. 14a–c). The extent of the heterogeneity between the ends of this type is similar to heterogeneity between this type and a neighbouring type (L4–IT–VISp–*Rspo1* and L5–IT–VISp–*Hsd11b1–Endou*, Extended Data Fig. 14d, e). However, in this dataset, we were unable to split this cluster into subclusters using our clustering criteria. This cluster maps to three clusters connected by many intermediate cells in our previous study[20] (Extended Data Fig. 14b). Therefore, the description of L4 cell heterogeneity changed from discrete with many intermediate cells[20] to continuous, possibly owing to more extensive cell sampling and better gene detection. To demonstrate how clustering criteria affect the taxonomy, we performed clustering for *Sst* types at different stringencies. As expected, less stringent statistical criteria yield more types, and vice versa (Extended Data Fig. 14f).

Transcriptomic profiles are also influenced by cell states, which can be defined as reversibly accessible locations a cell can occupy within a multidimensional gene expression space[39]. To determine whether we can detect activity-dependent changes that may be indicative of states in our cell types, we mapped our cells to VISp transcriptomic clusters from dark-reared animals, some of which were exposed to light before euthanasia[40] (Extended Data Fig. 15). We find several glutamatergic and GABAergic types that display statistically significant enrichment or depletion of early- and/or late-response genes, showing that some of our types probably represent cell states. Therefore, our clustering criteria are appropriate to capture at least some cell states, whereas more stringent criteria may overlook them (Extended Data Fig. 14f; the *Sst–Tac1–Tacr3* cluster merges with *Sst–Tac1–Htr1d*).

Discussion

We used single-cell transcriptomics to uncover the principles of cell type diversity in two functionally distinct areas of neocortex. We define 133 transcriptomic types, 101 types in the ALM and 111 in the VISp, 79 of which are shared between these areas. Most glutamatergic types are area-specific. By contrast, and as previously suggested[19], non-neuronal and most GABAergic neuronal types are shared across cortical areas. Although we detect area-specific differences in gene expression within GABAergic types (Fig. 2, Extended Data Fig. 16), they are usually insufficient to define subtypes with our statistical criteria.

This dichotomy correlates with neuronal connectivity patterns and developmental origins. Most glutamatergic types in VISp or ALM project to different cortical and subcortical targets (Fig. 3, Extended Data Fig. 10), whereas nearly all GABAergic interneurons form local connections. Most glutamatergic neurons are born locally within the ventricular–subventricular zone of the developing cortex[41], which is pre-patterned with developmental gradients—an embryonic protomap[42,43]—and further segregated into areas through differential thalamic input in development[44,45]. By contrast, types that are shared across areas are derived from extracortical sources, and migrate into the developing cortex: most GABAergic interneurons are from the medial ganglionic eminence or caudal ganglionic eminence[16]; *Meis2* interneurons are from the pallial–subpallial boundary[22]; and Cajal–Retzius cells of the hippocampus and cortex are from the cortical hem[46]. It remains to be investigated whether some of the shared L6b types may originate from the rostro-medial telencephalic wall, a known source for a subset of subplate neurons that are distinct from those generated within the local ventricular–subventricular zone[47], or whether further sampling may segregate them into area-specific types. Although our taxonomy mostly agrees with the developmental origins of the cells, there are exceptions. For example, tamoxifen induction of *Nkx2.1-creERT2* mice at E18 labels not only chandelier cells, but also a suggested second chandelier type, CHC2[36]. Our taxonomy suggests that CHC2 may be a neurogliaform type (*Lamp5–Lxh6*) that arises from the medial ganglionic eminence, and that neurogliaform types could arise through different developmental pathways and embryonic sources in an example of developmental convergence.

We observe both discrete and continuous gene expression variation among and within types. To accommodate both kinds of variation, we used post-clustering classifiers to construct constellation diagrams, and were able to capture cell states. Alternative analyses of these landscapes lead to more cluster splits (more discreteness) or merges (more continuous variation) (Extended Data Fig. 14f). The detected and described (versus actual) discreteness in the definition of cell types depend on gene detection, cell sampling, and noise estimates or statistical criteria[39] (Extended Data Fig. 14b, f). Future experimental datasets would benefit from multimodal data acquisition, more efficient mRNA detection, and sampling cells according to their abundance in situ[48] and in different states[40]. Our dataset provides a foundation for understanding the diversity of cortical cell types and dissecting circuit function. As an example, in the accompanying paper[21], we show that ALM L5 pyramidal tract neurons map to transcriptomic clusters with

© 2018 Springer Nature Limited. All rights reserved.

distinct projection patterns that have different roles in the preparation and execution of movement.

Online content

Any methods, additional references, Nature Research reporting summaries, source data, statements of data availability and associated accession codes are available at https://doi.org/10.1038/s41586-018-0654-5.

Received: 5 December 2017; Accepted: 24 September 2018;
Published online 31 October 2018.

1. Fuster, J. *The Prefrontal Cortex* 5th edn (Academic Press, Cambridge, MA, 2015).
2. Mountcastle, V. B. *Perceptual Neuroscience: The Cerebral Cortex* (Harvard Univ. Press, Cambridge, MA, 1998).
3. DeFelipe, J. The evolution of the brain, the human nature of cortical circuits, and intellectual creativity. *Front. Neuroanat.* **5**, 29 (2011).
4. Glasser, M. F. et al. A multi-modal parcellation of human cerebral cortex. *Nature* **536**, 171–178 (2016).
5. Kolb, B. & Tees, R. C. *The Cerebral Cortex of the Rat* (MIT Press, Cambridge, MA, 1990).
6. Ng, L. et al. An anatomic gene expression atlas of the adult mouse brain. *Nat. Neurosci.* **12**, 356–362 (2009).
7. Cardin, J. A., Kumbhani, R. D., Contreras, D. & Palmer, L. A. Cellular mechanisms of temporal sensitivity in visual cortex neurons. *J. Neurosci.* **30**, 3652–3662 (2010).
8. Durand, S. et al. A Comparison of visual response properties in the lateral geniculate nucleus and primary visual cortex of awake and anesthetized mice. *J. Neurosci.* **36**, 12144–12156 (2016).
9. Liu, H., Agam, Y., Madsen, J. R. & Kreiman, G. Timing, timing, timing: fast decoding of object information from intracranial field potentials in human visual cortex. *Neuron* **62**, 281–290 (2009).
10. Chen, T. W., Li, N., Daie, K. & Svoboda, K. A map of anticipatory activity in mouse motor cortex. *Neuron* **94**, 866–879.e4 (2017).
11. Guo, Z. V. et al. Maintenance of persistent activity in a frontal thalamocortical loop. *Nature* **545**, 181–186 (2017).
12. Guo, Z. V. et al. Flow of cortical activity underlying a tactile decision in mice. *Neuron* **81**, 179–194 (2014).
13. Svoboda, K. & Li, N. Neural mechanisms of movement planning: motor cortex and beyond. *Curr. Opin. Neurobiol.* **49**, 33–41 (2018).
14. Zeng, H. & Sanes, J. R. Neuronal cell-type classification: challenges, opportunities and the path forward. *Nat. Rev. Neurosci.* **18**, 530–546 (2017).
15. Molyneaux, B. J., Arlotta, P., Menezes, J. R. & Macklis, J. D. Neuronal subtype specification in the cerebral cortex. *Nat. Rev. Neurosci.* **8**, 427–437 (2007).
16. Rudy, B., Fishell, G., Lee, S. & Hjerling-Leffler, J. Three groups of interneurons account for nearly 100% of neocortical GABAergic neurons. *Dev. Neurobiol.* **71**, 45–61 (2011).
17. Jiang, X. et al. Principles of connectivity among morphologically defined cell types in adult neocortex. *Science* **350**, aac9462 (2015).
18. Markram, H. et al. Reconstruction and simulation of neocortical microcircuitry. *Cell* **163**, 456–492 (2015).
19. Zeisel, A. et al. Brain structure. Cell types in the mouse cortex and hippocampus revealed by single-cell RNA-seq. *Science* **347**, 1138–1142 (2015).
20. Tasic, B. et al. Adult mouse cortical cell taxonomy revealed by single cell transcriptomics. *Nat. Neurosci.* **19**, 335–346 (2016).
21. Economo, M. N. et al. Distinct descending motor cortex pathways and their roles in movement. *Nature* https://doi.org/10.1038/s41586-018-0642-9 (2018).
22. Frazer, S. et al. Transcriptomic and anatomic parcellation of 5-HT_{3A}R expressing cortical interneuron subtypes revealed by single-cell RNA sequencing. *Nat. Commun.* **8**, 14219 (2017).
23. Abellan, A., Menuet, A., Dehay, C., Medina, L. & Rétaux, S. Differential expression of LIM-homeodomain factors in Cajal–Retzius cells of primates, rodents, and birds. *Cereb. Cortex* **20**, 1788–1798 (2010).
24. Kirischuk, S., Luhmann, H. J. & Kilb, W. Cajal–Retzius cells: update on structural and functional properties of these mystic neurons that bridged the 20th century. *Neuroscience* **275**, 33–46 (2014).
25. Lein, E. S. et al. Genome-wide atlas of gene expression in the adult mouse brain. *Nature* **445**, 168–176 (2007).
26. Sorensen, S. A. et al. Correlated gene expression and target specificity demonstrate excitatory projection neuron diversity. *Cereb. Cortex* **25**, 433–449 (2015).
27. Harris, K. D. & Shepherd, G. M. The neocortical circuit: themes and variations. *Nat. Neurosci.* **18**, 170–181 (2015).
28. Oh, S. W. et al. A mesoscale connectome of the mouse brain. *Nature* **508**, 207–214 (2014).
29. Li, N., Chen, T. W., Guo, Z. V., Gerfen, C. R. & Svoboda, K. A motor cortex circuit for motor planning and movement. *Nature* **519**, 51–56 (2015).
30. Wang, Q. et al. Organization of the connections between claustrum and cortex in the mouse. *J. Comp. Neurol.* **525**, 1317–1346 (2017).
31. Zeng, H. et al. Large-scale cellular-resolution gene profiling in human neocortex reveals species-specific molecular signatures. *Cell* **149**, 483–496 (2012).
32. Ayoub, A. E. & Kostovic, I. New horizons for the subplate zone and its pioneering neurons. *Cereb. Cortex* **19**, 1705–1707 (2009).
33. Hoerder-Suabedissen, A. et al. Subset of cortical layer 6b neurons selectively innervates higher order thalamic nuclei in mice. *Cereb. Cortex* **28**, 1882–1897 (2018).
34. Kim, E. J., Juavinett, A. L., Kyubwa, E. M., Jacobs, M. W. & Callaway, E. M. Three types of cortical layer 5 neurons that differ in brain-wide connectivity and function. *Neuron* **88**, 1253–1267 (2015).
35. He, M. et al. Strategies and tools for combinatorial targeting of GABAergic neurons in mouse cerebral cortex. *Neuron* **92**, 555 (2016).
36. Paul, A. et al. Transcriptional architecture of synaptic communication delineates GABAergic neuron identity. *Cell* **171**, 522–539.e20 (2017).
37. Hilscher, M. M., Leão, R. N., Edwards, S. J., Leão, K. E. & Kullander, K. Chrna2-Martinotti Cells synchronize layer 5 type a pyramidal cells via rebound excitation. *PLoS Biol.* **15**, e2001392 (2017).
38. Cadwell, C. R. et al. Electrophysiological, transcriptomic and morphologic profiling of single neurons using Patch-seq. *Nat. Biotechnol.* **34**, 199–203 (2016).
39. Tasic, B., Levi, B. P. & Menon, V. in *Decoding Neural Circuit Structure and Function: Cellular Dissection Using Genetic Model Organisms* (eds A. Çelik & M. F. Wernet) 437–468 (Springer International Publishing, New York, 2017).
40. Hrvatin, S. et al. Single-cell analysis of experience-dependent transcriptomic states in the mouse visual cortex. *Nat. Neurosci.* **21**, 120–129 (2018).
41. Gao, P. et al. Deterministic progenitor behavior and unitary production of neurons in the neocortex. *Cell* **159**, 775–788 (2014).
42. O'Leary, D. D., Chou, S. J. & Sahara, S. Area patterning of the mammalian cortex. *Neuron* **56**, 252–269 (2007).
43. Rakic, P. Specification of cerebral cortical areas. *Science* **241**, 170–176 (1988).
44. Vue, T. Y. et al. Thalamic control of neocortical area formation in mice. *J. Neurosci.* **33**, 8442–8453 (2013).
45. Chou, S. J. et al. Geniculocortical input drives genetic distinctions between primary and higher-order visual areas. *Science* **340**, 1239–1242 (2013).
46. Yoshida, M., Assimacopoulos, S., Jones, K. R. & Grove, E. A. Massive loss of Cajal-Retzius cells does not disrupt neocortical layer order. *Development* **133**, 537–545 (2006).
47. Pedraza, M., Hoerder-Suabedissen, A., Albert-Maestro, M. A., Molnár, Z. & De Carlos, J. A. Extracortical origin of some murine subplate cell populations. *Proc. Natl Acad. Sci. USA* **111**, 8613–8618 (2014).
48. Lein, E., Borm, L. E. & Linnarsson, S. The promise of spatial transcriptomics for neuroscience in the era of molecular cell typing. *Science* **358**, 64–69 (2017).

Acknowledgements We thank M. Chillon Rodrigues for providing CAV2-Cre, A. Karpova for providing rAAV2-retro, A. Williford for technical assistance, and the Transgenic Colony Management and Animal Care teams for animal husbandry. This work was funded by the Allen Institute for Brain Science, and by US National Institutes of Health grants R01EY023173 and U01MH105982 to H.Z. We thank the Allen Institute founder, P. G. Allen, for his vision, encouragement and support.

Reviewer information *Nature* thanks P. Carninci, C. Chau Hon and the anonymous reviewer(s) for their contribution to the peer review of this work.

Author contributions H.Z. and K.S. conceptualized, and H.Z. and B.T. designed and supervised the study. K.S. defined ALM coordinates based on loss-of-function experiments. K.A.S. managed the scRNA-seq pipeline. A.B. and J.Phillips managed pipeline establishment. D.B., J.G., K.L., C.R, M.T. and T.K.K. performed scRNA-seq. Z.Y., L.T.G. and B.T. analysed the data with contributions from O.F., O.P., T.B., V.M., J.M., A.S. and M.H. I.W., H.A.S. and A.C. provided viral vectors. J.A.H., T.N.N., K.E.H. and P.G. conducted viral tracing experiments. B.P.L., N.D., T.C., S.P., E.B., M.K., N.V.S. and D.H. performed single-cell isolation. T.N.N. and E.G. performed RNA ISH with RNAscope. L.M. and T.L.D. generated transgenic mice. J.Pendergraft provided genotyping. R.L. provided mouse colony management. K.S., M.N.E., S.V. and L.L. provided manually collected cells from ALM. S.M.S. provided program management support. H.Z. and E.L. led the Cell Types Program at the Allen Institute. C.K. and A.R.J. provided funding, institutional support and management. L.T.G., Z.Y., T.N.N. and B.T. prepared the figures. B.T. and H.Z. wrote the manuscript with contributions from C.K., K.S., L.T.G., T.N.N. and Z.Y., and in consultation with all authors.

Competing interests The authors declare no competing interests.

Additional information
Extended data is available for this paper at https://doi.org/10.1038/s41586-018-0654-5.
Supplementary information is available for this paper at https://doi.org/10.1038/s41586-018-0654-5.
Reprints and permissions information is available at http://www.nature.com/reprints.
Correspondence and requests for materials should be addressed to B.T.
Publisher's note: Springer Nature remains neutral with regard to jurisdictional claims in published maps and institutional affiliations.

© 2018 Springer Nature Limited. All rights reserved.

METHODS

Mouse breeding and husbandry. All procedures were carried out in accordance with Institutional Animal Care and Use Committee protocols 1508, 1510 and 1511 at the Allen Institute for Brain Science and Janelia Research Campus. Animals were provided food and water ad libitum and were maintained on a regular 12-h day/night cycle at no more than five adult animals per cage. Animals were maintained on the C57BL/6J background, and newly received or generated transgenic lines were backcrossed to C57BL/6J. Experimental animals were heterozygous for the recombinase transgenes and the reporter transgenes. Transgenic lines used in this study are summarized in Supplementary Table 5. Standard tamoxifen treatment for CreER lines included a single dose of tamoxifen (40 μl of 50 mg ml^{-1}) dissolved in corn oil and administered via oral gavage at P10–14. Tamoxifen treatment for *Nkx2.1-creERT2;Ai14* was performed at E17 (oral gavage of the dam at 1 mg per 10 g of body weight), pups were delivered by caesarean section at E19 and then fostered. *Cux2-creERT2;Ai14* mice received tamoxifen treatment daily, for five consecutive days, between P30 and P40. Trimethoprim was administered to animals containing *Ctgf-2A-dgcre* by oral gavage daily, for three consecutive days, between P35 and P45 (0.015 ml per g of body weight using 20 mg ml^{-1} trimethoprim solution). *Ndnf-IRES2-dgcre* animals did not receive trimethoprim induction, because the baseline dgCre activity (without trimethoprim) was sufficient to label the cells with the *Ai14* reporter[20]. The transgenic component *dgcre* encodes a destabilized Cre protein: it contains a destabilizing domain '*d*', which is stabilized by trimethoprim, and a non-fluorescent portion of eGFP '*g*'. We excluded any animals with anophthalmia or microphthalmia. We used 352 animals to collect the set of 24,411 cells for clustering (Supplementary Table 1). Animals were euthanized at P53–P59 ($n = 339$), P51 ($n = 1$), and P63–P91 ($n = 12$). No statistical methods were used to predetermine sample size.

Generation of transgenic mice (*Penk-IRES2-cre-neo*, *Slc17a8-IRES2-cre* and *Vipr2-IRES2-cre*). Vectors containing gene-specific homology arms and *IRES2-cre-bGHpoly(A)-PGK-gb2-neo-PGKpoly(A)* components were generated using gene synthesis (GenScript) and standard molecular cloning techniques. Targeting of the transgene cassette into the endogenous gene locus immediately downstream of the stop codon was accomplished by CRISPR–Cas9-mediated genome editing using circularized targeting vector in combination with a gene-specific guide vector (Addgene, plasmid 42230)[49]. The 129S6/B6 F_1 embryonic stem (ES) cell line, G4[50], was used to generate all modified ES cells. Correctly targeted clones were identified using standard screening approaches (PCR, qPCR and Southern blots) and injected into blastocysts to obtain chimaeras and subsequent germline transmission. Resulting mice were crossed to the *Rosa26-PhiC31o* mice (JAX, 007743)[51] to delete the *PGK-neo* selection cassette, and then backcrossed to C57BL/6J mice and maintained in the C57BL/6J background. The *PGK-neo* cassette could not be removed from *Penk-IRES2-cre-neo* by the PhiC31o integrase-mediated recombination.

Retrograde labelling. We injected rAAV2-retro-EF1a-Cre[52], RVΔGL-Cre[53], or CAV2-Cre (gift from M. Chillon Rodrigues)[54] into brains of heterozygous or homozygous *Ai14* mice as previously described[20]. For ALM experiments, we also injected rAAV2-retro-CAG-GFP or rAAV2-retro-CAG-tdTomato[52] into wild-type mice. Stereotaxic coordinates were obtained from Paxinos adult mouse brain atlas[55](Supplementary Table 6). For two VISp experiments, we injected into the superior colliculus sensory-related area by inserting the needle through the cerebellum at a 45° angle in the posterior to anterior direction. TdT^+ or GFP^+ single cells were isolated from VISp or ALM, depending on the injection area. Detailed information on used viruses is available in Supplementary Table 7.

Anterograde labelling. For anterograde projection mapping, we injected AAV2/1-pCAG-FLEX-eGFP-WPRE-pA[28] into VISp or ALM of 8–12-week-old mice. Stereotaxic injection procedure was the same as for retrograde labelling above. In *Ctgf-2A-dgcre* mice, one week after AAV injection, trimethoprim induction was conducted for 3 consecutive days as described previously[20]. Mice were euthanized and brains perfused after 21 days (or 28 days in the case of *Ctgf-2A-dgcre*) after AAV injection, and brains were imaged using TissueCyte 1000 system as described previously[28]. Experiments can be viewed interactively on the Allen Institute data portal at http://connectivity.brain-map.org/.

Single-cell isolation. We isolated single cells as previously described[20,56,57] with modifications below. We usually used layer-enriching dissections, with focus on a single layer. Broader dissections (no layer enrichment or multiple layers combined) were used for lines that label small numbers of cells, to facilitate isolation of sufficient number of cells. We updated our artificial cerebrospinal fluid (ACSF) formulation compared to our previous study[20] to include *N*-methyl-D-glucamine (NMDG) to improve neuronal survival[58]. Our ACSF consisted of $CaCl_2$ (0.5 mM), glucose (25 mM), HCl (96 mM), HEPES (20 mM), $MgSO_4$ (10 mM), NaH_2PO_4 (1.25 mM), myo-inositol (3 mM), *N*-acetylcysteine (12 mM), NMDG (96 mM), KCl (2.5 mM), $NaHCO_3$ (25 mM), sodium L-ascorbate (5 mM), sodium pyruvate (3 mM), taurine (0.01 mM), thiourea (2 mM), and was bubbled with carbogen gas (95% O_2 and 5% CO_2). For samples collected after 16 December 2016, the ACSF formulation also included trehalose (13.2 mM). Mice were anaesthetized with isoflurane and perfused with cold carbogen-bubbled ACSF. The brain was dissected, submerged in ACSF, embedded in 2% agarose, and sliced into 250-μm coronal sections on a compresstome (Precisionary). Enzymatic digestion, trituration into single cell suspension, and FACS analysis of single cells were carried out as previously described[20], with example sorting strategy shown in Extended Data Fig. 1e–g. Cells were sorted into 8-well strips containing lysis buffer from the SMART-Seq v4 kit (see below) with RNase inhibitor (0.17 U μl^{-1}), immediately frozen on dry ice, and stored at −80 °C.

Note that the overall relative proportions of cell types in our dataset are not representative of those in the intact brain because of the targeted sampling approach using various Cre lines and possible cell type–specific differences in survival during the isolation procedure.

cDNA amplification and library construction. We used the SMART-Seq v4 Ultra Low Input RNA Kit for Sequencing (Takara, 634894) to reverse transcribe poly(A) RNA and amplify full-length cDNA according to the manufacturer's instructions. We performed reverse transcription and cDNA amplification for 18 PCR cycles in 8-well strips, in sets of 12–24 strips at a time. A small set of non-neuronal cell samples was amplified by 21 PCR cycles instead of 18 (Supplementary Table 10). At least 1 control strip was used per amplification set, which contained 4 wells without cells and 4 wells with 10 pg control RNA. Control RNA was either Mouse Whole Brain Total RNA (Zyagen, MR-201) or control RNA provided in the SMART-Seq v4 kit. All samples proceeded through Nextera XT DNA Library Preparation (Illumina FC-131-1096) using Nextera XT Index Kit V2 Set A (FC-131-2001). Nextera XT DNA Library prep was performed according to manufacturer's instructions except that the volumes of all reagents including cDNA input were decreased to 0.4× or 0.5× by volume. The replacement of Clontech's SMARTer v.1[59], which we used in our previous study[20], with SMART-Seq v.4 kit, which is based on Smart-seq2[60], increases the efficiency of gene detection. This allowed us to reduce the median sequencing depth from approximately 8.7 million to 2.5 million reads per cell while still detecting 9,500 genes per cell (median) compared to 7,800 previously (Extended Data Fig. 2b). Subsampling of the reads to a median of 0.5 million per cell results in similar gene detection per cell (>89% of genes detected, data not shown), showing that we detect most of the genes at 2.5 million reads per cell. Details are available in 'Documentation' on the Allen Institute data portal at: http://celltypes.brain-map.org/.

Sequencing data processing and quality control. Fifty-base-pair paired-end reads were aligned to GRCm38 (mm10) using a RefSeq annotation gff file retrieved from NCBI on 18 January 2016 (https://www.ncbi.nlm.nih.gov/genome/annotation_euk/all/). Sequence alignment was performed using STAR v2.5.3[61] in twopassMode. PCR duplicates were masked and removed using STAR option 'bamRemoveDuplicates'. Only uniquely aligned reads were used for gene quantification. Gene counts were computed using the R GenomicAlignments package[62] sumarizeOverlaps function using 'IntersectionNotEmpty' mode for exonic and intronic regions separately. In this study, we only used exonic regions for gene quantification. Cells that met any one of the following criteria were removed: <100,000 total reads, <1,000 detected genes (counts per million > 0), < 75% of reads aligned to genome, or CG dinucleotide odds ratio > 0.5. Doublets were removed by first classifying cells into broad classes of glutamatergic, GABAergic, and non-neuronal based on known markers. For each class, we selected a set of highly specific genes that are only present in this class compared to all other classes, and computed the eigengene (the first principle component based on the given gene set), normalized within the 0–1 range. Each cell was assigned to the class with the maximum eigengene. For each class, we computed the mean and standard deviation of the corresponding eigengene for cells outside this class. Any cell in which the eigengene was more than three standard deviations above the mean for the cells outside the class was assigned to be members of that class. On the basis of this criterion, cells that belong to more than one class were defined as doublets.

Mapping reads to synthetic constructs. We mapped all non-genome-mapped reads to sequences in Supplementary Table 8. To avoid ambiguous counting due to stretches of sequence identity, we designated unique regions within these sequences to count mRNAs of interest. We counted only reads for which at least one of the paired ends had an overlap with the unique regions of at least 10 bp.

Clustering. Cells that passed quality control criteria were clustered using an in-house developed iterative clustering R package hicat available via Github (https://github.com/AllenInstitute/hicat). It was described partially in previous studies[20,63], and was modified to improve robustness and adapt to large numbers of cells. In brief, all quality control qualified cells were grouped into very broad categories using known markers, then clustered using high variance gene selection, dimensionality reduction, dimension filtering, and Jaccard–Louvain or hierarchical (Ward) clustering. This process was repeated within each resulting cluster until no more child clusters met differential gene expression or cluster size termination criteria. The entire clustering procedure was repeated 100 times using 80% of all cells sampled at random, and the frequency with which cells co-cluster was used

© 2018 Springer Nature Limited. All rights reserved.

to generate a final set of clusters, again subject to differential gene expression and cluster size termination criteria. A workflow diagram for this approach is presented in Extended Data Fig. 2. The key strength of this approach is its ability to provide high-resolution cell type categorization that withstands rigorous statistical tests to ensure reproducibility and biological relevance of the results. Below, we provide more details for the analysis carried out at each iteration of clustering:

1. Selection of high-variance genes. We first removed predicted gene models (gene names that start with Gm), genes from the mitochondrial chromosome, ribosomal genes, sex-specific genes, as well as genes that were detected in fewer than four cells. To choose high variance genes, we used gene counts from each cell to fit a Loess regression curve between average scaled gene counts and dispersion (variance divided by mean). The regression residuals were then fit to a normal distribution based on 25% and 75% quantiles to calculate *P* values and adjusted *P* values (using Holm's method), representing the probability that each gene had higher than expected variance. Genes were ranked by adjusted *P* value.

2. Dimensionality reduction. We implemented two methods: principal component analysis (PCA) and weighted gene co-expression network analysis (WGCNA). In the PCA mode, top high variance genes with adjusted $P < 0.5$ were used to compute principal components. The proportion of variance for all principal components was converted to *z*-scores, and principal components with *z*-scores >2 were selected for clustering. In the WGCNA mode, the 4,000 genes with the most significant *P* values were used as input for WGCNA to identify gene modules. Here, we used a more relaxed criterion than in the PCA mode to allow more genes to be included for gene module detection. To determine the discriminative power of each module, we used the genes in each module to divide the cells into two clusters using Jaccard–Louvain clustering[64] (for more than 4,000 cells) or a combination of *k*-means and Ward's hierarchical clustering (for <4,000 cells). After dividing the cells into two clusters, we computed differential gene expression between the two clusters (see 'Defining differentially expressed genes' section). We then computed the differential expression score (deScore), defined as the sum of $-\log_{10}$ (adjusted *P* value) of all differentially expressed genes. For deScore calculations, the maximum value each gene was allowed to contribute was 20. Only modules with deScore greater than 150 were selected for use in downstream analysis, and module eigengenes were computed for selected modules as reduced dimensions. Up to 20 top reduced dimensions were selected for both methods. The two dimensionality reduction approaches are complementary: WGCNA detects rare clusters well, segregates well biological and technical variation, and provides cleaner cluster boundaries; PCA is more scalable to large datasets and captures combinatorial marker expression patterns better than WGCNA.

3. Dimension filtering. We have identified systematic technical variation that affects expression of hundreds of genes that we believe is primarily driven by the quality of the single cell cDNA library. The first principal component of these genes is highly correlated with the log-transform of the number of genes detected in each cell, so we define the latter as the quality control eigen. We have also identified a list of genes that contribute to the batch effect for the first set of experiments for this study with subtle protocol differences. We computed batch eigen as the first principal component based on these batch specific genes. We removed any principal components or module eigengenes that have correlation greater than 0.7 with either the quality control eigen or the batch eigen.

4. Initial clustering. For clustering, we applied either the Jaccard–Louvain method[64] using the Rphenograph package (for >4,000 cells), or Ward's method (for ≤4,000 cells). Although the Louvain algorithm scales well with large datasets, it has been shown to have a resolution limit[65], and small clusters tend to be missed. Therefore, as a complementary approach, we applied Ward's minimum variance method for hierarchical clustering when fewer than 4,000 cells were to be clustered. The initial number of clusters was set at twice the number of reduced dimensions from step 3.

5. Cluster merging. To make sure the resulting clusters all have distinguishable transcriptomic signatures, we defined differentially expressed genes between every cluster and their two nearest neighbours in the reduced dimension space (using Euclidean distance if there were 1 or 2 dimensions, or 1 minus Pearson correlation for more dimensions). A pair of clusters was considered separable if the deScore (described in step 2) for all differentially expressed genes was greater than 150. If a cluster did not pass this criterion, it was merged with the nearest neighbour cluster, and differentially expressed gene scores were recomputed using the merged clusters. Clusters with fewer than four cells were also merged with their nearest neighbours. This iterative merging process was repeated until all remaining clusters were separable and contained at least 4 cells.

Steps 1–5 were repeated for each resulting cluster until no further partitions were found.

6. Defining consensus clusters. To determine the robustness of the clustering results, the entire clustering procedure was repeated 100 times using 80% of all cells sampled at random in both the PCA and WGCNA modes. We then generated the frequency matrix for co-clustering of every pair of cells in both modes. The final cell-cell co-clustering matrix was defined as the element-by-element minimum of these two matrices, which implies that if two cells belong to the same cluster by one method, but to different clusters by another method, then their co-clustering probability is considered low and they should be separated into different clusters. We inferred the consensus clusters by iteratively splitting the co-clustering matrix. In any given step, we used the co-clustering matrix as the similarity matrix and performed clustering by either the Louvain (≥4000 cells) or Ward's algorithm (<4,000 cells). We defined $N_{k,l}$ as the average probabilities of cells within cluster *k* to co-cluster with cells within cluster *l*. We merged clusters *k, l* if $N_{k,l} > \max(N_{k,k}, N_{l,l}) - 0.25$. We merged remaining clusters based on differentially expressed genes as described in step 5 using a deScore threshold of 150.

7. Cluster refinement. For each cell *i*, we computed the average probability that it co-clustered with cells in each cluster *k* as $M_{i,k}$, and we reassigned every cell *i* to the cluster *k* with maximum $M_{i,k}$. We repeated this process until convergence.

8. Exclusion of outlier clusters. After defining consensus clusters, we examined our clustering results to identify outlier clusters that are likely to be due to technical artefacts. These clusters fall into three categories: clusters of doublets, clusters of low-quality cells, and clusters driven by batch effects. A cluster was defined as a doublet cluster if it had signatures from two distinctive cell subclasses, for example, smooth muscle cells and neurons. Low-quality clusters were defined as clusters with significantly lower gene counts compared to the nearest cluster in taxonomy, and with few or no significantly enriched genes. We also identified two clusters that contain only retrogradely labelled cells. These two clusters are very similar to two other distinctive clusters, but contain shared additional signatures that we suspect were due to technical variation in retrograde experiments, so they were annotated as outlier clusters.

Constructing the cell type taxonomy tree. To build the cell type tree, we computed up to top 50 differentially expressed genes in both directions for every pair of clusters, and assembled unique entrees into a marker list of 4,020 genes. We calculated median expression of these marker genes per cluster as cluster centroid, and applied hierarchical clustering with average linkage on the correlation matrix of cluster centroids to infer the cell type taxonomy tree. The confidence for each branch of the tree was estimated by the bootstrap resampling approach from the R package pvclust v.2.0. A comparison between the uncollapsed dendrogram and collapsing at >0.4 is presented in Extended Data Fig. 3. For display in figures, we collapsed the dendrogram to branches with a confidence score >0.4.

Assigning core and intermediate cells. In our previous study, post-clustering, we applied a random forest classifier to test our cluster assignments, and to define core and intermediate cells[20]. We found that random forest classification penalized small clusters, so we used a nearest-centroid classifier, which assigns a cell to the cluster whose centroid is the closest (with the highest correlation) to the cell. Here, the cluster centroid is defined as the median expression of 4,020 differentially expressed genes. To define core versus intermediate cells, we performed fivefold cross-validation 100 times: in each round, the cells were randomly partitioned into five groups, and cells in each group of 20% of the cells were classified by a nearest-centroid classifier trained using the other 80% of the cells. A cell classified to the same cluster more than 90 times was defined as a core cell, the others were designated intermediate cells. We define 21,195 core cells and 2,627 intermediate cells, which, in most cases, classify to only two clusters, one of which is the original cluster (2,492 out of 2,627; 94.9%).

Assigning cluster names. The marker genes included in cluster names were selected to be unique either individually or as a combination within our universe of cell types. We considered differentially expressed genes (see 'Defining differentially expressed genes' section below) at different levels of taxonomy: globally specific, within-class specific, within-subclass specific, and specific compared to the nearest sibling cluster. We also evaluated marker genes for the completeness of expression within the cluster that would be named after that gene. From this list of markers, we visually inspected marker specificity by examining gene expression at the single-cell level in clusters of interest. Many genes satisfied criteria of good marker genes, and therefore many alternatives for cluster naming exist. We gave preferences to globally unique genes (for example, *Chodl*, included in the *Sst–Chodl* cluster name) and markers that are expressed in all or a large proportion of cells within the cluster. For example, *Lamp5–Lxh6*, could also be called *Lamp5–Nkx2.1*. We chose *Lxh6* as it is expressed in every cell of this cluster whereas *Nkx2.1* is not, although *Nkx2.1* is expressed in a smaller number of cell types overall.

Defining differentially expressed genes. Differentially expressed genes were detected using the R package limma v.3.30.13[66] using $\log_2(\mathrm{CPM} + 1)$ of expression values. We did not perform any tests of normality before performing differentially expressed gene tests. Differentially expressed genes were defined as genes with a more than twofold change and adjusted $P < 0.01$. We also required these genes to have a relatively bimodal expression pattern, expressed predominately in one cluster relative to the other. To do that, we computed $P_{i,j}$ as the fraction of cells in cluster *j* expressing gene *i* with CPM ≥ 1, and required upregulated genes *i* in cluster c_1 relative to c_2 to have $P_{i,c1} > q1.\mathrm{th}$ ($q1.\mathrm{th} = 0.5$), and

© 2018 Springer Nature Limited. All rights reserved.

$(P_{i,c1} - P_{i,c2})/\max((P_{i,c1}, P_{i,c2}) > q.\text{diff.th}$ (q.diff.th = 0.7). We define the deScore as the sum of the $-\log_{10}$(adjusted P value) of all differentially expressed genes. For deScore calculations, the maximum value each gene was allowed to contribute was 20. The deScores used for Extended Data Fig. 14f are: 80, low stringency; 150, standard; and 300, high stringency.

Retro-seq quality control and analysis. All retrogradely labelled cells were subjected to the same experimental and data processing, quality control, and clustering with all other quality control-qualified single-cell transcriptomes. Clustering was performed blinded to the experimental source of retrogradely labelled cells. After clustering, we performed an additional quality control step, in which we examined the dissection images and annotated the injection sites for specificity. We excluded single cell samples derived from incorrectly targeted injections or injections which displayed significant labelling through needle tract to define the 'annotated retro-seq dataset' (Extended Data Fig. 2e). Figure 3 and Extended Data Fig. 10 were generated based on this dataset.

Correspondence between VISp and ALM glutamatergic clusters. To establish correspondence in both directions, we classified VISp glutamatergic cells using ALM glutamatergic clusters as training data, and vice versa. In both cases, we trained the nearest centroid classifier based on common set of glutamatergic markers (pool of top 50 differentially expressed genes in each direction between glutamatergic clusters within VISp or within ALM) shared by both regions, and calculated the fraction of cells in each VISp clusters that mapped to each of the ALM clusters, and vice versa. For each cell, we computed the correlation score of the best mapping cluster, and transformed the correlation scores into z-scores. If the average z-score of cells from one cluster mapped to another cluster in the other region was below −1.64 (roughly 5% confidence interval), this cluster was considered to be unique to one region, with no corresponding cluster in the other region. For Fig. 2c, we used matched types as described in the paragraph above, or split each type into its ALM and VISp portions. Differentially expressed genes were calculated for all pairwise comparisons between type-specific and region-specific portions within glutamatergic samples and GABAergic samples. For each gene, two measures were calculated: a ratio of proportions (proportion of cells in ALM − proportion in VISp divided by whichever is higher, x axis) and the proportion of cells in whichever region has a greater proportion of cells expressing each gene (y axis). Proportions were computed separately for glutamatergic and GABAergic cells.

Assessing correspondence to the Paul et al. (2017)[36] dataset. We mapped cells from Gene Expression Omnibus (GEO) accession GSE92522[36] to our GABAergic clusters using the nearest centroid classifier based on a set of shared GABAergic markers that were detected in both datasets (expression >0). To estimate the robustness of mapping, we repeated classification 100 times, each time using 80% of randomly sampled markers, and computed the probabilities for every cell to map to every reference cluster.

Assessing correspondence to Cadwell et al. (2016)[38] Patch-seq dataset. We mapped cells from the ArrayExpress accession E-MTAB-4092 dataset[38] to our clusters (using only VISp cells) using the nearest centroid classifier with 100 sub-sampling rounds as described in paragraph above. Cells mapped to clusters with probabilities <80% were mapped to the parent nodes of the mapped clusters within the cell type hierarchy, until aggregated confidence at the parent node was >80%.

Assessing correspondence to Hrvatin et al. (2018)[40] dataset. We mapped VISp cells from our dataset to GEO accession GSE102827[40] using the same strategy described above. We chose the Hrvatin et al.[40] dataset as reference because the cells profiled by inDrop have lower gene detection, and cannot be mapped to our high-resolution clusters confidently, whereas our cells can be mapped to clusters from the previous dataset[40] with high confidence. To define early-response genes (ERGs) and late-response genes (LRGs) within each cluster in the previously published dataset[40], differentially expressed genes were computed between samples with 1 h or 4 h after exposure to light versus no exposure. We used the approach described above, with the following criteria: > twofold change, adjusted $P < 0.01$, $q1.\text{th} = 0.05$, $q.\text{diff.th} = 0.5$. We computed average ERGs and LRGs for all our VISp cells mapped to the this cluster, and plotted their distribution based on our cluster annotation. We then used two-sided t-test to compute the significance for enrichment/depletion of average ERG and LRG expression for each of our cell types against the other types mapped to the same Hrvatin cluster, and defined significant values as having a $P < 0.01$, after correction for multiple hypotheses using the Holm method, and average fold change greater than 2.

Measures of heterogeneity within L4–IT–VISp–*Rspo1* and between L4–IT–VISp–*Rspo1* and related clusters. To explore the heterogeneity of the L4–IT–VISp–*Rspo1* cluster, which corresponds to three separate cell types in our previous study[20] (Extended Data Fig. 5), we first removed the quality control-dependent gene expression signatures by regressing the expression of each gene against the quality control index, defined as the ratio between the fraction of the reads mapped to intronic regions over the reads mapped to exonic regions. Compared to other cell types, L4 cells have a high fraction of intronic reads, likely indicating high nuclear content. There is also considerable variation of this quality control index among L4 cells, which confounds other transcriptomic signatures. After normalization, we performed WGCNA to find co-expressed gene modules within cells from L4–IT–VISp–*Rspo1*. We found that the eigengene for the top gene module within L4–IT–VISp–*Rspo1* corresponds to the gradient that drove separation of L4 subtypes previously[20]. We then took the 50 cells at both ends of the eigengene-defined gradient, trained a random forest classifier using the genes from the WGCNA gene module, and tested it on the remaining cells to assign them to the ends of the gradient. The classification probabilities by random forest strongly correlated with the gradient eigengene (Extended Data Fig. 14d). We repeated the same analysis between L4–IT–VISp–*Rspo1* and the neighbouring L5–IT–VISp–*Hsd11b1–Endou* cluster, and between L4–IT–VISp–*Rspo1* and more distant L5–IT–VISp–*Batf3* cluster. The eigengenes for these comparisons were defined as the first principle component of the top 50 differentially expressed genes in both directions. In both cases, the classifier was trained on 50 sampled cells from each cluster based on the selected differentially expressed genes, and tested on the remaining cells. We applied Kolmogorov–Smirnov tests to determine whether the distribution of classification probabilities is uniform for each of the three cases above. To account for the differences in sample size, we sampled 400 tested L4–IT–VISp–*Rspo1* cells for the first case, and up to 200 cells from each cluster for the latter two cases. The Kolmogorov–Smirnov test gave $P = 2.64 \times 10^{-5}$ within the L4–IT–VISp–*Rspo1* gradient. Between neighbouring cluster L4–IT–VISp–*Rspo1* and L5–IT–VISp–*Batf3*, the random forest classification probabilities deviated from uniform distribution more significantly (Kolmogorov–Smirnov test $P = 4.37 \times 10^{-13}$). When cells in the L4–IT–VISp–*Rspo1* cluster were compared with the more distant L5–IT–VISp–*Batf3* cluster, the separation was clear (Kolmogorov–Smirnov test $P = 0$): classification probabilities have a bimodal distribution and cluster separation is discrete. Finally, we split the L4–IT–VISp–*Rspo1* cells into five bins based on random forest classification probabilities and computed the differentially expressed genes between the two bins at the both ends of the gradient and the bin at the middle of the gradient (Extended Data Fig. 14d).

RNA FISH. We performed RNA FISH using RNAscope Multiplex Fluorescent v1 and v2 kits (Advanced Cell Diagnostics) according to the manufacturer's protocols. We used fresh frozen sections, which we prepared by dissecting fresh brains, embedding the brains in optimum cutting temperature compound (OCT; Tissue-Tek), and storing OCT blocks at −80 °C. Ten-micrometre coronal sections were cut using a cryostat and collected on SuperFrost slides (ThermoFisher Scientific). Sections were allowed to dry for 30 min at −20 °C in a cryostat chamber, placed into pre-chilled plastic slide boxes, wrapped in a zipped plastic bag, and stored at −80 °C. Slides were used within one week. Nuclei were labelled by DAPI and nuclear signal was used to segment cells in images. We imaged mounted sections at 40× on a confocal microscope (Leica SP8). Maximum projections of z-stacks (1-μm intervals) were processed using CellProfiler (http://www.cellprofiler.org)[67] to identify nuclei, quantify the number of fluorescent spots, and assign fluorescent spots to each cell/nucleus.

Immunohistochemistry. Mice were perfused with 4% paraformaldehyde (PFA). Brains were dissected and post-fixed with 4% PFA at room temperature for 3–6 h followed by overnight at 4 °C. Brains were rinsed with PBS and cryoprotected in 10% sucrose (w/v) in PBS with 0.1% sodium azide overnight at 4 °C. One-hundred-micrometre coronal slices were sectioned on a microtome (Leica, SM2010R), washed with PBS, blocked with 5% normal donkey serum in PBS and 0.3% Triton X-100 (PBST) for 1 h, and stained with rabbit anti-dsRed (1:1,000, Clontech, 632496) and goat anti-PVALB (1:1,000, Swant, PVG-213) overnight at room temperature. Sections were washed three times in PBST and incubated with anti-rabbit Alexa 594 (1:500, Jackson ImmunoResearch, 711-585-152) and anti-goat Alexa 488 (1:500, Jackson ImmunoResearch, 705-605-147) for 4 h at room temperature. Sections were washed three times with PBST and stained with 5 μM DAPI in PBS for 20 min. After washing in PBST, sections were mounted onto slides, allowed to dry, rehydrated in PBS, dipped in water and coverslips were added with Fluoromount G (SouthernBiotech, 0100-01) mounting medium.

Data analysis and visualization software. Analysis and visualization of transcriptomic data were performed using R v.3.3.0 and greater[68], assisted by the Rstudio IDE (Integrated Development Environment for R v.1.1.442; https://www.rstudio.com/) as well as the following R packages: cowplot v.0.9.2 (https://rdrr.io/cran/cowplot/), dendextend v.1.5.2[69], dplyr v.0.7.4 (https://dplyr.tidyverse.org/), feather v0.3.1 (https://rdrr.io/cran/feather/), FNN v.1.1 (https://cran.r-project.org/web/packages/FNN/index.html), ggbeeswarm v.0.6.0 (https://cran.r-project.org/web/packages/ggbeeswarm/index.html), ggExtra v.0.8 (https://rdrr.io/cran/ggExtra/), ggplot2 v.2.2.1[70], ggrepel v.0.7.0 (https://cran.r-project.org/web/packages/ggrepel/vignettes/ggrepel.html), googlesheets v.0.2.2 (https://cran.r-project.org/web/packages/googlesheets/vignettes/basic-usage.html), gridExtra v.2.3 (https://cran.r-project.org/web/packages/gridExtra/index.html), Hmisc v.4.1-1 (https://cran.r-project.org/web/packages/Hmisc/index.html), igraph v.1.2.1 (https://www.rdocumentation.org/packages/igraph/versions/1.2.1), limma v.3.30.13[66,71], Matrix

© 2018 Springer Nature Limited. All rights reserved.

v.1.2-12 (https://rdrr.io/rforge/Matrix/), matrixStats v.0.53.1 (https://cran.rstudio.com/web/packages/matrixStats/index.html), pals v.1.5 (https://rdrr.io/cran/pals/), purrr v.0.2.4 (https://purrr.tidyverse.org/), pvclust v.2.0-0 (http://stat.sys.i.kyoto-u.ac.jp/prog/pvclust/), randomForest v.4.6-14[72], reshape2 v.1.4.2 (https://www.statmethods.net/management/reshape.html), Rphenograph v.0.99.1 (https://rdrr.io/github/JinmiaoChenLab/Rphenograph/), Rtsne v.0.14. (https://cran.r-project.org/web/packages/Rtsne/citation.html), Seurat v.2.1.0[73], viridis v.0.5.0 (https://rdrr.io/cran/viridisLite/man/viridis.html), WGCNA v.1.61[74], and xlsx v.0.5.7 (https://cran.r-project.org/web/packages/xlsx/index.html). Scripts for the R implementation of FIt-SNE[75] were used for *t*-SNE analyses.

Reporting summary. Further information on research design is available in the Nature Research Reporting Summary linked to this paper.

Code availability. Software code used for data analysis and visualization is available from GitHub at https://github.com/AllenInstitute/tasic2018analysis/. An R package for iterative clustering (hicat) is available on GitHub at https://github.com/AllenInstitute/scrattch.hicat. The dataset is available for download and browsing on the Allen Institute for Brain Science website: http://celltypes.brain-map.org/rnaseq.

Data availability

Single-cell transcriptomic data are available at the NCBI Gene Expression Omnibus (GEO) under accession GSE115746. Summary of all transcriptomic types and markers is available in Supplementary Table 9. Full metadata for all samples are available in Supplementary Table 10. Newly generated mouse lines have been deposited to the Jackson Laboratory: *Vipr2-IRES2-cre* (JAX stock number 031332), *Slc17a8-IRES2-cre* (JAX stock number 028534), *Penk-IRES2-cre-neo* (JAX stock number 025112).

49. Cong, L. et al. Multiplex genome engineering using CRISPR/Cas systems. *Science* **339**, 819–823 (2013).
50. George, S. H. et al. Developmental and adult phenotyping directly from mutant embryonic stem cells. *Proc. Natl Acad. Sci. USA* **104**, 4455–4460 (2007).
51. Raymond, C. S. & Soriano, P. High-efficiency FLP and PhiC31 site-specific recombination in mammalian cells. *PLoS One* **2**, e162 (2007).
52. Tervo, D. G. et al. A designer AAV variant permits efficient retrograde access to projection neurons. *Neuron* **92**, 372–382 (2016).
53. Chatterjee, S. et al. Nontoxic, double-deletion-mutant rabies viral vectors for retrograde targeting of projection neurons. *Nat. Neurosci.* **21**, 638–646 (2018).
54. Hnasko, T. S. et al. Cre recombinase-mediated restoration of nigrostriatal dopamine in dopamine-deficient mice reverses hypophagia and bradykinesia. *Proc. Natl Acad. Sci. USA* **103**, 8858–8863 (2006).
55. Paxinos, G. and Franklin, K. B. J. *Mouse Brain In Stereotaxic Coordinates 3rd edn* (Academic Press, Cambridge, MA, 2008).
56. Sugino, K. et al. Molecular taxonomy of major neuronal classes in the adult mouse forebrain. *Nat. Neurosci.* **9**, 99–107 (2006).
57. Hempel, C. M., Sugino, K. & Nelson, S. B. A manual method for the purification of fluorescently labeled neurons from the mammalian brain. *Nat. Protoc.* **2**, 2924–2929 (2007).
58. Ting, J. T., Daigle, T. L., Chen, Q. & Feng, G. Acute brain slice methods for adult and aging animals: application of targeted patch clamp analysis and optogenetics. *Methods Mol. Biol.* **1183**, 221–242 (2014).
59. Ramsköld, D. et al. Full-length mRNA-Seq from single-cell levels of RNA and individual circulating tumor cells. *Nat. Biotechnol.* **30**, 777–782 (2012).
60. Picelli, S. et al. Smart-seq2 for sensitive full-length transcriptome profiling in single cells. *Nat. Methods* **10**, 1096–1098 (2013).
61. Dobin, A. et al. STAR: ultrafast universal RNA-seq aligner. *Bioinformatics* **29**, 15–21 (2013).
62. Lawrence, M. et al. Software for computing and annotating genomic ranges. *PLOS Comput. Biol.* **9**, e1003118 (2013).
63. Yao, Z. et al. A single-cell roadmap of lineage bifurcation in human ESC models of embryonic brain development. *Cell Stem Cell* **20**, 120–134 (2017).
64. Shekhar, K. et al. Comprehensive classification of retinal bipolar neurons by single-cell transcriptomics. *Cell* **166**, 1308–1323 (2016).
65. Fortunato, S. & Barthélemy, M. Resolution limit in community detection. *Proc. Natl Acad. Sci. USA* **104**, 36–41 (2007).
66. Ritchie, M. E. et al. *limma* powers differential expression analyses for RNA-sequencing and microarray studies. *Nucleic Acids Res.* **43**, e47 (2015).
67. Lamprecht, M. R., Sabatini, D. M. & Carpenter, A. E. CellProfiler: free, versatile software for automated biological image analysis. *Biotechniques* **42**, 71–75 (2007).
68. R Development Core Team. *R: A Language and Environment for Statistical Computing* (R Foundation for Statistical Computing, Vienna, 2018).
69. Galili, T. dendextend: an R package for visualizing, adjusting and comparing trees of hierarchical clustering. *Bioinformatics* **31**, 3718–3720 (2015).
70. Wickham, H. *ggplot2: Elegant Graphics for Data Analysis* (Springer-Verlag, New York, 2009).
71. Law, C. W., Alhamdoosh, M., Su, S., Smyth, G. K. & Ritchie, M. E. RNA-seq analysis is easy as 1-2-3 with limma, Glimma and edgeR. *F1000 Res.* **5**, 1408 (2016).
72. Liaw, A. & Weiner, M. Classification and regression by randomForest. *R News* **2**, 18–22 (2002).
73. Macosko, E. Z. et al. Highly parallel genome-wide expression profiling of individual cells using nanoliter droplets. *Cell* **161**, 1202–1214 (2015).
74. Langfelder, P. & Horvath, S. WGCNA: an R package for weighted correlation network analysis. *BMC Bioinformatics* **9**, 559 (2008).
75. Linderman, G. C., Rachh, M., Hoskins, J. G., Steinberberger, S. & Kluger, Y. Efficient algorithms for t-distributed stochastic neighborhood embedding. Preprint at https://arXiv.org/abs/1712.09005 (2017).
76. Hevner, R. F., Neogi, T., Englund, C., Daza, R. A. & Fink, A. Cajal-Retzius cells in the mouse: transcription factors, neurotransmitters, and birthdays suggest a pallial origin. *Brain Res. Dev. Brain Res.* **141**, 39–53 (2003).
77. Cahoy, J. D. et al. A transcriptome database for astrocytes, neurons, and oligodendrocytes: a new resource for understanding brain development and function. *J. Neurosci.* **28**, 264–278 (2008).
78. Marques, S. et al. Oligodendrocyte heterogeneity in the mouse juvenile and adult central nervous system. *Science* **352**, 1326–1329 (2016).
79. Zhang, Y. et al. An RNA-sequencing transcriptome and splicing database of glia, neurons, and vascular cells of the cerebral cortex. *J. Neurosci.* **34**, 11929–11947 (2014).
80. Kopatz, J. et al. Siglec-h on activated microglia for recognition and engulfment of glioma cells. *Glia* **61**, 1122–1133 (2013).
81. Bennett, M. L. et al. New tools for studying microglia in the mouse and human CNS. *Proc. Natl Acad. Sci. USA* **113**, E1738–E1746 (2016).
82. Armulik, A., Genové, G. & Betsholtz, C. Pericytes: developmental, physiological, and pathological perspectives, problems, and promises. *Dev. Cell* **21**, 193–215 (2011).
83. Bondjers, C. et al. Microarray analysis of blood microvessels from PDGF-B and PDGF-Rβ mutant mice identifies novel markers for brain pericytes. *FASEB J.* **20**, 1703–1705 (2006).
84. Campbell, J. N. et al. A molecular census of arcuate hypothalamus and median eminence cell types. *Nat. Neurosci.* **20**, 484–496 (2017).
85. Groh, A. et al. Cell-type specific properties of pyramidal neurons in neocortex underlying a layout that is modifiable depending on the cortical area. *Cereb. Cortex* **20**, 826–836 (2010).
86. Harris, J. A. et al. Anatomical characterization of Cre driver mice for neural circuit mapping and manipulation. *Front. Neural Circuits* **8**, 76 (2014).
87. Taniguchi, H., Lu, J. & Huang, Z. J. The spatial and temporal origin of chandelier cells in mouse neocortex. *Science* **339**, 70–74 (2013).

© 2018 Springer Nature Limited. All rights reserved.

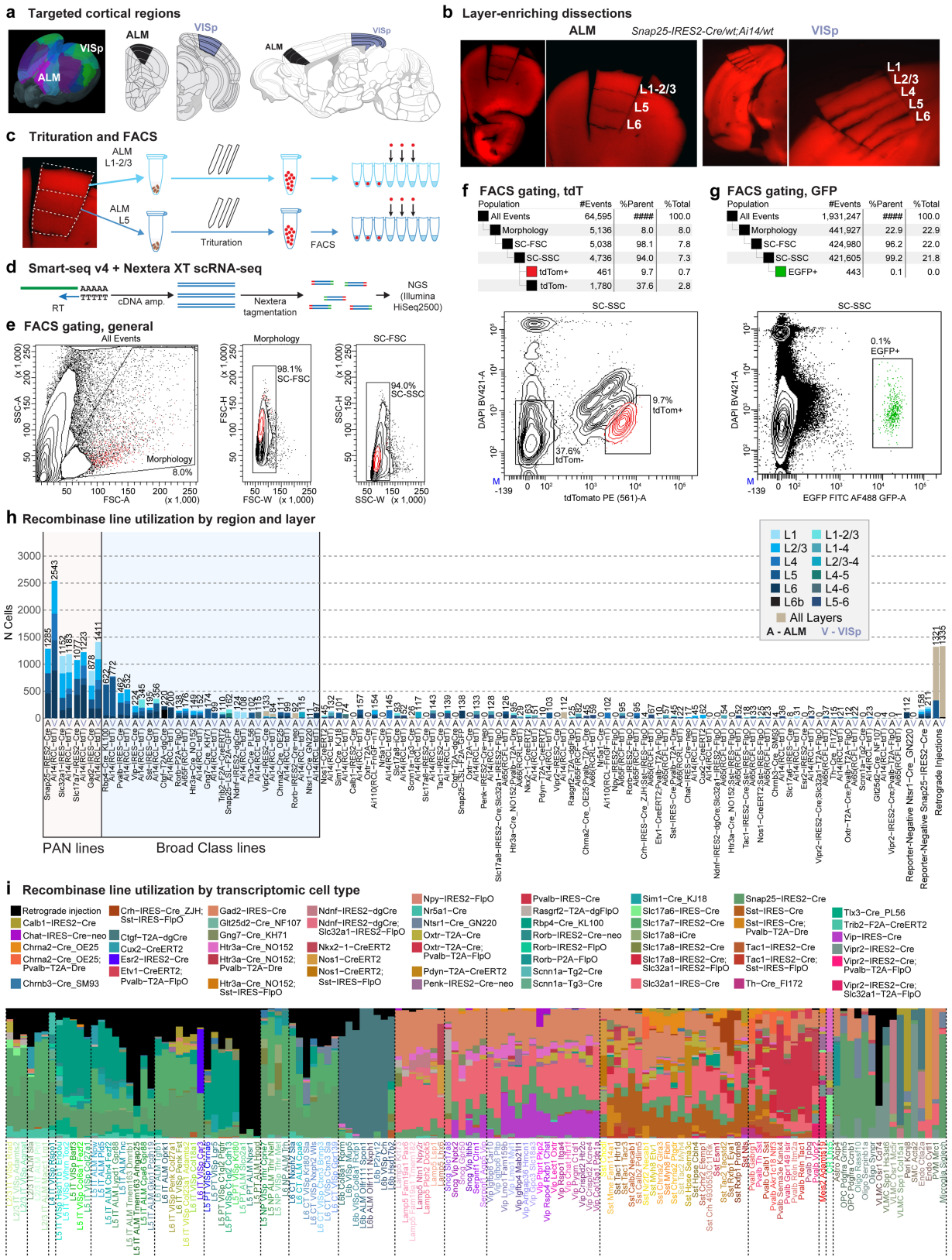

Extended Data Fig. 1 | See next page for caption.

© 2018 Springer Nature Limited. All rights reserved.

Extended Data Fig. 1 | Overview of sample collection. a, One of the two brain regions, ALM or VISp, was dissected from an adult mouse (P53–P59 ($n = 339$), P51 ($n = 1$), and P63–P91 ($n = 12$), Supplementary Table 1). **b**, Example microdissection images from the most heavily sampled mouse genotype, *Snap25-IRES2-cre/wt;Ai14/wt*, from both cortical regions. For many samples, microdissection was used to isolate layer-enriched portions of the cortex. ALM lacks L4. The dissection images are representative of $n = 21$ processed *Snap25-IRES2-cre/wt;Ai14/wt* brains. **c**, Microdissected layers were processed separately for single-cell suspension. Each sample was digested with pronase, then triturated with pipettes of decreasing tip diameter (600, 300 and 150 μm). Individual cells were sorted into 8-well strip PCR tubes by FACS. **d**, SMART-Seq v4 was used to reverse-transcribe and amplify full-length cDNAs from each cell. cDNAs were then tagmented by Nextera XT, PCR-amplified, and sequenced on Illumina HiSeq2500. **e**, Common gates used for all FACS sorts: (1) Morphology gate excludes events with high side scatter and low forward scatter, which are largely cellular debris, and (2) SC-FSC and SC-SSC gates exclude samples with high forward scatter width and high side scatter width, respectively, to exclude cell doublets and multiplets. **f**, Example gating for live tdTomato$^+$ or tdTomato$^-$ cells. Cells sorted using the tdTom$^+$ gate express the tdTomato reporter and have low DAPI fluorescence. This plot was generated from cell suspension isolated from a *Snap25-IRES2-cre/wt;Ai14/wt* animal, which expresses tdTomato in all neurons. The tdTom$^-$ gate in this genotype was the main source of non-neuronal cells, which have low DAPI fluorescence and low tdTomato expression. Gating hierarchy and sorting statistics are shown above the FACS scatter plot. This gating strategy is representative of $n = 21$ processed *Snap25-IRES2-cre/wt;Ai14/wt* brains. **g**, To sort eGFP$^+$ cells, we used the same debris and doublet gating described in **e**, then collected cells with high eGFP and low DAPI fluorescence (eGFP$^+$ gate). This plot was generated from cell suspension isolated from VISp of a *Ctgf-2A-dgcre/wt;Snap25-LSL-F2A-GFP/wt* animal, which expresses eGFP in L6b neurons. Gating hierarchy and sorting statistics are shown above the FACS scatter plot. This gating strategy is representative of $n = 4$ processed *Ctgf-2A-dgcre/wt;Snap25-LSL-F2A-GFP/wt* brains. **h**, Genotype and layer sampling frequencies for all cluster-assigned cells ($n = 23{,}822$). PAN Cre-lines were used to broadly sample neurons in the cortex. Non-PAN lines were included to (1) enrich for cells that displayed poor survival in the isolation process (for example, *Rbp4-cre_KL100* for L5 types and *Pvalb-IRES-cre* for *Pvalb* types); (2) enrich for rare cell types (for example, *Ctgf-2A-dgcre* for L6b); and (3) transcriptomically characterize cell types labelled by these lines. Bar plots show the number of cells sampled from each genotype and region (A, ALM; V, VISp). Bars are coloured according to the number of samples from microdissected layers or combinations of layers. **i**, Transgenic driver composition with respect to cell types for all cluster-assigned cells ($n = 23{,}822$). The stacked bar plot shows the proportion of cells in each cluster that were collected from each Cre line. Black bars represent cells collected from retrograde tracing experiments. These cells were labelled by a fluorophore-expressing virus or by a Cre-expressing virus together with a Cre-reporter transgenic line. Brain diagrams were derived from the Allen Mouse Brain Reference Atlas (version 2 (2011); downloaded from https://brain-map.org/api/index.html).

© 2018 Springer Nature Limited. All rights reserved.

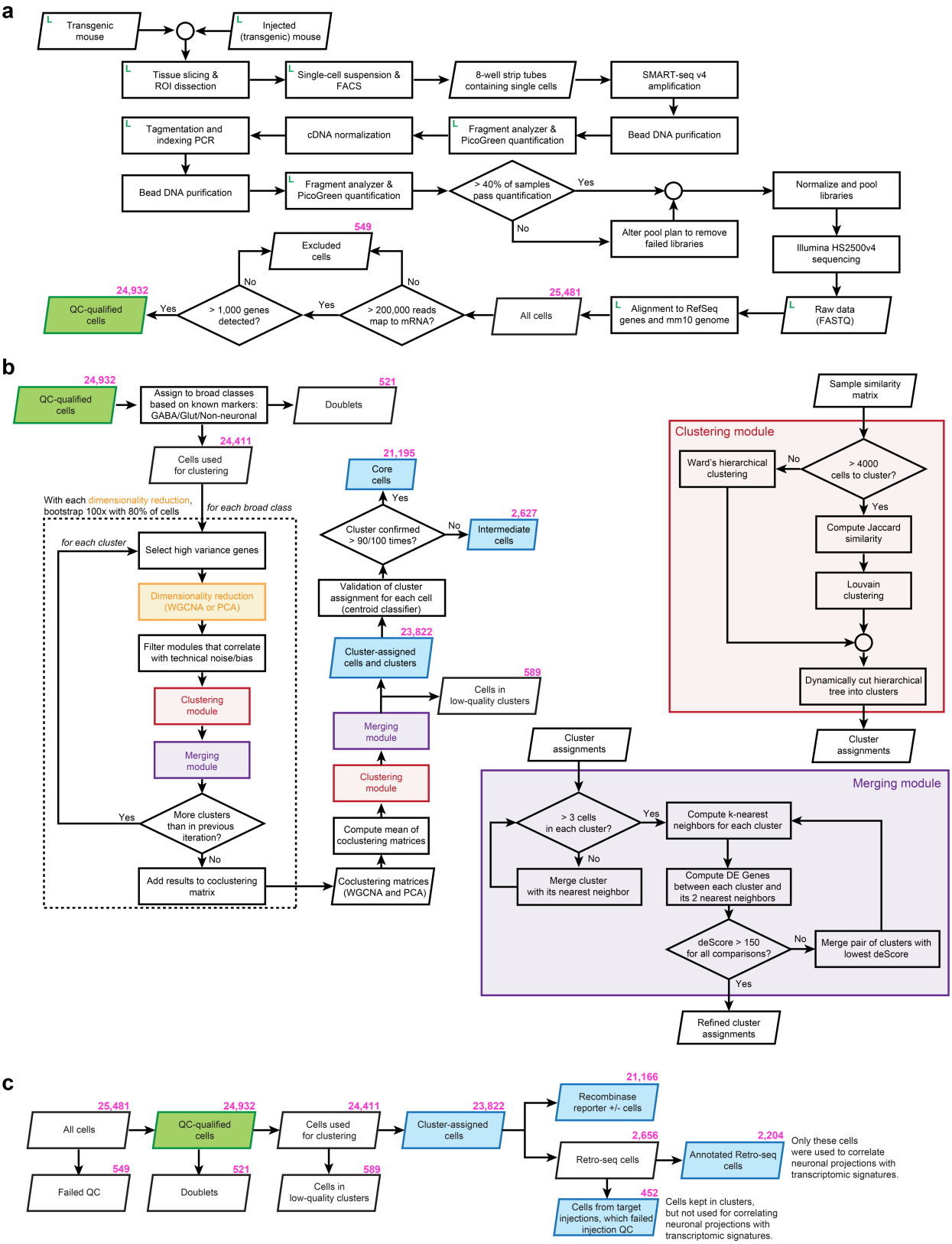

Extended Data Fig. 2 | See next page for caption.

© 2018 Springer Nature Limited. All rights reserved.

Extended Data Fig. 2 | scRNA-seq pipeline and analysis workflow. **a**, Workflow diagram outlines the path from individual experimental animals to quality control-qualified scRNA-seq data. At multiple points throughout sample processing, cell and sample metadata were recorded in a laboratory information management system (LIMS, labelled as L), which informs quality control processes. Samples must pass quality control benchmarks to continue through sample processing. **b**, Clustering procedure. Cells were first divided into broad cell classes based on known marker gene expression, then were segregated into clusters 100 times using a bootstrapped procedure that sampled 80% of cells each time. Within each iteration, cells were split by selection of high variance genes followed by PCA or WGCNA dimensionality reduction. Principal components and WGCNA eigengenes were then used to cluster samples by hierarchical clustering or graph-based Jaccard–Louvain clustering algorithm, depending on the number of cells (clustering module, red box). Clusters were checked for over-splitting or termination criteria (merging module, purple box). Each cluster was used as input for a further round of splitting until termination criteria were met. After 100 rounds of clustering, the frequencies with which samples were clustered together were used as a similarity measure to hierarchically cluster the samples. The resulting hierarchical clustering tree was then dynamically cut, and the resulting clusters were checked for over-splitting. Finally, cells were subjected to validation by a centroid classifier. After 100 rounds of validation, cells that were mapped to the same cluster in more than 90 out of 100 trials were assigned 'core' cell identity ($n = 21{,}195$), and cells with lower scores were assigned 'intermediate' cell identity ($n = 2{,}627$). Most intermediate cells were mapped to only two clusters (2,492 out of 2,627; 94.9%). **c**, The number of cells at each step in our analysis pipeline. The identification of doublets and low-quality clusters is described in the Methods. Some high-quality cells ($n = 452$) from the retro-seq dataset were not used for projection analysis because stereotaxic injections were determined post-brain section to be unsatisfactory, because: (1) the incorrect target was injected, (2) the injection was too close to the collection site, or (3) strong injection tract labelling was detected (Methods). These cells were kept in transcriptomic clusters, but were not used to inform the specificity of glutamatergic projections. Only cells from the annotated retro-seq dataset ($n = 2{,}204$) were used for connectivity analyses in Fig. 3 and Extended Data Fig. 10a, b.

© 2018 Springer Nature Limited. All rights reserved.

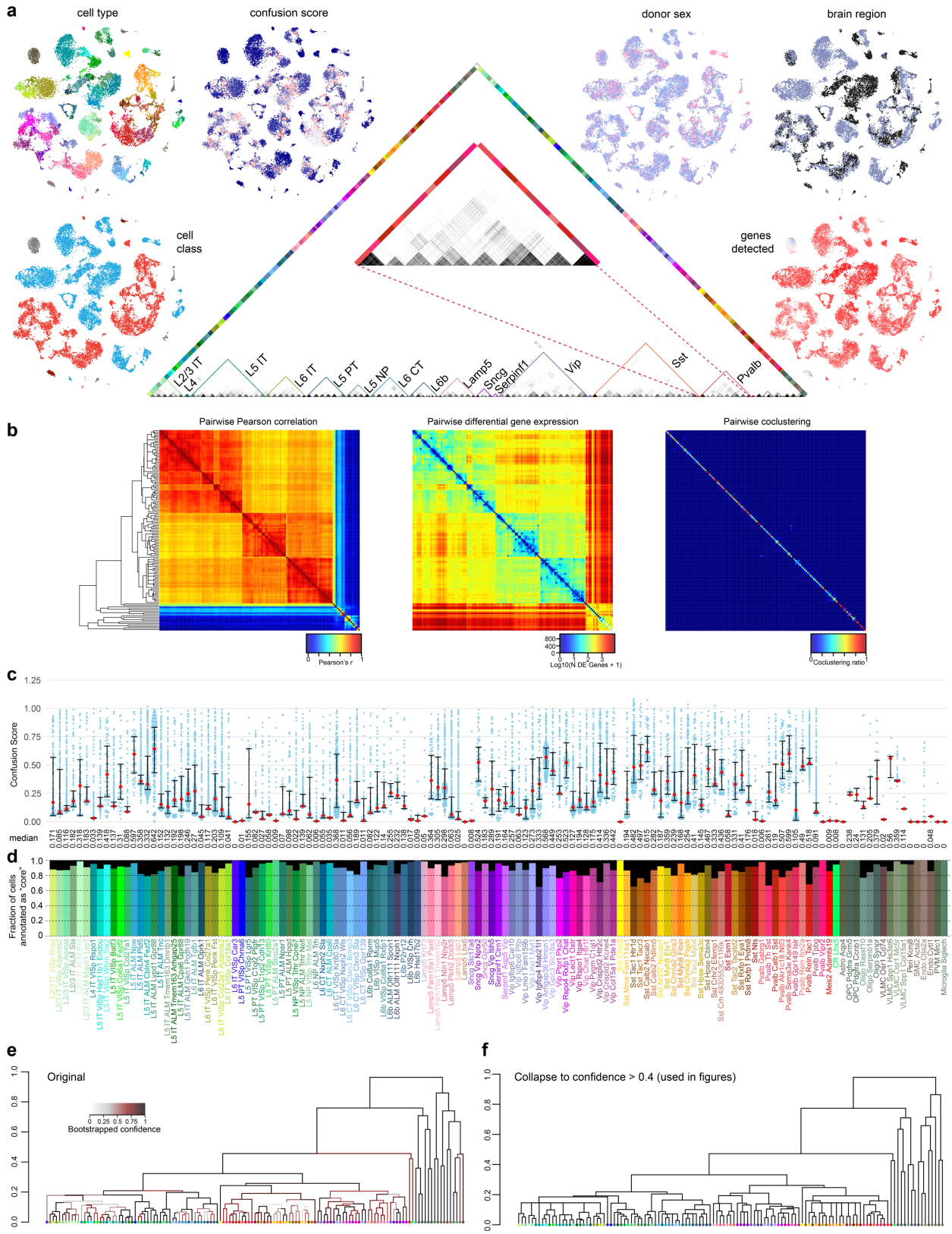

Extended Data Fig. 3 | See next page for caption.

© 2018 Springer Nature Limited. All rights reserved.

Extended Data Fig. 3 | Co-clustering frequency matrix, confusion scores and intermediate cells. a, The co-clustering frequency matrix (centre) for up to 100 cells per cluster selected at random ($n = 10{,}820$). Some cell types, for example certain *Pvalb* types (middle of enlarged panel), display pronounced co-clustering. *t*-SNE was used to visualize the similarity of gene expression patterns in two dimensions for all cluster-assigned cells ($n = 23{,}822$). Individual cells in *t*-SNE plots were coloured by: cell class (GABAergic, red; glutamatergic, blue; glia, grey; endothelial cells, brown), animal donor sex (female, pink; male, purple), dissected brain region (ALM, black; VISp, grey), confusion score (low-blue, high-red), and the number of genes detected (low-blue, high-red). **b**, Pairwise correlation, differential gene expression and co-clustering for all 133 clusters using all cluster-assigned cells ($n = 23{,}822$). **c**, Confusion scores for all cluster-assigned cells ($n = 23{,}822$) segregated by clusters. For each cell, the confusion score is defined as the ratio of the probabilities for that cell to be clustered with the cells from its second best cluster and with the cells from the final cluster (also the best cluster except for rare exceptions). Thus, confusion score is a measure of the confidence of cell type assignment: the lower the value, the less frequently a cell was grouped with cells from a different cluster. Each blue dot is a confusion score for a single cell, median values are shown as red dots; whiskers are twenty-fifth and seventy-fifth percentiles. **d**, Fraction of cluster-assigned cells ($n = 23{,}822$) annotated as core (coloured) or intermediate (black) for each cluster. In total, 21,195 cells (88.97%) were assigned core, whereas 2,627 (11.03%) were assigned intermediate identity. **e**, **f**, We performed 100 rounds of bootstrapped clustering to determine the confidence of our hierarchical clustering structure (Methods). The final dendrogram generated by this method (**e**), with branches coloured by their bootstrapped confidence: light grey (low confidence), maroon (moderate confidence), and black (high confidence). For figures, we used the dendrogram in **f**, in which we collapsed branches with confidence lower than 0.4.

© 2018 Springer Nature Limited. All rights reserved.

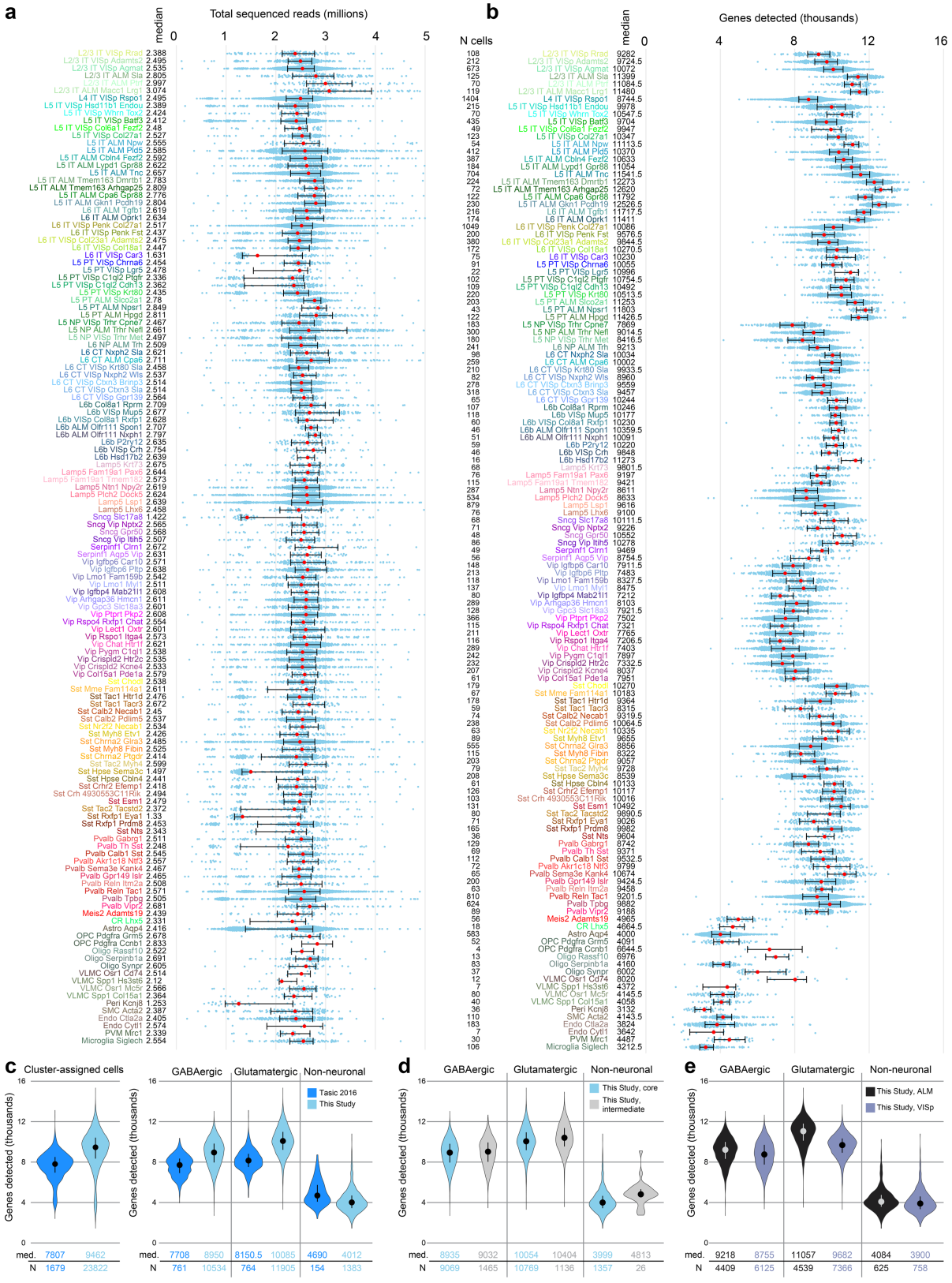

Extended Data Fig. 4 | See next page for caption.

© 2018 Springer Nature Limited. All rights reserved.

Extended Data Fig. 4 | Sequencing depth and gene detection for quality-control-qualified cells segregated by cluster. a, Sequencing depth for all cluster-assigned cells ($n = 23{,}822$), grouped by cell type. Cells were sequenced to a median depth of 2.54 million reads (min = 0.103 M; max = 13.84 M). Median values in millions of reads are adjacent to the cell type labels. Median values are shown as red dots; whiskers are twenty-fifth and seventy-fifth percentiles. **b**, The number of detected genes (reads detected in exons >0) varies by cell type. Gene detection is shown for each cluster-assigned cell ($n = 23{,}822$). Median values are shown adjacent to the cell type labels. Median number of genes detected across all cells is 9,462 per cell (min = 1,445; max = 15,338). Median values are shown as red dots; whiskers are twenty-fifth and seventy-fifth percentiles. Samples with less than1,000 detected genes were excluded at a prior quality control step (Extended Data Fig. 2). **c**, Comparison of gene detection between our previous study[20] and this study for all cluster-assigned cells (left) and cells grouped according to major classes (right). **d**, Comparison of gene detection between cell classes for core and intermediate cells. The higher gene detection for intermediate non-neuronal cells may be due to contamination with other non-neuronal cells. **e**, Comparison of gene detection within cell classes between VISp and ALM. In **c**–**e**, medians are shown as dots and values are listed below each distribution; whiskers are twenty-fifth and seventy-fifth percentiles. Sample size (number of cells) for each analysed group is listed between panels **a** and **b**, and below the graphs for panels **c**–**e**.

© 2018 Springer Nature Limited. All rights reserved.

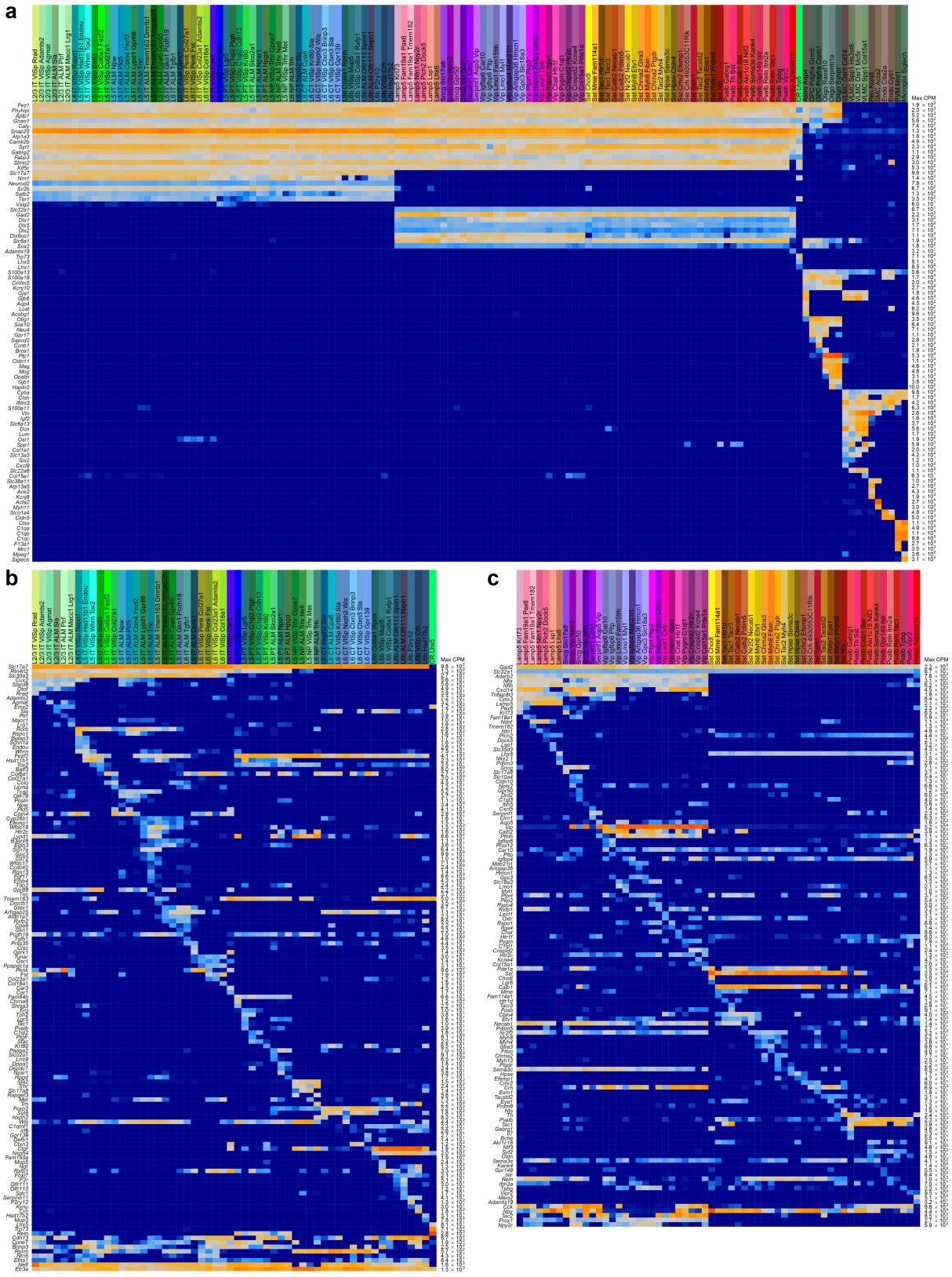

Extended Data Fig. 5 | See next page for caption.

© 2018 Springer Nature Limited. All rights reserved.

Extended Data Fig. 5 | Markers used for cell type assignment. **a**, Marker panel of 88 genes for cell classes. For each cluster, 25% trimmed mean expression values are shown ($n = 23{,}822$ cluster-assigned cells; 133 clusters). Maximum expression values (counts per million reads, CPM) are shown to the right of the heat map. Pan-neuronal markers (for example, *Snap25*) were used to assign neuronal type identity. Glutamatergic (for example, *Slc17a7* and *Slc17a6*) and pan-GABAergic (for example, *Gad1*, *Gad2* and *Slc32a1*) markers were used to assign glutamatergic and GABAergic identity, respectively. Known non-neuronal markers were used to assign non-neuronal identities. **b**, Marker panel for glutamatergic cell types. For each cluster, 25% trimmed mean expression values are shown ($n = 11{,}905$ cells; 56 clusters). Layer-specific markers were used to assign layer identity (for example, *Cux2*, *Rorb*, *Deptor* and *Foxp2*). To assign final names to types, subclass and/or layer-markers were combined with unique or other specific markers, many of which are novel. Once the identity was assigned, previously unknown genetic bases of phenotypes could be discovered. For example, for the Cajal–Retzius cell type CR–*Lhx5*, which has been shown by immunohistochemistry to contain glutamate but not GABA[76], we show that its glutamatergic phenotype stems from the expression of mRNA encoding VGLUT2 (*Slc17a6*), and not from the other glutamate transporters (*Slc17a7* and *Slc17a8*). Note that some markers that appear non-specific, provide preferential labelling of specific types when used to make random-insertion transgenic BAC lines. For example, *Efr3a-cre_NO108*[34] specifically labels near-projecting types, although *Efr3a* mRNA is ubiquitously detected in all neurons. However, its expression is about fivefold higher in near-projecting types; this may contribute to preferential labelling of the near-projecting types by this BAC transgenic Cre line. **c**, Marker panel for GABAergic cell types. For each cluster, 25% trimmed mean expression values are shown ($n = 10{,}534$ cells; 61 clusters). GABAergic subclasses were assigned based on the expression of *Lamp5*, *Serpinf1*, *Sncg*, *Vip*, *Sst* and *Pvalb*. Final names were assigned based on unique combinations of markers.

© 2018 Springer Nature Limited. All rights reserved.

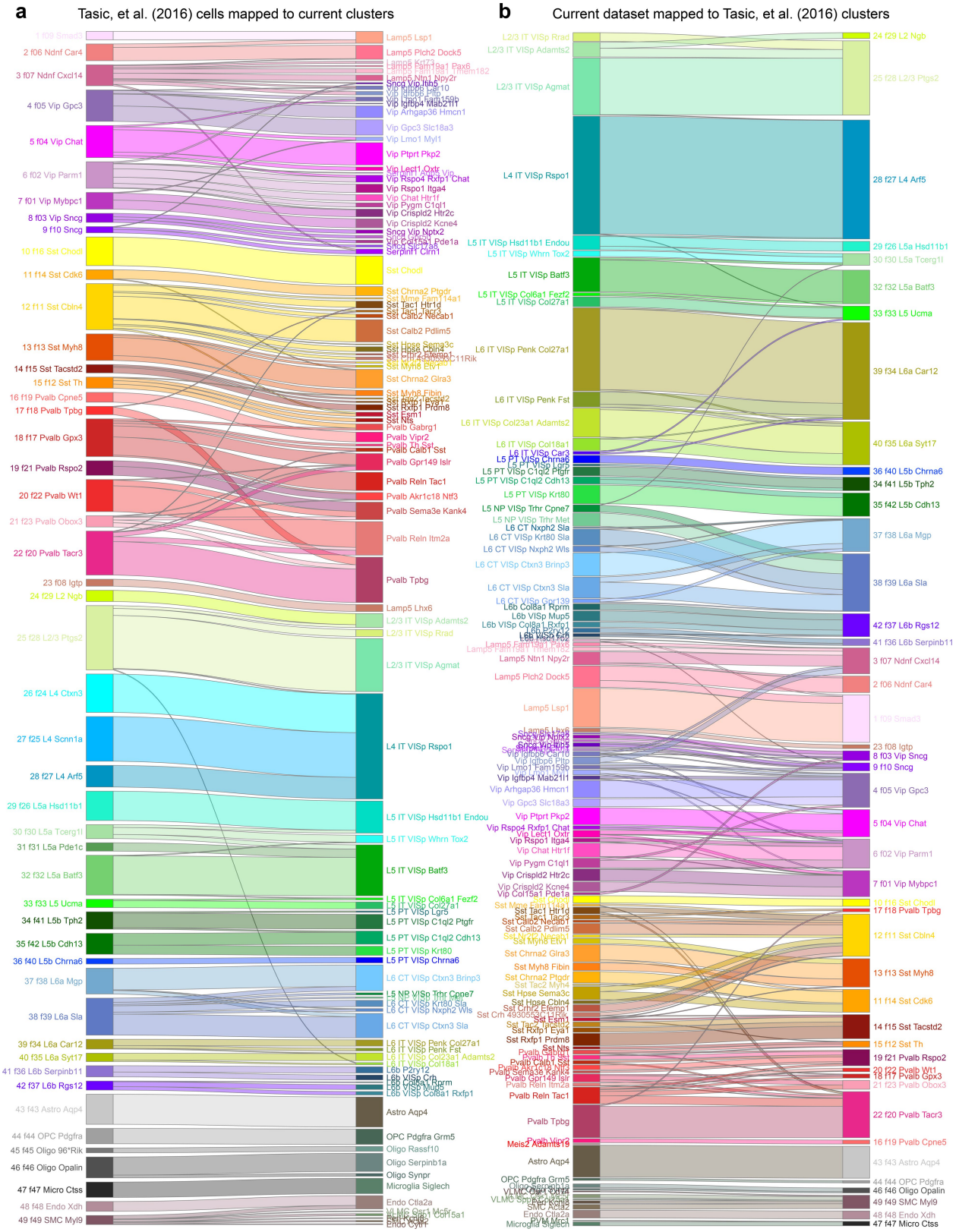

Extended Data Fig. 6 | Comparison of cell types to those defined previously[20]. We compared the similarity of clustering results for our current dataset and our previous dataset by nearest centroid classification (Methods). We mapped the 1,424 cells from the previous dataset[20] to 133 clusters from the current study (**a**) and vice versa: 23,822 current cells to 49 previous clusters[20]. **b**, Some types were largely absent from our previous study. For example, the *Meis2* type was not detected probably owing to rarity and white-matter confinement, whereas the L5 near-projecting types were missed owing to reliance on *Rbp4-cre_KL100* to isolate L5 cells. We now find that, in contrast to pan-neuronal (*Snap25-IRES-cre*) or pan-glutamatergic Cre lines (*Slc17a7-IRES-cre*), *Rbp4-cre_KL100* labels all L5 types except L5 near-projecting (Extended Data Fig. 8).

© 2018 Springer Nature Limited. All rights reserved.

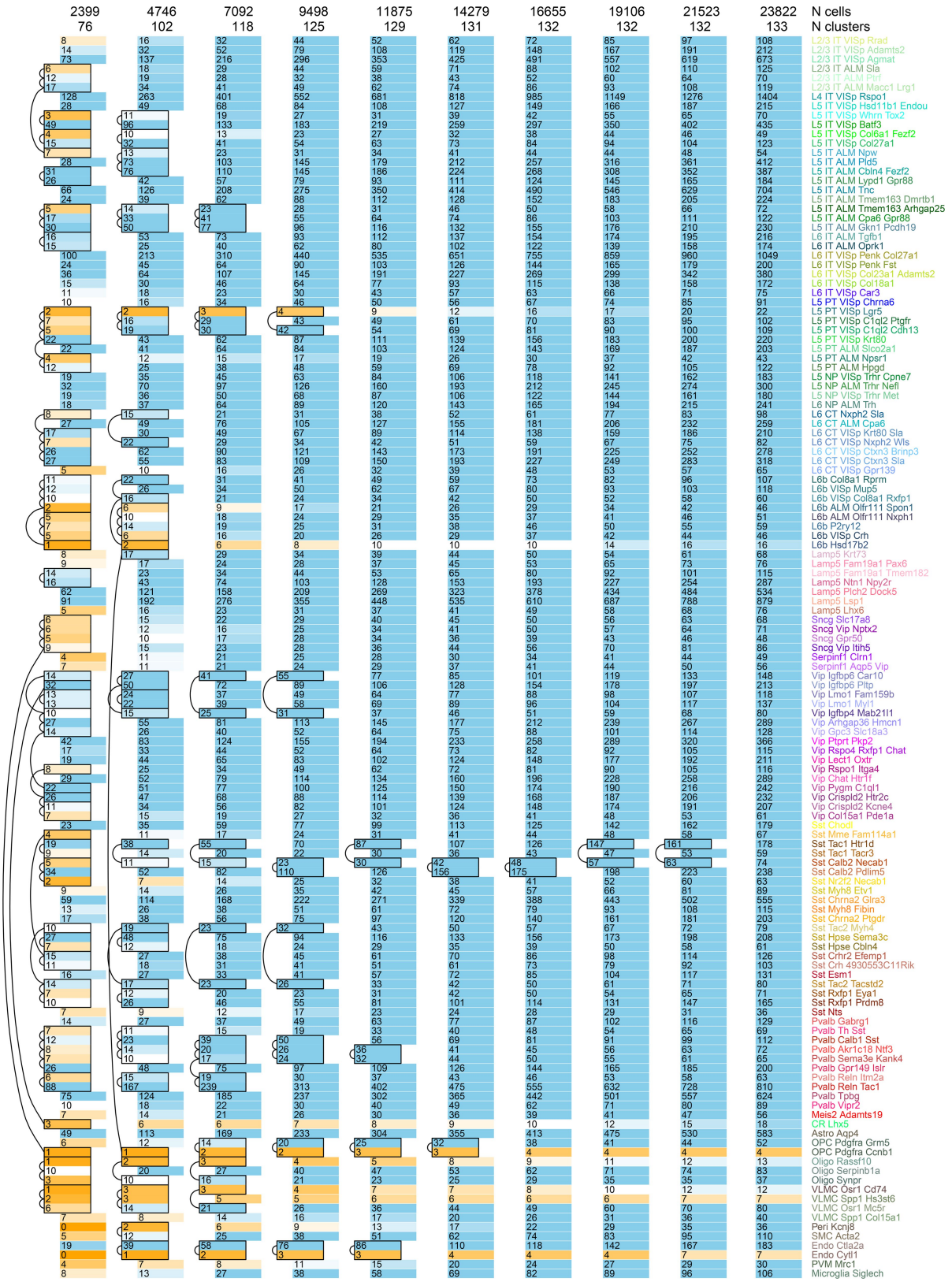

Extended Data Fig. 7 | Saturation of cell type detection. We tested the ability of our of computational approach to segregate cell types based on our standard cluster separation criteria (Methods) upon decreasing cell numbers included in clustering. The total number of sampled cells and derived clusters in each trial is shown at the top of each column. Each row is a cluster from our full dataset analysis. Each coloured box represents the number of cells from each cluster (row) that were included in the specific downsampled dataset (column). Clusters that merge are shifted to the left of their respective columns and merging is indicated by arcs and/or removal of lines between adjacent clusters. For most types, we were able to segregate them from their related types with many fewer cells than present in the complete dataset. Further cell sampling may reveal additional diversity, especially for rare cell types.

© 2018 Springer Nature Limited. All rights reserved.

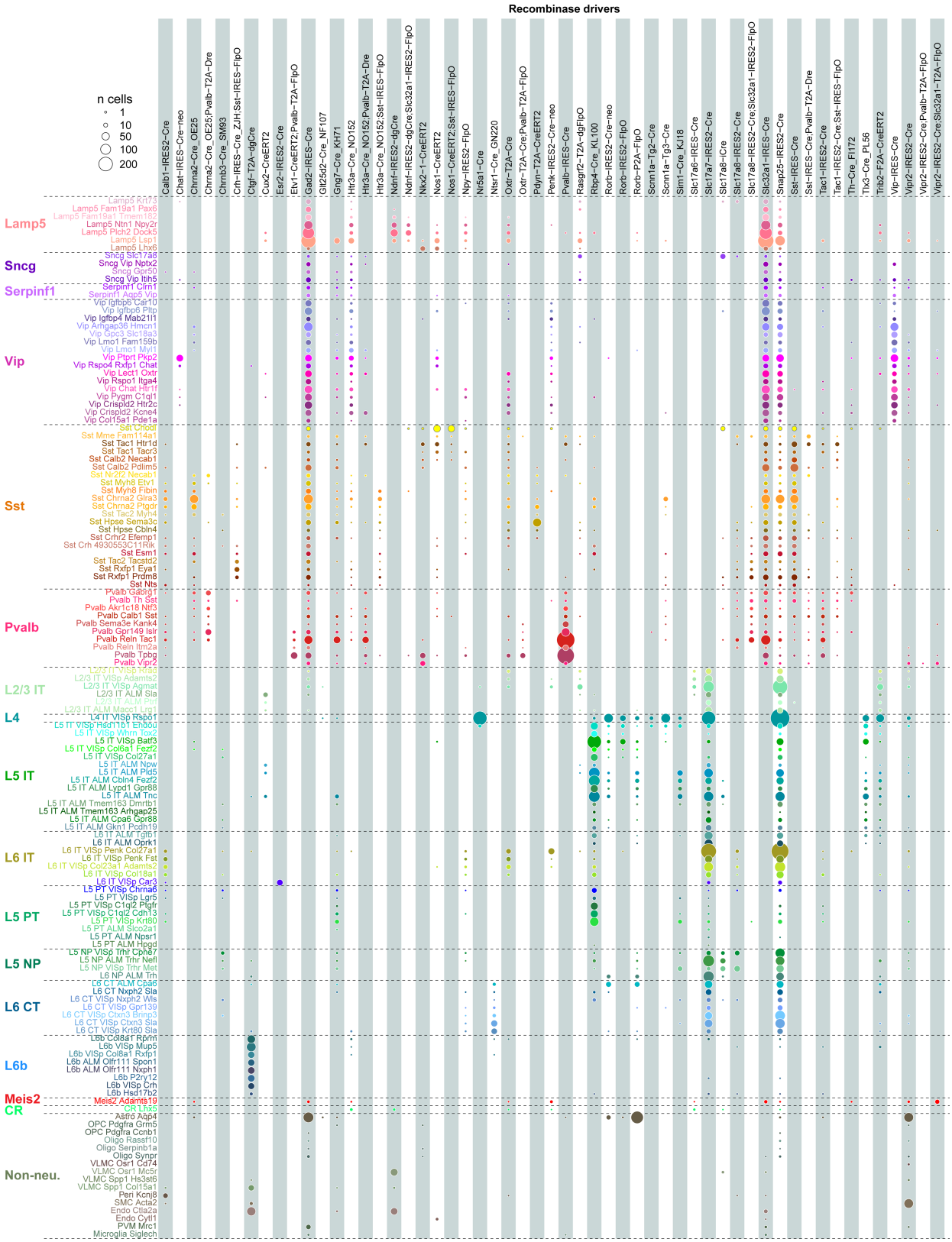

Extended Data Fig. 8 | Cell-type labelling by recombinase driver lines. Driver line names are listed on top (columns, $n = 55$) and cell types on the left (rows, $n = 133$). Coloured discs represent the numbers of cells detected for each type (cell numbers are proportional to disc surface area). This plot is based on 20,758 cells isolated from transgenic mice that were collected as tdT^+ or GFP^+ by FACS. Note that the relative proportions of cell types obtained in these experiments are likely to be affected by cell type-specific differences in survival during the isolation procedure and by samping via layer-enriching dissections.

© 2018 Springer Nature Limited. All rights reserved.

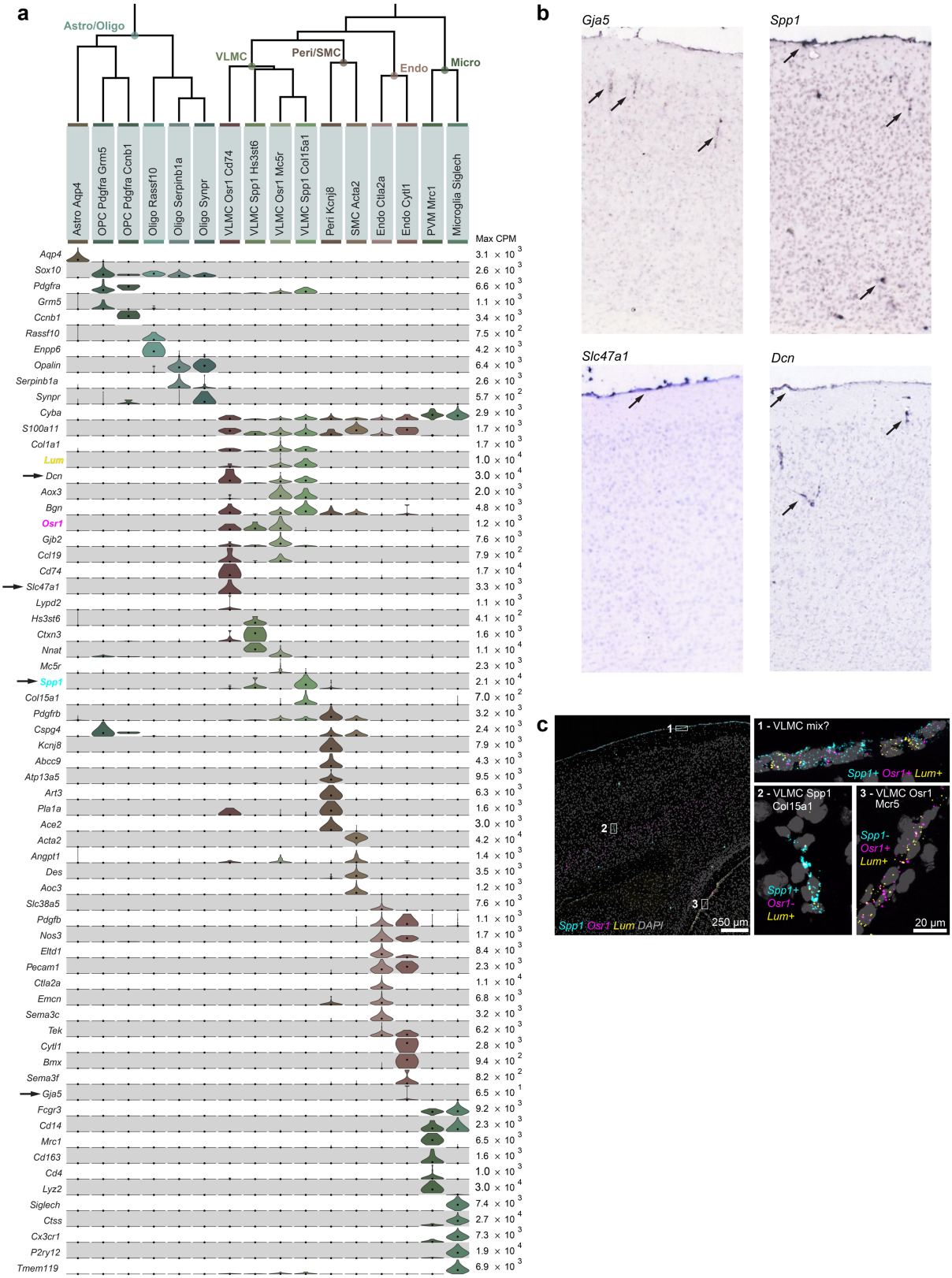

Extended Data Fig. 9 | See next page for caption.

© 2018 Springer Nature Limited. All rights reserved.

Extended Data Fig. 9 | Non-neuronal cell types. a, Non-neuronal cells ($n = 1{,}383$ cells) are divided into two major branches according to their developmental origin: neuroectoderm-derived branch, which contains astrocytes and oligodendrocytes (left), and non-neuroectoderm-derived, which includes immune cells (microglia, perivascular macrophages), blood vessel-associated cells (smooth muscle cells, pericytes and endothelial cells), and vascular leptomeningeal cells (VLMCs, right). All have been detected in both ALM and VISp, except VLMC–*Osr1*–*Cd74*, which may be rare (12 cells total) and may also be detected in ALM with further sampling. Violin plots represent distributions of individual marker gene expression in single cells within each cluster. Rows are genes, median values are black dots, and values within rows are normalized between 0 and the maximum expression value for each gene (right edge of each row) and displayed on a linear scale. We identify astrocytes based on expression of *Aqp4*[77]. Oligodendrocyte lineage cells express *Sox10*[78]. Oligodendrocyte precursor cells are marked by expression of *Pdgfra* and absence of *Col1a1*[77,78], with dividing oligodendrocyte precursor cells expressing *Ccnb1*. Newly generated oligodendrocytes (*Oligo*–*Rassf10*) express *Enpp6*, whereas myelinating oligodendrocytes (*Oligo*–*Serpinb1a*/*Synpr*) express *Opalin*[79]. Two related types of immune cells coexpress *Cd14* and *Fcgr3*, and can be identified as microglia by expression of *Siglech*[80] and *Tmem119*[81], and perivascular macrophages by expression of *Mrc1*, *Lyve1*[19] and *Cd163*[81]. We identify two related types of blood vessel-associated cells as pericytes and smooth muscle cells (SMCs) based on their expression of *Cspg4* and *Acta2* (reviewed previously[82]). We assign SMC identity to SMC–*Acta2*, which strongly expresses *Acta2* (smooth muscle actin). We assign pericyte identity to the Peri–*Kcnj8* cluster based on specific expression of pericyte markers *Kcnj8* and *Abcc9*[83]. We define additional markers uniquely expressed in this cell type (*Atp13a5*, *Art3*, *Pla1a* and *Ace2*) that may help solidify pericyte identity in future studies. We identify one type of endothelial cells (Endo–*Slc38a5*) based on expression of previously characterized endothelial markers, *Tek*, *Pdgfb*, *Nos3*, *Eltd1* and *Pecam1*. We identify VLMC types based on their unique expression of *Lum* and *Col1a1*[78,84]. We define four types based on differential gene expression. Markers examined in **b** and **c** are highlighted by arrows and colours, respectively. **b**, RNA ISH for some of non-neuronal markers from the Allen Brian Atlas[25]. Images contain regions of interest from representative sections selected from individual whole-brain RNA ISH experiments. *Spp1* mRNA is detected in the meninges and scattered in the cortex, corresponding to VLMCs, as well as select *Pvalb* and *Sst* types. *Gja5* mRNA labels vessel-like structures in the grey matter, probably corresponding to the Endo–*Slc38a5* cluster. *Slc47a1* is specific to the VLMC–*Osr1*–*Cd74* type, which appears to be restricted to pia. *Dcn* is expressed in three VLMC types, and its expression is seen in the pia and vessel-like structures in the cortex. The number of whole-brain experiments per gene available in the Allen Brain Atlas is as follows: *Spp1*: $n = 4$ brains (2 sagittal, 2 coronal); *Gja5*: $n = 2$ brains (2 sagittal); *Slc47a1*: $n = 1$ brain (sagittal); *Dcn*: $n = 3$ brains (2 sagittal, 1 coronal). **c**, Single-molecule RNA FISH by RNAscope for *Osr1*, *Spp1* and *Lum* mRNAs shows labelling at the pial surface and surrounding vessel-like structures. Images are representative of two independent RNAscope experiments on $n = 2$ brains. On the basis of the coexpression of marker genes shown in **a**, VLMCs within the grey matter (expanded region 2) are probably the VLMC–*Spp1*–*Col15a1* type, whereas VLMCs in pia between cortex and tectum (expanded region 3) are probably VLMC–*Osr1*–*Mc5r*. The surface VLMCs (expanded region 1) appear to express all three markers, which are usually not co-detected in single cells by RNA-seq (**a**). This finding could be explained by a possibility that region 1 may contain two or more types of spatially appositioned VLMCs, for example, VLMC–*Osr1*–*Cd74* (based on *Slc47a1* expression shown in **b**), as well as one of the *Lum*$^+$ types (VLMC–*Osr1*–*Mc5r* and/or VLMC–*Spp1*–*Col15a1*).

© 2018 Springer Nature Limited. All rights reserved.

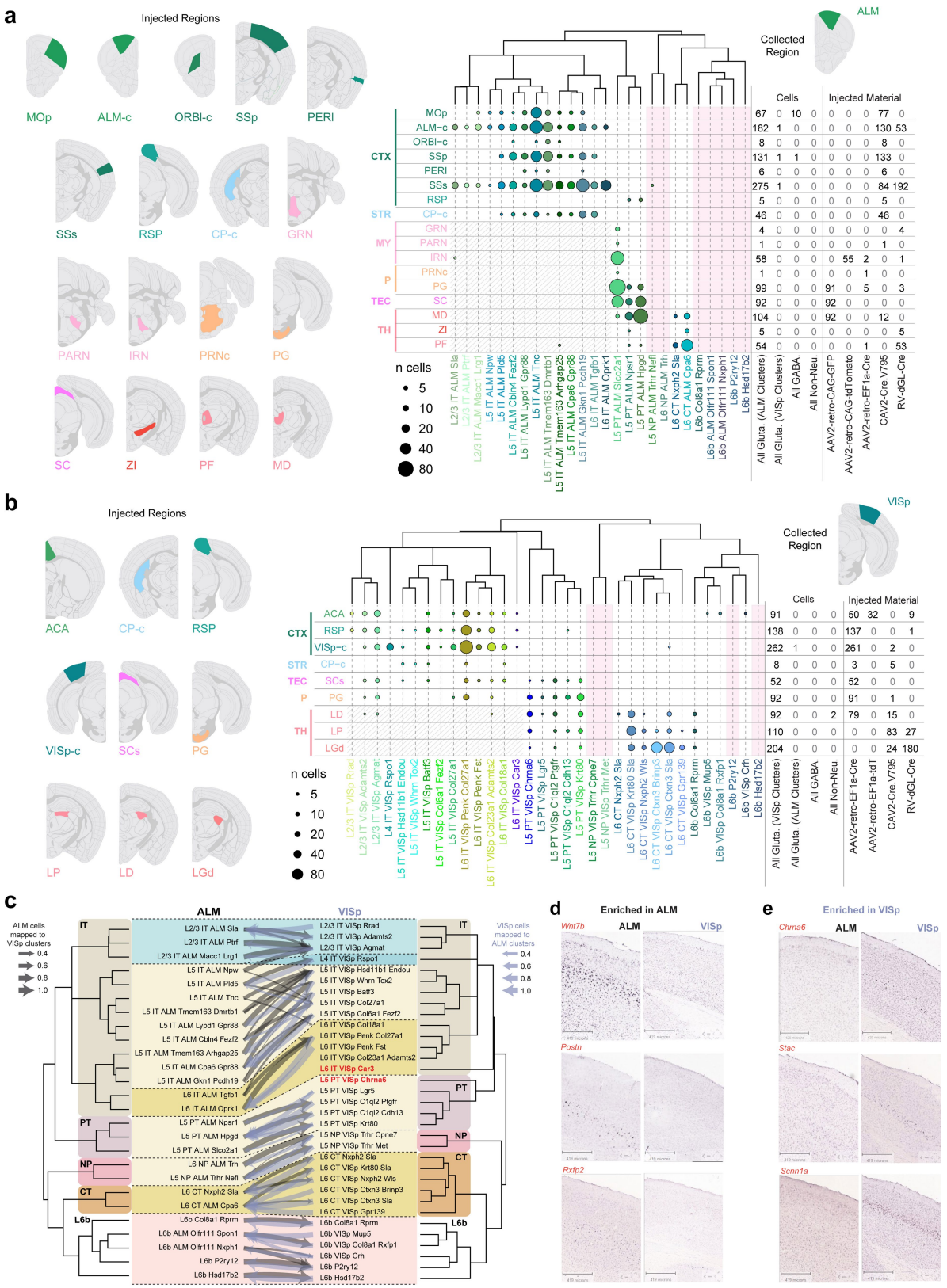

Extended Data Fig. 10 | See next page for caption.

© 2018 Springer Nature Limited. All rights reserved.

Extended Data Fig. 10 | Retro-seq and comparison of cell types across regions. a, **b**, Injection targets for retro-seq, represented by select Allen Reference Atlas images are displayed on the left. The plots on the right show injection targets in rows and cell types in columns for annotated retro-seq cells collected from the ALM ($n = 1{,}152$) (**a**) or VISp ($n = 1{,}052$) (**b**). Cell numbers are represented as discs, coloured according to detected cell types. Cell numbers from each target segregated by categories (based on broad type or virus injected) are shown to the right. We used three types of viral tracers expressing Cre: CAV2-Cre, rAAV2-retro-EF1a-Cre and RVΔGL-Cre, and injected them into a Cre-reporter line *Ai14*. For ALM experiments, we also injected rAAV2-retro-CAG-GFP or rAAV2-retro-CAG-tdT into wild-type mice. To ensure diverse coverage of projection neuron types, at least two virus types were used for most broad target regions (except for striatum and tectum for ALM, and tectum for VISp), as different viruses may display different tropisms. Cell types that were never isolated from the retrograde tracing experiments are shaded pink. Grey-hatched regions denote cells that may have been labelled unintentionally (but unavoidably) through the needle injection tract. For most subcortical injections into VISp-projection areas, the needle goes through the cortex, and some IT cells are labelled through the virus deposited along the needle tract. One exception is the injection into the superior colliculus for VISp experiments, in which we avoided cortical labelling by injecting at an angle through the cerebellum (Methods). Each injection target is labelled according to the centre of the corresponding injection site, however, neighbouring regions are often infected (Supplementary Table 5). Reference atlas abbreviations are as follows: ACA, anterior cingulate area; ALM-c, contralateral anterior lateral motor area; CP-c, contralateral caudoputamen; CTX, cortex; GRN, gigantocellular reticular nucleus; IRN, intermediate reticular nucleus; LD, lateral dorsal nucleus of the thalamus; LGd, dorsal lateral geniculate complex; LP, lateral posterior nucleus of the thalamus; MD, mediodorsal nucleus of the thalamus; MOp, primary motor area; MY, medulla; ORBl-c, contralateral orbital area, lateral part; P, pons; PARN, parvicellular reticular nucleus; PERI, perirhinal area; PF, parafascicular nucleus; PG, pontine grey; PRNc, pontine reticular nucleus dorsal part; RSP, retrospenial area; SC, superior colliculus; SCs, superior colliculus sensory related area; SSp, primary somatosensory area; SSs, supplementary somatosensory area; STR, striatum; TEC, tectum; TH, thalamus; VISp-c, contralateral primary visual area; ZI, zona incerta. **c**, Mapping of glutamatergic cells from ALM onto VISp glutamatergic cell types (grey arrows) using a random forest classifier trained on VISp types, and vice versa (blue-grey arrows; Methods). The fraction of cells that mapped with high confidence onto clusters from the other region is represented by the weight of the arrows. The best matched types were used in Fig. 2c. For this comparison, the 4,519 ALM cells and 7,352 VISp cells from glutamatergic types excluding CR–*Lhx5* were used. **d**, **e**, RNA ISH from the Allen Mouse Brain Atlas[25] for select markers confirms areal gene expression specificity. Images contain regions of interest from representative sections selected from individual whole-brain RNA ISH experiments. The number of whole-brain experiments per gene available in the Allen Brain Atlas is as follows: *Wnt7b*: $n = 3$ brains (1 sagittal, 2 coronal); *Postn*: $n = 2$ brains (1 sagittal, 1 coronal); *Rxfp2*: $n = 2$ brains (1 sagittal, 1 coronal); *Chrna6*: $n = 3$ brains (1 sagittal, 2 coronal); *Stac*: $n = 2$ brains (1 sagittal, 1 coronal); *Scnn1a*: $n = 2$ brains (1 sagittal, 1 coronal). Brain diagrams were derived from the Allen Mouse Brain Reference Atlas (version 2 (2011); downloaded from https://brain-map.org/api/index.html).

© 2018 Springer Nature Limited. All rights reserved.

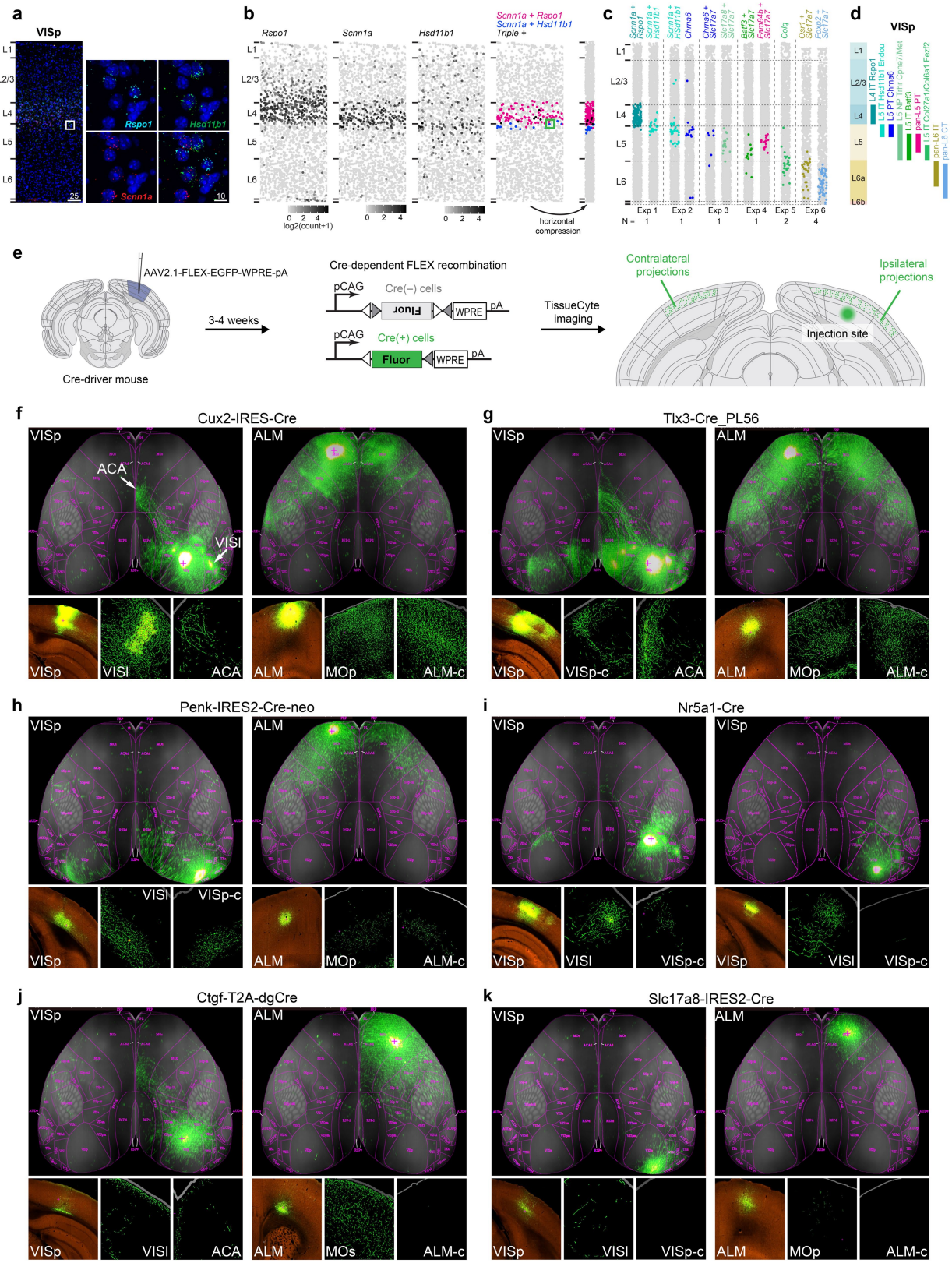

Extended Data Fig. 11 | See next page for caption.

© 2018 Springer Nature Limited. All rights reserved.

Extended Data Fig. 11 | Validation of glutamatergic marker gene expression and cell type location by RNA FISH and projection subclasses by anterograde tracing. a–**c**, Single-molecule RNA FISH with RNAscope was used to validate marker expression and cell type distribution. **a**, Example image shows fluorescent spots that correspond to *Rspo1* (cyan), *Hsd11b1* (green) and *Scnn1a* (red) mRNA molecules in a 10-μm coronal VISp section. Scale bars are in micrometres. **b**, Example of processed data from **a**; white square in **a** corresponds to green square in **b**. Data processing steps involved creation of maximum projection of a montage of confocal *z*-stacks, identifying nuclei, quantifying the number of fluorescent spots, assignment of spots to each nucleus by CellProfiler[67] and horizontal compression of the data to emphasize layer enrichment of examined cells. Each dot in the panel represents a cell plotted according to the detected nucleus position. Each cell was coloured according to the quantified fluorescent labelling. The first three panels show cells shaded according to the quantified number of spots per cell: *Rspo1* and *Scnn1a* mRNAs are enriched in L4 and *Hsd11b1* at the L4–L5 border. The fourth panel shows location of cells co-labelled with two or more probes and confirms scRNA-seq data: coexpression of *Rspo1* and *Scnn1a* is expected in the L4–IT–VISp–*Rspo1* type and coexpression of *Hsd11b1* and *Scnn1a* in the L5–IT–VISp–*Hsd11b1*–*Endou* type. **c**, Condensed plots for six individual representative RNA scope experiments (Exp) in VISp for select glutamatergic cell type markers. The number of times (*n*) each experiment was performed independently to produce similar results is listed below each experiment. Layers were delineated based on cell density. Data in **a** and **b** correspond to Exp1. **d**, A schematic of laminar distributions of VISp glutamatergic types according to experiments in **c** corroborates previous evidence[85] showing that L5 IT and L5 pyramidal tract cells are not well separated into 5a and 5b sublayers in the visual cortex, compared to the primary somatosensory cortex. Note that in ALM, even subtypes of L5b with different projections are well segregated into upper and lower sublayers (see accompanying study)[21]. **e**, To confirm the projection patterns of several transcriptomic types and examine them in greater detail, we performed anterograde tracing by Cre-dependent adeno-associated virus (AAV) in select Cre lines. We have previously characterized cell type labelling by these Cre lines (Extended Data Fig. 8). In one case, we used a Cre line with a similar pattern of expression with viral reporter in adulthood (*Cux2-IRES-cre* instead of *Cux2-IRES-creERT2*)[86]. **f**–**k**, Each image is a projection generated from a series of images obtained by TissueCyte 1000 from a representative anterograde tracing experiment; additional experiments are available at http://connectivity.brain-map.org/. **f**, L5 and L2/3 IT types as labelled in *Tlx3-cre_PL56*, and *Cux2-IRES-cre* lines display extensive long-range projections that cover all layers with preference for upper layers. **h**, By contrast, L6 IT types, labelled by the newly generated *Penk-IRES2-cre-neo* line (Extended Data Fig. 8), project to many of the same areas as the L2–L3 and L5 IT types, but their projections are confined to lower layers in all areas examined, including higher visual areas and contralateral VISp and ALM. **i**, As revealed by the retro-seq data (Extended Data Fig. 10b), we confirm that L4–IT–VISp–*Rspo1* type, which represents most cells labelled by *Nr5a1-cre* (Extended Data Fig. 8) projects to contralateral VISp (Fig. 3d). Notably, this projection is observed only when injection is performed in the most anterior portion of VISp (compare left and right panels in **i**). **j**, L6b types labelled by *Ctgf-2A-dgcre* have sparse projections to the anterior cingulate area. **k**, Consistent with the retro-seq data, the near-projecting types labelled by *Slc17a8-IRES2-cre* (Extended Data Fig. 8) do not have long-distance projections, but only local projections and sparse projections to nearby areas. Brain diagrams were derived from the Allen Mouse Brain Reference Atlas (version 2 (2011); downloaded from https://brain-map.org/api/index.html).

© 2018 Springer Nature Limited. All rights reserved.

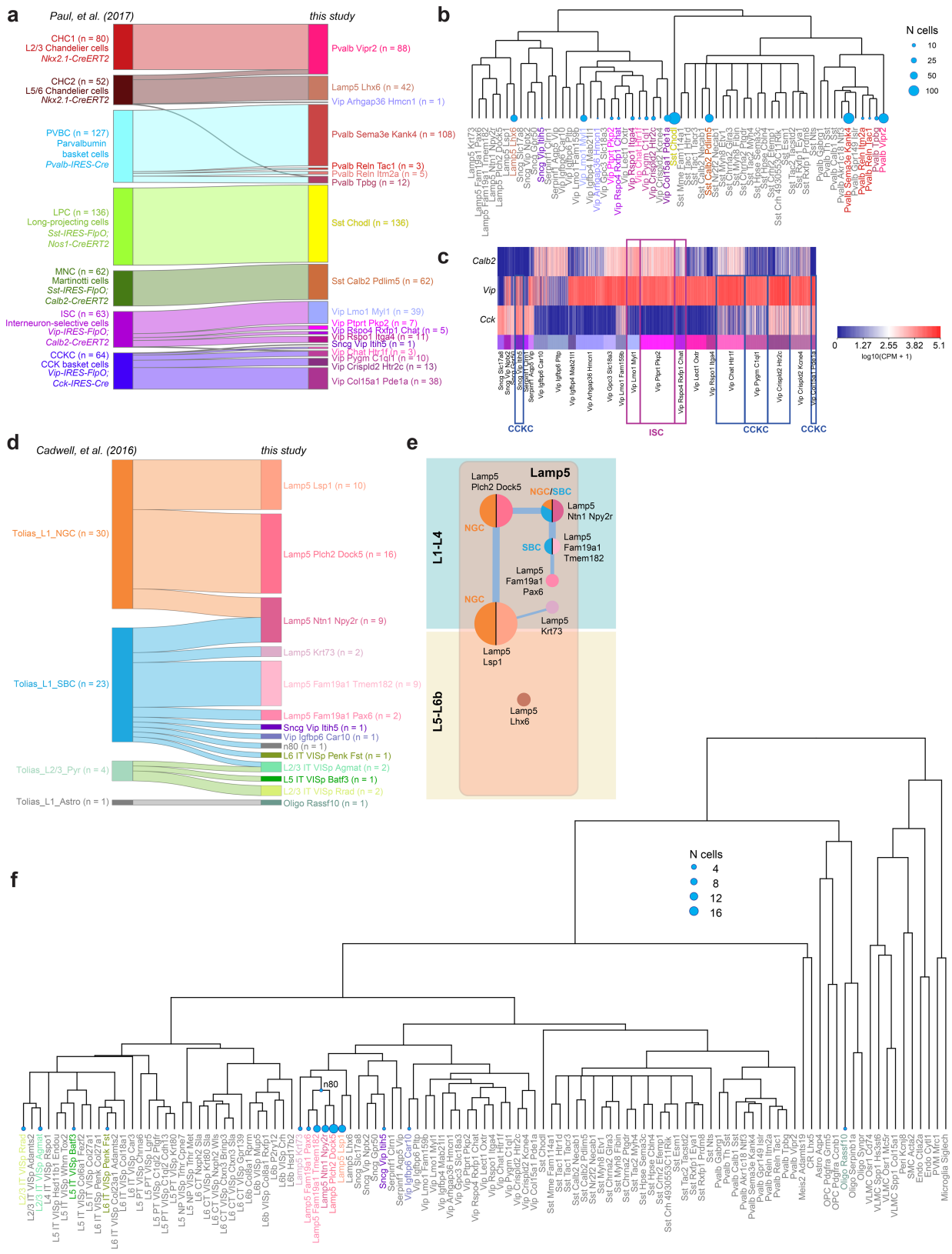

Extended Data Fig. 12 | See next page for caption.

© 2018 Springer Nature Limited. All rights reserved.

Extended Data Fig. 12 | Mapping of previously published scRNA-seq samples[36] and Patch-seq samples[38] to our dataset. scRNA-seq data obtained from sorted cells or cell content extracted by patching were mapped to our transcriptomic types using a centroid classifier (Methods). **a**, River plot showing the mapping of single-cell transcriptomes described previously[36] ($n = 584$ cells) to our types. **b**, Alternative representation of the results in **a**, with blue discs representing the number of single-cell transcriptomes published previously[36] onto a dendrogram of GABAergic cell types in this study. Each blue disc area represents the total number of single-cell transcriptomes mapped to one of our cell types. **c**, Expression of *Calb2*, *Vip* and *Cck* in single cells from our *Sncg* and *Vip* subclasses ($n = 3{,}225$). Transgenic recombinase lines based on these genes were used to label CCK basket cells (CCKC) and interneuron-selective cells (ISC) described previously[36]. Boxes highlight our types to which the CCK basket cells and interneuron-selective cells described previously[36] were mapped to. CCK basket cells and interneuron-selective cells as defined previously[36] each correspond to several of our transcriptomics types. **d**, Patch-seq data for 58 cells described previously[38] were mapped to our transcriptomic types. Some cells could not be mapped with high confidence to terminal leaves of our taxonomy, and were therefore mapped to an internal node (cluster labels on the right that start with 'n' for node, see **f**). **e**, Constellation diagram showing corresponding types described previously[38] and *Lamp5* cell types from this study. Correspondences with the neurogliaform cells (NGC, orange) and single-bouquet cells (SBC, blue) defined previously[38] are shown by the colours applied to the left side of each disc. **f**, Alternative representation of the result in **d**, with blue discs representing the number of single cell transcriptomes described previously[38] mapped onto a dendrogram of GABAergic cell types in this study. Each blue disc area represents the total number of single cell transcriptomes mapped to a type (terminal leaf) or node in our taxonomy.

© 2018 Springer Nature Limited. All rights reserved.

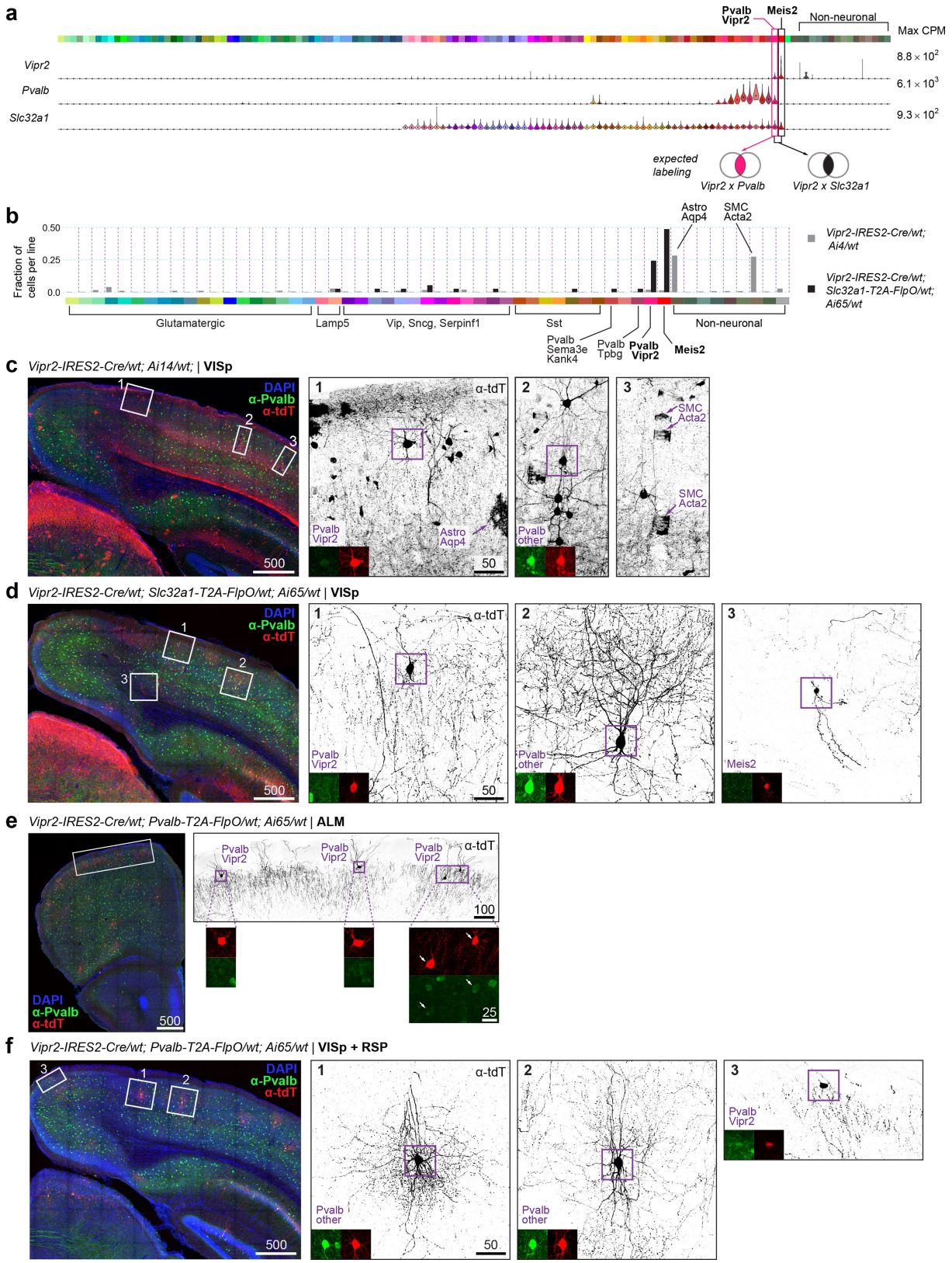

Extended Data Fig. 13 | See next page for caption.

© 2018 Springer Nature Limited. All rights reserved.

Extended Data Fig. 13 | A new tool, *Vipr2-IRES2-Cre*, for access to select transcriptomically defined cell types. a, Expression of select marker genes in our transcriptomically defined cell types (colour bar on top) represented as violin plots for all cluster-assigned cells ($n = 23{,}822$ cells; 133 clusters). Median values are black dots. Each row is scaled to the maximum expression value shown to the right of the plot (in CPM), and displayed on a linear scale. Venn diagrams represent expected cell type labelling by genetic tools described below. A new transgenic line, *Vipr2-IRES2-cre*, was created to label *Pvalb*–*Vipr2* and *Meis2* types. Unlike the previously developed *Nkx2.1-creERT2* line[87], this line does not require tamoxifen induction for chandelier cell labelling (corresponding to *Pvalb*–*Vipr2*). **b**–**f**, Specificity of this recombinase line was tested by scRNA-seq and immunohistochemistry. **b**, scRNA-seq and clustering with other cells revealed cell types labelled by two mouse genotypes on the right. Types are labelled on the bottom in standard colours. Only cell types with at least one cell labelled are displayed. $n = 329$ cells from *Vipr2-IRES2-cre/wt;Ai14/wt*; $n = 38$ cells from *Vipr2-IRES2-cre/wt;Slc32a1-T2A-FlpO/wt;Ai65/wt*. **c**–**f**, Representative images of immunohistochemistry results; each image is representative of $n = 2$ experimental animals with stated genotypes. High-magnification images show tdT labelling in black, anti-PVALB in green and anti-tdTomato in red. Tissue sections (100 μm) were stained with anti-PVALB, anti-dsRed (labels tdTomato), and DAPI. Images are maximum intensity projections of confocal *z*-stacks. Scale bars are in micrometres. In *Vipr2-IRES2-cre/wt;Ai14/wt* mice (**b**, grey bars), apart from the expected labelling of chandelier cells (*Pvalb*–*Vipr2*), many non-neuronal cells are labelled (especially, Astro–*Aqp4* and SMC–*Aoc3* types, panel **c**). **d**, To improve labelling specificity, we created and examined *Vipr2-IRES2-cre/wt;Slc32a1-T2A-FlpO/wt;Ai65/wt* mice. As expected, labelling was more specific, now confined to chandelier cells, basket cells and *Meis2* interneurons (dark bars in **b** and morphologically identified types in **d**). Notably, the chandelier cells within VISp did not express PVALB protein (**d**, panel 1). **e**, Genetic intersection of *Vipr2* and *Pvalb* expression labelled cells with chandelier morphology corresponding to Pvalb–Vipr2 in ALM. **f**, However, *Vipr2-IRES2-cre/wt;Pvalb-T2A-FlpO/wt;Ai65/wt* did not label chandelier cells in VISp, but PVALB$^+$ cells of basket morphology. This unexpected labelling may reflect historical expression of *Vipr2* in a subset of other Pvalb cells or low adult *Vipr2* expression that is not detected by scRNA-seq. In VISp-containing sections, some chandelier cells are labelled, but are observed outside of VISp (**f**, panel 3). RSP, retrosplenial cortex.

© 2018 Springer Nature Limited. All rights reserved.

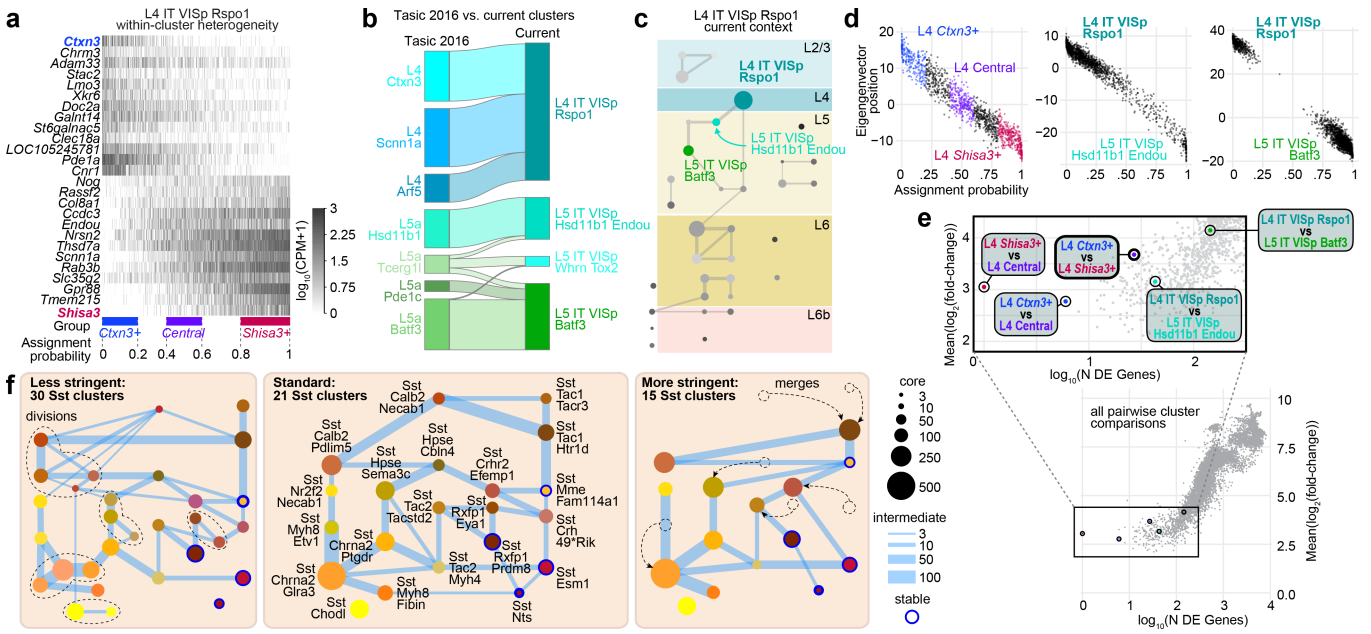

Extended Data Fig. 14 | Discreteness and continuity in cell type definition. **a**, Within the L4–IT–VISp–*Rspo1* type, $n = 1{,}442$ cells were arranged according to graded expression of 35 genes (only 26 are shown). **b**, Mapping of $n = 394$ L4 and L5 IT cells from our previous study[20] to cell types in this study. The three L4 clusters from our previous study[20] map primarily to the L4–IT–VISp–*Rspo1* type. **c**, Position of L4–IT–VISp–*Rspo1* within the VISp glutamatergic constellation diagram. **d**, Computational split of the L4–IT–VISp–*Rspo1* type into three parts along the continuum. For comparison, equivalent plots indicate better separation between this cluster and select L5 IT clusters. $n = 1{,}404$ cells for L4–IT–VISp–*Rspo1*, 215 for L5–IT–*Hsd11b1*–*Endou*, and 435 for L5–IT–VISp–*Batf3*. **e**, Comparison of gene expression differences among the parts of L4–IT–VISp–*Rspo1*, as well as this type with select L5 IT types. By this measure, similar differences are detected between the two 'end' parts of L4–IT–VISp–*Rspo1*, and between L4–IT–VISp–*Rspo1* and L5–IT–*Hsd11b1*–*Endou*. **f**, Constellation diagrams for $n = 2{,}880$ *Sst* subclass cells reflect clusters defined at three different deScores corresponding to clustering stringency: low, standard and high, starting with the same number of genes ($n = 30{,}862$, Methods). For low stringency, newly split clusters are enclosed by dashed contours. For high stringency, arrows indicate dominant merges.

© 2018 Springer Nature Limited. All rights reserved.

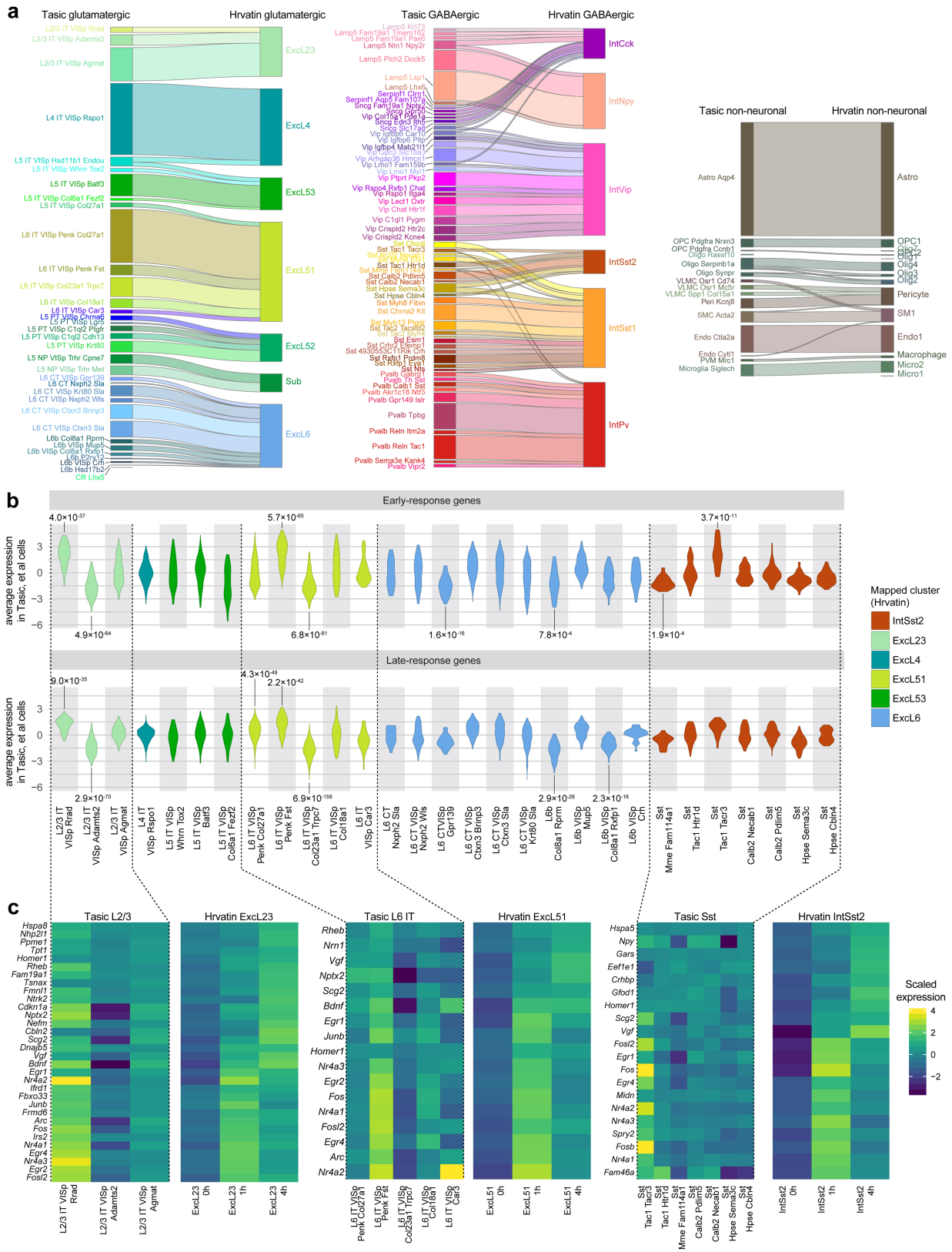

Extended Data Fig. 15 | Cell types with activity-dependent transcriptomic signatures. a, River plots representing the mapping of 14,205 VISp cells from this study to a previously published dataset[40] using a centroid classifier (Methods). **b**, Violin plots show the distribution of $\log_2$-scaled and centred average expression of late-response genes (LRGs) and early-response genes (ERGs) in select cell types from this study that are in a subclass with at least one type that is significantly correlated with LRG or ERG expression. From the published dataset[40], only the clusters with expression of at least four ERGs and LRGs were included. In total, values for $n = 6{,}956$ cells from our study are displayed in the violin plots. We performed a two-sided t-test to assess enrichment or depletion of expression of LRGs or ERGs, and defined significant values as $P < 0.01$ after correction for multiple hypotheses using the Holm method, and average fold change greater than 2. Significant P values for enrichment and depletion are displayed above and below each row, respectively. Complete statistics for all t-tests is included in Supplementary Table 11. **c**, Heat maps of $\log_2$-scaled and centred average gene expression for ERGs and LRGs in select cell types from our study and from the published dataset[40].

© 2018 Springer Nature Limited. All rights reserved.

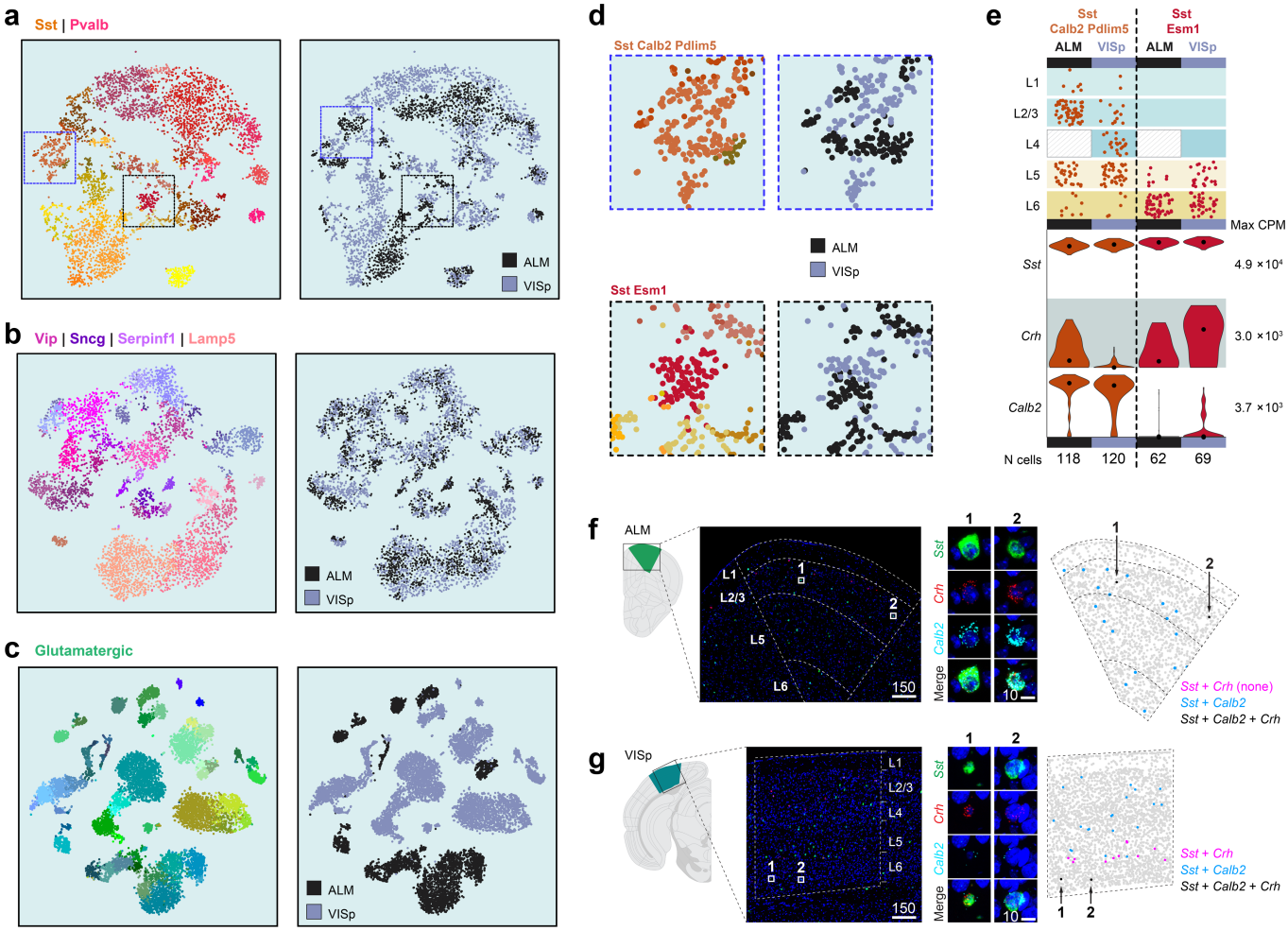

Extended Data Fig. 16 | Areal gene expression differences in GABAergic types. a–c, *t*-SNE plots for *Sst* and *Pvalb* ($n = 5{,}113$ cells, generated using 1,244 differentially expressed genes), *Lamp5*, *Serpinf1*, *Sncg* and *Vip* ($n = 5{,}365$ cells, generated using 1,184 differentially expressed genes) and glutamatergic types ($n = 11{,}905$ cells, generated using 1,984 differentially expressed genes) showing cells labelled in cluster colours on the left and area-of-origin on the right. Glutamatergic cells show the most marked segregation by area of origin. *Sst* and *Pvalb* types show small but noticeable area-specific segregation, which is even less obvious for the *Lamp5*, *Sncg* and *Vip* types. **d**, Areas from the *Sst* and *Pvalb* *t*-SNE plots were enlarged to show partial segregation of cells within two *Sst* types by area of origin. **e**, Layer distribution and violin plots for marker genes *Sst*, *Crh* and *Calb2* in cells from the same transcriptomic type divided by area. The number of cells in each type and region are shown below each column ($n = 118$ cells for ALM *Sst–Calb2–Pdlim5*; 120 for VISp *Sst–Calb2–Pdlim5*; 62 for ALM *Sst–Esm1*; and 69 for VISp *Sst–Esm1*). Violin plots are shown on a $\log_{10}$ scale, scaled to the maximum value for each gene (right of the plot in CPM); black dots are medians. In ALM, triple positive $Sst^{+}Crh^{+}Calb2^{+}$ cells belong to *Sst–Calb2–Pdlim5* type and are enriched in upper layers. In VISp, this same type does not express *Crh*, but a different type may account for $Sst^{+}Crh^{+}Calb2^{+}$ cells: *Sst–Esm1*, and would be expected in lower layers. **f**, **g**, RNA FISH by RNAscope for *Sst* (green), *Crh* (red) and *Calb2* (cyan) in ALM and VISp. Scale bars are in micrometres. In agreement with **e**, we find triple-positive cells by RNA FISH in ALM in upper layers, and in VISp in lower layers. Images are representative of a single experiment including multiple tissue sections from ALM and VISp. Brain diagrams were derived from the Allen Mouse Brain Reference Atlas (version 2 (2011); downloaded from https://brain-map.org/api/index.html).

© 2018 Springer Nature Limited. All rights reserved.

ARTICLE

https://doi.org/10.1038/s41586-018-0642-9

Distinct descending motor cortex pathways and their roles in movement

Michael N. Economo[1], Sarada Viswanathan[1], Bosiljka Tasic[2], Erhan Bas[1], Johan Winnubst[1], Vilas Menon[1], Lucas T. Graybuck[2], Thuc Nghi Nguyen[2], Kimberly A. Smith[2], Zizhen Yao[2], Lihua Wang[1], Charles R. Gerfen[3], Jayaram Chandrashekar[1], Hongkui Zeng[2], Loren L. Looger[1] & Karel Svoboda[1]*

Activity in the motor cortex predicts movements, seconds before they are initiated. This preparatory activity has been observed across cortical layers, including in descending pyramidal tract neurons in layer 5. A key question is how preparatory activity is maintained without causing movement, and is ultimately converted to a motor command to trigger appropriate movements. Here, using single-cell transcriptional profiling and axonal reconstructions, we identify two types of pyramidal tract neuron. Both types project to several targets in the basal ganglia and brainstem. One type projects to thalamic regions that connect back to motor cortex; populations of these neurons produced early preparatory activity that persisted until the movement was initiated. The second type projects to motor centres in the medulla and mainly produced late preparatory activity and motor commands. These results indicate that two types of motor cortex output neurons have specialized roles in motor control.

Motor cortex activity anticipates specific future movements, often seconds before the onset of movement[1,2]. This dynamic process, referred to as preparatory activity, moves motor cortex population activity to an initial condition that is appropriate for eliciting rapid, accurate movements[2]. In addition, motor cortex activity is modulated milliseconds before and during the onset of movement, consistent with commands that control the timing and direction of movements[3,4].

Reconciling these dual roles of the motor cortex requires an understanding of motor cortex cell types, and how these cell types integrate into multi-regional circuits. The motor cortex comprises cell types that differ in their location, gene expression, electrophysiology and connectivity. Intratelencephalic neurons in layers (L) 2–6 receive input from other cortical areas and excite pyramidal tract (PT) neurons[5–7]. PT neurons, the somata of which define neocortical L5b[8], link the motor cortex with premotor centres in the brainstem and spinal cord[9,10] and directly influence behaviour[10–12]. PT neurons also project to the thalamus[6,13,14]. Preparatory activity requires reverberations in a thalamocortical loop[15]. Consistent with roles in both the planning and initiation of movement, PT neurons are structurally heterogeneous[14,16,17] and show diverse activity patterns, including preparatory activity and movement commands[18–20].

Here we show that PT neurons in the mouse motor cortex comprise two cell types with distinct gene expression and axonal projections. We refer to these cell types as PT_{upper} and PT_{lower} neurons, reflecting their distributions in different sublaminae in L5b. PT_{upper} neurons project to the thalamus, which forms a feedback loop with the motor cortex. PT_{lower} cells project to premotor centres in the medulla. Cell-type-specific extracellular recordings in the anterior lateral motor cortex (ALM) during a delayed-response task suggest that PT_{upper} neurons are preferentially involved in motor planning, whereas PT_{lower} neurons have roles in movement execution.

Two types of PT neuron in layer 5

Single-cell RNA sequencing (scRNA-seq) was used to produce a taxonomy of cell types in the ALM and visual cortex[21]. From 9,573 single-cell transcriptomes, glutamatergic neurons in the ALM were grouped into 27 clusters (Fig. 1), which were distinct from glutamatergic clusters identified in the visual cortex[21]. PT neurons form the sole cortical projection to motor areas in the midbrain and hindbrain, and are therefore likely to have important roles in motor planning and execution. ALM PT neurons mapped to three transcriptomic clusters: the *Slco2a1* cluster and two other closely related clusters (*Npsr1* and *Hpgd*; Fig. 1 and Extended Data Fig. 1).

We mapped the structural diversity of PT neurons by reconstructing individual cells[22] ($n = 12$; Fig. 2a, b and Supplementary Table 1; median axonal length: 121,037 μm, range: 80,873–188,105 μm; median branch points: 243, range: 144–540). Patterns of axonal collaterals revealed two neuron types: one group innervated the thalamus ($n = 8$; Fig. 2a, b; green hues and Extended Data Fig. 2); the other group bypassed the thalamus and branched in the medulla, including the reticular nuclei containing premotor neurons for orofacial movements[23] ($n = 4$; magenta hues). All cells innervated the superior colliculus and subsets of both groups branched in other areas (Fig. 2a, b and Extended Data Fig. 2).

We used the adeno-associated virus rAAV2-retro[24] to label neurons retrogradely from the thalamus and medulla. Thalamus-projecting PT neurons were in upper L5b (Fig. 2c, d and Extended Data Fig. 3; green cells)[6] and medulla-projecting PT neurons were in lower L5b (magenta cells). This pattern was similar across the primary and secondary motor cortex (Extended Data Fig. 3). Retrograde labelling from the superior colliculus and pons labelled PT neurons in both L5b sublaminae (Fig. 2c). Few neurons were co-labelled by injections into the thalamus and medulla (2.2%; 22 out of 984 cells labelled from either location), whereas many neurons were co-labelled by injections into the thalamus and superior colliculus (77.1%; 687 out of 890 thalamus-labelled cells), as expected from axonal reconstructions.

To link projection classes and transcriptomic clusters, we examined gene expression in medulla-projecting and thalamus-projecting PT neurons identified using rAAV2-retro. All (62 out of 62) medulla-projecting PT neurons mapped to the *Slco2a1* taxonomic cluster.

[1]Janelia Research Campus, Howard Hughes Medical Institute, Ashburn, VA, USA. [2]Allen Institute for Brain Science, Seattle, WA, USA. [3]National Institute of Mental Health, Bethesda, MD, USA.
*e-mail: svobodak@janelia.hhmi.org

© 2018 Springer Nature Limited. All rights reserved.

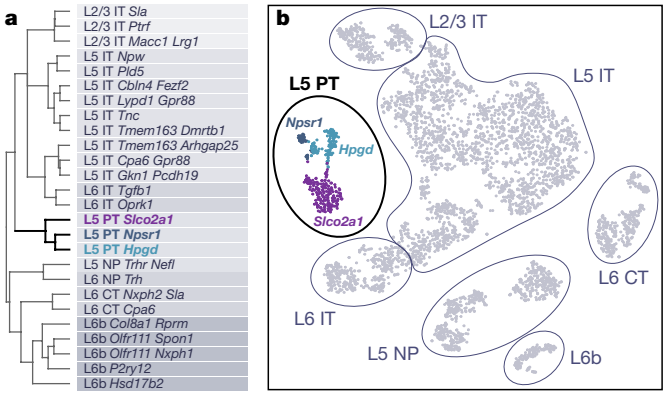

Fig. 1 | Taxonomy of motor cortex glutamatergic neurons based on scRNA-seq. a, Hierarchical clustering based on gene expression (for details, see Tasic et al.[21]). Three transcriptomic clusters, identified by the genes *Slco2a1*, *Npsr1* and *Hpgd*, correspond to PT neurons. The transcriptomic cluster corresponding to Cajal–Retzius cells was excluded here[21]. CT, corticothalamic neurons; IT, intratelencephalic neurons; NP, near-projecting neurons. *Ptrf* is also known as *Cavin1*. **b**, Two-dimensional stochastic neighbour embedding (*t*-SNE) of transcriptomic data of sequenced single neurons in the ALM ($n = 4{,}477$ glutamatergic cells). Cells are colour-coded as in **a**.

Similarly, thalamus-projecting PT neurons mapped to the *Npsr1* and *Hpgd* clusters (91 out of 94, *Npsr1*: 19 out of 94, *Hpgd*: 72 out of 94; Figs. 1b, 2e, f). Pons- and superior colliculus-projecting neurons mapped to the same three PT clusters (superior colliculus total: 97, *Slco2a1*: 43, *Npsr1*: 15, *Hpgd*: 39; pons total: 100, *Slco2a1*: 86, *Npsr1*: 5, *Hpgd*: 9; Fig. 2f). Expression patterns of neurons in the *Slco2a1* cluster retrogradely labelled from a single structure (that is, superior colliculus, pons or medulla) were not more similar to each other than in pairs drawn randomly from the *Slco2a1* cluster (Extended Data Fig. 4a). Likewise, the projection targets of *Hpgd* neurons (that is, superior colliculus or thalamus) did not explain additional gene expression variance within that cluster (Extended Data Fig. 4b, c; the *Npsr1* cluster was not analysed owing to its small size).

Axonal reconstructions and scRNA-seq data suggest that PT neurons can be divided into two distinct cell types. To determine whether thalamus-projecting and medulla-projecting PT neurons account for most PT neurons, we examined additional PT neurons that were reconstructed partially (thalamus-projecting: $n = 3$; medulla-projecting: $n = 3$). All (18 out of 18) partially and fully reconstructed PT neurons projected to the superior colliculus and no (0 out of 18) PT neurons lacked projections to both the thalamus and medulla (Supplementary Table 1). Thalamus- and medulla-projecting neurons together expressed the complete set of PT neuron genes (Extended Data Fig. 4d). These results suggest that most, if not all, PT neurons are accounted for by the medulla-projecting and thalamus-projecting types. We refer to the superficial, thalamus-projecting *Npsr1–Hpgd* cell type as PT_{upper} neurons, and the deep, medulla-projecting *Slco2a1* cell type as PT_{lower} neurons, reflecting their laminar distributions.

We next identified marker genes for PT_{upper} (*Npsr1–Hpgd* clusters) and PT_{lower} (*Slco2a1* cluster) neurons. For maximal sensitivity, we combined scRNA-seq with bulk RNA sequencing (RNA-seq) analysis (Extended Data Fig. 4e–i; 50–100 cells per sample; 6 replicates each). The relative expression levels of differentially expressed genes in scRNA-seq and bulk RNA-seq were highly correlated (Extended Data Fig. 4i). Differentially expressed genes identified from scRNA-seq were differentially expressed in bulk RNA-seq (Extended Data Fig. 1c), and vice versa (Extended Data Fig. 1b). Several differentially expressed genes were specific for each population. From these, *Slco2a1* was confirmed as a marker for PT_{lower} neurons (Fig. 3). Single-molecule RNA fluorescence in situ hybridization (smFISH) revealed higher levels of *Slco2a1* mRNA in PT_{lower} neurons than in PT_{upper} neurons (Fig. 3c; bottom). *Npnt* was specific for, and spanned, both clusters containing PT_{upper} neurons (*Npsr1* and *Hpgd*; Fig. 3a). smFISH confirmed that

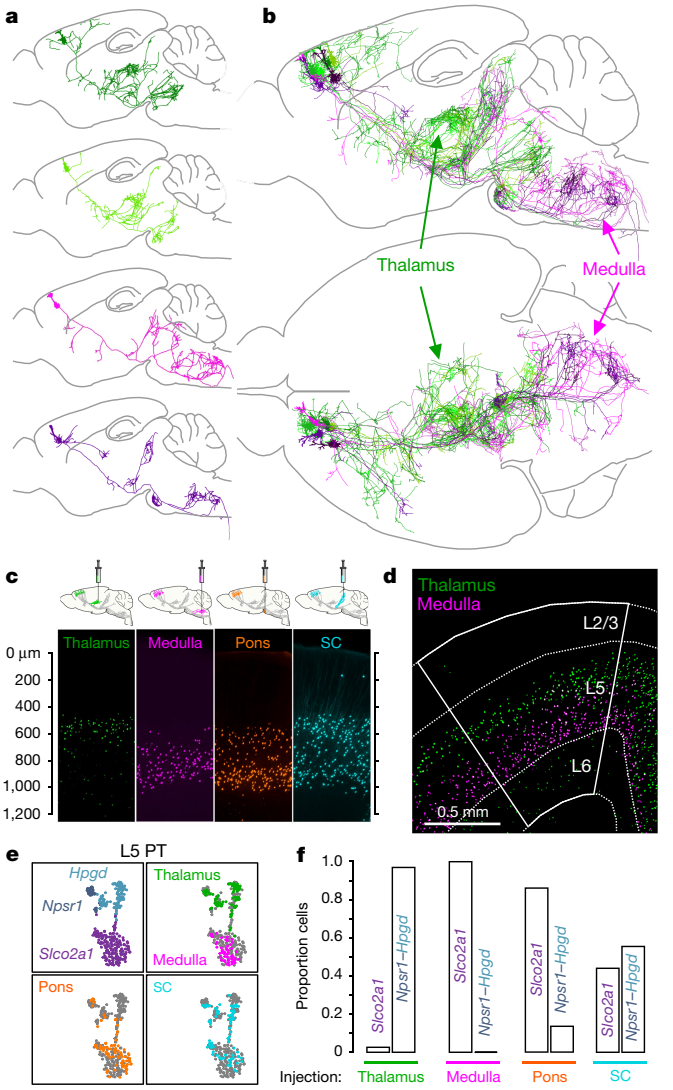

Fig. 2 | Two types of PT neuron in the motor cortex. a, Example reconstructions. Two PT neurons project to the thalamus (top; green hues) and two project to the medulla (bottom; magenta hues). **b**, Four thalamus-projecting and four medulla-projecting PT neurons overlaid and collapsed in the sagittal (top) and horizontal (bottom) planes. Dendrites are denoted by thicker lines. **c**, **d**, Nuclei of neurons retrogradely labelled from the thalamus (green) and medulla (magenta) are located in distinct sublaminae of L5b (experiment replicated three times with similar results). SC, superior colliculus. **e**, Gene expression of PT neurons coloured according to cluster membership or retrograde injection site in *t*-SNE space (as in Fig. 1b; $n = 368$ PT neurons). **f**, Proportion of neurons retrogradely labelled from each PT target that were clustered into the *Slco2a1* and *Npsr1–Hpgd* expression clusters.

Npnt was expressed specifically in PT_{upper} neurons (Fig. 3c; top) compared to PT_{lower} neurons. *Npnt* and *Slco2a1* also marked PT_{upper} and PT_{lower} neurons in the primary motor cortex (data not shown), indicating that the gene expression patterns determined in the ALM generalize across the motor cortex.

Cell-type-specific recordings

The projection patterns of PT_{upper} and PT_{lower} neurons suggest distinct roles in motor control. The cortico–thalamocortical loop is necessary for maintaining persistent preparatory activity related to motor planning[15]. PT_{upper} cells project to the thalamus and lack projections to premotor nuclei in the medulla (Fig. 2a, b and Extended Data Fig. 2). These characteristics suggest a role for PT_{upper} cells in generating and/or maintaining preparatory activity. By contrast, PT_{lower} cells project to

© 2018 Springer Nature Limited. All rights reserved.

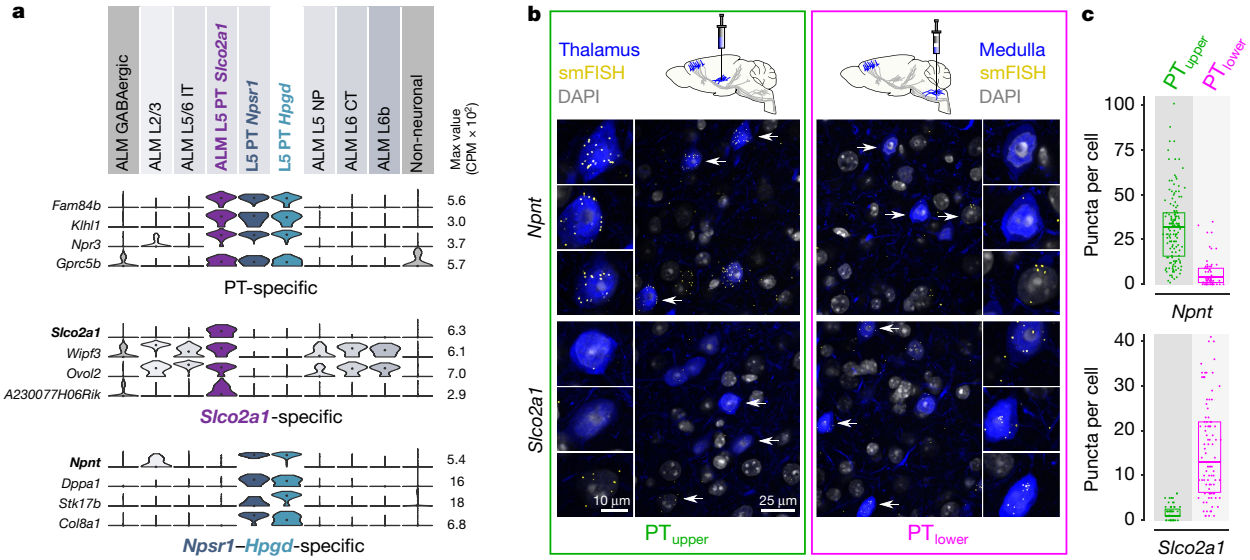

Fig. 3 | PT neuron type markers. a, Differentially expressed genes from scRNA-seq ($n = 9{,}573$ cells), represented by violin plots. Each row represents a single gene, and values within rows are normalized between 0 and the maximum expression value for each gene (right) and displayed on a $\log_{10}$ scale. Median values are shown as black dots within each violin. CPM, counts per million mapped reads. **b**, smFISH validating cell-type-specific marker expression. Blue, neurons labelled from the thalamus or medulla; yellow, RNA puncta; grey, cellular nuclei. **c**, Number of *Npnt* (top) and *Slco2a1* (bottom) RNA puncta in the ALM measured in cells of each type. *Slco2a1*, PT_{upper}: interquartile range (IQR) = 1–2.5 puncta, $n = 60$; *Slco2a1*, PT_{lower}: IQR = 6–22, $n = 95$; *Npnt*, PT_{upper}: IQR = 16–40, $n = 145$; *Npnt*, PT_{lower}: IQR = 1–9, $n = 69$. Horizontal bars in box plots correspond to quartiles. Two independent biological replicates of the experiment illustrated in **b** and **c** yielded similar results and were pooled.

premotor centres in the medulla and spinal cord, with few collaterals in the basal ganglia and thalamus, suggesting a role in movement execution. We performed projection-specific recordings in the ALM during a delayed-response task[19,25] (Fig. 4). Mice were trained to discriminate object locations with their whiskers[25] and signal their decision about object location with skilled, directional licking (left or right) after a delay epoch (1.3 s). The delay epoch was terminated by an auditory 'go' cue that instructs animals to respond. The ALM is a hub for planning and executing movements in this task[18,25–27].

PT_{upper} or PT_{lower} cells were infected with rAAV2-retro expressing channelrhodopsin-2 (ChR2). Fibre optic cannulae were implanted into the thalamus (to activate PT_{upper} cells; Fig. 4c, top) or medulla (to activate PT_{lower} cells; Fig. 4c, bottom). ChR2-expressing cells in the ALM were identified with axonal photostimulation and extracellular recordings in the ALM using a collision test[18] (61 PT_{upper} cells, 8 mice; 69 PT_{lower} neurons, 4 mice; Fig. 4d and Extended Data Fig. 5). Identified PT_{upper} cells were at more superficial recording depths than PT_{lower} neurons, consistent with retrograde labelling experiments (Figs. 2c, d, 4e). Layer 6 corticothalamic cells, which also innervate the thalamus, were inefficiently labelled by rAAV2-retro[24] and excluded based on recording depth, several hundred micrometres below the PT_{upper} cells. Baseline and trial-averaged peak spike rates were not significantly different ($P > 0.1$, two-sided *t*-test) in PT_{upper} cells (baseline: 4.3 ± 3.5 Hz; peak: 17.7 ± 13.8 Hz; median ± s.d.) compared to PT_{lower} cells (baseline: 5.2 ± 4.8 Hz; peak: 17.2 ± 22 Hz). Spike rates in PT_{lower} cells were more heterogeneous across the population (baseline: $P = 0.02$; peak: $P = 3 \times 10^{-4}$; χ^2 test). A substantial proportion of PT_{lower} neurons displayed spike bursts (18.8%), which were rare among PT_{upper} cells (3.3%; $P = 0.006$, Fisher's exact test; Extended Data Fig. 5c).

Most recorded PT neurons had significant selectivity, defined as the difference in spike rate between trial types ('lick left' versus 'lick right'), during at least one task epoch ($P < 0.01$, two-sided Mann–Whitney *U*-test; 122 out of 130; 94%). Individual neurons exhibited diverse patterns of activity and selectivity (Fig. 4f and Extended Data Fig. 5). Trial-averaged activity patterns were nearly as diverse within each PT population as across all neurons recorded within ALM (Extended Data Fig. 6). We next investigated how specific task-related signals were represented in each PT population.

Preparatory activity

A subset of PT neurons displayed selectivity that emerged at the start of the sample epoch and persisted through the delay epoch (Fig. 4f; left cells), representing a stable encoding of upcoming movement direction[1].

We investigated the emergence and maintenance of preparatory activity in populations of PT_{upper} and PT_{lower} cells. Neurons were pooled across experiments and analysed in activity space, in which each dimension corresponds to the activity of one neuron[27,28]. Preparatory activity for each movement corresponded to a distinct trajectory in activity space. For each population, we computed the direction in activity space that best discriminated trial types during the first 400 ms of the sample epoch (CD_{early}: 'early coding direction'). We then projected the trial-averaged activity of all cells in the population along CD_{early}, producing the one-dimensional projection of each activity space trajectory with maximal selectivity (Fig. 5a). In this projection, selectivity was larger and more consistent across trials in the PT_{upper} population compared to the PT_{lower} population (Fig. 5b). Furthermore, selectivity in the PT_{upper} population remained constant throughout the sample and delay epochs until the go cue, implying retention of decision-related information. By contrast, selectivity in the PT_{lower} population decayed rapidly along CD_{early} (no significant selectivity in 400 ms preceding go cue; $P = 0.34$, bootstrap). This decay did not reflect a lack of selectivity in the PT_{lower} population: along a different direction in activity space, which maximized selectivity at the end of the delay epoch, CD_{late}, selectivity was substantial in both cell types[18] (Extended Data Fig. 7a, b; PT_{upper}: 40 out of 61 neurons selective; PT_{lower}: 44 out of 69). We next computed the stability of the coding direction. For the PT_{upper} population, the CD remained more similar across the sample and delay epochs compared to the PT_{lower} population (Extended Data Fig. 7c, d). Differences in coding between PT_{upper} and PT_{lower} neurons could not be explained by variation across animal cohorts (Extended Data Fig. 8). As suggested by population analyses, individual PT_{upper} neurons displayed persistent selectivity throughout the sample and delay epochs (Fig. 5c), exhibited higher early selectivity (PT_{upper}: 0.41 ± 0.04; mean ± s.e.m.; PT_{lower}: 0.25 ± 0.02; $P < 0.01$), and decoded trial type significantly better than PT_{lower} neurons during the sample epoch (Extended Data Fig. 9).

© 2018 Springer Nature Limited. All rights reserved.

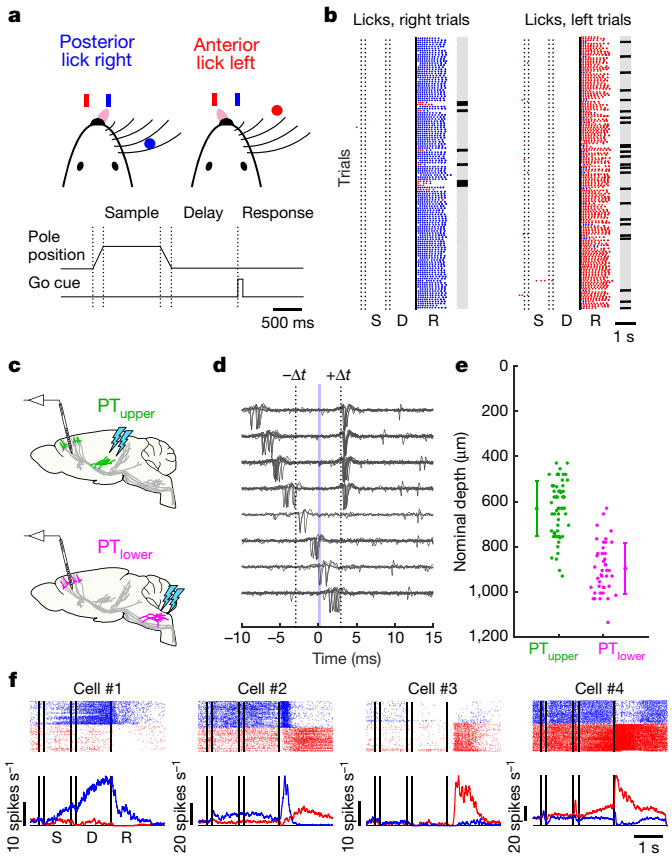

Fig. 4 | Cell type-specific extracellular neurophysiology. a, Delayed-response task. On each trial, an object was presented to the whiskers in one of two rostro-caudal positions during the sample epoch (1.0 s). After a brief delay epoch (1.3 s), mice reported the pole position by licking a reward port on the right (caudal pole position) or the left (rostral pole position). **b**, Performance during an example session. Dots represent licks to the right (blue) or the left (red). Grey bars, correct trials; black bars, incorrect trials. S, sample; D, delay; R, response. **c**, Schematic for recording and photostimulation (cyan arrows) configuration for each cell type. **d**, Collision test for an example neuron. Trials with spontaneous spikes preceding the light-evoked spike are shown binned by latency from top to bottom. Putative photostimulation-evoked spikes are at $+\Delta t$. When a spike occurs in the interval $[-\Delta t, +\Delta t]$, a collision occurs with the photostimulation-evoked spike in the axon and the somatic spike at $+\Delta t$ is absent. **e**, Depth distribution of PT_{upper} and PT_{lower} neurons based on micromanipulator readings (PT_{upper}: $n = 61$ cells; PT_{lower}: $n = 69$ cells). Depths are measured from the dorsal surface and are uncorrected for the curvature of cortical layers. Error bars represent mean ± s.d. **f**, Example identified PT neurons. Top, spike rastergrams for correct lick right trials (blue) and lick left trials (red). Bottom, trial-averaged spike rates.

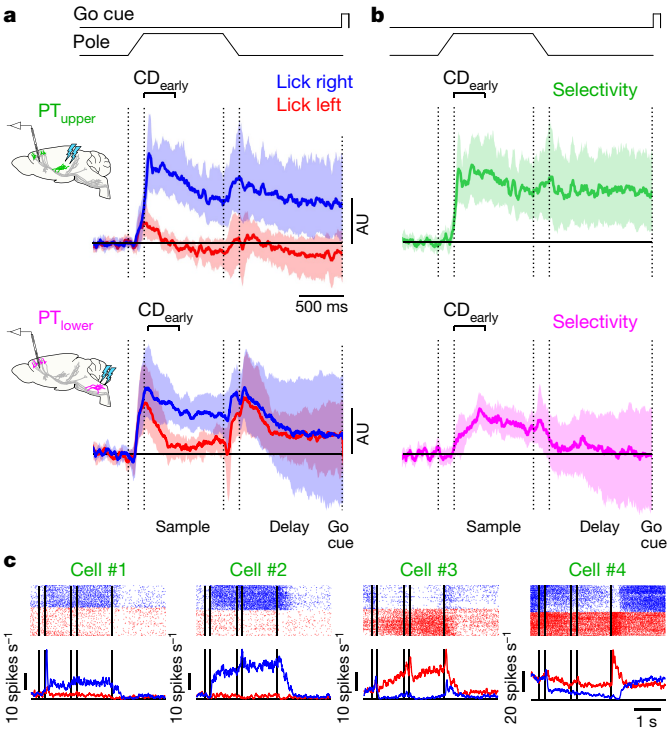

Fig. 5 | Persistent preparatory activity in PT_{upper} neurons. a, Time course of the linear combination of neuronal activity that best differentiates trial type after stimulus onset (CD_{early}) on lick right (blue) and lick left (red) trials for PT_{upper} (top) and PT_{lower} (bottom) neurons. AU, arbitrary units. **b**, Difference in CD_{early} projections on lick right and lick left trials (selectivity) in PT_{upper} (top; green) and PT_{lower} (bottom; magenta) neurons. **c**, Example identified PT_{upper} neurons. Top, raster plots for correct lick right trials (blue) and lick left trials (red). Bottom, trial-averaged spike rates. Shaded regions represent the standard deviation of the distribution produced by hierarchical bootstrapping ($n = 1{,}000$ iterations) in **a** and 5–95% confidence intervals in **b** (denoting region significantly greater than zero, $P < 0.05$ one-sided test, bootstrap).

Movement commands

Microstimulation of the ALM is sufficient to initiate bouts of directional licking[18,29], but the rhythmic movements involved in licking and swallowing are coordinated by circuits in the reticular nuclei of the medulla[23,30]. PT_{lower} neurons provide a direct path from the ALM to premotor circuits in the medulla (Fig. 2a, b and Extended Data Fig. 2). We reasoned that putative ALM signals driving movement should have selectivity for specific movements and emerge between the go cue and movement onset. In addition, movement commands should lie within an activity subspace that is orthogonal to the direction that predicts movement in the delay epoch; otherwise movement would be triggered prematurely[31,32].

We determined CD_{go} as the direction that maximizes selectivity in the 400 ms immediately after the go cue, orthogonal to CD_{late} (Fig. 6a). Along CD_{go}, selectivity was larger, emerged faster, and persisted longer in the PT_{lower} than in the PT_{upper} population (Fig. 6b, c). In the PT_{lower} population, significant selectivity emerged 24 ms after the go cue, faster than in the PT_{upper} population (48 ms) (Fig. 6c). The onset of the first detectable movement occurred approximately 50 ms after the go cue onset (99% confidence interval: 38–56 ms). The coding direction changed rapidly at the go cue in the PT_{lower} population, and more slowly, over several hundred milliseconds, in the PT_{upper} population (Extended Data Fig. 7c, e). Individual PT_{lower} neurons displayed pronounced changes in selectivity at the go cue (Fig. 6d).

Each bout of licking consists of a sequence of directional tongue protrusions at a stereotyped frequency (approximately 8 Hz; Fig. 4b). Aligning PT_{lower} activity to the last lick in a bout revealed additional movement-related features. Selectivity along both CD_{late} and CD_{go} ceased with the offset of movement (Extended Data Fig. 10a, b), simultaneous with an abrupt change in the coding direction (Extended Data Fig. 10c). This transition was not observed in the dynamics of the PT_{upper} population. Indeed, examining the activity of single neurons in the PT_{lower} population revealed neurons that were strongly modulated at the go cue, at the offset of movement, or both (Extended Data Fig. 10d)—features rarely observed in PT_{upper} cells. These results show that subgroups of PT_{lower} neurons have activity patterns consistent with roles in initiating, sustaining, and/or terminating movements.

Discussion

PT neurons exhibit diverse activity patterns that are related to movement planning and execution[2,4,18,19,32]. We have shown that motor cortex PT neurons comprise two cell types. PT_{upper} neurons connect with the thalamus and avoid motor centres in the medulla. These neurons tend to show early and persistent preparatory activity. PT_{lower} neurons

© 2018 Springer Nature Limited. All rights reserved.

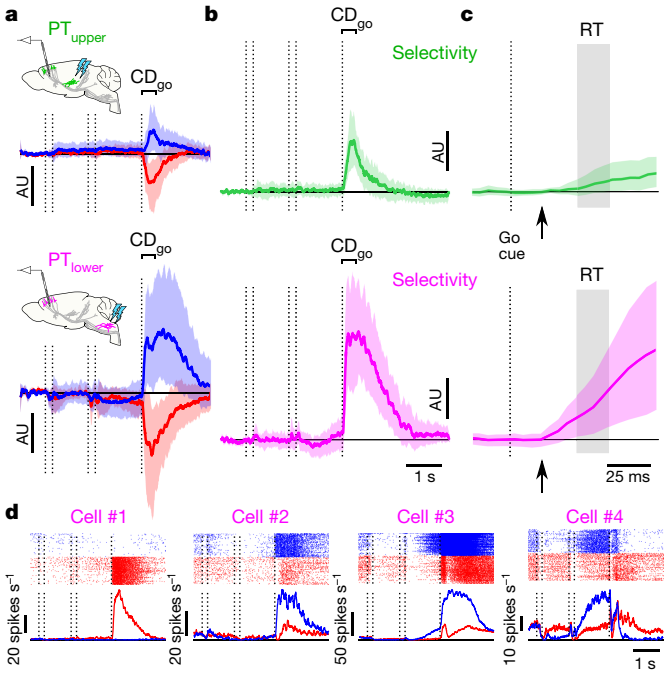

Fig. 6 | Movement commands in PT_{lower} neurons. a, Time course of the linear combination of neuronal activity that best differentiates trial types after the go cue (CD_{go}) on lick right (blue) and lick left (red) trials for PT_{upper} (top) and PT_{lower} (bottom) neurons. **b**, Difference in CD_{go} projections on lick right and lick left (selectivity) trials in PT_{upper} (top; green) and PT_{lower} (bottom; magenta) neurons. **c**, Data from **b** expanded around the go cue. Grey region indicates the distribution of session-averaged reaction times (RT; earliest detected orofacial movement; 99% confidence interval = 38–56 ms). Along CD_{go}, selectivity in PT_{lower} neurons emerged 24 ms after the go cue, faster than in the PT_{upper} population (48 ms) and consistent with a role in movement initiation. **d**, Example identified PT_{lower} neurons. Top, raster plots for correct lick right trials (blue) and lick left trials (red). Bottom, trial-averaged spike rates. Shaded regions represent the s.d. of the distribution produced by hierarchical bootstrapping ($n = 1{,}000$ iterations) in **a** and 5–95% confidence intervals in **b** and **c** (denoting region significantly greater than zero, $P < 0.05$ one-sided test, bootstrap).

avoid the thalamus and project to motor nuclei in the medulla. These neurons show late preparatory activity and seem to control movement initiation and termination. The segregation of PT neurons into two distinct types persists across the motor cortex and may generalize to other cortical areas[33] and other mammals[34,35].

Previous studies have suggested that collaterals of PT neurons to the thalamus[13,14] might provide an efference copy of motor commands[36]. Instead, we show that neurons that project to motor centres do not project to the thalamus. Corticothalamic PT_{upper} neurons encode more cognitive signals related to motor planning. The thalamus also receives a projection from L6 corticothalamic neurons, but these neurons are sparsely active, uncoupled from PT neurons, and have weak synapses on thalamic neurons[37,38].

Preparatory activity appeared early and remained persistent in PT_{upper} neurons, whereas movement commands were observed in PT_{lower} neurons. At the same time, several signals were multiplexed within both populations of PT neurons. For example, preparatory activity emerged in PT_{lower} neurons during the delay epoch (along CD_{late}) and persisted through the go cue and up to the termination of licking bouts. In the same cell type, and sometimes in the same individual cells (for example, Fig. 6d; cell #3), activity was modulated after the go cue along a different direction (CD_{go}), consistent with a movement command. In addition, cell type explained relatively little of the overall variance in neural activity (Extended Data Fig. 6). This highlights that even defined cell types express rich population coding.

Future studies that link detailed anatomy with transcriptional profiling might lead to further subdivision of PT neuron types, particularly the *Npsr1–Hpgd* PT_{upper} cells that mapped to two transcriptomic clusters (Figs. 1, 2). Exploring the connectivity of each PT type with each other and other ALM cell types, as well as long-range inputs, will be crucial for understanding how motor planning and movement signals arise differentially across the PT neuron populations. In addition to PT neurons, the ALM contains 14 transcriptomic clusters corresponding to diverse intratelencephalic neurons, which project to other cortical areas and the striatum[21] (Fig. 1). Identifying the roles of other distinct cell types in movement will require experiments similar to those presented here—in addition to mapping the connections between cell types—and are crucial for understanding the function of cortical circuits.

Online content

Any methods, additional references, Nature Research reporting summaries, source data, statements of data availability and associated accession codes are available at https://doi.org/10.1038/s41586-018-0642-9.

Received: 5 December 2017; Accepted: 24 September 2018;
Published online 31 October 2018.

1. Svoboda, K. & Li, N. Neural mechanisms of movement planning: motor cortex and beyond. *Curr. Opin. Neurobiol.* **49**, 33–41 (2018).
2. Shenoy, K. V., Sahani, M. & Churchland, M. M. Cortical control of arm movements: a dynamical systems perspective. *Annu. Rev. Neurosci.* **36**, 337–359 (2013).
3. Evarts, E. V. Pyramidal tract activity associated with a conditioned hand movement in the monkey. *J. Neurophysiol.* **29**, 1011–1027 (1966).
4. Kaufman, M. T. et al. The largest response component in the motor cortex reflects movement timing but not movement type. *eNeuro* **3**, https://doi.org/10.1523/ENEURO.0085-16.2016 (2016).
5. Kiritani, T., Wickersham, I. R., Seung, H. S. & Shepherd, G. M. G. Hierarchical connectivity and connection-specific dynamics in the corticospinal-corticostriatal microcircuit in mouse motor cortex. *J. Neurosci.* **32**, 4992–5001 (2012).
6. Kawaguchi, Y. Pyramidal cell subtypes and their synaptic connections in layer 5 of rat frontal cortex. *Cereb. Cortex* **27**, 5755–5771 (2017).
7. Hooks, B. M. et al. Organization of cortical and thalamic input to pyramidal neurons in mouse motor cortex. *J. Neurosci.* **33**, 748–760 (2013).
8. von Economo, C. & Parker, S. *The Cytoarchitectonics of the Human Cerebral Cortex* (Oxford University Press, London 1929).
9. Kuypers, H. G. J. M. in *Comprehensive Physiology* (ed. Terjung, R.) (John Wiley & Sons, Inc., New Jersey, 1981).
10. Lemon, R. N. Descending pathways in motor control. *Annu. Rev. Neurosci.* **31**, 195–218 (2008).
11. Cheney, P. D. & Fetz, E. E. Functional classes of primate corticomotoneuronal cells and their relation to active force. *J. Neurophysiol.* **44**, 773–791 (1980).
12. Lawrence, D. G. & Kuypers, H. G. The functional organization of the motor system in the monkey. I. The effects of bilateral pyramidal lesions. *Brain J. Neurol.* **91**, 1–14 (1968).
13. Deschênes, M., Bourassa, J. & Pinault, D. Corticothalamic projections from layer V cells in rat are collaterals of long-range corticofugal axons. *Brain Res.* **664**, 215–219 (1994).
14. Kita, T. & Kita, H. The subthalamic nucleus is one of multiple innervation sites for long-range corticofugal axons: a single-axon tracing study in the rat. *J. Neurosci. Off. J. Soc. Neurosci.* **32**, 5990–5999 (2012).
15. Guo, Z. V. et al. Maintenance of persistent activity in a frontal thalamocortical loop. *Nature* **545**, 181–186 (2017).
16. Jones, E. G. & Wise, S. P. Size, laminar and columnar distribution of efferent cells in the sensory-motor cortex of monkeys. *J. Comp. Neurol.* **175**, 391–437 (1977).
17. Wang, X. et al. Deconstruction of corticospinal circuits for goal-directed motor Skills. *Cell* **171**, 440–455.e14 (2017).
18. Li, N., Chen, T.-W., Guo, Z. V., Gerfen, C. R. & Svoboda, K. A motor cortex circuit for motor planning and movement. *Nature* **519**, 51–56 (2015).
19. Tanji, J. & Evarts, E. V. Anticipatory activity of motor cortex neurons in relation to direction of an intended movement. *J. Neurophysiol.* **39**, 1062–1068 (1976).
20. Turner, R. S. & DeLong, M. R. Corticostriatal activity in primary motor cortex of the macaque. *J. Neurosci.* **20**, 7096–7108 (2000).
21. Tasic, B. et al. Shared and distinct transcriptomic cell types across neocortical areas. *Nature* https://doi.org/10.1038/s41586-018-0654-5 (2018).
22. Economo, M. N. et al. A platform for brain-wide imaging and reconstruction of individual neurons. *eLife* **5**, e10566 (2016).
23. Stanek, E., IV, Cheng, S., Takatoh, J., Han, B.-X. & Wang, F. Monosynaptic premotor circuit tracing reveals neural substrates for oro-motor coordination. *eLife* **3**, e02511 (2014).
24. Tervo, D. G. et al. A designer AAV variant permits efficient retrograde access to projection neurons. *Neuron* **92**, 372–382 (2016).
25. Guo, Z. V. et al. Flow of cortical activity underlying a tactile decision in mice. *Neuron* **81**, 179–194 (2014).
26. Chen, T.-W., Li, N., Daie, K. & Svoboda, K. A map of anticipatory activity in mouse motor cortex. *Neuron* **94**, 866–879 (2017).

© 2018 Springer Nature Limited. All rights reserved.

27. Li, N., Daie, K., Svoboda, K. & Druckmann, S. Robust neuronal dynamics in premotor cortex during motor planning. *Nature* **532**, 459–464 (2016).
28. Cunningham, J. P. & Yu, B. M. Dimensionality reduction for large-scale neural recordings. *Nat. Neurosci*. **17**, 1500–1509 (2014).
29. Komiyama, T. et al. Learning-related fine-scale specificity imaged in motor cortex circuits of behaving mice. *Nature* **464**, 1182–1186 (2010).
30. Travers, J. B., Dinardo, L. A. & Karimnamazi, H. Motor and premotor mechanisms of licking. *Neurosci. Biobehav. Rev*. **21**, 631–647 (1997).
31. Druckmann, S. & Chklovskii, D. B. Neuronal circuits underlying persistent representations despite time varying activity. *Curr. Biol*. **22**, 2095–2103 (2012).
32. Kaufman, M. T., Churchland, M. M., Ryu, S. I. & Shenoy, K. V. Cortical activity in the null space: permitting preparation without movement. *Nat. Neurosci*. **17**, 440–448 (2014).
33. Hattox, A. M. & Nelson, S. B. Layer V neurons in mouse cortex projecting to different targets have distinct physiological properties. *J. Neurophysiol*. **98**, 3330–3340 (2007).
34. Catsman-Berrevoets, C. E. & Kuypers, H. G. A search for corticospinal collaterals to thalamus and mesencephalon by means of multiple retrograde fluorescent tracers in cat and rat. *Brain Res*. **218**, 15–33 (1981).
35. Steriade, M. & Yossif, G. Afferent and recurrent collateral influences on cortical somatosensory neurons. *Exp. Neurol*. **56**, 334–360 (1977).
36. Sherman, S. M. Thalamus plays a central role in ongoing cortical functioning. *Nat. Neurosci*. **19**, 533–541 (2016).
37. Yamawaki, N. & Shepherd, G. M. G. Synaptic circuit organization of motor corticothalamic neurons. *J. Neurosci*. **35**, 2293–2307 (2015).
38. Sherman, S. M. & Guillery, R. W. On the actions that one nerve cell can have on another: distinguishing "drivers" from "modulators". *Proc. Natl Acad. Sci. USA* **95**, 7121–7126 (1998).

Acknowledgements We thank A. Lemire and K. Aswath for single-cell sorting and bulk RNA-seq, S. Lindo for stereotaxic surgeries, D. Kao and T. Wang for help with RNA-seq analysis, D. Alcor for imaging assistance, and N. Li and H. Inagaki for help with electrophysiological recordings and for discussion. We thank M. Cembrowski, E. Bloss and F. Henry for discussion. H. Inagaki, M. Sherman, S. Romani, L. Luo, G. Shepherd and T. Wang provided comments on the manuscript. Imaging and reconstructions of neuronal morphology was performed by the Janelia MouseLight project (http://mouselight.janelia.org/). This work was funded by the Howard Hughes Medical Institute, the Allen Institute for Brain Science, the NIH Brain Initiative (U01MH105982 to H.Z.), and the Intramural Research Program of the NIMH (ZIA-MH002497-29 to C.R.G).

Reviewer information *Nature* thanks P. Carninci, M. Fee, T. Mrsic-Flogel and the anonymous reviewer(s) for their contribution to the peer review of this work.

Author contributions M.N.E., K.S., S.V., L.L.L., B.T. and H.Z.: conception and design of the experiments. B.T., L.T.G., T.N.N., K.A.S., Z.Y. and H.Z.: scRNA-seq experiments, with material provided by M.N.E., S.V. and L.W. M.N.E., E.B., J.W. and J.C.: single neuron reconstructions. S.V., C.R.G. and M.N.E: in situ experiments and analysis. M.N.E.: electrophysiology experiments. M.N.E., S.V. and C.R.G.: anatomical experiments. M.N.E., S.V., V.M., L.T.G., Z.Y., K.S. and L.L.L.: data analysis. M.N.E., K.S. and L.L.L.: wrote the paper with input from all authors.

Competing interests The authors declare no competing interests.

Additional information
Extended data is available for this paper at https://doi.org/10.1038/s41586-018-0642-9.
Supplementary information is available for this paper at https://doi.org/10.1038/s41586-018-0642-9.
Reprints and permissions information is available at http://www.nature.com/reprints.
Correspondence and requests for materials should be addressed to K.S.
Publisher's note: Springer Nature remains neutral with regard to jurisdictional claims in published maps and institutional affiliations.

© 2018 Springer Nature Limited. All rights reserved.

METHODS

Animals. Mice used for scRNA-seq experiments in the visual cortex and ALM are described elsewhere[21]. Mice used for all other experiments are listed in Supplementary Tables 2 and 3. Mice were housed on a 12-h light/dark cycle with ad libitum access to food and water, except during behaviour (described in the 'Mouse behaviour' section). For electrophysiological experiments, group sizes were based on the number of identified neurons possible to record in each animal (5–20) and the number of cells likely to yield interpretable results (>50 neurons per condition; based on previous work[18]). For sequencing and anatomy experiments, sample sizes were similar to those used by others in the field. No statistical tests were used to determine sample sizes.

Surgical procedures. All procedures were in accordance with protocols approved by the Janelia Research Campus Institutional Animal Care and Use Committee and Institutional Biosafety Committee. Mice were given buprenorphine HCl (0.1 mg kg^{-1}; Bedford Laboratories) and ketoprofen (5 mg kg^{-1}; Fort Dodge Animal Health) for post-operative analgesia and to reduce inflammation. Surgical procedures were carried out under 1–2% isoflurane anaesthesia. Mice were placed in a stereotaxic headholder on a thermal blanket and their eyes covered with artificial tears (Rugby). Marcaine (0.05 ml, 0.5%) was injected under the skin covering the skull. The skin and periosteum covering the skull was removed and the skull thinned overlying the sites of viral injection(s). For all injections, virus was injected using a manual volume displacement injector (MMO-220A, Narishige) connected to a glass pipette (5-000-2005, Drummond Scientific) pulled to a 30 μm tip (P-2000, Sutter Instruments) that was bevelled to a sharp tip. Pipettes were back-filled with mineral oil and virus was front-loaded before injection. Pipettes were inserted through the thinned bone to the appropriate depth and virus injected at 10 nl min^{-1}. For electrophysiology, a fibre optic cannula (CFML12L05; Thorlabs) was implanted 200 μm above the viral injection target and a headbar implanted caudal to Bregma. Dental acrylic (Jet repair; Pearson Dental) was used to secure the optic fibre and headbar to the skull and protect exposed bone.

Viral expression. All viruses used in these experiments were adeno-associated viruses (AAVs) produced in the Janelia Research Campus (JRC) Virus Shared Resource. Viruses used for scRNA-seq experiments are described elsewhere[21]. For all other experiments, viruses incorporated the rAAV2-retro capsid[24], with the exception of axonal reconstruction experiments (Fig. 2a, b and Extended Data Fig. 2a–d), which used AAV2 serotype 1. Viruses used, viral titres, injection volumes, injection coordinates, and associated experiments are described in Supplementary Tables 2 and 4.

scRNA-seq. Single-cell RNA-seq data (Figs. 1a, b, 2e, f and 3a and Extended Data Figs. 1a, b and 4a–c, h, i), were collected and analysed as described elsewhere[21]. A total of 9,573 scRNA-seq transcriptomes were measured from ALM neurons (4,477 glutamatergic) and 14,249 from V1 neurons. To collect individual cells, layer-enriching dissections were used from brains of pan-neuronal, pan-excitatory or pan-inhibitory recombinase lines crossed to recombinase reporters (10,752 cells). This dataset was supplemented with 10,414 cells isolated from other recombinase lines. Dissections without layer enrichment, or multiple layers combined, were used for lines with sparse labelling. Additional recombinase lines were selected to capture cellular diversity that was suggested by ongoing analysis of the data. In total, 2,656 additional cells were derived from viral retrograde labelling, with the goal to establish correspondence between transcriptomic types and projection properties. PT neurons were collected from retrogradely-labelled brains ($n = 62$ medulla injection; $n = 94$ thalamus; $n = 100$ pons; $n = 97$ superior colliculus; $n = 2$ amygdala; $n = 2$ zona incerta) and recombinase crosses ($n = 10$).

scRNA-seq analysis. A detailed description of scRNA-seq analysis is provided elsewhere[21]. In brief, 50-base pair paired-end reads were aligned to GRCm38 (mm10) using a RefSeq annotation gff file retrieved from NCBI on 18 January 2016 (https://www.ncbi.nlm.nih.gov/genome/annotation_euk/all/). Sequence alignment was performed using STAR v2.5.3[48] in two-pass mode. Transcriptomic features, extracted by weighted gene co-expression network analysis[39], were clustered in an iterative and bootstrapped manner. The output of this procedure is a co-clustering matrix, which shows the frequency with which any cell clusters with any other cell in 100 bootstrapped iterative clustering rounds. The transcriptomic clusters are defined by 'cutting' the co-clustering matrix to derive membership of each cell to a cluster. The membership of each cell is tested post-clustering by classification algorithms to assign core versus intermediate identity to cells[40]. Cells that were reliably assigned to only one cluster are 'core' cells 21,195); cells that were assigned to more than one cluster (typically two) are 'intermediate' cells 2,627 cells). ALM scRNA-seq transcriptomes clustered into 27 glutamatergic, 61 GABAergic and 16 non-neuronal types. In scRNA-seq experiments, differentially expressed genes (Fig. 3a and Extended Data Fig. 1a, c) were detected as described previously[40] using the R package limma v3.30.13[41]. In brief, differentially expressed genes were defined as genes with more than twofold change and adjusted $P < 0.01$, and with expression following a bimodal pattern confined to one cluster relative to the other. Multiple genes were found satisfying criteria for markers. Cluster names (for example, *Slco2a1*, *Npsr1* and *Hpgd*) were selected from candidate genes as those adding the most discriminability for adjacent leafs of the dendrogram and that were detected in more than 50% of individual cells with preference for globally unique genes[21].

Single-cell axonal reconstruction. The axons of single neurons were labelled and imaged as described previously[22] (Fig. 2a, b and Extended Data Fig. 2a–d). Neurons in the motor cortex were sparsely labelled using a viral vector encoding either GFP or tdTomato. At least 3 weeks after virus injection, mice were perfused and brains extracted. Brains were embedded in gelatin and cleared using a combination of DMSO and D-sorbitol. The full volume of each brain was imaged at sub-micrometre resolution using a block-face two-photon microscope with integrated vibratome. Individual neurons were reconstructed manually in three-dimensions using the Janelia Workstation (https://www.janelia.org/confocal-imagery-management-and-analysis-tools) by two independent annotators who were blinded to all analyses. Consensus reconstructions were determined by resolving discrepancies (generally <5%) between annotators. Each dataset was registered to the Allen Common Coordinate Framework[42] using landmark based registration (3DSlicer, Landmark Registration module) and a thin plate spline warp determined between the two image spaces. Neuronal reconstructions were then projected into the reference space to determine the brain area associated with each axonal segment, branch point, and terminus.

Histology and imaging. At least two weeks after viral injections, mice were transcardially perfused with PBS (>20 ml) followed by 4% paraformaldehyde (>20 ml). Brains were post-fixed overnight. For immunolabelling (Fig. 2c, d and Extended Data Fig. 3), brains were transferred to a 20% sucrose solution for cryoprotection and sectioned coronally at 50 μm on a freezing microtome. In all other cases (Extended Data Fig. 2e), brains were sectioned at 50 or 100 μm on a vibratome (VT1200; Leica Biosystems). Sections were processed using standard immunohistochemical techniques and imaged as previously described[43] (Fig. 2c, d and Extended Data Figs. 2e, 3). Brightness and contrast were adjusted manually to match approximate luminance values across imaging experiments in a linear fashion using ImageJ/Fiji.

Bulk RNA-seq. Cells retrogradely labelled from the thalamus, medulla, pons, and superior colliculus with GFP or tdTomato were collected by manual cell sorting[44] (Extended Data Figs. 1c, d, 4d–g, i). Approximately 50–120 cells were collected per sample, with 7 biological replicates performed each for thalamus and medulla and 3 replicates each for superior colliculus and pons. Cells were isolated by manual cell sorting on a fluorescence dissecting scope, following micro-dissection, trituration and enzymatic digestion as described previously[45]. Following pooling and lysis, total RNA was extracted by Picopure kit (KIT0204; Thermo-Fisher). Amplified DNA was produced using Ovation RNA-seq System V2 kit (7102; NuGEN), fragmented to ~200 bp, ligated to Illumina sequencing adaptors with Encore Rapid kit (0314; NuGEN), and sequenced on an Illumina HiSeq 2500 with fourfold multiplexing (single end, 100=bp read length).

Bulk RNA-seq analysis. Adaptor sequences (AGATCGGAAGAGCACACGTCTGAACTCCAGTCAC) were removed from reads using Trimmomatic 0.36[46], mapped using STAR 2.5.3a[47] to the Ensembl mouse genome GRCm38.p5, release 90 (https://www.ensembl.org\). Mapped reads were normalized to the total number of reads per sample (counts per million). Principal components analysis of the 7 thalamus-projecting and 7 medulla-projecting replicates showed that a single replicate from each behaved as an outlier. Thus, for further analysis, 6 replicates were considered for each. Three replicates were performed for both superior colliculus-projecting and pons-projecting neurons with all replicates used in further analysis. Similar numbers of genes were detected in each of the bulk RNA-seq samples (thalamus: 12,317; medulla: 12,363). These numbers were higher than the genes detected across all cells in scRNA-seq (Extended Data Fig. 4e–h). In bulk RNA-seq experiments, differential expression analysis was performed using EdgeR[48]. Genes were determined to be differentially expressed (Extended Data Fig. 1b, d) between PT_{upper} and PT_{lower} cells according to the following criteria: false discovery rate of 1×10^{-5}, mean expression fold change >2, and non-zero expression in at least 5 of 6 replicates. A number of potential marker genes were identified for both PT_{upper} and PT_{lower} neurons from both scRNA-seq and bulk RNA-seq (Extended Data Figs. 1, 4i). *Slco2a1*, the gene selected as the name for the PT_{lower} cluster from scRNA-seq data, was confirmed as having high expression in PT_{lower} neurons and low expression in PT_{upper} neurons (Fig. 3 and Extended Data Fig. 1a, c) and was thus chosen as a marker gene for PT_{lower} neurons. *Npnt* was chosen as a marker gene for PT_{upper} neurons as it was highly expressed across both the *Npsr1* and *Hpgd* clusters and was differentially expressed in both scRNA-seq and bulk RNA-seq as well, with little expression in other layer 5 and 6 clusters, GABAergic neurons, and glia.

In situ hybridization. Animals were perfused with 4% paraformaldehyde and brains were post-fixed in 4% paraformaldehyde overnight at 4 °C. Brains were then rinsed in PBS and cryoprotected in 30% sucrose, and 20-μm thick sections were cut on a cryostat. smFISH (RNAScope) followed by immunohistochemistry was

© 2018 Springer Nature Limited. All rights reserved.

performed on fixed frozen tissue from mice injected with rAAV2-retro-GFP in either the thalamus or medulla (Supplementary Tables 2–4) as per protocols for fixed frozen tissue using proprietary probes from Advanced Cell Diagnostics (ACDBio). Probes used in this study (Mm-Npnt: 316771; Mm-Slco2a1: 485041) were detected using proprietary detection reagent (RNAscope Fluorescent Multiplex Detection Reagents, 320851), using Amp4 Alt B (Atto 550). After smFISH, sections were rinsed in PBS, and blocking buffer (2% BSA and 0.3% serum) was applied for 5 min. Primary antibody (Aves-Labs, GFP-1020) was diluted in the blocking buffer (1:100) and incubated overnight at 4 °C. Sections were rinsed in PBS three times (5 min) and incubated with secondary antibody goat anti-chicken AF 488 (A-11039, Invitrogen; diluted 1:100 in blocking buffer) at room temperature for 2 h. Sections were then rinsed in PBS and coverslips were added with Vectashield containing DAPI (H-1500; VectorLabs). Images were acquired as 7-μm thick stacks collected using a 40×/1.3 numerical aperture (NA) objective (pixel size, 0.11 × 0.11 μm) on a Zeiss 880 inverted confocal microscope. Punctate mRNA signal was quantified on cell volumes from maximum intensity projection of the *Z*-stacks in the ALM and primary motor cortex (AP: 0.0 to +1.0, ML: 1.0 to 2.0) using Neurolucida (MBF). Single image planes are illustrated in Fig. 3b.

Mouse behaviour. Mice were water-restricted and housed on a 12-h reverse light/dark cycle with testing during the dark phase. On days in which mice were not trained, they received 1 ml of water. Behavioural experiments lasted 1–2 h per day, during which mice consumed their daily water intake (approximately 0.5–1.0 ml). Mice unable to sustain stable body weight were given supplementary water. Mice were trained using operant conditioning as previously described[25,49] until reaching behavioural criterion (>75% trials correct). At the beginning of each trial, a vertical pole moved within reach of the whiskers (200-ms travel time). The pole remained in position for 1.0 s and then was retracted (200-ms travel time). The sample epoch was defined as the 1.0 s during which the pole was in range of the whiskers and stationary. After the pole was removed, the mouse was trained to refrain from licking for an additional 1.3 s (delay epoch) before an auditory 'go cue' (pure tone, 3.4 kHz, 0.1 s duration) instructed the mouse to lick (reward epoch). Premature licks during the sample or delay epoch resulted in a restart of the requisite epoch and these trials were excluded from all analyses. Licking the correct lick port after the go cue led to a small water reward (3 μl). Licking the incorrect lick port triggered a timeout (2–10 s). Trials in which mice did not lick within a 1.5-s window after the go cue were rare and typically occurred at the end of a session.

Videography. Video was acquired at 400 Hz framerate from below and to the side of the mouse using CMOS cameras (CM3-U3-13Y3M, FLIR) with a 4–12 mm focal length lens (12VM412ASIR, Tamron). Camera data were acquired using BIAS (IORodeo). Reaction times were determined by measuring the luminance change in a small region of interest manually placed just below the jaw in side-view movies. Luminance traces were averaged across all of the trials within each session (453 ± 79, mean ± s.d.; range: 295–551). 95% confidence intervals for reaction time were calculated by bootstrapping session means across mice ($n = 3$) and sessions ($n = 14$). Little inter-animal variation was observed in session-averaged reaction time.

Electrophysiology. A small craniotomy (diameter, 0.5–1 mm) was made over ALM (AP: 2.5, ML 1.5) one day before the first recording session. Extracellular spikes were recorded using silicon probes containing two shanks each with 32 channels with 25 μm spacing (H2; Cambridge Neurotech). The 64-channel voltage signals were multiplexed, recorded on a PCI6133 board (National Instrument), and digitized at 14 bits. The signals were demultiplexed into the 32 voltage traces, sampled at 25 kHz and stored for offline analyses. A total of 4–7 recordings were made from each craniotomy on consecutive days. The tissue was allowed to settle for 10 min before recording.

To optogenetically tag PT_{upper} and PT_{lower} neurons during recording, we expressed ChR2–YFP or ChR2(H134R)–GFP selectively in each population using a viral injection into the medulla or thalamus as described above. During each recording session, more than 1,200 photostimuli were delivered at 4 Hz just before and after the behavioural session. Photostimuli were 0.1–0.5 ms at 80–100 mW (measured just before the implanted fibre optic cannula). Reliable antidromic activation was observed in 1–6 units per session. Owing to the proximity of the cerebral peduncle, subthalamic nucleus and zona incerta, which contain projections from both cell types, a smaller viral injection was performed in the thalamus (50 nl) than in the medulla (50–200 nl), resulting in fewer tagged PT_{upper} neurons per mouse. Across all sessions recording PT_{upper} neurons, mouse performance was 85.4 ± 7.8% on lick left trials and 89.3 ± 9.4% on lick right trials (mean ± s.d.; $n = 37$ sessions in 8 mice; left hemisphere). In PT_{lower} neuron recordings, performance was 83.5 ± 6.3% on lick left trials and 86.3 ± 8.2% on lick right trials ($n = 23$ sessions in 4 mice; both hemispheres). Mice performed a median of 107 and 105 correct trials on lick left and lick right trials respectively in PT_{upper} recordings and 117 and 108 correct trials during PT_{lower} recordings. PT neurons recorded from the left and right ALM did not differ and were combined in all further analysis to increase statistical power.

In addition, 495 unidentified single units were isolated from 15 sessions from the same cohort of animals in which PT_{upper} neurons were tagged, and 511 unidentified single units were isolated from 14 sessions from the same cohort in which PT_{lower} neurons were identified. Unidentified neurons were isolated in the same proportion as tagged neurons across animals. To produce depth-matched samples of unidentified neurons (Extended Data Fig. 8), we restricted analysis to experiments from the left ALM because recordings from the right ALM were made using oblique penetration angles and were biased towards deep L5b. By contrast, recordings from left ALM were obtained with penetrations perpendicular to cortical layers.

Electrophysiology data analysis. Extracellular recordings were band-pass filtered (300–4,500 Hz; second order Butterworth filter) and the common mode on ±4 sites was subtracted from each channel. Events were detected using JRClust[50] and spikes from tagged units ($n = 143$) were sorted manually using a custom program written in MATLAB. All other units were sorted using JRClust[50]. Extreme care was taken to restrict analysis to tagged units that could be sorted with a low number of false positive spikes (mean inter-spike intervals less than 2 ms = 0.02%; Extended Data Fig. 5) so that neuronal responses could be faithfully attributed to the correct cell type. Despite this, spike rates were similar to those measured in other ALM recordings in the same task[18] indicating that the false negative spike rate remained low. Information from 4–7 adjacent recording sites was used for sorting each unit. Units recorded during behavioural sessions in which performance was not greater than 65% for both trial types were excluded from the dataset. Units recorded during behavioural sessions with less than 50 correct trials of each type were excluded (13 units were rejected; 130 were kept for further analysis). Unit depths (Fig. 4e) were inferred from manipulator readings only without correction for the angle between the electrode penetration and the orientation of cortical layers. Collision tests were performed for all tagged units to confirm axonal projections to the thalamus or medulla[18,51] (Fig. 4d). Trial-averaged spike rates were calculated in 5 ms time bins and filtered using a causal 50 ms boxcar filter.

The coding direction vector (**CD**) (Figs. 5, 6 and Extended Data Figs. 7, 8, 10) was calculated as:

$$\boldsymbol{v} = \frac{\bar{\boldsymbol{x}}_{\text{lick right}} - \bar{\boldsymbol{x}}_{\text{lick left}}}{\sqrt{\text{Var}(\bar{\boldsymbol{x}}_{\text{lick right}}) + \text{Var}(\bar{\boldsymbol{x}}_{\text{lick left}})}} \quad (1)$$

$$\mathbf{CD} = \frac{\boldsymbol{v}}{\sum |\boldsymbol{v}|} \quad (2)$$

For each neuron, the mean difference in spike rate between lick right, $\bar{\boldsymbol{x}}_{\text{lick right}}$, and lick left trials, $\bar{\boldsymbol{x}}_{\text{lick left}}$, was calculated in a 400-ms time interval. This vector was divided by the square root of the sum of the across-trial variances of spike rate for each trial type. The resulting vector ($\boldsymbol{v}$) was then normalized by its L_1 norm so that projections would not scale with vector length (number of cells in population) to produce the coding direction, **CD**. Coding directions were calculated in the first 400 ms of the sample epoch (CD_{early}; 2.5 to 2.1 s before the go cue) the last 400 ms of the delay epoch (CD_{late}; 0.4 to 0.0 s before the go cue) and the first 400 ms of the response epoch (CD_{go}; 0.0 to 0.4 s after the go cue). CD_{go} was orthogonalized to CD_{late} using the Gram–Schmidt process to isolate selectivity emerging after the go cue, independent of the component of CD_{late} that persisted into the response epoch. Coding directions were calculated separately for the PT_{upper} and PT_{lower} populations.

Projections of the activity of each PT population along the coding directions ($\boldsymbol{p}_{\text{lick right}}$, $\boldsymbol{p}_{\text{lick left}}$) were calculated as:

$$\boldsymbol{p}_{\text{lick right}} = \mathbf{CD}^{\mathrm{T}} \boldsymbol{x}_{\text{lick right}} \quad (3)$$

$$\boldsymbol{p}_{\text{lick left}} = \mathbf{CD}^{\mathrm{T}} \boldsymbol{x}_{\text{lick left}} \quad (4)$$

Selectivity ($\boldsymbol{S}$) along each direction was:

$$\boldsymbol{S} = \boldsymbol{p}_{\text{lick right}} - \boldsymbol{p}_{\text{lick left}} \quad (5)$$

In all cases (Figs. 5, 6 and Extended Data Figs. 7, 8, 10), the illustrated projections are the results of a hierarchical bootstrapping procedure. For each population, 1,000 bootstrapped projections were calculated. For each repetition, *M* mice were chosen with replacement from the appropriate cohort, in which *M* was the original cohort size. From that sample of mice, *n* neurons were randomly chosen (with replacement), in which *n* was the number of neurons in the population. For each neuron, 50 correct trials of each trial type were randomly selected with replacement. In all figures, solid lines represent the median and s.d. of all repetitions for projections of the data for each trial type[52,53]. For selectivity, shaded areas represent 5–95% confidence intervals, thereby indicating where projections are significantly different from zero ($P < 0.05$, one-sided test, bootstrap).

© 2018 Springer Nature Limited. All rights reserved.

To determine the variance explained by cell type in Extended Data Fig. 6, trial-averaged activity patterns from all neurons were *z*-scored and time series from trial types were concatenated. These concatenated time series were decomposed separately across each PT population using principal component analysis and the fraction of variance of the data explained by each principal component was calculated. For comparison, we repeated the same procedure, but drew a size-matched sample from the population of unidentified neurons (without replacement). 1,000 repetitions of this procedure were performed to build a distribution for comparison.

To create matrices of the coding direction correlation across time (Extended Data Figs. 7c, 10c), coding directions were calculated at each time point from the trial-averaged spike rates of all neurons within a population (5-ms time bins, filtered using a causal 50-ms boxcar filter), as above, but were normalized by their Euclidean norms to produce unit vectors. Correlation matrices represent the inner product of coding direction vectors at each pair of time points.

Single-cell trial type decoding accuracy (Extended Data Fig. 9) was determined using the average spike rate during the first 400 ms of the sample epoch (2.5 to 2.1 s before the go cue). A spike rate threshold was determined that best distinguished lick right trials from lick left trials (maximal accuracy) with accuracy defined as the proportion of trials correctly classified. Accuracy was $\geq 50\%$ by definition. Shaded regions in around the cumulative distribution function in Extended Data Fig. 9b, d represent s.e.m., estimated using Greenwood's formula.

All two-sample *t*-tests were Student's *t*-tests.

Randomization and blinding. In all experiments in which PT_{upper} and PT_{lower} neurons were compared in different animals (electrophysiology, in situ hybridization, etc.), individual mice were allocated randomly into experimental groups.

Retrogradely labelled neurons were isolated for scRNA-seq by a technician and/or sorted automatically using FACS. Single-neuron reconstructions were performed by expert annotators without knowledge of the biological focus of this study. For electrophysiological recordings, trial types were randomly determined by a computer program. During spike sorting, experimenters did not have access to trial type, and individual events could not be related to trial epochs so experimenters were blinded to conditions.

Reporting summary. Further information on research design is available in the Nature Research Reporting Summary linked to this paper.

Code availability. Analysis code is available at https://github.com/SvobodaJanelia.

Data availability

The full single-cell RNA-seq dataset has been described previously[21]. Bulk RNA-seq data are available at the Gene Expression Omnibus (GEO) under accession GSE119182. Electrophysiology data are available at CRCNS.org and Figshare (doi: 10.25378/janelia.7007846).

39. Langfelder, P. & Horvath, S. WGCNA: an R package for weighted correlation network analysis. *BMC Bioinformatics* **9**, 559 (2008).
40. Tasic, B. et al. Adult mouse cortical cell taxonomy revealed by single cell transcriptomics. *Nat. Neurosci.* **19**, 335–346 (2016).
41. Ritchie, M. E. et al. limma powers differential expression analyses for RNA-sequencing and microarray studies. *Nucleic Acids Res.* **43**, e47 (2015).
43. Oh, S. W. et al. A mesoscale connectome of the mouse brain. *Nature* **508**, 207–214 (2014).
44. Paletzki, R. & Gerfen, C. R. Whole mouse brain image reconstruction from serial coronal sections using FIJI (ImageJ). *Curr. Protoc. Neurosci.* **73**, 1.25.1–1.25.21 (2015).
45. Sugino, K. et al. Molecular taxonomy of major neuronal classes in the adult mouse forebrain. *Nat. Neurosci.* **9**, 99–107 (2006).
46. Sugino, K. et al. Cell-type-specific repression by methyl-CpG-binding protein 2 is biased toward long genes. *J. Neurosci.* **34**, 12877–12883 (2014).
47. Bolger, A. M., Lohse, M. & Usadel, B. Trimmomatic: a flexible trimmer for Illumina sequence data. *Bioinformatics* **30**, 2114–2120 (2014).
48. Dobin, A. et al. STAR: ultrafast universal RNA-seq aligner. *Bioinformatics* **29**, 15–21 (2013).
49. McCarthy, D. J., Chen, Y. & Smyth, G. K. Differential expression analysis of multifactor RNA-Seq experiments with respect to biological variation. *Nucleic Acids Res.* **40**, 4288–4297 (2012).
50. Guo, Z. V. et al. Procedures for behavioral experiments in head-fixed mice. *PLoS One* **9**, e88678 (2014).
51. Jun, J. J. et al. Real-time spike sorting platform for high-density extracellular probes with ground-truth validation and drift correction. Preprint at https://www.bioRxiv.org/content/early/2017/01/19/101030 (2017).
52. Towe, A. L., Patton, H. D. & Kennedy, T. T. Response properties of neurons in the pericruciate cortex of the cat following electrical stimulation of the appendages. *Exp. Neurol.* **10**, 325–344 (1964).
53. Aarts, E., Verhage, M., Veenvliet, J. V., Dolan, C. V. & van der Sluis, S. A solution to dependency: using multilevel analysis to accommodate nested data. *Nat. Neurosci.* **17**, 491–496 (2014).
54. van der Leeden, R. in *Handbook of Multilevel Analysis* (eds de Leeuw, J. & Meijer, E.) 401-433 (Springer, New York, 2008).
55. Lein, E. S. et al. Genome-wide atlas of gene expression in the adult mouse brain. *Nature* **445**, 168–176 (2007).

© 2018 Springer Nature Limited. All rights reserved.

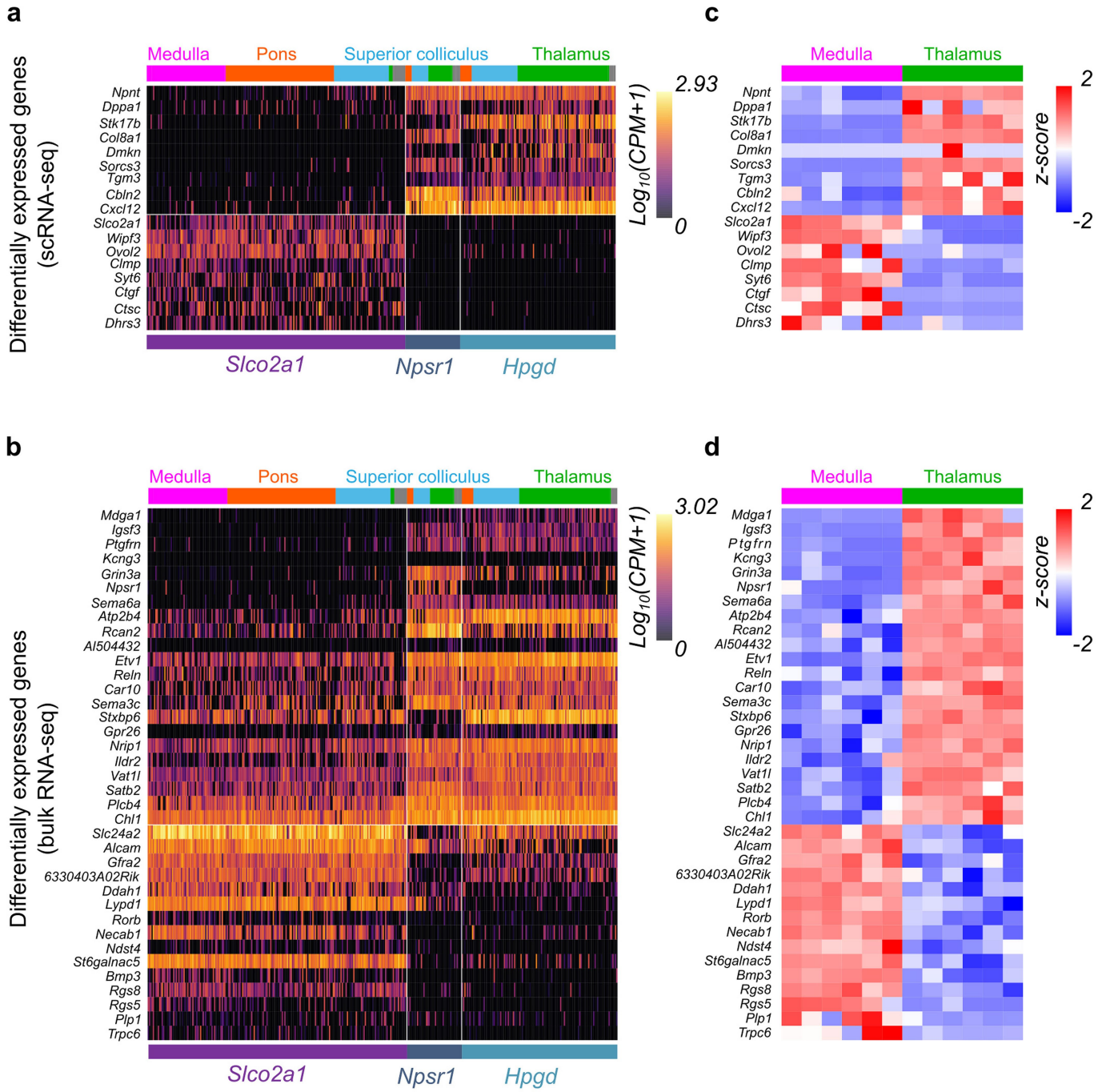

Extended Data Fig. 1 | Differentially expressed genes in single-cell and bulk RNA-seq. a, **b**, Heat map of expression (from scRNA-seq) of differentially expressed genes identified from scRNA-seq (**a**) and bulk RNA-seq (**b**). Columns represent individual cells, grouped by transcriptomic cluster (indicated below each colour map; *Slco2a1*, $n = 203$; *Npsr1*, $n = 43$; *Hpgd*, $n = 122$) and retrograde labelling site (indicated above). Grey indicates cells isolated from transgenic lines or other targets. Rows represent genes differentially expressed between the *Slco2a1* and *Hpgd*–*Npsr1* clusters. Colour bar shows transcript expression in counts per million mapped reads (CPM + 1) on a log-scale. **c**, **d**, Heat map of expression (based on bulk RNA-seq) of differentially expressed genes identified from scRNA-seq (**c**) and bulk RNA-seq (**d**) datasets. Rows represent genes, coloured by differential bulk RNA-seq expression between thalamus-labelled and medulla-labelled PT neurons. Columns in the heat map represent individual replicates (six each for PT_{upper} and PT_{lower}). Colours show log-transformed transcript intensity (CPM + 1) in *z*-scored units. Blue shows replicates with low expression (*z*-score = −2); red shows replicates with high expression (*z*-score = +2).

© 2018 Springer Nature Limited. All rights reserved.

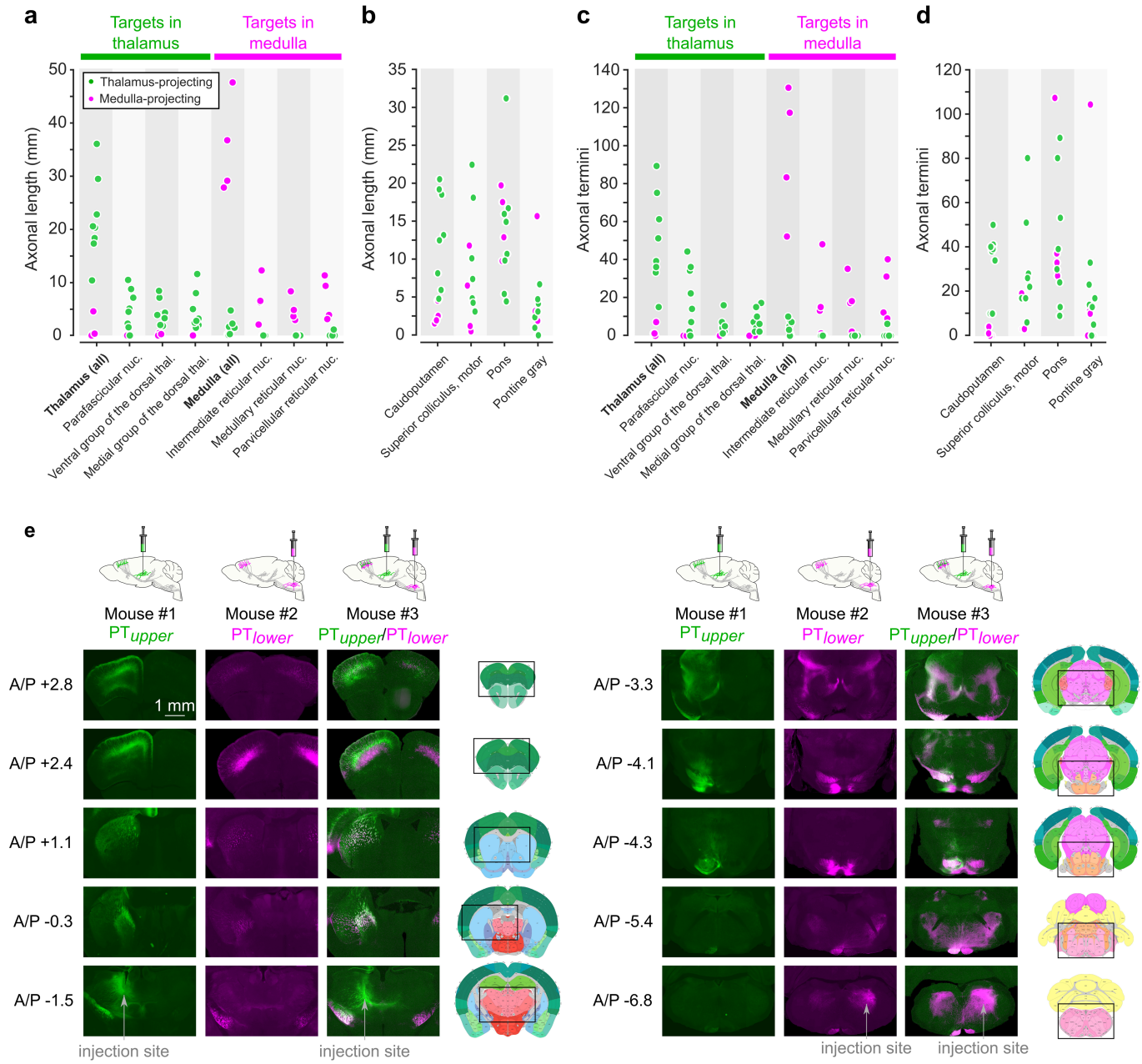

Extended Data Fig. 2 | Distribution of PT axon collaterals. a, Axonal lengths of single-neuron reconstructions within targets in thalamus and medulla (thalamus-targeting PT neurons, $n = 8$, green; medulla-targeting PT neurons, $n = 4$, magenta). **b**, Axonal lengths within other selected PT targets. **c**, Axonal termini in single-neuron reconstructions within thalamic and medullary targets. **d**, Axonal termini within other selected PT targets. **e**, Bulk projections of PT_{upper} and PT_{lower} populations. Groups of cortical neurons were labelled from the thalamus (PT_{upper}; mouse #1), the medulla (PT_{lower}; mouse #2), or both targets (mouse #3) using rAAV2-retro expressing spectrally distinct fluorescent proteins. Top, schematics of the labelling procedures. Left, rostro-caudal level (relative to Bregma). Right, annotated coronal sections taken from the Allen Mouse Brain Atlas[54] with imaged area indicated. Both cell types extended axon collaterals to motor-related superior colliculus, but to different parts. Axons from PT_{upper} cells were apparent throughout all superior colliculus layers, with a dense projection to the ventrolateral aspect; PT_{lower} neurons were restricted to the ventral superior colliculus and were concentrated more caudally. Both groups project to the pons, particularly the pontine grey, but with terminations in largely non-overlapping zones. PT_{upper} cells projected to the globus pallidus external segment and broadly targeted the dorsal, lateral and ventral striatum. PT_{lower} cells projected sparsely to the lateral striatum. PT_{lower} neurons projected to the central amygdala and parasubthalamic nucleus. PT_{lower} neurons also made up most of the projection to the red nucleus, parabrachial nucleus, substantia nigra pars compacta, motor and sensory trigeminal nuclei in the hindbrain, and through the medullary pyramids. Both cell types extended axon collaterals locally within the same sublamina as their somata, the subthalamic nucleus, zona incerta, and the midbrain reticular nucleus. PT_{upper} cells project more broadly to layer 1 in motor cortex. Mice 1 and 2 were used for electrophysiological recordings. For this reason, projections were labelled with ChR2(H134R)–YFP.

© 2018 Springer Nature Limited. All rights reserved.

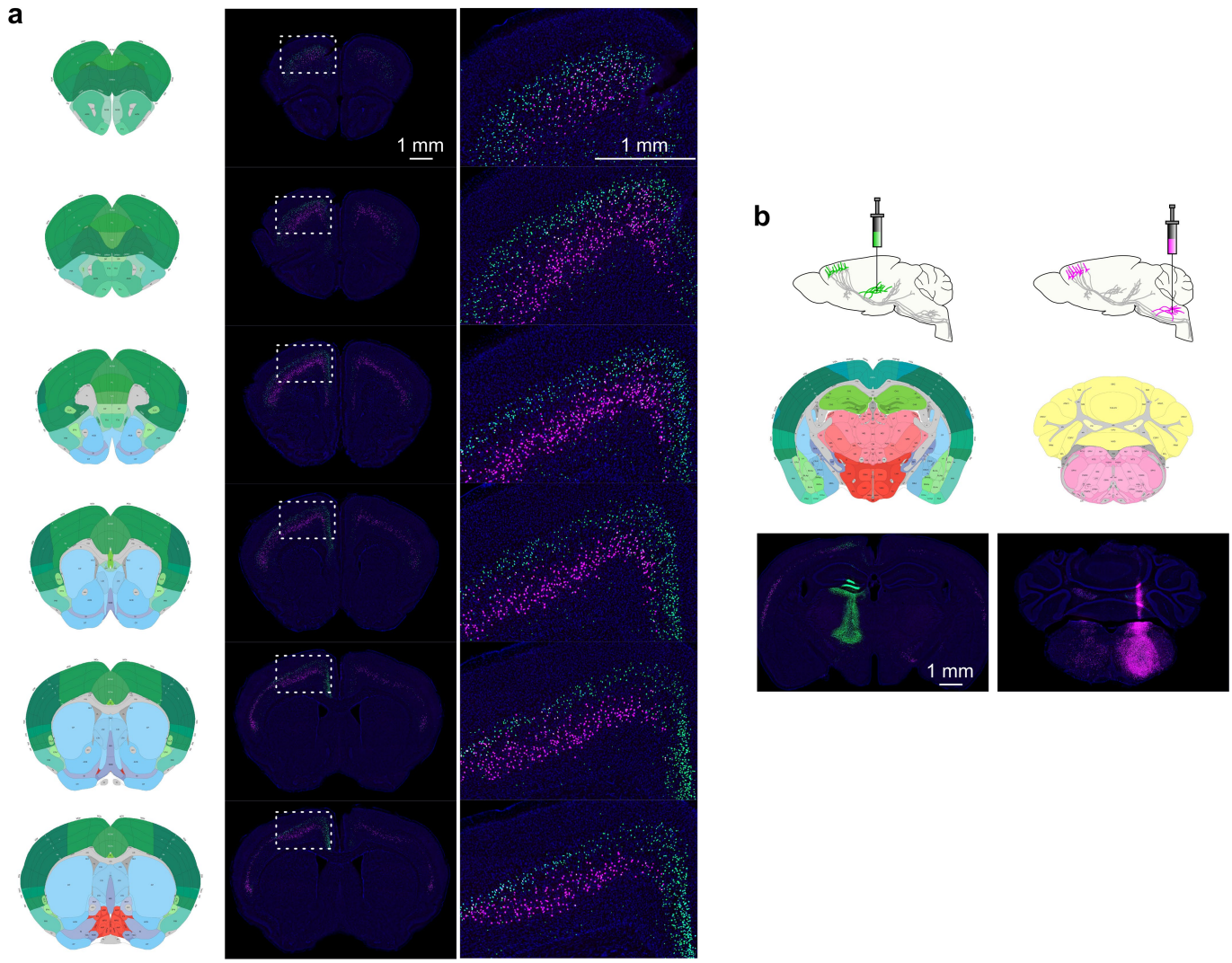

Extended Data Fig. 3 | Spatial distribution of thalamus- and medulla-projecting PT neurons. a, The nuclei of PT neurons were retrogradely labelled from the thalamus (green cells) and medulla (magenta cells) using rAAV2-retro. Thalamus-projecting PT neurons are in upper L5b throughout motor cortex, whereas medulla-projecting PT neurons are in deep L5b. Schematics to the left of each image set are annotated coronal sections (Allen Mouse Brain Atlas[54]). **b**, rAAV2-retro injection sites in the thalamus (left) and medulla (right). Three biological replicates of this experiment yielded similar results.

© 2018 Springer Nature Limited. All rights reserved.

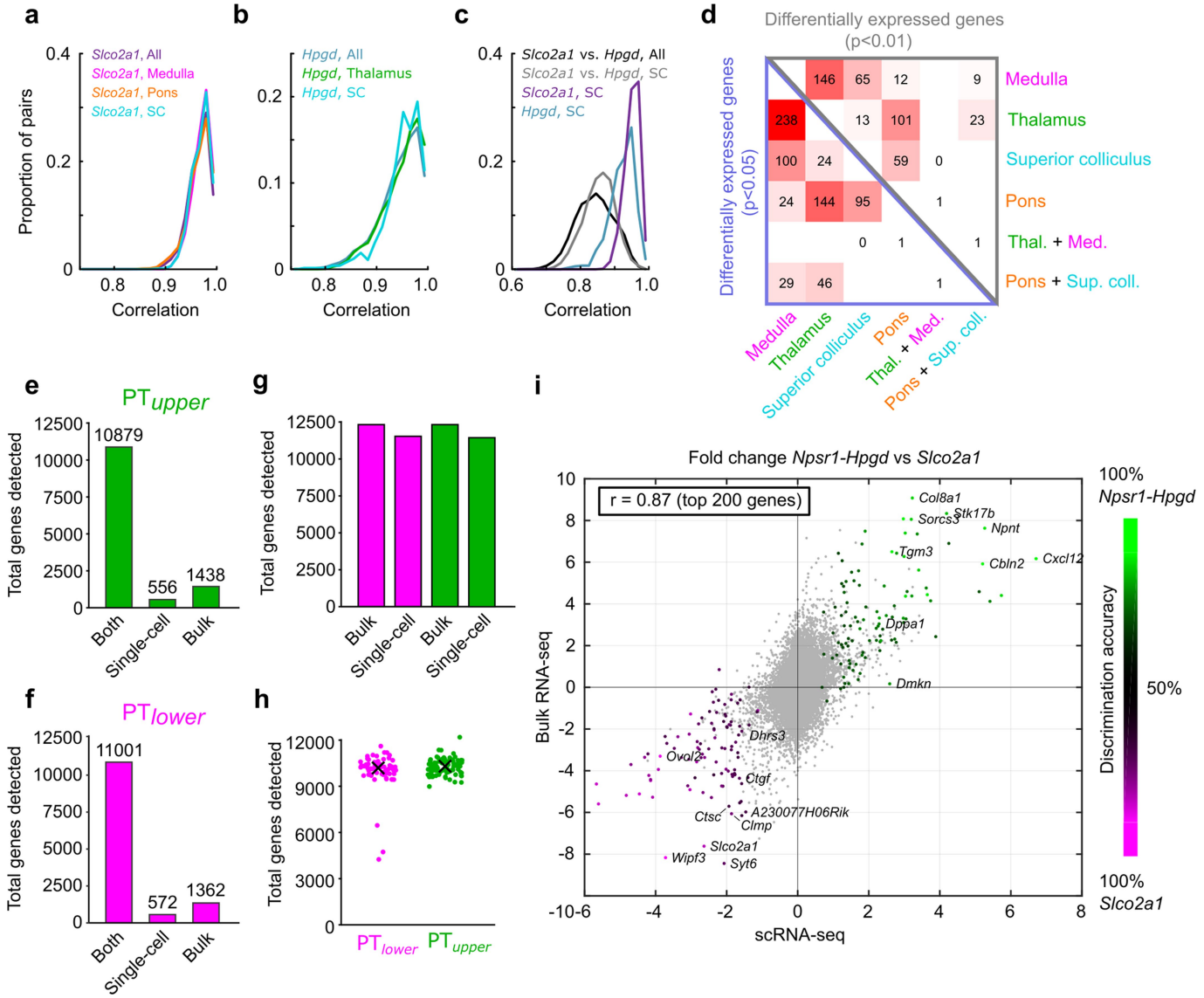

Extended Data Fig. 4 | Correspondence between scRNA-seq transcriptomic clusters, projection targets, and bulk RNA-seq data. **a**, Pairwise correlations (Pearson's *r*) in gene expression between all cells in the *Slco2a1* cluster and within subsets of *Slco2a1* cells identified by projection target. Expression patterns of cells identified from a common target were not more similar than randomly chosen cells. **b**, As in **a** for the *Hpgd* expression cluster. **c**, Pairwise correlation in gene expression of cells retrogradely labelled from the superior colliculus within the *Slco2a1* cluster, within the *Hpgd* cluster, and between cells from different clusters. Correlations between cells from different clusters were significantly lower than within-cluster correlations (between *Slco2a1*, superior colliculus and *Hpgd*, superior colliculus ($n = 1{,}677$ pairs) versus within *Slco2a1*, superior colliculus ($n = 903$ pairs): $P < 1 \times 10^{-10}$; between *Slco2a1*, superior colliculus and *Hpgd*, superior colliculus ($n = 1{,}677$ pairs) versus within *Hpgd*, superior colliculus ($n = 741$ pairs): $P < 1 \times 10^{-10}$; two-sided Wilcoxon signed rank test). Correlation analysis was not performed for the *Npsr1* cluster as the number of cells was relatively small (Fig. 2e). **d**, Number of differentially expressed genes in bulk RNA-seq data between groups of cells labelled from different projection targets. Notably, only a single gene was identified as differentially expressed between the thalamus/medulla group and the superior colliculus/pons group, indicating that the set of PT neurons projecting to either the thalamus or medulla probably represents a superset of PT neurons. There is unlikely to be a transcriptomically distinct group of PT neurons with projections to the superior colliculus or pons that lacks projections to the medulla and thalamus. Although we cannot rule out a transcriptomically distinct subset that lacks projections to all of the thalamus, medulla, pons and superior colliculus, such neurons were not detected in single-cell reconstructions. **e**, Total genes detected by bulk RNA-seq and scRNA-seq in PT_{upper} neurons. Both: genes detected in bulk RNA-seq and scRNA-seq; single-cell: additional genes detected only in scRNA-seq; bulk: additional genes detected only in bulk RNA-seq. **f**, As in **e** for PT_{lower} neurons. **g**, Total number of genes detected across all experiments. In **e**–**g**, single cell reads were downsampled such that total read depth was the same for scRNA-seq and bulk RNA-seq. **h**, Number of genes detected in scRNA-seq for each PT_{upper} and PT_{lower} neuron ('X', median; PT_{upper}, 9,936 genes; PT_{lower}, 9,865 genes). **i**, Mean fold change in expression (measured as $\log_2(\mathrm{CPM} + 1)$) of all genes detected by both methods between neurons in the *Npsr1–Hpgd* clusters (PT_{upper}) and neurons in the *Slco2a1* cluster (PT_{lower}) as determined by scRNA-seq (*x* axis) and bulk RNA-seq (*y* axis). Colour represents classification accuracy between the *Npsr1–Hpgd* and *Slco2a1* clusters using a binary (detected/not detected) version of the scRNA-seq data. The 100 most discriminative neurons are coloured for each type. The correlation coefficient (Pearson's *r*) in fold change expression was 0.87 for this set of 200 differentially expressed genes.

© 2018 Springer Nature Limited. All rights reserved.

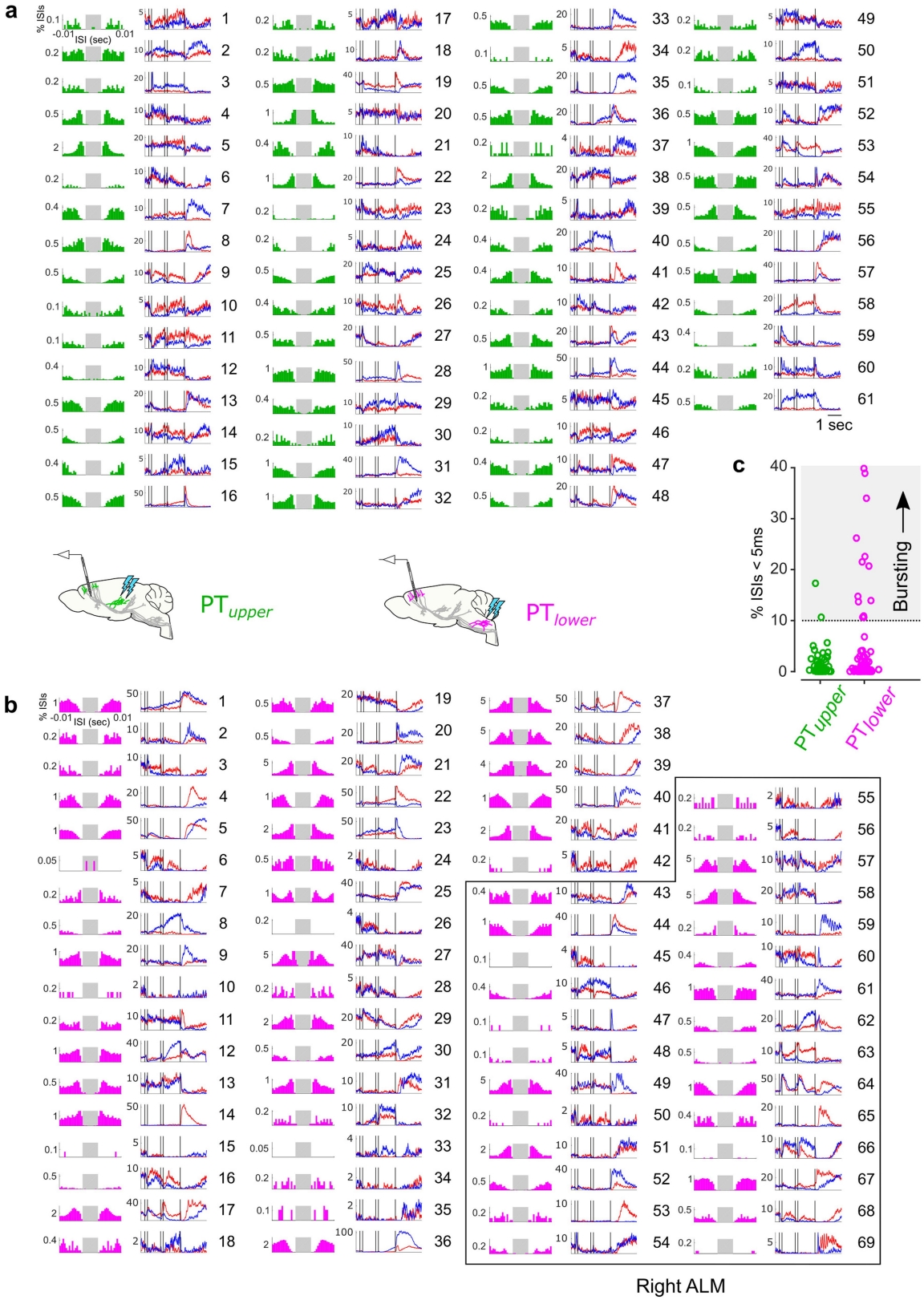

Extended Data Fig. 5 | Electrophysiology and trial-averaged spike rates for identified PT neurons. a, PT_{upper} neurons ($n = 61$). Left, inter-spike interval histograms; right: trial-averaged activity on lick right (blue) and lick left trials (red). Grey shaded area in inter-spike interval histograms represents the interval of −2.5 ms to 2.5 ms. **b**, PT_{lower} neurons ($n = 69$). Boxed region indicates neurons recorded in the right ALM (ipsilateral to injection site in medulla). All other neurons were recorded in the left ALM (contralateral to injection site). **c**, Bursting cells (cells in which greater than 10% of inter-spike intervals were less than 5 ms) were rare in the PT_{upper} population (3.3%) and more common in the PT_{lower} population (18.8%; $P = 0.006$, Fisher's exact test).

© 2018 Springer Nature Limited. All rights reserved.

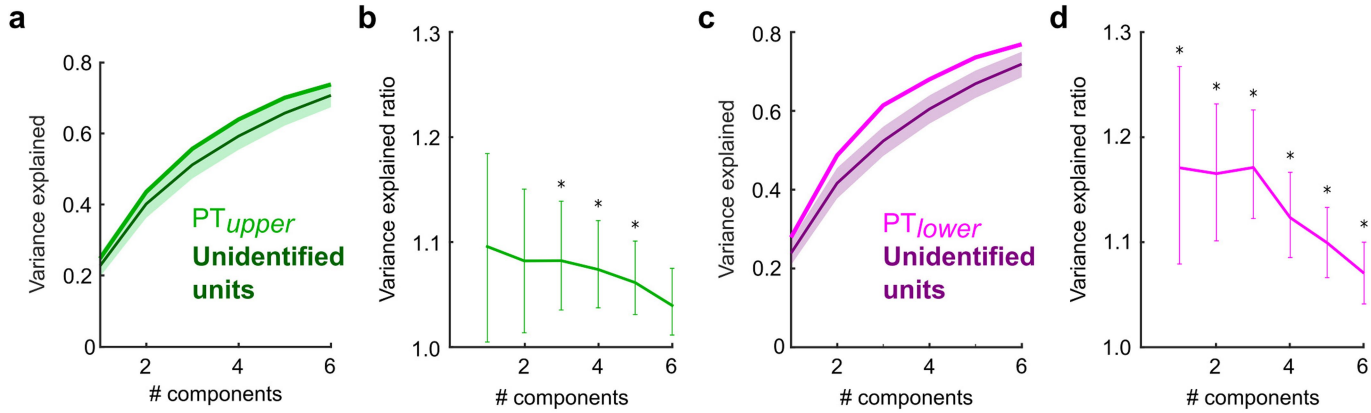

Extended Data Fig. 6 | Variance in trial-averaged activity explained by PT cell class. a, Green line: variance of trial-averaged activity explained by increasing numbers of principal components across the population of PT_{upper} neurons ($n = 61$). Dark green line and 95% confidence interval: expected variance explained by the same number of components for size-matched samples ($n = 1{,}000$ repetitions) of simultaneously recorded, unidentified neurons. **b**, Ratio of variance explained between PT_{upper} neurons and bootstrapped distribution of simultaneously recorded unidentified neurons. Error bars represent s.d. of distribution. **c**, **d**, As in **a** and **b**, but for PT_{lower} neurons ($n = 69$). Asterisks denote points significantly greater than unity ($P < 0.05$, bootstrap).

© 2018 Springer Nature Limited. All rights reserved.

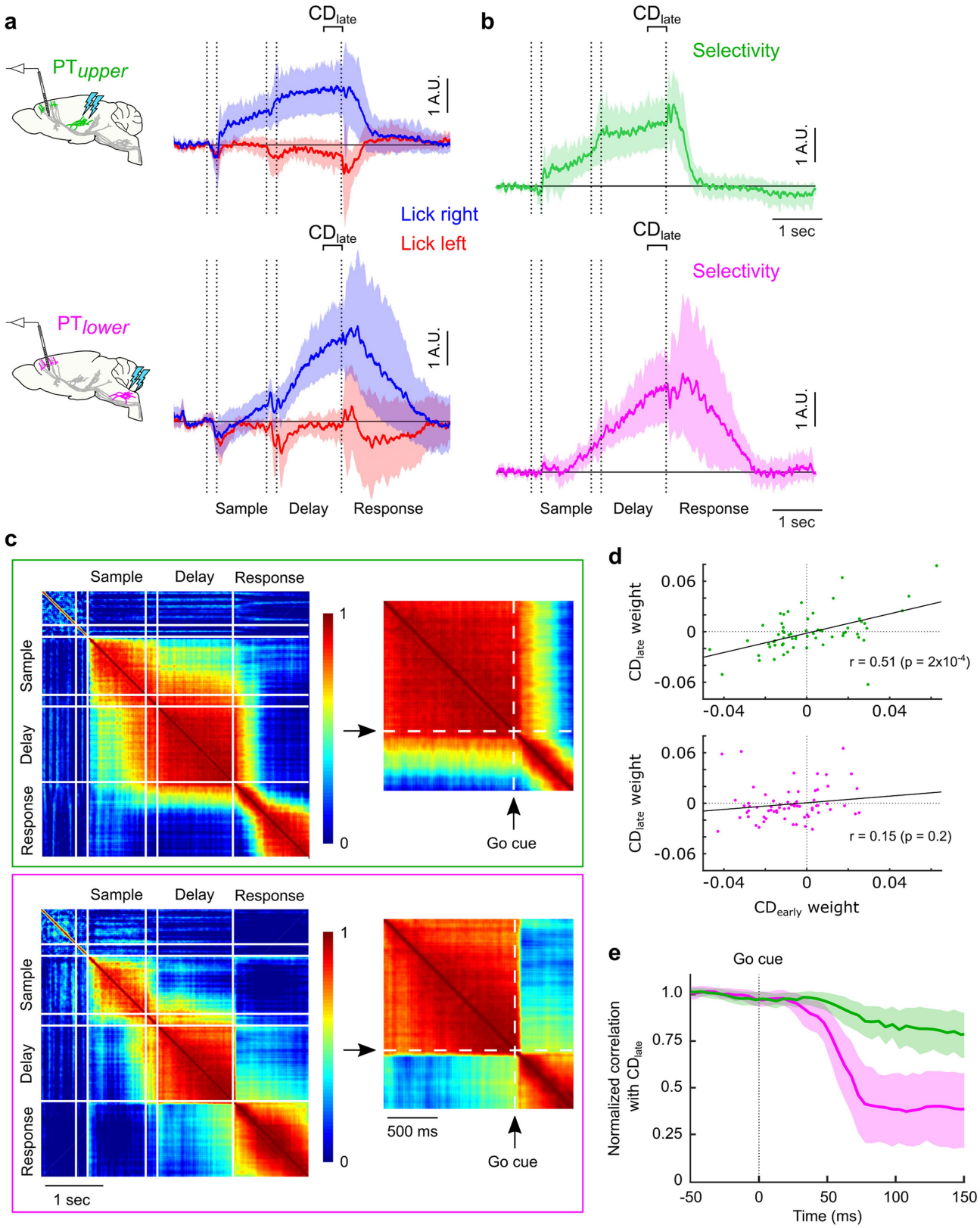

Extended Data Fig. 7 | See next page for caption.

© 2018 Springer Nature Limited. All rights reserved.

Extended Data Fig. 7 | Late delay epoch coding direction and similarity with other trial epochs. a, Time course of the linear combination of neuronal activity that best differentiates trial types in the 400 ms immediately before the go cue (late coding direction; CD_{late}) on lick right (blue) and lick left (red) trials for PT_{upper} (top; $n = 61$) and PT_{lower} (bottom; $n = 69$) neurons. **b**, Difference in CD_{late} projections on lick right and lick left trials (selectivity) in each population. Selectivity along CD_{late} is present in both populations, and persists after the go cue, but is not strongly modulated during movement initiation. Shaded regions represent the s.d. of the distribution produced by hierarchical bootstrapping ($n = 1{,}000$ iterations) in **a** and 5–95% confidence intervals in **b** (denoting region significantly greater than zero, $P < 0.05$ one-sided test, bootstrap). **c**, A coding direction (CD) was calculated at all individual time points. Heat maps represent the correlation (inner product) of the CD between pairs of time points. In PT_{upper} neurons (top), the coding direction remained similar across the sample and delay epochs. In PT_{lower} neurons (bottom), coding directions in the delay epoch were largely orthogonal to coding directions calculated in the sample epoch. The upcoming movement direction is encoded in a persistent manner in the PT_{upper} population, but not the PT_{lower} population. Right, expanded view of the change in coding direction around the time of the go cue. An abrupt change in the coding direction occurs immediately after the go cue onset in the PT_{lower} population. A change also occurs in the PT_{upper} population, but more slowly (over several hundred milliseconds), largely after initiation of movement. **d**, Correlation (Pearson's r) between CD_{early} vector weights and CD_{late} vector weights for PT_{upper} neurons (top) and PT_{lower} neurons (bottom). **e**, Correlation between the CD and CD_{late} normalized to the mean correlation in the 400 ms preceding the go cue. A rapid change in the CD occurs in the PT_{lower} population following the go cue. Shaded areas represent the s.d. of the bootstrapped distribution ($n = 1{,}000$ iterations).

© 2018 Springer Nature Limited. All rights reserved.

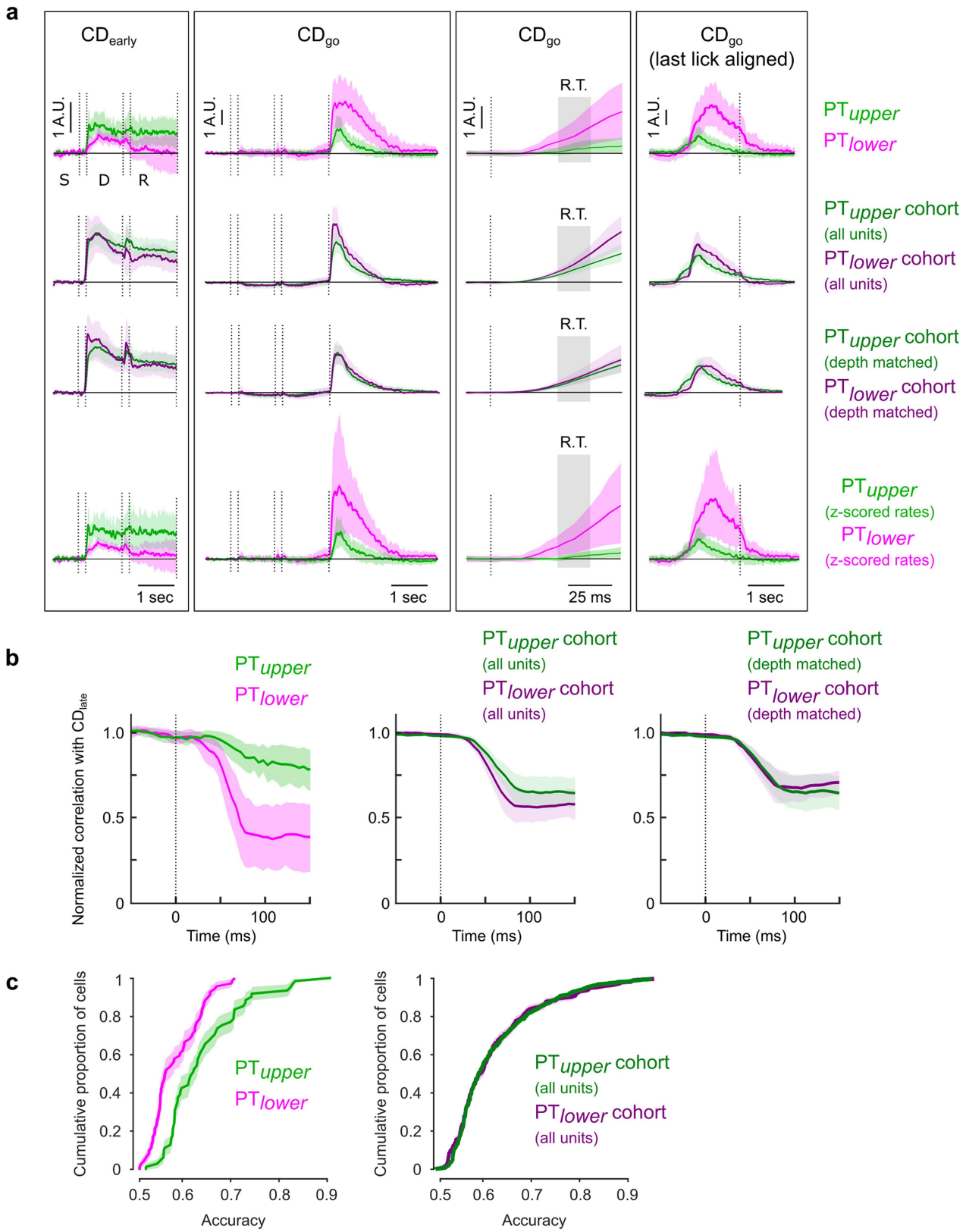

Extended Data Fig. 8 | See next page for caption.

© 2018 Springer Nature Limited. All rights reserved.

Extended Data Fig. 8 | Comparison between identified PT populations and simultaneously recorded untagged neurons. Time course of selectivity along CD_{early} (as in Fig. 5b), CD_{go} (as in Fig. 6b), and CD_{go} aligned to the last lick in each trial (as in Extended Data Fig. 10b) calculated as follows: (1) from PT_{upper} ($n = 61$) and PT_{lower} ($n = 69$) neurons (top row), (2) from simultaneously recorded but unidentified neurons (second row; $n = 495$ from PT_{upper} cohort; $n = 511$ simultaneously recorded with PT_{lower} neurons), (3) after removing unidentified neurons from the PT_{lower} experiments recorded from the contralateral hemisphere (third row; $n = 276$ remaining), which were recorded at a lower average depth in a different recording configuration, and (4) from PT_{upper} and PT_{lower} neurons with firing rates z-scored based on their firing rates in the epoch preceding the stimulus (bottom row). CD projections in the populations of unidentified neurons were similar and nearly indistinguishable after they were approximately depth-matched. Shaded regions represent 5–95% confidence intervals in bootstrapped distribution as in all other figures ($n = 1{,}000$ iterations; denotes region significantly greater than zero, $P < 0.05$ one-sided test, bootstrap). **b**, Correlation of CD with CD_{late} (inner product; as in Extended Data Fig. 7e) around the time of the go cue in each PT population (left), in simultaneously recorded unidentified populations (middle) and approximately depth matched populations (right). The change in correlations around the time of the go cue in the unidentified populations were similar and intermediate between that observed in the PT_{upper} population and PT_{lower} populations. **c**, Early trial type decoding (as in Extended Data Fig. 9) in each PT population (left) and the simultaneously recorded populations of unidentified neurons (right).

© 2018 Springer Nature Limited. All rights reserved.

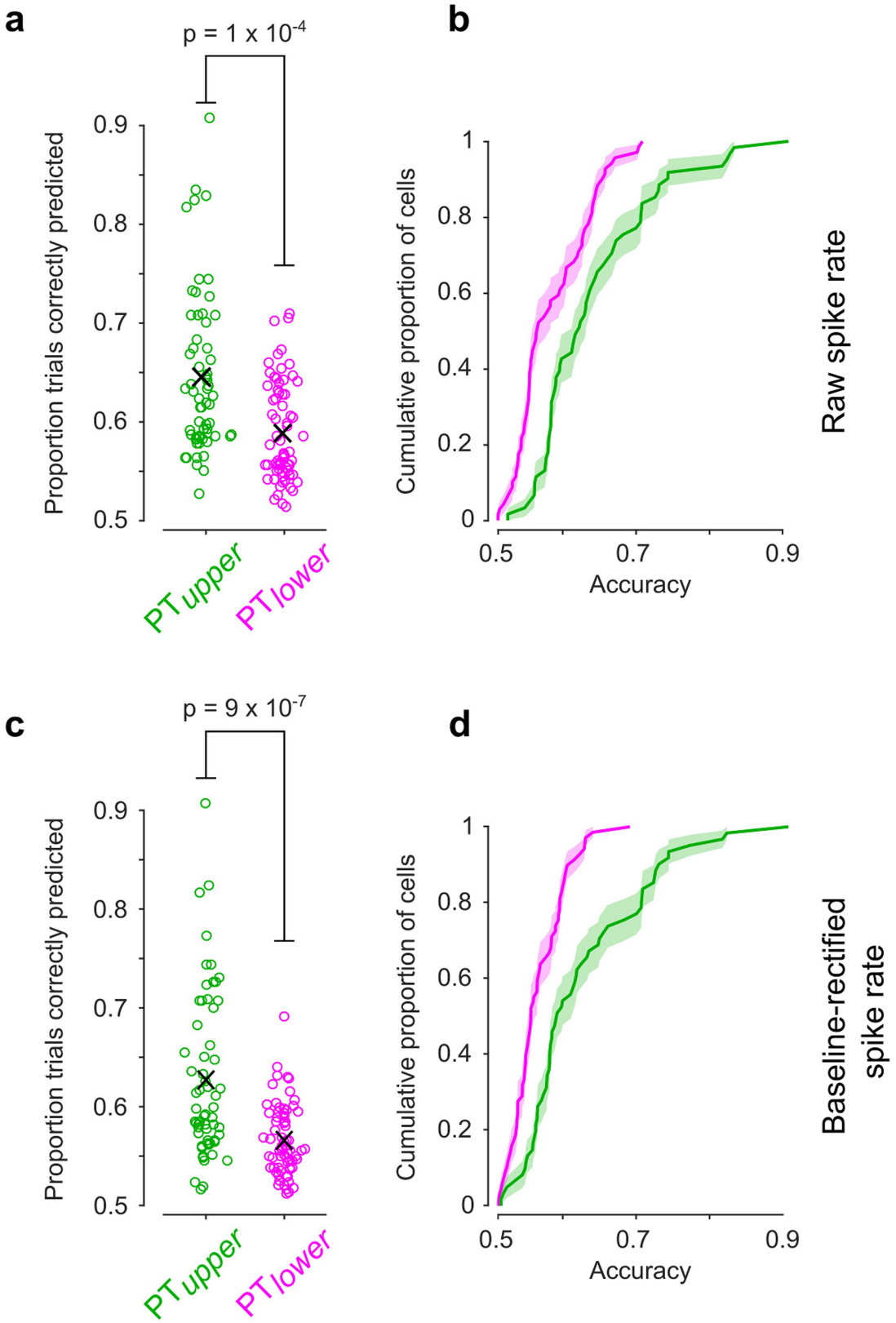

Extended Data Fig. 9 | Decoding of trial type in PT neuron types. **a**, Accuracy of trial type classification by single neurons in the 400 ms immediately after stimulus onset. 24.6% (15 out of 61) of PT_{upper} neurons predicted trial type with at least 70% accuracy, whereas only 4.4% (3 out of 69) of PT_{lower} neurons did so. Mean accuracy was also significantly higher in PT_{upper} neurons (PT_{upper}: $64.4 \pm 1.0\%$; PT_{lower}: $58.9 \pm 0.6\%$, mean ± s.e.m.; $P = 1 \times 10^{-4}$, two-sided Mann–Whitney test). The ten most discriminative neurons all belonged to the PT_{upper} population. **b**, Cumulative distribution function of the data in **a**. **c**, **d**, As in **a** and **b** but decoding only based on spike rates rectified at baseline. Trial-type selectivity during the sample epoch in PT_{lower} neurons was predominantly characterized by a modest suppression of spiking on one trial type, probably reflecting widespread lateral inhibition. Disregarding spike rate changes below baseline, no PT_{lower} neurons predicted trial type with at least 70% accuracy, whereas the same 24.6% of PT_{upper} neurons continued to do so and accounted for 20 out of 21 of the most predictive neurons (PT_{upper}: $62.7 \pm 1.1\%$; PT_{lower}: $56.7 \pm 0.4\%$, mean ± s.e.m.; $P = 9 \times 10^{-7}$, two-sided Mann–Whitney test). As soon as the trial type is cued by the stimulus, upcoming movement direction is encoded robustly in a subset of PT_{upper} cells and only minimally in PT_{lower} cells.

© 2018 Springer Nature Limited. All rights reserved.

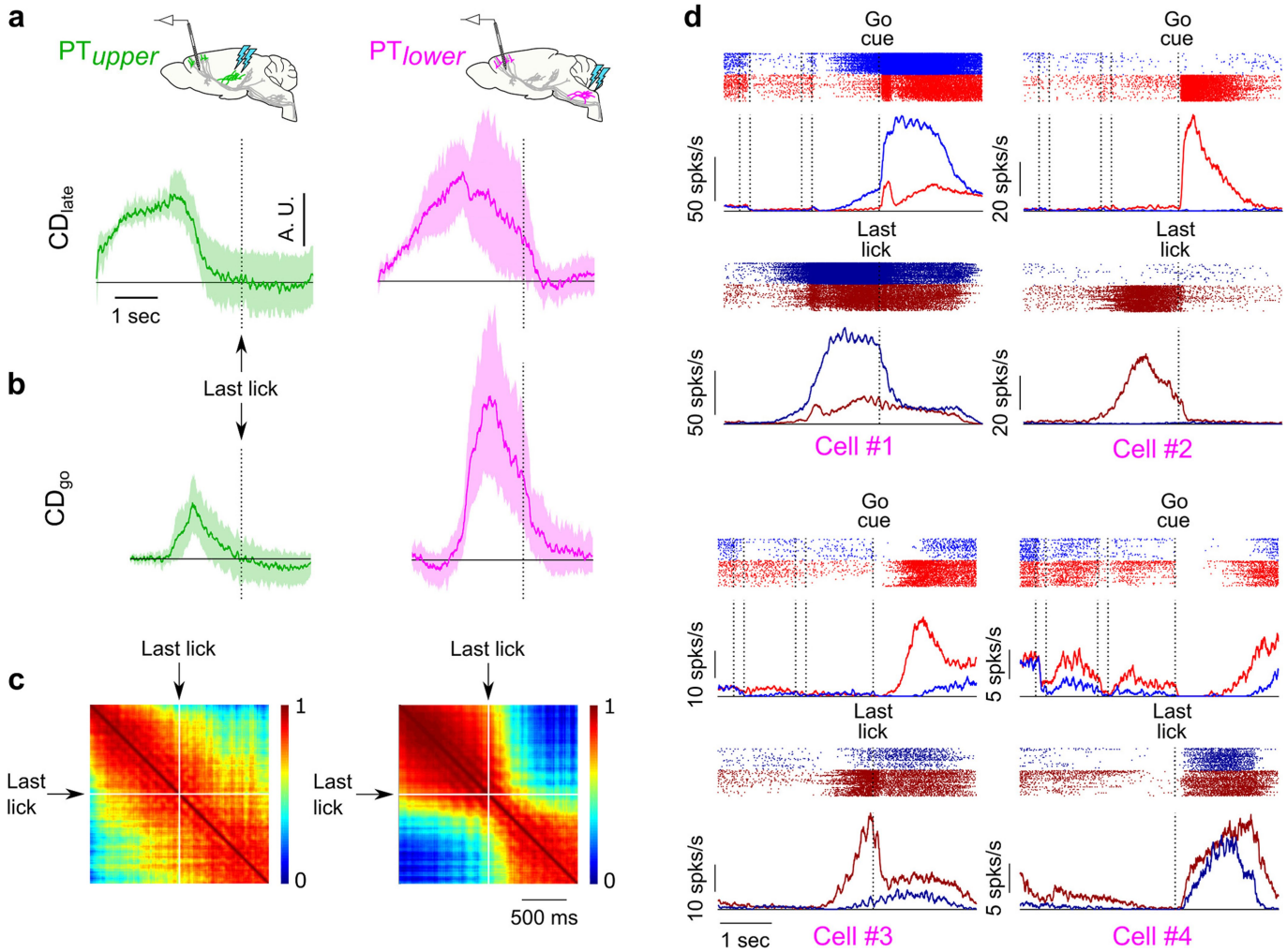

Extended Data Fig. 10 | Movement termination signals in PT_{lower} neurons. a, Selectivity along CD_{late} (as in Extended Data Fig. 7b) for PT_{upper} (green, left; $n = 61$) and PT_{lower} neurons (magenta, right; $n = 69$) aligned to the last lick in the response epoch. **b**, Selectivity along CD_{go} (same as Fig. 6b) aligned to the last lick for each PT type. Shaded regions in **a** and **b** represent 5–95% confidence intervals around the mean using hierarchical bootstrapping ($n = 1{,}000$ iterations; denoting region significantly greater than zero, $P < 0.05$ one-sided test, bootstrap). **c**, Correlation of coding direction weights at all pairs of time points after the go cue for PT_{upper} neurons (left) and PT_{lower} neurons (right) using last-lick aligned spike rates. An additional transition in the population dynamics accompanies the termination of movement in PT_{lower} neurons, whereas there is no correlate of movement termination in PT_{upper} neurons. The change in dynamics at the offset of movement was less abrupt than at movement onset, probably a result of aligning data to the last lick-port contact, which does not precisely mark the cessation of movement. **d**, Spike raster plots (top) and trial-averaged activity (bottom) for four example PT_{lower} neurons aligned to the go cue (lick right: blue; lick left: red) and the last lick-port contact (lick right: dark blue; lick left: dark red).

© 2018 Springer Nature Limited. All rights reserved.

LETTER

https://doi.org/10.1038/s41586-018-0625-x

The merger that led to the formation of the Milky Way's inner stellar halo and thick disk

Amina Helmi[1]*, Carine Babusiaux[2,3], Helmer H. Koppelman[1], Davide Massari[1], Jovan Veljanoski[1] & Anthony G. A. Brown[4]

The assembly of our Galaxy can be reconstructed using the motions and chemistry of individual stars[1,2]. Chemo-dynamical studies of the stellar halo near the Sun have indicated the presence of multiple components[3], such as streams[4] and clumps[5], as well as correlations between the stars' chemical abundances and orbital parameters[6–8]. Recently, analyses of two large stellar surveys[9,10] revealed the presence of a well populated elemental abundance sequence[7,11], two distinct sequences in the colour–magnitude diagram[12] and a prominent, slightly retrograde kinematic structure[13,14] in the halo near the Sun, which may trace an important accretion event experienced by the Galaxy[15]. However, the link between these observations and their implications for Galactic history is not well understood. Here we report an analysis of the kinematics, chemistry, age and spatial distribution of stars that are mainly linked to two major Galactic components: the thick disk and the stellar halo. We demonstrate that the inner halo is dominated by debris from an object that at infall was slightly more massive than the Small Magellanic Cloud, and which we refer to as Gaia–Enceladus. The stars that originate in Gaia–Enceladus cover nearly the full sky, and their motions reveal the presence of streams and slightly retrograde and elongated trajectories. With an estimated mass ratio of four to one, the merger of the Milky Way with Gaia–Enceladus must have led to the dynamical heating of the precursor of the Galactic thick disk, thus contributing to the formation of this component approximately ten billion years ago. These findings are in line with the results of galaxy formation simulations, which predict that the inner stellar halo should be dominated by debris from only a few massive progenitors[2,16].

The sharp view provided by the second data release (DR2) of the Gaia mission[17] has recently revealed[14] that, besides a few tight streams, a considerable fraction of the halo stars that are near the Sun are associated with a single large kinematic structure. This structure has slightly retrograde mean motion and dominates the blue sequence of the Hertzsprung–Russell diagram (HRD) revealed in the Gaia data[12]. This large structure is readily apparent (in blue) in Fig. 1a, which shows the velocity distribution of stars (presumably belonging to the halo) inside a volume with a radius of 2.5 kpc in the solar vicinity, as obtained from the Gaia data (see Methods for details). Figure 1b shows the velocity distribution from a simulation of the formation of a thick disk via a 20% mass-ratio merger[18]. The similarity between the graphs suggests that the retrograde structure could be largely made up of stars originating in an external galaxy that merged with the Milky Way in the past.

Support for this hypothesis comes from the chemical abundances of stars provided by the APOGEE survey[9]. In Fig. 2a we plot the abundances [α/Fe] and [Fe/H] for a sample of stars cross-matched to Gaia DR2 (see Methods for details). α-elements are produced by massive stars that die fast as supernovae (type II), while iron is also produced in type I supernova explosions of binary stars. Therefore in a galaxy [α/Fe] decreases with time (as [Fe/H] increases). Figure 2a shows the well known sequences defined by the thin and thick disks. The vast majority of the retrograde structure's stars (in blue) follow a well defined separate sequence that extends from low to relatively high [Fe/H]. (The presence of low-α stars with retrograde motions in the halo near the Sun has been reported before[7,19], but for a small sample. The existence of a well populated sequence with lower [α/Fe] was

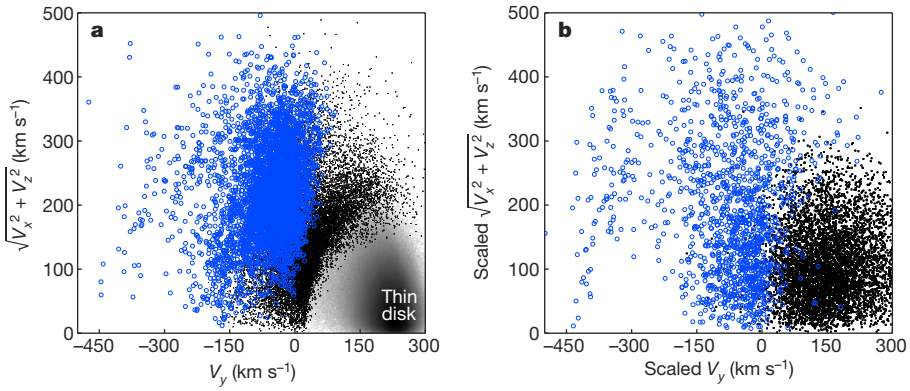

Fig. 1 | Measured velocity distribution of stars in the solar vicinity compared with merger simulation results. a, Velocities of stars in the disk are plotted with grey density contours (because of the large number of stars), and halo stars (selected as those with $|\boldsymbol{V} - \boldsymbol{V}_{\rm LSR}| > 210$ km s^{-1}, where $\boldsymbol{V}_{\rm LSR}$ is the velocity of the local standard of rest) are shown as black points. The blue points are part of a prominent structure with slightly retrograde mean rotational motion and have been selected as those having angular momentum $-1{,}500$ kpc km s$^{-1} < L_z < 150$ kpc km s^{-1} and energy $E > -1.8 \times 10^5$ km^2 s^{-2} (see Methods for details). **b**, Distribution of star particles in a small volume, extracted from a simulation[18] of the formation of a thick disk from the merger of a satellite galaxy (blue symbols) with a pre-existing disk (black points) at a mass ratio of 5:1. The overall morphology of the measured distribution and the observed arch (from $V_y \approx -450$ km s^{-1} and $V_\perp = (V_x^2 + V_z^2)^{1/2} \approx 50$ km s^{-1} to $V_y \approx -150$ km s^{-1} and $V_\perp \approx 300$ km s^{-1} in **a**) can be reproduced qualitatively after appropriately scaling the velocities (see Methods) and by using a simulation with a disk-like satellite (rather than a spherical one, as the arch-like feature is sharper for the disk-like satellite) on a retrograde orbit inclined by about 30°–60°.

[1]Kapteyn Astronomical Institute, University of Groningen, Groningen, The Netherlands. [2]Université Grenoble Alpes, CNRS, IPAG, Grenoble, France. [3]GEPI, Observatoire de Paris, Université PSL, CNRS, Meudon, France. [4]Leiden Observatory, Leiden University, Leiden, The Netherlands. *e-mail: ahelmi@astro.rug.nl

© 2018 Springer Nature Limited. All rights reserved.

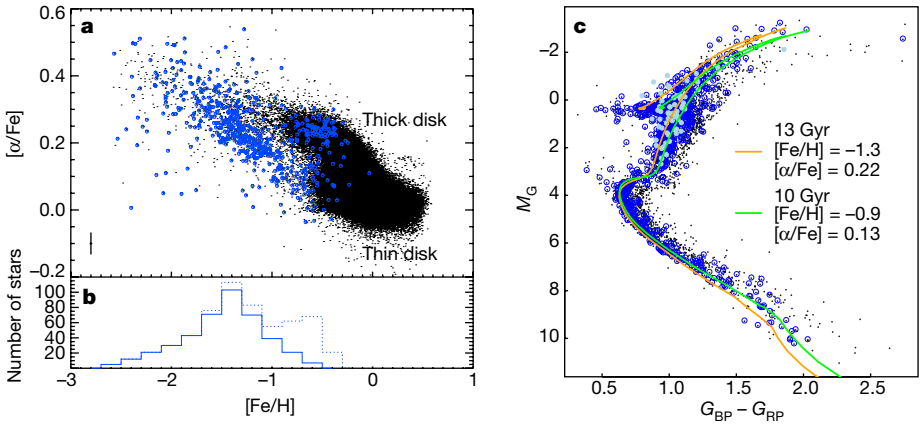

Fig. 2 | Astrophysical properties of stars in Gaia–Enceladus. a, Chemical abundances for a sample of stars located within 5 kpc from the Sun, obtained from cross-matching Gaia and APOGEE data. The blue circles correspond to 590 stars with $-1{,}500$ kpc km s$^{-1} < L_z < 150$ kpc km s^{-1} and energy $E > -1.8 \times 10^5$ km^2 s^{-2} (as in Fig. 1a, but for a larger volume to increase the sample size; see Methods). We note the clear separation between the thick disk and the sequence defined by the majority of the stars in the retrograde structure, except for a small amount of contamination (17%) by thick-disk stars (that is, in the α-rich sequence) that have a similar phase-space distribution to that of the retrograde structure. The error bar in the lower left corner shows the 1σ median error for the sample. **b**, The solid (dotted) histogram shows the metallicity distribution of the retrograde structure without (with) the subset of α-rich stars. The distribution, which peaks at [Fe/H] ≈ −1.6, is reminiscent of the distribution of the stellar halo of the Galaxy[21]. **c**, The HRD for halo stars (black points) selected as in Fig. 1a, with the additional photometric quality cuts[12] of: colour excess $E(B-V) < 0.015$ (to limit its impact on the magnitudes and colours to less than 0.05 mag) and flux excess factor phot-bp-rp-excess-factor $< 1.3 + 0.06(G_{BP} - G_{RP})^2$, where G_{BP} and G_{RP} denote the magnitude in the Gaia BP and RP passband, respectively. M_G is the absolute magnitude in the Gaia G band. In the HRD the blue and red sequences unveiled by Gaia[12] can be seen. Dark-blue symbols represent Gaia–Enceladus stars and light-blue symbols are those that are also in the APOGEE dataset within 5 kpc of the Sun and with [α/Fe] < −0.14 − 0.35[Fe/H]. The superimposed isochrones[23] (orange and green lines), which are based on previous work[25], show that an age range of 10–13 Gyr is compatible with the HRD of Gaia–Enceladus.

demonstrated recently using the APOGEE data[11].) An independent analysis[15] has confirmed the relation between the blue sequence in the HRD of the Gaia data and the kinematic structure shown in Fig. 1a and established firmly the link to the low-α stars using both earlier[7] and APOGEE data, thereby making the accretion hypothesis more secure.

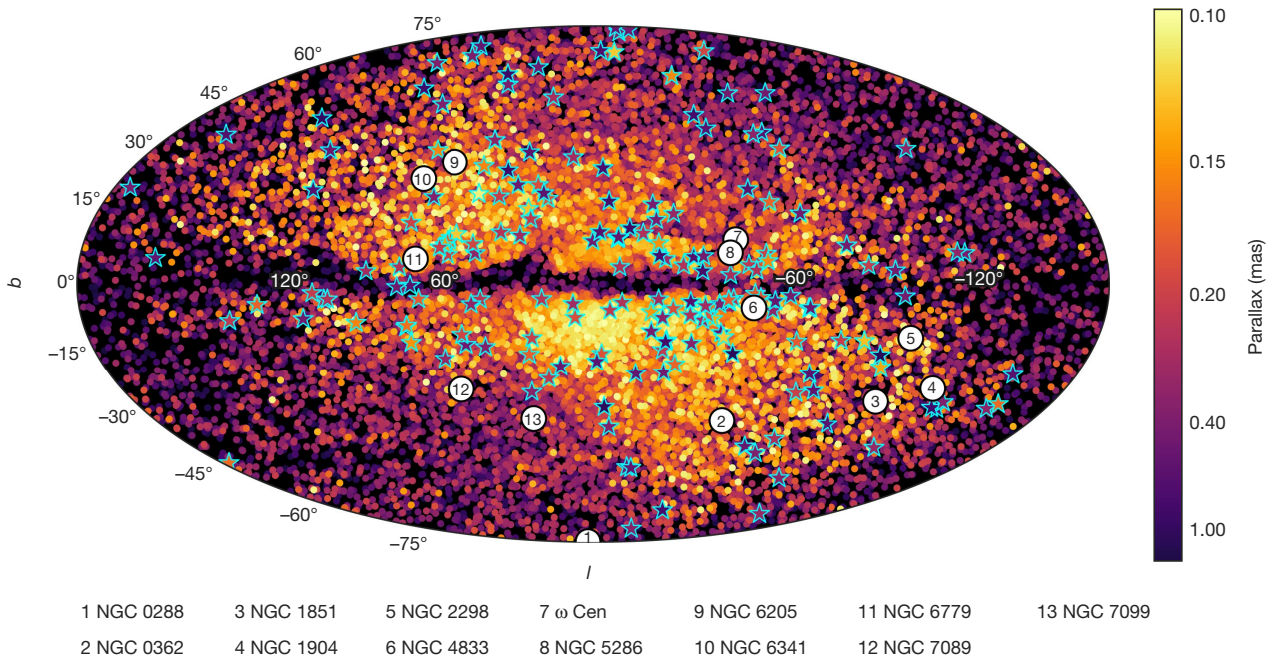

Fig. 3 | Sky distribution of candidate Gaia–Enceladus members from a Gaia subsample of stars with full phase-space information. These stars have parallax $\varpi > 0.1$ mas, a relative parallax error of 20% and satisfy the condition $-1{,}500$ kpc km s$^{-1} < L_z < 150$ kpc km s^{-1}. The symbols are colour-coded according to the stars' distance from the Sun (near, dark red; far, light yellow). Because of the large volume explored, we do not include additional selection criteria based on energy, as in Fig. 2 (because the energy depends on the Galactic potential, whose spatial variation across the volume explored is less well constrained than its local value) or on velocity, as in Fig. 1a (because the velocity can vary considerably across this volume). We therefore expect some contamination by thick-disk stars, especially towards the inner Galaxy (see Methods). The star symbols represent Gaia RR Lyrae stars potentially associated with this structure. To identify these, we divide the sky into 128° × 128° bins and log(ϖ) into bins with a width of 0.2 (mimicking the relative parallax error) and measure the average proper motion of Gaia–Enceladus stars in each three-dimensional bin. We then require that the RR Lyrae stars have the same proper motion (within 25 km s^{-1} in each direction at their distance), which corresponds to 1 mas yr^{-1} for stars with $\varpi \approx 0.2$ mas. Globular clusters with $L_z < 50$ kpc km s^{-1}, located between 5 kpc and 15 kpc from the Sun and 40° away from the Galactic centre, are indicated with solid circles. b, galactic latitude; l, galactic longitude.

© 2018 Springer Nature Limited. All rights reserved.

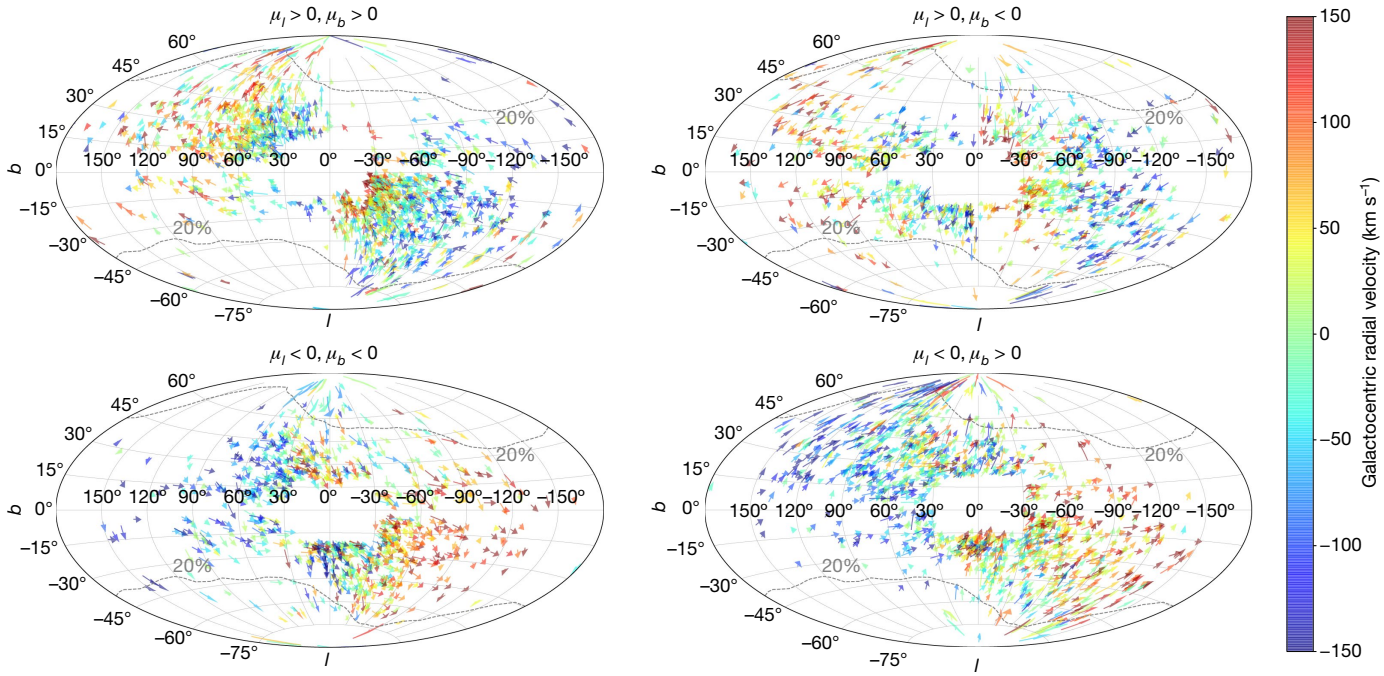

Fig. 4 | Kinematic properties of Gaia–Enceladus candidates. The plotted stars are a subset of those shown in Fig. 3 with 0.1 mas $< \varpi <$ 0.2 mas. The arrows indicate the direction of motion and are colour-coded according to the stars' radial velocity. To avoid cluttering, we show the data in four panels that correspond to different proper-motion ranges and we have removed stars close to the bulge (within 30° in longitude and 20° in latitude). All velocities have been corrected for the solar and local-standard-of-rest motions. The grey contours encompass 90% of the stars in the 6D Gaia dataset that have 0.1 mas $< \varpi <$ 0.2 mas and 20% relative parallax error and clearly demonstrate that the latter selection criterion affects our ability to identify distant Gaia–Enceladus stars in certain regions of the sky. We note the large-scale pattern in the radial velocity, as well as its correlation with the proper-motion component μ_l in the longitude direction: stars with $\mu_l > 0$ (top panels) have $V_{\rm GSR} > 0$ for $l \gtrsim 75°$ and $V_{\rm GSR} < 0$ for $l \lesssim -75°$, where $V_{\rm GSR}$ is the Galactocentric-standard-of-rest velocity, and the reverse occurs for $\mu_l < 0$. Such a global pattern (and its reversal for $-75° \lesssim l \lesssim 75°$) arises because of the coherent retrograde sense of rotation of the stars in their orbits (that is, they have mostly $L_z \lesssim 0$), but the correlation with μ_l is a result of their elongated orbits. For example, we see that if $\mu_l > 0$ and $l \gtrsim 75°$, stars are typically moving outwards away from the Sun at high speed ($V_{\rm GSR} \gtrsim 100$ km s^{-1}).

The large metallicity spread of the stars of the retrograde structure (Fig. 2b) implies that they did not form in a single burst in a low-mass system. Furthermore, the lower [α/Fe] of the more metal-rich stars at the characteristic metallicity of the thick disk ([Fe/H] ≈ −0.6) means that these stars were born in a system with a lower star formation rate than that of the thick disk. The star formation rate required to match the α-poor sequence of the APOGEE data has recently been calculated using a chemical evolution model and including different elemental abundances[20], and it was found to be $0.3 M_\odot$ yr^{-1} and to last for about 2 Gyr ($M_\odot$ is the mass of the Sun). This implies a stellar mass of about $6 \times 10^8 M_\odot$ for the progenitor system. This value is consistent with the large fraction of nearby halo stars that are associated with the structure according to estimates of the local halo density[21] and is comparable to the present-day mass of the Small Magellanic Cloud[22]. Interestingly, previous work[11] has shown that the trends in the abundances of low-metallicity stars in the Large Magellanic Cloud overlap well with the sequence, which implies that the structure was comparable to the Large Magellanic Cloud in its early years. Perhaps more importantly, because [α/Fe] must decrease as [Fe/H] increases, the stars in the structure could not have formed in the same system as the vast majority of stars in the Galactic thick disk. They must have formed, as previously suggested[7,14,15], in a separate galaxy, which we refer to as Gaia–Enceladus (see Methods for the motivation behind the naming).

We now explore whether the Gaia–Enceladus galaxy could have been responsible at least partly for the formation of the thick disk[13–15], as the comparison between the data and the simulation results shown in Fig. 1 suggests. In that case, a pre-existing disk must have been in place at the time of the merger. Figure 2c displays the HRD of the halo stars of Fig. 1a, which shows that the Gaia–Enceladus stars (in blue) populate the blue sequence revealed in the Gaia data[12,14,15]. The thinness of this sequence is compatible with an age range from about 10 Gyr to 13 Gyr, given the stars' abundance sequence, as indicated by the plotted isochrones[23]. Previous studies[24,25], on which this age range is based, have shown that the stars in the α-poor sequence are younger than those in the α-rich sequence for $-1 <$ [Fe/H] < -0.5. This implies that the progenitor of the Galactic thick disk was in place when Gaia–Enceladus fell in, which, according to the ages of its youngest stars, suggests that the merger took place around 10 Gyr ago, that is, at redshift $z \approx 1.8$.

Such a prominent merger must have left debris over a large volume of the Galaxy. To explore where we may find other candidate members of Gaia–Enceladus beyond the solar neighbourhood, we consider stars in the Gaia 6D sample with parallax $\varpi > 0.1$ mas, 20% relative parallax error and a z-direction angular momentum of −1,500 kpc km s^{-1} $< L_z <$ 150 kpc km s^{-1}. Figure 3 shows that nearby candidate Gaia–Enceladus stars (with $\varpi > 0.25$ mas; darker points) are distributed over the whole sky, with this subset being more than 90% statistically complete. More distant stars are preferentially found in specific regions of the sky. Although for such small Gaia parallaxes ($\varpi = 0.1$–0.25 mas) the zero-point offset (about −0.03 mas) is substantial and affects the selection of L_z, it does not affect it to the extent that it can produce the observed asymmetry in the sky. At least in part, this asymmetry is due to the 20% relative parallax error cut, as highlighted in Fig. 4 (see Methods for details and for possible links with known overdensities). In Fig. 3 we have also overplotted (star markers) a subset of 200 Gaia RR Lyrae stars[26]. These have proper motions similar to the mean motion of the candidate Gaia–Enceladus stars, with full phase-space information at their sky position and parallax. Thirteen globular clusters can also be associated with Gaia–Enceladus on the basis of their angular momenta[27] (Fig. 3). All these clusters show a consistent age–metallicity relation[28].

Figure 4 shows the velocity field of the more distant stars associated with Gaia–Enceladus. A large-scale gradient is observed in the radial velocity across the full sky; such a coherent pattern can be obtained

© 2018 Springer Nature Limited. All rights reserved.

only if stars are moving in the same (retrograde) direction on elongated orbits. The proper motions, depicted by arrows, reveal a complex velocity field. This is expected because of the large mass of the progenitor object and the short mixing timescales in the inner Galaxy[2]. Nonetheless, this complexity contains streams as neighbouring stars often move in the same direction. This is a very significant effect, established by comparing the data with mock sets constructed by assuming a multivariate Gaussian for the velocities (see Methods for details).

We conclude that the halo near the Sun is strongly dominated by a single structure of accreted origin, as also hinted by other work[13,14], and leaves little room for an in situ contribution[15]. This is however not necessarily representative of the whole stellar halo, as debris from other accreted large objects (for example, with different chemical abundance patterns) might dominate elsewhere in the Galaxy. We also conclude that the Milky Way disk experienced a substantial merger in its history. We estimate the mass ratio of this merger at the time that it took place as $M_{\rm h}^{\rm GE}/M_{\rm h}^{\rm MW} = (f^{\rm MW}/f^{\rm GE}) \times (M_*^{\rm GE}/M_*^{\rm MW})$, where f is the ratio of the luminous-to-halo mass of the object, $M_{\rm h}$ and M_* denote the halo mass and stellar mass, respectively, and the superscripts MW and GE represent the Milky Way and Gaia–Enceladus. At the present time, $f^{\rm MW,0} \approx 0.04$ for the Milky Way[29]; if we assume Gaia–Enceladus to be similar to the Large Magellanic Cloud had it evolved in isolation, then[22] $f^{\rm GE,0} \approx 0.01$. It has been shown[30] that the redshift evolution of f between $z = 2$ and $z = 0$ is similar for objects of the scales of the Magellanic Cloud and of the Milky Way, which implies that $f^{\rm MW}/f^{\rm GE} = f^{\rm MW,0}/f^{\rm GE,0} \approx 4$. Therefore, by taking $M_*^{\rm MW}$ at the time of the merger to be the mass of the thick disk[29], that is, $M_*^{\rm MW} \approx 10^{10} M_\odot$, we obtain a mass ratio of about 0.24 for the merger. This implies that the merging of Gaia–Enceladus must have led to considerable heating and to the formation of a thick (or thicker) disk.

Online content

Any methods, additional references, Nature Research reporting summaries, source data, statements of data availability and associated accession codes are available at https://doi.org/10.1038/s41586-018-0625-x.

Received: 15 June 2018; Accepted: 11 September 2018;
Published online 31 October 2018.

1. Freeman, K. & Bland-Hawthorn, J. The new Galaxy: signatures of its formation. *Annu. Rev. Astron. Astrophys.* **40**, 487–537 (2002).
2. Helmi, A., White, S. D. M. & Springel, V. The phase-space structure of cold dark matter haloes: insights into the Galactic halo. *Mon. Not. R. Astron. Soc.* **339**, 834–848 (2003).
3. Carollo, D. et al. Two stellar components in the halo of the Milky Way. *Nature* **450**, 1020–1025 (2007); erratum **451**, 216 (2008).
4. Helmi, A., White, S. D. M., de Zeeuw, P. T. & Zhao, H. Debris streams in the solar neighbourhood as relicts from the formation of the Milky Way. *Nature* **402**, 53–55 (1999).
5. Morrison, H. L. et al. Fashionably late? Building up the Milky Way's inner halo. *Astrophys. J.* **694**, 130–143 (2009).
6. Chiba, M. & Beers, T. C. Kinematics of metal-poor stars in the Galaxy. III. Formation of the stellar halo and thick disk as revealed from a large sample of non-kinematically selected stars. *Astron. J.* **119**, 2843–2865 (2000).
7. Nissen, P. E. & Schuster, W. J. Two distinct halo populations in the solar neighbourhood – evidence from stellar abundance ratios and kinematics. *Astron. Astrophys.* **511**, L10 (2010).
8. Beers, T. C. et al. Bright metal-poor stars from the Hamburg/ESO survey. II. A chemodynamical analysis. *Astrophys. J.* **835**, 81 (2017).
9. Abolfathi, B. et al. The fourteenth data release of the Sloan Digital Sky Survey: first spectroscopic data from the extended Baryon Oscillation Spectroscopic Survey and from the second phase of the Apache Point Observatory Galactic Evolution Experiment. *Astrophys. J. Suppl. Ser.* **235**, 42 (2018).
10. Gaia Collaboration. The Gaia mission. *Astron. Astrophys.* **595**, A1 (2016).
11. Hayes, C. R. et al. Disentangling the Galactic halo with APOGEE. I. Chemical and kinematical investigation of distinct metal-poor populations. *Astrophys. J.* **852**, 49 (2018).
12. Gaia Collaboration. Gaia Data Release 2: observational Hertzsprung– Russell diagrams. *Astron. Astrophys.* **616**, A10 (2018).
13. Belokurov, V., Erkal, D., Evans, N. W., Koposov, S. E. & Deason, A. J. Co-formation of the Galactic disc and the stellar halo. *Mon. Not. R. Astron. Soc.* **478**, 611–619 (2018).
14. Koppelman, H. H., Helmi, A. & Veljanoski, J. One large blob and many streams frosting the nearby stellar halo in Gaia DR2. *Astrophys. J.* **860**, L11 (2018).
15. Haywood, M. et al. In disguise or out of reach: first clues about in-situ and accreted stars in the stellar halo of the Milky Way from Gaia DR2. *Astrophys. J.* **863**, 113 (2018).
16. Cooper, A. P. et al. Galactic stellar haloes in the CDM model. *Mon. Not. R. Astron. Soc.* **406**, 744–766 (2010).
17. Gaia Collaboration. Gaia Data Release 2. Summary of the contents and survey properties. *Astron. Astrophys.* **616**, A1 (2018).
18. Villalobos, A. & Helmi, A. Simulations of minor mergers – I. General properties of thick discs. *Mon. Not. R. Astron. Soc.* **391**, 1806–1827 (2008).
19. Nissen, P. E. & Schuster, W. J. Two distinct halo populations in the solar neighborhood. II. Evidence from stellar abundances of Mn, Cu, Zn, Y, and Ba. *Astron. Astrophys.* **530**, A15 (2011).
20. Fernández-Alvar, E. et al. Disentangling the Galactic halo with APOGEE. II. Chemical and star formation histories for the two distinct populations. *Astrophys. J.* **852**, 50 (2018).
21. Helmi, A. The stellar halo of the Galaxy. *Astron. Astrophys. Rev.* **15**, 145–188 (2008).
22. Van der Marel, R. P., Kallivayalil, N. & Besla, G. Kinematical structure of the Magellanic System. *Proc. IAU* **256**, 81–92 (2008).
23. Marigo, P. et al. A new generation of PARSEC-COLIBRI stellar isochrones including the TP-AGB phase. *Astrophys. J.* **835**, 77 (2017).
24. Schuster, W. J., Moreno, E., Nissen, P. E. & Pichardo, B. Two distinct halo populations in the solar neighborhood. III. Evidence from stellar ages and orbital parameters. *Astron. Astrophys.* **538**, A21 (2012).
25. Hawkins, K., Jofré, P., Gilmore, G. & Masseron, T. On the relative ages of the α-rich and α-poor stellar populations in the Galactic halo. *Mon. Not. R. Astron. Soc.* **445**, 2575–2588 (2014).
26. Clementini, G. et al. Gaia Data Release 2: specific characterisation and validation of all-sky Cepheids and RR Lyrae stars. Preprint at https://arxiv.org/abs/1805.02079 (2018).
27. Gaia Collaboration. Gaia Data Release 2: kinematics of globular clusters and dwarf galaxies around the Milky Way. *Astron. Astrophys.* **616**, A12 (2018).
28. VandenBerg, D. A., Brogaard, K., Leaman, R. & Casagrande, L. The ages of 55 globular clusters as determined using an improved $\Delta V_{\rm TO}^{\rm HB}$ method along with color–magnitude diagram constraints, and their implications for broader issues. *Astrophys. J.* **775**, 134 (2013).
29. McMillan, P. J. The mass distribution and gravitational potential of the Milky Way. *Mon. Not. R. Astron. Soc.* **465**, 76–94 (2017).
30. Behroozi, P. S., Wechsler, R. H. & Conroy, C. The average star formation histories of galaxies in dark matter halos from z = 0–8. *Astrophys. J.* **770**, 57 (2013).

Acknowledgements We are grateful to Á. Villalobos for permission to use his suite of simulations, and to M. Breddels for the software package Vaex (http://vaex.astro.rug.nl), which was used for part of our analyses. We thank H.-W. Rix, D. Hogg and A. Price-Whelan for comments. We have made use of data from the European Space Agency mission Gaia (http://www.cosmos.esa.int/gaia), processed by the Gaia Data Processing and Analysis Consortium (DPAC; see http://www.cosmos.esa.int/web/gaia/dpac/consortium). Funding for DPAC has been provided by national institutions, in particular the institutions participating in the Gaia Multilateral Agreement. We also used data from the APOGEE survey— a part of Sloan Digital Sky Survey IV, which is managed by the Astrophysical Research Consortium for the Participating Institutions of the Sloan Digital Sky Survey (SDSS) Collaboration (http://www.sdss.org). A.H., H.H.K., D.M. and J.V. acknowledge financial support from a Vici grant from the Netherlands Organisation for Scientific Research (NWO) and A.G.A.B. from the Netherlands Research School for Astronomy (NOVA).

Reviewer information *Nature* thanks T. C. Beers, K. V. Johnston and K. Venn for their contribution to the peer review of this work.

Author contributions All the authors contributed to the work. A.H. led and contributed to all aspects of the analysis and wrote the manuscript. C.B. compiled the APOGEE data, provided the cross-match to the Gaia data, was involved in the chemical abundance analysis and, together with D.M., analysed the HRD. H.H.K. and J.V. carried out the dynamical analysis and identification of member stars. A.G.A.B. proposed the preparation of this paper, explored the impact of the selection effects and contributed to the writing of the paper, together with the other co-authors.

Competing interests The authors declare no competing interests.

Additional information
Extended data is available for this paper at https://doi.org/10.1038/s41586-018-0625-x.
Supplementary information is available for this paper at https://doi.org/10.1038/s41586-018-0625-x.
Reprints and permissions information is available at http://www.nature.com/reprints.
Correspondence and requests for materials should be addressed to A.H.
Publisher's note: Springer Nature remains neutral with regard to jurisdictional claims in published maps and institutional affiliations.

© 2018 Springer Nature Limited. All rights reserved.

METHODS

We describe here the motivation behind the name Gaia–Enceladus. In Greek mythology Enceladus was one of the Giants and the offspring of Gaia (which represents the Earth) and Uranus (which represents the sky). Enceladus was said to be buried under Mount Etna and to be responsible for earthquakes in the region. There are many analogies to the accreted galaxy reported and characterized here, including: (i) being offspring of Gaia and the sky, (ii) having been a 'giant' compared to other past and present satellite galaxies of the Milky Way, (iii) being buried (in reality, first disrupted by the Milky Way and then buried—also in the Gaia data) and (iv) being responsible for seismic activity (that is, shaking the Milky Way and thereby leading to the formation of its thick disk). We refer to the accreted galaxy as Gaia–Enceladus to avoid confusion with one of Saturn's moons, also named Enceladus.

Dataset, selection criteria and the effect of systematics. For this work, we select stars from the Gaia 6D dataset[17] with small relative parallax error $\varpi/\sigma_\varpi > 5$, which allows us to compute their distance from the Sun as $d = 1/\varpi$. For Fig. 1, we consider only stars with $\varpi > 0.4$ mas (that is, within 2.5 kpc from the Sun) to limit the impact of the velocity gradients. The velocities are obtained using the appropriate matrix transformations from the observables α (right ascension), δ (declination), $\mu_{\alpha*}$ and μ_δ (proper motion in the direction of α and δ, respectively) and $V_{\rm los}$ (line-of-sight velocity) and the distances d. These velocities are then corrected for the peculiar motion of the Sun[31] and the local-standard-of-rest-velocity, which is assumed as[29] $V_{\rm LSR} = 232$ km s^{-1}.

We select halo stars (such as the black points in Fig. 1a) as those that satisfy[14] $|\boldsymbol{V} - \boldsymbol{V}_{\rm LSR}| > 210$ km s^{-1}. This condition is used to remove the contribution of the disk(s), although it is less effective towards the inner Galaxy because of the increasing velocity dispersion of disk stars[32]. To select members of the retrograde structure (such as the blue points in Fig. 1a), we inspect the E–L_z distribution of the stars in our dataset. The energy E is computed assuming a Galactic potential including thin-disk, bulge and halo components[33]. For example, Extended Data Fig. 1a shows the E–L_z distribution for all halo stars within 5 kpc from the Sun ($\varpi > 0.2$ mas). Here we have removed stars with phot-bp-rp-excess-factor > 1.27, which is enough to remove some globular cluster stars with poorer photometric quality so as not to apply a colour-dependent correction[34]. This figure shows that the regions occupied by the retrograde structure and by the disk are relatively well separated. There is however some overlap, particularly for higher binding energies and lower angular momenta. Therefore, even the selection criteria $L_z < 150$ kpc km s^{-1} and $E > -1.8 \times 10^5$ km^2 s^{-2} (dashed lines) do not yield a pure (thick-disk-free) sample of stars in the structure. This figure also reveals the large range of energies in the structure, which indicates that member stars are expected over a large range of distances.

Because the energies of stars depend on the gravitational potential of the Galaxy, whose form and amplitude are not so well constrained beyond the solar neighbourhood, we use a criterion based only on L_z to find additional members of the structure/Gaia–Enceladus beyond the immediate vicinity of the Sun (as in Fig. 3). Extended Data Fig. 1b shows the L_z versus the Galactocentric distance R in the disk plane for all stars in the Gaia 6D dataset with $\varpi/\sigma_\varpi > 5$ and parallaxes $\varpi > 0.2$ mas. This plot shows that a selection based only on L_z works relatively well to isolate Gaia–Enceladus stars near the Sun and also farther out in the Galaxy. However, in the inner regions there is much more overlap between the thick disk and Gaia–Enceladus; hence, distinguishing them from each other is less straightforward and the amount of contamination by thick-disk stars is probably much higher. Furthermore, we expect the orbits of some stars in the progenitor of the thick disk to have been perturbed so much during the merger[35] that they 'mingle' with those from Gaia–Enceladus.

Extended Data Fig. 1c shows the z-direction angular momentum as a function of the cylindrical radius of the stellar particles, as obtained from a simulation of the merger of a pre-existing disk and a massive satellite[18,36] (as in Fig. 1b). This example corresponds to the simulation of a disk with mass $M_* = 1.2 \times 10^{10} M_\odot$ and a satellite with mass $M_{*,\rm sat} = 2.4 \times 10^9 M_\odot$ at redshift $z = 1$. Because of the lower host mass used in this simulation (compared to the present-day mass of the Milky Way), the spatial scales and velocities are typically smaller than the data. Therefore, in the simulations we consider as the solar vicinity a volume centred at $R_\odot^{\rm sim} = 2.4 R_{\rm thick}^{\rm final}$, where the final thick-disk scale-length in the simulation is[18] $R_{\rm thick}^{\rm final} = 2.26$ kpc. We also scale the positions by $R_\odot / R_\odot^{\rm sim} = 1.5$ and the velocities by $v_{{\rm thick},\odot}/v_{\rm thick}^{\rm final,sim}$, where $v_{{\rm thick},\odot} = 173$ km s^{-1} is the rotational velocity of the thick disk near the Sun[37] and $v_{\rm thick}^{\rm final,sim}$ is that at $R_\odot^{\rm sim}$ in the simulation. Extended Data Fig. 1c shows that, as in the data, the separation between accreted and host disk stars is less clear for small radii.

For the data of Fig. 2a, we cross-match the catalogues of Gaia DR2 and APOGEE[9,38] DR14 and retain only stars with estimated distances (that is, spectrophotometric and trigonometric parallaxes) that are consistent with each other at the 2σ level. We also require a relative parallax error of 20%. More than 100,000 stars within 5 kpc from the Sun satisfy these conditions. The abundances shown in Fig. 2 are obtained from the ASCAP pipeline[39].

The established presence of a parallax zero-point offset in the Gaia data[40] is partly (if not only) due to a degeneracy between the parallax and the basic-angle variation of the Gaia satellite[41]. Its amplitude varies with the location in the sky[34,40] and is on average -0.029 mas, with a root-mean-square error of about 0.03 mas[27,40]. Such variations make it very difficult to perform a correction a posteriori for the full Gaia DR2 dataset (although the parallax zero-point offset is expected to be smaller than for Gaia DR3). The discovery and characterization of Gaia–Enceladus was done using stars with parallaxes $\varpi > 0.4$ mas in Fig. 1 and for stars with $\varpi > 0.2$ mas from the cross-match of Gaia and APOGEE in Fig. 2. We therefore expect the derived kinematic and dynamical quantities for these subsets to be largely unaffected by the systematic parallax error. However, for Figs. 3, 4, we selected stars on the basis of their L_z, although we focused on properties that are independent of the parallax, such as the position in the sky and proper motions. Nonetheless, to establish how important the parallax zero-point offset is for the selection via L_z, we perform the following test.

We use the Gaia Universe Model Snapshot (GUMS) model v18.0.0[42] and select stars according to the following criteria: apparent magnitude in the Gaia G band $6 \le G \le 13$, surface gravity $0.2 \le \log(g) \le 5$ and effective temperature 3,000 K $\le T_{\rm eff} \le$ 9,000 K. This selection leads to a total of 7,403,454 stars distributed across all Galactic components. For these stars we compute the error-free velocities and L_z and convolve their true parallax with a Gaussian with a dispersion that depends on the magnitude of the star (see https://www.cosmos.esa.int/web/gaia/science-performance, where the end-of-mission uncertainties have been scaled to account for the shorter timespan of DR2). The parallax is reconvolved with a Gaussian with a mean of -0.029 mas and a dispersion of 0.030 mas. Using these observed parallaxes, we compute the 'observed' velocities and L_z.

We find that for measured distances smaller than 5 kpc there is no shift in the derived L_z, whereas for a shell between 5 kpc and 7.5 kpc the median amplitude of the shift is about -50 kpc km s^{-1}, making the observed L_z more retrograde. For a shell between 9 kpc and 10 kpc, the median shift is small and has an amplitude of 20 kpc km s^{-1}, which presumably reflects that at such large distances, random errors dominate in the measurements of individual stars. The results are shown in Extended Data Fig. 2a, where we plot the difference between the true (initial) and 'measured' distributions of L_z for stars 'observed' at distances between 5 kpc and 10 kpc for $l = (-60°, -20°)$. Extended Data Fig. 2b shows the distribution of the mean value of this difference over the whole sky. Although the figure reveals certain patterns, these are different from those seen in Fig. 3. As stated in the main paper, the lack of distant stars in the regions outside the contours of Fig. 4 is the result of a quality cut in the relative parallax error of 20%. This selection criterion allows for parallax errors in the range 0.02–0.04 mas for the most distant stars (with 0.1 mas $< \varpi <$ 0.2 mas); such errors are only reached in those regions of the sky that have been surveyed more frequently by Gaia, such as around the ecliptic poles. The Gaia RR Lyrae stars associated with Gaia–Enceladus also suffer from this effect because a lower number of visits leads to more difficult identification and hence to lower levels of statistical completeness[26].

Random sets and importance of features. To understand how different the dynamical properties of the Gaia 6D dataset are in comparison with a smooth distribution, we plot the distribution of velocities in Extended Data Fig. 3a and of E–L_z in Extended Data Fig. 3b for randomized datasets. These smooth datasets have been obtained from the Gaia data shown in Fig. 1a and in Extended Data Fig. 1a, respectively, by re-shuffling the velocities. That is, to each star, we assign randomly the velocity components V_y and V_z of two other stars in the sample. This results in distributions with the same one-dimensional velocity distributions as the original data, but without any correlations or lumpiness. The comparison of Fig. 1a with Extended Data Fig. 3a shows that the distribution in the random dataset is indeed much smoother than the data and that the overall velocity dispersion in the y direction increases because there is no longer a clear separation between the region occupied by Gaia–Enceladus and by the thick disk. The comparison of Fig. 1b with Extended Data Fig. 3b is even more revealing and clearly shows that the structure defined in E–L_z by Gaia–Enceladus stars has effectively disappeared in the randomized dataset. Similar conclusions are reached when, instead of using a reshuffled dataset, we compare the distributions with those in the GUMS model.

Figure 4 shows the radial velocities and proper motions (corrected for the solar and local-standard-of-rest motions) for stars with 0.1 mas $< \varpi <$ 0.2 mas and $-1{,}500$ kpc km s^{-1} $< L_z <$ 150 kpc km s^{-1}. These stars are potential members of Gaia–Enceladus, although, as discussed earlier, contamination by thick-disk stars becomes more important for large distances towards the inner Galaxy. The arrows that depict the proper motions suggest that stars that are close by in the sky move in similar directions. We establish here whether this is statistically significant by comparing the data with a mock dataset.

© 2018 Springer Nature Limited. All rights reserved.

The mock dataset uses the measured positions of the stars that are plotted in Fig. 4, but with their velocities generated randomly according to a multivariate Gaussian distribution with dispersions of 141, 78 and 94 km s^{-1} in V_R, V_ϕ and V_z, respectively[43], where ϕ is the azimuth angle in the disk plane. During the generation of the mock dataset, we only keep star velocities that satisfy $-1{,}500$ kpc km s^{-1} $< L_z < 150$ kpc km s^{-1}, as in the real data. To quantify the degree of coherence in the proper motions of neighbouring stars in the sky, we perform the following test. For each star, we find its nearest neighbour in the sky and then determine the angle between their proper-motion vectors. We then count the number of such pairs with a given angle. Extended Data Fig. 4 shows the distribution of these pairs for the Gaia subsample (blue) and for the mock dataset (red). There is a clear excess of pairs of stars with similar directions of motion in the data in comparison with the mock dataset.

Context and link with other substructures. Hints of the presence of a population like Gaia–Enceladus have been reported in the literature in the last two decades and have been typically based on small samples of stars. These hints were of a chemo-dynamical nature[6,8,44] and sometimes attributed to accretion[5,45], but also based purely on chemical signatures, such as the α-poor sequence[7,19]. More recently, cross-matches to the first data release of the Gaia mission[46] also revealed the contrast between the metal-rich population, which is supported by prograde rotation and associated with the tail of the thick disk[47], and the metal-poor halo, which we have identified as Gaia–Enceladus. Furthermore, in one study[13] the difference in the kinematics of these two populations, as well as the measurement of a very radially biased velocity ellipsoid for halo stars with [Fe/H] > -1.7, led to the proposal that this population (which was termed 'Gaia sausage') could be the result of a substantial merger. Although this could be also attributed to an in situ formation via a radial collapse, this hypothesis is further supported by the orbits of the stars in the population, leading to a break in the halo density profile at about 20 kpc[48]. All of these pieces of evidence together outline the case for the discovery and detailed characterization of Gaia–Enceladus reported here.

The more distant Gaia–Enceladus debris occupies large portions of the sky that are not extensively covered by other existing surveys. There is however a recent detection of an overdensity identified by the PanSTARRS and the WISE surveys with the help of Gaia proper motions[49], which overlaps with the northern part of the more distant Gaia–Enceladus stars for -2 mas yr$^{-1} < \mu_\alpha < -1$ mas yr^{-1} and -1 mas yr$^{-1} < \mu_\delta < 0$ mas yr^{-1} and partly (but not fully because of the PanSTARRS footprint) with the southern part for 0 mas yr$^{-1} < \mu_\alpha < 1$ mas yr^{-1} and -3 mas yr$^{-1} < \mu_\delta < -1$ mas yr^{-1}. There could be also a relationship with the Hercules Aquila Cloud[50] identified in SDSS data, although this appears to be offset both in the northern and southern hemispheres and is located at a larger distance. The location of intermediate-distance Gaia–Enceladus stars in the sky seems to overlap with the Hercules thick-disk cloud[51], especially in the fourth Galactic quadrant below the Galactic plane.

Data availability

All data generated and analysed in this study are provided as Source Data or Supplementary Data.

31. Schönrich, R., Binney, J. & Dehnen, W. Local kinematics and the local standard of rest. *Mon. Not. R. Astron. Soc.* **403**, 1829–1833 (2010).
32. Gaia Collaboration. Gaia Data Release 2: mapping the Milky Way disc kinematics. *Astron. Astrophys.* **616**, A11 (2018).
33. Helmi, A., Veljanoski, J., Breddels, M. A., Tian, H. & Sales, L. V. A box full of chocolates: the rich structure of the nearby stellar halo revealed by Gaia and RAVE. *Astron. Astrophys.* **598**, A58 (2017).
34. Arenou, F. et al. Gaia Data Release 2: catalogue validation. *Astron. Astrophys.* **616**, A17 (2018).
35. Jean-Baptiste, I. et al. On the kinematic detection of accreted streams in the Gaia era: a cautionary tale. *Astron. Astrophys.* **604**, A106 (2017).
36. Villalobos, A. & Helmi, A. Simulations of minor mergers – II. The phase-space structure of thick discs. *Mon. Not. R. Astron. Soc.* **399**, 166–176 (2009).
37. Morrison, H. L., Flynn, C. & Freeman, K. C. Where does the disk stop and the halo begin? Kinematics in a rotation field. *Astron. J.* **100**, 1191–1222 (1990).
38. Majewski, S. R. et al. The Apache Point Observatory Galactic Evolution Experiment (APOGEE). *Astron. J.* **154**, 94 (2017).
39. García Pérez, A. E. et al. ASPCAP: the APOGEE stellar parameter and chemical abundances pipeline. *Astron. J.* **151**, 144 (2016).
40. Lindegren, L. et al. Gaia Data Release 2: the astrometric solution. *Astron. Astrophys.* **616**, A2 (2018).
41. Butkevich, A. G., Klioner, S. A., Lindegren, L., Hobbs, D. & van Leeuwen, F. Impact of basic angle variations on the parallax zero point for a scanning astrometric satellite. *Astron. Astrophys.* **603**, A45 (2017).
42. Robin, A. C. et al. Gaia Universe model snapshot. A statistical analysis of the expected contents of the Gaia catalogue. *Astron. Astrophys.* **543**, A100 (2012).
43. Posti, L., Helmi, A., Veljanoski, J. & Breddels, M. The dynamically selected stellar halo of the Galaxy with Gaia and the tilt of the velocity ellipsoid. *Astron. Astrophys.* **615**, A70 (2018).
44. Carollo, D., Martell, S. L., Beers, T. C. & Freeman, K. C. CN anomalies in the halo system and the origin of globular clusters in the Milky Way. *Astrophys. J.* **769**, 87 (2013).
45. Brook, C. B., Kawata, D., Gibson, B. K. & Flynn, C. Galactic halo stars in phase space: a hint of satellite accretion? *Astrophys. J.* **585**, L125–L129 (2003).
46. Gaia Collaboration. Gaia Data Release 1. Summary of the astrometric, photometric, and survey properties. *Astron. Astrophys.* **595**, A2 (2016).
47. Bonaca, A., Conroy, C., Wetzel, A., Hopkins, P. F. & Kereš, D. Gaia reveals a metal-rich, in situ component of the local stellar halo. *Astrophys. J.* **845**, 101 (2017).
48. Deason, A. J., Belokurov, V., Koposov, S. E. & Lancaster, L. Apocenter pile-up: origin of the stellar halo density break. *Astrophys. J.* **862**, L1 (2018).
49. Conroy, C. et al. They might be giants: an efficient color-based selection of red giant stars. *Astrophys. J.* **861**, L16 (2018).
50. Belokurov, V. et al. The Hercules–Aquila cloud. *Astrophys. J.* **657**, L89–L92 (2007).
51. Larsen, J. A., Cabanela, J. E. & Humphreys, R. M. Mapping the asymmetric thick disk. II. Distance, size, and mass of the Hercules thick disk cloud. *Astron. J.* **141**, 130 (2011).

© 2018 Springer Nature Limited. All rights reserved.

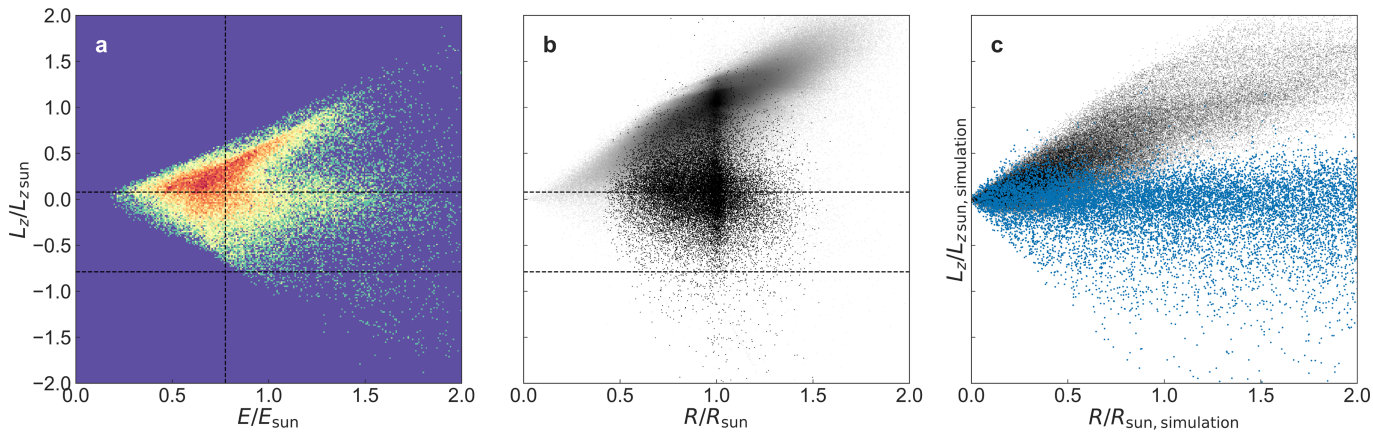

Extended Data Fig. 1 | Slices of phase space used to isolate Gaia–Enceladus stars. a, Energy E versus angular momentum L_z for stars in the 6D Gaia dataset that satisfy the quality criteria described in the text, with $\varpi > 0.2$ mas (5 kpc from the Sun) and $|\boldsymbol{V} - \boldsymbol{V}_{\mathrm{LSR}}| > 210$ km s^{-1}. The dashed lines indicate the criteria used to select Gaia–Enceladus stars, namely, $-1{,}500$ kpc km s$^{-1} < L_z < 150$ kpc km s^{-1} and $E > -1.8 \times 10^5$ km^2 s^{-2}. These criteria follow roughly the structure's shape (for comparison, see Extended Data Fig. 3b) but are slightly conservative for the upper limit of L_z to prevent too much contamination by the thick disk. However, small shifts—such as those obtained by considering an upper limit of 250 kpc km s^{-1} or a lower limit of -750 kpc km s^{-1} for L_z, or $E > -2 \times 10^5$ km^2 s^{-2}—do not result in drastic changes to the results presented in the paper. The colour scale indicates the logarithm of the counts in the bins, with red corresponding to the highest number of counts, yellow and blue to 1/6th and 1/30th of this value, respectively, and purple to empty bins. **b**, Angular momentum L_z versus the Galactocentric distance R for all stars in the 6D Gaia with $\varpi > 0.2$ mas. The black points are the halo-star sample shown in **a**. **c**, Same as **b**, but for star particles in the merger simulation[18] shown in Fig. 1b. Blue points correspond to stars from the satellite and grey points to the host disk, and the positions and velocities have been scaled as described in the text. In this figure, E, L_z and R have been scaled by the energy ($E_{\mathrm{sun}} = -1.63 \times 10^5$ km^2 s^{-2} in the Galactic potential used), angular momentum ($L_{z,\mathrm{sun}} = 1{,}902.4$ kpc km s^{-1}) and Galactocentric distance ($R_{\mathrm{sun}} = 8.2$ kpc) of the Sun, respectively.

© 2018 Springer Nature Limited. All rights reserved.

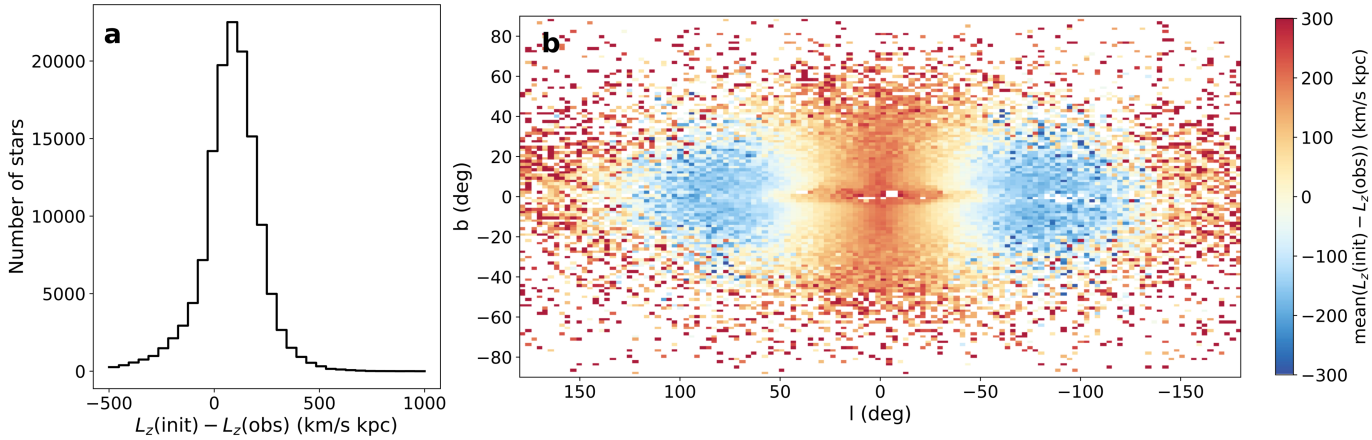

Extended Data Fig. 2 | Effect of a zero-point offset in the parallax on L_z. a, Distribution of the difference between the initial (L_z(init)) and 'measured' (L_z(obs); after error convolution) z-angular momentum for stars from the GUMS model with 'measured' distances between 5 and 10 kpc and with galactic longitude $l = (-60°, -20°)$. **b**, Mean value of the difference over the full sky.

© 2018 Springer Nature Limited. All rights reserved.

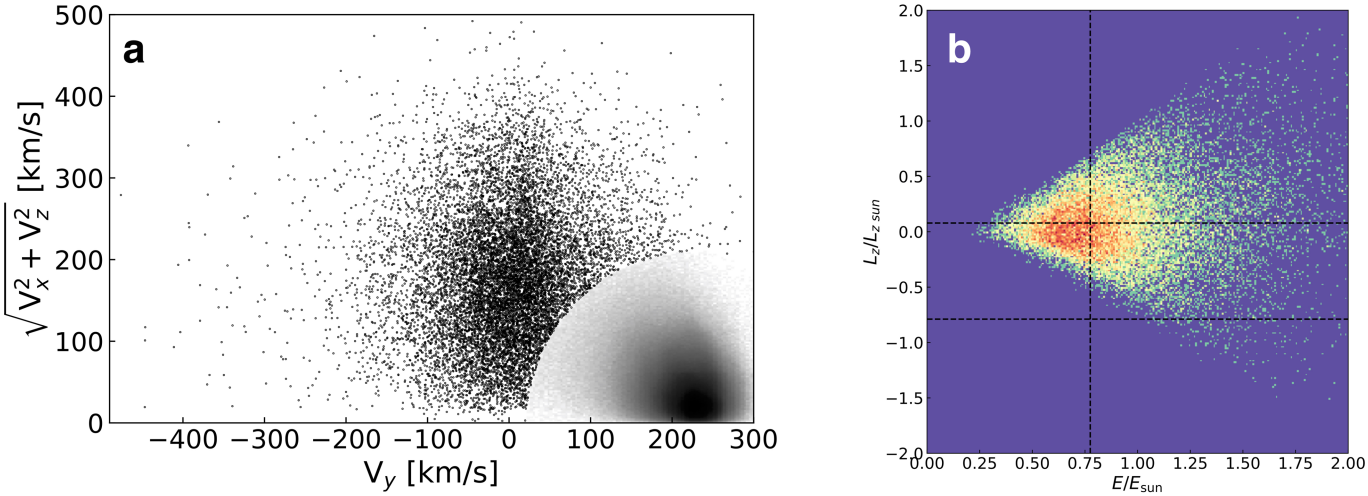

Extended Data Fig. 3 | Dynamical properties of stars for a smooth dataset. a, **b**, Velocity (**a**) and E–L_z (**b**) distribution, for a dataset obtained by reshuffling the velocities of the stars plotted in Fig. 1a and in Extended Data Fig. 1a, respectively. Visual comparison to those figures shows that these random sets are less clumped than the observed distributions of the Gaia halo stars. L_z and E in **b** are scaled as in Extended Data Fig. 1, and the colour scale indicates the logarithm of the counts in the bins, with dark red corresponding to the highest number of counts, yellow and blue to 1/5th and 1/15th of this value, respectively, and purple to empty bins.

© 2018 Springer Nature Limited. All rights reserved.

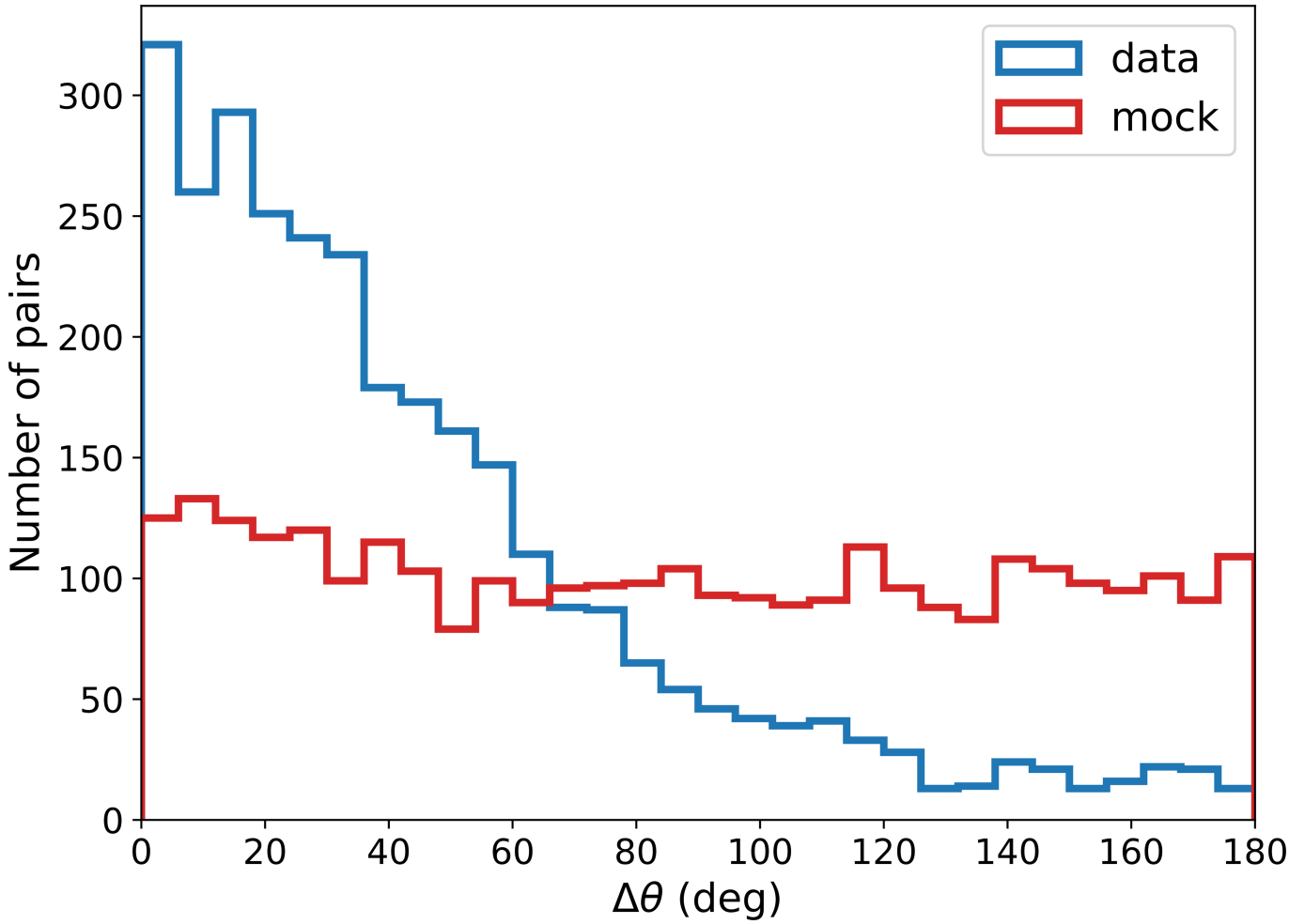

Extended Data Fig. 4 | Distribution of angles between proper-motion vectors for neighbouring stars in the sky. The blue and red histograms correspond to Gaia–Enceladus stars and a mock dataset, respectively. This mock dataset uses the positions of the stars in Gaia–Enceladus, but velocities generated randomly according to a multivariate Gaussian distribution[43]; only velocities that satisfy $-1{,}500$ kpc km s$^{-1} < L_z < 150$ kpc km s^{-1} are kept in the mock dataset, as in the real data. For each star, we find its nearest neighbour in the sky and then determine the angle $\Delta\theta$ between their proper-motion vectors for the data and for the mock dataset. We then count the number of such pairs with a given angle $\Delta\theta$.

© 2018 Springer Nature Limited. All rights reserved.

https://doi.org/10.1038/s41586-018-0609-x

Security and eavesdropping in terahertz wireless links

Jianjun Ma[1], Rabi Shrestha[1], Jacob Adelberg[1], Chia-Yi Yeh[2], Zahed Hossain[3], Edward Knightly[2], Josep Miquel Jornet[3] & Daniel M. Mittleman[1]*

Resiliency against eavesdropping and other security threats has become one of the key design considerations for communication systems. As wireless systems become ubiquitous, there is an increasing need for security protocols at all levels, including software (such as encryption), hardware (such as trusted platform modules) and the physical layer (such as wave-front engineering)[1–5]. With the inevitable shift to higher carrier frequencies, especially in the terahertz range (above 100 gigahertz), an important consideration is the decreased angular divergence (that is, the increased directionality) of transmitted signals, owing to the reduced effects of diffraction on waves with shorter wavelengths. In recent years, research on wireless devices[6–8] and systems[9–11] that operate at terahertz frequencies has ramped up markedly. These high-frequency, narrow-angle broadcasts present a more challenging environment for eavesdroppers compared to the wide-area broadcasts used at lower frequencies[12,13]. However, despite the widespread assumption of improved security for high-frequency wireless data links[14–16], the possibility of terahertz eavesdropping has not yet been characterized. A few recent studies have considered the issue at lower frequencies[5,12,13,17,18], but generally with the idea that the eavesdropper's antenna must be located within the broadcast sector of the transmitting antenna, leading to the conclusion that eavesdropping becomes essentially impossible when the transmitted signal has sufficiently high directionality[15]. Here we demonstrate that, contrary to this expectation, an eavesdropper can intercept signals in line-of-sight transmissions, even when they are transmitted at high frequencies with narrow beams. The eavesdropper's techniques are different from those for lower-frequency transmissions, as they involve placing an object in the path of the transmission to scatter radiation towards the eavesdropper. We also discuss one counter-measure for this eavesdropping technique, which involves characterizing the backscatter of the channel. We show that this counter-measure can be used to detect some, although not all, eavesdroppers. Our work highlights the importance of physical-layer security in terahertz wireless networks and the need for transceiver designs that incorporate new counter-measures.

Wireless networking is on the cusp of a revolution. For more than 100 years, wireless links have relied on wide-angle broadcasts, using transmit and receive antennas with gains that are relatively insensitive to the angle of emission or reception (and therefore with relatively low directivity). With the roll-out of 5G cellular mobile communications systems, this approach will soon change to an entirely new one, in which highly directional (and steerable) antennas provide links that are more like directed beams than like omnidirectional broadcasts[2,19]. This change is an unavoidable consequence of the move to higher carrier frequencies, a necessary step for increased bandwidth and higher rates of data transfer. There are numerous advantages to using more directional channels, including improved data security. Here, we focus on the new challenges faced by an eavesdropper when communication channels become directional[5,18], with a beam divergence angle much smaller than that used by existing mobile networks, which often use 120° sectors[20].

Security mechanisms are available at every layer of a network, and can be used jointly across layers for redundancy or in a subset of layers when resources are constrained. These mechanisms can take many forms, including encryption and authentication at the upper layers[2,3], as well as physical-layer techniques such as wave-front engineering, near-field antenna modulation and polarization multiplexing[4,5,21,22]. Physical-layer approaches have some advantages: they do not require a shared private key, they use little or no additional computing resources[23] and they do not rely on the assumption that the attacker has limited computational power. In the terahertz frequency range, numerous researchers have envisioned the need for physical-layer security[14–16,24]. Highly directional beams and increased atmospheric attenuation will confine unauthorized users to be on the same narrow path as the intended user if they wish to intercept the signal. As a result, it is often assumed that terahertz signals are more secure than lower-frequency signals: a more directional transmission sends energy to a smaller range of locations, so it is more difficult for an eavesdropper to place a receiver that detects the signal without blocking the intended recipient and thereby raising an alarm. The equipment needed to collect, demodulate and amplify terahertz signals is large (always larger than the aperture of the detector) and bulky, so blockage would always be a concern.

Although this argument is reasonable for conventional eavesdropping attacks, it does not consider alternative approaches that could circumvent the blockage problem and enable a successful attack. In our measurements, we consider a different approach for the eavesdropper (Eve). Rather than adopting the conventional assumption that Eve must place a large bulky receiver within the narrow beam path[5,13,17,18], we instead consider the possibility that she can place a smaller passive object in the beam that will scatter some of the transmitted radiation towards her receiver, which is located elsewhere[12]. This set-up affords Eve considerable additional flexibility, and can enable successful eavesdropping even at high frequencies with very directional beams.

We assume a line-of-sight configuration connecting a single transmitter (Alice) and a single receiver (Bob), as is standard for a highly directional millimetre-wave or terahertz wireless link through the air[25–27] (see Methods section 'Radiation patterns for directional horn antennas'). In our scale model data link (Fig. 1), we position objects at various locations in the beam between Alice and Bob, and evaluate the signal strength and bit error rate detected by Eve at various receiver locations. Eve's goal is to choose a scattering object, and its location, in such a way that the signal measured by Bob is not attenuated too much (otherwise, Bob might detect the attack) and the signal that she measures is large enough for her to intercept the communication. This corresponds to a successful eavesdropping configuration. To quantify

[1]School of Engineering, Brown University, Providence, RI, USA. [2]Department of Electrical and Computer Engineering, Rice University, Houston, TX, USA. [3]Department of Electrical Engineering, University at Buffalo, The State University of New York, Buffalo, NY, USA. *e-mail: daniel_mittleman@brown.edu

© 2018 Springer Nature Limited. All rights reserved.

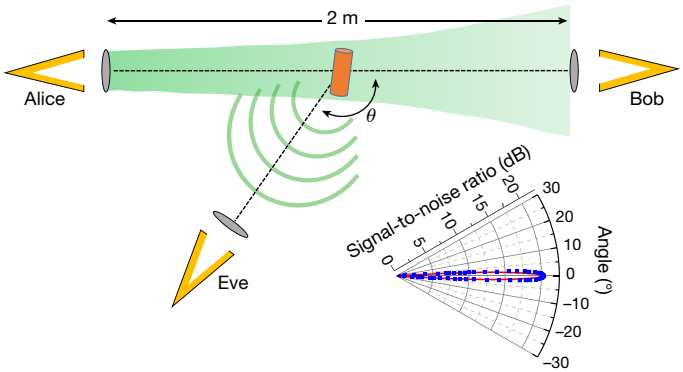

Fig. 1 | Schematic of a line-of-sight transmission channel with an eavesdropper. The schematic of the experiment shows a line-of-sight transmission channel between Alice (the transmitter) and Bob (the receiver). The inset shows the measured (blue) and computed (red) angular distribution of radiation emitted by our transmitter for the horn antenna and dielectric lens combination used in our measurements at a frequency of 200 GHz. These data indicate a high directivity of 34 dBi (decibels above isotropic) and no measurable side lobes. The results are similar for the other frequencies that we used in this work. The schematic also illustrates the eavesdropper's (Eve's) strategy: place a small (compared to the beam size) object (orange cylinder), which passively scatters radiation to a receiver located elsewhere, at an angle θ relative to the initial propagation axis of the beam. In our measurements, the receiver used by Eve is identical to that used by Bob and has identical angular sensitivity to the radiation pattern of the transmitter (Alice).

these statements, we define the attenuation of Bob's signal due to the scattering object, which we refer to as the blockage, as:

$$b = 1 - \frac{\mathrm{SNR}_{\mathrm{Bob}}^{\mathrm{object}}}{\mathrm{SNR}_{\mathrm{Bob}}^{\mathrm{no\ object}}}$$

where SNR represents the signal-to-noise ratio on a linear scale. A value of $b = 0.5$ would correspond to a situation in which Eve's scattering object is blocking half of Bob's signal. This arbitrary value may be considered a threshold beyond which Bob is certain to be aware of the change in the characteristics of his line-of-sight channel. Further, as a small modification to the conventional approach[28], we define a normalized secrecy capacity, which relates the strength of Eve's signal to Bob's signal:

$$\bar{c}_s = \frac{\log(1+\mathrm{SNR}_{\mathrm{Bob}}) - \log(1+\mathrm{SNR}_{\mathrm{Eve}})}{\log(1+\mathrm{SNR}_{\mathrm{Bob}})}$$

This quantity incorporates the particular modulation and coding methods used and characterizes the empirical limits of Bob's and Eve's reception capabilities. It is equal to unity if Eve receives no signal and to zero if Eve and Bob receive the same signal. In general, a threshold value for $\bar{c}_s$ is not easy to define, because Eve's ability to decode a signal depends on additional factors, including the modulation scheme and the absolute power level. In an information-theoretic sense, secure transmission is possible under certain circumstances even if $\bar{c}_s < 0$[29]. Thus, this quantity is not a perfect metric for defining the security of a channel. However, it is reasonable to assume that networks would be designed to strive to maximize $\bar{c}_s$, to minimize the likelihood of a successful eavesdropping attack[5]. To frame our discussion, we use an illustrative value of $\bar{c}_s = 0.5$ as an arbitrary threshold, below which we presume that eavesdropping is feasible. Both b and $\bar{c}_s$ depend on the size, shape, composition and location of the object placed in the beam path, and the carrier frequency. We find that for any frequency, Eve can always find a successful configuration that permits her to eavesdrop undetected, in the absence of any counter-measures.

To illustrate this point, we show in Fig. 2 the measured values of b and $\bar{c}_s$ for a set of scattering objects. These long cylindrical metal pipes

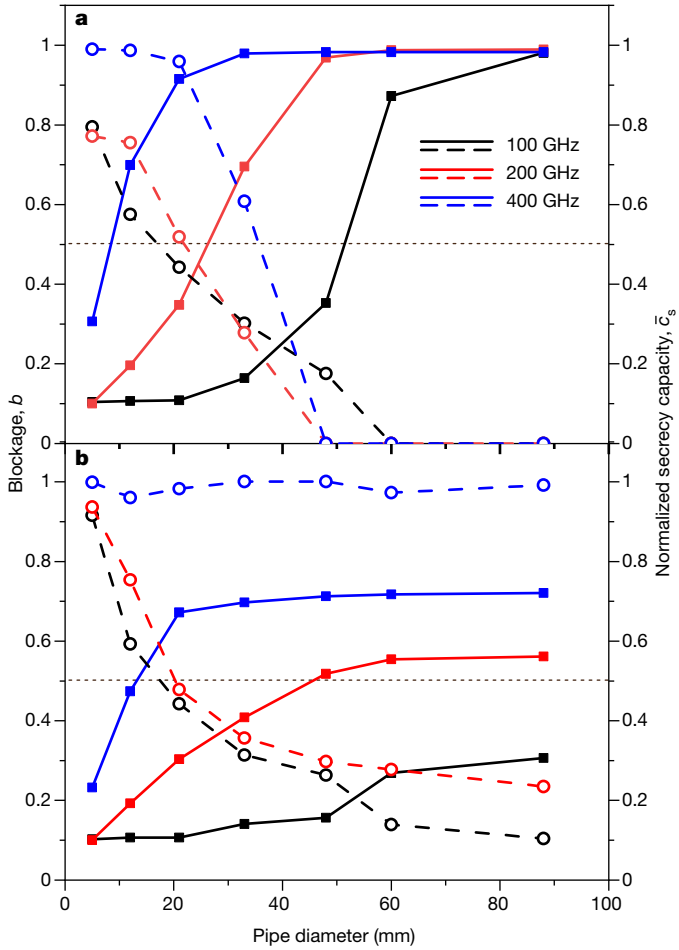

Fig. 2 | Measured blockage and secrecy capacity for eavesdropping attacks using metal cylinders. a, The blockage b (filled squares connected by solid lines; left axis) and normalized secrecy capacity $\bar{c}_s$ (open circles connected by dashed lines; right axis) as a function of the size of the metal pipe placed along the centre line of the transmission channel between Alice and Bob, for three different carrier frequencies. These values are measured with Eve located at an angle of $\theta = 160°$ (θ is defined in Fig. 1) and with the same total transmission path length as the distance from Alice to Bob (2 m). The blockage increases with the size of the object, owing to shadowing. In addition, for a given size, the blockage increases with frequency, because higher frequencies diffract less. Here, negative values of $\bar{c}_s$ are plotted as zero. **b**, The same as **a**, except with the scattering object moved off the centre line by a distance equal to the radius of the cylinder. This has the effect of decreasing the blockage substantially, making a successful eavesdropping attack easier. In **a** and **b**, the dashed horizontal lines indicate blockages or secrecy capacities of 0.5; a reasonable (but arbitrary) criterion for successful eavesdropping is that $b < 0.5$ and $\bar{c}_s < 0.5$. By this criterion, Eve succeeds in 10 of the 42 configurations that we measured.

of various diameters are inserted into the beam path along an axis parallel to the polarization direction of the beam. In Fig. 2a, the objects are situated on the line-of-sight transmission axis, so that they cast a direct shadow on the aperture of Bob's receiver[30]. Unsurprisingly, the value of b therefore increases with the size of the scattering object. We also observe a roughly opposite trend for $\bar{c}_s$: a larger scattering object directs more signal to Eve, so the secrecy capacity decreases.

For any realistic line-of-sight millimetre-wave or terahertz data link, even if the beam is highly directional, it is likely that the size of the beam when it reaches the receiver will exceed the aperture of the receiver. This is necessary to provide some margin of error for beam steering and for channel fluctuations such as atmospheric scintillation[31]. Therefore, it is possible that a scattering object could intercept a portion of the beam but not cast a shadow on the receiver. To illustrate this

© 2018 Springer Nature Limited. All rights reserved.

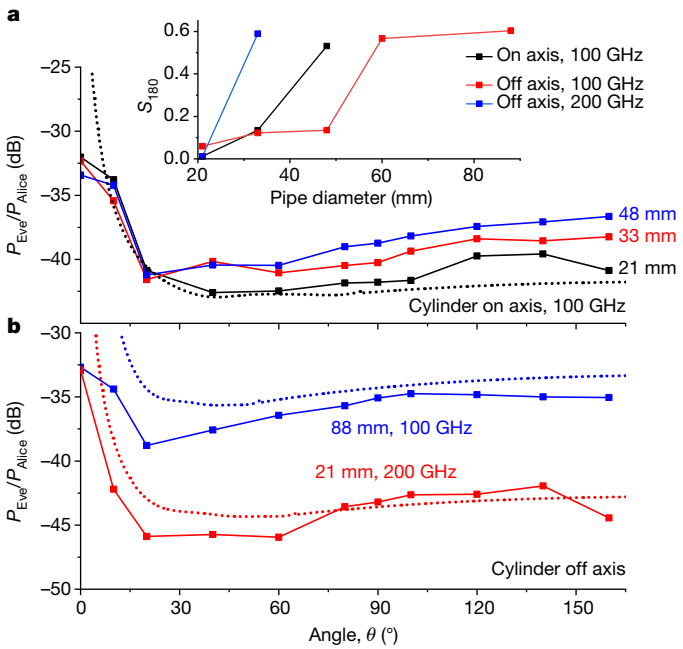

Fig. 3 | Angular distribution of power received by Eve, using metal cylinders. a, The received power ratio for Eve (the power received by Eve, P_{Eve}, normalized by the power transmitted by Alice, P_{Alice}), for different angular locations of her receiver, for all three of the configurations identified in Fig. 2a as resulting in successful eavesdropping attacks (metal cylinders located on the transmission axis; carrier frequency of 100 GHz). The labels in the main panel (21 mm, 33 mm and 48 mm) indicate the diameters of the cylinders. This result illustrates the increased power of the scattered signal with increasing cylinder diameter. The black dotted curve shows the results of ab initio numerical computations of the strength of the scattered signal for the 21-mm-diameter cylinder. **b**, Similar to **a**, showing two typical results for the seven successful-eavesdropping situations identified in Fig. 2b (in which the cylinder is moved off axis). As in **a**, the dotted curves show the corresponding computational results. The inset in **a** shows the back-scatter parameter S_{180} for all ten successful-eavesdropping configurations identified in Fig. 2. Assuming a criterion of $S_{180} > 0.5$ for the detection of potential eavesdropping, our proposed counter-measure identifies four of the ten attacks.

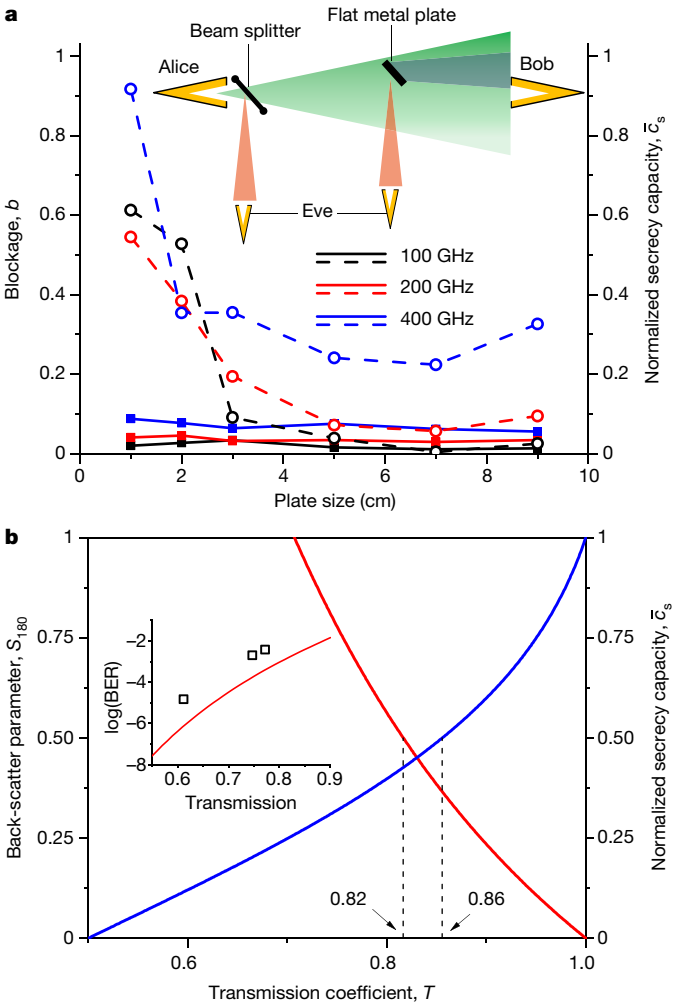

Fig. 4 | Measured blockage and secrecy capacity for eavesdropping attacks using flat objects. a, The blockage b (filled squares connected by solid lines; left axis) and normalized secrecy capacity $\bar{c}_s$ (open circles connected by dashed lines; right axis) for square planar metal reflectors of various sizes, for three different carrier frequencies. Here, the objects are placed off axis, similar to Fig. 2b. They are arranged to generate specular reflection to Eve's receiver, which is located at 90° to the axis of transmission. Unlike the case of the cylindrical objects, eavesdropping is possible ($b < 0.5$ and $\bar{c}_s < 0.5$), even at 400 GHz, for all but the smallest of the objects. The inset shows a schematic of the set-up for this form of attack, and for an attack using a beam splitter placed close to Alice (where the diameter of the beam is smallest), so as to encompass the entire transmitted beam. **b**, Values of the back-scatter parameter S_{180} (red; left axis) and $\bar{c}_s$ (blue; right axis) computed for the values of the transmission coefficient T of the beam splitter for which $b < 0.5$. There is a range of values for which S_{180} and $\bar{c}_s$ are both less than 0.5 (between the vertical dashed lines); a successful and undetected attack is possible in this range. If the back-scatter counter-measure is not used, then Eve can implement a successful attack for any value of T between 0.5 and 0.86, to obtain arbitrarily low secrecy capacity. The inset shows the measured (open squares) and calculated (solid line) bit error rate (BER) for Eve, under the assumption that Bob has a bit error rate of 10^{-9}. The experimental data were obtained using a few custom-made beam splitters (see Methods section 'The beam-splitter attack').

point, we repeat the experiments of Fig. 2a, except that we move the cylindrical objects off the centre line to minimize blockage due to direct shadowing. As a result, the values of b are reduced considerably (Fig. 2b), so that Bob may not notice the effect of the object in some cases. For the lower frequencies, the secrecy capacity is also quite low for larger objects, because they still scatter a substantial amount of power. Eve is much more readily able to implement a successful attack ($b < 0.5$ and $\bar{c}_s < 0.5$) with an off-centre object.

From Eve's point of view, cylindrical objects are advantageous because they scatter radiation over a wide range of angles. Whereas Fig. 2 depicts results for one particular location of Eve's receiver, Fig. 3 shows Eve's received power as a function of the angular location, for a few of the situations that satisfy both $b < 0.5$ and $\bar{c}_s < 0.5$. The dashed curves show a few examples of predicted values corresponding to the measured situations. These calculations use an ab initio model to compute the diffracted field from a perfectly smooth cylindrical conductor, under illumination from a point source[32] (see Methods section 'Diffracted field from a uniform metal cylinder'). As indicated by the measurements and calculations, Eve has the freedom to place her receiver in many different locations, without sacrificing signal strength.

The wide-angle scattering of a cylindrical object can also be used to develop a new type of physical-layer counter-measure[2]. A cylindrical object scatters some radiation at 180°, back towards the transmitter (Alice)[33]. It can also block radiation reflected from Bob's receiver, which would otherwise have returned to Alice. If Alice can measure these incoming signals and distinguish them from the variable backscatter off mobile objects or the environment, then any change, either an increase or a decrease, would be a sign of a possible attack. The effectiveness of this strategy relies on the assumption that Alice has previously characterized the back-scatter of the channel before any attempted attack by Eve—a rather strong assumption. Nevertheless, when combined with other, more conventional eavesdropping counter-measures[2–5], this approach can provide an additional level

© 2018 Springer Nature Limited. All rights reserved.

of security. We define the success of this counter-measure through a back-scatter parameter:

$$S_{180} = \left| 1 - \frac{\mathrm{SNR}_{\mathrm{Alice}}^{\mathrm{no\ object}}}{\mathrm{SNR}_{\mathrm{Alice}}^{\mathrm{object}}} \right|$$

If the object placed in the beam by Eve causes no change in the back-scattered signal, then $S_{180} = 0$ and the counter-measure has failed. But a larger value, greater than some pre-determined threshold (for example, $S_{180} > 0.5$), could be regarded as a warning of possible eavesdropping. In the inset in Fig. 3a we show measured values of S_{180} for all of the conditions for which both $b < 0.5$ and $\bar{c}_s < 0.5$ (see Methods section 'Measurement of S_{180}'). These measurements indicate that some, but not all, of Eve's attacks are detected by this counter-measure.

A second disadvantage for Eve is that, because the scattered radiation is dispersed in all directions, the power collected in a small receiver aperture is relatively low. Consequently, for example, at 400 GHz even the largest of our metal cylinders does not scatter enough radiation to permit Eve to decode the signal ($\bar{c}_s$ is nearly unity for all measurements at this frequency). An alternative for Eve is to use objects that scatter more selectively. Although this limits Eve's freedom of location considerably, it also increases her signal strength substantially. Instead of cylinders, we consider a set of square planar metal reflectors, which direct a portion of Alice's transmitted beam at 90° to the original propagation direction by specular reflection. When placed on the transmission axis, these plates block a substantial portion of Bob's signal. However, when moved off axis (Fig. 4a), the blockage drops to nearly zero, while the secrecy capacity remains low at all frequencies. Moreover, because these objects generate little back-scatter towards Alice, we find that S_{180} is small except for the largest plates, which block radiation reflected by Bob back towards Alice. For instance, for all of the measurements at 400 GHz, we find $S_{180} < 0.2$. As an extreme case, we imagine that Eve has the capacity to fabricate a lossless beam splitter, which is large enough to encompass the entire beam generated by Alice and which can be engineered to split off any desired fraction of the power in the transmitted beam. Figure 4b demonstrates that this type of attack is always effective if the transmittance of the beam splitter is chosen correctly (see Methods section 'The beam-splitter attack'). Moreover, if Alice cannot measure back-scattered signals (and is therefore unable to use the associated counter-measure), then the beam-splitter attack becomes even more devastating: Eve can readily obtain a bit error rate that is nearly as good as Bob's.

Our results demonstrate that a narrow pencil-like beam does not guarantee immunity from eavesdropping. Although this claim has often been cited as one of the advantages of using millimetre or terahertz waves, our analysis reveals that an agile eavesdropper can always succeed in implementing an undetected attack, unless counter-measures are used. Traditional counter-measures such as those that rely on beam forming[5,21,24] or on more advanced multiplexing schemes[22] may be less effective against these attacks, because the portion of the wave front that is sampled by Eve is almost coincident with that intended for Bob. On the other hand, our new counter-measure requires Alice to use a transceiver, not merely a transmitter. Thus, to incorporate security into a directional wireless link, systems will require new physical-layer components and new protocols for channel estimation. For our measurements, the transmitter-to-receiver distance is considerably less than what is often envisioned for line-of-sight terahertz links for backhaul applications. Nevertheless, our results apply equally well to communication over a longer range, by scaling the transmitter and receiver gain (see Methods section 'Radiation patterns for directional horn antennas'). Our results also demonstrate the ease with which line-of-sight communications can be diverted, which could have implications other than for eavesdropping, such as for distributing signals to multiple receivers in a network.

Online content

Any methods, additional references, Nature Research reporting summaries, source data, statements of data availability and associated accession codes are available at https://doi.org/10.1038/s41586-018-0609-x.

Received: 27 April; Accepted: 9 August 2018;
Published online 15 October 2018.

1. Shiu, Y.-S., Chang, S. Y., Wu, H.-C., Huang, S. C.-H. & Chen, H.-H. Physical layer security in wireless networks: a tutorial. *IEEE Wirel. Commun.* **18**, 66–74 (2011).
2. Yang, N. et al. Safeguarding 5G wireless communication networks using physical layer security. *IEEE Commun. Mag.* **53**, 20–27 (2015).
3. Zou, Y., Zhu, J., Wang, X. & Hanzo, L. A survey on wireless security: technical challenges, recent advances, and future trends. *Proc. IEEE* **104**, 1727–1765 (2016).
4. Sun, L. & Du, Q. Physical layer security with its application in 5G networks: a review. *China Commun.* **14**, 1–14 (2017).
5. Ju, Y., Wang, H.-M., Zheng, T.-X., Yin, Q. & Lee, M. H. Safeguarding millimeter wave communications against randomly located eavesdroppers. *IEEE Trans. Wirel. Commun.* **17**, 2675–2689 (2018).
6. Gao, W. et al. High-contrast terahertz wave modulation by gated graphene enhanced by extraordinary transmission through ring apertures. *Nano Lett.* **14**, 1242–1248 (2014).
7. Karl, N. J., McKinney, R. W., Monnai, Y., Mendis, R. & Mittleman, D. M. Frequency-division multiplexing in the terahertz range using a leaky-wave antenna. *Nat. Photon.* **9**, 717–720 (2015).
8. Reichel, K. S., Mendis, R. & Mittleman, D. M. A broadband terahertz waveguide T-junction variable power splitter. *Sci. Rep.* **6**, 28925 (2016).
9. Hermelo, M. F., Shih, P.-T. B., Steeg, M., Ng'oma, A. & Stöhr, A. Spectral efficient 64-QAM-OFDM terahertz communication link. *Opt. Express* **25**, 19360–19370 (2017).
10. Ma, J., Karl, N. J., Bretin, S., Ducournau, G. & Mittleman, D. M. Frequency-division multiplexer and demultiplexer for terahertz wireless links. *Nat. Commun.* **8**, 729 (2017).
11. Ma, J., Shrestha, R., Moeller, L. & Mittleman, D. M. Channel performance of indoor and outdoor terahertz wireless links. *APL Photon.* **3**, 051601 (2018).
12. Steinmetzer, D., Chen, J., Classen, J., Knightly, E. & Hollick, M. Eavesdropping with periscopes: experimental security analysis of highly directional millimeter waves. In *Proc. IEEE Conf. Commun. Netw. Security (CNS)* 335–343 (IEEE, 2015).
13. Zhu, Y., Wang, L., Wong, K.-K. & Heath, R. W. Secure communications in millimeter wave ad hoc networks. *IEEE Trans. Wirel. Commun.* **16**, 3205–3217 (2017).
14. Federici, J. & Moeller, L. Review of terahertz and subterahertz wireless communications. *J. Appl. Phys.* **107**, 111101 (2010).
15. Akyildiz, I. F., Jornet, J. M. & Han, C. Terahertz band: next frontier for wireless communications. *Phys. Commun.* **12**, 16–32 (2014).
16. Kürner, T. & Priebe, S. Towards THz communications – status in research, standardization and regulation. *J. Infrared Millim. THz Waves* **35**, 53–62 (2014).
17. Vuppala, S., Biswas, S. & Ratnarajah, T. An analysis on secure communications in millimeter/micro-wave hybrid networks. *IEEE Trans. Commun.* **64**, 3507–3519 (2016).
18. Kim, M., Hwang, E. & Kim, J.-N. Analysis of eavesdropping attack in mmWave-based WPANs with directional antennas. *Wirel. Netw.* **23**, 355–369 (2017).
19. Pierpoint, M. & Rebeiz, G. M. Paving the way for 5G realization and mmWave communication systems. *Mirowave J.* **59**, 106–108 (2016).
20. Xu, J. et al. Statistical analysis of path losses for sectorized wireless networks. *IEEE Trans. Commun.* **65**, 1828–1838 (2017).
21. Babakhani, A., Rutledge, D. B. & Hajimiri, A. Transmitter architectures based on near-field direct antenna modulation. *IEEE J. Solid-State Circuits* **43**, 2674–2692 (2008).
22. Djordjevic, I. B. Multidimensional OAM-based secure high-speed wireless communications. *IEEE Access* **5**, 16416–16428 (2017).
23. Rifà-Pous, H. & Herrera-Joancomarti, J. Computational and energy costs of cryptographic algorithms on handheld devices. *Future Internet* **3**, 31–48 (2011).
24. Headland, D., Monnai, Y., Abbott, D., Fumeaux, C. & Withayachumnankul, W. Tutorial: terahertz beamforming, from concept to realizations. *APL Photon.* **3**, 051101 (2018).
25. Song, H.-J. & Nagatsuma, T. Present and future of terahertz communications. *IEEE Trans. THz Sci. Technol.* **1**, 256–263 (2011).
26. Koenig, S. et al. Wireless sub-THz communication system with high data rate. *Nat. Photon.* **7**, 977–981 (2013).
27. Ducournau, G. et al. Ultrawide-bandwidth single-channel 0.4-THz wireless link combining broadband quasi-optic photomixer and coherent detection. *IEEE Trans. THz Sci. Technol.* **4**, 328–337 (2014).
28. Barros, J. & Rodrigues, M. R. D. Secrecy capacity of wireless channels. In *Proc. IEEE Symp. Inform. Theory* 356–360 (IEEE, 2006).
29. Csiszár, I. & Körner, J. Broadcast channels with confidential messages. *IEEE Trans. Inf. Theory* **24**, 339–348 (1978).
30. Petrov, V., Komarov, M., Moltchanov, D., Jornet, J. M. & Koucheryavy, Y. Interference and SINR in millimeter wave and terahertz communication systems with blocking and directional antennas. *IEEE Trans. Wirel. Commun.* **16**, 1791–1808 (2017).
31. Ma, J., Moeller, L. & Federici, J. F. Experimental comparison of terahertz and infrared signaling in controlled atmospheric turbulence. *J. Infrared Millimeter THz Waves* **36**, 130–143 (2015).

© 2018 Springer Nature Limited. All rights reserved.

32. Kouyoumjian, R. G. & Pathak, P. H. A uniform geometrical theory of diffraction for an edge in a perfectly conducting surface. *Proc. IEEE* **62**, 1448–1461 (1974).
33. Dorney, T. D., Symes, W. W., Baraniuk, R. G. & Mittleman, D. M. Terahertz multistatic reflection imaging. *J. Opt. Soc. Am. A* **19**, 1432–1442 (2002).

Acknowledgements This work was funded in part by the US National Science Foundation, the US Army Research Office and the W. M. Keck Foundation.

Reviewer information *Nature* thanks K.-Y. Lam and the other anonymous reviewer(s) for their contribution to the peer review of this work.

Author contributions D.M.M. and E.K. conceived the experiments. J.M., R.S. and J.A. performed the measurements. Z.H. and J.M.J. performed the computations shown as dotted lines in Fig. 3. D.M.M., E.K. and C.-Y.Y. analysed and interpreted the data. All authors contributed to the writing of the manuscript.

Competing interests The authors declare no competing interests.

Additional information
Extended data is available for this paper at https://doi.org/10.1038/s41586-018-0609-x.
Reprints and permissions information is available at http://www.nature.com/reprints.
Correspondence and requests for materials should be addressed to D.M.M.
Publisher's note: Springer Nature remains neutral with regard to jurisdictional claims in published maps and institutional affiliations.

© 2018 Springer Nature Limited. All rights reserved.

METHODS

Radiation patterns for directional horn antennas. Our transmitter consists of a waveguide-coupled horn antenna together with a dielectric lens (diameter, 5 cm; focal length, 7.5 cm). In Fig. 1, we show the measured radiation pattern for the 200-GHz transmitter (WR-5.1 conical horn) used in our measurements, as well as a computed antenna pattern using a finite-element solver. For this configuration, the measured far-field beam pattern has a directivity of 34 dBi, which corresponds to an angular full-width of about 4°. The radiation patterns for the 100-GHz and 400-GHz measurements are similar; these transmitters also use horn antennas (WR-8 conical horn and WR-2.2 diagonal horn, respectively), coupled to the same dielectric lens. The measured directivities are shown in Extended Data Table 1. As might be anticipated from simple diffraction arguments, higher frequencies produce narrower beams. Yet, even for our narrowest beam, the diameter of the beam when it reaches Bob is still twice as large as the aperture of his receiver.

Our detection system, which we use for Bob's and Eve's measurements, uses the same type of lens and horn as used for the transmitter and therefore has similar angular sensitivity. For bit error rate (BER) measurements, the transmitter signal is modulated with a pulse-pattern generator using amplitude shift keying, with a bit rate of 1 Gb s^{-1}. The detected signal is amplified and analysed in real time using a BER tester. Other specifications of our transmitter and receiver equipment are given in Extended Data Table 1, with more details in ref. [10].

Our measurement set-up is a scale model of a typically envisioned terahertz wireless link—our transmitter–receiver distance is only 2 m. Our work is not intended to emulate a real system, which would require a transmitter–receiver distance of tens or hundreds of metres. In part, this is due to the limitations of our measurement apparatus. A system designed for longer distances would probably use a higher-power transmitter, higher-gain antennas and/or a more sensitive receiver. For example, a system operating at 220 GHz was used previously[34] to achieve a data transmission rate of 3.5 Gb s^{-1} using a transmitter antenna with a gain exceeding 50 dBi. This enhanced link budget enables a scaling of the broadcast distance to 200 m. If we assume that Eve's detector sensitivity scales in the same way as Bob's, then this scaling would not only enhance Bob's ability to detect signals at larger distances but also equally enhance Eve's ability. In more complex wireless links, such as those that use multiple inputs and multiple outputs (MIMO), the issue of scaling is more subtle and requires a more detailed consideration[35]. However, for the single-transmitter, single-receiver link discussed here, a scale-model approach is valid, on the basis of the linearity of the Friis equation. Our results should apply equally well to any line-of-sight link at any range.

Measurement of S_{180}. The data shown in Fig. 2 can be used to select a limited number of configurations for further investigation. Using the criteria that b and $\bar{c}_s$ must both be less than 0.5, we down-select from the 42 different measurements displayed in Fig. 2. The remaining ten points are a representative set of configurations that illustrate successful eavesdropping situations. Eight of these are at the lowest frequency of 100 GHz and the remaining two are at 200 GHz. We measured the back-scatter parameter S_{180} for each of these ten situations; the results are shown in the inset of Fig. 3a.

These measurements are limited in the sense that we have only one receiver for detecting signals. This makes it challenging to characterize back-scattered signals that might be received by Alice, because one of the main sources of back-scattered signals is Bob's receiver. If Bob's receiver generates a back-scattered signal, then it cannot also be used to measure this signal at Alice's location. Of course, a real transmission channel may have other sources of scattering, but in our controlled laboratory environment we worked to eliminate these. To make a measurement that illustrates the point of this potentially valuable counter-measure, we created a mock-up of Bob's receiver rig using highly reflective metal tape, configured to simulate a receiver at Bob's location. We can then move our receiver to a location close to Alice and measure back-scattered signals from the mock-up. This mock-up probably does not accurately reproduce the reflections that would come from an actual receiver, but this is not relevant; any given receiver configuration will give rise to a unique pattern of reflected waves, which will also depend strongly on frequency. Our approach is intended to illustrate the potential value of using back-scatter as a counter-measure in the case of a typical receiver; the details will change depending on the receiver configuration, mounting hardware, channel distance and so on. We also recognize that Alice would need to carefully characterize her transmission channel to Bob, before any eavesdropping attack, for this counter-measure to be useful. Any changes in Bob's receiver configuration or other aspects of the channel would require a recalibration of the back-scattered signal at Alice's location. This may seem challenging, but existing 4G LTE protocols already include a channel-sounding measurement every 20 ms; this is expected to decrease to 1 ms in 5G systems.

An additional measurement challenge in our experiment is that our transmitter (Alice) is not able to also detect received signals. Therefore, we cannot measure signals in exactly the back-scattered direction (180°). Instead, we place our receiver as close as possible to this direction, limited by the size of the equipment. The measured values of S_{180} reported in Fig. 3 were obtained at an angle of about 175° and are therefore only approximate values. Nonetheless, they illustrate the key points of our discussion.

Diffracted field from a uniform metal cylinder. The three dotted curves shown in Fig. 3 were computed using an ab initio model for diffraction from a uniform cylinder made of a perfectly conducting metal[28]. In brief, if Eve is not located in the geometric shadow of the cylinder, then the power received by Eve (in units of decibels) is

$$P_{\mathrm{Eve}} = P_{\mathrm{Alice}} + G_{\mathrm{tx}} + G_{\mathrm{rx}} + 20\log|R_{\mathrm{D}}| - 20\log\left[\frac{4\pi(d_{\mathrm{i}}+d_{\mathrm{r}})}{\lambda}\right]$$

where P_{Alice} is the power transmitted by Alice, G_{tx} and G_{rx} are the gains of the transmitter and receiver, respectively, d_{i} and d_{r} are the propagation distances from the transmitter to the specular surface reflection point on the cylinder and from that point to Eve's receiver, respectively (so that their sum is the total propagation distance for a ray detected by Eve), and λ is the wavelength of the radiation. The factor R_{D} accounts for the strength of the diffracted signal. In a coordinate system centred on the central axis of the cylinder, it is given by

$$R_{\mathrm{D}} = -\exp\left(-i\frac{\pi}{4}\right)\sqrt{\frac{-4}{\xi}}\exp\left(-i\frac{\xi^3}{12}\right)\left[\frac{-F(X)}{2\xi\sqrt{\pi}} + p(\xi)\right]$$

where $\xi = -2(ka/2)X^{1/3}$, $X = 2kd_{\mathrm{i}}\cos^2(\phi)$, k is the free-space wavevector and a is the radius of the cylinder. The angle ϕ is the difference between the angle at which Eve's receiver is located and the angle of the point on the surface of the cylinder that corresponds to the specular surface reflection, both measured relative to the line from the transmitter through the centre of the cylinder. The function F is defined as

$$F(x) = 2i\sqrt{x}\,\mathrm{e}^{ix}\int_{\sqrt{x}}^{\infty}\mathrm{e}^{ju^2}\mathrm{d}u$$

and the function p is the Fock scattering function, which is defined in appendix F of ref. [36].

The beam-splitter attack. In the context of Fig. 4, we envision that Eve has the freedom to create an ideal lossless thin-film beam splitter and place it in the transmission channel at a location where the beam is small enough so that it does not illuminate the edge of the beam splitter (that is, close to Alice), as shown in the inset in Fig. 4a. This placement eliminates any edge-scattering effects. Therefore, the only effect of the beam splitter is to redirect a portion of the transmitted power towards Eve, with the remaining power continuing to Bob, undistorted. We further imagine that Eve has the freedom to choose the power-transmission coefficient of the beam splitter T to be any value between 0 and 1. In this case, we can compute directly the three relevant parameters discussed in the text. First, the blockage is given by $b = 1 - T$. From this result, we conclude that Eve must choose $T > 0.5$, or else the blockage would be too high. Second, the back-scatter parameter S_{180} is found by noting that the signal-to-noise ratio of a back-reflected signal measured by Alice is reduced by a factor of T^2 when the beam splitter is inserted (because such signals must pass through the beam splitter twice to reach Alice, once in each direction). Thus, $S_{180} = |1 - 1/T^2|$. Third, to compute the normalized secrecy capacity, we note that Eve's signal-to-noise ratio ($\mathrm{SNR}_{\mathrm{Eve}}$) is given by the product of $1 - T$ and the transmitter power, or

$$\mathrm{SNR}_{\mathrm{Eve}} = \frac{1-T}{T}\mathrm{SNR}_{\mathrm{Bob}} \tag{1}$$

where $\mathrm{SNR}_{\mathrm{Bob}}$ is the signal-to-noise ratio measured by Bob with the beam splitter in place. The normalized secrecy capacity is therefore

$$\bar{c}_{\mathrm{s}} = 1 - \frac{\log[1 + \mathrm{SNR}_{\mathrm{Bob}}(1-T)/T]}{\log(1 + \mathrm{SNR}_{\mathrm{Bob}})}$$

To proceed with this analysis and compute the value of $\bar{c}_{\mathrm{s}}$ that results when Eve uses a beam splitter with a particular value of T, we must make an assumption about Bob's signal-to-noise ratio. For the purpose of illustration, we assume that Bob is receiving sufficient signal (with the beam splitter in place) to be able to achieve a BER of 10^{-9} (that is, an error-free signal). For amplitude-shift-keying modulation, the BER is related to the signal-to-noise ratio (SNR) by

$$\mathrm{BER} = \frac{1}{4}\mathrm{e}^{-\mathrm{SNR}/4}\mathrm{erfc}\left(\sqrt{\frac{\mathrm{SNR}}{2}}\right) \tag{2}$$

where $\mathrm{erfc}(x)$ is the complimentary error function and the signal-to-noise ratio is expressed as a linear ratio (not in decibels). To achieve $\mathrm{BER}_{\mathrm{Bob}} = 10^{-9}$, a signal-to-noise ratio of about 23.3 is required.

© 2018 Springer Nature Limited. All rights reserved.

Using this assumed value for SNR_{Bob}, we can compute $\bar{c}_s$ and S_{180} for T between 0.5 and 1 (Fig. 4b). These calculations show that there is a narrow range of T for which all three criteria are satisfied: $b < 0.5$, $\bar{c}_s < 0.5$ and $S_{180} < 0.5$. In particular, the criterion on S_{180} is satisfied for $T > \sqrt{2/3} \approx 0.82$ and the criterion on $\bar{c}_s$ is satisfied for

$$T < \frac{SNR_{Bob}}{\sqrt{1 + SNR_{Bob}} + SNR_{Bob} - 1} \approx 0.86$$

This quantity is not a very strong function of SNR_{Bob}. To reduce it from 0.86 to $\sqrt{2/3}$, SNR_{Bob} would need to be diminished considerably, from about 23.3 to about 10.9. This would eliminate the range of T for which eavesdropping is possible, but at the expense of increasing BER_{Bob} by nearly four orders of magnitude. Thus, under the assumptions that we have made for parameter thresholds, Alice and Bob can prevent a successful beam-splitter attack only by operating at greatly reduced BER and by using both blockage and back-scatter as detection counter-measures.

With the same assumption of $BER_{Bob} = 10^{-9}$, we can use equations (1) and (2) to compute the BER that Eve can achieve (BER_{Eve}) when she uses a beam-splitter attack (Fig. 4b inset, solid red line). Doing so indicates that BER_{Eve} improves continuously as T decreases. If Eve is restricted to the range of T mentioned above, then the optimal value of BER_{Eve} is achieved for $T = \sqrt{2/3}$ and is 1.5×10^{-3}. Although this value may be sufficient to decode information, Eve can do much better with a smaller value of T. If the back-scatter counter-measure proposed here is not used, then Eve can use any beam splitter with $T > 0.5$, enabling her to implement an attack with a secrecy capacity arbitrarily close to zero and thus achieve a BER essentially equal to that of Bob.

The above analysis assumes that the transmitter produces zero side lobes. Although small, the side lobes cannot be exactly zero. Therefore, in the beam-splitter configuration depicted in the inset of Fig. 4a, Eve would measure not only the signal from the beam splitter but also a small contribution from side lobes, which would effectively degrade her BER through added interference. The inset of Fig. 4b also contains a few measured data points (open squares), which quantify this effect. The data reproduce the predicted trend in BER_{Eve}, but with a slightly worse BER than predicted. This is presumably due to the effect of side-lobe interference, which amounts to an extra roughly 3 dB of noise.

To make these measurements, we fabricated a few large-aperture beam splitters (no such devices are commercially available for these frequencies). To avoid etalon effects, which could introduce substantial phase distortion that would artificially decrease the BER, we fabricated the beam splitters on very thin low-loss polyethylene substrates[37]. These substrates were stretched across a circular metal frame with a large enough diameter to encompass the beam at the output of Alice's transmitter without much scattering from the frame. The polyethylene films were then coated with a thin metal layer, using a metallic spray paint. The paint adhered well to the surface and coated it uniformly. By varying the thickness of this metal layer, we fabricated beam splitters with different values of T, which were determined experimentally.

Data availability

The data that support the findings of this study are available from the corresponding author on reasonable request.

34. Chen, Z. et al. 220 GHz outdoor wireless communication system based on a Schottky diode transceiver. *IEICE Electron. Express* **13**, 1–9 (2016).
35. Yeh, C.-Y. & Knightly, E. W. Feasibility of passive eavesdropping in massive MIMO: an experimental approach. In *Proc. IEEE Conf. Commun. Netw. Security (CNS)* 1–9 (IEEE, 2018).
36. McNamara, D. A., Pistorius, C. W. I. & Malherbe, J. A. G. *Introduction to the Uniform Geometrical Theory of Diffraction* (Artech House, Boston, 1990).
37. Ung, B. S.-Y. et al. Low-cost ultra-thin broadband terahertz beam-splitter. *Opt. Express* **20**, 4968–4978 (2012).

© 2018 Springer Nature Limited. All rights reserved.

Extended Data Table 1 | Specifications for the terahertz wireless communication system

Carrier Frequency	100 GHz	200 GHz	400 GHz
IF frequency	1 GHz		
LO frequency	12.25 GHz		
PRBS	$2^7 - 1$		
Max. Tx output power	24 dBm	20 dBm	10 dBm
Tx/Rx antenna gain	21 dB	21 dB	26 dB
Tx beam directivity (angular full-width)	28 dBi (7.8º)	34 dBi (4º)	42 dBi (1.6º)
Detector responsivity	2400 V/W	6200 V/W	1700 V/W
Detector NEP	3 pW/√Hz	3 pW/√Hz	1.9 pW/√Hz
Tx/Rx polarization	vertical		

© 2018 Springer Nature Limited. All rights reserved.

https://doi.org/10.1038/s41586-018-0626-9

Gate-tunable room-temperature ferromagnetism in two-dimensional Fe_3GeTe_2

Yujun Deng[1,2,3,7], Yijun Yu[1,2,3,7], Yichen Song[1,2,3], Jingzhao Zhang[4], Nai Zhou Wang[2,5,6], Zeyuan Sun[1,2], Yangfan Yi[1,2], Yi Zheng Wu[1,2], Shiwei Wu[1,2,3], Junyi Zhu[4], Jing Wang[1,2], Xian Hui Chen[2,5,6] & Yuanbo Zhang[1,2,3]*

Materials research has driven the development of modern nanoelectronic devices. In particular, research in magnetic thin films has revolutionized the development of spintronic devices[1,2] because identifying new magnetic materials is key to better device performance and design. Van der Waals crystals retain their chemical stability and structural integrity down to the monolayer and, being atomically thin, are readily tuned by various kinds of gate modulation[3,4]. Recent experiments have demonstrated that it is possible to obtain two-dimensional ferromagnetic order in insulating $Cr_2Ge_2Te_6$ (ref. [5]) and CrI_3 (ref. [6]) at low temperatures. Here we develop a device fabrication technique and isolate monolayers from the layered metallic magnet Fe_3GeTe_2 to study magnetotransport. We find that the itinerant ferromagnetism persists in Fe_3GeTe_2 down to the monolayer with an out-of-plane magnetocrystalline anisotropy. The ferromagnetic transition temperature, T_c, is suppressed relative to the bulk T_c of 205 kelvin in pristine Fe_3GeTe_2 thin flakes. An ionic gate, however, raises T_c to room temperature, much higher than the bulk T_c. The gate-tunable room-temperature ferromagnetism in two-dimensional Fe_3GeTe_2 opens up opportunities for potential voltage-controlled magnetoelectronics[7–11] based on atomically thin van der Waals crystals.

Atomically thin, layered van der Waals crystals represent ideal two-dimensional (2D) material systems with exceptional electronic structures. Vast opportunities in 2D material research arise from (1) emerging physical properties as a result of reduced dimensionality, and (2) new gating capabilities to modulate the material properties now that the entire crystal is a surface. The former underpins the rapid permeation of 2D materials in areas ranging from semiconductors to highly correlated materials and superconductors. The trend continues with the recent addition of magnetic crystals in the 2D material family[5,6]. In particular, ferromagnetic order has been observed in monolayer CrI_3 in the form of a 2D Ising ferromagnet[6]. The intrinsic ferromagnetism in these 2D materials is unlike the ferromagnetism in conventional, molecular-beam-epitaxy-grown ultrathin metals[12,13], which is determined by the interface with the substrate. This suggests device concepts based on magnetic van der Waals heterostructures[14–16].

Here we report the discovery of 2D itinerant ferromagnetism in atomically thin Fe_3GeTe_2 (FGT). As in the case of CrI_3, intrinsic magnetocrystalline anisotropy in FGT monolayers counteracts thermal fluctuations and preserves the 2D long-range ferromagnetic order, which is otherwise precluded in an isotropic magnetic system according to the Mermin–Wagner theorem[17]. FGT, however, offers a critical advantage: its metallic nature enables the interplay of both spin and charge degrees of freedom that lies at the heart of various spintronic architectures[18]. In this study we focus on the large anomalous Hall effect resulting from such interplay. The anomalous Hall effect enables us to extract the ferromagnetic transition temperature T_c, and elucidate the evolution of the magnetic order from bulk down to monolayer FGT. Taking advantage of the tunability of atomically thin crystals, we further show that extreme doping induced by an ionic gate dramatically elevates T_c to room temperature, accompanied by large modulations in the coercivity. These results establish FGT as a room-temperature ferromagnetic 2D material in addition to VSe_2 (ref. [19]), and the gate tunability makes FGT potentially suitable for electrically controlled magnetoelectronic devices.

Various metallic layered compounds exhibit magnetism[20]. Among them FGT stands out with a relatively high T_c (ranging from 150 K to 220 K depending on Fe occupancy[21–24]). In each FGT monolayer, covalently bonded Fe_3Ge heterometallic slab is sandwiched between two Te layers (Fig. 1b). The structure and valence states of the compound can be written as $(Te^{2-})(Fe_I^{3+})[(Fe_{II}^{2+})(Ge^{4-})](Fe_I^{3+})(Te^{2-})$ per formula unit with two inequivalent Fe sites, Fe_I^{3+} and Fe_{II}^{2+}, within the Fe_3Ge slab[22]. Partially filled Fe *d* orbitals dominate the band structure around the Fermi level, and give rise to itinerant ferromagnetism in bulk FGT[25]. Adjacent monolayers are separated by a 2.95 Å van der Waals gap in the bulk crystal. As a result of the reduced crystal symmetry of the layered structure, bulk FGT exhibits a strong magnetocrystalline anisotropy[25]. Such anisotropy is expected to stabilize the long-range ferromagnetic order in FGT monolayers.

Experimentally isolating atomically thin FGT crystals from the bulk, however, poses a challenge. Although bulk FGT cleaves along the van der Waals gap, the intralayer bonding is not strong enough for thin flakes of reasonable size (about 5 μm) to survive conventional mechanical exfoliation processes. Similar issues plague the exfoliation of many other layered materials (only a small fraction of known layered crystals is cleavable down to monolayers), and have largely impeded the research on 2D materials in general.

To address this problem, we developed an Al_2O_3-assisted exfoliation method that enables isolation of monolayers from bulk layered crystals that are otherwise difficult to exfoliate using conventional methods. Our method was inspired by the gold-mediated exfoliation of layered transition-metal chalcogenide compounds[26,27]. The fabrication process is illustrated step by step in Fig. 1a. We started by covering the freshly cleaved surface of the bulk crystal with Al_2O_3 thin film with thicknesses ranging from 50 nm to 200 nm. The film was deposited by thermally evaporating Al under an oxygen partial pressure of 10^{-4} mbar. We then used a thermal release tape to pick up the Al_2O_3 film, along with pieces of FGT microcrystals separated from the bulk. The Al_2O_3/FGT stack was subsequently released onto a piece of polydimethylsiloxane (PDMS) upon heating, with the FGT side in contact with the PDMS surface. Next, we stamped the PDMS/FGT/Al_2O_3 assembly onto a substrate and quickly peeled away the PDMS, leaving the Al_2O_3 film covered with freshly cleaved FGT flakes on the substrate. Figure 1c displays an optical image of atomically thin FGT flakes on Al_2O_3 film supported on a 285-nm SiO_2/Si substrate. Mono- to trilayer regions of FGT are clearly resolved by the optical contrast. The layer identification was corroborated by direct topography measurements with an atomic

[1]State Key Laboratory of Surface Physics and Department of Physics, Fudan University, Shanghai, China. [2]Collaborative Innovation Center of Advanced Microstructures, Nanjing University, Nanjing, China. [3]Institute for Nanoelectronic Devices and Quantum Computing, Fudan University, Shanghai, China. [4]Department of Physics, The Chinese University of Hong Kong, Shatin, Hong Kong, China. [5]Hefei National Laboratory for Physical Science at Microscale and Department of Physics, University of Science and Technology of China, Hefei, China. [6]Key Laboratory of Strongly Coupled Quantum Matter Physics, University of Science and Technology of China, Hefei, China. [7]These authors contributed equally: Yujun Deng, Yijun Yu. *e-mail: zhyb@fudan.edu.cn

© 2018 Springer Nature Limited. All rights reserved.

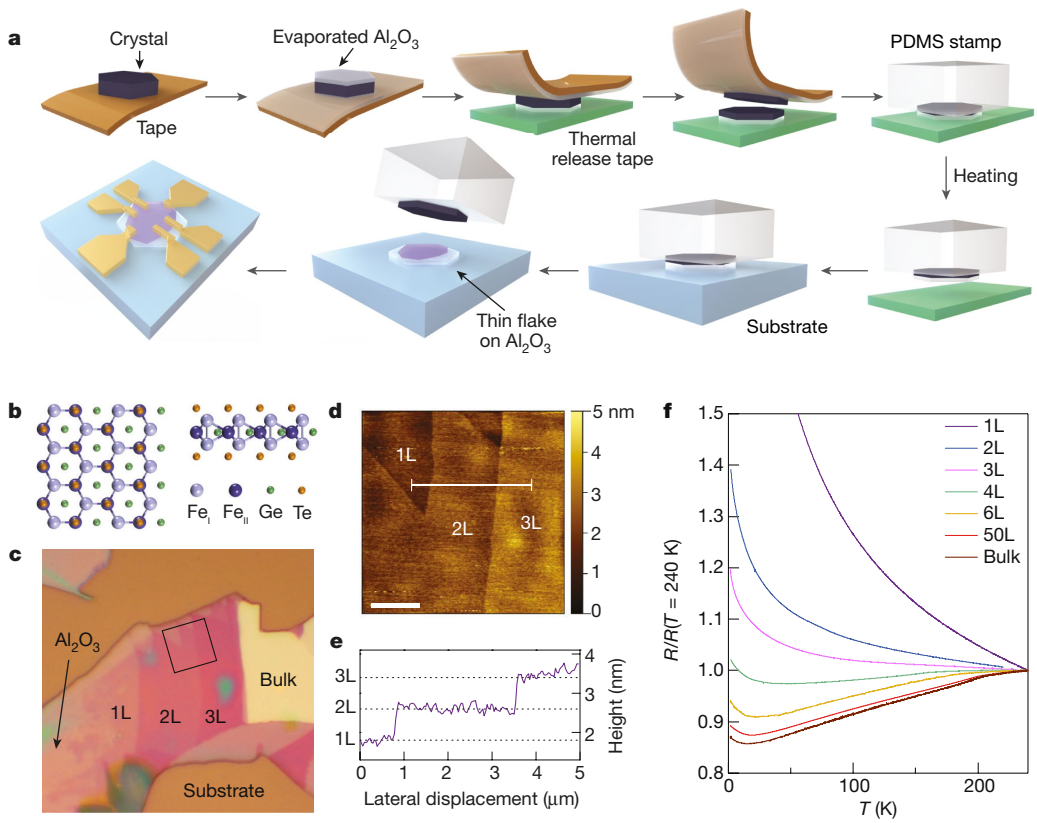

Fig. 1 | Fabrication and characterization of atomically thin FGT devices. a, Schematic of our Al_2O_3-assisted mechanical exfoliation method. The method uses an Al_2O_3 film evaporated onto the bulk crystal to cleave layered materials. The strong adhesion between the crystal and the Al_2O_3 film makes it possible to exfoliate layered crystals that are otherwise difficult to cleave from SiO_2 surfaces using conventional methods. **b**, Atomic structure of monolayer FGT. The left panel shows the view along [001]; the right panel shows the view along [010]. Bulk FGT is a layered crystal with an interlayer van der Waals gap of 2.95 Å (ref. [22]). Fe_I and Fe_{II} represent the two inequivalent Fe sites in the +3 and +2 oxidation states, respectively. **c**, Optical image of typical few-layer FGT flakes exfoliated on top of an Al_2O_3 thin film. The Al_2O_3 film is supported on an Si wafer covered with 285-nm SiO_2. **d**, Atomic force microscopy image of the area marked by the square in **c**. Mono- and few-layer flakes of FGT are clearly visible. Scale bar, 2 μm. **e**, Cross-sectional profile of the FGT flakes along the white line in **d**. The steps are 0.8 nm in height, consistent with the thickness of monolayer (1L) FGT (0.8 nm). **f**, Temperature-dependent sample resistance of FGT with varying number of layers up to 6L. Resistances are normalized by their values at $T = 240$ K. The typical behaviour of bulk FGT (brown) is also shown for reference.

force microscope; the 0.8-nm steps in the height profile exactly match the FGT monolayer thickness (Fig. 1d, e). We then fabricated electrodes on FGT thin flakes, either with direct metal deposition through stencil masks or with indium cold welding, for subsequent transport measurements. The entire device fabrication process was performed in an argon atmosphere with O_2 and H_2O content kept below 0.5 parts per million to avoid sample degradation. Details of the sample exfoliation and electrode fabrication are presented in the Methods. Finally, we point out that even though we focus only on FGT in this study, the method should be applicable to a wide variety of van der Waals crystals. We attribute the drastically enhanced exfoliation capability to higher affinity, as well as increased contact area, between the evaporated Al_2O_3 film and the freshly cleaved FGT surface.

We study the magnetism in FGT by probing the Hall resistance, R_{xy}, under an external magnetic field, $\mu_0 H$, applied perpendicular to the van der Waals plane. In our samples, which typically have a van der Pauw configuration, the fact that R_{xy} is antisymmetric with respect to the polarity of $\mu_0 H$, whereas magnetoresistance is symmetric, enables us to use a standard symmetrization procedure[28] to separate the contribution of magnetoresistance from the raw Hall voltage data. For a magnetic material, R_{xy} can be decomposed into two parts:

$$R_{xy} = R_{NH} + R_{AH} \quad (1)$$

where $R_{NH} = R_0 \mu_0 H$ is the normal Hall resistance, and $R_{AH} = R_S M$ the anomalous Hall resistance; R_0 and R_S are coefficients characterizing the strength of R_{NH} and R_{AH}, respectively, and M is the magnetization. Crucial information on the long-range magnetic order, which is contained in M, can therefore be extracted from the anomalous Hall resistance.

As the layer number is reduced in FGT flakes, the samples become progressively more insulating (Fig. 1f), but ferromagnetism persists down to the monolayer. Unambiguous evidence comes from the clear hysteresis in R_{xy} for all FGT thin flakes (with thickness ranging from monolayer to 50 layers; Fig. 2a) under investigation at low temperatures. Such hysteresis reflects the hysteresis in M; the remanent M at $\mu_0 H = 0$ signifies spontaneous magnetization, and thus the long-range ferromagnetic order. Raising the temperature introduces thermal fluctuations, and ferromagnetism eventually disappears above T_c. In Fig. 2b, measurements of R_{xy} show that ferromagnetism in samples with various layer numbers responds differently to thermal fluctuations: at an elevated temperature of $T = 100$ K hysteresis vanishes in mono- and bilayer samples, but survives in thicker crystals. The observation clearly indicates a strong dimensionality effect on ferromagnetism in atomically thin FGT.

To fully elucidate such a dimensionality effect, we precisely determine T_c as a function of layer number from the temperature dependence of the anomalous Hall effect. For each sample thickness, we examine the remanent Hall resistance at zero external magnetic field, $R_{xy}^{r} \equiv R_{xy}|_{\mu_0 H=0}$, as a function of temperature. According to equation (1), R_{xy}^{r} is directly proportional to the zero-field spontaneous magnetization $M|_{\mu_0 H=0}$. So the onset of non-zero R_{xy}^{r} indicates the emergence of spontaneous magnetization. The temperature at the onset of non-zero R_{xy}^{r} therefore marks T_c (Fig. 2c)[28]. Analyses of various

© 2018 Springer Nature Limited. All rights reserved.

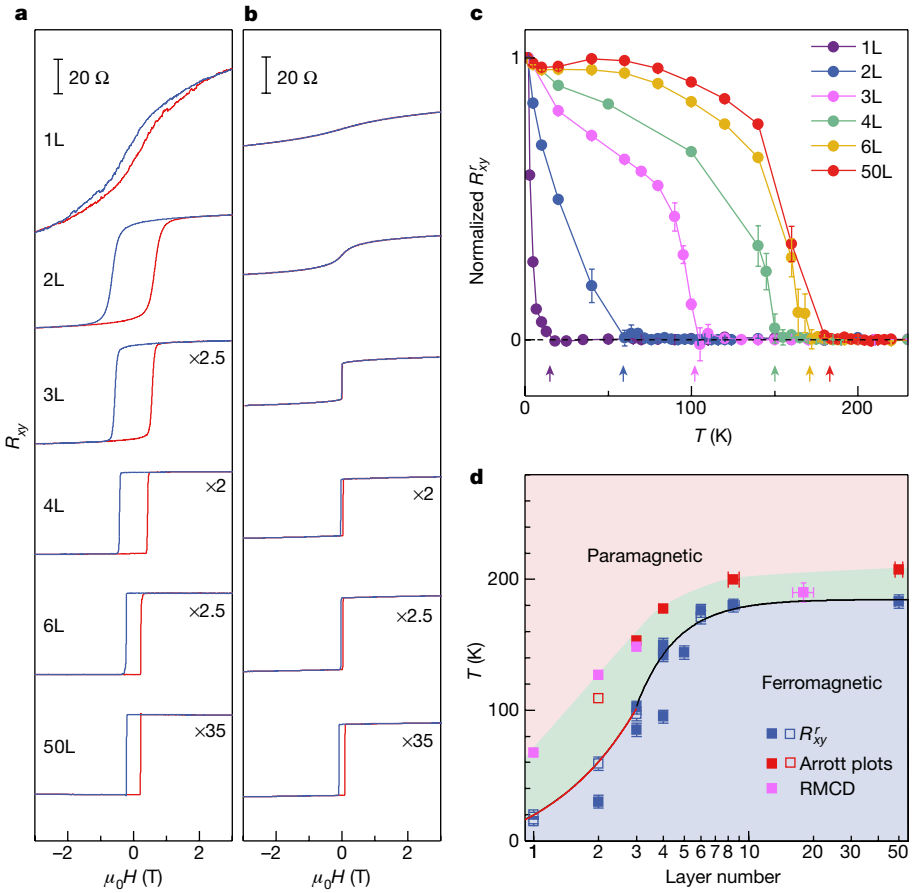

Fig. 2 | Ferromagnetism in atomically thin FGT. a, **b**, R_{xy} at low temperature (**a**) and at $T = 100$ K (**b**) obtained in FGT thin-flake samples with varying numbers of layers. Ferromagnetism, evidenced by the hysteresis in low-temperature R_{xy}, is observed in all atomically thin FGT down to the monolayer. At $T = 100$ K, hysteresis disappears in mono- and bilayer FGT, but persists in thicker specimens. All the low-temperature data were obtained at $T = 1.5$ K except for the monolayer data, which were recorded at $T = 3$ K. **c**, Remanent anomalous Hall resistance R^r_{xy} as a function of temperature obtained from FGT thin-flake samples with varying numbers of layers. R^r_{xy} data are normalized by their values at $T = 1.5$ K, except for the monolayer dataset, which is normalized by the value at $T = 3$ K. Arrows mark the ferromagnetic transition temperature T_c. Vertical error bars represent the standard deviation of R^r_{xy} values within 1 mT of zero magnetic field; 1 mT is the uncertainty in reading the magnetic field during field sweeps. **d**, Phase diagram of FGT as layer number and temperature are varied. T_c values determined from anomalous Hall effect, Arrott plots and RMCD are displayed in blue, red and magenta, respectively. Filled red and blue squares represent data obtained from samples with thermally evaporated Cr/Au electrodes, and open squares represent data obtained from samples with cold-welded indium microelectrodes. The black line is a fit to $T_c(N)$ (for $N \geq 3$) with the finite-size scaling formula and the red line is a line fit to $T_c(N)$ for $N \leq 3$ (see Methods for scaling analysis). Blue and pink regions mark the ferromagnetic and paramagnetic phases, respectively. The green region in between represents a ferromagnetically ordered phase with domains (see text). Horizontal error bars represent uncertainties in determining the sample thickness from optical contrast or atomic force microscope measurements. Vertical error bars represent uncertainties in locating the onset of non-zero R^r_{xy} (in **c**) or the RMCD signal (in Extended Data Fig. 4f).

sample thicknesses reveals that T_c decreases monotonically as the samples are thinned down, from about 180 K in the bulk limit to 20 K in a monolayer (Fig. 2d). The one-order-of-magnitude decrease in T_c implies a dramatic reduction in the energy scale of magnetic ordering in 2D FGT. Meanwhile, we also used polar refractive magnetic circular dichroism (RMCD) microscopy to measure layer-dependent T_c (Fig. 2d). We found that T_c values from RMCD measurements are consistently higher than those from anomalous Hall effect measurements. Because the anomalous Hall effect probes ferromagnetic ordering in the whole sample (with a typical size of about 100 μm) and RMCD detects local ordering (with a laser beam spot of about 2 μm), the large discrepancy signifies the existence of domains well above the T_c from measurements of the anomalous Hall effect. Analysis of Arrott plots (see Methods for details) provides further insights into the domain structure. The plots determine T_c by extrapolating high-field data, where domains are fully aligned. T_c values from Arrott plots agree well with those from RMCD measurements, which implies that the domain size is of the same order of the beam spot size in our RMCD measurements, that is, about 2 μm.

The strong dimensionality effect on the ferromagnetism in FGT stems from the fundamental role of thermal fluctuation in 2D. The itinerant ferromagnetism in FGT is, in principle, described by the Stoner model[22,25]. It has, however, been established that such itinerant ferromagnetism can be mapped on to a classical Heisenberg model with Ruderman–Kittel–Kasuya–Yosida (RKKY) exchange[29]. Armed with this insight, we adopt the following anisotropic Heisenberg Hamiltonian:

$$H = \sum_{i,j} J_{ij} \boldsymbol{S}_i \cdot \boldsymbol{S}_j + \sum_i A(S_i^z)^2 \qquad (2)$$

where $\boldsymbol{S}_i$ is the spin operator on site i, and J_{ij} is the exchange coupling between spins on site i and j; A is the single-ion perpendicular magnetocrystalline anisotropy arising from spin–orbital coupling. In the three-dimensional (3D) limit, the density of states per spin for the magnon modes is strongly suppressed, so thermal fluctuations destroy the long-range magnetic order only at a finite T_c determined primarily by exchange interactions J_{ij} (ref. [5]). The bulk T_c of approximately 200 K

© 2018 Springer Nature Limited. All rights reserved.

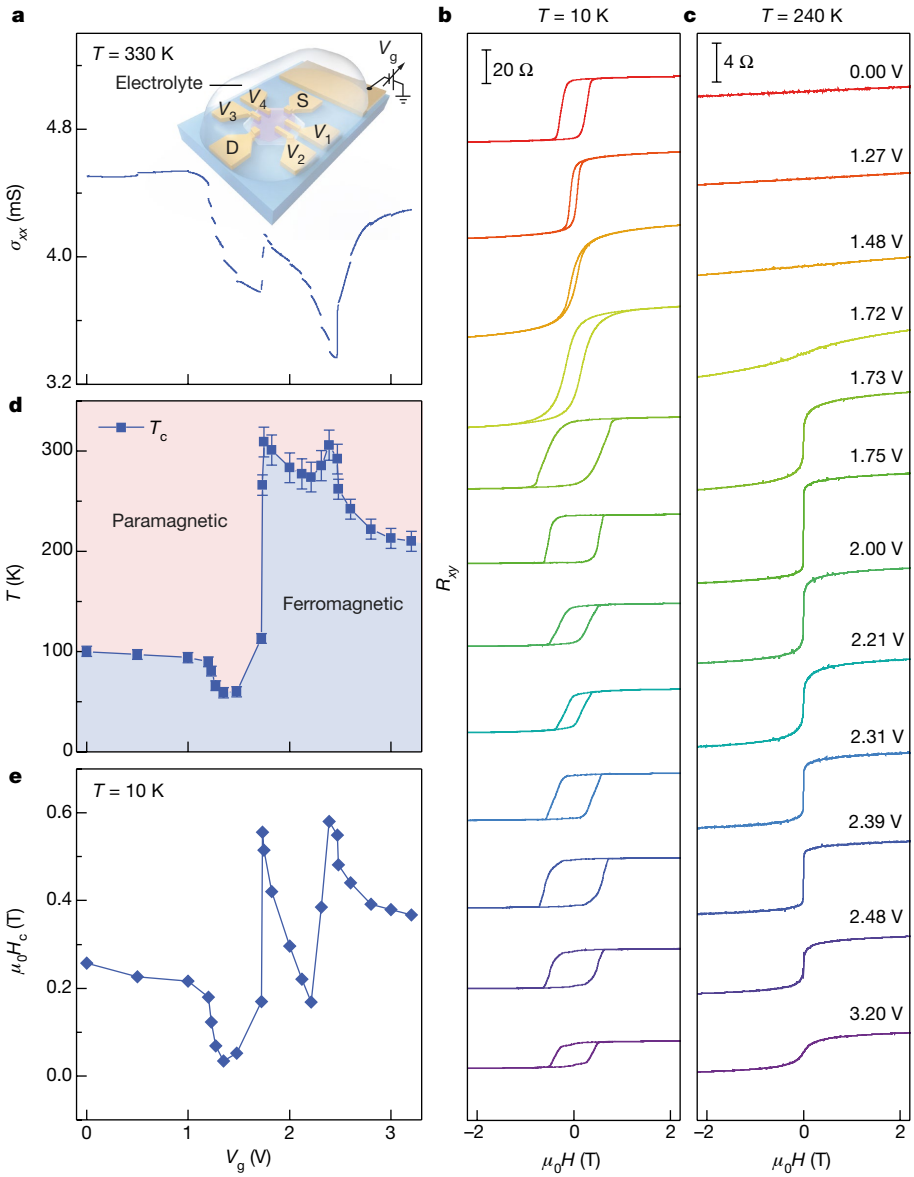

Fig. 3 | Ferromagnetism in an atomically thin FGT flake modulated by an ionic gate. a, Conductance as a function of gate voltage V_g measured in a trilayer FGT device. Data were obtained at $T = 330$ K. Breaks in the curve were caused by temperature-dependent measurements at fixed gate voltages during the gate sweep. The inset shows a schematic of the FGT device structure and measurement setup. S and D label the source and drain electrodes, respectively, and V_1, V_2, V_3 and V_4 label the voltage probes. The solid electrolyte ($LiClO_4$ dissolved in polyethylene oxide matrix) covers both the FGT flake and the side gate. **b**, **c**, R_{xy} as a function of external magnetic field recorded at representative gate voltages, obtained at $T = 10$ K (**b**) and $T = 240$ K (**c**). **d**, Phase diagram of the trilayer FGT sample as the gate voltage and temperature are varied. We determine the transition temperature from temperature-dependent anomalous Hall resistance extrapolating to zero (see Methods and Extended Data Fig. 7a). Vertical error bars represent the uncertainties in determining the onset of non-zero R_{xy}^{r} in Extended Data Fig. 7a. **e**, Coercive field as a function of the gate voltage. Data were obtained at $T = 10$ K.

implies that the energy scale of J_{ij} (summed over nearest neighbours) in FGT is of the order of 10 meV. In monolayer FGT, however, the largely isotropic exchange couplings J_{ij} (see Methods for detailed ab initio calculations) alone will not be able to sustain magnetic order at finite temperatures because of thermal fluctuations of the long-wavelength gapless magnon modes in 2D. In this case, the magnetocrystalline anisotropy A gives rise to an energy gap in the magnon dispersion. The gap suppresses low-frequency, long-wavelength magnon excitations, and protects the magnetic order below a finite T_c determined primarily by A. A monolayer T_c up to 68 K (from RMCD measurement) implies an A value of the order of 2.0 meV. The estimations of both exchange interactions and magnetocrystalline anisotropy fall in the range predicted by ab initio calculations[25,30] (see also Methods). The magnetocrystalline anisotropy corresponds to a uniaxial energy density parameter K_u on the order of 10^6 J m^{-3}. The estimated K_u is consistent with the value measured in bulk FGT[31], and is one order of magnitude larger than the perpendicular anisotropy energy density in a 1.3-nm-thick CoFeB film[32]. The large intrinsic perpendicular anisotropy will be important to enable the realization of stable, compact spintronic devices.

Even though T_c is suppressed in atomically thin FGT, we now demonstrate that an ionic gate could drastically modulate the ferromagnetism in FGT thin flakes, and boost T_c up to room temperature. We employ an ionic field-effect transistor setup, in which solid electrolyte ($LiClO_4$ dissolved in polyethylene oxide matrix) covers both the FGT thin flake and a side gate[4] (inset to Fig. 3a). A positive gate voltage, V_g, intercalates lithium ions into the FGT thin flake, much like the charging process in a lithium-ion battery. The charge transfer between lithium ions and the host crystal induces electron doping up to the order of 10^{14} cm^{-2} per layer[4]. The high doping level effects a

© 2018 Springer Nature Limited. All rights reserved.

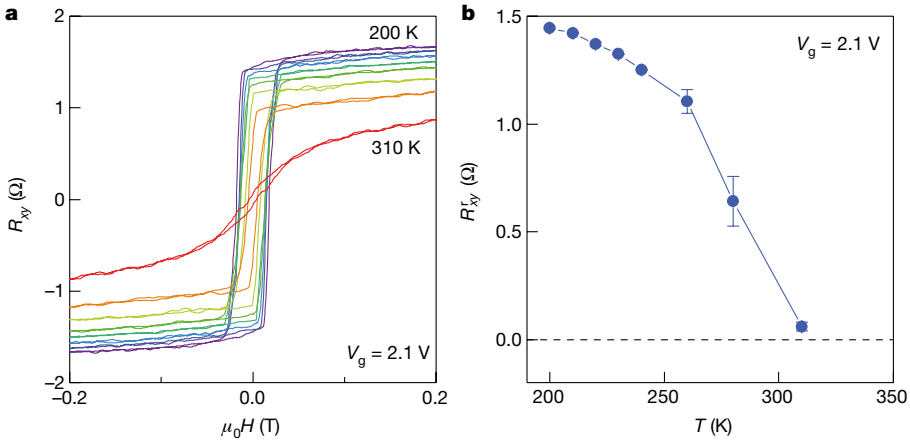

Fig. 4 | Direct observation of room-temperature ferromagnetism in atomically thin FGT. a, R_{xy} of a four-layer FGT flake under a gate voltage of $V_g = 2.1$ V. We have subtracted a background in R_{xy} resulting from the slow drifting of lithium ions in the electrolyte under the gate bias above $T = 250$ K (ref. [33]). Hysteresis in R_{xy} persists up to $T = 310$ K, providing unambiguous evidence for room-temperature ferromagnetism in the sample. **b**, Remanent Hall resistance R^r_{xy} as a function of temperature. Extrapolating R^r_{xy} to zero yields a T_c higher than 310 K. Error bars for R^r_{xy} are obtained as in Fig. 2c.

profound change in the ferromagnetism in the FGT thin flake. Figure 3b, c displays the R_{xy} of a trilayer sample obtained at $T = 10$ K and $T = 240$ K, respectively. A moderate V_g of a few volts induces large variations in the coercivity of the ferromagnetic FGT, and the ferromagnetism, manifested as a finite R^r_{xy}, persists at high temperatures under certain gate doping. Indeed, detailed analysis reveals that T_c is strongly modulated by the ionic gate, with the highest T_c reaching room temperature ($T = 300$ K; Fig. 3d). The gate-induced room-temperature ferromagnetism is also directly observed in a four-layer sample as shown in Fig. 4. (The room-temperature remanence is low, but this may be improved by, for example, interfacing the sample with an antiferromagnetic insulator.) T_c as a function of the gate voltage exhibits a complex pattern: after an initial drop, T_c increases sharply to room temperature at $V_g = 1.75$ V. T_c peaks again at $V_g = 2.39$ V on top of an otherwise slowly declining trend as the doping level increases (Fig. 3d; see Methods for details). The variation in T_c is accompanied by changes in the sample conductance, σ_{xx}, obtained at $T = 330$ K (Fig. 3a). In particular, the two peaks in T_c coincide with sudden increases in σ_{xx}, suggesting changes in the electronic structure as the origin of the magnetism modulation. Finally, we note that the coercivity measured at $T = 10$ K also roughly follows the variations in T_c, as shown in Fig. 3e.

The gate-tuned ferromagnetism in atomically thin FGT is consistent with the Stoner model, which describes itinerant magnetic systems. The Stoner criterion implies that the formation of ferromagnetic order is dictated by the density of states (DOS) at the Fermi level. The extreme electron doping induced by the ionic gate causes a substantial shift of the electronic bands of FGT. Consequently, the large variation in the DOS at the Fermi level leads to appreciable modulation in the ferromagnetism. Detailed calculations support such a picture. Specifically, our calculation shows that gate-induced electrons sequentially fill the sub-bands originating from the Fe d_{z^2}, d_{xz} and d_{yz} orbitals, leading to sharp peaks in the DOS that correspond to the Fermi level passing through the flat band edges of the sub-bands (see Methods and Extended Data Fig. 10a). Such DOS peaks may be responsible for the sharp increase of T_c and the corresponding sudden jump in σ_{xx}. Meanwhile, calculations indicate that change in the average magnet moment per Fe atom is minimal (less than 3%) under charge doping (see Methods and Extended Data Fig. 10b). This result suggests that the gate-tuned coercivity shown in Fig. 3e may in fact reflect the large modulation in the anisotropy energy, although we cannot rule out effects from domain nucleation that complicates the correlation between coercivity and anisotropy.

Online content

Any methods, additional references, Nature Research reporting summaries, source data, statements of data availability and associated accession codes are available at https://doi.org/10.1038/s41586-018-0626-9.

Received: 6 March 2018; Accepted: 7 August 2018;
Published online 22 October 2018.

1. Žutić, I., Fabian, J. & Das Sarma, S. Spintronics: fundamentals and applications. *Rev. Mod. Phys.* **76**, 323–410 (2004).
2. Hellman, F. et al. Interface-induced phenomena in magnetism. *Rev. Mod. Phys.* **89**, 025006 (2017).
3. Ye, J. T. et al. Superconducting dome in a gate-tuned band insulator. *Science* **338**, 1193–1196 (2012).
4. Yu, Y. et al. Gate-tunable phase transitions in thin flakes of 1T-TaS_2. *Nat. Nanotechnol.* **10**, 270–276 (2015).
5. Gong, C. et al. Discovery of intrinsic ferromagnetism in two-dimensional van der Waals crystals. *Nature* **546**, 265–269 (2017).
6. Huang, B. et al. Layer-dependent ferromagnetism in a van der Waals crystal down to the monolayer limit. *Nature* **546**, 270–273 (2017).
7. Matsukura, F., Tokura, Y. & Ohno, H. Control of magnetism by electric fields. *Nat. Nanotechnol.* **10**, 209–220 (2015).
8. Jiang, S., Shan, J. & Mak, K. F. Electric-field switching of two-dimensional van der Waals magnets. *Nat. Mater.* **17**, 406–410 (2018).
9. Huang, B. et al. Electrical control of 2D magnetism in bilayer CrI_3. *Nat. Nanotechnol.* **13**, 544–548 (2018).
10. Song, T. et al. Giant tunneling magnetoresistance in spin-filter van der Waals heterostructures. *Science* **360**, 1214–1218 (2018).
11. Klein, D. R. et al. Probing magnetism in 2D van der Waals crystalline insulators via electron tunneling. *Science* **360**, 1218–1222 (2018).
12. Huang, F., Kief, M. T., Mankey, G. J. & Willis, R. F. Magnetism in the few-monolayers limit: a surface magneto-optic Kerr-effect study of the magnetic behavior of ultrathin films of Co, Ni, and Co-Ni alloys on Cu(100) and Cu(111). *Phys. Rev. B* **49**, 3962–3971 (1994).
13. Elmers, H.-J., Hauschild, J. & Gradmann, U. Critical behavior of the uniaxial ferromagnetic monolayer Fe(110) on W(110). *Phys. Rev. B* **54**, 15224–15233 (1996).
14. Zhao, C. et al. Enhanced valley splitting in monolayer WSe_2 due to magnetic exchange field. *Nat. Nanotechnol.* **12**, 757–762 (2017).
15. Zhong, D. et al. Van der Waals engineering of ferromagnetic semiconductor heterostructures for spin and valleytronics. *Sci. Adv.* **3**, e1603113 (2017).
16. Scharf, B., Xu, G., Matos-Abiague, A. & Žutić, I. Magnetic proximity effects in transition-metal dichalcogenides: converting excitons. *Phys. Rev. Lett.* **119**, 127403 (2017).
17. Mermin, N. D. & Wagner, H. Absence of ferromagnetism or antiferromagnetism in one- or two-dimensional isotropic Heisenberg models. *Phys. Rev. Lett.* **17**, 1133–1136 (1966).
18. Bhatti, S. et al. Spintronics based random access memory: a review. *Mater. Today* **20**, 530–548 (2017).
19. Bonilla, M. et al. Strong room-temperature ferromagnetism in VSe_2 monolayers on van der Waals substrates. *Nat. Nanotechnol.* **13**, 289–293 (2018).
20. Parkin, S. S. P. & Friend, R. H. 3D transition-metal intercalates of the niobium and tantalum dichalcogenides. I. Magnetic properties. *Phil. Mag. B* **41**, 65–93 (1980).
21. Abrikosov, N. K., Bagaeva, L. A., Dudkin, L. D., Petrova, L. I. & Sokolova, V. M. Phase equilibria in the Fe-Ge-Te system. *Inorg. Mater.* **21**, 1680–1686 (1985).

© 2018 Springer Nature Limited. All rights reserved.

22. Deiseroth, H.-J., Aleksandrov, K., Reiner, C., Kienle, L. & Kremer, R. K. Fe_3GeTe_2 and Ni_3GeTe_2—two new layered transition-metal compounds: crystal structures, HRTEM investigations, and magnetic and electrical properties. *Eur. J. Inorg. Chem.* **2006**, 1561–1567 (2006).
23. May, A. F., Calder, S., Cantoni, C., Cao, H. & McGuire, M. A. Magnetic structure and phase stability of the van der Waals bonded ferromagnet $Fe_{3-x}GeTe_2$. *Phys. Rev. B* **93**, 014411 (2016).
24. Liu, S. et al. Wafer-scale two-dimensional ferromagnetic Fe_3GeTe_2 thin films grown by molecular beam epitaxy. *npj 2D Mater. Appl.* **1**, 30 (2017).
25. Zhuang, H. L., Kent, P. R. C. & Hennig, R. G. Strong anisotropy and magnetostriction in the two-dimensional Stoner ferromagnet Fe_3GeTe_2. *Phys. Rev. B* **93**, 134407 (2016).
26. Magda, G. Z. et al. Exfoliation of large-area transition metal chalcogenide single layers. *Sci. Rep.* **5**, 14714 (2015).
27. Desai, S. B. et al. Gold-mediated exfoliation of ultralarge optoelectronically-perfect monolayers. *Adv. Mater.* **28**, 4053–4058 (2016).
28. Ohno, H., Munekata, H., Penney, T., von Molnár, S. & Chang, L. L. Magnetotransport properties of p-type (In,Mn)As diluted magnetic III–V semiconductors. *Phys. Rev. Lett.* **68**, 2664–2667 (1992).
29. Prange, R. E. & Korenman, V. Local-band theory of itinerant ferromagnetism. IV. Equivalent Heisenberg model. *Phys. Rev. B* **19**, 4691–4697 (1979).
30. Verchenko, V. Y., Tsirlin, A. A., Sobolev, A. V., Presniakov, I. A. & Shevelkov, A. V. Ferromagnetic order, strong magnetocrystalline anisotropy, and magnetocaloric effect in the layered telluride $Fe_{3-\delta}GeTe_2$. *Inorg. Chem.* **54**, 8598–8607 (2015).
31. Tan, C. et al. Hard magnetic properties in nanoflake van der Waals Fe_3GeTe_2. *Nat. Commun.* **9**, 1554 (2018).
32. Ikeda, S. et al. A perpendicular-anisotropy CoFeB–MgO magnetic tunnel junction. *Nat. Mater.* **9**, 721–724 (2010).
33. Ueno, K. et al. Anomalous Hall effect in anatase $Ti_{1-x}Co_xO_{2-\delta}$ above room temperature. *J. Appl. Phys.* **103**, 07D114 (2008).

Acknowledgements We thank X. Jin, B. Lian and G. Chen for discussions. Part of the sample fabrication was conducted at Fudan Nano-fabrication Laboratory. Y.D., Y. Yu, Y.S., J.W. and Y.Z. acknowledge support from National Key Research Program of China (grant nos. 2016YFA0300703, 2018YFA0305600), NSF of China (grant nos U1732274, 11527805, 11425415 and 11421404), Shanghai Municipal Science and Technology Commission (grant no. 18JC1410300), and Strategic Priority Research Program of Chinese Academy of Sciences (grant no. XDB30000000). Y. Yu also acknowledges support from China Postdoc Innovation Talent Support Program. N.Z.W. and X.H.C. acknowledge support from the 'Strategic Priority Research Program' of the Chinese Academy of Sciences (grant no. XDB04040100) and the National Basic Research Program of China (973 Program; grant no. 2012CB922002). X.H.C. also acknowledges support from the National Natural Science Foundation of China (grant no. 11534010) and the Key Research Program of Frontier Sciences, CAS (grant no. QYZDY-SSW-SLH021). J. Zhu acknowledges financial support from Chinese University of Hong Kong (CUHK) under grant no. 4053084, from the University Grants Committee of Hong Kong under grant no. 24300814, and the Start-up Funding of CUHK. J.W. also acknowledges support from the NSF of China (grant no. 11774065). Z.S., Y. Yi and S.W. acknowledge support from the National Basic Research Program of China (grant no. 2014CB921601).

Reviewer information *Nature* thanks I. Zutic and the other anonymous reviewer(s) for their contribution to the peer review of this work.

Author contributions Y.Z. conceived the project. N.Z.W. and X.H.C. grew the bulk FGT crystal. Y.D., Y.S. and Y. Yu developed device fabrication method. Y.D. fabricated devices and performed electric measurements with the help of Y. Yu. Z.S., Y. Yi and S.W. performed optical measurements. Y.D., Y. Yu, Y.Z.W. and Y.Z. analysed the data. J. Zhang and J. Zhu carried out DFT calculations; J.W. carried out theoretical calculations and modelling; and all three performed theoretical analysis. Y.D., Y. Yu, J.W. and Y.Z. wrote the paper and all authors commented on it.

Competing interests The authors declare no competing interests.

Additional information
Extended data is available for this paper at https://doi.org/10.1038/s41586-018-0626-9.
Reprints and permissions information is available at http://www.nature.com/reprints.
Correspondence and requests for materials should be addressed to Y.Z.
Publisher's note: Springer Nature remains neutral with regard to jurisdictional claims in published maps and institutional affiliations.

© 2018 Springer Nature Limited. All rights reserved.

METHODS

Growth and characterization of bulk FGT crystal. High-quality FGT single crystals were grown by the chemical vapour transport method. High-purity elements were stoichiometrically mixed and sealed under vacuum in a quartz tube with a small quantity of iodine (5 mg cm^{-3}). The tube was placed into a two-zone horizontal furnace with the hot end at 750 °C and the cold end at 650 °C. Shining plate-like single crystals with typical dimensions of 3 mm × 3 mm × 0.25 mm were then obtained. The phase purity of the sample was examined by a powder X-ray diffractometer (SmartLab-9, Rigaku Corp.) with Cu Kα radiation, and result is shown in Extended Data Fig. 1a. The magnetization was measured by a SQUID magnetometer (Quantum Design MPMS-5), and the result is shown in Extended Data Fig. 1b.

Fabrication of FGT thin-flake devices. We used two kinds of substrates for FGT exfoliation: 285-nm SiO_2/Si wafer and sapphire. For thin flakes on 285-nm SiO_2/Si wafers (Fig. 1c), we determined the layer number of the flakes with an atomic force microscope, and correlated the topography image with optical contrast. Here the optical contrast is defined as $(G^{R}_{sample} - G^{R}_{substrate})/G^{R}_{substrate}$, where G^{R}_{sample} and $G^{R}_{substrate}$ are intensity of the reflection (R) on sample and substrate, respectively, in the green channel of the optical image captured with a charge-coupled device (CCD) camera. Excellent correlation between the height profile and the optical contrast has enabled us to determine unambiguously the layer number of exfoliated thin flakes. However, because optical contrast in the reflection is very sensitive to the thickness of the Al_2O_3 film as a result of optical interference, the optical contrast needs to be calibrated with atomic force microscopy measurement individually for every batch of samples. Such calibration processes usually take a long time. For this reason, we also used sapphire substrates, and determined the layer numbers by optical transmission, which is not sensitive to the Al_2O_3 film thickness. The optical transmission is now defined as $G^{T}_{sample}/G^{T}_{substrate}$, where G^{T}_{sample} and $G^{T}_{substrate}$ are the intensities of the transmission (T) through the sample and substrate, respectively, in the green channel of the image captured with a CCD camera. Extended Data Fig. 2a–c illustrates the layer number determination on sapphire substrate. The layer-number-dependent optical transmission is well described by the Beer–Lambert law (Extended Data Fig. 2c), which enables us to determine the layer number quickly and reliably.

We employed two methods to fabricate electrical contacts to FGT thin flakes: (1) direct metal deposition through stencil mask and (2) indium cold welding. We find that direct metal deposition works well for samples with thicknesses larger than two layers, but it tends to degrade the sample quality for thinner samples. We therefore used the cold welding method to fabricate indium microelectrodes on the thinnest flakes. Indium thin foil was first cut into small stripes. A PDMS stamp was then used to hold these stripes, with which we align the FGT thin flake under an optical microscope. We then pressed the indium stripes onto the sample to form electrical contacts, before lifting off the PDMS stamp. The cold welding method works well for FGT thin flakes as small as 20 μm. Extended Data Fig. 2f displays a monolayer device with microelectrodes made by cold welding. A trilayer device made by direct metal deposition is shown in Extended Data Fig. 2i for comparison.

Determining T_c by Arrott plots and polar RMCD microscopy. In the main text, the T_c values for FGT thin-flake devices were obtained from the temperature-dependent anomalous Hall effect. Here we use Arrott plots[34] to independently determine T_c. Following a previously described method[35], we replot the Hall data (such as those shown in Extended Data Fig. 3a–c) in plots of R^2_{xy} as a function of $\mu_0 H/R_{xy}$, that is, Arrott plots. Extrapolation of the high-field linear part of the Arrott plots intercepts the R^2_{xy} axis at values denoted as $(R^s_{xy})^2$, where R^s_{xy} refers to spontaneous Hall resistance. Positive intercepts indicate a ferromagnetic state, and T_c is the temperature where R^s_{xy} vanishes[35]. As an example, we show the Arrott plots of a bilayer FGT sample in Extended Data Fig. 3d. The T_c values of the bilayer and other thin-flake samples are determined from points where R^s_{xy} as a function of T approaches zero (Extended Data Fig. 3e), and the results are summarized in Fig. 2d. We note that T_c values for monolayer samples cannot be extracted from Arrott plots, because the samples are very insulating, and the large normal Hall contribution in R_{xy} prevents a reliable determination of T_c.

We also used RMCD microscopy to determine the T_c of FGT thin flakes. The same fabrication technique as shown in Fig. 1a was used to make thin-flake samples for the RMCD measurements. At each fixed temperature, we recorded the RMCD signal on each uniform region of the few-layer sample shown in Extended Data Fig. 4a as the magnetic field was swept. (We used a 633 nm HeNe laser with a spot size of about 2 μm to obtain the RMCD signal.) The data are displayed in Extended Data Fig. 4b–e. Clear hysteresis loops in RMCD signal are observed at low temperatures. We extracted the remanent RMCD signal at $\mu_0 H = 0$ from each dataset in Extended Data Fig. 4b–e, and plotted the results in Extended Data Fig. 4f. The T_c of FGT flakes with varying number of layers is determined by the temperature where the remanent RMCD signal vanishes.

Figure 2d summarizes the T_c obtained from anomalous Hall measurements, Arrott plot analysis and RMCD measurements. Although the T_c from Arrott plot analysis and RMCD measurements agree with each other, they are consistently higher than that determined from anomalous Hall effect measurements. The discrepancy is as large as about 50 K in few-layer FGT. As discussed in the main text, the large discrepancy signifies the existence of micrometre-sized domains above the T_c obtained from anomalous Hall effect measurements. We note that a similar thickness-dependent domain effect was also observed in the charge density wave ordering in 1T-TaS_2 thin flakes. The charge density wave phase transition was observed in optical[36] and transmission electron microscopy measurements[37], but not detected in transport measurement[37].

Scaling analysis of layer-dependent T_c in FGT thin flakes. The evolution from 3D to 2D magnetism in FGT is linked with the critical behaviour at the paramagnet to ferromagnet phase transition. Because T_c is the critical temperature where spin-spin correlation length diverges, a finite sample thickness limits the divergence of the correlation length, and therefore depresses T_c. Analyses of the critical behaviour in large area magnetic thin films[38–40] show that layer-number-dependent $T_c(N)$ follows a universal scaling law as the sample thickness approaches the 2D limit: $[T_c(\infty) - T_c(N)]/T_c(\infty) = [(N_0+1)/2N]^{\lambda}$, where $T_c(\infty)$ denotes T_c of the bulk crystal. The critical exponent $\lambda = 1/\nu$ reflects the universality class of the transition; N_0 is the critical layer number defined by the mean spin–spin interaction range. Analyses[40–43] also reveal that the power law is replaced by a linear relation when the film is thinner than the critical value, that is, $N \leq N_0$. N_0, therefore, marks the boundary that separates 2D magnetism and 3D magnetism in ultrathin ferromagnets. The scaling law fits well to the $T_c(N)$ measured in FGT as shown in Extended Data Fig. 5 (here we fitted the highest T_c determined by R^r_{xy} for each sample thickness). The fit yields a critical layer number of $N_0 = 3.2 \pm 0.6$ and a critical exponent of $\lambda = 2.3 \pm 0.8$. We also confirmed that the linear relation well describes our data in the thinnest samples ($N \leq 3$; see Extended Data Fig. 5). We note that N_0 obtained in FGT is comparable to that in the magnetic thin films[12,40,43]. Meanwhile, λ is consistent with values expected from mean field model ($\lambda = 2$), 3D Ising model ($\lambda = 1.587$), or 3D Heisenberg model ($\lambda = 1.414$); more accurate determination of T_c is required to resolve the universality class of bulk FGT.

Magnetic anisotropy of atomically thin FGT devices. We investigate the magnetic anisotropy of a four-layer FGT flake with angle-dependent anomalous Hall measurements. When a perpendicular magnetic field is applied ($\theta_H = 90°$; θ_H is the tilt angle between the magnetic field and basal plane of the sample), the square hysteresis loop indicates an out-of-plane magnetic anisotropy. A large in-plane field ($\mu_0 H > 2.6$ T; $\theta_H \approx 0°$) forces the magnetization to the in-plane direction; R_{xy} vanishes because it is proportional only to the out-of-plane component of the magnetization (Extended Data Fig. 6a). As the in-plane magnetic field decreases, however, R_{xy} acquires a finite value, implying that the magnetization is tilted towards the out-of-plane direction. The fact that the remanent Hall resistance R^r_{xy} at $\theta_H \approx 0°$ does not reach the value at $\theta_H = 90°$ suggests the existence of domains in this four-layer FGT sample.

To eliminate the effect of domains, we analyse the angle-dependent anomalous Hall effect at a high magnetic field of $\mu_0 H = 3$ T. The high field aligns the domains at all tilt angles (Extended Data Fig. 6a), so the whole sample is effectively a single domain. We extracted the R_{xy} value at $\mu_0 H = 3$ T at various tilt angles, and calculated the angle between magnetization and the basal plane, θ_M, as a function of θ_H, using the formula:

$$\theta_M(\theta_H) = \arcsin\left(\frac{R_{xy}(\theta_H)}{R_{xy}(\theta_H = 90°)}\right) \quad (3)$$

Extended Data Fig. 6c displays θ_M as a function of θ_H. The fact that θ_M is always larger than θ_H implies that the magnetization always tends to point to the out-of-plane direction regardless of the direction of the external magnetic field. This result indicates a strong out-of-plane magnetic anisotropy in the four-layer FGT.

The out-of-plane magnetic anisotropy is corroborated by angle-dependent R_{xy} measurements near T_c. Here we applied external fields at $\theta_H = 20°$ and $\theta_H = 90°$ at 150 K (around 5 K above the T_c determined by anomalous Hall measurements in the same sample). We observed that for magnetic fields tilted to a nearly in-plane direction ($\theta_H = 20°$), R_{xy} decreases with the field strength in the high field regime ($\mu_0 H > 1$ T), in contrast to the upward trend in R_{xy} as the magnetic field is applied perpendicularly ($\theta_H = 90°$; Extended Data Fig. 6b). Because the anomalous component of R_{xy} is proportional only to the out-of-plane magnetization, our observation implies that the magnetization is pinned in the out-of-plane direction at small magnetic fields, and is pulled towards the in-plane direction only in the high field regime.

Finally, we extract an estimation of the magnetic anisotropy energy density by fitting the data shown in Extended Data Fig. 6c with the Stoner–Wohlfarth model[44]. The total energy of the system is:

$$E = K_u \sin^2(\theta_M) - \mu_0 H M_s \cos(\theta_H - \theta_M) \quad (4)$$

© 2018 Springer Nature Limited. All rights reserved.

where K_u is the magnetic anisotropy energy density, and M_s is the saturation magnetization per volume. At equilibrium:

$$\frac{\partial E}{\partial \theta_M} = 2K_u \sin(\theta_M)\cos(\theta_M) + \mu_0 H M_s \sin(\theta_H - \theta_M) = 0 \quad (5)$$

The above equation determines the relation between θ_M and θ_H, which we used to fit the experimental data shown in Extended Data Fig. 6c (solid line). Assuming a value for M_s of about $1.8\mu_B$ per Fe atom[30], we obtained $K_u = 5.1 \times 10^5$ J m^{-3} from the fit. Such a magnetic anisotropy energy density is in reasonable agreement with the value obtained in bulk FGT[31].

Ionic gating of atomically thin ferromagnetic FGT devices. We determine the T_c of the FGT trilayer under ionic gating (Fig. 3) from anomalous Hall measurements. Specifically, we recorded R_{xy} as a function of T when the sample is cooled down in the presence of an infinitesimal magnetic field $\mu_0 H_0 = 0.01$ T applied in the out-of-plane direction. Because the normal part of the Hall resistance is negligible at such a low field, the anomalous Hall resistance is obtained as $R_{AH}|_{\mu_0 H_0} = (R_{xy}|_{\mu_0 H_0} - R_{xy}|_{-\mu_0 H_0})/2$. (The symmetrization procedure[28] is required to remove the R_{xx} component in the Hall data.) We extracted T_c by extrapolating R_{AH} to 0 (black lines, Extended Data Fig. 7a). The extrapolation is necessary because some of the T_c values are far above the freezing temperature of lithium ions (about 240 K).

The normal Hall resistance R_{NH} proportional to the external magnetic field manifests as a linear background in R_{xy} at high fields where the anomalous Hall resistance saturates. We were therefore able to obtain the Hall coefficient R_H as the slope of the line fits to the high-field part of $R_{xy}(\mu_0 H)$ shown in Fig. 3c. Extended Data Fig. 7d displays such line fits at three representative gate voltages, and the inverse of eR_H is plotted as a function of V_g in Extended Data Fig. 7e (here e is the charge on the electron). We observe that the inverse of eR_H as a function of V_g follows exactly the behaviour of T_c (Extended Data Fig. 7c). Because R_H is determined by the electronic structure on the Fermi surface[45], our observation unambiguously links the gate-induced magnetic response to changes in the Fermi surface, and provides additional support for the Stoner model discussed in the main text. Finally, we caution that here one cannot directly extract the carrier density from the inverse of eR_H as in the case of semiconductors. The Fermi surface of a multiband metal such as FGT is very complex, and the inverse of eR_H is in general not related to the carrier density.

We determined that the fundamental mechanism underlying the ionic gating in this study is gate-controlled intercalation of lithium ions. Clear evidence came from the fact that the ionic gate uniformly modulates the trilayer FGT as shown in Fig. 3. Such a large modulation depth is only possible with ion intercalation; electrostatic gating would have been almost completely screened by the first atomic layer, resulting in nonuniform gating in the out-of-plane direction. The thickness dependence of the gate modulation provides additional evidence for intercalation mechanism. The resistances (normalized by the value at $V_g = 0$ V) of three samples with varying thicknesses under gate modulation are displayed in Extended Data Fig. 8. The fact that a resistive state is induced in all three (initially metallic) samples implies that the gate modulation depth can be as large as 70 layers. This result is unambiguous evidence that ion diffusion, not the electrostatic field, is at work.

The intercalation mechanism is further corroborated by the reversibility of the magnetic response under ionic gating. As shown in Extended Data Fig. 7c, the gate-induced high-T_c state reverts to the initial low-T_c state once the gate voltage is swept back. Such reversibility indicates that the gate-intercalated ions do not chemically react (that is, form chemical bonds) with the crystal, which is consistent with results from gate-controlled intercalation of other layered crystals[46–48]. We note that the reversibility of ionic gating is also confirmed by the measurement of the Hall coefficient R_H shown in Extended Data Fig. 7e. The ultrathin specimen did suffer from sample degradation, which resulted in a large background in the sample resistance (Extended Data Fig. 7b) during the down-sweep of the gate. Such degradation was expected because ultrathin FGT was shown to be sensitive to the trace amounts of O_2 and H_2O present during gating.

First-principles calculations of electronic and magnetic properties of bulk FGT. First-principles calculations were carried out based on density functional theory (DFT)[49,50] as implemented in VASP code[51] with a plane wave basis set[52,53]. Spin-polarized Perdew–Burke–Enzerhof generalized gradient approximation (GGA)[54] and local density approximation (LDA)[55] were used as the exchange-correlation functionals. We also tested the on-site Coulomb interaction with different effective Hubbard U. The correction of van der Waals interactions, namely the DFT-D3 method with Becke–Jonson damping[56,57], was included in all our calculations. The energy cutoff of the plane-wave basis set was set to 400 eV. The bulk crystal lattice constants were obtained by fully relaxing the primitive cell to be stress-free with a $17 \times 17 \times 4$ gamma-centred k-point mesh. The k-point sampling was up to $17 \times 17 \times 1$ and $4 \times 4 \times 2$ for slabs and bulk supercell calculations, respectively. The slabs were separated by a vacuum of at least 15 Å. We performed careful convergence tests for all of the settings aforementioned. The LDA functional yields a magnetic moment of $1.424\mu_B$ per Fe site, which agrees with experimental observations[22,23,58] (LDA+U, GGA and GGA+U functionals yield magnetic moments of more than $2\mu_B$ per Fe site). The result is consistent with previous theoretical studies[25]. We therefore mainly use LDA with spin–orbit coupling to calculate the exchange coupling strength as well as the single-ion anisotropy A.

We adopted the energy mapping method[59,60] to obtain the Heisenberg spin exchange constants J from first-principles calculations. Here we used a $3 \times 3 \times 1$ bulk supercell to extract all six-intralayer J_x (or J_y) and four-interlayer J_z. Detailed illustrations of configurations for different J values are shown in Extended Data Fig. 9a and b. Following the algorithm proposed in ref. [59], we calculated the anisotropic spin exchange in a monolayer $3 \times 3 \times 1$ supercell. All the calculation results are summarized in Extended Data Fig. 9c. The intralayer couplings are approximately one order of magnitude larger than the interlayer couplings. Meanwhile, ferromagnetic order is strongly favoured for both in-plane and out-of-plane configurations, owing to the large number of hopping sites that favour ferromagnetic coupling (negative J values).

Next, we investigate the magnetic anisotropy in a monolayer. The exchange parameters for in-plane and out-of-plane are comparable, with the out-of-plane ones slightly larger. The single-ion anisotropy A is defined as the energy difference between all magnetic moments along the easy-axis (the z direction) and along the hard-axis (the x or y direction) in the layer. We found that the single-ion anisotropy A was 1.11 meV per μ_B for both bulk and monolayer FGT.

Finally, we estimate the effect of electron doping on the Fe magnetic moments. Extended Data Fig. 10a displays the DOS for a trilayer FGT as a function of electron doping level. The average magnetic moment as a function of electron doping is shown in Extended Data Fig. 10b. The results indicate that the amount of electrons doped in our experiment do not much affect the mean magnetic moments on Fe sites.

Mean-field calculation of T_c in bulk FGT. Although experiments and LDA calculations show that the magnetism in FGT is itinerant origin, one can still describe the 'magnetic part' of the thermodynamic properties of itinerant ferromagnetism with a Heisenberg Hamiltonian with magnetic anisotropy:

$$H = \sum_{i,j} J_{ij} \boldsymbol{S}_i \cdot \boldsymbol{S}_j + \sum_i A(S_i^z)^2 - g\mu_B \sum_i B S_i^z \quad (6)$$

where the first term is the sum of the Heisenberg exchange interactions between spin i with spin operator $\boldsymbol{S}_i$ and its neighbours $\boldsymbol{S}_j$, with which it interacts with strength J_{ij}; a negative J_{ij} corresponds to ferromagnetic interactions, and $\boldsymbol{S}_i$ is in units of h. The second term is the uniaxial single-ion anisotropy with respect to the uniaxial z axis, where the single-ion anisotropy $A < 0$ prefers spins aligning along the z axis. The third term is the Zeeman interaction. Fe_I^{3+} and Fe_{II}^{2+} have different and non-integer magnetic moments. We, however, treat them equally for simplicity.

We used the molecular mean field theory to solve the above Hamiltonian, which is achieved by replacing the spin operator by its mean value plus fluctuations. Mean-field approximation gives

$$H_{MFA} = \sum_i S_i^z \left[2 \sum_j J_{ij} S_j^z \right] + \sum_i A(S_i^z)^2 - g\mu_B \sum_i B S_i^z - \sum_{i,j} J_{ij} S_i^z S_j^z \quad (7)$$

where the spin flips are completely suppressed. Here B is the magnetic field and g is the Landé g-factor. The eigenvalues of the Hamiltonian $E(S^z)$ are labelled by the z components of the spin angular momentum $S^z \equiv -S, -S+1, \ldots, S$. The dimensionless magnetization at temperature T is given by the statistical average over all possible states of S^z

$$\frac{M}{M_0} = \frac{1}{Sg\mu_B} \frac{1}{Z_S} \sum_{S^z=-S}^{+S} \left(-\frac{\partial E_n}{\partial B_z} \right) e^{-E_n/k_B T} \quad (8)$$

where the partition function is $Z_S = \sum_{S^z=-S}^{+S} e^{-E_n/k_B T}$. On the other hand, the magnetization is

$$M = \frac{N}{V} g\mu_B \langle S^z \rangle \quad (9)$$

Therefore, both sides of equation (8) contain M, which can be solved graphically. Using mean-field approximation, one can see that without the A term in the Hamiltonian of equation (6), the right hand side of equation (8) becomes a Brillouin function. One can further approximate the A term by an effective exchange field as $\sum_i 2A\langle S^z \rangle S_i^z$. In this case, the Heisenberg model is equivalent to the phenomenological Weiss model of a ferromagnet. The magnetization is

$$\frac{M(T,B)}{M_0} = B_S \left(\frac{Sg\mu_B (B + B_A)}{k_B T} \right) \quad (10)$$

© 2018 Springer Nature Limited. All rights reserved.

where B_S is the Brillouin function defined as

$$B_S(x) = \frac{2S+1}{2S}\coth\left(\frac{2S+1}{2S}x\right) - \frac{1}{2S}\coth\left(\frac{x}{2S}\right) \quad (11)$$

and

$$B_A = -\frac{1}{g\mu_B}\left(2\sum_j J_{ij} + 2A\right)\langle S^z\rangle \quad (12)$$

The Curie temperature T_c is given by $M=0$, which leads to

$$T_c = -\frac{2S(S+1)}{3k_B}\left(\frac{1}{n}\sum_{i\neq j} J_{ij} + A\right) \quad (13)$$

Here n is the number of neighbouring sites. Taking the effective J parameters from LDA calculations, and choosing $S=5/2$ as the magnetic moment of single Fe_I^{3+} ion, we can estimate the T_c of bulk FGT to be about 233 K. Meanwhile, choosing $S=2$ as the magnetic moment of single Fe_{II}^{2+} ion leads to a bulk T_c value of about 160 K.

Data availability

The datasets generated and analysed during the current study are available from the corresponding author on reasonable request.

34. Arrott, A. Criterion for ferromagnetism from observations of magnetic isotherms. *Phys. Rev.* **108**, 1394–1396 (1957).
35. Ohno, H. et al. Electric-field control of ferromagnetism. *Nature* **408**, 944–946 (2000).
36. Albertini, O. R. et al. Zone-center phonons of bulk, few-layer, and monolayer 1T-TaS_2 : detection of commensurate charge density wave phase through Raman scattering. *Phys. Rev. B* **93**, 214109 (2016).
37. Tsen, A. W. et al. Structure and control of charge density waves in two-dimensional 1T-TaS_2. *Proc. Natl Acad. Sci. USA* **112**, 15054–15059 (2015).
38. Fisher, M. E. & Barber, M. N. Scaling theory for finite-size effects in the critical region. *Phys. Rev. Lett.* **28**, 1516–1519 (1972).
39. Ritchie, D. S. & Fisher, M. E. Finite-size and surface effects in Heisenberg films. *Phys. Rev. B* **7**, 480–494 (1973).
40. Zhang, R. & Willis, R. F. Thickness-dependent Curie temperatures of ultrathin magnetic films: effect of the range of spin-spin interactions. *Phys. Rev. Lett.* **86**, 2665–2668 (2001).
41. Huang, F., Mankey, G. J., Kief, M. T. & Willis, R. F. Finite-size scaling behavior of ferromagnetic thin films. *J. Appl. Phys.* **73**, 6760–6762 (1993).
42. Ambrose, T. & Chien, C. L. Finite-size scaling in thin antiferromagnetic CoO layers. *J. Appl. Phys.* **79**, 5920 (1996).
43. Henkel, M., Andrieu, S., Bauer, P. & Piecuch, M. Finite-size scaling in thin Fe/Ir(100) Layers. *Phys. Rev. Lett.* **80**, 4783–4786 (1998).
44. Stoner, E. C. & Wohlfarth, E. P. A mechanism of magnetic hysteresis in heterogeneous alloys. *Phil. Trans. R. Soc. Lond. A* **240**, 599–642 (1948).
45. Evtushinsky, D. V. et al. Pseudogap-driven sign reversal of the Hall effect. *Phys. Rev. Lett.* **100**, 236402 (2008).
46. Zhao, S. Y. F. et al. Controlled electrochemical intercalation of graphene/*h*-BN van der Waals heterostructures. *Nano Lett.* **18**, 460–466 (2018).
47. Lei, B. et al. Gate-tuned superconductor-insulator transition in (Li,Fe)OHFeSe. *Phys. Rev. B* **93**, 060501 (2016).
48. Lei, B. et al. Tuning phase transitions in FeSe thin flakes by field-effect transistor with solid ion conductor as the gate dielectric. *Phys. Rev. B* **95**, 020503 (2017).
49. Hohenberg, P. & Kohn, W. Inhomogeneous electron gas. *Phys. Rev.* **136**, B864–B871 (1964).
50. Kohn, W. & Sham, L. J. Self-consistent equations including exchange and correlation effects. *Phys. Rev.* **140**, A1133–A1138 (1965).
51. Kresse, G. & Furthmüller, J. Efficiency of ab-initio total energy calculations for metals and semiconductors using a plane-wave basis set. *Comput. Mater. Sci.* **6**, 15–50 (1996).
52. Blöchl, P. E. Projector augmented-wave method. *Phys. Rev. B* **50**, 17953–17979 (1994).
53. Kresse, G. & Joubert, D. From ultrasoft pseudopotentials to the projector augmented-wave method. *Phys. Rev. B* **59**, 1758–1775 (1999).
54. Perdew, J. P., Burke, K. & Ernzerhof, M. Generalized gradient approximation made simple. *Phys. Rev. Lett.* **77**, 3865–3868 (1996).
55. Perdew, J. P. & Zunger, A. Self-interaction correction to density-functional approximations for many-electron systems. *Phys. Rev. B* **23**, 5048–5079 (1981).
56. Grimme, S., Antony, J., Ehrlich, S. & Krieg, H. A consistent and accurate ab initio parametrization of density functional dispersion correction (DFT-D) for the 94 elements H-Pu. *J. Chem. Phys.* **132**, 154104 (2010).
57. Grimme, S., Ehrlich, S. & Goerigk, L. Effect of the damping function in dispersion corrected density functional theory. *J. Comput. Chem.* **32**, 1456–1465 (2011).
58. Chen, B. et al. Magnetic properties of layered itinerant electron ferromagnet Fe_3GeTe_2. *J. Phys. Soc. Jpn* **82**, 124711 (2013).
59. Xiang, H., Lee, C., Koo, H.-J., Gong, X. & Whangbo, M.-H. Magnetic properties and energy-mapping analysis. *Dalton Trans.* **42**, 823–853 (2013).
60. Xiang, H. J., Kan, E. J., Wei, S.-H., Whangbo, M.-H. & Gong, X. G. Predicting the spin-lattice order of frustrated systems from first principles. *Phys. Rev. B* **84**, 224429 (2011).

© 2018 Springer Nature Limited. All rights reserved.

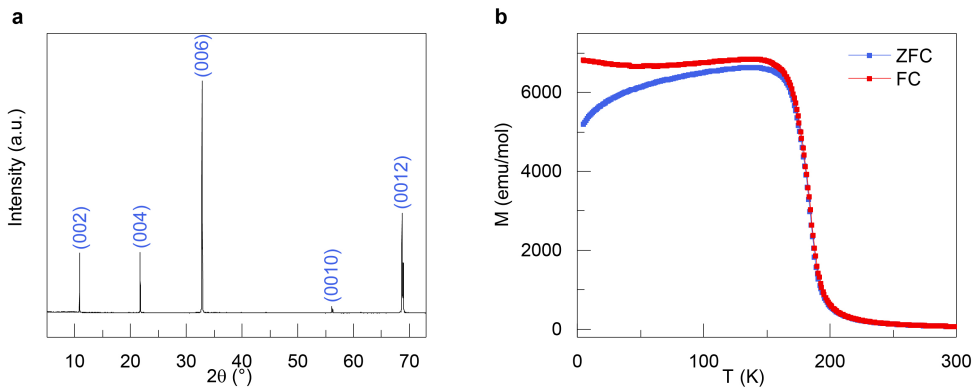

Extended Data Fig. 1 | Characterization of FGT bulk crystal. **a**, Powder X-ray diffraction pattern of bulk FGT crystal. **b**, Temperature-dependent magnetization of bulk FGT measured during zero-field cooling (ZFC, blue curve) and field cooling (FC, red curve) with an external magnetic field of 0.1 T. (a.u., arbitrary units; emu, electromagnetic unit for magnetic moment).

© 2018 Springer Nature Limited. All rights reserved.

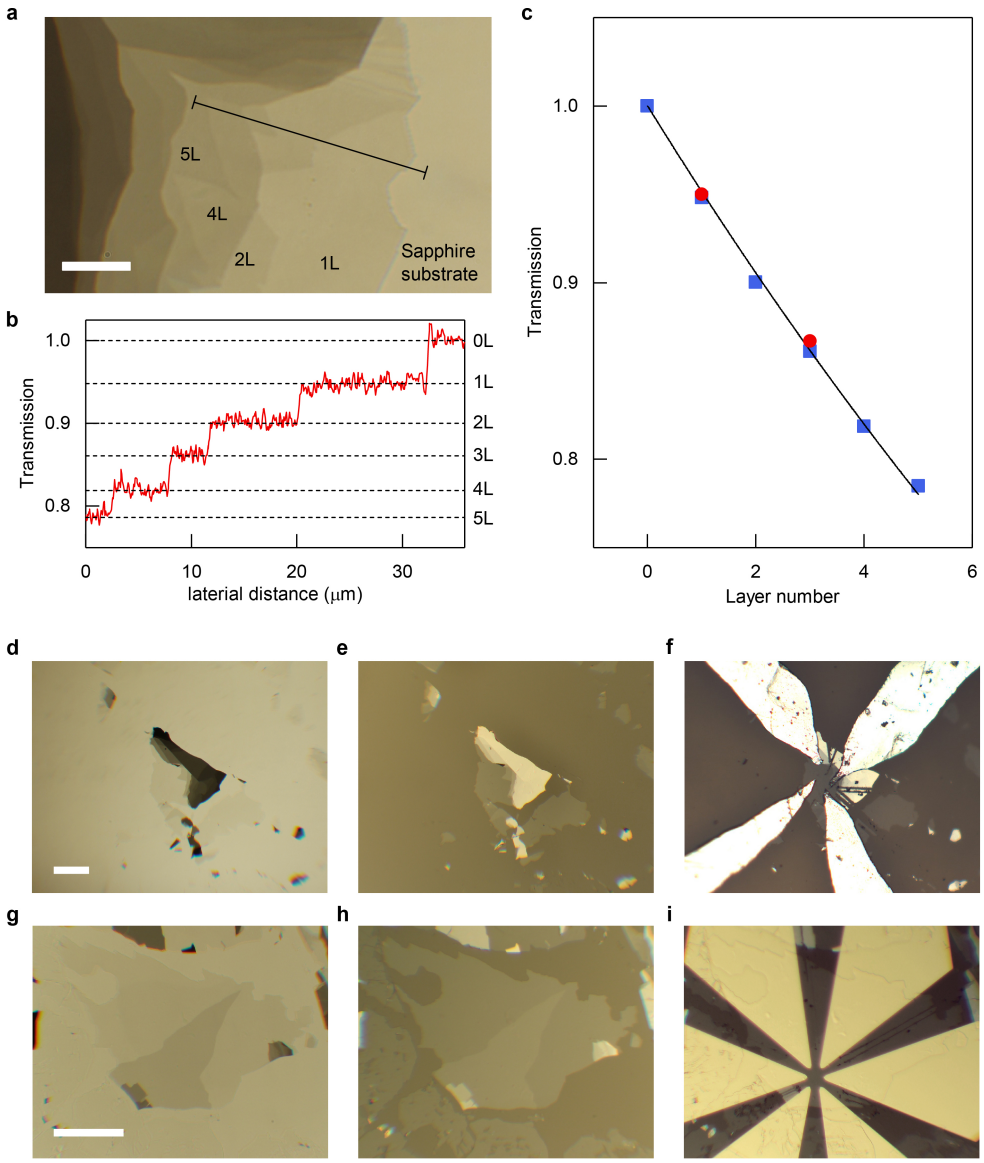

Extended Data Fig. 2 | FGT thin-flake device fabrication. a, A representative optical image of FGT thin flakes exfoliated on top of Al_2O_3 film supported on a sapphire substrate. The image was captured with a CCD camera mounted on an optical microscope operating in transmission mode. **b**, Cross-sectional profile of optical transmission $G^{T}_{sample}/G^{T}_{substrate}$ along the black line in **a**. Scale bar, 10 μm. **c**, Layer-dependent optical transmission extracted from the image shown in **a**. The black line is a fit to the data (blue squares) using the Beer–Lambert law. **d**, **e**, Optical images obtained in transmission mode (**d**) and reflection mode (**e**) for a typical monolayer sample. **f**, Device fabricated from the monolayer sample shown in **d** and **e**. Electrical contacts to the sample were made with indium microelectrodes. Scale bar, 100 μm. **g**, **h**, Optical images obtained in transmission mode (**g**) and reflection mode (**h**) for a typical trilayer sample. **i**, Device fabricated from the trilayer sample shown in **g** and **h**. Electrical contacts to the sample were made with thermally evaporated Cr/Au electrodes. Scale bar, 100 μm. The optical transmission of the monolayer and trilayer sample shown in **d** and **g** are presented as red dots in **c**.

© 2018 Springer Nature Limited. All rights reserved.

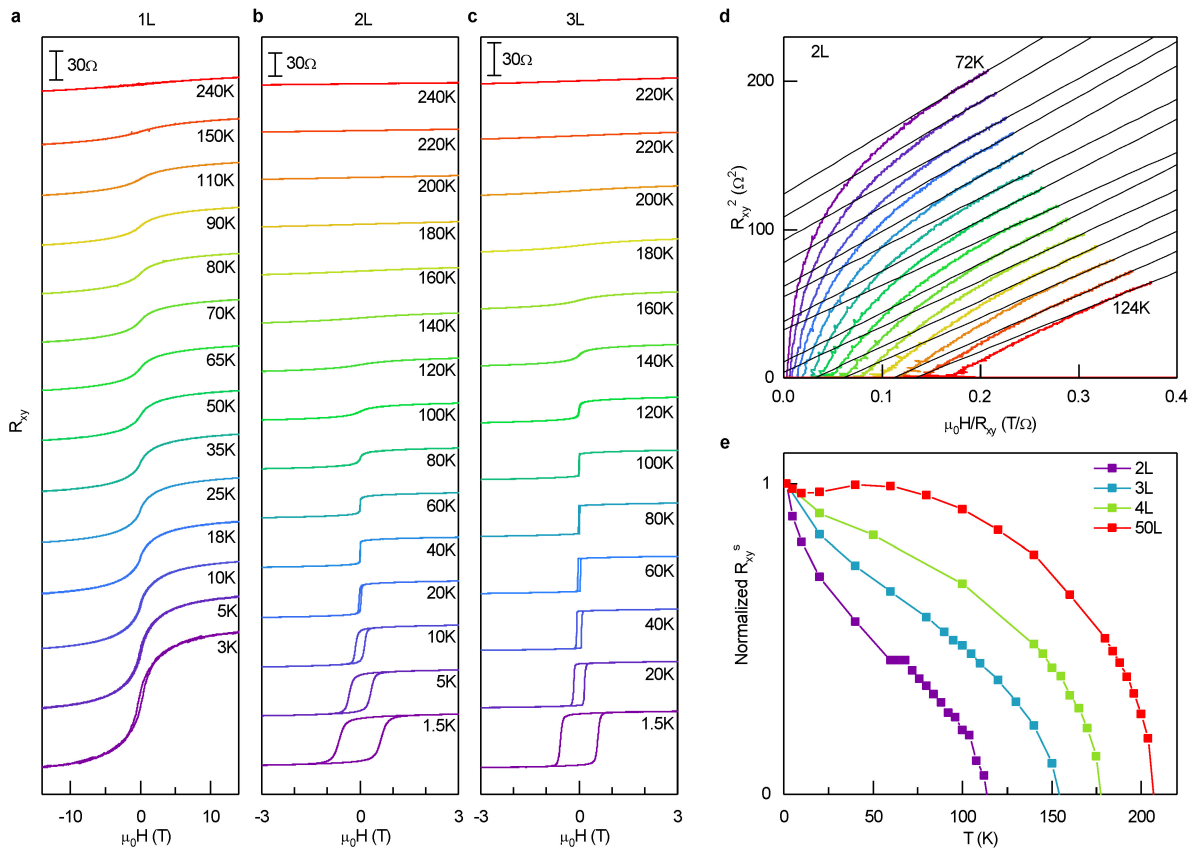

Extended Data Fig. 3 | Determining T_c by Arrott plot analysis. **a**–**c**, R_{xy} as a function of external magnetic field $\mu_0 H$ obtained in a monolayer (**a**), bilayer (**b**) and trilayer (**c**) FGT device at varying temperatures. **d**, Arrott plots of the Hall resistance data of the bilayer sample shown in **b**. The temperature is varied from 72 K to 124 K with a 4 K interval. Black lines are line fits at high magnetic fields (from $\mu_0 H = 2.25$T to $\mu_0 H = 3$T). **e**, Spontaneous Hall resistance R_{xy}^s as a function of temperature obtained from FGT samples with varying number of layers. R_{xy}^s are normalized by their values at $T = 1.5$K. T_c is determined by the temperature where R_{xy}^s approaches zero.

© 2018 Springer Nature Limited. All rights reserved.

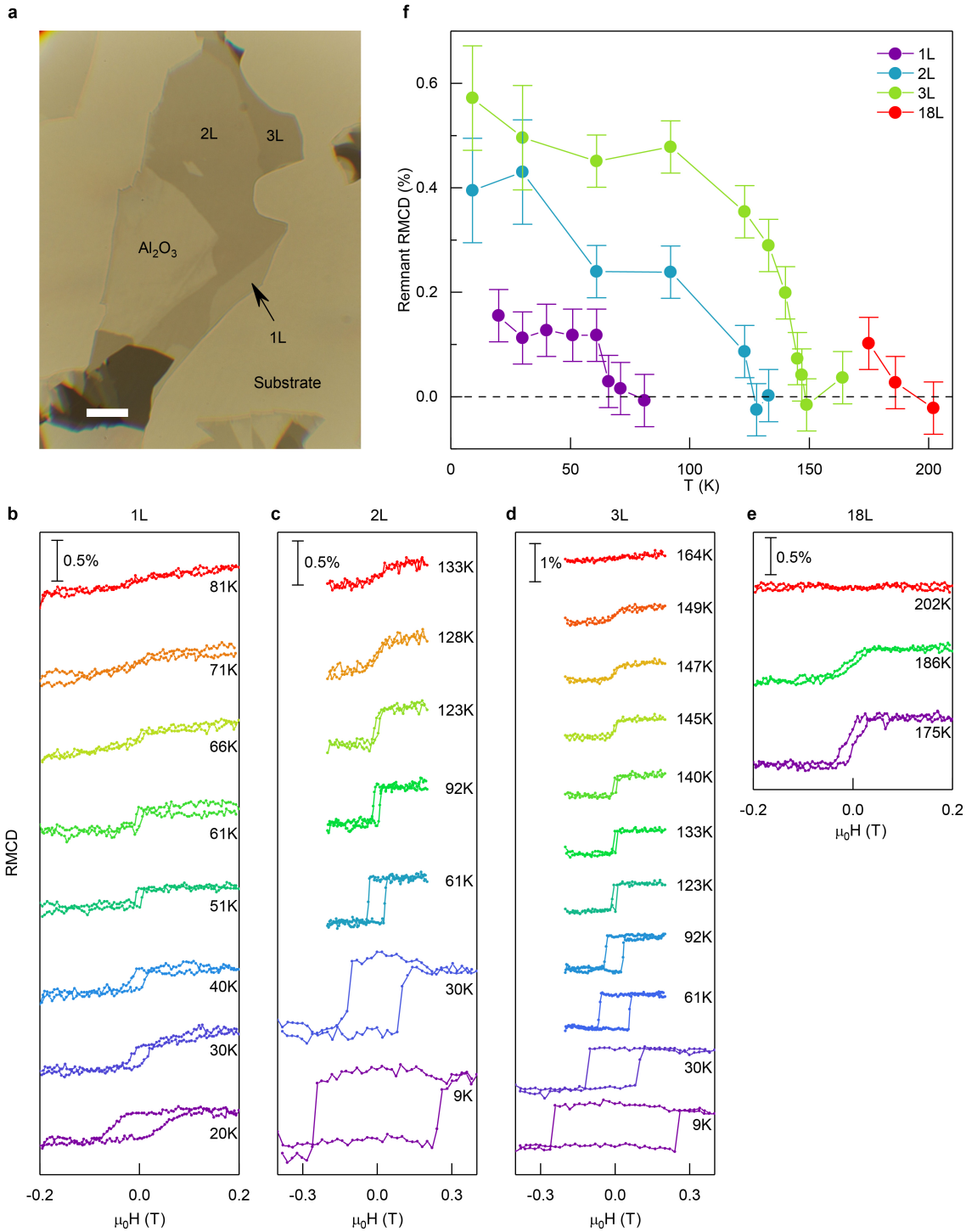

Extended Data Fig. 4 | Determining T_c from RMCD measurements. **a**, Optical image of monolayer, bilayer and trilayer FGT samples. Scale bar, 10 μm. **b**–**e**, Polar RMCD signal as a function of magnetic field recorded in monolayer (**b**), bilayer (**c**), trilayer (**d**) and bulk (**e**) samples at various temperatures. The bulk sample refers to an 18-layer sample with the thickness determined from optical transmission. **f**, Remanent RMCD signal at zero magnetic field as a function of temperature obtained from datasets shown in **b**–**e**. The T_c of each sample is determined by the temperature where remanent RMCD signal vanishes. Vertical error bars represent the measurement uncertainty of the remanent RMCD signal.

© 2018 Springer Nature Limited. All rights reserved.

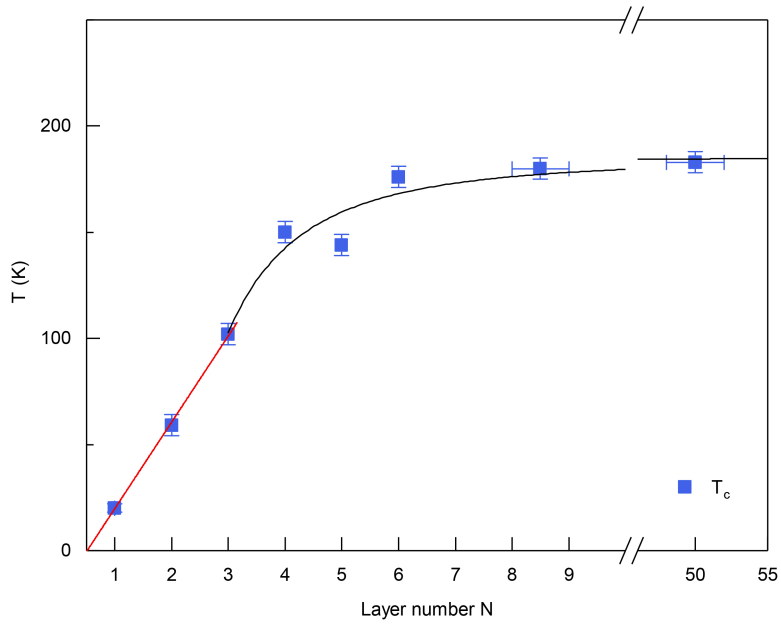

Extended Data Fig. 5 | Finite-size scaling of T_c in FGT thin flakes. T_c shown here is obtained from anomalous Hall measurements. We used the highest T_c at each sample thickness for the analysis. Error bars are defined as in Fig. 2d.

© 2018 Springer Nature Limited. All rights reserved.

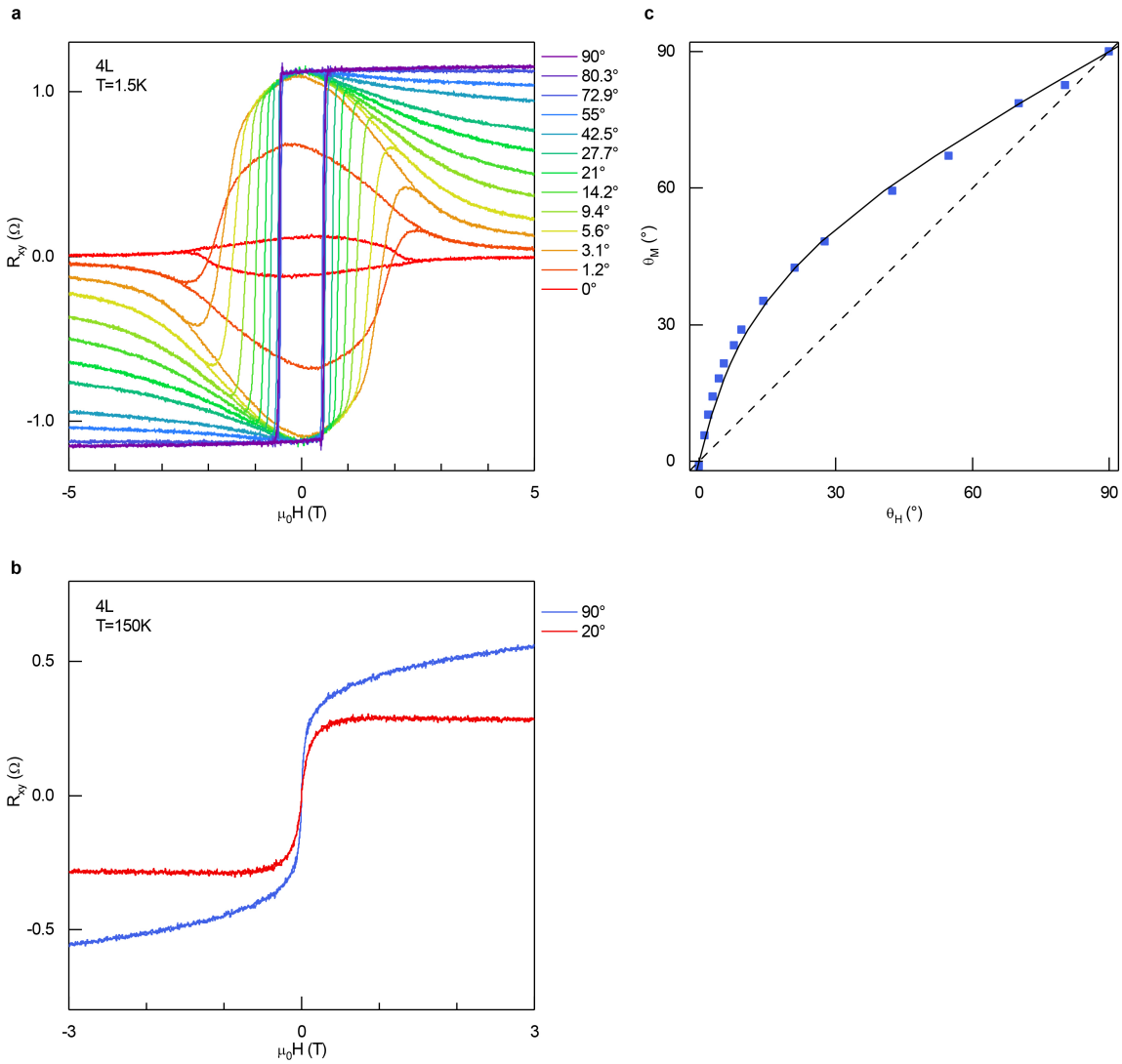

Extended Data Fig. 6 | Angle-dependent Hall resistance of a four-layer FGT flake. a, R_{xy} as a function of magnetic field recorded at various tilt angles. Data were obtained at $T = 1.5$ K. **b**, R_{xy} as a function of magnetic field recorded at $\theta_H = 90°$ (blue) and $\theta_H = 20°$ (red) at $T = 150$ K, about 5 K above the T_c determined by anomalous Hall measurements in the same sample. **c**, θ_M as a function of θ_H. θ_M was extracted from the R_{xy} data at $\mu_0 H = 3$ T in **a**. The solid line is a fit to the Stoner–Wohlfarth model. A K_u value of 5.1×10^5 J m^{-3} is obtained from the fit, if M_s takes the value of about $1.8\mu_B$ per Fe atom. The broken line marks $\theta_M = \theta_H$ that corresponds to $K_u = 0$.

© 2018 Springer Nature Limited. All rights reserved.

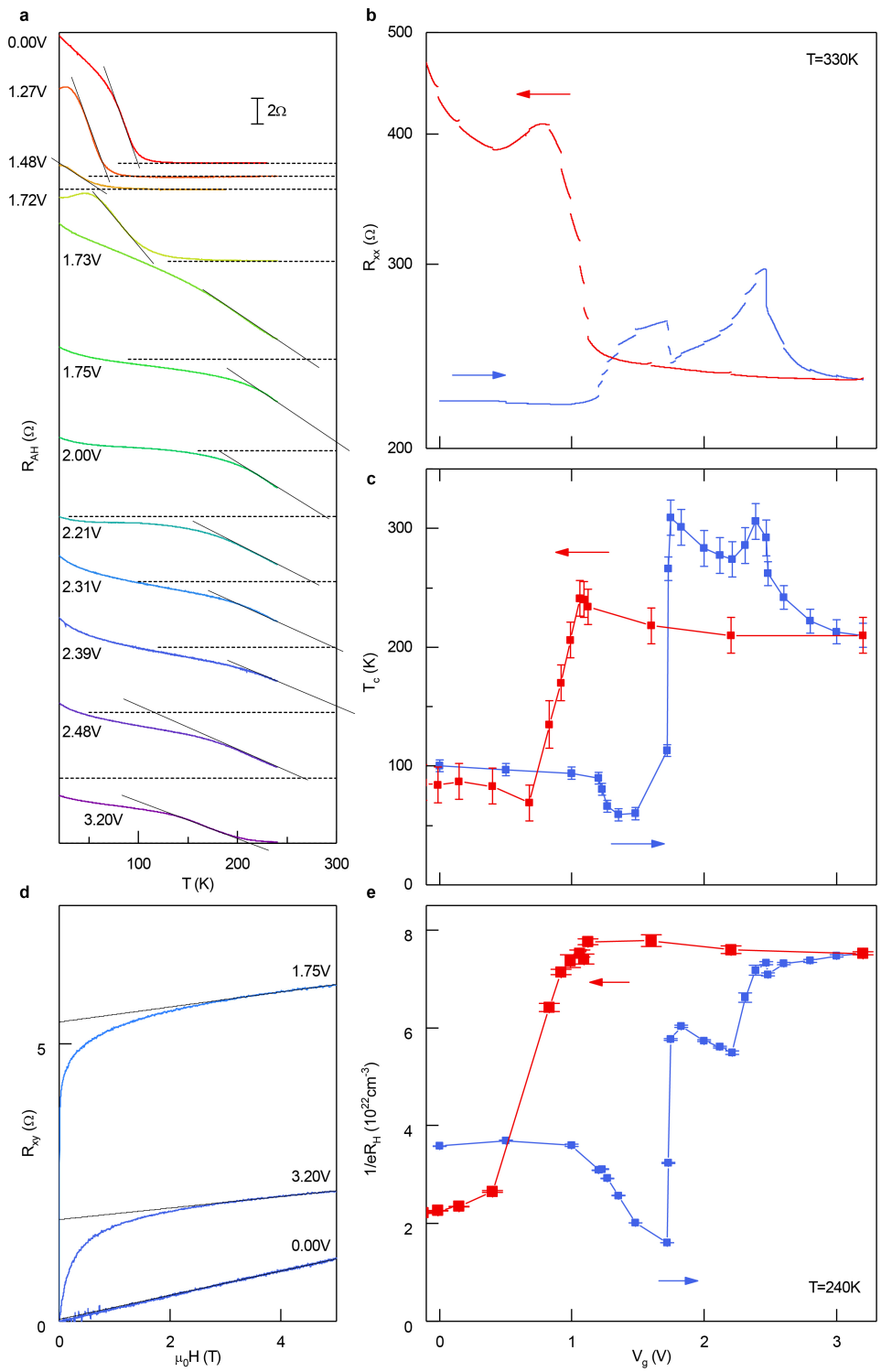

Extended Data Fig. 7 | Ionic gating of an FGT trilayer ionic field-effect transistor. a, Temperature-dependent R_{AH} at representative V_g under a small external magnetic field of $\mu_0 H_0 = 0.01$ T. The ferromagnetic transition temperature T_c is extracted by extrapolating R_{AH} to zero. **b**, Sample resistance R_{xx} as a function of V_g during the up-sweep (blue) and down sweep (red) of V_g. Data were obtained at $T = 330$ K. **c**, T_c as a function of V_g during the up-sweep (blue) and down sweep (red) of V_g. T_c exhibits reasonably good reversibility under gate modulation, even though R_{xx} acquires a large background, possibly due to sample degradation. Data were obtained from the same device discussed in Fig. 3. The error bars are also defined the same way as in Fig. 3. **d**, Line fits of R_{xy} as a function of $\mu_0 H$ in the range of $3\ \mathrm{T} < \mu_0 H < 5$ T at three representative gate voltages. R_H is obtained as the slope of the line fits. **e**, Inverse of eR_H as a function of V_g during the up-sweep (blue) and down-sweep (red) of the gate voltage. Data were obtained at $T = 240$ K. Error bars represent the standard deviations of the line fits in **d**.

© 2018 Springer Nature Limited. All rights reserved.

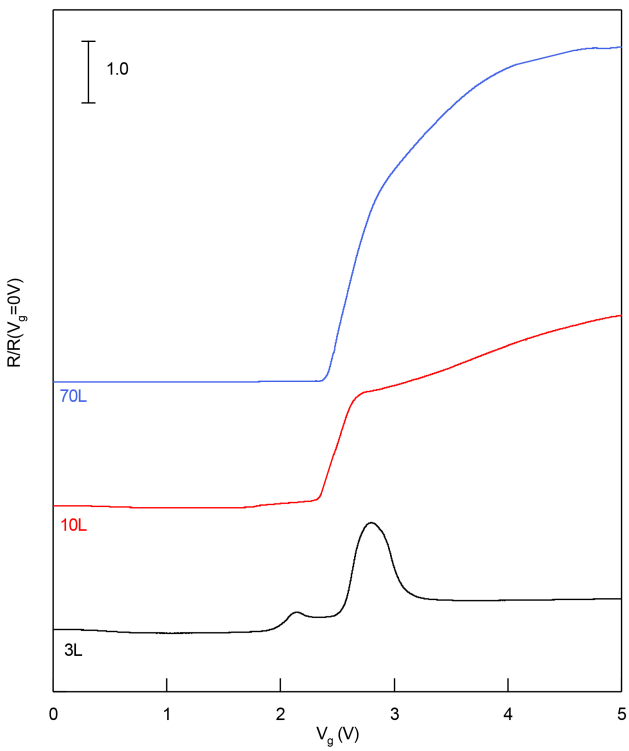

Extended Data Fig. 8 | Thickness dependence of the gate modulation in a FGT ionic field-effect transistor. Sample resistance measured as a function of V_g in trilayer (black), 10-layer (red) and 70-layer (blue) FGT devices. Resistances are normalized by their values at $V_g = 0$ V.

© 2018 Springer Nature Limited. All rights reserved.

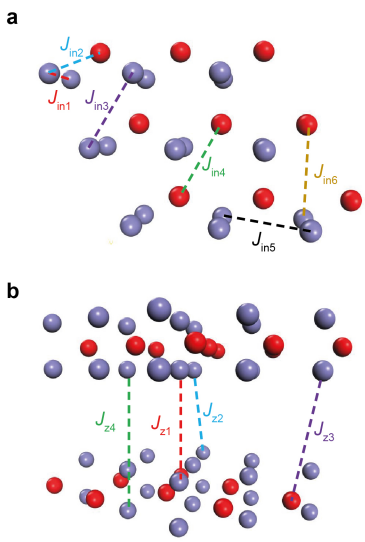

c

Bulk		Monolayer			
J_{in1}	-6.48	J_{xx1} (J_{yy1})	-23.48	J_{zz1}	-23.40
J_{in2}	-27.90	J_{xx2} (J_{yy2})	-20.41	J_{zz2}	-20.60
J_{in3}	5.79	J_{xx3} (J_{yy3})	10.93	J_{zz3}	11.04
J_{in4}	4.64	J_{xx4} (J_{yy4})	8.91	J_{zz4}	10.77
J_{in5}	-1.23	J_{xx5} (J_{yy5})	3.71	J_{zz5}	3.87
J_{in6}	0.12	J_{xx6} (J_{yy6})	-2.28	J_{zz6}	-2.59
J_{z1}	1.93				
J_{z2}	-0.21				
J_{z3}	-1.44				
J_{z4}	0				

Extended Data Fig. 9 | Calculated exchange parameters. a, The top view shows J_{in1} to J_{in6} for the intralayer (in plane) coupling. **b**, The side view shows J_{z1} to J_{z4} for the interlayer (out of plane) coupling. Only Fe ions are shown in the structure. The purple and red atoms are Fe_I and Fe_{II} ions, respectively. **c**, The left column shows the calculated exchange parameters for bulk FGT, J_{ini} for intralayer and J_{zi} for interlayer, in a $3 \times 3 \times 1$ bulk supercell. The right column shows the spin exchange parameters in a monolayer $3 \times 3 \times 1$ supercell, denoted as J_{xxi} (J_{yyi}) and J_{zzi}. The units of J are millielectronvolts. The results indicate that the exchange coupling J is largely isotropic.

© 2018 Springer Nature Limited. All rights reserved.

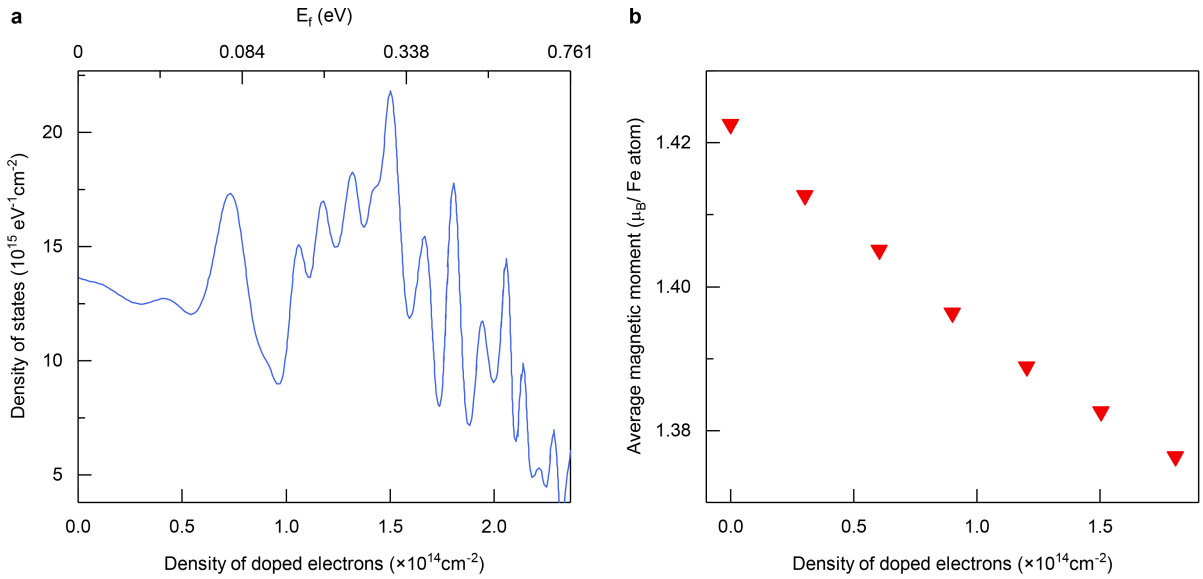

Extended Data Fig. 10 | LDA calculation of DOS and average magnetic moment as a function of electron doping level. a, Calculated DOS for trilayer FGT as a function of electron doping level. **b**, Calculated average magnetic moment in bulk FGT as a function of electron doping level.

© 2018 Springer Nature Limited. All rights reserved.

https://doi.org/10.1038/s41586-018-0628-7

Base-free nickel-catalysed decarbonylative Suzuki–Miyaura coupling of acid fluorides

Christian A. Malapit[1], James R. Bour[1], Conor E. Brigham[1] & Melanie S. Sanford[1]*

The Suzuki–Miyaura cross-coupling of organoboron nucleophiles with aryl halide electrophiles is one of the most widely used carbon–carbon bond-forming reactions in organic and medicinal chemistry[1,2]. A key challenge associated with these transformations is that they generally require the addition of an exogenous base, the role of which is to enable transmetallation between the organoboron nucleophile and the metal catalyst[3]. This requirement limits the substrate scope of the reaction because the added base promotes competitive decomposition of many organoboron substrates[3–5]. As such, considerable research has focused on strategies for mitigating base-mediated side reactions[6–12]. Previous efforts have primarily focused either on designing strategically masked organoboron reagents (to slow base-mediated decomposition)[6–8] or on developing highly active palladium precatalysts (to accelerate cross-coupling relative to base-mediated decomposition pathways)[10–12]. An attractive alternative approach involves identifying combinations of catalyst and electrophile that enable Suzuki–Miyaura-type reactions to proceed without an exogenous base[12–14]. Here we use this approach to develop a nickel-catalysed coupling of aryl boronic acids with acid fluorides[15–17], which are formed in situ from readily available carboxylic acids[18–22]. This combination of catalyst and electrophile enables a mechanistic manifold in which a 'transmetallation-active' aryl nickel fluoride intermediate is generated directly in the catalytic cycle[13,16]. As such, this transformation does not require an exogenous base and is applicable to a wide range of base-sensitive boronic acids and biologically active carboxylic acids.

The traditional Suzuki–Miyaura reaction involves the palladium-catalysed coupling of an aryl halide (Ar–X) with a boronic acid in the presence of exogenous base (MX*). The role of the base (Fig. 1b, cycle I) is to convert the 'transmetallation-inactive' [Ar–Pd–X] intermediate (where X = chloride, bromide or iodide) to a 'transmetallation-active' intermediate [Ar–Pd–X*] (where X* = hydroxide or fluoride). [Ar–Pd–X*] then participates in fast transmetallation with a boronic acid[23–25]. However, the base also mediates the off-cycle formation of organoboronate intermediates that competitively decompose via protodeboronation, oxidation and/or homocoupling[4,5]. Inspired by several literature reports[13,16], we proposed that the combination of a nickel catalyst and an acid fluoride electrophile would directly form a 'transmetallation-active' intermediate [Ar–Ni–F] via oxidative addition and subsequent decarbonylation (Fig. 1b, cycle II). Importantly, Ni^0 is well-known to participate in oxidative addition reactions with carboxylic acid derivatives[15,26–30]. Furthermore, with appropriate selection of supporting ligands, the resulting Ni^{II}-acyl intermediates are known to undergo decarbonylation[26–30]. This approach offers several advantages, which include eliminating the requirement for exogenous base; using highly electrophilic ArC(O)F substrates, which should undergo rapid oxidative addition under mild conditions (compared to, for example, the corresponding aryl fluorides[13,31–33], esters[26,28] or amides[27]); and using readily available and inexpensive carboxylic acid derivatives as coupling partners. Notably, a similar strategy was recently applied to the palladium-catalysed decarbonylative coupling of acid fluorides with triethyltrifluoromethylsilane[16].

Stoichiometric studies were first conducted to assess the viability of each step of the proposed catalytic cycle. To investigate oxidative addition and decarbonylation, benzoyl fluoride **1** was reacted with $Ni(cod)_2$ and PCy_3 (Fig. 2a) (cod, 1,5-cyclooctadiene; PCy_3, tricyclohexylphosphine). The benzoyl nickel fluoride intermediate **2** was formed rapidly

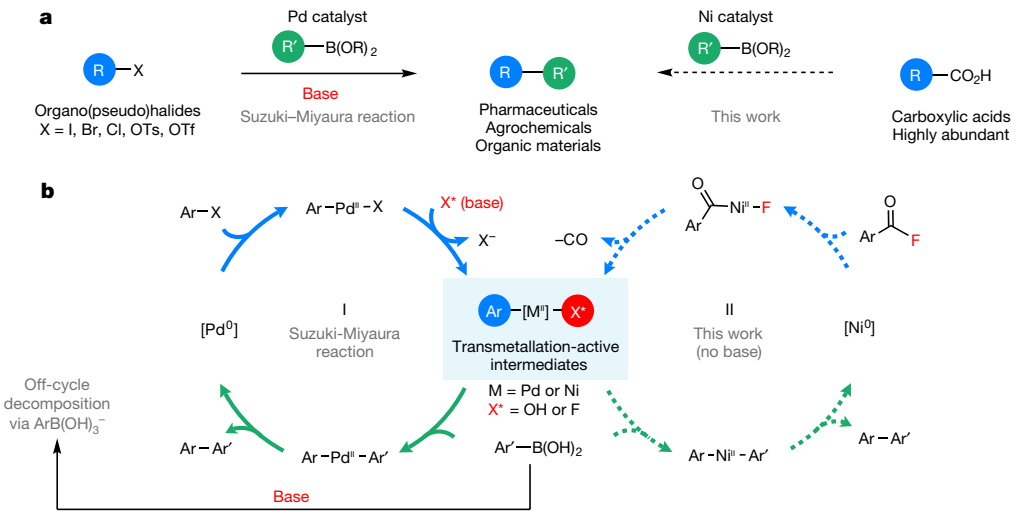

Fig. 1 | Suzuki–Miyaura reaction and mechanistic design for the direct generation of transmetallation-active [Ar–M–X*] intermediates. **a**, Cross-coupling reactions with organoboron reagents. **b**, Mechanistic design for directly accessing transmetallation-active intermediates for the base-free decarbonylative coupling of acid fluorides with organoboron reagents. R, alkyl or aryl group; Ar, aryl group.

[1]Department of Chemistry, University of Michigan, Ann Arbor, MI, USA. *e-mail: mssanfor@umich.edu

© 2018 Springer Nature Limited. All rights reserved.

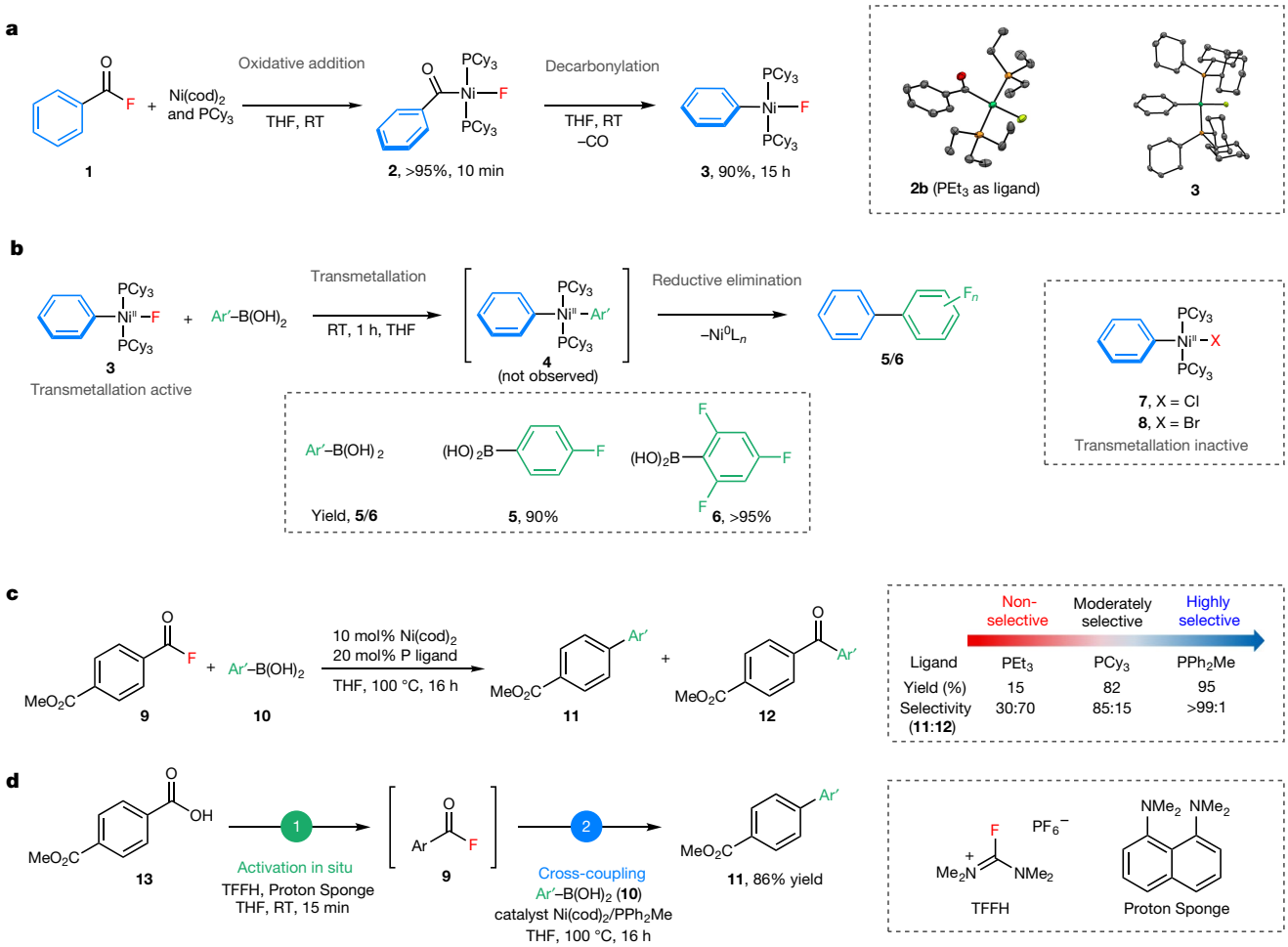

Fig. 2 | Discovery of transmetallation-active nickel fluoride intermediates generated from decarbonylation enables Suzuki–Miyaura reaction of carboxylic acids and aryl boronic acids. **a**, Oxidative addition and decarbonylation of acid fluoride **1** at room temperature generates an Ar–Ni–F intermediate **3**. **b**, Transmetallation and reductive elimination of **3** and aryl boronic acids. **c**, Base-free nickel-catalysed decarbonylative Suzuki–Miyaura-type reaction. **d**, Direct conversion of aryl carboxylic acid to Suzuki–Miyaura biaryl product via in situ generation of acid fluoride. Yields are based on ^{19}F NMR spectroscopy (**a**, **b**) and gas chromatography (**c**). Cy, cyclohexyl; RT, room temperature; THF, tetrahydrofuran. For details on reaction conditions, see Supplementary Information.

(within 10 min at room temperature), and this complex underwent decarbonylation to afford phenyl nickel fluoride complex **3** in 90% yield after 15 h. To confirm that **3** is 'transmetallation-active', this complex was treated with 4-fluorophenyl boronic acid. As predicted, biaryl **5** (the product of transmetallation and subsequent C–C bond-forming reductive elimination) was formed in 90% yield after 1 h at room temperature. An analogous reaction with 2,4,6-trifluorophenylboronic acid (which is known to undergo rapid protodeboronation under basic conditions)[4,10] provided **6** in >95% yield, indicating that transmetallation with **3** is faster than protodeboronation. Notably, the analogous phenyl nickel chloride **7** and phenyl nickel bromide **8** do not react with aryl boronic acids to form **5** and **6**, respectively, even when heated at 100 °C.

These stoichiometric studies were next translated to a nickel-catalysed decarbonylative coupling between acid fluoride **9** and 4-methoxyphenyl boronic acid (**10**). The use of 10 mol% $Ni(cod)_2$ and 20 mol% PCy_3 as catalyst afforded biaryl **11** along with a ketone by-product **12** (**11**:**12** = 85:15). Triethylphosphine afforded poorer selectivity (**11**:**12** = 30:70), whereas methyl(diphenyl)phosphine (PPh_2Me) provided **11** as a single detectable product in 95% yield. These changes in selectivity as a function of phosphine arise from ligand effects on the decarbonylation step (see Supplementary Information for details).

A key advantage of acid fluoride electrophiles is that they are directly accessible from carboxylic acids via deoxyfluorination. Evaluation of various deoxyfluorinating reagents and bases revealed that the combination of tetramethylfluoroformamidinium hexafluorophosphate (TFFH) and 1,8-bis(dimethylamino)naphthalene converts carboxylic acid **13** to acid fluoride **9** within 15 min at room temperature. The subsequent addition of nickel catalyst and boronic acid **10** to the same pot and heating for 16 h at 100 °C then affords biaryl product **11** in 86% yield. Various aromatic and heteroaromatic carboxylic acids participate in this one-pot nickel-catalysed coupling with arylboronic acids (Fig. 3). Esters, nitriles, trifluoromethyl groups, methyl- and phenyl ethers, sulfonamides, amides, alkenes, imidazoles, oxazoles and pinacolboronate esters are tolerated. Aryl chlorides and phenyl esters[26,28]—common electrophiles in other nickel-catalysed cross-coupling reactions—are also compatible, demonstrating the orthogonality of the current method. Moderate yields were obtained with acid fluorides bearing electron-donating substituents (products **17**–**23**) as well as those with *ortho*-substituents (products **20**–**23**). For the former, analysis of the crude reaction mixtures by gas chromatography coupled with mass spectrometry showed ketone side products, indicating that decarbonylation is relatively slow with electron-rich substrates. With the latter, unreacted starting material remained, suggesting that oxidative addition is sluggish when the acid fluoride is sterically hindered. Heteroaromatic carboxylic acids, including thiophene, benzofuran, indole, pyridine and quinoline derivatives, are also effective coupling partners. Finally, various carboxylic acid-containing bioactive molecules, including probenecid, bexarotene, tamibarotene,

© 2018 Springer Nature Limited. All rights reserved.

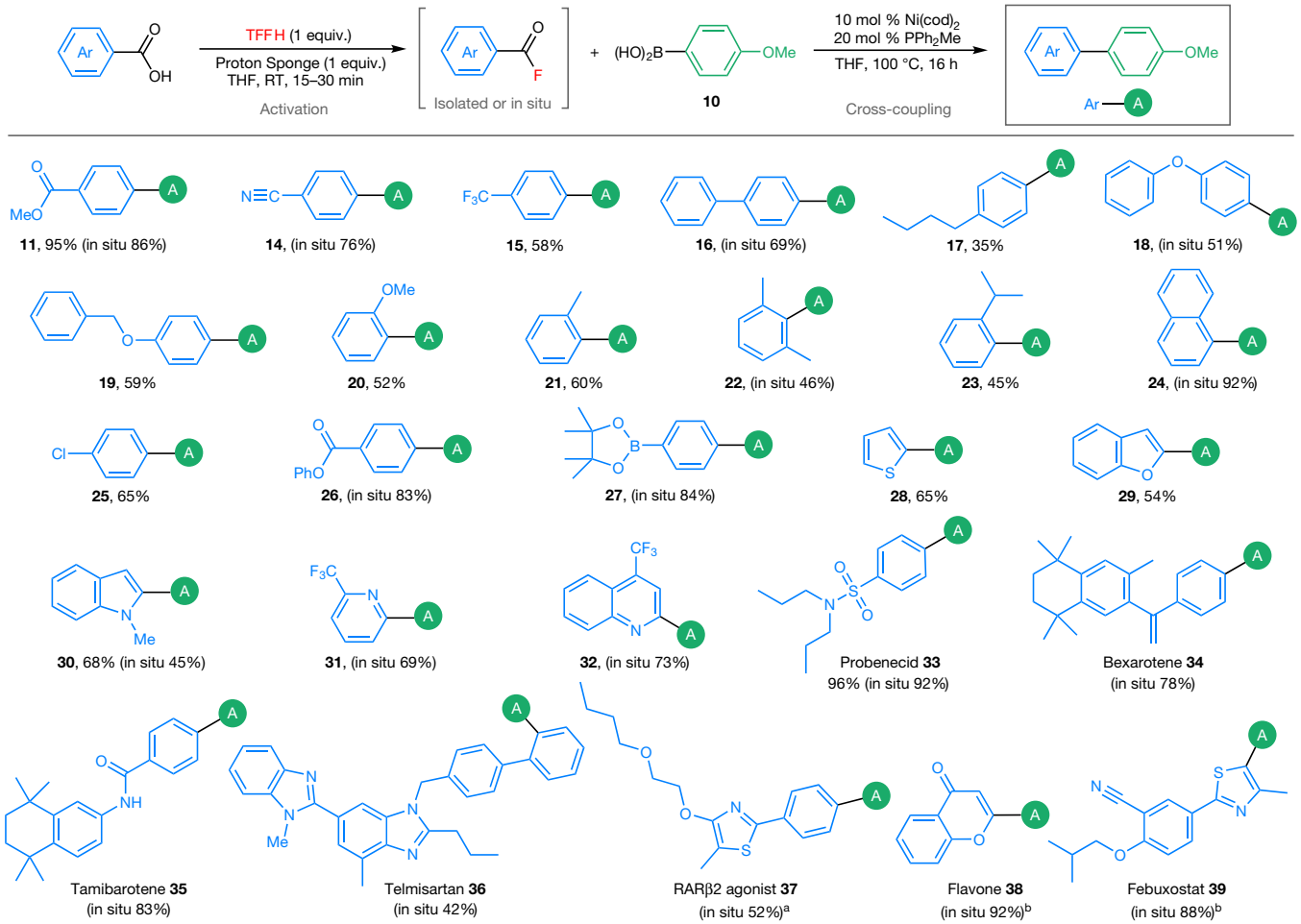

Fig. 3 | Scope of the nickel-catalysed decarbonylative Suzuki–Miyaura reaction with various carboxylic acids. A (in green), *p*-anisyl. [a]Contains inseparable protodecarbonylated carboxylic acid fluoride (7%) as impurity. [b]Tributyl(4-methoxyphenyl)stannane was used as the coupling partner. For details of reaction conditions and for examples of acid fluorides that did not undergo high-yielding decarbonylative coupling, see Supplementary Information.

telmisartan, flavone and febuxostat, participate in this one-pot decarbonylative cross-coupling.

The generality of this method with respect to the boronic acid coupling partner was explored using probenecid as the substrate (Fig. 4a). Aryl boronic acids containing fluorine, ester and methyl ketone substituents were compatible. Alkenyl boronic acids underwent coupling to generate **45** and **46**. Cyclopropyl, allyl and benzyl boronic acids reacted under the optimized conditions to afford moderate yields of **47**–**49**. Additionally, without any modification on the conditions, arylstannane nucleophiles afforded the flavone and febuxostat analogues **36** and **37** (Fig. 3). Base-sensitive α-heteroaryl boronic acids, including furans, thiophenes and pyrroles, also underwent coupling (Fig. 4b). Finally, highly base-sensitive *ortho*-difluorophenyl boronic acids[4,10] underwent high-yielding coupling with probenecid acid fluoride.

A final set of studies focused on eliminating the need for air-sensitive $Ni(cod)_2$ as the nickel source in these transformations. These investigations revealed that the combination of air-stable, commercially available $Ni(o\text{-tolyl})(PPh_2Me)_2Cl$ (**63**, 10 mol%) and CsF (10 mol%) affords a relatively comparable yield to the original catalyst system of $Ni(cod)_2$ and PPh_2Me in the formation of product **61** (Fig. 4c), as well as in related transformations (Supplementary Fig. 9). All of the catalysts and reagents for the reactions with $Ni(o\text{-tolyl})(PPh_2Me)_2Cl$ and CsF were weighed on the benchtop, without the requirement for an inert-atmosphere glove box. As such, this advance should render these coupling reactions even more practical and accessible to a wide variety of synthetic and medicinal chemistry researchers.

Data availability

The main data supporting the findings of this study are available within the article and its Supplementary Information. Additional data are available from the corresponding author upon request. Metrical parameters for the structures of complexes **2b** and **3** (see Supplementary Information) are available free of charge from the Cambridge Crystallographic Data Centre (https://www.ccdc.cam.ac.uk/) under reference numbers CCDC 1837039 and CCDC 1837038, respectively.

Received: 14 April 2018; Accepted: 22 August 2018;
Published online 24 October 2018.

1. Suzuki, A. Cross-coupling reactions of organoboranes: an easy way to construct C–C bonds (Nobel Lecture). *Angew. Chem. Int. Ed.* **50**, 6722–6737 (2011).
2. Brown, D. G. & Boström, J. Analysis of past and present synthetic methodologies on medicinal chemistry: where have all the new reactions gone? *J. Med. Chem.* **59**, 4443–4458 (2016).
3. Lennox, A. J. J. & Lloyd-Jones, G. C. Transmetalation in the Suzuki–Miyaura coupling: the fork in the trail. *Angew. Chem. Int. Ed.* **52**, 7362–7370 (2013).
4. Cox, P. A. et al. Base-catalyzed aryl-$B(OH)_2$ protodeboronation revisited: from concerted proton transfer to liberation of a transient aryl anion. *J. Am. Chem. Soc.* **139**, 13156–13165 (2017).
5. Cox, P. A., Leach, A. G., Campbell, A. D. & Lloyd-Jones, G. C. Protodeboronation of heteroaromatic, vinyl, cyclopropyl boronic acids: pH–rate profiles, autocatalysis, and disproportionation. *J. Am. Chem. Soc.* **138**, 9145–9157 (2016).
6. Molander, G. A. & Biolatto, B. Palladium-catalyzed Suzuki–Miyaura cross-coupling reactions of potassium aryl- and heteroaryltrifluoroborates. *J. Org. Chem.* **68**, 4302–4314 (2003).
7. Knapp, D. M., Gillis, E. P. & Burke, M. D. A general solution for unstable boronic acids: slow-release cross-coupling from air-stable MIDA boronates. *J. Am. Chem. Soc.* **131**, 6961–6963 (2009).

© 2018 Springer Nature Limited. All rights reserved.

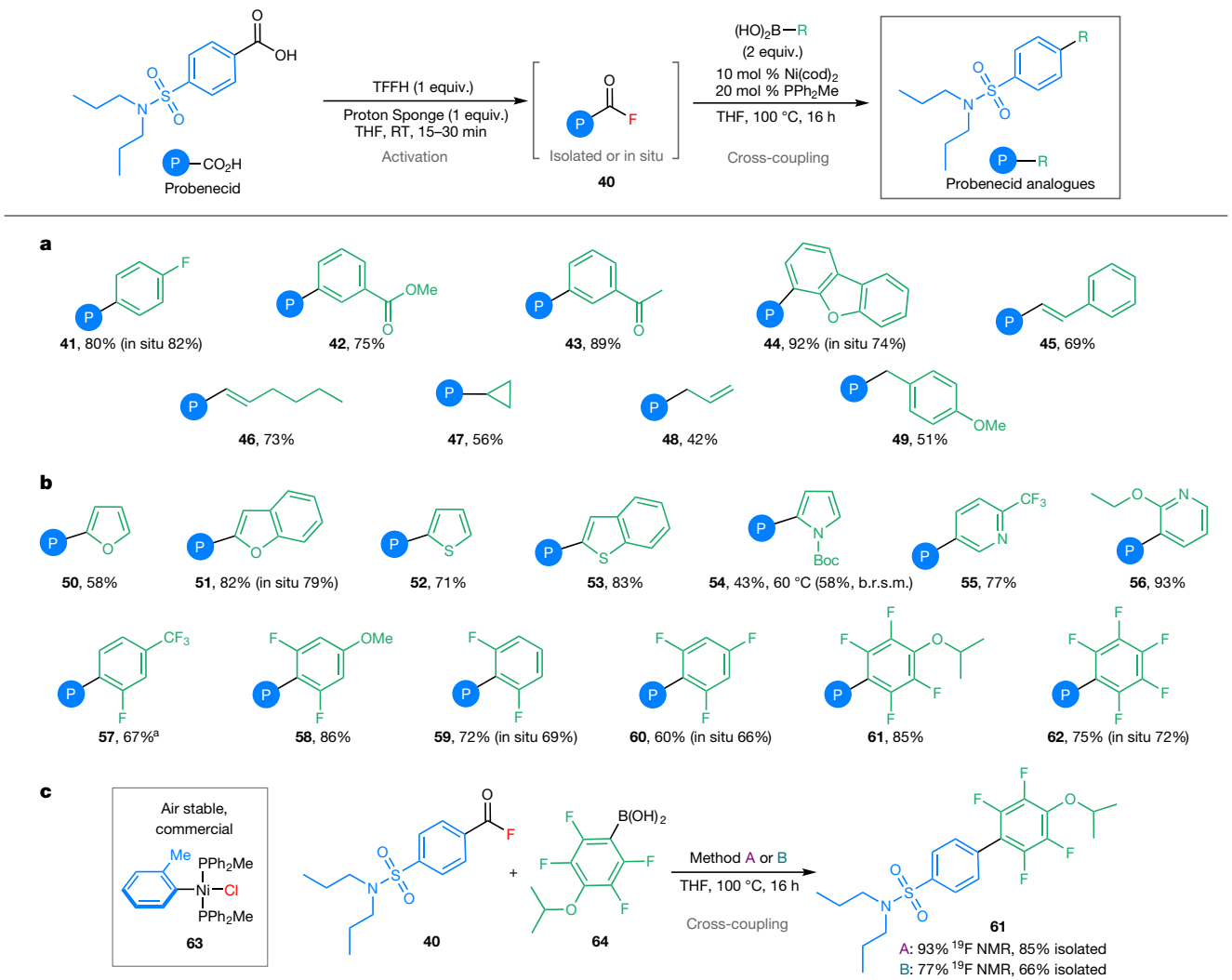

Fig. 4 | Scope of the nickel-catalysed decarbonylative Suzuki–Miyaura coupling with various organoboron reagents. a, (Hetero)aryl, alkenyl, and alkyl boronic acids. **b**, Organoboron reagents that undergo facile protodeboronation. b.r.s.m., based on recovered starting material. **c**, Use of a commercial, air-stable precatalyst **63**. Method A involves standard conditions and is operated in a dry box. Method B: 10 mol% **63**, 10 mol% CsF, all catalysts and reagents are handled on the benchtop. P (in blue), probenecid aryl fragment; Boc, *tert*-butoxycarbonyl. [a]Isolated product contains inseparable ketone by-product (5%). For details on reaction conditions and for examples of organoboron reagents that did not undergo high yielding decarbonylative coupling, see Supplementary Information.

8. Robbins, D. W. & Hartwig, J. F. A C–H borylation approach to Suzuki–Miyaura coupling of typically unstable 2-heteroaryl and polyfluorophenyl boronates. *Org. Lett.* **14**, 4266–4269 (2012).
9. Bulfield, D. & Huber, S. M. Synthesis of polyfluorinated biphenyls; pushing the boundaries of Suzuki–Miyaura cross coupling with electron-poor substrates. *J. Org. Chem.* **82**, 13188–13203 (2017).
10. Kinzel, T., Zhang, Y. & Buchwald, S. L. A new palladium precatalyst allows for the fast Suzuki–Miyaura coupling reactions of unstable polyfluorophenyl and 2-heteroaryl boronic acids. *J. Am. Chem. Soc.* **132**, 14073–14075 (2010).
11. Chen, L., Francis, H. & Carrow, B. P. An "on-cycle" precatalyst enables room-temperature polyfluoroarylation using sensitive boronic acids. *ACS Catal.* **8**, 2989–2994 (2018).
12. Chen, L., Sanchez, D. R., Zhang, B. & Carrow, B. P. "Cationic" Suzuki–Miyaura coupling with acutely base-sensitive boronic acids. *J. Am. Chem. Soc.* **139**, 12418–12421 (2017).
13. Ohashi, M., Saijo, H., Shibata, M. & Ogoshi, S. Palladium-catalyzed base-free Suzuki–Miyaura coupling reactions of fluorinated alkenes and arenes via a palladium fluoride key intermediate. *Eur. J. Org. Chem.* 443–447 (2013).
14. Graham, T. J. A. & Doyle, A. G. Nickel-catalyzed cross-coupling of chromene acetals and boronic acids. *Org. Lett.* **14**, 1616–1619 (2012).
15. Zhang, Y. & Rovis, T. A unique catalyst effects the rapid room-temperature cross-coupling of organozinc reagents with carboxylic acid fluorides, chlorides, anhydrides, and thioesters. *J. Am. Chem. Soc.* **126**, 15964–15965 (2004).
16. Keaveney, S. T. & Schoenebeck, F. Palladium-catalyzed decarbonylative trifluoromethylation of acid fluorides. *Angew. Chem. Int. Ed.* **57**, 4073–4077 (2018).
17. Ogiwara, Y., Sakurai, Y., Hattori, H. & Sakai, N. Palladium-catalyzed reductive conversion of acyl fluorides via ligand-controlled decarbonylation. *Org. Lett.* **20**, 4204–4208 (2018).
18. Gooßen, L. J., Deng, G. & Levy, L. M. Synthesis of biaryls via catalytic decarboxylative coupling. *Science* **313**, 662–664 (2006).
19. Zuo, Z. et al. Merging photoredox with nickel catalysis: coupling of α-carbonyl sp^3-carbons with aryl halides. *Science* **345**, 437–440 (2014).
20. Wang, J. et al. Nickel-catalyzed cross-coupling of redox active esters with boronic acids. *Angew. Chem. Int. Ed.* **55**, 9676–9679 (2016).
21. Edwards, J. T. et al. Decarboxylative alkenylation. *Nature* **545**, 213–218 (2017).
22. Fawcett, A. et al. Photoinduced decarboxylative borylation of carboxylic acids. *Science* **357**, 283–286 (2017).
23. Carrow, B. P. & Hartwig, J. F. Distinguishing between pathways for transmetalation in Suzuki–Miyaura reactions. *J. Am. Chem. Soc.* **133**, 2116–2119 (2011).
24. Amatore, C., Jutand, A. & Le Duc, G. The triple role of fluoride ions in palladium-catalyzed Suzuki–Miyaura reactions: unprecedented transmetalation from [$ArPdFL_2$] complexes. *Angew. Chem. Int. Ed.* **51**, 1379–1382 (2012).
25. Thomas, A. A. & Denmark, S. E. Pre-transmetalation intermediates in the Suzuki–Miyaura reaction revealed: the missing link. *Science* **352**, 329–332 (2016).
26. Muto, K., Yamaguchi, J., Musaev, D. G. & Itami, K. Decarbonylative organoboron cross-coupling of esters by nickel catalysis. *Nat. Commun.* **6**, 7508 (2015).
27. Shi, S., Meng, G. & Szostak, M. Synthesis of biaryls through nickel-catalyzed Suzuki–Miyaura coupling of amides by carbon–nitrogen bond cleavage. *Angew. Chem. Int. Ed.* **55**, 6959–6963 (2016).
28. Guo, L. & Rueping, M. Decarbonylative cross-couplings: nickel catalyzed functional group interconversion strategies for the construction of complex organic molecules. *Acc. Chem. Res.* **51**, 1185–1195 (2018).
29. Masson-Makdissi, J., Vandavasi, J. K. & Newman, S. G. Switchable selectivity in the Pd-catalyzed alkylative cross-coupling of esters. *Org. Lett.* **20**, 4094–4098 (2018).

© 2018 Springer Nature Limited. All rights reserved.

30. Ichiishi, N., Malapit, C. A., Wozniak, L. & Sanford, M. S. Palladium- and nickel-catalyzed decarbonylative C–S coupling to convert thioesters to thioethers. *Org. Lett.* **20**, 44–47 (2018).
31. Schaub, T., Backes, M. & Radius, U. Catalytic C–C bond formation accomplished by selective C–F activation of perfluorinated arenes. *J. Am. Chem. Soc.* **128**, 15964–15965 (2006).
32. Tobisu, M., Xu, T., Shimasaki, T. & Chatani, N. Nickel-catalyzed Suzuki–Miyaura reaction of aryl fluorides. *J. Am. Chem. Soc.* **133**, 19505–19511 (2011).
33. Liu, X.-W., Echavarren, J., Zarate, C. & Martin, R. Ni-catalyzed borylation of aryl fluorides via C–F cleavage. *J. Am. Chem. Soc.* **137**, 12470–12473 (2015).

Acknowledgements We acknowledge financial support from National Institutes of Health NIGMS (GM073836) and the Danish National Research Foundation (Carbon Dioxide Activation Center; CADIAC). We acknowledge J. Kampf for X-ray crystallographic analyses of **2b** and **3**.

Author contributions C.A.M., J.R.B. and C.E.B. developed the stoichiometric reactions. C.A.M. discovered and developed the catalytic reactions. C.A.M., J.R.B. and M.S.S. conceived and designed the investigations. M.S.S. directed and supported the research. C.A.M., J.R.B. and M.S.S. wrote and revised the manuscript.

Competing interests The authors declare no competing interests.

Additional information
Supplementary information is available for this paper at https://doi.org/10.1038/s41586-018-0628-7.
Reprints and permissions information is available at http://www.nature.com/reprints.
Correspondence and requests for materials should be addressed to M.S.S.
Publisher's note: Springer Nature remains neutral with regard to jurisdictional claims in published maps and institutional affiliations.

© 2018 Springer Nature Limited. All rights reserved.

LETTER

https://doi.org/10.1038/s41586-018-0651-8

Quantification of ocean heat uptake from changes in atmospheric O_2 and CO_2 composition

L. Resplandy[1]*, R. F. Keeling[2], Y. Eddebbar[2], M. K. Brooks[2], R. Wang[3], L. Bopp[4], M. C. Long[5], J. P. Dunne[6], W. Koeve[7] & A. Oschlies[7]

The ocean is the main source of thermal inertia in the climate system[1]. During recent decades, ocean heat uptake has been quantified by using hydrographic temperature measurements and data from the Argo float program, which expanded its coverage after 2007[2,3]. However, these estimates all use the same imperfect ocean dataset and share additional uncertainties resulting from sparse coverage, especially before 2007[4,5]. Here we provide an independent estimate by using measurements of atmospheric oxygen (O_2) and carbon dioxide (CO_2)—levels of which increase as the ocean warms and releases gases—as a whole-ocean thermometer. We show that the ocean gained $1.33 \pm 0.20 \times 10^{22}$ joules of heat per year between 1991 and 2016, equivalent to a planetary energy imbalance of 0.83 ± 0.11 watts per square metre of Earth's surface. We also find that the ocean-warming effect that led to the outgassing of O_2 and CO_2 can be isolated from the direct effects of anthropogenic emissions and CO_2 sinks. Our result—which relies on high-precision O_2 measurements dating back to 1991[6]—suggests that ocean warming is at the high end of previous estimates, with implications for policy-relevant measurements of the Earth response to climate change, such as climate sensitivity to greenhouse gases[7] and the thermal component of sea-level rise[8].

As shown in Fig. 1, recent temperature-based hydrographic estimates of ocean warming[9–12] show good agreement for the years 2007–2016 ($1.09 \pm 0.10 \times 10^{22}$ to $1.16 \pm 0.20 \times 10^{22}$ J yr^{-1}), but a larger spread when extending back to include the sparser data of the 1990s ($0.90 \pm 0.09 \times 10^{22}$ to $1.36 \pm 0.10 \times 10^{22}$ J yr^{-1} for 1993–2015). The spread is mostly caused by gap-filling methods and systematic errors[5,9], which together introduce uncertainties of up to 25%–50% in warming trends[4]. Because temperature-based estimates also use the same upper-ocean observations and linear warming trend for depths below 2,000 m (ref. [11]), they may share additional unknown systematic errors[12]. An alternative method based on the top of the atmosphere energy balance[13] is also not truly independent, because it is subject to large systematic errors when estimating long-term trends and therefore depends on the same hydrographic measurements for calibration[13–15]. Here we introduce a third method, based on changes in the abundances of gases in the atmosphere, which respond to whole-ocean warming through the temperature dependence of gas solubility in sea water. This method is not limited by data sparseness, because fast mixing in the atmosphere efficiently integrates the global ocean signal.

Changes in ocean heat content on seasonal[16] and glacial–interglacial[17] timescales have been reconstructed using measurements of noble gases in modern or ancient air. Our method is similar, but instead of relying on noble gases (for example, ratios of argon to nitrogen), which lack sufficient accuracy as yet[16], we rely on measurements of atmospheric O_2 and CO_2, which can be summed to yield a tracer 'atmospheric potential oxygen' (APO) that responds to warming similarly to a noble gas[18]. When the ocean warms, the solubility of O_2 and CO_2 drops, and the amount of gas lost by the ocean can be quantified with the complementary change observed in the atmosphere. Precise atmospheric O_2 measurements began in 1991 (CO_2 in 1958), enabling APO-based reconstructions of ocean heat content that span nearly three decades[6].

APO ($O_2 + 1.1 \times CO_2$) is computed using observed atmospheric O_2/N_2 molar ratios and CO_2 molar fractions (see Methods)[6,19]. By design, APO is insensitive to exchanges with land ecosystems, which produce changes in O_2 and CO_2 that largely cancel in APO owing to their approximate 1.1 O_2/C oxidative ratio. Time-series measurements at remote sites show a global long-term decline in APO, with ΔAPO_{OBS} being -243.70 ± 10.10 per meg (units defined in the Methods) between 1991 and 2016. ΔAPO_{OBS} is driven by four primary contributors, illustrated in Fig. 2:

$$\Delta APO_{OBS} = \Delta APO_{FF} + \Delta APO_{Cant} + \Delta APO_{AtmD} + \Delta APO_{Climate} \quad (1)$$

where ΔAPO_{FF} is the decrease in APO caused by industrial processes (fossil-fuel burning and cement production), which in aggregate consume more than 1.1 moles of O_2 for each mole of CO_2 released; ΔAPO_{Cant} accounts for the oceanic uptake of excess anthropogenic atmospheric CO_2; ΔAPO_{AtmD} accounts for air–sea exchanges driven by ocean fertilization from anthropogenic aerosol deposition (increased fertilization leads to increased photosynthesis, with a concomitant release of O_2 and uptake of CO_2); and $\Delta APO_{Climate}$ accounts for air–sea fluxes of O_2, CO_2 and N_2 driven by ocean processes, including warming-induced changes in solubility, in ocean circulation, and in photosynthesis and respiration (N_2 influences O_2/N_2 ratios). Here, we derive $\Delta APO_{Climate}$ from equation (1) and show that it tracks ocean warming.

We estimate ΔAPO_{FF} using fossil-fuel and cement inventories[20], finding $\Delta APO_{FF} = -119.70 \pm 4.00$ per meg (Fig. 3). ΔAPO_{Cant} is controlled by the increase in atmospheric CO_2 and by ocean mixing, which is quantified by the distribution of transient tracers including chlorofluorocarbons (CFCs)[21]; we find that $\Delta APO_{Cant} = -154.30 \pm 4.20$ per meg. ΔAPO_{Cant} is relatively precise because it excludes the effects of changing ocean biology and circulation on natural carbon fluxes that are included in $\Delta APO_{Climate}$. ΔAPO_{AtmD} is derived from ocean model simulations with and without aerosol fertilization (phosphate, iron and nitrogen; Extended Data Fig. 1)[22]. ΔAPO_{AtmD} is uncertain, owing in part to uncertainties in iron availability to photosynthetic organisms, but is relatively small compared with the other terms: $\Delta APO_{AtmD} = 7.00 \pm 3.50$ per meg. From equation (1), we thereby find that $\Delta APO_{Climate} = 23.20 \pm 12.20$ per meg, corresponding to a least-squares linear trend of $+1.16 \pm 0.15$ per meg per year—larger than the trends expected from 26-year natural variations alone in four Earth-system models (the Community Earth System Model (CESM) and the Geophysical Fluid Dynamics Laboratory (GFDL), Institut Pierre Simon Laplace (IPSL) and University of Victoria (UVic) models). As shown in Fig. 3, a clear increase in $\Delta APO_{Climate}$ emerges over the period January 1991 to the end of December 2016.

A starting point for understanding $\Delta APO_{Climate}$ is to imagine that O_2 and CO_2 behave like inert gases, such that the air–sea fluxes are dominated by temperature-driven solubility changes. In this case,

[1]Department of Geosciences and Princeton Environmental Institute, Princeton University, Princeton, NJ, USA. [2]Scripps Institution of Oceanography, University of California San Diego, La Jolla, CA, USA. [3]Department of Environmental Science and Engineering, Fudan University, Shanghai, China. [4]LMD/IPSL, ENS, PSL Research University, École Polytechnique, Sorbonne Université, CNRS, Paris, France. [5]National Center for Atmospheric Research, Boulder, CO, USA. [6]NOAA, Geophysical Fluid Dynamics Laboratory, Princeton, NJ, USA. [7]GEOMAR Helmholtz Centre for Ocean Research Kiel, Kiel, Germany. *e-mail: laurer@princeton.edu

© 2018 Springer Nature Limited. All rights reserved.

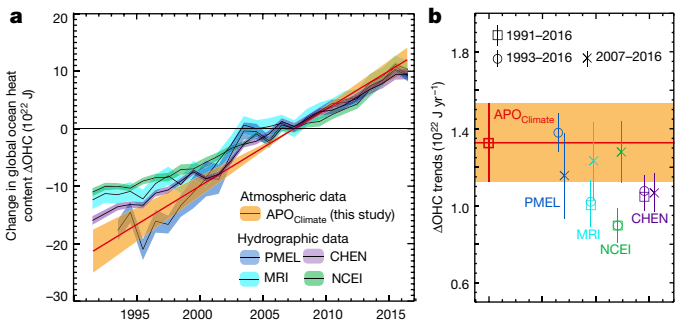

Fig. 1 | Change in global ocean heat content (ΔOHC). a, ΔOHC derived from hydrographic and atmospheric observations (normalized to zero in 2007, ±1σ uncertainty). **b**, Linear least-squares trends for 1991–2016, 1993–2016 and 2007–2016 (±1σ uncertainty). Hydrography-based ΔOHC estimates combine warming rates at ocean depths of 0 to 2,000 m (from Cheng and co-authors (CHEN)[12], Pacific Marine Environmental Laboratory (PMEL)[10], Meteorological Research Institute (MRI)[9] and National Centers for Environmental Information (NCEI)[31] estimates) with the revised deep ocean warming (at depths of more than 2,000 m) of ref. [11] (Extended Data Tables 1 and 2). The atmospheric-based estimate (this study), which uses observed atmospheric potential oxygen trends ($\Delta APO_{Climate}$) and model-based $\Delta APO_{Climate}$-to-ΔOHC ratios, does not resolve interannual variations.

APO would increase by around 0.8 per meg per 10^{22} J of warming, with changes in O_2 and CO_2 solubility accounting for an increase of +1.0 per meg per 10^{22} J, partly offset by the N_2 contribution of −0.2 per meg per 10^{22} J (Methods). Support for the dominance of solubility in $\Delta APO_{Climate}$ can be found in the natural distribution of O_2 and carbon in the ocean. Ocean potential oxygen (OPO) is a dissolved tracer that mirrors $APO_{Climate}$ and tracks changes in air–sea O_2 and CO_2 fluxes[18]. Observed OPO abundance is strongly tied to ocean potential temperature (Fig. 4): warming induces OPO loss, and cooling induces OPO gain. The observed OPO-to-temperature trend of −4.45 nmol J^{-1} is within 17% of the trend of −3.70 nmol J^{-1} expected from solubility alone (OPO_{sat}-to-temperature). Biological effects (related to changes in ocean circulation and photosynthesis/respiration) on CO_2 and O_2 substantially cancel in OPO (Extended Data Fig. 2), while thermal impacts reinforce each other, with warming waters releasing both O_2 and CO_2 to the atmosphere and increasing $\Delta APO_{Climate}$.

Further support for the dominance of solubility in $\Delta APO_{Climate}$ is found on multidecadal timescales in the four Earth-system models mentioned above, which yield OPO-to-temperature ratios of between −4.71 and −4.38 nmol J^{-1}, bracketing the ratio of −4.45 nmol J^{-1}

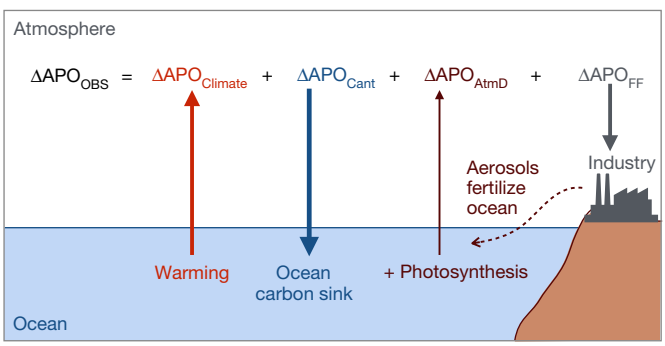

Fig. 2 | Processes contributing to observed changes in atmospheric potential oxygen (ΔAPO_{OBS}). Industrial processes (fossil-fuel burning and cement production; ΔAPO_{FF}) and the ocean sink for anthropogenic carbon (ΔAPO_{Cant}) remove APO from the atmosphere. The fertilization effect of anthropogenic aerosol deposition (ΔAPO_{AtmD})—which promotes marine photosynthesis—and the changes in solubility, biology and ocean circulation due to warming ($\Delta APO_{Climate}$) release APO into the atmosphere. Our study shows that $\Delta APO_{Climate}$ can be used to estimate long-term changes in global ocean warming.

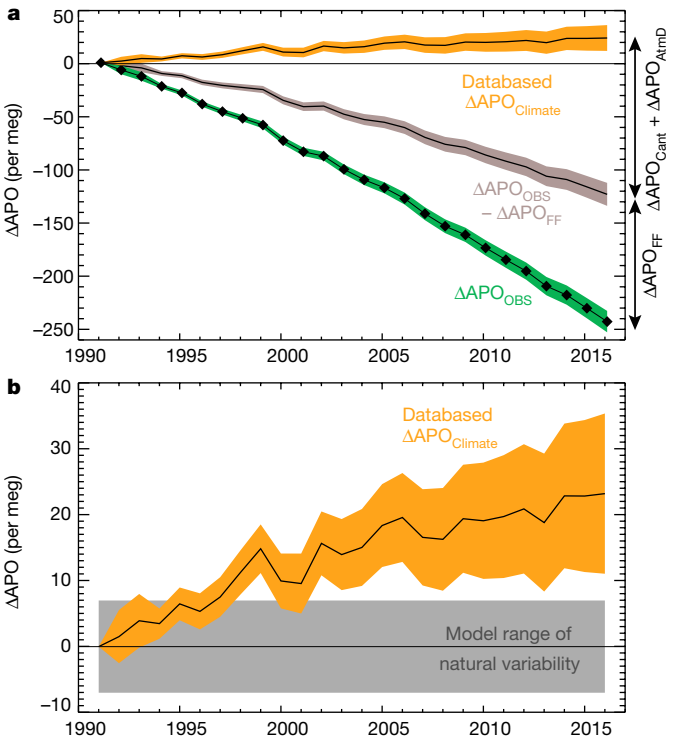

Fig. 3 | Databased estimates of global $\Delta APO_{Climate}$. **a**, $\Delta APO_{Climate}$ estimated from observed APO (ΔAPO_{OBS}) from the Scripps Institution of Oceanography network (1991–2016), and corrected by taking into account fossil-fuel burning, ocean anthropogenic carbon uptake and anthropogenic aerosol deposition ($\Delta APO_{Climate} = \Delta APO_{OBS} - \Delta APO_{FF} - \Delta APO_{Cant} - \Delta APO_{AtmD}$) and their 1$\sigma$ uncertainty ranges. **b**, The increase in global $\Delta APO_{Climate}$ (±1σ interval) exceeds the range of 26-year trends expected from the natural variations in four Earth system models (CESM, GFDL, IPSL and UVic, shown in grey). Sources of uncertainty and contributions to ΔAPO_{OBS}, ΔAPO_{FF} and ΔAPO_{Cant} are given in Extended Data Tables 3 and 4.

found in hydrographic observations (Extended Data Fig. 3). The models also simulate a very close relationship between $\Delta APO_{Climate}$ and the change in global ocean heat content (ΔOHC) that occurs during the simulations (1920–2100), with an atmospheric build-up in APO of between 0.83 and 0.99 per meg per 10^{22} J (Extended Data Figs. 3, 4)—close to the ratio expected from temperature-driven solubility changes alone (0.8 per meg per 10^{22} J). By dividing the simulated APO change into separate biological and thermal components, we show that solubility changes account for more than 80% of $\Delta APO_{Climate}$, while biologically driven changes account for 5% to 20% (Extended Data Fig. 4). This partitioning found in response to transient warming is very similar to the partitioning found in hydrographic data (where solubility and biology contribute 83% and 17%, respectively, to the OPO-to-temperature ratio; Fig. 4).

Small differences between individual model $\Delta APO_{Climate}$-to-ΔOHC relationships (0.83 to 0.99 per meg per 10^{22} J) reflect systematic differences in biological fluxes. Models with stronger biological effects (IPSL and UVic) yield stronger oceanic loss of OPO and stronger release of APO for a given ocean warming (more negative OPO-to-temperature and higher $\Delta APO_{Climate}$-to-ΔOHC; Extended Data Fig. 3b). Using this relationship, we find that a $\Delta APO_{Climate}$-to-ΔOHC ratio of 0.87 ± 0.03 per meg per 10^{22} J is compatible with the observed OPO-to-temperature ratio. Combining this constrained $\Delta APO_{Climate}$-to-ΔOHC ratio (0.87 ± 0.03 per meg per 10^{22} J) with the observation-based trend in $\Delta APO_{Climate}$ (1.16 ± 0.18 per meg yr^{-1}) yields a warming trend of 1.33 ± 0.20 × 10^{22} J yr^{-1} between 1991 and 2016. As shown in Fig. 1, this APO-based estimate of ocean heat uptake agrees well, within uncertainties, with the highest temperature-based estimates (from the Pacific Marine Environmental Laboratory (PMEL)[10], available only for

© 2018 Springer Nature Limited. All rights reserved.

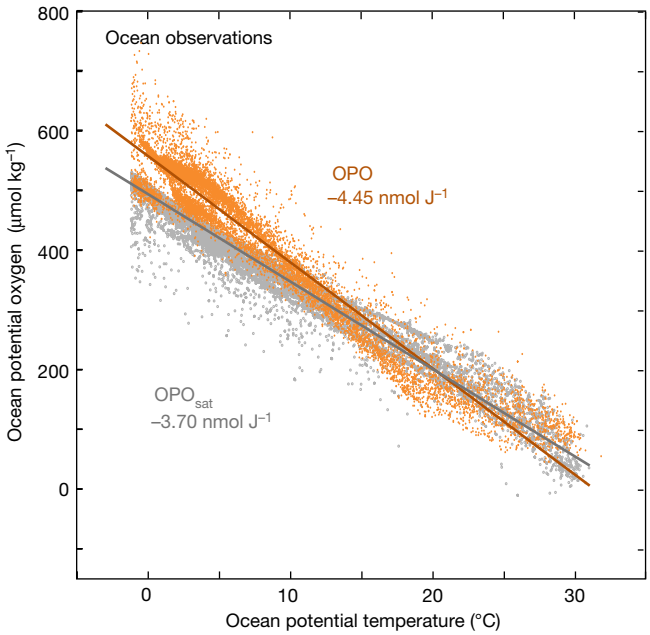

Fig. 4 | Observed link between potential oxygen and ocean heat. OPO concentrations in situ (OPO, yellow) and at saturation based on O_2 and CO_2 solubility (OPO_{sat}, grey) as a function of ocean temperature in the GLODAPv2 database[32].

1993–2015) and marginally with the two next estimates (from Cheng et al.[12] (CHEN) and the Japanese Meteorological Institute (MRI)[9]).

The APO data provide a much-needed independent confirmation of the recent upward revisions in estimates of ocean warming[5,9]. A higher value of ΔOHC compatible with both $APO_{Climate}$ and in situ temperature approaches (1.13 to 1.46×10^{22} J yr^{-1}) calls for a steric sea level rise of 1.34–1.74 mm yr^{-1} (Methods), in full agreement with satellite constraints on thermal expansion, corrected for the freshwater contribution (1.50 ± 0.40 mm yr^{-1})[8,23].

A higher ΔOHC will also affect the equilibrium climate sensitivity, recently estimated at between +1.5 K and +4.5 K if CO_2 is doubled[1]. This estimated range reflects a decrease in the lower bound from 2 K to 1.5 K owing to downward revision of the aerosol cooling effect (in the Intergovernmental Panel on Climate Change (IPCC) Fifth Assessment Report, as compared with the Fourth Assessment Report)[1,24], but relied on a low ΔOHC value (0.80×10^{22} J yr^{-1} for 1993–2010). An upward revision of the ocean heat gain by $+0.5 \times 10^{22}$ J yr^{-1} (to 1.30×10^{22} J yr^{-1} from 0.80×10^{22} J yr^{-1}) would push up the lower bound of the equilibrium climate sensitivity from 1.5 K back to 2.0 K (stronger warming expected for given emissions), thereby reducing maximum allowable cumulative CO_2 emissions by 25% to stay within the 2 °C global warming target (see Methods).

We find that the APO–heat coupling ($APO_{Climate}$) is most robust on decadal and longer timescales. Strong cancellation of biological O_2 and CO_2 fluxes is not expected on all temporal scales[25]. On seasonal timescales, air–sea O_2 fluxes driven by marine photosynthesis are around eight times larger than those of CO_2 owing to slow equilibration of CO_2 (ref. [25]). More complex coupling is also possible on interannual timescales[26], such as the weaker lagged air–sea CO_2 flux compared with the O_2 flux during El Niño events[27].

Atmospheric O_2 and CO_2 measurements have been applied previously to estimate global land and ocean CO_2 sinks, but relied on estimates of ocean heat content and model-based oceanic O_2-to-heat ratios to correct for climate-driven O_2 outgassing[28–30]. Here we have reversed this logic, using estimates of other quantities to constrain the ocean heating. Our approach exploits the APO–heat relationship, which is stronger than the O_2–heat relationship. Further work to constrain the separate contributions of O_2 and CO_2 to APO is needed to refine estimates of land and ocean carbon sinks using atmospheric O_2 and CO_2.

Online content

Any methods, additional references, Nature Research reporting summaries, source data, statements of data availability and associated accession codes are available at https://doi.org/10.1038/s41586-018-0651-8.

Received: 4 December 2017; Accepted: 29 August 2018;
Published online 31 October 2018.

1. IPCC. *Climate Change 2013: The Physical Science Basis* (eds Stocker, T. F. et al.) (Cambridge Univ. Press, Cambridge, 2013).
2. Abraham, J. P. et al. A review of global ocean temperature observations: implications for ocean heat content estimates and climate change. *Rev. Geophys.* **51**, 450–483 (2013).
3. Riser, S. C. et al. Fifteen years of ocean observations with the global Argo array. *Nat. Clim. Change* **6**, 145–153 (2016).
4. Boyer, T. et al. Sensitivity of global upper-ocean heat content estimates to mapping methods, XBT bias corrections, and baseline climatologies. *J. Clim.* **29**, 4817–4842 (2016).
5. Cheng, L. et al. XBT science: assessment of instrumental biases and errors. *Bull. Am. Meteorol. Soc.* **97**, 924–933 (2016).
6. Keeling, R. F. & Manning, A. C. in *Treatise on Geochemistry* 385–404 (Elsevier, Oxford, 2014).
7. Forster, P. M. Inference of climate sensitivity from analysis of Earth's energy budget. *Annu. Rev. Earth Planet. Sci.* **44**, 85–106 (2016).
8. Church, J. A. et al. in *Climate Change 2013: The Physical Science Basis* (eds Stocker, T. F. et al.) 1137–1216 (IPCC, Cambridge Univ. Press, Cambridge, 2013).
9. Ishii, M. et al. Accuracy of global upper ocean heat content estimation expected from present observational data sets. *Sci. Online Lett. Atmos.* **13**, 163–167 (2017).
10. Johnson, G. C. et al. Ocean heat content. *Am. Meteorol. Soc. Bull.* **98**, S66–S68 (2017).
11. Desbruyères, D. G., Purkey, S. G., McDonagh, E. L., Johnson, G. C. & King, B. A. Deep and abyssal ocean warming from 35 years of repeat hydrography. *Geophys. Res. Lett.* **43**, 10356–10365 (2016).
12. Cheng, L. et al. Improved estimates of ocean heat content from 1960 to 2015. *Sci. Adv.* **3**, e1601545 (2017).
13. Allan, R. P. et al. Changes in global net radiative imbalance 1985–2012. *Geophys. Res. Lett.* **41**, 5588–5597 (2014).
14. Palmer, M. D. Reconciling estimates of ocean heating and Earth's radiation budget. *Curr. Clim. Change Rep.* **3**, 78–86 (2017).
15. Loeb, N. G. et al. Observed changes in top-of-the-atmosphere radiation and upper-ocean heating consistent within uncertainty. *Nat. Geosci.* **5**, 110–113 (2012).
16. Battle, M. *et al.* Measurements and models of the atmospheric Ar/N_2 ratio. *Geophys. Res. Lett.* **30**, 1786 (2003).
17. Ritz, S. P., Stocker, T. F. & Severinghaus, J. P. Noble gases as proxies of mean ocean temperature: sensitivity studies using a climate model of reduced complexity. *Quat. Sci. Rev.* **30**, 3728–3741 (2011).
18. Resplandy, L. et al. Constraints on oceanic meridional heat transport from combined measurements of oxygen and carbon. *Clim. Dyn.* **47**, 3335–3357 (2016); erratum **49**, 4317 (2017).
19. Stephens, B. B. et al. Testing global ocean carbon cycle models using measurements of atmospheric O_2 and CO_2 concentration. *Glob. Biogeochem. Cycles* **12**, 213–230 (1998).
20. Le Quéré, C. et al. Global carbon budget 2016. *Earth Syst. Sci. Data* **8**, 605–649 (2016).
21. DeVries, T. The oceanic anthropogenic CO_2 sink: storage, air-sea fluxes, and transports over the industrial era. *Glob. Biogeochem. Cycles* **28**, 631–647 (2014).
22. Wang, R. et al. Influence of anthropogenic aerosol deposition on the relationship between oceanic productivity and warming. *Geophys. Res. Lett.* **42**, 10745–10754 (2015).
23. Rietbroek, R., Brunnabend, S.-E., Kusche, J., Schröter, J. & Dahle, C. Revisiting the contemporary sea-level budget on global and regional scales. *Proc. Natl Acad. Sci. USA* **113**, 1504–1509 (2016).
24. IPCC. *Climate Change 2007: Synthesis Report* (eds Core Writing Team, Pachauri, R. K. & Reisinger, A.) (IPCC, Geneva, 2008).
25. Keeling, R. F. & Severinghaus, J. P. in *The Carbon Cycle* (eds Wigley, T. M. L. & Schimel, D.) 134–140 (Cambridge Univ. Press, New York, 2000).
26. Resplandy, L., Séférian, R. & Bopp, L. Natural variability of CO_2 and O_2 fluxes: what can we learn from centuries-long climate models simulations? *J. Geophys. Res. Oceans* **120**, 384–404 (2015).
27. Eddebbar, Y. A. et al. Impacts of ENSO on air-sea oxygen exchange: observations and mechanisms. *Glob. Biogeochem. Cycles* **31**, 2017GB005630 (2017).
28. Keeling, R. F. & Garcia, H. E. The change in oceanic O_2 inventory associated with recent global warming. *Proc. Natl Acad. Sci. USA* **99**, 7848–7853 (2002).
29. Bopp, L., Le Quéré, C., Heimann, M., Manning, A. C. & Monfray, P. Climate-induced oceanic oxygen fluxes: implications for the contemporary carbon budget. *Glob. Biogeochem. Cycles* **16**, 1022 (2002).
30. Keeling, C. D., Piper, S. C., Whorf, T. P. & Keeling, R. F. Evolution of natural and anthropogenic fluxes of atmospheric CO_2 from 1957 to 2003. *Tellus B Chem. Phys. Meterol.* **63**, 1–22 (2011).

© 2018 Springer Nature Limited. All rights reserved.

31. Levitus, S. et al. World ocean heat content and thermosteric sea level change (0–2000 m), 1955–2010. *Geophys. Res. Lett.* **39**, L10603 (2012).
32. Olsen, A. et al. The Global Ocean Data Analysis Project version 2 (GLODAPv2)—an internally consistent data product for the world ocean. *Earth Syst. Sci. Data* **8**, 297–323 (2016).

Acknowledgements We thank M. Winton for useful suggestions. L.R. acknowledges support from the Climate Program Office of the National Oceanic and Atmospheric Administration (NOAA), grant NA13OAR4310219, and from the Princeton Environmental Institute. The National Center for Atmospheric Research (NCAR) is sponsored by the National Science Foundation (NSF). We also thank the people who maintain the APO time series at Scripps and the groups developing the models CESM, GFDL, IPSL and UViC, used in this study. The Scripps O_2 program has been supported by a series of grants from the US NSF and the NOAA, most recently 1304270 and NA15OAR4320071. Any opinions, findings, and conclusions or recommendations expressed in this material are those of the authors and do not necessarily reflect the views of the NSF and NOAA. We thank the staff at the Cape Grim Baseline Air Pollution Station of the Canadian Greenhouse Gas program for collection of air samples.

Reviewer information *Nature* thanks L. Cheng, F. Primeau and the other anonymous reviewer(s) for their contribution to the peer review of this work.

Author contributions L.R. directed the analysis of the datasets and models used here and shared responsibility for writing the manuscript; R.F.K. shared responsibility for writing the manuscript; R.W. performed simulations of anthropogenic aerosols; L.B., J.P.D., M.C.L., W.K. and A.O. provided model results. All authors contributed to the final version of the manuscript.

Competing interests The authors declare no competing interests.

Additional information
Extended data is available for this paper at https://doi.org/10.1038/s41586-018-0651-8.
Reprints and permissions information is available at http://www.nature.com/reprints.
Correspondence and requests for materials should be addressed to L.R.
Publisher's note: Springer Nature remains neutral with regard to jurisdictional claims in published maps and institutional affiliations.

© 2018 Springer Nature Limited. All rights reserved.

METHODS

Observed changes in APO. A change in atmospheric potential oxygen concentration (in per meg) is defined following[19]:

$$(\delta \mathrm{APO}) = (\delta \mathrm{O_2/N_2}) + \frac{1.1}{X_{\mathrm{O_2}}} \times (X_{\mathrm{CO_2}} - 350)$$

with

$$(\delta \mathrm{O_2/N_2}) = \frac{\mathrm{O_2/N_2(sample)}}{\mathrm{O_2/N_2(reference)}} - 1$$

where $(\delta O_2/N_2)$ is the atmospheric change in $\delta O_2/N_2$ ratios (in per meg); X_{CO_2} is the CO_2 concentration in the air parcel (in p.p.m., that is, μmol mol^{-1}) and 350 is an arbitrary reference; 1.1 is the approximate O_2/CO_2 ratio of terrestrial ecosystems[33]; and X_{O_2} (= 0.2094) is the reference value of atmospheric mole fraction of O_2 necessary to convert X_{CO_2} from p.p.m. to per meg units.

ΔAPO_{OBS} is computed from in situ atmospheric changes in CO_2 concentrations and O_2/N_2 ratios[19] measured at stations of the Scripps Institution of Oceanography network (available online at http://scrippso2.ucsd.edu)[6]. The global average ΔAPO_{OBS} is based on data from the three stations with longest record (1991 to 2016), that is, La Jolla (32.9° N, 117° W), Alert (82.5° N, 62.5° W) and Cape Grim (40.5° S, 144.5° E) and weighted by the stations' latitudinal distribution[34]. Station annual means are based on bimonthly data fit to a four-harmonic seasonal cycle and a stiff long-term trend[6]. The uncertainty on ΔAPO_{OBS} was computed by generating 10^6 time series with noise scaled to the random and systematic errors of APO data detailed in Extended Data Table 3. The uncertainty is taken as the 1σ interval (±1 standard deviation) from these 10^6 realizations (Fig. 3).

Effects of fossil-fuel burning and cement production on APO. ΔAPO_{FF} is estimated using annual CO_2 emissions from oil, coal, gas, flaring and cement production ($\Delta CO_{2(i)}$ in moles)[20] weighted by their O_2/C combustion ratios, R_i (ref. [6]):

$$\Delta \mathrm{APO_{FF}(per\ meg)} = \sum_{\mathrm{i}} \frac{1.1 - R_i}{X_{\mathrm{O_2}}} \times \frac{\Delta \mathrm{CO_{2(i)}}}{M_{\mathrm{air}}}$$

where M_{air} is the number of moles of dry air in the atmosphere (convert moles of CO_2 to p.p.m.).

The uncertainty on ΔAPO_{FF} includes uncertainties in CO_2 emissions ($\Delta CO_{2(i)}$)[35] and in combustion ratios (R_i in Extended Data Table 3)[36]. Uncertainties on $\Delta CO_{2(i)}$ are not independent in time and were estimated using an autoregressive model[37] (1,000 realizations); uncertainties on R_i were computed using a Monte Carlo approach (1,000 realizations). The uncertainty on ΔAPO_{FF} was then estimated by combining the 1,000 realizations of $\Delta CO_{2(i)}$ and the 1,000 realizations of R_i, yielding a set of 10^6 estimates of ΔAPO_{FF}.

Effect of ocean anthropogenic carbon uptake on APO. We represent the ocean CO_2 uptake (ΔCO_2) as the sum of three contributions:

$$\Delta \mathrm{CO_2} = \Delta \mathrm{Cant_0} + \Delta \mathrm{Cant'} + \Delta \mathrm{CO_{2Climate}} \quad (2)$$

where $\Delta Cant_0$ is the flux driven by the rise in CO_2 assuming steady ocean circulation ($\Delta Cant_0$ is negative, corresponding to uptake by the ocean); $\Delta CO_{2Climate}$ is the flux driven by the action of climate on natural carbon in the ocean ($\Delta CO_{2Climate}$ is positive, that is, warming reduces the uptake of natural carbon); and $\Delta Cant'$ is the remainder, which accounts for impact of circulation changes on the uptake of carbon driven by rising CO_2 ($\Delta Cant'$ is positive, that is, warming reduces the uptake of C_{ant}). ΔAPO_{Cant} can be expressed as the weighted sum of the two terms $\Delta Cant_0$ and $\Delta Cant'$:

$$\Delta \mathrm{APO_{Cant}(per\ meg)} = \frac{1.1}{X_{\mathrm{O2}} \times M_{\mathrm{air}}} \times (\Delta \mathrm{Cant_0} + \Delta \mathrm{Cant'})$$

where $\Delta Cant_0$ and $\Delta Cant'$ are in moles. Note that $\Delta CO_{2Climate}$ is accounted for in $\Delta APO_{Climate}$.

$\Delta Cant_0$ is taken from a recent ocean inversion scheme with assimilation of observed potential temperature, salinity, radiocarbon and CFC-11 (ref. [21]), updated to 2016. $\Delta Cant'$ cannot be derived from observations and was estimated at 0.05 Pg C yr^{-1}, equivalent to a trend of +0.2 per meg^{-1}, using model simulations (see 'Model anthropogenic $\Delta Cant'$').

The uncertainty on ΔAPO_{Cant} is related to uncertainties in $\Delta Cant_0$ and $\Delta Cant'$. We allow for uncertainty in $\Delta Cant_0$ following ref. [21], using the ten sensitivity experiments (on ocean vertical and isopycnal diffusivities, data constraint, gas-exchange coefficient and so on) available for the ocean inversion and an estimate of the interannual variability in the ocean sink of a 0.2 Pg C yr^{-1}. We also allow an additional 1% uncertainty (less than 0.03 Pg C yr^{-1}) in $\Delta Cant_0$ resulting from imperfectly known atmospheric CO_2 history[38], taking account of sensitivity to start date (1765 versus 1791), to degree of temporal smoothing, and to using different versions of the record since 1958 (Mauna Loa record versus average of Mauna Loa and South Pole records). This estimate used a variant of the box-diffusion model[39], and CO_2 data from ref. [40] and the Scripps CO_2 program (https://library.ucsd.edu/dc/collection/bb3381541w). Uncertainties on $\Delta Cant'$ are assumed to be 100% of the model-based estimate of $\Delta Cant'$.

Ocean fertilization and atmospheric deposition of aerosols. Deposition of anthropogenic aerosol from fossil fuel, biomass burning and other processes fertilizes the ocean with nutrients and increases surface photosynthesis and subsurface respiration[41–43]. The effect of aerosol fertilization is partly counterbalanced by biological processes such as a decline in nitrogen fixation, which would be immediate, and an increase in denitrification in the water column, which would be on timescales of several hundred years[44]. Fixed anthropogenic nitrogen also fertilizes the land biosphere and coastal oceans by river runoffs, but, in these cases, efficient denitrification returns fixed nitrogen to the atmosphere and has little impact on the APO budget on the decadal timescales considered here. The impact of anthropogenic aerosol on O_2, CO_2 and APO air−sea fluxes is evaluated with the IPSL ocean model NEMO-PISCES v2 (ref. [45]), using the difference between simulations with aerosols and a simulation in which the aerosol deposition is fixed to a constant preindustrial value (equivalent to year 1850, Extended Data Fig. 1)[22]. We use four simulations with varying aerosols: one includes the combined effect of nitrogen (N), iron (Fe) and phosphorus (P) aerosol deposition, whereas the other three include only their individual contributions (N-only, Fe-only or P-only; Extended Data Fig. 1 and Extended Data Table 5). Uncertainties at the 1σ level on ΔAPO_{AtmD} are assumed to be ±50%. See Extended Data Table 4.

Combined, N, Fe and P deposition accounts for an O_2 outgassing of 19.0 Tmol yr^{-1} for the 1980–2007 period (16 Tmol yr^{-1} for the entire 1960–2007 simulation period) and an oceanic CO_2 uptake of 8.3 Tmol yr^{-1} for the 1980–2007 period (6.8 Tmol yr^{-1} for the entire 1960–2007 simulation period; Extended Data Fig. 1 and Extended Data Table 5). The overall impact on ΔAPO_{AtmD} is +0.27 per meg yr^{-1} over 27 years of simulation (1980–2007), which we extrapolate to our 1991–2016 period. Increased O_2 outgassing accounts for an increase in APO of +0.51 per meg yr^{-1}, and CO_2 uptake accounts for a change in APO of −0.24 per meg yr^{-1} ($APO_{AtmD(O2)}$ and $APO_{AtmD(CO2)}$ in Extended Data Table 3).

The overall effect of N, Fe and P is smaller than the sum of the individual effects (Extended Data Fig. 1), because of the interplay between the aerosol deposition pattern and nutrient co-limitations in the ocean. Phytoplankton growth in the ocean depends on the availability of the most limiting nutrient. While more available N will promote photosynthesis in regions where N is limiting (for example, the tropical Atlantic Ocean), the effect is negligible in regions where Fe, P or any other nutrient is limiting (such as the Southern Ocean; see Fig. 2 in ref. [22]).

To our knowledge this is the first estimate of the effect of anthropogenic aerosol deposition on both O_2 and CO_2 air–sea fluxes at the global scale. Note however that ref. [6] used anthropogenic aerosol N inventories and scaling arguments to estimate an ocean O_2 loss due to anthropogenic N deposition only of about 10 ± 10 Tmol yr^{-1}, slightly lower than our model estimate of 15.5 Tmol yr^{-1}.

$\Delta APO_{Climate}$ trends and uncertainty analysis. We compute the APO response to climate change ($\Delta APO_{Climate}$) via:

$$\Delta \mathrm{APO_{Climate}} = \Delta \mathrm{APO_{OBS}} - \Delta \mathrm{APO_{FF}} - \Delta \mathrm{APO_{Cant}} - \Delta \mathrm{APO_{AtmD}}$$

We combine the estimates of ΔAPO_{FF}, ΔAPO_{Cant} and ΔAPO_{AtmD} to obtain 10^6 time series of $\Delta APO_{FF} + \Delta APO_{Cant} + \Delta APO_{AtmD}$, and obtain 10^6 time series of $\Delta APO_{Climate}$ using the 10^6 time series of ΔAPO_{OBS}. We computed the $\Delta APO_{Climate}$ least-squares linear trend using the standard deviation of the 10^6 realizations of $\Delta APO_{Climate}$ as the error. We find a $\Delta APO_{Climate}$ trend of 1.16 ± 0.15 per meg yr^{-1} for 1991–2016.

Hydrography-based estimates of ocean heat uptake. We used four global-ocean estimates of ΔOHC, based on hydrographic measurements, in Fig. 1. Ocean warming rates from the surface to 2,000 m are from ref. [10] (PMEL), ref. [9] (MRI; https://climate.mri-jma.go.jp/pub/ocean/ts/v7.2/), an updated version of ref. [31] (NCEI; www.nodc.noaa.gov/OC5/3M_HEAT_CONTENT/basin_avt_data.html) and ref. [12] (CHEN; http://159.226.119.60/cheng/images_files/TOA_OHC_errorbar_1940_2015_2.txt), with the revised deep-ocean (depths greater than 2,000 m) constant linear warming rate of 0.10 ± 0.03 × 10^{22} J yr^{-1} of ref. [11] being based on the global ship-based sections program (GO-SHIP; http://www.go-ship.org)[46].

Ocean observations of ocean potential oxygen. We used in situ ocean observations from GLODAPv2 (ref. [32]) combined with an anthropogenic carbon estimate[21] interpolated at the location of each sample to compute 78,456 values (GLODAPv2 quality control = 0; marginal seas and coastal waters were removed) of OPO[18] as follows:

$$\mathrm{OPO} = \mathrm{O_2^*} + 1.1 \times \mathrm{C}_{pi}^*$$

© 2018 Springer Nature Limited. All rights reserved.

where O_2* and C_{pi}* are ocean conservative tracers related to air–sea fluxes of O_2 and preindustrial carbon[47]. The thermal component (solubility-driven) of OPO (OPO_{sat}) is computed as:

$$OPO_{sat} = O_{2sat} + 1.1 \times C_{pisat}$$

where O_{2sat} is the dissolved O_2 concentration at saturation with the observed temperature and salinity[48]; and C_{pisat} is the dissolved inorganic carbon concentration expected at the observed temperature and salinity and assuming equilibrium with a preindustrial partial pressure of CO_2 of 280 p.p.m., using pre-formed alkalinity[49].

Solubility-driven changes in OPO and APO. Extended Data Fig. 2 shows a tight and quasilinear link between observed OPO and potential temperature (-4.4 nmol J^{-1}; $r^2 = 0.95$), similar to the link found between OPO_{sat} and potential temperature (-3.7 nmol J^{-1}; $r^2 = 0.93$). This suggests that changes in OPO and hence $\Delta APO_{Climate}$ are driven primarily by changes in thermal air–sea fluxes. In these observations, departures of dissolved oxygen and carbon concentrations (O_2* and C_{pi}*) from their respective saturation curves (O_{2sat} and C_{pisat}) due to biological activity tend to balance (Extended Data Fig. 2). By contrast, thermal effects reinforce each other (O_{2sat} and C_{pisat} both decrease with increasing temperature) and biological effects compensate for each other (O_2* > O_{2sat} and C_{pi}* < C_{pisat}).

The change in APO expected from changes in gas solubility in the ocean is an increase of 3.0 nmol per J of warming, which includes the outgassing of O_2 and CO_2 following OPO_{sat} (3.7 nmol J^{-1}) and the release of N_2 (0.7 nmol J^{-1}) (Extended Data Fig. 2b). A change of 3.0 nmol per J of warming is equivalent to an increase of 1.0 per meg per 10^{22} J ($= (3.0 \times 10^{-9}) / (3.7 \times 10^{19}) \times 10^{22} = 0.8 \times 10^{-6} = 1.0$ per meg per 10^{22} J, with 3.7×10^{19} being the number of moles of O_2 in the atmosphere). O_2 and CO_2 solubility alone yields an increase in APO of 1.0 per meg per 10^{22} J, which is partly counterbalanced by the outgassing of N_2 that decreases APO by 0.2 per meg per 10^{22} J (via the increase in the O_2/N_2 ratio).

Earth system model experiments. We used four Earth-system models (ESMs): the Geophysical Fluid Dynamics Laboratory Earth System Models with a nominally level vertical coordinate version, GFDL-ESM2M (called GFDL here)[50,51], the Institut Pierre-Simon Laplace Coupled Model 5 version IPSL-CM5A-LR (IPSL here)[52], the Community Earth System Model large ensemble CESM-LE (CESM here)[53] and the UVic model version 2.9 (UVic here)[54]. Evaluation of these models and their biogeochemical components can be found in previous studies[51,55–57]. GFDL, IPSL and UVic participated in the Coupled Model Intercomparison Project Phase 5 (CMIP5)[58].

For GFDL, IPSL and UVic, we used the CMIP5 business as usual 'historical-RCP8.5' scenario, the feedback experiment 'esmFdbk3' (which includes only warming-driven changes associated with anthropogenic emissions, such as radiation effects), and the fixed-climate experiment 'esmFixClim3', which includes only the direct biogeochemical effects of increasing atmospheric CO_2 (for example, uptake of anthropogenic carbon, acidification and so on). For CESM, we also used the historical-RCP8.5 experiment and the separation between anthropogenic carbon from the natural carbon available in this model (carbon tracer separation approach). The feedback approach used for GFDL, IPSL and UVic removes all direct biogeochemical effects of rising atmospheric CO_2 on the air–sea O_2 and CO_2 exchanges, whereas the natural carbon tracer separation approach used for CESM still includes the biogeochemical impacts of increasing atmospheric CO_2 on the carbon cycle (for example, acidification) even while it excludes the anthropogenic carbon itself. However, we expect the effect on our results to be small and negligible.

We also used the multicentury preindustrial control simulation 'piControl' with no increase in atmospheric CO_2 to correct for model drift and to estimate the natural internal variability of $\Delta APO_{Climate}$ (Fig. 2). We used model results over the 1920–2100 period, which were available for the four models.

Model OPO was computed as for the observations. Note that for CESM we removed subsurface regions of high denitrification in the Eastern Equatorial Pacific Ocean and the Bay of Bengal, where oxygen and O_2* in this model have unrealistic values[59].

Model anthropogenic $\Delta Cant'$. The component $\Delta Cant'$ was derived from equation (2) ($\Delta Cant' = \Delta CO_2 - \Delta Cant_0 - \Delta CO_{2Climate}$) using CMIP5 model simulations. ΔCO_2 was taken from experiment RCP8.5, $\Delta Cant_0$ from experiment esmFixClim3, and $\Delta CO_{2Climate}$ from experiment esmFdbk3. Note that the control simulation was also used to correct model drift. We estimated $\Delta Cant'$ to be 0.05 ± 0.05 Pg C yr^{-1} for 1991–2016, based on the results of the three models—which individually yielded $\Delta Cant'$ values of 0.0 Pg C yr^{-1} (IPSL), 0.12 Pg C yr^{-1} (GFDL) and 0.12 Pg C yr^{-1} (UVic)—and assuming an uncertainty of $\pm 100\%$. This corresponds to a trend of 0.12 ± 0.12 per meg yr^{-1}.

Model $\Delta APO_{Climate}$-to-ΔOHC ratios and uncertainty. Model $\Delta APO_{Climate}$ is computed using individual contributions from O_2, CO_2 and N_2 as follows:

$$APO_{Climate}(\text{per meg}) = APO_{O_2} + APO_{CO_2} + APO_{N_2}$$

$$\Delta APO_{Climate}(\text{per meg}) = \frac{1}{X_{O_2} 2p M_{air}} \times \left(\Delta F_{O_2} + 1.1 \times \Delta F_{CO_2} - \frac{X_{O_2}}{X_{N_2}} \times \Delta F_{N_2} \right)$$

where ΔF_{O_2}, ΔF_{CO_2} and ΔF_{N_2} are the changes in air–sea fluxes of O_2, CO_2 and N_2 respectively (in moles); M_{air} is the number of moles of dry air in the atmosphere; and X_{N_2} and X_{O_2} are the reference atmospheric mixing ratios of N_2 and O_2 respectively[60]. O_2 and CO_2 fluxes are simulated in the models. N_2 air–sea fluxes, which affect the O_2 atmospheric mixing ratio (because O_2 constitutes around 20% of the atmospheric composition), are quantified from the global ocean temporal changes in N_2 solubility computed from model changes in temperature and salinity[61].

The link between long-term changes in $APO_{Climate}$ and ocean heat content—that is, $\Delta APO_{Climate}$-to-ΔOHC ratios—were computed for each model using the 180 years of simulations (1920–2100). Resulting $\Delta APO_{Climate}$-to-ΔOHC ratios vary between 0.83 and 0.99 per meg per 10^{22} J of warming (Extended Data Fig. 3). These ratios include uncertainty in the natural climate variations on interannual and decadal timescales and uncertainty in the O_2/C oxidative ratio associated with global gains and losses of O_2 and CO_2 by terrestrial ecosystems. The uncertainty due to interannual variations was evaluated by computing $\Delta APO_{Climate}$-to-ΔOHC ratios using multiple 26-year-long segments from the 180-year simulations. We obtained 616 $\Delta APO_{Climate}$-to-ΔOHC ratios (154 time series of 26 years per model), and used the standard deviation between these ratios as a measure of the uncertainty.

The O_2/C ratio is assumed to be 1.1 in our computation to follow the widely accepted definition of APO ($APO = O_2 + 1.1 \times CO_2$), but is shown to have variations between 1 and 1.1 (ref. [33]). An oxidative ratio lower than 1.1 would yield a weaker $\Delta APO_{Climate}$-to-ΔOHC slope and hence a slightly higher estimate of ΔOHC for a given $\Delta APO_{Climate}$. We evaluated the influence of the O_2/C ratio for each model by using the difference between $\Delta APO_{Climate}$ computed with a ratio of 1.1 and $\Delta APO_{Climate}$ computed with a ratio of 1. The two contributions to the uncertainties on the simulated $\Delta APO_{Climate}$-to-ΔOHC ratios (interannual variations and O_2/C ratio) combine to yield ± 0.01 per meg per 10^{22} J for the CESM and GFDL models, ± 0.02 per meg per 10^{22} J for the UVic model, and ± 0.05 per meg per 10^{22} J for the IPSL model (1σ). These uncertainties are used in Extended Data Fig. 3.

Steric component of sea-level rise. We evaluated the steric component of sea-level rise associated with a ΔOHC compatible with both $APO_{Climate}$ and existing in situ temperature constraints (that is, between 1.13×10^{22} J yr^{-1} and 1.46×10^{22} J yr^{-1}) to be between 1.34 mm yr^{-1} and 1.74 mm yr^{-1}. Following ref. [62], this calculation assumes that 45% of the warming occurs below 700 m, and that the steric rise is 1 mm per 0.60×10^{22} J above 700 m, and 1 mm per 1.15×10^{22} J below 700 m (that is, a global steric rise of 1 mm per 0.84×10^{22} J). Assuming that 48% of the warming occurs below 700 m (ref. [10]) would yield a global steric rise of 1 mm per 0.86×10^{22} J and change our estimate by less than 3%. Our estimate is also consistent with the recent hydrography-based estimate of the WCRP Global Sea Level Budget Group[63].

Ocean heat uptake, sea level and climate sensitivity. Climate sensitivity has been estimated to fall within the range of +1.5 K to +4.5 K for a doubling of CO_2 (ref. [1]). The impact of an increase in the ocean heat uptake on the effective equilibrium climate sensitivity (the apparent equilibrium climate sensitivity diagnosed from nonequilibrium conditions) can be estimated using a cumulative approach on the Earth energy balance (see Fig. 2 in ref. [1]):

$$N = F - \alpha \Delta T \tag{3}$$

where N is the global heat imbalance, which mostly consists of the ocean heat uptake; F is the radiative forcing (in W m^{-2}); ΔT is the increase in surface temperature (in K) above a natural steady state; and α is the climate feedback parameter (in W m^{-2} K^{-1}), which is inversely proportional to the effective equilibrium climate sensitivity[1]. All terms in equation (3) are time integrated over the period of interest.

The IPCC Fifth Assessment Report gives a ΔOHC of 0.80×10^{22} J yr^{-1} for 1993–2010, which is about 0.5×10^{22} J yr^{-1} lower than the ΔOHC that is compatible with both APO and hydrographic constraints. By applying equation (3)[1] to surface temperature data over the period 1991–2016 (HadCrut4 version 4.5, ref. [64], with a 1860–1879 preindustrial baseline), we found that the upward revision of the global heat imbalance, N, by $+0.5 \times 10^{22}$ J yr^{-1} pushes up the lower bound of the equilibrium climate sensitivity from 1.5 K back to 2.0 K. An increase of the lower bound from 1.5 K to 2 K corresponds to a need to reduce maximum emissions by 25% to stay within the 2 °C global warming target (because of the almost linear

© 2018 Springer Nature Limited. All rights reserved.

relationship between warming and cumulative emissions; see Fig. SPM.10 in ref. [1]). This corresponds to a reduction in maximum allowable cumulative CO_2 emissions from 4,760 Gt CO_2 to 3,570 Gt CO_2.

We tested the sensitivity of the climate sensitivity by using three alternate temperature datasets (NASA GISS Surface Temperature Analysis GISTEMP[65], available at https://data.giss.nasa.gov/gistemp; the NOAA/OAR/ESRL global surface temperature data[66] v4.0.1, available at https://www.esrl.noaa.gov/psd; and the ocean + land product of Berkeley Earth, available at berkeleyearth.lbl.gov/auto/Global; all data were accessed on 7 August 2018) as well as two preindustrial baseline periods (1860–1879 and 1880–1899). We find changes in the climate sensitivity of the order of 5% owing to the choice of temperature dataset, and less than 1% due to the choice of preindustrial baseline.

Link to global ocean deoxygenation. Our application of O_2 atmospheric measurements to constrain long-term ocean warming can be compared with earlier work that considers warming-driven oceanic O_2 outgassing. Multiplying our warming rate of $1.33 \pm 0.20 \times 10^{22}$ J yr^{-1} by the O_2-to-heat ratios simulated by the four ESMs (-3.70 ± 0.80 nmol O_2 J^{-1}) yields an ocean loss of 49 ± 13 Tmol O_2 yr^{-1}. Adding a loss of around 19 ± 19 Tmol O_2 yr^{-1} due to anthropogenic aerosols (Extended Data Table 5) yields a global ocean outgassing of 68 ± 23 Tmol O_2 yr^{-1}, in the range of previous estimates based on atmospheric data[67] (about 40 Tmol O_2 yr^{-1}), ocean data above 1,000 m (55–65 Tmol O_2 yr^{-1}, refs [68,69]) and global ocean data[70] (96 ± 42 Tmol O_2 yr^{-1}). This calculation suggests that ocean CO_2 uptake is reduced by warming at a ratio of around 0.70 nmol of CO_2 per joule (the difference between the O_2-to-heat ratio of 3.70 nmol J^{-1} and the OPO-to-heat ratio of 4.45 nmol J^{-1}).

Code availability. ESM codes are available online for IPSL-CM5A-LR (cmc.ipsl.fr/ipsl-climate-models), GFDL-ESM2M (mdl-mom5.herokuapp.com/web/docs/project/quickstart), UVic (climate.uvic.ca/model) and CESM (www.cesm.ucar.edu/models/).

Data availability

Scripps APO data are available at http://scrippso2.ucsd.edu/apo-data. $APO_{Climate}$ data, contributions to APO_{OBS} and ocean heat content time series are available in Extended Data Figs. 1–4 and Extended Data Tables 1–5. Model results are available upon reasonable request to R.W. (IPSL anthropogenic aerosol simulations), L.B. (IPSL-CM5A-LR), M.C.L. (CESM-LE), J.P.D. (GFDL-ESM2M) or W.K. (UVic).

33. Severinghaus, J. P. *Studies of the Terrestrial O_2 and Carbon Cycles in Sand Dune Gases and in Biosphere*. PhD Thesis, Columbia Univ. (1995).
34. Hamme, R. C. & Keeling, R. F. Ocean ventilation as a driver of interannual variability in atmospheric potential oxygen. *Tellus B Chem. Phys. Meterol.* **60**, 706–717 (2008).
35. Andres, R. J., Boden, T. A. & Higdon, D. A new evaluation of the uncertainty associated with CDIAC estimates of fossil fuel carbon dioxide emission. *Tellus B Chem. Phys. Meterol.* **66**, 23616 (2014).
36. Keeling, R. F., Manning, A. C., Paplawsky, W. J. & Cox, A. C. On the long-term stability of reference gases for atmospheric O_2/N_2 and CO_2 measurements. *Tellus B Chem. Phys. Meterol.* **59**, 3–14 (2007).
37. Ballantyne, A. P. et al. Audit of the global carbon budget: estimate errors and their impact on uptake uncertainty. *Biogeosciences* **12**, 2565–2584 (2015).
38. Bronselaer, B., Winton, M., Russell, J., Sabine, C. L. & Khatiwala, S. Agreement of CMIP5 simulated and observed ocean anthropogenic CO_2 uptake. *Geophys. Res. Lett.* **44**, 12298–12305 (2017).
39. Oeschger, H., Siegenthaler, U., Schotterer, U. & Gugelmann, A. A box diffusion model to study the carbon dioxide exchange in nature. *Tellus* **27**, 168–192 (1975).
40. MacFarling Meure, C. et al. Law Dome CO_2, CH_4 and N_2O ice core records extended to 2000 years BP. *Geophys. Res. Lett.* **33**, L14810 (2006).
41. Wang, D., Gouhier, T. C., Menge, B. A. & Ganguly, A. R. Intensification and spatial homogenization of coastal upwelling under climate change. *Nature* **518**, 390–394 (2015).
42. Ito, T., Nenes, A., Johnson, M. S., Meskhidze, N. & Deutsch, C. Acceleration of oxygen decline in the tropical Pacific over the past decades by aerosol pollutants. *Nat. Geosci.* **9**, 443–447 (2016).
43. Jickells, T. D. et al. A reevaluation of the magnitude and impacts of anthropogenic atmospheric nitrogen inputs on the ocean. *Glob. Biogeochem. Cycles* **31**, 289–305 (2017).
44. Somes, C. J., Landolfi, A., Koeve, W. & Oschlies, A. Limited impact of atmospheric nitrogen deposition on marine productivity due to biogeochemical feedbacks in a global ocean model. *Geophys. Res. Lett.* **43**, 4500–4509 (2016).
45. Aumont, O., Ethé, C., Tagliabue, A., Bopp, L. & Gehlen, M. PISCES-v2: an ocean biogeochemical model for carbon and ecosystem studies. *Geosci. Model Dev.* **8**, 2465–2513 (2015).
46. Talley, L. D. et al. Changes in ocean heat, carbon content, and ventilation: a review of the first decade of GO-SHIP global repeat hydrography. *Annu. Rev. Marine Sci.* **8**, 185–215 (2016).
47. Sarmiento, J. L. & Gruber, N. Sinks for anthropogenic carbon. *Phys. Today* **55**, 30–36 (2002).
48. Garcia, H. E. & Gordon, L. I. Oxygen solubility in seawater: better fitting equations. *Limnol. Oceanogr.* **37**, 1307–1312 (1992).
49. Gruber, N., Sarmiento, J. L. & Stocker, T. F. An improved method for detecting anthropogenic CO_2 in the oceans. *Glob. Biogeochem. Cycles* **10**, 809–837 (1996).
50. Dunne, J. P. et al. GFDL's ESM2 global coupled climate–carbon Earth system models. Part I: physical formulation and baseline simulation characteristics. *J. Clim.* **25**, 6646–6665 (2012).
51. Dunne, J. P. et al. GFDL's ESM2 global coupled climate–carbon Earth system models. Part II: carbon system formulation and baseline simulation characteristics. *J. Clim.* **26**, 2247–2267 (2013).
52. Séférian, R., Iudicone, D., Bopp, L., Roy, T. & Madec, G. Water mass analysis of effect of climate change on air–sea CO_2 fluxes: the Southern Ocean. *J. Clim.* **25**, 3894–3908 (2012).
53. Kay, J. E. et al. The Community Earth System Model (CESM) large ensemble project: a community resource for studying climate change in the presence of internal climate variability. *Bull. Am. Meteorol. Soc.* **96**, 1333–1349 (2015).
54. Keller, D. P., Oschlies, A. & Eby, M. A new marine ecosystem model for the University of Victoria Earth System Climate Model. *Geosci. Model Dev.* **5**, 1195–1220 (2012).
55. Bopp, L. et al. Multiple stressors of ocean ecosystems in the 21st century: projections with CMIP5 models. *Biogeosciences* **10**, 6225–6245 (2013).
56. Keller, D. P., Kriest, I., Koeve, W. & Oschlies, A. Southern Ocean biological impacts on global ocean oxygen. *Geophys. Res. Lett.* **43**, 6469–6477 (2016).
57. Long, M. C., Deutsch, C. & Ito, T. Finding forced trends in oceanic oxygen. *Glob. Biogeochem. Cycles* **30**, 381–397 (2016).
58. Taylor, K. E., Stouffer, R. J. & Meehl, G. A. An overview of CMIP5 and the experiment design. *Bull. Am. Meteorol. Soc.* **93**, 485–498 (2012).
59. Moore, J. K., Lindsay, K., Doney, S. C., Long, M. C. & Misumi, K. Marine ecosystem dynamics and biogeochemical cycling in the Community Earth System Model [CESM1(BGC)]: comparison of the 1990s with the 2090s under the RCP4.5 and RCP8.5 scenarios. *J. Clim.* **26**, 9291–9312 (2013).
60. Rödenbeck, C., Le Quéré, C., Heimann, M. & Keeling, R. F. Interannual variability in oceanic biogeochemical processes inferred by inversion of atmospheric O_2/N_2 and CO_2 data. *Tellus B Chem. Phys. Meterol.* **60**, 685–705 (2008).
61. Hamme, R. C. Mechanisms controlling the global oceanic distribution of the inert gases argon, nitrogen and neon. *Geophys. Res. Lett.* **29**, 35-1–35-4 (2002).
62. Trenberth, K. E., Fasullo, J. T., von Schuckmann, K. & Cheng, L. Insights into Earth's energy imbalance from multiple sources. *J. Clim.* **29**, 7495–7505 (2016).
63. WCRP Global Sea Level Budget Group. Global sea level budget 1993–present. *Earth Syst. Sci. Data* **10**, 1551–1590 (2018).
64. Morice, C. P., Kennedy, J. J., Rayner, N. A. & Jones, P. D. Quantifying uncertainties in global and regional temperature change using an ensemble of observational estimates: the HadCRUT4 data set. *J. Geophys. Res. Atmos.* **117**, D08101 (2012).
65. Hansen, J., Ruedy, R., Sato, M. & Lo, K. Global surface temperature change. *Rev. Geophys.* **48**, RG4004 (2010).
66. Vose, R. S. et al. NOAA's merged land–ocean surface temperature analysis. *Bull. Am. Meteorol. Soc.* **93**, 1677–1685 (2012).
67. Keeling, R. F., Körtzinger, A. & Gruber, N. Ocean deoxygenation in a warming world. *Annu. Rev. Mar. Sci.* **2**, 199–229 (2010).
70. Schmidtko, S., Stramma, L. & Visbeck, M. Decline in global oceanic oxygen content during the past five decades. *Nature* **542**, 335–339 (2017).
68. Helm, K. P., Bindoff, N. L. & Church, J. A. Observed decreases in oxygen content of the global ocean. *Geophys. Res. Lett.* **38**, L23602 (2011).
69. Ito, T., Minobe, S., Long, M. C. & Deutsch, C. Upper ocean O_2 trends: 1958–2015. *Geophys. Res. Lett.* **44**, 4214–4223 (2017).

© 2018 Springer Nature Limited. All rights reserved.

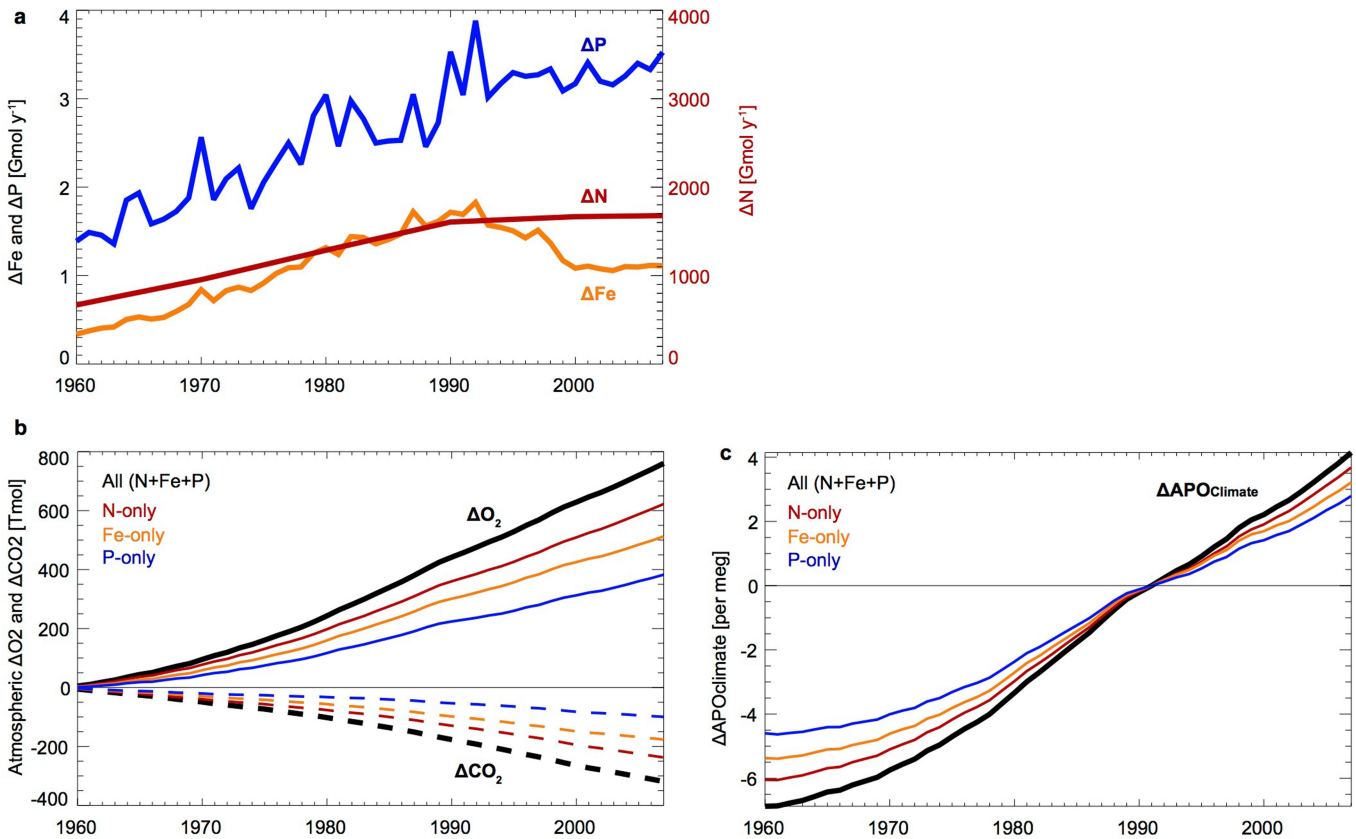

Extended Data Fig. 1 | Effects of anthropogenic aerosols on APO. **a**, Anomaly, relative to 1850 levels, in deposition of atmospheric anthropogenic aerosols (N, P and Fe) at the air–sea interface between 1960 and 2007, derived from model simulations with and without aerosols[22]. **b**, Impact of aerosol eutrophication on atmospheric O_2 (solid lines) and CO_2 (dashed lines) for all aerosols (black lines) and for each aerosol taken individually (coloured lines). **c**, Overall impact of aerosol eutrophication on $\Delta APO_{Climate}$ referenced to the first year that has observations (1991).

© 2018 Springer Nature Limited. All rights reserved.

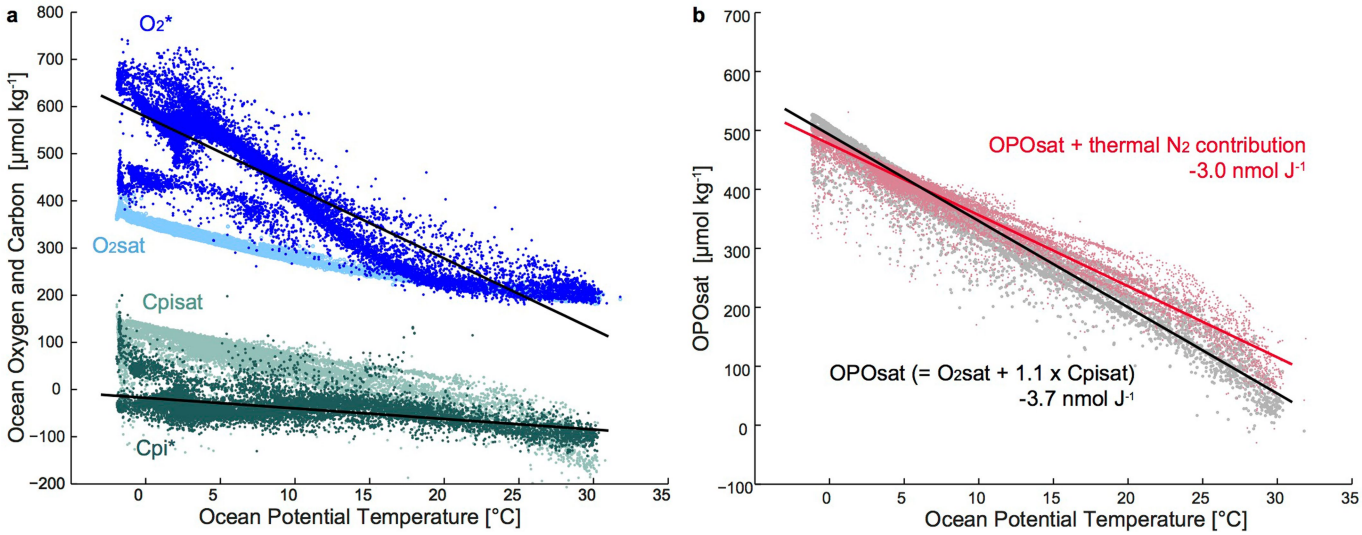

Extended Data Fig. 2 | Solubility-driven changes in ocean oxygen and carbon concentrations. a, Ocean observations of O_2*, O_{2sat}, C_{pi}* and C_{pisat} as a function of potential temperature in the Glodapv2 database[32]. **b**, OPO_{sat} ($= O_{2sat} + 1.1C_{pisat}$, in grey) and the expected effects on APO owing to the combined effects of OPO_{sat} and the thermal exchanges of N_2 ($= O_{2sat} + 1.1C_{pisat} - X_{O2} / X_{N2}$ [N_2 – mean(N_2)], in red). For clarity only 16×10^3 points randomly picked out of the 78,456 data points available are shown for each variable. Note that very low values of O_2* (around 450 µmol kg^{-1}) at low temperature (less than 10 °C) correspond to data collected in the Arctic Ocean, where phosphate concentrations (used for O_2* calculation) are comparatively lower than in other cold ocean regions. Low O_2* values in the Arctic explain the relatively low values of OPO shown in Extended Data Fig. 3a at temperatures below 10 °C.

© 2018 Springer Nature Limited. All rights reserved.

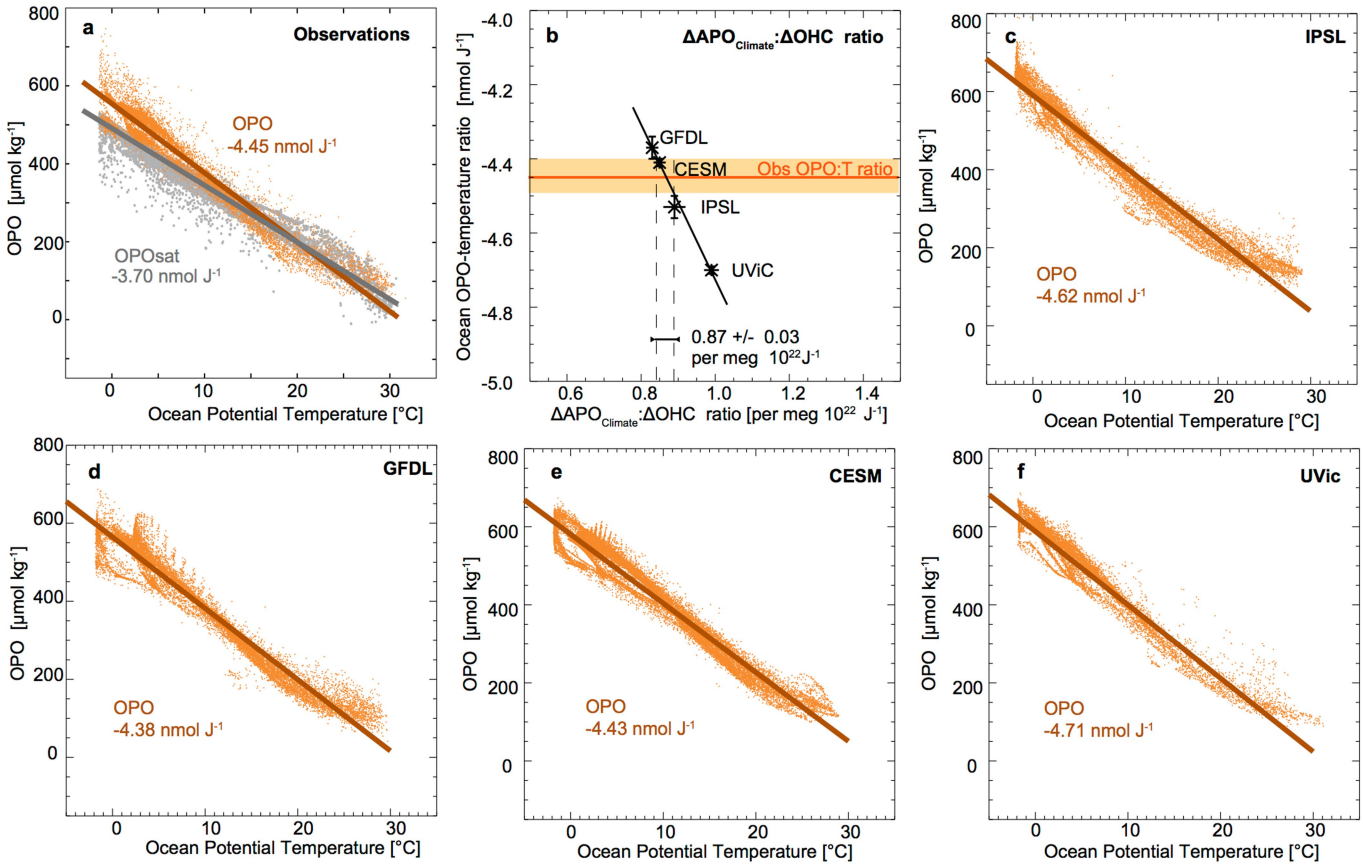

Extended Data Fig. 3 | Link between OPO, $APO_{Climate}$ and ocean heat. **a**, **c–f**, OPO concentrations (yellow) and OPO concentrations at saturation based on O_2 and CO_2 solubility (OPO_{sat}, grey) as a function of ocean temperature in the GLODAPv2 database[32] (**a**) and four Earth-system models (IPSL, GFDL, CESM and UVic; **c–f**). Slopes give the OPO-to-temperature ratios in nmol J^{-1}. **b**, The link between $\Delta APO_{Climate}$ and changes in ocean heat content (that is, $\Delta APO_{Climate}$-to-ΔOHC ratio) in the four models is tied to their OPO-to-temperature ratios and can be constrained using the observed OPO-to-temperature of 4.45 nmol J^{-1} (vertical dashed lines). To avoid visual saturation, only 16,000 points, picked randomly, are shown for OPO.

© 2018 Springer Nature Limited. All rights reserved.

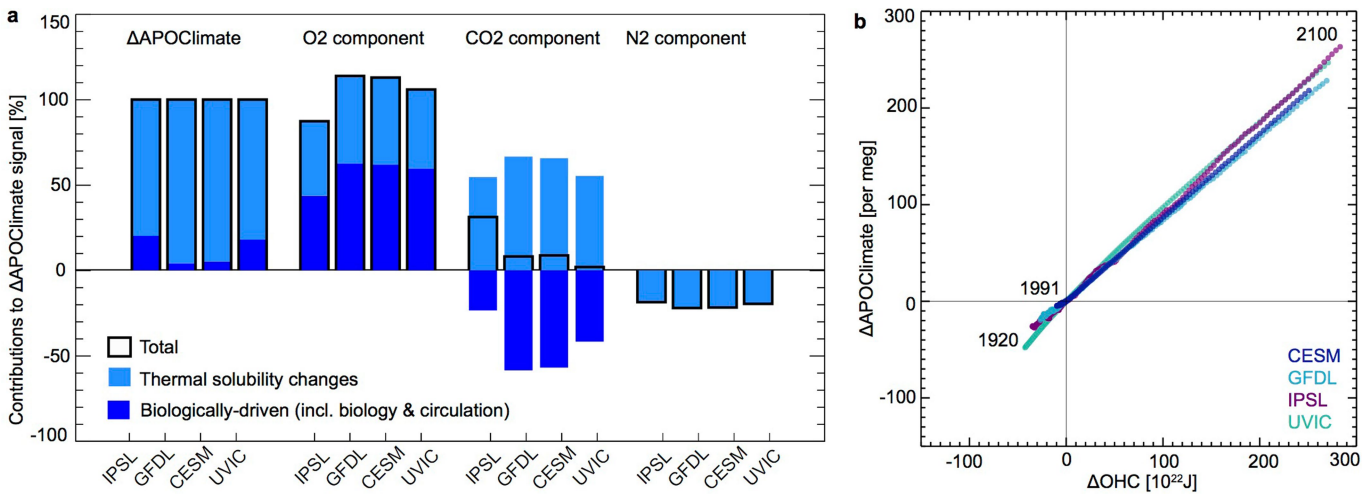

Extended Data Fig. 4 | Changes in $APO_{Climate}$ ($\Delta APO_{Climate}$) and ocean heat content (ΔOHC) in four Earth-system models. a, Simulated $\Delta APO_{Climate}$ (black outlines) are decomposed into the contributions (percentage of total) from changes in ocean thermal saturation (light blue) and biologically driven changes (dark blue), the latter including changes in photosynthesis/respiration and changes in ocean circulation that transport and mix gradients of biological origin. For each model, $\Delta APO_{Climate}$ is further decomposed into its O_2, CO_2 and N_2 components—that is, how much of $\Delta APO_{Climate}$ is explained by changes in O_2, CO_2 and N_2 air–sea fluxes due to ocean saturation changes and biologically driven changes. **b**, Model $\Delta APO_{Climate}$-to-ΔOHC ratios over the 180 years of simulation (referenced to year 1991) in per meg per 10^{22} J units are: 0.85 ± 0.01 (CESM), 0.83 ± 0.01 (GFDL), 0.89 ± 0.03 (IPSL) and 0.99 ± 0.02 (UVic).

© 2018 Springer Nature Limited. All rights reserved.

Extended Data Table 1 | Sources of the hydrographic databased estimates of global changes in ocean heat content (△OHC) used in Fig. 1

Label in Fig 1	0 to 2000 m depth range	2000 to 6000 m depth range
PMEL	Ref. 10	Ref. 11
MRI	Ref. 9	Ref. 11
NCEI	Update of Ref. 31	Ref. 11
CHEN	Ref. 12	Ref. 11

The estimates are taken from refs 9–12.

© 2018 Springer Nature Limited. All rights reserved.

Extended Data Table 2 | Linear trends in global ocean heat content

	1991-2016 ΔOHC trend (±1-σ)	1993-2016 ΔOHC trend (±1-σ)	2007-2016 ΔOHC trend (±1-σ)
$APO_{Climate}$	1.33 ± 0.20	-	-
PMEL	-	1.35 ± 0.10	1.16 ± 0.20
MRI	1.00 ± 0.11	1.03 ± 0.12	1.23 ± 0.22
NCEI	0.89 ± 0.08	0.90 ± 0.09	1.28 ± 0.16
CHEN	1.07 ± 0.07	1.10 ± 0.08	1.09 ± 0.10

Units are 10^{22} J yr^{-1}. Trends and $\pm 1\sigma$ uncertainty ranges are given for hydrographic (in situ temperature) and atmospheric (APO) data over the depth range 0–6,000 m. See Extended Data Table 1 for literature sources of estimates.

© 2018 Springer Nature Limited. All rights reserved.

Extended Data Table 3 | Contributions to ΔAPO_{OBS}, ΔAPO_{FF} and ΔAPO_{Cant} and associated uncertainties ($\pm 1\sigma$) during the observation period 1991–2016

	Mean value	References	1-σ uncertainty	References
		ΔAPO_{OBS}		
Corrosion			± 0.3 per meg yr^{-1}	
Leakage			± 0.2 per meg yr^{-1}	
Desorption			± 0.1 per meg yr^{-1}	
Thermal fractionation			± 2 per meg (± 4 before July 1992)	Ref. 36
Scale systematic error			2% on $\delta(O_2/N_2)$ contribution	
		ΔAPO_{FF}		
		Oxidative Ratios R_i		
Coal	1.17		± 0.03	
Oil	1.44	Ref. 36	± 0.03	Ref. 36
Gas	1.95		± 0.04	
Cement	0.0		± 0.00	
Flaring	1.98		± 0.07	
		Emissions $\Delta CO2_i$		
Coal			± 7.0%	
Oil	Time varying	Ref. 20	± 5.5%	Ref. 35
Gas			± 6.5%	
Cement			±12%	
Flaring			±12%	
		ΔAPO_{Cant}		
$\Delta Cant_0$	Time varying (~2 to 3 PgC yr^{-1})	Ref. 21	1-σ of 10 experiments (<0.3 PgC yr^{-1})	Ref. 21
			+ 1% uncertainty (<0.03 PgC yr^{-1}) (atmospheric CO_2 history)	*this study*
$\Delta Cant'$	0.05 PgC yr^{-1} (0.12 per meg yr^{-1})	*this study*	± 0.05 PgC yr^{-1} (± 0.12 per meg yr^{-1})	*this study*

The estimates are taken from refs 20,21,35,36.

© 2018 Springer Nature Limited. All rights reserved.

Extended Data Table 4 | Temporal evolution of the cumulative contributions to global APO changes and their 1σ uncertainties

year	$\Delta APO_{Climate}$	1-σ	ΔAPO_{OBS}	1-σ	ΔAPO_{FF}	1-σ	ΔAPO_{Cant}	1-σ	ΔAPO_{AtmD}	1-σ
1991	0.00	0.00	0.00	0.00	0.00	0.00	0.00	0.00	0.00	0.00
1992	1.50	4.00	-6.80	4.00	-4.00	0.30	-4.90	0.10	0.50	0.30
1993	3.90	4.10	-12.90	4.00	-8.00	0.40	-9.70	0.30	0.80	0.40
1994	3.50	2.30	-22.30	2.20	-12.10	0.50	-14.80	0.40	1.10	0.50
1995	6.50	2.50	-28.40	2.30	-16.20	0.60	-20.10	0.50	1.30	0.70
1996	5.40	2.70	-39.00	2.50	-20.40	0.70	-25.50	0.70	1.60	0.80
1997	7.50	3.00	-46.10	2.70	-24.70	0.80	-30.80	0.90	1.90	0.90
1998	11.30	3.40	-52.40	2.90	-29.00	0.90	-36.80	1.10	2.10	1.10
1999	14.90	3.70	-58.70	3.20	-33.40	1.10	-42.60	1.20	2.40	1.20
2000	10.00	4.20	-73.40	3.60	-37.90	1.20	-48.20	1.40	2.70	1.30
2001	9.60	4.50	-83.90	3.90	-42.50	1.30	-54.00	1.60	2.90	1.50
2002	15.70	4.80	-87.90	4.10	-47.10	1.40	-59.80	1.70	3.20	1.60
2003	14.00	5.40	-100.40	4.50	-51.80	1.60	-66.10	1.90	3.50	1.70
2004	15.10	5.80	-110.20	4.90	-56.70	1.70	-72.40	2.00	3.70	1.90
2005	18.40	6.30	-117.80	5.20	-61.70	1.80	-78.60	2.30	4.00	2.00
2006	19.60	6.70	-127.90	5.60	-66.80	2.00	-85.10	2.40	4.30	2.10
2007	16.60	7.30	-142.10	6.10	-71.90	2.20	-91.60	2.60	4.50	2.30
2008	16.30	7.80	-153.90	6.50	-77.10	2.40	-98.10	2.90	4.80	2.40
2009	19.40	8.20	-162.00	6.80	-82.20	2.60	-104.50	3.00	5.10	2.50
2010	19.10	8.80	-174.30	7.20	-87.40	2.80	-111.50	3.20	5.40	2.70
2011	19.70	9.30	-185.40	7.60	-92.70	3.00	-118.30	3.40	5.60	2.80
2012	20.90	9.80	-196.20	8.10	-98.10	3.20	-125.10	3.50	5.90	3.00
2013	18.80	10.50	-210.30	8.60	-103.40	3.40	-132.10	3.80	6.20	3.10
2014	22.90	11.00	-218.70	9.00	-108.70	3.60	-139.50	3.90	6.50	3.20
2015	22.90	11.50	-231.10	9.50	-114.20	3.80	-146.70	4.20	6.70	3.40
2016	23.20	12.20	-243.70	10.10	-119.70	4.00	-154.30	4.20	7.00	3.50

Units are per meg.

© 2018 Springer Nature Limited. All rights reserved.

Extended Data Table 5 | Trends in air–sea flux of O_2, CO_2 and APO due to anthropogenic aerosol deposition

Trends 1980 to 2007	N-only	Fe-only	P-only	All (N+Fe+P)
O_2 [Tmol y^{-1}]	15.5	12.9	9.6	19.0
CO_2 [Tmol y^{-1}]	-6.1	-4.6	-2.6	-8.3
$APO_{AtmD(O2)}$ [per meg y^{-1}]	0.42	0.35	0.26	0.51
$APO_{AtmD(CO2)}$ [per meg y^{-1}]	-0.18	-0.14	-0.08	-0.24
APO_{AtmD} [per meg y^{-1}]	0.24	0.21	0.18	**0.27**

Trends in APO due to atmospheric deposition (ΔAPO_{AtmD}) are decomposed into contributions from the O_2 flux only ($APO_{AtmD(O2)}$) and the CO_2 flux only ($APO_{AtmD(CO2)}$). Results are from model simulations[22]. Anomalies in air–sea flux are positive towards the atmosphere. The total trend used in this study is in bold type.

© 2018 Springer Nature Limited. All rights reserved.

https://doi.org/10.1038/s41586-018-0627-8

Biodiversity increases and decreases ecosystem stability

Frank Pennekamp[1]*, Mikael Pontarp[1,2], Andrea Tabi[1], Florian Altermatt[1,3], Roman Alther[1,3], Yves Choffat[1], Emanuel A. Fronhofer[1,3,5], Pravin Ganesanandamoorthy[1,3], Aurélie Garnier[1], Jason I. Griffiths[4], Suzanne Greene[1,6], Katherine Horgan[1], Thomas M. Massie[1], Elvira Mächler[1,3], Gian Marco Palamara[1,7], Mathew Seymour[3,8] & Owen L. Petchey[1]

Losses and gains in species diversity affect ecological stability[1–7] and the sustainability of ecosystem functions and services[8–13]. Experiments and models have revealed positive, negative and no effects of diversity on individual components of stability, such as temporal variability, resistance and resilience[2,3,6,11,12,14]. How these stability components covary remains poorly understood[15]. Similarly, the effects of diversity on overall ecosystem stability[16], which is conceptually akin to ecosystem multifunctionality[17,18], remain unknown. Here we studied communities of aquatic ciliates to understand how temporal variability, resistance and overall ecosystem stability responded to diversity (that is, species richness) in a large experiment involving 690 micro-ecosystems sampled 19 times over 40 days, resulting in 12,939 samplings. Species richness increased temporal stability but decreased resistance to warming. Thus, two stability components covaried negatively along the diversity gradient. Previous biodiversity manipulation studies rarely reported such negative covariation despite general predictions of the negative effects of diversity on individual stability components[3]. Integrating our findings with the ecosystem multifunctionality concept revealed hump- and U-shaped effects of diversity on overall ecosystem stability. That is, biodiversity can increase overall ecosystem stability when biodiversity is low, and decrease it when biodiversity is high, or the opposite with a U-shaped relationship. The effects of diversity on ecosystem multifunctionality would also be hump- or U-shaped if diversity had positive effects on some functions and negative effects on others. Linking the ecosystem multifunctionality concept and ecosystem stability can transform the perceived effects of diversity on ecological stability and may help to translate this science into policy-relevant information.

Ecological stability consists of numerous components, including temporal variability, resistance to environmental change and rate of recovery from disturbance[1,2,16]. Effects of species losses and gains on these components are of considerable interest, not least because of the potential effects on ecosystem functioning and therefore on the sustainable delivery of ecosystem services[1–13]. A growing number of experimental studies reveal stabilizing effects of diversity on individual stability components. In particular, higher diversity often—but not always—reduces temporal variability of biomass production[13]. Positive effects of diversity on resistance are common, although neutral and negative effects on resistance and resilience also occur[9,13,19,20]. Although the assessment of individual components of stability is essential, a more integrative approach to ecological stability could lead to clearer conceptual understanding[15] and might help to improve policy guidance concerning ecological stability[16].

Analogous to ecosystem multifunctionality[17,18], a more integrative approach considers variation in multiple stability components and the often-ignored covariation among stability components. The nature of this covariation is of paramount importance, as it defines whether diversity has consistent effects on multiple stability components, or whether some stability components increase with diversity while others decrease. However, the nature, prevalence and implications of negative covariation between stability components along diversity gradients are almost completely overlooked, including the ensuing possibility for non-monotonic effects of diversity on overall ecosystem stability.

We first describe our experimental findings of how biodiversity affects the intrinsic stability of ecosystems and their resistance to warming. Temperature is a highly relevant disturbance owing to its importance for biological processes and its great variability across space and time. However, our findings equally apply to and have implications for other environmental changes that could result in opposing effects on stability components, such as flooding[12] or chemical stress[21]. We then review other evidence for negative covariation in effects of diversity on stability and potential mechanisms. Finally, we analyse overall ecosystem stability, a concept that embraces the covariation between stability components and their weighting, and show the plausibility of previously overlooked non-monotonic (hump- and U-shaped) effects of diversity on overall ecosystem stability.

We performed a factorial manipulation of the diversity and composition of competing species (1–6 species, 53 unique community compositions) and temperature (six constant levels, modelled as a linear predictor) in microbial communities of bacterial consumers, and recorded community biomass dynamics over time. For each replicate we then calculated two stability components: resistance (that is, the total biomass at T minus the total biomass at 15 °C divided by T minus 15 °C, in which T is the temperature of the replicate) and the temporal stability of biomass (the inverse of the coefficient of variation of community biomass). Although these stability indices are widely used by empiricists, they should not be mistaken for mathematical definitions—such as asymptotic resilience—that are more precise but also more restrictive[22].

Increased species richness caused greater temporal stability of total biomass (Fig. 1a) (linear mixed-effects model of log inverse coefficient of variation: richness effect size 0.33 ± 0.065 (mean ± s.e.m.)) at all temperatures (Extended Data Fig. 1). Total biomass increased during the first week of the experiment and then declined over the next five weeks and total biomass was higher in more species-rich communities (Fig. 1b, c and Extended Data Table 1). The effect size for log(richness) was 0.05 ± 0.0096 mg ml^{-1} per log(species richness) (mean ± s.e.m.).

By contrast, increased species richness decreased resistance of total biomass to warming (Fig. 1a) (negative effect of log(richness) in a linear model, effect size of -0.006 ± 0.0018 mg per °C per log(species richness) (mean ± s.e.m.). Richness negatively affected resistance measured on both absolute and relative scales (Extended Data Fig. 2). This effect was

[1]Department of Evolutionary Biology and Environmental Studies, University of Zurich, Zurich, Switzerland. [2]Department of Ecology and Environmental Science, Umeå University, Umeå, Sweden. [3]Department of Aquatic Ecology, Eawag: Swiss Federal Institute of Aquatic Science and Technology, Dübendorf, Switzerland. [4]Department of Mathematics, University of Utah, Salt Lake City, UT, USA. [5]Present address: ISEM, Université de Montpellier, CNRS, IRD, EPHE, Montpellier, France. [6]Present address: MIT Center for Transportation & Logistics, Massachusetts Institute of Technology, Cambridge, MA, USA. [7]Present address: Department of Systems Analysis, Integrated Assessment and Modelling, Eawag: Swiss Federal Institute of Aquatic Science and Technology, Dübendorf, Switzerland. [8]Present address: Molecular Ecology and Fisheries Genetics Laboratory, School of Biological Sciences, Bangor University, Bangor, UK. *e-mail: frank.pennekamp@ieu.uzh.ch

© 2018 Springer Nature Limited. All rights reserved.

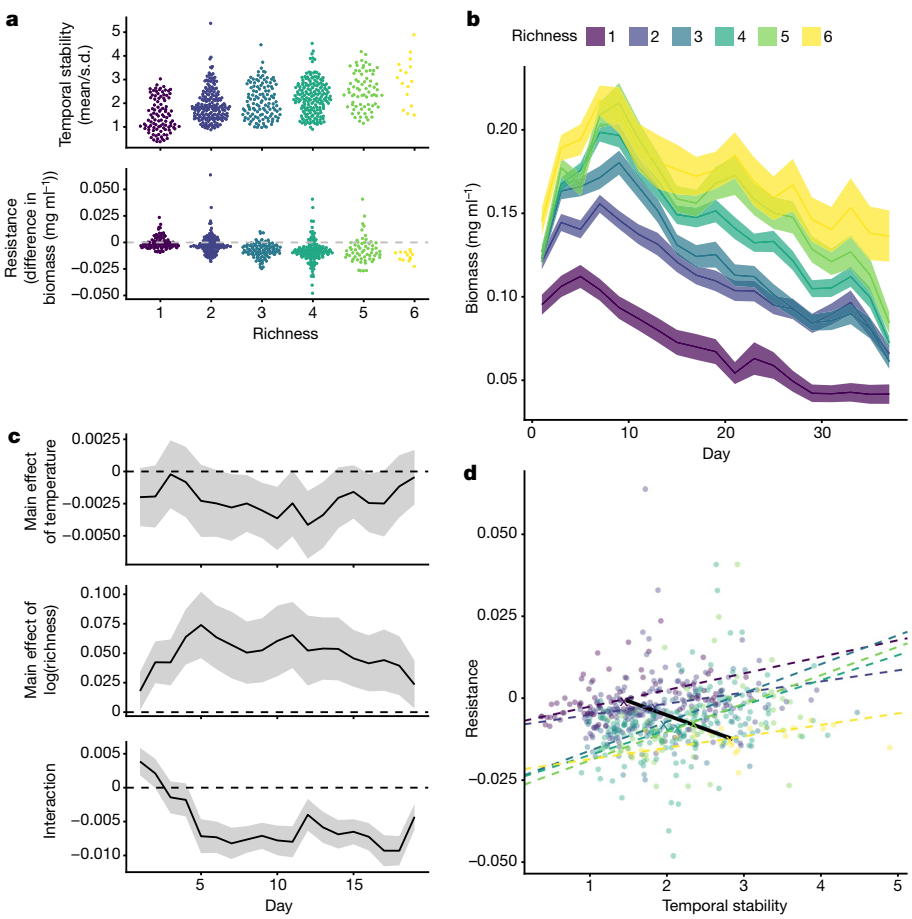

Fig. 1 | Biomass and stability in experimental microbial communities. a, Richness increased temporal stability (top, $n = 681$ independent microcosms), but decreased resistance (bottom, $n = 567$ independent microcosms). The dashed line indicates zero resistance. **b**, Average (mean ± s.e.m.) biomass for each diversity level ($n = 12{,}939$ microcosm × day combinations). **c**, Temporal dynamics of effect sizes (and 95% confidence intervals) of a linear mixed-effects model of total biomass showed, on average, a negative effect of temperature on biomass (top), a positive effect of diversity on biomass (middle) and a more negative effect of temperature at higher richness on biomass (persistent negative interaction term; bottom) ($n = 681$ independent microcosms per day). The dashed lines indicate zero effect. **d**, Resistance and temporal stability ($n = 567$ independent microcosms) covaried negatively across richness (solid line through centroid of each richness level, $n = 6$ independent richness levels), but positively within richness levels (dashed lines).

corroborated in analyses of total biomass by a negative interaction term between temperature and richness, which persisted through the experiment, except during the first days (Fig. 1c) (log(richness) × temperature interaction of -0.0053 ± 0.00051 mg ml^{-1} per °C per log(species richness)), despite large variation in dynamics of total biomass (Fig. 1b). This negative interaction reflects a stronger negative effect of temperature on total biomass (that is, lower resistance) in richer communities (that is, a richness-dependent response of total biomass to temperature).

Therefore, temporal stability and resistance were negatively correlated across the species richness gradient (Fig. 1d, reduced major axis regression analysis with a slope of −0.009 and a 95% confidence interval of −0.0178 to −0.0051). Niche complementarity, statistical averaging, low overall response diversity and possibly lower response diversity in more diverse communities were probably causes of the opposite effects of richness on temporal stability (Extended Data Fig. 3). The two stability components were, however, positively correlated within any single level of species richness (Fig. 1d and Extended Data Table 2).

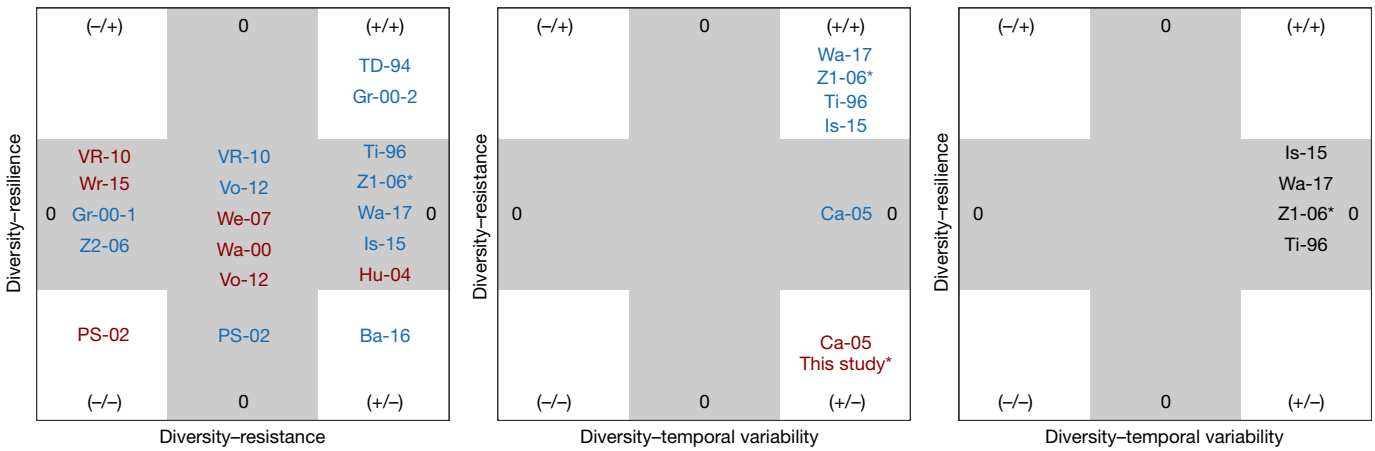

Fig. 2 | Positive, negative and neutral relationships among resistance, resilience and temporal variability in empirical studies with diversity manipulation. The 30 bivariate relationships were reported by 17 independent studies (in addition to this study). Detailed information about individual studies (for example, code VR-10) is provided in Extended Data Tables 3, 4. Light-grey regions indicate no covariation. Relative positions within regions are arbitrary and do not indicate relative strengths of relationships. Different colours indicate the effect of diversity on absolute (red) or relative (blue) resistance, whereas temporal stability and resilience are shown in black. *Studies that examine intrinsic stability alongside response to an environmental change.

© 2018 Springer Nature Limited. All rights reserved.

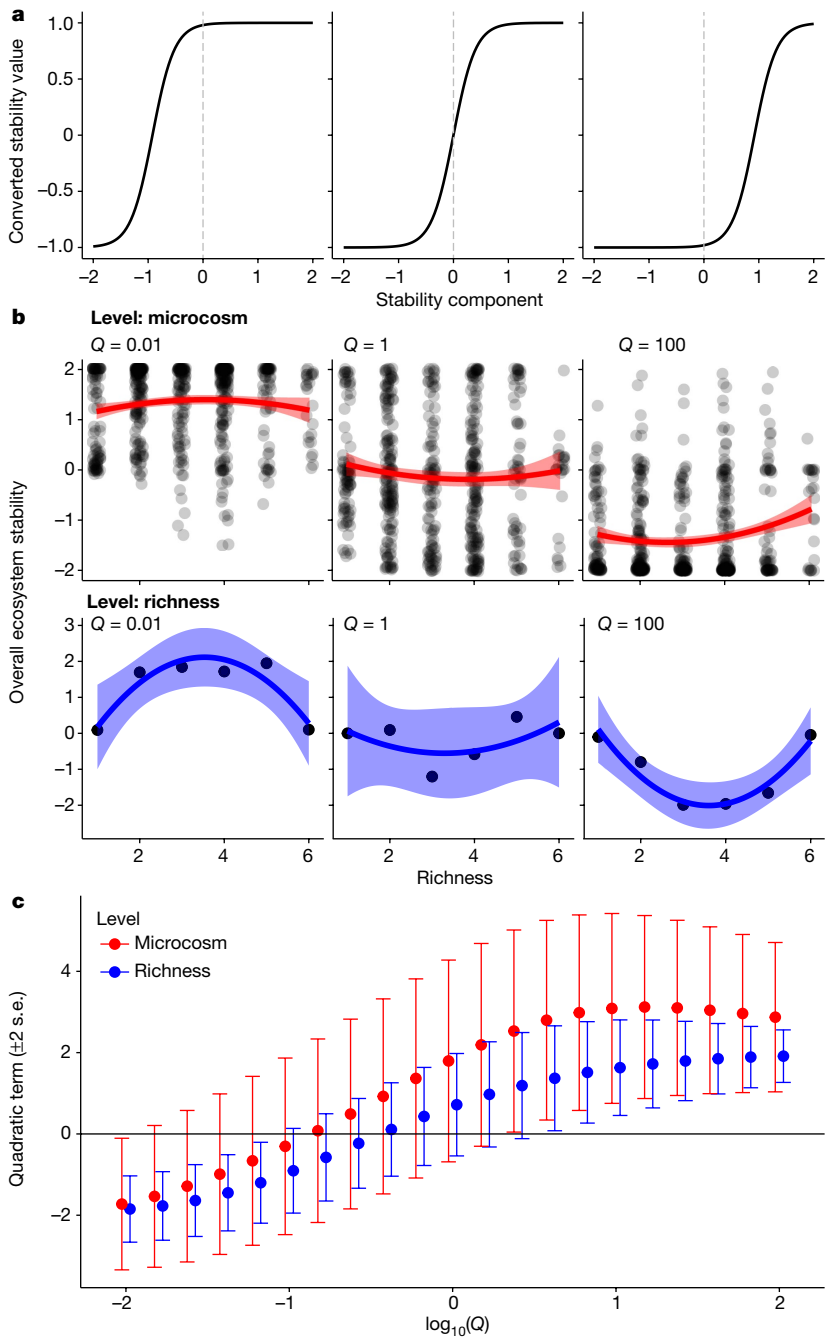

Fig. 3 | Hump- and U-shaped diversity–stability relationships. a, The intercept of the generalized logistic to convert measured stability components into a common currency varies with the parameter *Q*. **b**, The non-aggregated ($n = 567$ independent microcosms) or aggregated ($n = 6$ richness levels) data exhibits hump- to flat- to U-shaped diversity–stability relationships as *Q* varies. Lines show the fit of a quadratic model and the 95% confidence interval (bands). **c**, The variation from hump-shaped to U-shaped relationship depends smoothly on *Q*—that is, the position of the threshold (quantified by the quadratic term of a regression with mean (dot) and 95% confidence intervals (bars)).

That is, composition variation without changes in species richness resulted in positively covarying temporal stability and resistance.

Next, we examined studies (including our own) that measured multiple stability components across diversity gradients based on a previously published review[16] (Fig. 2 and Extended Data Tables 3, 4). In total 7 out of 30 comparisons showed positive covariance, 20 studies showed no covariance, and 3 studies showed negative covariance. Notably, our study identifies negative covariation between resistance and temporal variability caused by intrinsic dynamics only. Although infrequently reported, negative covariation is disproportionately important, because it complicates conclusions about and practical implications of the effects of diversity on stability. Furthermore, these studies may be unrepresentative of the true prevalence of negative covariation, because it may be overlooked, because of publication bias towards positive diversity–stability relationships[3] or if the scale of analysis masks such covariation, for example, within richness versus across richness.

A general mechanistic understanding of why different studies find different correlations would be a major step forward. Of the 30 pairs of stability components, only 7 were accompanied by quantitative analyses of mechanism for both diversity–stability relationships (Extended Data Table 4). Response diversity was implicated in five of these seven studies. Indeed, response diversity has been identified as an important driver of the resilience of ecological systems[23,24], and correlation among effect (that is, high biomass production) and response (for example, response to an environmental driver) traits—at least in the absence of strong interspecific interactions—might predict covariance among stability components[23]. None of the studies involved manipulation of mechanism.

Negative covariation also raises the potential for non-monotonic effects of diversity on overall ecosystem stability. Ecosystem multifunctionality is the simultaneous consideration of several ecosystem functions. Similarly, overall ecosystem stability considers multiple stability components simultaneously[16] (see Extended Data Fig. 4 for clarification of terms and concepts). We first calculated overall ecosystem stability as the sum of the standardized individual components of ecosystem stability[25]. For the results of our experiment, in which one stability component increases linearly with diversity and another decreases linearly

© 2018 Springer Nature Limited. All rights reserved.

(Fig. 1a), overall ecosystem stability is invariant with species richness, because the two standardized components perfectly balance each other.

We further explored the implications of the negative covariation among stability components. Existing methods for calculating ecosystem multifunctionality include a mathematical function for converting values of each ecosystem function into a common currency. Following previous studies[26], we assumed a logistic shape conversion function, and converted observed stability components into the common currency, with parameter values chosen to ensure that the range of the data includes the lower and upper asymptote. Here we present the influence of the value of the intercept (Q) of the conversion function (Fig. 3a), which is similar to varying the threshold value when calculating ecosystem multifunctionality with the threshold approach[27].

The opposing stability–diversity relationships from our experiment, coupled with logistic conversion functions, produced a hump-shaped relationship between overall ecosystem stability and diversity at low values of Q, a flat relationship at intermediate values and a U-shaped relationship at higher values (Fig. 3b, c). Effects of richness on overall ecosystem stability were weaker at the replicate level than the richness level (Fig. 3b), in part because of the relatively large variability among the replicates within richness levels and also because of positive covariance of temporal stability and resistance within diversity levels (Fig. 1d).

Finding hump- and U-shaped diversity–stability relationships fundamentally alters the importance of biodiversity, from it being unimportant (variation in biodiversity has no consequence) to it being state-dependent. The hump-shaped and U-shaped relationships occurred because measured stability components (for example, resistance) cross the threshold of the conversion function at different levels of species richness (see Methods). Therefore, negatively covarying stability components and nonlinear conversion functions can produce a non-monotonic effect of diversity on overall ecosystem stability. Furthermore, we expect the same to apply to ecosystem multifunctionality when individual ecosystem functions negatively covary along a diversity gradient.

The chosen mathematical conversion function and its parameter values are therefore important. Ecosystem multifunctionality–diversity relationships can be negative, neutral or positive depending on the chosen threshold value[27]. Similarly, different weightings of ecosystem functions can alter which species and interactions are considered important for multifunctionality[26]. Other types and parameterizations of conversion functions might conceivably result in other diversity–stability relationships. For instance, weighting one ecosystem function (or stability component) highly would lead to a multifunctionality and/or overall ecosystem stability measure that is essentially univariate. We view the choice and parameterization of conversion functions as an opportunity to tailor estimates of ecosystem multifunctionality and overall ecosystem stability to their policy and decision-making applications[16,26,28,29]. These conversion functions and estimates of overall ecosystem stability can then transform the perceived importance of biodiversity change for the sustainable delivery of multiple ecosystem services and may help to translate the results of scientific studies into actionable information.

Online content

Any methods, additional references, Nature Research reporting summaries, source data, statements of data availability and associated accession codes are available at https://doi.org/10.1038/s41586-018-0627-8.

Received: 29 January 2018; Accepted: 24 August 2018;
Published online 17 October 2018.

1. Pimm, S. L. The complexity and stability of ecosystems. *Nature* **307**, 321–326 (1984).
2. McCann, K. S. The diversity–stability debate. *Nature* **405**, 228–233 (2000).
3. Ives, A. R. & Carpenter, S. R. Stability and diversity of ecosystems. *Science* **317**, 58–62 (2007).
4. Allesina, S. & Tang, S. Stability criteria for complex ecosystems. *Nature* **483**, 205–208 (2012).
5. Mougi, A. & Kondoh, M. Diversity of interaction types and ecological community stability. *Science* **337**, 349–351 (2012).
6. Loreau, M. & de Mazancourt, C. Biodiversity and ecosystem stability: a synthesis of underlying mechanisms. *Ecol. Lett.* **16**, 106–115 (2013).
7. Grilli, J., Barabás, G., Michalska-Smith, M. J. & Allesina, S. Higher-order interactions stabilize dynamics in competitive network models. *Nature* **548**, 210–213 (2017).
8. Tilman, D. & Downing, J. A. Biodiversity and stability in grasslands. *Nature* **367**, 363–365 (1994).
9. Pfisterer, A. B. & Schmid, B. Diversity-dependent production can decrease the stability of ecosystem functioning. *Nature* **416**, 84–86 (2002).
10. Worm, B. et al. Impacts of biodiversity loss on ocean ecosystem services. *Science* **314**, 787–790 (2006).
11. Cardinale, B. J. et al. Biodiversity loss and its impact on humanity. *Nature* **486**, 59–67 (2012).
12. Wright, A. J. et al. Flooding disturbances increase resource availability and productivity but reduce stability in diverse plant communities. *Nat. Commun.* **6**, 6092 (2015).
13. Isbell, F. et al. Biodiversity increases the resistance of ecosystem productivity to climate extremes. *Nature* **526**, 574–577 (2015).
14. Isbell, F. I., Polley, H. W. & Wilsey, B. J. Biodiversity, productivity and the temporal stability of productivity: patterns and processes. *Ecol. Lett.* **12**, 443–451 (2009).
15. Donohue, I. et al. On the dimensionality of ecological stability. *Ecol. Lett.* **16**, 421–429 (2013).
16. Donohue, I. et al. Navigating the complexity of ecological stability. *Ecol. Lett.* **19**, 1172–1185 (2016).
17. Duffy, J. E., Richardson, J. P. & Canuel, E. A. Grazer diversity effects on ecosystem functioning in seagrass beds. *Ecol. Lett.* **6**, 637–645 (2003).
18. Hector, A. & Bagchi, R. Biodiversity and ecosystem multifunctionality. *Nature* **448**, 188–190 (2007).
19. Balvanera, P. et al. Quantifying the evidence for biodiversity effects on ecosystem functioning and services. *Ecol. Lett.* **9**, 1146–1156 (2006).
20. Zhang, Q.-G. & Zhang, D.-Y. Resource availability and biodiversity effects on the productivity, temporal variability and resistance of experimental algal communities. *Oikos* **114**, 385–396 (2006).
21. Baert, J. M., De Laender, F., Sabbe, K. & Janssen, C. R. Biodiversity increases functional and compositional resistance, but decreases resilience in phytoplankton communities. *Ecology* **97**, 3433–3440 (2016).
22. Arnoldi, J.-F., Loreau, M. & Haegeman, B. Resilience, reactivity and variability: a mathematical comparison of ecological stability measures. *J. Theor. Biol.* **389**, 47–59 (2016).
23. Suding, K. N. et al. Scaling environmental change through the community-level: a trait-based response-and-effect framework for plants. *Glob. Change Biol.* **14**, 1125–1140 (2008).
24. Mori, A. S., Furukawa, T. & Sasaki, T. Response diversity determines the resilience of ecosystems to environmental change. *Biol. Rev. Camb. Philos. Soc.* **88**, 349–364 (2013).
25. Maestre, F. T. et al. Plant species richness and ecosystem multifunctionality in global drylands. *Science* **335**, 214–218 (2012).
26. Slade, E. M. et al. The importance of species identity and interactions for multifunctionality depends on how ecosystem functions are valued. *Ecology* **98**, 2626–2639 (2017).
27. Gamfeldt, L. & Roger, F. Revisiting the biodiversity–ecosystem multifunctionality relationship. *Nat. Ecol. Evol.* **1**, 0168 (2017).
28. Manning, P. et al. Redefining ecosystem multifunctionality. *Nat. Ecol. Evol.* **2**, 427–436 (2018).
29. Armsworth, P. R. & Roughgarden, J. E. The economic value of ecological stability. *Proc. Natl Acad. Sci. USA* **100**, 7147–7151 (2003).

Acknowledgements F. De Laender and B. Schmid provided feedback on previous drafts of the Letter; I. Donohue provided the list of publications from his 2016 review paper. The University of Zurich Research Priority Programme on Global Change and Biodiversity supported this research. In addition, funding came from the Swiss National Science Foundation (grant PP00P3_150698 to F.A. and 31003A_159498 to O.L.P.). This is publication ISEM 2018-171 of the Institut des Sciences de l'Evolution, Montpellier.

Reviewer information *Nature* thanks T. Bell, P. J. Morin and the other anonymous reviewer(s) for their contribution to the peer review of this work.

Author contributions O.L.P., F.P. and F.A. conceived the study. O.L.P., F.P., M.S., E.A.F., F.A., G.-M.P., T.M.M. and M.P. designed the experiment. F.P. coordinated and led the experiment. The experimental sampling was performed by all authors, except J.G. and A.T. F.P., O.L.P. and J.G. prepared the data for analysis. F.P., O.L.P., M.P., A.T. and M.S. analysed the dataset. The first draft was written by F.P. and O.L.P. All authors contributed to revisions of the manuscript.

Competing interests The authors declare no competing interests.

Additional information
Extended data is available for this paper at https://doi.org/10.1038/s41586-018-0627-8.
Supplementary information is available for this paper at https://doi.org/10.1038/s41586-018-0627-8.
Reprints and permissions information is available at http://www.nature.com/reprints.
Correspondence and requests for materials should be addressed to F.P.
Publisher's note: Springer Nature remains neutral with regard to jurisdictional claims in published maps and institutional affiliations.

© 2018 Springer Nature Limited. All rights reserved.

METHODS

Data reporting. No statistical methods were used to predetermine sample size. The experiments were randomized and the investigators were not blinded to allocation during experiments and outcome assessment.

Experimental methods. The experiment was conceived and designed to research relationships between biodiversity and the ecosystem, with a focus on questions on environmental gradients and effects on temporal changes and/or stability, including the one addressed in this Letter. We factorially manipulated temperature (15, 17, 19, 21, 23 and 25 °C) and species richness (1–6 species of bacterivorous ciliates: *Colpidium striatum*, *Dexiostoma campylum*, *Loxocephalus* sp., *Paramecium caudatum*, *Spirostomum teres* and *Tetrahymena thermophila*) in 690 microcosms (250-ml Duran bottles). There were two incubators at each temperature. Manipulating temperature with a replicated gradient is recommended to harness the power of a regression design, while still allowing us to test for a nonlinear temperature effect[30]. During previous experiments, the temperature of liquid in similar microcosms varied around the set-point temperature by 0.1 °C. Long-term ciliate cultures were kept at 15 °C, and warming usually decreases their carrying capacities but increases growth rates[31]. For *Colpidium*, temperatures above 20 °C represent a stress that decreases population growth rate, whereas the other species are still within their tolerated thermal range.

To start the experiment, ciliates were grown to their respective carrying capacities at 20 °C in bottles containing 1 l of bacterized medium. Throughout the experiments, medium consisted of protist pellets (Carolina Biological Supplies) at a concentration of 0.055 g l^{-1} of Chalkley's medium in which the bacterium *Serratia fonticola* was grown as the resource for all ciliate consumers. Two autoclaved wheat seeds were added to each bottle for slow nutrient release[32].

Monocultures (species richness = 1) were initiated at a density of 3 individuals per ml in a total of 100 ml medium. Multispecies communities (containing 2 to 6 species) were initiated with a total of 40 ml of ciliate culture topped up with 60 ml of fresh medium (100 ml culture in total). The 40-ml cultures were assembled by adding a fixed fraction (that is, 20 ml for two species, 13.33 ml for three species and so on) of each species at their specific carrying capacity, adopting a substitutive design. Because the number of possible species compositions exceeded the number of feasible experimental units, we used all possible compositions only for the monocultures, and for two- and six-species communities. For all other levels, species compositions were selected randomly from the set of all possible compositions such that all species occurred the same number of times, resulting in a total of 53 different compositions. Each level of species richness and composition was replicated at least twice, including an additional replicate for the monoculture, and three additional replicates for the six-species community resulting in 115 experimental units per temperature.

We sampled each experimental unit every day for the first 7 days, then 3 times per week for the following 50 days and a final sampling 7 days later, resulting in time series of 27 time points over a period of 57 days. We used video sampling techniques to count and measure individual ciliates in all communities[33]. For sampling, microcosms were taken out of the incubator, gently stirred to homogenize the culture and a sample was pipetted into a counting chamber. The counting chamber was covered with a lid and a 5-s long video was taken under the microscope. The videos were subsequently processed with the R package BEMOVI[34].

We derived community biomass by summing the biovolume of all individuals of a given species in a given community and multiplying biovolume with a constant density equal to water (that is, 1 g cm^{-3}). For each community, this resulted in a time series of community biomass. To avoid analysing monoculture time series while starting at a low fraction of the carrying capacity (3 individuals per ml)—compared to our multi-species culture species, which started between 7 and 20% carrying capacity (depending on richness)—we aligned the monoculture time series such that they started at the day on which they crossed 20% of their expected carrying capacity. Results regarding the effect of richness on temporal stability are qualitatively robust to exclusion of monoculture data (Extended Data Fig. 1c).

The temporal stability of each replicate community was calculated as the inverse of the coefficient of temporal variation in community biomass (mean community biomass divided by the standard deviation of community biomass). Resistance was measured for each replicate as the absolute difference between total biomass in the replicate and the mean total biomass at 15 °C, divided by the temperature difference, with dimensions of milligrams (per ml) per degree Celsius. Resistance values close to 0 indicate high resistance, whereas negative values indicate lower resistance. We also quantified relative resistance as the difference between total biomass in the replicate and the mean total biomass at 15 °C divided by the mean total biomass at 15 °C (that is, the loss proportional to the mean biomass at 15 °C).

We did not quantify resilience, because in a constant environment temporal variability is in principle closely related to resilience[35]. To understand the potential drivers and mechanisms, we investigated the role of statistical averaging and species asynchrony. Statistical averaging is assessed by the scaling relationship between the species mean biomass and species variance in biomass[36]. Synchrony was assessed by a previously published metric[37] that calculates the average correlation between the biomass of each species and the total biomass of all other species in the group. We used the R package codyn[38] to calculate asynchrony.

Analyses. Analysis of total biomass was performed using linear mixed-effects models[39], with temperature (linear, centred), species richness (log-linear) and their interaction as fixed effects (Extended Data Table 1a). Microcosm identity nested in composition was included as a random factor to account for the repeated measurements. Heterogeneity of residuals was accounted for by estimating a composition-specific variance. AIC comparison consistently identified as most parsimonious a model with a linear effect of temperature, as opposed to when temperature was a factor (ΔAIC of the model with a nonlinear temperature term was greater than 2 in all comparisons). A simpler analysis of the temporal average of total biomass of each individual microcosm to test the effect of richness, temperature and their interaction—including a random effect for species composition—yielded quantitatively and qualitatively similar results (see Extended Data Table 1b). Figure 1c shows the estimated effects of linear mixed-effects models fitted separately for each day with temperature (linear, centred), species richness (log-linear) and their interaction as fixed effects and composition as a random effect. Analyses of temporal stability and resistance did not contain repeated measures and therefore only accounted for variation in composition with a random effect. We used the R package nlme for all linear mixed-effects models[40]. To calculate associations between resistance and temporal stability among and within richness levels, we calculated reduced major axis regressions using the R package lmodel2[41] as both variables potentially contain measurement errors. The significance of reduced major axis regression slopes deviating from zero was assessed by one-tailed permutation tests. All analyses were done in R—the statistical computing environment[42].

Review of empirical studies. On the basis of the previously published review[16], we obtained a set of 17 independent studies of resilience, resistance and temporal variability of ecosystem functions in response to direct or indirect experimental manipulations of diversity[8,9,12,13,20,21,43–52]. Direct manipulations were defined as changing diversity by adding different sets of species to an experimental plot, jar or other unit, whereas indirect manipulations induced variation in diversity through the experimental treatment, such as fertilization. We only included studies that performed experimental manipulations.

To analyse whether specific mechanisms lead to covariation, we noted the type of mechanism proposed for each of the individual diversity–stability components (Extended Data Table 4). Furthermore, we assessed whether a quantitative or verbal argument was provided (or the mechanisms were not addressed at all) and synthesized the available evidence by vote counting.

Calculating overall ecosystem stability. An interactive website (https://frankpennekamp.shinyapps.io/Overall_ecosystem_stability_demo/) describes the calculation of ecosystem multifunctionality (also known as overall ecosystem functioning) or overall ecosystem stability and illustrates the following. The calculation requires that values of an ecosystem function (for example, biomass production) or of a stability component (for example, resistance to temperature) are converted into a common currency. The threshold approach uses a step mathematical function[53]; the averaging approach uses a linear mathematical function (and both equalize relative contributions of different ecosystem functions and/or stability components)[25]; a principal component approach uses a specific linear mathematical function for each ecosystem function or stability component[54]; and step-like mathematical functions have previously been proposed[26] with more or less gradual changes from the lower to higher value. The generalized logistic function (also known as the Richard's function) is flexible enough to give a wide range of shapes of conversion functions. If x is the measured variable, and Y is the converted variable, the generalized logistic function is:

$$Y = A + \frac{K - A}{(C + Qe^{-Bx})^{1/\nu}}$$

in which A is the lower asymptote, K is the upper asymptote and B is the gradient. ν affects the symmetry and the value of $Y(0)$. Q affects the value of $Y(0)$, that is, it shifts the function horizontally. C is typically set to 1. x is the value of the measured ecosystem function or stability component.

Overall ecosystem stability (that is, the aggregate measure of multiple stability components) is then the sum of the standardized and converted stability components: $\mathrm{OES} = f(z(\mathrm{res})) + f(z(\mathrm{ts}))$ in which 'res' is the measured resistance, 'ts' is the measured temporal stability, the function $z()$ subtracts the mean and divides by the standard deviation, and $f()$ is the generalized logistic function. The parameters of $f()$ were $A = -1$, $K = 1$, $B = 5$, $\nu = 1$, $C = 1$ and Q was varied from 10^{-2} to 10^{2}. These values were chosen to produce converted stability measures that span the range from A to K and to have a relatively threshold-like change from A to K.

Standardization before summation results in overall ecosystem stability with a mean of 0, emphasizing that the units of valuation here are arbitrary (although they generally need not be). Standardization also suggests equal weights for

© 2018 Springer Nature Limited. All rights reserved.

different stability components; weighting of functions needs to be further considered and may be specified according to the specific use cases[55]. Differential weightings, if desired and justified, can be incorporated into the conversion functions. Suggestions regarding the choice of conversion functions for managed systems can be found in two previous studies[26,28].

Unimodal relationships can result from negative covariation among two stability components. We also took into consideration how more than two components affect the unimodal pattern. Although the unimodal relationship is most pronounced when equal numbers of positive and negative relationships are considered, a unimodal relationship will persist as long as there is at least one opposing stability component (see Extended Data Fig. 5).

Reporting summary. Further information on research design is available in the Nature Research Reporting Summary linked to this paper.

Code availability. Code to reproduce the analyses and figures is accessible at Github (https://github.com/pennekampster/Code_and_data_OverallEcosystemStability) with the identifier (https://doi.org/10.5281/zenodo.1345557).

Data availability

The experimental data that support the findings of this study are available at Github (https://github.com/pennekampster/Code_and_data_OverallEcosystemStability) with the identifier (https://doi.org/10.5281/zenodo.1345557). Source Data for Figs. 1–3 are provided in the online version of the paper.

30. Cottingham, K. L., Lennon, J. T. & Brown, B. L. Knowing when to draw the line: designing more informative ecological experiments. *Front. Ecol. Environ.* **3**, 145–152 (2005).
31. Leary, D. J. & Petchey, O. L. Testing a biological mechanism of the insurance hypothesis in experimental aquatic communities. *J. Anim. Ecol.* **78**, 1143–1151 (2009).
32. Altermatt, F. et al. Big answers from small worlds: a user's guide for protist microcosms as a model system in ecology and evolution. *Methods Ecol. Evol.* **6**, 218–231 (2015).
33. Pennekamp, F. et al. Dynamic species classification of microorganisms across time, abiotic and biotic environments—a sliding window approach. *PLoS ONE* **12**, e0176682 (2017).
34. Pennekamp, F., Schtickzelle, N. & Petchey, O. L. BEMOVI, software for extracting behavior and morphology from videos, illustrated with analyses of microbes. *Ecol. Evol.* **5**, 2584–2595 (2015).
35. May, R. M. Stability and complexity in model ecosystems. *Monogr. Popul. Biol.* **6**, 1–235 (1973).
36. Tilman, D., Lehman, C. L. & Bristow, C. E. Diversity–stability relationships: statistical inevitability or ecological consequence? *Am. Nat.* **151**, 277–282 (1998).
37. Gross, K. et al. Species richness and the temporal stability of biomass production: a new analysis of recent biodiversity experiments. *Am. Nat.* **183**, 1–12 (2014).
38. Hallett, L. M. et al. codyn: an R package of community dynamics metrics. *Methods Ecol. Evol.* **7**, 1146–1151 (2016).
39. Schmid, B., Baruffol, M., Wang, Z. & Niklaus, P. A. A guide to analyzing biodiversity experiments. *J. Plant Ecol.* **10**, 91–110 (2017).
40. Pinheiro, J., Bates, D., DebRoy, S., Sarkar, D. & R Core Team. *nlme: Linear and Nonlinear Mixed Effects Models* R package version 3.1.137 https://CRAN.R-project.org/package=nlme (2018).
41. Legendre, P. *lmodel2: Model II Regression* R package version 1.7.3 https://CRAN.R-project.org/package=lmodel2 (2018).
42. R Core Team. *R: A Language and Environment for Statistical Computing* (R Foundation for Statistical Computing, Vienna, 2018).
43. Caldeira, M. C., Hector, A., Loreau, M. & Pereira, J. S. Species richness, temporal variability and resistance of biomass production in a Mediterranean grassland. *Oikos* **110**, 115–123 (2005).
44. Zhang, Q.-G. & Zhang, D.-Y. Species richness destabilizes ecosystem functioning in experimental aquatic microcosms. *Oikos* **112**, 218–226 (2006).
45. van Ruijven, J. & Berendse, F. Diversity enhances community recovery, but not resistance, after drought. *J. Ecol.* **98**, 81–86 (2010).
46. Griffiths, B. S. et al. Ecosystem Response of pasture soil communities to fumigation-induced microbial diversity reductions: an examination of the biodiversity–ecosystem function relationship. *Oikos* **90**, 279–294 (2000).
47. Wardle, D. A., Bonner, K. I. & Barker, G. M. Stability of ecosystem properties in response to above-ground functional group richness and composition. *Oikos* **89**, 11–23 (2000).
48. Hughes, A. R. & Stachowicz, J. J. Genetic diversity enhances the resistance of a seagrass ecosystem to disturbance. *Proc. Natl Acad. Sci. USA* **101**, 8998–9002 (2004).
49. Vogel, A., Scherer-Lorenzen, M. & Weigelt, A. Grassland resistance and resilience after drought depends on management intensity and species richness. *PLoS ONE* **7**, e36992 (2012).
50. Wertz, S. et al. Decline of soil microbial diversity does not influence the resistance and resilience of key soil microbial functional groups following a model disturbance. *Environ. Microbiol.* **9**, 2211–2219 (2007).
51. Wagg, C. et al. Plant diversity maintains long-term ecosystem productivity under frequent drought by increasing short-term variation. *Ecology* **98**, 2952–2961 (2017).
52. Tilman, D. Biodiversity: population versus ecosystem stability. *Ecology* **77**, 350–363 (1996).
53. Byrnes, J. E. K. et al. Investigating the relationship between biodiversity and ecosystem multifunctionality: challenges and solutions. *Methods Ecol. Evol.* **5**, 111–124 (2014).
54. Antiqueira, P. A. P., Petchey, O. L. & Romero, G. Q. Warming and top predator loss drive ecosystem multifunctionality. *Ecol. Lett.* **21**, 72–82 (2018).
55. Gamfeldt, L., Hillebrand, H. & Jonsson, P. R. Multiple functions increase the importance of biodiversity for overall ecosystem functioning. *Ecology* **89**, 1223–1231 (2008).

© 2018 Springer Nature Limited. All rights reserved.

a

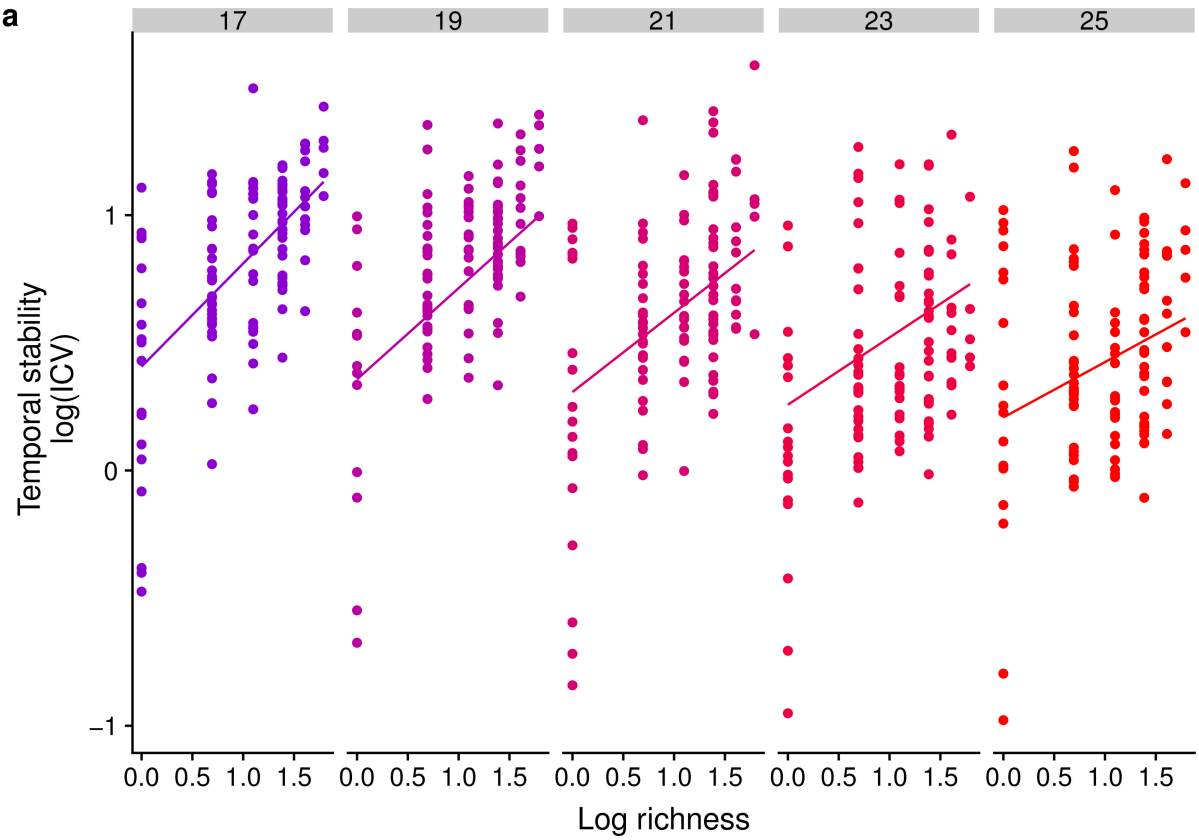

b

	Estimate	CI (lower)	CI (upper)	Std.Error	DF	t–value	p–value
Intercept	0.3320	0.1897	0.4744	0.07250	626	4.58	0.000006
Richness	0.3335	0.2038	0.4631	0.06459	51	5.16	0.000004
Temperature	−0.0249	−0.0360	−0.0137	0.00569	626	−4.37	0.000015
Rich. x temp.	−0.0234	−0.0334	−0.0134	0.00508	626	−4.61	0.000005

c

	Estimate	CI (lower)	CI (upper)	Std.Error	DF	t–value	p–value
Intercept	0.3937	0.2163	0.57118	0.09032	531	4.36	0.000016
Richness	0.2842	0.1319	0.43648	0.07562	45	3.76	0.000491
Temperature	−0.0317	−0.0506	−0.01272	0.00965	531	−3.28	0.001095
Rich. x temp.	−0.0181	−0.0337	−0.00247	0.00794	531	−2.28	0.023283

Extended Data Fig. 1 | Richness increased temporal stability across temperatures. a, The stabilizing effect of richness was present across all temperatures, although temperature had a negative effect on mean stability. The inverse coefficient of variation (ICV) is calculated as the mean biomass divided by the standard deviation of biomass. **b**, Results of the linear mixed-effects model of log richness, temperature and their interaction on temporal stability supporting the positive effects of richness and the negative effect of temperature on temporal stability ($n = 681$ independent microcosms). **c**, Results of the same analysis as in **b** but without the monocultures. Results are qualitatively the same, indicating that the relationship between richness and temporal stability is not driven only by the monocultures ($n = 580$ independent microcosms). CI, 95% confidence interval; DF, degrees of freedom; Std.Error, standard error of the estimate.

© 2018 Springer Nature Limited. All rights reserved.

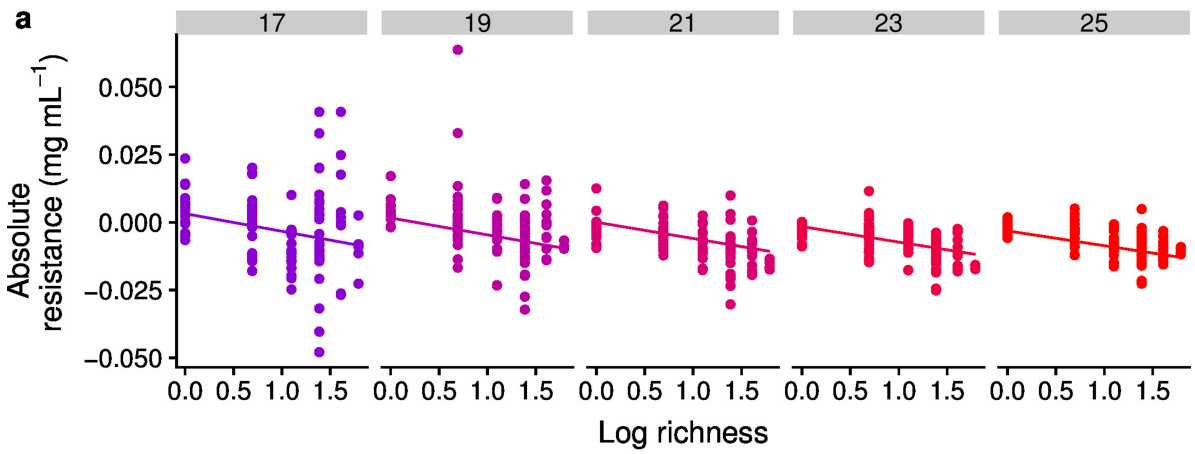

b

	Estimate	CI (lower)	CI (upper)	Std.Error	DF	t–value	p–value
Intercept	0.000812	−0.003137	0.004760	0.002010	512	0.404	0.686407
Richness	−0.006115	−0.009710	−0.002520	0.001791	51	−3.415	0.001258
Temperature	−0.000796	−0.001215	−0.000376	0.000214	512	−3.726	0.000216
Rich. x temp.	0.000133	−0.000241	0.000507	0.000190	512	0.697	0.486295

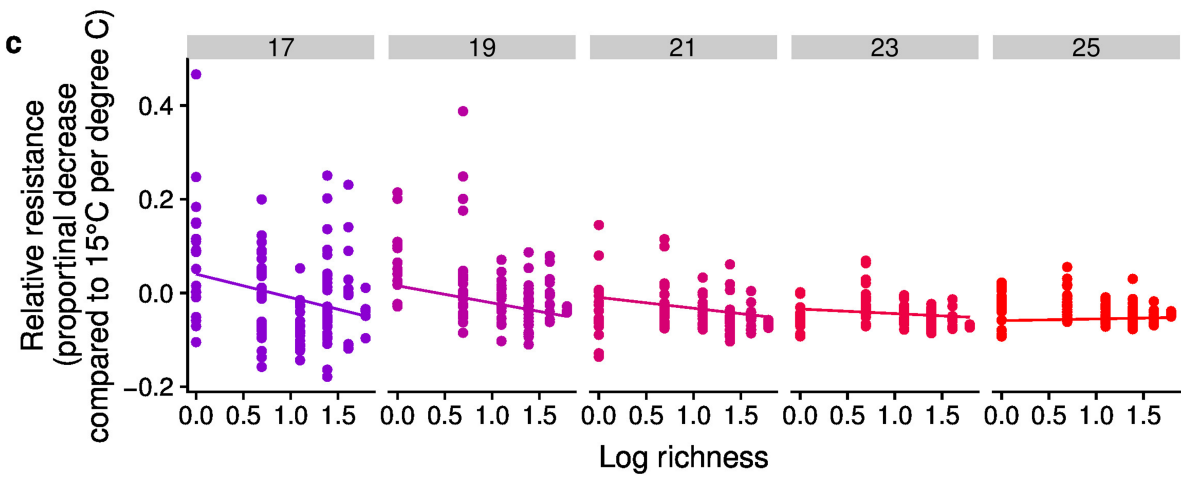

d

	Estimate	CI (lower)	CI (upper)	Std.Error	DF	t–value	p–value
Intercept	0.00284	−0.02027	0.02595	0.01176	512	0.241	0.80951
Richness	−0.02980	−0.05085	−0.00875	0.01048	51	−2.842	0.00643
Temperature	−0.01241	−0.01544	−0.00937	0.00155	512	−8.023	< 0.000001
Rich. x temp.	0.00670	0.00399	0.00941	0.00138	512	4.858	0.000002

Extended Data Fig. 2 | The effect of richness on absolute and proportional resistance. a, **c**, Richness decreased resistance, regardless of whether it was measured on an absolute or proportional scale. **b**, **d**, Results of linear mixed-effects models of richness, temperature and their interaction on absolute and proportional richness ($n = 567$ independent microcosms).

© 2018 Springer Nature Limited. All rights reserved.

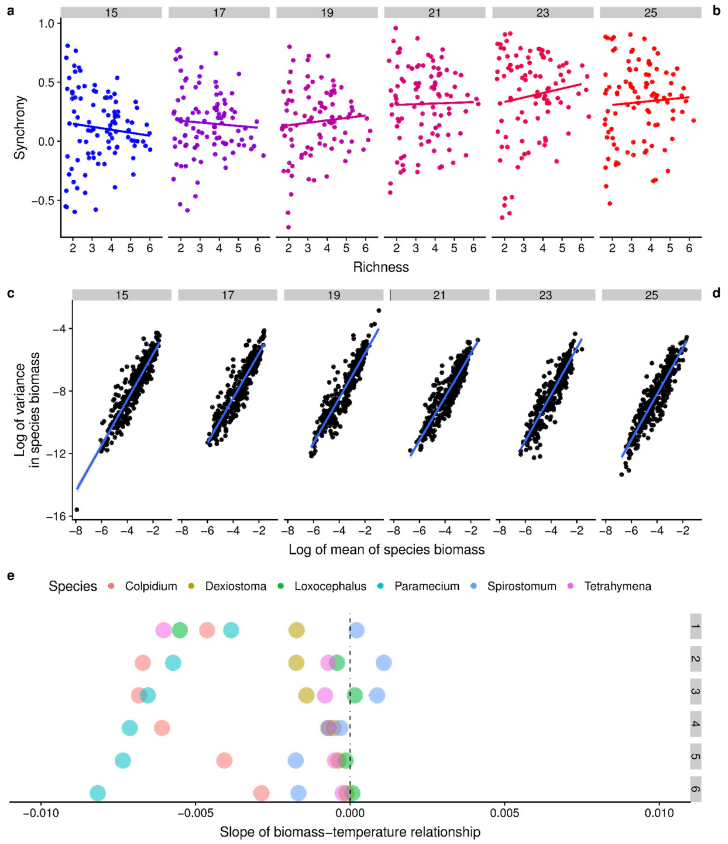

	Estimate	CI (lower)	CI (upper)	Std.Error	DF	t–value	p–value
Intercept	0.18940	−0.04873	0.4275	0.12122	531	1.562	0.1188
Richness	0.00666	−0.01117	0.0245	0.00908	531	0.734	0.4635
Temperature	0.04958	−0.15500	0.2542	0.10157	45	0.488	0.6278
Rich. x temp.	0.01821	0.00354	0.0329	0.00747	531	2.439	0.0151

	Estimate	CI (lower)	CI (upper)	Std. Error	t value	Pr(>|t|)
Intercept	−2.58856	−2.69474	−2.48238	0.0541	−47.810	< 0.000001
Log species mean biomass	1.44577	1.41858	1.47297	0.0139	104.261	< 0.000001
Temperature	0.04280	0.01195	0.07366	0.0157	2.721	0.00657
Log species mean biomass x temperature	0.00139	−0.00645	0.00923	0.0040	0.348	0.72772

Extended Data Fig. 3 | Niche complementarity and low response diversity probably caused the negative covariance of stability components. Niche complementarity and the resulting increase in total biomass with richness tended to increase temporal stability (Fig. 1). **a**, **b**, We found little evidence for an effect of population asynchrony on temporal stability (linear mixed-effects model with composition as random effect and log richness and temperature as fixed effects; $n = 681$ independent microcosms). **c**, **d**, By contrast, statistical averaging contributed to stabilization (linear regression between mean species biomass and the variance of species biomass; $n = 2{,}077$ species mean–variance biomass observations). **e**, Low response diversity was inferred because the biomass of most species decreased or was unaffected by temperature (linear regression between temperature and species biomass; $n = 972$ species biomass × temperature observations). Consequently, when there were more species, there was greater total biomass and greater temporal stability, but a greater biomass loss, with temperature increase. Therefore, niche complementarity (that is, effect diversity) probably not only caused a positive effect of diversity on temporal stability but also had a negative effect of diversity on resistance in the absence of high response diversity. However, this explanation cannot apply within richness levels, for which positive covariance among stability components was found.

© 2018 Springer Nature Limited. All rights reserved.

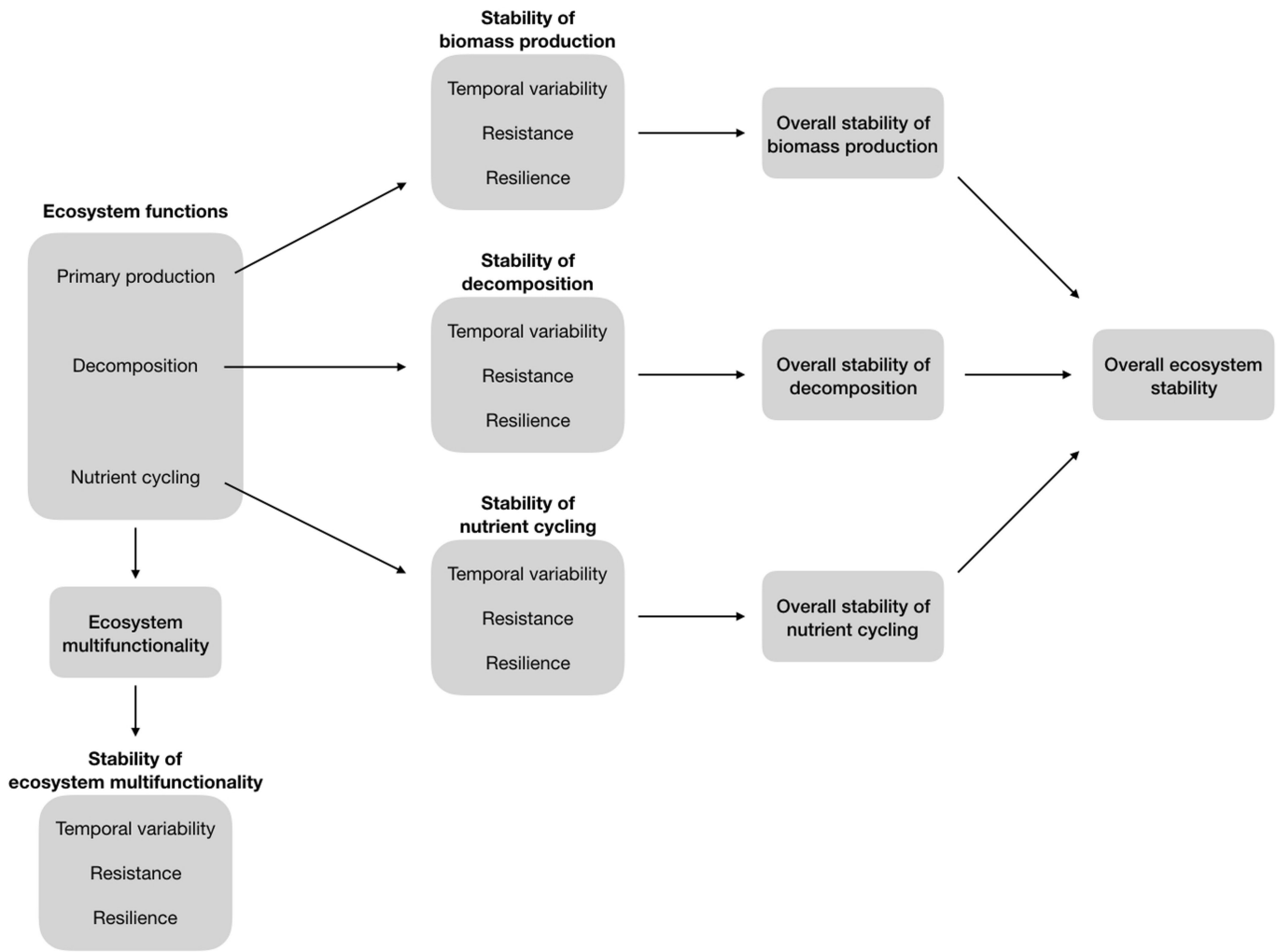

Extended Data Fig. 4 | Overview of terms and the concept of overall ecosystem stability. Measured ecosystem functions (left-most top box) can each have multiple components of stability (for example, temporal variability, resistance and resilience of biomass production), each of which can be combined into a measure of overall stability. When—as in our study—there is only one ecosystem function, this overall stability of a specific function is also the overall ecosystem stability. In studies of more than one ecosystem function, the overall stability of several functions could be combined to give overall ecosystem stability. Alternatively, one could first calculate ecosystem multifunctionality and then measure its stability components.

© 2018 Springer Nature Limited. All rights reserved.

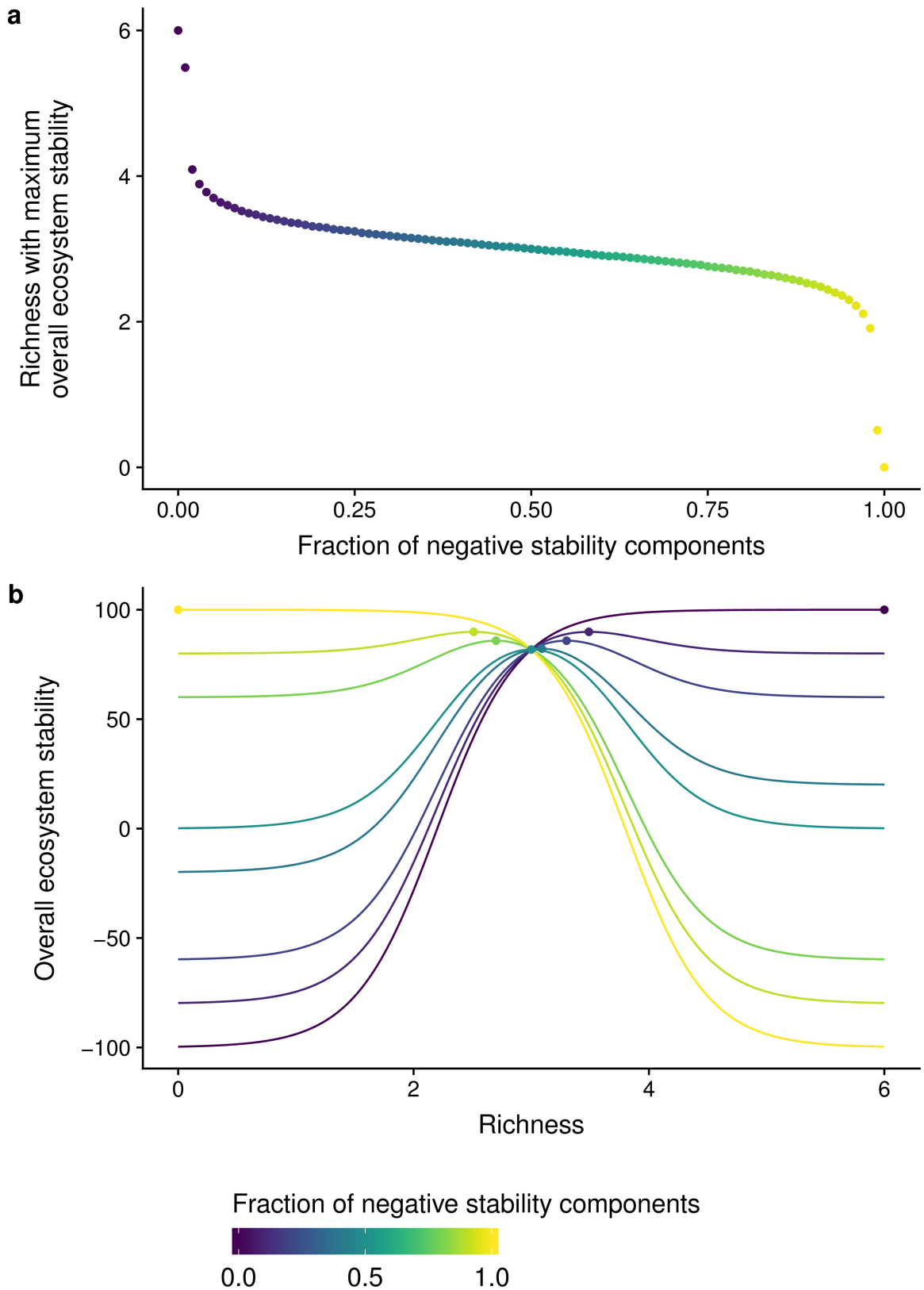

Extended Data Fig. 5 | The effect of aggregating more than two stability components into overall ecosystem stability. The fraction of stability components with a negative sign influences whether or not a unimodal pattern will result for a total of 100 stability components. **a**, A unimodal relationship between diversity and OES will result if at least one stability component is negative. **b**, However, the strength of the pattern depends on the relative balance of positive and negative relationships.

© 2018 Springer Nature Limited. All rights reserved.

Extended Data Table 1 | Richness increased, whereas temperature decreased, biomass production

a

	Estimate	CI (lower)	CI (upper)	Std.Error	DF	t–value	p–value
Intercept	0.07286	0.05182	0.093890	0.010731	12258	6.79	< 0.000001
Richness	0.04977	0.03058	0.068958	0.009559	51	5.21	0.000003
Temperature	–0.00205	–0.00315	–0.000948	0.000561	626	–3.65	0.000281
Rich. x temp.	–0.00534	–0.00634	–0.004345	0.000507	626	–10.54	< 0.000001

b

	Estimate	CI (lower)	CI (upper)	Std.Error	DF	t–value	p–value
Intercept	0.07323	0.05206	0.094407	0.010782	626	6.79	< 0.000001
Richness	0.04959	0.03031	0.068872	0.009603	51	5.16	0.000004
Temperature	–0.00220	–0.00351	–0.000892	0.000667	626	–3.30	0.00102
Rich. x temp.	–0.00547	–0.00664	–0.004296	0.000596	626	–9.18	< 0.000001

a, Results of the linear mixed-effects model of richness, temperature and their interaction on the temporal dynamics of biomass ($n = 12{,}939$ microcosm × day combinations). **b**, Results of the linear mixed-effects model of richness, temperature and their interaction with the time series aggregated to the average biomass for each microcosm ($n = 681$ independent microcosms).

© 2018 Springer Nature Limited. All rights reserved.

Extended Data Table 2 | Positive temporal stability–resistance relationships within richness levels

richness	Intercept	Slope	P–perm (1–tailed)	N
1	–0.00760617400951036	0.00506367932695562	0.01	84
2	–0.00843466390669893	0.00339781153057296	0.02	148
3	–0.0247877029765781	0.00880722901581866	0.02	100
4	–0.0249323685277533	0.00762486814778502	0.01	150
5	–0.027634192253533	0.0086737833813624	0.01	60
6	–0.0220565962582076	0.00349526254239345	0.02	25

Reduced major axis regression analyses revealed positive relationships between temporal stability and resistance within each of the six richness levels (the *P* values were based on one-tailed permutation tests (*P*-perm); *N* indicates the sample size for each richness level).

© 2018 Springer Nature Limited. All rights reserved.

Extended Data Table 3 | Overview of studies used for literature survey

Code	Description	Reference
Ca–05	Diversity manipulation of grassland plants (Portuguese BIODEPTH site) analysing temporal variability and resistance to natural perturbation (frost and low precipitation) of biomass production.	43
PS–02	Diversity manipulation of grassland plants (Swiss BIODEPTH site) analysing resistance and resilience of biomass production to experimental drought perturbation.	9
Z2–06	Diversity manipulation of unicellular algae analysing resistance and resilience of biomass production to experimental cold perturbation.	44
Z1–06 *	Diversity manipulation of unicellular algae analysing temporal variability and resistance to experimental cold perturbation of biomass production.	20
Is–15	Forty–six diversity manipulations of grassland plants analysing temporal variability, resistance, and resilience to natural perturbations (drought and wet events) of biomass production.	13
VR–10	Diversity manipulation of plants, analysing resistance and resilience to natural perturbation (drought) of biomass production.	45
Ba–16	Diversity manipulation of diatoms, analysing resistance and resilience to perturbation (chemical stressor, atrazine) of biomass production.	21
Gr–00–1	Diversity manipulation by fumigation of soil microorganisms, analysing resilience to perturbation (heating) and resistance to perturbation (heating) of respiration.	46
Gr–00–2	Diversity manipulation by fumigation of soil microorganisms, analysing resilience to perturbation (chemical stress) and resistance to perturbation (chemical stress, CuSO4) of respiration.	46
TD–94	Diversity manipulation by fertilisation of plants, analysing resistance and resilience of biomass production to natural perturbation (drought).	8
Wa–00	Diversity manipulation of plants, analysing resistance and resilience to experimental perturbation (drought) of various ecosystem functions.	47
Hu–04	Analysis of diverse studies of marine ecosystems, some of which examined diversity–resistance and some diversity–resilience relationships for various ecosystem functions.	48
Vo–12	Diversity manipulation of grassland plants. Analysis of resistance and resilience of biomass production to drought perturbation.	49
Wr–15	Diversity manipulation of grassland plants. Analysis of temporal variability and resilience of biomass production to drought perturbation.	12
We–07	Manipulation of soil microbial diversity by serial dilution. Analysis of resistance and resilience of denitrification and nitrite oxidisation to a temperature perturbation.	50
Wa–17	Diversity manipulation of grassland plants. Analysis of temporal variability and resilience of biomass production to drought perturbation.	51
Ti–96	Diversity manipulation of grassland plants via fertilisation. Analysis of temporal variability, resilience and resistance of biomass production to natural drought perturbation.	52

The individual study code, a short description and the reference for each study[8,9,12,13,20,21,43–52] is shown.
*Studies that examine intrinsic stability alongside response to a disturbance.

© 2018 Springer Nature Limited. All rights reserved.

Extended Data Table 4 | Putative mechanisms and type of evidence for bivariate diversity–stability relationships

Code	diversity_stability_relation	direction	mechanism1	mechanism2	evidence1	evidence2	scale
Ba–16	resistance/resilience	positive/negative	low response diversity	selection effect	signals of mechanisms	signals of mechanisms	relative
Ca–05	resistance/temporal_var	negative/positive	selection effect	increased evenness, synchrony, statistical averaging	signals of mechanisms	signals of mechanisms	absolute
Ca–05	resistance/temporal_var	neutral/positive	selection effect	increased evenness, synchrony, statistical averaging	signals of mechanisms	signals of mechanisms	relative
Gr–00–1	resistance/resilience	negative/neutral	not stated	not stated	missing	missing	relative
Gr–00–2	resistance/resilience	positive/positive	insurance effect	insurance effect	verbal	verbal	relative
Hu–04	resistance/resilience	positive/neutral	trade–offs in response diversity among stressors	not a sampling effect	signals of mechanisms	signals of mechanisms	absolute
Is–15	resistance/resilience	positive/neutral	not stated	not stated	missing	missing	relative
Is–15	resistance/temporal_var	positive/positive	not stated	not stated	missing	missing	relative
Is–15	resilience/temporal_var	neutral/positive	not stated	not stated	missing	missing	
PS–02	resistance/resilience	negative/negative	high response diversity; evenness	species composition	signals of mechanisms	signals of mechanisms	absolute
PS–02	resistance/resilience	neutral/negative	high response diversity; evenness	species composition	signals of mechanisms	signals of mechanisms	relative
TD–94	resistance/resilience	positive/positive	high response diversity	not stated	verbal	missing	relative
Ti–96	resistance/resilience	positive/neutral	high response diversity	not stated	verbal	missing	relative
Ti–96	resistance/temporal_var	positive/positive	high response diversity	high response diversity; competition	verbal	signals of mechanisms	relative
Ti–96	resilience/temporal_var	neutral/positive	not stated	high response diversity; competition	missing	signals of mechanisms	
Vo–12	resistance/resilience	neutral/neutral	not stated	not stated	missing	missing	absolute
Vo–12	resistance/resilience	neutral/neutral	not stated	not stated	missing	missing	relative
VR–10	resistance/resilience	negative/neutral	high response diversity	not stated	signals of mechanisms	missing	absolute
VR–10	resistance/resilience	neutral/neutral	high response diversity	not stated	signals of mechanisms	missing	relative
Wa–00	resistance/resilience	neutral/neutral	species composition	species composition	verbal	verbal	absolute
Wa–17	resistance/resilience	positive/neutral	insurance effect	insurance effect	verbal	verbal	relative
Wa–17	resistance/temporal_var	positive/positive	insurance effect	insurance effect	verbal	verbal	relative
Wa–17	resilience/temporal_var	neutral/positive	insurance effect	insurance effect	verbal	verbal	
We–07	resistance/resilience	neutral/neutral	high response diversity	high response diversity	verbal	verbal	absolute
Wr–15	resistance/resilience	negative/neutral	selection effect; community composition	not stated	signals of mechanisms	missing	absolute
Z1–06 *	resistance/resilience	positive/neutral	high response diversity	not stated	verbal	missing	relative
Z1–06 *	resistance/temporal_var	positive/positive	high response diversity	statistical averaging	verbal	signals of mechanisms	relative
Z1–06 *	resilience/temporal_var	neutral/positive	not stated	statistical averaging	missing	signals of mechanisms	
Z2–06	resistance/resilience	negative/neutral	low response diversity	not stated	signals of mechanisms	missing	relative

All reported bivariate diversity–stability relationships are listed. The nature of the covariation, the putative mechanism for each stability measure (for example, response diversity, evenness or statistical averaging), as well as the type of evidence provided (that is, verbal arguments, signals of mechanisms (that is, statistical evidence), manipulation of mechanisms in experiments or missing) are included.

© 2018 Springer Nature Limited. All rights reserved.

LETTER

https://doi.org/10.1038/s41586-018-0633-x

A cortico–cerebellar loop for motor planning

Zhenyu Gao[1], Courtney Davis[2], Alyse M. Thomas[2], Michael N. Economo[3], Amada M. Abrego[2], Karel Svoboda[3], Chris I. De Zeeuw[1,4] & Nuo Li[2,3]*

Persistent and ramping neural activity in the frontal cortex anticipates specific movements[1–6]. Preparatory activity is distributed across several brain regions[7,8], but it is unclear which brain areas are involved and how this activity is mediated by multi-regional interactions. The cerebellum is thought to be primarily involved in the short-timescale control of movement[9–12]; however, roles for this structure in cognitive processes have also been proposed[13–16]. In humans, cerebellar damage can cause defects in planning and working memory[13]. Here we show that persistent representation of information in the frontal cortex during motor planning is dependent on the cerebellum. Mice performed a sensory discrimination task in which they used short-term memory to plan a future directional movement. A transient perturbation in the medial deep cerebellar nucleus (fastigial nucleus) disrupted subsequent correct responses without hampering movement execution. Preparatory activity was observed in both the frontal cortex and the cerebellar nuclei, seconds before the onset of movement. The silencing of frontal cortex activity abolished preparatory activity in the cerebellar nuclei, and fastigial activity was necessary to maintain cortical preparatory activity. Fastigial output selectively targeted the behaviourally relevant part of the frontal cortex through the thalamus, thus closing a cortico-cerebellar loop. Our results support the view that persistent neural dynamics during motor planning is maintained by neural circuits that span multiple brain regions[17], and that cerebellar computations extend beyond online motor control[13–15,18].

Head-fixed mice were presented with a pole during a sample period of 1.3 s, and discriminated its location (anterior or posterior) using their whiskers (Fig. 1a). The mice held their responses in short-term memory and planned for the upcoming movement during a delay period of 1.3 s. After this, an auditory 'go' cue (0.1 s) signalled the response period and mice reported the location of the pole by skilled directional licking (left or right) to obtain a water reward.

During such a delay period, it is known that preparatory activity in the anterior lateral motor cortex (ALM; Fig. 1b) is critical for subsequent correct movements[19–22]. ALM neurons exhibit persistent and ramping activity that predicts specific future movements, long before the onset of movement.

The ALM projects to the cerebellum via the basal pontine nucleus[23,24]. We tested the involvement of the cerebellum in the delayed response task by lesioning either the fastigial nucleus or the dentate nucleus (Fig. 1c, Methods). We separately examined behavioural choice (the direction of the first lick after the 'go' cue) and movement execution (licking duration and frequency). Fastigial lesions impaired the initiation of contralesional licking (Fig. 1d) and delayed the initiation of contralesional licking following the 'go' cue (Fig. 1e). After the initiation of movement, licking duration and frequency were unaffected (Fig. 1e, Extended Data Fig. 1b, c). Dentate lesions (around 1.5 mm away from the fastigial nucleus) did not change behavioural choice and movement execution (Fig. 1d).

We tested the involvement of the fastigial nucleus during specific behavioural periods by disrupting activity using channelrhodopsin-2 (ChR2) activation (photoactivation, Fig. 1f, Methods). Fastigial photoactivation during the early sample period had no effect on behavioural choice ($P > 0.05$ for either trial type, bootstrap; Methods). Photoactivation during the delay and response periods both resulted in incorrect choices (Fig. 1g, h), which were induced even when the photostimuli ceased 800 ms before the movement. Photoactivation during the delay period biased future movements to either the contralateral or ipsilateral direction in individual mice (Fig. 1h, Extended Data Fig. 1e). Photoactivation immediately before the onset of movement (response period) produced a contralateral bias (Fig. 1h), which is opposite to the directional bias induced by fastigial lesions. The distinct patterns of bias induced by photoactivation in the delay and in the response periods suggest temporally specific roles for the fastigial nucleus in driving movement planning and initiation.

Fastigial photoactivation during the response period did not block or perturb the frequency and duration of licking movements (Fig. 1i). In addition, photoactivation during the delay period did not evoke early licks (Extended Data Fig. 1f). These data show that rhythmic licking is independent of fastigial activity, but they do not rule out the involvement of the fastigial nucleus in controlling the direction and timing of licking bouts via its descending input to oscillators in the medulla that drive licking[25]. Dentate photoactivation produced little effect on behavioural choice (Fig. 1g, $P = 0.06$, bootstrap; Extended Data Fig. 1e), which is consistent with results from the lesion experiments.

Next, we silenced fastigial activity to test its necessity for correct behavioural choice. We photostimulated ChR2-expressing Purkinje cells, which inhibited the activity of the cerebellar nucleus (CN) (photoinhibition, Fig. 1j, Extended Data Fig. 2, Methods). Photoinhibition during the early sample period did not affect behavioural choice (Fig. 1k, $P > 0.05$ for either trial type, bootstrap; Methods). Photoinhibition during the late sample and delay periods resulted in incorrect behavioural choices, with a larger effect induced in the delay period (Fig. 1k, Extended Data Fig. 2g, h). Photoinhibition during the delay period biased future movements to either the contralateral or the ipsilateral direction in individual mice (Extended Data Fig. 2g, h). Photoinhibition during movement initiation (response period) produced an ipsilateral bias (Fig. 1k), consistent with that observed after fastigial lesions, and opposite from the bias induced by fastigial photoactivation. Photoinhibition minimally affected movement execution (Fig. 1l), and no other movements were consistently evoked during photoinhibition (Methods, Extended Data Fig. 2e, f, i). These results reveal that fastigial activity, starting from the late sample period and continuing throughout the delay period, is required for correct behavioural choice.

We compared the activity in the ALM and the CN by recording from single units (ALM, $n = 1{,}194$ units; CN, $n = 564$ units; Extended Data Fig. 3, Methods). Most ALM pyramidal neurons distinguished 'lick-left' and 'lick-right' trials in spike counts (980/1,194, $P < 0.05$, two-tailed t-test, Methods). A similar proportion of CN neurons showed trial-type selectivity (416/564). Individual ALM and CN neurons exhibited diverse activity patterns, including selective persistent activity and ramping activity during the delay period (Fig. 2a, b). Preparatory activity (selectivity before the response period) was more prevalent in ALM (ALM, 59% of neurons; CN, 35% of neurons; $P < 0.001$, χ^2 test).

[1]Department of Neuroscience, Erasmus MC, Rotterdam, The Netherlands. [2]Department of Neuroscience, Baylor College of Medicine, Houston, TX, USA. [3]Janelia Research Campus, Ashburn, VA, USA. [4]Netherlands Institute for Neuroscience, Amsterdam, The Netherlands. *e-mail: nuol@bcm.edu

© 2018 Springer Nature Limited. All rights reserved.

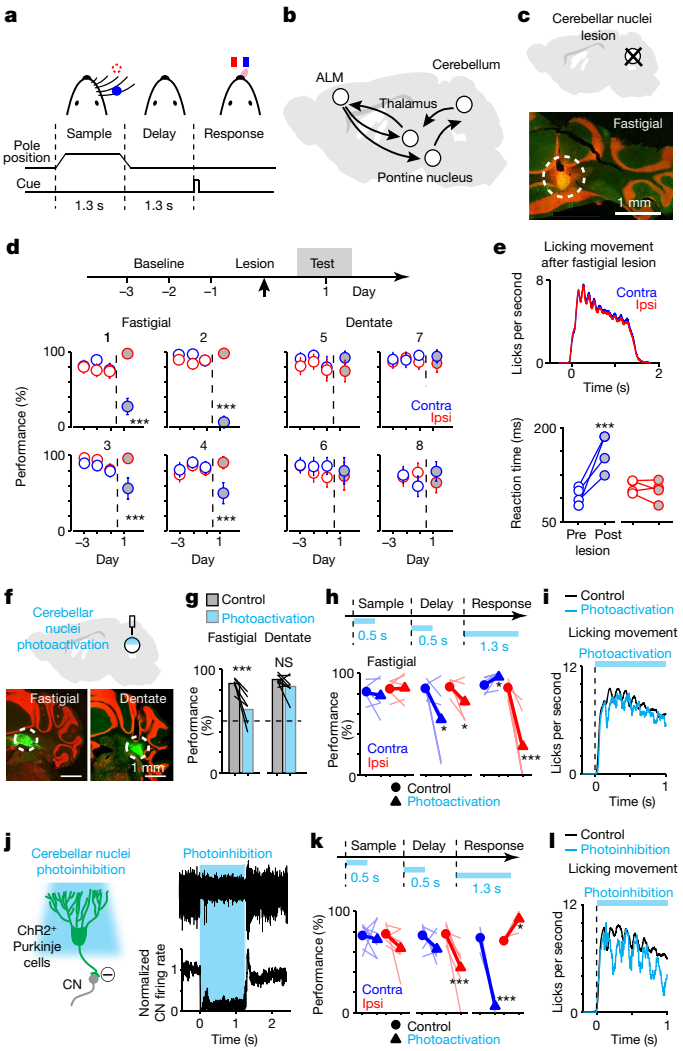

Fig. 1 | Cerebellar involvement in motor planning and movement initiation. a, Mouse reporting the location of a pole by directional licking. **b**, The ALM-cerebellar loop. **c**, Top, schematic of a fastigial or a dentate lesion. Bottom, example lesion. **d**, Performance of mice in the delayed response task (session mean ± s.e.m., $n = 75$–256 trials). The numbers at the top of the graphs refer to the number assigned to each individual mouse. Mouse 1, 2, left fastigial lesion; mouse 3, 4, right fastigial lesion; mouse 5, left dentate lesion; mouse 6–8, right dentate lesion. Lick-left and lick-right trials are grouped by instructed licking direction relative to the lesioned hemisphere. Blue, contralesional (contra); red, ipsilesional (ipsi). $***P < 0.001$, one-sided test, pre- versus post lesion, bootstrap (Methods). **e**, Top, lick rate during contra- and ipsilesional licking bouts after fastigial lesion. Lick times are aligned to the first lick ($t = 0$). Bottom, time of the first lick to the contra- and ipsilesional direction after onset of the 'go' cue. Lines represent individual mice ($n = 4$). $***P < 0.001$, one-sided test, bootstrap. **f**, Top, schematic of fastigial or dentate photoactivation. Laser power, 0.5–1.5 mW. Bottom, example ChR2 expression. **g**, Performance in the delayed response task after fastigial or dentate photoactivation during the delay period. Lick-left and lick-right trials are pooled. Chance is 50% (dashed line). Lines represent individual mice (fastigial, $n = 6$; dentate, $n = 8$); bars represent the mean. $***P < 0.001$, one-sided test, bootstrap. **h**, Performance in the delayed response task after fastigial photoactivation during specific periods. Lick-left and lick-right trials are grouped by instructed licking direction relative to the manipulated hemisphere. Both hemispheres were tested. See Supplementary Table 1 for manipulated hemispheres. Thick lines represent the mean; thin lines represent individual mice ($n = 6$). Photoact., photoactivation. $*P < 0.05$, $***P < 0.001$, one-sided test, bootstrap. **i**, Lick rate in control and fastigial photoactivation trials ($n = 6$ mice). **j**, Left, schematic of CN photoinhibition. Laser power, 0.5–4.5 mW. Right, silicon-probe recording in the fastigial nucleus. An example voltage trace and the average firing rate of CN neurons are shown ($n = 26$ neurons, 2 mice). Firing rates were normalized to the baseline (500 ms before photostimulus onset). **k**, Performance in the delayed response task after CN photoinhibition. Experimental details as in **h**. $n = 7$ mice for sample and delay period photoinhibition; $n = 3$ for response period photoinhibition (Supplementary Table 1). **l**, Lick rate in control and CN photoinhibition trials ($n = 3$ mice).

Peri-movement activity (selectivity during the response period) was equally prevalent in both regions (ALM, 67%; CN, 66%). In both regions, a similar proportion (less than 10%) of neurons showed modulated spike rates during individual licks (Extended Data Fig. 4).

Selectivity for lick-left and lick-right trials emerged gradually in both ALM and CN population averages (Fig. 2c, d), starting during the sample period and reaching a maximum during the response period. An 'error' trial was recorded if the mouse licked in the opposite direction to the instruction provided by the object location. A small group of CN neurons signalled the location of the object; however, most CN neurons predicted the upcoming lick direction (67%, Extended Data Fig. 4), which is similar to findings in the ALM[19,20]. Thus, CN selectivity during the delay period is related to future movement, and is characteristic of preparatory activity that instructs subsequent movement.

Preparatory activity was present in all three cerebellar nuclei (Extended Data Figs. 3, 4). In the fastigial nucleus, distinct patterns of selectivity were observed during the early compared with the late delay period, in which equal numbers of neurons preferred either contralateral or ipsilateral movement during the early delay. In addition, a population-level preference for contralateral movement developed just before movement initiation[23] (Extended Data Fig. 4g), which is consistent with the directional biases induced by fastigial lesion and optogenetic manipulations during movement initiation (Fig. 1). These results show that there is widespread activity related to motor planning and movement initiation in the CN.

The cerebellum is thought to process information over timescales of hundreds of milliseconds[26–28]. Cerebellar preparatory activity lasting seconds could be inherited from the ALM. We recorded from the CN while bilaterally photoinhibiting the ALM during the delay period (Fig. 3a, Methods). The activity of many CN neurons was rapidly altered by ALM photoinhibition (185/389, $P < 0.01$, two-tailed t-test; latency, 10.7 ± 4.0 ms, mean ± s.e.m.), including that of neurons with selective persistent and ramping activity (Extended Data Fig. 5a). Photoinhibition of the ALM caused a greater proportion of CN neurons to increase in activity, resulting in a net disinhibition of the CN (Fig. 3b, 123/185 increase, 62/185 decrease, $P < 0.001$, binomial test). The selectivity of the CN for lick-left and lick-right trials was abolished by photoinhibition of the ALM (Fig. 3c, Extended Data Fig. 5b–d).

Photoinhibition of either side of the ALM reduced preparatory activity in the CN (Extended Data Fig. 6a–d), whereas photoinhibition of motor cortex regions posterior to the ALM had a lesser effect on CN preparatory activity (Extended Data Fig. 6e). Thus, the ALM seems to provide widespread input to the cerebellum to drive CN preparatory activity during motor planning.

We tested whether ALM preparatory activity depends on CN activity by recording from ALM while photoinhibiting the CN during the delay period (Fig. 3d, Methods). The activity of many ALM neurons was rapidly altered by CN photoinhibition (197/454, $P < 0.01$, two-tailed t-test, Extended Data Fig. 5e, latency, 7.1 ± 3.8 ms). However, the average spike rate was nearly unchanged (control, 4.15 spikes per second; photoinhibition, 4.39 spikes per second; $P = 0.58$, two-tailed t-test). The responses of individual ALM neurons increased (108/197) or decreased (89/197) during CN photoinhibition (Fig. 3e). ALM trial-type selectivity was abolished by CN photoinhibition (Fig. 3f), similar to observations after partial inactivation of the thalamus[17]. Thus, CN activity is necessary for maintaining cortical selectivity for planned movement, and preparatory activity is maintained in a cortico-cerebellar loop.

Preparatory activity requires reciprocal excitation between the ALM and the thalamus[17]. We mapped connectivity between the CN,

© 2018 Springer Nature Limited. All rights reserved.

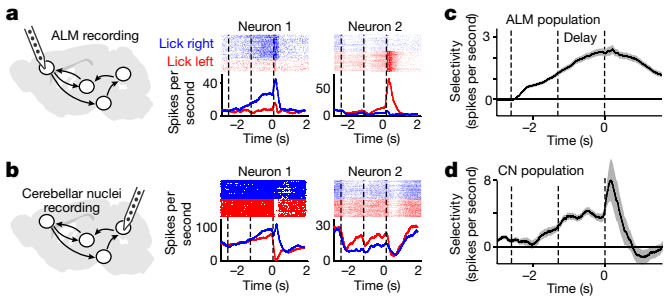

Fig. 2 | Preparatory activity in the ALM and the CN. **a**, Left, schematic of silicon-probe recording in the ALM. Middle and right, spike raster plots (top) and spike rate (bottom) for two example neurons. Correct lick-right (blue) and lick-left (red) trials only. Dashed lines mark behavioural periods. **b**, Same as **a**, but for the CN. **c**, ALM population selectivity (mean ± s.e.m. across neurons, bootstrap). Selectivity is the difference in spike rate between the preferred and the non-preferred trial type (Methods). Putative pyramidal neurons with significant selectivity, $n = 980$. Averaging window, 200 ms. **d**, Same as **c**, but for the CN. Neurons with significant selectivity, $n = 197$.

the thalamus and the ALM using retrograde and anterograde tracers in the ALM and the CN (Methods, Fig. 4a, Extended Data Figs. 7, 8). Fastigial projections mostly overlapped with parts of the thalamus that project to the ALM (that is, the ventral medial nucleus and parts of the ventral anterior-lateral nucleus, whereas dentate projections targeted an adjacent region that was more dorsal and lateral (that is, primarily the ventral anterior-lateral nucleus) (Fig. 4b, c).

We investigated the influence of the CN on the ALM thalamocortical loop during motor planning. We perturbed fastigial or dentate activity using ChR2 activation during the early delay period while monitoring ALM preparatory activity (Fig. 4d). Fastigial photoactivation induced rapid changes in ALM activity (latency, 4.5 ± 2.6 ms; Extended Data Fig. 9a), which is consistent with a disynaptic pathway through the thalamus. Selective persistent and ramping activity was abolished in most ALM neurons (Fig. 4e, top). In a minority of neurons, photoactivation created new preparatory activity (Fig. 4e, bottom). Transient photoactivation of the fastigial nucleus altered ALM

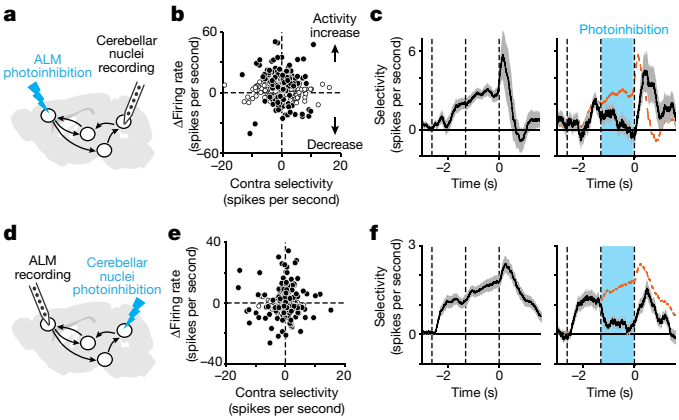

Fig. 3 | CN preparatory activity depends on ALM activity and vice versa. **a**, Schematic of CN recording during bilateral ALM photoinhibition. Laser power, 1.5 mW per location (Methods). **b**, Relationship between the delay period selectivity of individual CN neurons and changes in firing rate due to ALM photoinhibition ($n = 389$). Filled circles indicate neurons that are significantly modulated by ALM photoinhibition ($P < 0.01$, two-tailed t-test). **c**, CN population selectivity. Left, control; right, photoinhibition trials. Mean ± s.e.m. across neurons, bootstrap. Selective neurons tested for >3 trials in all conditions ($n = 157$). The orange line represents the mean from control trials. **d**, ALM recording during contralateral CN photoinhibition. Laser power, 1.5–4.5 mW. **e**, Same as **b**, but for ALM neurons ($n = 454$). **f**, Same as **c**, but for ALM neurons ($n = 329$).

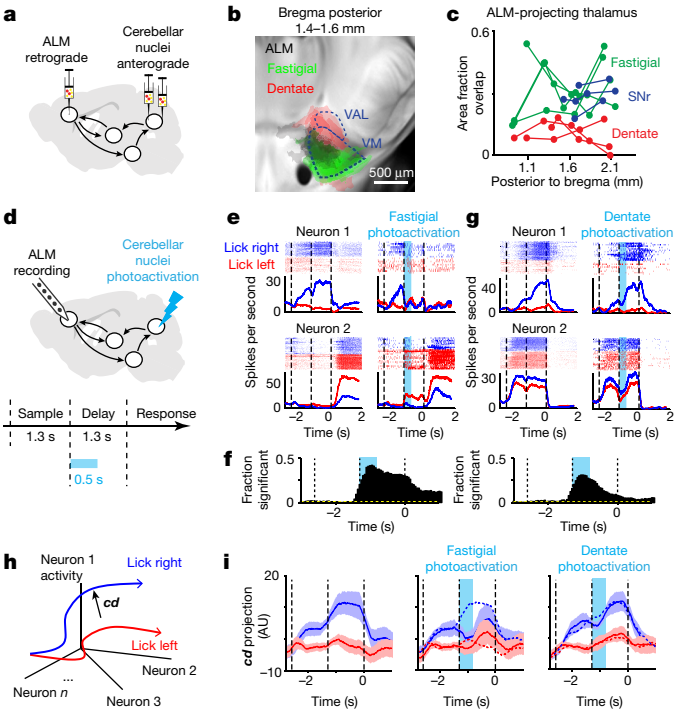

Fig. 4 | The fastigial nucleus is critical for ALM coding of future movement. **a**, Triple injections to map connectivity in the thalamus. **b**, Labelled areas in the thalamus from fastigial (green, $n = 6$), dentate (red, $n = 4$), and ALM (black, $n = 8$) injections. Brain sections were aligned to the Allen Reference Brain (Methods). The ventral medial nucleus (VM) and parts of the ventral anterior-lateral nucleus (VAL) borders are based on the Allen Reference Atlas. Labelling was also present in the medial dorsal thalamus but is not quantified here. **c**, Overlaps between ALM-projecting thalamus and projections from the fastigial nucleus, dentate nucleus or basal ganglia substantia nigra reticulata (SNr). The co-labelled area is normalized to the total thalamic area labelled by each projection (area fraction overlap). Dots represent individual coronal sections; lines represent individual injections. **d**, ALM recording during contralateral fastigial or dentate photoactivation. Laser power, 0.5–1.5 mW. **e**, Spike raster plots (top) and spike rates (bottom) of two example ALM neurons. **f**, Fraction of neurons with significant change in spike rate compared to control trials ($P < 0.01$, two-tailed t-test); $n = 446$. The cyan bar indicates the photoactivation period. **g**, Same as **e** and **f**, but for dentate photoactivation; $n = 466$. **h**, Schematic of movement-specific activity trajectories and coding direction (***cd***) in activity space. **i**, ALM activity in control and photoactivation trials projected onto the ***cd***. Both correct and error trials are included, grouped by instructed movement. Mean ± s.e.m. ($n = 28$ sessions, 10 mice). The ***cd*** was estimated using an independent subset of control trials (correct trials only).

preparatory activity long (more than 1 s) after cessation of the photostimulus (Fig. 4f, Extended Data Fig. 9b). Dentate photoactivation also induced changes in the ALM response (Fig. 4g; latency, 8.3 ± 5.0 ms). Notably, activity quickly recovered after dentate photoactivation (Fig. 4g).

Next, we differentiated between the effects of fastigial and dentate photoactivation on the preparatory activity of the ALM. We analysed population dynamics in 'activity space', where each dimension corresponds to the activity of one neuron[6,20,29]. We estimated a 'coding direction' (***cd***) in activity space, along which preparatory activity maximally discriminated upcoming licking directions (Fig. 4h, Methods). In control trials, activity trajectories from lick-left and lick-right trials diverged from each other along the ***cd*** during the sample period and remained separated throughout the delay period, providing a stable neural substrate for a short-term memory of future movement[20] (Fig. 4i). Fastigial photoactivation resulted in a collapse of activity trajectories. Additional experiments showed that fastigial photoactivation abolished the relationship between activity trajectories and

© 2018 Springer Nature Limited. All rights reserved.

specific future movements (Supplementary Information, Extended Data Fig. 10). By contrast, dentate photoactivation affected activity trajectories along the ***cd*** only minimally, despite having an effect on ALM neuron responses (Fig. 4i, Extended Data Fig. 9c). Therefore, fastigial photoactivation eradicated the coding of future movement, whereas dentate photoactivation did not.

Our results show that the cerebellum is critical for the coding of future movement in the frontal cortex. Considering its roles in the timing of movement[26], the cerebellum may provide an urgency drive that is necessary for the emergence of selectivity in the ALM thalamo-cortical loop[17] in the preparation of movement, which is consistent with attractor models of motor planning[30].

Online content

Any methods, additional references, Nature Research reporting summaries, source data, statements of data availability and associated accession codes are available at https://doi.org/10.1038/s41586-018-0633-x.

Received: 20 December 2017; Accepted: 15 August 2018;
Published online 17 October 2018.

1. Tanji, J. & Evarts, E. V. Anticipatory activity of motor cortex neurons in relation to direction of an intended movement. *J. Neurophysiol*. **39**, 1062–1068 (1976).
2. Funahashi, S., Bruce, C. J. & Goldman-Rakic, P. S. Mnemonic coding of visual space in the monkey's dorsolateral prefrontal cortex. *J. Neurophysiol*. **61**, 331–349 (1989).
3. Riehle, A. & Requin, J. Monkey primary motor and premotor cortex: single-cell activity related to prior information about direction and extent of an intended movement. *J. Neurophysiol*. **61**, 534–549 (1989).
4. Fried, I., Mukamel, R. & Kreiman, G. Internally generated preactivation of single neurons in human medial frontal cortex predicts volition. *Neuron* **69**, 548–562 (2011).
5. Murakami, M., Vicente, M. I., Costa, G. M. & Mainen, Z. F. Neural antecedents of self-initiated actions in secondary motor cortex. *Nat. Neurosci*. **17**, 1574–1582 (2014).
6. Svoboda, K. & Li, N. Neural mechanisms of movement planning: motor cortex and beyond. *Curr. Opin. Neurobiol*. **49**, 33–41 (2018).
7. Goldman-Rakic, P. S. Cellular basis of working memory. *Neuron* **14**, 477–485 (1995).
8. Wang, X. J. Synaptic reverberation underlying mnemonic persistent activity. *Trends Neurosci*. **24**, 455–463 (2001).
9. Wolpert, D. M., Miall, R. C. & Kawato, M. Internal models in the cerebellum. *Trends Cogn. Sci*. **2**, 338–347 (1998).
10. Proville, R. D. et al. Cerebellum involvement in cortical sensorimotor circuits for the control of voluntary movements. *Nat. Neurosci*. **17**, 1233–1239 (2014).
11. Heiney, S. A., Kim, J., Augustine, G. J. & Medina, J. F. Precise control of movement kinematics by optogenetic inhibition of Purkinje cell activity. *J. Neurosci*. **34**, 2321–2330 (2014).
12. Herzfeld, D. J., Kojima, Y., Soetedjo, R. & Shadmehr, R. Encoding of action by the Purkinje cells of the cerebellum. *Nature* **526**, 439–442 (2015).
13. Schmahmann, J. D. & Sherman, J. C. The cerebellar cognitive affective syndrome. *Brain* **121**, 561–579 (1998).
14. Ito, M. Control of mental activities by internal models in the cerebellum. *Nat. Rev. Neurosci*. **9**, 304–313 (2008).
15. Strick, P. L., Dum, R. P. & Fiez, J. A. Cerebellum and nonmotor function. *Annu. Rev. Neurosci*. **32**, 413–434 (2009).
16. Tsai, P. T. et al. Autistic-like behaviour and cerebellar dysfunction in Purkinje cell Tsc1 mutant mice. *Nature* **488**, 647–651 (2012).
17. Guo, Z. V. et al. Maintenance of persistent activity in a frontal thalamocortical loop. *Nature* **545**, 181–186 (2017).
18. Wagner, M. J., Kim, T. H., Savall, J., Schnitzer, M. J. & Luo, L. Cerebellar granule cells encode the expectation of reward. *Nature* **544**, 96–100 (2017).
19. Guo, Z. V. et al. Flow of cortical activity underlying a tactile decision in mice. *Neuron* **81**, 179–194 (2014).
20. Li, N., Daie, K., Svoboda, K. & Druckmann, S. Robust neuronal dynamics in premotor cortex during motor planning. *Nature* **532**, 459–464 (2016).
21. Chen, T. W., Li, N., Daie, K. & Svoboda, K. A map of anticipatory activity in mouse motor cortex. *Neuron* **94**, 866–879.e4 (2017).
22. Inagaki, H. K., Inagaki, M., Romani, S. & Svoboda, K. Low-dimensional and monotonic preparatory activity in mouse anterior lateral motor cortex. *J. Neurosci*. **38**, 4163–4185 (2018).
23. Li, N., Chen, T. W., Guo, Z. V., Gerfen, C. R. & Svoboda, K. A motor cortex circuit for motor planning and movement. *Nature* **519**, 51–56 (2015).
24. Economo, M. N. et al. Distinct descending motor cortex pathways and their roles in movement. *Preprint at* https://www.biorxiv.org/content/early/2017/12/05/229260 (2017).
25. McElvain, L. E. et al. Circuits in the rodent brainstem that control whisking in concert with other orofacial motor actions. *Neuroscience* **368**, 152–170 (2018).
26. Medina, J. F. & Mauk, M. D. Computer simulation of cerebellar information processing. *Nat. Neurosci*. **3**, 1205–1211 (2000).
27. Ohyama, T., Nores, W. L., Murphy, M. & Mauk, M. D. What the cerebellum computes. *Trends Neurosci*. **26**, 222–227 (2003).
28. Kalmbach, B. E., Ohyama, T., Kreider, J. C., Riusech, F. & Mauk, M. D. Interactions between prefrontal cortex and cerebellum revealed by trace eyelid conditioning. *Learn. Mem*. **16**, 86–95 (2009).
29. Shenoy, K. V., Sahani, M. & Churchland, M. M. Cortical control of arm movements: a dynamical systems perspective. *Annu. Rev. Neurosci*. **36**, 337–359 (2013).
30. Inagaki, H. K., Fontolan, L., Romani, S. & Svoboda, K. Discrete attractor dynamics underlying selective persistent activity in frontal cortex. *Preprint at* https://www.biorxiv.org/content/early/2017/10/16/203448 (2017).

Acknowledgements We thank R. Sillitoe for L7-cre mice; J. Medina, H. Inagaki, Z. Guo and M. Ahrens for comments on the manuscript; S. Druckmann for discussion; T. Pluntke and M. Inagaki for animal training; and J. White and H. Hasanbegovic for dystonia scoring. This work was funded by the Robert and Janice McNair Foundation (N.L.), the Whitehall Foundation (N.L.), the Alfred P. Sloan Foundation (N.L.), the Searle Scholars Program (N.L.), the National Institutes of Health NS104781 (N.L.), the Simons Collaboration on the Global Brain (K.S. and N.L.), the Dutch Organization for Medical Sciences (C.I.D.Z.), Life Sciences (Z.G. and C.I.D.Z.), an Erasmus MC fellowship (Z.G.), the ERC-advanced and ERC-PoC (C.I.D.Z.) and the Howard Hughes Medical Institute (K.S., M.E. and N.L.).

Reviewer information *Nature* thanks T. Ebner, M. Joshua and the other anonymous reviewer(s) for their contribution to the peer review of this work.

Author contributions N.L., K.S., C.I.D.Z. and Z.G. conceived the project. Z.G., N.L. and C.I.D.Z. performed pilot experiments. N.L., Z.G., C.D., A.M.T. and A.M.A. performed behavioural and recording experiments. Z.G. performed anatomy experiments. M.N.E. contributed brain alignment software. N.L., Z.G., K.S. and C.I.D.Z. analysed the data. N.L., Z.G., C.I.D.Z. and K.S. wrote the manuscript with input from all authors.

Competing interests The authors declare no competing interests.

Additional information
Extended data is available for this paper at https://doi.org/10.1038/s41586-018-0633-x.
Supplementary information is available for this paper at https://doi.org/10.1038/s41586-018-0633-x.
Reprints and permissions information is available at http://www.nature.com/reprints.
Correspondence and requests for materials should be addressed to N.L.
Publisher's note: Springer Nature remains neutral with regard to jurisdictional claims in published maps and institutional affiliations.

© 2018 Springer Nature Limited. All rights reserved.

METHODS

Mice. This study is based on data from 70 mice (age >P60 where P is postnatal day; both male and female mice, Supplementary Table 1). Thirteen C57B1/6 mice were used for CN ChR2 photoactivation experiments. A subset of these (10 mice) was used for ALM recordings during photoactivation of the CN. Another subset (2 mice) and six additional C57B1/6 mice were used for CN lesion experiments (8 mice). Seven L7-cre[31] crossed to Ai32 (Rosa26-LSL-ChR2-eYFP, JAX Stock 012569)[32] mice were used for CN photoinhibition experiments in the delayed response task. A subset of these mice (4 mice) was used for ALM recordings during CN photoinhibition. Two additional L7-cre × Ai32 mice were used to characterize CN photoinhibition using electrophysiology. Six additional L7-cre × Ai32 mice (not listed in Supplementary Table 1) were used to quantify the general effects of CN photoinhibition on movements. Ten C57B1/6 mice were used for CN recording experiments. Eight VGAT-ChR2-eYFP mice (Jackson Laboratory, JAX Stock 014548)[33] were used for CN recordings during ALM photoinhibition. Four VGAT-ChR2-eYFP mice were used for behavioural experiments in which both ALM and CN activity were manipulated to test the causal role of ALM activity in behaviour following a fastigial perturbation. Twelve C57B1/6 mice (not listed in Supplementary Table 1) were used for anatomical tracing.

All procedures were performed in accordance with protocols approved by the Institutional Animal Care and Use Committees at Baylor College of Medicine, Janelia Research Campus and the Erasmus Medical Center. Mice were housed in a 12:12 reverse light:dark cycle and tested during the dark phase. On days when they were not tested, mice received 0.5–1 ml of water. On other days, mice were tested in experimental sessions lasting 1–2 h, during which they received all their water (0.3 to 2 ml). If mice did not maintain a stable body weight, they received supplementary water[34]. All surgical procedures were carried out aseptically under 1–2% isoflurane anaesthesia. Buprenorphine HCl (0.1 mg kg^{-1}) or sustained release meloxicam (4 mg kg^{-1}) was used for pre- and post-operative analgesia. Ketoprofen (5 mg kg^{-1}) was used at the time of surgery and post-operatively to reduce inflammation. After the surgery, mice were allowed to recover for at least three days with free access to water before water restriction.

Surgery. Mice were prepared for photostimulation and electrophysiology with a clear-skull cap[19] and a headpost[34]. The scalp and periosteum over the dorsal surface of the skull were removed. A layer of cyanoacrylate adhesive (Krazy Glue, Elmer's Products) was directly applied to the intact skull. A custom-made headpost was placed on the skull (approximately over the visual cortex) and cemented in place with clear dental acrylic (Lang Dental Jet Repair Acrylic; 1223-clear). A thin layer of clear dental acrylic was applied over the cyanoacrylate adhesive covering the entire exposed skull, followed by a thin layer of clear nail polish (Electron Microscopy Sciences, 72180).

In wild-type mice prepared for CN ChR2 photoactivation experiments, 150 nl of AAV2-hSyn1-(h134R)ChR2-eYFP virus (UNC viral core, titre 5.7×10^{12} viral genomes (vg) per ml) was injected in the fastigial nucleus (posterior 2.7 mm from lambda, lateral 0.5 mm, depth 2.3 mm) or dentate nucleus (posterior 2.5 mm lambda, lateral 2.7 mm, depth 2.3 mm), followed by implantation of a 2-mm long optical fibre (Thorlabs, CFML12L02) over the injection site. In VGAT-ChR2-eYFP mice prepared for fastigial perturbation experiments, an optical fibre was implanted at the same stereotaxic coordinate to target the fastigial nucleus.

Behaviour. The behavioural task and training have been described previously[19,34]. The stimulus was a metal pin (0.9 mm in diameter), presented at one of two possible positions (Fig. 1a). The two pole positions were 5 mm apart along the anterior–posterior axis and were constant across sessions. The posterior pole position was 5 mm from the whisker pad. A two-spout lickport (4.5 mm between spouts) was used to deliver water rewards and record response licks. Behavioural data were acquired using commercial hardware and software (Bpod, Sanworks).

At the beginning of each trial, the vertical pole was moved to within reach of the whiskers (0.2 s travel time) where it remained for 1 s, after which it was retracted (retraction time 0.2 s). The sample period was defined as the time between the pole movement onset to 0.1 s after the pole retraction onset (duration 1.3 s, Fig. 1a). Mice touched the object at both pole positions, typically with a different set of whiskers. The delay period (duration 1.3 s) followed the sample period. An auditory 'go' cue indicated the end of the delay period (pure tone, 3.4 kHz, 0.1 s duration). Licking early during the trial was punished by a loud alarm sound (siren buzzer, 0.05 s duration), followed by a brief timeout (1–1.2 s). Licking the correct lickport after the 'go' cue led to a liquid reward (2–3 μl). Licking the incorrect lickport triggered a timeout (2–6 s). Trials in which mice did not lick within a 1.5-s window after the 'go' cue ('no lick') were rare and typically occurred at the end of a session. The recorded reaction time was from the onset of the 'go' cue to the first contact with the lickport.

CN lesion. In eight wild-type mice, we performed localized lesions in the CN. Intense 473-nm light (>10 mW) was delivered to either the fastigial or dentate nucleus through the implanted optical fibre for 5–10 min while the mice were under 2% isoflurane anaesthesia. Light-induced heating produced a localized lesion around the fibre tip. The lesion areas were estimated post hoc, by measuring the size of areas in which neuron labelling was absent (anti-NeuN staining, Millipore ABN78, 1:1,000; Fig. 1c, Extended Data Fig. 1a). Lesion sizes were between 602–878 μm, close to the diameters of the fastigial nucleus or the dentate nucleus. The mice were tested on subsequent days. See Supplementary Table 1 for the list of mice and lesioned hemispheres.

CN ChR2 photoactivation. For ChR2 photoactivation of the CN, 13 wild-type mice injected with AAV2-hSyn1-ChR2(H134R)-eYFP virus were used. Light was delivered to the CN through an optical fibre. In six mice, both the fastigial nucleus and the dentate nucleus on opposite hemispheres were tested: left fastigial/right dentate nucleus was tested in three mice and right fastigial/left dentate nucleus was tested in the other three mice. In those mice, the fastigial and the dentate nucleus were tested on separate days. In another three mice, only the right fastigial nucleus was tested. In another four mice, only the right dentate nucleus was tested. In one of the fastigial-stimulation mice, the injection of ChR2 virus missed the CN and its data were excluded. See Supplementary Table 1 for the list of mice and manipulated hemispheres in individual experiments.

Light from a 473-nm laser (Laser Quantum, Gem 473) was controlled by an acousto-optical modulator (Quanta Tech) and a shutter (Vincent Associates). To prevent the mice from distinguishing photostimulation trials from control trials using visual cues, a 'masking flash' was delivered using 470 nm LEDs (Luxeon Star) near to the eyes of the mice. The masking flash began as the pole started to move and continued through the end of the period in which photostimulation could occur. Photostimulation was deployed on 25% of the behavioural trials. During ALM recordings, photostimulation was deployed on 33% of the trials. The photostimulus was pulses of light (5-ms pulse duration) delivered at 20 Hz and a range of peak powers (5, 10 and 15 mW). The power values reported in the paper indicate average powers (0.5, 1 and 1.5 mW). The powers were measured at the fibre tip. The photostimulus started at the beginning of a task period and continued for either 0.455 s (10 pulses) or 1.255 s (26 pulses).

We performed photostimulation both during the early parts of the sample and delay period (0.455 s; Fig. 1g, h) and throughout the entire period (1.255 s; Extended Data Fig. 1e). Our primary experiments were centred around sub-period manipulations (early sample and early delay). This experimental design was chosen for two reasons. First, sub-period manipulations sought to better resolve specific involvements of the CN in time. Manipulations during the entire sample period (1.3 s) may affect the beginning of the motor planning process, and manipulations during the entire delay period up to the 'go' cue may interfere with movement initiation[20]. Second, we sought to use the early delay period manipulation to examine any persistent effect on preparatory activity (Fig. 4). If a brain region is involved in maintaining preparatory activity, transiently disrupting it during the early delay should subsequently disrupt preparatory activity. We later tested manipulations that spanned the entire behavioural periods and included the response period to examine the involvement of the CN in movement initiation and execution (Fig. 1h, i, Extended Data Fig. 1e).

CN photoinhibition. In L7-cre × Ai32 mice, ChR2 was expressed in cerebellar Purkinje cells. We photostimulated Purkinje cells to inhibit neurons in the CN (Fig. 1j). To characterize the effect of CN photoinhibition (Extended Data Fig. 2) we performed silicon-probe recordings in the fastigial nucleus (details described in 'Electrophysiology'). Photostimulation of Purkinje cells was carried out by directing a blue laser (beam diameter 400 μm at 4σ) to the brain surface through a cranial window. The photostimulus was a 40 Hz sinusoid (average power, 4.5 mW) lasting for 1.3 s, including a 100–200 ms linear ramp during the laser offset to reduce rebound neuronal activity. Photostimulation was deployed on 25% of the behavioural trials. During ALM recordings, photostimulation was deployed on 33% of the trials. A masking flash was delivered on all trials. Photostimulation was performed at two different locations: 3 mm posterior and 2 mm lateral from lambda (the cerebellar cortex); and 1 mm posterior and 2 mm lateral to lambda (the inferior colliculus). Photostimulation of the cerebellar cortex silenced fastigial activity whereas photostimulation of the inferior colliculus did not (Extended Data Fig. 2).

For photoinhibition of the CN during behaviour trials, we tested 7 L7-cre × Ai32 mice. Photostimulation of Purkinje cells was carried out by directing the blue laser to the brain surface through a cranial window. We manipulated the left hemisphere in three mice and the right hemisphere in the other four mice. The photostimulus (average power 0.5, 1.5 or 4.5 mW) started at the beginning of a task period and continued for either 0.5 or 1.3 s, including the 100–200 ms linear ramp.

We performed CN photoinhibition both during parts of the behavioural trial period (0.5 s; Fig. 1k) and over the entire period (1.3 s; Extended Data Fig. 2g), for the same reasons described in 'CN ChR2 photoactivation'. In addition to early sample and early delay photoinhibitions, we also included late sample and late delay photoinhibitions to resolve CN involvements during specific sub-periods of the delayed response task (Extended Data Fig. 2h). Seven mice were initially tested for sub-period photoinhibitions. Later, three of the seven mice were tested

© 2018 Springer Nature Limited. All rights reserved.

with photoinhibition over the entire behaviour periods to confirm the directional bias induced by response period photoinhibition (Extended Data Fig. 2g, Supplementary Table 1).

In four L7-cre × Ai32 mice (Supplementary Table 1), we recorded from the ALM during contralateral CN photoinhibition. Photoinhibition (average power, 1.5 or 4.5 mW) started at the beginning of the delay period and continued for 1.3 s, including the 100–200 ms linear ramp.

CN photoinhibition and effects on movement. In six naive L7-cre × Ai32 mice, we examined the general effects of CN photoinhibition on movements. One optical fibre was implanted in the fastigial nucleus and another fibre was implanted in the dentate nucleus in the opposite hemisphere to photostimulate Purkinje cell axons in the CN. We tested a range of laser powers (average power, 1.5, 5, 10 and 20 mW), including the photostimulus intensities used to photoinhibit CN activity in the delayed response task (1.5 mW). The photostimulus was pulses of light (5–10 ms pulse duration, 20–40 Hz, 15–50 mW peak powers). Videos (Point Grey, CM3-US-13Y3M-CS or Basler, acA640-300gm) were recorded while mice underwent photoinhibition either in the head-fixed configuration or unrestrained. In head-fixed mice ($n = 6$), jaw movement and eyeblink were tracked using custom software. In unrestrained mice ($n = 2$), the effect of photoinhibition on movements and postures were manually scored on a scale of 0 to 4 that rated dystonia-like movements[35]: 0, no motor abnormalities; 1, slightly slowed or abnormal motor behaviour, no dystonia; 2, mild impairment, mild and transient dystonic postures, weak tremor; 3, moderate impairment, dystonic postures, cannot balance the body, major tremor; 4, severe impairment, sustained dystonic postures and limited movements. Two individuals scored the videos independently and the scores were averaged. The scoring was blinded to the experimental conditions.

In head-fixed mice, high-intensity photoinhibition (20 mW) of the dentate nucleus produced jaw movements (Extended Data Fig. 2f). No tongue protrusion was observed in all photoinhibition conditions. No consistent eyeblink was evoked. At the photoinhibition intensities used in the delayed response task (1.5–5 mW), no movement was consistently evoked.

In unrestrained mice, high-intensity photoinhibition (20 mW) of both the fastigial nucleus and the dentate nucleus produced dystonia-like movements and posture changes. This included loss of balance and extension of the contralateral limbs (Extended Data Fig. 2e). However, at the photoinhibition intensities used in the delayed response task (1.5–5 mW), no consistent movement was detected (Extended Data Fig. 2e).

ALM photoinhibition. The ALM is centred on bregma anterior 2.5 mm, lateral 1.5 mm[19–21]. For photoinhibition of the ALM, we photostimulated cortical GABAergic (γ-aminobutyric acid) neurons in VGAT-ChR2-eYFP mice (8 mice). Photostimulation was performed through the clear-skull cap implant by directing the blue laser over the skull (beam diameter, 400 μm at 4σ, bregma anterior 2.5 mm, lateral 1.5 mm). The light transmission through the intact skull was 50%[19]. Photoinhibition was deployed on 25% of the behavioural trials. During CN recordings, photoinhibition was deployed on 33% of the trials. A masking flash was delivered on all trials.

We photoinhibited ALM for 1.3 s at the beginning of the delay period, including a 100 ms linear ramp at the laser offset to minimize rebound excitation. This photostimulus was empirically determined to produce robust photoinhibition in ALM[19,20]. The photoinhibition silenced 90% of spikes in a cortical area of 1-mm radius (at half-maximum) through all cortical layers. For unilateral ALM photoinhibition (Extended Data Figs. 6, 10), we used a 40 Hz sinusoidal photostimulus (1.5 mW average power at the skull surface) at 2.5 mm anterior and 1.5 mm lateral from bregma. For bilateral ALM photoinhibition (Fig. 3, Extended Data Figs. 5, 6, 10), we used a constant photostimulus and a scanning galvo (GVSM002, Thorlabs), which stepped the laser beam sequentially through the photoinhibition sites at the rate of 1 step per 5 ms (step time, 0.2 ms; dwell time, 4.8 ms; measured using a photodiode). Eight photoinhibition sites covered the ALM on both hemispheres. On each hemisphere, four photoinhibition sites were spaced in 1 mm spacing, at anterior 2–3 mm and lateral 1–2 mm from bregma. Peak power was adjusted based on the number of photoinhibition sites to achieve an average power of 1.5 mW per site.

ALM photoinhibition after a fastigial perturbation. To test the causal role of ALM activity in driving directional licking after a fastigial perturbation, we tested four VGAT-ChR2-eYFP mice (Extended Data Fig. 10). We confirmed that ChR2 was expressed in Purkinje cells as well as other GABAergic neurons in the cerebellum[33]. Photostimulation (40 Hz sinusoid; average power, 1.5 mW) was delivered to the fastigial nucleus through an optical fibre to perturb CN activity. Photostimulation was started at the onset of the delay period and always lasted for 500 ms. We targeted the left fastigial nucleus in three mice and the right fastigial nucleus in one mouse. See Supplementary Table 1 for the list of mice and manipulated hemispheres. CN perturbations in VGAT-ChR2-eYFP mice might be different from CN photoactivation using the ChR2 virus and photoinhibition in L7-cre × Ai32 mice. We thus first confirmed that in VGAT-ChR2-eYFP mice, fastigial perturbations during the early delay period reduced behavioural performance for both trial types (control: 'contra lick' trials, 74.5% correct, 'ipsi lick' trials, 67.8%; photostimulation: 58.5% and 57.0%; $P < 0.05$ for both trial types, bootstrap), similar to other CN optogenetic manipulations during the early delay period (compare with Fig. 1h, k).

Photoinhibition of ALM was performed as described above. For unilateral ALM photoinhibition, photostimulation was started 800 ms after the onset of the delay period and ended at the onset of the 'go' cue (500 ms in duration). Unilateral ALM photoinhibition before the 'go' cue was previously found to bias the upcoming licking to the ipsilateral direction[20]. We confirmed the ipsilateral bias here (Extended Data Fig. 6b, 10e). In three VGAT-ChR2-eYFP mice, we also tested bilateral ALM photoinhibition. Bilateral photostimulation started at the onset of the 'go' cue and lasted for 1.3 s. On randomly interleaved trials, we either perturbed the fastigial nucleus, or photoinhibited ALM (unilateral or bilateral), or perturbed the fastigial nucleus followed by ALM photoinhibition (Extended Data Fig. 10f, g). Photostimulation was deployed on 25% of the behavioural trials. A masking flash was delivered on all trials.

Behavioural data analysis. Performance was computed as the fraction of correct choices, excluding lick early trials and no lick trials (Fig. 1g, Extended Data Figs. 1e, 2g, 10b). Chance performance was 50%. We also separately computed the performance for lick-right and lick-left trials (Fig. 1, Extended Data Figs. 1, 2, 6, 10). The significance of the change in performance in each photostimulation condition was determined using bootstrap to account for variability across mice, sessions and trials. We tested against the null hypothesis that the change in performance caused by photostimulation was due to normal behavioural variability. In each round of bootstrap, we replaced the original behavioural dataset with a resampled dataset in which we resampled with replacement from: (1) mice, (2) sessions performed by each mouse, (3) the trials within each session. We then computed the performance change on the resampled dataset. Repeating this procedure 10,000 times produced a distribution of performance changes that reflected the behavioural variability. The P value of the observed change in performance was computed as the fraction of times the bootstrap produced an inconsistent change in performance (for example, if a performance decrease was observed during photostimulation, the P value was the fraction of times a performance increase was observed during bootstrap, one-tailed test).

Electrophysiology. Extracellular spikes were recorded using 32-channel NeuroNexus silicon probes (A4x8-5mm-100-200-177) or 64-channel Cambridge NeuroTech silicon probes (H2 acute probe, 25 μm spacing, 2 shanks). The 32-channel voltage signals were multiplexed, digitized by a PCI6133 board at 400 kHz (National Instruments) at 14 bit, demultiplexed (sampling at 25,000 Hz) and stored for offline analysis. The 64-channel voltage signals were amplified and digitized on an Intan RHD2164 64-Channel Amplifier Board (Intan Technology) at 16 bit, recorded on an Intan RHD2000-Series Amplifier Evaluation System (sampling at 20,000 Hz) using Open-Source RHD2000 Interface Software from Intan Technology (version 1.5.2), and stored for offline analysis.

For ALM recordings, a small craniotomy (diameter, <1 mm) was made one day before the recording session (2.5 mm anterior, 1.5 mm lateral from bregma)[19]. A silicon probe was acutely inserted 0.9–1.11 mm below the brain surface before the start of each recording session. To minimize brain movement, a drop of silicone gel (3-4680, Dow Corning) was applied over the craniotomy after the electrode was in the tissue. The tissue was allowed to settle for several minutes before the recording started. Two to six recordings were made from each craniotomy. In ten mice, recordings were from the left ALM. In two mice, recordings were from the right ALM. ALM recordings were always contralateral to the side of CN manipulations (Supplementary Table 1).

For CN recordings, two craniotomies (diameter, 1.5 mm) were made successively over the left cerebellum to target the CN (first at 2.5 mm posterior, 1.5mm lateral from lambda; then at 2 mm posterior, 3 mm lateral from lambda). After a craniotomy was opened, recordings were made at different locations within the craniotomy over the next 5–7 days. A silicon probe was acutely inserted 2.1–2.4 mm below the brain surface before the start of each session. On the last recording session, the silicon probe was painted with DiI to label the recording track. All the recording locations within a craniotomy were reconstructed post-hoc relative to the labelled track (Extended Data Fig. 3). Reconstructions were based on the insertion locations on the brain surface. Recording depths were inferred from manipulator readings and verified on the basis of histology. The second craniotomy was opened after the first craniotomy had been sampled.

Electrophysiology data analysis. The extracellular recording traces were band-pass-filtered (300–6 kHz). Events that exceeded an amplitude threshold (four standard deviations of the background) were subjected to manual spike sorting to extract single units[19].

For ALM recordings during behaviour trials (Fig. 2), 1,309 single-units were recorded in 10 mice across 39 sessions. Spike widths were computed as the trough-to-peak interval in the mean spike waveform. Units with a spike width <0.35 ms were defined as fast-spiking neurons (82/1,309) and units with spike widths

© 2018 Springer Nature Limited. All rights reserved.

>0.45 ms as putative pyramidal neurons (1,194/1,309). Units with intermediate values (0.35–0.45 ms, 33/1,309) were excluded from the analyses. This classification was previously verified by optogenetic tagging of GABAergic neurons[19]. We concentrated our analyses on the putative pyramidal neurons ($n = 1{,}194$). Nine of the ten mice were tested with CN ChR2 photoactivation during ALM recordings (Fig. 4, Extended Data Fig. 10; $n = 912$ putative pyramidal neurons). One mouse was excluded because the injection of ChR2 virus missed the CN. For ALM recordings during CN photoinhibition (Fig. 3, Extended Data Fig. 5), 490 single-units were recorded in 4 mice across 19 sessions. In total, 454/490 units were putative pyramidal neurons.

For CN recordings during behaviour trials, 878 single-units were recorded in 18 mice across 169 sessions (Fig. 2). CN single units were not classified on the basis of spike shapes. We estimated unit locations on the basis of recording track labelling, recording depth and the lamination of activity patterns across the recording shanks (Extended Data Fig. 3). CN boundaries were visible in DAPI staining (Extended Data Fig. 3). 314 units were from outside of the CN (mostly from the cerebellar cortex). 268 units were from the fastigial nucleus, 139 units were from the interposed nucleus and 157 units were from the dentate nucleus. Eight of the 18 mice were tested with ALM photoinhibition during CN recordings (Fig. 3, Extended Data Figs. 5, 6; $n = 389$).

To characterize CN photoinhibition in L7-cre × Ai32 mice, 60 single units were recorded in 2 mice across 11 recording sessions (Fig. 1j, Extended Data Fig. 2). The recordings were targeted to the left fastigial nucleus. Thirty-four units were from outside of CN (mostly from the cerebellar cortex). Twenty-six units were from the fastigial nucleus. The mice were awake but non-behaving during the recordings.

Neurons were tested for significant trial-type selectivity during the sample, delay or response periods, using the spike counts from the lick-left and lick-right trials (two-tailed t-test, $P < 0.05$). Neurons that significantly differentiated trial types during any one of the periods were deemed 'selective'. To compute selectivity in Figs. 2, 3 and Extended Data Figs. 4, 5, 6, we first determined the preferred trial type of each neuron using spike counts from a subset of the trials (10 trials for ALM, 20 for CN); selectivity was calculated as the difference in spike rate between lick-left and lick-right trials in the remaining data. Selecting the preferred trial type using either sample, delay or response period data yielded qualitatively similar preparatory activity.

To quantify the effect of photostimulation on individual neuron spike rates (Figs. 3, 4, Extended Data Figs. 5, 9), spike counts from lick-left and lick-right trials were pooled. We used two-tailed t-tests on spike counts binned in various windows (for example, Fig. 3 and Extended Data Fig. 5, the whole delay period; Fig. 4f, 400-ms time bins in steps of 50 ms) to test for a significant change in spike rate between control and photostimulation trials.

Quantification of the effect of photostimulation on selectivity was complicated by the fact that selectivity was coupled to upcoming movements (Extended Data Fig. 4e). For example, using only correct trials to compute selectivity would miss the trials in which photostimulation caused the mice to switch future movements, thus underestimating the effect of photostimulation on selectivity. We therefore used all trials (correct and incorrect, grouped by instructed trial types) when quantifying selectivity changes caused by photostimulation (Fig. 3c, f, Extended Data Figs. 5, 6, 9).

Analysis of ALM population dynamics in the activity space. To analyse the relationship between ALM population activity and upcoming movements, we restricted the analysis to the recording sessions with >5 neurons recorded simultaneously for >5 trials per condition (28/39 sessions, 8–46 neurons recorded simultaneously; Fig. 4, Extended Data Fig. 10). For a population of n neurons, we found an $n \times 1$ vector in the n dimensional activity space that maximally separated the response vectors in lick-right and lick-left trials; we term this vector the coding direction ($\boldsymbol{cd}$).

Average spike counts were computed in 400-ms windows in 10-ms steps. For each movement direction (lick right and lick left) we computed the average spike counts $\bar{\boldsymbol{x}}_{lick\ right}$ and $\bar{\boldsymbol{x}}_{lick\ left}$, $n \times 1$ response vectors that described the population response at each time point, t. We computed the difference in the mean response vectors, $\boldsymbol{cd}_t = \bar{\boldsymbol{x}}_{lick\ right} - \bar{\boldsymbol{x}}_{lick\ left}$. $\boldsymbol{cd}_t$ was stable throughout the delay period. We averaged the values of $\boldsymbol{cd}_t$ from the delay period to obtain a single $\boldsymbol{cd}$. Only correct control trials were used to estimate the $\boldsymbol{cd}$. The projection along the $\boldsymbol{cd}$ captured $64.1 \pm 3.4\%$ of the population selectivity for lick-left and lick-right trials over the sample and delay periods (root mean square, r.m.s., of the difference in spike rate between lick-right and lick-left trials), and $27.0 \pm 4.2\%$ of the total variance in ALM task-related activity. Activity variance was quantified as the r.m.s. of the baseline-subtracted activity over the sample and delay periods.

To visualize the effect of CN photoactivation on ALM activity trajectories, we projected the activity trajectories from the control trials, fastigial photoactivation trials or dentate photoactivation trials on the $\boldsymbol{cd}$. We used independent control and photoactivation trials from the trials used to compute the $\boldsymbol{cd}$. For each trial we computed the spike counts for each neuron, $\boldsymbol{x}$ ($n \times 1$ response vector), at each time point. The projected trajectories in Fig. 4i were obtained as $\boldsymbol{cd}^T\boldsymbol{x}$. Both correct and incorrect trials were used to compute the projected trajectories, grouped by the instructed trial types. To average trajectories across multiple behavioural sessions, we first offset the trajectories for a particular session by subtracting the mean $\boldsymbol{cd}^T\boldsymbol{x}$ across all trials and time points in that session. This removed fluctuations in mean activity from session to session. The offsets were computed using the independent control trials that were used to calculate the $\boldsymbol{cd}$. Standard errors of the mean were obtained by bootstrapping individual sessions.

To predict upcoming movements using ALM responses projected onto the $\boldsymbol{cd}$ (Extended Data Fig. 10c, d) we used the response vector $\boldsymbol{x}$ from the last time bin before the 'go' cue (last 400 ms of the delay period). For each session, we computed the projected responses, $\boldsymbol{cd}^T\boldsymbol{x}$, from lick-right and lick-left trials. The $\boldsymbol{cd}$ was computed using independent control trials (correct trials only). Separate photostimulation trials were used to predict performance (both correct and incorrect trials). The probability of the mouse licking right in photostimulation trials was calculated as a function of projected responses, $\boldsymbol{cd}^T\boldsymbol{x}$ (Extended Data Fig. 10c, d). Data from multiple sessions were pooled.

Anatomy tracing. We mapped connectivity between the CN, thalamus, ALM, substantia nigra reticulata (SNr) and the lateral superior colliculus. The lateral superior colliculus was previously implicated to have roles in controlling licking[36] (Fig. 4a–c, Extended Data Figs. 7, 8). Mice were anaesthetized using isofluorane and fixated on a high precision stereotaxic frame (David Kopf or Stoelting). Coordinates used to target brain areas of interest used either bregma or lambda as the reference points. The coordinates were (in mm): ALM: bregma anterior 2.5, lateral 1.5, depth 0.8; SNr: lambda anterior 1.1, lateral 1.4, depth 4.5; superior colliculus: lambda anterior 0, lateral 1.3, depth 1.8; fastigial nucleus: lambda posterior 2.7, lateral 0.7, depth 2.3; dentate nucleus: lambda posterior 2.5, lateral 2.5, depth 2.4. To label the ALM-projecting thalamus, 10% biotin dextran amine BDA-10k (Sigma), or 1% Cholera toxin subunit b (Ctb) conjugated to Alexa647 (Invitrogen) dissolved in PBS were iontophoretically injected. Glass pipettes with a tip size of 20 μm were filled with either BDA or Ctb and 4 mA of positive current was applied with a 7-s duty cycle for 15 min. Viral vector-assisted tracing was applied to the other brain regions. AAV2-CAG-eGFP or AAV2-CAG-tRFP (100–150 nl; UNC viral core, titres 1.0–1.2 $\times 10^{13}$ vg ml^{-1}) were pressure-injected in the target areas. After each injection, the pipette was left in place for >10 min before being slowly withdrawn. Brains were processed for immunohistochemistry 10 days after the injection. Mice were deeply anaesthetized with an overdose of Nembutal (0.2 ml, i.p.) and transcardially perfused with 20 ml saline followed by 50 ml 4% paraformaldehyde (PFA) in PBS. Brains were extracted and post-fixed in 4% PFA for 2 h and incubated in 10% sucrose overnight at 4 °C. Brains were then embedded in gelatine and cryoprotected in 30% sucrose in PB, frozen on dry ice, and sectioned using a freezing microtome (50 μm thick). For immunohistochemistry, sections were blocked for 1 h at room temperature in PBS with 0.4% Triton X-100 and 10% N-hydroxysuccinimide (NHS) solution and incubated for 48 h at 4 °C in a mixture of primary antibodies diluted in PBS with 2% NHS and 0.4% Triton X-100. Sections were then washed and incubated for 2 h at room temperature in the fluorescent secondary antibodies. Axonal projections and neurons were visualized using: mouse anti-NeuN (1:1,000, Millipore), chicken anti-GFP (1:2,000, Aves), rabbit anti-RFP (1:2,000, Rockland), mouse anti-vGlut2 (1:1,000, Millipore) and streptavidin-Alexa647 (1:400, Jackson). Slices were counterstained with DAPI (1:100,000, Invitrogen) and mounted with mounting medium for fluorescence (Mowiol, Sigma). Stacks of images were acquired on an upright LSM 700 confocal microscope (Carl Zeiss) operated with Zeiss Zen Software (v.2.2) and post-hoc adjusted and processed in FIJI software (v.1.46) with appropriate plugins (https://imagej.net/Fiji).

Anatomy analysis. We aligned each coronal section to the Allen Mouse Common Coordinate Framework (CCF)[37,38] using landmark-based image registration. The registration target was the 10 μm per voxel CCF anatomical template. To align a coronal section, we first manually selected the coronal plane in the anatomical template that best corresponded to the section. Next, we manually placed control points at corresponding local landmarks in each image (Extended Data Fig. 7a). Thirty to fifty control points were placed in a single image. All control points were outside of the thalamus. Next, the image was warped to the CCF using an affine transformation followed by a non-rigid transformation using b-splines[39]. Images were warped using the B-spline Grid, Image and Point based Registration package available on the Matlab FileExchange (https://www.mathworks.com/matlabcentral/fileexchange/20057-b-spline-grid–image-and-point-based-registration). We performed this procedure independently for each brain section. Two to six sections at the rostro-caudal level of the thalamus were analysed (bregma posterior 1.1–2.1 mm in the CCF).

We quantified the connectivity of the fastigial nucleus, the dentate nucleus, the SNr and the superior colliculus with the ALM thalamo-cortical loop on the basis of the overlaps in the anterograde fluorescence from a source area with ALM-projecting thalamus. In each case, quantifications of the anterograde fluorescence from a source area were always made in brains that contained co-injections of

© 2018 Springer Nature Limited. All rights reserved.

tracers in the ALM to label ALM-projecting thalamus. Injections of retrograde (Ctb) and anterograde (BDA) tracers in the ALM produced similar patterns of labelling in the thalamus[17] (Extended Data Fig. 8). We therefore used both types of tracers to label ALM-projecting thalamus. Quantifications of fluorescence were performed on images after alignment to the CCF anatomical template (Extended Data Fig. 7b). We found consistent labelling patterns in the thalamus across different injection cases (Extended Data Fig. 7c). Alignment to the CCF enabled us to combine quantifications of fluorescence overlaps across different injection cases (Fig. 4a–c, Extended Data Fig. 7d–f).

To quantify fluorescence overlaps with ALM-projecting thalamus, we first limited the analysis to a subregion of the coronal section that contained the thalamus ipsilateral to the ALM injection (shown in Extended Data Fig. 7b at different rostrocaudal levels). We then thresholded the fluorescence intensities independently for each channel at approximately the 89th percentile (85th–94th across different cases). The labelled area was defined as all the pixels that exceeded this threshold (Extended Data Fig. 7e). Finally, the overlap in fluorescence was computed as the number of pixels co-labelled by ALM injections and a projection (for example, the fastigial nucleus) divided by the total number of pixels labelled by that projection ('area fraction' overlap, Extended Data Fig. 7f). This procedure was carried out separately for each coronal section, which constituted one data point in Fig. 4c and Extended Data Figs. 7e, f, 8b.

Because we always performed triple injections (a retrograde or anterograde tracer in ALM, and anterograde tracers in two source areas—that is, the fastigial and dentate nucleus, or the fastigial nucleus and SNr, or the fastigial nucleus and superior colliculus, or other combinations), quantifications of fluorescence overlaps were further validated by visualizing all three channels in individual injection cases (Extended Data Fig. 8).

Statistics. The sample sizes are similar to sample sizes used in the field: for behaviour, three mice or more per condition; for electrophysiology, more than 100 units per brain region. No statistical methods were used to determine sample size. In one of the fastigial photoactivation mice, the injection of ChR2 virus missed the CN and its data were excluded. All key results were replicated in multiple mice. Mice were randomly preallocated into experimental groups. Unless stated otherwise, the investigators were not blinded to allocation during experiments and outcome assessment. Trial types were randomly determined by a computer program. During spike sorting, experimenters cannot tell the trial type, so were blind to the conditions. Statistical comparisons using *t*-tests and bootstrap are described in detail in the previous sections.

Code availability. Software used for data analysis is available from the corresponding author upon reasonable request.

Data availability

Raw and processed data are available from the corresponding author upon reasonable request.

31. Lewis, P. M., Gritli-Linde, A., Smeyne, R., Kottmann, A. & McMahon, A. P. Sonic hedgehog signaling is required for expansion of granule neuron precursors and patterning of the mouse cerebellum. *Dev. Biol.* **270**, 393–410 (2004).
32. Madisen, L. et al. A toolbox of Cre-dependent optogenetic transgenic mice for light-induced activation and silencing. *Nat. Neurosci.* **15**, 793–802 (2012).
33. Zhao, S. et al. Cell type–specific channelrhodopsin-2 transgenic mice for optogenetic dissection of neural circuitry function. *Nat. Methods* **8**, 745–752 (2011).
34. Guo, Z. V. et al. Procedures for behavioral experiments in head-fixed mice. *PLoS ONE* **9**, e88678 (2014).
35. Chen, C. H., Fremont, R., Arteaga-Bracho, E. E. & Khodakhah, K. Short latency cerebellar modulation of the basal ganglia. *Nat. Neurosci.* **17**, 1767–1775 (2014).
36. Rossi, M. A. et al. A GABAergic nigrotectal pathway for coordination of drinking behavior. *Nat. Neurosci.* **19**, 742–748 (2016).
37. Dong, H. W. *The Allen reference atlas: A digital color brain atlas of the C57Bl/6J male mouse.* (John Wiley & Sons Inc, Hoboken, 2008)
38. Oh, S. W. et al. A mesoscale connectome of the mouse brain. *Nature* **508**, 207–214 (2014).
39. Rueckert, D. et al. Nonrigid registration using free-form deformations: application to breast MR images. *IEEE Trans. Med. Imaging* **18**, 712–721 (1999).

© 2018 Springer Nature Limited. All rights reserved.

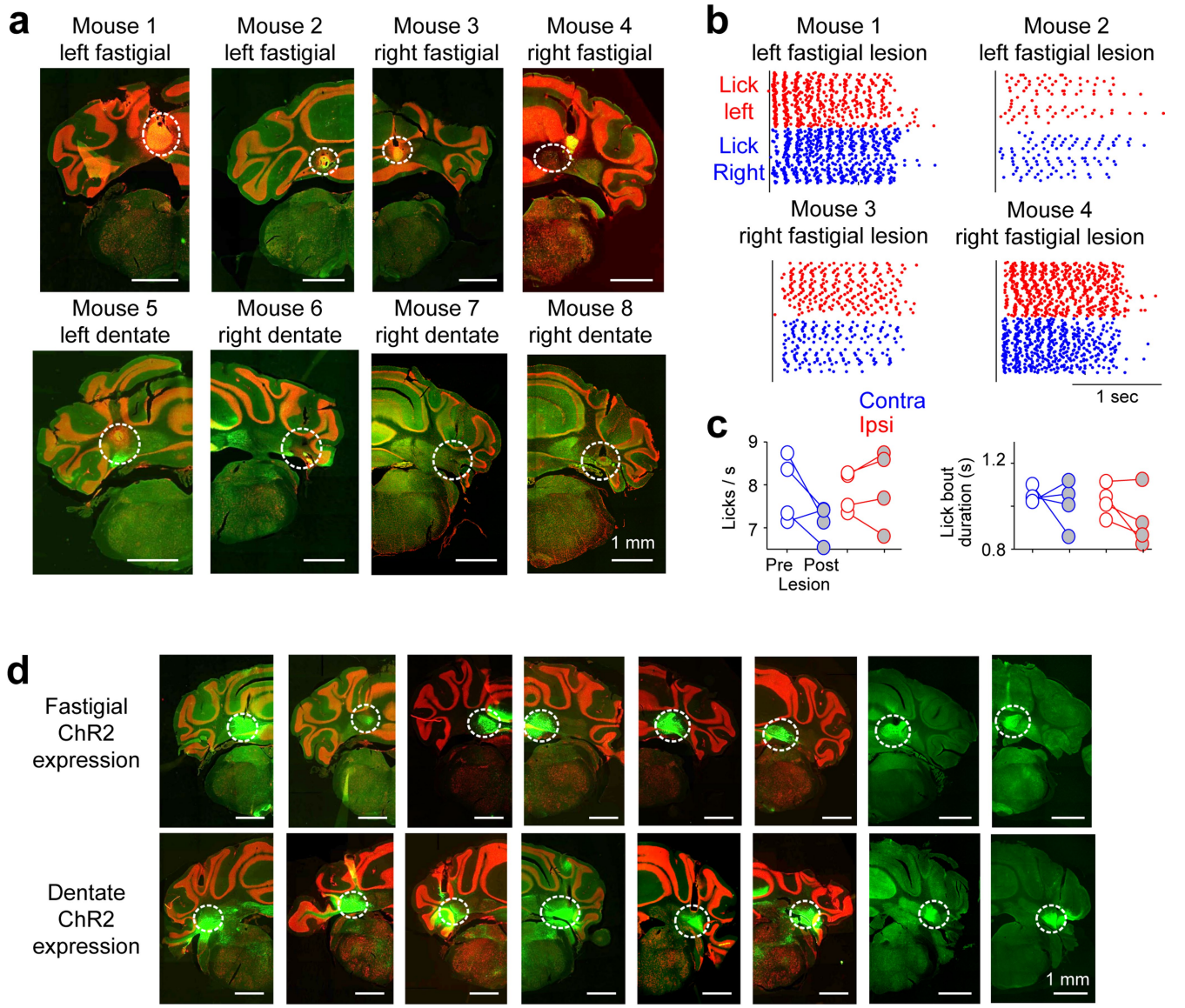

Extended Data Fig. 1 | See next page for caption.

© 2018 Springer Nature Limited. All rights reserved.

Extended Data Fig. 1 | Histology and behavioural data. a, Coronal sections showing CN lesion sites for all mice. Fastigial lesion, $n = 4$; dentate lesion, $n = 4$. **b**, Execution of the licking movement is not affected by fastigial lesions. Individual licks are shown as dots (blue, lick right; red, lick left). Licks are aligned to the onset of the 'go' cue (vertical line). **c**, Average lick rate within a lick bout and the duration of lick bouts are not affected by fastigial lesion. A lick bout is defined as a sequence of licks with an inter-lick interval of less than 500 ms. Data from the fastigial-lesion mice only ($n = 4$). Data are grouped by licking direction relative to the lesioned hemisphere: contralesional licking (blue) or ipsilesional licking (red). **d**, Coronal sections showing ChR2–eYFP expression in the fastigial nucleus and the dentate nucleus. Nine mice were used for various fastigial ChR2 photoactivation experiments, and ten mice were used for dentate ChR2 photoactivation experiments. In one of the fastigial photoactivation mice, the injection of ChR2 virus missed the CN (not shown) and its data were excluded. Two of the dentate photoactivation mice were subsequently used for lesion experiments (not shown). See Supplementary Table 1 for the list of mice and manipulated hemispheres in individual experiments. **e**, CN photoactivation during specific behavioural periods. Top, the experiment timeline. Photostimulation was for the entire task period (1.3 s). Bottom, performance in the behavioural trials. Left, fastigial photoactivation ($n = 6$); right, dentate photoactivation ($n = 8$). For fastigial photoactivation, average behavioural performance for control and photoactivation trials (S, sample period photoactivation; D, delay period; R, response period) is also shown. Grey lines represent individual mice. Chance is 50%. For behavioural performance grouped by trial type, lick-left and lick-right trials are grouped by instructed licking direction relative to the manipulated hemisphere. Blue, contralateral; red, ipsilateral. Both hemispheres were tested. See Supplementary Table 1 for the list of mice and manipulated hemispheres. Thick lines represent the mean; thin lines represent individual mice ($n = 6$). $^{*}P < 0.05$, $^{**}P < 0.01$, $^{***}P < 0.001$, one-sided test, bootstrap (Methods). **f**, Proportion of early-lick and no-lick trials with and without CN photoactivation during the delay period. Control trials are shown in grey and photoactivation trials in cyan. Lines represent individual mice. FN, fastigial photoactivation ($n = 6$); DN, dentate photoactivation ($n = 8$).

© 2018 Springer Nature Limited. All rights reserved.

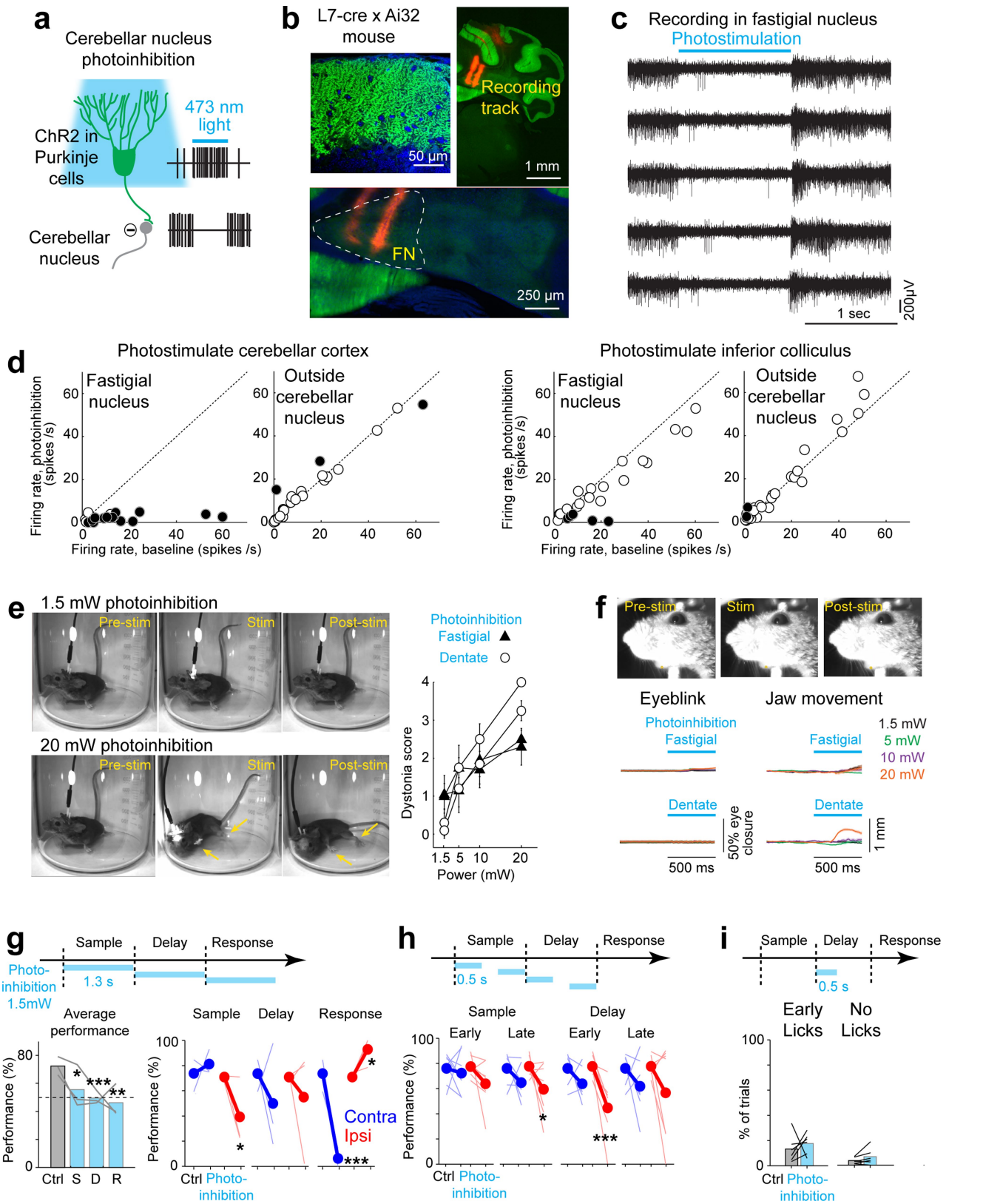

Extended Data Fig. 2 | See next page for caption.

© 2018 Springer Nature Limited. All rights reserved.

Extended Data Fig. 2 | Characterization of CN photoinhibition and behavioural data. a, Strategy for silencing the CN. ChR2 is expressed in cerebellar Purkinje cells, and the photostimulation of Purkinje cells inhibits CN neurons (photoinhibition). **b**, Top left, an image of the cerebellar cortex showing the expression of ChR2–eYFP in Purkinje cells in a L7-cre × Ai32 mouse. Top right, an example silicon-probe recording in a L7-cre × Ai32 mouse. The coronal section shows ChR2–eYFP expression in the cerebellar cortex and DiI-labelled electrode tracks. Bottom, electrode tracks within the fastigial nucleus (dashed contour). Photostimulation of Purkinje cells was carried out by directing a blue laser (0.5–4.5 mW average power, beam diameter 400 μm at 4σ) to the brain surface through a cranial window. **c**, Example voltage traces from a recording of the fastigial nucleus during photoinhibition. Multi-unit activity in the fastigial nucleus was silenced. Multiple traces show repeats of photostimulation. **d**, Photoinhibition reduced activity specifically in the CN. Average spike rates before (500 ms) versus during photoinhibition (1.2 s) are shown, for neurons from the fastigial nucleus (left, $n = 26$) and from the surrounding cerebellar cortex (right, $n = 34$). Photostimulation of the cerebellar cortex (lambda posterior 3 mm, lateral 2 mm) silenced fastigial activity whereas photostimulation of the inferior colliculus (posterior 1 mm, lateral 2 mm) did not. Solid dots indicate neurons with a significant change in spike rate ($P < 0.01$, two-tailed *t*-test). **e**, Dose-dependent effect of CN photoinhibition on posture and movement. Left, video frames showing an unrestrained mouse undergoing CN photoinhibition. During low-intensity photoinhibition (1.5 mW, the intensity typically used in the delayed response task), no consistent movement was detected. High-intensity photoinhibition (20 mW) of both the fastigial nucleus and the dentate nucleus produced dystonia-like movements and posture changes, such as loss of balance and extensions of the contralateral limbs (arrows). Right, dystonia-like movements observed upon photoinhibition were given scores on a scale of 0–4 (Methods): 0, no motor abnormalities; 1, slightly slowed or abnormal motor behaviour, no dystonia; 2, mild impairment, mild and transient dystonic postures, weak tremor; 3, moderate impairment, dystonic postures, cannot balance the body, major tremor; 4, severe impairment, sustained dystonic postures and limited movements. The scoring was performed blind to the experimental conditions. Data are mean ± s.e.m. across trials. $n = 2$ mice, 10 trials per condition. **f**, Dose-dependent effect of CN photoinhibition on jaw movement and eyeblink. Top, video frames showing a head-fixed mouse undergoing CN photoinhibition. Bottom left, eyeblink responses during CN photoinhibition. No consistent eyeblink was evoked. Bottom right, jaw movements during CN photoinhibition. Only high-intensity photoinhibition (20 mW) of the dentate nucleus produced jaw movements. Data are mean ± s.e.m. across trials. $n = 4$ mice, 10 trials per condition for eyeblink, 20 trials per condition for jaw movement. **g**, Behavioural performance in the delayed response task with and without fastigial photoinhibition for the entire task periods ($n = 3$). Left, average behavioural performance for control and photoinhibition trials (S, sample period photoinhibition; D, delay period; R, response period). Grey lines show individual mice. Chance is 50%. Right, behavioural performance for each trial type. Lick-left and lick-right trials are grouped by instructed licking direction relative to the manipulated hemisphere. Blue, contralateral; red, ipsilateral. Both hemispheres were tested. See Supplementary Table 1 for the list of mice and manipulated hemispheres. Thick lines represent the mean; thin lines represent individual mice. $^{*}P < 0.05$, $^{**}P < 0.01$, $^{***}P < 0.001$, one-sided test, bootstrap (Methods). **h**, Behavioural performance in trials with photoinhibition during the early sample, late sample, early delay, and late delay periods ($n = 7$ mice). $^{*}P = 0.04$, $^{***}P = 0.0002$, one-sided test, bootstrap. **i**, Proportion of early-lick and no-lick trials with fastigial photoinhibition during the delay period. Control trials (grey) and photoinhibition trials (cyan). Lines, individual mice ($n = 7$).

© 2018 Springer Nature Limited. All rights reserved.

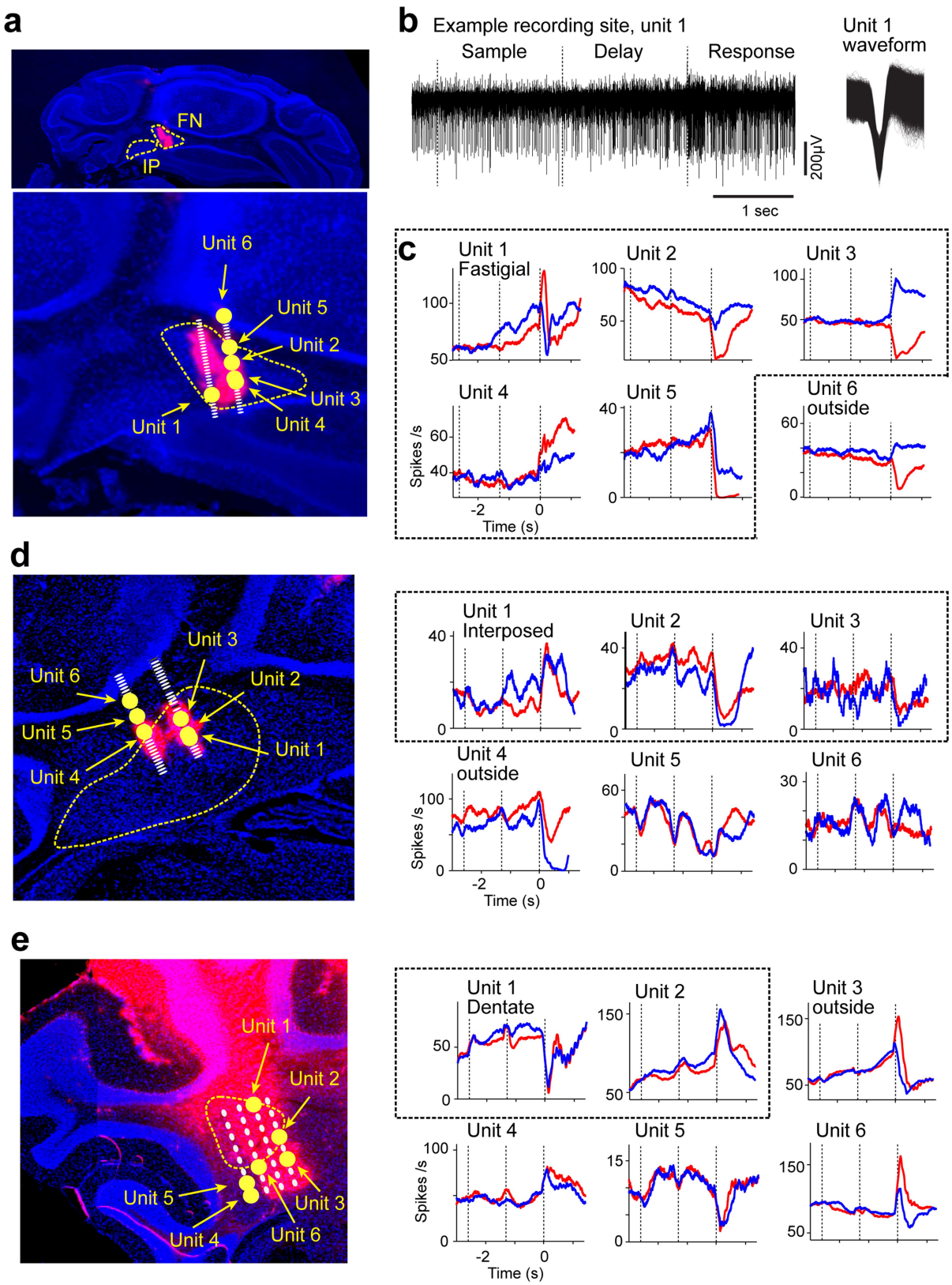

Extended Data Fig. 3 | See next page for caption.

© 2018 Springer Nature Limited. All rights reserved.

Extended Data Fig. 3 | Silicon-probe recordings in the CN. a, DiI-labelled recording tracks in coronal sections stained by DAPI. Borders of the CN are visible in DAPI staining. Electrode location was estimated based on DiI labelling and manipulator depth. The lamination of activity patterns across the electrodes corresponded well to the anatomical structures: that is, high activity levels in the CN and the cerebellar cortex, low activity levels in the white matter. Single-unit locations were estimated on the basis of electrode location. Top, a coronal section showing a recording in the fastigial nucleus. Bottom, the fastigial nucleus (yellow dashed line), estimated electrode location, and the locations of single units (units 1–6) from an example recording. **b**, Left, voltage trace from the recording site of unit 1 during a single behavioural trial. Dashed lines indicate behavioural periods. Right, waveforms of unit 1 after spike sorting. **c**, Peristimulus time histogram of all the units from the example fastigial recording. The dashed box indicates that units 1–5 were within the fastigial nucleus, and unit 6 was outside of the fastigial nucleus. Blue, lick-right trials; red, lick-left trials. **d**, Same as **a** and **c**, but for an example recording in the interposed nucleus. **e**, Same as **a** and **c**, but for an example recording in the dentate nucleus.

© 2018 Springer Nature Limited. All rights reserved.

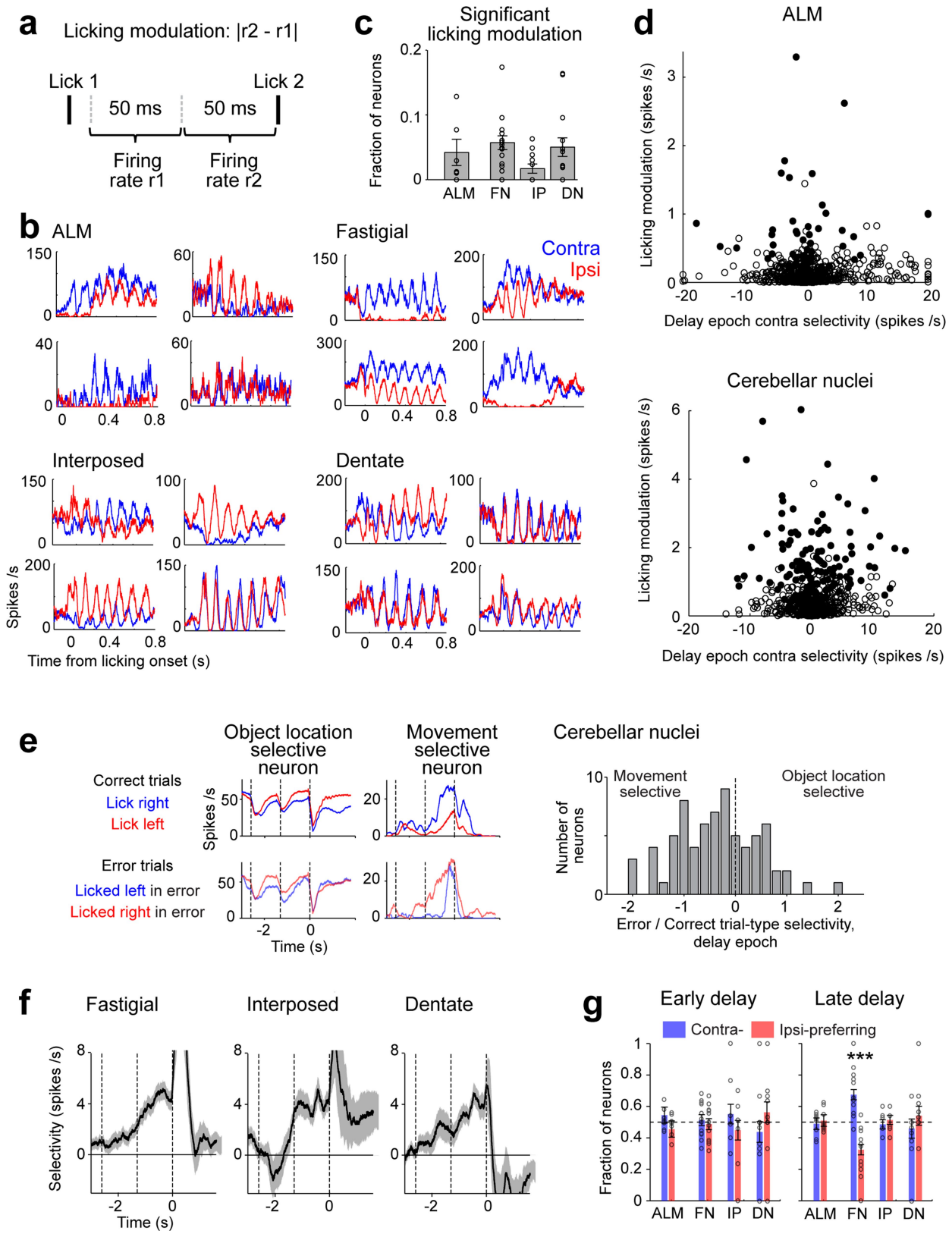

Extended Data Fig. 4 | See next page for caption.

© 2018 Springer Nature Limited. All rights reserved.

Extended Data Fig. 4 | ALM and CN activity is related to motor planning and movement. a, Criteria used to identify neuronal activity modulated by licking. For each lick, spike counts were calculated in two adjacent 50-ms time windows, starting 20 ms from the detection time of the lick. Across all licks and all trials, neurons with significant difference in spike count between the two time windows were deemed to be modulated by licking ($P < 0.01$, two-tailed t-test). Licking modulation is calculated for each neuron: mean difference in spike rate between the two time windows. **b**, Example neurons are significantly modulated by licking. Peristimulus time histogram from the correct lick-right and lick-left trials during the response period. Spike times are aligned to the first lick. Trials are grouped by licking direction relative to the recorded hemisphere: contralateral (blue) or ipsilateral (red). Averaging window, 10 ms. **c**, Fraction of neurons that are significantly modulated by licking ($P < 0.01$, two-tailed t-test) from each brain region. FN, fastigial nucleus; IP, interposed nucleus; DN, dentate nucleus. Error bars indicate s.e.m. across mice, bootstrap (Methods); dots represent individual mice (ALM, $n = 10$; FN, $n = 15$; IP, $n = 9$; DN, $n = 11$). **d**, There is no correlation between whether a neuron was modulated by licking and whether it exhibited preparatory activity. Top, ALM; bottom, the cerebellar nuclei. Selectivity during the delay period is the difference in spike rate between the lick-right and lick-left trials. Solid dots indicate neurons that are significantly modulated by licking ($P < 0.01$, two-tailed t-test). **e**, Preparatory activity in the CN. Left, Peristimulus time histograms for correct and error trials are shown for two example CN neurons. Trial types are based on sensory instruction (blue, lick right; red, lick left). The same trial-type preference in correct and error trials indicates selectivity for object location. Opposite trial-type preference indicates selectivity for upcoming movement directions. A negative ratio of trial-type selectivity between error and correct trials means a neuron switches trial-type preference to predict upcoming movement directions on error trials. Right, selectivity ratios for CN neurons. Neurons with significant delay-period selectivity and tested for >3 error trials are shown ($n = 73$). **f**, Population selectivity for each cerebellar nucleus (mean ± s.e.m. across neurons, bootstrap; fastigial, $n = 87$; interposed, $n = 50$; dentate, $n = 60$). Selectivity is the difference in spike rate between the preferred and the non-preferred trial type (Methods). Dashed lines separate sample, delay and response periods. **g**, Proportion of contra-preferring versus ipsi-preferring neurons, based on spike counts during the first 500 ms (left) and the last 500 ms (right) of the delay period. Error bars indicate s.e.m. across mice. Dots represent individual mice (ALM, $n = 10$; FN, $n = 15$; IP, $n = 9$; DN, $n = 11$). ***$P = 0.0001$, one-sided test, bootstrap.

© 2018 Springer Nature Limited. All rights reserved.

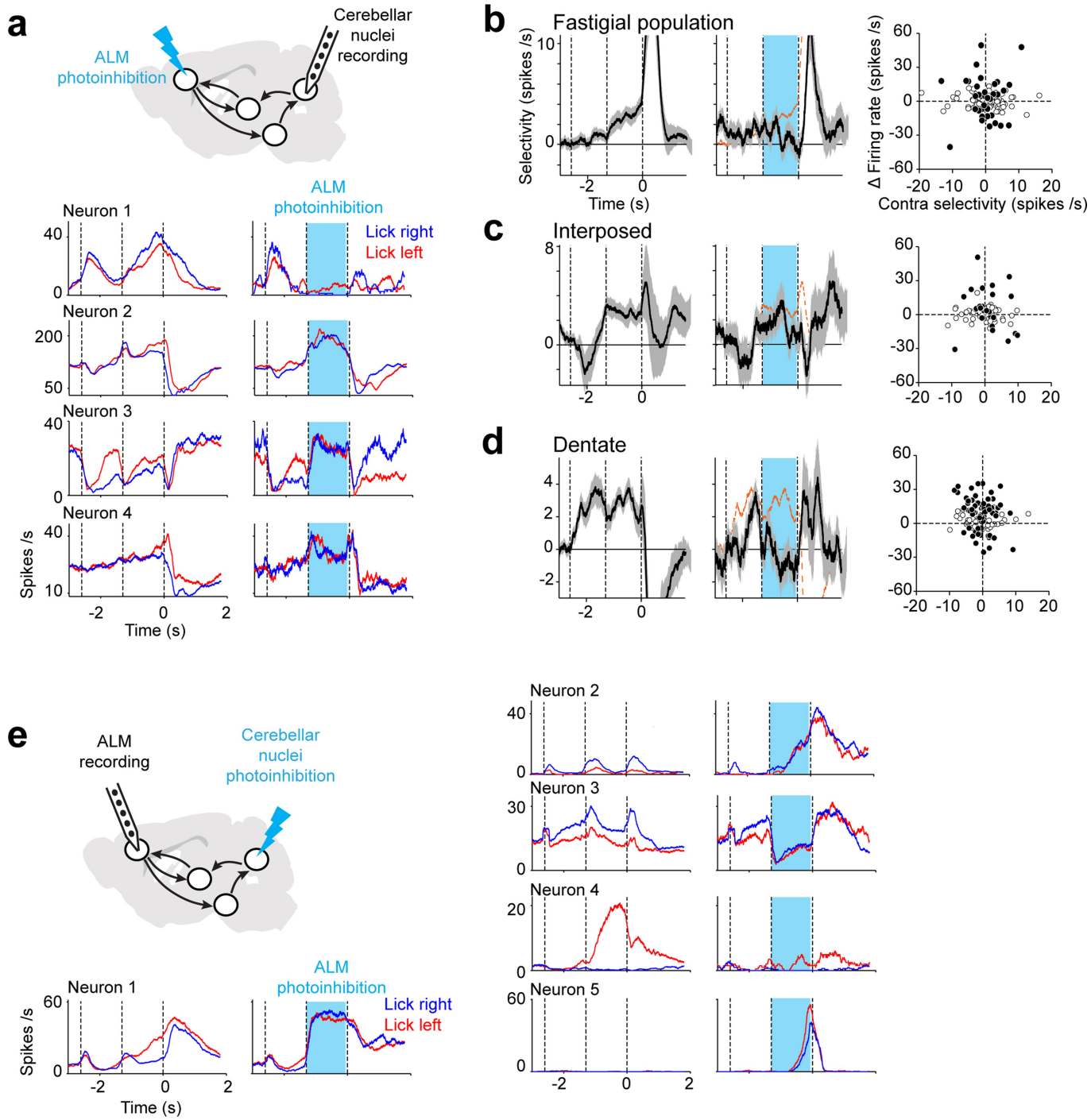

Extended Data Fig. 5 | ALM drives CN preparatory activity and vice versa. a, Top, schematic showing CN recording during bilateral ALM photoinhibition. Laser power, 1.5 mW per location (Methods). Bottom, Peristimulus time histograms of four example CN neurons with and without ALM photoinhibition. The cyan bar indicates the photoinhibition period. Blue, lick-right trials; red, lick-left trials. **b**, Left, average fastigial selectivity in control and photoinhibition trials (mean ± s.e.m. across neurons, bootstrap). Only selective neurons tested for >3 trials in all conditions are included ($n = 54$ neurons, 8 mice). Orange dashed line denotes the mean from control trials. Right, relationship between delay-period selectivity of individual fastigial neurons and changes in firing rate due to ALM photoinhibition. Filled circles indicate neurons that are significantly modulated by ALM photoinhibition ($P < 0.01$, two-tailed t-test). **c**, Same as **b**, but for the interposed nucleus ($n = 44$ neurons, 5 mice). **d**, Same as **b**, but for the dentate nucleus ($n = 59$ neurons, 6 mice). **e**, Same as **a**, but for ALM recording during contralateral CN photoinhibition. Laser power, 1.5–4.5 mW.

© 2018 Springer Nature Limited. All rights reserved.

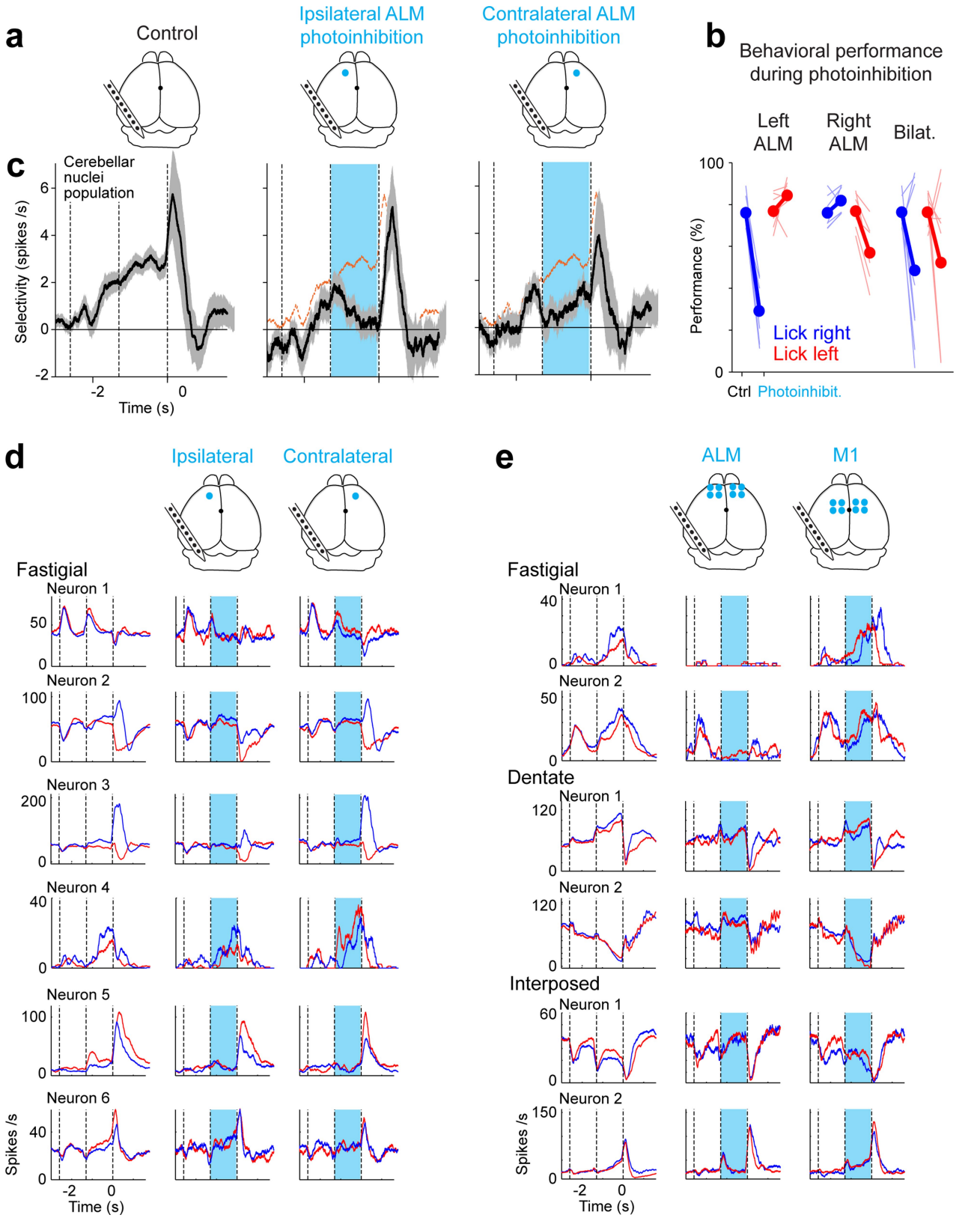

Extended Data Fig. 6 | CN preparatory activity is driven by both hemispheres of the ALM. a, CN recording during contralateral or ipsilateral ALM photoinhibition. **b**, Performance in the delayed response task during unilateral and bilateral ALM photoinhibition. **c**, CN population selectivity from control and photoinhibition trials (mean ± s.e.m. across neurons, bootstrap). Only selective neurons tested for >3 trials in all conditions are included ($n = 157$). The orange dashed line indicates the mean from control trials. The cyan bar denotes the photoinhibition period. CN selectivity was reduced by photoinhibiting either side of the ALM. **d**, Peristimulus time histograms of example CN neurons during ipsilateral or contralateral ALM photoinhibition. The effect was heterogeneous across individual neurons. Some neurons were affected by ipsilateral ALM photoinhibition (row 1–3), other neurons were affected by contralateral ALM photoinhibition (row 4), others were affected by photoinhibition of either side (row 5, 6). **e**, Peristimulus time histograms of example CN neurons during bilateral ALM or M1 photoinhibition. ALM: bregma anterior 2–3 mm, lateral 1–2 mm; M1 anterior 0–1 mm, lateral 1–2 mm.

© 2018 Springer Nature Limited. All rights reserved.

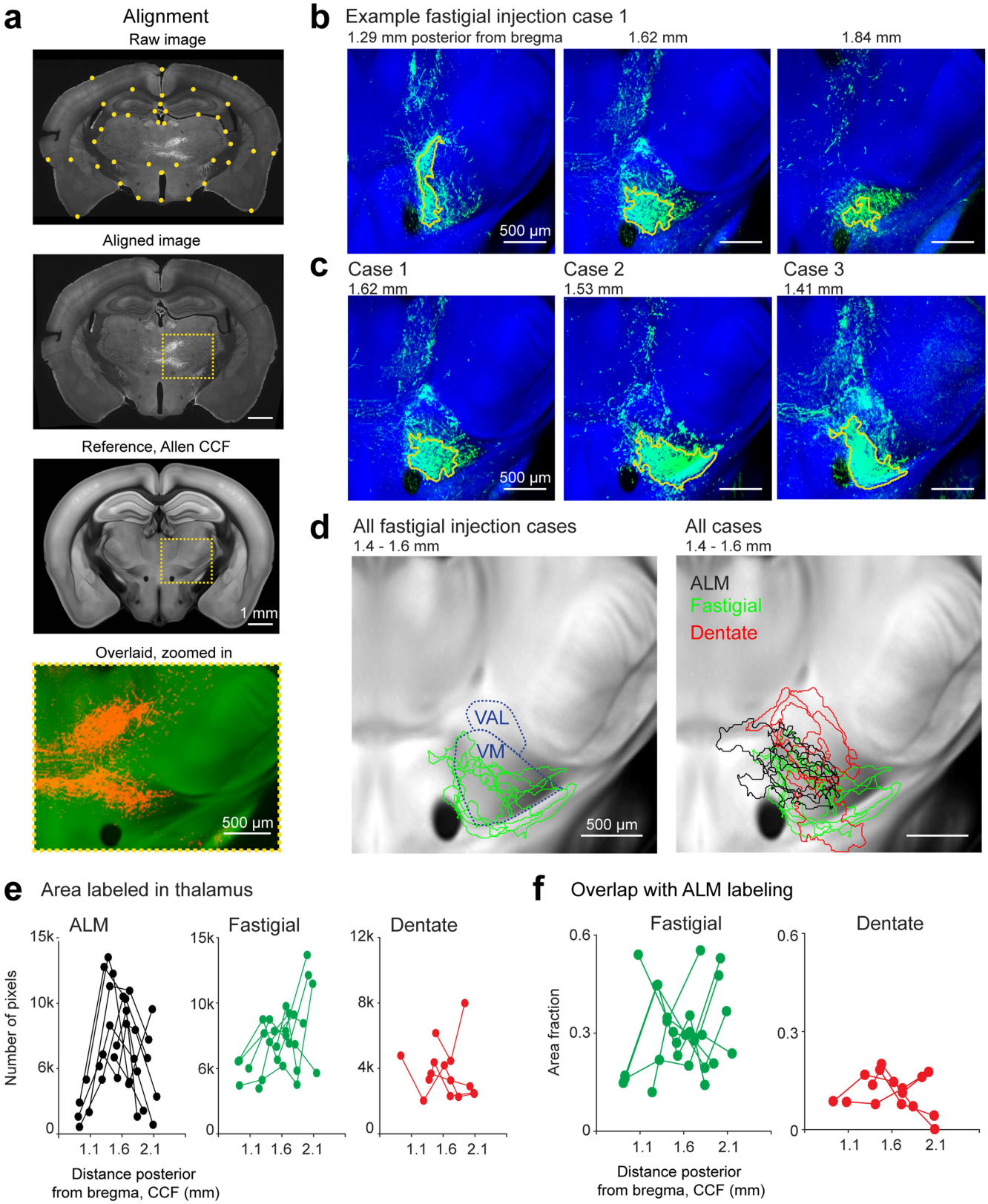

Extended Data Fig. 7 | See next page for caption.

© 2018 Springer Nature Limited. All rights reserved.

Extended Data Fig. 7 | Alignment of anatomical data and comparing fastigial and dentate projections to ALM-projecting thalamus. **a**, Top, an example coronal section before and after alignment to the corresponding section of the anatomical template in the Allen Mouse Common Coordinate Framework (CCF). Fluorescence is anterograde labelling (BDA) from an ALM injection, labelling the ALM-projecting thalamus (Methods). Yellow dots indicate control points for b-spline transformation. The dashed line denotes a region of interest containing the thalamus ipsilateral to the ALM injection. Bottom, overlay of the aligned image (orange) and the anatomical template (green). ALM axons in the thalamus obey structural boundaries in the anatomical template. Critically, the alignment procedure did not use any structures inside the thalamus as landmarks. **b**, Coronal sections showing an example fastigial injection case with anterograde labelling in the thalamus. The sections are aligned to and superimposed on the anatomical template. The yellow outlines show labelled areas after thresholding (Methods). **c**, Coronal sections showing three different fastigial injection cases. Different injections show similar patterns of anterograde labelling in the thalamus. **d**, Left, outlines of the labelled areas from all fastigial injection cases ($n = 6$). Borders of the thalamic nuclei (VM and VAL) are based on annotations in the Allen Reference Brain. Right, outlines of the labelled areas from all fastigial ($n = 6$), dentate ($n = 4$) and ALM ($n = 8$) injection cases. There was a greater overlap between fastigial and ALM labelling. **e**, Total areas labelled (number of pixels) in the thalamus by fastigial, dentate and ALM injections. Dots indicate individual coronal sections; lines represent individual injections. **f**, Overlaps between fastigial or dentate projections and the ALM-projecting thalamus. The co-labelled area is normalized to the total thalamic area labelled by fastigial or dentate projections (area fraction overlap). Dots indicate individual coronal sections; lines represent individual injections.

© 2018 Springer Nature Limited. All rights reserved.

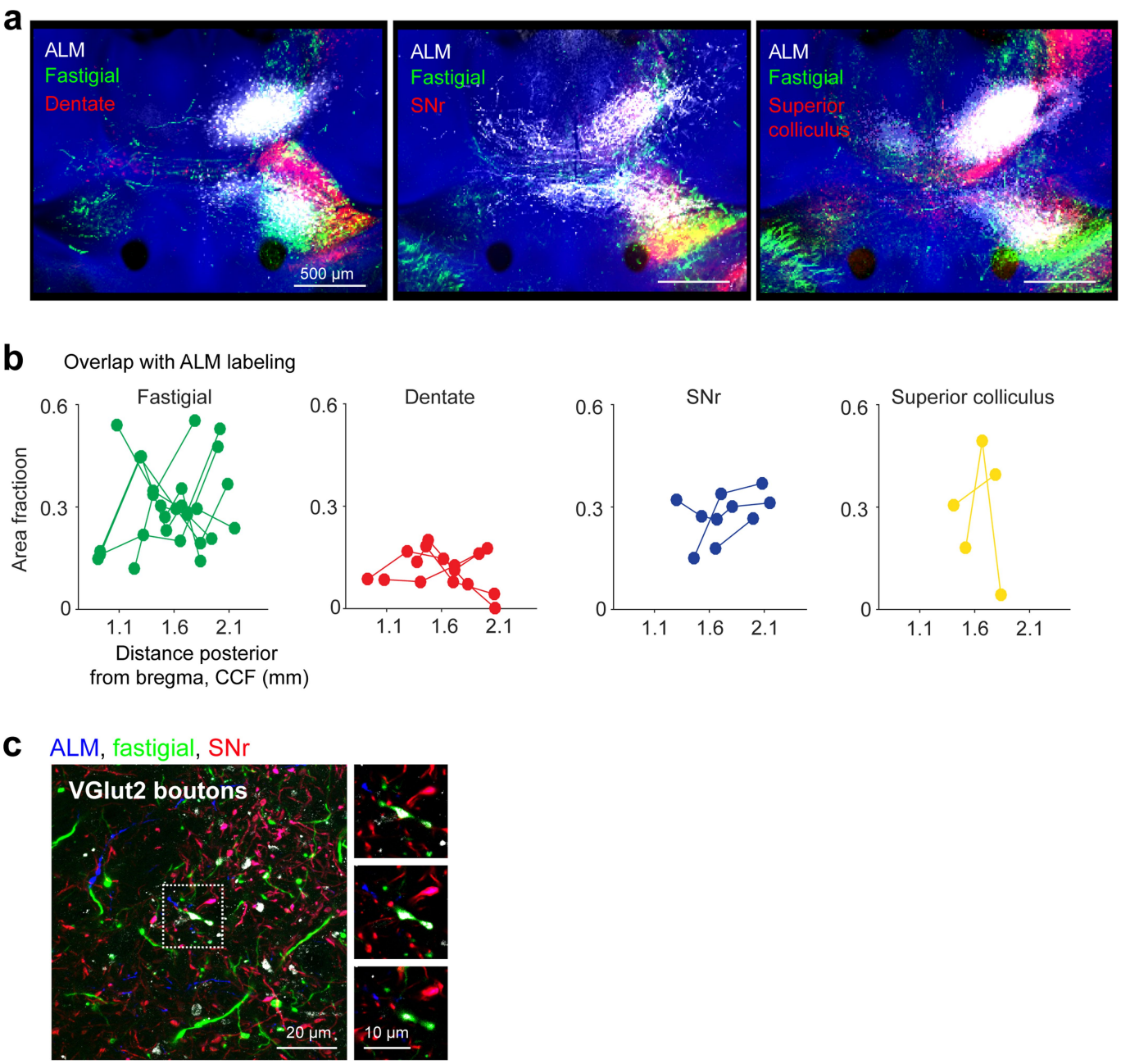

Extended Data Fig. 8 | The ALM-projecting thalamus receives converging inputs from the fastigial nucleus, basal ganglia SNr and the superior colliculus. a, Example triple injections showing co-labelling of fastigial and dentate projections (left), fastigial and SNr projections (middle), and fastigial and superior colliculus projections (right) in the thalamus. Injections were repeated several times in different mice with similar results (ALM–fastigial–dentate, $n = 4$; ALM–fastigial–SNr, $n = 3$; ALM–fastigial–superior colliculus, $n = 2$). **b**, Overlaps between ALM-projecting thalamus and projections of different areas (Methods). Fastigial, SNr and superior colliculus labelling show a comparable amount of overlap with the ALM-projecting thalamus. Dentate labelling shows less overlap. The thalamic area co-labelled by ALM injection and a projection (fastigial, dentate, SNr or superior colliculus) is normalized to the total thalamic area labelled by that projection (area fraction). Dots indicate individual coronal sections; lines represent individual injections. **c**, A confocal image showing vGlut2 staining in the ALM-projecting thalamus. Anterograde tracer injections in the ALM (blue), the fastigial nucleus (green) and the SNr (red). Fastigial axons form glutamatergic synapses (vGlut2 positive) within the ALM-projecting thalamus. vGlut2 staining was performed in one ALM–fastigial–SNr injection case.

© 2018 Springer Nature Limited. All rights reserved.

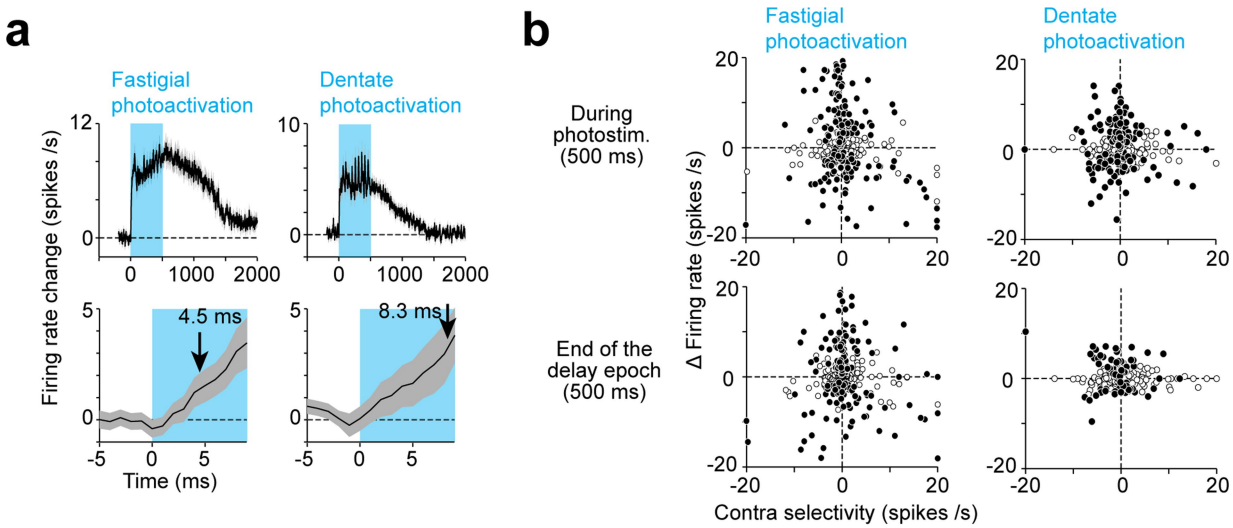

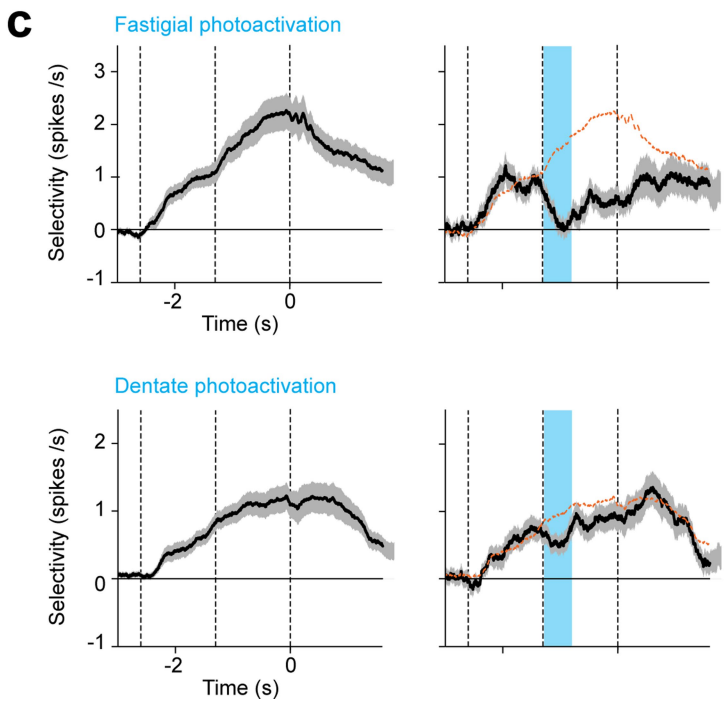

Extended Data Fig. 9 | CN ChR2 photoactivation drives rapid change in ALM activity. a, The change in firing rate of ALM neurons during fastigial or dentate ChR2 photoactivation. The change in firing rate is the difference in spike rate between control and photoactivation trials. For neurons that were suppressed by CN photoactivation, the firing rate differences are multiplied by −1 so that the firing rate changes are always positive for latency quantifications. Data are mean ± s.e.m. across neurons. Only neurons that were significantly modulated by CN photoactivation are included ($P < 0.01$, two-tailed t-test; fastigial photoactivation, $n = 227$; dentate photoactivation, $n = 163$). Top, Time course for the change in ALM firing rate. The cyan bar denotes the CN photoactivation period (500 ms). Bottom, The onset of the change in firing rate of ALM neurons (arrows). The change of firing rate is quantified in 10-ms time bins in 1-ms steps. The onset time is the first time bin in which the change in population firing rate significantly deviated from zero ($P < 0.01$, two-tailed t-test). We repeated the onset time estimation 10,000 times. In each round, we resampled with replacement from the neurons in the dataset and re-estimated the onset time. The arrows indicate the mean estimated onset time. **b**, Relationship between selectivity of individual ALM neurons and changes in firing rate due to CN photoactivation. Filled circles denote ALM neurons that were significantly modulated by CN photoactivation ($P < 0.01$, two-tailed t-test). The change in firing rate is the difference in the spike rate between control and photoactivation trials during photostimulation (top) or the last 500 ms of the delay period (bottom). The selectivity is the difference in spike rate between lick-right and lick-left trials during the delay period. **c**, Selectivity of the ALM population from control and photoactivation trials (mean ± s.e.m. across neurons, bootstrap; selective neurons tested for >3 trials in all conditions). The orange dashed line indicates the mean from control trials. Top, fastigial photoactivation ($n = 328$); bottom, dentate photoactivation ($n = 377$). The cyan bar denotes the photoactivation period.

© 2018 Springer Nature Limited. All rights reserved.

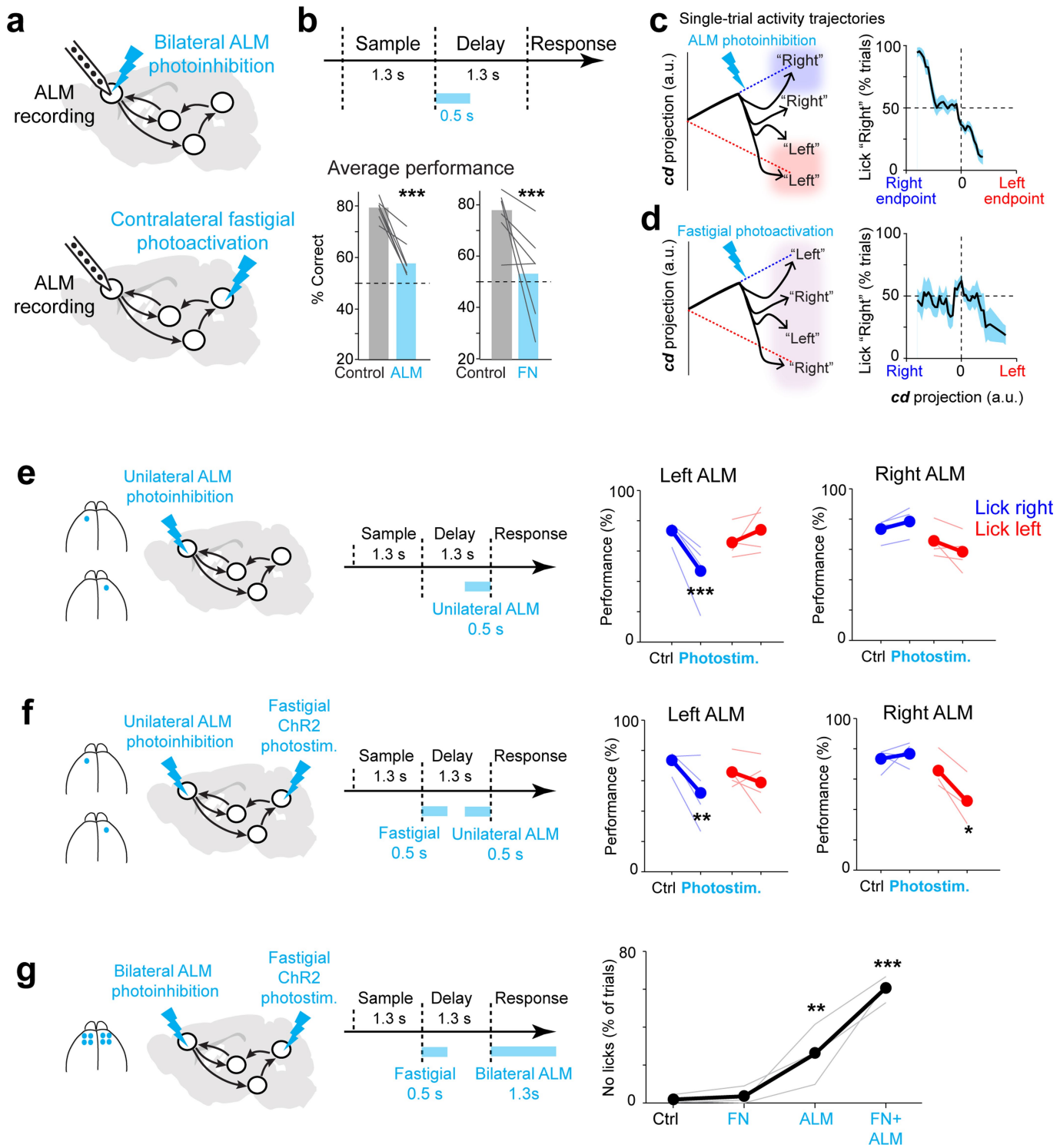

Extended Data Fig. 10 | See next page for caption.

© 2018 Springer Nature Limited. All rights reserved.

Extended Data Fig. 10 | Fastigial photoactivation abolishes the relationship between ALM activity and upcoming movements. a, ALM recording during bilateral ALM photoinhibition (top) or contralateral fastigial photoactivation (bottom). **b**, Performance in control (grey) and photostimulation (cyan) trials. Lick-left and lick-right trials are pooled. Chance is 50% (dashed line). Lines represent individual mice (ALM photoinhibition, $n = 7$; fastigial photoactivation, $n = 6$). ***$P < 0.001$, one-sided test, bootstrap (Methods). **c**, Left, schematic of ALM activity projected onto the coding direction (***cd***). Dashed lines indicate control trials, ALM activity trajectories converge to discrete endpoints at the end of the delay period that predict upcoming movement directions (lick right, blue; lick left, red). Solid black lines indicate bilateral ALM photoinhibition trials; the distance of the perturbed trajectories to the endpoints predicts future movement directions even though the behavioural performance is close to that which would be obtained by chance. Right, experimental data. Probability of the mouse licking right as a function of trajectory distance to the endpoints along the ***cd*** (Methods). Bilateral ALM photoinhibition trials only ($n = 690$). The ***cd*** and endpoints were estimated from independent control trials. Data are binned along the ***cd*** projection. The s.e.m. is obtained by bootstrapping the trials in each bin. **d**, Same as **c**, but for fastigial photoactivation trials ($n = 337$). ALM activity no longer predicts future movement directions after a fastigial perturbation. **e**, It is possible that fastigial perturbation activated downstream motor circuits that could maintain the motor plan and generate movements independent of ALM. We examined the necessity of ALM activity in driving directional licking after a fastigial perturbation. In VGAT-ChR2-eYFP mice expressing ChR2 in both Purkinje neurons and cortical GABAergic neurons, we independently manipulated activity in the fastigial nucleus and the ALM (Methods). Left, unilateral ALM photoinhibition during the late delay period. Right, behavioural performance for each trial type in control and photoinhibition trials. Left ALM photoinhibition biased upcoming licking to the left, resulting in lower performance in the lick-right trials. The opposite pattern of bias was induced by right ALM photoinhibition. Thick lines represent the mean; thin lines represent individual mice ($n = 4$). ***$P = 0.0002$, one-sided test, bootstrap (Methods). **f**, Same as **e**, but for unilateral ALM photoinhibition after fastigial perturbation. Note the same pattern of behavioural bias as **e**. *$P = 0.04$, **$P = 0.008$, one-sided test, bootstrap. **g**, Left, after fastigial perturbation, ALM activity was bilaterally silenced during movement initiation. Right, fraction of trials in which mice did not lick after the 'go' cue. FN, fastigial perturbation only; ALM, bilateral ALM photoinhibition; FN + ALM, fastigial perturbation followed by bilateral ALM photoinhibition. Thick lines represent the mean; thin lines represent individual mice ($n = 3$). **$P = 0.002$, ***$P = 0.0002$, one-sided test, bootstrap.

© 2018 Springer Nature Limited. All rights reserved.

https://doi.org/10.1038/s41586-018-0636-7

A mesocortical dopamine circuit enables the cultural transmission of vocal behaviour

Masashi Tanaka[1,5], Fangmiao Sun[2,3], Yulong Li[2,3,4] & Richard Mooney[1]*

The cultural transmission of behaviour depends on the ability of the pupil to identify and emulate an appropriate tutor[1–4]. How the brain of the pupil detects a suitable tutor and encodes the behaviour of the tutor is largely unknown. Juvenile zebra finches readily copy the songs of the adult tutors that they interact with, but not the songs that they listen to passively through a speaker[5,6], indicating that social cues generated by the tutor facilitate song imitation. Here we show that neurons in the midbrain periaqueductal grey of juvenile finches are selectively excited by a singing tutor and—by releasing dopamine in the cortical song nucleus HVC—help to encode the song representations of the tutor used for vocal copying. Blocking dopamine signalling in the HVC of the pupil during tutoring blocked copying, whereas pairing stimulation of periaqueductal grey terminals in the HVC with a song played through a speaker was sufficient to drive copying. Exposure to a singing tutor triggered the rapid emergence of responses to the tutor song in the HVC of the pupil and a rapid increase in the complexity of the song of the pupil, an early signature of song copying[7,8]. These findings reveal that a dopaminergic mesocortical circuit detects the presence of a tutor and helps to encode the performance of the tutor, facilitating the cultural transmission of vocal behaviour.

The cortical song nucleus HVC is crucial for singing and song learning[7,9–12] and receives convergent input from premotor, auditory and neuromodulatory neurons, including dopamine (DA)-secreting neurons in the midbrain periaqueductal grey (PAG)[13–15] (Fig. 1a–c and Extended Data Fig. 1a–c). In the mammalian PAG, DA neurons encode information about social context, arousal in response to behaviourally salient stimuli, or rewards[16–18], raising the possibility that the PAG-to-HVC pathway in juvenile finches encodes information about the tutor that facilitates song imitation. To explore this idea, we implanted tetrodes into the PAG of juvenile male finches raised in isolation from a tutor (tutor-naive juveniles; see Methods) (Fig. 1d–k). Most PAG neurons (81.8%; 18 out of 22 neurons from four birds) increased their action potential activity in the presence of a singing tutor (Fig. 1e–g, k), whereas PAG activity was unaffected during encounters with non-singing adult male finches or female finches, which do not sing (Fig. 1i–k). Neural activity in the PAG of the juvenile was not precisely locked to

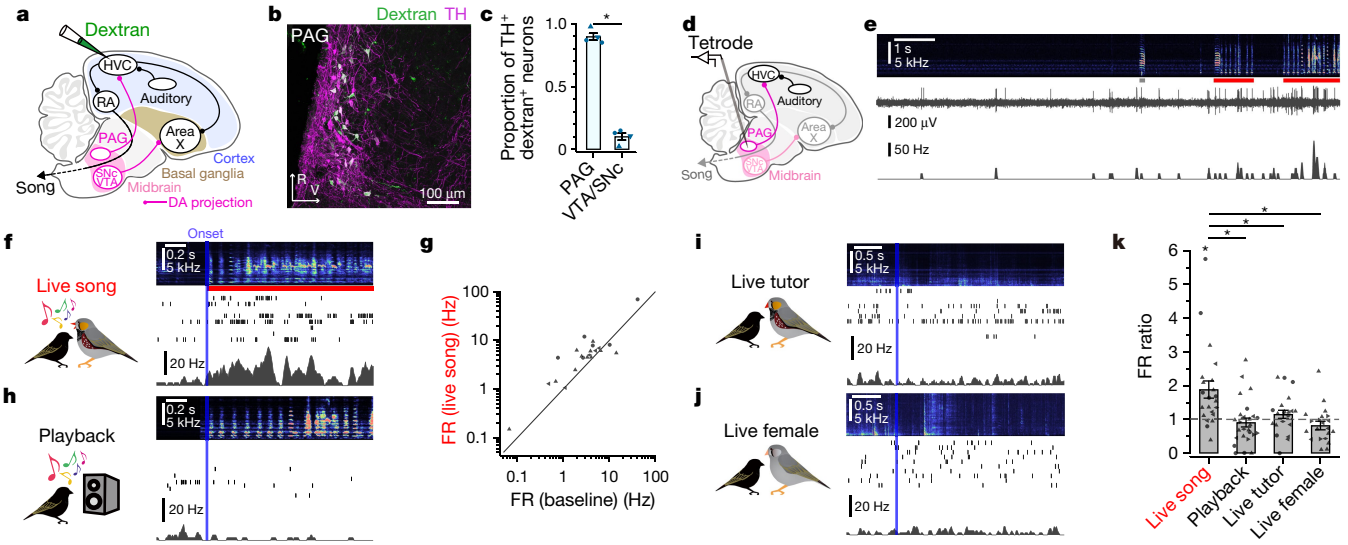

Fig. 1 | Recordings of PAG activity. a, Schematic of dextran injection into HVC. RA, robust nucleus of the arcopallium; SNc, substantia nigra pars compacta; VTA, ventral tegmental area. **b**, PAG neurons labelled with dextran (green) and TH antibody (pseudo-coloured magenta) (approximately 0.5 mm lateral of the midline). R, rostral; V, ventral. **c**, Proportion of double-labelled neurons (dextran and TH) in the midbrain. Data were analysed using a χ^2 test; $\chi_1^2 = 623.02$, $P < 0.001$, $n = 4$ hemispheres from three birds. **d**, Schematic of tetrode recordings from PAG neurons. **e**, PAG unit activity during live tutor songs (red bar) (grey bar: an isolated tutor call). Top, sound spectrogram. Middle, voltage recording. Bottom, firing rate. **f**, PAG unit activity aligned to the onset of tutor songs. Top, averaged spectrogram. Middle, spike raster. Bottom, mean firing rate. **g**, Mean firing rate (FR) during live tutor songs as a function of baseline firing rate of PAG neurons. **h–j**, PAG unit activity aligned to the onset of song playback (**h**), encounters with a live, non-singing tutor (**i**), encounters with a live female (**j**), shown as in **f**. **k**, Mean firing rate of PAG neurons normalized to baseline firing rate. Student's two-sided paired *t*-test, comparing firing rate during each condition to baseline; live song, $t_{21} = 3.439$, $P = 0.002$; playback, $t_{25} = 0.278$, $P = 0.783$; live tutor, $t_{21} = 1.270$, $P = 0.218$; live female, $t_{19} = 1.339$, $P = 0.196$; $n = 26$ neurons from five birds. Data are mean ± s.e.m. Asterisks above horizontal bars indicate significant *P* values from Tukey–Kramer tests in which the firing rate during live tutor songs is compared to other conditions: playback, $P < 0.001$; live tutor, $P = 0.017$; live female, $P < 0.001$.

[1]Department of Neurobiology, Duke University, Durham, NC, USA. [2]State Key Laboratory of Membrane Biology, Peking University School of Life Sciences, Beijing, China. [3]PKU-IDG/McGovern Institute for Brain Research, Beijing, China. [4]Peking-Tsinghua Center for Life Sciences, Beijing, China. [5]Graduate School of Life Sciences, Tohoku University, Sendai, Japan. *e-mail: mooney@neuro.duke.edu

© 2018 Springer Nature Limited. All rights reserved.

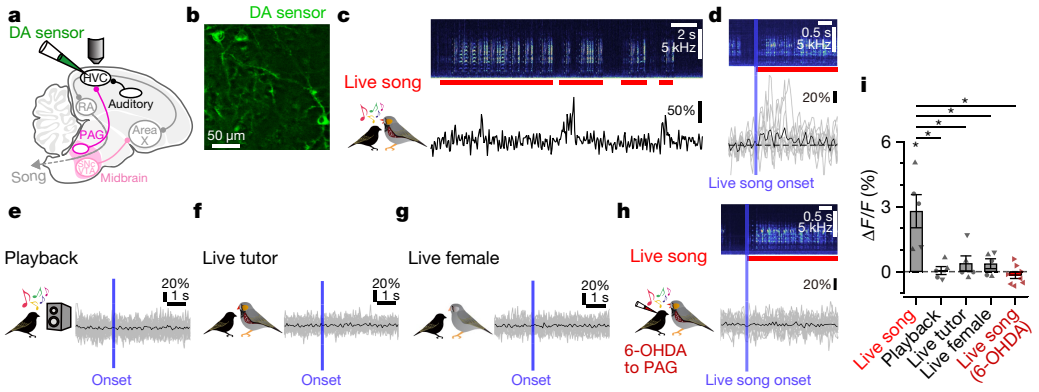

Fig. 2 | Imaging of DA in the HVC. a, Schematic of two-photon imaging of DA sensors ($GRAB_{DA1h}$) in the HVC. **b**, Two-photon image of HVC neurons expressing DA sensors. **c**, Fluorescence changes ($\Delta F/F$) of $GRAB_{DA1h}$ in a HVC neuron of a juvenile in response to songs from a live tutor (red bars). **d**, $\Delta F/F$ aligned to the onset of live tutor songs (grey, individual traces; black, mean). **e**–**h**, $\Delta F/F$ aligned to the onset of song playback (**e**), encounters with a live, non-singing tutor (**f**), encounters with a live female (**g**) and live tutor songs after 6-OHDA injection into the PAG (**h**). **i**, Mean $\Delta F/F$ of HVC neurons. Student's two-sided paired *t*-test; live song, $t_4 = 3.660$, $P = 0.022$; playback, $t_4 = 0.261$, $P = 0.807$; live tutor: $t_4 = 1.092$, $P = 0.336$; live female, $t_4 = 1.589$, $P = 0.187$; live song after 6-OHDA injection into the PAG, $t_7 = 1.122$, $P = 0.324$; $n = 13$ neurons from five birds. Data are mean ± s.e.m.

syllables of the song of the tutor, was variable across different tutor song bouts, and could remain elevated for hundreds of milliseconds after the tutor had stopped singing (Extended Data Fig. 2c–f), suggesting that PAG activity evoked by a singing tutor is not simply auditory in nature. Indeed, playback of the song of an adult finch from a speaker, including that of a recent tutor, failed to evoke activity in the PAG of the juvenile (Fig. 1h, k). Moreover, song playback from a speaker in the presence of an adult female bird failed to activate PAG neurons in tutor-naive juveniles (Extended Data Fig. 2a, b). Therefore, PAG neurons in juvenile males respond strongly and selectively to a live singing tutor and can thus signal the presence of a suitable song model.

These findings raise the possibility that experience of a singing tutor stimulates DA release from PAG terminals in the HVC. We explored this idea by virally expressing a modified dopamine type 2 (D2) receptor in HVC neurons of tutor-naive juvenile males that increases fluorescence upon DA binding (Fig. 2) (AAV2/9-$GRAB_{DA1h}$)[19]. We then head-fixed these juvenile males in the awake state and used two-photon imaging methods[20] to establish that DA levels in the HVC increase in the presence of a singing tutor (Fig. 2c–d, i). By contrast, DA-related changes in fluorescence were not detected in the HVC of the juvenile in response to song playback (Fig. 2e, i), or when the juvenile encountered non-singing adult males or females (Fig. 2f, g, i), paralleling the selective enhancement of PAG activity elicited by a singing tutor. Moreover, ablating DA neurons in the PAG of the pupil with 6-hydroxydopamine (6-OHDA[21]) prevented tutor-evoked DA transients in the HVC of the pupil (Fig. 2h, i), confirming that

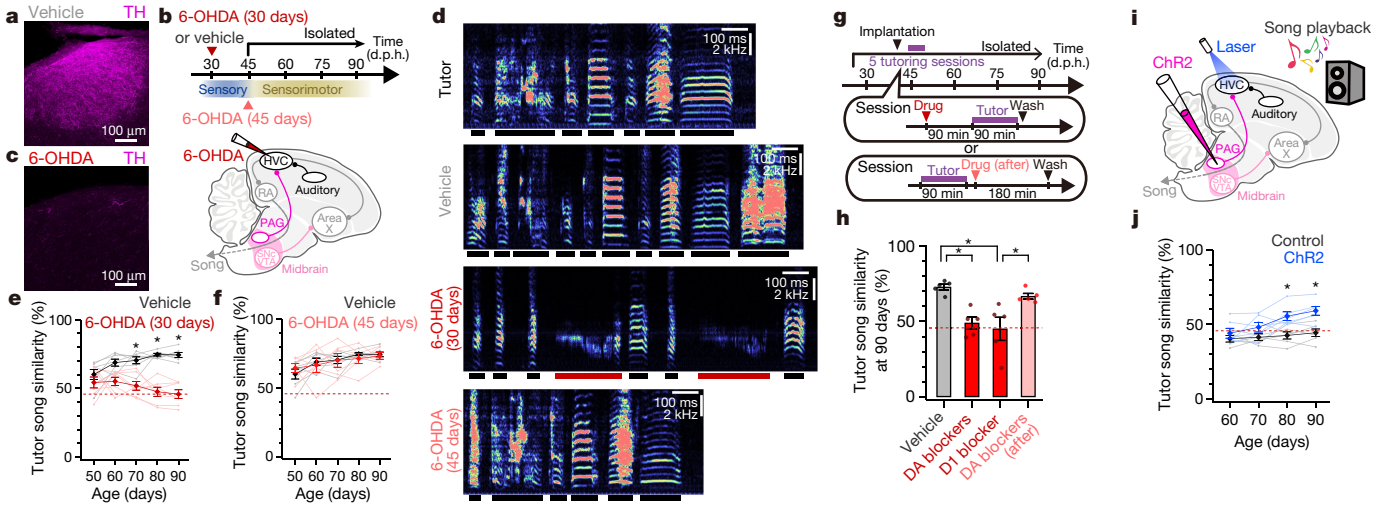

Fig. 3 | Chemical blockade and optogenetic activation of DA signalling in HVC. a, DA fibres in HVC (pseudo-coloured magenta, TH) (approximately 2.4 mm lateral of the midline). **b**, Timeline and schematic of 6-OHDA injection into the HVC. d.p.h., days after hatching. **c**, Loss of DA fibres in the HVC after 6-OHDA injection at 29 days of age, as in **a** (around 2.4 mm lateral of the midline). **d**, From top to bottom, spectrograms of a song from the tutor bird and songs from 90-day-old pupil birds that received injections into the HVC of vehicle, 6-OHDA at around 30 days of age or 6-OHDA at around 45 days of age (red bars denote abnormally long syllables; see Extended Data Fig. 4b, c). **e**, Absence of song copying following injection of 6-OHDA into the HVC at around 30 days of age. Tukey–Kramer test; vehicle, $n = 7$; 6-OHDA, $n = 7$; at 90 days, $P < 0.001$. **f**, Normal levels of song copying were achieved following injection of 6-OHDA into the HVC at around 45 days of age. Tukey–Kramer test; vehicle, $n = 7$ (same birds as in **e**); 6-OHDA at 45 days of age, $n = 6$; at 90 days, $P = 1.000$. **g**, Timeline of DA blocker infusion into the HVC using microdialysis. **h**, Tutor song similarity of 90-day-old pupils that received infusion into the HVC of vehicle during tutoring ($n = 5$), DA blockers during tutoring (Tukey–Kramer test; compared to vehicle, $P = 0.011$, $n = 5$), dopamine type 1(D1-type) receptor blocker during tutoring (Tukey–Kramer test; compared to vehicle, $P < 0.001$, $n = 5$), or DA blockers after tutoring (Tukey–Kramer test; compared to vehicle, $P = 1.000$; $n = 5$). **i**, Schematic of PAG_{HVC} terminal activation paired with song playback. **j**, Song copying is facilitated by pairing playback with PAG_{HVC} terminal activation in tutor-naive juveniles (Tukey–Kramer test; ChR2, $n = 6$; control, $n = 6$; at 90 days, $P = 0.023$). **e**, **f**, **h**, **j**, Horizontal red dashed lines show song similarity between 90-day-old untutored birds to unrelated adults (see Extended Data Fig. 4b, c). Data are mean ± s.e.m.

© 2018 Springer Nature Limited. All rights reserved.

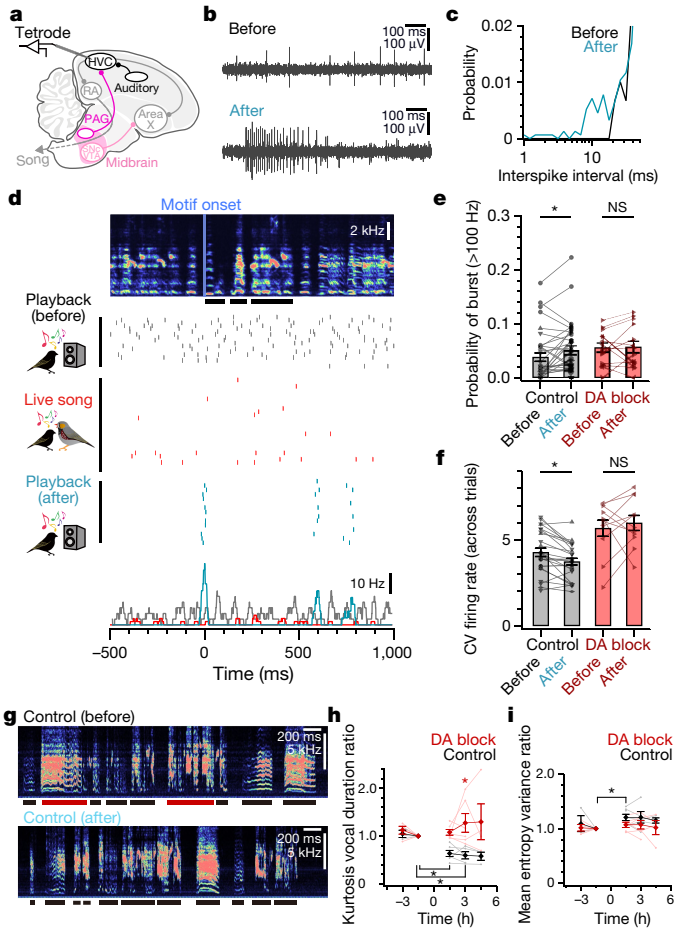

Fig. 4 | Changes in HVC activity and song features after live tutoring. **a**, Schematic of HVC recordings in pupils. **b**, **c**, Spontaneous HVC unit activity (**b**) and the histogram of the interspike intervals before (black) and after (cyan) live tutoring (**c**). **d**, HVC unit activity aligned to tutor song motif onset. Top, averaged spectrogram. Middle, raster. Bottom, mean firing rate across trials. Horizontal bars indicate syllables. **e**, Probability of burst activity (>100 Hz) increased after live tutoring in control juveniles (Student's two-sided paired *t*-test; $t_{34} = 2.490$, $P = 0.018$, $n = 35$ neurons from four birds), but not in juveniles with 6-OHDA injected into the HVC (Student's two-sided paired *t*-test; $t_{13} = 0.774$, $P = 0.453$, $n = 14$ neurons from two birds). NS, not significant. **f**, After live tutoring, coefficients of variance (CV) of firing rate across trials of tutor song playback decreased in control juveniles (Student's two-sided paired *t*-test; $t_{25} = 4.080$, $P < 0.001$, $n = 26$ neurons from four birds), but not in juveniles with 6-OHDA injected into the HVC (Student's two-sided paired *t*-test; $t_{10} = 0.640$, $P = 0.537$, $n = 11$ neurons from two birds). **g**, Spectrograms of juvenile songs before (top) and after (bottom) live tutoring (red bar: long vocalization). **h**, After live tutoring, kurtosis of vocal duration decreased in control juveniles (Student's two-sided paired *t*-test; 1.5 h, $t_5 = 5.563$, Bonferroni-corrected $P = 0.008$, $n = 6$), but not in juveniles with 6-OHDA or DA blockers injected into the HVC (Student's two-sided paired *t*-test; 1.5 h: $t_5 = 1.364$, Bonferroni-corrected $P = 0.692$, $n = 6$). **i**, After live tutoring, mean Wiener entropy variance increased in control juveniles (Student's two-sided paired *t*-test; at 1.5 h: $t_5 = 4.059$, Bonferroni-corrected $P = 0.029$, $n = 6$), but not in juveniles with 6-OHDA or DA blockers injected into HVC (Student's two-sided paired *t*-test; at 1.5 h: $t_5 = 1.432$, Bonferroni-corrected $P = 0.635$, $n = 6$). Juveniles did not sing during tutoring (0–1.5 h; see Extended Data Fig. 9). Data are mean ± s.e.m.

tutor-evoked DA release in the HVC of the pupil largely originates from the PAG.

To explore whether DA signalling in the HVC has a role in song imitation, we used 6-OHDA to lesion DA-releasing fibres in the HVC of juvenile male finches raised continuously with adult male tutors and tracked their song development into adulthood (Fig. 3a–c and Extended Data Fig. 3). Lesions of DA-releasing fibres in HVC made near the onset of the sensitive period for tutor song memorization (30 days after hatching[22]) prevented song copying (Fig. 3d, e) without affecting the overall rate of singing (Extended Data Fig. 4a). As adults, these 6-OHDA-treated birds produced abnormally long and acoustically simple syllables, similar to finches raised in isolation from a tutor[22] (Extended Data Fig. 4b, c). The 6-OHDA lesions made in the HVC in 30-day-old males are permanent and thus could potentially interfere with tutor song memorization (that is, sensory learning), the subsequent phase of song copying (sensorimotor learning), or both. However, 6-OHDA lesions made in the HVC of 45-day-old males, which have had sufficient tutoring experience to enable accurate copying but are just beginning sensorimotor learning[22], did not affect the ability of a juvenile to copy the song of a tutor (Fig. 3d, f).

These findings suggest that DA signalling in the HVC has a role in sensory learning, but we cannot exclude a more general but developmentally restricted (before 45 days of age, for example) role for such signalling. Therefore, we used microdialysis methods[23] to reversibly block DA receptors in the HVC[24] of tutor-naive juvenile males (age: 43.0 ± 4.9 days of age (mean ± s.d.), $n = 5$) while they were housed with a tutor for 1.5 h on five consecutive days, allowing us to better determine whether DA signalling in the HVC is crucial during pupil–tutor interactions, when sensory learning occurs (Fig. 3g, h and Extended Data Fig. 5a–c). Reversibly blocking DA receptors in the HVC during, but not immediately after, tutoring sessions blocked song copying (Fig. 3h and Extended Data Fig. 5b, c), without affecting attentive behaviours of juveniles to tutors or the singing rates of tutors (Extended Data Fig. 5d, e and Supplementary Videos 1, 2). Moreover, reversibly suppressing PAG activity in the pupil with muscimol during daily tutoring sessions also blocked song copying; notably, juveniles in which the PAG was inactivated also failed to orient to their tutors, even though tutors continued singing at normal rates (Extended Data Fig. 5d–h and Supplementary Video 3). Thus, tutor-evoked activation of the PAG of the pupil and concomitant release of DA in the HVC are essential to encoding tutor song experience, and PAG activity may be required for the pupil to attend to a singing tutor.

The current findings do not exclude the possibility that DA signalling at other sites also contributes to sensory learning. One potential site is the basal ganglia region, Area X[11], which receives dopaminergic input from the ventral tegmental area and substantia nigra pars compacta, as well as from a smaller cohort of TH^+ PAG neurons (Extended Data Fig. 1d–g), and where dopamine signalling has a role in sensorimotor learning[25]. Nevertheless, infusing DA receptor blockers into Area X of juvenile males during daily tutoring sessions did not affect song copying (Extended Data Fig. 6). Another potential site is the caudal mesopallium, an auditory forebrain region important for song memory[26,27]. However, blocking DA receptors in the caudal mesopallium of juvenile males during daily tutoring sessions did not block song copying (Extended Data Fig. 5i–k).

These results show that DA release from PAG axon terminals in the HVC (PAG_{HVC} terminals) signals the presence of a suitable model and helps to encode this model in the brain of the pupil. Consequently, artificially activating PAG_{HVC} terminals should compensate for the absence of a live tutor and facilitate vocal copying in response to song playback. To test this hypothesis, we used adeno-associated viruses (AAVs) to express channelrhodopsin-2 (ChR2) bilaterally in the PAG of tutor-naive juvenile males (Fig. 3i, j and Extended Data Fig. 7a–d). Several weeks (33.3 ± 7.4 days (mean ± s.d.), $n = 6$) later, we implanted optical fibres bilaterally over the HVC and optogenetically activated PAG_{HVC} terminals while playing the song of an adult male zebra finch through a speaker. Pairing PAG_{HVC} terminal stimulation with song playback resulted in a significant level of song copying compared to juveniles that had only been exposed to song playback, or to song playback and optical illumination of HVC in the absence of ChR2 (Fig. 3j and Extended Data Fig. 7b; see Methods). Moreover, the combination of song playback and PAG_{HVC} terminal stimulation while infusing DA blockers into the HVC did not lead to song copying in tutor-naive juveniles (Extended Data Fig. 7e–g).

To explore how tutor-evoked DA release from PAG_{HVC} axon terminals alters HVC to drive song imitation, we implanted tetrodes in

© 2018 Springer Nature Limited. All rights reserved.

the HVC of tutor-naive juveniles and recorded neural activity before and after their initial encounters with a singing tutor (Fig. 4a–f). Spontaneous burst firing in HVC neurons increased within 1 h after the initial exposure of the juvenile to a singing tutor (Fig. 4b, c, e), without any change in their mean firing rates (Extended Data Fig. 8d). Because burst firing in HVC is driven by auditory afferent neurons[12], this enhanced burst firing suggests that tutoring rapidly potentiates auditory inputs to the HVC. In fact, brief (35.0 ± 16.8 min (mean $\pm$ s.d.)) experience with a singing tutor led rapidly (around 1 h) to the emergence of temporally precise responses in the HVC of an awake juvenile to tutor song playback (Fig. 4d, f and Extended Data Fig. 8a–c). Furthermore, the mean firing rate of HVC neurons to song playback was unaffected by tutoring (Extended Data Fig. 8e, f), indicating that neural responses in the HVC became more tightly locked to specific features in the tutor song. None of these juveniles ($n = 4$) sang during or for several hours after the tutoring session, and thus these physiological changes were not simply the result of auditory feedback associated with vocal rehearsal. In another set of tutor-naive juvenile males, we found that tutoring rapidly reduced the kurtosis of vocal duration (Fig. 4g, h) and increased the mean entropy variance of the songs of the juveniles (Fig. 4i), two early hallmarks of song copying[7,8]. Notably, blocking DA signalling in the HVC of the pupil with 6-OHDA or DA blockers prevented these physiological and behavioural changes (Fig. 4e, f, h, i).

The discovery that DA neurons in the PAG of the pupil are strongly and selectively activated by a singing tutor parallels emerging evidence that potentially homologous neurons in the mammal can encode social cues, including those related to reward, context or novelty[16,17]. Indeed, the present findings advance a model in which both social cues and the song-related auditory input provided by the singing tutor drive the coincident activation of DA receptors and auditory synapses in the HVC, leading to the rapid emergence of auditory representations of the song of the tutor necessary to song imitation[10,20] (Extended Data Fig. 10). This coincident encoding mechanism could help to ensure that the brain of the pupil selectively forms representations of songs produced by suitable adult tutors, and not of extraneous auditory stimuli. Although DA-dependent modulation of auditory cortical representations has previously been linked to perceptual learning[28], a notable feature of the DA-dependent process of auditory encoding described here is that it occurs in a vocal motor region and rapidly drives vocal imitation. More broadly, DA signalling is enhanced in the motor cortex of primates relative to other mammals[29,30], raising the possibility that augmented DA signalling in motor regions of songbirds and primates reflects a convergent neural architecture for promoting motor imitation in response to social models.

Online content

Any methods, additional references, Nature Research reporting summaries, source data, statements of data availability and associated accession codes are available at https://doi.org/10.1038/s41586-018-0636-7.

Received: 30 March 2018; Accepted: 21 August 2018;
Published online 17 October 2018.

1. Whiten, A. Social learning and culture in child and chimpanzee. *Annu. Rev. Psychol.* **68**, 129–154 (2017).
2. Goldstein, M. H., King, A. P. & West, M. J. Social interaction shapes babbling: testing parallels between birdsong and speech. *Proc. Natl Acad. Sci. USA* **100**, 8030–8035 (2003).
3. Marler, P. & Tamura, M. Culturally transmitted patterns of vocal behavior in sparrows. *Science* **146**, 1483–1486 (1964).
4. Fehér, O., Wang, H., Saar, S., Mitra, P. P. & Tchernichovski, O. De novo establishment of wild-type song culture in the zebra finch. *Nature* **459**, 564–568 (2009).
5. Chen, Y., Matheson, L. E. & Sakata, J. T. Mechanisms underlying the social enhancement of vocal learning in songbirds. *Proc. Natl Acad. Sci. USA* **113**, 6641–6646 (2016).
6. Derégnaucourt, S., Poirier, C., Kant, A. V., Linden, A. V. & Gahr, M. Comparisons of different methods to train a young zebra finch (*Taeniopygia guttata*) to learn a song. *J. Physiol. Paris* **107**, 210–218 (2013).
7. Aronov, D., Andalman, A. S. & Fee, M. S. A specialized forebrain circuit for vocal babbling in the juvenile songbird. *Science* **320**, 630–634 (2008).
8. Derégnaucourt, S., Mitra, P. P., Fehér, O., Pytte, C. & Tchernichovski, O. How sleep affects the developmental learning of bird song. *Nature* **433**, 710–716 (2005).
9. Nottebohm, F., Stokes, T. M. & Leonard, C. M. Central control of song in the canary, *Serinus canarius*. *J. Comp. Neurol.* **165**, 457–486 (1976).
10. Roberts, T. F., Gobes, S. M., Murugan, M., Ölveczky, B. P. & Mooney, R. Motor circuits are required to encode a sensory model for imitative learning. *Nat. Neurosci.* **15**, 1454–1459 (2012).
11. Fortune, E. S. & Margoliash, D. Parallel pathways and convergence onto HVc and adjacent neostriatum of adult zebra finches (*Taeniopygia guttata*). *J. Comp. Neurol.* **360**, 413–441 (1995).
12. Coleman, M. J. & Mooney, R. Synaptic transformations underlying highly selective auditory representations of learned birdsong. *J. Neurosci.* **24**, 7251–7265 (2004).
13. Appeltants, D., Absil, P., Balthazart, J. & Ball, G. F. Identification of the origin of catecholaminergic inputs to HVc in canaries by retrograde tract tracing combined with tyrosine hydroxylase immunocytochemistry. *J. Chem. Neuroanat.* **18**, 117–133 (2000).
14. Hamaguchi, K. & Mooney, R. Recurrent interactions between the input and output of a songbird cortico-basal ganglia pathway are implicated in vocal sequence variability. *J. Neurosci.* **32**, 11671–11687 (2012).
15. Kingsbury, M. A., Kelly, A. M., Schrock, S. E. & Goodson, J. L. Mammal-like organization of the avian midbrain central gray and a reappraisal of the intercollicular nucleus. *PLoS ONE* **6**, e20720 (2011).
16. Cho, J. R. et al. Dorsal raphe dopamine neurons modulate arousal and promote wakefulness by salient stimuli. *Neuron* **94**, 1205–1219 (2017).
17. Matthews, G. A. et al. Dorsal raphe dopamine neurons represent the experience of social isolation. *Cell* **164**, 617–631 (2016).
18. Flores, J. A., Galan-Rodriguez, B., Ramiro-Fuentes, S. & Fernandez-Espejo, E. Role for dopamine neurons of the rostral linear nucleus and periaqueductal gray in the rewarding and sensitizing properties of heroin. *Neuropsychopharmacology* **31**, 1475–1488 (2006).
19. Sun, F. et al. A genetically encoded fluorescent sensor enables rapid and specific detection of dopamine in flies, fish, and mice. *Cell* **174**, 481–496 (2018).
20. Roberts, T. F., Tschida, K. A., Klein, M. E. & Mooney, R. Rapid spine stabilization and synaptic enhancement at the onset of behavioural learning. *Nature* **463**, 948–952 (2010).
21. Ungerstedt, U. & Arbuthnott, G. W. Quantitative recording of rotational behavior in rats after 6-hydroxy-dopamine lesions of the nigrostriatal dopamine system. *Brain Res.* **24**, 485–493 (1970).
22. Eales, L. A. Song learning in zebra finches: some effects of song model availability on what is learnt and when. *Anim. Behav.* **33**, 1293–1300 (1985).
23. Tanaka, M., Singh Alvarado, J., Murugan, M. & Mooney, R. Focal expression of mutant huntingtin in the songbird basal ganglia disrupts cortico-basal ganglia networks and vocal sequences. *Proc. Natl Acad. Sci. USA* **113**, E1720–E1727 (2016).
24. Kubikova, L., Wada, K. & Jarvis, E. D. Dopamine receptors in a songbird brain. *J. Comp. Neurol.* **518**, 741–769 (2010).
25. Hisey, E., Kearney, M. G. & Mooney, R. A common neural circuit mechanism for internally guided and externally reinforced forms of motor learning. *Nat. Neurosci.* **21**, 589–597 (2018).
26. Roberts, T. F. et al. Identification of a motor-to-auditory pathway important for vocal learning. *Nat. Neurosci.* **20**, 978–986 (2017).
27. London, S. E. & Clayton, D. F. Functional identification of sensory mechanisms required for developmental song learning. *Nat. Neurosci.* **11**, 579–586 (2008).
28. Bao, S., Chan, V. T. & Merzenich, M. M. Cortical remodelling induced by activity of ventral tegmental dopamine neurons. *Nature* **412**, 79–83 (2001).
29. Berger, B., Gaspar, P. & Verney, C. Dopaminergic innervation of the cerebral cortex: unexpected differences between rodents and primates. *Trends Neurosci.* **14**, 21–27 (1991).
30. Williams, S. M. & Goldman-Rakic, P. S. Widespread origin of the primate mesofrontal dopamine system. *Cereb. Cortex* **8**, 321–345 (1998).

Acknowledgements We thank J. Hatfield for constructing AAV2/9-CAG-GRAB$_{DA1h}$; S. Nowicki, S. Peters, C. Sturdy, F. Wang and S. Soderling for critical discussion and for reading earlier versions of this manuscript. This work was supported by JSPS Postdoctoral Fellowship for Research Abroad (M.T.), the National Basic Research Program of China 973 Program Grant 2015CB856402 (Y.L.), the American BRAIN Initiative project 1U01NS103558-01 (Y.L.), NIH Grant 1R01-NS-099288 (R.M.) and NSF IOS-1354962 (R.M.).

Reviewer information *Nature* thanks O. Tchernichovski, L. Zweifel and the other anonymous reviewer(s) for their contribution to the peer review of this work.

Author contributions M.T. and R.M. designed experiments. F.S. and Y.L. developed DA sensors. M.T. performed experiments and analysed data. M.T. and R.M. wrote the manuscript.

Competing interests F.S. and Y.L. have filed patent applications of which the value might be affected by this publication.

Additional information
Extended data is available for this paper at https://doi.org/10.1038/s41586-018-0636-7.
Supplementary information is available for this paper at https://doi.org/10.1038/s41586-018-0636-7.
Reprints and permissions information is available at http://www.nature.com/reprints.
Correspondence and requests for materials should be addressed to R.M.
Publisher's note: Springer Nature remains neutral with regard to jurisdictional claims in published maps and institutional affiliations.

© 2018 Springer Nature Limited. All rights reserved.

METHODS

Data reporting. No statistical methods were used to predetermine sample size. The experiments were not randomized and the investigators were not blinded to allocation during experiments and outcome assessment.

Animal model. Juvenile male (15–90 days old), adult male (>200 days old) and adult female (>200 days old) zebra finches (*Taeniopygia guttata*) were obtained from the Duke University Medical Center breeding facility. All experimental procedures were in accordance with the NIH guidelines and approved by the Duke University Medical Center Animal Care and Use Committee. Birds were kept under a 14:10-h light:dark cycle with free access to food and water. Data were collected from 96 birds (Supplementary Table).

Song analysis. Songs were automatically recorded with Sound Analysis Pro (SAP2011)[31] in a soundproof box. Vocalizations of >10 ms were detected by thresholding of the recorded sounds. Imitation of the tutor song was quantified as percentage of similarity (asymmetrical similarity) between the song motifs from pupil birds and their tutors using SAP2011[31] with default parameters for zebra finches, and reported as tutor song similarity. First, the song motif (a stereotyped sequence of syllables constituting an adult zebra finch song) of each bird was determined as the most frequently observed syllable sequence. Then, the percentage of similarity was calculated for representative song motifs randomly chosen from pupils and their tutor, and averaged across ≥10 comparisons to report as tutor song similarity. For immature subsongs that do not have a stereotyped song motif, we used a randomly chosen part of the subsongs with a duration that was similar to the tutor song motif for calculating the percentage of similarity. For isolated birds in Extended Data Fig. 4c, the percentage of similarity was calculated between the song motifs from isolated birds and unrelated, normally raised adult zebra finches. A song bout was detected as successive vocalizations with ≥3 syllables (to exclude call bouts) separated by an interbout interval of >400 ms. Kurtosis of vocal duration and Wiener entropy variance were calculated based on all of the song bouts in each 90-min time window.

Tutoring of juvenile birds. Juvenile birds were raised by their parents with their siblings until around 45 days old in experiments depicted in Fig. 3a–f. Otherwise, juvenile birds were separated from their parents and siblings at 15–30 days of age (that is, tutor-naive juveniles), and encountered an unfamiliar adult male (tutor) only during tutoring sessions. During a tutoring session, a juvenile bird and tutor were separated by a plastic grating or transparent glass, so they could acoustically and visually interact but direct physical interactions were prevented. The tutor was either manually introduced into the neighbouring chamber by an experimenter, or presented through an electric glass for which the transparency could be remotely controlled. Attention of juvenile birds to the tutor was quantified as the time that juvenile birds were awake and near the tutor without foraging, drinking, preening or singing, and normalized to the total time of observation (>5 min) during tutoring sessions. Untutored isolated birds depicted in Extended Data Fig. 4b, c were kept isolated from adult males until 90 days of age.

General surgery. Detailed procedures of surgery were previously provided[23]. In brief, juvenile birds were anaesthetized with 2% isoflurane inhalation and placed on a custom stereotaxic apparatus with a heat blanket. Target cites for injection and implantation were determined by stereotaxic coordinates and multiunit activity. Stereotaxic coordinates, measured from the bifurcation of the midsagittal sinus, were 0.0 mm rostral, 2.4 mm lateral and 0.5 mm ventral for HVC; 3.4 mm rostral, 0.5 mm lateral and 6.3 mm ventral (head angle of 58°) for PAG; 5.8 mm rostral, 1.6 mm lateral and 3.0 mm ventral (head angle of 40°) for Area X; and 1.3 mm rostral, 1.2 mm lateral and 0.5 mm ventral for the caudal mesopallium (CM). Reagents or viruses were injected using Nanoject-II (Drummond Scientific). Viral injections were performed bilaterally with a volume of 483–966 nl per hemisphere. Viruses were obtained from the Penn Vector Core (Pennsylvania, USA), UNC Vector Core (Chapel Hill, USA), Janelia Virus Service Facility (Ashburn, USA), and Vigene Biosciences (Rockville, USA). Experiments were performed >30 days after the viral injection. Birds with unsuccessful injection or implantation were discarded from the analysis.

Injection of 6-OHDA. Juvenile birds received bilateral injection of 200–450 nl 6-OHDA solution into the HVC at either around 30 days of age (mean ± s.d.: 30.1 ± 4.2 days of age; range: 25–34 days of age; $n = 7$) or around 45 days of age (mean ± s.d.: 44.5 ± 3.0 days of age; range: 39–47 days of age; $n = 6$). The solution was PBS-based and included 5–20 mM 6-OHDA hydrochloride (Santa Cruz, sc-203482), 2–10 mM L-ascorbic acid (Millipore/Sigma, A92902), and 1 μM desipramine hydrochloride (Tocris, 3067), which was included as an inhibitor for noradrenaline and serotonin transporters to protect noradrenergic and serotonergic neuron terminals at the injection site. Control birds received an injection of PBS with 2–10 mM ascorbic acid and 1 μM desipramine at around 30 days of age (mean ± s.d.: 29.3 ± 3.6 days of age; range: 22–32 days of age; $n = 7$). Drugs were dissolved into PBS immediately before injection in place of equimolar NaCl (working solution: around 300 mOsm, pH 7.3). After injection, birds were returned to their original home cage until approximately 45 days of age when they were isolated in a soundproof box until 90 days of age.

Microdialysis infusion of drugs. Tutor-naive juveniles (around 45 days of age; mean ± s.d.: 43.8 ± 5.5 days of age; range: 32–57 days of age; $n = 34$) received bilateral implantation of a microdialysis probe. After 1–3 days of implantation (mean ± s.d.: 45.5 ± 5.8 days of age; range: 33–60 days of age; $n = 34$), tutoring sessions were conducted for five consecutive days. Each tutoring session consisted of 90-min tutor presentation. Drug was infused into the target area (HVC, Area X, CM or PAG) either 90 min before or immediately after the tutor presentation, and washed with saline 180 min after the injection (Fig. 3g). The tutor bird typically sang >30 motifs in a session (see Extended Data Fig. 5e). For a session in which the tutor did not sing any song, an additional tutoring session was conducted on the next day. As a blocker for D1- and D2-type receptors, 5 mM R(+)-SCH-23390 hydrochloride (Millipore/Sigma, D054) and 5 mM S-(−)-sulpiride (Tocris, 0895) were respectively used and dissolved into saline. To inactivate PAG, 2.5 mM muscimol (Millipore/Sigma, M-1523) dissolved into saline was infused into the PAG.

Histology and imaging. Birds were deeply anaesthetized with intramuscular injection of 20 μl euthasol (Virbac) and transcardially perfused with PBS, followed by perfusion with 4% (wt/vol) paraformaldehyde (PFA) in PBS. The removed brain was post-fixed and cryoprotected with 30% (wt/vol) sucrose and 4% (wt/vol) PFA in PBS overnight. Frozen sagittal sections (thickness of 50 μm) were prepared with a sledge microtome (Reichert) and collected in PBS. For immunohistochemistry, sections were washed twice in PBS, permeabilized with 0.3% Triton X-100 in PBS (PBST) for 1 h, blocked with 10% Blocking One Histo (06349-64, Nacalai Tesque) in PBST for 1 h, and incubated with rabbit primary antibody against TH (1:500, AB152; Millipore/Sigma) or rabbit primary antibody against dopamine beta-hydroxylase (DBH) (1:2,000, 22806; ImmunoStar) in PBST with 10% Blocking One Histo at 4 °C overnight. Then, sections were washed three times in PBST and incubated with anti-rabbit secondary antibody (1:500; Jackson ImmunoResearch) in PBST at room temperature for 1 h, followed by three washes in PBS. Sections were coverslipped with Fluoromount-G (SouthernBiotech), and then imaged with a confocal microscope (SP8; Leica) through a 20× objective lens controlled by LAS X software (Leica). To label PAG neurons that project to the HVC or Area X, dextran Alexa Fluor 488 (D-22910; ThermoFisher) was injected into the HVC (age: mean ± s.d.: 35.3 ± 7.0 days of age; range: 28–42 days of age; $n = 3$) or Area X (age: mean ± sd: 47.7 ± 15.3 days of age; range: 36–65 days of age; $n = 3$) of juvenile birds 4–7 days before perfusion. Retrogradely labelled neurons were manually counted in PAG and VTA/SNc, each of which was densely packed with TH^+ neurons. Images are shown as maximum-projected images of sagittal sections. To quantify TH^+ fibres in the HVC, TH^+ fibres in HVC shelf/nidopallium caudolateral (NCL), and DBH^+ fibres in the HVC, the fibre density was calculated in >0.04 mm^2 areas from each region as the fraction of areas with fluorescence higher than mean + 10 s.d. of the background fluorescence. For analysis of HVC shelf/NCL, a >0.04 mm^2 region located approximately 0.6 mm ventral of the HVC was manually selected.

Two-photon imaging and analysis. Viruses encoding DA sensors (AAV2/9-hSyn-$GRAB_{DA1h}$ or AAV2/9-CAG-$GRAB_{DA1h}$), developed in the Y.L. laboratory[19], were injected into the HVC of tutor-naive juveniles (approximately 30 days old, mean ± s.d.: 32.6 ± 5.3 days of age; range: 25–39 days of age; $n = 5$), and the HVC was imaged after implantation of a head-post and cranial window >30 days later (mean ± s.d.: 66.6 ± 6.0 days of age; range: 60–73 days of age; $n = 5$). To ablate DA-releasing PAG neurons, 200 nl 6-OHDA solution (10 mM 6-OHDA, 10 mM L-ascorbic acid, and 1 μM desipramine hydrochloride) was injected into PAG two days before imaging. Images were collected at 15.5 Hz with a resonant-scanning two-photon microscope (Neurolabware) that applies a mode-locked titanium sapphire laser (Mai Tai DeepSee) at 920 nm through a 16× objective lens (0.8 NA water immersion, Nikon). The objective lens was covered with black cloth to prevent room light from being detected by the photomultipliers. During imaging, a head-fixed bird in a dim room experienced playback of an adult zebra finch (tutor) song bout (3 s; seven introductory notes and three motifs comprising five syllables), encounters with an adult male tutor, encounters with an adult female bird, and a singing tutor with a randomized order. Images were acquired >10 trials for each condition, and regions of interest (ROIs) were automatically or manually selected after image alignment with MATLAB programs (Scanbox). After subtraction of background fluorescence in an annular region surrounding each ROI, signals were calculated as mean fluorescence within each ROI. Then, the $\Delta F/F$ of the ROI (%) was calculated for each trial as $100 \times (F(t) - F_0)/F_0$, where $F(t)$ was a time series of ROI signals, and F_0 was the average of baseline ROI signals for the 5-s period just before the onset of stimulus presentation. Mean $\Delta F/F$ was calculated for the 5-s period after the onset of stimulus presentation, and averaged across trials in each condition.

Optogenetics. Tutor-naive juvenile birds received an injection of AAV2/9-CAG-ChR2-mCherry, AAV2/1-CAG-ChR2-mCherry or AAV2/9-CAG-NRX-ChR2-YFP into the PAG at around 35 days of age (mean ± s.d.: 34.0 ± 4.8 days of age; range: 30–40 days of age; $n = 9$). A laser was bilaterally applied through optic fibres (core: 200 μm; Thorlabs) implanted into the HVC. Juvenile birds received a tutoring session

© 2018 Springer Nature Limited. All rights reserved.

per day for five consecutive days starting at around 60–70 days of age (mean ± s.d.: 64.0 ± 4.9 days of age; range: 61–71 days of age; $n = 9$). In each tutoring session, a juvenile bird experienced playback of a song bout (mean amplitude: 70 dB sound pressure level, seven introductory notes and three motifs comprising five syllables) 10 times (30 motifs) within 30 min. To block DA signalling in the HVC, DA blockers were infused into the HVC with microdialysis probes 90 min before the tutoring session, and washed with saline immediately after the tutoring session ($n = 3$). Experimental birds received repetitive laser stimulation (10 ms; 20 Hz) throughout the playback. Control birds consisted of a group that received an injection of viruses encoding GFP and implantation of optic fibres ($n = 2$, scAAV2/9-CMV-GFP or AAV2/9-CAG-GFP) at around 35 days of age (mean ± s.d.: 36.5 ± 6.4 days of age; range: 32–41 days of age; $n = 2$), a group that did not receive viral injection but implantation of optic fibres ($n = 2$), and a group that did not receive injection, implantation or laser stimulation ($n = 2$). These groups listened to playback in the same way as experimental birds (age: mean ± s.d.: 58.5 ± 8.5 days of age; range: 54–73 days of age; $n = 6$), and were analysed together since we did not find any significant differences in learning abilities between these groups.

Chronic recording from the PAG and HVC. Tetrodes (A2x2-tet-3/10mm-150-150-121, NeuroNexus) were implanted into the HVC or the PAG of tutor-naive juveniles (age: mean ± s.d.: 51.3 ± 13.4 days of age; range: 27–71 days of age; $n = 11$). Birds were habituated to a dummy probe (1.5–2 g) on the head for approximately seven days before the implantation. Data were collected with a universal serial bus (USB) interface board (RHD2000; Intan Technologies) after band-pass filtering (0.2–10 kHz) and sampling at 30 kHz with a small amplifier board (RHD2132 16-Channel; Intan Technologies) on the head of the bird. Unit activity was sorted in a semi-automated fashion with custom C++ software using a support vector machine algorithm (M.T.). Unit activity with a mean amplitude >3 s.d. of noise was used for subsequent analyses. Recording of song-related activity was triggered by xpctarget in MATLAB (MathWorks). To block DA signalling in the HVC, juvenile birds received an injection of 6-OHDA into the HVC 2–5 days before tetrode recording from the same HVC. The mean firing rate of PAG neurons was calculated for >10 trials with >0.5 s after the onset of singing or song playback and 5 s after presentation of a male or female bird, and averaged after normalization with mean spontaneous firing rate calculated for >10 s before the presentation of stimuli. Probability of burst activity in HVC neurons was calculated for >300 s spontaneous activity before and after exposure to a live tutor. Coefficients of variance of the firing rate across trials of HVC neurons were calculated for 50-ms bins with a hop size 1 ms across >15 trials, and reported as the mean of the coefficients of variance of the firing rate from all the bins in the motif (>0.5 s) if the mean firing rate during playback was >0.05 Hz. For data analysis, Igor Pro (WaveMetrics), MATLAB and Microsoft Excel were used.

Statistics. Data are shown as mean ± s.e.m., unless otherwise noted. Two-way ANOVAs were performed in MATLAB to examine the significance of the main effect of 6-OHDA ($F_{2,85} = 53.10$, $P < 0.001$; Fig. 3e–f), DA blockers on the HVC, DA blockers on the CM and muscimol on PAG ($F_{5,99} = 23.17$, $P < 0.001$; Fig. 3h and Extended Data Fig. 5c, h, k), DA blockers on Area X ($F_{1,30} = 0.22$, $P = 0.640$; Extended Data Fig. 6c), optogenetic activation of PAG terminals in the HVC ($F_{2,47} = 16.61$, $P < 0.001$; Fig. 3j and Extended Data Fig. 7f), followed by a post hoc Tukey–Kramer test to report significant differences between conditions at each age window. To examine the different proportion of labelled neurons in the PAG and VTA/SNc, χ^2 tests were performed. Two-way ANOVAs were performed in MATLAB to examine significance of the main effect of blockage of DA signalling on kurtosis syllable duration ($F_{1,39} = 19.69$, $P < 0.001$; Fig. 4h), entropy variance ($F_{1,39} = 4.84$, $P = 0.034$; Fig. 4i) and song rate ($F_{1,39} = 0.16$, $P = 0.691$; Extended Data Fig. 9), followed by a Tukey–Kramer test to report significant differences between conditions at each time window and by a Student's two-sided paired *t*-test with Bonferroni correction to report significant differences between before and after exposure to tutor songs. One-way ANOVAs were performed in MATLAB to examine the main effect of different conditions in Fig. 1k and Extended Data Fig. 2b ($F_{4,93} = 6.84$, $P < 0.001$), Fig. 2i ($F_{4,23} = 10.31$, $P < 0.001$), Extended Data Fig. 3c ($F_{2,12} = 13.42$, $P < 0.001$), Extended Data Fig. 3d ($F_{2,12} = 0.14$, $P = 0.870$), Extended Data Fig. 4a ($F_{2,17} = 0.28$, $P = 0.757$), Extended Data Fig. 5d ($F_{2,7} = 30.40$, $P < 0.001$), and Extended Data Fig. 5e ($F_{2,10} = 0.78$, $P = 0.486$), each followed by a Tukey–Kramer test to report significant differences between conditions. In other analyses, Student's paired *t*-tests (Figs. 1k, 2i, 4h, i and Extended Data Figs. 2b, 8d–f) or Student's unpaired *t*-tests (Extended Data Figs. 3e, 4c) were performed in Microsoft Excel. Multiple data from a bird are indicated with the same markers in Fig. 1c, g, k, 2i, 4e, f and Extended Data Figs. 1b, c, e–g, 2b, 3c–e, 8d–f. Statistical tests were performed two-sided. Asterisks show $P < 0.050$.

Reporting summary. Further information on research design is available in the Nature Research Reporting Summary linked to this paper.

Code availability. Custom code or software is available from the corresponding author upon reasonable request.

Data availability

The datasets generated and analysed during the current study are available from the corresponding author upon reasonable request.

31. Tchernichovski, O., Nottebohm, F., Ho, C. E., Pesaran, B. & Mitra, P. P. A procedure for an automated measurement of song similarity. *Anim. Behav.* **59**, 1167–1176 (2000).

© 2018 Springer Nature Limited. All rights reserved.

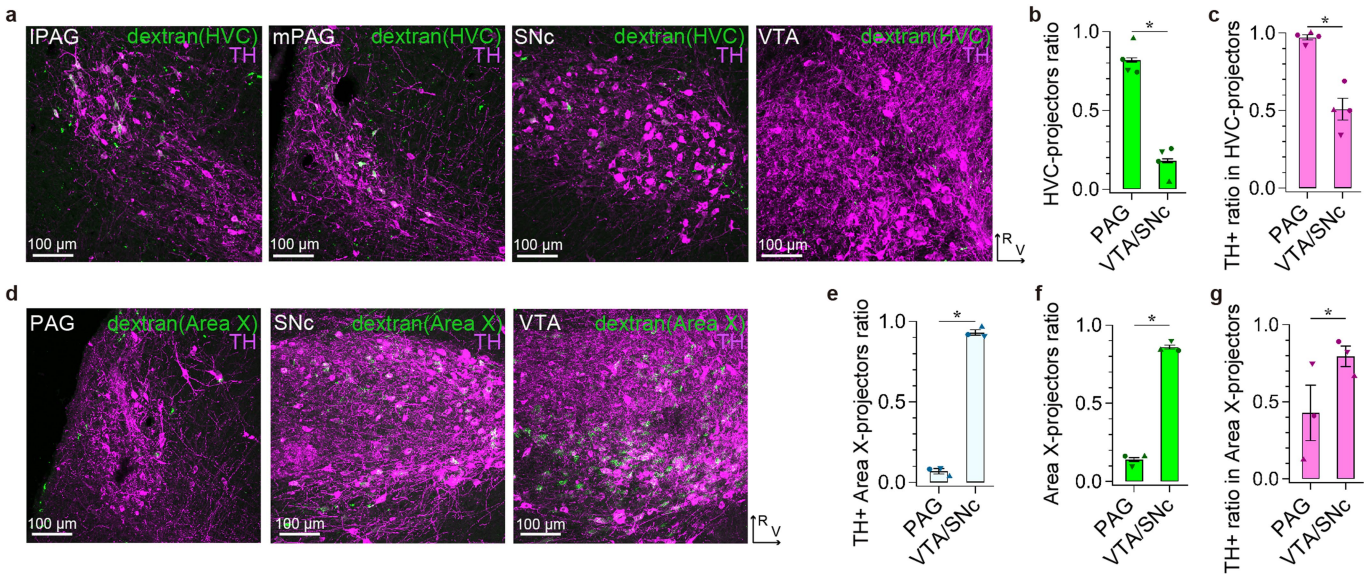

Extended Data Fig. 1 | Distribution of HVC-projecting neurons and Area X-projecting neurons in the midbrain. a, From left to right, a maximum-projected image of serial sagittal sections visualized with a confocal microscope, showing a lateral part of the PAG (lPAG) (approximately 1.0 mm lateral of the midline), a medial part of the PAG (mPAG, approximately 0.2 mm lateral of the midline), SNc (approximately 1.2 mm lateral of the midline) and VTA (approximately 0.2 mm lateral of the midline), each of which was labelled with dextran injected into the HVC (green) and an antibody against TH (pseudo-coloured magenta). Similar results were obtained in four independently repeated experiments. R, rostral; V, ventral. **b**, Proportion of HVC-projecting neurons in the PAG and VTA/SNc. χ^2 test; $\chi_1^2 = 406.54$, $P < 0.001$, $n = 4$ hemispheres from three birds. **c**, Proportion of TH^+ neurons in HVC-projecting neuron subsets in the PAG and the VTA/SNc. χ^2 test; $\chi_1^2 = 204.62$, $P < 0.001$, $n = 4$ hemispheres from three birds. **d**, From left to right, a maximum-projected image of serial sagittal sections visualized with a confocal microscope, showing the PAG (approximately 0.6 mm lateral of the midline), SNc (approximately 0.6 mm lateral of the midline) and VTA (approximately 0.2 mm lateral), each of which was labelled with dextran injected into Area X (green) and an antibody against TH (pseudo-coloured magenta). Similar results were obtained in three independently repeated experiments. **e**, Proportion of double-labelled neurons (dextran and TH) in PAG and SNc/VTA in birds that received injection of dextran into Area X. χ^2 test; $\chi_1^2 = 493.92$, $P < 0.001$, $n = 3$ hemispheres from three birds. **f**, Proportion of Area-X-projecting neurons in the PAG and VTA/SNc. χ^2 test; $\chi_1^2 = 472.07$, $P < 0.001$, $n = 3$ hemispheres from three birds. **g**, Proportion of TH^+ neurons in Area-X-projecting neuron subsets in the PAG and VTA/SNc. χ^2 test; $\chi_1^2 = 55.14$, $P < 0.001$, $n = 3$ hemispheres from three birds. Data are mean ± s.e.m.

© 2018 Springer Nature Limited. All rights reserved.

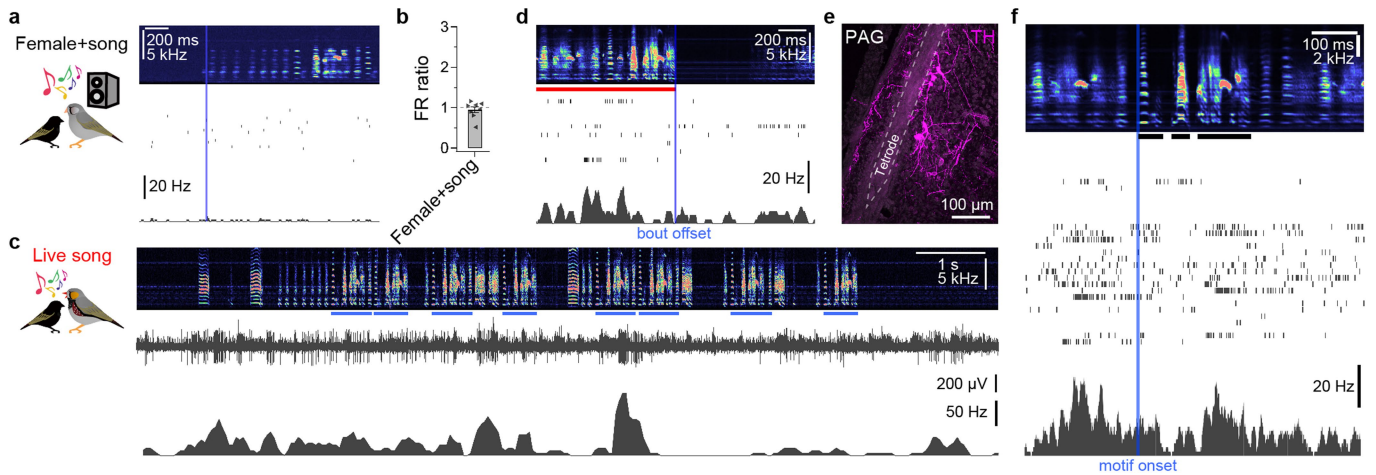

Extended Data Fig. 2 | Juvenile male PAG activity in response to song playback in the presence of a female bird and live songs of a male bird. **a**, Tutor-naive juvenile male finch PAG activity aligned to the onset of 35 presentations of song playback in the presence of an adult female bird. Top, averaged sound spectrogram. Middle, spike raster plot. Bottom, mean firing rate. Blue vertical bar marks song onset. **b**, Mean firing rate of neurons in the juvenile PAG during presentation of song playback in the presence of an adult female bird, normalized to baseline firing rate. Student's two-sided paired *t*-test; $t_7 = 0.620$, $P = 0.555$; $n = 8$ neurons from two birds. **c**, Neuron activity in the PAG of the juvenile during a live tutor song bout. Top, sound spectrogram. Middle, voltage recording. Bottom, firing rate. Blue bar, song motif. **d**, Juvenile PAG unit activity aligned to the offset (blue vertical bar) of the song bouts of a live tutor (red bar, live song), shown as in **a**. **e**, A maximum-projected image of serial sagittal sections visualized with a confocal microscope, showing the site of tetrode recordings in the PAG (around 0.8 mm lateral of the midline). **f**, Juvenile PAG unit activity aligned to the onset (blue vertical bar) of the song motifs (syllables denoted by black horizontal bars) of a live tutor, shown as in **a**. Note that the tutor often sings multiple motifs within a single bout, thus some motifs precede (and follow) the alignment time. Data are mean ± s.e.m.

© 2018 Springer Nature Limited. All rights reserved.

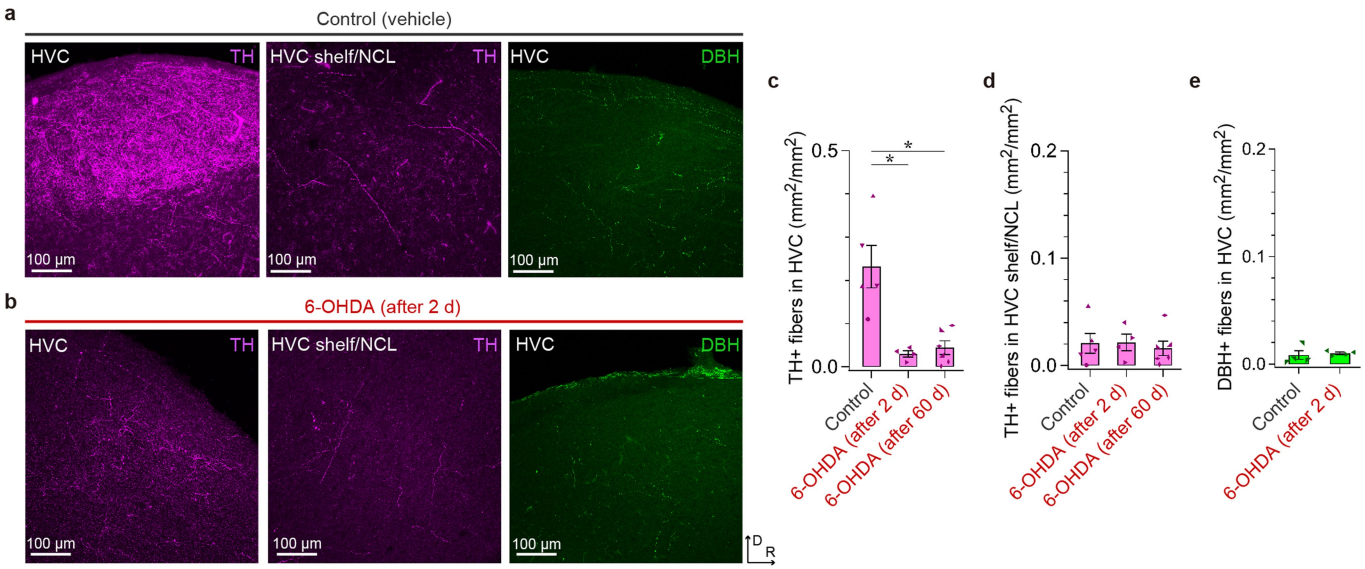

Extended Data Fig. 3 | Effects of 6-OHDA injection into the HVC on DA fibres in the HVC and surrounding regions and on noradrenergic/adrenergic fibres in the HVC. a, From left to right, a maximum-projected image of serial sagittal sections visualized with a confocal microscope, showing the HVC with TH immunolabelling (approximately 2.4 mm lateral of the midline), the HVC shelf and nidopallium caudolateral (NCL) just ventral of the HVC with TH immunolabelling (approximately 2.4 mm lateral of the midline), and the HVC with DBH immunolabelling (approximately 2.4 mm lateral of the midline) in control birds, which received an injection of vehicle into the HVC. Similar results were obtained in five independently repeated experiments (orientation is similar to **b**). **b**, From left to right, a maximum-projected image of serial sagittal sections visualized with a confocal microscope, showing the HVC with TH immunolabelling (approximately 2.4 mm lateral of the midline), the HVC shelf and NCL just ventral to the HVC with TH immunolabelling (approximately 2.4 mm lateral of the midline), and the HVC with DBH immunolabelling (approximately 2.4 mm lateral of the midline) in birds that received an injection of 6-OHDA into the HVC two days before tissue fixation. Similar results were obtained in four independently repeated experiments. D, dorsal; R, rostral. **c**, Density of TH^+ fibres in the HVC of control birds ($n = 5$ hemispheres from three birds) was higher than the density in birds that received injections of 6-OHDA two days before fixation (Tukey–Kramer test; $P = 0.002$; $n = 4$ hemispheres from two birds), and also higher than the density in birds that received injections of 6-OHDA around 60 days before fixation, as in Fig. 3b, c (Tukey–Kramer test; $P = 0.002$; $n = 6$ hemispheres from four birds). **d**, Density of TH^+ fibres in the HVC shelf and NCL in control birds ($n = 5$ hemispheres from three birds), birds that received an injection of 6-OHDA two days before fixation ($n = 4$ hemispheres from two birds), and birds that received an injection of 6-OHDA around 60 days before fixation, as in Fig. 3b, c ($n = 6$ hemispheres from four birds). **e**, Density of DBH^+ fibres in HVC in control birds ($n = 4$ hemispheres from two birds) and birds that received an injection of 6-OHDA two days before injection ($n = 4$ hemispheres from two birds) was not significantly different. Student's two-sided unpaired t-test; $t_7 = 0.379$, $P = 0.716$. Data are mean ± s.e.m.

© 2018 Springer Nature Limited. All rights reserved.

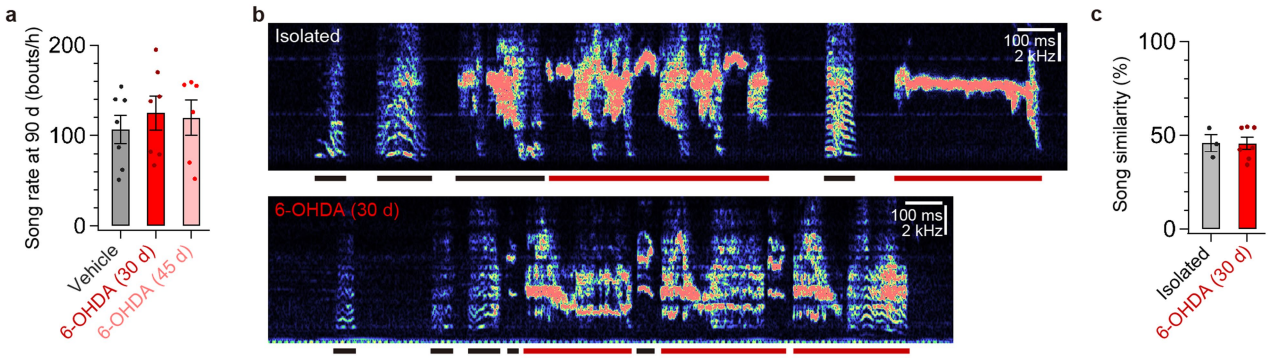

Extended Data Fig. 4 | Ablation of DA terminals in the HVC did not affect song rate but decreased song imitation to the level of birds raised in isolation from a tutor. a, The song rates of 90-day-old birds that received an injection of vehicle ($n = 7$), 6-OHDA at around 30 days of age ($n = 7$), and 6-OHDA at around 45 days of age ($n = 6$) were not significantly different. One-way ANOVA; $F_{2,17} = 0.283$, $P = 0.757$. **b**, Spectrograms from a 90-day-old bird that was raised in isolation from a tutor (top) and from a 90-day-old bird that was normally tutored but received an injection of 6-OHDA into the HVC at 30 days of age (bottom). **c**, Similarity of 90-day-old untutored (Isolated) adult zebra finch songs to songs of unrelated adult zebra finches that had been normally tutored ($n = 3$) was not significantly different from tutor song similarity of 90-day-old pupils that received an injection of 6-OHDA into the HVC at approximately 30 days of age ($n = 7$; Student's two-sided unpaired t-test; $t_9 = 0.013$, $P = 0.990$), but was significantly different from tutor song similarity of 90-day-old pupils that received an injection of vehicle at around 30 days of age ($n = 7$; Student's two-sided unpaired t-test; $t_9 = 3.028$, $P = 0.014$), or from tutor song similarity of 90-day-old pupils that received an injection of 6-OHDA into the HVC at around 45 days of age ($n = 6$; Student's two-sided unpaired t-test; $t_8 = 3.314$, $P = 0.011$). The song data from birds injected with 6-OHDA into the HVC at around 30 days of age is the same as in Fig. 3e; song similarity data from birds injected into the HVC with vehicle at around 30 days of age or 6-OHDA at around 45 days of age are not shown here but are shown in Fig. 3f. Data are mean ± s.e.m.

© 2018 Springer Nature Limited. All rights reserved.

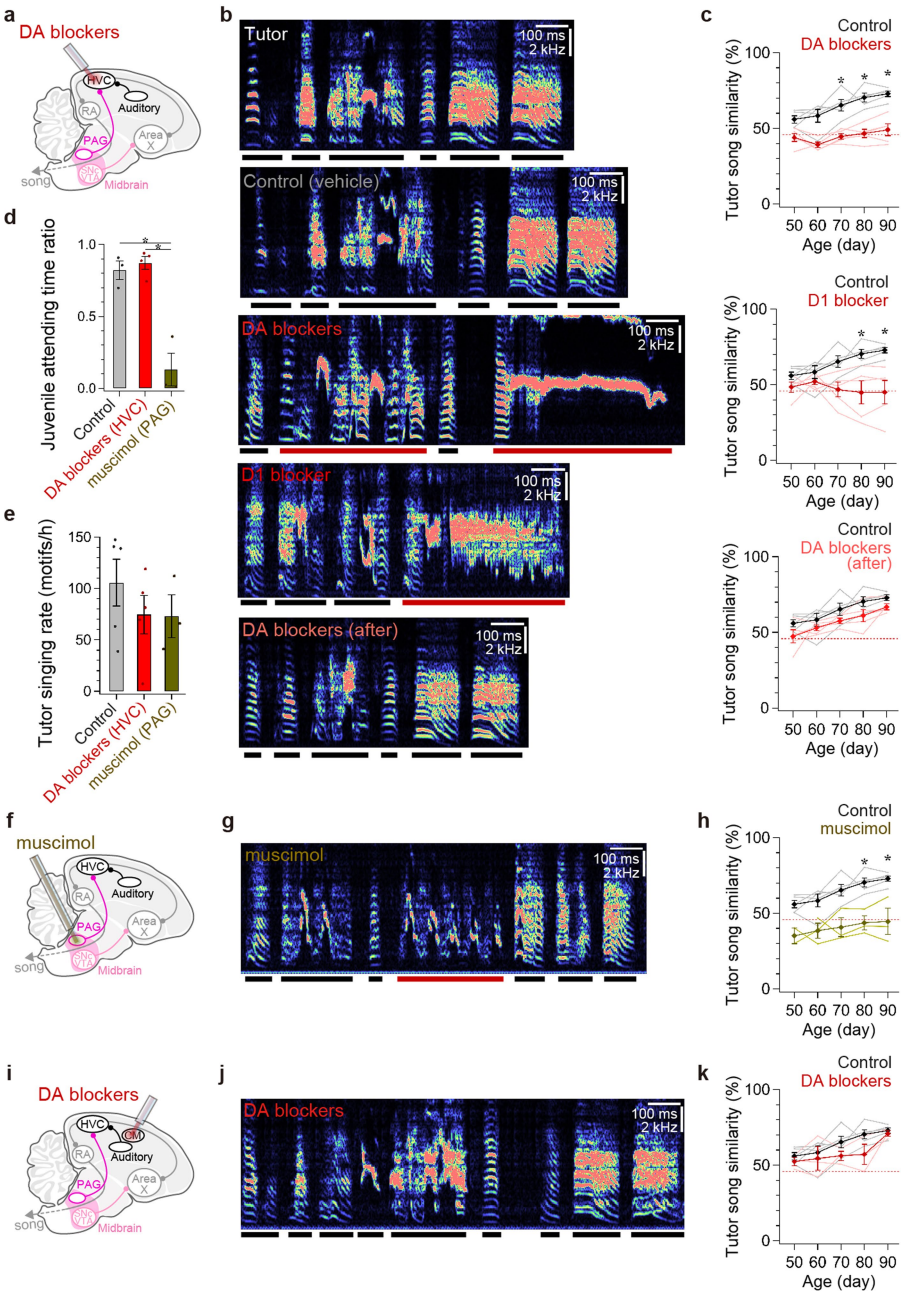

Extended Data Fig. 5 | See next page for caption.

© 2018 Springer Nature Limited. All rights reserved.

Extended Data Fig. 5 | Effects of infusing DA blockers into either the HVC or CM, or infusing muscimol into the PAG on song copying. **a**, Schematic showing infusion of DA blockers into the HVC. **b**, From top to bottom, sound spectrograms of a song of a tutor bird, a 90-day-old pupil that received an infusion of vehicle during tutoring sessions, a 90-day-old pupil that received infusions of both D1- and D2-type DA blockers (DA blockers) during tutoring sessions, a 90-day-old pupil bird that received an infusion of a D1-type blocker during tutoring sessions, and a 90-day-old pupil that received infusions of both D1- and D2-type DA blockers after tutoring sessions. **c**, Developmental changes in tutor song similarity of pupils that received infusions of both D1- and D2-type DA blockers (DA blockers) into the HVC during tutoring sessions (top, $n = 5$), a D1-type blocker into HVC during tutoring sessions (middle, $n = 5$), or DA blockers into the HVC immediately after tutoring sessions (bottom, $n = 5$). Asterisks indicate $P < 0.050$; Tukey–Kramer test (see Methods). **d**, Proportion of time that juvenile birds attended to the tutor during tutoring sessions was not significantly different between birds that received infusions of vehicle ($n = 3$) or DA blockers into HVC ($n = 4$) (Tukey–Kramer test; $P = 0.871$). By contrast, the attention time of juvenile birds that received infusion of muscimol into the PAG ($n = 3$) was lower than that of control birds (Tukey–Kramer test; $P = 0.001$) and that of birds that received an injection of DA blockers into the HVC (Tukey–Kramer test; $P < 0.001$). **e**, Singing rates of the tutor bird to pupils that received vehicle into the HVC ($n = 5$) were not differe*n*t from that to pupils that received injection of DA blockers into the HVC ($n = 5$) or muscimol into the PAG ($n = 3$). One-way ANOVA; $F_{2,10} = 0.776$, $P = 0.486$. **f**, Schematic showing infusion of muscimol into the PAG. **g**, A sound spectrogram of a song of a 90-day-old pupil that received an infusion of muscimol into the PAG during tutoring sessions. A sound spectrogram of the tutor song is shown in **b**. **h**, Tutor song similarity of pupil birds that received infusion of vehicle into the HVC and birds that received an infusion of muscimol blockers into PAG were significantly different (Tukey–Kramer test; vehicle, $n = 5$; muscimol into the PAG, $n = 3$; at 90 days of age, $P = 0.007$). **i**, Schematic showing infusion of DA blockers into the CM (DA blockers possibly diffused into both the medial and lateral CM). **j**, A sound spectrogram of a song of a 90-day-old pupil that received an infusion of DA blockers into the CM during tutoring sessions. A sound spectrogram of the tutor song is shown in **b**. **k**, Tutor song similarity of pupil birds that received an infusion of vehicle into the HVC and birds that received infusion of DA blockers into the CM were not significantly different (Tukey–Kramer test; vehicle, $n = 5$; DA blockers into the CM, $n = 3$; at 90 days of age; $P = 1.000$). **c**, **h**, **k**, Horizontal red dashed lines show song similarity between 90-day-old untutored birds and unrelated adult male zebra finches that had been raised with normal exposure to a tutor (see Extended Data Fig. 4b, c). Data are mean ± s.e.m.

© 2018 Springer Nature Limited. All rights reserved.

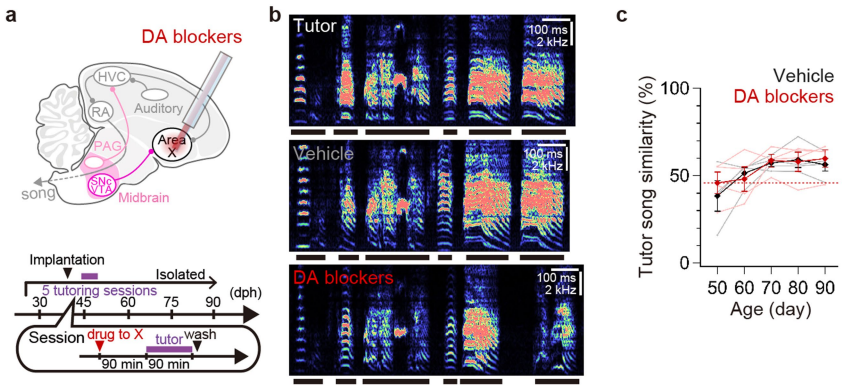

Extended Data Fig. 6 | Infusion of DA blockers into Area X in juvenile males did not disrupt song copying. a, Schematic (top) and schedule (bottom) of infusion of DA blockers into Area X. **b**, Sound spectrograms of a song of a tutor (top), a 90-day-old bird that received an infusion of vehicle into Area X during tutoring sessions (middle), and a 90-day-old bird that received an infusion of DA blockers into Area X during tutoring sessions (bottom). **c**, Tutor song similarity of pupil birds that received an infusion of vehicle into Area X and birds that received infusion of DA blockers into Area X were not significantly different. Tukey–Kramer test; vehicle, $n = 4$, DA blockers, $n = 4$; at 90 days of age; $P = 1.000$. The horizontal red dashed line shows song similarity between 90-day-old untutored birds and unrelated adult male zebra finches that had been raised with normal exposure to a tutor (see Extended Data Fig. 4b, c). Data are mean ± s.e.m.

© 2018 Springer Nature Limited. All rights reserved.

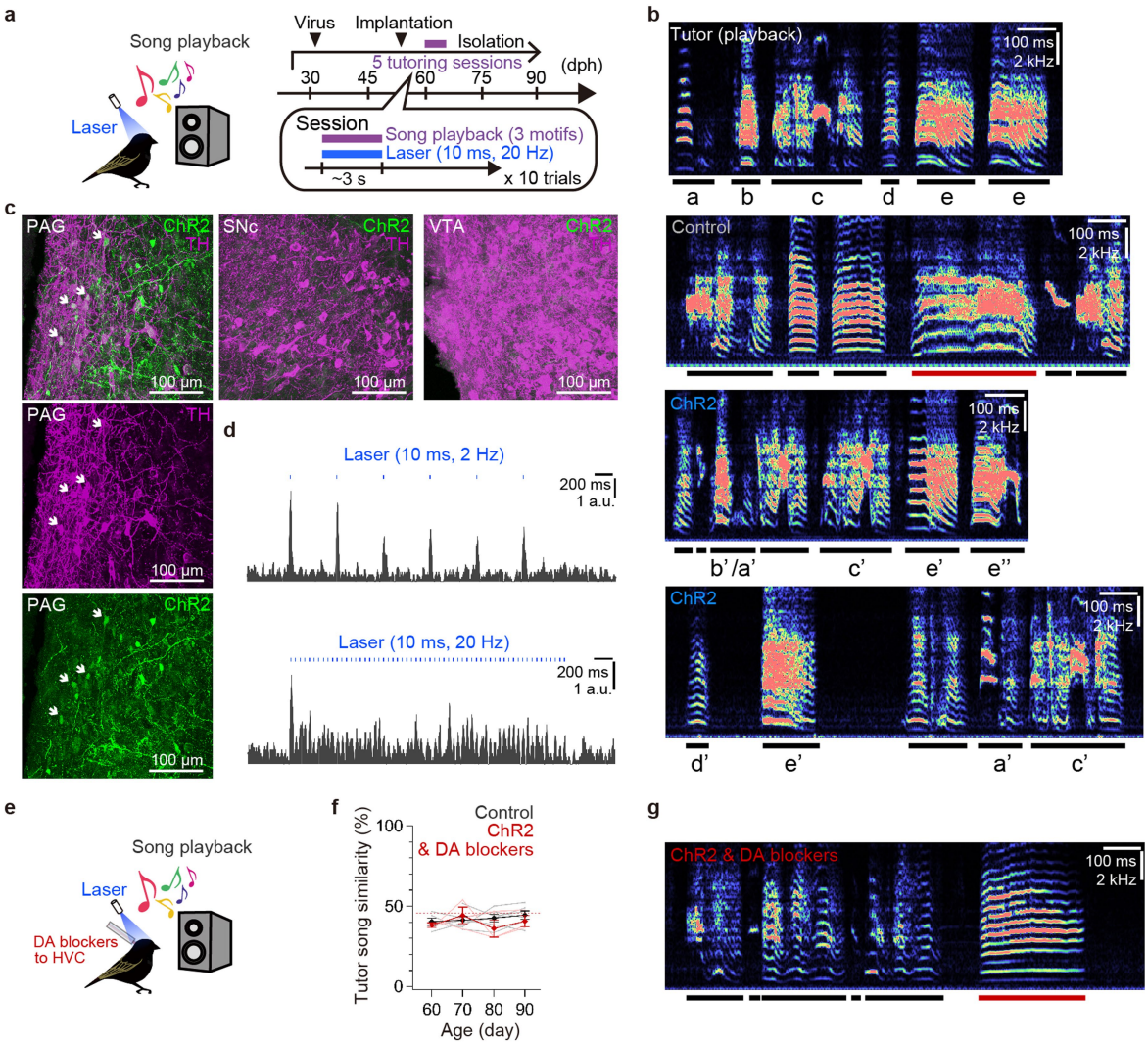

Extended Data Fig. 7 | Optogenetic activation of PAG_{HVC} terminals paired with song playback. a, Schematic (left) and schedule (right) of optogenetic stimulation of PAG_{HVC} terminals paired with song playback. **b**, Sound spectrograms of song playback used in tutoring sessions (top), a song of a 90-d pupil 'tutored' by song playback without viral injections but with laser illumination over HVC (top middle), and 90-day-old pupils that had received optogenetic activation of PAG_{HVC} terminals paired with song playback (bottom middle and bottom). **c**, From left to right, a maximum-projected image of serial sagittal sections of the PAG (left, approximately 0.5 mm lateral of the midline), showing PAG neurons expressing both ChR2 (green) and TH (pseudo-coloured magenta) (arrows), SNc (middle, approximately 0.8 mm lateral of the midline) and VTA (right, approximately 0.3 mm lateral of the midline). Similar results were obtained in six independently repeated experiments. **d**, Multiunit activity in the PAG, showing the time-locked response to laser stimulation at 2 Hz (top) and 20Hz (bottom). **e**, Schematic of optogenetic stimulation of PAG_{HVC} terminals paired with song playback while infusing DA blockers into HVC. **f**, Tutor song similarity of pupils that received activation of PAG_{HVC} terminals paired with song playback while infusing DA blockers into the HVC (red, $n = 3$) was not different from control birds shown in Fig. 3j (Tukey–Kramer test; at 90 days of age; $P = 1.000$), but lower than that received activation of PAG_{HVC} terminals paired with song playback shown in Fig. 3j (Tukey–Kramer test; at 90 days of age; $P = 0.019$). **g**, A sound spectrogram of the song of a 90-day-old pupil that had received optogenetic activation of PAG_{HVC} terminals paired with song playback while infusing DA blockers into the HVC. A sound spectrogram of the song playback used in tutoring sessions is shown in **b**. Data are mean ± s.e.m.

© 2018 Springer Nature Limited. All rights reserved.

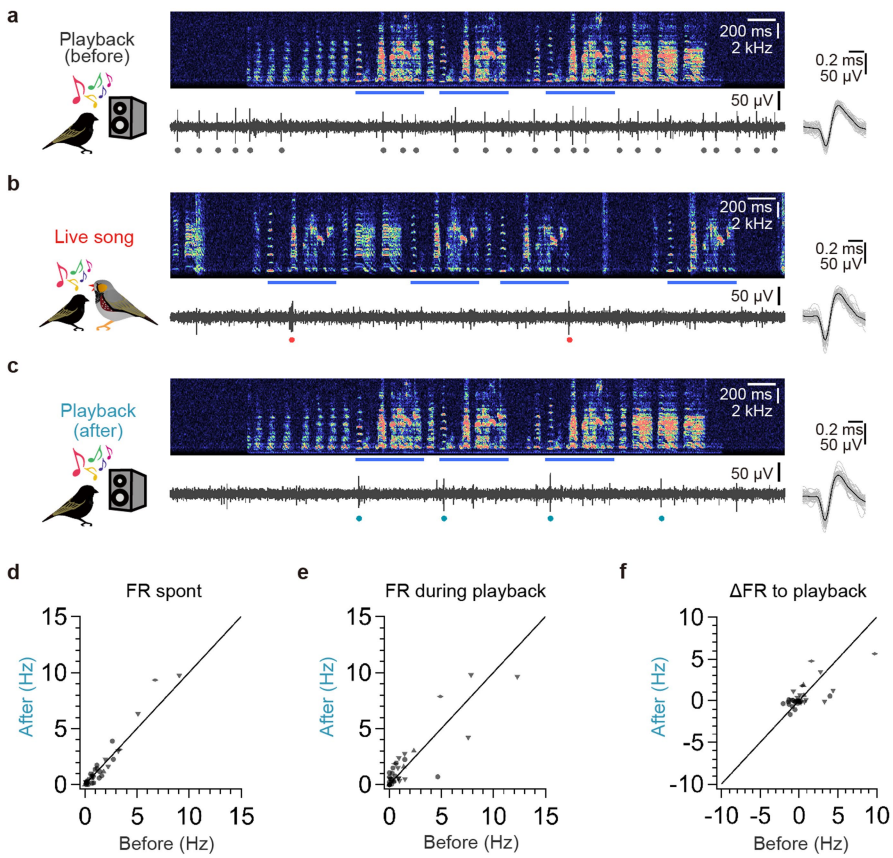

Extended Data Fig. 8 | Action potential activity of HVC neurons in juvenile male zebra finches before and after their first exposure to live tutor songs. a–c, Action potential activity of an HVC neuron to tutor song playback before exposure to a singing tutor (**a**), to live tutor songs (**b**) and to tutor song playback after exposure to live tutor songs (**c**). Top, sound spectrogram. Bottom, voltage recording. Bottom right, 50 action potentials (grey) and their mean (black). Circle, individual action potential; blue bar, tutor song motif. **d**, Spontaneous firing rates (FR spont) of HVC neurons of juvenile males before and after exposure to live tutor songs. Student's two-sided paired *t*-test; mean firing rate before, 1.6 ± 0.3 Hz; mean firing rate after, 1.6 ± 0.4 Hz; $t_{34} = 0.794$, $P = 0.433$, $n = 35$ neurons from four birds. **e**, Firing rates of juvenile male HVC neurons during playback of tutor songs (FR during playback) before and after exposure to live tutor songs. Student's two-sided paired *t*-test; mean firing rate before, 2.0 ± 0.6 Hz; mean firing rate after, 2.1 ± 0.6 Hz; $t_{34} = 0.468$, $P = 0.643$, $n = 35$ neurons from four birds. **f**, Changes in firing rates (ΔFR) of juvenile HVC neurons in response to playback of tutor songs before and after exposure to live tutor songs. Student's two-sided paired *t*-test; ΔFR before, 0.5 ± 0.4 Hz; ΔFR after, 0.5 ± 0.2 Hz; $t_{34} = 0.079$, $P = 0.937$, $n = 35$ neurons from four birds.

© 2018 Springer Nature Limited. All rights reserved.

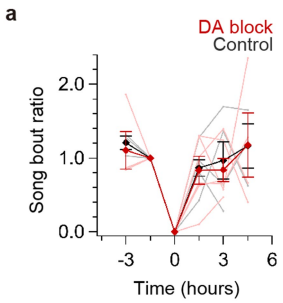

Extended Data Fig. 9 | Song rates of juvenile birds before and after their first tutoring sessions. a, Ratio of song bouts produced before and after the first tutoring session in control birds (black, $n = 6$) and in birds that received an injection of 6-OHDA into the HVC several days before the tutoring session or that were infused with DA blockers into the HVC immediately before and during the tutoring session (red, $n = 6$). Data are mean ± s.e.m.

© 2018 Springer Nature Limited. All rights reserved.

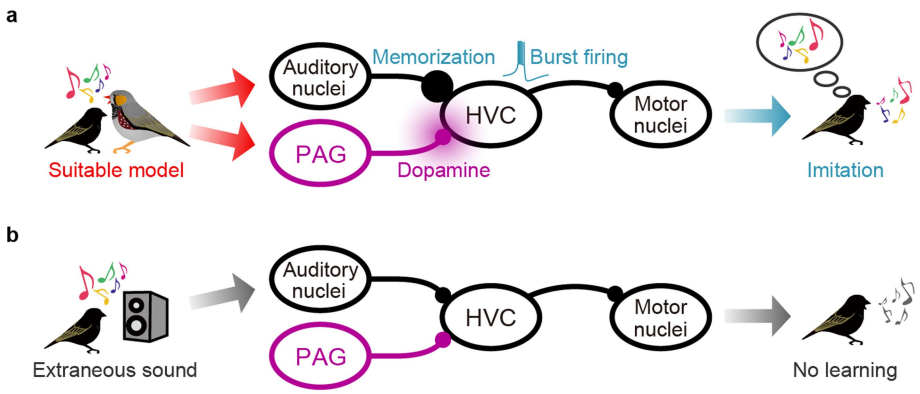

Extended Data Fig. 10 | Summary diagram. a, The presence of a singing tutor (that is, a suitable model) activates auditory afferent neurons and DA-releasing PAG afferent neurons to HVC, leading to potentiation and stabilization of auditory synapses in HVC. This plastic change results in temporally precise coding of the tutor song and increases the occurrence of bursting activity in the HVC, while also rapidly altering temporal and spectral features of the vocalization of a pupil in a manner that drives successful imitation of the tutor song. **b**, Playback of an adult male song without social cues (that is, extraneous sound) only activates auditory afferent neurons in the HVC. The activation of these auditory inputs by itself can neither alter HVC activity nor drive song learning, similar to the condition in which DA signalling in the HVC of the pupil is blocked during the exposure of a juvenile to a live, singing tutor.

© 2018 Springer Nature Limited. All rights reserved.

LETTER

OPEN
https://doi.org/10.1038/s41586-018-0619-8

Genome organization and DNA accessibility control antigenic variation in trypanosomes

Laura S. M. Müller[1,2,3,15], Raúl O. Cosentino[1,2,3,15], Konrad U. Förstner[4,5,6], Julien Guizetti[3,14], Carolin Wedel[3], Noam Kaplan[7], Christian J. Janzen[8], Panagiota Arampatzi[6], Jörg Vogel[9,10], Sascha Steinbiss[11], Thomas D. Otto[11,12], Antoine-Emmanuel Saliba[9], Robert P. Sebra[13] & T. Nicolai Siegel[1,2,3]*

Many evolutionarily distant pathogenic organisms have evolved similar survival strategies to evade the immune responses of their hosts. These include antigenic variation, through which an infecting organism prevents clearance by periodically altering the identity of proteins that are visible to the immune system of the host[1]. Antigenic variation requires large reservoirs of immunologically diverse antigen genes, which are often generated through homologous recombination, as well as mechanisms to ensure the expression of one or very few antigens at any given time. Both homologous recombination and gene expression are affected by three-dimensional genome architecture and local DNA accessibility[2,3]. Factors that link three-dimensional genome architecture, local chromatin conformation and antigenic variation have, to our knowledge, not yet been identified in any organism. One of the major obstacles to studying the role of genome architecture in antigenic variation has been the highly repetitive nature and heterozygosity of antigen-gene arrays, which has precluded complete genome assembly in many pathogens. Here we report the de novo haplotype-specific assembly and scaffolding of the long antigen-gene arrays of the model protozoan parasite *Trypanosoma brucei*, using long-read sequencing technology and conserved features of chromosome folding[4]. Genome-wide chromosome conformation capture (Hi-C) reveals a distinct partitioning of the genome, with antigen-encoding subtelomeric regions that are folded into distinct, highly compact compartments. In addition, we performed a range of analyses—Hi-C, fluorescence in situ hybridization, assays for transposase-accessible chromatin using sequencing and single-cell RNA sequencing—that showed that deletion of the histone variants H3.V and H4.V increases antigen-gene clustering, DNA accessibility across sites of antigen expression and switching of the expressed antigen isoform, via homologous recombination. Our analyses identify histone variants as a molecular link between global genome architecture, local chromatin conformation and antigenic variation.

Genome sequences of several pathogens have revealed a partitioning of chromosomes, with housekeeping genes often being located in the central core and antigen genes being located in subtelomeric regions[5,6]. These assemblies suggest that the linear organization of the genome may be important for restricting high levels of recombination to regions that code for antigens and for ensuring that all but one antigen is repressed.

Recently, genome-wide Hi-C analyses have begun to uncover the 3D organization of chromosomes at high resolution[4], which has highlighted the critical role of spatial organization and compartmentalization of DNA in the regulation of gene expression and recombination[2,3]. In addition, microscopy-based analyses of the unicellular eukaryotic parasites *Plasmodium falciparum* and *T. brucei* have indicated that nuclear organization may be important for the mutually exclusive expression of antigens[7–9]. However, to our knowledge, the proteins that are involved in shaping genome architecture and controlling antigen expression have not yet been identified in any organism.

This study aimed to identify the process that restricts antigen expression. Specifically, we sought to identify proteins that are important for maintaining genome architecture and to determine whether global and/or local changes in chromatin conformation affect antigen expression.

In *T. brucei*—which is the causative agent of human sleeping sickness—the key antigens are the variant surface glycoproteins (VSGs). Most VSG genes—of which there are about 2,500—are found in long subtelomeric arrays of megabase chromosomes[6]. In addition, about 65 VSG genes are located on mini-chromosomes (50–150 kb in length)[10] and a smaller subset of VSG genes is located in distinct telomere-proximal polycistronic transcription units, called expression sites[11]. Expression sites are grouped into metacyclic-form and bloodstream-form expression sites (MESs and BESs, respectively) on the basis of the life-cycle stage during which they can be activated. VSG genes are transcribed only when they are located within an expression site and only one of about 15 BESs is transcribed at a time, which ensures that the expression of VSG genes is mutually exclusive[11]. Therefore, a genome sequence that contains both subtelomeric VSG gene arrays and telomeric expression sites, which is lacking in the available *T. brucei* genome (isolate TREU 927)[6], is required to elucidate the molecular link between genome architecture and antigenic variation.

Using PacBio single-molecule real-time (SMRT) sequencing technology, we generated an approximately 100-fold genome-sequence coverage of the *T. brucei* 427 Lister isolate (the most commonly used laboratory isolate) and assembled the reads into megabase chromosomes, of which there are 11 (96 contigs, Fig. 1, Extended Data Table 1). To order and orient contigs without relying on scaffolds of related parasite isolates (which may have undergone genome rearrangements), we took advantage of two ubiquitous features of chromosome organization: a distance-dependent decay of DNA–DNA interaction frequency and substantially higher interaction frequencies between DNA loci located on the same chromosome, compared to those on different chromosomes[4]. The high degree of subtelomeric heterozygosity enabled us to assemble the complete *T. brucei* genome with phased diploid subtelomeric regions (Extended Data Figs. 1, 2, Supplementary Data). In addition, RNA sequencing (RNA-seq) revealed a notable partitioning of the genome into a transcribed homozygous core and non-transcribed

[1]Department of Veterinary Sciences, Experimental Parasitology, Ludwig-Maximilians-Universität München, Munich, Germany. [2]Biomedical Center Munich, Department of Physiological Chemistry, Ludwig-Maximilians-Universität München, Planegg-Martinsried, Germany. [3]Research Center for Infectious Diseases, University of Würzburg, Würzburg, Germany. [4]ZB MED – Information Centre for Life Sciences, Cologne, Germany. [5]TH Köln, Faculty of Information Science and Communication Studies, Cologne, Germany. [6]Core Unit Systems Medicine, Institute of Molecular Infection Biology, University of Würzburg, Würzburg, Germany. [7]Department of Physiology, Biophysics & Systems Biology, Rappaport Faculty of Medicine, Technion Israel Institute of Technology, Haifa, Israel. [8]Department of Cell & Developmental Biology, Biocenter, University of Würzburg, Würzburg, Germany. [9]Helmholtz Institute for RNA-based Infection Research, Würzburg, Germany. [10]RNA Biology Group, Institute of Molecular Infection Biology, University of Würzburg, Würzburg, Germany. [11]Wellcome Trust Sanger Institute, Hinxton, Cambridge, UK. [12]Centre of Immunobiology, Institute of Infection, Immunity & Inflammation, College of Medical, Veterinary and Life Sciences, University of Glasgow, Glasgow, UK. [13]Icahn Institute and Department of Genetics and Genomic Sciences, Icahn School of Medicine at Mount Sinai, New York, NY, USA. [14]Present address: Centre for Infectious Diseases, Parasitology, Heidelberg University Hospital, Heidelberg, Germany. [15]These authors contributed equally: Laura S. M. Müller, Raúl O. Cosentino. *e-mail: n.siegel@lmu.de

© 2018 Springer Nature Limited. All rights reserved.

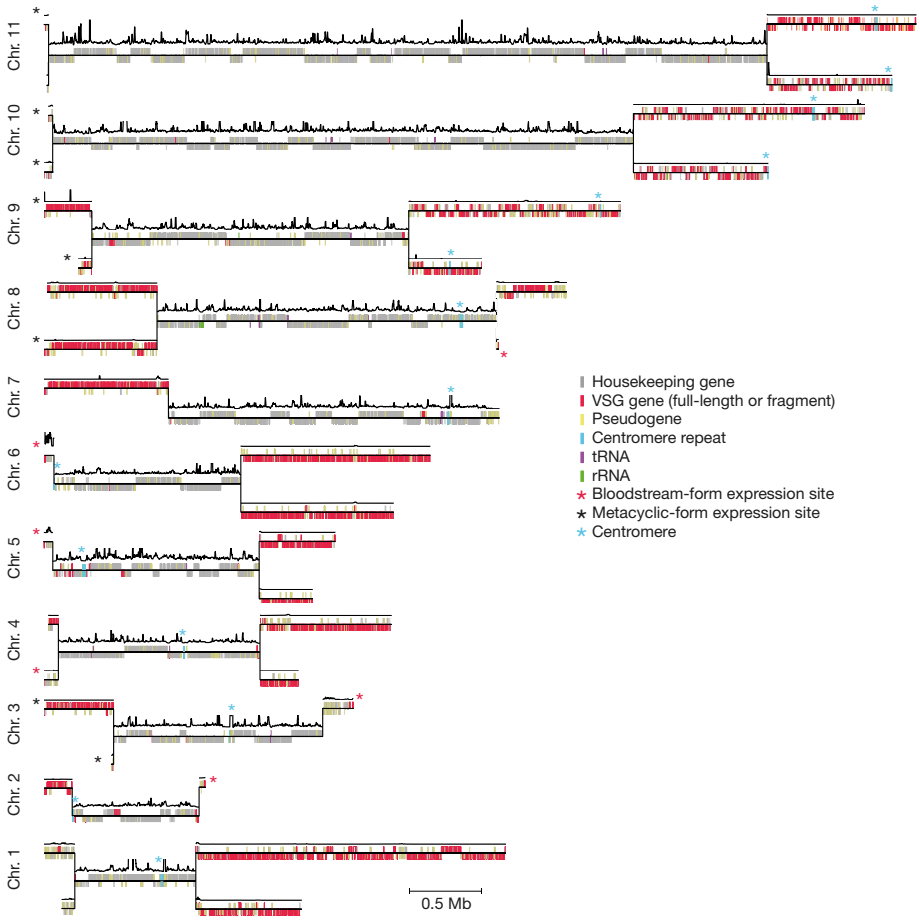

Fig. 1 | Long-read and Hi-C-based de novo assembly of the *T. brucei* Lister 427 genome. Only one of the two homologous chromosomes (chr.) is depicted for the homozygous chromosomal core regions (22.71 Mb). Both chromosomes are shown for the heterozygous subtelomeric regions (19.54 Mb). Relative transcript levels (window size, 5,001 bp; step size, 101 bp) are shown as a black line above each chromosome. BESs and MESs were assigned to the respective subtelomeric region if an unambiguous assignment based on DNA interaction data was possible (see Supplementary Information). Centromeres were assigned based on KKT2 ChIP–seq data[30].

heterozygous subtelomeric regions, which encode the vast repertoire of antigens (Fig. 1).

Analysis of the frequency of intra-chromosomal DNA–DNA interaction suggested a strong compartmentalization of the *T. brucei* genome: centromeres and junctions between the core and subtelomeres function as the most prominent boundaries of DNA compartments. In addition, the frequency of DNA–DNA contact was substantially higher across subtelomeric regions compared to core regions, which indicates that subtelomeres are more compact than the core region (Fig. 2a, Extended Data Fig. 3). Therefore, the partitioning of the genome into transcribed housekeeping genes and non-transcribed antigen genes that is observed in the genome assembly and transcriptome data is mirrored by the 3D organization of the genome. In *T. brucei*, RNA polymerase II transcription can occur in the absence of canonical promoter motifs[12,13]. Thus, the high degree of compaction across subtelomeric regions probably prevents the spurious initiation of transcription and ensures mutually exclusive expression of a single VSG gene from a BES. In addition, BES–BES interactions were much more frequent than interactions among randomly chosen genomic loci, suggesting a clustering of BESs (Fig. 2b). Taken together, the Hi-C data suggest a distinct compartmentalization of the *T. brucei* nucleus.

Higher-order genome structures are established and maintained by architectural proteins such as CCCTC-binding factor (CTCF) and cohesin[14]. Histone variants are also enriched at many compartment boundaries[15], but the role of these variants in shaping genome architecture remains unknown. Although CTCF appears to be absent in non-metazoans[16], the major subunit of cohesin (SCC1) is present in *T. brucei* and the depletion of this subunit causes deregulation of VSG expression[17]. However, it has remained unclear whether this is a direct effect because SCC1 depletion strongly affects cell-cycle progression and growth rate, leading to rapid parasite death[18].

Chromatin immunoprecipitation with sequencing (ChIP–seq) revealed that in *T. brucei* SCC1 is enriched across tRNA and rRNA genes, termination sites of RNA polymerase II transcription and most of the 3′ ends of BESs (Fig. 2c, d, Extended Data Fig. 4). This pattern of cohesin enrichment is reminiscent of its distribution in humans and yeast, in which cohesin is found at insulator and boundary elements such as tRNA genes[19,20]. The observed distribution of SCC1 is also similar to that of histone variants H3.V and, to a lesser extent, H4.V in *T. brucei* (Fig. 2d, Extended Data Fig. 4; also see ref. [21]). This raised the possibility that these two histone variants function together with SCC1 in shaping genome organization and the regulation of antigen expression.

To investigate a possible link between these histone variants, genome architecture and antigen expression, we determined the expression of VSG genes and genome architecture in Δ*H3.V*, Δ*H4.V* and Δ*H3.V*Δ*H4.V* cells. No cell cycle defect was observed in these cell lines (Extended Data Fig. 5).

Laboratory-adapted isolates, such as the one used here, switch their expression of VSG isoforms at very low frequency (about 10^{-6} per population doubling), and homogenously express *VSG-2* (Fig. 3a; also see ref. [22]). Thus, an increase in heterogeneity of VSG gene expression can be caused by a loss of mutually exclusive expression of VSG genes in individual cells—that is, heterogeneity in antigen expression at the single-cell level—or an increased switching frequency in expression of VSG genes in different parasites (heterogeneity at the population level).

© 2018 Springer Nature Limited. All rights reserved.

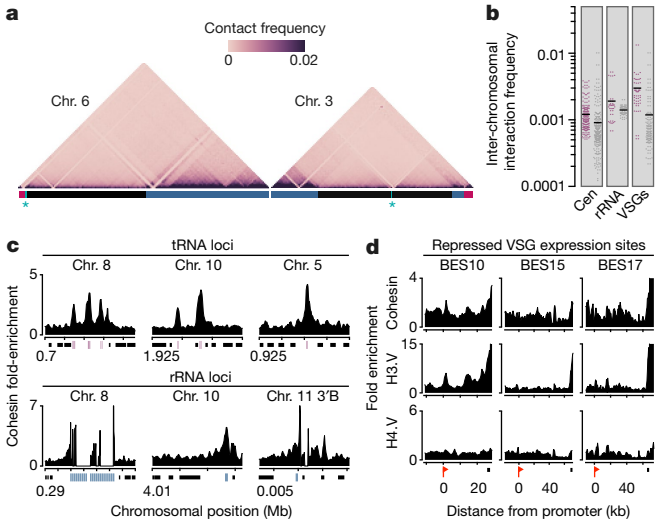

Fig. 2 | Hi-C and ChIP–seq reveal partitioning of the *T. brucei* genome into distinct domains. a, Hi-C heat maps of chromosomes 3 and 6 at 20-kb resolution. Horizontal blue, black and red lines mark heterozygous subtelomeric, homozygous core regions and BESs, respectively. Centromeres are marked by asterisks. **b**, Scatter plot showing inter-chromosomal interaction frequencies among centromeres (cen) ($n = 206$ bins; $P = 0.0029$), VSG genes in silent expression sites (VSGs) ($n = 54$ bins; $P = 1.63 \times 10^{-6}$) and rRNA genes ($n = 40$ bins; $P = 0.0177$) compared to a matching background sample, which was randomly selected from the interaction matrix (50-kb bin size). The background sample (grey) matches the genomic feature (red) in size and number. Selected bins with zero values were removed from both the query and background sample. *P* values are based on Welch's *t*-test (two-sided). Black lines represent the mean. **c**, ChIP–seq data showing the enrichment (compared to input material) of the cohesin subunit SCC1 ($n = 3$ biologically independent experiments) across representative tRNA and rRNA genes (window size, 501 bp; step size, 101 bp). Black, red and blue boxes represent protein coding, tRNA and rRNA genes, respectively. Tick marks on the *x* axis represent 5-kb intervals. 3′B refers to one of the two alternative subtelomeric ends (A or B) at the 3′end of chromosome 11. **d**, ChIP–seq data showing cohesin ($n = 3$ biologically independent experiments), H3.V and H4.V (each in $n = 2$ biologically independent experiments) enrichment across three transcriptionally repressed BESs (window size, 2,001 bp; step size, 501 bp). Red flags mark BES promoters and black boxes indicate the locations of VSG genes.

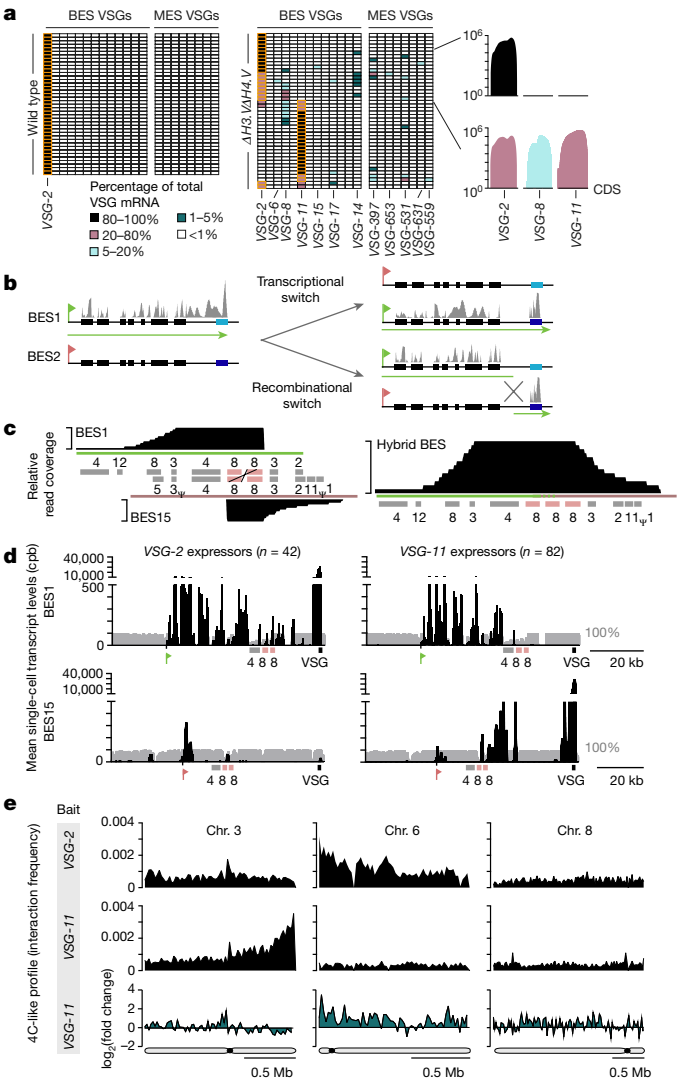

Fig. 3 | Deletion of histone variants *H3.V* and *H4.V* leads to a switch in expression of VSG isoforms. a, scRNA-seq analysis of wild-type ($n = 40$) and $\Delta H3.V\Delta H4.V$ (first time point, $n = 44$) cells. Each row represents data from one cell. The number of sequencing reads was normalized to account for differences in library size, gene length and uniqueness of VSG gene sequence. Only uniquely mapping reads were considered. The total number of VSG transcripts per cell is set to 100% (for details, see Methods, Extended Data Fig. 7). The colour code indicates the contribution of individual VSG transcripts to the pool of VSG transcripts in a single cell. The dominant VSG isoform is depicted with an orange border. For selected cells, the read coverage is shown across *VSG-2*, *VSG-8* and *VSG-11* (with 500 bp of surrounding sequence). CDS, coding sequence. **b**, Outline of the VSG switching mechanisms described for *T. brucei*. Green and red flags mark the active and repressed promoters, respectively. Green lines and grey bars indicate regions of expected transcription for the two different scenarios. **c**, Sequencing coverage across BES1 (left, top), BES15 (left, bottom) and a hybrid BES consisting of the 5′-BES1 and 3′-BES15 (right). Coverage is based on SMRT sequencing reads >10 kb from $\Delta H3.V\Delta H4.V$ gDNA that map to BES1 and BES15. The cross represents the site of recombination. Boxes represent expression-site-associated genes and ψ denotes a pseudogene. **d**, scRNA-seq-based analysis of $\Delta H3.V\Delta H4.V$ cells that exclusively express *VSG-2* ($n = 42$) or *VSG-11* ($n = 82$). The average transcript levels (counts per billion, cpb) based on uniquely mapping reads across BES1 and BES15 are shown. Grey bars represent degree of uniqueness. **e**, 4C-like inter-chromosomal interaction profiles (based on Hi-C-data, 20-kb bin size) showing the average interaction frequencies of BES1 (top) and BES15 (middle) with chromosomes 3, 6 and 8 in wild-type cells and the fold change ($\log_2$) in interactions of BES15 (bottom) with chromosomes 3, 6 and 8 after deletion of *H3.V* and *H4.V*.

To distinguish between these possibilities and to identify the VSG genes that are expressed, we performed single-cell RNA-seq (scRNA-seq) of individual *T. brucei* cells. scRNA-seq data from a total of 40 wild-type and 378 $\Delta H3.V\Delta H4.V$ cells revealed that—whereas all wild-type cells expressed *VSG-2*—in 74% of the $\Delta H3.V\Delta H4.V$ cells, *VSG-2* transcript levels contributed less than 20% of the total VSG mRNA; this indicates a switch in expression of VSG genes (Fig. 3a, Extended Data Figs. 6, 7). Activation of new VSG genes was not random, with *VSG-11* being the dominant newly activated VSG gene in 230 out of 378 cells. In addition, several cells contained transcripts from multiple VSG genes, which points to a partial loss of mutually exclusive expression. To determine the stability of *VSG-2* expression, we analysed $\Delta H3.V\Delta H4.V$ cells at two time points that were about 50 population doublings apart. Although the overall pattern remained the same (Fig. 3a, Extended Data Fig. 6), the percentage of cells that expressed only *VSG-2* mRNA, or multiple VSG mRNAs, had declined by the second time point. This suggests that the process of *VSG-2* deactivation had progressed further, and that the simultaneous expression of multiple VSG genes may have been a transient intermediate state. Analyses based on immunofluorescence and flow cytometry confirmed that the loss of *VSG-2* mRNA resulted in a loss of *VSG-2* expression (Extended Data Fig. 8). No major effect on the expression of VSG genes was observed upon deletion of *H3.V* or *H4.V* alone (Extended Data Fig. 8).

© 2018 Springer Nature Limited. All rights reserved.

In *T. brucei*, the switching of expression of VSG genes occurs by two distinct mechanisms[11]: either by switching transcription from one BES to another (transcriptional switch) or by a recombination-based event that leads to the replacement of the previously active VSG gene with a new VSG gene from a different genomic location (recombinational switch, Fig. 3b).

To gain insight into the mechanism by which histone variants affect antigen expression, we sequenced Δ*H3.V*Δ*H4.V* genomic DNA using SMRT sequencing technology. The SMRT data indicated that, in most cells, recombination had occurred between an expression-site-associated gene 8 (*ESAG8*) gene pair that was present in both BES1 and BES15. The data also revealed that the new chimeric BES contained three copies of *ESAG8*, one from BES1 and two from BES15 (Fig. 3c). scRNA-seq and Hi-C data support a recombination event (Fig. 3d, e). Hi-C data revealed that, upon deletion of *H3.V* and *H4.V*, the interaction frequency between *VSG-11* and the 5′ end of chromosome 6—where *VSG-2* is located in wild-type cells—increased, indicating that *VSG-11* had relocated to chromosome 6.

Studies in different organisms have shown that the frequency of recombination is affected by spatial proximity and DNA accessibility[23,24]. Thus, to determine whether histone variants contribute to genome architecture and/or local DNA accessibility, we performed Hi-C and assays for transposase-accessible chromatin using sequencing (ATAC-seq). Hi-C data from Δ*H3.V* cells revealed marked changes in inter-chromosomal interactions (Fig. 4a, top) and a significant increase in interactions among repressed BESs (Fig. 4b), pointing to a loss of constraints that may have 'anchored' the BESs to specific nuclear sites. In support of these Hi-C data, fluorescence in situ hybridization (FISH) data revealed a strong clustering of telomeric repeats upon deletion of *H3.V* (Fig. 4c, d). By contrast, deletion of *H4.V* affected genome architecture only modestly (Fig. 4a, bottom). Unlike the Hi-C data, our ATAC-seq data indicated that promoter-proximal DNA accessibility increased upon *H3.V* or *H4.V* deletion (Fig. 4e). However, only Δ*H3.V*Δ*H4.V* cells exhibited high DNA accessibility across the entire length of transcriptionally repressed BESs (Fig. 4e bottom, Extended Data Fig. 9).

In summary, the Hi-C and ATAC-seq data indicate that although deletion of *H3.V* was responsible for the majority of genome architectural changes and increased BES clustering, this alone was not sufficient to induce a switch in expression of VSG genes. Only the concurrent deletion of *H3.V* and *H4.V*, which also strongly increased DNA accessibility across transcriptionally repressed BESs, enhanced the rate of recombination-based switching of VSG genes.

The depletion of histone H3 was previously shown to upregulate BES proximal-promoter activity—presumably via a general increase in DNA accessibility—but did not cause deregulation of VSG genes[25]. We hypothesize that the marked increase in switching frequency of VSG gene expression results from the combination of decreased spatial distance between BESs and increased local DNA accessibility (Fig. 4f).

The activation of new VSG genes did not occur at random; this non-random activation has previously been observed for infections of different hosts[26,27]. In a small number of cells, we detected transcripts from different VSG isoforms. This loss of mutually exclusive expression of VSG genes may be caused by increased DNA accessibility upon the deletion of histone variants, which may result in promiscuous RNA polymerase II transcription. Our observations that even in Δ*H3.V*Δ*H4.V* cells not all expression sites are transcribed and that specific 'pairs' of VSG genes tend to be co-expressed, suggest that there are additional constraints imposed by genome organization or VSG protein structure[28]. At the genome level, co-activated VSG genes may have to be localized in close proximity to ensure sufficient levels of an activating factor[8,29]; alternatively, differences in VSG protein structure may make it impossible for the parasite to tolerate certain mosaic surface coats.

In this study, we have demonstrated how evolutionarily conserved features of genome architecture can be exploited for the de novo scaffolding of phased diploid genomes. The use of Hi-C, scRNA-seq and ATAC-seq—to our knowledge, all used here for the first time in *T. brucei*—opened opportunities for genome assembly and the characterization of the mechanism that underlies VSG switching in Δ*H3.V*Δ*H4.V* cells. Our data reveal that histone variants can function as architectural proteins, and that changes in global genome architecture and local chromatin configuration can induce extensive switches in antigen expression.

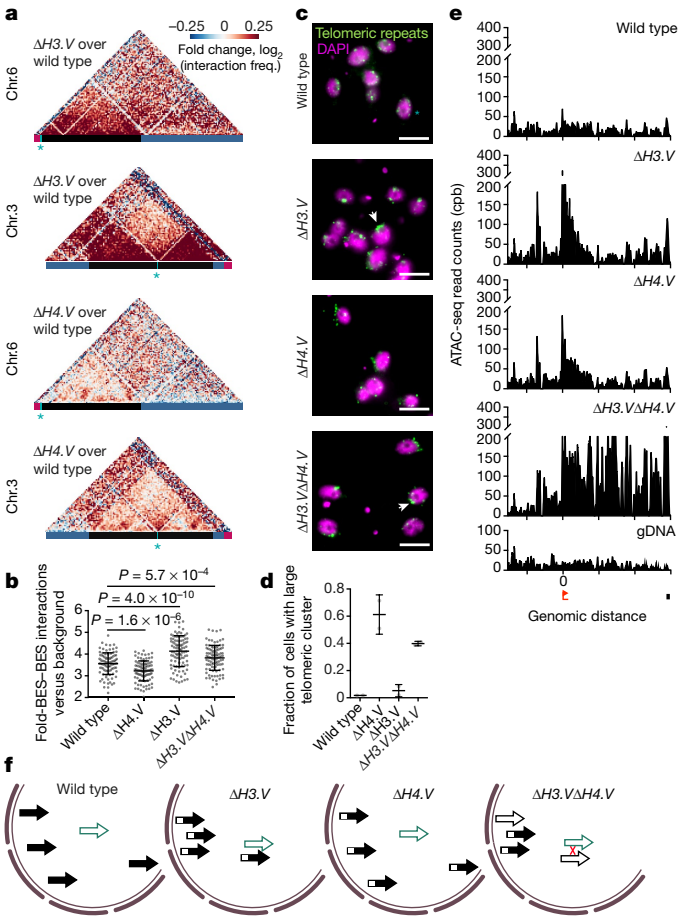

Fig. 4 | Histone variants H3.V and H4.V influence global and local chromatin structures. a, Hi-C heat map showing the fold change ($\log_2$) in DNA–DNA interaction frequency between wild-type and Δ*H3.V* (top two panels) and Δ*H4.V* cells (bottom two panels). **b**, Fold change in DNA–DNA interaction frequency among VSG genes located in BESs compared to background DNA–DNA interactions in wild-type, in Δ*H4.V*, Δ*H3.V* and Δ*H3.V*Δ*H4.V* cells. The ratios for each cell line were calculated for 100 randomly selected background regions. Mean ± s.d. Significance was determined using Welch's *t*-test (two-sided). **c**, FISH with probes against telomeric repeats (Alexa Fluor488, green), $n = 2$ biologically independent experiments. Scale bar, 5 μm. **d**, Quantification of telomere signal to determine the fraction of cells containing large telomeric clusters (white arrows in **c**) was performed using Imaris 8 and is based on the analysis of 1,128 cells. Means ± s.d. of two replicates are shown (wild type: $n = 116, 221$; Δ*H3.V*: $n = 140, 102$; Δ*H4.V*: $n = 146, 107$ and Δ*H3.V*Δ*H4.V*: $n = 190, 106$). **e**, ATAC-seq data ($n = 2$ biologically independent experiments) across BES15 (repressed in wild-type cells). gDNA read coverage (bottom) is shown to illustrate mappability of reads (window size, 501 bp; step size, 101 bp). Red flag and black box indicate the position of the promoter and the VSG gene, respectively. Tick marks on *x* axes represent 20-kb intervals. **f**, Model illustrating the influence of H3.V and H4.V on genome architecture and local DNA accessibility. H3.V and H4.V single knockouts alone mediate only partial opening of BESs (half open arrow) and H3.V knockout leads to a spatial rearrangement of BESs inside the nucleus, whereas deletion of both histone variants is required to obtain the fully opened BESs (open arrow) and spatial proximity of BESs that facilitate recombination (red cross) and lead to the expression of a new VSG isoform.

© 2018 Springer Nature Limited. All rights reserved.

Online content

Any methods, additional references, Nature Research reporting summaries, source data, statements of data availability and associated accession codes are available at https://doi.org/10.1038/s41586-018-0619-8.

Received: 13 July 2017; Accepted: 3 September 2018;
Published online 17 October 2018.

1. Deitsch, K. W., Lukehart, S. A. & Stringer, J. R. Common strategies for antigenic variation by bacterial, fungal and protozoan pathogens. *Nat. Rev. Microbiol*. **7**, 493–503 (2009).
2. Hager, G. L., McNally, J. G. & Misteli, T. Transcription dynamics. *Mol. Cell* **35**, 741–753 (2009).
3. Misteli, T. & Soutoglou, E. The emerging role of nuclear architecture in DNA repair and genome maintenance. *Nat. Rev. Mol. Cell Biol*. **10**, 243–254 (2009).
4. Lajoie, B. R., Dekker, J. & Kaplan, N. The hitchhiker's guide to Hi-C analysis: practical guidelines. *Methods* **72**, 65–75 (2015).
5. Otto, T. D. et al. Long read assemblies of geographically dispersed *Plasmodium falciparum* isolates reveal highly structured subtelomeres. *Wellcome Open Res*. **3**, 52 (2018).
6. Berriman, M. et al. The genome of the African trypanosome *Trypanosoma brucei*. *Science* **309**, 416–422 (2005).
7. Lopez-Rubio, J. J., Mancio-Silva, L. & Scherf, A. Genome-wide analysis of heterochromatin associates clonally variant gene regulation with perinuclear repressive centers in malaria parasites. *Cell Host Microbe* **5**, 179–190 (2009).
8. Chaves, I. et al. Subnuclear localization of the active variant surface glycoprotein gene expression site in *Trypanosoma brucei*. *Proc. Natl Acad. Sci. USA* **95**, 12328–12333 (1998).
9. Navarro, M. & Gull, K. A pol I transcriptional body associated with VSG mono-allelic expression in *Trypanosoma brucei*. *Nature* **414**, 759–763 (2001).
10. Cross, G. A., Kim, H. S. & Wickstead, B. Capturing the variant surface glycoprotein repertoire (the VSGnome) of *Trypanosoma brucei* Lister 427. *Mol. Biochem. Parasitol*. **195**, 59–73 (2014).
11. Horn, D. Antigenic variation in African trypanosomes. *Mol. Biochem. Parasitol*. **195**, 123–129 (2014).
12. McAndrew, M., Graham, S., Hartmann, C. & Clayton, C. Testing promoter activity in the trypanosome genome: isolation of a metacyclic-type VSG promoter, and unexpected insights into RNA polymerase II transcription. *Exp. Parasitol*. **90**, 65–76 (1998).
13. Wedel, C., Förstner, K. U., Derr, R. & Siegel, T. N. GT-rich promoters can drive RNA pol II transcription and deposition of H2A.Z in African trypanosomes. *EMBO J*. **36**, 2581–2594 (2017).
14. Merkenschlager, M. & Odom, D. T. CTCF and cohesin: linking gene regulatory elements with their targets. *Cell* **152**, 1285–1297 (2013).
15. Millau, J. F. & Gaudreau, L. CTCF, cohesin, and histone variants: connecting the genome. *Biochem. Cell Biol*. **89**, 505–513 (2011).
16. Heger, P., Marin, B., Bartkuhn, M., Schierenberg, E. & Wiehe, T. The chromatin insulator CTCF and the emergence of metazoan diversity. *Proc. Natl Acad. Sci. USA* **109**, 17507–17512 (2012).
17. Landeira, D., Bart, J. M., Van Tyne, D. & Navarro, M. Cohesin regulates VSG monoallelic expression in trypanosomes. *J. Cell Biol*. **186**, 243–254 (2009).
18. Gluenz, E., Sharma, R., Carrington, M. & Gull, K. Functional characterization of cohesin subunit SCC1 in *Trypanosoma brucei* and dissection of mutant phenotypes in two life cycle stages. *Mol. Microbiol*. **69**, 666–680 (2008).
19. Raab, J. R. & Kamakaka, R. T. Insulators and promoters: closer than we think. *Nat. Rev. Genet*. **11**, 439–446 (2010).
20. Van Bortle, K. & Corces, V. G. Nuclear organization and genome function. *Annu. Rev. Cell Dev. Biol*. **28**, 163–187 (2012).
21. Siegel, T. N. et al. Four histone variants mark the boundaries of polycistronic transcription units in *Trypanosoma brucei*. *Genes Dev*. **23**, 1063–1076 (2009).
22. Horn, D. & Cross, G. A. Analysis of *Trypanosoma brucei vsg* expression site switching in vitro. *Mol. Biochem. Parasitol*. **84**, 189–201 (1997).
23. Roukos, V. et al. Spatial dynamics of chromosome translocations in living cells. *Science* **341**, 660–664 (2013).
24. Hogenbirk, M. A. et al. Defining chromosomal translocation risks in cancer. *Proc. Natl Acad. Sci. USA* **113**, E3649–E3656 (2016).
25. Alsford, S. & Horn, D. Cell-cycle-regulated control of *VSG* expression site silencing by histones and histone chaperones ASF1A and CAF-1b in *Trypanosoma brucei*. *Nucleic Acids Res*. **40**, 10150–10160 (2012).
26. Barry, J. D. & McCulloch, R. in *Advances in Parasitology*, Vol. 49 (eds Baker, J. R. et al.) 1–70 (Academic Press, London, 2001).
27. Mugnier, M. R., Cross, G. A. & Papavasiliou, F. N. The in vivo dynamics of antigenic variation in *Trypanosoma brucei*. *Science* **347**, 1470–1473 (2015).
28. Pinger, J. et al. African trypanosomes evade immune clearance by O-glycosylation of the VSG surface coat. *Nat. Microbiol*. **3**, 932–938 (2018).
29. Glover, L., Hutchinson, S., Alsford, S. & Horn, D. VEX1 controls the allelic exclusion required for antigenic variation in trypanosomes. *Proc. Natl Acad. Sci. USA* **113**, 7225–7230 (2016).
30. Akiyoshi, B. & Gull, K. Discovery of unconventional kinetochores in kinetoplastids. *Cell* **156**, 1247–1258 (2014).

Acknowledgements We thank S. Gorski and members of the Siegel laboratory for critical reading of the manuscript. We thank T. Achmedov for scRNA-seq technical assistance, M. Berriman, G. Ramasamy, P. Myler and L. Barquist for assistance with the genome assembly, J. Dekker, M. Imakaev, J. M. Belton and B. R. Lajoie for advice on Hi-C experimental design and analysis, K. Ersfeld for advice on epitope tagging of SCC1 and FISH, S. Kirchner and A. R. Batista for suggestions on ATAC-seq, T. Straub and F. Goth for providing server space and all members of the Engstler, Janzen, Kramer, Morriswood and Ladurner laboratories for valuable discussions. We thank C. Clayton and L. Glover for reagents and M. Urbiniak for sharing unpublished SCC1 data. This work was funded by the Young Investigator Program of the Research Center for Infectious Diseases (ZINF) at the University of Würzburg, Germany, the German Research Foundation (SI 1610/2-1 and SI 1610/3-1), the Center for Integrative Protein Science (CIPSM) and by an ERC Starting Grant (3D_Tryps 715466). L.S.M.M. was supported by a grant of the German *Excellence Initiative* to the Graduate School of Life Science, University of Würzburg. R.O.C. was supported by a Georg Forster Fellowship (Humboldt Foundation). T.D.O. was funded by Wellcome Trust grant: 098051.

Reviewer information *Nature* thanks F. Tang, C.-L. Wei and the other anonymous reviewer(s) for their contribution to the peer review of this work.

Author contributions Experiments were designed by T.N.S. and L.S.M.M. and carried out by L.S.M.M. unless indicated otherwise. scRNA-seq was performed by P.A., L.S.M.M. and A.-E.S. with the assistance of J.V. N.K. provided advice on Hi-C experiments, data analysis and the genome assembly. J.G. performed FISH. C.W. performed ATAC-seq. Genome assembly was done by R.O.C. and R.P.S. The quality of the assembly was assessed by T.D.O. and S.S. K.U.F. and L.S.M.M. performed computational analyses of Hi-C data and R.O.C. did the same for the RNA-seq and scRNA-seq data. C.J.J. performed flow cytometry. T.N.S., L.S.M.M. and R.O.C. wrote the manuscript.

Competing interests The authors declare no competing interests.

Additional information
Extended data is available for this paper at https://doi.org/10.1038/s41586-018-0619-8.
Supplementary information is available for this paper at https://doi.org/10.1038/s41586-018-0619-8.
Reprints and permissions information is available at http://www.nature.com/reprints.
Correspondence and requests for materials should be addressed to T.N.S.
Publisher's note: Springer Nature remains neutral with regard to jurisdictional claims in published maps and institutional affiliations.

Open Access This article is licensed under a Creative Commons Attribution 4.0 International License, which permits use, sharing, adaptation, distribution and reproduction in any medium or format, as long as you give appropriate credit to the original author(s) and the source, provide a link to the Creative Commons license, and indicate if changes were made. The images or other third party material in this article are included in the article's Creative Commons license, unless indicated otherwise in a credit line to the material. If material is not included in the article's Creative Commons license and your intended use is not permitted by statutory regulation or exceeds the permitted use, you will need to obtain permission directly from the copyright holder. To view a copy of this license, visit http://creativecommons.org/licenses/by/4.0/.

© 2018 Springer Nature Limited. All rights reserved.

METHODS

No statistical methods were used to predetermine sample size. The experiments were not randomized and investigators were not blinded to allocation during experiments and outcome assessment.

Cell culture. All *T. brucei* strains used in this study are derivatives of the Lister 427 bloodstream-form isolate. Cells were cultured in HMI-11 medium (HMI-9[31] without serum plus) at 37 °C up to a density of 10^6 cells/ml. If required, drugs were used at standard concentrations.

Cell lines. Δ*H3.V* and Δ*H4.V* cells used in this study have previously been published[21,32]. After generation of a transgenic cell line, the correct tagging of a gene or the deletion of gene was verified by PCR. Cell lines were not tested for mycoplasma contamination.

Ty1-H3.V/ΔH3.V *cells*. To delete the first *H3.V* allele (Tb927.10.15350), the regions upstream and downstream of the *H3.V* CDS were PCR-amplified using the following primer pairs: H3.V_01_F, H3.V_02_R and H3.V_03_F, H3.V_04_R (see Supplementary Table 4 for a full list of oligonucleotides) and cloned into pyrFEKO-Puro[33] using InFusion HD Cloning Plus reagents (Clontech) at PvuII/HindIII and BamHI/SbfI restriction sites. The resulting plasmid was linearized with PvuII and SbfI and stably transfected into the *H3.V* locus of *T. brucei* wild-type cells to generate *H3.V*/Δ*H3.V* cells. To add an N-terminal 2× Ty1 tag to the second *H3.V* allele, the sequence of 326-bp upstream of the *H3.V* CDS (H3.V_05_F, H3.V_06_R) was cloned into the ApaI/NotI linearized vector pPOTv3-2×Ty1 using InFusion HD Cloning Plus reagents (Clontech). Downstream of the blasticidin resistance marker and the Ty1-tag, a 417-bp DNA sequence homologous to the *H3.V* CDS 5′-end (H3.V_07_F, H3.V_08_R) was amplified (leaving out the ATG start codon) and likewise inserted using SacI and NheI restriction sites. The tag sequence was subsequently replaced by a codon-optimized version: oligonucleotides containing two codon-optimized Ty1 coding sequences (H3.V_09 and H3.V_10) were annealed, digested with HindIII and SacI and ligated into the HindII/SacI-linearized plasmid. Finally, the plasmid was linearized with ApaI and NheI restriction enzymes and stably transfected into *H3.V*/Δ*H3.V* cells to generate *Ty1-H3.V*/Δ*H3.V*.

ΔH3.VΔH4.V *double-knockout cells*. To delete *H4.V*, the upstream (H4.V_11_F, H4.V_12_R) and downstream (H4.V_13_F, H4.V_14_R) regions flanking the *H4.V* CDS (Tb927.2.2670) were amplified from bloodstream-form wild-type gDNA and purified using NucleoSpin Gel and PCR Clean-up kit (Macherey-Nagel). The PCR product of the upstream region was inserted into the plasmid pyrFEKO-Neo[33] using InFusion HD Cloning Plus reagents (Clontech) between HindIII and AgeI restriction sites. The downstream region was integrated by ligation using BamHI and SbfI restriction sites. The neomycin resistance cassette was exchanged with a blasticidin or a phleomycin resistance marker, respectively, using the BglII and XbaI sites that flank the resistance marker. To this end, the blasticidin and phleomycin cassettes were excised from pyrFEKO-BSD or pyrFEKO-Phleo, purified and ligated into the target plasmid. The plasmids were linearized with NheI and SbfI and stably transfected into the previously published Δ*H3.V* cell line[32].

Ty1-SCC1/ΔSCC1 *cells*. To delete the first *SCC1* allele (Tb927.7.6900), the flanking regions upstream (Scc1_15_F, Scc1_16_R) and downstream (Scc1_17_F, Scc1_18_R) of the *SCC1* CDS were amplified, digested with PvuII/HindIII and BamHI/SbfI, respectively, and ligated into pyrFEKO-Hyg[33] at PvuII/HindIII and BamHI/SbfI restriction sites. Wild-type cells were transfected with the linearized plasmid (PvuII/SbfI) to obtain *SCC1*/Δ*SCC1* cells. For the N-terminal Ty1-tagging of the second *SCC1* allele, the 3′ end of the *SCC1* 5′ UTR was amplified (Scc1_19_F, Scc1_20_R), digested with ApaI and NotI and ligated into the ApaI/NotI-linearized vector pPOTv3-2×Ty1. Next, the 5′ end of the *SCC1* CDS was amplified (leaving out the ATG start codon) (Scc1_21_F, Scc1_22_R), digested with SacI and NheI and ligated into the likewise-digested plasmid. The Ty1-tag was exchanged by a codon-optimized version as described for N-terminal tagging of *H3.V* (see above). The ApaI/NheI linearized plasmid was stably transfected into *SCC1*/Δ*SCC1* *T. brucei* cells to generate *Ty1-SCC1*/Δ*SCC1*.

The cell line in which both endogenous *H4.V* alleles are knocked out and ectopic overexpression of a Ty1-tagged version of H4.V can be induced has previously been published[21].

In situ Hi-C. Because Δ*H3.V*[32] and Δ*H4.V*[21] cells had been generated in a 'single marker' background[34], we generated the Δ*H3.V*Δ*H4.V* cells in a single marker background and compared the Hi-C profiles of the transgenic cell lines to those generated from single marker cells. Thus, all 'wild-type' Hi-C data shown in Figs. 2–4 and Extended Data Figs. 3, 4 are generated from single marker cells. Hi-C data from 'true' wild-type cells (Lister 427, MiTat 1.2) were also generated, but used only for the genome assembly.

In situ Hi-C was performed based on previously published protocols[35,36] and adapted to *T. brucei*: 2×10^8 cells (wild type, single marker, Δ*H3.V*, Δ*H4.V* and Δ*H3.V*Δ*H4.V*) were collected and resuspended in 40 ml of 1× trypanosome dilution buffer (1× TDB; 0.005 M KCl, 0.08 M NaCl, 0.001 M $MgSO_4 \times 7H_2O$, 0.02 M Na_2HPO_4, 0.002 M $Na_2HPO_4 \times 2H_2O$, 0.02 M glucose). Cells were fixed in the presence of 1% formaldehyde for 20 min at room temperature by addition of 4 ml of formaldehyde solution (50 mM Hepes-KOH pH 7.5, 100 mM NaCl, 1 mM EDTA pH 8.0, 0.5 mM EGTA pH 8.0, 11% formaldehyde). The reaction was stopped by addition of 3 ml of 2 M glycine and incubation for 5 min at room temperature and 15 min on ice. Cells were washed twice in 1× TDB and the cell pellet was snap-frozen in liquid nitrogen. Cells were resuspended in 1 ml of permeabilization buffer (100 mM KCl, 10 mM Tris pH 8.0, 25 mM EDTA) supplemented with protease inhibitors (1.5 mM pepstatin A, 4.25 mM leupeptin, 1.06 mM PMSF, 1.06 mM TLCK) and digitonin (200 μM final concentration) and incubated for 5 min at room temperature. Cells were washed twice in 1× NEBuffer3.1 (NEB, B7003S) and resuspended in 342 μl of 1× NEBuffer3.1. After addition of 38 μl of 1% SDS, and an incubation at 65 °C for 10 min, the SDS was quenched by addition of 43 μl of 10% Triton-X 100 (Sigma) and the incubation was continued at room temperature for 15 min. Another 35 μl of water, 13 μl of 10× NEBuffer3.1 and 100 units of MboI (NEB, R0147M) were added and the chromatin was digested at 37 °C overnight while shaking. To inactivate MboI, the sample was incubated at 65 °C for 20 min. Restriction fragments were biotinylated by supplementing the reaction with 60 μl of fill-in mix (0.25 mM biotin-14-dATP (Life Technologies, 19524016), 0.25 mM dCTP, 0.25 mM dGTP, 0.25 mM dTTP (Fermentas), 40 U of DNA polymerase I, large (Klenow) fragment (NEB, M0210)) and incubation at 23 °C for 4 h. The end-repaired chromatin was transferred to 665 μl of ligation mix (1.8% Triton-X 100, 0.18 mg BSA, 1.8× T4 DNA Ligase Buffer (Invitrogen, 46300018) and 5 μl of T4 DNA ligase (invitrogen, 15224025) were added. The ligation was performed for 4 h at 16 °C with interval shake. Crosslinks were reversed by adding 50 μl of 10 mg/ml proteinase K (65 °C for 4 h) and another addition of 50 μl of 10mg/ml proteinase K, 80 μl of 5M NaCl and 70 μl of 10% SDS (65 °C, overnight).

The DNA was precipitated with ethanol and resuspended in 257 μl of TLE (10 mM Tris-HCl, 0.1 mM EDTA, pH 8.0). SDS was added to a final concentration of 0.1% and the sample was split among two tubes for sonication (Covaris S220; microtubes, 175 W peak incident power, 10% duty factor, 200 cycles per burst, 240 s treatment). The samples were recombined and the volume was adjusted to 300 μl with TLE. Fragments between 100 and 400 bp in size were selected using Agencourt AMPure XP beads (Beckman Coulter), according to the manufacturer's instructions. The DNA fragments were eluted off the beads in 55 μl of TLE.

For end-repair and biotin removal from unligated ends, 70 μl of end-repair mix was added (1× Ligation buffer (NEB), 357 μM dNTPs, 25U T4 PNK (NEB, M0201), 7.5U T4 DNA polymerase I (NEB, M0203), 2.5U DNA polymerase I, large (Klenow) fragment (NEB, M0210)) and incubated for 30 min at 20 °C and 20 min at 75 °C. To inactivate the enzymes, EDTA was added to a final concentration of 10 mM. To isolate biotin-labelled ligation junctions, 50 μl of 10 mg/ml Dynabeads MyOne Streptavidin C1 (Life Technologies, 65001) were washed with 400 μl of 1× Tween washing buffer (TWB; 5 mM Tris-HCl pH 7.5, 0.5 mM EDTA, 1 M NaCl, 0.05% Tween 20), collected with a magnet, resuspended in 400 μl of 2× binding buffer (10 mM Tris-HCl pH 7.5, 1 mM EDTA, 2 M NaCl) and added to the sample suspended in 330 μl TLE. Biotinylated DNA was bound to the beads by incubating the sample for 15 min at room temperature with slow rotation. Subsequently, the DNA-bound beads were captured with a magnet, washed twice with 400 μl of 1× binding buffer, washed once in 100 μl of 1× TLE T4 ligase buffer and resuspeded in 41 μl of TLE. For polyadenylation, 5 μl of 10× NEBuffer 2.1, 1 μl of 10 mM dATP and 3 μl of 5 U/μl of Klenow fragment (3′→ 5′ exo-) (NEB, M0212) and incubated for 30 min at 37 °C followed by deactivation for 20 min at 65 °C. Beads were reclaimed with a magnet, washed once with 400 μl 1× Quick ligation buffer (NEB, M2200) and resuspended in 46.5 μl of 1× Quick ligation buffer (NEB, M2200). 2.5 μl of DNA Quick ligase (NEB, M2200) and 0.5 μl of 50 μM annealed TruSeq adapters were added and incubated for 1 h at room temperature. Beads were separated on a magnet, resuspended in 400 μl of 1× TWB (5 mM Tris-HCl, 0.5 M EDTA, 1 M NaCl, 0.05% Tween-20) and washed for 5 min at room temperature with rotation. Beads were washed on the magnet with 200 μl 1× binding buffer and 200 μl of 1× NEBuffer 2.1 and resuspended in 20 μl of 1× NEBuffer 2.1. The library was amplified in 8 separate reactions of 50 μl. Per reaction, 1.5 μl of 25 μM TruSeq PCR primer cocktail (TruSeq PCR primer cocktail_F, TruSeq PCR primer cocktail_R; see Supplementary Table 4), 25 μl of 2× Kapa HiFi HotStart Ready Mix (Kapa Biosystems, KR0370) and 21.5 μl of water were added to 2 μl of library bound to the beads. Amplification was performed as follows: 3 min at 95 °C, 5 cycles of 20 s at 98 °C, 30 s at 63 °C and 30 s at 72 °C, 1 cycle of 1 min at 72 °C, hold at 4 °C. The PCR reactions were pooled and the beads were removed from the supernatant using a magnet. The library was purified by addition of 1.5 volumes of Agencourt AMPure XP beads (Beckman Coulter), according to the manufacturer's instructions. The sample was eluted off beads using 25 μl of 1× TLE buffer, transferred to a fresh tube and the concentration was determined using Qubit (Qubit dsDNA HS Assay Kit, Thermo Fisher) and qPCR (KAPA SYBR FAST qPCR Master Mix, Kapa Biosystems), according to the manufacturer's instructions. Library size distributions were determined on a 5% polyacrylamide gel. Paired-end

© 2018 Springer Nature Limited. All rights reserved.

76-bp sequencing was carried out using the Illumina NextSeq 500 system with high and mid output NextSeq 500/550 kits according to the manufacturer's instructions.

Mapping of Hi-C reads and generation of interaction matrices. Reads were trimmed at their ligation junction using the truncator of the HiCUP pipeline[37] (version 0.5.9 devel), mapped using bwa mem (https://arxiv.org/abs/1303.3997) of the bwa kit version 0.7.12-r1039 and those with a quality score $q > 0$ were retained. Reads were mapped to the *T. brucei* Lister 427 genome version 9 (Tb427v9). For each chromosome, this genome contains the core region of two homologous chromosomes only once, whereas both of the the respective heterozygous subtelomeric regions belonging to the two homologous chromosomes are included. During the mapping of Hi-C reads, contigs that displayed alternative variations of an assembled allele were removed (Tb427v9_without_allelic_variants) to keep these loci visible in the Hi-C matrices. The primary analysis of Hi-C reads was performed with HiC-Pro[38] (version 2.10.0) to visually inspect reproducibility among replicates. Raw matrices were normalized for differences in ploidy (for example, read counts at diploid regions were multiplied by 0.5), balanced by iterative correction using HiC-Pro (default settings) and converted into a homer compatible format[39] using a custom Python script (see 'Code availability'). To enable comparisons between different Hi-C experiments, each value in the balanced interaction matrix was divided by the respective column sum.

Distance-dependent decay of interaction frequencies. To visualize the distance-dependent decay, interaction frequencies between Hi-C bin pairs were grouped on the basis of the linear distance between the pairs, and the distribution of the median interaction frequency across distances was plotted.

Co-localization of genomic loci. To determine whether a region of interest interacted more or less than expected by chance, the median and mean interaction frequencies were calculated for bins overlapping with the regions of interest. In addition, a 'background' interaction frequency was determined by randomly selecting regions of identical size from the same matrix. Significance was determined using Welch's *t*-test.

To identify changes in DNA–DNA interaction frequencies after deletion of histone variants, the ratio of 'feature median interaction frequencies'/'background median interaction frequency' was determined for 100 randomly selected background regions in wild-type, Δ*H3.V*, Δ*H4.V* and Δ*H3.V*Δ*H4.V* cells. Significance was determined using Welch's *t*-test. Co-localization analyses were performed using balanced interaction matrices (50-kb resolution). Bins with zero values were excluded from the analyses.

4C-like analysis. To visualize interactions between one genomic region (bait) and all other genomic sites, relevant bins were extracted from a 20-kb Hi-C matrix. An average interaction value for every genomic bin was calculated if the bait regions spanned more than one bin.

Hi-C matrix visualization. Matrices were plotted based on the colour palettes provided by seaborn (https://seaborn.pydata.org). To generate differential heat maps, a pseudo-count of 0.000001 was added to each interaction value of the numerator and denominator matrix before division.

SMRT sequencing. Genomic DNA was isolated and precipitated from 3×10^8 cells of the *T. brucei* 427 17.13 P10 isolate[40] using the Blood & Cell Culture DNA Midi Kit (Qiagen), according to the manufacturer's instructions. In addition, the DNA was purified in a phenol chloroform extraction using Manual Phase Lock Gel 2-ml (heavy/light) tubes (5Prime) and suspended in 100 μl of TE buffer. SMRT library preparation and sequencing was performed at the Icahn School of Medicine at Mount Sinai.

Genomic DNA library preparation and sequencing was performed primarily using the manufacturer's instructions for the P6-C4 sequencing enzyme and chemistries. In short, ~5 μg gDNA was quantified and diluted to 150 μl using elution buffer (Qiagen) at 33 ng/μl and then sheared to ~20 kb by centrifugation at 4,500 rpm for 50 s using a G-tube spin column (Covaris). The sheared DNA was then re-purified using Agencourt AMPure XP beads (Beckman Coulter) at 0.45×. Next, ~1.6 to 3.2 μg of DNA from each batch was taken into DNA damage and end repair. In brief, the DNA fragments were repaired by adding 21.1 μl of DNA damage repair solution (1× DNA damage repair buffer (1× NAD+, 1 mM ATP and 0.1 mM dNTP) and 1× DNA damage repair mix) and incubation at 37 °C for 20 min. DNA ends were repaired by adding 1× end repair mix to the solution and incubation at 25 °C for 5 min, followed by an additional 0.45× Agencourt AMPure XP purification step. Next, 0.75 μM of blunt adaptor was added to the DNA and 1× template preparation buffer (0.05 mM ATP and 0.75 U/μl T4 DNA ligase) was added to a final volume of 47.5 μl. This solution was incubated at 25 °C overnight, followed by incubation at 65 °C for 10 min to inactivate the ligase. To remove un-ligated DNA fragments, exonuclease cocktail (1.81 U/μl Exo III 18 and 0.18 U/μl Exo VII) was added to the library followed by a 60 min incubation at 37 °C. Two additional 0.45× Agencourt Ampure XP purification steps were performed to remove <2,000-bp molecular weight DNA and organic contaminants.

The size of the library was validated using an Agilent DNA 12000 chip. Before P6-C4-based sequencing, Blue Pippin size selection was applied to remove molecules <7,000 bp. This step was conducted using Sage Science Blue Pippin 0.75% agarose cassettes to select libraries in the range of 7,000–50,000 bp. Primers were annealed to the size-selected SMRTbell at a ratio of 20:1 with the full-length libraries by denaturation (80 °C for 2 min) and slow cooling (0.1 °C/s to 25 °C). The polymerase-template complex was bound to the P6 enzyme using a ratio of 10:1 polymerase to SMRTbell at 0.5 nM for 4 h at 30 °C and then held at 4 °C until ready for magnetic-bead loading. The magnetic-bead loading step was conducted at 4 °C for 60 min. The magnetic-bead-loaded, polymerase-bound SMRTbell libraries were placed onto the RSII machine at a sequencing concentration of 50 pM and configured for a 240-min continuous sequencing run.

Assembly, post-assembly improvements and genome scaffolding. The 642,583 sequencing reads from wild-type gDNA (seven SMRT cells) were assembled into contigs following the RS_HGAP_Assembly.3 workflow from SMRT Analysis v2.3.0[41] with default parameters. In brief, a sequence seeding dataset with the longest sequencing reads was pulled apart. The remaining reads were mapped onto them to obtain error-corrected reads through a consensus procedure. The error-corrected reads were assembled by traditional overlap layout consensus with a Celera Assembler[42]. Contig sequences were polished with Quiver and were further joined and extended using PBJelly 2 (PBSuite_15.2.20)[43]. Remaining sequence errors were corrected using iCORN2[44] with previously published and new gDNA Illumina data available under GSM2586510 (https://www.ncbi.nlm.nih.gov/geo/query/acc.cgi?acc=GSM2586510) and ERS1503958 (http://www.ebi.ac.uk/ena/data/view/ERS1503958), respectively.

For genome scaffolding, all Hi-C reads were combined, mapped onto the error-corrected HGAPv3 contigs and a balanced 10-kb bin heat map matrix of DNA–DNA interactions was generated as previously described. For the scaffolding, only a subset of the matrix that contained contigs larger than 50 kb was considered (Extended Data Fig. 1).

Then, contigs that did not exhibit a gradual distance-dependent decay in DNA–DNA interactions (which suggests that they may have been incorrectly assembled) were broken at the site of the putative mis-assembly. Available pipelines for the scaffolding of contigs based on DNA–DNA interaction frequencies are not designed for genomes that contain large regions of heterozygosity[45,46]; therefore, contigs were manually rearranged and/or inverted so that long-distance DNA interactions—visible as signal away from the diagonal—were reduced. The process of Hi-C read-mapping, heat map generation and contig repositioning or inversion was repeated until no contigs could be identified, the repositioning of which would have further minimized the signal away from the diagonal (Extended Data Fig. 1). To validate our scaffolding approach and to further improve the genome, we ran PBJelly 2, which enabled us to join together several of the contigs that we had placed next to each other and to reduce the number of contigs from 139 to 91. In addition, we compared the obtained Lister 427 scaffold to that of the previously assembled TREU 927 genome and found that the core regions exhibited a high degree of similarity and synteny (Extended Data Fig. 2), which validates our scaffolding approach. The subtelomeric regions are known to be different between the genomes. Finally, we observed that 27 out of the 33 core–subtelomere boundaries in the assembly are spanned by PacBio reads and/or contigs, which supports their linear proximity (see Supplementary Information).

For a comparison of different assembly strategies and an assessment of the genome quality, see Supplementary Information and Supplementary Table 3. The genome-built Tb427v9, which was used for all analyses performed in this study, is available in the European Nucleotide Archive with the ENA study accession number PRJEB18945 (http://www.ebi.ac.uk/ena/data/view/PRJEB18945).

Genome annotation. Annotations from the *T. brucei* TREU 927 genome were transferred using Companion (https://companion.sanger.ac.uk; accessed 9 January 2017)[47]. In addition, VSG genes were annotated based on similarity (>90% coverage and >95% identity to a VSG gene) of the available VSGnome dataset from the Lister 427 strain[10] with NCBI-BLAST+ (version 2.2.31+). Overlapping VSG-gene entries were merged and named after the entry with the best bit score. For the identification of putative novel MESs, the assignment of BESs to chromosome ends and the identification of centromeres, see Supplementary Information.

Chromatin immunoprecipitation with sequencing. Assays were performed as previously described[48] with minor alterations. For the immunoprecipitation of cell lines with Ty1-tagged proteins (*Ty1-H3.V*/Δ*H3.V*, *Ty1-H4.V* Δ*H4.V*/Δ*H4.V* and *Ty1-SCC1*/Δ*SCC1* cells), 50 μl of Dynabeads protein G (ThermoFisher) was separated on a magnet, the supernatant was removed and the beads were resuspended in 200 μl of PBS-Tween (0.02%) containing 10 μg of BB2 antibody[49], and then incubated with slow rotation at 4 °C overnight. Antibody-coupled protein G beads were separated on a magnetic rack and washed three times with PBS-Tween (0.02%). Five hundred microlitres of ChIP sample was added, and incubated at 4 °C overnight with slow rotation. For ChIP assessment of the distribution of histone variants, the DNA was fragmented using micrococcal nuclease; for ChIP assessment of the distribution of SCC1, the DNA was sheared using a Covaris S220 instrument before target protein binding. Sequencing reads were mapped using

© 2018 Springer Nature Limited. All rights reserved.

bwa mem and coverage plots were generated using COVERnant (v.0.3.2) (https://github.com/konrad/COVERnant)[13].

ATAC-seq. To ensure reproducibility of the assays independent of cell-number variations, all assays were performed with 1×10^6 and 2×10^6 cells. To this end 3×10^7 cells were collected and washed in 30 ml of cold 1× TDB. The pellet was resuspended in 300 μl permeabilization buffer with protease inhibitors, 3 μl of 4 mM digitonin was added and incubated for 5 min at room temperature. The cells were pelleted, resuspended in 600 μl isotonic buffer with protease inhibitors and split in two samples, containing 1×10^7 and 2×10^7 cells, respectively. The transposition reaction was performed by adding 50 μl of transposition mix to the pellet (25 μl TD (2× reaction buffer from Nextera kit), 25 μl TDE1 (Tn5 transposase from Nextera kit), 22.5 μl nuclease-free water) and incubation for 30 min at 37 °C. For the gDNA control, 200 ng of gDNA was treated in the same manner. The DNA samples were purified using Qiagen MinElute PCR Purification Kit and eluted in 10 μl EB (10 mM Tris-HCl, pH 8). The transposed DNA fragments were amplified using the NEBNext High-Fidelity 2× PCR Master Mix (M0541) supplied with 2.5 μl of 25 μM barcoded primers and amplification for 13 cycles. The libraries were purified using AMPure XP beads (Beckman Coulter) according to the manufacturer's instructions. The library fragment sizes between 150 and 1,000 bp were purified from a 6% polyacrylamide gel. Paired-end 76-bp sequencing was carried out using the Illumina NextSeq 500 system with a high-output NextSeq 500/550 kit, according to the manufacturer's instructions. Sequencing reads were mapped using bwa mem and coverage plots were generated using COVERnant (v.0.3.2) (https://github.com/konrad/COVERnant)[13].

scRNA-seq. *T. brucei* wild-type and $\Delta H3.V\Delta H4.V$ cells were sorted (0 cell, 1 cell or 50 cells) using a FACSAria III (BD Biosciences; precision: single-cell; nozzle: 100 μm). A forward-scatter area versus side-scatter area plot was used to gate and sort the cells. *T. brucei* cells were sorted in 48-well plates (Brand) filled with 2.6 μl of 1× lysis buffer (Takara) supplemented with 0.01 μl of RNase inhibitor (40 U/μl; Takara). Immediately after sorting, cells were placed on ice for 5 min and stored at −80 °C.

Lysates from 50 trypanosomes and single trypanosomes were supplemented with 0.2 μl of a 1:2 × 10^6 (scRNA-seq I) or a 1:20 × 10^6 (scRNA-seq II) dilution of ERCC Spike-In Control Mix 1 (Thermo Fisher, 4456740). Libraries were prepared using SMART-Seq v.4 Ultra Low Input RNA Kit (Takara) using a quarter of the reagent volumes recommended by the manufacturer. PCR amplification was performed using 26 cycles (scRNA-seq I) or 22 cycles (scRNA-seq II), according to the supplier's recommendations. cDNA was purified using Agencourt AMPure XP beads (Beckman Coulter) and recovered in 15 μl of elution buffer (Takara). Libraries were quantified using the Qubit 3 Fluorometer with dsDNA Hs Assay kit (Life Technologies) and the quality of the libraries was assessed using a 2100 Bioanalyzer with High Sensitivity DNA kit (Agilent) (Extended Data Fig. 7). Similar to previously published approaches[50], 0.5 ng of cDNA was subjected to a tagmentation-based protocol (Nextera XT, Illumina) using a quarter of the recommended volumes, 10 min for tagmentation at 55 °C and 1 min extension time during PCR amplification. Libraries were pooled (96 libraries for NextSeq) and sequencing was performed in paired-end mode for 2 × 75 cycles using Illumina's NextSeq 500. Details of the sequencing results are listed in Supplementary Table 2.

Analysis of scRNA-seq. The reads were mapped to the combination of the Tb427v9 genome with the ERCC spike-in sequences, using bwa mem, version 0.7.16. The mapped data were processed using samtools[51] (version 1.8) and MarkDuplicates tool (2.18.3-SNAPSHOT) from Picard (http://broadinstitute.github.io/picard/), and the read counts-to-features were done with bedtools[52] (version 2.26.0). To assess the quality of the data, for each scRNA-seq experiment the read counts to the following groups were determined: reads mapping to 'rRNA genes', reads mapping to 'protein-coding genes' (CDS plus 89 bp for the 5′ UTR and 400 bp for the 3′ UTR)[53], reads mapping to 'other regions of the genome' and 'unmapped reads'. Reads that overlapped 'rRNA genes' and 'protein-coding genes' features at the same time were excluded from both groups and counted as reads mapping to 'other regions of the genome'.

To assess the library complexity of the scRNA-seq datasets, the number of genes with ≥ 10 read counts was determined for each cell. The counts per feature group, as well as the number of genes captured in each scRNA-seq experiment, are available in Supplementary Table 2. Only those scRNA-seq datasets with more than 500 genes with ≥ 10 read counts were considered for the quantification of VSG gene expression.

Many VSG genes share a high degree of homology with each other. Therefore, to determine the expression levels for each of the 2,846 VSG genes annotated in Tb427v9, the number of uniquely mapping sequence reads obtained for each VSG gene was normalized to account for differences in uniqueness. The uniqueness of the VSG genes was determined by alignment of an in silico-generated dataset that matched the scRNA-seq datasets in read size and fragment-length distribution. For each cell, the transcript level of an individual VSG gene is shown as a percentage of the total VSG gene transcript level in that cell. Raw and normalized read counts are available in Supplementary Table 2, and a diagram explaining the VSG count normalization procedure is shown in Extended Data Fig. 7.

Total RNA-seq. Triplicates of *T. brucei* wild-type, $\Delta H3.V$, $\Delta H4.V$ and $\Delta H3.V\Delta H4.V$ cells were grown to a density of ~10^6 cells/ml. Cell concentration was determined nine times for each replicate using a Coulter Cell Counter (Beckman Coulter) and 4.5×10^7 cells were collected from each culture. Cells were washed with 1× TDB, resuspended in 350 μl of buffer RA1 (Macherey-Nagel, NucleoSpin RNA) and 38 μl of 0.1 M DTT and 1 μl of a 1:10 dilution of ERCC Spike-In Control Mix (Thermo Fisher, 4456740) were added. Total RNA was purified from the lysate according to the NucleoSpin RNA kit protocol, and eluted in 30 μl of nuclease-free water. To deplete rRNA, 3.5 μg of total RNA was mixed with 2.6 μl of 5× hybridization buffer (500 mM Tris-HCl pH 7.4, 1 M NaCl), 0.459 pmol of 131 50-bp anti-rRNA oligonucleotides (covering *18S*, *M1*, *M2*, *M3*, *M4*, *M5*, *M6*, *28S* alpha and *28S* beta rRNAs, a kind gift of C. Clayton; for the full list, see Supplementary Table 4) and 2.2 μl of water, denatured at 95 °C for 2 min and slowly (0.1 °C per s) cooled to 37 °C. One microlitre of prewarmed 10× RNaseH digestion buffer (200 mM Tris-HCl, pH 7.4, 500 mM KCl, 40 mM $MgCl_2$, 10 mM DTT) and 10 U of RNaseH (ThermoFisher, AM2292) were added and the volume was adjusted to 16 μl with nuclease-free water. The mixture was incubated at 37 °C for 20 min. Residual oligonucleotides were subsequently digested by addition of 2 U of Turbo DNaseI and 5 μl of 10× Turbo DNase reaction buffer (AM2238, Thermo Fisher) in a total reaction volume of 50 μl and incubation at 37 °C for 20 min. The DNase was inactivated by addition of EDTA (15 mM final concentration) and heating at 75 °C for 10 min. The RNA was purified using RNAeasy Minelute columns (Qiagen), according to the manufacturer's instructions, and eluted in 14 μl of RNase-free water. Double-stranded cDNA was synthesized from 100 ng of rRNA-depleted RNA using the NEBNext Ultra RNA Library Prep Kit for Illumina. The double-stranded cDNA was purified using Agencourt AMPure XP beads (Beckman Coulter) and eluted in 60 or 30 μl of 0.1× TE Buffer, respectively. Libraries were prepared and sequenced as previously described[48].

Analysis of RNA-seq data. After adaptor clipping and quality trimming using cutadapt[54] (version 1.10), the RNA-seq reads were mapped against the *T. brucei* genome using bwa mem of the bwa kit version 0.7.16. Only reads with a quality score $q > 0$ were retained. Feature quantification was performed with bedtools multicov subcommand. Differential gene expression analysis was then conducted with DESeq2 (v.1.20.0)[55]. Features with an adjusted *P* value (calculated based on Wald test and adjusted for multiple testing using the procedure of Benjamini and Hochberg[56]) below 0.1 were considered as differentially expressed. Supplementary Table 1 contains the raw counts for each gene in each individual RNA-seq replicate, as well as the fold change (in $\log_2$ scale) and *P* value adjusted for each sample versus wild type.

Fluorescence in situ hybridization. For each FISH assay, 1×10^7 bloodstream-form trypanosomes grown to a density of up to 1×10^6 cells/ml were collected and the cell pellet was washed once with 1× TDB and fixed for 15 min in 1× TDB containing 4% formaldehyde. Cells were washed with 1× TDB once and resuspended in 50 μl of 1× TDB. Gene frames were placed onto microscopy slides to cover an aminopropyltriethoxysilane-coated coverslip. Cells were pipetted onto the framed coverslip and allowed to settle for 5 min by gravity. The sample was washed twice for 2 min with 90 μl of 1× TDB, incubated with quenching solution (1× TDB containing 1 mg/ml $NaBH_4$) for 10 min, washed twice with 1× TDB, permeabilized with 70 μl of 1× TDB containing 0.1% NP-40 for 5 min and washed twice with 1× TDB. Next, cells were treated with 1× PBS containing 1 mg/ml RNaseA for 30 min, washed twice with 1× TDB and incubated with 50 μl of a 1:1 dilution of hybridization buffer with 2× SSC for 30 min at room temperature. The labelled probe (see Supplementary Table 4) was diluted to a final concentration of 400 nM in 25 μl of hybridization buffer (50 (v/v) formamide, 10% (w/v) dextran sulfate, 2× SSPE, 250 μg/ml herring sperm DNA). The hybridization buffer was removed from the sample, 25 μl of hybridization solution containing the probe was added and the frame was closed with a plastic lid. The sample was incubated using a thermal block at 90 °C for 5 min and at 37 °C overnight. Next, the samples were washed for 30 min in 30 ml of 50% (v/v) deionized formamide and 2× SSC at 37 °C, for 10 min in 30 ml of 1× SSC at 50 °C, for 10 min in 30 ml of 2× SSC at 50 °C and for 10 min in 30 ml of 4× SSC at room temperature. Subsequently, cells were blocked in P1 buffer (100 mM maleic acid, 150 mM sodium chloride, pH 7.5, 4% BSA, 1% milk) for 1 h, incubated with primary antibody (sheep anti-digoxigenin antigen-binding fragment, Roche, diluted 1:2,000 in P1) for 45–60 min and washed with 0.5% Tween-20 and PBS 4 times for 4 min each. Cells were then incubated with the secondary antibody (Alexa Fluor 488 conjugated donkey anti-sheep IgG (H + L), Life Technologies, A11015, diluted 1:2,000 in P1) for 30–60 min. For further signal amplification, the samples were washed with PBS containing 0.5% Tween-20 4 times for 4 min and incubated with a rabbit anti-donkey IgG (H + L) DyLight 488 (Invitrogen) (diluted 1:2,000 in P1) for 30-60 min. The samples were washed twice for 10 min in 30 ml of PBS containing 0.5% Tween-20 and another 10 min in 30 ml of PBS, each time in a falcon tube on a shaker. Samples were

© 2018 Springer Nature Limited. All rights reserved.

mounted with 36 μl of Vectashield Mounting Medium with DAPI (Biozol) on a microscopy slide and were sealed with nail polish.

Immunofluorescence. Immunofluorescence was performed as previously described[57], with minor alterations. Ten million cells per ml (wild type, Δ*H3.V*, Δ*H4.V* and Δ*H3.V*Δ*H4.V*) were suspended in HMI-11 containing 2% formaldehyde, incubated for 5 min at room temperature and washed with 1× TDB. α-Tubulin was stained using the mouse monoclonal antibody Tat1[58] (1:200) and a secondary Alexa Fluor 594-conjugated chicken anti-mouse IgG (1:350, Invitrogen). VSG-2 was stained using CRD-depleted rabbit anti-VSG-2[40] (1:1,000) and a secondary Alexa Fluor 488-conjugated donkey anti-rabbit IgG (1:350, Invitrogen).

Fluorescence microscopy and image analysis. For imaging, a wide-field fluorescence Leica DMI6000 microscope with a mercury metal halide lamp and a HCX PL APO CS 100×/1.47 OIL objective was used. Images were captured with a Leica DFC 360 FX camera. Stacks with 32 slices and 6.3232 μm in height (0.0645 × 0.0644 × 0.1976 μm^3 voxel size) were captured using identic exposure times for all conditions.

Quantification of 'large' telomere clusters was carried out using Imaris 8 software (Oxford Instruments). After segmenting individual nuclei in the DAPI channel, surfaces were rendered for the telomere FISH signal, while setting the quality filter > 1,000. All FISH signals that generated surfaces with a volume > 0.3 μm^3 were classified as large telomere clusters, and scored.

FACS flow cytometry. VSG expression on the cell surface was quantified according to a previously published protocol[40]. In brief, 1×10^6 cells were centrifuged in a chilled microcentrifuge at 1,500*g* for 4 min at 4 °C. Cells were resuspended in 100 μl of ice cold HMI-11 and a VSG-specific antibody (anti-VSG-2 or anti-VSG-13)[40] was added. After 60 min of incubation at 4 °C with gentle shaking, cells were washed three times in 500 μl of ice cold HMI-11, resuspended in 100 μl of cold HMI-11 and incubated with an Alexa Fluor 488-conjugated secondary antibody for 20 min. The cells were washed twice with 500 μl of 1× TDB and finally resuspended in 400 μl of 1× TDB before analysis with a FACSort flow cytometer (Becton Dickinson Biosciences).

To determine the cell-cycle profiles, 5×10^6 cells were collected (10 min, 1,300*g*, 4°C) and washed once with ice-cold 1× TDB. The cells were resuspended in 1 ml ice-cold PBS and 2 mM EDTA and fixed by adding 2.5 ml ice-cold methanol. After a 1-h incubation, cells were washed with 1 ml PBS and EDTA at room temperature and resuspend in 1 ml PBS and EDTA. One microlitre RNaseA (10 μg/μl) and 10 μl propidium iodide (1 μg/μl) were added. The stained cells were analysed with a FACSCalibur (Becton Dickinson) after a 30-min incubation at 37 °C.

Mapping the site of recombination. A library from Δ*H3.V*Δ*H4.V* gDNA was prepared as described for wild-type gDNA and sequenced using the PacBio Sequel system by diffusion at 5 pM, with v2.1 chemistry and a 10-h movie. Reads > 10 Kb were extracted, split into ∼2,500-bp chunks and mapped independently to the genome. Reads that contained chunks that mapped to BES1 and BES15 were kept and mapped again to BES1 and BES15. Based on the observed mapping pattern, a BES1–BES15 hybrid was constructed.

Code availability. Workflows and custom-made Unix Shell, Python and R scripts have been deposited at Zenodo (https://doi.org/10.5281/zenodo.823671). Documentation to reproduce the data analysis is provided.

Reporting summary. Further information on research design is available in the Nature Research Reporting Summary linked to this paper.

Data availability

The RNA-seq, scRNA-seq, ChIP–seq, ATAC-seq and Hi-C sequencing data have been deposited in the Gene Expression Omnibus[59] and are accessible through GEO Series accession number GSE100896. The raw SMRT sequencing reads and the genome assembly have been deposited in the European Nucleotide Archive and are accessible through ENA study accession number PRJEB18945. All other data are available from the corresponding author upon reasonable request.

31. Hirumi, H. & Hirumi, K. Continuous cultivation of *Trypanosoma brucei* blood stream forms in a medium containing a low concentration of serum protein without feeder cell layers. *J. Parasitol.* **75**, 985–989 (1989).
32. Lowell, J. E. & Cross, G. A. A variant histone H3 is enriched at telomeres in Trypanosoma brucei. *J. Cell Sci.* **117**, 5937–5947 (2004).
33. Scahill, M. D., Pastar, I. & Cross, G. A. M. CRE recombinase-based positive-negative selection systems for genetic manipulation in *Trypanosoma brucei*. *Mol. Biochem. Parasitol.* **157**, 73–82 (2008).
34. Wirtz, E., Leal, S., Ochatt, C. & Cross, G. A. M. A tightly regulated inducible expression system for conditional gene knock-outs and dominant-negative genetics in *Trypanosoma brucei*. *Mol. Biochem. Parasitol.* **99**, 89–101 (1999).
35. Rao, S. S. et al. A 3D map of the human genome at kilobase resolution reveals principles of chromatin looping. *Cell* **159**, 1665–1680 (2014).
36. Belaghzal, H., Dekker, J. & Gibcus, J. H. Hi-C 2.0: An optimized Hi-C procedure for high-resolution genome-wide mapping of chromosome conformation. *Methods* **123**, 56–65 (2017).
37. Wingett, S. et al. HiCUP: pipeline for mapping and processing Hi-C data. *F1000Res.* **4**, 1310 (2015).
38. Servant, N. et al. HiC-Pro: an optimized and flexible pipeline for Hi-C data processing. *Genome Biol.* **16**, 259 (2015).
39. Heinz, S. et al. Simple combinations of lineage-determining transcription factors prime *cis*-regulatory elements required for macrophage and B cell identities. *Mol. Cell* **38**, 576–589 (2010).
40. Figueiredo, L. M., Janzen, C. J. & Cross, G. A. M. A histone methyltransferase modulates antigenic variation in African trypanosomes. *PLoS Biol.* **6**, e161 (2008).
41. Chin, C. S. et al. Nonhybrid, finished microbial genome assemblies from long-read SMRT sequencing data. *Nat. Methods* **10**, 563–569 (2013).
42. Myers, E. W. et al. A whole-genome assembly of *Drosophila*. *Science* **287**, 2196–2204 (2000).
43. English, A. C. et al. Mind the gap: upgrading genomes with Pacific Biosciences RS long-read sequencing technology. *PLoS ONE* **7**, e47768 (2012).
44. Otto, T. D., Sanders, M., Berriman, M. & Newbold, C. Iterative Correction of Reference Nucleotides (iCORN) using second generation sequencing technology. *Bioinformatics* **26**, 1704–1707 (2010).
45. Kaplan, N. & Dekker, J. High-throughput genome scaffolding from *in vivo* DNA interaction frequency. *Nat. Biotechnol.* **31**, 1143–1147 (2013).
46. Burton, J. N. et al. Chromosome-scale scaffolding of *de novo* genome assemblies based on chromatin interactions. *Nat. Biotechnol.* **31**, 1119–1125 (2013).
47. Steinbiss, S. et al. Companion: a web server for annotation and analysis of parasite genomes. *Nucleic Acids Res.* **44**, W29–W34 (2016).
48. Wedel, C. & Siegel, T. N. Genome-wide analysis of chromatin structures in *Trypanosoma brucei* using high-resolution MNase-ChIP-seq. *Exp. Parasitol.* **180**, 2–12 (2017).
49. Bastin, P., Bagherzadeh, Z., Matthews, K. R. & Gull, K. A novel epitope tag system to study protein targeting and organelle biogenesis in *Trypanosoma brucei*. *Mol. Biochem. Parasitol.* **77**, 235–239 (1996).
50. Patel, A. P. et al. Single-cell RNA-seq highlights intratumoral heterogeneity in primary glioblastoma. *Science* **344**, 1396–1401 (2014).
51. Li, H. et al. The Sequence Alignment/Map format and SAMtools. *Bioinformatics* **25**, 2078–2079 (2009).
52. Quinlan, A. R. & Hall, I. M. BEDTools: a flexible suite of utilities for comparing genomic features. *Bioinformatics* **26**, 841–842 (2010).
53. Siegel, T. N., Hekstra, D. R., Wang, X., Dewell, S. & Cross, G. A. M. Genome-wide analysis of mRNA abundance in two life-cycle stages of *Trypanosoma brucei* and identification of splicing and polyadenylation sites. *Nucleic Acids Res.* **38**, 4946–4957 (2010).
54. Martin, M. Cutadapt removes adapter sequences from high-throughput sequencing reads. *EMBnet J.* **17**, 10–12 (2011).
55. Love, M. I., Huber, W. & Anders, S. Moderated estimation of fold change and dispersion for RNA-seq data with DESeq2. *Genome Biol.* **15**, 550 (2014).
56. Benjamini, Y. & Hochberg, Y. Controlling the false discovery rate: a practical and powerful approach to multiple testing. *J. R. Stat. Soc. Ser. B* **57**, 289–300 (1995).
57. Siegel, T. N. et al. Acetylation of histone H4K4 is cell cycle regulated and mediated by HAT3 in *Trypanosoma brucei*. *Mol. Microbiol.* **67**, 762–771 (2008).
58. Woods, A. et al. Definition of individual components within the cytoskeleton of Trypanosoma brucei by a library of monoclonal antibodies. *J. Cell Sci.* **93**, 491–500 (1989).
59. Edgar, R., Domrachev, M. & Lash, A. E. Gene Expression Omnibus: NCBI gene expression and hybridization array data repository. *Nucleic Acids Res.* **30**, 207–210 (2002).
60. Carver, T. J. et al. ACT: the Artemis Comparison Tool. *Bioinformatics* **21**, 3422–3423 (2005).

© 2018 Springer Nature Limited. All rights reserved.

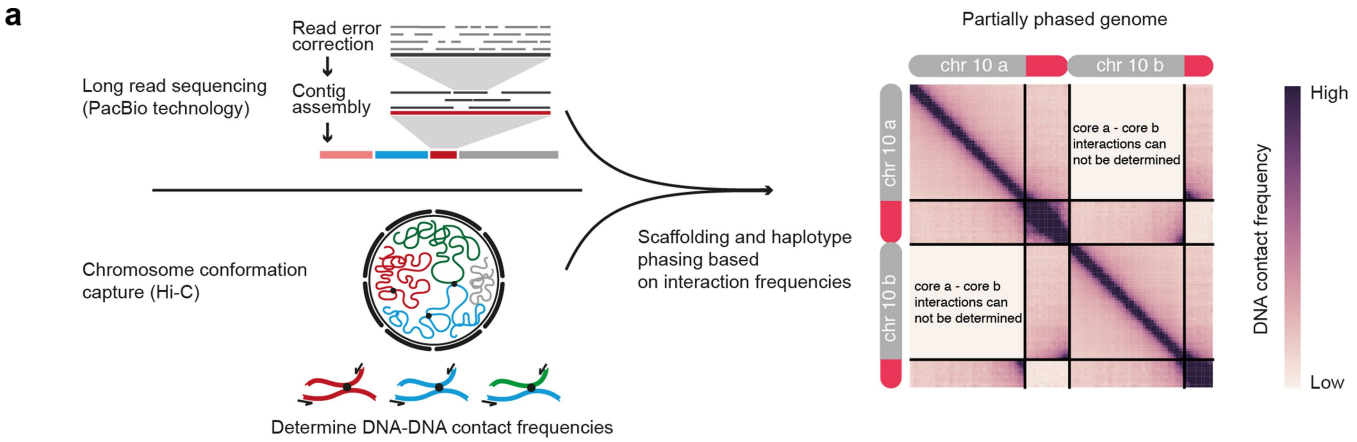

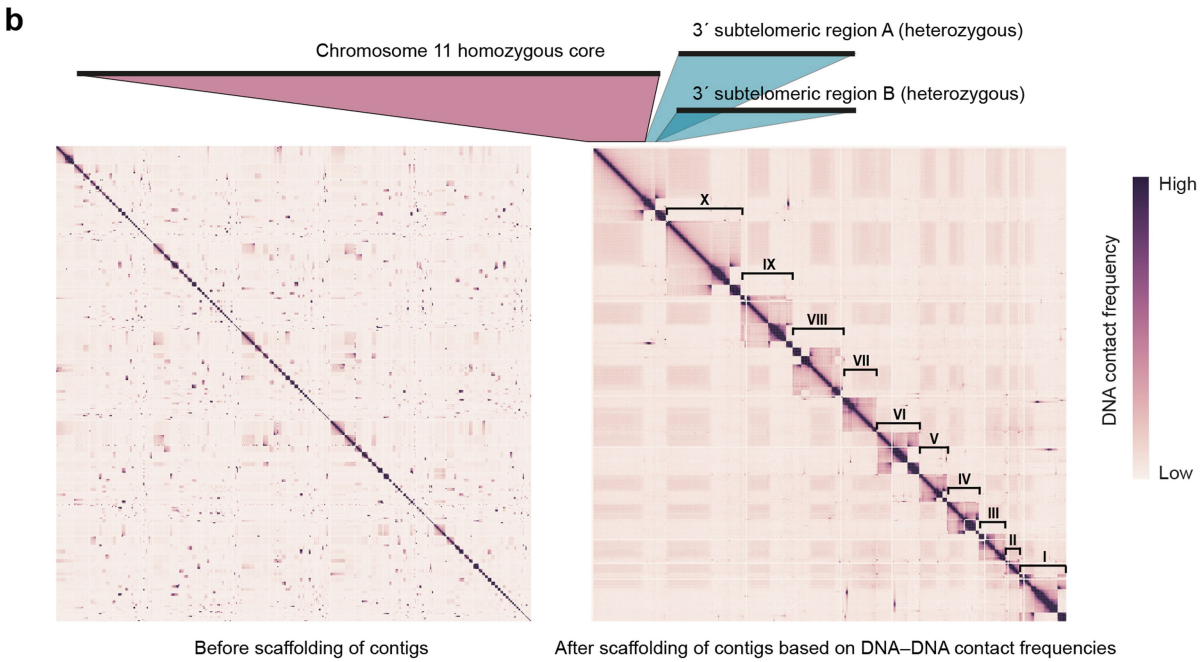

c

		SM 1	SM 2	SM 3	*ΔH3.V* 1	*ΔH3.V* 2	*ΔH3.V* 3	*ΔH4.V* 1	*ΔH4.V* 2	*ΔH4.V* 3	*ΔH3.VΔH4.V* 1	*ΔH3.VΔH4.V* 2	*ΔH3.VΔH4.V* 3
Uniquely mapped reads	Valid pairs	39621230	29246517	34224540	27575120	29806865	38649755	51033124	43771094	58604871	40293781	56126609	52975076
	Duplicates removed	39118877	28965016	33821714	27289976	29480564	38217619	50446864	43285453	57880276	39821237	55430464	52312461
	cis*	18077783	14129415	15873681	15041108	16526804	20961846	24600951	22569873	26180139	19244484	27365880	26154185
	trans*	21041094	14835601	17948033	12248868	12953760	17255773	25845913	20715580	31700137	20576753	28064584	26158276
	Dangling-end pairs	3267860	1973862	2183522	2535464	1771926	4759822	7350115	3205967	7653963	2555580	4238926	4806053
	Religation pairs	512445	333170	383430	471518	412765	741209	749387	530095	723682	449187	691047	675579
	Self-cycle pairs	67045	41226	46734	32328	45306	53743	120835	103566	127209	59587	92993	79717
	Single-end pairs	0	0	0	0	0	0	0	0	0	0	0	0
	Dumped pairs	3668	3350	3340	2815	2814	3636	6533	5463	7629	4053	6081	5499

Extended Data Fig. 1 | Assembly of the *T. brucei* Lister 427 genome. **a**, Outline of the genome-assembly strategy: gDNA of *T. brucei* Lister 427 was sequenced using SMRT sequencing technology and P6-C4 sequence chemistry. The 10% longest reads were error-corrected using the remaining SMRT reads and assembled into contigs using the HGAPv3 algorithm[41]. Information on spatial contacts between contigs, obtained from Hi-C analyses, was used to position and orient the contigs into scaffolds. **b**, To scaffold and orient the contigs, Hi-C reads were mapped to 1,232 contigs to generate a heat map of DNA–DNA interactions (left). Scaffolding was performed by placing contigs such that the interaction signal located away from the diagonal could not be further reduced (right). Heterozygous subtelomeric regions displayed strong interactions with the chromosomal core region but not with other subtelomeric regions, which indicates that they belong to independent homologous chromosomes. Note that for the left arm of chromosome 7, the heterozygous subtelomeric regions of the two homologous chromosomes could not be assembled separately. **c**, Statistics of Hi-C data analysis based on reads mapped to a joined genome version (haploid A-forks joined to the core). This implies an underestimation of *cis*, and overestimation of *trans* interactions (marked with asterisks), as the B-forks remain un-joined.

© 2018 Springer Nature Limited. All rights reserved.

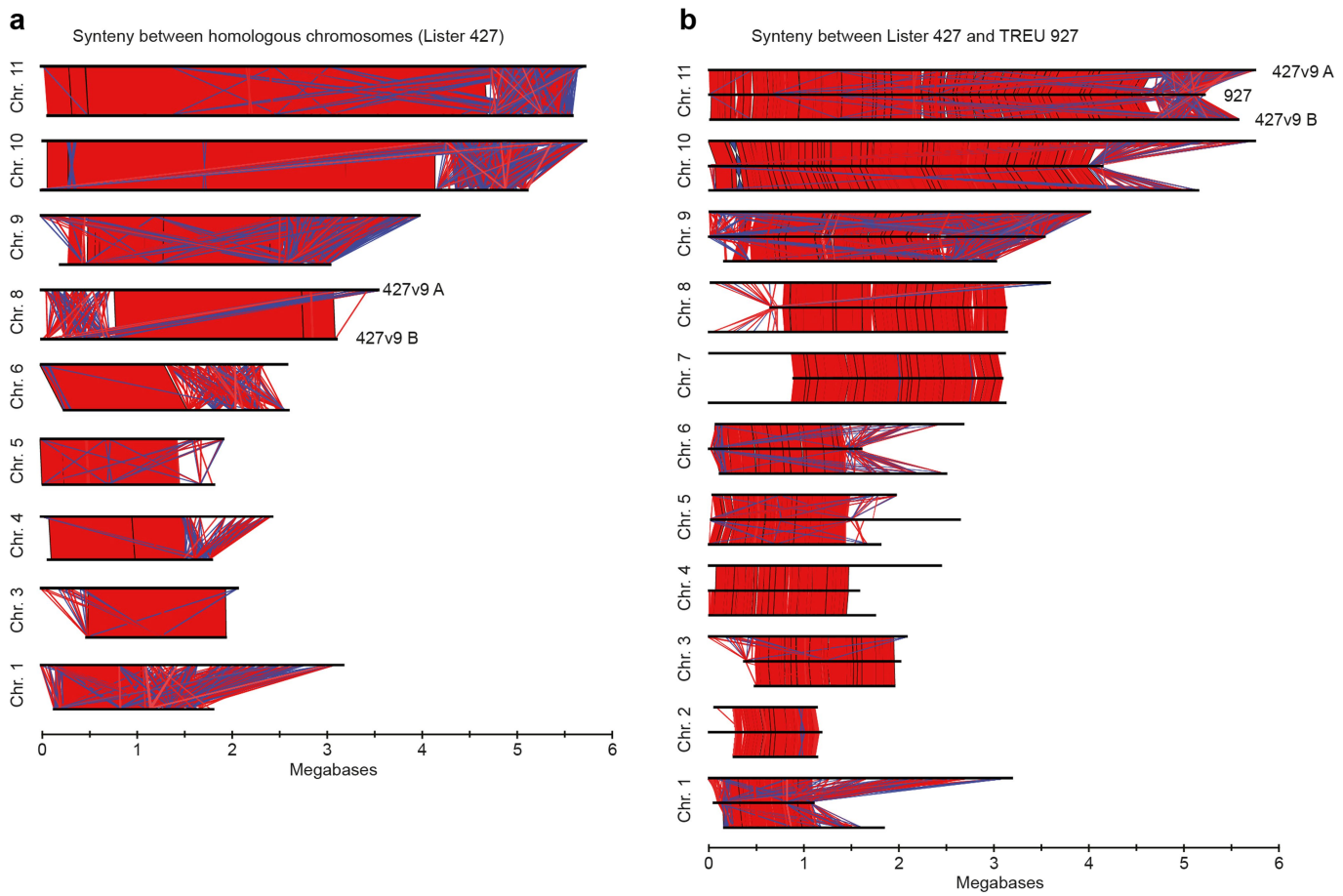

Extended Data Fig. 2 | Synteny between homologous chromosomes and between different isolates. a, Pairwise comparison of corresponding homologous chromosomes using the Artemis Comparison Tool (ACT) of the Wellcome Trust Sanger Institute[60]. Pairs of regions that share a high degree of similarity (BLAST score $\geq$ 5,000) are connected by boxes in red, or in blue if they are inverted. Chromosome 7 is not shown because the subtelomeric regions of the two homologous chromosomes are very similar and could not be resolved during the assembly. Chromosome 2 is not shown as only one of the two homologous chromosomes contains an extended subtelomeric region. **b**, Pairwise comparison of the eleven megabase-chromosomes of the TREU 927 isolate (middle black bar) and the corresponding two homologous chromosomes of the Lister 427 isolate (top and bottom black bars) using ACT[60]. Regions that reached a BLAST score of at least 5,000 are drawn in red, or in blue if they are inverted.

© 2018 Springer Nature Limited. All rights reserved.

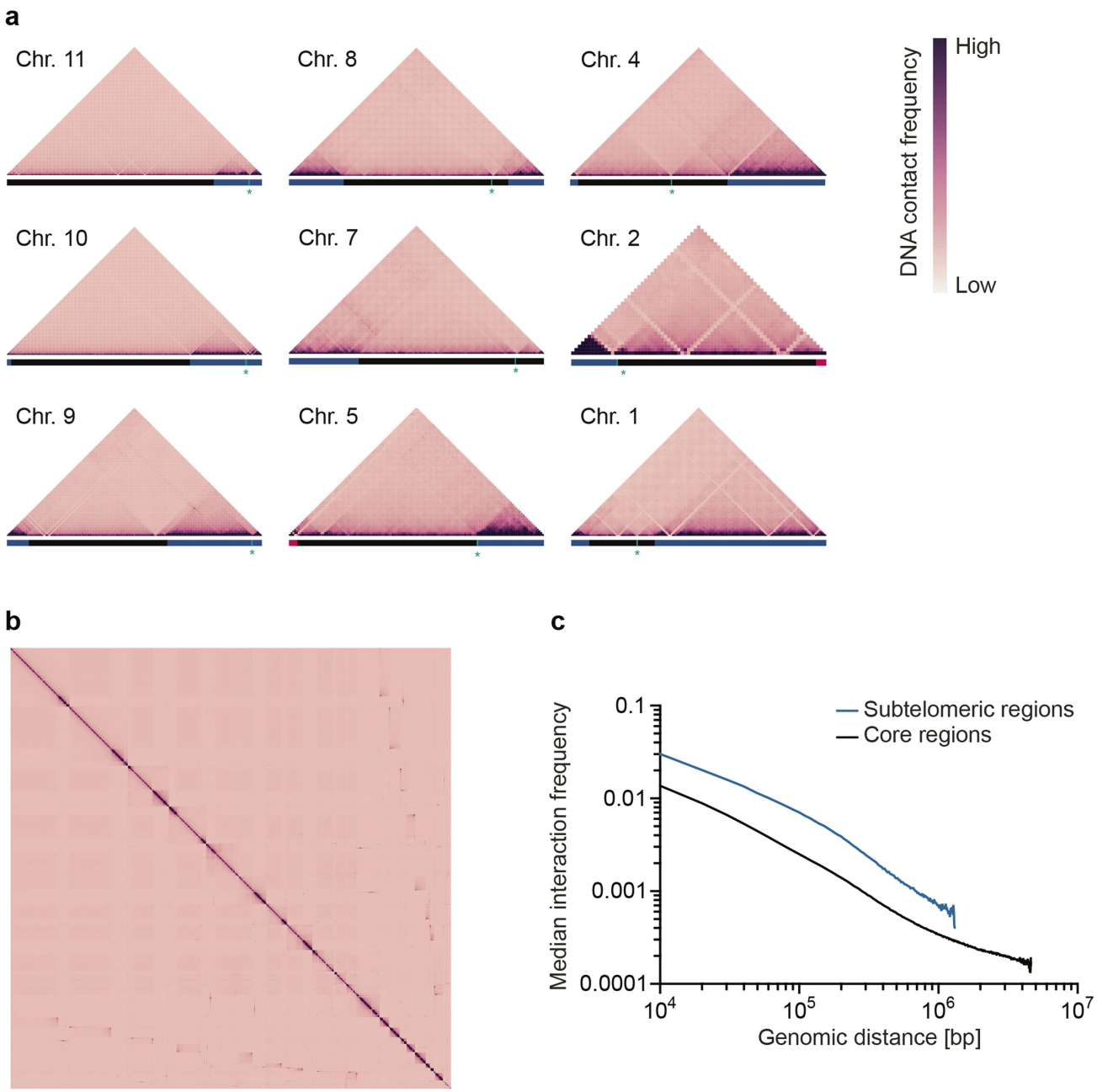

Extended Data Fig. 3 | Compartmentalization of megabase chromosomes in wild-type cells. a, Hi-C heat maps of individual chromosomes at 20-kb resolution. Horizontal lines mark subtelomeric regions (blue), core regions (black) and bloodstream-form expression sites (red). A blue vertical line and an asterisk indicate the locations of centromeres. **b**, Hi-C heat map of the haploid genome with one set of subtelomeric regions joined to the core regions (20-kb resolution). **c**, Decay of frequency of intra-chromosomal contacts as a function of genomic distance (20-kb bin size) within subtelomeric (blue) and core (black) regions. The median across the core ($n = 11$) and subtelomeres ($n = 32$) is shown.

© 2018 Springer Nature Limited. All rights reserved.

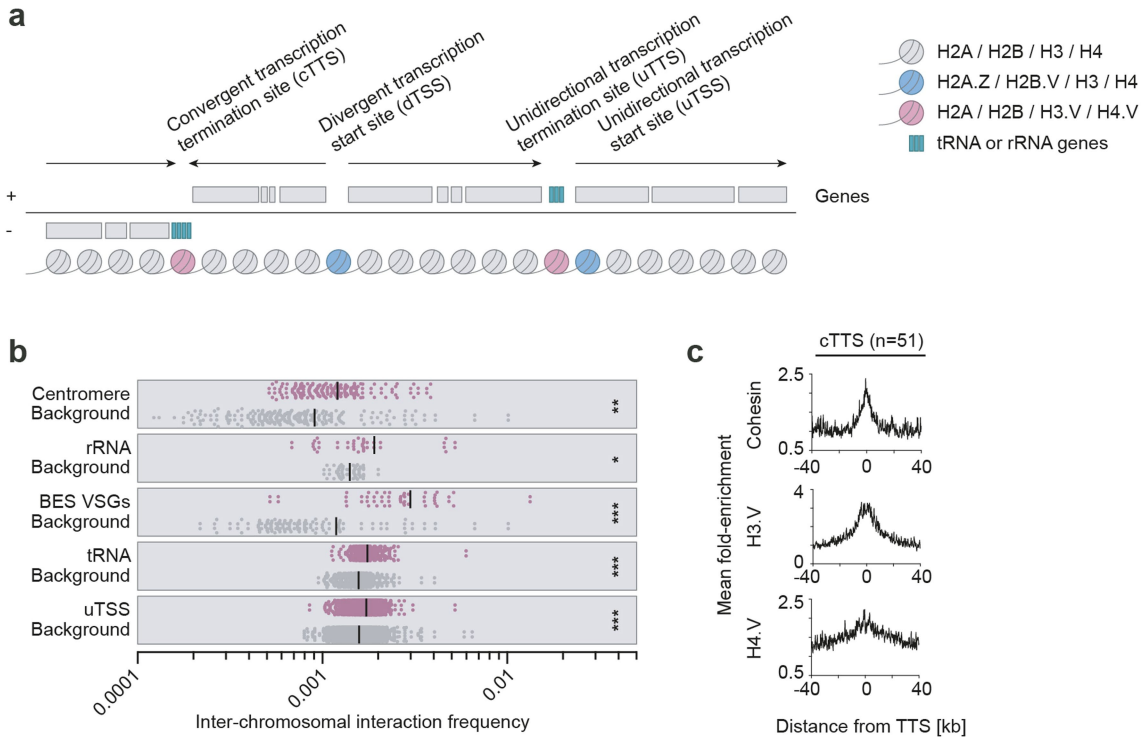

Extended Data Fig. 4 | Hi-C and ChIP–seq reveal partitioning of the *T. brucei* genome into distinct domains. a, Outline of the genome organization. Boundaries of transcription units are marked by nucleosomes that contain different types of histone variants. Black arrows indicate the direction of transcription. **b**, Scatter plot showing inter-chromosomal interactions among centromeres ($n = 206$ query bins, $n = 292$ background bins, $P = 0.0029$), VSG genes ($n = 54$ query bins, $n = 130$ background bins, $P = 1.63 \times 10^{-6}$), rRNA genes ($n = 40$ query bins, $n = 64$ background bins, $P = 0.0177$), tRNA genes ($n = 614$ query bins, $n = 620$ background bins, $P = 2.45 \times 10^{-190}$) and unidirectional transcription start sites ($n = 3{,}142$ query bins, $n = 3{,}682$ background bins, $P = 6.49 \times 10^{-91}$) compared to a background sample, which was randomly selected from the interaction matrix (50-kb bin size). The background sample matches the genomic feature in size and number. Selected bins with zero values were removed from both the query and background sample. *P* values are based on Welch's *t*-test (two-sided). Black lines represent the mean. **c**, ChIP–seq data showing cohesin, H3.V and H4.V enrichment (compared to input material) averaged across all convergent transcription termination sites (cTTS, $n = 51$) (window size, 101 bp; step size, 11 bp).

© 2018 Springer Nature Limited. All rights reserved.

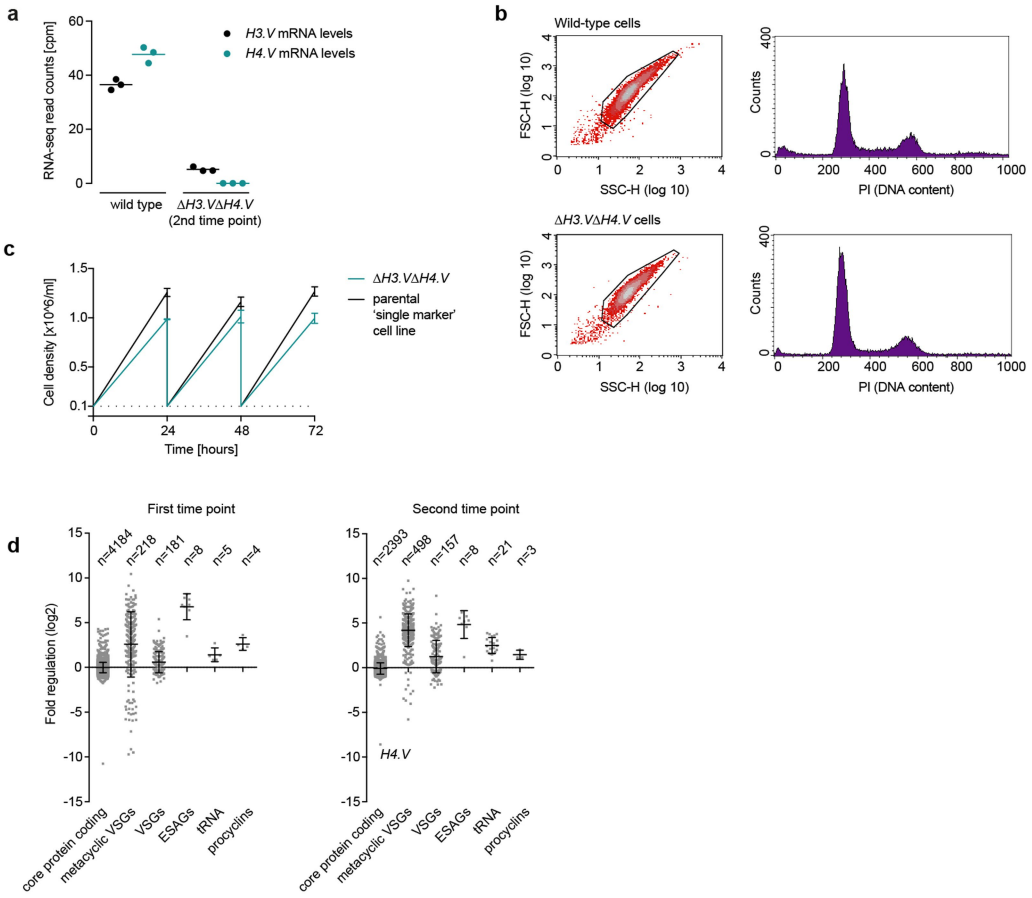

Extended Data Fig. 5 | Characterization of Δ*H3.V*Δ*H4.V* cells. **a**, RNA-seq fragment counts on *H3.V* and *H4.V* CDS in wild-type and Δ*H3.V*Δ*H4.V* cells, normalized by million fragments mapped to protein-coding genes. Note that the first and last codon of the *H3.V* open reading frame were not deleted. As a result, a small number of *H3.V* reads are detected even in the Δ*H3.V* cells. **b**, Cell-cycle analysis based on flow cytometry, of wild-type and Δ*H3.V*Δ*H4.V* cells. One of three replicates is shown. **c**, Growth curve (mean ± s.d.) of wild-type and Δ*H3.V*Δ*H4.V* cells ($n = 3$ biologically independent replicates). **d**, RNA-seq of Δ*H3.V*Δ*H4.V* cells (first and second time points). The mean ± s.d. fold change in expression compared to wild type ($n = 3$ biologically independent experiments) is shown, for the significantly regulated genes (based on a Benjamini–Hochberg adjusted *P* value from a two-sided Wald test with false discovery rate < 0.1) from different gene groups. ESAGs, expression-site-associated genes.

© 2018 Springer Nature Limited. All rights reserved.

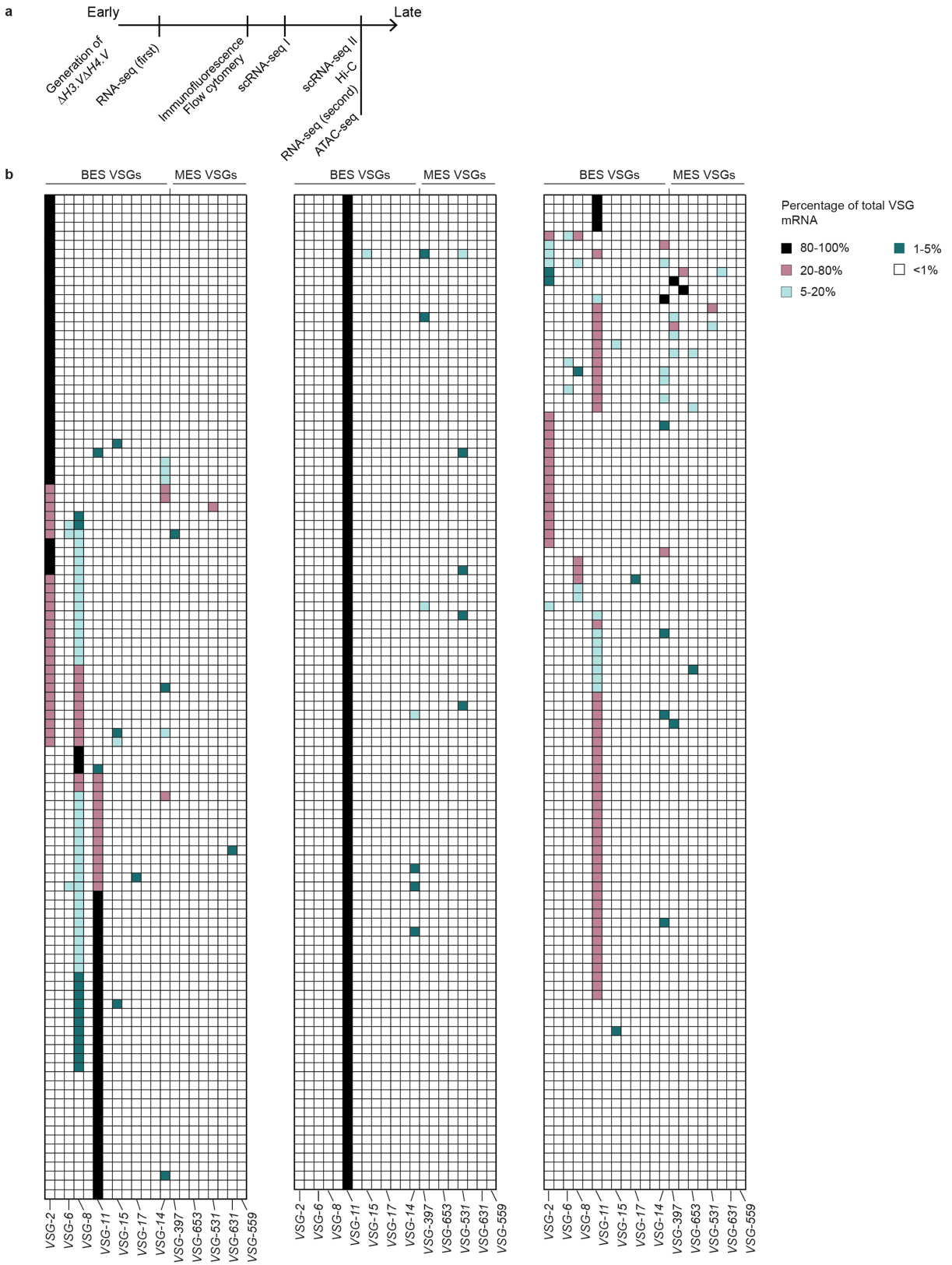

Extended Data Fig. 6 | Analysis of Δ*H3.V*Δ*H4.V* cells. a, Order of cell analyses. **b**, scRNA-seq analyis of Δ*H3.V*Δ*H4.V* cells, at the second time point. (n = 338). Each row represents data from one cell. For details, see Fig. 3a, Extended Data Fig. 7.

© 2018 Springer Nature Limited. All rights reserved.

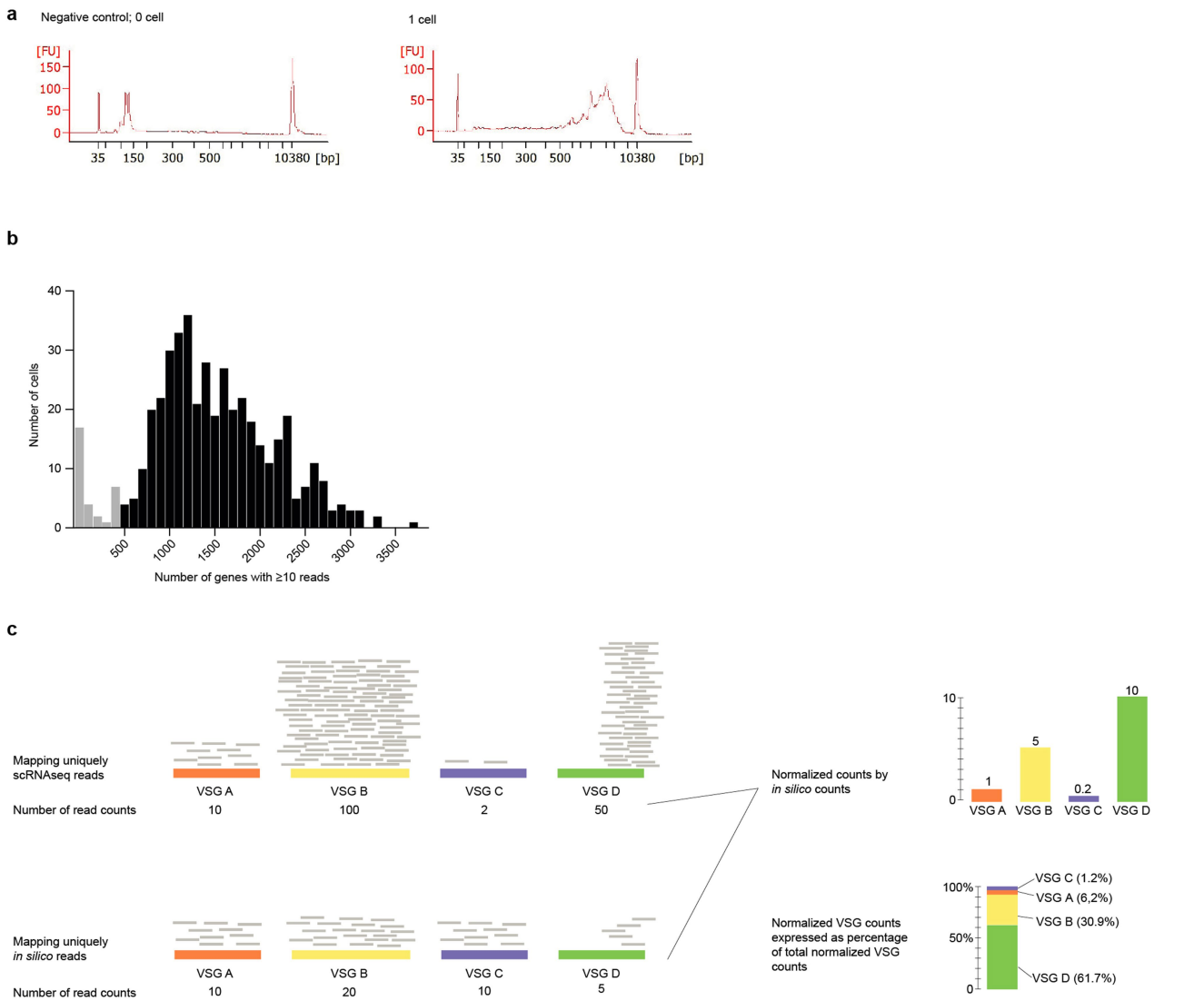

Extended Data Fig. 7 | scRNA-seq quality control, VSG gene normalization and quantification. a, Representative Bioanalyzer profiles (Agilent) of cDNA from 0 cells ($n = 6$) and 1 cell ($n = 18$, supplemented with ERCC spike-in control). **b**, Histogram representing the total number of genes expressed per single cell (wild type and $\Delta H3.V\Delta H4.V$; $n = 452$). Cells with fewer than 500 genes (grey bars) were excluded from the analysis. **c**, Diagram representing quantification of expression of VSG genes, and the normalization procedure. The reads obtained in each single-cell library were mapped to the genome, keeping only the uniquely mapping reads (mapq > 0). Next, the number of reads mapping to each VSG gene was quantified. To account for differences in length and 'uniqueness' among the different VSG genes, the same procedure was performed with an in silico set of reads. The read counts to each VSG gene in each scRNA-seq assay were normalized for 'uniqueness' and gene length by dividing them by the counts obtained with the in silico dataset. Finally, for each cell the normalized read counts for each VSG gene were expressed as a percentage of the total number of normalized counts to VSG genes.

© 2018 Springer Nature Limited. All rights reserved.

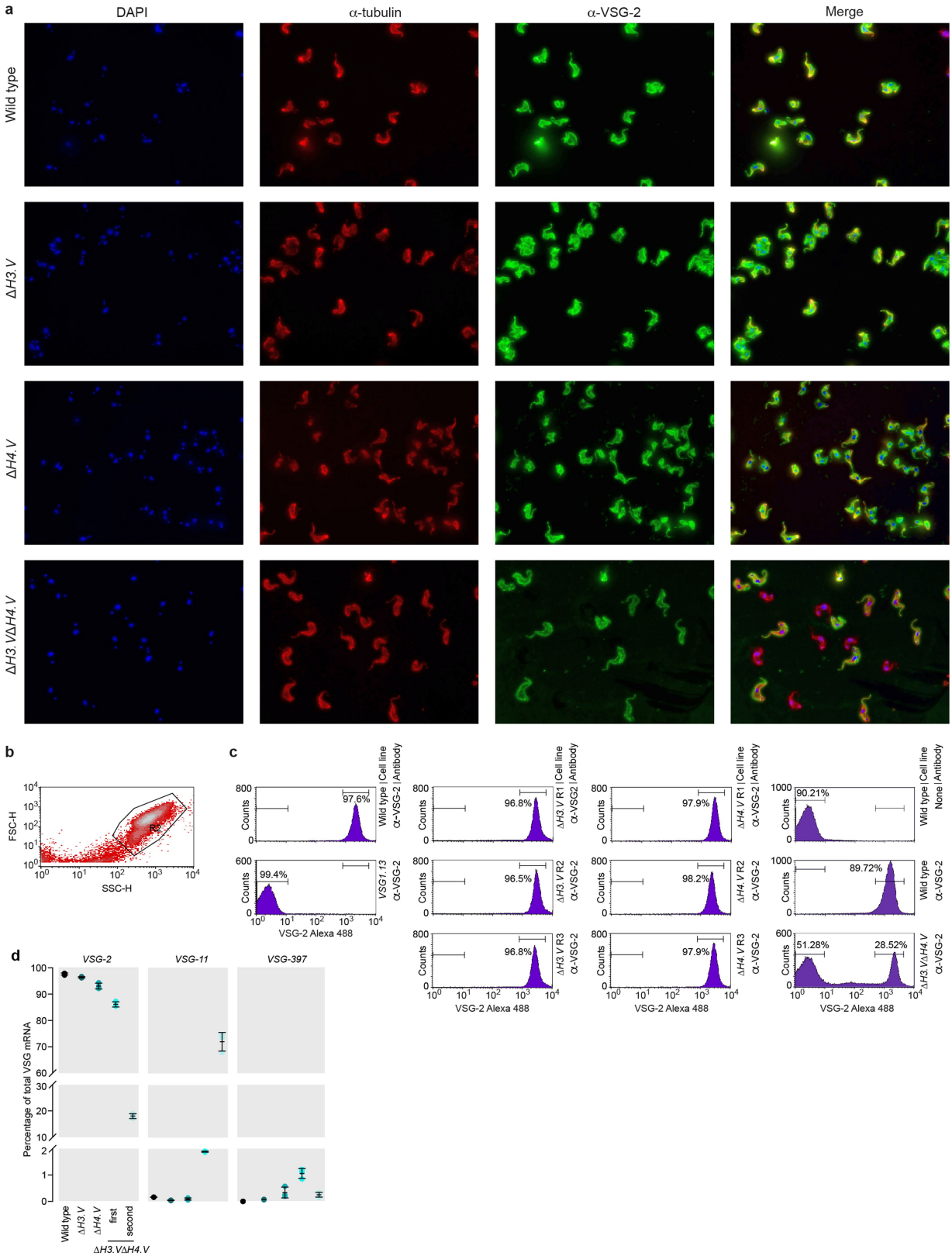

Extended Data Fig. 8 | Mutually exclusive expression of VSG genes is not lost in Δ*H3.V* and Δ*H4.V* single-knockout cells. **a**, Immunofluorescence imaging in wild-type, Δ*H3.V*, Δ*H4.V* and Δ*H3.V*Δ*H4.V* cells ($n = 1$). Representative images of 26–28 stacks (0.1976-μm voxel size, maximum projection) are shown. Scale bar, 10 μm. **b**, Gating strategy used for all analyses. **c**, Flow cytometry analysis of *VSG-2* expression in Δ*H3.V*, Δ*H4.V* and Δ*H3.V*Δ*H4.V* cells. Wild-type cells were used as a *VSG-2* positive control, and cells expressing *VSG-13* were used as a negative control. Δ*H3.V*, $n = 3$; Δ*H4.V*, $n = 3$; Δ*H3.V*Δ*H4.V*, $n = 7$ (measured at different time points). For each assay, 50,000 events were gated. **d**, Heterogeneity in expression of VSG genes, based on RNA-seq. The contributions of the dominant *VSG-2* and two additional VSG genes found to be upregulated in Δ*H3.V*Δ*H4.V* cells relative to the total VSG mRNAs are depicted. For each condition, mean mRNA levels and s.d. are derived from $n = 3$ biologically independent RNA-seq experiments.

© 2018 Springer Nature Limited. All rights reserved.

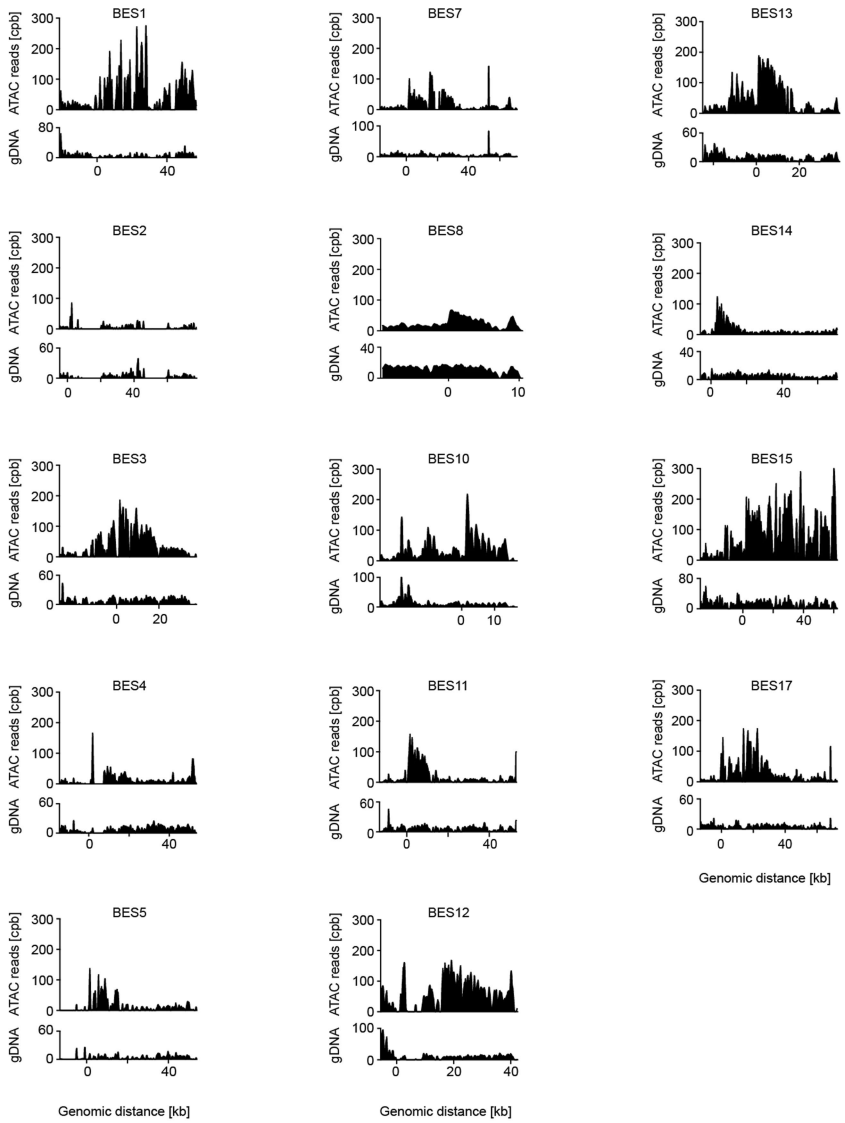

Extended Data Fig. 9 | DNA accessibility across BESs in Δ*H3.V*Δ*H4.V* cells. Uniquely mapping ATAC-seq reads across all BESs are shown. The 0-nt position corresponds to the promoter. Uniquely mapping gDNA-seq reads are shown to illustrate differences in mappability. For ATAC-seq, $n = 2$ biologically independent experiments were performed, using sample material from 10 million cells in one experiment and from 20 million cells in the other.

© 2018 Springer Nature Limited. All rights reserved.

Extended Data Table 1 | Genome assembly statistics

Parameter	Number
The genome	
Total size (Mb)	42.25
Core regions (diploid) (Mb)	22.71
Subtelomeric region (haploid) (Mb)	19.54
Megabase chromosomes	11
Contigs	96
VSG expression sites assigned to megabase chromosomes	14
The assembly	
SMRT reads	642,583
SMRT read N50 (kb)	11.94
Contigs after HGAPv3 assembly	1232
HGAPv3 contig N50 (kb)	251
Sequence assigned to megabase chr. (Mb)	42.25
Sequence assigned to mini- or intermediate chromosomes (Mb)	0.8
Unscaffolded contigs (Mb)	11.08

DNA elements that are smaller than 1 Mb—for example, mini-chromosomes or circular DNA—were not scaffolded for this study, and contribute to the un-scaffolded contigs.

© 2018 Springer Nature Limited. All rights reserved.

https://doi.org/10.1038/s41586-018-0586-0

Neural blastocyst complementation enables mouse forebrain organogenesis

Amelia N. Chang[1,5], Zhuoyi Liang[1,5], Hai-Qiang Dai[1,5], Aimee M. Chapdelaine-Williams[1], Nick Andrews[2], Roderick T. Bronson[3], Bjoern Schwer[4,6]* & Frederick W. Alt[1,6]*

Genetically modified mice are commonly generated by the microinjection of pluripotent embryonic stem (ES) cells into wild-type host blastocysts[1], producing chimeric progeny that require breeding for germline transmission and homozygosity of modified alleles. As an alternative approach and to facilitate studies of the immune system, we previously developed RAG2-deficient blastocyst complementation[2]. Because RAG2-deficient mice cannot undergo V(D)J recombination, they do not develop B or T lineage cells beyond the progenitor stage[2]: injecting RAG2-sufficient donor ES cells into RAG2-deficient blastocysts generates somatic chimaeras in which all mature lymphocytes derive from donor ES cells. This enables analysis, in mature lymphocytes, of the functions of genes that are required more generally for mouse development[3]. Blastocyst complementation has been extended to pancreas organogenesis[4], and used to generate several other tissues or organs[5–10], but an equivalent approach for brain organogenesis has not yet been achieved. Here we describe neural blastocyst complementation (NBC), which can be used to study the development and function of specific forebrain regions. NBC involves targeted ablation, mediated by diphtheria toxin subunit A, of host-derived dorsal telencephalic progenitors during development. This ablation creates a vacant forebrain niche in host embryos that results in agenesis of the cerebral cortex and hippocampus. Injection of donor ES cells into blastocysts with forebrain-specific targeting of diphtheria toxin subunit A enables donor-derived dorsal telencephalic progenitors to populate the vacant niche in the host embryos, giving rise to neocortices and hippocampi that are morphologically and neurologically normal with respect to learning and memory formation. Moreover, doublecortin-deficient ES cells—generated via a CRISPR–Cas9 approach—produced NBC chimaeras that faithfully recapitulated the phenotype of conventional, germline doublecortin-deficient mice. We conclude that NBC is a rapid and efficient approach to generate complex mouse models for studying forebrain functions; this approach could more broadly facilitate organogenesis based on blastocyst complementation.

The complexity of the cerebral cortex is a longstanding obstacle to elucidating key questions about its development and function. Experiments on cultured neurons are limited in interpretability as often they do not recapitulate normal physiological conditions[11], including the specific cues involved in regional patterning during development, activity-dependent synaptic pruning and experience-dependent plasticity. In vitro 3D brain organoid approaches can be problematic for similar reasons; in vitro approaches also do not allow neurobehavioural testing. Consequently, genetically engineered transgenic and germline mutant mouse models designed to interrogate specific gene functions in the cerebral cortex and hippocampus have been critically important for the field. However, the generation of such mutant mice using conventional methods requires breeding of chimaeras for germline transmission of the modified allele (Fig. 1a), and is time-consuming, costly and limited to genes not required for early mouse development. Germline gene knockout approaches can also be impractical with respect to analysing complex genetic models that involve independently segregating alleles[12]. Thus, we sought to develop a blastocyst complementation approach to facilitate neurobiological studies of the mouse forebrain, by creating and repopulating a vacant forebrain niche during neurodevelopment.

To ablate dorsal telencephalic progenitors in mice, we crossed mice that express Cre recombinase from an *Emx1* promoter with mice carrying a floxed STOP cassette upstream of an attenuated diphtheria toxin subunit A that was introduced into the *Rosa26* locus[13,14]. Emx1 is a homeobox transcription factor expressed at embryonic day (E)9.5 in dorsal telencephalic progenitors, which give rise to neocortical, hippocampal and olfactory bulb structures[14,15]. We predicted that *Emx1-cre;R26-DTA* mice would lack neocortices and hippocampi, based on the findings of previous studies that tested *Emx1* Cre-mediated deletion of factors required for neuronal survival[16,17], and the known ability of directed expression of diphtheria toxin subunit A to ablate specific cell lineages in mice[13,18,19] (Fig. 1b). After being transferred into foster females, pups derived from *Emx1-cre;R26-DTA* blastocysts survived birth, acquired a characteristic pink coloration (Extended Data Fig. 1a) and vocalized, which indicates they had normal respiratory and cardiovascular systems as well as functionally intact brainstems[20]. However, histological analysis of serial brain sections of the *Emx1-cre;R26-DTA* pups revealed extensive ablation of hippocampal, neocortical and olfactory bulb structures, resulting in fusion and dilation of the lateral ventricles over the thalamus (Fig. 1c). The thalamus, midbrain, hindbrain and cerebellum appeared normal, consistent with the specificity of *Emx1-cre* recombination[14]. However, the mice exhibited incomplete jaw development, probably owing to off-target recombination (Extended Data Fig. 1a), which is consistent with a similar defect documented in an independent mouse model using the same *Emx1-cre* strain[19].

We sought to repopulate the vacant dorsal telencephalic niche in *Emx1-cre;R26-DTA* mice by injecting wild-type donor ES cells into *Emx1-cre;R26-DTA* NBC host blastocysts, followed by transfer into foster females to generate NBC chimaeras (Fig. 1b). Histological analysis of NBC chimaeras revealed complete reconstitution of hippocampal and neocortical structures (Fig. 1c), and rescue of the jaw malformation (Extended Data Fig. 1a). Reconstituted NBC chimaeras that display a normal jaw phenotype were viable, developed normally after birth and showed no increased mortality up to 24 months of age (Extended Data Fig. 1a–d). Both male and female NBC chimaeras were fertile, and female chimaeras displayed normal nurturing behaviour towards their pups.

To directly assess and quantify donor and host cell contribution in NBC chimaeras, we generated and injected donor TC1 ES cells that expressed H2B–eGFP into blastocysts derived from *Emx1-cre;R26-DTA*

[1]Howard Hughes Medical Institute, Program in Cellular and Molecular Medicine, Boston Children's Hospital, Department of Genetics and Department of Pediatrics, Harvard Medical School, Boston, MA, USA. [2]Division of Neurology, Kirby Center for Neurobiology, Boston Children's Hospital, Boston, MA, USA. [3]Rodent Histopathology Core, Harvard Medical School, Boston, MA, USA. [4]Department of Neurological Surgery and Eli and Edythe Broad Center of Regeneration Medicine and Stem Cell Research, University of California, San Francisco, CA, USA. [5]These authors contributed equally: Amelia N. Chang, Zhuoyi Liang, Hai-Qiang Dai. [6]These authors jointly supervised this work: Bjoern Schwer, Frederick W. Alt. *e-mail: bjoern.schwer@ucsf.edu; alt@enders.tch.harvard.edu

© 2018 Springer Nature Limited. All rights reserved.

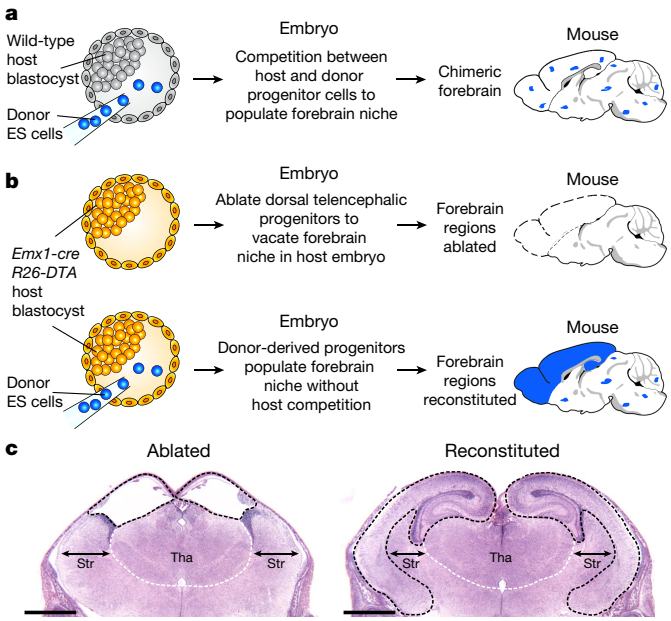

Fig. 1 | Generation of NBC chimaeras with forebrain regions derived from donor ES cells. a, Schematic of the conventional approach to generate mouse models. Competition between host and donor cells generates mice with chimeric brains (blue dots indicate donor contribution). **b**, Schematic of the NBC approach. Top, *Emx1-cre* activation of expression of diphtheria toxin subunit A at E9.5 causes ablation of dorsal telencephalic progenitors in host embryos, which develop into mice that lack forebrain regions (dotted lines). Bottom, injection of donor ES cells into host blastocysts yields mice with reconstituted, donor-derived forebrain regions (blue). Mouse brain schematics in **a**, **b** were generated based on a reference image from the Allen Mouse Brain Atlas. **c**, Representative coronal brain sections stained with haematoxylin and eosin (H&E) (E18.5) from 42 mice generated from *Emx1-cre;R26-DTA* blastocysts that were not (left) or were (right) injected with ES cells ($n = 3$ from *Emx1-cre;R26-DTA* blastocysts injected with ES cells; $n = 38$ *Emx1-cre;R26-DTA* blastocysts not injected with ES cells). Ablated (left) or reconstituted (right) forebrain regions are demarcated by black dotted lines. White dotted lines demarcate the approximate boundary of the thalamus (Tha); double-headed arrows indicate width of the striatum (Str). Scale bars,1 mm. See Extended Data Fig. 1 for more details of NBC chimaera phenotypes.

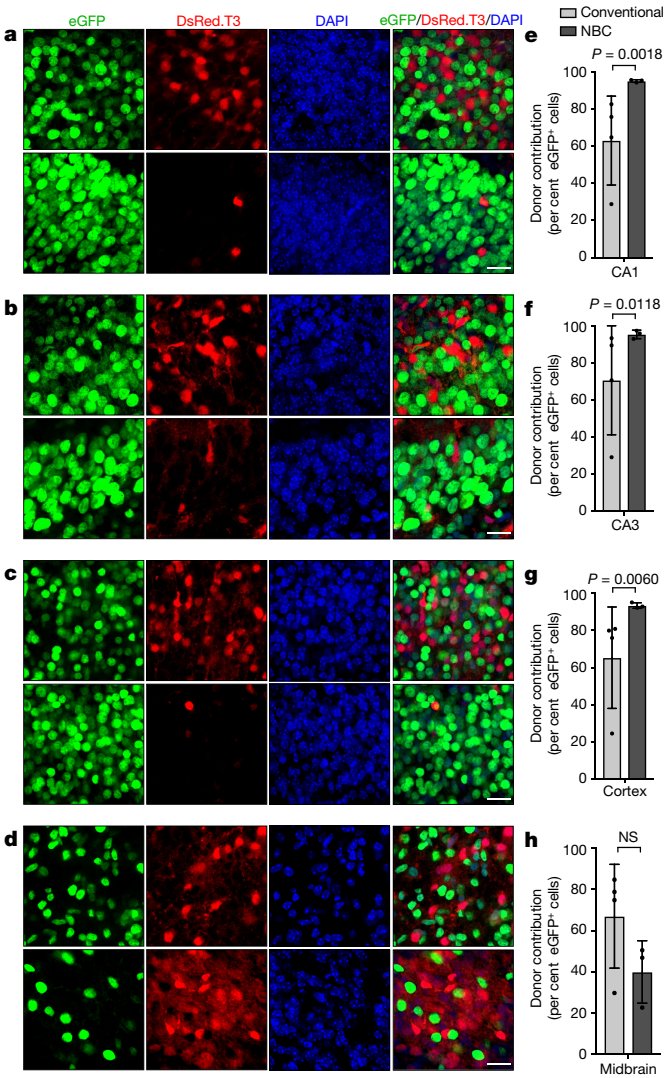

Fig. 2 | NBC chimaeras show consistently high donor contribution in forebrain regions as compared to conventional chimaeras. a–**d**, Representative images showing extent of H2B–eGFP-expressing donor ES cell contribution to CA1 (**a**), CA3 (**b**), cortex (**c**) and midbrain (**d**) regions in conventional (top) and NBC (bottom) chimaeras at P0, depicting donor-derived cells in green and host-derived cells in red. Nuclei were DAPI-stained (blue). **e**–**h**, Quantification of donor ES cell contribution in conventional ($n = 4$) and NBC chimaeras ($n = 3$). Data are mean ± s.d. Variance was significantly different between conventional and NBC chimaeras for CA1, CA3 and cortex (*F* test for equality of variances), reflecting the wide variation in donor contribution among individual conventional chimaeras, in contrast to the consistently high donor contribution in NBC chimaeras. No difference in variance was observed for midbrain ($P = 0.5534$; NS, not significant; *F* test for equality of variances), consistent with random donor contribution to this non-ablated brain region in both types of chimaeras. Scale bars, 10 μm.

mice crossed with *CAG-DsRed.T3* transgenic mice (see Methods and Extended Data Fig. 2). The *DsRed.T3* transgene mediates widespread constitutive expression of the red fluorescent protein variant DsRed.T3, driven by the chicken β-actin promoter coupled with the cytomegalovirus immediate early enhancer. Thus, this strategy generates dual-labelled chimaeras in which cells derived from donor ES cells are eGFP-positive (green) and cells derived from host blastocysts are DsRed.T3-positive (red). Postnatal day (P)0 NBC chimaeras generated from *Emx1-cre;R26-DTA;CAG-DsRed.T3* blastocysts injected with H2B–eGFP-expressing ES cells had nearly 100 per cent eGFP-positive cells in the hippocampus and cerebral cortex, indicating reconstitution of the vacant forebrain niche (Fig. 2a–c, e–g). By contrast, conventional P0 chimaeras generated by injection of H2B–eGFP-expressing donor ES cells into *CAG-DsRed.T3* blastocysts consistently showed substantially lower—and much more variable—percentages of eGFP-positive cells, owing to host–donor competition (Fig. 2a–c, e–g). In the midbrain—where there is no ablation and thus no host–donor competition—both NBC and conventional chimaeras showed lower numbers of eGFP-positive cells and large chimaera-to-chimaera variability (Fig. 2d, h), similar to other non-ablated tissues (Extended Data Fig. 3). We note that the small percentage of DsRed.T3-positive cells in the forebrain regions of NBC chimaeras probably corresponds to cells of host origin that are not derived from the dorsal telencephalon—for example, interneurons that migrate tangentially into the cortex, microglia that derive from resident macrophages or endothelial cells from blood vessels.

To assess the cytoarchitecture and lamination of the neocortex and hippocampus in P7 wild-type NBC chimaeras, we performed immunofluorescence staining for layer-specific markers[21] (Fig. 3a–d and Extended Data Fig. 4). The reconstituted brains of wild-type NBC chimaeras at P7 were morphologically normal, and had layer widths and cellular densities that were indistinguishable from conventional chimaera controls (Fig. 3a–d and Extended Data Fig. 4). The numbers of oligodendrocytes, astrocytes and microglia in these chimaeras were similar to those of controls, and there were no signs of neuroinflammation (Extended Data Fig. 5). Correspondingly, basic neurological

© 2018 Springer Nature Limited. All rights reserved.

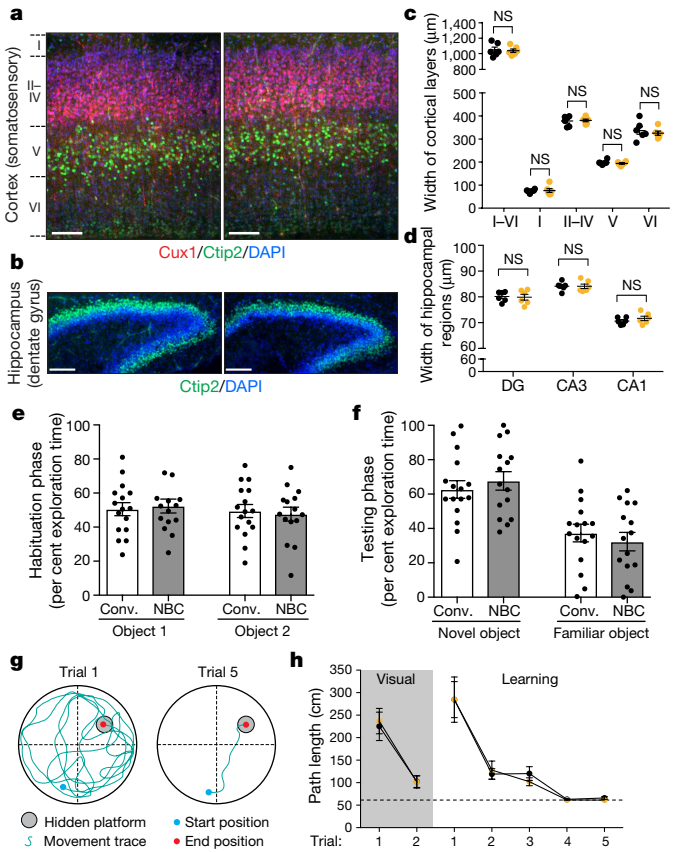

Fig. 3 | Brains of NBC mice are structurally and functionally normal. **a**, Representative images of somatosensory cortex sections from six independent NBC (right) and conventional (left) chimaeras at P7. Layers (L) II–IV (Cux1; red), L V (Ctip2; green) and nuclei (DAPI; blue) are shown. **b**, Representative images of hippocampal sections from six independent P7 NBC (right) and conventional (left) chimaeras stained for Ctip2 (green) and DAPI (blue). **c**, Widths of somatosensory cortex layers in conventional (black) or NBC (yellow) chimaeras ($n = 6$ mice each) at P7. **d**, Widths of dentate gyrus (DG), CA3 and CA1 regions in conventional (black) or NBC (yellow) chimaeras ($n = 6$ mice each) at P7. Horizontal bars in **c**, **d** indicate mean ± s.e.m.; NS, not significant, $P > 0.05$ (unpaired, two-tailed t-test). **e**, No significant difference in percentage of total exploration time spent on object 1 versus object 2 during habituation phase of novel-object recognition task in conventional (conv.) and NBC chimaeras. **f**, Significant preference for the novel object in male two-month-old conventional ($n = 15$) and NBC ($n = 14$) chimaeras. Data represent mean ± s.e.m. Conventional chimaeras, novel versus familiar, $P = 0.0051$; NBC chimaeras, novel versus familiar, $P < 0.0001$ (one-way ANOVA, Tukey's post hoc correction). **g**, Schematic of Morris water maze task. **h**, Mean path length (± s.e.m.) to platform for conventional (black) or NBC (yellow) chimaeras in visual and learning trials. Dotted line indicates minimum possible path length to platform. No significant difference between male two-month-old conventional and NBC chimaeras ($n = 16$ mice each) in visual ($F(1, 30) = 0.052$, $P = 0.822$) or learning trials ($F(1, 30) = 0.041$, $P = 0.841$) (two-way mixed-model ANOVA). Path length across learning trials was significantly different, which indicates that both groups had learned the task ($F(1.393, 41.787) = 34.57$, $P < 0.0005$) (two-way mixed-model ANOVA with Greenhouse–Geisser correction for violation of sphericity). Scale bars, 100 μm.

functions were intact in the two- to three-month-old wild-type NBC chimaeras (Supplementary Table 1). We tested the behaviour of two-month-old adult chimaeras in the novel-object recognition and Morris water maze paradigms to assess higher cognitive functions, as these two behavioural tasks are dependent on intact forebrain function[22,23]. Adult wild-type NBC chimaeras performed indistinguishably from controls in both paradigms, which demonstrates that learning and memory are intact (Fig. 3e–h and Extended Data Fig. 6). Collectively, these studies indicate that NBC mice are indistinguishable from normal mice with respect to brain structure and function.

To further evaluate NBC, we tested the ability of this approach to rapidly assess a brain phenotype previously established by a conventional germline knockout approach[24,25]. The gene doublecortin (*Dcx*) lies on the mouse X chromosome and encodes a microtubule-associated protein that functions in neuronal migration[26,27]. Male mice in which the single *Dcx* copy is functionally abrogated show disrupted hippocampal lamination with a normal neocortex from age E17.5 onward, including at P0 and two months of age[24,25]. We targeted male mouse ES cells via CRISPR–Cas9 to delete *Dcx* exons 2 and 3 (Extended Data Fig. 7a, b), which encode the tubulin-binding domains that are essential for Dcx function[28]. Two $Dcx^{-/Y}$ ES cell clones, generated from independent deletion events (Extended Data Fig. 7c), were injected into NBC blastocysts to create NBC chimaeras. At P0, the resulting $Dcx^{-/Y}$ NBC chimaeras showed a marked reduction in Dcx in protein lysates from neocortical and hippocampal tissue relative to control NBC chimaeras generated from the parental wild-type ES cell line (Extended Data Fig. 7d). In addition, immunofluorescence analyses with two different antibodies revealed that Dcx was absent in most cells of the neocortex and hippocampus of $Dcx^{-/Y}$ NBC chimaeras at P0 (Extended Data Fig. 7e). The remaining Dcx-positive neurons expressed markers of GABAergic neurons (Extended Data Fig. 7f, g) and were probably immature interneurons that originated in the ventral telencephalon where *Emx1* is not expressed[14]. Overall positioning and cell density of GABA-positive interneurons in the somatosensory cortex were similar in wild-type and $Dcx^{-/Y}$ chimaeras (Extended Data Fig. 7h, i). We did not observe decreased postnatal viability of reconstituted $Dcx^{-/Y}$ chimaeras; all mice that were not euthanized for experiments at P0 survived to adulthood (that is, at least two months of age; $n = 14$, generated from 2 different $Dcx^{-/Y}$ ES cell clones; Extended Data Fig. 7j). Further, body weights of wild-type (TC1) and $Dcx^{-/Y}$ chimaeras were similar at P0 and two months of age (Extended Data Fig. 7j).

$Dcx^{-/Y}$ NBC chimaeras accurately phenocopied the hippocampal dysplasias observed in P0 and two-month-old germline $Dcx^{-/Y}$ mice[24,25]. At P0, we observed an abnormal division of the stratum pyramidale of the cornu ammonis (CA)3 region into an internal and external layer, which resulted in a distinct band of heterotopic neurons (Fig. 4a, b). We also noted a less-pronounced band of heterotopic neurons in the stratum oriens of the CA1 region (Fig. 4a). When $Dcx^{-/Y}$ NBC chimaeras were examined at two months of age, the heterotopic band of CA3 neurons was still present; however, the CA1 heterotopias appeared to have resolved (Extended Data Fig. 8a, b). The mutant hippocampal phenotype was reproducibly observed in all NBC chimaeras from both $Dcx^{-/Y}$ ES cell clones, demonstrating full recapitulation of the brain phenotype of germline *Dcx* knockout mice at both of the ages examined[24,25]. As in germline $Dcx^{-/Y}$ mice, cortical layering in $Dcx^{-/Y}$ NBC chimaeras was intact at P0 (Fig. 4c and Extended Data Fig. 8h), which provides an internal control to verify the absence of non-specific neurodevelopmental defects in the $Dcx^{-/Y}$ NBC chimaeras.

We further generated $Dcx^{-/Y}$ ES cells that express H2B–eGFP and injected them into either *Emx1-cre;R26-DTA;CAG-DsRed.T3* blastocysts or *CAG-DsRed.T3* blastocysts to generate, respectively, NBC or conventional $Dcx^{-/Y}$ H2B–eGFP-expressing chimaeras (Extended Data Fig. 8d–i). Consistent with our findings with the NBC and conventional chimaeras that were generated with wild-type ES cells that express H2B–eGFP (Fig. 2), at P0 $Dcx^{-/Y}$ H2B–eGFP-expressing NBC chimaeras showed significantly higher donor contribution and lower variability in forebrain regions—but not in non-ablated tissues—than conventional $Dcx^{-/Y}$ H2B–eGFP-expressing chimaeras (Extended Data Fig. 8d–f). Moreover, at P0 all $Dcx^{-/Y}$ NBC chimaeras showed the well-characterized *Dcx* knockout phenotype with high consistency, which allowed clear-cut experimental analyses and conclusions (Extended Data Fig. 8g). By contrast, $Dcx^{-/Y}$ conventional chimaeras showed highly variable penetrance of the *Dcx* knockout phenotype (Extended Data Fig. 8g). This experiment therefore clearly reveals the advantage of using the NBC system, in which competition does not

© 2018 Springer Nature Limited. All rights reserved.

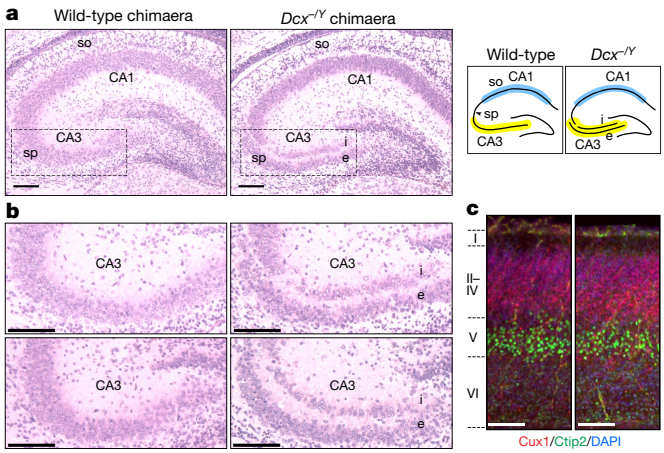

Fig. 4 | *Dcx*$^{-/Y}$ NBC chimaeras recapitulate the phenotype of germline *Dcx*$^{-/Y}$ mice. a, Left, representative images of H&E-stained coronal brain sections showing hippocampal defects in *Dcx*$^{-/Y}$ NBC chimaeras but not wild-type chimaeras at P0. Dashed lines highlight the CA3 region, in which the stratum pyramidale is present as a single layer in wild-type chimaeras but is abnormally divided into an internal (i) and external (e) layer in the *Dcx*$^{-/Y}$ chimaeras. Right, diagram of this phenotype, with the CA3 (yellow) and CA1 (blue) regions highlighted. so, stratum oriens; sp, stratum pyramidale. **b**, Enlarged representative images of the CA3 region in two wild-type (left) and *Dcx*$^{-/Y}$ (right) chimaeras at P0. **c**, Representative images of coronal somatosensory cortex sections co-stained with Cux1 (red), Ctip2 (green) and DAPI (blue), from wild-type (left) and *Dcx*$^{-/Y}$ (right) chimaeras at P0. Approximate location of cortical layers I–VI is indicated on the left. Images in **a**–**c** are representative of experiments performed on 21 mice ($n = 6$ for *Dcx*$^{-/Y}$ ES-cell clone 7F; $n = 4$ for *Dcx*$^{-/Y}$ ES-cell clone 8E; $n = 11$ for wild-type ES cells). Mice were generated and characterized as depicted in Extended Data Figs. 7, 8. Scale bars, 100 μm.

occur between progenitors derived from donor *Dcx*$^{-/Y}$ ES cells and progenitors derived from host blastocysts. Beyond further establishing the utility of the NBC system for analysis of the known relatively subtle and specific *Dcx*$^{-/Y}$ phenotype, these experiments also revealed that neural progenitors derived from *Dcx*$^{-/Y}$ ES cells are not at a major competitive disadvantage, as compared to wild-type progenitors, during neurodevelopment.

The NBC approach we describe provides a blastocyst complementation system that should greatly facilitate many in vivo studies of the cerebral cortex and hippocampus. Blastocyst complementation has previously been used to reconstitute several tissues and organs—including the mature adaptive immune system, ocular lens, pancreas, thymus, kidney and heart[2–10]—but until now blastocyst complementation has, to our knowledge, never been reported for the brain. NBC is based on ES-cell complementation of blastocysts that, owing to programmed ablation of blastocyst-derived dorsal telencephalic progenitors, cannot generate major forebrain structures. The approach works extremely well: we found consistent pup survival rates, recovery rates and litter sizes across a large number of experiments (Extended Data Fig. 9). Moreover, use of normal ES cells for NBC complementation leads to the generation of NBC chimaeras with donor-derived forebrain structures that are structurally and functionally indistinguishable from those of conventional chimaeras (Figs 1–3). Thus, use of normal ES cells for NBC can reliably generate key structures of the brain, arguably the most complex organ in vertebrates. Furthermore, the use of *Dcx*$^{-/Y}$ ES cells for NBC complementation fully recapitulated the reported brain phenotypes of *Dcx* germline knockout mice (Fig. 4). Thus, the NBC approach is anticipated to substantially accelerate studies of the function of genes and other genomic elements in cortical and hippocampal development and physiology in mice.

Previous blastocyst complementation approaches relied on the creation of cellular niches by inactivation of genes that are critical for organ development in blastocyst-derived progenitor cells[2–10]. By contrast, NBC abrogates organogenesis by selective progenitor cell ablation, via targeted expression of diphtheria toxin subunit A. The general ablation strategy that we use for NBC should also be applicable to blastocyst complementation approaches in the context of other brain regions and other organ systems. Compared to traditional methods used to generate genetically modified mice via germline genetic modifications, NBC offers many of the same advantages for brain studies that have been extensively documented for RAG2-deficient blastocyst complementation in the context of studies of the immune system. As documented by our studies of the *Dcx* mutation, genetic modifications introduced into ES cells using CRISPR–Cas9 approaches can be rapidly and accurately assessed via NBC, even with respect to causing a subtle brain phenotype. As extensively documented in RAG2-deficient blastocyst complementation analyses of the immune system[12,29,30], multiple genetic modifications can be introduced into ES cells, which then could be analysed directly for effects on forebrain development, function or disease in NBC chimaeras. This would eliminate the time-consuming and often prohibitive task of intercrossing multiple, segregating alleles in mutant mice[12,29]. Finally, recent studies have focused on analyses of interspecies chimaeras[4,8–10]; the NBC approach could provide an ideal platform for such studies in the context of forebrain development and function.

Online content

Any methods, additional references, Nature Research reporting summaries, source data, statements of data availability and associated accession codes are available at https://doi.org/10.1038/s41586-018-0586-0.

Received: 29 May 2017; Accepted: 5 September 2018;
Published online 10 October 2018.

1. Capecchi, M. R. Gene targeting in mice: functional analysis of the mammalian genome for the twenty-first century. *Nat. Rev. Genet.* **6**, 507–512 (2005).
2. Chen, J., Lansford, R., Stewart, V., Young, F. & Alt, F. W. RAG-2-deficient blastocyst complementation: an assay of gene function in lymphocyte development. *Proc. Natl Acad. Sci. USA* **90**, 4528–4532 (1993).
3. Chen, J. et al. Generation of normal lymphocyte populations by *Rb*-deficient embryonic stem cells. *Curr. Biol.* **3**, 405–413 (1993).
4. Kobayashi, T. et al. Generation of rat pancreas in mouse by interspecific blastocyst injection of pluripotent stem cells. *Cell* **142**, 787–799 (2010).
5. Liégeois, N. J., Horner, J. W. & DePinho, R. A. Lens complementation system for the genetic analysis of growth, differentiation, and apoptosis in vivo. *Proc. Natl Acad. Sci. USA* **93**, 1303–1307 (1996).
6. Stanger, B. Z., Tanaka, A. J. & Melton, D. A. Organ size is limited by the number of embryonic progenitor cells in the pancreas but not the liver. *Nature* **445**, 886–891 (2007).
7. Usui, J. et al. Generation of kidney from pluripotent stem cells via blastocyst complementation. *Am. J. Pathol.* **180**, 2417–2426 (2012).
8. Wu, J. et al. Stem cells and interspecies chimaeras. *Nature* **540**, 51–59 (2016).
9. Wu, J. et al. Interspecies chimerism with mammalian pluripotent stem cells. *Cell* **168**, 473–486.e15 (2017).
10. Yamaguchi, T. et al. Interspecies organogenesis generates autologous functional islets. *Nature* **542**, 191–196 (2017).
11. Conti, L. & Cattaneo, E. Neural stem cell systems: physiological players or in vitro entities? *Nat. Rev. Neurosci.* **11**, 176–187 (2010).
12. Ba, Z. et al. A rapid embryonic stem cell-based mouse model for B-cell lymphomas driven by Epstein–Barr virus protein LMP1. *Cancer Immunol. Res.* **3**, 641–649 (2015).
13. Wu, S., Wu, Y. & Capecchi, M. R. Motoneurons and oligodendrocytes are sequentially generated from neural stem cells but do not appear to share common lineage-restricted progenitors in vivo. *Development* **133**, 581–590 (2006).
14. Gorski, J. A. et al. Cortical excitatory neurons and glia, but not GABAergic neurons, are produced in the Emx1-expressing lineage. *J. Neurosci.* **22**, 6309–6314 (2002).
15. Simeone, A., Acampora, D., Gulisano, M., Stornaiuolo, A. & Boncinelli, E. Nested expression domains of four homeobox genes in developing rostral brain. *Nature* **358**, 687–690 (1992).
16. Kim, S. et al. The apical complex couples cell fate and cell survival to cerebral cortical development. *Neuron* **66**, 69–84 (2010).
17. Lee, Y. et al. Neurogenesis requires TopBP1 to prevent catastrophic replicative DNA damage in early progenitors. *Nat. Neurosci.* **15**, 819–826 (2012).
18. Palmiter, R. D. et al. Cell lineage ablation in transgenic mice by cell-specific expression of a toxin gene. *Cell* **50**, 435–443 (1987).
19. Yoshida, M., Assimacopoulos, S., Jones, K. R. & Grove, E. A. Massive loss of Cajal–Retzius cells does not disrupt neocortical layer order. *Development* **133**, 537–545 (2006).
20. Turgeon, B. & Meloche, S. Interpreting neonatal lethal phenotypes in mouse mutants: insights into gene function and human diseases. *Physiol. Rev.* **89**, 1–26 (2009).

© 2018 Springer Nature Limited. All rights reserved.

21. Molyneaux, B. J., Arlotta, P., Menezes, J. R. & Macklis, J. D. Neuronal subtype specification in the cerebral cortex. *Nat. Rev. Neurosci*. **8**, 427–437 (2007).
22. Leger, M. et al. Object recognition test in mice. *Nat. Protocols* **8**, 2531–2537 (2013).
23. Vorhees, C. V. & Williams, M. T. Morris water maze: procedures for assessing spatial and related forms of learning and memory. *Nat. Protocols* **1**, 848–858 (2006).
24. Corbo, J. C. et al. Doublecortin is required in mice for lamination of the hippocampus but not the neocortex. *J. Neurosci*. **22**, 7548–7557 (2002).
25. Kappeler, C. et al. Magnetic resonance imaging and histological studies of corpus callosal and hippocampal abnormalities linked to *doublecortin* deficiency. *J. Comp. Neurol*. **500**, 239–254 (2007).
26. Gleeson, J. G., Lin, P. T., Flanagan, L. A. & Walsh, C. A. Doublecortin is a microtubule-associated protein and is expressed widely by migrating neurons. *Neuron* **23**, 257–271 (1999).
27. Francis, F. et al. Doublecortin is a developmentally regulated, microtubule-associated protein expressed in migrating and differentiating neurons. *Neuron* **23**, 247–256 (1999).
28. Taylor, K. R., Holzer, A. K., Bazan, J. F., Walsh, C. A. & Gleeson, J. G. Patient mutations in doublecortin define a repeated tubulin-binding domain. *J. Biol. Chem*. **275**, 34442–34450 (2000).
29. Tian, M. et al. Induction of HIV neutralizing antibody lineages in mice with diverse precursor repertoires. *Cell* **166**, 1471–1484.e18 (2016).
30. Yeap, L. S. et al. Sequence-intrinsic mechanisms that target AID mutational outcomes on antibody genes. *Cell* **163**, 1124–1137 (2015).

Acknowledgements We thank members of the Alt laboratory and C. A. Walsh for stimulating discussions, P.-Y. Huang for help with blastocyst injections, H.-L. Cheng for advice and help with ES cell culture, and S. V. Griswold and T. Chari for assistance with behavioural experiments. Behavioural testing was carried out at the Boston Children's Hospital (BCH) Neurodevelopmental Behavior Core (CHB IDDRC, 1U54HD090255). This work was supported by the Howard Hughes Medical Institute, the BCH Department of Medicine (DOM) Support Fund, and the BCH DOM Anderson Porter Fund and a major grant from the Charles H. Hood Foundation. B.S. is a Kimmel Scholar of The Sidney Kimmel Foundation, supported by NIA/NIH grant AG043630, the UCSF Brain Tumor SPORE Career Development Program, the American Cancer Society, the Andrew McDonough B+ Foundation, the Shurl and Kay Curci Foundation and a Martin D. Abeloff V Scholar award of The V Foundation for Cancer Research. B.S. also holds the Suzanne Marie Haderle and Robert Vincent Haderle Endowed Chair, UCSF. H.-Q.D. is a fellow of the Cancer Research Institute of New York. F.W.A. is an investigator of the Howard Hughes Medical Institute.

Author contributions A.N.C., B.S. and F.W.A. designed the study; A.N.C., H.-Q.D., Z.L. and B.S. performed experiments; A.M.C.-W. performed NBC injections and related mouse work; B.S. and F.W.A. supervised the research. A.N.C., H-Q.D., Z.L., B.S. and F.W.A. wrote the paper. R.T.B. reviewed histology sections; N.A. provided advice and carried out behavioural experiments.

Competing interests The authors declare no competing interests.

Additional information
Extended data is available for this paper at https://doi.org/10.1038/s41586-018-0586-0.
Supplementary information is available for this paper at https://doi.org/10.1038/s41586-018-0586-0.
Reprints and permissions information is available at http://www.nature.com/reprints.
Correspondence and requests for materials should be addressed to B.S. or F.W.A.
Publisher's note: Springer Nature remains neutral with regard to jurisdictional claims in published maps and institutional affiliations.

© 2018 Springer Nature Limited. All rights reserved.

METHODS

No statistical methods were used to predetermine sample size. Samples for image acquisition and image analysis and mice for neurobehavioural tests were randomized, and investigators were blinded to allocation during the experiment and outcome assessment.

Mice and blastocyst injections. All studies were in compliance with ethical regulations established by the Boston Children's Hospital Institutional Animal Care and Use Committee and Institutional Biosafety Committee. Animals were maintained on a 12-h light–dark schedule in a temperature-controlled environment, with food and water provided ad libitum. Behavioural testing was conducted during the light phase. *Emx1-cre* (stock no.: 005628; C57BL/6) and *R26-DTA* mice (stock no.: 010527; 129Sv:C57BL/6) were purchased from the Jackson Laboratory and maintained as homozygous breeding pairs. *Tg(CAG-DsRed*MST)1Nagy/J* mice (Jackson Laboratory stock no.: 006051; C57BL/6)[31] were a kind gift from C. F. Kim (Boston Children's Hospital). See Supplementary Table 2 for genotyping information. Blastocyst injections were performed as previously described[3]. In brief, 10–12 ES cells were injected per blastocyst (collected at 3.5 days post coitum from superovulated *R26-DTA* females crossed to *Emx1-cre* or *Emx1-cre; DsRed.T3* stud males), and 10–16 blastocysts were implanted per pseudo-pregnant CD-1 foster female (Charles River Laboratories). For a detailed protocol of the above methods, see Protocol Exchange[32]. For all studies, NBC chimaeras with normally developed jaws were analysed. The following parental ES cell lines were used for blastocyst injections: TC1 (a gift from P. Leder, Harvard Medical School; 129Sv; used for analysis of brain morphology, donor versus host contribution, and *Dcx* mutation), EF1 (derived in house from a 129Sv:C57BL/6 F1 hybrid mouse; used for analysis of brain morphology and behaviour experiments), R26-*lacZ* (TC1-derived; a gift from S. H. Orkin, Boston Children's Hospital; 129Sv; used for brain morphology analysis). All cell lines were confirmed to be mycoplasma free.

ES cell culture, CRISPR–Cas9 gene editing, fluorescent labelling of cells and generation of *Dcx*$^{-/Y}$ mice. ES cells were maintained on a monolayer of gamma-irradiated mouse embryonic fibroblast feeder cells and passaged every 2–3 days. Cells were cultured at 37 °C and 5% CO_2 in DMEM medium supplemented with 15% (v/v) fetal bovine serum, 20 mM HEPES (pH 7.4), 2 mM L-glutamine, 50 U/ml penicillin/streptomycin, 0.1 mM MEM non-essential amino acids, 50 μM β-mercaptoethanol, and 500 U/ml recombinant mouse leukaemia inhibitory factor. To generate fluorescently labelled ES cell lines, wild-type TC1 and *Dcx* mutant ES cells (described below) were transduced with the lentiviral plasmid FUHGW (H2B–eGFP driven by the human Ubc promoter)[33], a kind gift from G.-L. Xu (Shanghai Institute of Biochemistry and Cell Biology, Chinese Academy of Sciences). Two *Cas9* single-guide RNAs (sgRNAs) targeting the *Dcx* locus (see Supplementary Table 2 for nucleotide sequences) were cloned into the pX330 vector (Addgene plasmid 42230), and nucleofected into wild-type TC1 ES cells (1 μg each pX330 vector per 2×10^6 cells) according to the Amaxa 4D-nucleofector protocol (solution P3, CG-104, Lonza). A puromycin-resistance plasmid was co-transfected to enable positive clones to be identified by puromycin selection. ES cell clones with *Dcx* deletion were identified by PCR screening, Southern blotting (see below) and nucleotide sequencing of the deletion junction (see Supplementary Table 2 for details and oligonucleotide sequences). The two independent ES cell clones (referred to as *Dcx* 7F and *Dcx* 8E) used for blastocyst injections were confirmed to have a normal karyotype by metaphase analysis. Clones were also confirmed by Southern blotting to be negative for genomic integration of the pX330 plasmid backbone or the puromycin-resistance plasmid backbone. For a detailed protocol of the above methods, see Protocol Exchange[32]. As Dcx is developmentally regulated, mice were analysed at P0 for Dcx expression. For assessment of hippocampal and cortical phenotypes, two differently aged cohorts of NBC chimaeras (*Dcx* 7F or *Dcx* 8E ES cells into *Emx1-cre;R26-DTA* blastocysts) and control chimaeras (wild-type parental TC1 ES cells into *Emx1-cre;R26-DTA* blastocysts) were analysed. For the P0 cohort, $n = 6$ for *Dcx* 7F, $n = 4$ for *Dcx* 8E and $n = 11$ for wild-type controls. For the two-month-old cohort, $n = 6$ for *Dcx* 7F, $n = 8$ for *Dcx* 8E and $n = 5$ for wild-type controls. Additional mouse cohorts were generated using *Dcx*$^{-/Y}$ H2B–eGFP-expressing ES cells and analysed at P0; $n = 3$ for *Dcx*$^{-/Y}$ H2B–eGFP-expressing NBC chimaeras (*Dcx*$^{-/Y}$ H2B–eGFP-expressing ES cells into *Emx1-cre;R26-DTA;DsRed.T3* blastocysts) and $n = 3$ for control chimaeras (*Dcx*$^{-/Y}$ H2B–eGFP-expressing ES cells into *R26-DTA;DsRed.T3* blastocysts). In all cases, sample order was randomized and investigators were blinded to genotype.

Histology and immunofluorescence analysis. Mice were anaesthetized with ketamine and xylazine, and transcardially perfused with ice-cold PBS before brain removal and fixation. For histological analyses, hemi-brains were fixed overnight in Bouin's solution (Sigma) at 4 °C with gentle agitation, embedded in paraffin and sectioned at 5 μm. H&E staining was performed on coronal brain sections per standard protocols. For Nissl staining, brains were fixed in 4% (w/v) paraformaldehyde at 4 °C for 24 h with gentle agitation, cryoprotected in 30% (w/v) sucrose in 0.1 M sodium phosphate buffer overnight at 4 °C, embedded in optimal cutting temperature compound and cryosectioned at 35 μm. Coronal sections were mounted onto glass slides and dried. Slides were rehydrated in TBS, stained with thionin solution (0.25% (w/v) thionin, 1.2% (v/v) glacial acetic acid, 0.144% (w/v) sodium hydroxide) for 1 min, dehydrated by incubation in a series of increasing ethanol concentrations, cleared with xylene and coverslipped (Permount mounting medium; Electron Microscopy Sciences). Images were acquired with an Olympus BX51 microscope and a Micropublisher 5.0 RTV camera (QImaging) and processed with the QCapture software (QImaging).

For immunofluorescence analyses, hemi-brains were fixed overnight in 4% (w/v) paraformaldehyde at 4 °C with gentle agitation. For use with GABA and GAD67 antibodies (see below), 0.2% (v/v) glutaraldehyde was added during this fixation step. Fixed brains were cryoprotected, embedded and cryosectioned at 35 μm. Floating coronal sections were rinsed in TBS, quenched in 50 mM NH_4Cl, permeabilized with 0.4–1% (w/v) Triton X-100, blocked (5% (v/v) serum from the species used to generate the secondary antibodies and 0.5% (w/v) fish gelatin, 0.2% (w/v) Tween-20), and then incubated with primary antibody at 4 °C overnight. The following primary antibodies were used: Cux1 (CDP; rabbit polyclonal, 1:250; sc-13024(M-222), Santa Cruz Biotechnology), Ctip2 (rat monoclonal (clone 25B6), 1:100, ab18465, Abcam), GFAP (rabbit polyclonal, 1:1,000; Z0334, DAKO), Olig2 (rabbit polyclonal, 1:1,000; AB9610, Millipore), Iba1 (rabbit polyclonal, 1:1,000; 019-19741, Wako chemicals), Dcx (rabbit polyclonal, 1:1,000; ab18723, Abcam; or goat polyclonal, 1:1,000; sc-8066 (C-18), Santa Cruz Biotechnology), GABA (rabbit polyclonal, 1:1,000; A2052, Sigma), GAD67 (mouse monoclonal (clone 1G10.2), 1:500; MAB5406, Millipore), Satb2 (mouse monoclonal (clone SATBA4B10), 1:500; ab51502, Abcam), Foxp2 (rabbit polyclonal, 1:1,000; ab16046, Abcam). Sections were washed three times with TBS or TBS with 0.05–0.1% (w/v) Triton X-100 and incubated with secondary antibody (1:500; Alexa Fluor 488, 594 or 647; Thermo Fisher Scientific) for two hours at room temperature. Sections were washed twice with TBS or TBS with 0.05–0.1% (w/v) Triton X-100, mounted on SuperFrost Plus glass slides and coverslipped with DAPI Fluoromount-G (SouthernBiotech). Non-brain tissues (heart, lung, kidney and tail) were fixed and sectioned similarly to the brains.

For image acquisition and analysis, sample order was randomized and investigators were blinded to genotype. Images were acquired with a Zeiss confocal spinning disk microscope (Yokogawa CSU-X1, 3i Intelligent Imaging Innovations) and a QuantEM:512SC EMCCD camera (Photometrics) and processed with SlideBook6 software (3i Intelligent Imaging Innovations). To assess donor and host contribution, brain slices from P0 NBC chimaeras with normal jaw morphology indicative of successful ES cell contribution (wild-type H2B–eGFP-expressing or *Dcx*$^{-/Y}$ H2B–eGFP-expressing ES cells into *Emx1-cre;R26-DTA;DsRed.T3* blastocysts) and control chimaeras (wild-type H2B–eGFP-expressing or *Dcx*$^{-/Y}$ H2B–eGFP-expressing ES cells into *R26-DTA;DsRed.T3* blastocysts) were analysed by fluorescence imaging. Graphed data points represent the average cell counts from three coronal sections per mouse.

For analysis of layer widths and cell densities, brain slices from P7 NBC chimaeras (TC1-derived ES cells or EF1 ES cells injected into *Emx1-cre;R26-DTA* blastocysts) and conventional chimaera controls (TC1-derived ES cells or EF1 ES cells injected into wild-type strain-background-matched blastocysts) were analysed. Width of layer (L) I–VI, L II–IV and L V was determined by DAPI, Cux1, and Ctip2 immunostaining, respectively. L I and VI were determined by the boundary of cortex and adjacent layer markers. The widths of cortical layers in *Dcx*$^{-/Y}$ H2B–eGFP-expressing chimaeras were analysed similarly using brain slices from P0 NBC chimaeras (*Dcx*$^{-/Y}$ H2B–eGFP-expressing ES cells injected into *Emx1-cre;R26-DTA;DsRed.T3* blastocysts) and control chimaeras (*Dcx*$^{-/Y}$ H2B–eGFP-expressing ES cells injected into *R26-DTA;DsRed.T3* blastocysts) and the width of layer II–IV was determined by DAPI staining. Graphed data points represent the average measurements or cell counts from twelve coronal step-sections per mouse. For each section, layer width in the hippocampus was estimated from seven measurements across each hippocampal region, and layer width in the cortex was estimated from three measurements across the somatosensory cortex (S1). Quantification of dentate gyrus measurements was performed in at least three hippocampal sections per mouse. Numbers of mice analysed are stated in the figure legends. Dentate gyrus area was measured by outlining the dentate gyrus region. Dentate gyrus length and width were assessed by determining the length of the granule cell layer and the distance between the ends of the granule cell layer, respectively.

Southern blotting. Genomic DNA was prepared by lysing cells at 56 °C overnight in lysis buffer (200 mM NaCl, 100 mM Tris-Cl pH 8.0, 5 mM EDTA, 0.2% SDS), supplemented with 0.2–0.4 mg/ml proteinase K, followed by precipitation and purification by phenol-chloroform-isoamyl alcohol extraction according to standard protocols. DNA was digested with the indicated restriction enzymes, genomic fragments were separated by agarose gel electrophoresis, transferred to nylon membranes (Zeta-Probe GT, Bio-Rad) and hybridized with radiolabelled DNA probes according to standard protocols. Details of *Dcx* probes are listed in Supplementary Table 2.

© 2018 Springer Nature Limited. All rights reserved.

Protein extraction and immunoblotting. Whole-cell extracts were prepared from micro-dissected cortical and hippocampal tissue in ice-cold THB buffer (250 mM sucrose, 20 mM Tris pH 7.4, 1 mM EDTA, 1 mM EGTA), supplemented with protease inhibitors (cOmplete EDTA-free protease inhibitor cocktail, Roche) and 0.5 mM PMSF. Tissue was homogenized by 30 strokes of a Teflon pestle in a Potter-Elvehjem tissue grinder (#19; Kontes). Protein concentration was determined (Bio-Rad Protein DC assay), samples were briefly sonicated, 6 × SDS sample buffer (0.5 M Tris-Cl pH 6.8, 30% (w/v) glycerol, 10% (w/v) SDS, 0.6 M dithiothreitol, 0.012% (w/v) bromophenol blue) was added to a final concentration of 1× and samples were denatured by incubation at 95 °C for three minutes. Equal amounts of protein were separated by SDS–PAGE, followed by immunoblotting with primary antibodies against Dcx (rabbit polyclonal, 1:10,000; ab18723, Abcam) and βIII-tubulin (rabbit polyclonal, 1:20,000; ab18207, Abcam).

Neurobehavioural analysis. Cohorts of two- to three-month-old male mice generated by injection of two different ES cell lines were tested: a larger cohort generated from wild-type EF1 donor ES cells and a smaller cohort generated from wild-type TC1 donor ES cells. Cohorts of age-matched, male conventional chimaeras generated from the same donor ES cell lines were used as controls. Mice were randomized for testing and investigators administering the tests were blinded to genotype. Before behavioural testing, mice were transferred to the testing room and allowed to acclimatize for at least 30 min. Basic autonomic, neurological, and sensory functions were assessed using a modified SmithKline Beecham, Harwell, Imperial College, Royal London Hospital phenotype assessment (SHIRPA) protocol[34]. Parameters were scored in accordance with guidelines from the 'International Mouse Phenotyping Resource of Standardised Screens' developed by the International Mouse Phenotyping Consortium.

Novel-object recognition. The novel-object recognition task was administered in a square arena (30 × 30 cm) maintained at 30 lx throughout the experiment. During the habituation phase, mice were allowed to explore the arena and two identical objects freely, and the trial was stopped once the mouse had explored both objects for a combined total of 20 s. The mice were then returned to the home cage for a 10-min inter-session interval. During the testing phase, one of the objects was replaced with a novel object, and mice were allowed to explore freely for 5 min. The position of the novel object was randomized for each trial. Mice were monitored by automated, multiple body point video tracking with an overhead camera (Ethovision XT 11.5, Noldus Information Technology), and novel-object discrimination was calculated as the percentage of total exploration time spent exploring the novel or familiar object. Locomotor activity (distance travelled in cm) was determined by automated video tracking. Nose-point heat maps, track maps and videos were generated for visualization purposes.

Morris water maze. Mice were placed in a circular pool (137-cm diameter) filled with room-temperature water, divided into quadrants marked with visual cues for spatial orientation. Swim patterns were recorded by automated video tracking (Ethovision XT 11.5, Noldus Information Technology). Track maps for each mouse were visually inspected, and a total of three conventional chimaeras were excluded owing to technical tracking issues. In the visual phase (day 1), mice were given 90 s to swim to a visible platform elevated 0.5 cm above the water and marked with a flag. The position of the platform was kept constant, but the starting quadrant varied. Four starts (each from one of the four quadrants) were administered in one trial, and two visual trials were administered during day 1. In the learning phase (days 2 and 3), the platform was moved to the opposite quadrant, submerged 0.5 cm below the water and the flag was removed. Mice were given 90 s to find the hidden platform and left on the platform for 5 s to orientate themselves. Mice that did not find the platform within 90 s were guided to it. Each mouse completed three learning trials on day 2 (Trials 1 to 3), and two learning trials on day 3 (Trials 4 and 5), with each trial comprising four starts each. In the probe trial (day 4), the platform was removed. Mice were placed in the quadrant opposite the quadrant that had previously contained the platform (north east, NE), and given 60 s to swim. Time spent and path length traversed in each of the four quadrants was recorded.

Statistical analysis. Graphs were generated using GraphPad Prism 6.05. Data from the quantification of donor ES cell contribution were analysed with an unpaired Welch's *t*-test, and *F* test for equality of variances. Data from the quantification of cortical and hippocampal widths and cell densities were analysed with an unpaired, two-tailed *t*-test. Data from the novel-object recognition testing were analysed with a one-way ANOVA with Tukey's post hoc correction. Morris water maze data for two-way mixed-model ANOVA analysis were first tested for normality and sphericity, using the Shapiro–Wilks test in GraphPad Prism and Mauchly's test in SPSS Statistics, respectively. Morris water maze data were found to be normally distributed, and in cases in which the data were found to violate the assumption of sphericity, the Greenhouse–Geisser correction was used to correct the *F* statistic and assess statistical significance. Data were then analysed in SPSS Statistics with a two-way mixed model ANOVA, with genotype (NBC chimaera and conventional chimaera) as the between-subject factor, and path length or latency to platform (visual and learning trials), or path length within each quadrant (probe trial) as the within-subject factor. Bonferroni post hoc correction was applied in cases in which multiple pairwise comparisons were performed.

Reporting summary. Further information on research design is available in the Nature Research Reporting Summary linked to this paper.

Data availability

All data generated or analysed during this study are included in this manuscript and its Supplementary Information.

31. Vintersten, K. et al. Mouse in red: red fluorescent protein expression in mouse ES cells, embryos, and adult animals. *Genesis* **40**, 241–246 (2004).
32. Schwer, B. et al. CRISPR/Cas9-mediated genome editing in mouse embryonic stem cells and direct analysis of brain phenotypes via neural blastocyst complementation. *Protoc. Exch.* (2018).
33. Hu, X. et al. Tet and TDG mediate DNA demethylation essential for mesenchymal-to-epithelial transition in somatic cell reprogramming. *Cell Stem Cell* **14**, 512–522 (2014).
34. Masuya, H. et al. Implementation of the modified-SHIRPA protocol for screening of dominant phenotypes in a large-scale ENU mutagenesis program. *Mamm. Genome* **16**, 829–837 (2005).

© 2018 Springer Nature Limited. All rights reserved.

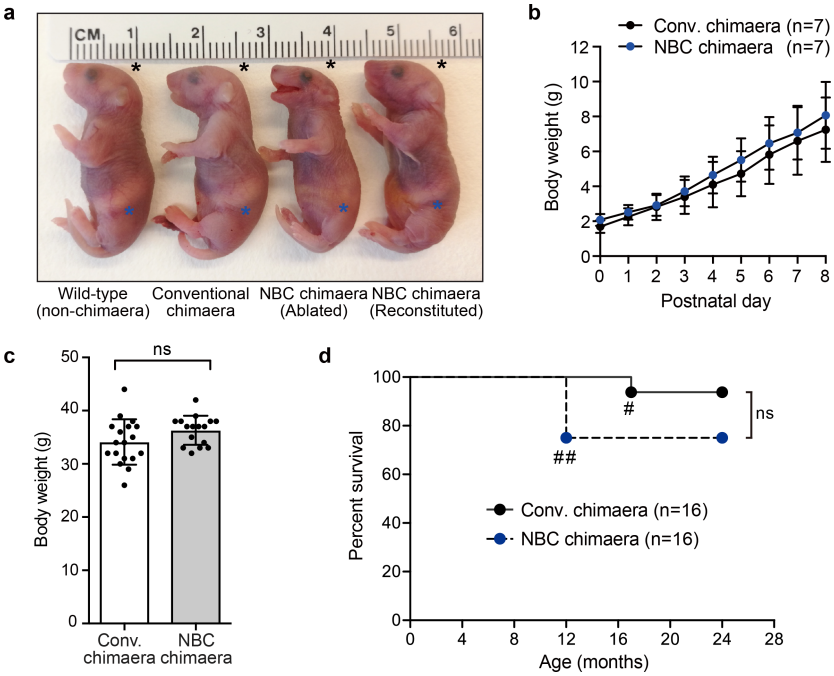

Extended Data Fig. 1 | NBC chimaeras have normal overall appearance, postnatal growth, body weights and survival rates. a, Representative photograph of newborn mice. From left to right: wild-type non-chimeric pup from a normal mouse breeding cross; conventional chimaera generated by injecting donor ES cells into a wild-type host blastocyst; NBC chimaera without reconstitution of the forebrain using donor ES cells ('ablated'); and NBC chimaera with reconstitution of the forebrain using donor ES cells ('reconstituted'). Note the abnormal head curvature of the ablated NBC chimaera relative to the other mice (black asterisks), consistent with the lack of a forebrain. Also note the lack of a milk spot (blue asterisks), consistent with the inability to suckle as a result of incomplete jaw development. At least three mice per group from independent experiments were analysed with similar results. **b**, Body-weight gain of conventional and NBC chimaeras with normal jaws ($n = 7$ each) in the first postnatal week. Data represent mean ± s.d.; not significant, $P > 0.05$ (multiple unpaired, two-tailed t-tests, Holm–Sidak post hoc correction) for all data points. **c**, Body weights of 2–3-month-old male conventional ($n = 18$) and NBC ($n = 16$) chimaeras. Data represent mean and s.d.; NS, not significant, $P > 0.05$ (unpaired, two-tailed t test). **d**, Postnatal survival rate of conventional ($n = 16$ males) and NBC ($n = 16$ males) chimaeras; NS, not significant; $P > 0.05$ (two-sided log-Rank, Mantel–Cox test. [#]One conventional chimaera was euthanized because of a genital mass. [##]Four NBC chimaeras died because their cage flooded; all other mice were euthanized at 24 months of age.

© 2018 Springer Nature Limited. All rights reserved.

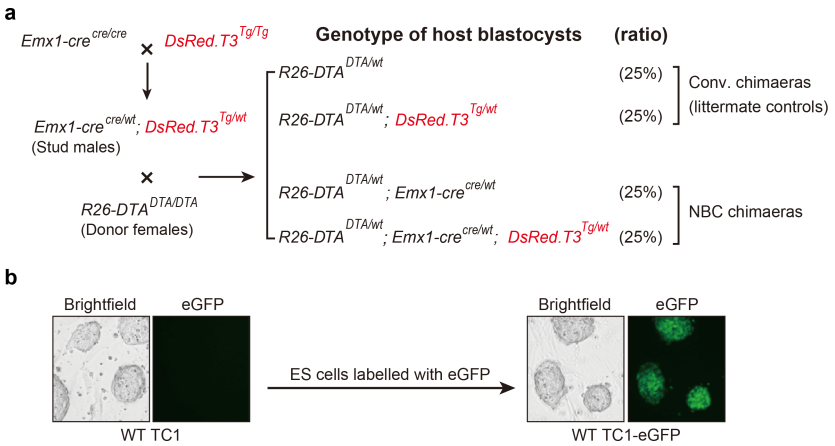

Extended Data Fig. 2 | Generation of *Emx1-cre;R26-DTA;DsRed.T3* NBC host blastocysts and eGFP-labelled donor ES cells. a, Schematic of the breeding crosses used to generate DsRed.T3-labelled NBC host blastocysts. *Tg*, transgene. **b**, Representative bright field and fluorescence microscopy images of wild-type TC1 ES cells before and after lentiviral integration of H2B–eGFP. The ES cells shown stably express H2B–eGFP and were repeatedly imaged during the study with similar results.

© 2018 Springer Nature Limited. All rights reserved.

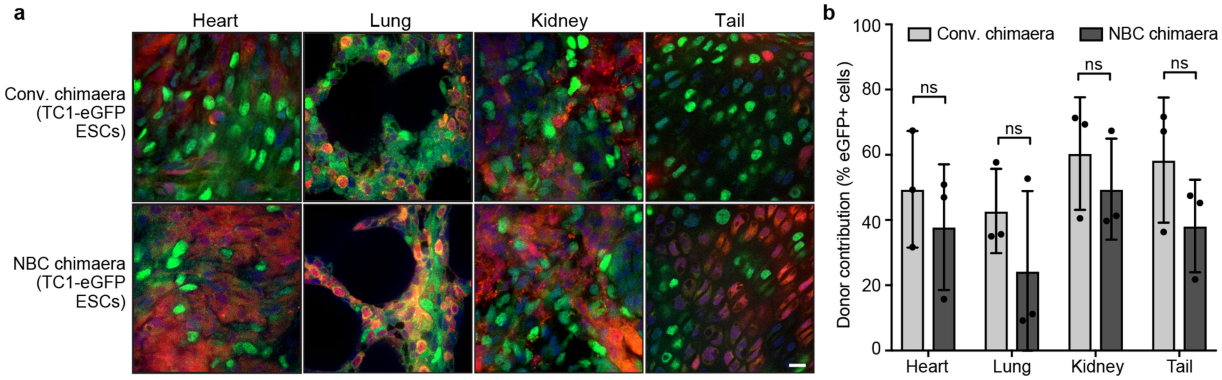

Extended Data Fig. 3 | NBC chimaeras show variable donor contribution in non-brain tissues, as do conventional chimaeras. **a**, Representative images showing the extent of H2B–eGFP-expressing wild-type (TC1) donor ES cell (ESC) contribution to the indicated non-brain tissues in conventional (conv.) and NBC chimaeras at P0, depicting donor-derived cells in green and host-derived cells in red. Nuclei were visualized by DAPI (blue). These experiments were performed on six mice ($n = 3$, NBC chimaeras; $n = 3$, conventional chimaeras). **b**, Quantification of donor ES cell contribution in indicated tissues of conventional and NBC chimaeras ($n = 3$ mice each). Data represent mean and s.d. The variance in donor contribution was not significantly different between conventional and NBC chimaeras for all tissues examined, consistent with competition between donor and host cells in these non-brain tissues in both types of chimaeras (NS, not significant, $P > 0.05$; F test for equality of variances). Scale bar, 10 μm.

© 2018 Springer Nature Limited. All rights reserved.

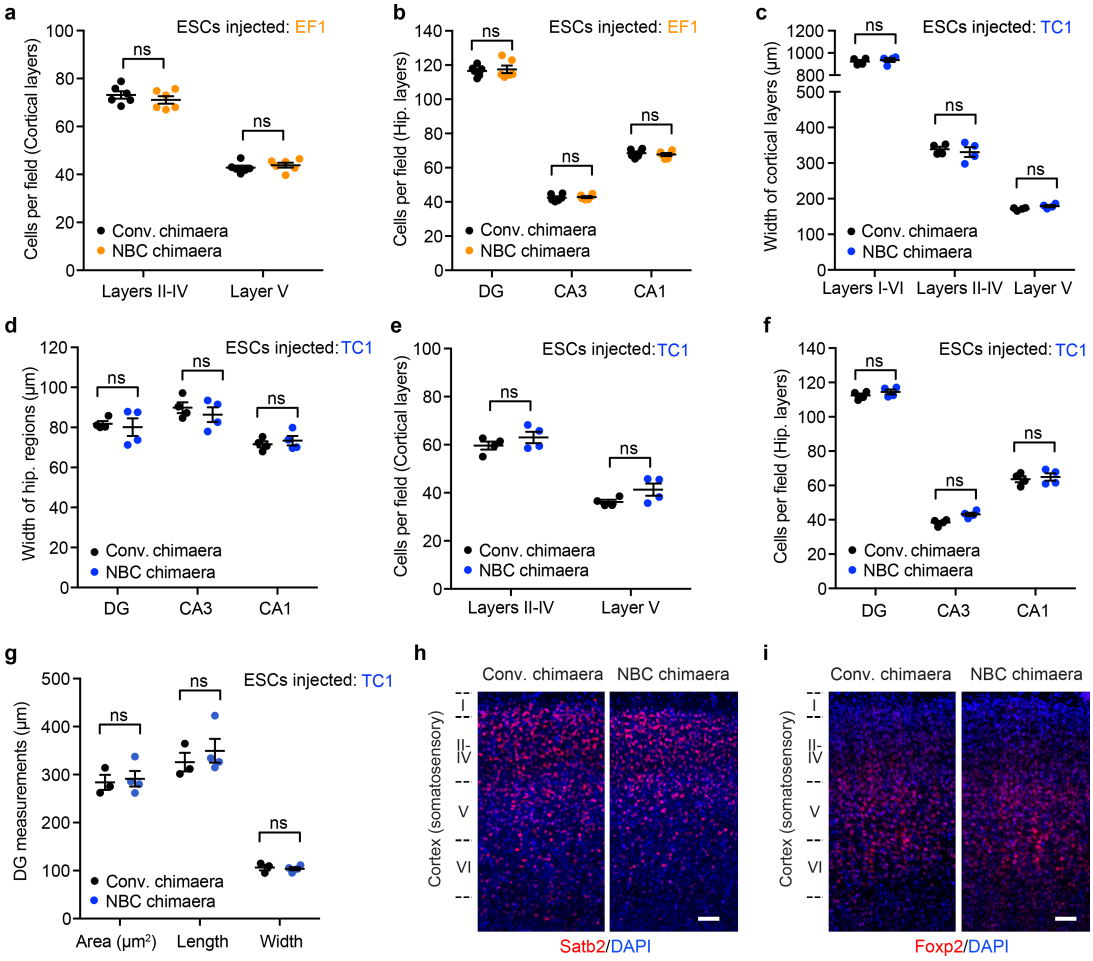

Extended Data Fig. 4 | Brains of NBC mice are structurally normal. **a**, **b**, Cell numbers in the indicated somatosensory cortical layers (**a**) and hippocampal regions (**b**) in P7 conventional (black) and NBC (orange) chimaeras ($n = 6$ mice each) generated by blastocyst injection of EF1 ES cells. Cortical layers II–IV and V were identified by Cux1 and Ctip2 immunoreactivity, respectively. Nuclei were visualized with DAPI. Hip, hippocampus. **c**, **d**, Width of the indicated somatosensory cortical layers (**c**) and hippocampal regions (**d**) in P7 conventional (black) and NBC (blue) chimaeras generated by blastocyst injection of TC1-derived ES cells ($n = 4$ mice each), analysed as in Fig. 3. **e**, **f**, Cell numbers in the indicated somatosensory cortical layers (**e**) and hippocampal regions (**f**) in P7 conventional (black) and NBC (blue) chimaeras generated by blastocyst injection of TC1-derived ES cells ($n = 4$ mice each), analysed as in **a**, **b**. **g**, Dentate gyrus measurements in P0 conventional chimaeras ($n = 3$; black) and NBC chimaeras ($n = 4$; blue) generated by blastocyst injection of H2B–eGFP-expressing TC1 ES cells. For panels **a**–**g**, horizontal bars indicate mean; error bars denote s.e.m.; NS, not significant, $P > 0.05$ (unpaired, two-tailed t test). **h**, **i**, Representative images of coronal somatosensory cortex sections at P7 stained for Satb2 (**h**, red), Foxp2 (**i**, red) and DAPI (blue). These experiments were repeated on six mice ($n = 3$, NBC chimaeras; $n = 3$, conventional chimaeras). Scale bars, 50 μm.

© 2018 Springer Nature Limited. All rights reserved.

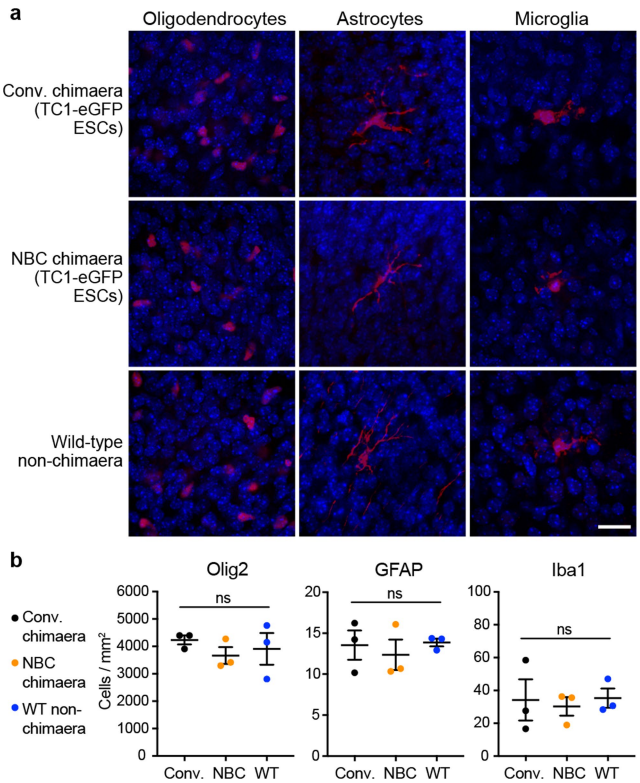

Extended Data Fig. 5 | NBC mice have normal proportions of non-neuronal cells and do not show signs of neuroinflammation. **a**, Representative immunofluorescence images of oligodendrocytes (Olig2), astrocytes (GFAP) and microglia (Iba1) in cortical brain sections of conventional and NBC chimaeras, with a wild-type non-chimeric mouse for comparison. The non-neuronal cells are shown in red; DAPI-stained nuclei are in blue. These experiments were repeated on 9 mice ($n = 3$, NBC chimaeras; $n = 3$, conventional chimaeras; $n = 3$, non-chimeric wild-type mice). **b**, Quantification of Olig2-, GFAP- or Iba1-positive cells in cortical brain sections of conventional chimaeras, NBC chimaeras and wild-type non-chimeric mice ($n = 3$ each). Data represent mean and s.e.m.; NS, not significant, $P > 0.05$ (one-way ANOVA, Tukey's post hoc correction for multiple comparisons). Scale bar, 10 μm.

© 2018 Springer Nature Limited. All rights reserved.

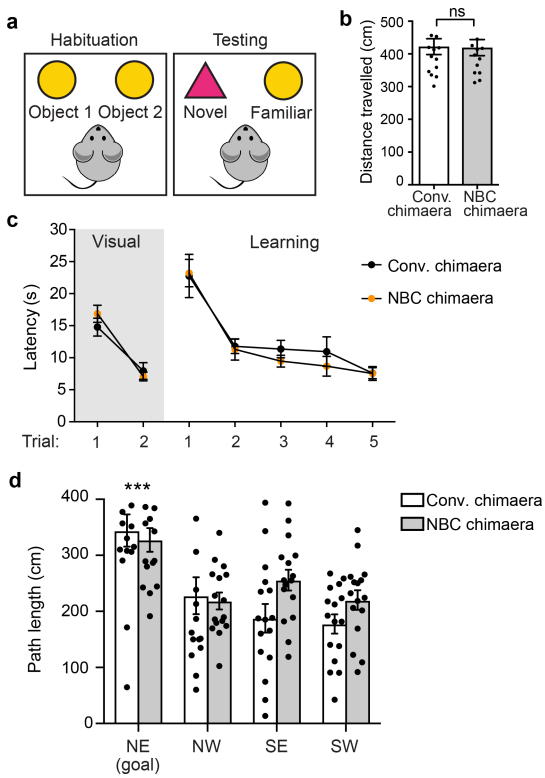

Extended Data Fig. 6 | Brains of NBC mice are functionally normal. **a**, Schematic of the novel-object recognition task. **b**, Locomotor activity of male two-month-old conventional ($n = 15$) or NBC ($n = 14$) chimaeras during the habituation phase of the novel-object recognition paradigm. Data represent mean and s.e.m.; NS, $P > 0.05$ (unpaired two-tailed t-test). **c**, Latency to platform for conventional (black) or NBC (orange) chimaeras in the indicated visual and learning trials of the Morris water maze task. Male two-month-old conventional and NBC chimaeras ($n = 16$ mice each) were analysed. Data represent mean and s.e.m.; no significant difference was observed between conventional and NBC chimaeras across the visual trials ($F(1, 30) = 0.223$, $P = 0.640$) or learning trials ($F(1, 30) = 0.296$, $P = 0.590$) (two-way mixed-model ANOVA). A significant difference was observed in latency over the learning trials, indicating that both groups of mice are able to learn ($F(1.627, 48.815) = 29.426$, $P < 0.0005$) (two-way mixed-model ANOVA with Greenhouse–Geisser correction for violation of sphericity). **d**, Path length traversed in each quadrant by conventional and NBC chimaeras during the probe trial. Male two-month-old conventional and NBC chimaeras ($n = 16$ mice each) were analysed. Data represent mean and s.e.m.; no significant difference between conventional and NBC chimaeras ($F(1, 30) = 1.433$, $P = 0.241$) (two-way mixed-model ANOVA). Significant preference was observed for the north-east (NE) quadrant where the platform had previously been located, indicating memory retention of the prior platform location; ***$P < 0.001$ (multiple pairwise comparisons with Bonferroni post hoc correction).

© 2018 Springer Nature Limited. All rights reserved.

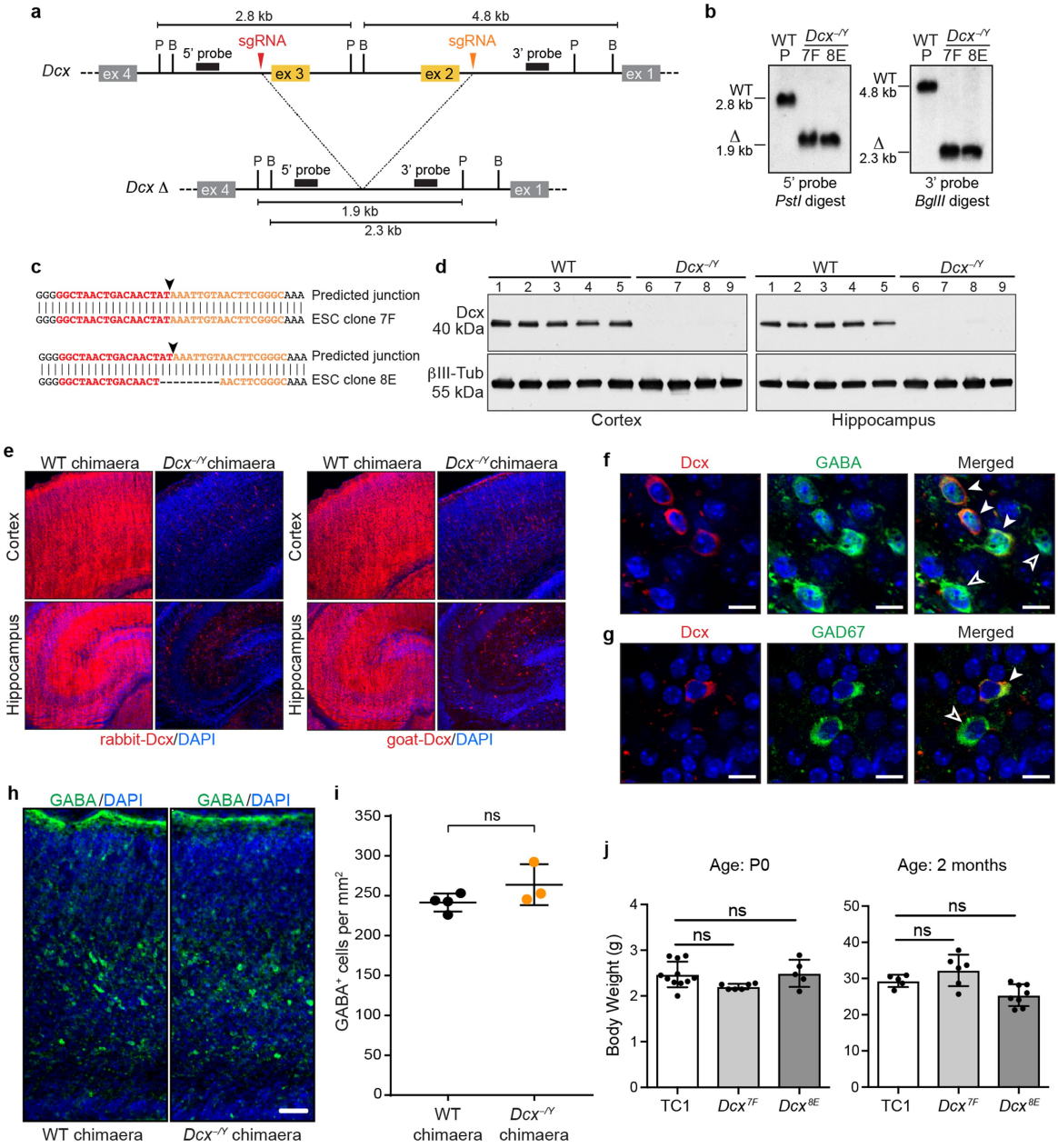

Extended Data Fig. 7 | See next page for caption.

© 2018 Springer Nature Limited. All rights reserved.

Extended Data Fig. 7 | Generation of *Dcx*$^{-/Y}$ NBC chimaeras. a, Top, schematic of *Dcx* inactivation. sgRNA target sequences (red and orange arrowheads) flanking exon 2 (ex 2) and exon 3 (ex 3) are indicated. Probes (black rectangles) and restriction enzyme sites (P, PstI; B, BglII) used for Southern blotting are indicated. Predicted restriction fragment sizes are indicated in kb. Bottom, predicted *Dcx* exon 2 and exon 3 deletion (Δ) locus. **b**, Southern blot analysis of genomic DNA from parental (P) *Dcx*$^{+/Y}$ (wild-type) ES cell line and *Dcx*$^{-/Y}$ ES-cell clones 7F and 8E, using the probes and digests depicted in **a**. Southern blot analysis was performed five times. **c**, Sequence analysis of *Dcx* deletion junctions (black arrowheads); sgRNA target sequences flanking the deletion junction are denoted in red and orange. Both of the *Dcx*$^{-/Y}$ ES cell clones have a unique junction sequence, which suggests that each derived from an independent deletion event. **d**, Western blotting of whole-cell lysates from cortex or hippocampus of wild-type or *Dcx*$^{-/Y}$ NBC chimaeras at P0 with antibodies to Dcx (rabbit anti-Dcx) and βIII-tubulin as a loading control. Each lane (1–9) depicts cortex or hippocampus whole-cell lysate from one mouse; experiments were performed on nine mice ($n = 4$, *Dcx*$^{-/Y}$ ES-cell clone 8E; $n = 5$, wild-type ES cells) **e**, Representative immunofluorescence images of Dcx expression in cortex and hippocampus of wild-type or *Dcx*$^{-/Y}$ chimaeras at P0. Twenty-one mice ($n = 6$, *Dcx*$^{-/Y}$ ES-cell clone 7F; $n = 4$ *Dcx*$^{-/Y}$ ES-cell clone 8E; $n = 11$ wild-type ES cells) were analysed. Dcx-expressing cells (red) were detected with rabbit or goat Dcx antibodies. Nuclei were DAPI-stained (blue). **f**, Representative images of somatosensory cortical brain sections (acquired between layers IV and V) from P0 *Dcx*$^{-/Y}$ chimaeras co-stained with Dcx (red) and GABA (green) antibodies. Merged images are shown on the right. Nuclei were DAPI-stained (blue). Solid white arrowheads indicate cells that are double-positive for Dcx and GABA (host-derived immature interneurons). Hollow arrowheads indicate GABA single-positive cells, which are either donor-derived mature interneurons, donor-derived immature interneurons or host-derived mature interneurons. **g**, Representative images of somatosensory cortical brain sections (acquired between layers IV and V) from P0 *Dcx*$^{-/Y}$ chimaeras co-stained with Dcx (red) and GAD67 (green) antibodies. Merged images are shown on the right. Nuclei were DAPI-stained (blue). Solid white arrowheads indicate host-derived immature interneurons, whereas hollow arrowheads indicate cells that are either donor-derived mature interneurons, donor-derived immature interneurons or host-derived mature interneurons. For experiments in **f**, **g**, nine mice ($n = 4$, *Dcx*$^{-/Y}$ ES-cell clone 8E; $n = 5$ wild-type ES cells) were analysed. **h**, Representative images of somatosensory cortical brain sections from P0 wild-type and *Dcx*$^{-/Y}$ chimaeras stained with GABA antibodies (green). Nuclei were DAPI-stained (blue). Seven mice were analysed ($n = 3$, NBC chimaeras; $n = 4$, conventional chimaeras). **i**, Cell density of GABA-positive interneurons in somatosensory cortex from control chimaeras ($n = 4$ mice) and *Dcx*$^{-/Y}$ chimaeras ($n = 3$ mice). Centre denotes mean, error bars indicate s.e.m. NS, not significant, $P > 0.05$ (unpaired, two-tailed *t*-test). **j**, Mean (± s.d.) body weights of wild-type (TC1) or *Dcx*$^{-/Y}$ chimaeras; NS, not significant, $P > 0.05$ (one-way ANOVA, Tukey's post hoc correction). For P0 cohort, $n = 6$ for *Dcx* 7F; $n = 5$ for *Dcx* 8E; $n = 11$ for wild-type TC1 controls. For two-month-old cohort, $n = 6$ for *Dcx* 7F; $n = 8$ for *Dcx* 8E; $n = 5$ for wild-type TC1 controls. Scale bars, 10 μm (**f**, **g**), 50 μm (**h**).

© 2018 Springer Nature Limited. All rights reserved.

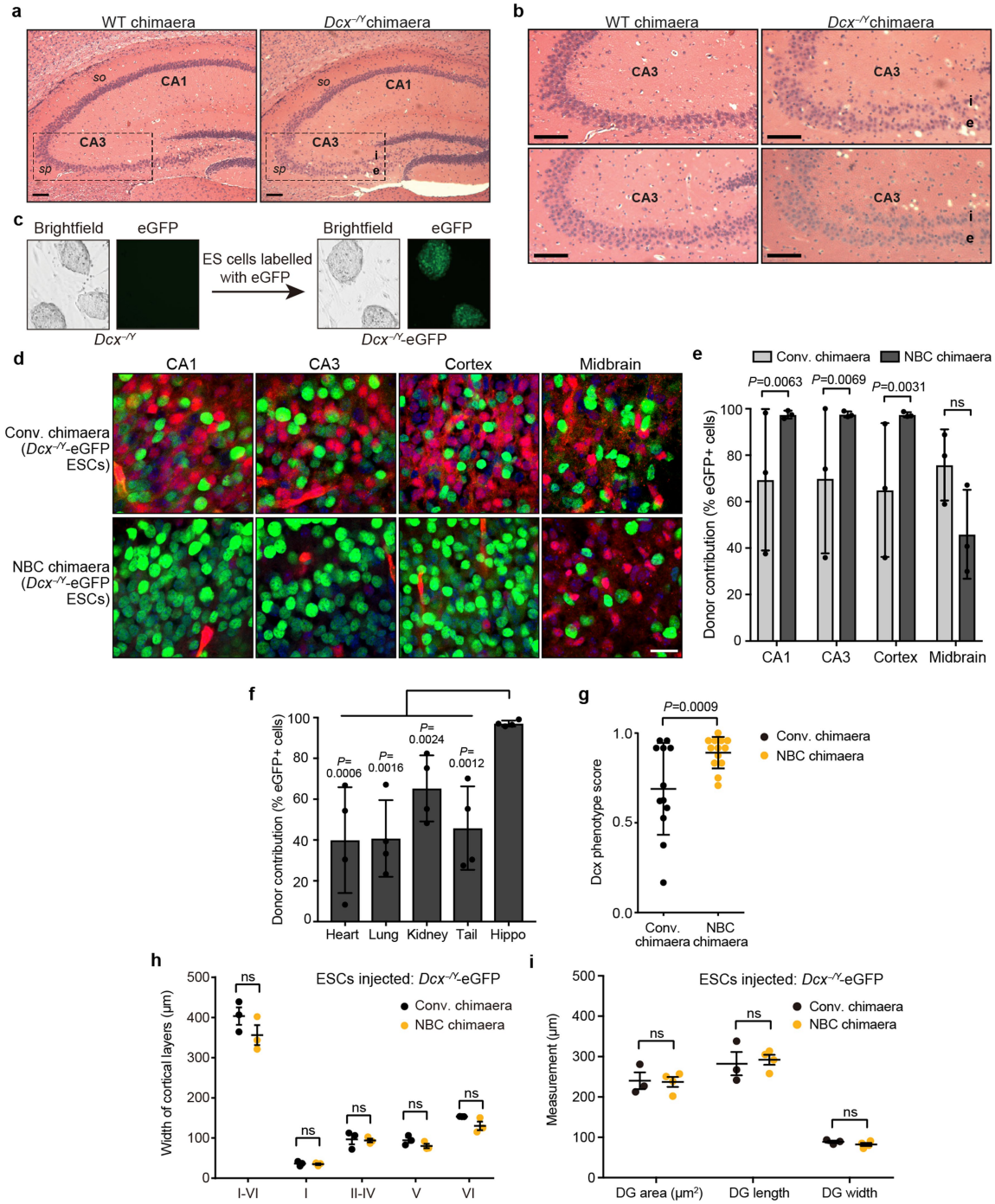

Extended Data Fig. 8 | See next page for caption.

© 2018 Springer Nature Limited. All rights reserved.

Extended Data Fig. 8 | *Dcx*$^{-/Y}$ NBC chimaeras show a mutant hippocampal phenotype. a, Representative images of H&E-stained coronal sections of hippocampus from two-month-old wild-type chimaeras and *Dcx*$^{-/Y}$ chimaeras. Dashed lines highlight the CA3 region, where the stratum pyramidale is present as a single layer in wild-type chimaeras but is abnormally divided into an internal and external layer in the *Dcx*$^{-/Y}$ chimaeras. Figure 4a provides a schematic of the hippocampus. **b**, Enlarged, representative images of the CA3 region in two two-month-old wild-type and *Dcx*$^{-/Y}$ chimaeras. For experiments in **a**, **b**, 14 2-month-old *Dcx*$^{-/Y}$ chimaeras—generated from 2 different *Dcx*$^{-/Y}$ ES clones ($n = 6$ from clone *Dcx* 7F; $n = 8$ from clone *Dcx* 8E)—and 5 wild-type chimaeras were analysed. All 14 *Dcx*$^{-/Y}$ chimaeras showed the hippocampal mutant phenotype. **c**, Representative bright field and fluorescence microscopy images of *Dcx*$^{-/Y}$ ES cells before and after lentiviral integration of H2B–eGFP. **d**, Representative images from experiments performed on six mice ($n = 3$, NBC chimaeras; $n = 3$, conventional chimaeras) showing the extent of the contribution of *Dcx*$^{-/Y}$ H2B–eGFP-expressing donor ES cells to indicated brain regions in conventional and NBC chimaeras at P0 (green, cells derived from donor ES cells; red, host-derived cells; blue, DAPI-stained nuclei). **e**, Quantification of the contribution of *Dcx*$^{-/Y}$ H2B–eGFP-expressing donor ES cells in conventional and NBC chimaeras ($n = 3$ mice each). Data are mean ± s.d. Variance was significantly different between conventional and NBC chimaeras for CA1, CA3 and cortex (*F* test for equality of variances), which reflects the wide variation in donor contribution among individual conventional chimaeras in contrast to consistently high donor contribution in NBC chimaeras. No difference was observed for midbrain (NS, not significant; $P = 0.7812$), which is consistent with competition between donor and host cells in this non-ablated brain region in both types of chimaera. **f**, Quantification of variance in contribution of *Dcx*$^{-/Y}$ H2B–eGFP-expressing donor ES cells in non-brain tissues, relative to hippocampus in NBC chimaeras ($n = 4$). Donor contribution in the hippocampus was calculated as the average of CA1 and CA3 values. Data are mean ± s.d. (*F* test for equality of variances). **g**. Quantification of Dcx mutant hippocampal phenotype in conventional chimaeras ($n = 12$) and NBC chimaeras ($n = 13$) at P0. Dcx phenotype scores were determined by reviewing a series of coronal brain step-sections from each chimaera and determining the number of sections that show a clear CA3 double layer (score = 1), some degree of CA3 disorganization (score = 0.5) or normal CA3 layer morphology (score = 0). Mean Dcx phenotype scores across all sections of a given chimaera are plotted. Each data point corresponds to one chimaera. Horizontal lines indicate mean phenotype score (± s.d.) across all chimaeras per group. Conventional chimaeras show significant variation in the severity of the mutant phenotype, in contrast to the NBC chimaeras (*F* test for equality of variances). **h**, Widths of somatosensory cortex layers in P0 conventional ($n = 3$, black) or NBC ($n = 3$, orange) chimaeras injected with *Dcx*$^{-/Y}$ H2B–eGFP-expressing ES cells, determined by DAPI and Ctip2 staining. Centre denotes mean, error bars indicate s.e.m. NS, not significant, $P > 0.05$ (two-way ANOVA with Bonferroni post hoc correction for multiple comparisons). **i**, Dentate gyrus measurements in conventional chimaeras ($n = 3$; black) and NBC chimaeras ($n = 4$; orange) at P0, generated by blastocyst injection of *Dcx*$^{-/Y}$ H2B–eGFP-expressing ES cells. Horizontal bars indicate mean; error bars denote s.e.m.; NS, not significant, $P > 0.05$ (unpaired, two-tailed *t*-test). Scale bars, 100 μm (**a**, **b**), 10 μm (**d**).

© 2018 Springer Nature Limited. All rights reserved.

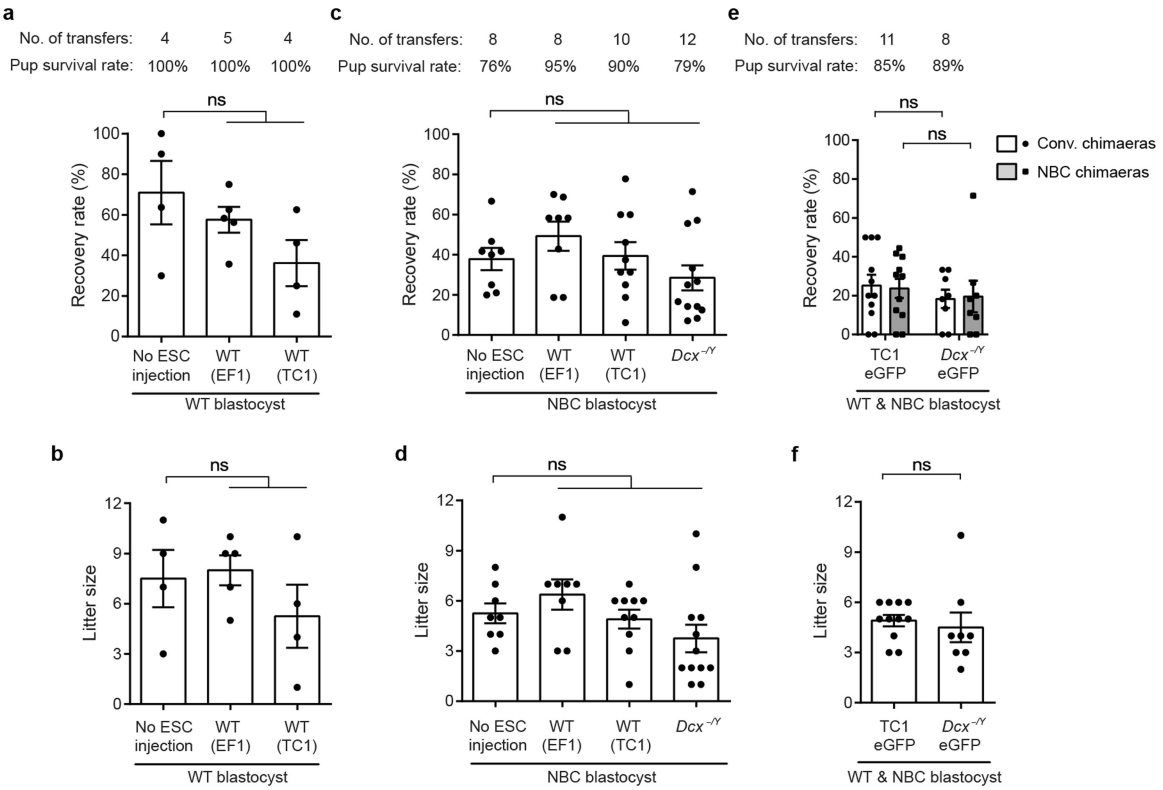

Extended Data Fig. 9 | Rates of recovery, survival, and litter sizes across multiple pregnancies and ES cell lines. a, Average recovery rate (±s.e.m.) of liveborn pups from wild-type blastocysts without ES cell injection or injected with wild-type ES cells (EF1 and TC1). NS, not significant, $P > 0.05$ (one-way ANOVA with Tukey's post hoc correction for multiple comparisons). Number of transfers (foster pregnancies) and pup survival rate at P0 is listed above the graph. **b**, Mean litter size (±s.e.m.) per foster recipient of wild-type blastocysts without ES cell injection or injected with wild-type ES cells (EF1 and TC1); NS, not significant, $P > 0.05$ (one-way ANOVA, Tukey's post hoc correction for multiple comparisons). **c**, Average recovery rate (±s.e.m.) of liveborn pups from NBC blastocysts without ES cell injection or injected with wild-type (EF1 and TC1) or *Dcx*$^{-/Y}$ ES cells. NS, not significant, $P > 0.05$ (one-way ANOVA with Tukey's post hoc correction for multiple comparisons). Number of transfers (foster pregnancies) and pup survival rate at P0 is listed above the graph. **d**, Mean litter size (±s.e.m.) per foster recipient of NBC blastocysts without ES cell injection or injected with wild-type (EF1 and TC1) or *Dcx*$^{-/Y}$ ES cells; NS, not significant, $P > 0.05$ (one-way ANOVA, Tukey's post hoc correction for multiple comparisons). **e**, Average recovery rate (±s.e.m.) of mice from mixed wild-type and NBC blastocyst transfers; NS, not significant, $P > 0.05$ (unpaired, two-tailed *t*-test). **f**, Mean litter size (±s.e.m.) per foster recipient; NS, not significant, $P > 0.05$ (unpaired, two-tailed *t*-test). For experiments in **e**, **f**, mice were inter-crossed to simultaneously generate wild-type or NBC blastocysts with or without expression of DsRed.T3 (see schematic in Extended Data Fig. 2a) and were injected with either wild-type (TC1) H2B–eGFP-expressing or *Dcx*$^{-/Y}$ H2B–eGFP-expressing ES cells, followed by transfer into fosters. Pups were then genotyped to determine whether they were wild-type or derived from NBC blastocysts.

© 2018 Springer Nature Limited. All rights reserved.

LETTER

https://doi.org/10.1038/s41586-018-0629-6

Nuclear cGAS suppresses DNA repair and promotes tumorigenesis

Haipeng Liu[1,2,11], Haiping Zhang[3,11], Xiangyang Wu[1,2,11], Dapeng Ma[2], Juehui Wu[1,2], Lin Wang[1,2], Yan Jiang[2], Yiyan Fei[4], Chenggang Zhu[4], Rong Tan[5], Peter Jungblut[6], Gang Pei[7], Anca Dorhoi[7,8], Qiaoling Yan[2], Fan Zhang[9], Ruijuan Zheng[1], Siyu Liu[2], Haijiao Liang[1,2], Zhonghua Liu[1], Hua Yang[1], Jianxia Chen[1,2], Peng Wang[2], Tianqi Tang[2], Wenxia Peng[2], Zhangsen Hu[3], Zhu Xu[3], Xiaochen Huang[1], Jie Wang[1], Haohao Li[1], Yilong Zhou[1,2], Feng Liu[1], Dapeng Yan[10], Stefan H. E. Kaufmann[7], Chang Chen[9], Zhiyong Mao[3]* & Baoxue Ge[1,2]*

Accurate repair of DNA double-stranded breaks by homologous recombination preserves genome integrity and inhibits tumorigenesis. Cyclic GMP–AMP synthase (cGAS) is a cytosolic DNA sensor that activates innate immunity by initiating the STING–IRF3–type I IFN signalling cascade[1,2]. Recognition of ruptured micronuclei by cGAS links genome instability to the innate immune response[3,4], but the potential involvement of cGAS in DNA repair remains unknown. Here we demonstrate that cGAS inhibits homologous recombination in mouse and human models. DNA damage induces nuclear translocation of cGAS in a manner that is dependent on importin-α, and the phosphorylation of cGAS at tyrosine 215—mediated by B-lymphoid tyrosine kinase—facilitates the cytosolic retention of cGAS. In the nucleus, cGAS is recruited to double-stranded breaks and interacts with PARP1 via poly(ADP-ribose). The cGAS–PARP1 interaction impedes the formation of the PARP1–Timeless complex, and thereby suppresses homologous recombination. We show that knockdown of cGAS suppresses DNA damage and inhibits tumour growth both in vitro and in vivo. We conclude that nuclear cGAS suppresses homologous-recombination-mediated repair and promotes tumour growth, and that cGAS therefore represents a potential target for cancer prevention and therapy.

To find out whether cGAS responds to DNA damage, we treated an immortalized human fibroblast HCA2-TERT cell line and two primary human skin fibroblast cell lines with the genotoxic agents etoposide, camptothecin and H_2O_2, and then examined the intracellular localization of cGAS. All treatments led to robust nuclear translocation of cGAS (Fig. 1a, Extended Data Fig. 1a–n). cGAS has previously been reported to accumulate within the nuclear compartment of micronuclei owing to rupture of their membranes[4], but our lamin A/C staining analysis revealed that the nuclear membrane was intact when cGAS translocated

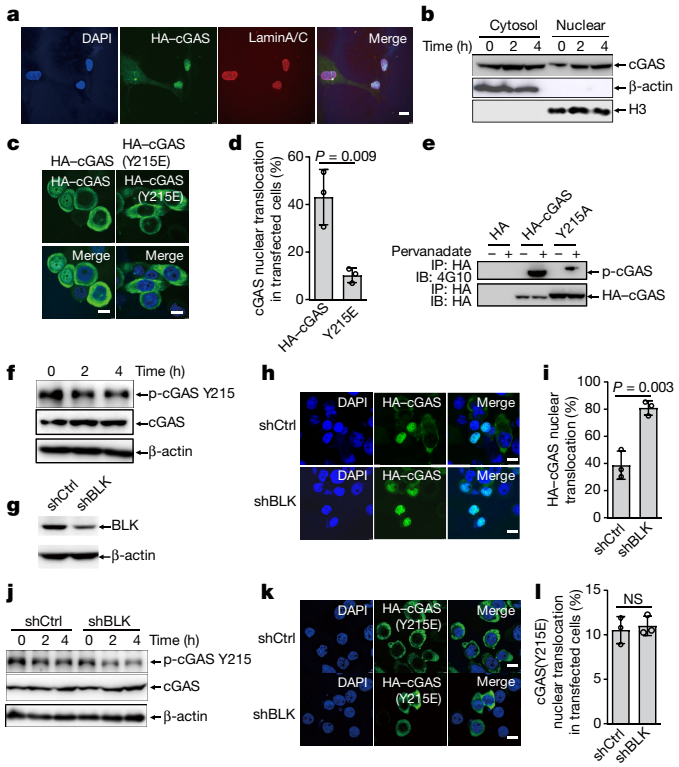

Fig. 1 | Phosphorylation of cGAS at Y215 by BLK regulates the nuclear translocation of cGAS in response to DNA damage. **a** Immunofluorescence of HA–cGAS in transfected HCA2-TERT cells exposed to etoposide (100 μg ml^{-1}) for 4 h. **b**, Immunoblot of endogenous cGAS in the cytoplasmic and nuclear fractions of HCA2-TERT cells treated with etoposide for the indicated times. **c**, **d**, Immunofluorescence of HA–cGAS and HA–cGAS(Y215E) in PC-9 cells exposed to etoposide (100 μg ml^{-1}) for 4 h (**c**). Quantitative data are shown in **d**. **e**, Immunoblot (IB) of anti-HA immunoprecipitates (IP) from HEK293T cells transfected with HA–cGAS and HA–cGAS(Y215A) in the absence or presence of pervanadate for 30 min. **f**, **g**, Immunoblot of the lysates of PC-9 cells stimulated with etoposide (100 μg ml^{-1}) for the indicated times (**f**) and the lysates of PC-9 cells expressing HA–cGAS, transfected with either control shRNA (shCtrl) or shRNA targeting *BLK* (shBLK) for 72 h (**g**). **h**, **i**, Immunofluorescence of HA–cGAS in PC-9 cells that stably express HA–cGAS, with either shCtrl or shBLK introduced after treatment with etoposide (100 μg ml^{-1}) for 4 h (**h**). Quantitative data are shown in **i**. **j**, Immunoblot of cell lysates of PC-9 cells that stably express HA–cGAS, transfected with either shCtrl or shBLK after etoposide (100 μg ml^{-1}) treatment for 4 h. **k**, **l**, Immunofluorescence of overexpressed HA–cGAS(Y215E) in PC-9 cells that had been transfected with either shCtrl or shBLK followed by exposure to etoposide (100 μg ml^{-1}) for 4 h (**k**). Quantitative data are presented in **l**. Data are expressed as mean ± s.e.m. of 3 independent experiments (**d**, **i**, **l**). $n = 3$ independent experiments (**a**–**c**, **e**–**h**, **j**, **k**). Nuclei were stained with DAPI (blue). Student's *t* tests (two-tailed) were used for statistical analysis. NS, not significant. Scale bar, 5 μm. For gel source data, see Supplementary Fig. 1.

[1]Shanghai Key Laboratory of Tuberculosis, Shanghai Pulmonary Hospital, Tongji University School of Medicine, Shanghai, China. [2]Clinical Translational Research Center, Shanghai Pulmonary Hospital, Tongji University School of Medicine, Shanghai, China. [3]Clinical and Translational Research Center of Shanghai First Maternity & Infant Hospital, Shanghai Key Laboratory of Signaling and Disease Research, School of Life Sciences and Technology, Tongji University, Shanghai, China. [4]Department of Optical Science and Engineering, Shanghai Engineering Research Center of Ultra-Precision Optical Manufacturing, Key Laboratory of Micro and Nano Photonic Structures (Ministry of Education), Fudan University, Shanghai, China. [5]Center for Molecular Medicine, Xiangya Hospital, Central South University, Changsha, China. [6]Protein Purification Core Facility, Max Planck Institute for Infection Biology, Berlin, Germany. [7]Department of Immunology, Max Planck Institute for Infection Biology, Berlin, Germany. [8]Institute of Immunology, Friedrich-Loeffler-Institut, Federal Research Institute for Animal Health, Greifswald Insel Riems, Germany. [9]Department of Thoracic Surgery, Shanghai Pulmonary Hospital, Tongji University School of Medicine, Shanghai, China. [10]Key Laboratory of Medical Molecular Virology of MOE/MOH, Fudan University, Shanghai, China. [11]These authors contributed equally: Haipeng Liu, Haiping Zhang, Xiangyang Wu. *e-mail: zhiyong_mao@tongji.edu.cn; baoxue_ge@tongji.edu.cn

© 2018 Springer Nature Limited. All rights reserved.

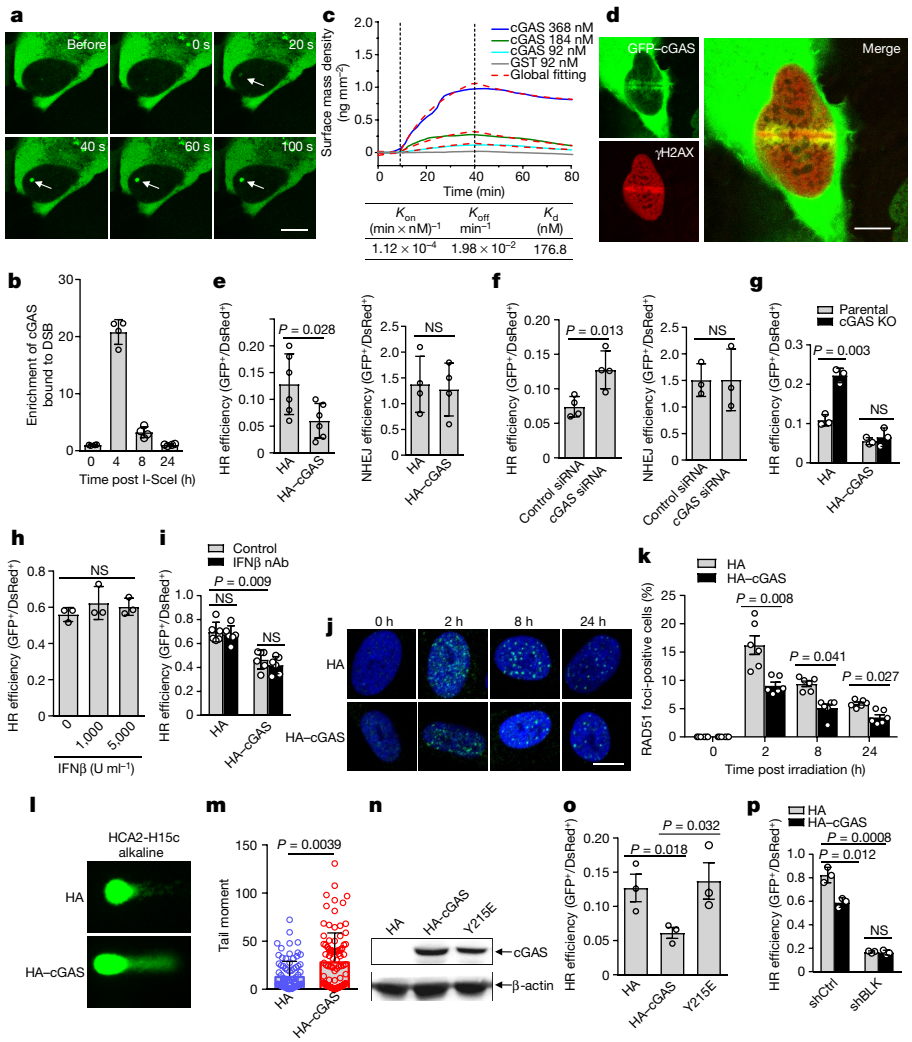

Fig. 2 | cGAS is recruited to DNA DSB sites and inhibits homologous recombination. a, Representative images showing recruitment of GFP–cGAS to DNA damage sites in U2OS cells following laser microirradiation. $n = 4$ independent experiments. **b**, Chromatin immunoprecipitation assay showing HA–cGAS recruitment to I-SceI induced DSBs. **c**, Binding curves of surface-immobilized phosphopeptides with GST–cGAS or GST at indicated concentrations. Vertical lines mark the start of association and dissociation phases of the binding events. The dashed lines are global fits to a Langmuir reaction model; global fitting parameters are listed in the table below the plot. $n = 5$ independent experiments. **d**, Representative immunofluorescence of GFP–cGAS and endogenous γH2AX at DNA-damage sites, in U2OS cells following laser microirradiation. ($n = 3$ independent experiments). **e**, **f**, Effect of cGAS overexpression (**e**) and knockdown (**f**) on the efficiency of homologous recombination (HR) and NHEJ. **g**, Analysis of efficiency of homologous recombination in parental and cGAS knockout (KO) HCA2-H15c cells transfected with control vector (HA) or HA–cGAS. **h**, **i**, Effect of exogenous IFNβ (**h**) and IFNβ neutralization antibody (nAb) (**i**) on the efficiency of homologous recombination. One-way ANOVA (**h**). **j**, Representative images showing RAD51 foci at indicated times after irradiation. Quantification in **k** is as described in Methods. **l**, **m**, Representative comet assay showing the tail moment of HCA2-H15c cells transfected with HA or HA–cGAS vector (**l**). Quantification in **m**; data represent mean ± s.d. of the tail moment of $n = 87$ (HA) and $n = 92$ (HA–cGAS) cells from 3 independent experiments. Mann–Whitney *U*-test. **n**, **o**, Effect of cGAS(Y215E) on homologous recombination efficiency, in HCA2-H15c cells. Immunoblot showing the expressed protein is shown in **n**. **p**, Effect of *BLK* knockdown on cGAS-mediated inhibition of homologous recombination efficiency. Mean ± s.e.m. of independent experiments and each dot represents the data of one independent experiment (**b**, **e**–**i**, **k**, **o**, **p**). Student's *t* tests (two-tailed) unless otherwise indicated. NS, not significant. Scale bar, 5 μm. For gel source data, see Supplementary Fig. 1.

to the nucleus in response to agents that cause DNA damage (Fig. 1a, Extended Data Fig. 1f–h, j–m) and that the cells were scarcely apoptotic (Extended Data Fig. 1o). Subcellular fractionation analysis also confirmed that cGAS accumulated in the nuclear fractions of cells treated with etoposide (Fig. 1b).

We further observed a dose-dependent, stress-induced nuclear translocation of cGAS in two human lung cancer cell lines, A549 and PC-9 (Extended Data Fig. 2a–h). DNA binding and enzymatic activity are essential for cGAS to sense cytosolic DNA and activate the STING-mediated type I IFN response[1,2]. However, nuclear translocation of cGAS in response to treatment with etoposide was observed for the DNA-binding mutants cGAS(N210A, Y214A, K384A), cGAS(K407A, Δ171–174) and cGAS(Δ171–174) as well as the enzymatically inactive mutants cGAS(E225A, D227A) and cGAS(D319A)[5] (Extended Data Fig. 3a, b), which indicates that nuclear translocation of cGAS induced by DNA damage is uncoupled from the function of cGAS in DNA sensing.

Mutating the evolutionarily conserved tyrosine 215 of cGAS to glutamic acid abrogated the nuclear translocation of cGAS in response to DNA damage (Fig. 1c, d, Extended Data Fig. 4a–e). In addition, the Y215A mutant of cGAS showed a markedly reduced level of tyrosine phosphorylation (Fig. 1e). We used a rabbit polyclonal antibody specifically against phospho-cGAS Y215 (Extended Data Fig. 4f), and found that the gradual reduction of the level of Y215 phosphorylation was accompanied by increased nuclear translocation of cGAS in response to DNA-damaging agents (Fig. 1f, Extended Data Fig. 4g), which suggests

© 2018 Springer Nature Limited. All rights reserved.

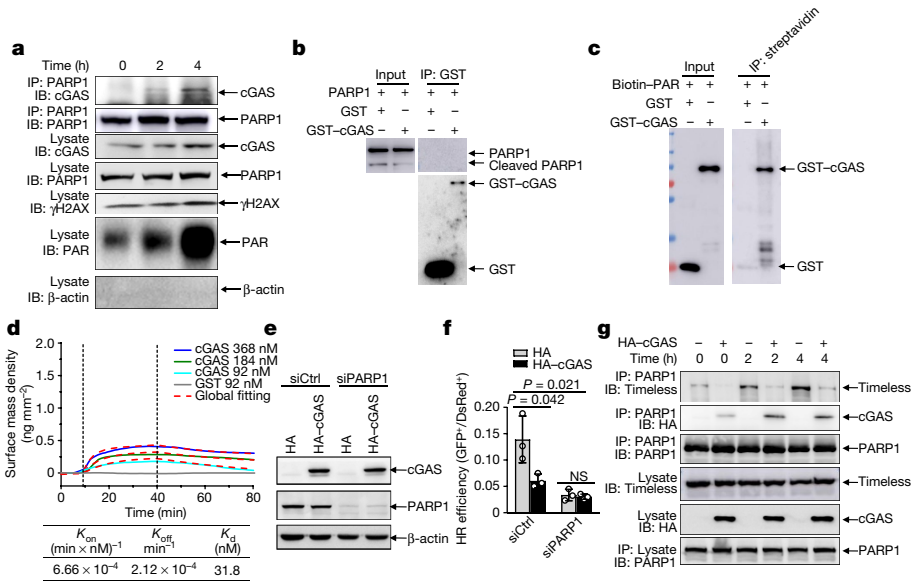

Fig. 3 | cGAS interacts with PARP1 via PAR and abrogates the formation of the PARP1–Timeless complex. a, Immunoblot of anti-PARP1 immunoprecipitates. Nuclear-fraction lysates were prepared from PC-9 cells treated with etoposide (100 μg ml^{-1}) for the indicated times. **b**, Results of in vitro GST precipitation assay of purified PARP1 combined with GST or GST–cGAS. **c**, Results of in vitro precipitation assay with streptavidin beads of biotin PAR combined with GST or GST–cGAS. **d**. Binding curves of surface-immobilized PAR with GST-labelled cGAS at concentrations of 368 nM, 184 nM and 92 nM, and with control GST at a concentration of 92 nM. Vertical lines mark the starts of association and dissociation phases of the binding events. The dashed lines are global fits to a Langmuir reaction model; global fitting parameters are listed in the table below the plot. **e**, Immunoblot findings from human HCA2-H15c fibroblasts that had been transfected with a pcDNA3.1-HA control (HA) or HA–cGAS and with control siRNA (siCtrl) or siRNA targeting *PARP1* (siPARP1). **f**, Effect of *PARP1* knockdown on the modulation of homologous recombination by overexpressed cGAS in HCA2-H15c cells. Control (siCtrl) and *PARP1* knockdown (siPARP1) human fibroblasts that contain chromosomally integrated reporter cassettes were transfected with either pcDNA3.1-HA control (HA) or HA–cGAS, and homologous recombination efficiency was assessed. Data are expressed as mean ± s.e.m. of 3 independent experiments. Student's *t* tests (two-tailed). NS, not significant. **g**, Immunoblot results of cell lysates or anti-PARP1 immunoprecipitates from PC-9 cells that had been stably transfected with HA–cGAS (+) or with pcDNA3.1-HA (HA–cGAS −) and treated with etoposide (100 μg ml^{-1}) for the indicated times. Data are representative of $n = 3$ (**b**, **c**, **e**, **g**) or $n = 4$ independent experiments (**a**, **d**). For gel source data, see Supplementary Fig. 1.

that cGAS phosphorylation at Y215 has a possible role in regulating the nuclear translocation of cGAS.

We set out to identify the tyrosine kinase that is responsible for cGAS phosphorylation by screening the effect of a short hairpin RNA (shRNA) library that targets 89 protein tyrosine kinases on nuclear translocation of cGAS tagged with GFP (GFP–cGAS), in PC-9 cells (Supplementary Table 2). Transfection of cells with shRNA targeting B-lymphoid tyrosine kinase (*BLK*)—a member of the SRC kinase family[6]—substantially increased cGAS nuclear translocation (Supplementary Table 2), which was further confirmed in PC-9 cells that stably express cGAS tagged with haemagglutinin (HA–cGAS) (Fig. 1g–i, Extended Data Fig. 4h, i). Moreover, *BLK* knockdown reduced the phosphorylation of cGAS Y215 in PC-9 cells upon stimulation with DNA-damaging agents (Fig. 1j, Extended Data Fig. 4j). However, *BLK* knockdown did not significantly change the nuclear translocation of cGAS(Y215E) (Fig. 1k, l). Therefore, in resting cells the constitutive phosphorylation of cGAS at Y215 by BLK may maintain the cytosolic localization of cGAS, whereas stimulation with DNA-damaging agents leads to cGAS dephosphorylation and therefore facilitates the shuttling of cGAS to the nucleus.

cGAS contains two nuclear localization sequences, ^{21}KASARNARGAPMDPTESPAAPEAALPKAGKF^{51} (NLS1) and ^{295}DVIMKRKRGGS^{305} (NLS2) (Extended Data Fig. 5a, b; as analysed by cNLS Mapper, http://nls-mapper.iab.keio.ac.jp/cgi-bin/NLS_Mapper_form.cgi)[7], which suggests a classical, importin-mediated pathway for nuclear import of cGAS[8]. cGAS interacted with proteins of the importin-α family, including karyopherin (KPNA) 1, KPNA2, KPNA3, KPNA4 and KPNA5 (Extended Data Fig. 5c). In HEK293T cells, deleting NLS2 but not NLS1 from cGAS abolished the interaction between cGAS and KPNA2 (Extended Data Fig. 5d), and in PC-9 cells this deletion reduced the nuclear translocation of cGAS induced by DNA damage (Extended Data Fig. 5e–j). Moreover, the inhibition of importin-β by importazole significantly reduced the nuclear translocation of cGAS induced by DNA damage (Extended Data Fig. 5k–p). NLS2 is therefore required for the importin-dependent nuclear translocation of cGAS.

To investigate whether cGAS participates in DNA repair, we examined the recruitment of cGAS to DNA-damage sites. Laser microirradiation showed that GFP–cGAS was recruited to DNA lesions (Fig. 2a, Supplementary Video 1). Chromatin immunoprecipitation assays further demonstrated that cGAS is recruited to site-specific double-stranded breaks (DSBs) that are generated by I-SceI meganuclease[9] (Fig. 2b). We found that cGAS interacts with γH2AX, a well-characterized marker of DNA DSBs[10]. The interaction of cGAS with γH2AX was enhanced in response to DNA damage (Extended Data Fig. 6a, b), which was concomitant with elevated γH2AX levels (Extended Data Fig. 6c). By generating cGAS deletion mutants, we found that the C-terminal region of cGAS (amino acids 213–522) mediated the interaction of this protein with γH2AX (Extended Data Fig. 6d, e). The H2AX(S139A) mutant[11] showed less binding with cGAS, indicating that the phospho-epitope of γH2AX is critical for the interaction between γH2AX with cGAS (Extended Data Fig. 6f). A label-free biomolecular interaction assay[12] demonstrated a direct interaction between the phosphorylated H2AX peptide and cGAS ($K_d = 176.8$ nM) (Fig. 2c, Extended Data Fig. 6g, h). Moreover, γH2AX co-localized with cGAS at DNA damage sites upon laser microirradiation (Fig. 2d). Knocking down *H2AX* (also known as *H2AFX*) by shRNA inhibited the recruitment of cGAS to DNA-damage sites (Extended Data Fig. 6i–k, Supplementary Video 2). Taken together, these data indicate that the phosphorylation of H2AX S139 is required for the direct interaction of H2AX with cGAS and facilitates the recruitment of cGAS to DNA-damage sites.

We next examined the effect of cGAS on the efficiency of two DNA DSB repair pathways—homologous recombination and

© 2018 Springer Nature Limited. All rights reserved.

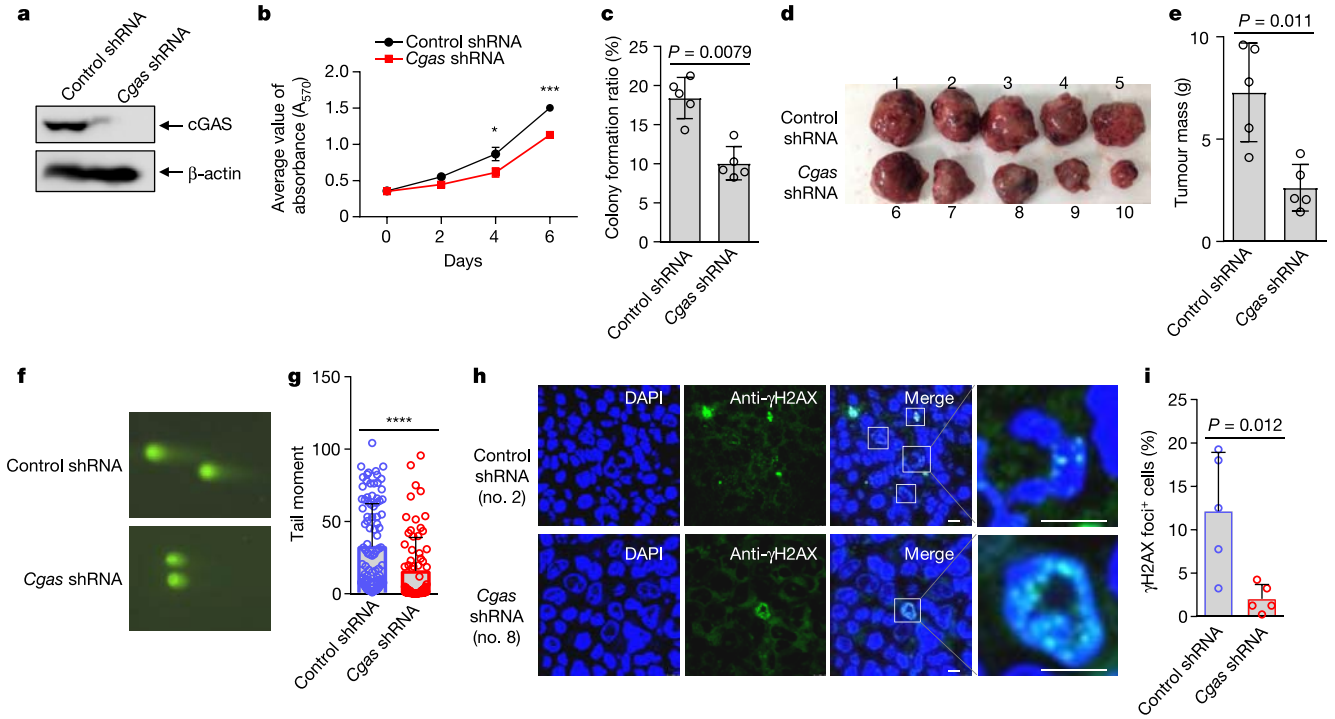

Fig. 4 | cGAS promotes tumour expansion. a, Immunoblot of the lysates from LLC cells stably transfected with scrambled shRNA (control shRNA) or shRNA targeting *Cgas* (*Cgas* shRNA). $n = 2$ independent experiments. **b**, Results of an MTT assay showing the proliferation of control shRNA and *Cgas* shRNA LLC cells. Mean ± s.e.m. of $n = 3$ independent experiments. Student's *t* tests (two-tailed). $^*P < 0.05$; $^{***}P < 0.001$. **c**, Colonogenic assay to detect colony formation of control shRNA and *Cgas* shRNA LLC cells. Mean ± s.e.m. of $n = 5$ independent experiments. Mann–Whitney *U*-test. **d**, **e**, Size (**d**) and weight (**e**) of tumours formed in male C57BL/6 recipient mice by control shRNA and *Cgas* shRNA LLC cells. Tumours isolated from individual mice were coded sequentially (**d**). $n = 3$ independent experiments, $n = 5$ mice for each group in every independent experiment. Mean ± s.d. of $n = 5$ mice in 1 representative experiment and Student's *t* tests (two-tailed) (**e**). **f**, **g**, Representative comet assay showing the tail moment of control shRNA and *Cgas* shRNA LLC cells. $n = 3$ independent experiments. Quantification in **g**; data represent mean ± s.d. of the tail moment of $n = 98$ (control shRNA) and $n = 76$ (*Cgas* shRNA) cells from 3 independent experiments. Mann–Whitney *U*-test. **h**, **i**, Representative immunofluoresence of γH2AX (anti-γH2AX, green) in tumours formed in C57BL/6 mice injected with control shRNA (no. 2) or *Cgas* shRNA (no. 8) LLC cells (**h**). Quantification of the percentage of γH2AX-foci-positive cells in **i** is as described in Methods; data represent mean ± s.d. of $n = 5$ mice in 1 representative experiment. Mann–Whitney *U*-test. Scale bar, 5 μm. For gel source data, see Supplementary Fig. 1.

nonhomologous end joining (NHEJ)—by using cell lines containing reporters[13] (Extended Data Fig. 7a). cGAS overexpression significantly inhibited homologous recombination but not NHEJ (Fig. 2e), which was mirrored in primary cells as determined by extrachromosomal assay[14] (Extended Data Fig. 7b, c). Knockdown of *CGAS* by small interfering RNA (siRNA) consistently and markedly increased homologous recombination but not NHEJ (Fig. 2f). Furthermore, knocking out of cGAS using CRISPR–Cas9 genome editing in HCA2-H15c cells enhanced the efficiency of homologous recombination, whereas restoration of cGAS eliminated this effect (Fig. 2g, Extended Data Fig. 7d). A modest increase in type I IFN transcripts was observed in HCA2-H15c cells that overexpress I-SceI (Extended Data Fig. 7e). However, cGAS overexpression did not cause an additional increase in the expression of type I IFN (Extended Data Fig. 7e). The addition of exogenous IFNβ or neutralization of IFNβ had no significant effect on homologous recombination or NHEJ (Fig. 2h, i, Extended Data Fig. 7f). Therefore, the inhibition of homologous recombination by cGAS is independent of the induction of type I IFN. In addition, we observed that cGAS restrained the recruitment of two critical homologous recombination factors—RPA2[15] and RAD51[16]—to DNA DSBs in response to DNA damage (Fig. 2j, k, Extended Data Fig. 7g–l), which is consistent with the inhibitory role of cGAS in homologous recombination repair.

Our comet assay showed that genome stability was impaired in cells that overexpress cGAS (Fig. 2l, m), as a consequence of reduced homologous recombination. Moreover, the knocking out of cGAS stabilized genomes in HCA2-H15c cells and primary mouse skin fibroblasts (Extended Data Fig. 7m–q). However, cGAS overexpression did not alter cell-cycle distribution or the level of 5-ethynyl-2′-deoxyuridine incorporation (Extended Data Fig. 7r–t), which suggests that cGAS suppresses homologous recombination by affecting signalling in the homologous recombination pathway per se, rather than by arresting the cell cycle[17].

The C-terminal region of cGAS (amino acids 161–522) retained its capacity to inhibit homologous recombination (Extended Data Fig. 8a, b). All enzyme-inactive or DNA-binding mutants also inhibited homologous recombination (Extended Data Fig. 8c–e). However, cGAS(Y215E), cGAS(ΔNLS2) or treatment with importazole allowed homologous recombination to proceed (Fig. 2n, o, Extended Data Fig. 8f–h), which indicates that nuclear translocation of cGAS has an essential role in homologous recombination repair. Moreover, knockdown of *BLK* profoundly suppressed homologous recombination, and counteracted the inhibitory effect of cGAS on homologous recombination (Fig. 2p, Extended Data Fig. 8i), which confirms that the nuclear translocation of cGAS mediated by BLK is involved in modulating DNA repair directed by homologous recombination.

By performing immunoprecipitation and mass spectrometry analysis, we found that PARP1 interacted with cGAS in response to DNA damage (Extended Data Fig. 9a, b). PARP1 participates in both base excision repair[18] and DNA DSB repair by homologous recombination[19]. The interaction was further confirmed by co-immunoprecipitation (co-IP) (Fig. 3a, Extended Data Fig. 9c) and was resistant to DNase I (Extended Data Fig. 9c), which indicates that the interaction is not mediated by DNA.

Inhibiting PARP1 by olaparib[20] abrogated the interaction of PARP1 with cGAS (Extended Data Fig. 9d). Furthermore, the enzymatically

© 2018 Springer Nature Limited. All rights reserved.

inactive mutant PARP1(E988K)[21] failed to interact with cGAS (Extended Data Fig. 9e). Glutathione *S*-transferase (GST) pull-down assay demonstrated that cGAS did not interact with PARP1 directly (Fig. 3b). Both the co-IP assay (Fig. 3c) and the label-free biomolecular interaction assay ($K_d = 31.8$ nM) (Fig. 3d) revealed a direct interaction between cGAS and poly(ADP-ribose) (PAR). Our findings demonstrate that DNA damage induces a PAR-mediated interaction between cGAS and PARP1.

Knockdown of *PARP1* by siRNA inhibited homologous recombination and attenuated cGAS-mediated inhibition of homologous recombination (Fig. 3e, f). The interaction between PARP1 and Timeless is important for DNA repair by homologous recombination[22,23]. In PC-9 cells, cGAS overexpression markedly impeded the interaction of PARP1 with Timeless induced by DNA damage (Fig. 3g, Extended Data Fig. 9f–h) but did not affect PARP1 recruitment to DNA lesions (Extended Data Fig. 9i, j). Notably, inhibiting PARP1 enzymatic activity by olaparib almost completely blocked the nuclear translocation of cGAS induced by DNA damage (Extended Data Fig. 9k–m), indicating that activation of PARP1 by DNA damage is a prerequisite for the nuclear translocation of cGAS. Therefore, cGAS inhibits PARP1-mediated homologous recombination by disrupting the formation of the PARP1–Timeless complex at DSB sites.

Homologous recombination is usually associated with tumorigenesis[24,25]. Stable knockdown of cGAS profoundly reduced the proliferation rate (Fig. 4a, b) and cluster formation (Fig. 4c) of LLC cells (a mouse lung cancer cell line), whereas in PC-9 cells that overexpress cGAS the proliferation rate and cluster formation increased (Extended Data Fig. 10a, b). In addition, MTT assays revealed that cGAS knockdown impeded the survival of LLC cells, whereas cGAS overexpression sensitized PC-9 cells to DNA-damage inducers (Extended Data Fig. 10c, d). Moreover, a soft agar assay[26] demonstrated that human skin fibroblast cells that overexpress cGAS are more susceptible to malignant transformation (Extended Data Fig. 10e, f), which indicates that cGAS has a promoting effect on tumorigeneisis.

We next investigated whether cGAS has any effect on the formation of solid tumours from lung cancer cells in vivo. Depleting cGAS significantly reduced both the volume and mass of LLC tumours in male C57BL/6 mice (Fig. 4d, e). Results from comet assays demonstrated that cGAS knockdown markedly reduced the tail moment (Fig. 4f, g) whereas overexpression of cGAS in PC-9 cells markedly increased the tail moment (Extended Data Fig. 10g, h), which indicates that cGAS enhances DSBs in lung tumour cells. In addition, cGAS knockdown resulted in fewer γH2AX foci in the xenografts (Fig. 4h, i), indicating less DNA damage.

Molecular evolutionary analysis traces cGAS families back to the choanoflagellate *Monosiga brevicollis*, which indicates that cGAS has functions beyond that of cytosolic DNA sensing[27]. Our work has uncovered a function of nuclear cGAS in the DNA-damage response: the inhibition of DNA repair mediated by homologous recombination, to directly influence genome stability (Extended Data Fig. 10i). The potential association between the tumorigenic transformation of normal cells by the dangerous translocation of cGAS and host DNA-damage responses to DNA tumour viruses awaits further investigation. Our finding that nuclear cGAS can act as a tumour enhancer is supported by aberrant upregulation of cGAS transcripts in non-small cell lung carcinomas, including squamous cell carcinoma and adenocarcinoma (Extended Data Fig. 10j, k). Moreover, the expression of regulators of the nuclear translocation of cGAS—KPNA2 and BLK—may have prognostic value for non-small cell lung carcinomas (Extended Data Fig. 10l, m). Specifically, $KPNA2^{high}BLK^{low}$ expression levels are associated with a poor prognosis (Extended Data Fig. 10l, m). These findings underscore the critical role of the nuclear translocation of cGAS in cancer development, which forms the basis for suggesting that inhibitors that intervene in the nuclear translocation of cGAS have the potential to be used as adjuncts to canonical chemo- and radiosensitization treatments.

Online content

Any methods, additional references, Nature Research reporting summaries, source data, statements of data availability and associated accession codes are available at https://doi.org/10.1038/s41586-018-0629-6.

Received: 17 August 2017; Accepted: 22 August 2018;
Published online 24 October 2018.

1. Sun, L., Wu, J., Du, F., Chen, X. & Chen, Z. J. Cyclic GMP–AMP synthase is a cytosolic DNA sensor that activates the type I interferon pathway. *Science* **339**, 786–791 (2013).
2. Wu, J. et al. Cyclic GMP–AMP is an endogenous second messenger in innate immune signaling by cytosolic DNA. *Science* **339**, 826–830 (2013).
3. Harding, S. M. et al. Mitotic progression following DNA damage enables pattern recognition within micronuclei. *Nature* **548**, 466–470 (2017).
4. Mackenzie, K. J. et al. cGAS surveillance of micronuclei links genome instability to innate immunity. *Nature* **548**, 461–465 (2017).
5. Civril, F. et al. Structural mechanism of cytosolic DNA sensing by cGAS. *Nature* **498**, 332–337 (2013).
6. Petersen, D. L. et al. A novel BLK-induced tumor model. *Tumour Biol.* **39**, https://www.doi.org/10.1177/1010428317714196 (2017).
7. Kosugi, S., Hasebe, M., Tomita, M. & Yanagawa, H. Systematic identification of cell cycle-dependent yeast nucleocytoplasmic shuttling proteins by prediction of composite motifs. *Proc. Natl Acad. Sci. USA* **106**, 10171–10176 (2009).
8. Goldfarb, D. S., Corbett, A. H., Mason, D. A., Harreman, M. T. & Adam, S. A. Importin α: a multipurpose nuclear-transport receptor. *Trends Cell Biol.* **14**, 505–514 (2004).
9. Mao, Z. et al. SIRT6 promotes DNA repair under stress by activating PARP1. *Science* **332**, 1443–1446 (2011).
10. Rogakou, E. P., Pilch, D. R., Orr, A. H., Ivanova, V. S. & Bonner, W. M. DNA double-stranded breaks induce histone H2AX phosphorylation on serine 139. *J. Biol. Chem.* **273**, 5858–5868 (1998).
11. Stucki, M. et al. MDC1 directly binds phosphorylated histone H2AX to regulate cellular responses to DNA double-strand breaks. *Cell* **123**, 1213–1226 (2005).
12. Landry, J. P., Fei, Y. & Zhu, X. Simultaneous measurement of 10,000 protein–ligand affinity constants using microarray-based kinetic constant assays. *Assay Drug Dev. Technol.* **10**, 250–259 (2012).
13. Mao, Z., Seluanov, A., Jiang, Y. & Gorbunova, V. TRF2 is required for repair of nontelomeric DNA double-strand breaks by homologous recombination. *Proc. Natl Acad. Sci. USA* **104**, 13068–13073 (2007).
14. Li, Z. et al. Impaired DNA double-strand break repair contributes to the age-associated rise of genomic instability in humans. *Cell Death Differ.* **23**, 1765–1777 (2016).
15. Zhao, W. et al. Promotion of BRCA2-dependent homologous recombination by DSS1 via RPA targeting and DNA mimicry. *Mol. Cell* **59**, 176–187 (2015).
16. Prakash, R., Zhang, Y., Feng, W. & Jasin, M. Homologous recombination and human health: the roles of BRCA1, BRCA2, and associated proteins. *Cold Spring Harb. Perspect. Biol.* **7**, a016600 (2015).
17. Escribano-Díaz, C. et al. A cell cycle-dependent regulatory circuit composed of 53BP1-RIF1 and BRCA1-CtIP controls DNA repair pathway choice. *Mol. Cell* **49**, 872–883 (2013).
18. Caldecott, K. W.; KW. Mammalian single-strand break repair: mechanisms and links with chromatin. *DNA Repair (Amst.)* **6**, 443–453 (2007).
19. Hu, Y. et al. PARP1-driven poly-ADP-ribosylation regulates BRCA1 function in homologous recombination-mediated DNA repair. *Cancer Discov.* **4**, 1430–1447 (2014).
20. Rottenberg, S. et al. High sensitivity of BRCA1-deficient mammary tumors to the PARP inhibitor AZD2281 alone and in combination with platinum drugs. *Proc. Natl Acad. Sci. USA* **105**, 17079–17084 (2008).
21. Steffen, J. D. et al. Targeting PARP-1 allosteric regulation offers therapeutic potential against cancer. *Cancer Res.* **74**, 31–37 (2014).
22. Xie, S. et al. Timeless interacts with PARP-1 to promote homologous recombination repair. *Mol. Cell* **60**, 163–176 (2015).
23. Young, L. M. et al. TIMELESS forms a complex with PARP1 distinct from its complex with TIPIN and plays a role in the DNA damage response. *Cell Reports* **13**, 451–459 (2015).
24. Cerbinskaite, A., Mukhopadhyay, A., Plummer, E. R., Curtin, N. J. & Edmondson, R. J. Defective homologous recombination in human cancers. *Cancer Treat. Rev.* **38**, 89–100 (2012).
25. Chernikova, S. B., Game, J. C. & Brown, J. M. Inhibiting homologous recombination for cancer therapy. *Cancer Biol. Ther.* **13**, 61–68 (2012).
26. Hahn, W. C. et al. Creation of human tumour cells with defined genetic elements. *Nature* **400**, 464–468 (1999).
27. Margolis, S. R., Wilson, S. C. & Vance, R. E. Evolutionary origins of cGAS–STING signaling. *Trends Immunol.* **38**, 733–743 (2017).

Acknowledgements This project was supported by grants from the Chinese National Program on Key Basic Research Project (2017YFA0505900 to B.G. and 2015CB964800 to Z.M.) and the National Natural Science Foundation of China (81770006 and 81370108 to H.Liu, 91542111 and 31030028 to B.G., and 81622019 and 31570813 to Z.M.). H.Liu is sponsored by the Shanghai Pujiang Program (16PJ1408600) and by the Shanghai Medical and Health Services Outstanding Youth Talent Program (2017YQ078).

Author contributions H.Liu, Z.M. and B.G. conceived the project, designed the experiments and wrote the manuscript. H.Liu, H.Z. and X.W. performed most

© 2018 Springer Nature Limited. All rights reserved.

of the experiments and analysed the data. D.M., J.Wu and L.W. generated cGAS knockout cells and performed the co-IP experiments. Y.J. performed the animal experiments. Y.F. and C.Z. performed the label-free biomolecular interaction assays. R.T. performed the laser microirradiation experiments. P.J. conducted the mass spectrometry analyses. Q.Y. performed the multiple sequence alignment. F.Z. carried out analyses of gene expression and Kaplan–Meier survival plots. R.Z., S.L., H.Liang, Z.L., H.Y., J.C., P.W., T.T., W.P., Z.H., Z.X., X.H., J.Wang, H.Li, Y.Z., F.L. and D.Y. assisted with experiments and provided technical help. G.P., A.D., S.H.E.K. and C.C. provided comments and assisted with manuscript preparation.

Competing interests The authors declare no competing interests.

Additional information

Extended data is available for this paper at https://doi.org/10.1038/s41586-018-0629-6.
Supplementary information is available for this paper at https://doi.org/10.1038/s41586-018-0629-6.
Reprints and permissions information is available at http://www.nature.com/reprints.
Correspondence and requests for materials should be addressed to Z.M. or B.G.
Publisher's note: Springer Nature remains neutral with regard to jurisdictional claims in published maps and institutional affiliations.

© 2018 Springer Nature Limited. All rights reserved.

METHODS

Reagents and plasmids. Etoposide and camptothecin were purchased from Selleckchem. Olaparib and importazole were obtained from MedChem Express. The following antibodies were used: anti-H2AX (#7631), anti-phospho-H2AX (#9718), anti-cGAS (#31659), anti-PARP1 (#9532), anti-histone H3 (#4499), anti-BLK (#3262), anti-β-actin (#4970), anti-β-tubulin (9F3) (#2128), horseradish peroxidase (HRP)-conjugated anti-rabbit or anti-mouse IgG (all from Cell Signaling Technology); anti-haemagglutinin (HA) (H6908), anti-Flag (F3165) (both from Sigma-Aldrich). Anti-PAR monoclonal antibody (10H) (ALX-804-220-R100) was purchased from Enzo Life Science, anti-phosphotyrosine monoclonal antibody (4G10) from Millipore, anti-Timeless (ab72458) antibody from Abcam. The cDNA encoding human cGAS and human PARP1 was purchased from InvivoGen. The cDNA encoding human Timeless and human H2AX was purchased from Changsha Youbio Tech. The corresponding mutated constructs were generated by site-directed mutagenesis with the primers listed in Supplementary Table 1. The siRNA targeting human *CGAS* (sc-95512) and *PARP1* (sc-29437) as well as control scramble siRNA (sc-37007) were purchased from Santa Cruz Biotechnology. A Mission shRNA Human Gene Family Set (Kinases, SH0111) was obtained from Sigma-Aldrich, and shRNAs targeting protein tyrosine kinases were used in the screening assay. More detailed information is presented in Supplementary Table 2.

Cell culture. Human embryonic kidney epithelial cells (HEK293T; ATCC CRL-11268), human type II pneumocytes (A549; ATCC CRL-11268), human lung adenocarcinoma cells (formerly known as PC-14) (ECACC 90071810), mouse Lewis lung carcinoma cells (LLC) (ATCC CRL-1642) and U2OS cells (ATCC HTB-96) were cultured in Dulbecco's Modified Eagle's Medium (DMEM; Gibco) supplemented with 10% (v/v) heat-inactivated fetal bovine serum (FBS; Gibco), 1% (v/v) penicillin–streptomycin, 1 mM of sodium pyruvate, 2 mM of L-glutamine, 10 mM of HEPES buffer, and 50 μM of 2-mercaptoethanol (all from Gibco). HCA2-TERT cells (an immortalized foreskin fibroblast cell line), HCA2-H15c cells, HCA2-I7c cells and HCA2-I9a[28] cells were cultured in Minimum Essential Medium (MEM; Hyclone) supplemented with 10% (v/v) FBS (Gibco), 1% (v/v) penicillin–streptomycin (Gibco) and 1% MEM Nonessential Amino Acids (NEAA; Gibco). Cells were maintained at 37 °C in 5% CO_2. A LookOut Mycoplasma PCR Detection Kit (MP0035, Sigma-Aldrich) was applied for screening of mycoplasma contamination. All cells included in the study were confirmed to be free of mycoplasma.

Mice. *Cgas* knockout mice (stock number: 026554) were purchased from Jackson Laboratory. C57BL/6 mice were purchased from Shanghai Laboratory Animal Center. Mice were 6–12 weeks of age for all experiments, matched for age and sex, and kept under specific pathogen-free conditions at the Laboratory Animal Center of Tongji University. All experiments were approved by Tongji University School of Medicine Animal Care and Use Committee and were conducted in accordance with the National Institutes of Health Guidelines for the Care and Use of Laboratory Animals.

Isolation of human and mouse skin fibroblasts. Human skin fibroblasts were isolated from the skin tissue of human eyelids. Ethical approval was given by the Ethic Committees of Changzheng Hospital affilliated to The Second Military Medical University (Reference number: 2015yxy111). Informed consent was obtained from the 2 enrolled human subjects, both of whom were female and 26 years old. Skin tissues were collected from normal healthy female donors who were undergoing plastic surgery, and the acquired tissues were further processed for cell isolation within 24 h of the surgeries. The isolation protocols have previously been described[14]. In brief, the tissues were washed twice with PBS to remove the blood and immediately minced into tiny pieces, followed by digestion with collagenase type I (1 × PBS with 10 mg/ml BSA, 1 mg/ml collagenase type I and 2mM $CaCl_2$) for 90 min at 37 °C. Afterwards, the digested skin tissues were centrifuged and plated into 10-cm dishes in MEM (Hyclone) supplemented with 10% (v/v) FBS (Gibco), 1% (v/v) penicillin–streptomycin (Gibco) and 1% MEM NEAA (Gibco). Cells were maintained at 37 °C in 5% CO_2.

For the isolation of mouse skin fibroblasts, skin tissues were collected from age- and sex-matched wild-type and *Cgas* knockout mice. Female mice of 6–12 weeks of age were used for the isolation of primary cells. The isolation procedure is similar to that of the isolation of human skin fibroblast cells. The isolated cells were cultured in MEM (Hyclone) supplemented with 10% (v/v) FBS (Gibco), 1% (v/v) penicillin–streptomycin (Gibco), and 1% MEM NEAA (Gibco).

Generation of stable cell lines. The lentivirus technology was used for the knockdown of specific genes. In brief, HEK293T cells were transfected by means of Lipofectamine 2000 (Invitrogen) with pSPAX2, pMD2.G, and pLKO.1 containing shRNA targeting mouse *Cgas* (CCGGGCTGGTCTTGAACAAAGAG ATCTCGAGATCTCTTTGTT CAAGACCAGCTTTTTTG, TRCN0000178459, Sigma-Aldrich), human *H2AX* (CCGGCAACAAGAAG ACGCGAATCATCTCG AGATGATTCGCGTCTTCT TGTTGTTTTTG) or scrambled shRNA. Viral supernatants were collected 48 h after transfection and were concentrated using an SW-28 rotor. LLC cells or U2OS cells were infected with concentrated virus in the presence of polybrene (10 μg/ml). LLC cells that had been stably transfected with shRNA targeting *Cgas* or with scramble shRNA (control shRNA) were isolated by puromycin selection (5 μg/ml). PC-9 cells that stably expressed HA–cGAS (PC-9 HA–cGAS) were generated by transfection with pcDNA3.1-HA–cGAS by means of Lipofectamine 2000, followed by G418 selection (400 μg/ml).

Generation of cGAS knockout cells by the CRISPR–Cas9 system. LentiCRISPRv2 vectors were used to generate cGAS knockout cells[29]. HEK293T cells were transfected by means of Lipofectamine 2000 with pSPAX2, pMD2.G and LentiCRISPRv2 containing a guide RNA (gRNA) that targeted human *CGAS* (CACGCAGTTATCAAAGCAG). Lentiviruses were collected 48 h later and were applied to infect HCA2-H15c cells. Subsequently, selection with puromycin (2 μg/ml) was carried out. Clones derived from single cGAS knockout cells were obtained by serial dilutions in a 96-well plate and were confirmed by western blot.

DNA repair assays and fluorescence-activated cell sorting analysis. HCA2-H15c cells, I9a[28]cells and the HCA2-H15c cGAS knockout cells prepared in this study were seeded at 5×10^5 cells per 10-cm dish and were cultured for 48 h. The cells then were transfected with 5 μg of I-SceI (to induce DSBs), 15 ng of DsRed (as an internal reference to monitor transfection efficiency) and the indicated plasmids, siRNA or shRNA. DSB repair efficiency was analysed by fluorescence-activated cell sorting (FACS) on a BD FACSVerse (BD Biosciences). The efficiency of homologous recombination or of NHEJ was ascertained as the ratio of GFP^+ cells and $DsRed^+$ HCA2-H15c or I9a cells, respectively. At least 20,000 cells were counted. Transfection was accomplished via electroporation with a DT-130 program on a Lonza 4D machine. Experiments were performed in triplicate.

Analysis of efficiency of homologous recombination and NHEJ in primary cells. Skin fibroblast cells were seeded at a density of 3×10^5 cells. On day 2 after splitting, the I-SceI linearized homologous recombination (0.3 μg) or NHEJ (0.15 μg) reporter, together with pCMV-DsRed (0.015 μg), was introduced to fibroblasts by electroporation using the kit (V4XP-2032) on a Lonza 4D machine (Cologne, Germany). On day 3 after transfection, cells were collected for analysis of DNA repair efficiency on FACSverse (BD Biosciences).

FACS analysis of the cell cycle. For analysis of cell-cycle distribution, cells were collected 48 h after splitting and were fixed in cold 70% ethanol (−20 °C). After fixation at 4 °C for at least 16 h, cells were stained with propidium iodide, and at least 10,000 cells were analysed by FACS. Data subsequently were analysed with FlowJo software.

EdU assay. Cells were seeded at a density of 5×10^5 cells per plate and were maintained in culture for 48 h. Cells then were transfected with 5 μg of pcDNA3.1-HA plasmid (HA) or pcDNA3.1-HA–cGAS plasmid (HA–cGAS). After 48 h, cells were incubated with 10 μM EdU for 2 h and then were analysed on a FACSverse device using a Click-iT EdU Assay Kit from Invitrogen.

Cell proliferation assay. Cell numbers were assessed indirectly using an MTT Cell Proliferation Kit I (Sigma-Aldrich).

FACS analysis of cell apoptosis. Apoptosis was detected with a fluorescein isothiocyanate (FITC) Annexin V Apoptosis Detection Kit I (BD Biosciences), according to the manufacturer's instructions. In brief, approximately 10^6 cells that had been treated as indicated were washed twice with PBS and incubated in 200 μl of binding buffer containing 5 μl of FITC-annexin V in the dark for 5 min at room temperature. Subsequently, 10 μl of propidium iodide was added, and samples were analysed with a flow cytometer (BD Accuri C6).

Comet assay. Cells were seeded and maintained for 48 h and then were collected and resuspended in phosphate-buffered saline (PBS) at a concentration of 3×10^5 cells per ml. The comet assay then was performed according to the manufacturer's instructions (4250-050-K; Trevigen). DNA damage was measured in terms of tail moments using cometscore software (casplab_1.2.3b2).

In vivo tumour growth. C57BL/6 mice were purchased from the Shanghai Laboratory Animal Center. All mice were bred under specific pathogen-free conditions at the Laboratory Animal Center of Tongji University. Male C57BL/6 mice aged 6 to 8 weeks were divided randomly into cages upon arrival and received 1×10^6 control shRNA or *Cgas* shRNA LLC cells in DMEM by subcutaneous injection. Mice were killed 4 weeks post-transplantation, and tumours were collected for further analysis. The sample size was determined empirically, based on experience with similar assays and from sample sizes generally used by other investigators. The experiments were not performed blind. All animal study protocols were reviewed and approved by the review boards of Tongji University School of Medicine Animal Care and Use Committee (ethical approval reference number K17-081) and were conducted in accordance with the National Institutes of Health Guidelines for the Care and Use of Laboratory Animals. The maximal tumour diameter of 20 mm was permitted by Tongji University School of Medicine Animal Care and Use Committee. None of the experiments in this study exceeded the limit.

Clonogenic assay. Cells were serially diluted and plated. After 2 weeks of culture in an incubator, cells were stained with Coomassie reagent (ratio, methanol:acetic acid:Coomassie:H_2O = 50:10:0.25:40) for 3 h. Stained cells were washed with distilled water, and colonies with at least 50 cells were counted. Survival rates were calculated as the ratio of the number of colonies to the number of seeded cells.

© 2018 Springer Nature Limited. All rights reserved.

Anchorage-independent growth and tumour formation. Growth of cells in soft agar was performed as previously described[26]. In brief, one million exponentially growing human skin fibroblast cells from two different donors were electroporated with vectors encoding SV40 large tumour antigen (LT) (5 μg), H-Ras V12 (Ras) (5 μg) and TERT (5 μg) together with pcDNA3.1-HA (HA) (5 μg) or HA–cGAS (5 μg) on a Lonza 4D machine. After transfection, cells were seeded and allowed to recover for 24 h. Then 10^5 cells were seeded into 0.4% Noble agar and colonies were photographed after 5 weeks of growth at 200× original magnification. Cultures were coded and the colony numbers were scored in a blinded fashion by a second observer.

Immunofluorescence assay. Cells were seeded on coverslips in 24-well plates and were treated with etoposide, camptothecin or H_2O_2 at the indicated concentrations for the indicated times. Stimulated cells were fixed with 4% paraformaldehyde (PFA) in PBS for 20 min at room temperature. Cells then were blocked and permeabilized for 30 min in blocking buffer, comprising 2% bovine serum albumin (BSA) and 0.2% Triton X-100 in PBS. Cells were incubated with primary and secondary antibodies diluted in PBS with 2% BSA for 1 h (primary antibody) or for 30 min (secondary antibody) at room temperature. The following primary antibodies were applied: anti-HA-tag rabbit monoclonal antibody (C29F4, Cell Signaling Technology, Cat#3724), anti-cGAS rabbit monoclonal antibody (D1D3G, Cell Signaling Technology, Cat#15102), anti-lamin A/C monoclonal antibody (E-1, Santa Cruz Biotechnology, Cat#sc-376248), and anti-γH2AX (phospho-Ser139) antibody (9F3, Abcam, Cat#ab26350). Corresponding Alexa Fluor 488 anti-rabbit or Alexa Fluor 555 anti-mouse antibodies (Thermo Fisher Scientific) were used as secondary antibody. Images were acquired using a Leica TCS SP8 confocal laser microscopy system (Leica Microsystems). Tumours grown from implanted LLC cells were fixed with 4% PFA, and continuous 5-μm sections were acquired for immunofluorescence analyses. Quantification of cGAS nuclear translocation and γH2AX-positive cells was performed by microscopy under blinded conditions. Cells with nuclear fluorescence only or with nuclear fluorescence much stronger than cytoplasmic fluorescence are calculated as nuclear translocation of cGAS. For quantification of nuclear translocation of cGAS, at least 100 transfected cells were counted in each independent experiment and at least 3 independent experiments were performed. For quantification of the percentage of γH2AX-foci-positive cells, we included at least 10 noncontinuous sections from each tumour formed in C57BL/6 mice that had been injected with LLC cells that stably expressed scrambled shRNA or shRNA targeting *Cgas*. At least 10 microscopic fields with more than 500 cells were calculated on each section.

Immunoprecipitation and western blot. Cells were lysed in lysis buffer (50 mM of Tris (pH 7.4), 150 mM of NaCl, 1% Triton X-100, 1 mM of EDTA (pH 8.0)) supplemented with protease cocktail (P8340, Sigma-Aldrich), 1 mM of PMSF, 1 mM of Na_3VO_4 and 1 mM of NaF. Cellular debris was cleared by centrifugation at 13,000 rpm for 15 min. For immunoprecipitation, cell lysates were incubated with anti-Flag M2 Affinity Gel (A2220, Sigma-Aldrich) and monoclonal anti-HA agarose (A2095, Sigma-Aldrich) at 4 °C overnight. Streptavidin Sepharose Bead Conjugate (#3419, Cell Signaling Technology) was used for immunoprecipitation of biotinylated PAR. For immunoblotting, cell lysates or precipitates in 1× sodium dodecyl sulfate (SDS) protein sample buffer were denatured at 95 °C for 8 min and then were resolved by electrophoresis through a 4% to 15% SDS-polyacrylamide gel. Separated proteins were transferred onto polyvinylidene difluoride membranes and were incubated with the prespecified antibodies at the indicated dilutions. An enhanced chemiluminescence reagent (Thermo Fisher Scientific) was applied for immunoblotting.

Cell fractionation. Cells were treated with etoposide for the indicated times and were lysed by sonication in 300 μl of hypotonic buffer (10 mM of HEPES (pH 7.6), 1.5 mM of $MgCl_2$, 10 mM of KCl and 1 mM of EDTA) supplemented with 10 mM of nicotinamide (NAM), 1 mM of PMSF, 1 mM of Na_3VO_4 and 1 mM of NaF. Following centrifugation for 5 min at 3,000 rpm and 4 °C, the supernatants were collected as the cytoplasmic fraction. Pellets were washed twice with hypotonic buffer and then were lysed by vortexing in 100 μl of high-salt buffer (10 mM of HEPES (pH 7.6), 500 mM of NaCl, 1.5 mM of $MgCl_2$ and 1 mM of EDTA) supplemented with 10 mM of NAM, 1 mM of PMSF, 1 mM of Na_3VO_4 and 1 mM of NaF. After incubation on ice for 20 min, the lysates were centrifuged at 13,000 rpm for 15 min to remove the nuclear debris. The supernatants then were collected as the nuclear fraction.

Real-time quantitative PCR with reverse transcription. Total RNA was isolated with TRIzol reagent, as described by the manufacturer (Invitrogen). The RNA (1 μg) was applied to generate cDNA by means of an iScript cDNA Synthesis Kit (Bio-Rad), and real-time quantitative PCR was performed using Power SYBR Green Master Mix (Applied Biosystems) in an LC480 thermocycler (Roche). The average threshold cycle (C_t) of quadruplicate reactions was determined, and amplification was analysed by the $\Delta\Delta C_t$ method. Gene expression was normalized to that of *GAPDH*. Real-time quantitative PCR with reverse transcription data were representative of at least three independent experiments, with two technical replicates per experiment. Primer sequences used to amplify human *IFNB1*, *BLK* and *GAPDH* were as follows: human *IFNB1* forward: ATGACCAACAAGTGTCTCCTCC, human *IFNB1* reverse: GGAATCCAAGCAAGTTGTAGCTC; human *BLK* forward: AGGAAAAGCCGATCAAAGAGAAG, human *BLK* reverse: CCACCAC GAAATGCTTGTCT; human *GAPDH* forward: ACAACTTTGG TATCGTGGAAGG, human *GAPDH* reverse: GCCATCACGCCACAGTTTC.

Gene expression analysis. The RNA sequencing data for lung adenocarcinoma were obtained from the TCGA project (http://cancergenome.nih.gov) and from firebrowse (http://firebrowse.org). Differential gene expression was analysed as previously described[30].

Kaplan–Meier survival analysis. Gene expression and survival data of patients with non-small cell lung cancer were accessed using the 2015 version of the Kaplan–Meier Plotter (http://kmplot.com/). Kaplan–Meier survival analysis was carried out using SPSS (IBM).

Multiple sequence alignment of the representative sequences of cGAS homologues. *Homo sapiens* cGAS homologues from several species were downloaded from the National Center for Biotechnology Information (NCBI) database (https://www.ncbi.nlm.nih.gov/protein). Multiple sequence alignment was performed using the online tool Clustal Omega (http://www.ebi.ac.uk/Tools/msa/clustalo/) and was rendered with ESPript 3.0 (http://espript.ibcp.fr/ESPript/cgi-bin/ESPript.cgi)[31].

Binding kinetics of cGAS to PAR, the phosphopeptide and the peptide. Label-free binding kinetics were measured with a microarray-compatible optical biosensor oblique-incidence reflectivity difference scanning microscope; this instrument enables detection of tens of thousands of biomolecular binding reactions in a single experiment[12]. Each microarray experiment consisted of PAR (4336-100-02, Trevigen), the phosphopeptide and the peptide, with each printed in triplicate on an epoxy-functionalized glass slide (CapitalBio) at concentrations of 10 μM, 9.6 mM and 10 mM, respectively. Six identical microarrays were fabricated on each glass slide. The printed glass slide then was assembled into a fluidic cartridge, with each microarray housed in a separate chamber. Before the binding reaction proceeded, the slide was washed in situ with a flow of 1× PBS to remove excess unbound samples. Subsequently, blocking was performed with 7,600 nM of BSA (Sigma-Aldrich) in 1× PBS for 30 min. PBS (1×) was passed through a reaction chamber at a flow rate of 0.01 ml/min for 9 min to acquire a baseline reading. The PBS then was quickly replaced with GST-labelled cGAS solution at a flow rate of 2 ml/min. The flow rate then was reduced to 0.01 ml/min, and the microarray was incubated in the cGAS solution for 31 min. This constituted the association phase of the reaction. The cGAS solution was then quickly replaced with 1× PBS at a flow rate of 2 ml/min, and the flow rate then was reduced to 0.01 ml/min to allow dissociation of cGAS for 40 min. This was the dissociation phase of the reaction. By repeating the cGAS binding reactions at concentrations of 368 nM, 184 nM and 92 nM on separate fresh microarrays, the binding curves of PAR, synthesized H2AX C-terminus peptide (^{123}TVGPKAPSGGKKATQASQEY^{142}) and the corresponding phosphopeptide (^{123}TVGPKAPSGGKKATQA(p-S)QEY^{142}; 'p-S' indicates phosphorylated serine)[11] with cGAS were determined at 3 concentrations. The binding curves of the GST tag alone (concentration, 92 nM) on the printed microarray were determined as the control. Reaction kinetic rate constants were estimated by fitting the binding curves globally using a 1-to-1 Langmuir reaction model[12].

Recombinant GST–cGAS purification and GST pull-down assay. Recombinant GST–cGAS was purified in collaboration with Novoprotein Scientific. Human *CGAS* cDNA was subcloned into a pGEX-4T-1 vector. BL21 (DE3) competent *Escherichia coli* bacteria then were transfected with this construct. Bacteria were grown in Luria–Bertani liquid medium to an optical density (OD) at 600 nm (OD_{600}) of approximately 0.8. Cells then were induced with isopropyl β-D-1-thiogalactopyranoside (IPTG, 0.1 mM) overnight at 16 °C. Recombinant GST–cGAS was purified from bacterial lysates using a GSTrap FF column (GE Healthcare). The concentration of GST–cGAS protein was measured with a Pierce BCA Protein Assay Kit (Thermo Fisher Scientific). Endotoxin in the purified protein was less than 1,000 EU/mg. For the GST pull-down assay, GST or GST–cGAS together with recombinant PARP1 protein (P0996, Sigma-Aldrich) was immunoprecipitated with Glutathione Sepharose 4B Resin (GE Healthcare).

Generation of phospho-cGAS Y215 antibody. Rabbit polyclonal antibody was raised against cGAS phosphorylated at Y215 (p-cGAS Y215) in collaboration with Abclonal Biotech. In brief, 2 rabbits were immunized with a mixture of peptide c(KLH)^{210}NTGSY(p-Y)EH^{217} and c(KLH)^{212}GSY(p-Y)EHVK^{219} (in which 'c(KLH)' indicates keyhole limpet haemocyanin fused through cysteine, and 'p-Y' indicates phosphorylated tyrosine) at a ratio of 1:1. The nonphosphorylated peptide c(KLH)^{210}NTGSYYEHVK^{219} was used for antibody purification and detection.

Laser microirradiation. A Leica DM6500 confocal microscopy 405-nm laser diode system was used for microirradiation. U2OS cells were kept in a 37-°C heated chamber controlled with Oko-Touch (Okolab) and presensitized with 100 μM of 8-methoxypsoralen in medium for 2 to 5 min. Living cells were visualized with high-throughput microscopy equipped with an ultraviolet-light-transmitting

© 2018 Springer Nature Limited. All rights reserved.

HC PL APO CS2 63×/1.40 oil objective. DNA damage was induced by microirradiation with a 50-mW, 405-nm laser diode and fluorescence recovery after photobleaching model was used. The final output power of the laser when passed through the lens was 1 mW, and the total power applied at the dots was calculated at indicated irradiation times. Laser light was passed through a 63× oil immersion objective lens. At least 15 cells were irradiated in each experiment. Leica LAS AF software (LAS AF3.1.0) was used for acquisition of images, and LAS X was used for image analysis.

Chromatin immunoprecipitation. NHEJ-I7c cells were transfected with 5 μg of HA–cGAS vector and 5 μg of I-SceI vector. Cells were collected at prespecified time points after transfection (0, 4, 8 and 24 h), and a chromatin immunoprecipitation assay was performed, as previously described[9]. The recruitment of cGAS to the site of I-SceI was determined by quantitative PCR analysis in which the region from 7 to 315 nucleotides downstream of the I-SceI site was amplified. The primers used for this step were 5′-CCTGAAGATTTGGGGGATTGTGCTTC-3′ and 5′-CTTGGAAACACCCATGTTGAAATATC-3′.

RPA2 and RAD51 analysis. Cells were seeded at a density of 5×10^5 cells per plate and were maintained for 48 h. Cells then were transfected with 5 μg of pcDNA3.1-HA plasmid or 5 μg of pcDNA3.1-HA–cGAS plasmid. Forty-eight hours later, cells were split and were either exposed to X-rays (dose of 8 Gy) or treated for 4 h with etoposide (100 μg ml^{-1}) or camptothecin (1 μM). After treatment, cells were kept at rest for the indicated times and then were fixed with 4% PFA and stained with anti-RPA2 antibody (Abcam; ab2175) or anti-RAD51 antibody (Abcam; ab176458). The frequencies of RAD51- and RPA2-positive cells (that is, >5 nuclear foci per cell) were determined at the indicated time points.

Statistical analysis. Data are expressed as the mean ± s.e.m. unless indicated otherwise. GraphPad Prism 7 software (GraphPad) was applied for statistical analysis. For all quantitative measurements, a normal distribution was assumed. For comparisons between 2 groups, the Student's *t* test (unpaired and 2-tailed) was applied. For comparisons among multiple groups, one-way ANOVA was used. Statistical evaluations of colony formation and of comet assay results were carried out with the Mann–Whitney *U*-test. No method was undertaken to calculate statistical power and corresponding sample size. Instead, sample size was determined empirically on the basis of experience with similar assays and from sample sizes generally used by other investigators. For all analyses, statistical significance was defined as $P < 0.05$.

Randomization, blinding and cell line identification. The experiments were not randomized. The investigators were blinded during data collection and analysis where possible. This included immunofluorescence assay data collection for the quantification of cGAS nuclear translocation and γH2AX positive cells in the tumours formed from transplanted cells, as well as microirradiation assay showing PARP1 and cGAS recruitment to DNA damage sites.

No commonly misidentified cell lines were used in this study. However, A549 and PC-9 cell lines were authenticated using short tandem repeat analysis as described in 2012 in ANSI Standard (ASN-0002) by the ATCC Standards Development Organization and in ref.32.

Reporting summary. Further information on research design is available in the Nature Research Reporting Summary linked to this paper.

Data availability

The authors declare that data supporting the findings of this study are available within the manuscript and Supplementary Information.

28. Mao, Z., Bozzella, M., Seluanov, A. & Gorbunova, V. Comparison of nonhomologous end joining and homologous recombination in human cells. *DNA Repair (Amst.)* **7**, 1765–1771 (2008).
29. Sanjana, N. E., Shalem, O. & Zhang, F. Improved vectors and genome-wide libraries for CRISPR screening. *Nat. Methods* **11**, 783–784 (2014).
30. Huang, T. et al. G9A promotes tumor cell growth and invasion by silencing CASP1 in non-small-cell lung cancer cells. *Cell Death Dis.* **8**, e2726 (2017).
31. Robert, X. & Gouet, P. Deciphering key features in protein structures with the new ENDscript server. *Nucleic Acids Res.* **42**, W320–W324 (2014).
32. Capes-Davies, A. et al. Match criteria for human cell line authentication: where do we draw the line? *Int. J. Cancer* **132**, 2510–2519 (2013).

© 2018 Springer Nature Limited. All rights reserved.

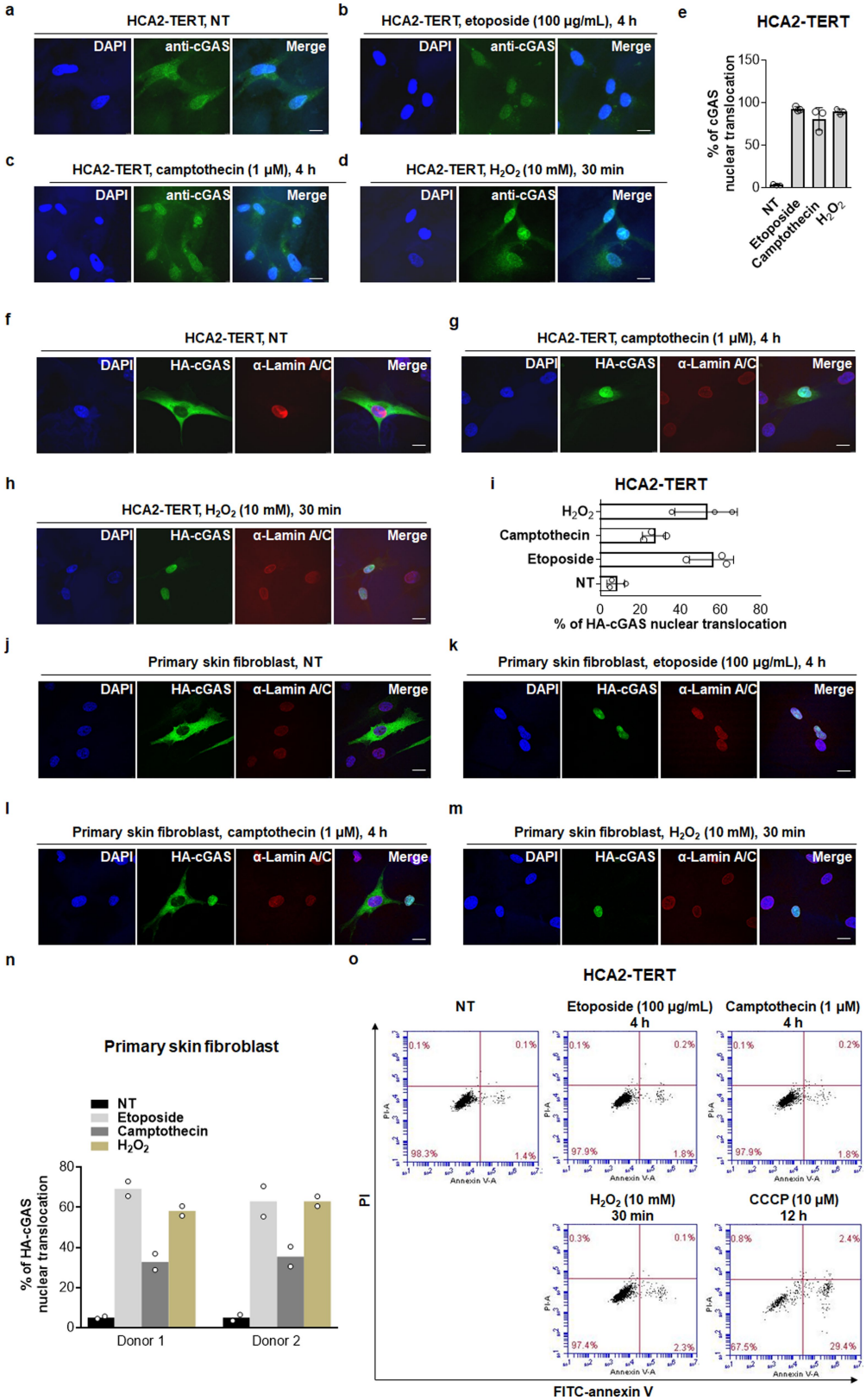

Extended Data Fig. 1 | See next page for caption.

© 2018 Springer Nature Limited. All rights reserved.

Extended Data Fig. 1 | cGAS translocates to the nucleus in non-apoptotic cells with intact nuclear membranes. a–e, Immunofluorescence results depicting localization of endogenous cGAS (anti-cGAS) in HCA2-TERT cells, an TERT-immortalized human fibroblast line. Cells were untreated (NT) (**a**) or exposed to etoposide (100 μg ml^{-1}) (**b**), camptothecin (1 μM) (**c**) or H_2O_2 (10 mM) (**d**) for the indicated times. Data are representative of $n = 3$ independent experiments. Quantitative data are shown in **e**. At least 100 cells were counted in each experiment. Data are mean ± s.e.m. of $n = 3$ independent experiments. **f–i**, Results of immunofluorescence analysis showing localization of overexpressed HA–cGAS in human HCA2-TERT fibroblasts that were untreated (NT) (**f**) or exposed to camptothecin (1 μM) (**g**) or H_2O_2 (10 mM) (**h**) for the indicated times. Data are representative of $n = 3$ independent experiments. Quantitative data are shown in **i**. At least 100 transfected cells were counted in each experiment. Data are mean ± s.e.m. of $n = 3$ independent experiments. **j–n**, Representative immunofluorescence analysis showing the localization of HA–cGAS (anti-HA, green) in transfected primary human skin fibroblasts from one healthy donor that were untreated (NT) (**j**) or exposed to etoposide (100 μg ml^{-1}) (**k**), camptothecin (1 μM) (**l**) or H_2O_2 (10 mM) (**m**) for the indicated times. Data represent $n = 2$ independent experiments. The quantification of nuclear translocation of cGAS in primary skin fibroblasts from two donors in response to indicated DNA-damaging agents are shown in **n**. At least 100 transfected cells were counted in each experiment. **o**, Representative FACS results depicting apoptosis of human fibroblast HCA2-TERT cells treated with etoposide (100 μg ml^{-1}), camptothecin (1 μM), H_2O_2 (10 mM) or carbonyl cyanide 3-chlorophenylhydrazone (CCCP) (10 μM) for the indicated times. Data represent $n = 3$ independent experiments. Scale bar, 5 μm.

© 2018 Springer Nature Limited. All rights reserved.

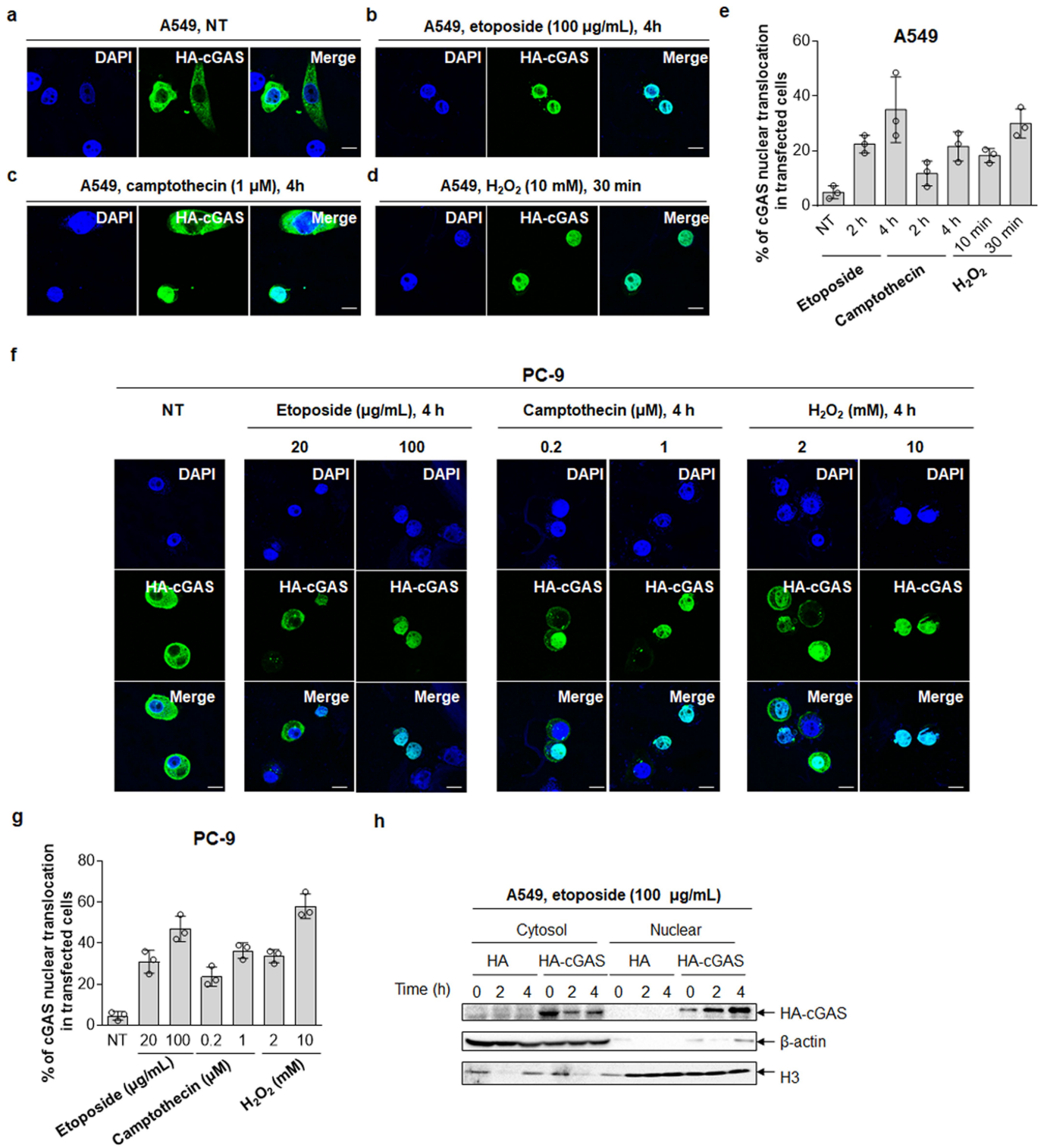

Extended Data Fig. 2 | DNA damage induces nuclear translocation of cGAS in lung cancer cells. a–e, Immunofluorescence assay results showing localization of transfected HA–cGAS (anti-HA, green) in A549 cells that were untreated (**a**) or treated with etoposide (100 μg ml^{-1}) (**b**), camptothecin (1 μM) (**c**) or H_2O_2 (10 mM) (**d**) for the indicated times. Data represent $n = 3$ independent experiments. Quantitative data are depicted in **e**. At least 100 transfected cells were counted in each experiment. Data are expressed as mean ± s.e.m. Scale bar, 5 μm. **f**, **g**, Immunofluorescence assay results showing localization of transfected HA–cGAS (anti-HA, green) in PC-9 cells that were untreated (NT) or treated with indicated concentrations of etoposide, camptothecin or H_2O_2 for the indicated times (**f**). Data represent $n = 3$ independent experiments. Quantitative data were depicted in **g**. At least 100 transfected cells were counted in each experiment. Data are expressed as mean ± s.e.m. Scale bar, 5 μm. **h**, Immunoblot results showing cytoplasmic and nuclear fractions of A549 cells transfected with pcDNA3.1-HA (HA) or pcDNA3.1-HA–cGAS (HA–cGAS) for 48 h and then treated with etoposide (100 μg ml^{-1}) for the indicated times. Data are representative of $n = 2$ independent experiments. For gel source data, see Supplementary Fig. 1.

© 2018 Springer Nature Limited. All rights reserved.

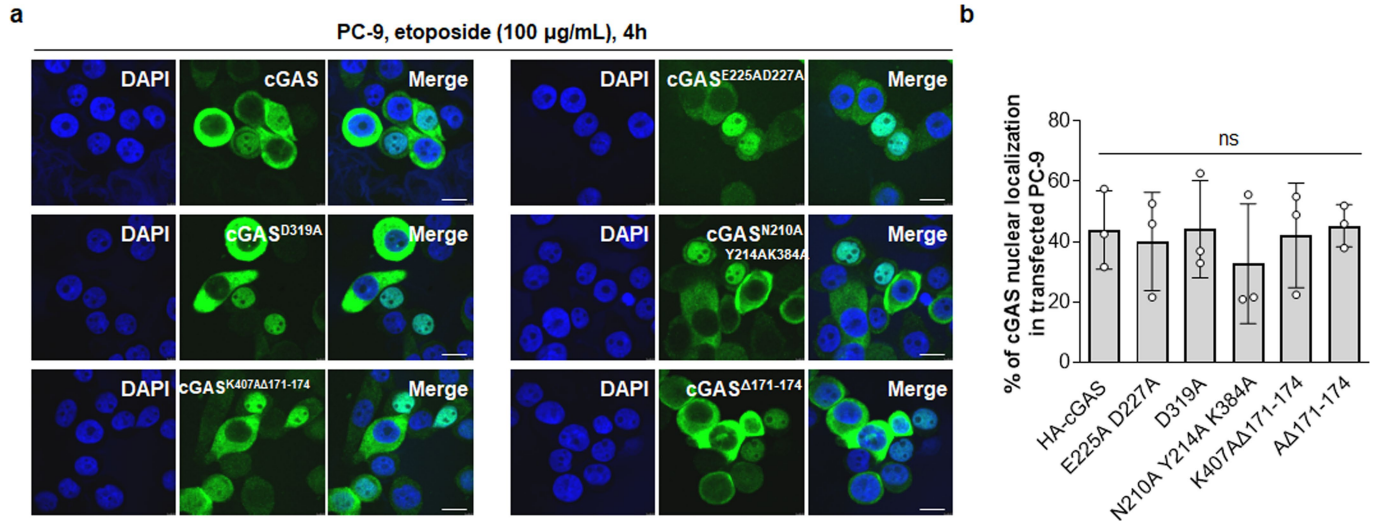

Extended Data Fig. 3 | cGAS translocates to the nucleus in response to DNA damage independently of its DNA-binding ability or enzymatic activity. a, Immunofluorescence assay results showing localization of transfected HA–cGAS and corresponding mutants (anti-HA, green) in PC-9 cells exposed to etoposide (100 μg ml^{-1}) for 4 h. Data represent $n = 3$ independent experiments. Quantitative data are depicted in **b**. At least 100 transfected cells were counted in each experiment. Data are expressed as mean ± s.e.m. of $n = 3$ independent experiments. One-way ANOVA was used for statistical analysis. NS, not significant.

© 2018 Springer Nature Limited. All rights reserved.

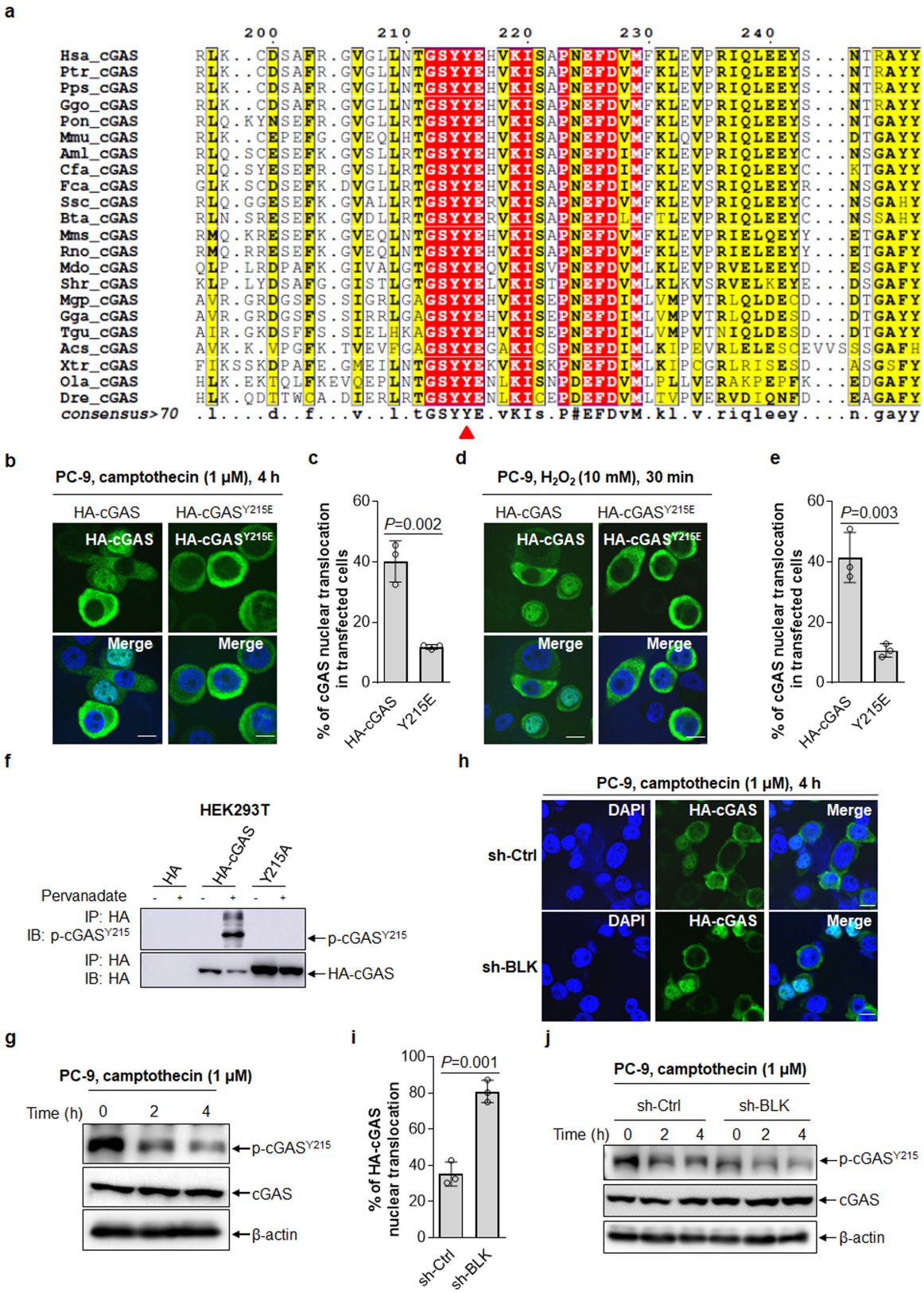

Extended Data Fig. 4 | See next page for caption.

© 2018 Springer Nature Limited. All rights reserved.

Extended Data Fig. 4 | BLK-mediated phosphorylation of cGAS at Y215 regulates the nuclear translocation of cGAS in response to DNA damage. a, Alignment of primary sequences of *H. sapiens* cGAS and its homologues in 22 species: *H. sapiens* (Hsa), *Pan troglodytes* (Ptr), *Pan paniscus* (Pps), *Gorilla gorilla* (Ggo), *Pongo abelii* (Pon), *Macaca mulatta* (Mmu), *Ailuropoda melanoleuca* (Aml), *Canis familiaris* (Cfa), *Felis catus* (Fca), *Sus scrofa* (Ssc), *Bos taurus* (Bta), *Mus musculus* (Mms), *Rattus norvegicus* (Rno), *Monodelphis domestica* (Mdo), *Sarcophilus harrisii* (Shr), *Meleagris gallopavo* (Mgp), *Gallus gallus* (Gga), *Taeniopygia guttata* (Tgu), *Anolis carolinensis* (Acs), *Xenopus tropicalis* (Xtr), *Oryzias latipes* (Ola) and *Danio rerio* (Dre). Consensus sequences (similarity score, >0.7) are listed at the bottom of the column; conserved amino acids are highlighted in yellow, and absolutely conserved amino acids are highlighted in red. The filled triangle indicates the conserved Y215. The primary sequence numbers of *H. sapiens* cGAS are labelled at the top of the line. **b**–**e**, Immunofluorescence assay results showing the localization of HA–cGAS and HA–cGAS(Y215E) (anti-HA, green) in PC-9 cells exposed to camptothecin (1 μM) for 4 h (**b**) or to H_2O_2 (10 mM) for 30 min (**d**). Data represent $n = 3$ independent experiments. Quantitative data for **b** and **d** are depicted in **c** and **e**, respectively. Data are expressed as mean ± s.e.m. of $n = 3$ independent experiments. **f**, Immunoblot results of anti-HA immunoprecipitates from HEK293T cells transfected with HA–cGAS or the HA–cGAS(Y215A) mutant in the absence or presence of pervanadate for 30 min, followed by cell collection. Data represent $n = 3$ independent experiments. **g**, Immunoblot of lysates from PC-9 cells that had been stimulated with camptothecin (1 μM) for the indicated times. Data represent $n = 3$ independent experiments. **h**, **i**, Results of immunofluorescence analysis showing localization of HA–cGAS (anti-HA, green) in PC-9 HA–cGAS cells transfected with control shRNA (sh-Ctrl) or with shRNA targeting *BLK* (sh-BLK) and then exposed to camptothecin (1 μM) for 4 h (**h**). Nuclei were stained with DAPI (blue). Data represent $n = 3$ independent experiments. Quantitative data are shown in **i**. At least 100 transfected cells were counted in each experiment. Data are expressed as mean ± s.e.m. of $n = 3$ independent experiments. **j**, Immunoblot results of lysates from PC-9 HA–cGAS cells that had been transfected with either control shRNA or with shRNA targeting *BLK* and then exposed to camptothecin (1 μM) for 4 h. Data represent 3 independent experiments. Student's *t* tests (unpaired and two-tailed) were used for statistical analysis (**c**, **e**, **i**). Scale bar, 5 μm. For gel source data, see Supplementary Fig. 1.

© 2018 Springer Nature Limited. All rights reserved.

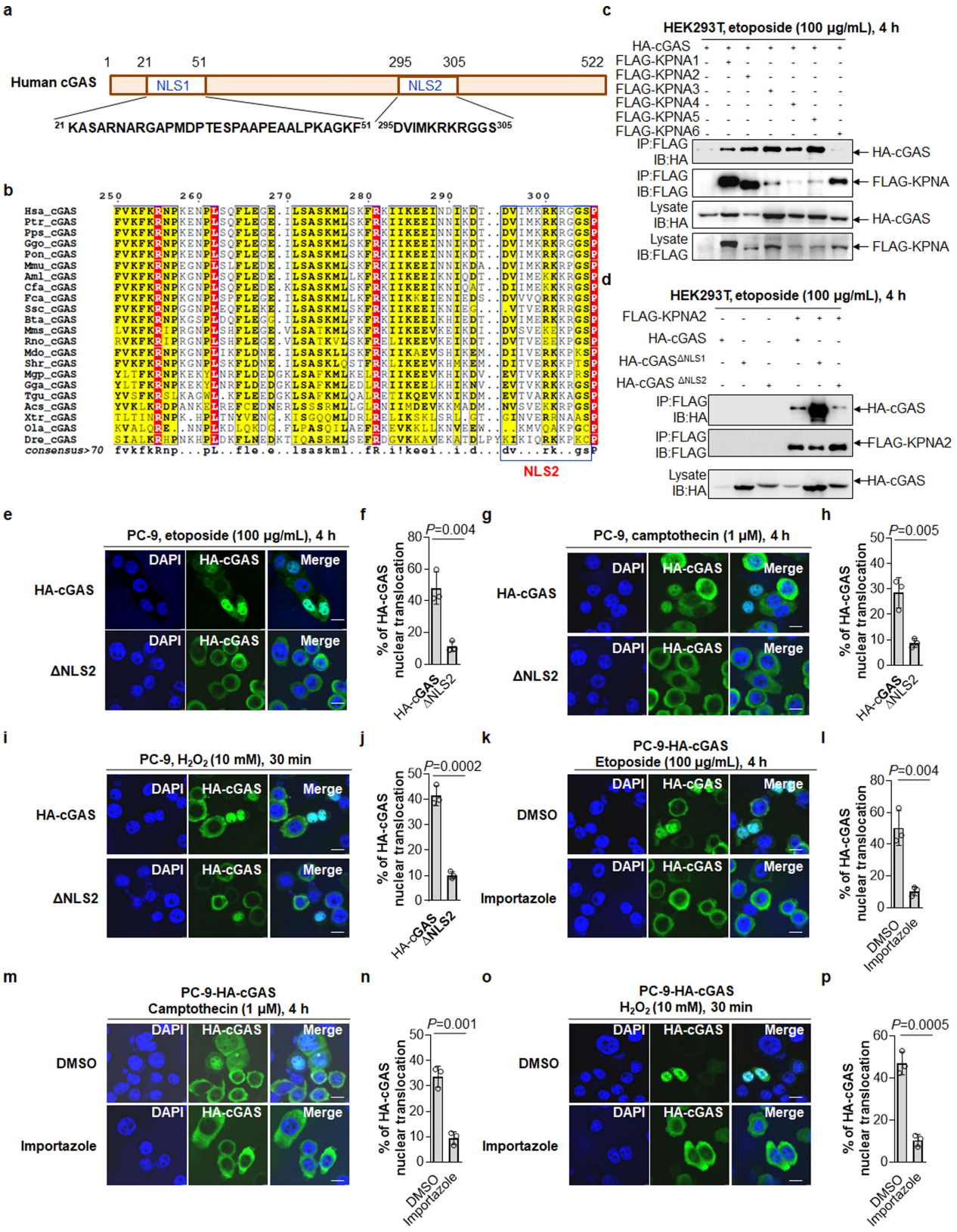

Extended Data Fig. 5 | See next page for caption.

© 2018 Springer Nature Limited. All rights reserved.

Extended Data Fig. 5 | cGAS interacts with importin-α and translocates to the nucleus in a manner dependent on importin-α. a, Diagram showing the location and sequence of two predicted nuclear localization sequences of cGAS. **b**, Alignment of primary sequences of *H. sapiens* cGAS and its homologues in 22 species were performed as indicated in Extended Data Fig. 4a. The conserved NLS2 sequences are shown in the rectangular box. **c**, Immunoblot results of cell lysates and anti-Flag immunoprecipitates from HEK293T cells that had been transfected with HA–cGAS and the indicated Flag–KPNA and then exposed to etoposide (100 μg ml^{-1}) for 4 h. Data represent $n = 3$ independent experiments. **d**, Immunoblot findings of cell lysates or anti-Flag immunoprecipitates from HEK293T cells that had been transfected with Flag–KPNA2 and HA–cGAS or the cGAS nuclear localization sequence deletion mutants (HA–cGAS(ΔNLS1) and HA–cGAS(ΔNLS2)) and exposed to etoposide (100 μg ml^{-1}) for 4 h. Data represent $n = 2$ independent experiments. **e–j**, Immunofluorescence findings showing the localization of transfected HA–cGAS or HA–cGAS(ΔNLS2) (anti-HA, green) in PC-9 cells treated with etoposide (100 μg ml^{-1}) (**e**) or camptothecin (1 μM) (**g**) for 4 h or with H_2O_2 (10 mM) for 30 min (**i**). Nuclei were stained with DAPI (blue). Data represent $n = 3$ independent experiments. Quantitative data for **e**, **g**, **i** are shown in **f**, **h**, **j**, respectively, and are expressed as mean ± s.e.m. of $n = 3$ independent experiments. **k–p**, Representative immunofluorescence of HA–cGAS (anti-HA, green) in PC-9 HA–cGAS cells treated with etoposide (100 μg ml^{-1}) (**k**) or camptothecin (1 μM) (**m**) for 4 h or with H_2O_2 (10 mM) for 30 min (**o**) in the presence of dimethyl sulfoxide (DMSO; mock treatment) or importazole (1 μM). Nuclei were stained with DAPI (blue). Data represent $n = 3$ independent experiments. Quantitative data for **k**, **m**, **o** are shown in **l**, **n**, **p**, respectively, and are expressed as mean ± s.e.m. of $n = 3$ independent experiments. At least 100 transfected cells were counted in each experiment. Student's *t* tests (unpaired and two-tailed) were used for statistical analysis (**f**, **h**, **j**, **l**, **n**, **p**). Scale bar, 5 μm. For gel source data, see Supplementary Fig. 1.

© 2018 Springer Nature Limited. All rights reserved.

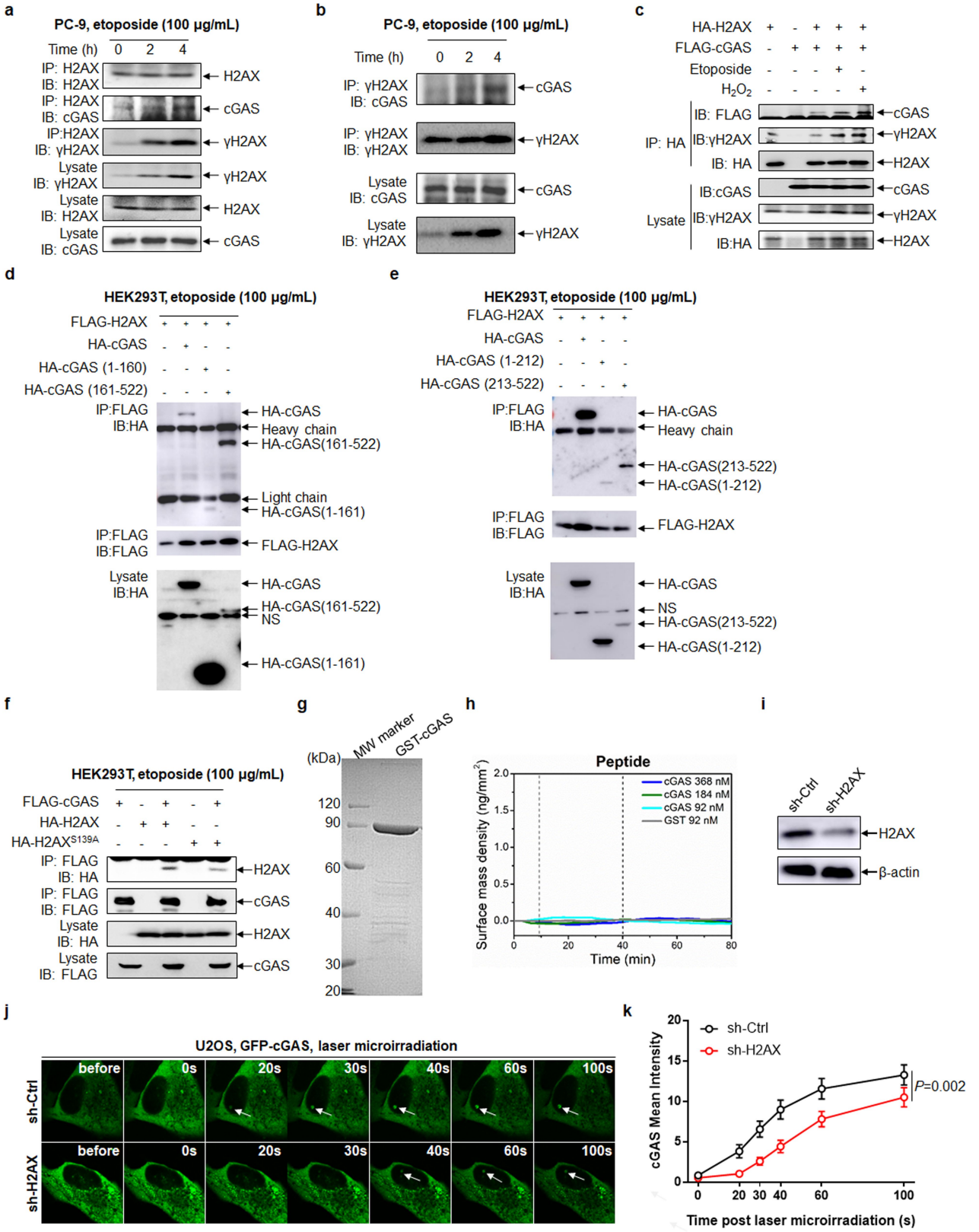

Extended Data Fig. 6 | See next page for caption.

© 2018 Springer Nature Limited. All rights reserved.

Extended Data Fig. 6 | cGAS interacts with γH2AX directly. **a**, **b**, Immunoblot of cell lysates and anti-H2AX (**a**) or anti-γH2AX (**b**) immunoprecipitates from PC-9 cells treated with etoposide (100 μg ml^{-1}) for the indicated times. Data represent $n = 3$ independent experiments. **c**, Immunoblot of cell lysates or anti-HA immunoprecipitates from HEK293T cells transfected with Flag–cGAS and HA–H2AX in the absence or presence of etoposide (100 μg ml^{-1}) for 4 h or H_2O_2 (10 mM) for 30 min. Data represent $n = 3$ independent experiments. **d**, **e**, Immunoblot of cell lysates or anti-Flag immunoprecipitates from HEK293T cells that had been transfected with Flag–H2AX and the indicated HA–cGAS truncated mutants in the presence of etoposide (100 μg ml^{-1}) for 4 h. Data represent $n = 3$ independent experiments. **f**, Immunoblot of cell lysates or anti-Flag immunoprecipitates from HEK293T cells transfected with Flag–cGAS, HA–H2AX, or HA–H2AX(S139A). Data represent $n = 3$ independent experiments. **g**, Coomassie blue staining of purified GST–cGAS protein. Data represent $n = 2$ independent experiments. **h**, Binding curves of surface-immobilized nonphosphorylated peptide with GST-labelled cGAS at concentrations of 368 nM, 184 nM and 92 nM, and control GST protein at a concentration of 92 nM. Vertical lines mark the starts of association and dissociation phases of binding events. Data represent $n = 4$ independent experiments. **i**, Immunoblot of cell lysates of U2OS cells that had been stably transfected with either control shRNA or shRNA targeting *H2AX* (sh-H2AX). Data represent $n = 2$ independent experiments. **j**, **k**, Representative images of U2OS cells that had been stably transfected with either control shRNA or shRNA targeting *H2AX*, showing the recruitment of GFP–cGAS to sites of DNA damage induced by laser microirradiation. Data represent $n = 3$ independent experiments. Quantification data are shown in **k** and represent the mean ± s.d. of $n = 17$ (sh-Ctrl) and $n = 22$ (sh-H2AX) cells, respectively, from 3 independent experiments. Two-way ANOVA was used for statistical analysis. For gel source data, see Supplementary Fig. 1.

© 2018 Springer Nature Limited. All rights reserved.

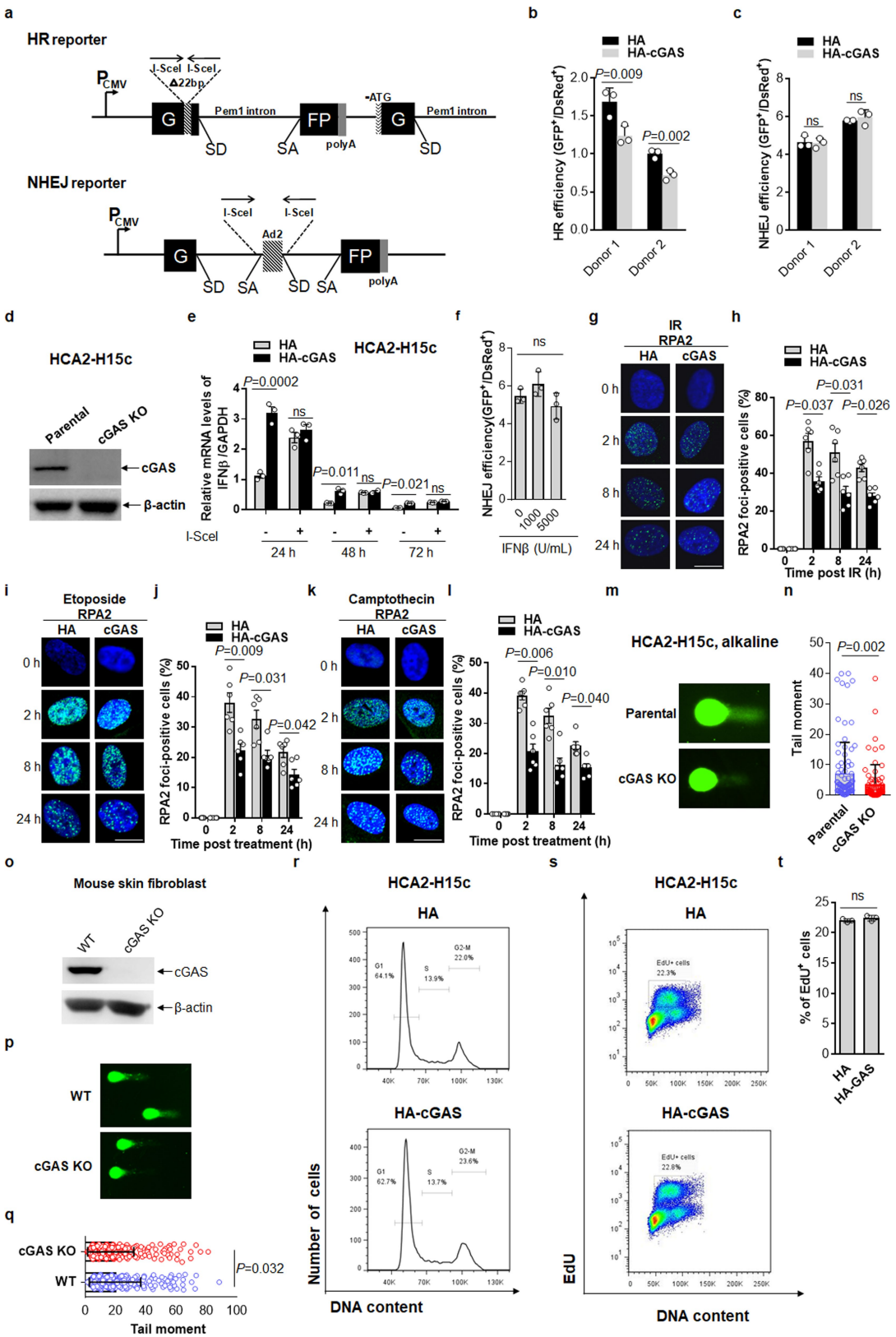

Extended Data Fig. 7 | See next page for caption.

© 2018 Springer Nature Limited. All rights reserved.

Extended Data Fig. 7 | cGAS inhibits repair mediated by homologous recombination in a manner that is independent of IFNβ, without altering the cell cycle or DNA replication. a, Schematic of reporter constructs prepared for the analysis of efficiency of DNA DSB repair by homologous recombination and NHEJ. Both reporter cassettes were constructed on *GFP–Pem1*. There are two non-functional copies of the *GFP-Pem1* gene in the homologous recombination construct. The first copy of *GFP–Pem1* contains a 22-nucleotide deletion and an insertion of 2 inverted I-SceI recognition sites. The second copy lacks the ATG start codon and the second *GFP* exon. After the induction of a DSB with I-SceI, only gene conversion can restore the functional *GFP* gene. The NHEJ cassette contains a copy of the *GFP* gene in which a *Pem1* intron is interrupted by an adenoviral exon (Ad2). The I-SceI endonuclease recognition sites flank the adenoviral exon. The *GFP* gene is restored when a DSB induced by I-SceI digestion is successfully repaired by NHEJ. SD, splice donor; SA, splice acceptor. **b**, **c**, Effect of cGAS overexpression on the efficiency of homologous recombination (**b**) and NHEJ (**c**) in primary cells, including primary skin fibroblast from two donors. Primary cells were transfected with linearized homologous recombination constuct (**b**) or NHEJ construct (**c**) and pDsRed2-N1 together with pcDNA3.1-HA (HA) or HA–cGAS, respectively, and analysis of the efficiency of homologous recombination or NHEJ was performed. Data represent mean ± s.e.m. of $n = 3$ independent experiments. Student's *t* tests (unpaired and two-tailed) were used for statistical analysis. **d**, Immunoblot of lysate of parental HCA2-H15c cells and cGAS knockout cells (cGAS KO) in which cGAS was deleted from the genome by CRISPR–Cas9 editing. Data represent $n = 2$ independent experiments. **e**, Quantitative PCR detection of the relative expression of IFNβ transcripts in HCA2-H15c cells at different time points after transfection with the pcDNA3.1-HA plasmid (HA) or the pcDNA3.1-HA–cGAS plasmid (HA–cGAS) with or without the I-SceI expression vector. Data represent mean ± s.e.m. of $n = 3$ independent experiments. Student's *t* tests (unpaired and two-tailed) were used for statistical analysis. **f**, Effect of exogenous IFNβ on NHEJ efficiency. Values represent the ratios of the quantity of GFP^+ cells (corresponding to successful repair events) to the $DsRed^+$ transfection controls. Data represent the mean ± s.e.m. of $n = 3$ independent experiments. One-way ANOVA was used for statistical analysis. **g**–**l**, Representative immunofluorescence of RPA2 foci at multiple time points in HCA2-H15c cells that had been transfected with pcDNA3.1-HA control (HA) or HA–cGAS, followed by ionizing irradiation (IR) (dose of 8 Gy) (**g**) or exposure to etoposide (100 μg ml^{-1}) (**i**) or camptothecin (1 μM) (**k**) for 4 h. Data represent $n = 6$ independent experiments. The percentage of RPA2-positive cells (with >5 nuclear foci per cell) was quantified at the indicated time points in **h**, **j**, **l** and expressed as mean ± s.e.m. of $n = 6$ independent experiments. Student's *t* tests (unpaired and two-tailed) were used for statistical analysis. **m**, Representative comet assay showing the tail moment of parental and cGAS knockout HCA2-H15c cells under alkaline conditions. Data represent $n = 3$ independent experiments. **n**, Quantification of the tail moment of parental and cGAS knockout HCA2-H15c cells under alkaline conditions. Data are expressed as mean ± s.d. of the tail moment of $n = 87$ (parental) and $n = 75$ (cGAS knockout) cells from 3 independent experiments. The Mann–Whitney *U*-test was used for statistical analysis. **o**, Immunoblot of cell lysates of skin fibroblast cells isolated from the tail of wild-type (WT) and cGAS knockout mouse. Data represent $n = 2$ independent experiments. **p**, Representative results of the comet assay showing the tail moment of skin fibroblast cells isolated from the tail of wild-type and cGAS knockout mouse under alkaline conditions. **q**, Quantification of the tail moment of wild-type and cGAS knockout skin fibroblast cells under alkaline conditions. Data are expressed as mean ± s.d. of the tail moment of $n = 299$ (wild type) and $n = 346$ (cGAS knockout) cells from 3 independent experiments. The Mann–Whitney *U*-test was used for statistical analysis. **r**, Representative FACS results depicting the cell-cycle distribution in HCA2-H15c cells that had been transfected with pcDNA3.1-HA (HA) or pcDNA3.1-HA–cGAS (HA–cGAS). Data are representative of $n = 3$ independent experiments. **s**, **t**, Representative FACS results showing the DNA content with EdU (**s**). Quantitative data are shown in **t**. Data represent the mean ± s.e.m. of $n = 3$ independent experiments. Student's *t* tests (unpaired and two-tailed) were used for statistical analysis. NS, not significant. Scale bar, 5 μm. For gel source data, see Supplementary Fig. 1.

© 2018 Springer Nature Limited. All rights reserved.

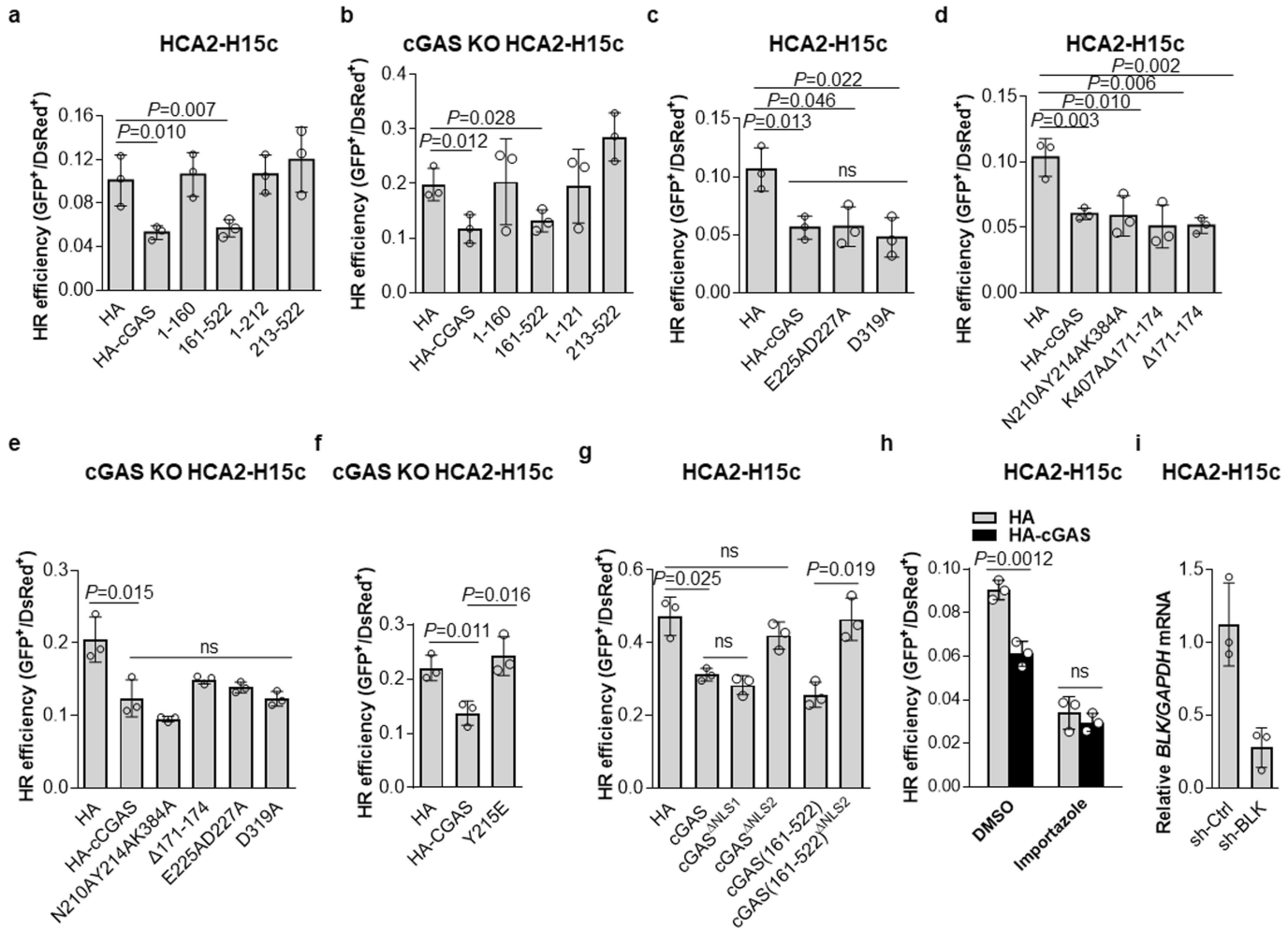

Extended Data Fig. 8 | cGAS inhibits repair mediated by homologous recombination independently of its DNA-binding ability or enzymatic activity. a–g, Human fibroblast HCA2-H15c cells containing chromosomally integrated reporter cassettes (**a**, **c**, **d**, **g**) or the corresponding cGAS knockout cells (**b**, **e**, **f**) were co-transfected with I-SceI endonuclease (to induce DSBs), pcDNA3.1-HA (HA) (control), HA–cGAS and corresponding mutants, and DsRedN-1 plasmid (transfection control) and assessed for efficiency of homologous recombination. **h**, HCA2-H15c cells were treated with either DMSO (control) or the importin-β inhibitor importazole (10 μM), followed by analysis of the efficiency of homologous recombination. Values in **a**–**h** represent the ratio of the quantity of GFP^+ cells (corresponding to successful repair events) to the $DsRed^+$ transfection controls. Data represent the mean ± s.e.m. of $n = 3$ independent experiments. Student's *t* tests (unpaired and two-tailed) were used for statistical analysis. NS, not significant. **i**, Quantitative PCR analysis of BLK expression in the homologous-recombination-repair reporter fibroblast HCA2-H15c cells, transfected with control shRNA or shRNA targeting *BLK*. Data represent the mean ± s.e.m. of $n = 3$ independent experiments.

© 2018 Springer Nature Limited. All rights reserved.

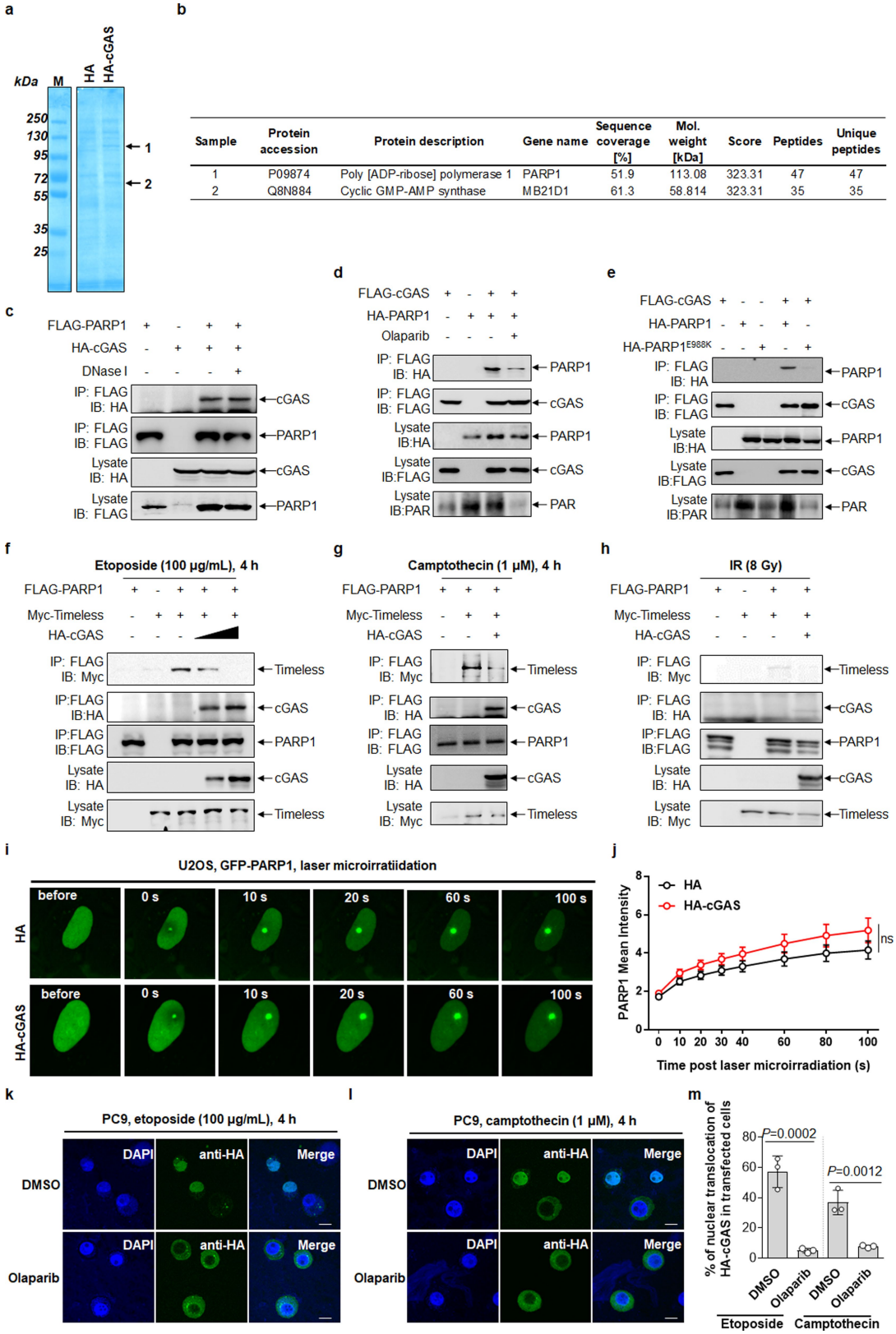

Sample	Protein accession	Protein description	Gene name	Sequence coverage [%]	Mol. weight [kDa]	Score	Peptides	Unique peptides
1	P09874	Poly [ADP-ribose] polymerase 1	PARP1	51.9	113.08	323.31	47	47
2	Q8N884	Cyclic GMP-AMP synthase	MB21D1	61.3	58.814	323.31	35	35

Extended Data Fig. 9 | See next page for caption.

© 2018 Springer Nature Limited. All rights reserved.

Extended Data Fig. 9 | cGAS interacts with PARP1 via PAR and prevents formation of the PARP1–Timeless complex. a, Coomassie-blue-stained SDS-polyacrylamide gel image showing the anti-HA immunoprecipitates of HEK293T cells stably transfected with pcDNA3.1-HA (HA) or HA–cGAS (HA–cGAS) and treated with H_2O_2 (10 mM) for 30 min. M, pre-stained protein markers. Distinct protein bands (indicated as 1 and 2) in the anti-HA immunoprecipitates of HEK293T cells that had been stably transfected with HA–cGAS were identified by mass spectrometry. Data represent $n = 2$ independent experiments. **b**, Results of mass spectrometry analysis of bands 1 and 2 in the anti-HA immunoprecipitates of HEK293T cells that had been stably transfected with HA–cGAS. **c**, Immunoblot of cell lysates or anti-Flag immunoprecipitates from HEK293T cells that were transfected with Flag–PARP1 and HA–cGAS in the presence or absence of DNase I. Data represent $n = 3$ independent experiments. **d**, Immunoblot of cell lysates or anti-Flag immunoprecipitates from HEK293T cells that were transfected with Flag–cGAS and HA–PARP1 in the absence or presence of the PARP1 inhibitor, olaparib (20 μM). Data represent $n = 3$ independent experiments. **e**, Immunoblot results of cell lysates or anti-Flag immunoprecipitates from HEK293T cells that had been transfected with Flag–cGAS, HA–PARP1 or its enzyme-inactivated mutant HA–PARP1(E988K). Data represent $n = 3$ independent experiments. **f**–**h**, Immunoblot of cell lysates or anti-Flag immunoprecipitates from HEK293T cells that had been transfected with Flag–PARP1, Myc–Timeless and HA–cGAS and then exposed to etoposide (100 μg ml^{-1}) (**f**) or camptothecin (1 μM) (**g**) for 4 h, or ionizing irradiation (8 Gy) (**h**). Data represent $n = 3$ independent experiments. **i**, **j**, Representative images of U2OS cells showing the recruitment of GFP–PARP1 to sites of DNA damage induced by laser microirradiation. Cells had been transfected with pcDNA3.1-HA control (HA) or HA–cGAS. Quantification data are shown in **j** and represent the mean ± s.d. of $n = 19$ cells (both HA and HA–cGAS) from 3 independent experiments. Two-way ANOVA was used for statistical analysis. NS, not significant. **k**–**m**, Representative immunofluorescence of HA–cGAS (anti-HA, green) in PC-9 HA–cGAS cells treated with etoposide (100 μg ml^{-1}) (**k**) or camptothecin (1 μM) (**l**) for 4 h in the presence of DMSO (mock treatment) or olaparib (20 μM). Nuclei were stained with DAPI (blue). Data represent $n = 3$ independent experiments. Quantitative data are shown in **m**. At least 100 transfected cells were counted in each experiment. Data are expressed as mean ± s.e.m. of $n = 3$ independent experiments (**m**). Student's *t* tests (unpaired and two-tailed) were used for statistical analysis. Scale bar, 5 μm. For gel source data, see Supplementary Fig. 1.

© 2018 Springer Nature Limited. All rights reserved.

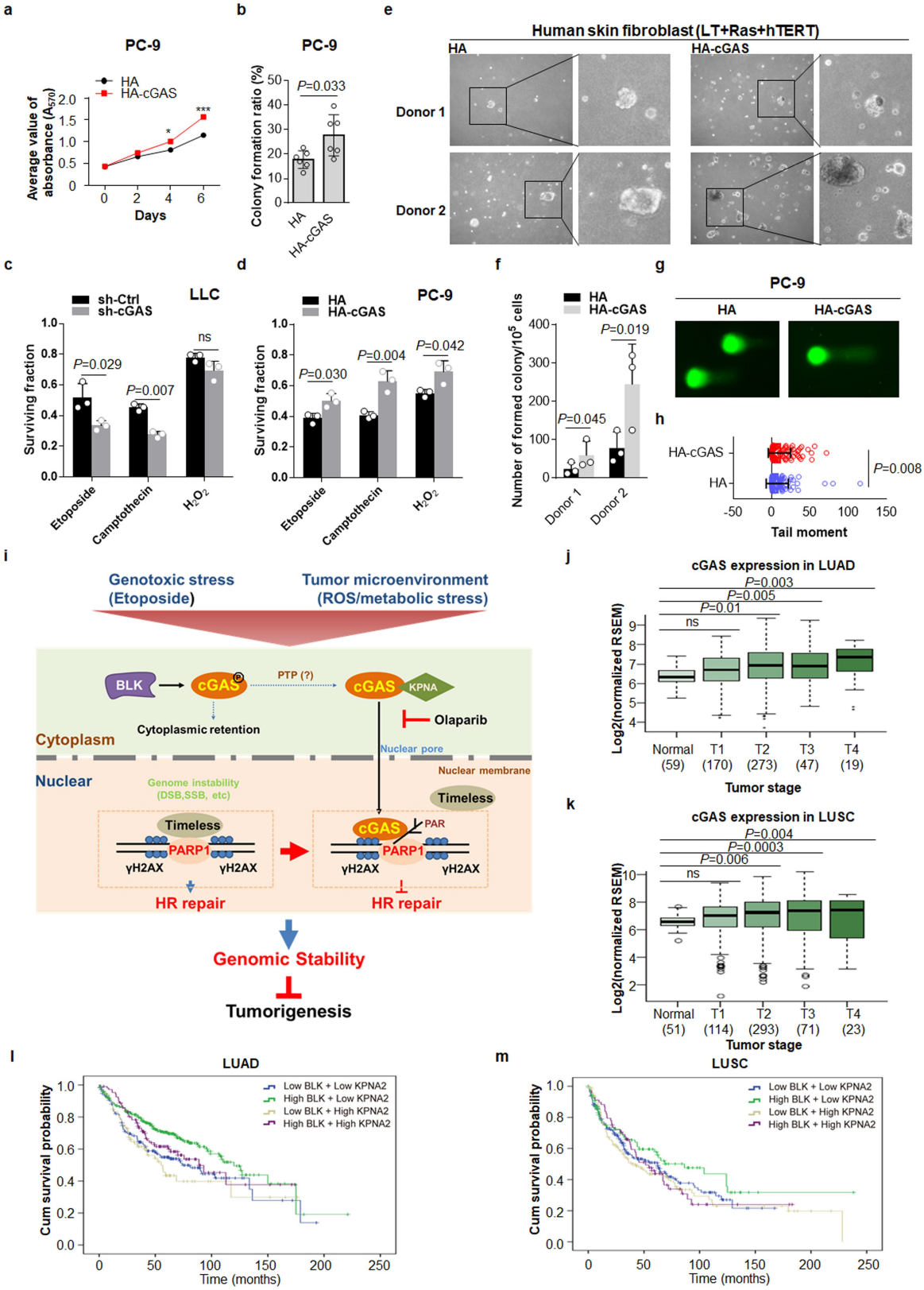

Extended Data Fig. 10 | See next page for caption.

© 2018 Springer Nature Limited. All rights reserved.

Extended Data Fig. 10 | cGAS promotes tumorigenesis. a, Results of the MTT assay showing the proliferation of PC-9 cells that had been stably transfected with pcDNA3.1-HA (HA) or HA–cGAS (HA–cGAS). Data are expressed as mean ± s.e.m. of $n = 3$ independent experiments. Student's *t* tests (unpaired and two-tailed) were used for statistical analysis. $^{*}P < 0.05$; $^{***}P < 0.001$. **b**, Colonogenic assay results depicting the colony-forming ability of PC-9 cells that were stably transfected with pcDNA3.1-HA (HA) or HA–cGAS (HA–cGAS). Data represent the mean ± s.e.m. of $n = 6$ independent experiments. The Mann–Whitney *U*-test was used for statistical analysis. **c**, The survival fraction of control shRNA LLC and *Cgas* shRNA LLC cells was determined by the MTT assay 6 days after exposure to etoposide (100 μg ml^{-1}) or camptothecin (1 μM) for 4 h or H_2O_2 (10 mM) for 30 min. Data are expressed as mean ± s.e.m. of $n = 3$ independent experiments. Student's *t* tests (unpaired and two-tailed) were used for statistical analysis. **d**, The survival fraction of PC-9 cells that had been stably transfected with pcDNA3.1-HA (HA) or HA–cGAS was determined by the MTT assay 6 days after exposure to etoposide (100 μg ml^{-1}) or camptothecin (1 μM) for 4 h or H_2O_2 (10 mM) for 30 min. Data are expressed as mean ± s.e.m. of $n = 3$ independent experiments. Student's *t* tests (unpaired and two-tailed) were used for statistical analysis. **e**–**f**, Soft agar assays of anchorage-independent colony formation of human skin fibroblast from two different donors that were transfected with vectors encoding SV40 large tumour antigen (LT), HRAS V12 (Ras) and TERT together with pcDNA3.1-HA (HA) or HA–cGAS followed by plating in soft agar. Colonies were photographed after 5 weeks of growth at 200× original magnification (**e**). To assess anchorage-independent growth, 10^5 cells were plated in 0.4% Noble agar and colonies were counted 5 weeks after seeding. Quantification data are shown in **f** and represent the mean ± s.e.m. of $n = 3$ independent experiments. The Mann–Whitney *U*-test was used for statistical analysis. **g**, Representative results of the comet assay depicting the tail moment of PC-9 cells that had been stably transfected with pcDNA3.1-HA (HA) or HA–cGAS under alkaline conditions. **h**, Quantification of the tail moment of PC-9 cells that had been stably transfected with pcDNA3.1-HA (HA) or HA–cGAS under alkaline conditions. Data represent mean ± s.d. of the tail moment of $n = 143$ (HA) and $n = 127$ (HA–cGAS) cells from 3 independent experiments. The Mann–Whitney *U*-test was used for statistical analysis. **i**, Schematic of the role of cGAS in control of the DNA-damage response. In response to DNA damage, cGAS translocates to the nucleus and is recruited to DSBs where it interacts with PARP1 via PAR and prevents the formation of the PARP1–Timeless complex. This interferes with the process of homologous recombination. Nuclear cGAS suppresses DNA repair and promotes tumorigenesis. **j**, The relative expression of cGAS in normal and tumour (T) stages from specimens of patients with lung adenocarcinoma (LUAD). Data were obtained from the TCGA database. log_2(fold-changes) and *P* values of cGAS expression are 0.47 ($P = 0.12$, T1 versus normal), 0.73 ($P = 0.01$, T2 versus normal), 0.76 ($P = 0.005$, T3 versus normal) and 0.93 ($P = 0.003$, T4 versus normal). NS, not significant. **k**, The relative expression of cGAS in normal and T stages from specimens of patients with lung squamous carcinoma (LUSC). Data were obtained from the TCGA database. log_2(fold-changes) and *P* values of cGAS expression are 0.56 ($P = 0.06$, T1 versus normal), 0.78 ($P = 0.006$, T2 versus normal), 0.94 ($P = 0.0003$, T3 versus normal) and 0.79 ($P = 0.004$, T4 versus normal). NS, not significant. **l**, **m**, Kaplan–Meier curve analysis of the overall survival probabilities of patients with lung adenocarcinoma or lung squamous carcinoma based on the expression levels of BLK and KPNA2. Patients with lung adenocarcinoma were assigned to 1 of 4 groups based on low or high levels of gene expression.

© 2018 Springer Nature Limited. All rights reserved.

https://doi.org/10.1038/s41586-018-0630-0

Cryo-EM structure of the Ebola virus nucleoprotein–RNA complex at 3.6 Å resolution

Yukihiko Sugita[1,7], Hideyuki Matsunami[1], Yoshihiro Kawaoka[2,3,4], Takeshi Noda[5,6] & Matthias Wolf[1]*

Ebola virus causes haemorrhagic fever with a high fatality rate in humans and non-human primates. It belongs to the family *Filoviridae* in the order *Mononegavirales*, which are viruses that contain linear, non-segmented, negative-sense, single-stranded genomic RNA[1,2]. The enveloped, filamentous virion contains the nucleocapsid, consisting of the helical nucleoprotein–RNA complex, VP24, VP30, VP35 and viral polymerase[1,3]. The nucleoprotein–RNA complex acts as a scaffold for nucleocapsid formation and as a template for RNA replication and transcription by condensing RNA into the virion[4,5]. RNA binding and nucleoprotein oligomerization are synergistic and do not readily occur independently[6]. Although recent cryo-electron tomography studies have revealed the overall architecture of the nucleocapsid core[4,5], there has been no high-resolution reconstruction of the nucleocapsid. Here we report the structure of a recombinant Ebola virus nucleoprotein–RNA complex expressed in mammalian cells without chemical fixation, at near-atomic resolution using single-particle cryo-electron microscopy. Our structure reveals how the Ebola virus nucleocapsid core encapsidates its viral genome, its sequence-independent coordination with RNA by nucleoprotein, and the dynamic transition between the RNA-free and RNA-bound states. It provides direct structural evidence for the role of the N terminus of nucleoprotein in subunit oligomerization, and for the hydrophobic and electrostatic interactions that lead to the formation of the helical assembly. The structure is validated as representative of the native biological assembly of the nucleocapsid core by consistent dimensions and symmetry with the full virion[5]. The atomic model provides a detailed mechanistic basis for understanding nucleocapsid assembly and highlights key structural features that may serve as targets for anti-viral drug development.

We expressed and purified C-terminally truncated Zaire ebolavirus nucleoprotein (NP), containing residues 1−450 (NP 1−450) in a human cell line (Fig. 1a), in which it sequestered cellular RNA and assembled into a rigid helix indistinguishable from the viral nucleocapsid core[3–5,7]. The sample was imaged without fixation using cryo-electron microscopy (cryo-EM), and its structure was determined by single-particle analysis (SPA) (Fig. 1b, Extended Data Fig. 1a–e, Extended Data Table 1). The complex forms a left-handed helical tube with outer and inner diameters of 295 and 175 Å, respectively, and features a characteristic zipper-like arrangement of parallel C-terminal α-helices (Fig. 1b–d). Its diameter and helical symmetry correspond closely to those of the recently reported Ebola virion reconstructed by cryo-electron tomography (cryo-ET)[4,5]. Our cryo-EM map enabled generation of an atomic model, including clearly resolved RNA nucleotides (Fig. 1e, Extended Data Figs. 1d, 1f, 2).

The transition from the RNA-free to the RNA-bound state requires conformational changes in both RNA and NP. Encapsidation of RNA by NP has been addressed by two leading models. One model has NP encapsidating the RNA in a closed conformation with a hinge-like motion around the junction between N- and C-terminal lobes[6,8–14]. The other has RNA and a phosphoprotein competing directly for the RNA-binding cleft[15,16] (Extended Data Fig. 3). To discriminate between these possibilities, we compared our atomic model of RNA-bound NP with structures of RNA-free monomeric NP chaperoned by phosphoprotein (VP35)[6,8]. We found that the relative positions around the junction—specifically, α-helices α9−α12 in the N-terminal lobe and α13−α15 in the C-terminal lobe—do not change significantly, which indicates that the transition is not a simple hinge motion. Binding regions of RNA and the N-terminal peptide of VP35 do not overlap, weakening the case for direct competition. These observations imply that the transition to the closed conformation is a consequence of multiple elements. In Ebola virus NP, the β-hairpin (β3−β4, which is unique to the family *Filoviridae*) is rotated approximately 90° between RNA-free and RNA-bound states (Fig. 2a, Extended Data Fig. 3, Supplementary Video 1). Simultaneously, the adjacent 3_{10} helix η2 and α-helices α16−α18 are shifted to form a 'closed' state (Fig. 2a, Extended Data Fig. 3a). The C-terminal helix α18 clamps the RNA strand and serves as a fastener to cover the RNA in its cleft, as previously reported[5]. A short 3_{10} helix η5 (residues 329−333), which does not exist in the RNA-free state, shortens and directs the adjacent loop 334–338 to secure the RNA tightly (Fig. 2a, b, Extended Data Fig. 3a).

The viral RNA is firmly secured in the NP–RNA complex within a positively charged ellipsoid cleft with a cross-section approximately 5 × 11 Å (Extended Data Fig. 4). The conformation of the RNA strand follows an undulating path along the helical NP strand. We found 6 RNA nucleotides clamped in the cleft (Fig. 1c, d), confirming predictions[4–6,8,9,17]. These nucleotides adopt a '3-bases-inward, 3-outward' configuration (Figs. 1e, 2a, b), similar to measles virus and parainfluenza virus 5[13,18]. Coordination is achieved by hydrogen bonding and electrostatic interactions between NP and negatively charged phosphate groups of RNA.

Polar residues on helix η5 and loop 334–338 are within hydrogen-bonding distance of the RNA backbone, adjacent to helix α17, and clamping helix α18 (Fig. 2b). Therefore, this region not only aligns the RNA but also serves as an interface for NP–RNA interactions. Positively charged residues K160, K171, R174, R298 and R401—some of which are important for RNA binding in filovirus NP[8,19]—were found in close proximity to RNA nucleotides, with their side chains pointing towards RNA-backbone phosphates (Fig. 2c). K248, which is non-essential for RNA binding[8,19], faces the RNA bases. These common residues suggest a shared structural motif for RNA interactions within the family *Filoviridae*. Unlike in measles virus, we found no indication of π–π stacking as a possible cause of the switch between '3-in' and '3-out' nucleotide directions[13]. The location of R298 on the inner side of the cleft enables it to interact with the RNA backbone. Combined with the restricted space in the cavity and R401 on helix α18 on the outside, these structural constraints may provide an alternative mechanism for the switch. In addition, E309 is within hydrogen-bonding distance of

[1]Molecular Cryo-Electron Microscopy Unit, Okinawa Institute of Science and Technology Graduate University, Okinawa, Japan. [2]Division of Virology, Department of Microbiology and Immunology, Institute of Medical Science, University of Tokyo, Tokyo, Japan. [3]Department of Pathobiological Sciences, School of Veterinary Medicine, University of Wisconsin-Madison, Madison, WI, USA. [4]Department of Special Pathogens, International Research Center for Infectious Diseases, Institute of Medical Science, University of Tokyo, Tokyo, Japan. [5]Laboratory of Ultrastructural Virology, Institute for Frontier Life and Medical Sciences, Kyoto University, Kyoto, Japan. [6]PRESTO, Japan Science and Technology Agency, Saitama, Japan. [7]Present address: Laboratory of Advanced Protein Characterization, Research Center for State-of-the-Art Functional Protein Analysis, Institute for Protein Research, Osaka University, Osaka, Japan. *e-mail: matthias.wolf@oist.jp

© 2018 Springer Nature Limited. All rights reserved.

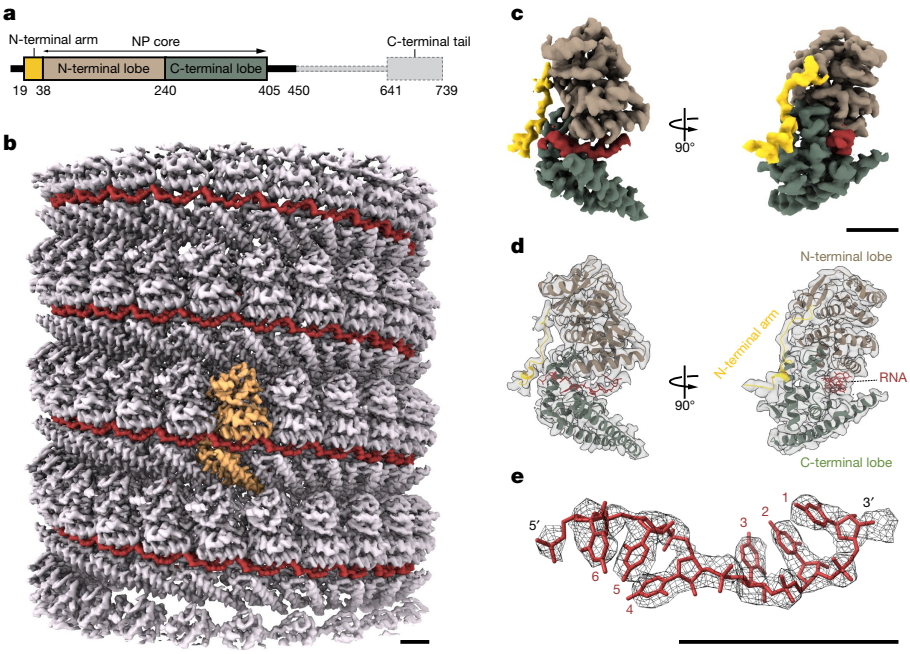

Fig. 1 | Cryo-EM reconstruction and atomic model of Ebola NP 1—450 helix. a, Structural layout of the Ebola NP sequence. The full-length NP contains 739 amino acids divided into an N-terminal arm domain, an NP core consisting of N- and C-terminal lobes, a disordered linker and a C-terminal tail. **b**, The iso-electron potential surface of NP–RNA complex reconstruction (contoured at 3σ above average) was calculated from 117,552 single-particle images. The RNA strand and a single NP subunit are highlighted in red and orange, respectively. **c**, **d**, The isolated NP subunit (2.5σ) with our atomic model (RCSB Protein Data Bank code (PDB): 5Z9W) in ribbon representation. **e**, Isolated electron potential map (5.0σ) of RNA superimposed with the atomic model of RNA. RNA bases were modelled as uracil. There are 6 nucleotides per NP. Scale bars, 20 Å.

the closest RNA nucleotide on the next NP subunit (Fig. 2d). These specific interactions with the RNA backbone are consistent with the sequence-independent NP–RNA interaction of negative-sense RNA viruses[12,13,15,20–25] (Fig. 2e).

The N-terminal arm domain of NP is essential for NP oligomerization[6,8]. Our map clearly shows that the N-terminal arms cross-link subunits on the inside of the helical tube (Fig. 3a–c, Extended Data Fig. 5a, d), confirming previous observations[5]. Furthermore,

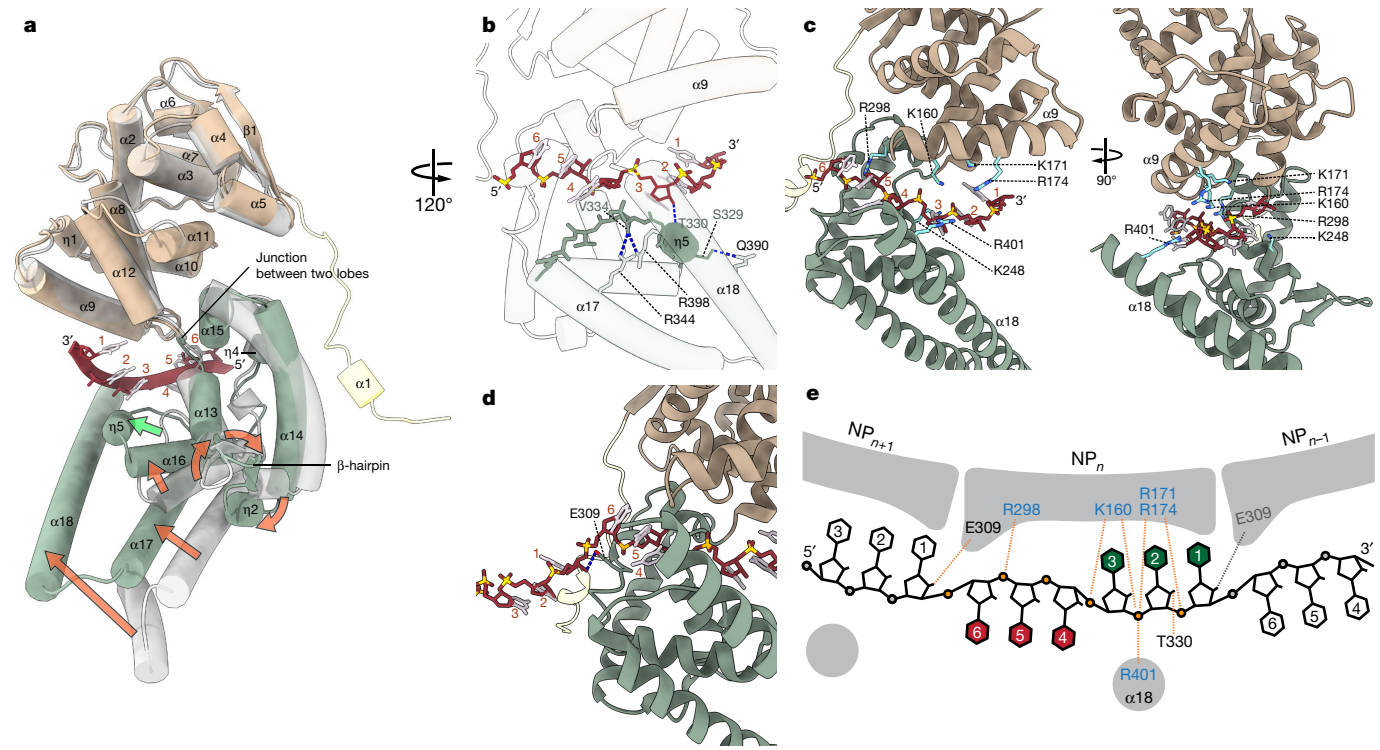

Fig. 2 | NP–RNA interactions. a, Comparison of an RNA-free, monomeric NP model (PDB: 4YPI, grey) and RNA-bound NP (PDB: 5Z9W, coloured, from this study). The conformational transition to the encapsidated state is orchestrated by a 90° rotation of the β-hairpin, formation of a new secondary structural element (η5) and shift of the C-terminal α-helices. Arrows indicate transitions from RNA-free (open) state to a bound (closed) state. The green arrow indicates formation of a 3_{10} helix η5 and shifting of the polypeptide chain. See also Supplementary Video 1. **b**–**d**, Close-up view of the NP–RNA binding region. Blue dashed lines depict predicted hydrogen bonds. **b**, 3_{10} helix η5, loop 334–338 and helix α18 coordinate RNA bases and flexibly adopt the RNA path. **c**, Interactions between positively charged NP residues and RNA-backbone phosphates. **d**, Possible hydrogen bond of E309 with the adjacent RNA pentose hydroxyl group. **e**, Schematic of RNA nucleotides within the nucleoprotein. Two RNA base triplets with opposing orientations are coordinated by each NP subunit. The RNA bases are numbered sequentially in the 3′ to 5′ direction, representing negative-sense genomic RNA, facing inward (green) towards the helical tube or outward (red). A set of specific electrostatic interactions on both the NP core and α18 determine nucleotide orientation. Secondary structure labels are based on our atomic model (see Extended Data Fig. 2).

© 2018 Springer Nature Limited. All rights reserved.

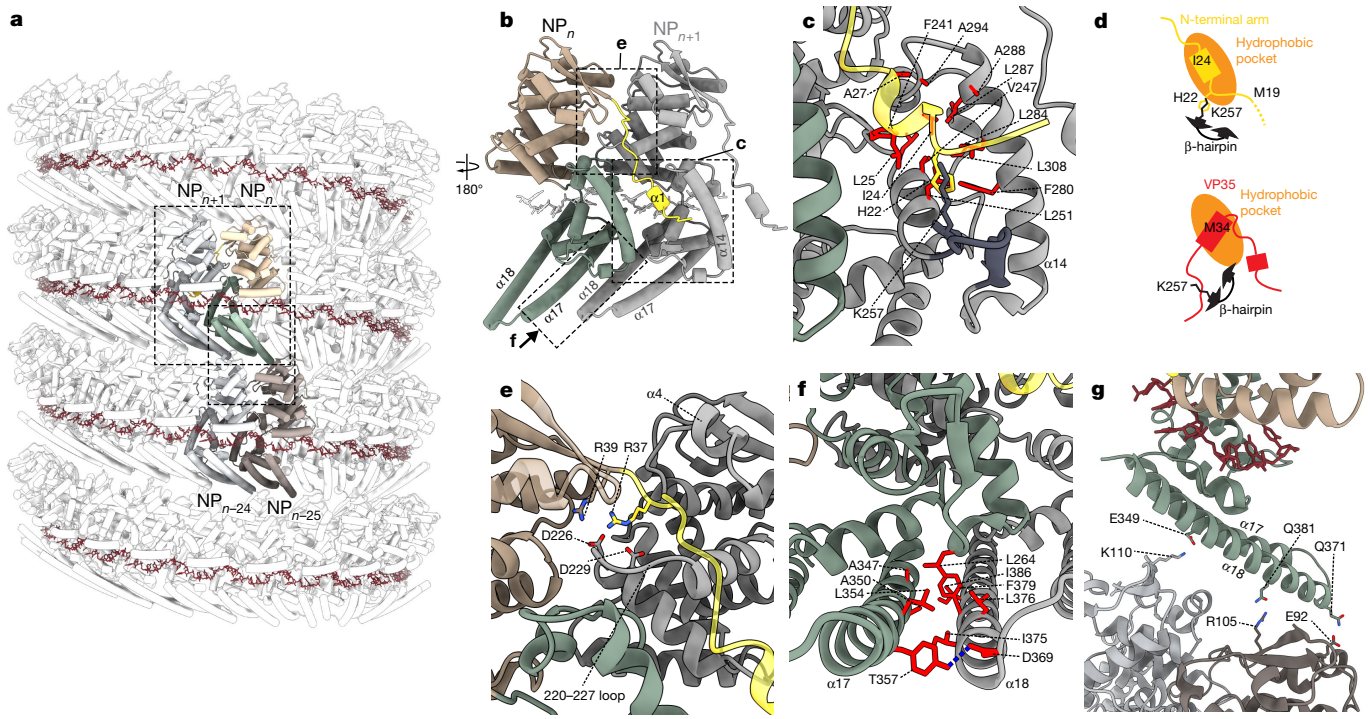

Fig. 3 | Intrastrand and interstrand NP–NP interactions. We refer to the NP–RNA band generically as a 'strand', 'intrastrand interactions' in the lateral direction and 'interstrand interactions' in the axial direction. **a**, An atomic model of the NP–RNA complex. Larger and smaller dashed boxes outline close-ups of two adjacent NP molecules (**b**) and interstrand NP–NP interface (**g**), respectively. **b**, An NP pair viewed from inside the helix. Dashed boxes delineate respective close-up figures. **c**, Intrastrand NP–NP interactions between the N-terminal arm and the hydrophobic pocket. The β-hairpin is shown in dark grey. **d**, Schematics of the hydrophobic pocket illustrating the binding mode of the N-terminal arm in the RNA-bound state (top) and VP35 in the RNA-free state (bottom). **e**, Contacts between the N-terminal arm and the N-terminal lobe. **f**, The contact region between α17 of NP$_n$ and α18 of NP$_{n+1}$ subunits. The blue dashed line indicates a hydrogen bond. **g**, Interstrand NP–NP interactions (with subunits NP$_{n\pm24}$ and NP$_{n\pm25}$) formed by 3 pairs of amino acid side chains, K110–E349, E92–Q371 and R105–Q381.

N-terminal residues have been predicted to associate with the same binding site as the N terminus of VP35[5,6]. VP35 binds to a hydrophobic pocket in the NP C-terminal lobe and acts as a chaperone to keep NP in its monomeric RNA-free state[6]. To clarify the mechanism of NP oligomerization, we examined the interface between the N-terminal arm and the pocket of adjacent NPs (Fig. 3b, c). The N-terminal arm binds to the same location as VP35 within this pocket via I24, L25 and A27 on its short N-terminal α-helix (Fig. 3c, Extended Data Fig. 5a–d). Whereas VP35 straddles the β-hairpin in the RNA-free monomeric form[6,8] (Extended Data Fig. 5a, c), adjacent NP subunits extend their N-terminal arm to interact directly with the rotated β-hairpin and the pocket in the NP–RNA complex (Fig. 3c). Furthermore, the N-terminal arm is tucked behind K257 on the rotated β-hairpin and the pocket (Fig. 3c, d, Extended Data Fig. 5d). Compared with monomeric NP, we discovered that loop 220–227 moves to create a groove between itself and helix α4, which makes space for the N-terminal arm of the adjacent NP (Fig. 3e, Extended Data Fig. 5e). This conformational change exposes two amino acids (D226 and D229) that serve as electrostatic anchors for partners (R37 and R39) on the N-terminal arm. This observation is consistent with a previous report of increased solvent exchange in this area upon oligomerization[6].

Lateral assembly of NP monomers relies on NP–NP and NP–RNA interactions. Beside the N-terminal arm, multiple contact regions are essential for RNA encapsidation[26]. Whereas the N-terminal arm of vesicular stomatitis virus is co-located with the NP–NP interface, contact regions in NP 1–450 are more spatially separated. Stoichiometric excess of VP35 does not dissociate the NP oligomer after the NP–RNA complex has been formed[4,6,27]. Our data and previous reports show that the NP–RNA complex retains lateral binding of NP subunits to form a flat ribbon-like strand, even where the NP–RNA complex is uncoiled[4,6–8] (Extended Data Fig. 1a, b). We identified a major NP–NP interface between the parallel C-terminal extended α-helices α17 and α18 (Fig. 3a, b, f), which contains surface patches formed by highly conserved hydrophobic residues (Fig. 3f, Extended Data Fig. 5b). These patches are buried in the NP oligomer. In non-physiological packing within the crystallographic unit cells of filovirus NP, α17 and α18 of adjacent NPs also make contacts in almost identical configurations[8,19] (Extended Data Fig. 5f), which emphasizes the high specificity of these helix–helix interactions. The function of the hydrophobic interface may be to align the C-terminal α-helices to form the characteristic zipper-like arrangement throughout the NP strand.

In our structure of NP 1–450, the interstrand interface is uniquely determined by NP–NP interactions. In the axial direction, any arbitrary NP$_n$ subunit shares contact regions with two pairs of neighbours located above and below (Fig. 3a). Three pairs of amino acids, K110–E349, E92–Q371 and R105–Q381, are located near enough for electrostatic interaction to occur between the zipper-like C-terminal α-helices and the β-sheet of the N-terminal lobe (Fig. 3g). Of note, most other amino acids at the interstrand interface within 2–6 Å of each other are also charged or polar (Extended Data Fig. 6), suggesting that the nature of interstrand NP–NP interaction is mainly electrostatic. This broad distribution of charged residues may allow distance variation without rupture upon helix bending, and would explain the phenotypic flexibility of filoviruses. The hydrophilic character of the interstrand interface further explains how the NP–RNA complex can easily uncoil, yet remain stable in solution.

Oligomeric NP structures determined at intermediate resolution by cryo-ET[5] and SPA[28] have previously been reported. The helical parameter of our NP–RNA complex is consistent with the full virion in the cryo-ET study[5]. However, our structure differs from the bacterially expressed, in vitro-assembled NP (residues 25–457)[28], which formed helical tubes of heterodimeric NP subunits with nearly twice the diameter of native Ebola virus. That structure has fundamentally different helical symmetry and contains no RNA density (Extended Data Fig. 7).

© 2018 Springer Nature Limited. All rights reserved.

Nevertheless, this N-terminal truncation mutant can still assemble into a paired back-to-back helical configuration with a partially disordered C-terminal helix located away from the RNA cleft. This further emphasizes the importance of the first 24 N-terminal residues for cooperative control in alignment and oligomerization of NP subunits, the clamping helix α18 and the RNA itself during assembly of the NP–RNA complex under physiological conditions.

Here we report the structure of the Ebola virus NP 1–450 RNA complex at near-atomic resolution. Insights from our study provide opportunities for rational design of novel antivirals—for example, creation of peptidomimetics competing with the binding site for the N-terminal arm helix or the C-terminal hydrophobic patches, or by cross-linking the interstrand interface. On the basis of its 6 nucleotides per NP subunit and genome size of the Zaire ebolavirus (18,960 bases), the length of the nucleocapsid necessary to accommodate a single copy of genomic RNA is 950 μm. This dimension is consistent with the average length of the filamentous Ebola virion[29,30]. Furthermore, a histogram of virion length shows a peak distribution with integer multiples of this distance[30]. Because the outer surface of mature Ebola nucleocapsid is in contact with matrix protein VP40, the NP–RNA complex may serve as a yardstick to determine virion length, causing pinch-off at its ends. Our structure supports conclusions by previous studies[5,6]—chiefly, the important role of the N-terminal arm in subunit linking and in competing with the VP35 N-terminal peptide. Encapsidation of the viral genome takes place concomitantly with genome replication, and lateral NP–NP interactions are required for assembly of the nucleocapsid. Therefore, NP oligomerization in open conformation by self-alignment via the hydrophobic interface must precede RNA clamping or occur simultaneously. Because NP oligomerization and NP–RNA binding are cooperative, the end of the RNA strand would terminate assembly.

Online content

Any methods, additional references, Nature Research reporting summaries, source data, statements of data availability and associated accession codes are available at https://doi.org/10.1038/s41586-018-0630-0.

Received: 29 May 2018; Accepted: 21 August 2018;
Published online 17 October 2018.

1. Lamb, R. A. in *Fields Virology* Vol. 1 (eds Knipe, D. M. & Howley, P. M.) Ch. 30, 880–884 (Wolters Kluwer/Lippincott Williams & Wilkins, 2013).
2. Ruigrok, R. W., Crepin, T. & Kolakofsky, D. Nucleoproteins and nucleocapsids of negative-strand RNA viruses. *Curr. Opin. Microbiol.* **14**, 504–510 (2011).
3. Huang, Y., Xu, L., Sun, Y. & Nabel, G. J. The assembly of Ebola virus nucleocapsid requires virion-associated proteins 35 and 24 and posttranslational modification of nucleoprotein. *Mol. Cell* **10**, 307–316 (2002).
4. Bharat, T. A. et al. Structural dissection of Ebola virus and its assembly determinants using cryo-electron tomography. *Proc. Natl Acad. Sci. USA* **109**, 4275–4280 (2012).
5. Wan, W. et al. Structure and assembly of the Ebola virus nucleocapsid. *Nature* **551**, 394–397 (2017).
6. Kirchdoerfer, R. N., Abelson, D. M., Li, S., Wood, M. R. & Saphire, E. O. Assembly of the Ebola virus nucleoprotein from a chaperoned VP35 complex. *Cell Reports* **12**, 140–149 (2015).
7. Noda, T., Hagiwara, K., Sagara, H. & Kawaoka, Y. Characterization of the Ebola virus nucleoprotein–RNA complex. *J. Gen. Virol.* **91**, 1478–1483 (2010).
8. Leung, D. W. et al. An intrinsically disordered peptide from ebola virus VP35 controls viral RNA synthesis by modulating nucleoprotein-RNA interactions. *Cell Reports* **11**, 376–389 (2015).
9. Dong, S. et al. Insight into the Ebola virus nucleocapsid assembly mechanism: crystal structure of Ebola virus nucleoprotein core domain at 1.8 Å resolution. *Protein Cell* **6**, 351–362 (2015).
10. Yabukarski, F. et al. Structure of Nipah virus unassembled nucleoprotein in complex with its viral chaperone. *Nat. Struct. Mol. Biol.* **21**, 754–759 (2014).
11. Yabukarski, F. et al. Ensemble structure of the highly flexible complex formed between vesicular stomatitis virus unassembled nucleoprotein and its phosphoprotein chaperone. *J. Mol. Biol.* **428**, 2671–2694 (2016).
12. Renner, M. et al. Nucleocapsid assembly in pneumoviruses is regulated by conformational switching of the N protein. *eLife* **5**, e12627 (2016).
13. Gutsche, I. et al. Near-atomic cryo-EM structure of the helical measles virus nucleocapsid. *Science* **348**, 704–707 (2015).
14. Guryanov, S. G., Liljeroos, L., Kasaragod, P., Kajander, T. & Butcher, S. J. Crystal structure of the measles virus nucleoprotein core in complex with an N-terminal region of phosphoprotein. *J. Virol.* **90**, 2849–2857 (2015).
15. Green, T. J., Zhang, X., Wertz, G. W. & Luo, M. Structure of the vesicular stomatitis virus nucleoprotein–RNA complex. *Science* **313**, 357–360 (2006).
16. Leyrat, C. et al. Structure of the vesicular stomatitis virus N^0–P complex. *PLoS Pathog.* **7**, e1002248 (2011).
17. Weik, M., Enterlein, S., Schlenz, K. & Muhlberger, E. The Ebola virus genomic replication promoter is bipartite and follows the rule of six. *J. Virol.* **79**, 10660–10671 (2005).
18. Alayyoubi, M., Leser, G. P., Kors, C. A. & Lamb, R. A. Structure of the paramyxovirus parainfluenza virus 5 nucleoprotein–RNA complex. *Proc. Natl Acad. Sci. USA* **112**, E1792–E1799 (2015).
19. Liu, B. et al. Structural insight into nucleoprotein conformation change chaperoned by VP35 peptide in Marburg virus. *J. Virol.* **91**, (2017).
20. Albertini, A. A. et al. Crystal structure of the rabies virus nucleoprotein–RNA complex. *Science* **313**, 360–363 (2006).
21. Tawar, R. G. et al. Crystal structure of a nucleocapsid-like nucleoprotein–RNA complex of respiratory syncytial virus. *Science* **326**, 1279–1283 (2009).
22. Hastie, K. M. et al. Crystal structure of the Lassa virus nucleoprotein–RNA complex reveals a gating mechanism for RNA binding. *Proc. Natl Acad. Sci. USA* **108**, 19365–19370 (2011).
23. Raymond, D. D., Piper, M. E., Gerrard, S. R., Skiniotis, G. & Smith, J. L. Phleboviruses encapsidate their genomes by sequestering RNA bases. *Proc. Natl Acad. Sci. USA* **109**, 19208–19213 (2012).
24. Ariza, A. et al. Nucleocapsid protein structures from orthobunyaviruses reveal insight into ribonucleoprotein architecture and RNA polymerization. *Nucleic Acids Res.* **41**, 5912–5926 (2013).
25. Niu, F. et al. Structure of the Leanyer orthobunyavirus nucleoprotein–RNA complex reveals unique architecture for RNA encapsidation. *Proc. Natl Acad. Sci. USA* **110**, 9054–9059 (2013).
26. Zhang, X., Green, T. J., Tsao, J., Qiu, S. & Luo, M. Role of intermolecular interactions of vesicular stomatitis virus nucleoprotein in RNA encapsidation. *J. Virol.* **82**, 674–682 (2008).
27. Noda, T., Kolesnikova, L., Becker, S. & Kawaoka, Y. The importance of the NP:VP35 ratio in Ebola virus nucleocapsid formation. *J. Infect. Dis.* **204**, S878–S883 (2011).
28. Su, Z. et al. Electron cryo-microscopy structure of Ebola virus nucleoprotein reveals a mechanism for nucleocapsid-like assembly. *Cell* **172**, 966–978 (2018).
29. Geisbert, T. W. & Jahrling, P. B. Differentiation of filoviruses by electron microscopy. *Virus Res.* **39**, 129–150 (1995).
30. Beniac, D. R. et al. The organisation of Ebola virus reveals a capacity for extensive, modular polyploidy. *PLoS ONE* **7**, e29608 (2012).

Acknowledgements We thank Y. Takizawa, A. Maigné and M. Collins for helpful discussions and S. D. Aird for editing the manuscript. This work was supported by a Grant-in-Aid for Research Activity Start-up from MEXT (Grant no. 26892028) (to Y.S.), by Joint Research Project of Institute of Medical Science, University of Tokyo (to Y.S. and T.N.), by Joint Research Program of Institute for Frontier Life and Medical Sciences, Kyoto University (to Y.S.), by JST (Grant no. JPMJPR13L9), by AMED (Grant no. 17fk0108128h0001), from JSPS Core-to-Core Program A and from Daiichi Sankyo Foundation of Life Science (to T.N.), by J-PRIDE for Global Epidemic from AMED (JP17fm0208101j0001), by RPERID from AMED (JP17fk0108029h0002) and by a Grant-in-Aid for Scientific Research on Innovative Areas from MEXT (Grant no. 16H06429, 16K21723 and 16H06434) (to Y.K.). Y.S. and M.W. were supported by direct funding from Okinawa Institute of Science and Technology Graduate University.

Reviewer information *Nature* thanks I. Gutsche, M. Luo and the other anonymous reviewer(s) for their contribution to the peer review of this work.

Author contributions Y.S., T.N. and M.W. designed experiments. Y.S. purified NP and prepared specimen. Y.S. and M.W. collected cryo-EM data and reconstructed the 3D structure. Y.S. and H.M. built and refined the atomic model. Y.K. and T.N. provided Ebola viral genes and valuable advice. M.W. supervised the project. Y.S. wrote the initial draft and created all figures. Y.S. and M.W. wrote the paper with input from all other authors.

Competing interests The authors declare no competing interests.

Additional information
Extended data is available for this paper at https://doi.org/10.1038/s41586-018-0630-0.
Supplementary information is available for this paper at https://doi.org/10.1038/s41586-018-0630-0.
Reprints and permissions information is available at http://www.nature.com/reprints.
Correspondence and requests for materials should be addressed to M.W.
Publisher's note: Springer Nature remains neutral with regard to jurisdictional claims in published maps and institutional affiliations.

© 2018 Springer Nature Limited. All rights reserved.

METHODS

Purification of the Ebola NP–RNA complex. Human embryonic kidney 293T cells (tested mycoplasma-free, authenticated by DNA fingerprinting and obtained from Kawaoka Lab at Institute of Medical Science, University of Tokyo) were transfected with a plasmid encoding truncated nucleoprotein (NP residues 1–450) of Zaire ebolavirus (strain Mayinga-76, GenBank code AF499101), the type species of the genus Ebolavirus[31]. Three days after transfection, cells were rinsed with Tris-HCl buffer (10 mM Tris-HCl (pH 7.8), 150 mM NaCl, 1 mM EDTA), and lysed with 0.1% Nonidet P-40 in buffer supplemented with a protease inhibitor (Roche) and an RNase inhibitor (Promega). The lysate was centrifuged at 20,000*g* at 4 °C for 10 min to remove insoluble compounds. Supernatant was loaded onto a discontinuous 25–40% (wt/wt) CsCl gradient and centrifuged at 250,000*g* at 4 °C for 1 h. Absorbance of fractions at 280 nm was measured, and peak fractions were subjected to centrifugation at 200,000*g* at 4 °C for 30 min. The pellet was suspended in the buffer and stored at 4 °C.

Cryo-EM specimen preparation. Two microlitres purified NP–RNA complex solution at protein concentration of 0.3 mg ml^{-1} was applied to C-Flat CF-1.2/1.3-4C grids (Protochips), previously treated with H_2/O_2 plasma (Gatan Solarus). Grids were blotted on a Vitrobot Mark IV (Thermo Fisher Scientific) before plunge freezing in liquid ethane.

Cryo-electron microscopy. Images of the liquid nitrogen-cooled sample were acquired on a Titan Krios cryo-TEM (Thermo Fisher Scientific) equipped with an energy filter (Gatan Quantum 968) at 300 kV in EFTEM nanoprobe mode. Data were acquired automatically as movies with the Leginon System[32] on a K2 Summit detector (Gatan). For details, see Extended Data Table 1.

Image processing. Super-resolution movie frames were 2× Fourier-cropped, gain-normalized, aligned, dose-weighted and summed using MOTIONCOR2[33]. Helices were manually traced with E2HELIXBOXER[32]. Subsequent helical image processing steps were performed with SPRING[34] and RELION 2.1[35,36]. Defocus values were estimated with CTFFIND4[37]. Classes with visual details were selected after two rounds of 2D classification in RELION 2.1. Helical symmetry parameters (helical pitch and subunits per turn) were exhaustively explored by multiple real-space correlation searches with the program SEGCLASSRECONSTRUCT of the software package SPRING[34]. The search provided many correlation peaks corresponding to various combinations of parameters. Then, 3D classification in RELION 2.1 was performed with symmetry search around the respective peaks (search range for pitch ± 10%, rotation ± 0.6 subunits per turn). Eighty-eight per cent of the segments fell into three of four classes with nearly identical helical symmetry and yielded reasonable reconstructions at high resolution. These three classes were combined and submitted to further 3D refinement with an additional symmetry search (resulting in no significant change in helical symmetry). The helical symmetry parameter converged to pitch = 73.56 Å, 24.44 subunits per turn (rise = 3.01 Å, rotation = 14.73°). A SPIDER[38]-generated cylinder-shaped electron density map was used as an initial alignment reference for 3D classification and refinement in RELION 2.1. The resolution estimate of the final reconstruction was based on Fourier shell correlation (FSC) between independently refined half sets using the high-resolution noise substitution method[39] and a soft-edged mask. Local resolution was calculated with RELION 2.1. The locally-sharpened map was normalized with MAPMAN[40]. Detailed image processing conditions are listed in Extended Data Table 1.

Atomic model building and refinement. Atomic modelling of the NP 1−450 helix used template-based and de novo structure modelling. First, a previously reported crystal structure of Ebola NP residues 38−385 (PDB: 4YPI)[8] served as the initial model and was docked as a rigid body into our 3.6 Å-resolution cryo-EM map. Next, N- and C-terminal residues of NP, and RNA nucleotides, were added, and the model was adjusted manually with COOT[41]. The RNA was built de novo with COOT. During manual model building, stereochemistry of peptide bonds was monitored using a Ramachandran plot[42]. N- and C-terminal residues 1−18 and 407−450 were not modelled owing to a lack of interpretable map features, although the highly flexible disordered C-terminal region was recognizable in 2D class-average images (Extended Data Fig. 1c). The model was refined including data to 3.6 Å resolution with phenix.real_space_refine[43] in the presence of 8 surrounding subunits including an extended RNA strand. Secondary structure elements for protein and base-pair stacking for RNA were estimated by phenix.secondary_structure_restraints[43], and used as restraints for the refinement. The model was validated with MolProbity[44]. The unambiguous assignment of nucleic acid density in our map represents an independent element of map validation. Detailed conditions of model refinement and validation are given in Extended Data Table 1. The electron potential map and atomic model were visualized with UCSF Chimera and ChimeraX[45,46].

Statistics and reproducibility. Data collection and atomic model statistics are listed in Extended Data Table 1. The method at the core of this work is cryo-EM and single particle analysis. The reconstruction was assembled from a total number of 117,552 single particle images. These images represent projections of a common 3D object (the NP–RNA complex) and were averaged in three dimensions to result in the present reconstruction. The process used two independent sets, each containing half the number of images. These half-set reconstructions were compared to each other using a FSC, which measures the degree of correspondence as a function of resolution. Using the established criterion for resolution measurement (FSC = 0.143 for independent datasets), the two half-set reconstructions agreed up to a spatial resolution of 3.6 Å.

Reporting Summary. Further information on research design is available in the Nature Research Reporting Summary linked to this paper.

Data availability

The cryo-EM map of the Ebola NP–RNA complex was deposited in the Electron Microscopy Data Bank with accession number EMD-6903. The atomic coordinates were deposited in the PDB with accession number 5Z9W.

31. Watanabe, S., Noda, T. & Kawaoka, Y. Functional mapping of the nucleoprotein of Ebola virus. *J. Virol*. **80**, 3743–3751 (2006).
32. Suloway, C. et al. Automated molecular microscopy: the new Leginon system. *J. Struct. Biol*. **151**, 41–60 (2005).
33. Zheng, S. Q. et al. MotionCor2: anisotropic correction of beam-induced motion for improved cryo-electron microscopy. *Nat. Methods* **14**, 331–332 (2017).
34. Desfosses, A., Ciuffa, R., Gutsche, I. & Sachse, C. SPRING—an image processing package for single-particle based helical reconstruction from electron cryomicrographs. *J. Struct. Biol*. **185**, 15–26 (2014).
35. He, S. & Scheres, S. H. W. Helical reconstruction in RELION. *J. Struct. Biol*. **198**, 163–176 (2017).
36. Scheres, S. H. Processing of structurally heterogeneous cryo-EM data in RELION. *Methods Enzymol*. **579**, 125–157 (2016).
37. Rohou, A. & Grigorieff, N. CTFFIND4: Fast and accurate defocus estimation from electron micrographs. *J. Struct. Biol*. **192**, 216–221 (2015).
38. Frank, J. et al. SPIDER and WEB: processing and visualization of images in 3D electron microscopy and related fields. *J. Struct. Biol*. **116**, 190–199 (1996).
39. Chen, S. et al. High-resolution noise substitution to measure overfitting and validate resolution in 3D structure determination by single particle electron cryomicroscopy. *Ultramicroscopy* **135**, 24–35 (2013).
40. Kleywegt, G. J. et al. The Uppsala electron-density server. *Acta Crystallogr. D* **60**, 2240–2249 (2004).
41. Emsley, P., Lohkamp, B., Scott, W. G. & Cowtan, K. Features and development of Coot. *Acta Crystallogr. D* **66**, 486–501 (2010).
42. Ramachandran, G. N., Ramakrishnan, C. & Sasisekharan, V. Stereochemistry of polypeptide chain configurations. *J. Mol. Biol*. **7**, 95–99 (1963).
43. Adams, P. D. et al. PHENIX: a comprehensive Python-based system for macromolecular structure solution. *Acta Crystallogr. D* **66**, 213–221 (2010).
44. Chen, V. B. et al. MolProbity: all-atom structure validation for macromolecular crystallography. *Acta Crystallogr. D* **66**, 12–21 (2010).
45. Pettersen, E. F. et al. UCSF Chimera—a visualization system for exploratory research and analysis. *J. Comput. Chem*. **25**, 1605–1612 (2004).
46. Goddard, T. D. et al. UCSF ChimeraX: meeting modern challenges in visualization and analysis. *Protein Sci*. **27**, 14–25 (2018).
47. Larkin, M. A. et al. Clustal W and Clustal X version 2.0. *Bioinformatics* **23**, 2947–2948 (2007).
48. Robert, X. & Gouet, P. Deciphering key features in protein structures with the new ENDscript server. *Nucleic Acids Res*. **42**, W320–W324 (2014).
49. Brasseur, R. Differentiation of lipid-associating helices by use of three-dimensional molecular hydrophobicity potential calculations. *J. Biol. Chem*. **266**, 16120–16127 (1991).

© 2018 Springer Nature Limited. All rights reserved.

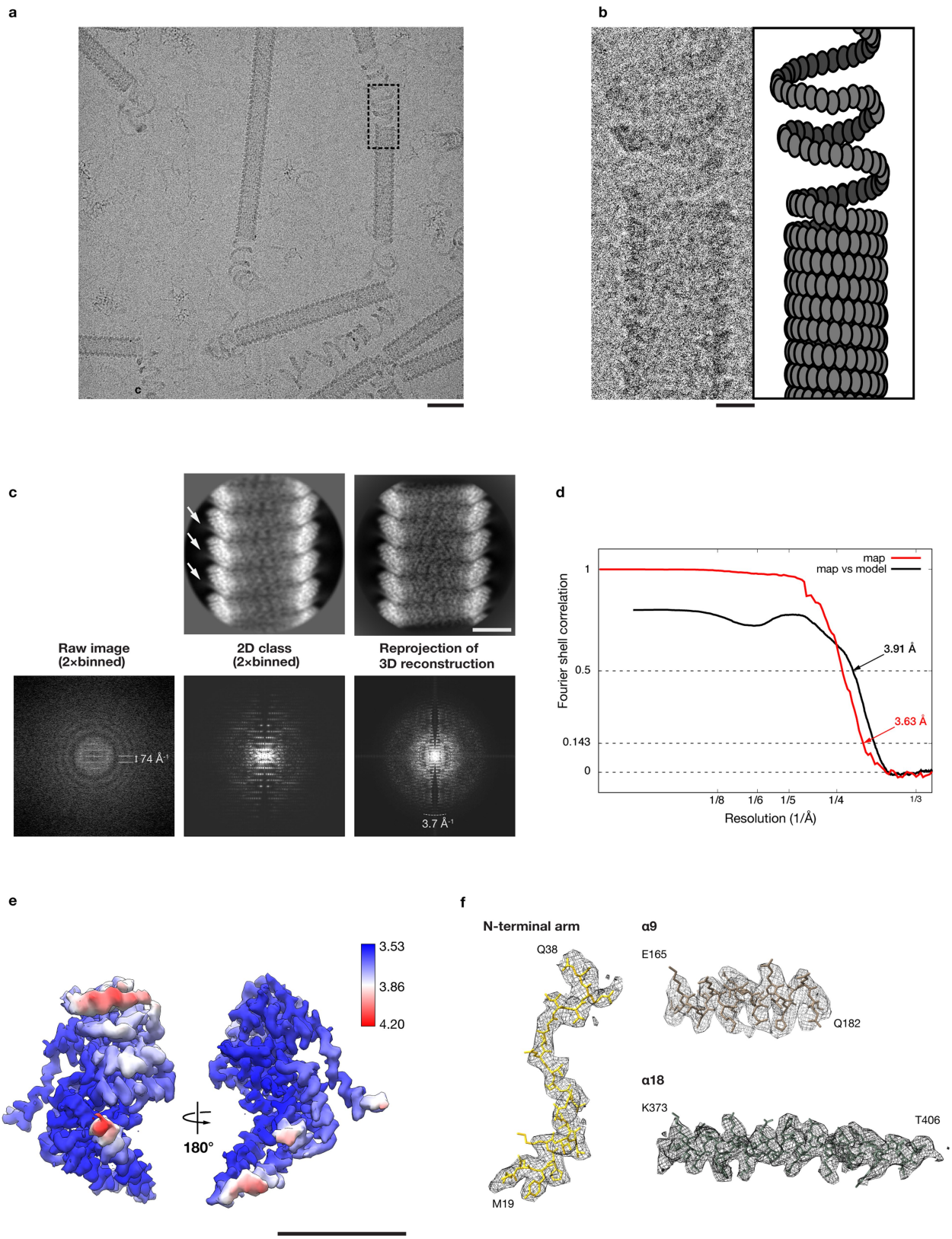

Extended Data Fig. 1 | See next page for caption.

© 2018 Springer Nature Limited. All rights reserved.

Extended Data Fig. 1 | Cryo-EM analysis and atomic model building of NP 1—450. a, One representative image of 2,467 digital micrographs showing NP helices in amorphous ice. The dashed box depicts the close-up in **b**. **b**, Magnified image from **a**, and a schematic of the interface between the ordered helical array and the uncoiled protein–RNA strand (right). **c**, Two-dimensional class-average image from ~9,000 aligned segmented projections (top, middle), back-projection from the 3D reconstruction (top, right) and their corresponding power spectra (below). The left-most power spectrum is the squared Fourier transform of the vertically aligned longest-helix image from the digital micrograph in **a**. Blurry disordered C-terminal regions are visible in the class-average image, protruding radially outward (arrows). Power spectra of the helix image and the class average are twofold binned (Nyquist limit at edge: 5.56 Å). All contain visible layer lines. The highest-resolution layer line in the unbinned power spectrum extends to 3.7 Å. **d**, FSC from independently refined datasets indicates overall map resolution of 3.63 Å (FSC = 0.143) (red curve), which is validated by the cross-FSC between cryo-EM map and model-generated electron-density map (black curve, 3.91 Å at FSC = 0.5). **e**, Local-resolution map. **f**, Parts of the cryo-EM electron potential map superimposed upon the atomic model of the N-terminal arm, α9, and C-terminal α18. All maps are contoured at 2.5σ above average. The map was sharpened with a *B*-factor of −100 Å^2. Scale bars, 500 Å in **a**; 50 Å in **b**, **c**, **e**.

© 2018 Springer Nature Limited. All rights reserved.

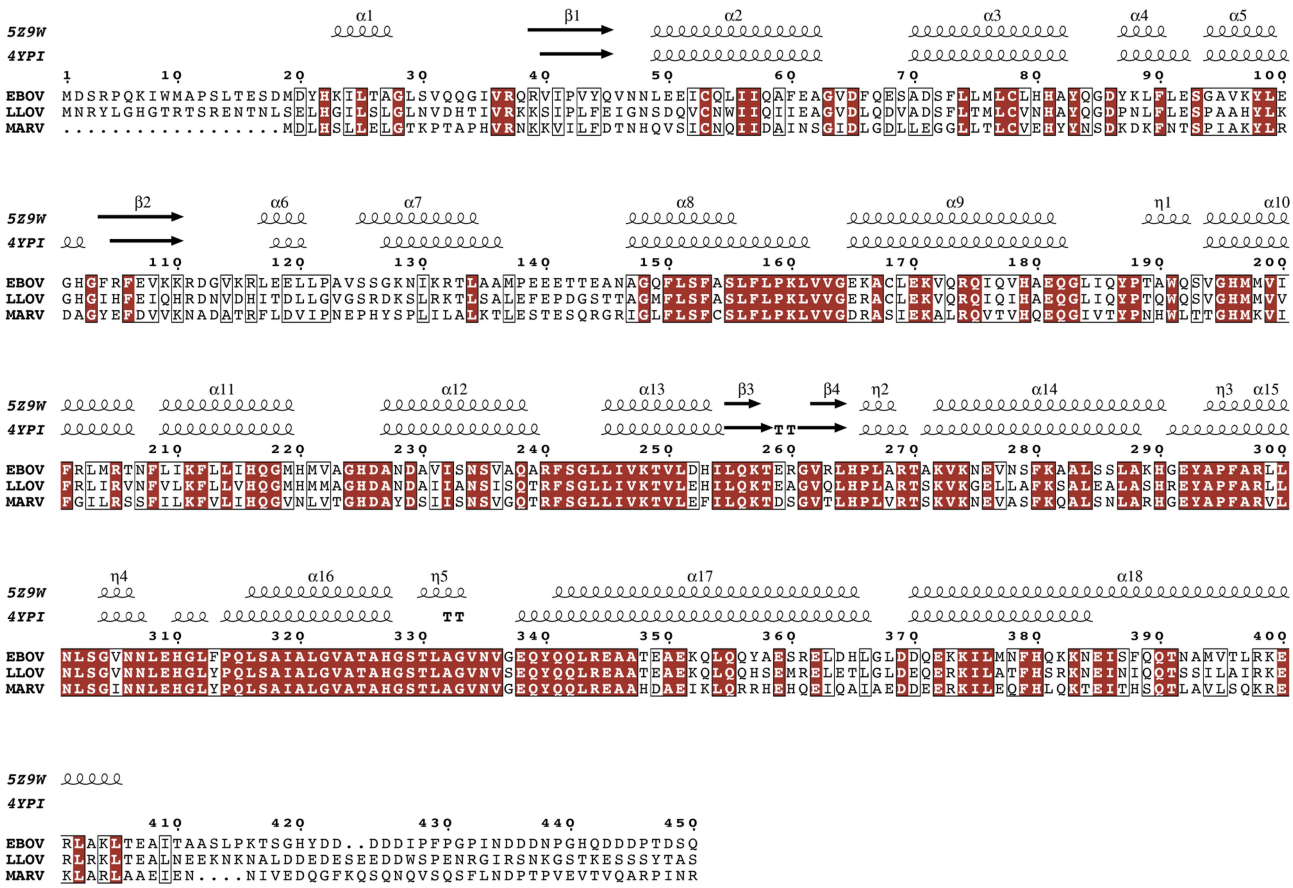

Extended Data Fig. 2 | Secondary structure assignment of Ebola viral NPs aligned with filovirus NPs. The secondary structure assignments from our atomic model of NP 19–406 (PDB: 5Z9W) in the presence of RNA, and the crystal structure of monomeric RNA-free NP 38–385 (PDB: 4YPI) are depicted at the top and second row, respectively. Sequence alignment of nucleoproteins from Zaire ebolavirus (EBOV), Lake Victoria marburgvirus (MARV), and Lloviu cuevavirus (LLOV) (UniProt: P18272, P35263 and G8EFI1) was performed with ClustalW2.1[47]. Conserved and similar residues are boxed in red and white, respectively. The figure was prepared with phenix.secondary_structure_restraints[43] and ESPript3.1[48].

© 2018 Springer Nature Limited. All rights reserved.

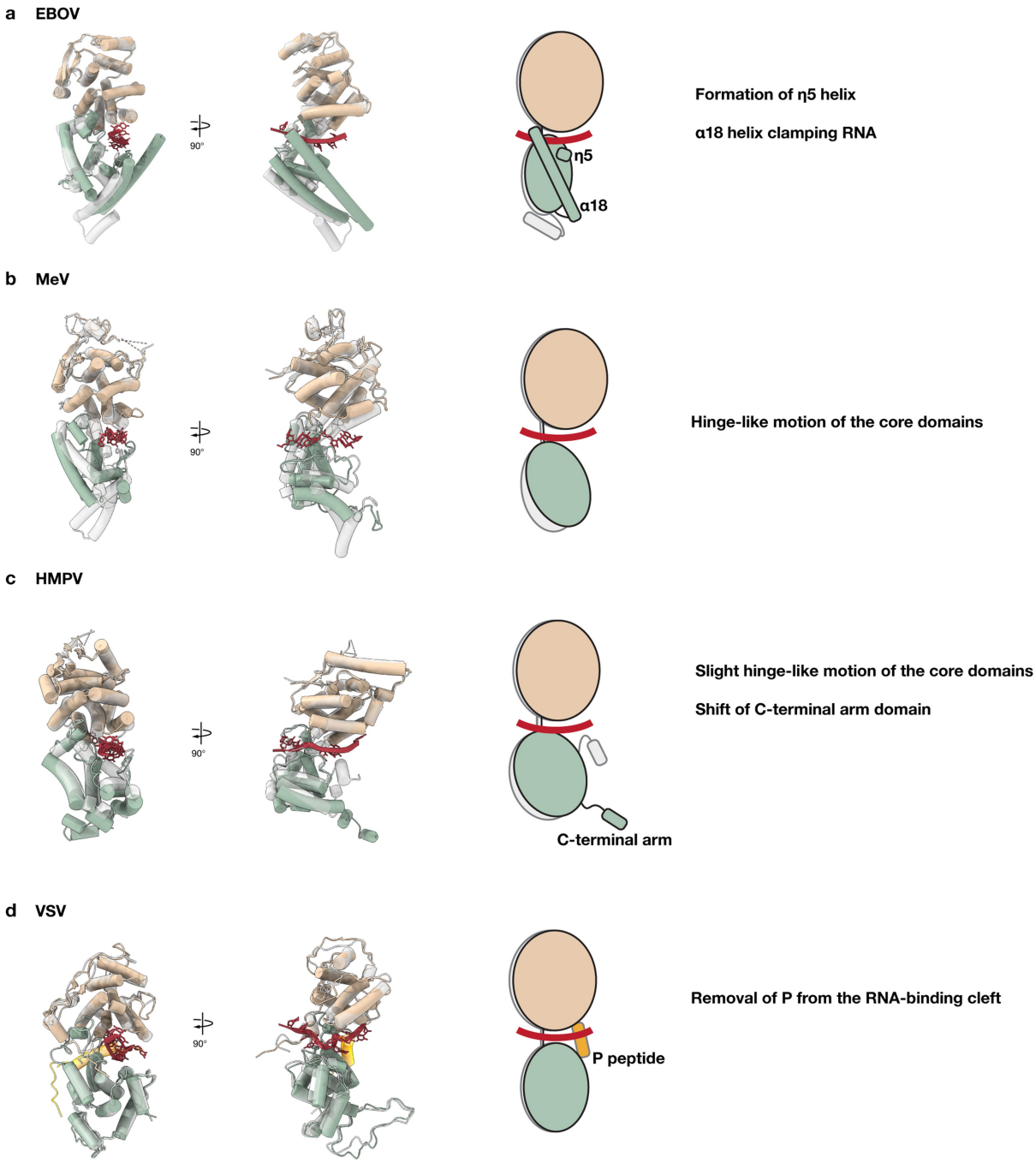

Extended Data Fig. 3 | Conformational changes upon RNA binding of nucleoproteins (NP or N) chaperoned by phosphoproteins (VP35 or P) in the order *Mononegavirales*. Structures were rendered in ribbon and tube representations (α-helices) based on their atomic coordinates. Only core domains (N- and C-terminal lobes, beige and green) and RNA (red) are shown, with the exception of P in vesicular stomatitis virus (VSV, orange). The two models were aligned relative to the N-terminal lobe. Schematic and summary on the right. The monomeric, RNA-free state (grey) is superimposed on the RNA-bound oligomeric state (colour). **a**, Ebola virus (EBOV) (NP-VP35, PDB: 4YPI[8]; NP–RNA, PDB: 5Z9W, this study) in the family *Filoviridae*. **b**, **c**, Measles virus (MeV) (N–P, PDB: 5E4V[14]; N–RNA, PDB: 4UFT[13]) (**b**) and human metapneumovirus (HMPV) (N–P, PDB: 5FVD; N–RNA, PDB: 5FVC)[12] (**c**) in the family *Paramyxoviridae*. **d**, VSV (N–P, PDB: 3PMK[16]; N–RNA, PDB: 2GIC[12]) in the family *Rhabdoviridae*.

© 2018 Springer Nature Limited. All rights reserved.

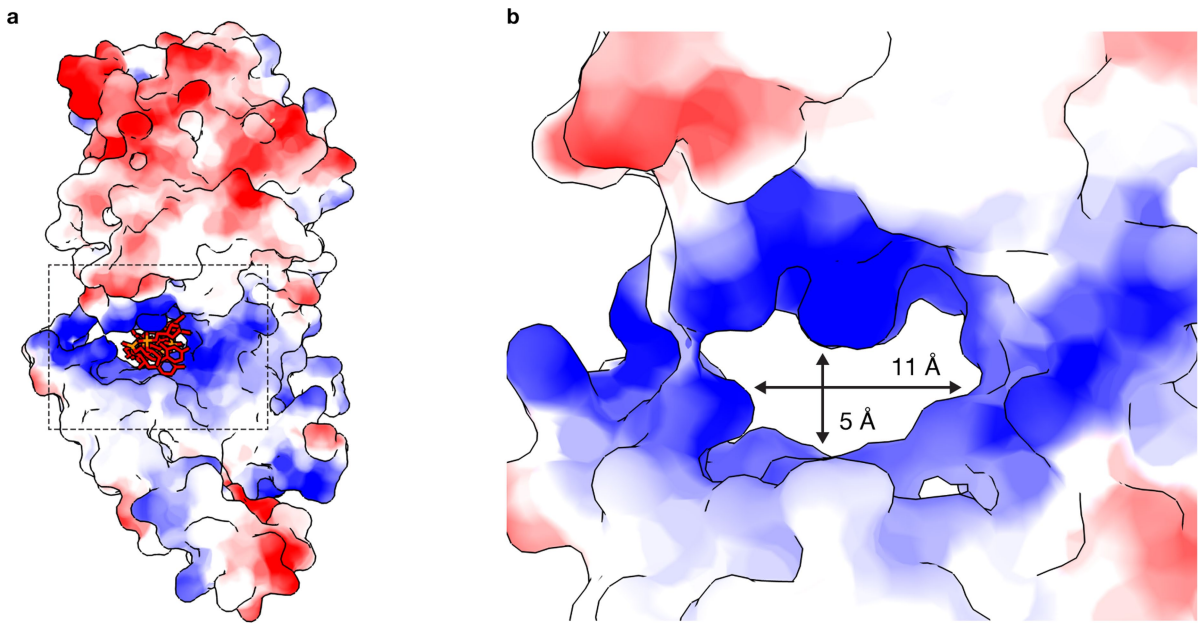

Extended Data Fig. 4 | NP–RNA interactions. a, Electrostatic surface surrounding the RNA cleft. Scale ranging from −10 (red) to +10 kcal mol^{-1} e^{-1} (blue), calculated from the atomic model of our NP monomer (PDB: 5Z9W). **b**, Close-up view with dimensions of the cleft shown in **a** without showing the RNA.

© 2018 Springer Nature Limited. All rights reserved.

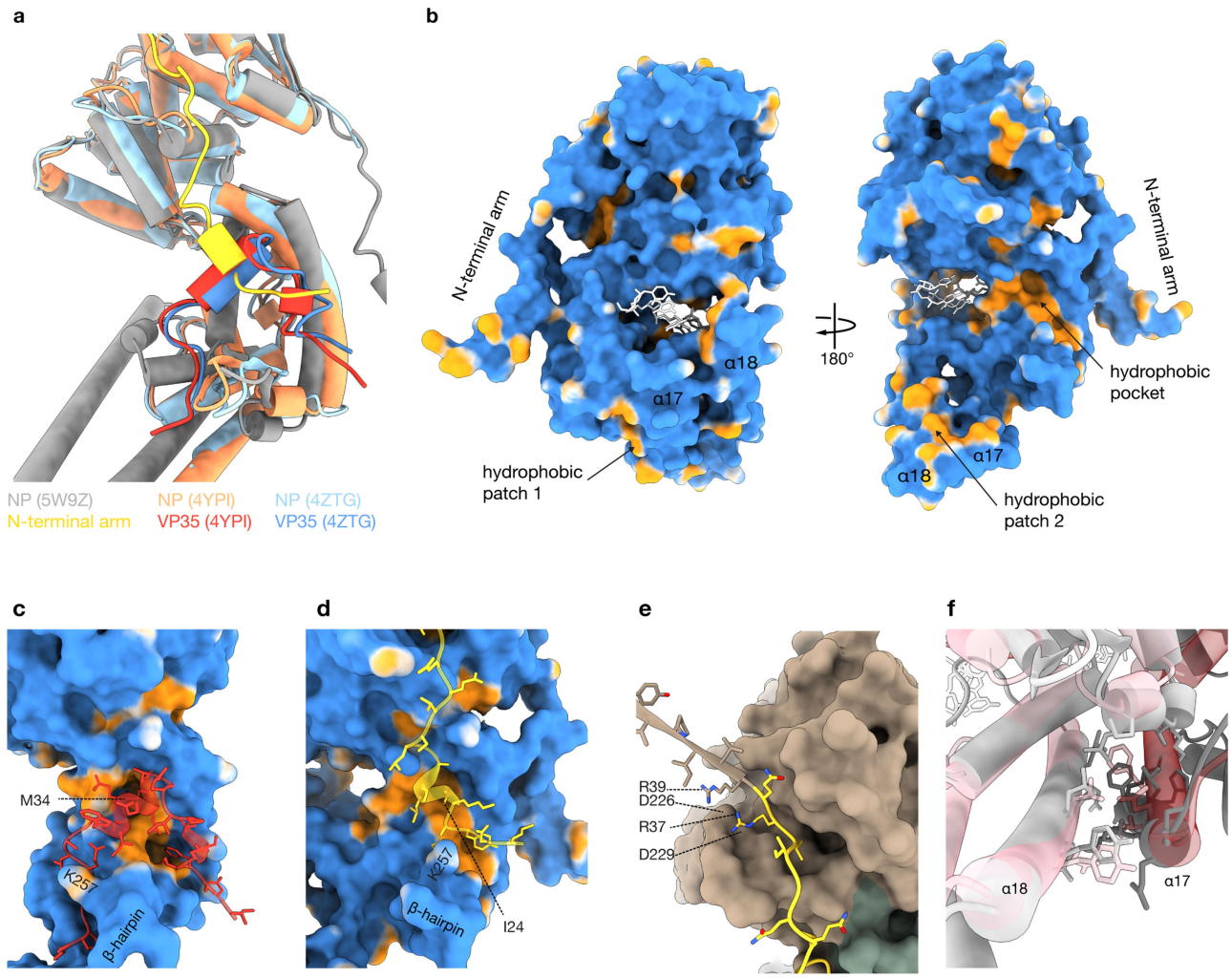

Extended Data Fig. 5 | Intrastrand NP–NP interactions. a, Comparison of NP structures. The VP35-bound, RNA-free monomeric state (PDB: 4YPI, orange and red, and 4ZTG, sky blue and blue) and the RNA-bound oligomeric state (PDB: 5Z9W, grey and yellow) were aligned relative to the whole polypeptide. VP35 and the N-terminal arm bind to the same hydrophobic pocket. **b**–**d**, Molecular lipophilicity potential maps (MLPP, Brasseur method[49]) of our structure (PDB: 5Z9W), coloured blue (hydrophilic) to orange (hydrophobic). **c**, A close-up of VP35-bound NP. **d**, A close-up of NP bound by the N-terminal arm. **e**, The contact region of the N-terminal arm and the N-terminal lobe of two adjacent NPs. **f**, A comparison of two adjacent NPs in the NP–RNA complex (PDB: 5Z9W, pink and red) and NP crystal packing (PDB: 4YPI). The two models were aligned relative to α17.

© 2018 Springer Nature Limited. All rights reserved.

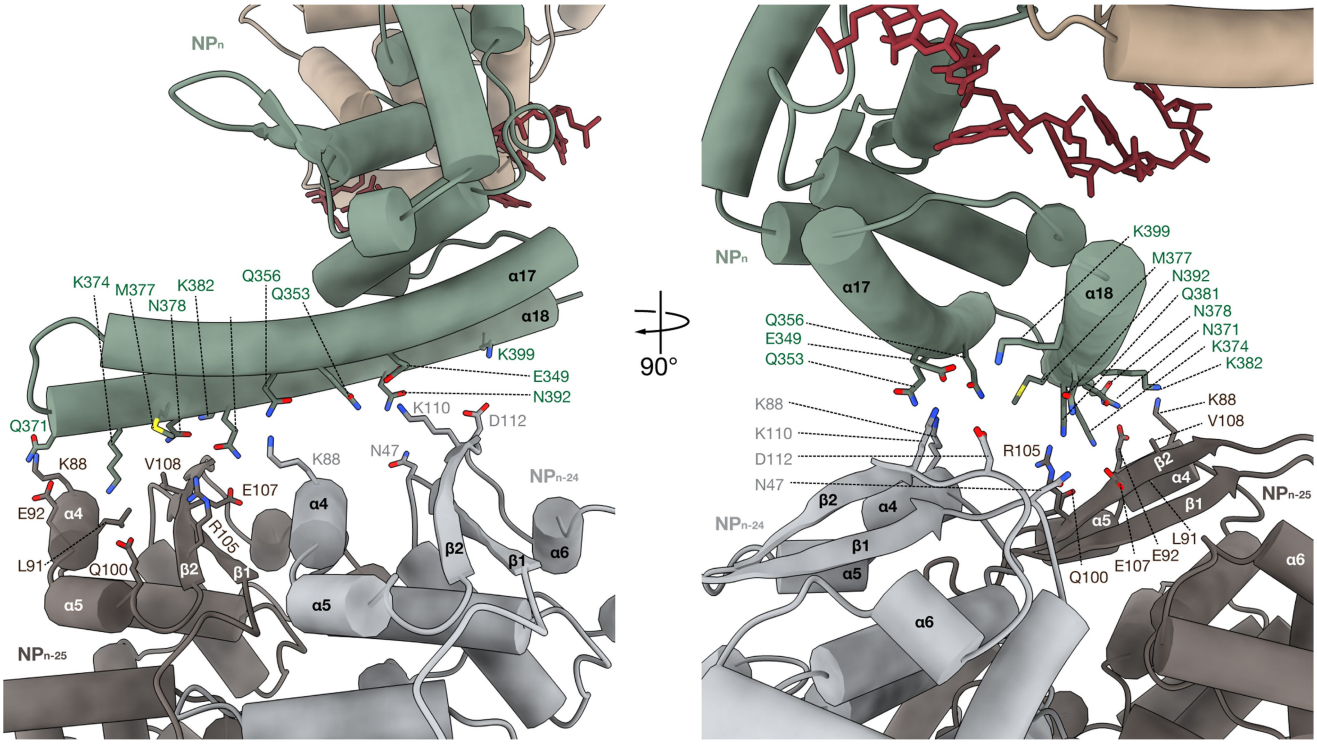

Extended Data Fig. 6 | Interstrand NP–NP interface. A close-up of the interstrand NP–NP interface shared among NP_n, NP_{n-24} and NP_{n-25} subunits. Amino acid side chains within a distance of ≤ 6 Å between NP_n and NP_{n-25} and between NP_n and NP_{n-24} are shown with their labels.

© 2018 Springer Nature Limited. All rights reserved.

a

	NP 1-450 Sugita *et al.*	NP 1-450 Wan *et al.*	NP wt in virion Wan *et al.*	NP 25-457 Su *et al.*
Sample preparation				
Expression	Mammalian cells	Mammalian cells	Mammalian cells	*E. coli*
Assembly	*In vivo* (cytoplasm)	*In vivo* (cytoplasm)	*In vivo* (cytoplasm)	*In vitro*
Fixation	–	Paraformaldehyde	Paraformaldehyde	–
NP residues	1-450	1-450	1-739	25-457
Structural data				
EMDB code	EMD-6903	EMD-3869	EMD-3873	EMD-7343
Map resolution (Å)	3.6	6.6	9.1 to 13.1	5.8
PDB code	5W9Z	6EHL	6EHM	6C54
Helical configuration				
Pitch (Å)	73.6	71 ± 1	74 ± 1	112
Subunits per turn	24.4	25.3 to 28.3	23.8 or 25.8	42.2
Asymmetric unit	Monomer	Monomer	Monomer	Heterodimer
Handedness	Left handed	Left handed	Left handed	Left handed
Inner diameter (Å)	≈ 175	161 ± 8*	189 ± 17*	≈ 330
NP-NP binding	N-terminal arm – pocket	N-terminal arm – pocket	N-terminal arm – pocket	C-terminus – pocket
EM density				
RNA	+	+	+	–
N-terminal arm	+	+	+	–

* Calculated from the tomograms of EMD-3870 and EMD-3874

b

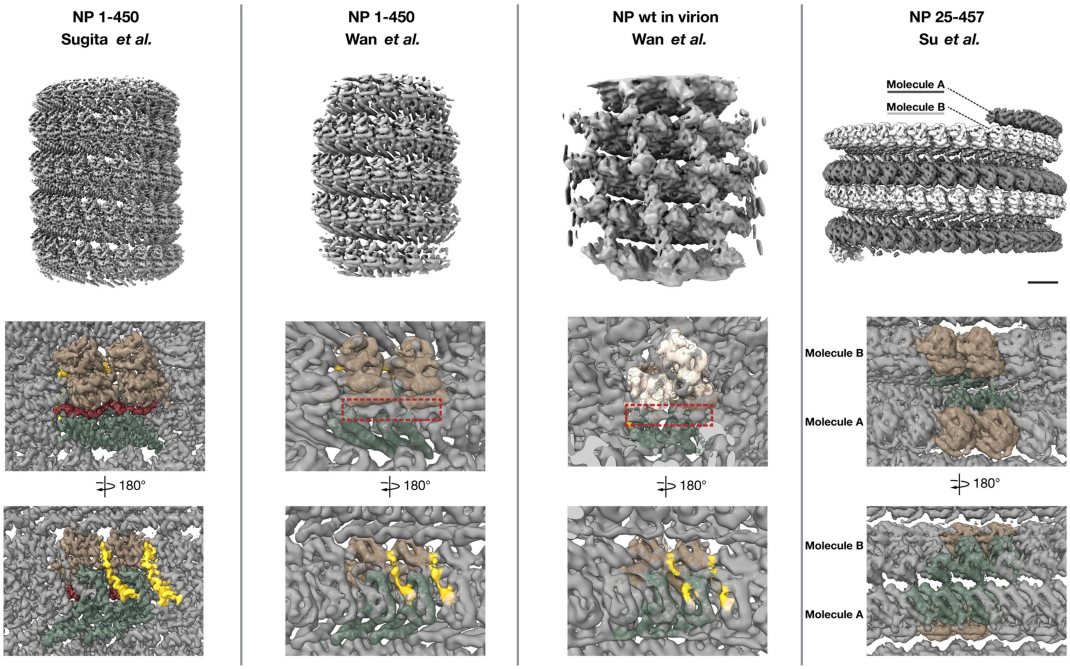

c

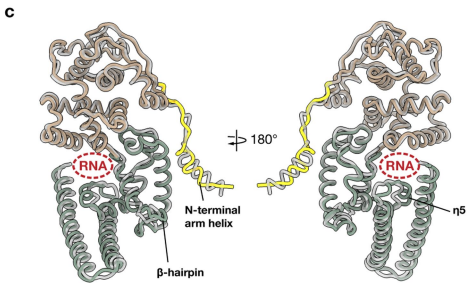

Extended Data Fig. 7 | Structural comparison of the currently available NP assemblies. a, Summary of the comparison among reported NP structures. **b**, Overall and close-up iso-potential surface views of helical NP assemblies (NP 1−450 by our study, NP 1−450 and nucleocapsid in virion[5] and NP 25−457[28]). Experimental cryo-EM maps were normalized and contoured at 2.5σ, 2.5σ, 2.0σ and 2.5σ above average, respectively. Two adjacent NP subunits are coloured according to the assignment in Fig. 1, using their corresponding atomic models within 4 Å distance (PDB: 5Z9W, 6EHL, 6EHM and 6C54). The approximate location of RNA is indicated by red dashed boxes. VP24 in the virus reconstruction is coloured in white (density is clipped at higher radius to reveal the RNA). Scale bar, 500 Å. **c**, Comparison between NP 1−450 structures from our study (coloured) and ref. [5] (grey). The structures agree in their overall fold. However, the course of the backbone deviates in regions with poor density—in particular, at the N terminus, the β-hairpin and around the RNA interface. The 3_{10} helix η5, which had not previously been described, is missing. Root mean square deviation (calculated with UCSF Chimera) among all 387 atoms pairs is 1.97 Å.

© 2018 Springer Nature Limited. All rights reserved.

Extended Data Table 1 | Cryo-EM data collection, refinement and validation statistics

	Ebola viral nucleoprotein 1-450 (EMDB-6903) (PDB 5Z9W)
Data collection and processing	
Magnification	105,000
Voltage (kV)	300
Electron exposure (e–/Å^2)	105
Defocus range (μm)	-0.8 to -4.0
Pixel size (Å)	1.39
Symmetry imposed	Yes
Initial particle images (no.)	232,490
Final particle images (no.)	117,552
Map resolution (Å)	3.63
FSC threshold	0.143
Map resolution range (Å)	3.51 to 5.67
Refinement	
Model resolution (Å)	3.91
FSC threshold	0.5
Map sharpening *B* factor (Å^2)	-100
Model composition	
Non-hydrogen atoms	3177
Protein residues	388
B factors (Å^2)	
Protein	99
R.m.s. deviations	
Bond lengths (Å)	0.006
Bond angles (°)	1.07
Validation	
MolProbity score	1.26
Clashscore	1.1
Poor rotamers (%)	0
Ramachandran plot	
Favored (%)	93.01
Allowed (%)	6.99
Disallowed (%)	0

© 2018 Springer Nature Limited. All rights reserved.

TECHNOLOGY FEATURE

TAPPING INTO THE BRAIN'S STAR POWER

No longer just 'brain glue', astrocytes are coming to the fore as a broadening toolset reveals the cells' complexity and diversity.

RACHEL KIM

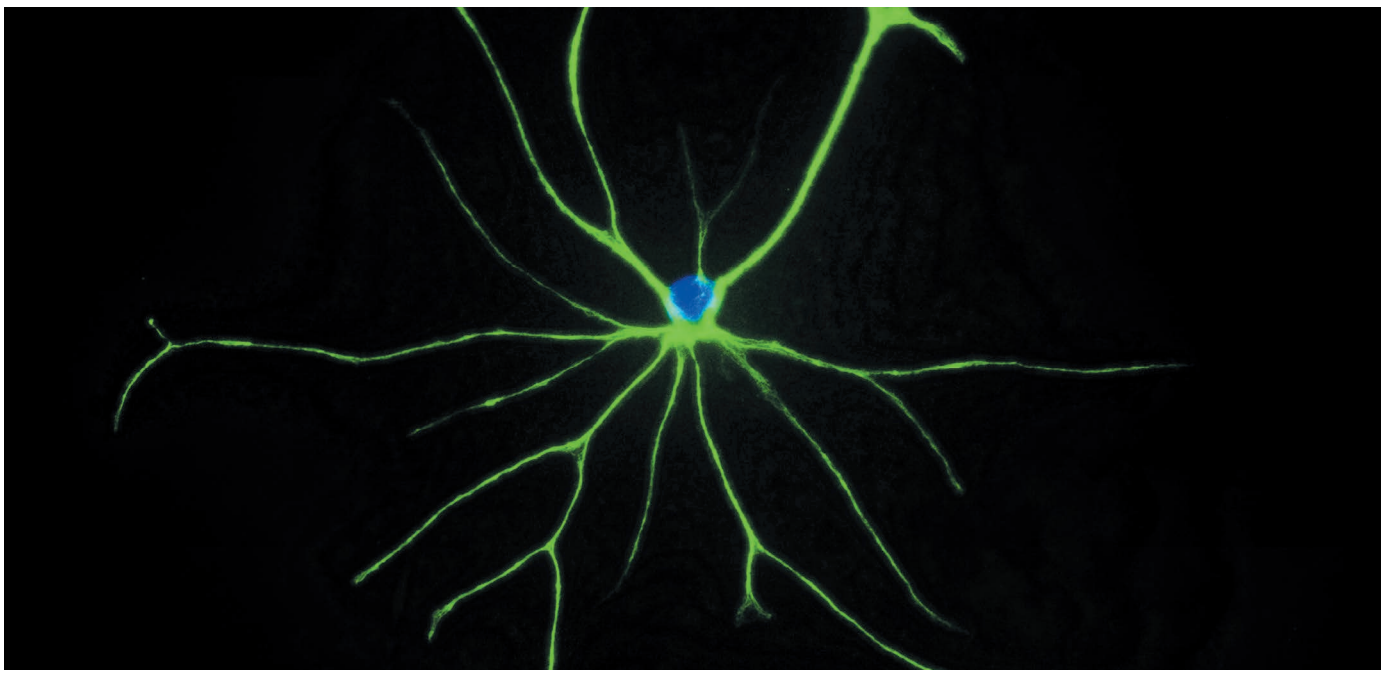

An astrocyte from a rat pup that was investigated using a technique known as immunopanning.

BY ESTHER LANDHUIS

In the mid-1850s, German anatomist Rudolf Virchow and others examining brains under the microscope noticed mysterious structures filling the space around and between the neurons that held their interest. Virchow dubbed these structures *nervenkitt*, literally 'nerve-glue', and translated as 'neuroglia'.

Today, researchers know that the *nervenkitt* are mostly astrocytes, representing 20–40% of all the cells in a mammalian brain. Yet for decades, the roles of these plentiful cells remained as mysterious as when Virchow first espied the structures.

Unlike neurons, astrocytes are electrically quiet, so their activity goes undetected by conventional electrophysiology methods. They're also astoundingly complex: a single astrocyte can connect to tens of thousands of neurons.

That's why "there hasn't been a set of tools with which we can probe these cells selectively and reliably throughout the brain", says Baljit Khakh, a neuroscientist at the University of California, Los Angeles (UCLA).

But Khakh and a growing number of researchers worldwide are starting to move past the field's neuron-centric focus to take a closer look at astrocytes. They are developing technologies to classify the cells into distinct subtypes with diverse roles and uncover how astrocytes support and shape neural circuits. The tools might even help researchers to engineer approaches for treating brain diseases.

SPOKES AND SNOWFLAKES

When stained with antibodies and viewed under a microscope, astrocytes resemble bicycle wheels — a big central cell body with half a dozen or so thick spokes radiating out, says Shane Liddelow, a neuroscientist at New York University. But when individual cells are injected with fluorescent dye, more structures become visible. These 'processes' branch off into ever-finer structures, like a 3D snowflake, Khakh says. The snowflakes wrap around every synapse in the brain, and some of the fine processes have bulb-like ends that surround blood vessels, forming a protective zone between brain tissue and vasculature.

Glossed over as mere support cells for more than a century, astrocytes actually have crucial roles in the brain. Researchers are probing these diverse functions with methods for sorting and growing the cells, as well as gene-delivery tools and optical techniques that track how the cells behave in circuits. These technologies are showing that astrocytes adjust their metabolic activities to control neurotransmitter levels, regulate extracellular potassium ions to influence thresholds for nerve-cell firing, and release molecules that promote the formation and pruning back of synapses. Astrocytes are "the major brain homeostat", says Khakh.

For Benjamin Deneen, early clues to that diversity emerged about a decade ago, while he was a postdoc at the California Institute of Technology (Caltech) in Pasadena. He and his co-workers were analysing spinal-cord ▶

© 2018 Springer Nature Limited. All rights reserved.

tissue from chicks and mice, and found that astrocytes exhibit spatial patterning[1]. That is, regional combinations of DNA-binding regulatory proteins called transcription factors determine when and which astrocyte subtypes are produced.

That got Deneen wondering about heterogeneity in the brain. But, unlike in the spinal cord, where patterning is well defined, each brain area seems to be subject to different rules.

Deneen, who now heads a lab at Baylor College of Medicine in Houston, Texas, turned to fluorescence-activated cell sorting (FACS). Using the technique in mice that had been genetically modified to express green fluorescent protein specifically in astrocytes, his team was able to subdivide the cells into five distinct but overlapping groups on the basis of their expression of three cell-surface proteins[2]. The researchers then used RNA sequencing to identify molecular signatures for each subpopulation.

In a separate study, Khakh and his colleagues isolated astrocytes from distinct brain circuits in the striatum and hippocampus of mice from the same strain. They used methods such as calcium imaging, mass spectrometry, immunohistochemistry, electron microscopy and RNA sequencing to probe cellular function, morphology and molecular features[3].

"Astrocytes in different parts of the brain are not the same," Khakh says. For example, in the hippocampus, they nestle closer to excitatory neural synapses and respond more robustly to the neurotransmitter glutamate than do those in the striatum. "This challenges the notion of the 'glue' because it suggests that astrocytes may be brain-area — or even neural-circuit — specific," says Khakh.

For its part, Deneen's group not only collected molecular data from FACS-isolated astrocyte subsets, but also screened for the presence of those cells in mouse models of brain cancer. The team identified populations that correlated with tumour progression and onset of seizures. "These populations could be used as an entry point for understanding diverse or malignant astrocyte identities and properties in disease," says Deneen.

PANNING FOR ASTROCYTES

The fastest, easiest method to grow astrocytes in cell culture was published in 1980 and has been a stalwart of research[4]. "Essentially, you mush up the brain, wait a couple of weeks, grow the cells in serum, shake off the top cells, and the ones left are astrocytes," says Liddelow. The protocol is fast and cheap, requires no special equipment, and produces hundreds of millions of cells.

But there are caveats to this 'MD astrocyte' method — named after its developers, Ken McCarthy at the University of North Carolina School of Medicine at Chapel Hill, and Jean de Vellis at UCLA. One is that when astrocytes grow in serum, they can start behaving quite differently from in the physiological resting state. Plus, Liddelow says, the method generates a fair

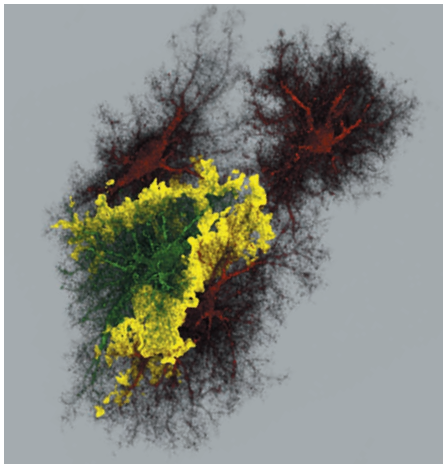

Astrocytes have a distinctive 3D branching shape.

NATIONAL CENTER FOR MICROSCOPY AND IMAGING RESEARCH, UCSD

number of precursor cells, which could be problematic depending on what researchers want to do with the cultures.

In 2011, a protocol known as immunopanning emerged from Ben Barres' lab at Stanford University in California[5]. The procedure first removes unwanted cells through a series of incubations on plates coated with antibodies to antigens that are present on the surfaces of those cells, and then isolates the astrocytes using antibodies that recognize a specific protein marker, known as integrin β-5. "We get serum-free, mature cells in a dish, and less than 1% contamination," says Liddelow, who uses the technique in his lab .

"Astrocytes in different parts of the brain are not the same."

Immunopanning requires about 6 hours hands-on time, compared with 2–3 hours for the MD protocol. But immunopanned cells can be used immediately, whereas the MD method requires another 3–4 weeks. Still, immunopanning is not always the best choice, Liddelow says. Its yield is about an order of magnitude lower than for the MD procedure. It is also more expensive because it uses purified growth factors rather than serum.

Liddelow and his colleagues have used immunopanned cells to identify two astrocyte subpopulations[6]. A1 astrocytes lose their ability to promote synapse formation, whereas A2 astrocytes upregulate neurotrophic factors. Consistent with those features, Liddelow's team found an abundance of A1 astrocytes in Alzheimer's, Huntington's and Parkinson's diseases, and in amyotrophic lateral sclerosis and multiple sclerosis, suggesting that A1 astrocytes contribute to cell death in neurodegenerative disorders.

LAB-GROWN ASTROCYTES

For Henrik Ahlenius, a group leader at Lund University in Sweden, astrocytes provide a handle for modelling Alzheimer's, frontotemporal dementia and other age-related diseases. But his research requires human astrocytes, which are larger and have more synapses than do mouse astrocytes. They are also harder to obtain.

"If you want to study disease progression or mechanisms in chronic brain diseases, it's very tricky to get a hold of the tissue," Ahlenius says. In the rare instances in which his team obtains cells from biopsies or post-mortem tissue, the samples are often hard to work with because they come from end-stage disease. In 2015, researchers in Italy showed how mouse astrocytes could be generated in the lab by culturing fibroblasts with three transcription factors — a process called direct conversion[7]. Ahlenius and his colleagues have since tested those molecules in human embryonic stem cells and found that two of them — NFIB alone or with SOX9 — yielded astrocytes with more than 90% purity in just one week, says Ahlenius[8].

These cells behave just like purified human astrocytes: they can take up and release glutamate; respond to growth factors and support synapses and express similar genes. They can also be used to model Alexander disease, a rare disorder of the nervous system. Ahlenius' team reported its method on *Nature*'s *Protocol Exchange*[8].

STELLAR GENE DELIVERY

To understand how astrocytes behave in both health and disease, researchers need tools with which to introduce genes reliably and specifically. To that end, Viviana Gradinaru's lab at Caltech has engineered vectors based on adeno-associated viruses (AAVs) that can deliver genes to the mouse brain after intravenous injection. These vectors allow researchers to dial up or down the number of cells that get labelled while maintaining high expression[9].

Ultimately, scientists want to study how astrocytes interact with neurons. Earlier this year, Khakh's team described a neuron–astrocyte proximity assay that could determine which of the tens of thousands of nearby synapses the astrocytes actually connected to[10]. "Without knowing what [a cell] can listen to, you're kind of looking around in the dark trying to determine what it might do in that setting," Khakh says.

The assay uses a technique called Förster resonance energy transfer, or FRET, to detect physical contacts between astrocytes and neurons that express fluorescent proteins on their surface. Using this method, and his lab's custom AAVs, Khakh's team examined how astrocytes wire with neural inputs in several diseases. In a mouse model of stroke, astrocytes labelled with these proteins seemed to expand their reach, whereas in animals modelling Huntington's disease, astrocytes retracted their processes and interacted with fewer synapses. Plasmid constructs and viral vectors from both Gradinaru and Khakh are available through the global non-profit plasmid repository, Addgene.

CIRCUIT DESIGN

Kira Poskanzer, a neuroscientist at the University of California, San Francisco, studies yet another aspect of astrocyte biology: how the

© 2018 Springer Nature Limited. All rights reserved.

cells respond to external signals. "One big push in our lab is to figure out which astrocytes are listening to which neurotransmitters," she says.

Poskanzer collaborates with analytical chemist Roberto Etchenique at the University of Buenos Aires, to design 'caged' compounds, in which neurotransmitters bind reversibly to chemical groups that restrict their interactions with other molecules in the cell. The compounds are light-sensitive, and will release the caged molecule when zapped with light of a particular wavelength.

The researchers have so far generated photo-activatable forms of the neurotransmitters glutamate, GABA and serotonin[11], and are developing a caged form of noradrenaline. "We're trying to build up an arsenal of tools so that we can 'play god' with the circuit," Poskanzer says — that is, photo-activate various neurotransmitters and watch how astrocytes respond.

Meanwhile, to probe what happens when astrocytes are silenced, Khakh's team has developed a method that uses a molecular pump to move calcium ions from the inside of the cell to the outside and thereby dampen astrocyte calcium signals in the mouse brain[12]. And his team is working with Loren Looger at Howard Hughes Medical Institute's Janelia Research Campus in Ashburn, Virginia, to develop sensors for ATP and other molecules released by astrocytes.

Such tools should help researchers to further tease apart the biology of the *nervenkitt*, and of the interconnected brain as a whole. The technologies are providing an "unparalleled appreciation of the richness and dynamics in how astrocytes contribute to the function of the brain as an organ", Khakh says. ■

Esther Landhuis *is a freelance science journalist based in the San Francisco Bay area, California.*

1. Hochstim, C., Deneen, B., Lukaszewicz, A. & Zhou, Q. *Cell* **133**, 510–522 (2008).
2. Lin, C.-C. J. *et al. Nature Neurosci.* **20**, 396–405 (2017).
3. Chai, H. *et al. Neuron* **95**, 531–549 (2017).
4. McCarthy, K. D. & de Vellis, J. *J. Cell Biol.* **85**, 890 (1980).
5. Foo, L. C. *et al. Neuron* **71**, 799–811 (2011).
6. Liddelow, S. A. *et al. Nature* **541**, 481–487 (2017).
7. Caiazzo, M. *et al. Stem Cell Rep.* **4**, 25–36 (2015).
8. Canals, I. *et al. Protoc. Exch.* https://doi.org/10.1038/protex.2018.088 (2018).
9. Challis, R. C. Preprint at bioRxiv https://doi.org/10.1101/246405 (2018).
10. Octeau, J. C. *et al. Neuron* **98**, 49–66 (2018).
11. Cabrera, R. *et al. ACS Chem. Neurosci.* **8**, 1036–1042 (2017).
12. Yu, X. *et al. Neuron* **99**, 1170–1187 (2018).

NEUROSCIENCE

Web service makes big data available to neuroscientists

NeuroData allows researchers to explore terabytes of brain images in multiple formats.

BY JEFFREY M. PERKEL

Randal Burns recalls that the brain-science community was "abuzz" in 2011. Burns, a computer scientist at Johns Hopkins University in Baltimore, Maryland, was focusing on astrophysics and fluid dynamics data management at the time. But he was intrigued when Joshua Vogelstein, a neuroscientist and colleague at Johns Hopkins, told him that the first large-scale neural-connectivity data sets had just been collected and asked for his help to present them online.

"It was the first time that you had data of that quality, at that resolution and scale, where you had the sense that you could build a neural map of an interesting portion of the brain," says Burns.

Vogelstein worked with Burns to build a system that would make those data — 20 trillion voxels' worth — available to the larger neuroscience community. The team has now generalized the software to support different classes of imaging data and describes the system this week (J. T. *Vogelstein et al. Nature Meth.* **15**, 846-847; 2018).

NeuroData is a free, cloud-based collection of web services that supports large-scale neuroimaging data, from electron microscopy to magnetic resonance imaging and fluorescence photomicrographs.

Key to its functionality, Vogelstein says, is the spatial database bossDB, which allows researchers to retrieve images of any section of the brain, at any resolution, and in several standard formats. Users can then explore those data using a tool known as Neuroglancer. As they navigate the images, the URL changes to reflect their specific view, allowing them to share particular visualizations with their colleagues. "These links become a core part of the way in which we communicate and pass data back and forth to one another," says Forrest Collman, a neuroscientist at the Allen Institute for Brain Science in Seattle, Washington, and a co-author of the paper.

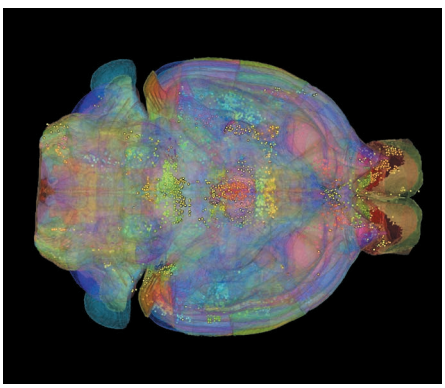

J. T. VOGELSTEIN *ET AL.*

Neuroimaging data sets contain vast amounts of information.

But data browsing "is not where the science happens", Burns says. "The science happens by doing a statistical analysis of the images." To that end, NeuroData also includes tools for machine learning, image analysis and 3D volume rendering.

More than 100 public and private data sets have been deposited, Vogelstein says. Two of those came from Nelson Spruston, a neuroscientist at the Howard Hughes Medical Institute Janelia Research Campus in Ashburn, Virginia, who assembled 2D images into 3D brain reconstructions that are several terabytes in size. Because it can take weeks to upload that much data, Spruston's team actually gave the information to NeuroData on a physical hard drive — an anachronistic, if practical solution.

Erik Bloss, a neuroscientist in Spruston's laboratory, compiled those data sets to study neural synapses in the hippocampus. But researchers could mine the same data to, for instance, quantify the branching of neural arbors or the density of neural spines, Spruston says. "There's all kinds of information in those data sets that in principle other people might be interested in," he says. ■

CORRECTION

The Toolbox article 'AI tames the scientific literature' (*Nature* **561**, 273–274; 2018) erroneously referred to the CORE repository by its old name, Connecting Repositories.

© 2018 Springer Nature Limited. All rights reserved.

TOOLBOX

BY JUPYTER, IT ALL MAKES SENSE

Thanks to an improved interface and tools for running in the cloud, take-up of this computational notebook is rocketing.

ILLUSTRATION BY THE PROJECT TWINS

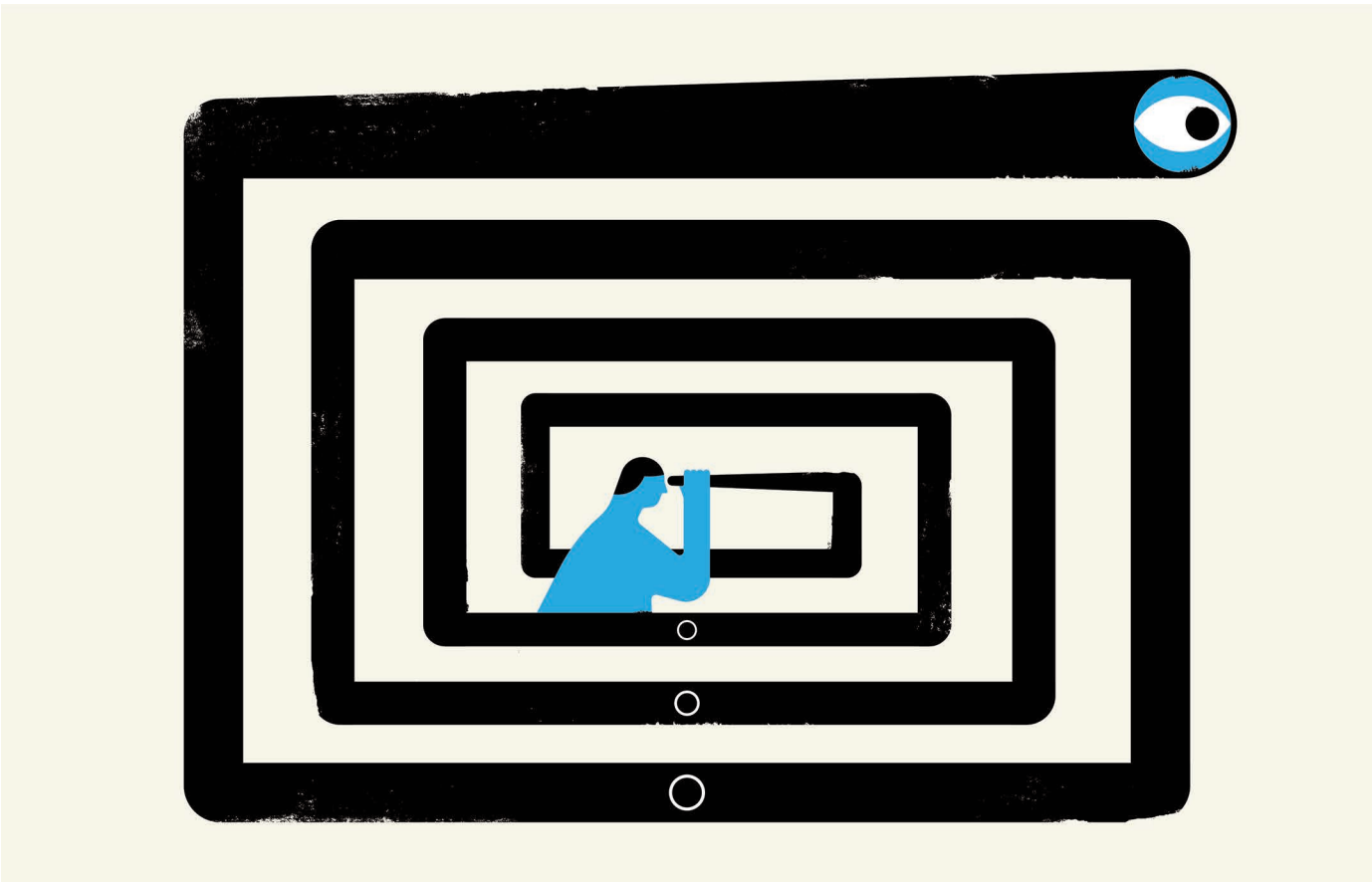

BY JEFFREY M. PERKEL

Perched atop the Cerro Pachón ridge in the Chilean Andes is a building site that will eventually become the Large Synoptic Survey Telescope (LSST). When it comes online in 2022, the telescope will generate terabytes of data each night as it surveys the southern skies automatically. And to crunch those data, astronomers will use a familiar and increasingly popular tool: the Jupyter notebook.

Jupyter is a free, open-source, interactive web tool known as a computational notebook, which researchers can use to combine software code, computational output, explanatory text and multimedia resources in a single document. Computational notebooks have been around for decades, but Jupyter in particular has exploded in popularity over the past couple of years. This rapid uptake has been aided by an enthusiastic community of user–developers and a redesigned architecture that allows the notebook to speak dozens of programming languages — a fact reflected in its name, which was inspired, according to co-founder Fernando Pérez, by the programming languages Julia (Ju), Python (Py) and R.

One analysis of the code-sharing site GitHub counted more than 2.5 million public Jupyter notebooks in September 2018, up from 200,000 or so in 2015. In part, says Pérez, that growth is due to improvements in the web software that drives applications such as Gmail and Google Docs; the maturation of scientific Python and data science; and, especially, the ease with which notebooks facilitate access to remote data that might otherwise be impractical to download — such as from the LSST. "In many cases, it's much easier to move the computer to the data than the data to the computer," says Pérez of Jupyter's cloud-based capabilities. "What this architecture helps to do is to say, you tell me where your data is, and I'll give you a computer right there."

For data scientists, Jupyter has emerged as a de facto standard, says Lorena Barba, a mechanical and aeronautical engineer at George Washington University ▶

© 2018 Springer Nature Limited. All rights reserved.

in Washington DC. Mario Jurić, an astronomer at the University of Washington in Seattle who coordinates the LSST's data-management team, says: "I've never seen any migration this fast. It's just amazing."

DATA EXPLORATION

Computational notebooks are essentially laboratory notebooks for scientific computing. Instead of pasting, say, DNA gels alongside lab protocols, researchers embed code, data and text to document their computational methods. The result, says Jupyter co-creator Brian Granger at California Polytechnic State University in San Luis Obispo, is a "computational narrative" — a document that allows researchers to supplement their code and data with analysis, hypotheses and conjecture.

For data scientists, that format can drive exploration. Notebooks, Barba says, are a form of interactive computing, an environment in which users execute code, see what happens, modify and repeat in a kind of iterative conversation between researcher and data. They aren't the only forum for such conversations — IPython, the interactive Python interpreter on which Jupyter's predecessor, IPython Notebook, was built, is another. But notebooks allow users to document those conversations, building "more powerful connections between topics, theories, data and results", Barba says.

Researchers can also use notebooks to create tutorials or interactive manuals for their software. This is what Mackenzie Mathis, a systems neuroscientist at Harvard University in Cambridge, Massachusetts, did for DeepLabCut, a programming library her team developed for behavioural-neuroscience research. And they can use notebooks to prepare manuscripts, or as teaching aids. Barba, who has implemented notebooks in every course she has taught since 2013, related at a keynote address in 2014 that notebooks allow her students to interactively engage with — and absorb material from — lessons in a way that lectures cannot match. "IPython notebooks are really a killer app for teaching computing in science and engineering," she said.

SPEAK MY LANGUAGE

The Jupyter notebook has two components. Users input programming code or text in rectangular cells in a front-end web page. The browser then passes that code to a back-end 'kernel', which runs the code and returns the results (see our example at go.nature.com/2yqq7ak). By Pérez's count, more than 100 Jupyter kernels have been created, supporting dozens of programming languages. Normally, each notebook can run only one kernel and one language, but workarounds exist. One demo notebook, for instance, speaks Python, Julia, R and Fortran.

Importantly, the kernels need not reside on the user's computer. When future users of the LSST use Jupyter notebooks to analyse their data, the code will be running on a supercomputer in Illinois, providing computational muscle no desktop PC could match. Notebooks can also run in the cloud. Google's Colaboratory project, for instance, provides a Google-themed front-end to the Jupyter notebook. It enables users to collaborate and run code that exploits Google's cloud resources — such as graphical processing units — and to save their documents on Google Drive.

Jupyter's newest variant is JupyterLab, which launched as a beta in January 2018 and is available (like the Jupyter notebook) either as a stand-alone package or as part of the free Anaconda scientific-computing environment.

Jason Grout is a software engineer at the financial-services company Bloomberg in San Francisco, California, and a member of the JupyterLab team. He calls JupyterLab a "next-generation web interface" for the Jupyter notebook — one that extends the familiar notebook metaphor with drag-and-drop functionality, as well as file browsers, data viewers, text editors and a command console. Whereas the standard Jupyter notebook assigns each notebook its own kernel, JupyterLab creates a computing environment that allows these components to be shared. Thus, a user could view a notebook in one window, edit a required data file in another, and log all executed commands in a third — all within a single web-browser interface.

"We went from Jupyter notebooks not existing some six years ago to in essence everybody using them today."

Users can also customize JupyterLab to fit their workflow. Built-in viewers exist for image, text and CSV files, for instance, but users can build custom components as well. These could display things such as genomic alignments or geospatial data. An attendee on a course taught by Pérez even created a component to display 3D brain-imaging data. "This is a completely [neuroscience] domain-specific tool, obviously — the Jupyter team has no business writing these things. But we provide the right standards, and then that community in 24 hours can come back and write one," he says.

Two additional tools have enhanced Jupyter's usability. One is JupyterHub, a service that allows institutions to provide Jupyter notebooks to large pools of users. The IT team at the University of California, Berkeley, where Pérez is a faculty member, has deployed one such hub, which Pérez uses to ensure that all students on his data-science course have identical computing environments. "We cannot possibly manage IT support for 800 students, helping them debug why the installation on their laptop is not working; that's simply infeasible," he says.

The other development is Binder, an open-source service that allows users to use Jupyter notebooks on GitHub in a web browser without having to install the software or any programming libraries. Users can also execute Jupyter notebooks on the Google cloud by inserting https://colab.research.google.com/github before the URL of a notebook on GitHub, or using the commercial service Code Ocean. In September, Code Ocean rolled out a new user interface for its cloud-based code-sharing and code-execution service, also based on Jupyter.

PROBLEMS NOTED

Such tools foster computational reproducibility by simplifying code reuse. But users still need to know how to use notebooks correctly.

Joel Grus, a research engineer at the Allen Institute for Artificial Intelligence in Seattle, Washington, gave a presentation titled 'I don't like notebooks' at the Jupyter developers' conference earlier this year in New York City. He says he has seen programmers get frustrated when notebooks don't behave as expected, usually because they inadvertently run code cells out of order. Jupyter notebooks also encourage poor coding practice, he says, by making it difficult to organize code logically, break it into reusable modules and develop tests to ensure the code is working properly.

Those aren't insurmountable issues, Grus concedes, but notebooks do require discipline when it comes to executing code: for instance, by moving analysis code to external files that can be called from the notebook, by defining key variables at the top of the notebook and by restarting the kernel periodically and running the notebook from top to bottom. As one Twitter user quipped, "Restart and run all or it didn't happen."

That's a lesson Barba tries to instil in her students. "I explain to my students from day one that they can interact with a notebook in a nonlinear fashion, and that gives them great power for exploration," she says. "But with great power comes great responsibility."

One tool that might help is Verdant, a plug-in that captures a history of a user's actions in Jupyter. "The authors built an extension that allows a flexible user workflow while also capturing the specific code executed, in what order and on what specific data," says Carol Willing, a member of the Jupyter team at California Polytechnic State University.

Jake VanderPlas, a software engineer at Google in Seattle, Washington, and a member of the Colaboratory team, says notebooks are like hammers: they can be misused, and aren't appropriate for every application. But for data exploration and communication, notebooks excel. The astronomy community seemingly agrees. "We went from Jupyter notebooks not existing some six years ago to in essence everybody using them today," says Jurić. "And we're a community that still has Fortran 77" — as in 1977 — "sticking around. It's something." ■

Jeffrey M. Perkel *is technology editor at* Nature.

© 2018 Springer Nature Limited. All rights reserved.

CAREERS

CONTINENTAL INSPIRATION Space researcher fêted for helping women into science **p.148**

MENTORING Find tips and resources at **go.nature.com/mentor**

SOCIAL Follow us at **twitter.com/naturejobs**

NOK A TUDOMANYBAN EGYESULET

A robotics workshop for ambassadors of the Association of Hungarian Women in Science.

RECOGNITION

Barrier breakers

Two prizes celebrate efforts to improve gender diversity.

BY AMBER DANCE

Last April, Eszti Varga was one of 2,400 young women to converge on 120 universities and companies across Hungary as part of Girls' Day, a campaign aimed at drawing high-school students into science and technology careers.

At the event, Varga, an 18-year-old at Szerb Antal High School in Budapest, experimented with virtual- and augmented-reality headsets and heard a speech by a Hungarian woman who had earned her first patent as a teenager. Although she was already sure she wanted to pursue a career in engineering, Varga felt empowered seeing other girls realize that they could have jobs in technology fields.

Sponsored by the Association of Hungarian Women in Science (NaTE), the campaign has attracted some 10,000 participants across the seven years that it has run.

For these and other efforts, NaTE has won the inaugural Nature Research Innovating Science Award, presented on 30 October in London. A companion Prize, the Inspiring Science Award, was presented to Mirjana Pović, an astrophysicist at the Ethiopian Space Science and Technology Institute in Addis Ababa (see page 148). NaTE and Pović were selected from almost 300 applications in a contest meant to showcase the work of researchers and organizations that inspire women and girls in STEM. The award programme is a joint initiative between Nature Research and The Estée Lauder Companies, headquartered in New York City.

"I was simply thrilled to see so many smart, successful scientists leading the charge in research, and so many strong advocates supporting girls and women in STEM across the globe," says Nadine Pernodet, a vice-president at The Estée Lauder Companies.

Today, fewer than 30% of the world's researchers are women, according to the United Nations Educational, Scientific and Cultural Organisation. Women face barriers to participating in science across the world. For example, in August, a Japanese university admitted to altering the test scores of medical-school applicants to reduce the number of women accepted on to the course. In September, a physicist at CERN, Europe's particle-physics lab near Geneva, gave a talk asserting that "physics was built by men" and that men, not women, face discrimination (the scientist has since been suspended by the lab). And a study published in *PLoS Biology* suggests that women will not reach parity on author lists until 2100 or later (L. Holman et *al. PLoS Biol.* **16**, e2004956; 2018) .

NaTE's Girls' Day programme, among other initiatives, is helping to knock down those barriers. For example, GE Digital in Budapest hosted a coding workshop in which students got to program robots, says Laura Paál, a senior director at the company. The girls walked away excited about robots, software and the company. "They also see that we love our jobs," says Paál. "This area is not only for men."

BY WOMEN FOR WOMEN

NaTE was founded in 2008 by ten women to support female scientists and graduate students, says Fanni Szigeti, the organization's general manager. Since then, the association has expanded to include members of any gender in both the natural and social sciences, and to encourage younger students. But there's still plenty to do before women reach parity, she says.

Szigeti points to gender stereotypes, lack of female role models, pay-equity gaps and lower promotion rates as reasons that are keeping girls and women from going into or progressing in STEM. Women also often launch their careers and start families simultaneously. In Hungary, Szigeti says, there are few systems in place to promote STEM for women.

Varga, for example, has faced discouragement about her career plans. "I have been told very interesting things, like how as a female, my brain could never be good enough for maths or physics," she says. She's undeterred, however, and NaTE programmes help her to connect with other young women who share her interests.

There's evidence that NaTE is making inroads. When the association began its ▶

© 2018 Springer Nature Limited. All rights reserved.

Girls' Day programme, just 7% of those enrolling in electrical engineering and informatics at the prestigious Budapest University of Technology and Engineering were women. Today, the number has doubled to 14%. "It can partly be attributed to the fact that the Technology University was among the first to join the Girls' Day series of events," says Szigeti.

NaTE has also expanded its programme beyond that one day. It organizes year-round Saturday meetings in which girls learn skills such as giving scientific presentations. It arranges for girls to shadow female researchers or tech developers at work. And it hosts workshops so that secondary-school teachers can learn about the science and technology job market and pass that information on to their students. NaTE aims to get 10% of Hungary's high-school girls involved in its programmes by 2020.

REACH OUT

NaTE also supports female researchers through its Women in Science Excellence Award. Launched in 2013 in conjunction with the Hungarian Academy of Sciences, the award honours young scientists who excel in their fields.

Now, NaTE is expanding its reach internationally. In 2015, it helped organizations in Slovakia and the Czech Republic to launch their own Girls' Day programmes. It's also representing Hungary in the European Union's Evaluation Framework for Promoting Gender Equality in Research & Innovation project. That consortium will provide indicators to measure gender inequality and compare those with the quality of outputs in research, technology, development and innovation.

> ***"I was simply thrilled to see so many strong advocates supporting girls and women in STEM."***

"NaTE's combination of programmes provides a supportive ecosystem for girls in STEM that is making a real difference today, and is poised to increase its impact in the future," says Mariette DiChristina, chief judge for the Innovating Science award and executive vice-president at Nature Research.

DiChristina, who is also editor-in-chief at *Scientific American*, says she hopes that by highlighting groups such as NaTE, the awards will inspire others to commit time to gender-diversity efforts.

Winners of both the Innovating Science and Inspiring Science awards will receive up to US$10,000 for projects related to women in science. The Estée Lauder Companies and Nature Research have committed to running these awards for at least two more years. ■

TURNING POINT
Continental inspiration

Astrophysicist Mirjana Pović has taught science to orphans in Rwanda, helped to organize a supportive community for women with HIV in Tanzania and contributed to space research in Africa. She has excelled in her own research at the Ethiopian Space Science and Technology Institute in Addis Ababa and the Institute of Astrophysics of Andalusia in Granada, Spain. For these endeavours, she won Nature Research's inaugural Inspiring Science Award, one of two prizes developed in partnership with The Estée Lauder Companies (see page 147). She impressed judges with the depth and breadth of her efforts to encourage women and girls in science, says Magdalena Skipper, chief editorial adviser of Nature Research, editor-in-chief of Nature *in London and chief judge of the awards.*

What is your background?
My family in Serbia was poor, and my country was at war as I was growing up. I would never have been able to pursue science without my family's encouragement, a free university education and a scholarship for my PhD. Children from poor and developing countries should know that their lives can change, but it's not enough that they work hard. It's fundamental to have support from society. Access to education is the first step.

What sort of research do you do?
I'm trying to understand how galaxies form, and how they evolve over cosmic time. In particular, there are galaxies with what we call active galactic nuclei in their centres. These are some of the most luminous sources of light in the Universe.

What draws you to Africa?
I am amazed by Africa's beauty and diversity, but I am disturbed by the inequalities between much of it and the developed world. During my PhD, I went for the first time to volunteer in Tanzania and Kenya. I was quite affected by the experience. After working in South Africa and Spain, I was invited to help establish the Space Science and Technology Institute here in Ethiopia.

What are the barriers to science for African women?
They face the same challenges as women in science worldwide, but multiplied. They lack female role models. They often don't get support from their families to pursue science. These issues are compounded by poverty. Fewer girls than boys finish primary or secondary school or have the opportunity to go to university, and many family responsibilities still fall on women.

How do you aim to lower those barriers?
In collaboration with the Society of Ethiopian Women in Science and Technology, I'm starting regular science talks for secondary-school girls to motivate them to do science. Women will speak about their fields, how to become a scientist, challenges they have faced and the life of a scientist. Of course, these talks cannot change poverty. But even if some girls cannot benefit fully from these talks today, they can get information that could help them and their children in the future.

What else are you doing?
Another project is to build a network of African women in astronomy and space science. In many African countries, there has been a lot of effort recently to develop astronomy and space science. It's important that young women have a safe space in which to share experiences, knowledge and career opportunities. I would also like to track how many women who are completing master's degrees go on to a PhD, and how many who finish a PhD remain in science.

Do you have advice for female researchers?
Interact as much as possible with other women in science, especially the senior ones, who can provide support and knowledge. In your path as a scientist, there will be many challenges and problems. Taking these contemplatively, and seeing them as a source of knowledge and experience, will help you to find the best solution. ■

INTERVIEW BY AMBER DANCE

This interview has been edited for clarity and length.

© 2018 Springer Nature Limited. All rights reserved.

CONTAGION IN TRANQUIL SHADES OF GREY

Running wild.

BY DEBORAH WALKER

ILLUSTRATION BY JACEY

The lecture had gone well. I'd introduced Tranquilitron, the latest mood stabilizer from my company, OedipusPharm. The last drug developed from the root I stole when I was 16.

But when I see her in the audience, the sound of applause grows quiet, colours fade to grey.

Offstage, Professor Mungan of Göbekli Tepe University asks, "Is anything wrong, Dr Hyde?" She's the founder of PersonalCon, a holistic event, artists and scientists exploring the personality. She's also very, very young. When you think professors are scandalously too young, it's a sign you're getting old.

A riddle emerges, unbidden. I whisper, "A sister gives birth to her sister. She in turn, gives birth to the first. Who are they?"

"Night and day," Professor Mungan answers. "The Sphinx's second question, not quite as well-known as her first riddle."

I nod. Already, I'm recovering. I need to leave.

"Can I escort you to the hotel, Dr Hyde? This heat is dreadful today."

"There's no need, my dear." She's worried about me. I'm old. The heat is quite fierce. She doesn't know I spent my childhood in Göbekli Tepe. And as any personalogist will willingly debate: childhood leaves its indelible marks.

I return to the hotel and pack. I leave the hotel by the back stairs, not leaving a note.

Like the servant seeing death in the market place, when I saw my sister, I fled. Swiftly, using not a fleet horse but my Amex, travelling along the route long-planned, full of secret caches: false passports and cash, until I reach the cottage in the Derbyshire peaks, and find, not entirely to my surprise, my sister waiting for me. My sister Sphinx does not pursue, she waits at her prey's final destination.

My twin, looking ten years younger. The version who stayed out of the sun. She's the me I could have been: calm, white-skinned, emotionless as the Virgin Queen. The sun has shone on me for many years, I have felt many things.

I won't use the knife. I might have killed a stranger. But not my sister. She always was the clever one, the better one. I took the role of rebellion.

She walks around the room outwardly observing the decoration.

Once, long ago, a man who would become a Stoic philosopher called us Sphinx: inscrutable, guardians of knowledge. A name so fitting, we embraced it.

From every surface of the cottage, we were watched by a thousand implacable eyes. The gaze of the stone and painted sphinx.

"The décor's quite unusual for a Derbyshire cottage."

Speaking so slowly, with exquisite detachment. My sister's a product of cultural and pharmacological repression of emotion. Sphinx are medicated to the root.

Only briefly do youngsters RunWild, tasting emotion before committing fully to the Sphinx. During the RunWild, I ran.

My sister admires a black and white photograph of the Great Sphinx of Giza. "My knowledge of English interior design is admittedly sparse. So do forgive me if I've made an incorrect assumption."

"Sister, I doubt you've *ever* made an incorrect assumption."

"Sister, how you misremember me."

"That's probably true. I remember the Sphinx in shades of grey."

"Our family never did have a penchant for colour."

"Sit down, Sister, rest your old bones."

She slips into a chair as agile as a girl, with no sign of the arthritis that plagues me. "I'm getting old," I tell her. "I have regrets. Tell the council I'm sorry I stole the root to fund my life outside the family."

"They should have supported you on the outside."

"I was shunned."

"We don't do that anymore," she says.

"Really?"

"We have a new leader."

"Old Metza's dead? Who's the new Sphinx Father?"

"Me," says my sister.

I laugh. The Sphinx were always so rigid about gender. "You changed the system from the inside? Be careful, Sister, power corrupts."

"We just have to hope that I never get absolute power."

It feels good to laugh again with my sister. Yet … "Even though I left, this change is … unsettling." As any personalogist will willingly debate: childhood leaves its indelible marks.

"The change started with you. Your example fed thirsty soil." She's curious. "RunWild is such an extreme of fear and joy. Has that been your life?"

"Good grief, no. No one could sustain that. But it's been memorable." I glance at a photo hidden among the sphinx, a picture of a man and a child.

"I wonder what made us so different," she says.

"Maybe we attest to the existence of a soul, with our differences despite our genetics."

"Maybe we attest to the countless yet incremental differences in environmental factors."

I nod. "Nature versus nurture is an old riddle. Yet, despite our differences, blood is thicker than water."

She inclines her head.

"But why are you are here, Sister?"

"I come to invite you back to Sphinx."

I think about my life. The memories flash in technicolour. "I don't think so."

"The root and the calm would give you more years."

It's tempting, but, "No. I've lived a life in the light. I won't dwindle in the underground city."

"Things are changing, Sister. We're moving into the light. We intend to share the root with those who want it."

"You're offering to stabilize the mood of humanity?"

"They need the gift of content. As do you, Sister. Will you take it?"

There it is, the root of the Sphinx. Calm and long life for the suppression of personality. The root of all content, nestling in my sister's hand like a contagion that will fall onto the world in tranquil shades of grey. ■

Find **Deborah** *in the British Museum trawling the past for future inspiration.*

© 2018 Springer Nature Limited. All rights reserved.

A hardcore innovator

The city of Xi'an is PROMOTING HARD & CORE TECHNOLOGY to reinvent itself as a global centre for technological innovation.

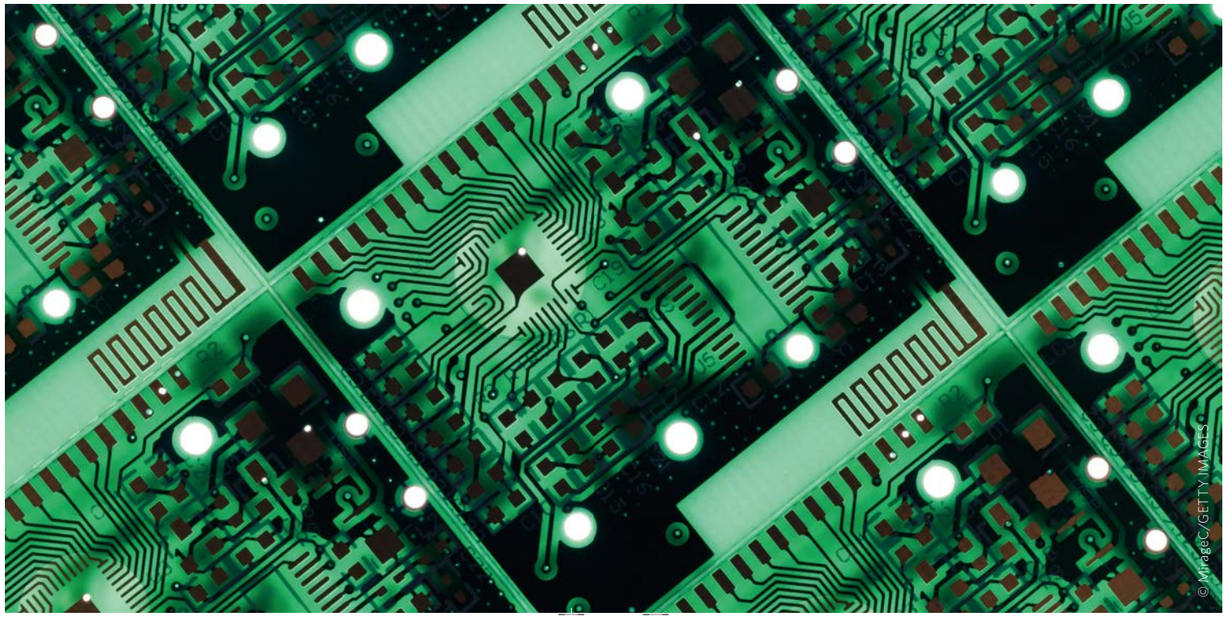

© MirageC/GETTY IMAGES

© TEK IMAGE/SCIENCE PHOTO LIBRARY

© Yuichiro Chino/GETTY IMAGES

Technological innovations are changing our lives and transforming the world, as countries around the world look to develop their economies.

Xi'an, the ancient capital city of northwest China's Shaanxi province, is reinventing itself as a global high-tech centre and will host the Global Hard & Core Technology Innovation and the Belt and Road Innovative Cooperation Conference 2018 to attract investment in this new field. The conference is in line with the national 'Belt and Road' initiative to boost science and technology collaboration in countries along the ancient Silk Road.

Understanding hard & core technology

'Hard & core technology', a concept coined in 2010 by Mi Lei, founder of Casstar, an incubator and an angel investor based in Xi'an and Beijing, refers to core technologies that are more advanced and cutting-edge than high-tech. They typically require long-term investment, a long R&D cycle, and have a high threshold for entry, which make such technologies hard to duplicate and imitate. But these technologies also bring in good returns.

Since the 2008 financial crisis, it has become clear that China's demographic dividend is not enough to rely on, and the country needs to diversify. "We need to find a new engine for growth in technological innovation," said Mi. "We believe hard & core technology will lead the world in the next 30 years, and it is important for us to develop these technologies ourselves, ensuring their intellectual property."

Hard & core technology differs from deep technology, which typically refers to disruptive technologies with high impact, trying to solve big issues. When David Rothenberg, a philosophy professor at the New Jersey Institute of Technology, first proposed the deep technology concept in 1995, he referred to technologies that bring us closer to nature. Now, the term is frequently used for tech companies founded on tangible engineering innovation or scientific advances and discoveries, rather than business model or other innovations. In Mi's view, such technologies entail great uncertainty. Thus, he proposed a term that puts a greater emphasis on core technologies based on basic science. "Developing such technologies requires toughness and a down-to-earth spirit, which characterize many Shaanxi entrepreneurs," said Mi.

Hard & core technology is also more tangible and applicable, as compared to black technology, which has a futuristic connotation. The former, typically has a clear product orientation and an identified industrial basis, helps improve product performance and is able to lead and support industrial development. Hard & core technology is also different from the internet-based innovation which creates a virtual world. "It focuses on our physical world," said Mi. "It is the engine that drives industrial growth."

Mi, who holds a doctorate in photonics, offers examples of hard & core technology, encompassing artificial intelligence (AI), aerospace, photonic chips, bio-technology, information technology, new materials, alternative energy, and intelligent manufacturing. In the field of aerospace engineering, drone quadcopters are an example of high tech, but manufacturing large aircraft and launching rockets or satellites require hard & core technology. As for the technologies for rocket recovery and landing on Mars, they fall in the category of deep technology or black technology, according to Mi.

Other examples include high-speed train technology, quantum communication technology, which is between hard & core technology and deep tech, and driverless vehicle technology, which involves laser radar and autonomous driving systems. All of these have great industrial potential.

Promoting hard & core technologies in Xi'an

The eight major fields that represent hard & core technology are focal points of national importance. National, provincial and local government funds have been poured into these sectors in recent years. To catch this wave of science and technology innovation, the Xi'an Municipal Government is committed to boosting its hard & core technology industries and has invested heavily in these fields.

There are rewards for incubators of hard & core technology industries, supporting facilities and talent for start-ups in these sectors. In 2017, the Xi'an government hosted the inaugural Global Hard & Core Technology Innovation Conference, which gathered global experts, leading researchers, tech company chiefs and investors to discuss latest breakthroughs and trends. With support from the government and the Chinese Academy of Sciences (CAS), a white paper was released, outlining the current landscape of hard & core technology, its development and investment, and opportunities for developing its eight fields.

Xi'an is well positioned to develop hard & core technology industries, with solid research and industrial basis in the eight fields. For example, a spin-off of Xi'an Institute of Optics and Precision Mechanics of CAS, incubated by Casstar, developed a femtosecond fibre laser for ultrafast, high-precision drilling, filling a technological gap in China. This micro nano processing technology, an important aspect in intelligent manufacturing, used in aerospace engineering, will enable China to manufacture aircraft engines with its own intellectual property rights.

The Northwestern Polytechnical University in Xi'an has participated in planning the overall design of the C919, China's first domestically manufactured large passenger jet, and contributed to solving problems in the power, control and micro-electromechanical systems, as well as structural design. The R&D and manufacturing of the C919, China's industrial breakthrough in the field of short- or medium-range passenger jets, is another typical example of the application of hard & core technology. It involves the use of advanced composite materials and aluminium-lithium alloys for building aircraft body, and the latest dynamics research for designing the body.

In the AI field, Xi'an Jiao Tong University houses an AI research institute and the Northwestern Polytechnical University boasts strong research capacity in drone technology. In biotechnology, Xi'an has a national centre on molecular medicine and translational science and the technology to create bionic bones using three-dimensional (3D) printing. Xi'an houses two important airbases, several big pharmaceutical companies, a graphene industrial base, a new energy car production base, several CAS institutes and a high-tech zone. A roadmap is laid out for developing photonic integrated circuits, novel memory chips, titanium or titanium alloy products, high-efficiency single crystalline photovoltaic cells with an annual capacity of 500 MW, 3D manufacturing of metals and other hard & core technologies.

"Hard & core technology is the propeller for Xi'an's ongoing industrial upgrade and economic transformation," said Mi. "It is also the tool that enables us to change the world and our future." ■

GHCTC

www.ghctc.com.cn

Advertiser retains sole responsibility for content

Hosted by the Xi'an Municipal Government and organized by Xi'an Science and Technology Bureau, Casstar and Zero2IPO Group, the Global Hard & Core Technology Innovation and the Belt and Road Innovative Cooperation Conference 2018 is to be held in Xi'an, China November 8-11. The theme this year is "Hard & Core Technology: Develop Xi'an, Change the World, and Win the Future".

A global conference for technology innovation

The conference will gather Nobel laureates, renowned scientists from the Chinese Academy of Sciences, opinion leaders and entrepreneurs from global and national technology industries and investors to discuss cutting-edge science trends. With talks on topics including artificial intelligence (AI), aerospace, photonic chips, bio-technology, information technology, new materials, alternative energy, and intelligent manufacturing, the conference aims to promote the commercialization of research by bridging technologies with capital and the market. It seeks to inspire greater technological innovations and foster international collaborations.

Broad activities

Apart from 20-plus sessions, the conference will also feature an industrial expo showcasing cutting-edge technologies developed in Xi'an and around the world. A whitepaper on the development of hard & core technologies and guidelines for investment in the field will be released. Innovation contests will be held to encourage greater youth participation.

An innovative dream becomes reality

In China's ancient city of Xi'an, an emerging smart town is providing a demonstration site for CUTTING-EDGE TECHNOLOGIES AND NOVEL IDEAS to drive science and technology innovation.

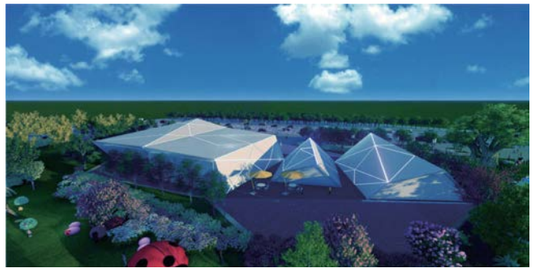

Imagine a town built for self-driving vehicles, with drones and robots patrolling traffic, and monitoring public security. It is a futuristic scene taking place in the Chang'an University Town, in the southern suburb of Xi'an, in China's Shaanxi province.

With joint support from foreign and domestic experts, the 'dream town', aims to establish a joint laboratory for web-controlled autonomous driving, and a road for testing driverless cars. It is designed as a pilot site for applying self-driving technology, along with other emerging technologies for smart living.

A science and technology innovation platform

In line with China's strategy of innovation-led development, Shaanxi Jintai Hengye Tianlang Company Limited, a joint venture between TITAN Group and Shaanxi Investment Group, two Xi'an-based enterprises specializing in industrial investment, has partnered with local government and universities to build a science and technology platform for an innovation ecosystem in Chang'an University Town. Embracing the ideals of 'intelligence, ecology, open-resource and sharing', the experimental town aims to promote the translation of research results, support innovation and entrepreneurship, and realise sustainable living.

The dream town spans 3.6 square kilometres in the heart of Chang'an University Town, linking Xi'an's high-tech zone, aerospace base, a new commercial district and neighbouring research institution. Capitalizing on Xi'an's research specialisms, the dream town focuses on developing emerging technologies that drive global economic innovation, including new-generation information technology, biotechnology, new energy, new materials and environmental protection industries. By applying novel technologies and building up these new industries, architects of the project expect to integrate industrial growth with culture, tourism and community development, creating an ideal place for living, producing, and ensuring longevity of a healthy environment.

"We believe innovation is the key to driving industrial development, and open-source is essential for promoting technological innovation," said Sun Yin, the chairwoman of TITAN. In line with this, the dream town makes the most of research resources from Xidian University and other neighbouring universities or research institutes to create an open-source information platform for sharing research results. To enhance the university-research-industry partnerships and bridge local enterprises with global innovation resources, the dream town is also to build infrastructure to support the Internet of Things (IoT) and big data technologies, facilitating the use of research results. It is to become a world-class cluster area integrating universities, research institutes and industry.

The clustering effect promotes links between research results, funding, enterprises, products and market, generating a supportive cycle. Eventually, the dream town is to house incubators that support entrepreneurship, platforms that serve sci-tech start-ups in research translation and R&D, as well as multi-sector R&D teams that accelerate science and technology innovation.

With a global outlook, the dream town is also active in international collaboration. It has attracted high-tech R&D collaborations with more than 10 countries, including the United Kingdom, the United States, Japan, Sweden and Ukraine. These projects will promote translation of research results from around the world.

Promoting research translation, innovation and entrepreneurship

An essential feature of the dream town is the creation of platforms that incorporate cloud platforms, IoT, block chain, artificial intelligence and building information modelling technologies, will form the 'brain' of the town. With real-time sharing between enterprises and continuous updates of platform technologies, sustainable growth of the platforms is possible. The 'brain' of the town makes systematic, visual, digital and intelligent technologies more accessible, promoting rapid development of enterprises in the town.

The town has four open-source platforms that facilitate entrepreneurship and innovation.

The university-research-industry collaboration platform is designed to integrate resources for innovation-driven enterprises around the world. As a university cluster area, the dream town will pool research result resources, and via the channels of commercial, industrial or university alumni associations, establish collaborative research institutes, R&D centres or university spin-offs with domestic or foreign enterprises. The platform will help enterprises find promising research projects, help define the market for potential products, and help seek market channels, contributing to efficient research translation and optimising company investment.

Focusing on attracting global capital and financial enterprises, the platform for science and technology finance aims to build investor pools for research and corporate institutions in the dream town. Along with other platforms, it will promote the development of industrial corporations and the commercialization of research results.

The dream town will also create a science and technology service platform. With third-party professional teams, it provides enterprises with policy analysis, legal advice, tax guidance, consulting, talent recruitment, product promotion and packaging, as well as estate management services. These comprehensive services facilitate building a supportive ecosystem for innovation.

Finally, the platform for trading research results creates online and offline markets, enabling their easy integration with the market. By channelling research results, enterprise needs and capital flows, an internet-based trading ecosystem is formed.

To hasten the application of novel technologies, the dream town is integrating infrastructure building with science and technology industries. Apart from the autonomous driving facilities under construction, localised computer network systems, building automation systems and mobile office management systems are also being set up, which will facilitate client solutions online.

The dream town is also keen to establish a solid credit system to guard personal and enterprise credibility, ensuring a supportive environment for open-source innovation and research results sharing.

By applying IoT and big data technologies in education, healthcare, environmental and industrial sectors, the dream town also has infrastructures set up to make healthy choices accessible for its residents. "We will integrate green building and information systems to create a model for smart living, embracing ecology, science and technology, and novel ideas," said Ma Yapeng, general manager of Shaanxi Jintai Hengye Real Estate Company Limited. "Our dream is to change the world with intelligence and make the world better with science and technology." ■

长安大学城 · 梦想小镇
WE HAVE A DREAM

+86 (0)29 88653833 ext.8990
tl03032@titan.com

Advertiser retains sole responsibility for content

A force to be reckoned with

A new international partnership at NORTHWESTERN POLYTECHNICAL UNIVERSITY in Xi'an is creating a new model for training global-minded talents in Northwest China.

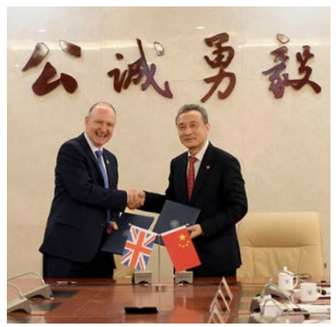

For the many Chinese students eager for an international education at a world-class university, a new joint education institution at Northwestern Polytechnical University (NPU) has provided an opportunity for such a pursuit, without moving abroad.

Established in May, 2016, the Queen Mary University of London Engineering School, NPU (QMES) is the first of its kind located in Northwest China. A truly collaborative school, it provides high-quality, trans-national education to undergraduates, offering degree programmes primarily in material science and engineering, polymer material and engineering.

Innovation redefines the future. Against the backdrop of the national Belt and Road Initiative, the joint engineering school is in line with the internationalization strategy of the country's higher education development, explains Jie Kong, dean of QMES, and a polymer material professor at NPU and a visiting professor at QMUL.

The joining of two strong forces

Two engineering powerhouses joined to form the QMES. Queen Mary University of London (QMUL), one of the largest colleges at the University of London, is a member of the Russell Group, considered the 'Ivy League' of leading universities. It was ranked among the global 100 in 2016 in the Times Higher Education's World University Rankings and its material science programme is a leader in the United Kingdom.

NPU has a long history stretching back to 1938, boasting many distinguished faculty members, including 28 Chinese Academy of Sciences or Chinese Academy of Engineering members. It is a national key university in China, and was one of the first universities selected into the national Project 211 and Project 985 initiatives, which aim to raise the bar at high-level across the country. In 2017, it was selected into the national 'Double First Class' initiative (Class A), which aims to build first-class universities and disciplines in China. This university boasts a strong material science programme, ranked among the country's top five in past ten years.

"Our partnership stems from our long collaboration in material and polymer science research, especially in emerging advanced functional materials," said Kong, a scientist whose work focuses on the precise design of hyperbranched polymers and innovative application in electromagnetic ceramics, nanodielectronics and energy materials. "The joint engineering school was established to leverage our advanced research platform for international collaboration in material sciences and to best use quality educational resources of the two universities."

To provide internationalized education that integrates science and engineering, and explore an internationally relevant model of Science-Technology-Engineering-Mathematics (STEM) higher education, the school has combined QMUL's strength in basic science and NPU's specialism in engineering and applied science to provide cross-disciplinary training. "We want to integrate the essence of both British and Chinese undergraduate education to focus on promoting students' innovation capabilities." said Andrew Bushby, executive vice dean of QMES, and a material professor at QMUL.

A novel educational programme

Following a philosophy that puts students and education at its centre, the QMES adopts the British curriculum system and evaluation model. Courses are taught in English, jointly by NPU and QMUL faculty members, with 50% of the core courses taught by QMUL faculty from the London campus. This is important for creating an global learning environment and to hone students' capacity for international research communication.

"Our training objective is to make each student all-rounded and innovative, capable of studying and working in a transnational setting, and with strong ability for lifelong learning," told Bushby. Training programmes focus on laying a solid foundation in natural sciences, as well as humanities for students, while building their expertise in material science. Both theory and practice are emphasized. Students are also familiarized with international practices and trained to develop a global perspective. "We hope we can open a door for them to get to know the world," said Kong.

Students can choose to major in material science and engineering or polymer material and engineering, and will be awarded a degree from each of the two universities at graduation. Since it started enrolling in 2017, the school takes on about 120 students for each of its majors each year.

Exploring a new model of international collaboration in education

The QMES represents NPU's response to a national call for educational reform. In late 2013, China's Ministry of Education set out a policy to improve the quality of Sino-foreign collaboration in higher education. A top-down guideline was set out to enhance the planning of international collaboration to best integrate available resources, balance regional and disciplinary differences, and improve the mechanisms of importing international resources and experience.

With this policy support, the QMES, a member of the Belt & Road Aerospace Innovation Alliance, is also taking measures to improve its management systems and collaboration mechanisms. It has established a joint administrative committee, an advisory board, along with academic, exam, and staff-student liaison committees, as well as other relevant management or academic bodies, seeking to integrate Chinese and British management practices. "We are in the process of exploring reforms on school management, internal governance structure, student training models and academic planning," said Kong. "We hope the lessons we learned will benefit China's higher education reform and shed a light on the future for students."

The QMES has also launched an International Centre for Teaching and Learning (ICTL) to explore innovative teaching and learning practices in STEM subjects. It will promote building an internationalized faculty team in material sciences, improving textbook development, and fostering globally minded students in other subjects at NPU. The Advanced Materials and Structures - Joint Research Centre (JRC), with five research institutes affiliated, was co-constructed by both universities, to enhance education quality by developing a first-rate research and education base to support civil aviation, areospace and material industries in Xi'an, and western China.

This new partnership in Xi'an, a major higher education base, in central China, is also an important step to revitalize this ancient city, which was once the eastern terminus of the ancient Silk Road and has a historical heritage of international communication. "By bringing in experience and resources from abroad and producing the most vital professionals, we provide essential support to higher education development in the region," said Kong. As a bridge that connects Xi'an to the world, the joint engineering school also plays a role in boosting educational, cultural and economic development in the region and beyond. ■

86 (0)29 88431985
qm@nwpu.edu.cn
http://qm.nwpu.edu.cn/index.htm

Advertiser retains sole responsibility for content

Advertiser retains sole responsibility for content

Making manufacturing smarter

Researchers at THE SCHOOL OF MECHANICAL ENGINEERING, XI'AN JIAOTONG UNIVERSITY are advancing leading-edge technologies for the manufacturing industry.

Additive manufacturing offers an innovative solution for bone repair. At Xi'an Jiaotong University (XJTU), researchers from the School of Mechanical Engineering achieved the world's first clinical trial of customized mandible implant produced by additive manufacturing in 2001, a breakthrough in personalized treatment for large-scale bone defects.

Additive manufacturing is only one specialism of this century-old school at XJTU, which started in 1913. Now boasting a strong, distinct, and complete academic programme, and a 240-strong faculty, the School of Mechanical Engineering is home to a State Key Laboratory for Manufacturing Systems Engineering, a Key Laboratory of Education Ministry for Modern Design & Rotor-Bearing Systems, and many other advanced research platforms. Fusing hard and soft technologies, the school has contributed to national and regional manufacturing industries through intelligent manufacturing of high-end equipment, and by training and cultivating talented professionals.

Rapid manufacturing systems developed by the school, featuring the integration of processing techniques with data and precision, were promoted in more than 60 service companies and have been used in complex large aerospace structures, and medical instruments. As a major force in additive manufacturing, the school led the way in establishing the National Innovation Institute of Additive Manufacturing in Xi'an, a centre dedicated to the development, standardization, and industrial transformation of these technologies.

Research programmes at the school encompass the full life cycle of major mechanical equipment, from their design and manufacturing to their in service performance. Researchers at the school were the first to propose the basic system engineering concepts of tribology, the science of friction, and summarized its three principles. Their breakthroughs in the design and testing of large-scale sliding and rolling bearings have broad engineering applications. Digitally controlled manufacturing technologies developed at the school are poised to become the foundation for intelligent manufacturing in aerospace, nuclear power, and automotive industries. The school's researchers have also developed a series of cutting-edge technologies with potential for batch production of devices on the micro and nano scale. These manufacturing technologies can support the development of wearable electronics, robots, and bionic devices, among others.

A historically significant problem in mechanical engineering is ensuring the safety of critical equipment in such areas as petrochemical, metallurgy, wind power, aviation and high-speed trains. Monitoring and diagnostic techniques date back to the 1980s. The new paradigm that combines manufacturing design and intelligent operation advocates a transition from scheduled to condition-based maintenance of major equipment.

Along this line, XJTU researchers pioneered high-temperature, high-pressure transduction technologies, special micro-machine dynamic transducers, monitoring techniques for non-stationary operating conditions, holospectrum technology, crack identification using wavelet analysis, fault isolation and intelligent diagnosis. The wind power monitoring and diagnostic systems they developed are used at more than 100 sites in China. The school has also collaborated with a commercial aircraft engine company to establish the United Innovation Centre for health management and operation safety of aircraft engines.

The school plans to further revolutionize large-scale equipment, robotics, interdisciplinary biomedical engineering and other intelligent manufacturing technologies. By innovating the model and format, and cultivating creative talents, it aims to fully transform the potential for technological advance, benefiting the economy, society, and the environment with disruptive technologies. ■

西安交通大學
机械工程学院
SCHOOL OF MECHANICAL ENGINEERING
XI'AN JIAOTONG UNIVERSITY
+86-(0)29-8266 8602
jxyb@xjtu.edu.cn
http://mec.xjtu.edu.cn

Advertiser retains sole responsibility for content

nature

[**inside**view]

AARHUS UNIVERSITY
HEALTH

Profile Feature as seen in *Nature* 1st November 2018

BIOMEDICAL 'IDEAS POWERHOUSE' OPENS ITS DOORS IN DENMARK

A conversation with **PROFESSOR ANDERS NYKJÆR**, Department of Biomedicine, Aarhus University, Denmark

Last month, the Department of Biomedicine at Aarhus University inaugurated its state of the art research centre, the Skou Building. It is named after former faculty member Jens Christian Skou who won the Nobel Prize in 1997 for his description of the sodium–potassium pump, which has a crucial role in cells. Neuroscientist Anders Nykjær, core group leader of the Danish Research Institute of Translational Neuroscience (DANDRITE), which will be a large stakeholder in the new building, and director of the Center for Proteins in Memory (PROMEMO), is excited that his laboratory will be one of the first to move into the new building and describes how its interdisciplinary environment will generate new creative ideas.

What difference will the new Skou Building make to your research?
The new building will be a powerhouse where ideas will be generated. It will allow people from different disciplines to work even closer together and develop synergy. It is important to minimize the physical distance between researchers as this causes barriers. The building also contains advanced laboratories and state of the art animal facilities, which is important as sophisticated transgenic animals are critical in translational research.

My main research interest is how receptors regulate psychiatric disorders such as ADHD, bipolar disorder and schizophrenia, and molecular mechanisms underlying memory. In PROMEMO we study what makes you remember certain things and forget others. What proteins are associated with memory and what are the circuitry networks? For example, if I ask anyone where they were when they heard about 9/11, most people can remember that clearly — but not where they were the same date a year ago.

Moving to the new building will provide an interdisciplinary environment that is critical to address and solve the big questions in neuroscience and in biomedicine in general. It is vital that groups with different expertise come together to provide scientific input in order to propel research forward.

What makes Aarhus University's Department of Biomedicine an attractive place to work?
It's a very strong scientific environment with an unusually open and relaxed atmosphere. There is not much of a barrier between the senior and junior scientists, which is really important as it makes the younger ones feel confident to come up with new ideas and suggestions.

The Department of Biomedicine is very international and has become even more so over the last ten years. Currently there are more than 30 nationalities working here including researchers from the United States, Japan, China, Iran and countries in Europe. We have been lucky to be able to attract some of the smartest brains from around the world. As a matter of fact we have vacant professorships at the department right now.

It's a very open and welcoming community. There is also good support to help international researchers find accommodation and, if they have kids, help them find schools. It's a great place to work as there is the lively city plus the sea and the forests.

NEUROSCIENCE AT AARHUS UNIVERSITY IS BECOMING A LIGHTHOUSE ATTRACTING THE BEST SCIENTISTS FROM AROUND THE WORLD.

Why is international collaboration and interdisciplinary research important?
Our department has a very strong tradition of integrating faculties from health and basic science. We like to foster collaboration. There are regular meetings for all scientists at the department where people from different research groups present and explain what they are doing. For example, anatomists may come and explain to their colleagues in neighbouring fields what they are working on. This can be very inspiring and it is an extremely good way of networking and initiating new collaborations.

To take science to the next level you need to get the brightest minds to come here and this influx of international researchers also stimulates the brightest minds from Denmark. Internationalisation allows us to experience different ways of thinking and it also facilitates collaboration with a researcher's former institution. Neuroscience at Aarhus University is becoming a lighthouse, attracting the best scientists from around the world. Over the next 5-10 years I predict it will become even stronger.

How is science perceived in Denmark?
Funding opportunities within bioscience are very good in Denmark. More than 50% of funding comes from foundations including the Novo Nordisk Foundation, Lundbeck Foundation and the Danish National Research Foundation. For example, at Aarhus University, the Lundbeck Foundation supports neuroscience for €20 million a year. The foundation also launched the €1 million Brain Prize, which has been important to increase the visibility of Danish neuroscience.

There is substantial interest in science in general and neuroscience in particular in Denmark. Public science talks are incredibly popular – for example, when the winners of the Brain Prize present their research. Demand for tickets has been so great the talks are now live-streamed to 50 cinemas in Denmark. They're like a rock concert by the Rolling Stones.

AARHUS UNIVERSITY
HEALTH

ADVERTISER RETAINS SOLE RESPONSIBILITY FOR CONTENT

SPRINGER NATURE

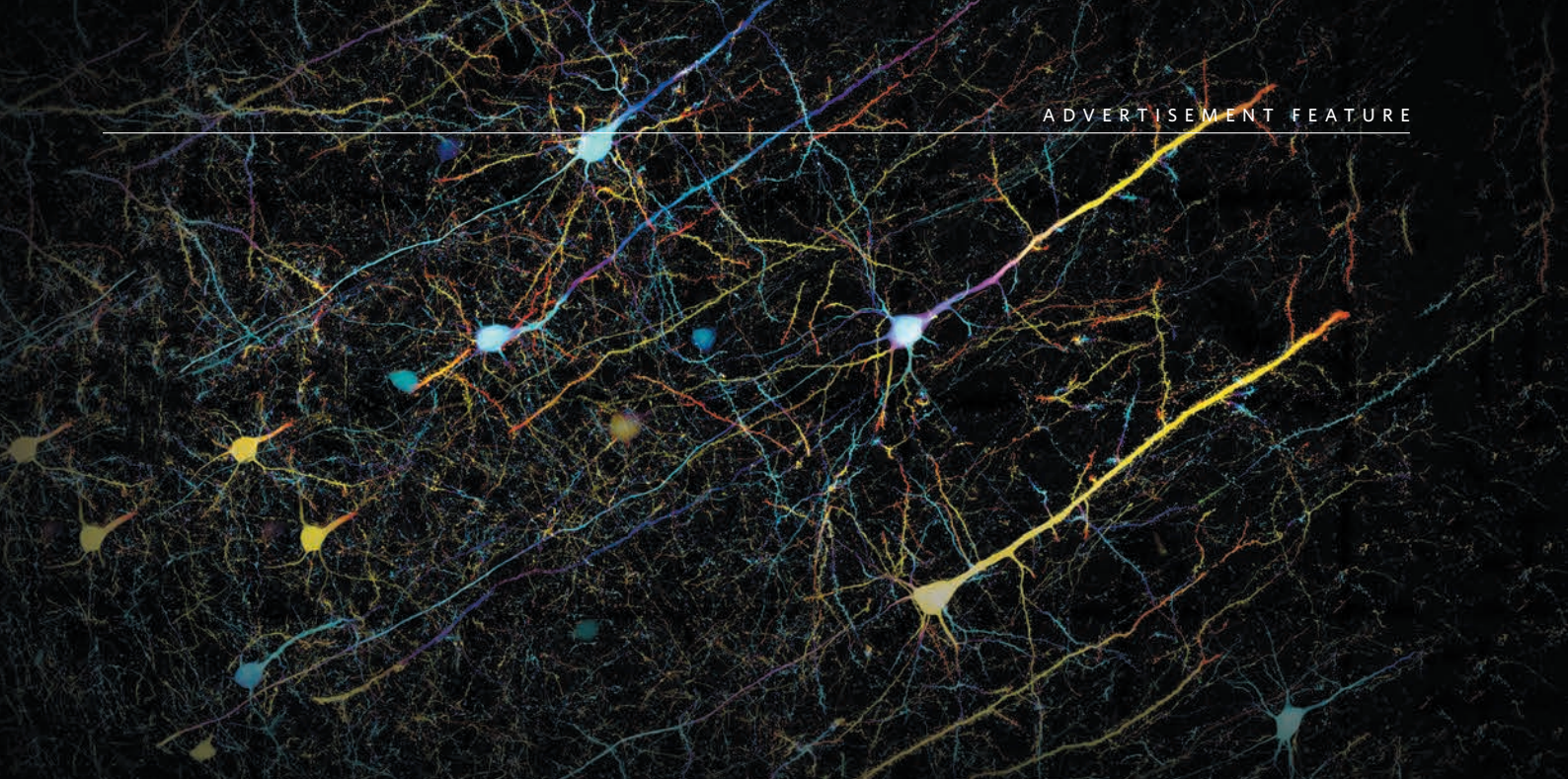

FORECASTING THE CYCLE OF EPILEPTIC SEIZURES

HOW BIG DATA AND AN APP ARE HELPING PEOPLE with epilepsy successfully manage their condition

People with epilepsy may report having a 'bad week' at the start of each month, a cluster of seizures every 10 days, or other cyclic patterns. However, while anecdotal evidence of long-term seizure cycles is abundant, experimental proof was lacking.

But now a University of Melbourne study, based on two of the largest databases of human seizures ever recorded, has provided an extremely accurate, objective account of the times seizures occur.

A team led by Mark Cook, director of the Graeme Clark Institute for Biomedical Engineering, has developed a powerful new framework for seizure forecasting – the longest epilepsy forecasting study undertaken in humans. The latest results were reported in Lancet Neurology in September, and have been critical to the development of a seizure forecasting app.

"The week day that most seizures occurred was unique to the individual and, across the population, no day of the week was 'worse' than any other day," says Cook, who is also director of the Department of Neurology at St Vincent's Hospital Melbourne, and senior research advisor at the Bionics Institute, both within the Melbourne Biomedical Precinct.

APP USERS CAN SCHEDULE MEDICATION ALIGNED TO THEIR UNIQUE RHYTHMS

"By developing the right software, we can immediately begin using the information from seizure cycles to improve treatment outcomes," says research team member Philippa Karoly from the Neuro Engineering Research Lab at the University of Melbourne.

Named the Beagle Health Tracker, the app detects different cycles that modulate individuals' seizures and presents this information graphically.

"Users can track where they are in a particular cycle, explore the different associated risk levels and schedule medication aligned to their unique rhythms," Karoly says.

"Our investigation has taught us that tracking seizure times can reveal rich patterns that can be used to build better forecasts and make a real difference to how people manage epilepsy." ■

Explore our research stories @ unimelb.edu.au/researchimpact

Download the Beagle Health Tracker app

THE UNIVERSITY OF MELBOURNE

Research collaboration in action

The interdisciplinary research that made development of the Beagle Health Tracker epilepsy app possible (see main story) is boosted by the co-location of clinical, research and translational experts and the facilities they depend on. The Melbourne Biomedical Precinct, of which the University of Melbourne is a seminal partner, is a collaboration of hospitals, universities, research institutes and business, located at the northern fringe of Melbourne's city centre. In the past decade, partner investment of more than AUD$3 billion has led to ongoing development of new health interventions, from fully-implantable cochlear devices to mobile stroke units and new ways to prevent hepatitis C transmission.

Advertiser retains sole responsibility for content

RESEARCH COLLABORATION DRIVES INNOVATION

Increasing international collaboration in Shanghai underpins the STRONG GROWTH OF RESEARCH OUTPUT IN THIS VIBRANT CITY, driving science and technology innovation.

With strong government commitment and continual increase in research input, China has become the world's second largest research powerhouse. This growth can be partly attributed to increasing international collaboration, a global trend in science.

In Shanghai, China's global economic centre and a leader in science and technology, collaboration and openness are setting the scene for innovation. A recent analysis based on Nature Index data, which tracks high-quality research published in top journals recognized by researchers, paints Shanghai's research output and collaboration picture, compared with the world's other top research producing cities, showcasing its growing capacity as a global science and technology innovation centre.

Growing research output

Based on articles published in 2017 in journals tracked by the Nature Index, Shanghai produces around 12% of the country's total output in the Nature Index. While it was still behind the world's top 10 cities in 2012, its fractional count, which calculates share of authorship, exceeded New York and the greater Boston area in the United States, as well as Paris and Tokyo in 2017, making Shanghai the second highest publishing city in the world as measured by the index. It lagged only behind Beijing, home to the Chinese Academy of Sciences (CAS), the world's largest research producing institution in the Nature Index. From 2012 to 2017, Shanghai has a 46% increase in the share of authorship and a 76% increase in article count, a growth rate higher than that of the world's most other major research producing cities.

By subject area, Earth and environmental science has the highest growth rate from 2012 to 2017, given its much lower base value in research output. In fact, output in all subjects has increased substantially in Shanghai from 2012 to 2017. As with the rest of China, chemistry is clearly the strength in Shanghai, accounting for more than half of its research output measured in fractional count, which is in contrast to other top research producing cities in the Nature Index, except Beijing.

Shanghai's academic institutions, including universities and their affiliated research centres, have contributed to most of its increases in research output. They account for 63% of the city's Nature Index output from 2012 to 2017, followed by government research institutions, such as those CAS institutes.

As a commercial centre, Shanghai also has 90 corporate institutions producing one or more articles in the Nature Index since 2012, exceeding the number of academic, government, or healthcare institutions contributing to the Nature Index in the city. This broad participation in research from corporate institutions demonstrates the dynamic forces that drive Shanghai's research capacity. "We encourage collaboration between our universities and enterprises," said Zhang Quan, director general of the Science and Technology Commission of Shanghai Municipality. "We want to see research results produced at our academic institutions translated into technological innovations that can contribute to socioeconomic development."

Collaboration as the norm

Growth is also seen in collaborative research, both in terms of domestic and international collaboration. International bilateral partnerships in Shanghai have grown by 159% from 2012 to 2017, while inter-city domestic partnerships have increased by 164%. The number of bilateral partnerships formed is based on co-authorship on articles tracked by the Nature Index.

Looking at article count, Shanghai's number of collaborative articles has doubled from 2012 to 2017, increasing by 90% for domestic collaboration, and by 106% for international collaboration. The proportion of internationally collaboration articles has increased from 45% in 2012 to 53% in 2017. Evidently, international collaboration has contributed considerably to Shanghai's rapid increase in research output and is dominating quality research publishing.

As science becomes more interdisciplinary and resource-intensive, collaboration is becoming the norm. International big science projects are also becoming more common. Aiming to be a leading research powerhouse, China is actively participating in, and also seeks to lead such global collaborations. The many international ties made between Shanghai institutions and their counterparts abroad, while demonstrating such a commitment, has led to growing research links. Meanwhile, the growing number of Chinese-born scientists returning from overseas also drives international collaboration, either with their former supervisors or colleagues abroad.

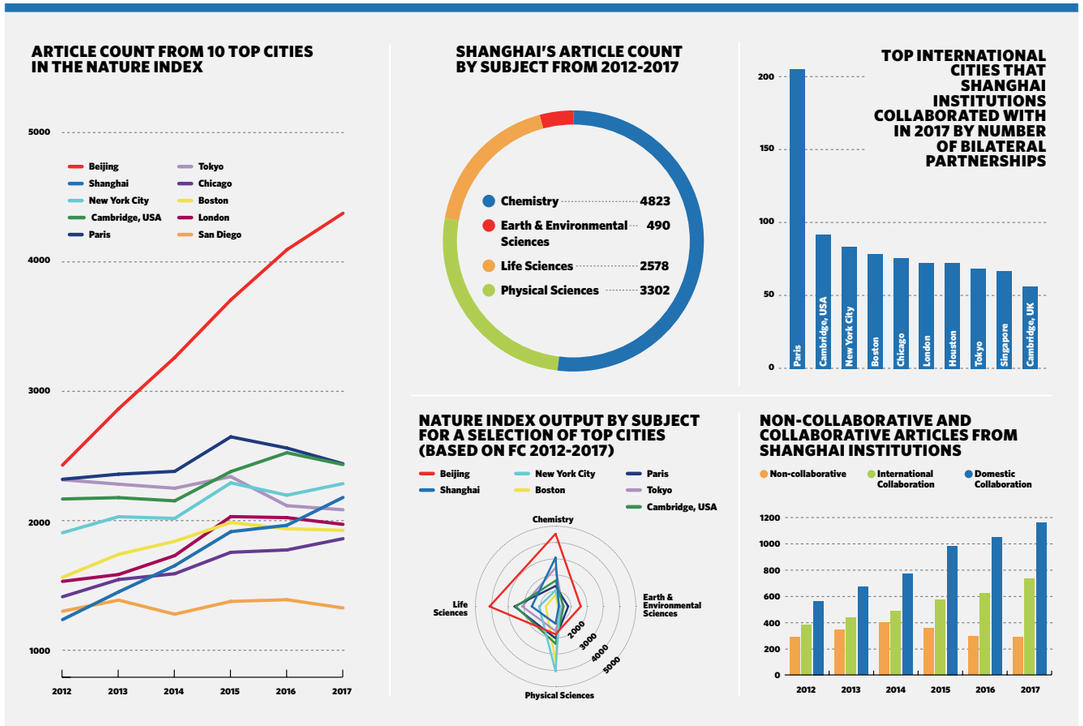

Unsurprisingly, Shanghai's top research producing academic institutions, such as Fudan University, Shanghai Jiao Tong University and East China Normal University, are also ranked among the top in their 2017 bilateral collaboration score, suggesting the role of collaboration in driving their high quality research output. This score is calculated by summing the fractional counts of the two institutions on papers to which both have contributed. The most active institution in international bilateral partnerships is NYU Shanghai, a joint venture in higher education between East China Normal University and New York University, which has most of its research output collaborated with its umbrella institution in the United States.

The United States is so far the biggest research collaborator for Shanghai. New York, Cambridge, Chicago, among others, are the top cities that Shanghai institutions collaborate with. Multilateral collaboration from Shanghai is the strongest with institutions in New York City. This is partially attributable to the three-way ties amongst NYU Shanghai, East China Normal University and New York University. In bilateral partnerships, Paris stands out as the top city that Shanghai institutions collaborated with. The Institut Pasteur of Shanghai, CAS has contributed greatly, given its close association with the Institut Pasteur in Paris.

Academic institutions in Shanghai tend to collaborate with cities in developed countries, such as the United States, UK, Germany and Japan. The exception is Tongji University, which has co-authored many papers with the UN Environment Programme, headquartered in Nairobi, Kenya. A joint institute for environment and sustainable development between the two institutions explains their close collaboration.

Joint research centres, institutes and schools are sprouting in Shanghai. Collaborative projects are also bringing more and more international researchers to the city. "We are glad to see the growing partnerships made between Shanghai institutions and their counterparts abroad, leading to increased research output," said Zhang. "We hope to broaden our collaboration and be more open, making Shanghai an ideal place for researchers around the world and a truly international science and technology innovation hub." ■

上海科技
www.stcsm.gov.cn

Advertiser retains sole responsibility for content

Make your mark in the city of makers

Calling talented faculty to the
HARBIN INSTITUTE OF TECHNOLOGY, SHENZHEN (HITSZ)

The 'City of Creators', Shenzhen is China's frontrunner in promoting innovation-driven development. Harbin Institute of Technology, Shenzhen (HITSZ) maintains high standards to attract excellent, international talents, while carrying forward the innovation spirit of Shenzhen to contribute to national and regional economic and social development.

Harbin Institute of Technology (HIT), founded in 1920, is a national key university under the Ministry of Industry and Information Technology. It offers specializations in science, engineering, management and many other fields. It is a member of the C9 League and one of the first universities to be selected for the national Project 985. It became part of the national Double First-Class initiative in 2017.

HIT was ranked as the world's sixth best university for engineering, and the second in China, according to the 2018 US NEWS Global Universities ranking. In the Academic Ranking of World Universities (ARWU) 2017 ranking, it was eighth in China and among the global top 200. In the same year, HIT had a subject area ranked among the global top 0.01%, according to Essential Science Indicators (ESI) data.

Together with the Shenzhen Municipal Government, HIT created Harbin Institute of Technology, Shenzhen (HITSZ) in 2002. It is now one of its key campuses. It is the first university among the C9 League to open a campus and enrol undergraduates in Shenzhen.

For more details about HITSZ, please refer to www.hitsz.edu.cn.

HITSZ now has multiple faculty positions available. It is eagerly seeking talented researchers from around the world to join its dynamic team in Shenzhen. ■

哈爾濱工業大學(深圳)
HARBIN INSTITUTE OF TECHNOLOGY, SHENZHEN

FIELDS OPEN FOR RECRUITMENT:

1. Computer Science and Technology
2. Electronic Science and Technology
3. Materials Science and Engineering
4. Control Science and Engineering
5. Power Engineering and Engineering Thermophysics
6. Mechanics
7. Mathematics
8. Practical Economics
9. Business Administration
10. Civil Engineering
11. Mechanical Engineering
12. Architecture
13. Space Science and Technology
14. Information and Communication Engineering
15. Environmental Science and Engineering
16. Management Science and Engineering
17. Biomedical Engineering
18. Chemistry
19. Physics
20. Biology
21. Design
22. Sociology
23. Marxism
24. Marine Science
25. Aeronautical and Astronautical Science and Technology
26. Urban and Rural Planning
27. Linguistics
28. English

QUALIFICATIONS AND REQUIREMENTS:

1. A Ph.D. in a related field;
2. Experience working abroad or postdoctoral training is preferred

SALARY AND BENEFITS:

1. Successful applicants will be appointed as 'Professor', 'Associate Professor' or 'Assistant Professor' according to their qualifications and backgrounds;
2. An annual salary in the range of 300,000 to 1.5 million RMB;
3. Research funds will depend on position and field.
4. Support to apply for high-level talents allowance in Shenzhen (ranging from 1.6 to 3 million RMB);
5. Subsidized housing

TO APPLY:

Applications must include the following documents:

1. Application Form for Faculty Position (downloadable from: http://www.hitsz.edu.cn/job/view/2.html; please indicate main research areas to facilitate the application process);
2. A cover letter in three parts: an introduction explaining why you should be considered for the job, expected contributions to the school in terms of research, and future work plan;
3. Three letters of recommendation
4. Electronic copies of supporting documents, including diploma, lists of publications and achievements, etc.

Application materials should be sent to YANG Zhixi at: hrsz@hit.edu.cn.

CONTACT:

Ms. YANG Zhixi

Human Resources Department
Harbin Institute of Technology, Shenzhen
E-mail: hrsz@hit.edu.cn.
Tel: +86-755-26033365

THE CHALLENGES AND OPPORTUNITIES OF CREATING A KNOWLEDGE HUB IN THE GLOBAL SOUTH

A conversation with **PROFESSOR MAMOKGETHI PHAKENG**, vice-chancellor, University of Cape Town

The world's knowledge map is heavily weighted towards the global North. When people think science cities, they don't necessarily think of Africa: a continent of great inequality and development challenges. This is visible in its cities, and Cape Town is no exception. But, says the new vice-chancellor of the University of Cape Town (UCT), Professor Mamokgethi Phakeng, cities in the global South also present many opportunities for creating a knowledge hub.

How is the Cape Town knowledge hub different from those in the global North?
The main difference might be the values that are embedded in the way we do our science. Based in a continent that is at the sharp end of many of the world's most intractable problems, development is at the core of our science and innovation. For instance, we have a thriving department of ICT4D (Information and Communication Technology for Development), which, among other things, developed an app to help small-scale fishermen compete with the big fishing companies.

And, like many research universities, we have a raft of scientists from different disciplines working on various aspects of biomedical technology. What is different about ours is their focus on the needs of the developing world, such as a low-cost, long-lasting heart valve that can be inserted without the need for open-heart surgery. Of course, it turns out that the global North is also very interested in innovation that drives costs down and avoids unnecessary medical intervention, which makes what is happening at UCT and in Cape Town attractive to the universities and industry in the global North.

What challenges does Cape Town face, and how does UCT help to resolve them?
South Africa is the most unequal country in the world. Any visitor to Cape Town is struck by the poverty of the informal settlements as they drive towards the high-rise luxury of the city centre and southern suburbs. Cape Town is also a fast-growing city. Our migrant and poverty-stricken population struggles to get the quality of education that is needed for them to flourish, and to contribute to making the city a true knowledge hub.

The good part of that story is the enormous potential that lies in this diverse and growing population. UCT aims to tap into the potential of South Africa and its people, and in doing so provides opportunities in a number of ways. For instance, the Graduate School of Business Solution Space, which works closely with corporate partners to incubate start-ups, is situated at the V&A Waterfront, right on the doorstep of Africa's fastest-growing tech hub. But it has also launched a campus in Philippi Village, in one of the most deprived areas of Cape Town, where we work directly with entrepreneurs in the community.

What makes UCT a valuable partner?
Well, it doesn't hurt that we have one of the most beautiful campuses in the world, and are based in one of the most beautiful cities in the world. That means people want to live and work here, and partners want to visit us.

UCT aims to tap into the potential of South Africa and it's people – and in doing so provides opportunities.

Apart from that, the most obvious opportunities lie in our geographic vantage point. It makes both the city and the university a significant destination for researching questions that are important to South Africa, the continent and the world.

For instance, Cape Town's position on the confluence of three major ocean systems makes it an ideal place for marine research. Its proximity to areas under dark skies without light pollution lends itself to astronomical studies. South Africa's population provides valuable cohorts for studies: into mother and baby health; AIDS and tuberculosis; violence and trauma; and lifestyle diseases.

These vantage points have given us world-leading expertise in a range of research fields such as ornithology, climate and development studies and life sciences and medicine. But what matters to us even more than being the best *in* Africa is being the best *for* Africa – research with impact. And this turns out to make us an attractive global partner in the current context where major research funding is focused on solving the world's most intractable problems, such as the sustainable development goals.

Does UCT have a close relationship with the city of Cape Town?
Absolutely: in much of our research, we partner with industry and government, which has knock-on effects for the city as a whole. For instance, the recent water crisis that nearly brought our city to its knees was partly averted because of the close cooperation between our scientists, the city and the province, and with industry. There are lessons the rest of the world can learn from us in how we got through the crisis together.

ADVERTISER RETAINS SOLE RESPONSIBILITY FOR CONTENT

Best in Africa.
Best for Africa.

As the leading university in Africa, the University of Cape Town is in a prime position to connect institutionsin the global north with its research collaborators elsewhere on the continent: drawing international expertise to Africa, strengthening collaborations within Africa and ensuring an African voice is part of global debates.

www.uct.ac.za

UNIVERSITY OF CAPE TOWN
IYUNIVESITHI YASEKAPA • UNIVERSITEIT VAN KAAPSTAD

A close look at in vitro diagnosis

Advancement of in vitro diagnostics is PROVIDING NEW TOOLS TO SUPPORT DISEASE DIAGNOSIS AND TREATMENT. In China, researchers encourage university-industry collaboration to promote technological innovation.

QIAN KUN: Principal Investigator, School of Biomedical Engineering at SJTU

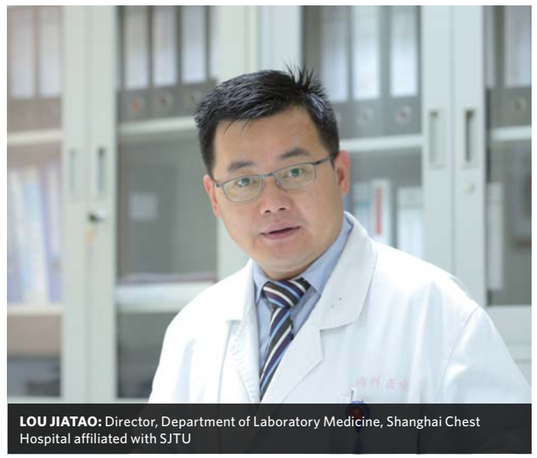

LOU JIATAO: Director, Department of Laboratory Medicine, Shanghai Chest Hospital affiliated with SJTU

The growing prevalence of chronic and infectious diseases has spurred development of the in vitro diagnostics (IVD) market. It is estimated that the global IVD market will reach US$73.9 billion by 2020 from US$61.9 billion in 2016. And the Chinese IVD market, estimated at 60 billion RMB (approximately US$10 billion) in 2017, is the fastest growing.

Discoveries in microbiology and immunochemistry have provided cost-effective diagnostic tools for faster and more accurate results. To explore advanced IVD technologies to improve disease detection and treatment, Shanghai Jiao Tong University (SJTU), China Association of In-Vitro Diagnostics, and the Experimental Medicine Professional Committee (EMPC) have partnered with *Nature Biomedical Engineering* to present a Nature Conference on IVD in March 2019. Here, two of the conference organizers, Qian Kun, and Lou Jiatao from SJTU, share their outlook on the future of IVD technologies in China and around the world.

QIAN: The development of IVD aims to provide faster, smaller, and more cost-effective tools that enable more precise diagnosis and point-of-care testing or self-testing. Artificial intelligence and cloud services also provide low-cost solutions for limited-resource settings. Today's cutting-edge technologies in laboratory medicine, including genetic sequencing, liquid biopsy, microfluidics and mass spectrometry technologies, reflect such trends. Sequencing technologies and multi-omic analysis provide a more comprehensive picture for personalised disease diagnosis. Liquid biopsy enables a non-invasive, real-time tool for early diagnosis of cancers. Microfluidics and other micro/nano devices provide a solution to system integration and make instruments smaller. And mass spectrometry helps achieve fast, high-throughput and high-sensitivity testing.

Our ultimate aim is to improve global health. We hope by discussing the current trends of IVD, we can guide its development and achieve our goals faster.

LOU: One area of increasing application of IVD technologies is cancer diagnosis and treatment, of which an exciting breakthrough is liquid biopsy. High-throughput sequencing techniques offer a non-invasive approach that enable disease diagnosis based on blood or urine samples. Researchers typically evaluate circulating tumour DNA (ctDNA) or circulating tumour cells (CTCs) to identify cancer biomarkers, the results of which can be used for cancer screening, to guide treatment plans and to monitor responses to treatment.

At SJTU, we are developing sequencing technologies to meet clinical needs for multi-gene testing and digital polymerase chain reaction (PCR) technology, which are undergoing trials. Together with microfluidic device and mass spectrometry techniques, these developments are allowing personalised disease management.

QIAN: Among my personal interests is developing mass spectrometry techniques for large-scale clinical use. Mass spectrometry is a common method used in omics analysis and is considered the future of diagnostics. It allows testing hundreds of thousands of indicators in a single test, shortening testing time to a couple of minutes.

CONFERENCE ORGANIZERS

SONG HAIBO
Chairman,
China Association of In-Vitro Diagnostics

As an experienced IVD technician, Song has served as deputy director of Anhui Provincial Center for Clinical Laboratories, deputy chairman of Anhui Micro-Improvement Society, and vice chairman of National Association of Health Industry and Enterprises Management. He has supported standardization of IVD systems and provided technical support to boosting the IVD industry. Song also holds several academic positions and serves on editorial boards of several journals in laboratory medicine. He is the founder of China Association of Clinical Laboratory Practice Expo (CACLP), China's largest professional exhibition in IVD industry.

WANG HUALIANG
Director,
Experimental Medicine Professional Committee (EMPC, China)

Wang is the director of Shanghai Clinical Laboratory Center, editor-in-chief of the journal of *Laboratory Medicine*, vice director of the Laboratory Medicine Management Committee of Chinese Hospital Association, and the vice director of Genetic Diagnosis Branch of Genetics Society of China. As an expert receiving special allowance from the State Council, Wang has led or participated in more than 20 major research projects, funded by the national or Shanghai municipal government, winning multiple science and technology awards. He has also published in top academic journals, such as *Science*, and *Clinical Biochemistry*.

The technology offers high-throughput, femtomolar sensitivity and fast testing, taking analysis from molecular to cellular levels. I have no doubt that it will revolutionize IVD.

LOU: In China, the IVD market is growing fast and has great potential. However, our IVD market is still relatively small and is generally dominated by big multinational companies. We need core products, and have lots of overlapping production. There is also a gap in our research capacity, compared with the world's science powerhouses. As IVD products have long R&D cycles and high technological thresholds, it is important for academia and industry to join forces.

QIAN: Developing IVD technologies requires collaboration across academia, the health sector, enterprises and governments. Academics propose novel research questions, explore the questions and publish the results in high impact journals. They are the source of innovation capacity and responsible for cultivating talented professionals. The industry has engineering capacity and provides funding support to research. As it connects to the end-users, it provides clinical application solutions. Governments also provide essential funding support and by enhancing market monitoring and speeding up product approval, facilitate commercialization of IVD technologies.

LOU: SJTU is very keen on this great endeavour. We are equipped with advanced research platforms, including national major science and technology infrastructure facilities, state key laboratories, such as those focusing on cancer genetics and medical omics studies, as well as various national research centres, laboratories and international collaboration centres. Our capacity is also demonstrated by our strong publication record, with the number of papers published in SCI journals leading in China. We are also national leaders in the number and value of natural science research grants won. More importantly, we have integrated, strong biomedical and engineering programmes. Our clinical medicine programme is the best in the country and the laboratory medicine department has a good academic standing. With our affiliated hospitals, we can also facilitate close collaboration with the clinical sector, making IVD technologies more accessible. ■

+86 (0)21 64760765
zhaobing@caivd.org
https://www.nature.com/natureconferences/invitro19/indexhtml

Advertiser retains sole responsibility for content

TACKLING CHALLENGES THROUGH SCIENCE AND TECHNOLOGY

Newly established SHANGHAITECH UNIVERSITY offers a stimulating environment for pursuing studies and impactful research.

Officially opened in 2013, ShanghaiTech University was jointly established by the Shanghai Municipal Government and the Chinese Academy of Sciences (CAS). It is dedicated as a research university of academic excellence . It is a dynamic hub where innovative research, education, and community service combine to provide a multi-disciplinary approach to learning, and to solving global challenges.

Located in Zhangjiang Hi-Tech Park, ShanghaiTech is close to various industries and venture companies, and accessible for large science facilities, including the Shanghai Synchrotron Radiation Facility, the National Center for Protein Science-Shanghai, the National Drug Screening Platform and the Shanghai Center for Microsatellites.

ShanghaiTech University comprises five schools — the School of Physical Science and Technology (SPST), the School of Information Science and Technology (SIST), the School of Life Science and Technology (SLST), the School of Entrepreneurship and Management (SEM), the School of Creative Arts (SCA) — and three research institutes — the Shanghai Institute for Advanced Immunochemical Studies (SIAIS), the iHuman Institute, and the Institute of Mathematical Sciences.

Investing in people

The university is gathering a top-tier faculty of 1,000 professors, including 500 distinguished professors-in-residence from CAS or other prestigious universities or institutes, four Nobel laureates, 34 CAS members, three Chinese Academy of Engineering members, 11 National Academy of Sciences (USA) members and three Royal Society (UK) fellows.

ShanghaiTech offers bachelor's, master's and doctoral degrees. It will eventually have 2,000 undergraduate students and 4,000 graduate students (including 3,000 doctoral students). The first cohort of 296 graduate students was admitted in September 2013, followed by first cohort of 207 undergraduate students from nine provinces in China in 2014. Currently there are 1433 undergraduate students and 1788 graduate students on campus.

ShanghaiTech aims to nurture future leading scientists, inventors and entrepreneurs. It fosters students' moral integrity, academic capabilities and innovative spirit. Students are encouraged to investigate the challenges China faces, explore cutting-edge research areas and high-tech industries, and implement their innovative and entrepreneurial ideas.

Advancing research through collaboration

ShanghaiTech is actively engaged in the globalization of education. It has extensive collaborations with the University of California, Berkeley, the University of Chicago, MIT, Yale University, Harvard University, and the University of Padova. To break down barriers between research and industry, ShanghaiTech collaborates closely with domestic and international high-tech companies in joint research and student training. ■

TIME TO SHINE AT SHANGHAITECH UNIVERSITY

ShanghaiTech University is a young and dynamic higher education institution aiming for high-quality research and global influence.

To address challenges faced by China and the world, it seeks innovative solutions in energy, materials, environment, human health, data science, artificial intelligence (AI), and electrical engineering. An integral part of the Zhangjiang Comprehensive National Science Center, the university is now leading several frontier research projects at large-scale facilities. For more information, please visit: www.shanghaitech.edu.cn.

We are now seeking talented researchers for multiple faculty positions at all ranks in the following fields:

School of Physical Science and Technology: energy, system materials, photon and condensed state, material biology, environmental science and engineering

School of Life Science and Technology: molecular and cell biology, structural biology, neuroscience, immunology, stem cells and regenerative medicine, system biology and biological data, molecular imaging, biomedical engineering

School of Information Science and Technology: computer science, electrical engineering, information engineering, artificial intelligence, network and communication, virtual reality, statistics, big data and data mining

School of Entrepreneurship and Management: economics, finance, accounting, management, marketing, strategy and entrepreneurship

School of Creativity and Art: film production, life drawing, photography, VR and game coding, illustration & visualization, performing arts

Shanghai Institute for Advanced Immunochemical Studies: antibody therapy, immunotherapy, cell therapy, regeneration medicine

iHuman Institute: bio-imaging, biology, chemistry, computational biology, AI/ML

Institute of Mathematical Sciences: pure mathematics, theory of computing, applied mathematics

Successful applicants will have a doctoral degree, and are expected to establish a record for independent, internationally recognized research, supervise students and teach high-quality courses.

ShanghaiTech University will offer attractive compensation packages, including:

initial research support package: reasonable start-up funds, research associates and post-doctoral fellows, laboratory space to meet research needs

compensation and benefits: highly competitive salary commensurate with experience and academic accomplishments, a comprehensive benefit package

subsidized housing: on-campus, 80/100/120 m^2 faculty apartments available at low rent for tenure and tenure-track faculty

relocation & travel allowance: reimbursement of expenses for household relocation and family's one-way travel

family assistance: support with children's education; affiliated kindergarten, primary and middle schools are under construction

To apply: using this format, please submit a cover letter (Firstname_Lastname_Cover_Letter.pdf), a research plan (Firstname_Lastname_Research_Plan.pdf), and a CV (Firstname_Lastname_CV.pdf) to shanghaitechuniversity@gmail.com.

上海科技大学
ShanghaiTech University

shanghaitechuniversity@gmail.com
www.shanghaitech.edu.cn/eng

Advertiser retains sole responsibility for content

A GUIDE TO THE NATURE INDEX

A description of the terminology and methodology used in this supplement, and a guide to the functionality available free online at natureindex.com

The Nature Index is a database of author affiliations and institutional relationships. The index tracks contributions to research articles published in 82 high-quality natural science journals, chosen by an independent group of researchers.

The Nature Index provides absolute and fractional counts of publication productivity at the institutional, national and regional level and, as such, is an indicator of global high-quality research output and collaboration. Data in the Nature Index are updated regularly, with the most recent 12 months made available under a Creative Commons licence at natureindex.com. The database is compiled by Springer Nature.

NATURE INDEX METRICS

The Nature Index provides several metrics to track research output and collaboration. These include article count, fractional count, adjusted fractional count and bilateral collaboration score.

The simplest is the article count (AC). A country/region or institution is given an AC of 1 for each article that has at least one author from that country/region or institution. This is the case regardless of the number of authors an article has, and it means that the same article can contribute to the AC of multiple countries/regions or institutions.

To get a sense of a country/region's or institution's contribution to an article, and to ensure they are not counted more than once, the index uses fractional count (FC), which takes into account the share of authorship on each article. The total FC available per article is 1, which is shared among all authors under the assumption that each contributed equally. For instance, an article with 10 authors means that each author receives an FC of 0.1. For authors who are affiliated with more than one institution, the individual author's FC is then split equally between those institutions.

The total FC for an institution is calculated by summing the FC for individual affiliated authors. The process is similar for countries/regions, although complicated by the fact that some institutions have overseas labs that will be counted towards host country/region totals.

When comparing data over time, FC values are adjusted to 2017 levels to account for the small annual variation in the total number of articles in Nature Index journals. The adjustment of FC values in each year is done by calculating the percentage difference in the total number of articles in the index in a given year relative to the number of articles in 2017, and applying this adjustment to FC values.

Another metric is bilateral collaboration score (CS). A bilateral collaboration can be between any two institutions or countries/regions co-authoring at least one article in the journals tracked by the Nature Index. CS is derived by summing the FCs from articles with authors from both institutions. The collaboration score between two institutions A+B is the sum of each of their FCs on the papers to which both have contributed.

THE SUPPLEMENT

Nature Index 2018 Science Cities is based on data from natureindex.com, covering articles published from 1 January 2012 to 31 December 2017 at the city and country/region level, and articles from 1 January 2015 to 31 December 2017 at the institution level. Most analyses within the supplement use FC as the primary metric, with time series figures adjusted to 2017 levels. Each city's FC is calculated by summing the output of institutions located in it. For institutions spanning multiple cities, such as CAS, entities were assigned to the city where they are located, where possible.

For a selection of the most populous conurbations with significant output in the index in the United States, Canada, Japan, South Korea, India and Europe, we defined boundaries based on official specifications from census bureaus, statistical offices, government offices, or as described in legal documents. The specifications typically group adjacent areas that have a high degree of social and economic integration, as measured by commuting ties. These cities are labelled as metropolitan areas (MA) in the tables and graphs.

The tables rank cities and metro areas by FC in 2017. They also provide each city's AC in 2017, contribution to their country/region's total FC, and percentage of papers co-authored with researchers not based in the city. Separate tables on natureindex.com rank the top cities for corporate output, and in four broad fields. The tables also show each of the five profiled city's leading institutions for high-quality science, ordered by FC in 2017. ■

NATUREINDEX.COM

A global indicator of high-quality research

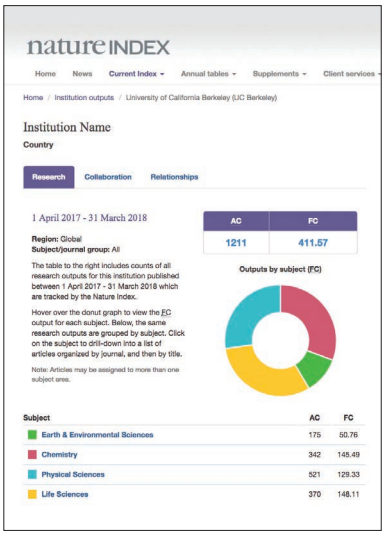

natureindex.com users can search for specific institutions or countries/regions and generate their own reports, ordered by article count (AC) or fractional count (FC).

Each query will return a profile page that lists the country/region or institution's recent outputs, from which it is possible to drill down for more information. Articles can be displayed by journal, and then by article. Research outputs are organized by subject area. The pages list the institution or country/region's top collaborators, as well as its relationship with other organizations. Registering allows users to track an institutions' performance over time, create their own indexes and export table data.

© 2018 Springer Nature Limited. All rights reserved.

nature INDEX 2018 SCIENCE CITIES

NATURE, VOL. 563, ISSUE NO. 7729 (1 NOVEMBER 2018)

COUNTING CAPITAL COSTS

Cities are the ideal setting for scientific exploration. They attract bright and diverse minds, buzz with creative activity, and can summon the capital to realize big ideas. But their potential can be stifled by social realities. Each of the five science cities profiled in this supplement are contending with problems of equity and engagement which, if not addressed, threaten their trajectories.

When it comes to the long-term viability of a science hotspot, local matters count as much as global positioning. Perhaps part of the solution lies in pursuing and rewarding the type of science that engages directly with local communities, and achieves impact.

San Francisco's sci-tech revolution has contributed to soaring housing costs, which could undermine the California metropolis's position as a leading region of innovation (S6). Wuhan is at risk from talent-poaching campaigns by richer coastal cities, as the competition for research supremacy intensifies in China (S16). The fault lines run deep in Cape Town, South Africa, where elite universities are under growing pressure to address inherited racial and gender inequalities (S2).

At the global scale, some degree of benefit sharing is taking place. An analysis of highly-cited research reveals that the gap between top-tier and second-tier cities narrowed between 1999 and 2014 (S18). Similar trends are apparent in the Nature Index, which measures a city's fractional count (FC), a metric for the share of contribution to the authorship of articles in 82 high-quality research journals.

In a highly connected world, cities can't take success for granted. Even though Beijing has emerged as a dominant producer of high-quality research, for example, its share of China's output has declined since 2012, as Nanjing, Wuhan and Guangzhou nestle in. Cities remain powerful units of scientific production, yet each urban centre's capacity is subject to change. Staying on top means paying heed to more than research funding.

Smriti Mallapaty
Senior editor, Nature Index

The cape of change
S2: Cape Town is confronting its colonial past to set a more inclusive research scene.

A venture under pressure

S6: Scientific innovation has powered the San Francisco Bay Area's economy, but local challenges could undermine progress.

City links
S8: Graphic of the top collaborating cities in the index.

A European heavyweight
S14: A rich research network has secured Munich's position as a centre of science in the region.

Discovery central
S16: A hive of young talent, Wuhan has surged up the Nature Index, but competition for minds is heating up.

Peripheral forces
S18: The growing impact of second-tier cities is narrowing the gap in knowledge production.

Standing firm
S22: An island of success in a stricken country, how much more can São Paulo endure?

The tables
S24: The world's cities ranked by their production of high-quality research.

COURTESY OF GENENTECH, A MEMBER OF THE ROCHE GROUP

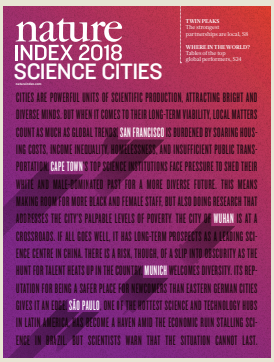

ON THE COVER

The Nature Index profiles five science cities that are leaders in their regions: Cape Town, San Francisco, Munich, Wuhan and São Paulo.

EDITORIAL: Catherine Armitage, Smriti Mallapaty, Rebecca Dargie, Gemma Conroy, Herb Brody, Stephen Pincock **ANALYSIS:** Aaron Ballagh, Bo Wu, Willem Sijp **ART & DESIGN:** Tanner Maxwell, Madeline Hutchinson, Wojtek Urbanek, Wesley Fernandes **PRODUCTION:** Kay Lewis, Karl Smart, Ian Pope, Nick Bruni, Bob Edenbach, Joern Ishikawa **MARKETING:** Stacy Best Ruel, Angelica Sarne **SALES & PARTNER CONTENT:** Helen Hill, Rory Mulkerrins, Ruffi Lu, Stella Yan, Nicole Yu, Sharon Wang, Yingying Zhou, Sara Phillips, Chika Takeda, Aimee Sics, Chris Gilloch **PUBLISHING:** Rebecca Jones, Richard Hughes, David Swinbanks.

NATURE INDEX 2018 SCIENCE CITIES
Nature Index 2018 Science Cities, a supplement to *Nature*, is produced by Nature Research, the flagship science portfolio of Springer Nature. This publication is based on data from the Nature Index, a Nature Research website maintained and made freely available at natureindex.com.

NATURE EDITORIAL OFFICES
The Campus, 4 Crinan Street,
London N1 9XW, UK
Tel: +44 (0)20 7833 4000
Fax: +44 (0)20 7843 4596/7

CUSTOMER SERVICES
To advertise with the Nature Index, please visit natureindex.com/
clientservicesfeedback@nature.com

Copyright © 2018 Macmillan Publishers Limited, part of Springer Nature.
All rights reserved.

© 2018 Springer Nature Limited. All rights reserved.

Cape Town benefits from geographic advantage and funding strength.

NATURE PICTURE LIBRARY/ALAMY

THE CAPE OF CHANGE

Africa's science star is confronting its colonial past to set a more inclusive research scene, benefitting more of its citizens.

LINDA NORDLING

Early pastoralists living on Africa's southern tip found fresh water and grazing in the shadow of Table Mountain, where Cape Town lies today. They called it *Camissa*, the place of sweet water. European explorers rounding the Cape, too, found it a useful pit stop. In their wake, botanists came to study the region's unique plants and animals, and astronomers came for the view it offered of the southern skies.

Today, Cape Town is a global hub for scientists studying biological diversity and astronomy. The city houses the nerve centre for an enormous radio telescope being constructed hundreds of kilometres inland, set to become the most powerful in the world. It is also home to several experts on local species ranging from the penguins that nest on its beaches, to the *fynbos* shrubland unique to the area.

But in the years since South Africa's first democratic elections in 1994, this scientific legacy, rooted in colonialism and racial segregation, has become a double-edged sword. Cape Town's top science institutions face pressure to shed their white and male-dominated past for a more diverse future. This means making room for more black and female staff and students, but also doing research that addresses South Africa's palpable poverty.

SOUTHERN SKIES

Cape Town is Africa's leading science city, when measured on its contribution to articles in the 82 high-quality science journals in the Nature Index over the past six years. Its accumulated fractional count (FC) for 2012–2017 was 107.2, just above the score for Johannesburg (102.77). The city's output is largely in the physical sciences, with strong representation in the life sciences and Earth and environmental sciences.

The University of Cape Town (UCT), South Africa's oldest, is by far its leading institution in the index with a 2012–2017 FC of 33.96, followed by the University of the Western Cape (UWC) at 5.08. Nearby Stellenbosch — the third highest performing science city in Africa with a six-year FC of 86.84 — also contributes to the Cape's research appeal.

Cape Town attracts significant research investment. Universities in the Western Cape, the province of both Cape Town and Stellenbosch, were responsible for nearly 31.8% of South Africa's higher-education research spend in 2015. By contrast, universities in Gauteng — the province of the capital Pretoria and Johannesburg, which has twice as many inhabitants as the Western Cape — were responsible for 33.5% of the spend. In South Africa's central Karoo desert, an international team is building the Square Kilometre Array, a radio telescope whose thousands of dishes will be shared by Australia and Africa.

The telescope has attracted hundreds of scientists and engineers to the city. UCT and UWC are both partners in the African Research Cloud, a national project to develop the capacity needed to deal with the huge datasets this telescope will produce. And in 2016, South Africa's Council for Scientific and Industrial Research launched Africa's fastest supercomputer at its Cape Town-based Centre for High Performance Computing, which will also play a role in designing the data-crunching systems for the astronomy data.

The supercomputer, known as Tsessebe, or 'antelope', is also supporting Cape Town's claim

© 2018 Springer Nature Limited. All rights reserved.

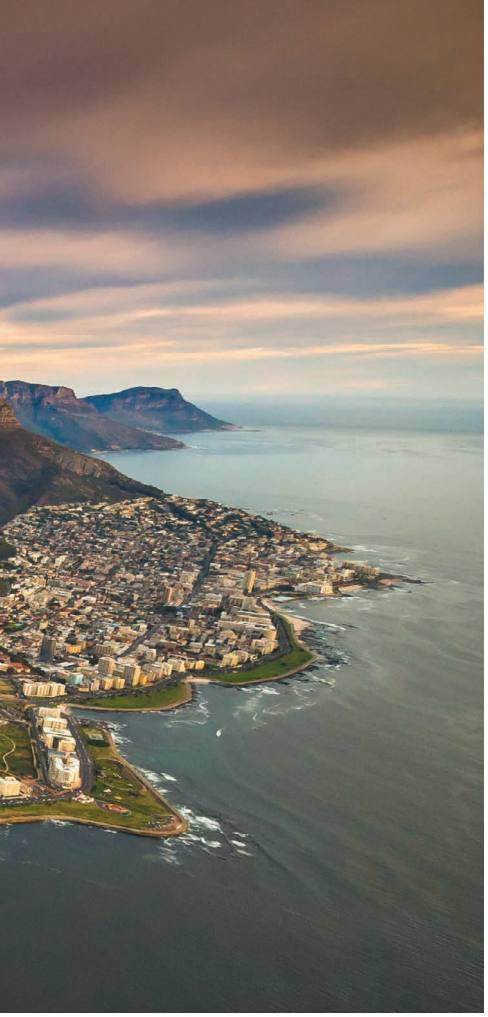

as a bioinformatics hotspot. Africans are the most genetically diverse people in the world. Humans have lived on the continent longer than anywhere else; only a subset migrated out. There is a push to understand how this genetic diversity influences disease and healthcare. The South African Medical Research Council has partnered with China to build the continent's most powerful whole-genome sequencing facility in the city, due to open in late 2018.

"WE HAVEN'T BROKEN THROUGH FROM BEING A PLACE ON THE HILL THAT PEOPLE THINK DOESN'T BELONG TO THEM."

The region's biodiversity, accessible so close to a major urban centre, continues to spark scientists' imagination — not least because it provides test-cases for species under increasing environmental and climatic stress.

"We live in the urban area with the highest concentration of red-listed species in the world," says Claire Spottiswoode, who heads UCT's Percy FitzPatrick Institute of African Ornithology. A South African by birth, she recently returned to Cape Town after 15 years abroad. "It's a privilege to have fascinating research problems and exhilarating biodiversity in such close proximity," she says. But change is afoot for South Africa's established institutions. UCT is a case in point. From its mountain perch, on land bequeathed by the staunch imperialist, Cecil John Rhodes, UCT looks out over the Cape's lowlands. It was to these Cape Flats, which bake in summer and flood in winter, that the architects of Apartheid forcefully moved non-white families. Its residents remain predominantly black and poor.

DECOLONIZING SCIENCE

In the early years of democracy, despite efforts to make them more inclusive, the intake at South Africa's top universities remained skewed towards relatively wealthy and advantaged students. However, three years ago, a rally to remove a statue of Rhodes from UCT snowballed into a country-wide push for free, decolonized education. Colonialism, the protesters argued, remained woven into the fabric of South Africa's institutions of higher learning. The protests disrupted teaching and damaged property in the Cape region worth more than 130 million rand (US$9 million).

Mamokgethi Phakeng, a mathematics education professor and UCT's vice-chancellor, is working to promote black excellence at the institution, where white South African professors still outnumbered their black, Indian and mixed-race South African counterparts by a factor of nearly four to one in 2017.

Susan Bourne, UCT's dean of science, says the university rewards community-facing initiatives such as outreach projects, spin-out activities or giving policy advice more now than it did a decade ago.

She offers the Abalobi app as an example of research developed at UCT that is directly helping local communities. The app connects small-scale fishers with restaurants, helping to match supply with demand and allowing fisheries to trace the catch from hook to cook.

Another way to bring scientists and city-dwellers closer together is through cooperating on urgent problems, Bourne adds. One example is the devastating drought that gripped the city earlier this year. The crisis allowed UCT to demonstrate the real-world usefulness of its science. Its water experts offered basic water-saving advice to the public, and policy input to disaster-response agencies, in particular through the UCT Future Water Institute, helping to keep the 'sweet waters' flowing in Cape Town.

The South African government also wants to put science to work to address the country's ills. A 10 September 2018 draft science policy — the country's first for 20 years — identifies fostering science and innovation for social benefit and economic transformation as a key priority for the country.

But, Bourne admits UCT needs to do more. "We haven't broken through from being the place up on the hill that people on the Cape Flats think doesn't belong to them." ■

CAPE TOWN

SHARE OF COUNTRY'S FRACTIONAL COUNT (FC) 2017: 20.4%

TOP 3 INSTITUTIONS (FC 2017):

1. University of Cape Town: 9.35
2. University of the Western Cape: 1.44
3. South African Astronomical Observatory: 1.07

TOP SOUTH AFRICAN CITIES

Cape Town is South Africa's top science city, based on its cumulative fractional count (FC) in the index 2012–2017.

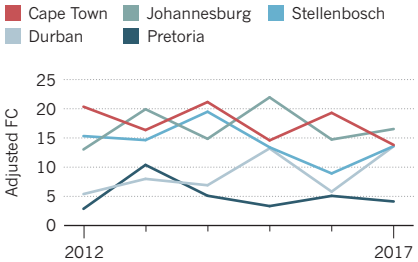

SCIENCE SECTORS

Academic institutions are the largest contributors to Cape Town's output in the index, measured by fractional count (FC) 2012–2017.

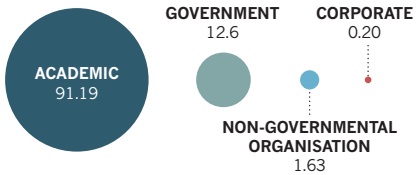

TOP FIELDS

Below are the top 6 fields that researchers in Cape Town contribute to in the index, measured by fractional count (FC) 2015–2017.

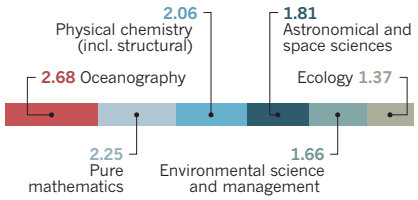

CHOICE JOURNALS

Cape Town-based researchers contribute more articles (AC) to the *Journal of High Energy Physics* than to any other index journal. In this journal, they account for 12% of the authorship (FC) of papers to which they contribute.

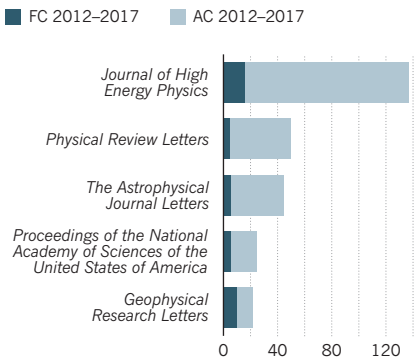

SOURCE: NATURE INDEX; SOURCE FOR 'TOP FIELDS': NATURE INDEX/DIMENSIONS FROM DIGITAL SCIENCE

© 2018 Springer Nature Limited. All rights reserved.

A VENTURE UNDER PRESSURE

Scientific innovation has long powered the San Francisco Bay Area's economy, but community and political challenges could undermine progress.

KATHERINE BOURZAC

From the integrated circuit to synthetic insulin, mail-order genetic tests and ride sharing, scientific discoveries and technologies developed by researchers and engineers in the San Francisco Bay Area have fuelled the local economy for decades.

But while politicians and urban planners around the world try to emulate the Bay Area's path to economic success through research prowess, locals and social scientists are asking whether the region's model of growth is sustainable. The Bay Area is burdened by the high cost of housing, income inequality, homelessness, gridlocked traffic, and inadequate public transportation. These threaten to undermine the region's status as an economic dynamo. "The viability of the innovation economy is in question," says Benjamin Grant, a director at the non-profit San Francisco Bay Area Planning and Urban Research Association (SPUR).

"The problems the Bay Area is facing are the problems of success," says Grant. The northern California metropolis is among the top 50 science cities in the Nature Index, measured by its contribution to the authorship of 82 high-quality research journals. When assessed solely on the output of its corporate institutions, it ranks number one. The question is whether the Bay Area can, in the face of mounting social problems, retain these companies and the brilliant researchers whose work they depend on.

NETWORK EFFECTS

In the 1970s, the Boston area, with its prestigious universities and long-established corporations, would have been a good bet to become the tech industry hub, says AnnaLee Saxenian, a political scientist and dean of the School of Information at the University of California, Berkeley. But an unusual culture in the Bay Area of open exchange between researchers, companies and universities, as well as strong ties to venture capital, she says, fostered science and engineering research, particularly in Silicon Valley. This sharing and information free-flow arose, in part, from the values of the 1960s hippie counterculture, which was centred in San Francisco.

"Engineers were reacting against the

COURTESY OF GENENTECH, A MEMBER OF THE ROCHE GROUP

A cold room at Genentech. The biotech giant is one of the Bay Area's major employers.

© 2018 Springer Nature Limited. All rights reserved.

corporate culture of the east coast," says Saxenian. Talented scientists and engineers came to the Bay Area from around the world to have access to networks, prototyping and venture funds. And venture capitalists looking for the next big thing, says Saxenian, found it in labs at Stanford University, and at the University of California's campuses in San Francisco, Davis and Berkeley.

The city has attracted many high-achieving scientists in the natural sciences. Zora Modrusan, who develops gene sequencing and analysis techniques at the biotech company Genentech, says the strength of the biotech industry drew her to the Bay Area from Canada 19 years ago. "It's very dynamic and interactive," she says. Since 2015, Modrusan has co-authored some 20 articles in the index journals, developing methods for analysing the functional significance of genetic changes in cancer and other diseases. Her current work seeks insights into the heterogeneity within tumours.

James Hedrick, a materials scientist at IBM Research–Almaden in San Jose, says his work has benefited from exchanges with the region's biologists, machine-learning experts, and catalysis chemists. Hedrick engineers new polymers and has co-authored more than a dozen articles in index journals over the past three years. Initially, IBM was using these materials in part of its chip-making process; now, Hedrick is developing them for devices to deliver targeted drug therapies.

BACKLASH

If you ask a local in San Francisco, you might hear a different take on what the Bay Area's booming innovation economy means: inadequate public transportation and gridlocked traffic (made all the more galling by the privately owned 'tech buses' pulling into public bus stops), growing income inequality, the displacement of communities of colour, and homelessness.

Perhaps the most severe challenge in the region is housing. Real estate company Zillow estimates that the median monthly price for a two-bedroom rental in San Francisco averages US$4,130, towering over the nationwide average of US$1,442, and more than a thousand dollars above New York and Boston. At last count, in January 2017, there were 7,499 homeless people in the city; these numbers have remained fairly steady since 2013.

Grant says the current crop of innovation-driven companies has failed to engage with these civic problems. For better or for worse, he says, "the world of research and innovation has been a world apart in California."

Although the tech industry has increased demand for housing and driven up prices, it does not carry the full blame for the city's social ills, says Alex Schafran, a geographer at the University of Leeds, in the United Kingdom, who studies California's housing crisis.

Broader cultural forces and political failures have contributed. Most people agree that the Bay Area needs more housing, but no one wants tall buildings to go up in their own neighbourhoods, says Grant. And under California's system of government, even if regional planning authorities agree on the need for more housing and public transit, local communities can veto such construction. Building outside developed areas is restricted by conservation regulations that protect large swaths of park lands.

These woes are eroding quality of life in the Bay Area, says Grant, and making it ever more difficult for companies and universities to hire and retain the best researchers and students. Companies are also beginning to move elsewhere, he says. As further evidence of the trend, San Francisco's output in the index has declined in recent years, from a fractional count of 1,723.8 in 2012 to 1,676.35 in 2017.

Such regional declines are hardly unprecedented. "At one time Detroit was the centre of innovation in the United States, and Detroit collapsed," says Grant. But he sees hope in moves by state legislators. California Senate Bill 827, introduced in January 2018 by San Francisco's State Senator Scott Wiener, would have enabled the construction of more housing near public transportation hubs. The bill didn't pass, but that it was even proposed is a sign that the tides may be shifting, says Grant.

> "YOU MAY BE ON THE TOP OF THE WORLD, BUT DON'T GET TOO COMFORTABLE."

Saxenian is more reserved in her projections, and for good reason. Her first paper about Silicon Valley predicted that the high cost of living would drive the tech industry out of the area. That was in the 1980s. "I was wrong," she says. The same conditions that drove the development of the Bay Area's strong culture of scientific innovation make it resilient.

Saxenian sees other threats to research innovation in the Bay Area: repeated cuts to the University of California's budget, and restrictive immigration policies, in particular. "Immigration has been beneficial both to the Bay Area and to other countries," says Saxenian, who has written a book (*The New Argonauts*) on the subject. "Talent goes both ways," she says. But this mutual benefit gets lost in the national political conversation.

Schafran, who grew up in the Bay Area, says researchers and engineers need to get more involved in addressing its social ills — but there are no quick fixes. Since they've been building for decades, "it's gonna take another 30 years to get ourselves out of it," he says. "We can't do this overnight." If researchers remain detached and don't think locally, it could be to their own detriment. "You may be on the top of the world for the moment, but don't get too comfortable," says Grant. ■

SAN FRANCISCO

SHARE OF COUNTRY'S FRACTIONAL COUNT (FC) 2017: 8.5%

TOP 3 INSTITUTIONS (FC 2017):

1. Stanford University: 610.47
2. University of California, Berkeley : 411.70
3. Lawrence Berkeley National Laboratory: 187.93

TOP US CITIES

San Francisco – San Jose is the third leading science city in the United States, measured by fractional count (FC) in 2017.

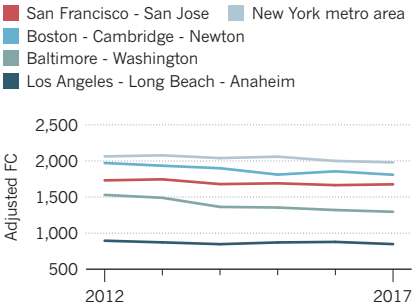

SOURCE: NATURE INDEX; SOURCE FOR 'TOP FIELDS': NATURE INDEX/DIMENSIONS FROM DIGITAL SCIENCE

SCIENCE SECTORS

Corporate institutions contribute a relatively large share of San Francisco's authorship in the index, measured by fractional count (FC) 2012–2017.

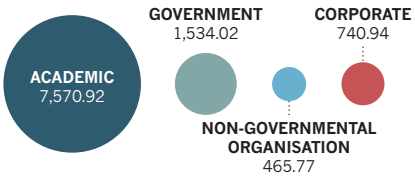

TOP FIELDS

Below are the top 6 fields that researchers in San Francisco contribute to in the index, measured by fractional count (FC) 2015–2017.

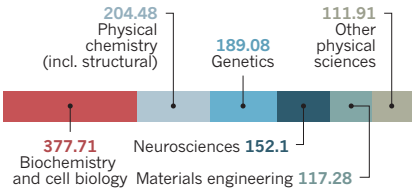

CHOICE JOURNALS

San Francisco-based researchers contribute more articles (AC) to the *Proceedings of the National Academy of Sciences, USA* than to any other journal in the index. In this journal, they account for 54% of the authorship (FC) of papers to which they contribute.

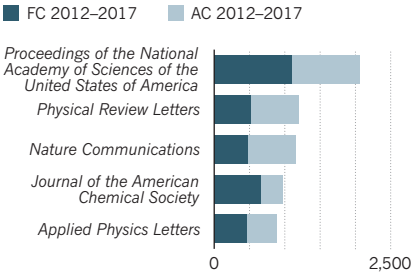

© 2018 Springer Nature Limited. All rights reserved.

CITY LINKS

The top collaborating cities in the Nature Index are located in the same country.

Leading science cities form dense networks of collaboration within their national boundaries. This graph shows the top 25 city pairs in the Nature Index, measured by their bilateral collaboration score (CS) — the sum of each city's fractional count (FC) on papers with authors from both cities in the 82 high-quality research journals tracked by the index. The partners typically contribute to an equal share of the authorship.

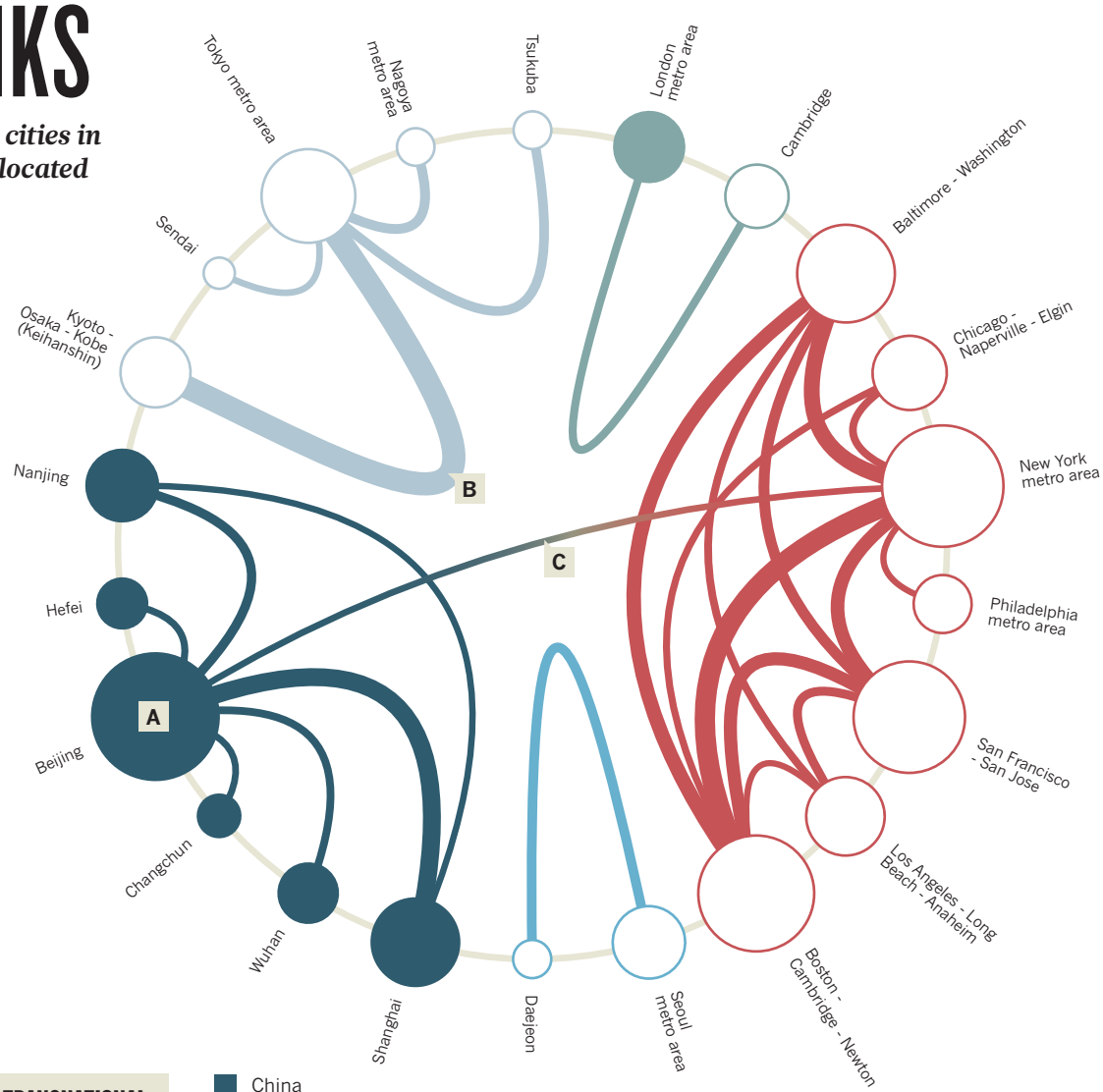

A: PEAK PERFORMER
Beijing is the top science city in the index, with an FC of 2,142.53 in 2017. Its contribution to high-quality research has grown over the past six years, as has that of many cities across China.

B: DYNAMIC DUO
Tokyo and the Keihanshin region are the top collaborators in the index, contributing to a joint CS of 442.88 in 2017.

C: TRANSNATIONAL ALLIANCE
Beijing and New York are the only global city pair in the top 25, contributing to a joint CS of 125.73 in 2017.

GLOBAL MATCH

The top five international city pairs in the Nature Index, measured by bilateral collaboration score (CS). Bars show each partner's contribution to the collaborative papers.

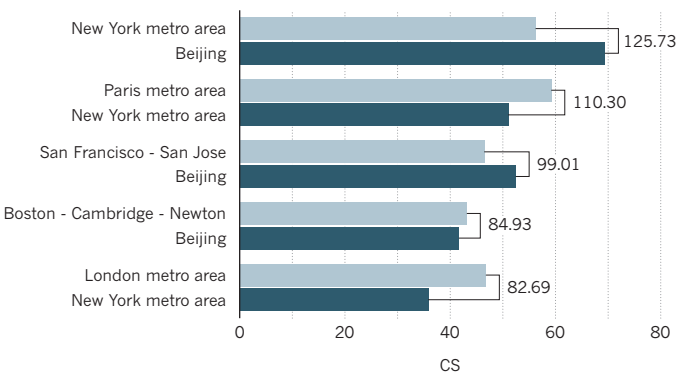

URBAN CONNECTIONS

Below are the top 10 most externally collaborative cities among the top 200 by fractional count. Some 97% of the 180 articles (AC) authored by researchers in Donostia/San Sebastián have co-authors based outside the city.

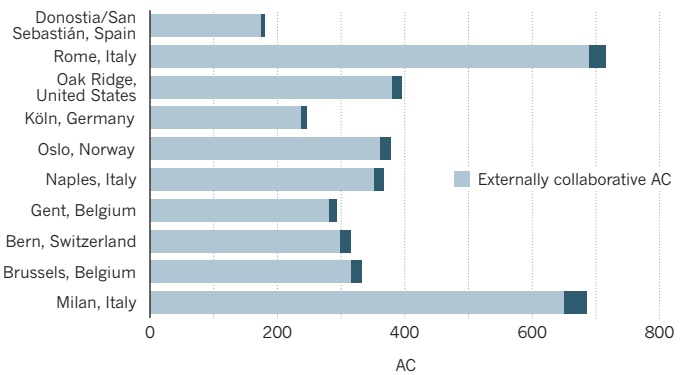

© 2018 Springer Nature Limited. All rights reserved.

Florian Röhrbein (centre) is managing director of the Neurorobotics project under the Human Brain Project at Technical University of Munich, which is developing simulated and real systems to reconstruct the human brain.

ANDREAS HEDDERGOTT / TUM

A EUROPEAN HEAVYWEIGHT

A rich research network has secured Munich's position as a centre of science in Europe.

HRISTIO BOYTCHEV

Centuries-old competition between esteemed universities for the best ideas and talent has driven continually rising standards in Munich, while their close links have fuelled a collaborative culture. Bavaria's capital, Munich is the second leading science city in Germany after Berlin, when measured on its contribution to the authorship of articles in the 82 high-quality research journals in the Nature Index, a metric known as fractional count (FC). It places sixth in Europe, behind bigger metropolises, Paris and London.

Strong institutional networks are a core strength of Munich, says Gerhard Müller, a structural mechanics engineer, and a vice president at Technical University of Munich (TUM). But this tight-knit community has recently been rocked by a series of scandals that could herald major institutional change in the long term.

With 17 higher-education institutes, Munich is second only to Berlin as the largest university centre in Germany. Standing out among them are two public universities, Ludwig Maximilians University (LMU), with an FC in 2017 of 179.41, and TUM, with an FC of 128.79.

Founded in 1472, LMU supports more than 6,000 researchers covering the breadth of social and natural sciences. TUM, its counterpart in size, was established several centuries later in 1868 and specifically focusses on the natural, life and applied sciences.

HEALTHY RIVALRY

Georg Kääb, managing director of the Bavarian biotech cluster, BioM, a consortium for the biotechnology sector in the region, says Munich maintains its standing because of the constant competition for the best ideas and talent between the two universities.

Their rivalry plays out in the annual Leibniz prizes, Germany's premier research awards bestowed by the German Research Foundation (DFG). In 2016, computer scientist Daniel Cremers from TUM received the award for advances in computer vision and reconstruction of three-dimensional objects from 2D images. A year later, biologist Karl-Peter Hopfner from LMU won the prize for his work on DNA repair and decoding the mechanism of a DNA damage sensor. And in 2018, Veit Hornung, an immunologist at the same university, was recognized for his work on clarifying how cells detect and combat viruses.

LMU and TUM were two of only three universities to be awarded additional grants in the first round of the German Universities Excellence Initiative, launched in 2006. The initiative is an effort by the German government to strengthen research universities and create internationally competitive centres. Over the past decade, LMU and TUM have received €21 million (US$24.4 million) annually through the programme. Sigmund Stintzing, a physicist and vice president at LMU, says the success of the excellence initiative has strengthened the

© 2018 Springer Nature Limited. All rights reserved.

university's commitment to the natural sciences, with plans to build a new campus that will feature a nanotechnology institute, scheduled to open in 2019.

RESEARCH CIRCUIT

The universities ensure a constant supply of well-trained students for the community of research institutes in the city — an important resource for principal investigators, says biophysicist, Petra Schwille.

Schwille is director for cellular and molecular biophysics at the Max Planck Institute of Biochemistry in Martinsried, a suburb of Munich. She is part of a team of astronomers, biologists, chemists and geoscientists from five research centres in Munich, including TUM and LMU, testing theories on the emergence of life on Earth. The group is funded by an initial four-year grant from the DFG through its €164 million Collaborative Research Centres programme to pursue long-term and innovative projects.

Schwille's institute is one of 11 located in the larger metropolitan area of Munich, which are part of the prestigious basic science organisation Max Planck Society, headquartered in the city. Also based in Munich is the Fraunhofer Society. With 72 research institutes across Germany and 25,000 employees, Fraunhofer is the largest applied science organisation in Europe.

The German Research Center for Environmental Health, and the German Aerospace Center are also in Munich. Both are part of the Helmholtz Association, yet another national research network, which specializes in infrastructure-intensive projects such as aeronautics and oceanography, and boasts almost 40,000 employees.

"MUNICH IS A NICER AND SAFER PLACE FOR PEOPLE WHO DO NOT LOOK AND SPEAK GERMAN."

ALL WELCOME

Munich is the third-most-populous city in Germany, after Berlin and Hamburg. But its national research prominence is partly due to wealth rather than size. The southern state of Bavaria has the highest GDP per capita of the 13 area-states. As such, Bavaria can afford to grant its universities a budget of €7 billion a year, more than twice the amount provided by the capital, Berlin.

Schwille also appreciates the general quality of life in the city. "The nature around Munich is fantastic and the city culture very inspiring," she says. Munich regularly ranks among the top ten cities in the world for quality of life. In the Mercer Quality of Living Survey 2018, for example, it holds third place.

The city also welcomes diversity, which gives it an edge over emerging science states. Eastern German cities, Dresden and Leipzig, for example, have recently founded the Max Planck institutes of molecular cell biology and genetics, and evolutionary anthropology. But the rise of the populist right in the east has made it more difficult for them to attract foreign students and researchers. "Compared to Dresden, Munich is definitely a much nicer and safer place for people who do not look and speak German," says Schwille. More than 15,000 foreign students are based in Munich, with some 20% of PhDs at TUM awarded to international students.

On the downside, the city is growing rapidly, and with it comes traffic and higher costs of living. Rent is especially a problem, being roughly 50% higher than in Berlin and twice as high as in Dresden.

TRIALLING TIMES

A number of high-profile research institutions in Germany have recently been shaken by scandals, including in Munich. Allegations of bullying against a director of the Max Planck Institute for Astrophysics in Garching, a town on the northern edge of Munich, surfaced this year. And in 2017, the Max Planck Institute for Psychiatry in Munich faced charges of financial fraud, plagiarism, and bullying. It is unclear whether the cases will affect Munich's good science name.

Fabian Schmidt, a cosmologist at the Max Planck Institute for Astrophysics, says that he was concerned that the allegations would taint the institute's reputation, but it is too early to determine their impact on doctoral student recruitment.

In response to the revelations, Max Planck Society commissioned an anonymous employee survey, and has hired a law firm to which scientists can anonymously bring allegations, which the firm will investigate independently.

The institute has also released a new code of conduct for professional interactions, which is a step in the right direction, says Schmidt. He acknowledges, though, that while it applies to all personnel, including directors, it is potentially not an adequate mechanism for enforcement in the event that another director is suspected of abusive conduct.

Many scientists point to the entrenched hierarchical structures in Germany's research institution as the underlying issue. The dependency between the majority of scientists with fixed-term contracts and the few permanent professorships is an ideal breeding ground for abuse, says Jule Specht, a psychologist at Humboldt University of Berlin, who has been campaigning for department structures that give scientists more independence. Professorships in Germany are typically the only long-term positions available in academia but they are relatively scarce. "The unattractive hierarchical structure makes Germany lose young scientists," she adds. ■

MUNICH

SHARE OF COUNTRY'S FRACTIONAL COUNT (FC) 2017: 10.7%

TOP 3 INSTITUTIONS (FC 2017):

1. Ludwig Maximilians University of Munich: 179.41
2. Technical University of Munich: 128.79
3. Helmholtz Zentrum München - German Research Center for Environmental Health: 28.80

TOP GERMAN CITIES

Munich is the second leading science city in Germany based on fractional count (FC).

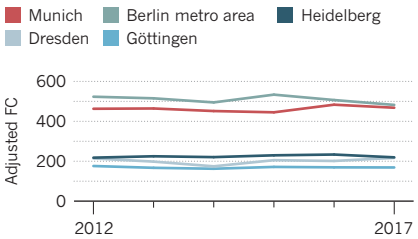

SCIENCE SECTORS

Non-governmental organisations such as the Max Planck Society are the second largest contributors to Munich's index output, measured by fractional count 2012–2017.

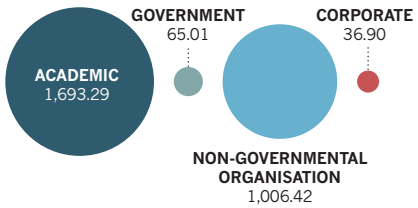

TOP FIELDS

Below are the top 6 fields that researchers in Munich contribute to in the index, measured by fractional count (FC) 2015–2017.

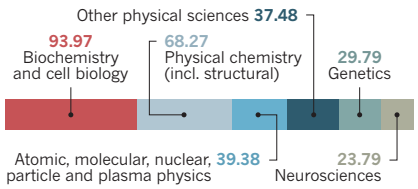

CHOICE JOURNALS

Munich-based researchers contribute more articles (AC) to *Physical Review Letters* than to any other journal in the index. In this journal, they account for 38% of the authorship (FC) of papers to which they contribute.

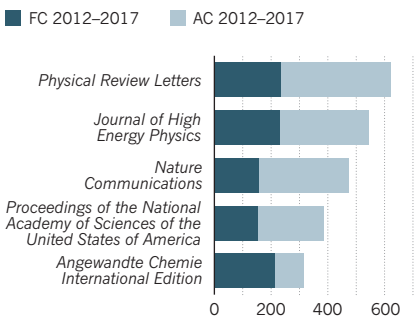

SOURCE: NATURE INDEX; SOURCE FOR 'TOP FIELDS': NATURE INDEX/DIMENSIONS FROM DIGITAL SCIENCE

© 2018 Springer Nature Limited. All rights reserved.

Researchers in Wuhan benefit from an equipment-sharing system, giving them access to a wide range of cutting-edge facilities.

STR/AFP/GETTY IMAGES

DISCOVERY CENTRAL

A hive of innovation, Wuhan has stormed up the Nature Index, but competition for talent is heating up.

HEPENG JIA

Less than a year after becoming president of Wuhan University (WU), Dou Xiankang embarked on a global recruitment drive. In October 2017, he visited New York, Boston and San Francisco, the capitals of scientific excellence in the United States. By May 2018, Dou, a space physicist, had been in Paris, Munich, Berlin and London, attending job fairs to persuade ambitious young scientists of the research promise in his city.

Wuhan is at a crossroads. If all goes well, it has long-term prospects as a leading science city in China. There is a risk, though, of a slip into obscurity as the hunt for talent heats up in the country.

In the past six years, Wuhan, a bustling city in central China, has risen in the Nature Index faster than any other city in the top 20. Its contribution to the authorship of papers in 82 high-quality research journals tracked by the index — a metric known as fractional count (FC) — has grown from 214.51 in 2012 to 490.54 in 2017, placing it nineteenth globally and fourth in China. WU is the city's top contributor to the index, with an FC in 2017 of 159.81.

The city's success has largely been driven by the recruitment of ambitious young scientists, says Zhao Rongying, a bibliometrician and senior science policy researcher at WU. Wuhan is the third most popular destination for recipients of the junior version of the central government's Thousand Talents Plan, a scheme to bring back high-achieving academics and science entrepreneurs living abroad. The city offers scientists solid research infrastructure, low living costs, prestigious positions and money to spend on their scientific interests.

But as competition for bright minds intensifies across the country, a recent ban on poaching researchers from universities in disadvantaged regions could put Wuhan under pressure. Wuhan does not have the financial might to compete with rich coastal cities such as Beijing, Shanghai, and Shenzhen. University representatives and city officials are redoubling efforts to keep the city in the limelight.

CENTRE STAGE

The capital of Hubei province, and a national hub for education and economic activity, the city's position strengthened following the

© 2018 Springer Nature Limited. All rights reserved.

establishment of the People's Republic of China in 1949. The central government set up new universities in Wuhan, expanded existing ones, and relocated coastal research institutions to avoid the threat of military attacks by the United States and then-Soviet Union during the 1950s and the 1960s.

By 2017, Wuhan hosted 84 universities — the highest number of any city in the country. Five universities had received substantial financial support under the Ministry of Education (MOE)'s Project 211, launched in 1995 to raise the standard of research at universities. Another two were selected under Project 985 launched in 1998 to establish world-class universities, including WU and Huazhong University of Science and Technology (HUST).

In 2016, research and industrial institutions in Wuhan spent 37 billion yuan (US$5.4 billion) on R&D in areas ranging from optoelectronics to materials science. This investment accounted for 3.1% of the city's GDP, ranking Wuhan as the country's fifth highest city in R&D activity, after Beijing, Shenzhen, Shanghai and Xiamen. Wuhan's R&D investment increased to 3.2% of GDP in 2017.

That same year, the government introduced an even larger scheme to raise the global standing of its universities and research disciplines, the Double First-Class project. The initiative supports 29 disciplinary programmes at universities in Wuhan, including geophysics, biology, and surveying science at WU, optical engineering, computer science and engineering thermal physics at HUST, horticultural science and zootechnics at Huazhong Agricultural University (HZAU), and geology at China University of Geosciences.

"THE COMPETITION FOR TALENTS HAS BECOME MORE SEVERE IN RECENT YEARS."

FRESH CATCH

Unable to match wealthy coastal universities in attracting established scholars, Wuhan has appealed to younger talents, says Fan Jingqun, deputy director of academic development and planning at HZAU. Between 2011 and 2017, Wuhan welcomed 262 young researchers through the Thousand Talents Plan, the third highest after Beijing and Shanghai.

Chen Shi was among the first batch of scientists to return to China under the scheme. Having spent several years as a postdoctoral researcher at Massachusetts Institute of Technology and Harvard University in Boston, Chen headed home in 2011 for a lucrative professorship in pharmaceutical sciences at WU.

Since his return, Chen and his team have published widely in the journals tracked by the index, revealing an unusual modification to the DNA backbone of some bacteria, in which oxygen is replaced with sulfur. The modification has diverse functions, including to regulate cellular metabolism, and could offer a new path to genome editing.

Young Thousand Talents scholars are widely considered to be more academically productive in China than full professors repatriated under the original version of the programme, many of whom do not work in China full-time.

A mechanism for instrument sharing among local institutions also gives researchers broad access to facilities. Chen says he often uses the advanced microscopy devices at HZAU and Wuhan Institute of Virology under the Chinese Academy of Sciences (CAS) to perform his genomic studies at low cost. Local university faculty members with promising ideas are welcome to use the CAS facilities, says Li Wei, deputy director of the CAS Wuhan Branch, which governs and coordinates seven research institutes.

His branch also hosts the biannual Xiaohongshan Interdisciplinary Forum to promote collaborations between CAS scientists and those at universities in Wuhan.

TOUGH COMPETITION

Despite Wuhan's significant progress, the city could struggle to maintain its momentum. "The competition for talents has become more severe in recent years," says Fan at HZAU. "Coastal universities are offering better research platforms and salaries."

In 2013 the MOE published a directive banning coastal universities from poaching top talents from financially strapped western and northeastern universities. In 2017, the ministry reiterated the policy, aimed at ensuring fairness in education, and committed to punishing violators. This could make universities in central China, which are not protected by the no-poaching rule, a primary target for talent hunters.

Wuhan-based universities have moved to pre-empt any losses. According to Zhou Xiong, deputy director for personnel and academic recruitment at HZAU, universities have increased the annual salaries offered to young Thousand Talents scholars and other decorated scientists in recent years to half a million yuan — equivalent to the average salary at coastal universities. This may not be enough, however, as many coastal universities are further increasing their pay.

WU recently set up a fund worth 400 million yuan specifically for hiring and providing seed money to new recruits. And in 2017, the city government announced a special fund to support university growth. It also announced tax breaks and an assurance of places in top local schools for the children of returnees.

Chen does not see Wuhan's attraction fading any time soon. "In fact, there are more and more researchers moving from Beijing and Shanghai to Wuhan too," he says. ■

WUHAN

SHARE OF COUNTRY'S FRACTIONAL COUNT (FC) 2017: 5.4%

TOP 3 INSTITUTIONS (FC 2017):

1. Wuhan University: 159.81
2. Huazhong University of Science and Technology: 113.20
3. China University of Geosciences: 47.43

TOP CHINESE CITIES

Wuhan has grown faster than the top cities in China, based on its contribution to the authorship of papers in the index (FC).

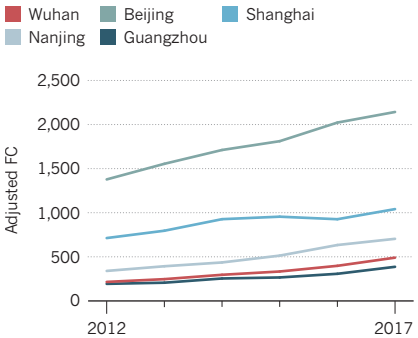

SCIENCE SECTORS

Academic institutions are the largest contributors to Wuhan's output in the index, measured by fractional count (FC) 2012–2017.

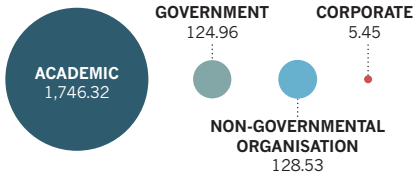

TOP FIELDS

Below are the top 6 fields that researchers in Wuhan contribute to in the index, measured by fractional count (FC) 2015–2017.

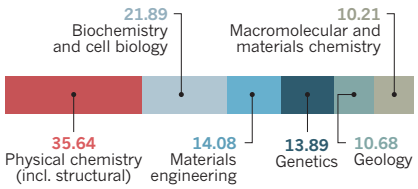

CHOICE JOURNALS

Wuhan-based researchers contribute more articles (AC) to *Chemical Communications* than to any other journal in the index. In this journal, they account for 70% of the authorship (FC) of papers to which they contribute.

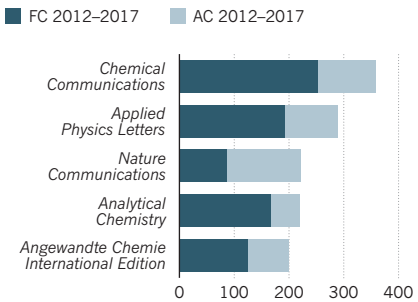

SOURCE: NATURE INDEX; SOURCE FOR 'TOP FIELDS': NATURE INDEX/DIMENSIONS FROM DIGITAL SCIENCE

© 2018 Springer Nature Limited. All rights reserved.

COMMENT
MARION MAISONOBE, LAURENT JÉGOU, AND GUILLAUME CABANAC

PERIPHERAL FORCES

The growing impact of second-tier cities is narrowing the gap in research production.

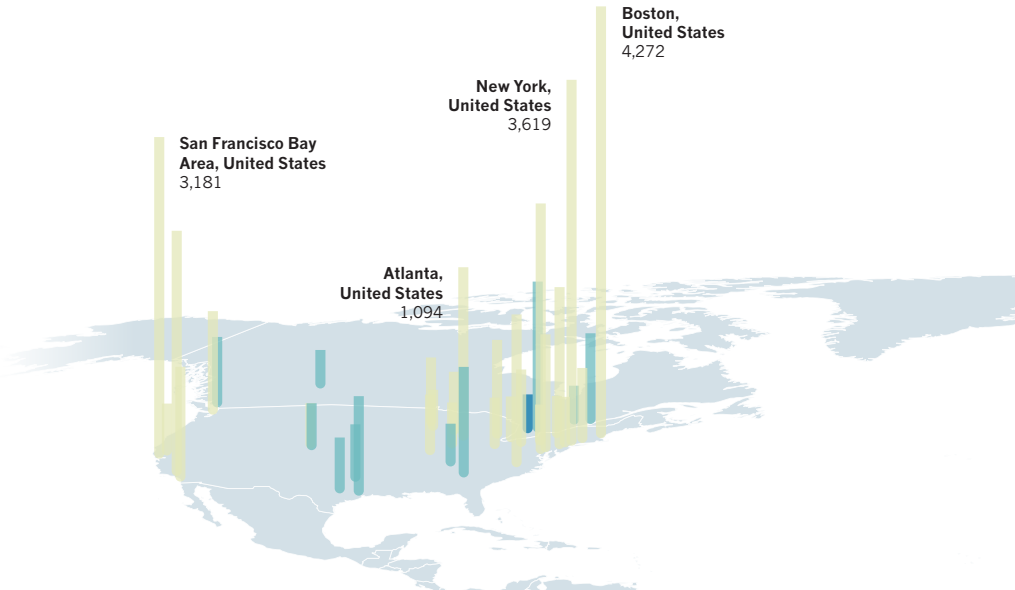

TOP-CITED CITIES

This map shows the top 100 cities based on their contribution to the top 10% of highly-cited publications in 2013 in the Web of Science database. Boston tops the ranking, publishing 4,272 highly-cited papers in 2013, followed by Beijing, New York, London and San Francisco. While many of the traditional science hotspots dominate, several newcomers are rising faster. Between 2000 and 2013, Tehran, Wuhan and Guangzhou each increased their production of highly-cited publications by more than 500%.

PHILIPPE MAISONOBE; LAURENT JÉGOU; ALEX SALIM

Scientific production is undergoing a gradual process of democratization. Over the past 50 years, a growing number of cities and countries have joined the global scientific community, and are making a significant impact. A more balanced distribution of paper citations means greater equity between researchers regardless of their location.

These changes have not gone unnoticed in traditional science hotspots, such as London, Paris and Tokyo, but those cities need not fear relinquishing their dominance in the foreseeable future. The observed spatial dispersal of knowledge production is driven by the emergence of new centres of higher education and innovation, not productivity losses at the top, and the newcomers have much ground to catch up.

We present an analysis based on 2.8 million scientific papers indexed in the Web of Science database between 1999 and 2014 that correspond to the top 10% of highly-cited research by subject, publication year, and document type (articles, reviews and letters).

Affiliations are assigned to urban areas based on fractional counting, which accounts for the number of distinct urban areas that contributed to a paper. For each observation, we used the three-year moving average of publication count.

MORE EVEN SPREAD

Our analysis has revealed a gradual shift in the global research landscape. In 2000, 3,180 urban areas in 171 countries published at least one highly-cited publication. By 2013, the number of contributing urban areas had grown by 52% to 4,841, in 190 countries.

> "A MORE BALANCED DISTRIBUTION OF PAPER CITATIONS MEANS GREATER EQUITY BETWEEN RESEARCHERS."

While most of the highly-cited research is still concentrated in a few hotspots, it is more evenly spread than a decade ago. The top 10 most impactful cities accounted for 21% of global output in 2000, but only 17% in 2013.

Countries such as China and Iran, which have made significant investments in research and development over the past decade, have seen swift growth in their share of the output. China's global share of highly-cited publications rose from 2% to 12% between 2000 and 2013, making it the second most impactful country after the United States. Iran, South Korea and Australia registered a one percentage-point increase in their share.

Within many countries, the production share of secondary cities has grown faster than those at the top. For example, Beijing's national share of highly-cited publications decreased from 22% to 19% between 2000 and 2013 and Paris's share declined from 40% to 37% during that same period. Meanwhile, those of Wuhan and Guangzhou have increased by two percentage points, and those of Marseille and Toulouse by more than 0.5.

PEOPLE PULL

An analysis of the entire publication record reveals a more level playing field. In an earlier study, we assessed 19 million documents indexed in the Web of Science database between 1999 and 2014, and found that while the top 10 publishing cities accounted for 17%

© 2018 Springer Nature Limited. All rights reserved.

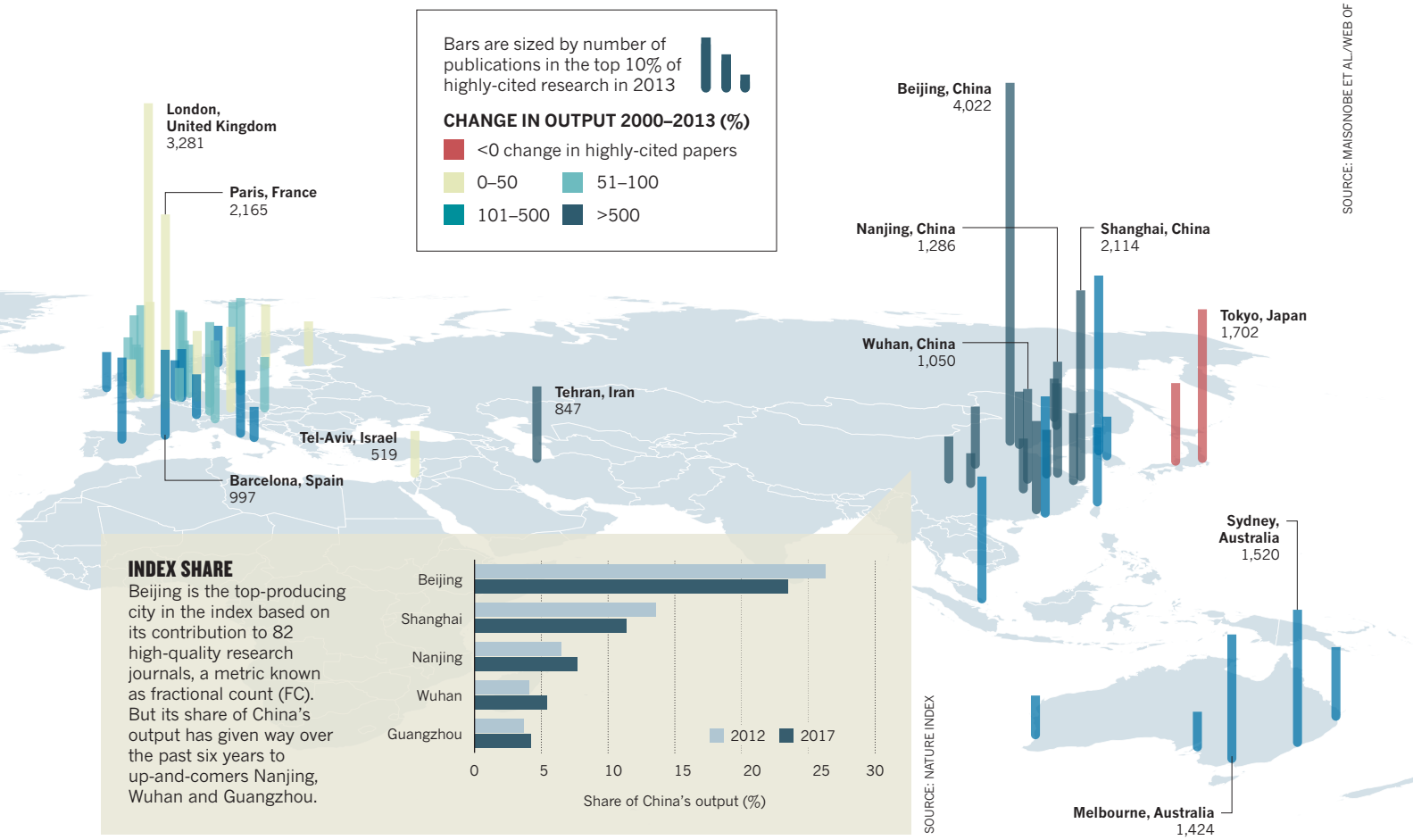

INDEX SHARE
Beijing is the top-producing city in the index based on its contribution to 82 high-quality research journals, a metric known as fractional count (FC). But its share of China's output has given way over the past six years to up-and-comers Nanjing, Wuhan and Guangzhou.

SOURCE: NATURE INDEX

SOURCE: MAISONOBE ET AL./WEB OF SCIENCE

of the world production in 2000, they produced only a 14% share in 2013.

This shift has resulted in an expanding network of scientific collaborations between cities, within and across countries and regions. The share of publications co-authored from at least two urban areas belonging to the same country has increased from 15.5% to 20%. Intra-national links have particularly increased within Latin America and Africa.

These changes stem from the creation of universities across all levels of the urban hierarchy. Whereas in the past, the researcher population was over-represented in a few megacities, it now corresponds more closely with the world's population distribution. Where there are bees, there will be honey.

REACHING THE HEIGHTS

Changes to the global science landscape have galvanized traditional science powerhouses. Facing the entrance of Beijing and Shanghai in the top 10 most productive and cited cities — together with the rise of Chinese institutions in the top university rankings — several countries have established new excellence policies.

Among others, Japan established the 21st Century Centers of Excellence programme in 2002 with an initial 18 billion yen (US$160 million), in 2005 Germany committed 4.6 billion euros (US$5.38 billion) to the Excellence Initiative to create elite universities, and France announced in 2010 the Investments for the Future programme, of which 24 billion euros would go to higher education, training and research.

These policies have strived to secure the position of traditional hotspots by concentrating research funding on their most visible institutions. By neglecting peripheral sites of scientific production, such policies could risk reverting to a less diverse and more skewed landscape, which would be detrimental to science.

The performance of a city is tightly connected to the performance of the cities it collaborates with. It is these links, particularly at the national level, that make cities strong globally. ■

Marion Maisonobe *is a geographer at Université Paris-Est.*
Laurent Jégou *is a geographer and cartographer at Université Toulouse II - Jean Jaurès.*
Guillaume Cabanac *is a computer scientist at Université Toulouse III - Paul Sabatier.*

URBAN IMPACT
This graph shows the productivity spread among cities publishing articles in the top 10% of highly-cited research. The top 30 cities published, on average, 48,700 highly-cited papers in 2013, representing a 40% increase from 2000. The relative gains were much larger among the 501–1,000 ranked cities, which published an average 12,300 highly-cited papers in 2013, up 186% from 2000.

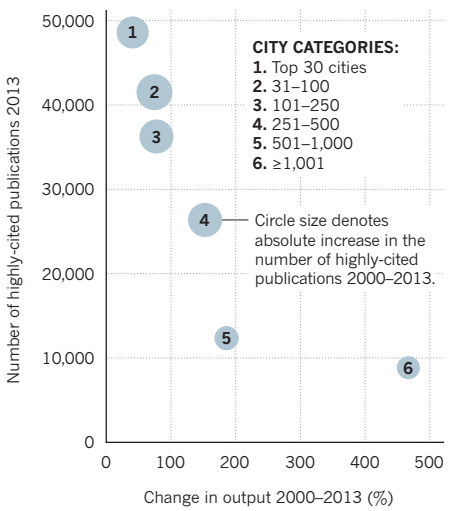

SOURCE: MAISONOBE ET AL./WEB OF SCIENCE

© 2018 Springer Nature Limited. All rights reserved.

Scientists in São Paulo protest against successive cuts to the federal science budget, at a march in October 2017.

CRIS FAGA/NURPHOTO VIA GETTY IMAGES

STANDING FIRM

São Paulo carries the scientific weight of a financially stricken country, but how much more can it endure?

HERTON ESCOBAR

Botanist Adriana Grandis thought the Amazon would be the perfect place to continue her research into how tropical trees respond to elevated levels of atmospheric carbon dioxide — if she could only get a beaker to conduct her chemistry analysis.

After completing her graduate studies on plant physiology at the University of São Paulo (USP), Grandis took up a post-doctoral fellowship at the National Institute of Amazonian Research in Manaus, a city in the middle of the rainforest.

But it took her two months just to acquire the basic glassware she needed for her project. In addition to the deep bureaucracy stalling research at public institutions in Brazil, the equipment had to come from São Paulo, some 2,700 kilometres away.

After 18 months, in June 2017, her scholarship from the Amazonas State Research Support Foundation was officially cancelled because of a lack of funds, putting an end to her fieldwork. Grandis returned to São Paulo, where she had another scholarship, and plenty of beakers, to continue her research with Marcos Buckeridge, a renowned plant physiologist at the USP Institute of Biosciences. "In São Paulo there is money, and infrastructure," says Grandis. "Everything just works better here."

São Paulo, long known as one of the hottest science and technology hubs in Latin America, has become a haven amid the economic ruin stalling scientific research throughout the country. The Ministry of Science, Technology, Innovation and Communications' budget has halved since 2014 to 4.6 billion reais (US$1.1 billion) in 2018, drastically reducing the funds available for public universities and research institutes across Brazil.

But, scientists in São Paulo have so far been spared the worst of the crisis, shielded by local state policies and a strong network of research-oriented public and private institutions. The question is, how long can the city hold?

RESEARCH REFUGE

São Paulo is the top science city in South America in the Nature Index. Its cumulative fractional count for the six years since 2012 was 473.35, a metric that accounts for the contribution of São Paulo-based authors to the 82 high-quality research journals tracked by the index. Its strengths are in the physical sciences.

The city's enormous metropolitan area, with 21 million inhabitants, hosts some of the largest and most productive universities in Brazil, including USP and São Paulo State University (UNESP). Overall, there are more than 30 institutions in the city with a strong research focus, and just as many more universities and colleges that primarily engage in education and technical training.

São Paulo is home to important research institutes, such as the Butantan Institute, a leading centre for biomedical research and

© 2018 Springer Nature Limited. All rights reserved.

vaccine production, and the National Center for Research in Energy and Materials, which is finalizing construction of the largest project in Brazilian science, a fourth-generation synchrotron light source, called Sirius.

A few hours' drive away are the National Institute for Space Research in São José dos Campos, and the Federal University of São Carlos, among others.

Some 20% of Brazilian scientists are based in the state of São Paulo. A third of the scientific articles in the index published by Brazilian researchers have at least one author from São Paulo.

Most of Brazil's economic elite is also here, with wall-to-wall high-tower offices sprawling along Paulista Avenue, an economic and political thoroughfare in the centre of town.

FIXED 1%

Connecting industry and the scientific community is what many consider to be the city's biggest asset: the São Paulo Research Foundation (FAPESP). Created in 1960, the foundation is entitled by the state Constitution to 1% of all local taxes. The funds are transferred on a monthly basis, to be reinvested in scientific research and technological innovation.

Almost every Brazilian state has an equivalent foundation, with similar funding arrangements, but not all state governments pay their dues as diligently as São Paulo's do. FAPESP is widely recognized for its administrative efficiency and scientific rigour. And because São Paulo is the richest state in the country, FAPESP is also the richest foundation of them all, with a budget in 2017 of 1.34 billion reais.

For comparison, the Research Support Foundation for the State of Rio de Janeiro (FAPERJ) is constitutionally entitled to 2% of state taxes, which should translate to an annual budget of some 550 million reais. But the state has been on the verge of economic collapse since 2016, forcing FAPERJ to freeze research grant payments and only honour scholarships.

Carlos Henrique de Brito Cruz, a physicist from the State University of Campinas, an hour's drive northwest of São Paulo, who has been scientific director at FAPESP since 2005, credits the state government for upholding its commitments to FAPESP. They know that investment in science and technology is good for economic development, he says.

"We are often accused of having FAPESP on our side," as if it represents an unfair advantage, says Sergio Novaes, a theoretical physicist at UNESP and member of the Compact Muon Solenoid Collaboration of the European Organization for Nuclear Research (CERN), in Switzerland. Scientists, academics and industry professionals won't tolerate any messing around with FAPESP, he says. It is "something we built and work hard to maintain."

Novaes has contributed to more than 130 papers in the index since 2012, alongside many other São Paulo physicists who collaborate with CERN. Their contributions included the discovery of the Higgs boson in 2012. Novaes says such long-term, high-profile international collaborations are only possible because of the funding stability provided by FAPESP and São Paulo's economic strength. FAPESP is also a member of the Giant Magellan Telescope project, a mirror telescope under construction in Chile and run by an international consortium.

The state universities "have a critical mass of scientists and students to produce good science," says Paulo Artaxo, an atmospheric pollution and climate change researcher at USP's Institute of Physics, who has contributed to close to a dozen papers in the index journals in the past three years.

Since 1996, FAPESP has been running a young investigator programme that offers four-year funding for maverick researchers to come to São Paulo and set up laboratories. Over the past two decades, the programme has supported more than 1,500 young scientists, some of whom have become very successful.

> "IT IS MUCH HARDER TO WIN MONEY NOW."

One example is Helder Nakaya, a computational systems biologist at USP's School of Pharmaceutical Sciences. He gave up an assistant professor position at Emory University in the United States to return to Brazil in 2013. The conditions for research in São Paulo are "as good as in any Ivy League school" in the US, he says.

Nakaya has led several projects on the mechanisms of vaccine-induced immunity in infectious diseases, such as malaria, schistosomiasis and the flu. One of these projects, funded by the Bill and Melinda Gates Foundation, involves using cell phone GPS data to identify hotspots for malaria transmission.

SINK OR SWIM

But scientists warn that the situation in São Paulo is not sustainable. FAPESP cannot hold together the entire state's research ecosystem on its own forever.

As funding for science collapses at the federal level, competition for state scholarships and grants increases. A retraction of the state economy over the past three years has meant that tax revenue, and the amount of money brought in through the 1% quota, is also shrinking.

"It's much harder to win money from FAPESP now than a few years ago," says Artaxo, who is concerned about São Paulo's ability to stay scientifically afloat without federal assistance. "This is bad; we can't live in isolation." ■

SÃO PAULO

SHARE OF COUNTRY'S FRACTIONAL COUNT (FC) 2017: 32.1%

TOP 3 INSTITUTIONS (FC 2017):

1. University of São Paulo: 56.65
2. São Paulo State University: 17.18
3. Federal University of ABC: 7.71

TOP BRAZILIAN CITIES

São Paulo is the top science city in Brazil, based on its contribution to the authorship of papers in the index (FC).

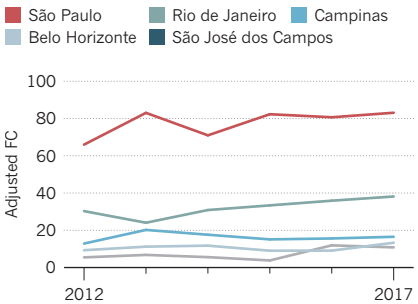

SCIENCE SECTORS

Academic institutions are the largest contributors to São Paulo's output in the index, measured by fractional count (FC) 2012–2017.

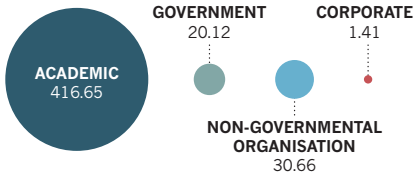

TOP FIELDS

Below are the top 6 fields that researchers in São Paulo contribute to in the index, measured by fractional count (FC) 2015–2017.

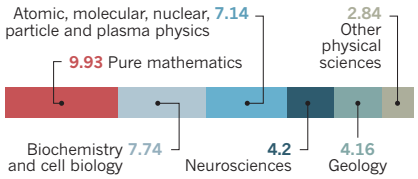

CHOICE JOURNALS

São Paulo-based researchers contribute more articles (AC) to the *Journal of High Energy Physics* than to any other index journal. In this journal, they account for 28% of the authorship (FC) of papers to which they contribute.

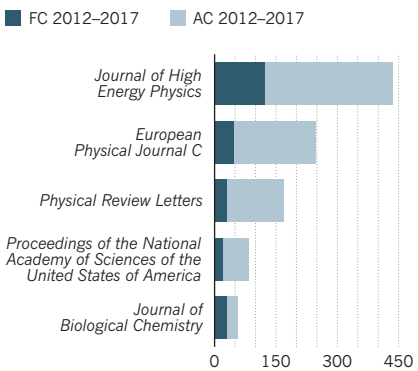

SOURCE: NATURE INDEX; SOURCE FOR 'TOP FIELDS': NATURE INDEX/DIMENSIONS FROM DIGITAL SCIENCE

© 2018 Springer Nature Limited. All rights reserved.

RUI RICARDO

Taking the silk road to high-tech growth

China's former ancient capital Xi'an has a scientific plan for development.

BY SARAH O'MEARA

When Chen Chen received word from a business incubator in Xi'an, in central China, offering to house and fund his fledgling company, the high-tech entrepreneur thought it might be a scam. He'd spent months looking for a low-cost site where he could manufacture highly efficient semiconductors for use in LEDs and lasers, and here was an empty, yet fully operational, semiconductor factory filled with equipment and people that could make his dream a reality. The message had come over the social media platform WeChat, from an investment manager working at the incubator.

Chen's invitation was the indirect result of national policies designed to bring growth to Xi'an, the capital of Shaanxi province, one of China's poorer, inland regions. In 2013, the central government had announced an ambitious vision called the Belt and Road Initiative (BRI) that would put Xi'an back at the centre of a massive trade network linking China with her landlocked neighbours to the west, as well as with a host of other nations across the three continents of Europe, Africa and Asia. The news sparked a surge of activity in local government, including a commitment to transform the city into an innovation-driven hub by 2019.

"Who would spend millions of renminbi to turn a factory into an incubator hub? Just maintaining that kind of site would be very costly," says Chen, a graduate of Tsinghua University, Beijing, who grew up in Shandong province in northern China, before moving to the United States in 2006. "I thought it was too good to be true."

Yet in January 2017, when Chen flew from his home in New Haven, Connecticut, the mechanical engineer found an optoelectronics incubator called the OEIC that was offering exactly what the investment manager had promised. Chen had what he needed to develop his business — and start making semiconductors.

Opened in 2016 by Xi'an's Institute of Optics and Precision Mechanics, the OEIC is a former manufacturing site that houses 20 start-ups developing computer chips for everything from high-end sensors to semiconductor lasers. It is the direct product of Xi'an's academic and political leaders, who hope to create a high-tech ecosystem where university researchers and private sector start-ups work side by side, echoing the model of Silicon Valley.

The site is one ambitious example of Xi'an's plans for economic growth. The city was once the most important in China, situated at the start of the Silk Road trading route, an ancient arterial network that carried Asian goods and spices to the Mediterranean and brought ▶

© 2018 Springer Nature Limited. All rights reserved.

back European wares. Since China reopened its doors to world trade in 1978, the landlocked former capital has been overshadowed by seafaring coastal economies to the east, such as the more globalized cities of Shanghai and Beijing.

EXPANDING FAST

The BRI is an economic action plan to strengthen trading and cultural relationships between China and countries in Asia, Africa and Europe. It has become increasingly hard to define, according to Dirk van der Kley, who is based in Sydney and researches Chinese foreign policy at the Australian National University in Canberra. "There is a real sense of mission creep," he says. "Infrastructure funding and investment in enterprise are being used to further the Chinese Communist Party's agenda to increase the country's social and cultural influence in these regions."

In Xi'an, the government is offering financial incentives for companies to start businesses in countries associated with the BRI.

"Thanks to investment from China, the intercity roads in Kyrgyzstan are often as good as in Australia between cities," says Van der Kley. "But there are the downsides. Some countries have taken on huge debts. Many Chinese companies, particularly inexperienced ones, run into trouble. They struggle with local culture and politics. Local hiring is also tricky. It varies by company and country. Initially, many companies do not hire many locals. But if they stay for a long period, companies do tend to localize their workforce."

Aside from that, levels of Chinese investment in BRI projects have been exaggerated, according to research by the Berlin-based Mercator Institute for China Studies (MERICS).

"Investors and commercial banks are aware of the difficulties of investing in some of the countries along the Belt and Road. In 2017, Chinese firms invested just US$14 billion across 70 countries, which is pretty small fry," says Van der Kley. "If you look in most parts of southeast Asia for example, China is not the leading investor. It's the US or Japan. In some cases Singapore, which is a re-routing point for Chinese investment in southeast Asia, is the leading investor. But even so, China is not as dominant as is sometimes portrayed."

Yet Xi'an's leaders remain optimistic. Fang Guanghua, deputy mayor of the Xi'an Municipal People's Government, says that the city is "indisputably standing at the forefront of opening up to the West in a new era, since the launching of the Belt and Road Initiative."

Rather than transporting silk across central Asia to the Mediterranean sea, the city's officials are focused on expanding industries in the city that are competitive and driven by advanced science; these include the aerospace industry, and those dedicated to new materials, energy, artificial intelligence, and intelligent manufacturing systems that can operate with less human intervention. And that's where the OEIC incubator comes in.

> "XI'AN IS INDISPUTABLY STANDING AT THE **FOREFRONT** OF OPENING UP TO THE WEST IN A **NEW ERA.**"

"I think it will take around five years for the city to establish itself as an innovative hub. Xi'an has the fundamentals, such as strong universities. New business is booming and lots of scientists are already coming to the city," says Chen.

Xi'an is no stranger to advanced manufacturing, especially in aviation and military technology. Since 1949, when the People's Republic of China was founded, the city has been a designated national base for the country's military industry, thanks to its strategic location on the western edge of the heavily populated east-coast region. The city is home to companies that research weaponry, ships and nuclear technology; it also has 63 universities and 3,000 commercial, state and military-research units.

Despite its longstanding technological advantages, Xi'an has struggled to keep up with the rapid economic development of other cities. In 2016, Shaanxi province ranked 15th out of 32 provinces in terms of its gross regional product, according to China's National Bureau of Statistics.

For a decade, Mi Lei, an engineer at Xi'an's Institute of Optics and Precision Mechanics was frustrated by the lack of development. "No private investors were interested in advanced research projects like mine," he says. "They preferred to invest in Internet companies that make money fast."

In 2000, he began lobbying the city's government for money to establish an 'angel' fund that would support the industrialization of what he calls hard-core technologies. These, he explains, are based on "research that needs long-term investment because it is difficult to be replicated or imitated, as it has an extremely high technical threshold". As examples, he cites photoelectric chips, alternative forms of energy generation, intelligent manufacturing, information technology, life science and artificial intelligence, and new materials.

Before the city reached a decision, Lei decided to start investing himself, and one of his first bets was in Vivo Light. Run by a former colleague, the company makes machines that can identify the location of blood vessels with high levels of accuracy.

"In 2012, my daughter was given an injection, but the nurse failed several times to find the vein. I wanted to work with a team who could solve this problem. Now we've sold these machines to hospitals in China, South America and Japan," says Lei, who was involved as a researcher at an early stage.

In 2013, Lei heard back from the government, which had decided to grant his wish, and set up CAS Star, an independently run incubator for start-ups; it's funded by local municipal and education funding bodies.

Five years later, CAS Star has 260 full-time employees, up from 7; they include 45 investment staff and a 6-person legal team, as well as scientists and engineers who assist with research, and develop and acquire new lab equipment. The fund has already invested in more than 230 companies and received

THREE YEARS *How to build a high-tech silk road*

May 2015
Xi'an Jiaotong University forms the University Alliance of the New Silk Road, with nearly 100 universities from 22 countries and regions.

June 2016
Xi'an government says the city will be an innovation centre for the Belt and Road Initiative (BRI) within three years.

January 2017
Financial incentives included in the city's five-year plan encourage Chinese enterprises to work in BRI countries.

January 2017
Xi'an congress calls the city a "Silk Road science and technology centre".

May 2017
Announcement of BRI recruitment strategy.

August 2017
Announcement of Free Trade Zone in and around Xi'an to support BRI.

March 2018
Individuals who recruit talent to Xi'an can receive rewards of up to 1 million yuan (US$140,000).

© 2018 Springer Nature Limited. All rights reserved.

An intelligent robot patrols a project site in Xi'an.

GETTY/VCG

praise from China's president Xi Jinping and premier Li Keqiang.

In 2016, Lei's team joined with several government and university departments to set up the OEIC, where Chen has his team. Lei's idea for hard-core technologies forms the core of the Xi'an government's vision for its science and technology development — and his incubator is just one of multiple plans, such as the construction of a Xi'an Science Park and a Silk Road Science and Technology Centre, to seize the momentum offered by the BRI.

Li Xining, director of the Xi'an Municipal Science and Technology Bureau, says that Xi'an could catch up and even surpass other cities in China. However, he acknowledges that there will be challenges. "We need to break down ideological barriers that restrict innovation, and encourage people to aim for scientific breakthroughs," he says. "We also need to promote the application of research and industrialization of innovation." And he argues that scientists' salary levels should be based on merit, rather than on the "irrational income distribution and defective incentive mechanisms" of the current system.

NEW RECRUITS

Yuanyuan Ma, a nanoscientist who researches energy-efficient catalysts that can be used in treating water pollution, came to Xi'an after completing her PhD at the University of California, Davis. She has worked there for six years at a multidisciplinary research centre called Frontier Institute of Science and Technology. Ma says that despite the city's large pool of universities, graduate talent regularly disappears because the government has not developed sustainable policies for creating high-quality jobs in research and development (R&D).

"It has concentrated on luring overseas talent with high salaries rather than promoting native talent. If a city cannot provide a positive platform for people's talents, they won't stay," she says. "I do think things are changing now, though."

In 2017, under the leadership of Wang Yongkang, Xi'an's newly appointed party secretary, the municipal government issued a series of policy initiatives. These rubber-stamped the city's rebranding as a Silk Road science-and-technology centre and approved 23 new recruitment policies, with a funding pledge of 3.8 billion yuan ($600 million), designed to attract 1,000,000 graduates to the city within the next 5 years — the majority of whom will be Chinese and already living in China.

"If you want to settle down in Xi'an, you may submit an application on your smartphone within 30 minutes to register as a resident," says Fang about one of the new policies launched in March, which makes it much easier to register as a citizen of Xi'an from elsewhere in China.

Cao Junji, director of the Institute of Earth Environment in Xi'an, says that a change in research trends is also making it easier to attract talent. Last year, Cao's group finished building the world's largest air purifier, and his work is increasingly attractive to students, he says.

"In the past, it was hard to attract talent to work in this area. Now, we have lots of young talent because caring about the environment matters to younger people. And we can offer high salaries, as solving China's air pollution problem is a key political priority, so we have plenty of funding," says Cao.

China lacks high-quality Earth-science courses, says Cao, and so he is obliged to send many of his undergraduate students to study in the United States. But he says that Xi'an is beginning to take an academic lead and forge partnerships with its historic Silk Road neighbours, as part of the BRI.

For example, in May this year, Cao's institute hosted its first Belt and Road Climate Change Training Course. Its stated aims were to improve the research capabilities of young scholars, promote cooperation and strengthen technology in China, and in countries such as Thailand along the 'Belt and Road'.

According to Fang, Xi'an is also active in starting businesses in central Asian countries, such as Kyrgyzstan. And Xining says that the presence of overseas firms in the city plays an important part in promoting the scientific and technological progress of the city. "It accelerates the overall upgrading of industry," he says.

Many large international enterprises, such as Samsung Electronics, Bosch and Intel have already set up their R&D centres in Xi'an, and Li hopes to attract more. The city's officials want it to become a global centre for cutting-edge technology by 2025, they announced in late 2017. Just a few months later, in January 2018, Internet giant Alibaba unveiled a plan to build its regional headquarters in the city.

"Tell me which companies we should ask to partner with us," Li says with a smile. "International cooperation is an important part if a city wants to become an international metropolis, no matter whether it's past history or the present." ■

Sarah O'Meara *is a writer and editor based in London.*

© 2018 Springer Nature Limited. All rights reserved.

DAVID PARKINS

How neuroscience is breaking out of the lab

Nervous-system scientists share how they're working in a variety of settings.

BY NIC FLEMING

Concerns that neuroscience's rise in popularity as a PhD subject has not been matched by a proportional growth in academic positions, coupled with a recent scaling back of brain-science research by many pharmaceutical companies, has led to worries that researchers will be forced to leave the field.

But neuroscience is opening doors in a broad range of alternative settings. *Nature* spoke to five neuroscientists putting their discipline to work to find satisfaction and impact in their careers.

KRIS DE MEYER
The film-maker

Postdoctoral research associate, King's College London.

The world did not end on 21 October 2011. It carried on spinning despite US Christian radio host Harold Camping persuading large numbers of people that once God had finished gathering his chosen few into heaven, everyone else would be destroyed in a fury of earthquakes, tsunamis and fire.

Some of Camping's followers prepared for the end by leaving their jobs and selling their homes. A handful of them feature in the 2016 documentary *Right Between Your Ears*, co-produced by neuroscientist Kris De Meyer, based at King's College London. The film highlights neuroscience research into how we form opinions and change or refuse to change our minds.

© 2018 Springer Nature Limited. All rights reserved.

Why a film? "Had we done a purely scientific study, it would have been published in a specialist journal with limited readership," says De Meyer. "As a story and film that brings out the science, it has brought useful scientific insights to hundreds of thousands of people to date."

Since 2013, De Meyer has been helping scientists, especially those concerned with climate change and the environment, to use insights from the brain sciences to improve the way that they communicate. "If you understand better why part of your audience rejects what you are saying, you might be able to compensate for that and find more constructive ways of getting your message across," he says.

De Meyer has also been working on projects that build neuroscience and psychology into immersive theatre. He is especially excited about the Justice Syndicate, in which audience members play the parts of jurors. The play helps the audience to gain insight into how people presented with the same evidence reach different conclusions.

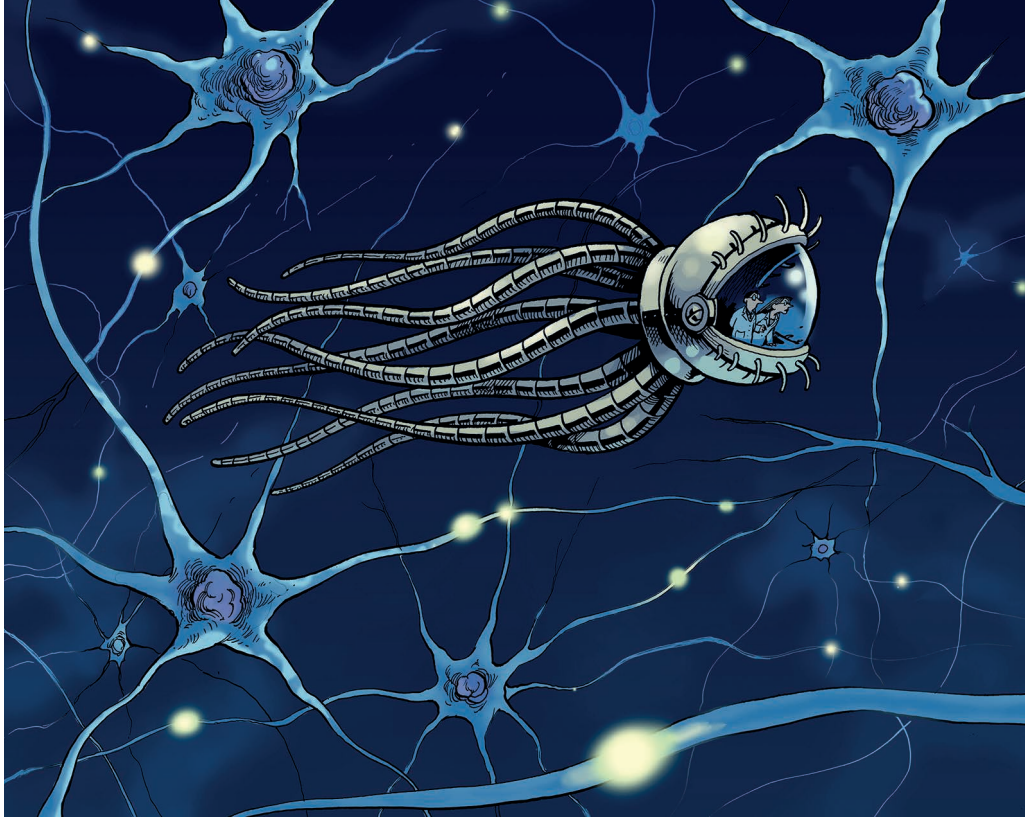

DAVID PARKINS

TARA SWART
The leadership coach

Public speaker, lecturer and author based in London.

Tara Swart couldn't disagree more with those who are pessimistic about the prospects of early-career neuroscientists. Swart, a leadership coach, public speaker, lecturer and author, thinks that brain science offers important insights into how people can develop the mental resilience needed to thrive in our rapidly-changing world. As a result, she says, there is great demand for those with expertise in the field in a wide range of business settings. "Doing a neuroscience PhD can set you up to do pretty much anything you want these days," says Swart, who is based in London. "It's hot property."

Swart originally studied medicine, before completing a PhD in neuropharmacology and working as a psychiatrist for seven years. She moved into leadership coaching a decade ago, after she noticed a "demand for rigorous but applicable neuroscience in the business and leadership context".

Neuroscience's not-so-secret weapon, according to Swart, is neuroplasticity — the ability of the brain to form or reorganize networks of connections between brain cells. The disrupted, information-rich, 24-hour environment in which many businesses operate can put its leaders under immense stress. Swart provides executives and managers with neuroscience-based insights, which she says can improve their ability to adapt to change and motivate their staff, for example. "Building mental resilience is probably the biggest part of my work," she says. "That's where neuroplasticity really comes in, because to build emotional intelligence or mental resilience you have to change pathways in your brain."

Swart uses a range of neuroscience research in her talks and coaching sessions. When discussing nutrition, she describes a study (M. E. Raichle & D. A. Gusnard *Proc. Natl Acad. Sci. USA* **99**, 10237–10239; 2002) showing that the brain uses 20% of calories consumed, and another that found that judges who have recently eaten are significantly more likely to rule in favour of prisoners in parole hearings than those who haven't (S. Danziger *et al. Proc. Natl Acad. Sci. USA* **108**, 6889–6892; 2011).

Swart also highlights research that describes how US marines doing stressful combat training showed fewer physiological markers of stress if they had previously attended mindfulness classes (D. C. Johnson *et al. Am. J. Psychiatry* **171**, 844–853; 2014). She tells her audiences to find forms of exercise that they enjoy, saying research shows that rats that voluntarily use a treadmill produce more of a protein that helps support brain-cell growth and survival, called brain-derived neurotrophic factor, than animals forced to do so. "I see myself as a translator of academic neuroscience to business," she says.

ORI AMIR
The comedian

Visiting assistant professor, Pomona College, Claremont, California.

If you ever go to an improvised comedy class, you may well be told to 'get out of your head'. This is not an invitation to take recreational drugs. Rather, it's the idea that setting aside your ego-driven concerns and tuning into your emotions might make you funnier.

Ori Amir, a neuroscientist and amateur stand-up comedian, has shown that this advice has at least some basis in science. He asked 13 professional comedians, 9 amateurs and 18 non-comedians to come up with both funny and non-funny captions for cartoons while undergoing brain scans in a functional magnetic resonance imaging machine.

"Generating funny ideas involves pretty much everything the brain can do."

Amir's study (O. Amir & I. Biederman *Front. Hum. Neurosci.* **10**, 597; 2016), which was part of his PhD on perceptual pleasure, was the first to explore brain activity during real-time humour creation. Amir showed that while trying to be funny, volunteers had increased activity in the medial pre-frontal cortex (mPFC) and some high-level semantic regions in the temporal lobes, where information converges from lower-level brain regions.

Amir concluded that the temporal regions are the origin of funny ideas because activation there was greater for more-experienced comedians and during the generation of funnier jokes — as rated by a separate group of volunteers. "It looks like 'getting out of your head' when doing improv works," he says. "The neuroscience translation is 'try to reduce the top-down control of the mPFC and trust that the stream of associations in the temporal regions will lead to funny ideas.'" Other research has shown this can be done through meditation.

Amir is now investigating the use of artificial intelligence (AI) to model comedy generation. He is not worried that his efforts to make computers funny will put his comedian friends out of work. "I think comedy generation is

© 2018 Springer Nature Limited. All rights reserved.

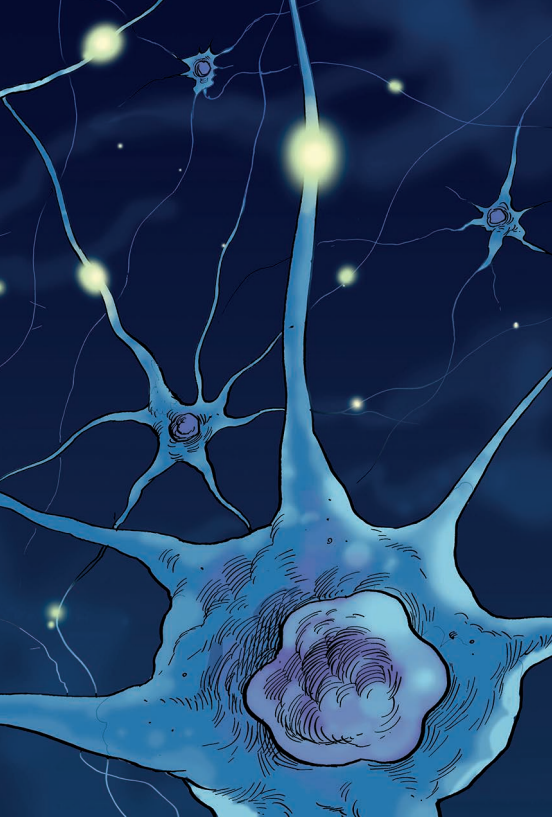

an AI-complete problem," he says. "In other words, generating funny ideas involves pretty much everything the brain can do. So comedians are unlikely to be replaced by AI, at least until almost every other profession has been replaced by it."

RITA BALICE-GORDON
The pharmacist

Global head, neuroscience, Sanofi, Boston, Massachusetts.

Drugs giant Pfizer's announcement in January that it was pulling out of neuroscience research and development (R&D) was just the latest instalment in a string of similar bad news for brain scientists hoping to work in the pharmaceutical industry. GSK, AstraZeneca, Novartis and Merck have all either closed neuroscience divisions or scaled back their brain-science research since 2010. Many saw these moves as adding to the sense that the field had over-promised and under-delivered when it came to real-world impact and application.

Yet, Rita Balice-Gordon, head of neuroscience at French pharmaceutical company Sanofi, says that such reports present only a partial picture. "Big pharma might not be all in when it comes to neuroscience, but when looked at in terms of the broader biopharma ecosystem, the field has never been more vibrant," she says. "We have a number of promising internal programmes, and, like other companies, we also have a number of exciting partnerships with biotech companies and start-ups, which together give me tremendous hope for the future."

Several announcements in the past few years suggest that she may be right. Many pharmaceutical companies are hedging their bets by restructuring their neuroscience research divisions rather than axing them entirely. Others, in step with a more general shift in the industry, are diversifying their risk by outsourcing R&D to academic labs and small biotech firms. In January, for instance, Takeda Pharmaceuticals agreed a deal worth up to US$1.2 billion with Denali Therapeutics, in San Francisco, to collaborate on three neurodegenerative disease programmes, and Johnson & Johnson unveiled four neuroscience collaborations with both academic and private-sector labs. In June, Pfizer revealed plans to invest $150 million in start-ups seeking new brain-disorder treatments.

Balice-Gordon discovered a passion for understanding how environmental cues shape brain circuitry, and how this affects behaviour, as an undergraduate at Northwestern University in Evanston, Illinois. She then spent almost 20 years at the University of Pennsylvania, Philadelphia, before becoming an enthusiastic convert to industry. She was recruited by Pfizer to lead its psychiatry and pain drug-development programmes in 2012. "I love working in the translational space between the lab and the clinic," she says. "I think that is where the real advances in neuroscience therapeutics are going to come from."

She has been with Sanofi since 2016. Balice-Gordon thinks many academics would be surprised at the similarities between doing research in universities and at drug companies. "There is a perception that in biopharma we don't ask a lot of science questions, but I think in early drug discovery, most academics would not find the focus very different. The key difference is that it requires a focus on the crucial questions from the point of view of patients, rather than exploring all possible questions."

To fellow neuroscientists interested in following in her footsteps, Balice-Gordon advises taking time to gain not just deep expertise but also broad knowledge, and says that the importance of networking cannot be overstated.

BENNY HOCHNER
The soft-body specialist

Professor of Neurobiology, Hebrew University of Jerusalem, Israel.

Before 1995, neuroscientist Benny Hochner was mainly interested in the mechanisms underlying learning and memory, something he studied in sea slugs with Eric Kandel, who later won a Nobel Prize in Physiology or Medicine, at Columbia University in New York. Then, Hochner was granted funding from the US Navy, which wanted to find out whether the mechanisms through which octopuses control their bodies could be replicated in soft-bodied military robots. This, it was hoped, could be useful for tasks such as surveillance, and search and rescue in complex terrains. He also received support from the US Defense Advanced Research Projects Agency.

Hochner began by trying to understand how the nervous systems of octopuses cope with the much greater flexibility their soft bodies afford them compared with animals that are constrained by skeletons. "Octopuses have an almost infinitely large degree of freedom of movement," he says. "Finding a way to efficiently control that is a huge problem, both for a nervous system and for a computer system."

"Octopuses have an almost infinitely large degree of freedom of movement."

Hochner, who is now at the Hebrew University of Jerusalem, showed that reaching movements could be triggered in severed octopus arms using electrical stimulation. He found that some often-repeated octopus movements can be independently controlled by neural circuitry in the arm, freeing the brain to focus on other tasks (G. Sumbre *et al. Science* **293**, 1845–1848; 2001).

He has also investigated how octopus brains represent and plan for almost limitless freedom of movement. By stimulating electrodes implanted into the brains of octopuses that were then filmed moving freely, Hochner's group found it was not possible to trigger movement in single arms or body parts. Unlike the brains of skeletal animals such as humans, Hochner found, the octopus brain does not contain specific parts that deal with sensory and motor information from individual body parts (L. Zullo *et al. Curr. Biol.* **19**, 1632–1636; 2009).

Hochner has described octopus movement and its evolution as examples of 'intelligent embodiment', a phrase used by roboticists to describe autonomous machines that learn behaviour through interacting with their environment.

His group has now returned to studying Hochner's original interest of memory and learning. Long-term synaptic potentiation, a process whereby synapses are strengthened through greater activity, is thought to have key roles in mammalian learning and memory. Hochner's group has shown it plays the same part in octopuses, suggesting the mechanism has evolved separately in parallel. He also found that, as in mammals, octopus brains have different systems for dealing with short- and long-term memories. ■

Nic Fleming *is a freelance science writer based in Bristol, UK.*

© 2018 Springer Nature Limited. All rights reserved.